FLUID COUPLING AND RESPONSE CHARACTERISTICS OF CYLINDER CLUSTERS IN AXIAL FLOW

by

Jean O. Gagnon
Department of Mechanical Engineering
McGill University, Montreal

July 1989

VOLUME 1: TEXT

A Thesis submitted to the Faculty of Graduate Studies and Research in partial fulfillment of the requirements for the Degree of Doctor of Philosophy

© Jean O. Gagnon 1989

National Library of Canada
Bibliothèque nationale du Canada

Canadian Theses Service
Service des thèses canadiennes

Ottawa, Canada
K1A 0N4

The author has granted an irrevocable non-exclusive licence allowing the National Library of Canada to reproduce, loan, distribute or sell copies of his/her thesis by any means and in any form or format, making this thesis available to interested persons.

L'auteur a accordé une licence irrévocable et non exclusive permettant à la Bibliothèque nationale du Canada de reproduire, prêter, distribuer ou vendre des copies de sa thèse de quelque manière et sous quelque forme que ce soit pour mettre des exemplaires de cette thèse à la disposition des personnes intéressées.

The author retains ownership of the copyright in his/her thesis. Neither the thesis nor substantial extracts from it may be printed or otherwise reproduced without his/her permission.

L'auteur conserve la propriété du droit d'auteur qui protège sa thèse. Ni la thèse ni des extraits substantiels de celle-ci ne doivent être imprimés ou autrement reproduits sans son autorisation.

ISBN 0-315-57222-1

Canada

Abstract

This Thesis examines the experimental and theoretical lateral vibration characteristics of flexible (rubber) cylinder clusters, subjected to axial incompressible (water) flow, within a rigid circular containment channel. The cylinders, some of which were instrumented with embedded strain gages, were clamped at both their upstream and downstream ends, to streamlined rigid fin assemblies.

The theory is a random vibration model, with cylinder deflections based on natural beam mode summation, and response dependent on both the effects of the mean flow along the cylinders, and of turbulent boundary layer pressure fluctuations.

Various bundles with different numbers of cylinders, as well as with combinations of flexible and rigid cylinders, were investigated, both experimentally and theoretically. It is shown that the theory is in excellent qualitative agreement with experiments, in terms of power spectral densities, and coherences and phases between cylinders; nevertheless, predicted amplitude levels are one order of magnitude higher than those measured.

Sommaire

Cette Thèse traite des vibrations latérales de faisceaux de cylindres (en caoutchouc) flexibles, soumis à l'écoulement longitudinal d'un fluide (eau) incompressible, à l'intérieur d'un conduit circulaire rigide. Les cylindres, dont certains étaient munis de jauges d'élongation implantées, étaient fixés aux deux extrémités (amont et aval), à un assemblage rigide d'ailettes profilées.

La théorie est un modèle d'oscillations aléatoires, avec les déflections des cylindres basées sur une sommation des modes propres d'une poutre, la réponse étant fonction des effets de l'écoulement moyen le long des cylindres, ainsi que des fluctuations de pression dans la couche limite de l'écoulement turbulent.

Divers faisceaux, ayant différents nombres de cylindres ainsi qu'un nombre de combinaisons de cylindres flexibles et rigides, furent analysés, aussi bien expérimentalement que théoriquement. Il est démontré ici que la théorie est en accord qualitatif excellent avec les essais expérimentaux, en terme de densités spectrales de puissance, et des cohérences et phases entre cylindres; néanmoins, les niveaux prédits des amplitudes sont d'un ordre de grandeur plus élevés que ceux qui ont été mesurés.

Preface

The dynamics of cylinder bundles subjected to axial flow, differs from that of isolated cylinders basically for one of two reasons: (i) dependence of excitation pressure field characteristics on the geometry of the systems, and possibly on the very motion of those systems, and (ii) existence of inter-cylinder fluid coupling, implying that the motion of cylinders in a bundle is inter-dependent.

The main objective of this research work was to investigate item (ii) above, based on random vibration theory, that is in terms of averaged frequency domain quantities (power- and cross-spectral densities). Of course, the latter (CSD's) include phase information, which allows measurement of (rms) motion of a given cylinder with respect to another in the cluster, i.e. the study of fluid coupling.

The original contributions of this Thesis, to new knowledge in the field, are as follows.

(1) Extensive experimental data on random vibration of flexible cylinders in axial flow, designed to provide a critical assessment of the latest theoretical model in the field, and also constituting a data bank for possible later evaluation of alternative theories.

(2) Design of special tests and extension of the current theoretical model, to allow in depth investigation of the dynamics of fluid coupling; this involves the use of combination of flexible and rigid cylinders, for the first time to the author's knowledge.

(3) The development of a new method to derive differential pressures, from the (simpler) measurement of single point pressures and their corresponding coherence function. This method also relaxes requirements for the matching of pressure transducer gains, when direct differential measurements are impractical. This technique was used to measure in situ some of the pressure characteristics of the test channel.

The large volume of data, together with relatively lengthy text and appendices, made the use of a second volume desirable. An unusual format has been chosen for material presentation, to facilitate reference to figures: all text, including appendices, has been bound in volume 1, and all figures grouped separately, in volume 2.

Acknowledgments

The author wishes to thank Professor M.P. Paidoussis for guidance, and for financial support through les Fonds pour la formation de Chercheurs et l'Aide à la Recherche du Québec (FCAR) and the Natural Sciences and Engineering Research Council of Canada.

Likewise, sincere thanks are forwarded to Mr. Josef Dubik for various mechanical tasks related to the experimental programme, and Messrs. George Dedic and George Tewfik for technical support in the area of instrumentation. Furthermore, I am indebted to Prof. A. Misra, for access to his computer, which proved very helpful for completing the word processing of this Thesis.

Special thanks are due to my wife Sally, for constant support during the course of this work, as well as for proofreading the text.

Finally, I wish to make special mention of two of my colleagues, namely: Mr. L.R. Curling for discussions on various theoretical aspects, especially random vibrations, inclusive of his own work in the field, and Mr. Bill Mark, whose knowledge in hardware and software was often instrumental in finding prompt solutions to computer related problems.

Table of Contents

Volume 1

Volume 2

Terminology

a_1, a_2, a_3 Constants (-) [see eqn.(2.240)].

a_k Lumping parameters (-) [see eqn.(2.64)].

a_{sq} Integration constant, natural beam modes (-) [see eqn.(2.85)].

a Index function (-) [see eqn.(2.162)].

b Constant (-) [see eqn.(2.213)].

b_1, b_2, b_3 Constants (-) [see eqs.(2.255) and (2.256)].

b_k Lumping parameters (-) [see eqn.(2.65)].

b_{sq} Integration constant, natural beam modes (-) [see eqn.(2.85)].

b Index function (-) [see eqn.(2.162)].

c Constant (-) [see eqn.(2.213)].

c Coefficient, drag ("linearized"), cylinder(s) (-) [see eqn.(2.52)].

c_1, c_2 Constants (-) [see eqs.(2.255) and (2.256)].

c_{b_0} Coefficient, base drag, reference cylinder (-) [see eqn.(2.52)].

c_f Coefficient of friction, longitudinal flow (-) [see eqn.(2.52)].

c_k Lumping parameters (-) [see eqn.(2.66)].

c_{sq} Integration constant, natural beam modes (-) [see eqn.(2.85)].

d Constant (-) [see eqn.(2.213)].

d_r Frequencies, modal, imaginary part (rad/s) [see eqn.(2.21)].

d_{sq} Integration constant, natural beam modes (-) [see eqn.(2.85)].

d_r Frequencies, modal, imaginary parts (-) [see eqn.(2.98)].

e_{ki} Coefficients, virtual mass, i^{th} direction, cylinder k (-) [see eqn.(2.27)].

f_1 Frequency, fundamental, real part (rad/s) [see eqn.(2.22)].

f_r Frequencies, modal, real part (rad/s) [see eqn.(2.21)].

f_r Frequencies, modal, real part (-) [see eqn.(2.98)].

g Acceleration due to gravity (m/s^2).

$g_{d_i d_j}$ Transfer function factor, response to pressure excitation (-) [see eqn.(2.271)].

g_{ki} Coefficients, virtual viscosity, i^{th} direction, cylinder k (-) [see eqn.(2.29)].

h Diameter ratio (-) [see eqn.(2.52)].

h_{ab} Components, impulse response function (-) [see eqn.(2.170)].

k Index, usually denotes the k^{th} cylinder (-).

k_{ki} Coefficients, virtual mass, i^{th} direction, cylinder k {-} [see eqn.(2.28)].

l_M Lateral distance, minimum, cylinder pair {m} [see eqn.(2.242)].

m Mass per unit length, individual cylinder {Kgm/m}.

m_0 Mass per unit length, reference cylinder {Kgm/m}.

m_k Mass per unit length, cylinder k {Kgm/m}.

p Pressure, fluid {KPa}.

$\overline{p}$ Pressure, average static {KPa} [see eqn.(2.15)].

p_a Pressure, acoustic {KPa} [see eqn.(2.276)].

p_d Pressure, differential {KPa} [see eqn.(2.278)].

p_{d_M} Pressure, differential, measured {KPa} [see eqn.(2.281)].

p_i Pressure, fluid, cylinder i {KPa} [see eqn.(2.195)].

p_i Pressure, fluid, cylinder i {-} [see eqn.(2.195)].

p_{A_n} Pressure, acceleration induced {KPa} [see eqn.(2.276)].

p_{c_n} Pressure, coherent {KPa} [see eqn.(2.286)].

p_{M_n} Pressure, measured {KPa} [see eqn.(2.276)].

p_S Pressure, static {KPa} [see eqn.(2.276)].

p_{T_n} Pressure, turbulence induced {KPa} [see eqn.(2.276)].

p_{U_n} Pressure, uncorrelated {KPa} {KPa} [see eqn.(2.304)].

q_{sq} Integration constant, natural beam modes {-} [see eqn. (J.18)].

$p_{[\omega,\Delta\omega]}$ Pressure, bandpass filtered {-} [see eqn.(2.208)].

r Index function {-} [see eqn.(2.197)].

s_{ki} Coefficients, virtual viscosity, i^{th} direction, cylinder k {-} [see eqn.(2.30)].

t Time {s}.

$trig_i$ Trigonometric function {-} [see eqn.(2.198)].

$trig_{ni}$ Trigonometric functions {-} [see eqn.(2.246)].

u Velocity (bulk), fluid, axial direction {-} [see eqn.(2.51)].

u_c Velocity, convection {-} [see eqn.(2.214)].

u_{qrk} Real part of P_{qrk} {-} [see eqn.(2.99)].

v_k Displacement, lateral, y-direction, cylinder k {m} [see eqn.(2.39)].

v_k Displacement, lateral, y-direction, cylinder k {m} [see eqn.(2.112)].

v_{rk} Displacement, harmonic, lateral (y), cylinder k {m} [see eqn.(2.39)].

v_{rk} Displacement, harmonic, lateral (y), cylinder k {m} [see eqn.(2.112)].

v_{qrk} Imaginary part of P_{qrk} {-} [see eqn.(2.99)].

w_k Displacement, lateral, z-direction, cylinder k (m) [see eqn.(2.36)].

w_k Displacement, lateral, z-direction, cylinder k (m) [see eqn.(2.112)].

w_{rk} Displacement, harmonic, lateral (z), cylinder k (m) [see eqn.(2.36)].

w_{rk} Displacement, harmonic, lateral (z), cylinder k (m) [see eqn.(2.112)].

x Displacement, longitudinal, along cylinder(s) (m).

y Displacement, lateral, single cylinder (m).

y_r Displacements, modal, lateral, cylinder(s) (m) [see eqs.(2.20) and (2.107)].

A Area, cross-sectional, single cylinder (m^2).

A Function, pressure measurements (-) [see eqn.(2.318)].

A_0 Area, cross-sectional, reference cylinder (m^2).

A_2 Area, downstream support, single cylinder (m^2) [see eqn.(2.13) and Fig. 3].

A_{2_k} Area, downstream support, cylinder k (m^2) [see eqn.(2.35)].

A_k Area, cross-sectional, cylinder k (m^2) [see eqs.(2.27) and (2.28)].

A_N Area, net cross-sectional, fluid (m^2) [see eqn.(2.6)].

A_{qrk} Modulus of P_{qrk} (-) [see eqn.(2.101)].

B Function, pressure measurements (-) [see eqn.(2.318)].

C Function, pressure measurements (-) [see eqn.(2.318)].

C_b Coefficient, base drag, single cylinder (-) [see eqn.(2.12)].

C_{b_0} Coefficient, base drag, reference cylinder (-) [see eqn.(2.52)].

C_{b_k} Coefficient, base drag, cylinder k (-) [see eqn.(2.34)].

C_D Coefficient, drag ("linearized"), cylinder(s) (m/s) [see eqs.(2.29) and (2.30)].

C_f Coefficient of friction, longitudinal flow (-) [see eqn.(2.2)].

D Diameter, cylinder (m).

D_0 Diameter, reference cylinder (m) [see eqn.(2.52)].

D_k Diameter, cylinder k (m) [see eqs.(2.45) and (2.46)].

D_h Diameter, hydraulic (m) [see eqn.(2.9)].

E Modulus of elasticity, cylinder (N/m^2).

E_0 Modulus of elasticity, reference cylinder (N/m^2) [see eqn.(2.52)].

E_k Modulus of elasticity, cylinder k (N/m^2) [see eqn.(2.45) and (2.46)].

F_{ij} Function, lateral pressure correlation (-) [see eqn.(2.267)].

F_A Force per unit length, lateral, single cylinder, inviscid fluid {N/m} [see $F_{A(z)k}$].

$F_{A(z)k}$, $F_{A(y)k}$ Forces per unit length, lateral, cylinder k, induced by fluid acceleration, z- and y-directions {N/m} [see eqs.(2.27) and (2.28)].

F_F Friction force per unit length, longitudinal, tunnel and cylinders {N/m} [see eqn.(2.5)].

F_L Friction force per unit length, longitudinal, single cylinder {N/m} [see eqn.(2.2)].

F_{L_k} Friction force per unit length, longitudinal, cylinder k {N/m} [see eqn.(2.31)].

F_N Force per unit length, lateral, single cylinder, viscous fluid {N/m} [see $F_{N(z)k}$].

$F_{N(z)k}$, $F_{N(y)k}$ Forces per unit length, lateral, cylinder k, induced by fluid velocity, z- and y-directions {N/m} [see eqs.(2.29) and (2.30)].

F_P Force per unit length, lateral, single cylinder, static pressure {N/m} [see eqn.(2.26)].

$F_{P(z)k}$, $F_{P(y)k}$ Forces per unit length, lateral, cylinder k, induced by static pressure, z- and y-directions [see eqs.(2.38) and (2.41)].

F_T Force per unit length, lateral, cylinder(s), turbulence induced [see eqn.(2.105)].

$F_{T(z)k}$, $F_{T(y)k}$ Forces per unit length, lateral, cylinder k, induced by random pressure fluctuations, z- and y-directions {N/m} [analogous to $F_{P(z)k}$ and $F_{P(y)k}$, see eqn.(2.116)].

$G_{d_i d_j}$ Dimensionless one-sided cross spectral density function, response, based on diameter {-} [see eqn.(2.268)].

$G_{p_{d_M}}$ Measured one-sided power spectral density function, differential pressure {$N^2 \cdot s/m^4 \cdot rad$} [see eqn.(2.339)].

$G_{p_{M_n}}$ One-sided spectral density function, measured pressure(s) {$N^2 \cdot s/m^4 \cdot rad$} [see eqn.(2.339)].

G_{p_T} Calculated one-sided power spectral density function, single point pressure {$N^2 \cdot s/m^4 \cdot rad$} [see eqn.(2.340)].

$G_{p_m p_m}$ One-sided power spectral density function, pressure, generalized $(N^2 \cdot s/m^4 \cdot rad)$ [see eqn.(2.273)].

$G_{p_m p_m}$ Dimensionless one-sided power spectral density function, pressure, generalized (-) [see eqn.(2.273)].

G_n Gain, pressure transducer(s) (-) [see eqn.(2.274)].

ΔG Gain difference (-) [see eqn.(2.283)].

H_{ab} Components of H matrix (-) [see eqs.(2.183) and (2.158)].

I Second moment of area, cylinder (m^4).

I_0 Second moment of area, reference cylinder (m^4) [see eqn.(2.52)].

I_k Second moment of area, cylinder k (m^4) [see eqs.(2.45) and (2.46)].

K Number of cylinders in the bundle (-).

$K_{ij,\theta}$ Function, lateral pressure correlation, individual cylinder (-) [see eqn.(2.237)].

$K_{ij,\xi}$ Function, longitudinal pressure correlation, individual or cylinder pair (-) [see eqn.(2.266)].

$K_{ij,\phi'}$ Function, lateral pressure correlation, cylinder pair (-) [see eqn.(2.251)].

L Length, cylinder(s) (m).

L_W Weighted length, downstream support, cylinder (m) [see eqn.(2.13)].

L_{W_k} Weighted length, downstream support, cylinder k (m) [see eqn.(2.35)].

L_1, L_2 Length, downstream support (m) [see eqn.(2.13)].

M Moment, bending, cylinder(s) $(N \cdot m)$ [see eqn.(2.16)].

M_{ij} Trigonometric function (-) [see eqn.(2.263)].

N Number of natural beam modes (comparison functions) (-).

N_{ij} Logical flag, used in F_{ij} function (-) [see eqn.(2.264)].

P Ratio, measured pressures spectral densities (-) [see eqn.(2.314)].

P_{qr} Amplitudes, modal (-) [see eqs.(2.20) and (2.107)].

P_{qrk} Amplitudes, harmonic, modal (-) [see eqs.(2.37) and (2.40)].

Q Force, lateral shear, cylinder(s) (N) [see eqn.(2.16)].

R Radius, cylinder (m).

R Ratio, pressures spectral densities (-) [see eqn.(2.315)].

R_k Radius, cylinder k (m) [see eqn.(2.32)].

R_C Radius, channel (m).

R_{rs} Inter-cylinder distance, center to center (m) [see Fig. 7].

$R_{p_{M_1} p_{M_2}}$ Cross correlation function, measured pressures {-} [see eqn.(2.305)].

$R_{pp'}$ Cross correlation function, pressure, individual cylinder {-} [see eqn.(2.206)].

$R_{pp'}$ Normalized cross correlation function, pressure, individual cylinder {-} [see eqn.(2.207)].

$R_{pp'[\omega,\Delta\omega]}$ Cross correlation function, pressure, bandpass filtered, individual cylinder {-} [see eqn.(2.208)].

$R_{pp'[\omega,\Delta\omega]}$ Normalized cross correlation function, pressure, bandpass filtered, individual cylinder {-} [see eqn.(2.210)].

$R_{p_i p_j}$ Cross correlation function, pressure, generalized {-} [see eqn.(2.202)].

$R_{\eta_i \eta_j}$ Cross correlation function, response {-} [see eqn.(2.173)].

$R_{\Phi_i \Phi_j}$ Cross correlation function, dimensionless force per unit length {-} [see eqn.(2.180)].

$S_{p_{C_n}}$ Spectral density function, coherent pressure(s) $\{N^2 \cdot s/m^4 \cdot rad\}$ [see eqn.(2.292)].

S_{p_d} Spectral density function, differential pressure $\{N^2 \cdot s/m^4 \cdot rad\}$ [see eqn.(2.335)].

$S_{p_{d_M}}$ Spectral density function, measured differential pressure $\{N^2 \cdot s/m^4 \cdot rad\}$ [see eqn.(2.336)].

$S_{p_{M_n}}$ Spectral density function, measured pressure(s) $\{N^2 \cdot s/m^4 \cdot rad\}$ [see eqn.(2.312)].

$S_{p_{T_n}}$ Spectral density function, turbulence induced pressure(s) $\{N^2 \cdot s/m^4 \cdot rad\}$ [see eqn.(2.321)].

$S_{p_{U_n}}$ Spectral density function, uncorrelated pressure(s) $\{N^2 \cdot s/m^4 \cdot rad\}$. [see eqn.(2.320)].

$S_{p_{C_1} p_{C_2}}$ Cross spectral density function, coherent pressures $\{N^2 \cdot s/m^4 \cdot rad\}$ [see eqn.(2.291)].

$S_{p_{M_1} p_{M_2}}$ Cross spectral density function, measured pressures $\{N^2 \cdot s/m^4 \cdot rad\}$ [see eqn.(2.306)].

$S_{p_i p_j}$ Cross spectral density function, pressure, generalized {-} [see eqn.(2.200)].

$S_{pp'}$ Cross spectral density function, pressure, individual cylinder {-} [see eqn.(2.219)].

$S_{p_i p_j}$ Cross spectral density function, dimensionless pressure, generalized {-} [see eqn.(2.200)].

S_R Strouhal number, radial {cycle} [see eqn.(2.239)].

$S_{\eta_i \eta_j}$ Cross spectral density function, response {-} [see eqn.(2.186)].

$S_{\Phi_i \Phi_j}$ Cross spectral density function, dimensionless force per unit length {-} [see eqn.(2.187)].

S_ξ Strouhal number, longitudinal {-} (cycle) [see eqn.(2.211)].

S_θ Strouhal number, angular, individual cylinder {-} (cycle) [see eqn.(2.212)].

S_θ Strouhal number, angular, cylinder pair {-} (cycle) [see eqn.(2.241)].

T Tension, cylinder {N} [see eqn.(2.1)].

T_k Tension, cylinder k {N} [see eqn.(2.33)].

T_{qrk} Displacement, lateral, harmonic {-} [see eqn.(2.97)].

$\bar{T}$ Tension, cylinder, externally imposed {N} [see eqn.(2.12)].

$\bar{T}_0$ Tension, reference cylinder, externally imposed {N} [see eqn.(2.52)].

$\bar{T}_k$ Tension in cylinder k, externally imposed {N} [see eqs.(2.45) and (2.46)].

U Velocity (bulk) of fluid, axial direction {m/s} [see eqn.(2.2)].

U_c Velocity, convection {m/s} [see u_c].

$U_{pp'}$ Coincident spectral density, pressure, individual cylinder {-} [see eqs.(2.220) and 2.221)].

$V_{pp'}$ Quadrature spectral density, pressure, individual cylinder {-} [see eqs.(2.220) and 2.221)].

Y_q Beam modes, natural {m} [see eqs.(2.20) and (2.23)].

W Weight, downstream support, individual cylinder {N} [see eqn.(2.12)].

W_0 Weight, downstream support, reference cylinder {N} [see eqn.(2.53)].

W_k Weight, downstream support, cylinder k {N} [see eqs.(2.45) and (2.46)].

α Viscous damping coefficient, cylinder (material) {-} [see eqn.(2.52)].

β Mass ratio {-} [see eqn.(2.52)].

β Index function {-} [see eqn.(2.161)].

β_ξ Phase angle, convection delay {-} (rad) [see eqn.(2.231)].

$\beta_{pp'}$ Phase angle of $S_{pp'}$ {-} (rad) [see eqn.(2.226)].

γ Gravitational acceleration parameter {-} [see eqn.(2.52)].

γ^2_{ab} Coherence function, "processes" a and b {-} [e.g. see eqn.(2.289)].

γ_C Gravitational acceleration parameter, (reference) cylinder {-} [see eqn.(2.54)].

γ_F Gravitational acceleration parameter, fluid {-} [see eqn.(2.54)].

δ Logical flag, cylinder(s) lower end condition {-} [see eqn.(2.14)].

δ_{sq} Kronecker delta {-} [see eqn.(2.86)].

ε Slenderness ratio {-} [see eqn.(2.52)].

ϵ Inter-cylinder spacing parameter {-} [see eqn.(2.254)].

ε_W Slenderness ratio, downstream support {-} [see eqn.(2.53)].

ε_1 Slenderness ratio, downstream support {-} [see eqn.(2.53)].

ε_{ki} Coefficients, virtual mass, i^{th} direction, cylinder k {-} [see eqn.(2.27)].

ζ_{ki} Coefficients, virtual viscosity, i^{th} direction, cylinder k {-} [see eqn.(2.29)].

θ Angle, point on cylinder {rad} [see $\Delta\theta$].

η_k Displacement, lateral, cylinder k, z-direction (or if k>K, cylinder k-K, y-direction) {-} [see eqn.(2.48)].

η_k Displacement, lateral, cylinder k, z-direction (or if k>K, cylinder k-K, y-direction) {-} [see eqn.(2.117)].

η_{rk} Displacements, harmonic, lateral, cylinder k, z-direction (or if k>K, cylinder k-K, y-direction) {-} [see eqn.(2.59)].

η_{rk} Displacements, phasor, lateral, cylinder k, z-direction (or, if k>K, cylinder k-K, y-direction) {-} [see eqn.(2.69) and (2.118)].

η_{mn} Displacement, Fourier Transformed {-} [see eqn.(2.159)].

$\Delta\theta$ Angle difference, individual cylinder {rad} [see eqn.(2.204)].

$\Delta\theta_{eq}$ Angle difference (equivalent), cylinder pair {rad} [see eqn.(2.242)].

κ_{ki} Coefficients, virtual mass, i^{th} direction, cylinder k {-} [see eqn.(2.28)].

λ Hysteretic damping coefficient, cylinder (material) {N/m^2} [see eqn.(2.18)].

λ_0 Hysteretic damping coefficient, reference cylinder (material) {N/m^2} [see eqn.(2.52)].

λ_k Hysteretic damping coefficient, cylinder k (material) {N/m^2} [see eqs.(2.45) and (2.46)].

λ_q Eigenvalue, q^{th} natural beam modes {-} [see eqn.(2.84) and Appendix G].

μ Viscous damping coefficient, cylinder (material) {$N \cdot s/m^2$} [see eqn.(2.18)].

μ_0 Viscous damping coefficient, reference cylinder (material) {$N \cdot s/m^2$} [see eqn.(2.52)].

μ_k Viscous damping coefficient, cylinder k (material) {$N \cdot s/m^2$} [see eqs.(2.45) and (2.46)].

ν Poisson ratio, cylinder (material) {-} [see eqn.(2.12)].

ν_k Poisson ratio, cylinder k (material) {-} [see eqs.(2.45) and (2.46)].

ξ Displacement, longitudinal {-} [see eqn.(2.47)].

ξ_0 Location, longitudinal, calculations of experimental and theoretical lateral displacements {-} [see eqn.(2.269)].

$\Delta\xi$ Longitudinal separation {-} [see eqn.(2.204)].

ρ Density of fluid {Kgm/m^3} [see eqn.(2.2)].

σ_q Characteristic constant, q^{th} natural beam mode {-} [see eqn.(2.84) and Appendix G].

σ_{ki} Coefficients, virtual viscosity, i^{th} direction, cylinder k {-} [see eqn.(2.30)].

τ Time {-} [see eqn.(2.49)].

τ_1 Period, fundamental {-} [see eqn.(2.139)].

τ_ξ Time, convection delay {-} [see eqn.(2.230)].

ϕ_q Normalized beam modes, natural {-} [see eqs.(2.60) and (2.84)].

ϕ_{qrk} Phase of P_{qrk} {-} (rad) [see eqn.(2.101)].

ψ_{ab} Components of η_{mn} {-} [see eqn.(2.166)].

ψ_{rs} Inter-cylinder angle, center to center {-} (rad) [see Fig. 7].

ω Frequency {-} [see eqn.(2.50)].

ω_1 Frequency, fundamental {-} [see eqn.(2.139)].

ω_r Frequencies, modal {-} [see eqn.(2.62)].

ω_r Frequencies, modal, real {-} [see eqn.(2.120)].

$\Delta\omega_r$ Frequency differential {-} [see eqn.(2.140)].

Γ Tension, externally imposed (-) [see eqn.(2.52)].

Γ_A Weight, downstream support, reference cylinder (-) [see eqn.(2.53)].

T Hysteretic damping coefficient (-) [see eqn.(2.52)].

Φ_k Forces per unit length, lateral, cylinder k, z-direction (or if k>K, cylinder k-K, y-direction), induced by random pressure fluctuations (-) [see eqn.(2.116)].

Φ_{mn} Force, Fourier Transformed (-) [see eqn.(2.160)].

Ω Frequency (rad/s) [see eqn.(2.50)].

Ω_r Frequencies, modal (rad/s) [see eqn.(2.21)].

$\{a\}_r$ Velocity and displacement vector, lateral, harmonic {-} [see eqn.(2.92)].

$\{0\}$ Null vector {-} [see eqn.(2.93)].

$\{p\}_{qr}$ Amplitude vector, lateral, harmonic {-} [see eqn.(2.123)].

$\{P\}_{qr}$ Displacement vector, lateral, harmonic {-} [see eqn.(2.78)].

$\{P\}_r$ Displacement vector, lateral, harmonic {-} [see eqn.(2.89)].

$\{P\}_{sr}$ Coefficient, Fourier series, for $\{\eta\}_s$ {-} [see eqn.(2.133)].

$\{Q\}_{sr}$ Coefficient, Fourier series, for $\{\Phi\}_s$ {-} [see eqn.(2.128)].

$\{\eta\}$ Displacement vector, lateral {-} [see eqn.(2.130)].

$\{\eta\}_s$ Displacement vector, lateral, modal {-} [see eqs.(2.131) and (2.146)].

$\{\eta_G\}_s$ Displacement vector, lateral, global (Fourier Transform) {-} [see eqn.(2.154)].

$\{\eta_H\}_s$ Hilbert transform of $\{\eta\}_s$ {-} [see eqn.(2.151)].

$\{\Phi\}$ Force (lateral) per unit length vector {-} [see eqn.(2.124)].

$\{\Phi\}_s$ Force (lateral) vector, modal {-} [see eqs.(2.126) and (2.147)].

$\{\Phi_G\}_s$ Force (lateral) vector, global (Fourier Transform) {-} [see eqn.(2.155)]

$[A]$ Global eigenvalue problem matrix (-) [see eqn.(2.94)].

$[C]$ Damping matrix (-) [see eqn.(2.82)].

$[C_G]$ Global viscosity matrix (-) [see eqn.(2.90)].

$[C_V]$ "Virtual" viscosity matrix (-) [see eqn.(2.83)].

$[E]$ Lumped parameters matrix (-) [see eqn.(2.82)].

$[F]$ Lumped parameters matrix (-) [see eqn.(2.82)].

$[G]$ Lumped parameters matrix (-) [see eqn.(2.82)].

$[H]$ Transfer function matrix (-) [see eqn.(2.157)].

$[I]$ Identity matrix (-).

$[K_1]$ Stiffness matrix (-) [see eqn.(2.82)].

$[K_2]$ Stiffness matrix (-) [see eqn.(2.82)].

$[K_G]$ Global stiffness matrix (-) [see eqn.(2.90)].

$[M]$ Mass matrix (-) [see eqn.(2.82)].

$[M_G]$ Global mass matrix (-) [see eqn.(2.90)].

$[M_V]$ "Virtual" mass matrix (-) [see eqn.(2.83)].

$[O]$ Null matrix (-).

$[R]$ Lumped parameters matrix (-) [see eqn.(2.82)].

$[R_m]$ Ratio matrix (-) [see eqn.(2.80)].

$[R_A]$ Ratio matrix (-) [see eqn.(2.81)].

$[R_{C_b}]$ Ratio matrix (-) [see eqn.(2.80)].

$[R_D]$ Ratio matrix (-) [see eqn.(2.80)].

$[R_E]$ Ratio matrix (-) [see eqn.(2.80)].

$[R_I]$ Ratio matrix (-) [see eqn.(2.81)].

$[R_{L_0}]$ Ratio matrix (-) [see eqn.(2.80)].

$[R_T]$ Ratio matrix (-) [see eqn.(2.80)].

$[R_W]$ Ratio matrix (-) [see eqn.(2.80)].

$[R_\lambda]$ Ratio matrix (-) [see eqn.(2.80)].

$[R_\mu]$ Ratio matrix (-) [see eqn.(2.80)].

$[R_\nu]$ Ratio matrix (-) [see eqn.(2.80)].

$[S]$ Lumped parameters matrix (-) [see eqn.(2.82)].

$[T]$ Lumped parameters matrix (-) [see eqn.(2.82)].

$[X]$ Lumped parameters matrix (-) [see eqn.(2.82)].

$[Y]$ Lumped parameters matrix (-) [see eqn.(2.82)].

REMARKS

System parameters that are subscripted with a "zero", for example, R_0 , represent reference values for non-dimensionalisation (see eqs.(2.49) to (2.54) inclusively).

1. INTRODUCTION

The field of flow induced vibration, usually involving flow within or over slender structures (e.g. long cylinders), has been classified for research purposes, into two categories, namely vibration resulting from cross-flow and that resulting from axial flow. Main differences lie (i) in the fluid mechanics, as there is (usually) no separation in the axial case whereas the opposite is true in cross flow; (ii) in the system's geometry in the sense that flow (usually) "encounters" structural elements sequentially in the case of cross flow, whereas in axial flow the fluid streams along the length of a given structure.

We will be concerned with axial flow induced vibration. Although most of the studies relate to cylindrical structures, the field is nevertheless quite varied, as one may consider flow that is steady or unsteady, compressible or incompressible, and so on; inner, outer or annular flow (or combinations thereof); one- or two-phase flow; pipes that are articulated or continuous, straight or curved, thick- or thin-walled (shells); cylinders with various end (boundary) conditions; and so on. Only papers closely related to the subject of interest here, namely axial incompressible flow over cylinder bundles inside a bounding rigid channel, will be reviewed. Work in the field can generally be classified either as (i) the study of stability, which relates to the effect of mean (bulk) fluid flow on the system, neglecting turbulence, near- and far-field noise, or (ii) the study of (finite amplitude) vibration induced by fluctuating fluid forces. Note that the overall system response involves both of the above categories. The following review is chronological and, since developments on "stability" and on "vibration" were interdependent, it will prove necessary to alternate between categories as we proceed.

Early studies* were concerned with the stability of cantilevered pipes subjected to internal flow, for example Bourrières' in 1939 [1], or were

---

* None of the earlier reviews can be said to be exhaustive, hence (involuntary) omissions of publications may have occurred here.

motivated by the existence of bending vibration of the Trans-Arabian pipeline, in the early 1950's, such as by Ashley and Haviland [2], Feodos'ev [3], Housner [4] and Niordson [5] (see Paidoussis and Issid [6]). Then, late in that decade, the development of nuclear power plants required the study of vibration induced by external axial flow over arrays of cylinders, modelling fuel elements in reactor cores. We shall now review related work, outlining the evolution of mathematical models, leading to the theory generally thought to best represent the physics of the phenomenon.

The earliest studies were done in the U.S.A.: Experiments conducted by Burgreen, Byrnes and Benforado [7], on loosely packed arrays and at relatively low flow velocities, indicated (individual) rod vibration at a dominant frequency, corresponding to the first beam deflection mode; a semi-empirical model to predict deflection amplitudes was produced, based on dimensional analysis of a basic equation of motion involving rod flexural restoring and lateral inertial forces, viscous damping forces on the rod oscillating in stationary fluid, and assuming the forcing function to be proportional to the dynamic pressure of the main flow. Next, Shields' [8] experimental results also suggested rod vibration at a dominant frequency, and so did Quinn's [9,10] work on a single cylinder in a channel. The latter proposed a model for a self-excitation mechanism, as follows: (i) the equation of lateral motion of the rod, integrated using an assumed first beam mode deflection, involves a "centrifugal" term, dependent on rod bow (i.e. lateral deflection) and fluid longitudinal velocity, which affects rod motion (and hence deflection), and (ii) an integrated (along the rod length) momentum equation, assuming constant pressure drop over the length of the rod, yields a relationship between flow velocity and rod deflection; the latter affects the hydraulic diameter of the channel hence the overall longitudinal friction pressure drop. (i) and (ii) interact to complete the feedback mechanism. It should be noted that Quinn considered the added mass (lateral accelerations) due to the fluid. Later Avanzini [11] would propose another self-excitation mechanism, but the latter is really semi-empirical (see Reference [12]). We shall not discuss further self-excitation mechanisms as they have never been very well substantiated.

Shortly afterwards, experimental studies were conducted in France [13] and Sweden [14,15,16] (see Reference [12]), reaching basically the same conclusion about cylinders vibrating independently at a dominant frequency corresponding to a first beam mode (for the given boundary conditions). This was to steer research mostly towards the prediction of vibration amplitudes, with the exception of work on stability (to be examined shortly). An early attempt at producing an empirical expression to optimally fit previous experimental data was made by Paidoussis [17]; it was based on a non-dimensionalized equation of motion including a number of new fluid inertial and frictional effects, the details of which were to be published shortly thereafter (see Reference [19] below). Later, Paidoussis [18] was to publish a systematic experimental study on the effects of varying various parameters, in an effort to improve his empirical expression. He also conducted ad hoc tests (i) on the effect of large scale turbulence and swirl on vibration of single cylinders and (ii) on bundles. Results, sometimes apparently contradictory, pointed to a definite need for fundamental research on system behaviour.

The first study on instabilities induced by external (axial) flow was by Paidoussis [19] in the mid-1960's. As in earlier studies, rod elastic and inertial forces were taken into account, but fluid damping forces were modified to include mean flow effects, and lateral and longitudinal drag forces resolved using Taylor's [20] approach. Cylinder tension,* induced by (longitudinal) drag forces as well as externally applied at the cylinder ends, was incorporated in the model. Finally, fluid added mass effects were included, making use of Lighthill's [21] slender-body theory. A pinned-pinned cylinder was investigated, both theoretically and experimentally (using a flexible rubber cylinder to allow manageably low fluid velocities, so as to reach instabilities easily); in addition to providing evidence that fluidelastic instabilities, both divergence and flutter, are possible, the work provided the first indications of the effect of mean

---

* Although Paidoussis (see Reference [43]) later discovered an error relative to that term, the system's essential (qualitative) features remained unaffected.

flow on system dynamics; more specifically, flow induced damping and lowering of vibration frequencies.* At that time, Paidoussis postulated that sub-critical vibration (i.e. vibration at flow velocities less than that for the first instability) are caused by departures from purely axial and steady flow. Note that instabilities are not of practical concern [19], but nevertheless can serve to test mean flow effect theories. System dynamics were further investigated in a subsequent paper by Paidoussis [22], where a more general theory was presented, considering various boundary conditions (pinned-pinned, clamped-clamped, clamped-free); the effect of various parameters on stability was investigated theoretically, supplemented by experiments. It was shown that, in the case of cylinders supported at both ends, oscillatory instabilities are specifically caused by frictional forces and that, without hydrodynamic drag, only buckling is possible.

Reavis, in 1967 [23,24], was the first to assume that cylinder motion is forced by random pressure fluctuations in the turbulent boundary layer (hence ignoring far-field noise§ and turbulence induced by upstream structural components, grids, supports, etc...); he considered that the pressure is homogeneous and unaffected by cylinder motion and that the process is ergodic. Furthermore, the cylinder was taken as lightly damped and response assumed in the first beam mode. The rod was modelled as a pinned-pinned beam, and the pressure characteristics used were those measured by Bakewell [25,26], el Baroudi et al. [27] and Corcos [28]. Those characteristics included power spectral densities and, longitudinal and circumferential correlations which were considered independent, following Corcos' [28] phenomenological model. The effects of mean flow and of the fluid added mass were ignored.† An explicit expression was obtained for the

---

* At least for cylinders fixed at both ends. Also note that this latter effect would not necessarily be clearly evident in practical systems, where flow velocities are relatively low.

§ Propagating acoustically.

† In retrospect, this is acceptable if rod density is high (compared to fluid), cluster is sparse, and flow velocities low (compared to instability velocities).

r.m.s. deflection of the rod, versus a number of system parameters (such as rod length, damping ratio, etc.); although trends obtained corresponded to those of available data, the theory underestimated displacements by more than one order of magnitude. A major step towards improving the model's predictions was to measure both pressure and vibration characteristics in the same test rig: Gorman's [29] work involved vibration measurements of a pinned-pinned rod in water flow and pressure measurements at the wall of the flow channel;* the theory used was essentially that of Reavis [23]. The modal damping was also measured (log decrement), for the first time in the flow, and for various velocities. Experimental and theoretical results agreed well (except at very low velocities where spurious vibration was deemed induced by the motion of mountings), lending support to the mechanism of turbulence induced vibration. Later, Gorman [30] reported results on two-phase flow, and agreement between theory and experiments was remarkable,§ leading to the conclusion that the so-called forced (by pressure fluctuations at the surface of the cylinder) vibration model is correct.† Among other facts, Gorman concluded that higher amplitudes in two-phase flow result from higher circumferential correlations.

Beam mode summation (to account for higher deflection modes) was used by Kanazawa and Boresi [31], and by Chen and Wambsganss [32]. The latter also incorporated the effects of mean flow by using Paidoussis' [22] equation of motion, and used Corcos' [28] phenomenological model for pressure disturbances. New data on turbulent wall pressure fluctuations, on a body of revolution (in water flow), by Bakewell [33], was also used. A Coriolis force term in the equation of motion was neglected so as to allow the use of normal beam modes for the solution, and agreement with experimental results also tended to confirm the forced vibration model. Again, response in the first beam mode was concluded to be dominant and damping was found

---

* Measurements were differential, thereby eliminating static pressure fluctuations.

§ Better than liquid flow, possibly because far-field effects, ignored in the theory, are negligible in two-phase flows.

† At least for single cylinders (as opposed to bundles).

to be proportional to flow velocity. The need for reliable pressure data at low (dimensionless) frequency was stressed, as considerable scatter was found among various researchers' measurements.

Approaching the problem from a different point of view, Y.N. Chen [34]* argued that vibration stems from a kind of instability, initiated mainly by turbulence-induced longitudinal fluctuations in the flow velocity, resulting in a variable compressible load in the cylinder which in turn affects the cylinder bow. More energy can be extracted from the flow as the mean velocity follows a "curved" path along the cylinder, inducing centrifugal forces tending to deflect it further. The number of assumptions required for this parametric oscillation (by analogy to a beam's response to harmonic end loading) model makes it more semi-empirical, and comparisons with experiments really do not confirm the theory (see Reference [12]).

In a follow-up paper to Reference [32], in 1972, Chen and Wambsganss [35] extended their model (i) to take into account more general boundary conditions (inclusive of lateral and torsional spring stiffnesses at the ends) and (ii) to add to Paidoussis' [22] equation of motion other damping effects, namely due to the internal dissipation in the rod (Kelvin type) and to the stationary fluid. Furthermore, the concept of the added mass being increased by confinement was introduced, and a potential flow technique§ to calculate it was applied to the case of a single cylinder positioned centrally in a confining channel. Also, damping was measured in flow, using a more refined technique than Gorman's [29], namely an electromagnetic motion excitation technique (see below). Finally, the response to random pressure excitation was obtained after making use of Galerkin's method and decoupling the resulting second order matrix equation of motion by neglecting some of the damping and Coriolis forces. In situ pressure measurements, on the surface of the rod, by Wambsganss and Zaleski [39],

---

* As opposed to S.S. Chen, mentioned previously.

§ Earlier work on the subject is quoted later by Chen [36], namely Mazur [37] and Shimogo and Inui [38].

were used; the latter included new and more reliable low dimensionless frequency data, where considerable scatter previously existed. Agreement with experiments was generally very good and can be said to validate the (single cylinder) turbulence excitation model. A further major contribution was the result that added mass can be significantly increased by confinement.

Pursuing the study of virtual mass, Chen [40] introduced the important concept of fluid coupled structural motion, investigating theoretically the free vibration of a cantilevered cylinder submerged in a quiescent ideal fluid bounded by a channel (also treated as a cantilevered beam); coupled natural frequencies and beam modes were calculated. In similar studies, Chen [41, 36] studied the response of two parallel, as well as a row of, circular cylinders in a liquid. In a later paper, Chen, Wambsganss and Jendrzejczyk [42] examined the effects of various (viscous) fluids on the added mass and damping of a cantilevered cylinder forced to oscillate harmonically within a rigid circular confinement channel. An homogeneous equation for the velocity potential, a form of linearized Navier-Stokes equation, was used. The electromagnetic technique mentioned earlier was utilized: a frequency sweep was employed and resonant frequencies and damping coefficients determined from the response amplitude and power required to sustain vibration, respectively. The channel-to-cylinder diameter ratio was also varied. Very good agreement was found between theory (taking into account fluid coupling) and experiments.

Meanwhile, the mean flow theory (i.e. stability) was further improved: in 1973 Paidoussis [43] incorporated the effects of (i) gravity* (which induces tension/compression in vertical cylinders), (ii) external pressurization (yielding a compressive load on a cylinder fixed at both ends), (iii) material damping (similarly to Chen and Wambsganss [35]), and modified the equation of motion to take into account (iv) the higher longitudinal pressure gradient found in bundles (frictional losses). In addition,

---

* Useful for cylinders with comparatively low flexural rigidity (compared to mass x length squared).

a more general method for calculating the response to random pressure excitation was presented, which included a matrix method for decoupling the equations of motion (rendering the assumptions used by Chen and Wambsganss [35] unnecessary). Drawing on the work by Chen et al, lateral-motion zero-flow fluid damping, and added mass were included. Also, a correction was brought to an otherwise undetected inconsistency in one of the frictional forces terms in the equation of motion. Finally, the general theoretical behaviour of cantilevered and pinned-pinned cylinders, with increasing flow, was examined; the dynamics of the latter was found to have been altered significantly by the newly corrected error on the friction forces. Comparisons were made with experiments, in terms of stability, and good agreement found, supporting this latest mean flow dynamical model. An important finding was that close spacing can severely destabilize the system. The physics of the problem was also extensively discussed, and so was the influence of various parameters on stability.

In 1975, Chen applied his theory on fluid coupled motion [40,41,36] to bundles [44]: Mean flow behaviour was analyzed for a two-cylinder (coupled) system with the basic equation of motion based on Paidoussis' [43] latest and also making use of Lighthill's [21] slender-body theory to get hydrodynamic forces (in flow). Matrix equations were decoupled using an adjoint eigenvalue system (see Paidoussis [43]). The overall calculation procedure was outlined, and it was shown that the effect of the flowing fluid is to decrease natural frequencies and increase damping, similarly to cases of isolated cylinders (see Paidoussis [19]). Also, for a two- and three-cylinder system in still fluid and corresponding to the first beam mode, coupled frequencies (numbering twice the number of cylinders) were shown to broaden in range (simultaneously from both the lower and upper ends) as cluster spacing is decreased, and the corresponding inter-cylinder (coupled) vibration modes were illustrated. The response of a four-cylinder bundle to forced harmonic excitation of one of them also showed the effect of fluid coupling (induced motion of adjacent cylinders). Subsequently, Chen [45] further illustrated the (zero-flow) behaviour of the coupled system; there are groups of frequencies, each group corresponding to successive beam deflection modes and centered approximately about the

in-fluid solitary beam frequency. Furthermore, a cross-sectional inter-cylinder motion pattern is common to each group. Among conclusions are that (i) the response to random excitation is primarily in the frequency range of the groups (i.e. like bandpass filtering) and (ii) only cylinders in the immediate vicinity of any one under analysis significantly affect its response. In a follow-up to Reference [42], Yeh and Chen [46] further studied theoretically the effect of fluid viscosity on coupled vibration; one conclusion was that viscosity becomes important, in terms of determining frequencies, only for very small gaps; otherwise, the potential flow approach is sufficient.

Experiments were later conducted on coupling in still fluid and results strongly supported the theoretical model. For example Lubin, Haslinger, Puri and Goldberg [47] tested a three-by-five cylinder bundle and basically obtained the theoretically predicted (first beam mode group) vibration frequency range. Chen and Jendrzejczyk [48] and Chen, Jendrzejczyk and Wambsganss [49] conducted extensive testing on cantilevered tube bundles (three to seven rods) and compared with theory, the frequencies, (cross-sectional) modes and coupled response (power spectral densities) when one of the cylinders is harmonically excited, with generally very good agreement. Various confinement schemes were used, namely, "no confinement" (large reservoir), circular channel (positioned eccentrically or not) and in proximity to a flat wall.

Paidoussis and Suss [50] investigated theoretically the stability of clusters of cylinders in a bounding circular channel, taking into account "viscous" in addition to inviscid hydrodynamic fluid coupling. Principal conclusions were that (i) the behaviour of coupled systems (versus flow velocity) is qualitatively similar to that of uncoupled ones (see also Chen [44]) but quantitatively different, close spacing destabilizing the system;* (ii) since the frequency response of the coupled system is broader (see Chen [44]), more energy can be extracted from the flow; (iii) orbital cross-sectional motion is possible (due to viscous coupling and cylinder

---

* See also Paidoussis [43].

material dissipation, see below), contrary to what was previously thought. Later, Paidoussis, Suss and Pustejovsky [51] presented a finite-element method, for free vibration of cylinder clusters in still fluid; comparisons with the classical method of solution showed the latter to be more efficient, but with the finite-element technique being able to solve more complex geometries. Moreover, it was shown that the cylinder cross-sectional orbital motion was due to either viscous hydrodynamic coupling or to material dissipation (in the cylinder).

On another front, Mulcahy, Yeh and Miskevics [52] tested a single rod in flow and at various upstream turbulence levels, also changing the hydraulic diameter by varying the confining channel size. An important conclusion was that turbulence propagated well, altering rod vibration levels, only for larger hydraulic diameters; in closely packed arrays, boundary layer pressure fluctuations are expected to be the dominant excitation. Among other such reports, Lin, Wambsganss and Jendrzejczyk [53] later established that, for low upstream turbulence, pressure power spectral densities are not only dependent on hydraulic diameter, but also on the system geometry, from seven-rod array tests (compared with the annulus experiments of Reference [52]). Results such as these provide much insight into the pressure forces deemed to cause vibration and shall be used to interpret experimental measurements.

In 1979, incorporating hydrodynamic coupling fully into his model, Paidoussis [54] presented extensive results on the system's free vibration* behaviour (frequencies and damping) with increasing flow. It was shown that, for higher flows, although cross-sectional modes remained constant,§ the axial modes departed, especially at higher flow velocities, from the pure beam deflection shapes found earlier (at zero flow) by Chen [45]. Experiments on stability agreed well with the theoretically predicted critical (first instability) flow velocity. This was followed in the early 1980's by a series of experiments by Paidoussis, Curling and Gagnon [55]

---

* Effects of mean flow.

§ At least for non-repeated eigenfrequencies.

which further supported the theory in terms of frequency bands versus flow velocity, leading to a zero frequency instability (divergence or buckling).* Flexible rubber cylinders were used so as to permit low (critical) flow velocities (see Paidoussis [19]).

Further experimental work, concentrating on the subcritical vibration aspects of the problem, was carried out. Paidoussis and Gagnon [56,57] and Paidoussis, Gagnon and C. Chen [58] analyzed motion of strain-gage instrumented flexible rubber cylinders in flowing fluid (water). Displacement power spectral densities, mostly for a cluster of four cylinders, reproduced very well the trends predicted in theory: As flow velocities increase, the oscillation frequencies decrease, faster at the lower than at the upper end of the frequency band (i.e. a broadening of the frequency band takes place), until the lowest frequency reaches zero, signifying the onset of buckling. Higher vibration mode groups were also detected (the second and the third). Furthermore, from simultaneous power spectral density measurements in orthogonal planes of motion§ on a cylinder in the bundle, the sequence of dominant frequencies in each direction corresponded to that of the respective eigenvalues of the cross-sectional inter-cylinder coupling modes. Data was also obtained on the r.m.s. vibration amplitudes versus flow rate, and the study of hydrodynamic coupling (in flow) initiated by testing solitary cylinders and a single flexible cylinder adjacent to rigid ones. Finally, preliminary data was gathered on relative phase in inter-cylinder motion (simultaneous motion measurement on two different cylinders).

The current state of knowledge on both the forced vibration and mean flow (free vibration) models was assembled into a "global" theory by Paidoussis and Curling [59]. The "only" required input, other than geometric material and fluid characteristics, it is hoped, is the fluctuating pressure characteristics within the bundle. The latter, and also a paper by

---

* Cylinders fixed at both ends.

§ In the principal directions predicted in theory.

Curling and Gagnon [60], presented experimental phase measurements* which confirm the existence of the cross-sectional modes, as predicted by the mean flow theory, but more work was required to validate all aspects of the forced vibration model, a most important aspect of this work being the prediction of vibration levels.

The interested reader can refer to general reviews in the field of flow induced vibration, the most recent ones being by Paidoussis [62,63, 64], Pettigrew [65], and Chen [66,67].

This Thesis is primarily meant to provide a critical experimental assessment of the forced vibration model, especially as applied to bundles. The experimental part also provides a data bank for subsequent comparisons. Vibration power and cross spectral density as well as coherence measurements were made in water flow, varying such parameters as flow velocity and bundle geometry (number and spacing of cylinders). Furthermore, hydrodynamic coupling was investigated by testing special arrangements, for example a single flexible rubber cylinder adjacent to "rigid" aluminium ones. Upstream turbulators had to be developed so as to obtain symmetric and repeatable results. The test tunnel was characterized by turbulence intensities and (integral) scale measurements, as well as by mean velocity profiles.§ Pressure spectra, to be used as input to the forced vibration model, were also measured, and a mathematical method to eliminate coherent (for example static) pressure fluctuations from power spectral densities was developed. The theory was expanded to include dissimilar (e.g. moduli of elasticity) cylinders in the cluster, and is presented in concise form, with appendices to provide detail where required; classical random vibration theory was used for the forced vibration model development, rather than the more rigorous but mathematically cumbersome approach originally used by Curling [61]. Qualitatively, predictions of the forced vibration theory agree very well with measurements, but not quantitatively, as r.m.s. amplitudes are experimentally lower. The reasons for this are discussed at the end.

---

* Part of this Thesis.

§ Earlier work (Masters Thesis).

2. THEORY

The random (forced) vibration theory for clusters of hydrodynamically coupled clamped-clamped* cylinders in a rigid containment channel (see Fig. 1) and subjected to turbulent flow pressure fluctuations, is developed from consideration of lateral forces on an element of beam (see Fig. 2). Note that, as longitudinal forces along a deflected beam possess lateral components, the latter had to be taken into account.

Before deriving the equation of motion for an arbitrary beam in the bundle, we discuss the two "types" of forces present in the system, specifically (i) beam (material) forces and (ii) fluid forces.

2.1: BEAM FORCES

Beam (material) forces exist without immersion in a fluid (e.g. in vacuo); they consist in lateral (i) elastic restoring forces, (ii) damping forces (viscous and hysteretic), (iii) inertial forces, and longitudinal (iv) gravity forces.§

Since in practice the cylinders are slender and deflections small, the following assumptions are made: (i) lateral deflections can be resolved into two orthogonal planes, and in each plane, we neglect the effects of (ii) shear deformations, (iii) rotary inertia and, (iv) longitudinal elastic (tension) or dynamic (damping and inertia) forces due to beam elongations (under deflections, with both ends fixed). Note that, as discussed later, compression induced in the cylinder(s) by static fluid pressure (which is not deflection dependent) is taken into account.

2.2: FLUID FORCES

There are normal (pressure) and tangential (shear) fluid forces present. Considered purely normal are (i) the inviscid hydrodynamic forces,

---

* Other boundary conditions (e.g. pinned-pinned) could have been used, had they been required.

§ Note that only nominally vertical beams are investigated here.

(ii) the static pressure forces (which yield stabilizing forces on a deflected cylinder and destabilizing compressive longitudinal ones dependent on Poisson's ratio), and (iii) the turbulent boundary layer pressure fluctuations. There are also combined normal and shear forces from form drag, calculated from bulk fluid velocities across cylinders. Finally, pure shear forces are assumed to arise from the (longitudinal) mean flow along the cylinders (since small motion is assumed, flow separation is absent).

2.3: TWO-DIMENSIONAL EQUATIONS OF MOTION

Now that the various forces considered to influence the system's dynamics have been qualitatively described, the equations of motion in a plane are derived in detail.

2.3-1: Longitudinal force balance

The tension in the cylinder is altered mainly by (i) gravitational forces, (ii) by static pressure induced compression (because ends are fixed), and by (iii) longitudinal friction forces. Item (i) is a "beam" (body) force, item (ii) is categorized as a " fluid" force (although it is really a combination fluid-beam), and item (iii) is a "fluid" force. Note that the buoyancy term F_{p_x} (see Fig. 2) is only second order (see Appendix A) and therefore, negligible.

The static pressure induced (negative) tension, item (ii) above, is constant throughout the beam (see Appendix B), hence, does not appear in the following "tension gradient" equation. From Fig. 2, we see that

$$\frac{\partial T}{\partial x} + mg + F_L = 0 \ , \tag{2.1}$$

where x is the longitudinal coordinate, T and m are the cylinder tension and mass per unit length respectively, F_L is the longitudinal friction (shear) force per unit length, and g the gravitational acceleration.

Paidoussis [43] used Taylor's [20] approach for the longitudinal friction forces on the cylinder(s). For low angles of incidence, we can write (see Appendix C)

$$F_L = \frac{1}{2} \rho D U^2 C_f \ , \tag{2.2}$$

where D is the cylinder diameter, ρ and U are the fluid density and mean (longitudinal) flow velocity respectively, and C_f is a constant friction coefficient.

It shall prove convenient to group T and the product pA (static pressure and cylinder cross-sectional area) in the lateral equations of motion. For a cylinder with constant cross-sectional area, we have

$$\frac{\partial}{\partial x} (pA) = \frac{\partial p}{\partial x} A \ , \tag{2.3}$$

which used in eqn. (2.1), together with eqn. (2.2) yields

$$\frac{\partial}{\partial x} (T + pA) = \frac{\partial p}{\partial x} A - mg - \frac{1}{2} \rho D U^2 C_f \ . \tag{2.4}$$

Now, the pressure gradient is assumed to stem from (i) gravity, and (ii) fluid friction losses along all wetted surfaces in the bundle, inclusive of the confining channel (see Fig. 1):

$$\frac{\partial p}{\partial x} = \rho g - \frac{F_F}{A_N} \ , \tag{2.5}$$

where F_F is the total friction force per unit length and A_N is the net fluid cross-sectional area. We have

$$A_N = \pi (R_C^2 - KR^2) \ , \tag{2.6}$$

R_C and R being the channel and cylinder radii respectively, and K is the number of cylinders in the cluster. If the longitudinal shear stress at the channel wall is taken as equal to that at the cylinder(s), then we can write

$$F_F = F_L \frac{KR + R_C}{R} \ , \tag{2.7}$$

for the whole cluster.

Combining eqs. (2.5), (2.6), and (2.7), and making use of eqn. (2.2), we get

$$\frac{\partial p}{\partial x} = \rho g - \frac{1}{2}\,\rho U^2 C_f \cdot \frac{4}{\pi} \cdot \frac{1}{D_h} \,, \tag{2.8}$$

where we have used the hydraulic diameter

$$D_h = \frac{2\,(R_c^2 - KR^2)}{(R_c + KR)} \,. \tag{2.9}$$

Substitution of eqn.(2.8) into eqn.(2.4) yields

$$\frac{\partial\,(T + pA)}{\partial x} = (\rho A - m)g - \frac{1}{2}\,\rho D U^2 C_f \left[1 + \frac{D}{D_h}\right] \,. \tag{2.10}$$

Integrating the latter equation simply yields, at location x :

$$T + pA = \left[(m - \rho A)g + \frac{1}{2}\,\rho D U^2 C_f \left[1 + \frac{D}{D_h}\right]\right](L - x) + (T + pA)\Big|_{x = L} \,, \tag{2.11}$$

where L is the beam length (and other parameters have been defined previously).

The last term, at $x = L$, depends on the lower support geometry and weight, and on the cylinder mounting procedure (e.g. hung vertically before clamping, etc.). Appendix C gives pertinent details; for cylinders clamped at both ends (but the lower end may be allowed to slide axially), we have*

$$(T + pA)\Big|_{x = L} = \delta\left[W + \bar{T} + (1 - 2\nu)\,\bar{p}\,A + \frac{1}{2}\,\rho A g L - \frac{1}{2}\,\rho D U^2 C_f \frac{L}{2}\left[1 + \frac{D}{D_h}\right]\right]$$

$$+ (1 - \delta)\cdot\left[W - \rho A g L_w + \frac{1}{2}\,\rho D^2 U^2 C_b + \frac{1}{2}\,\rho D U^2 C_f \left[L_1 + L_w \frac{D}{D_h}\right]\right] \,, \tag{2.12}$$

where

$$L_w = L_1 + L_2 \frac{A_2}{A} \,. \tag{2.13}$$

Here we have introduced new parameters: L_1, L_2, and A_2 are lengths and area related to the lower attachment and W is its weight (see Figs. 3, 4 and 5),

---

* This expression is similar to Paidoussis' [43], but has been modified to account for actual experimental conditions.

$$\delta = \begin{cases} 0 \text{ , if axial sliding is allowed,} \\ 1 \text{ , if axial sliding is not allowed,} \end{cases} \tag{2.14}$$

at the lower (downstream) end, $\bar{T}$ is an externally imposed (pre-) tension (applies only if $\delta = 1$), C_b is a base drag coefficient (applies only if $\delta = 0$), ν is Poisson's ratio. The latter affects the compression induced in the cylinders, when $\delta = 1$, by the fluid static pressure (see Appendix B), the average of which is

$$\bar{p} = p \Big|_{x = \frac{L}{2}} \text{ ,} \tag{2.15}$$

since the pressure gradient is constant (see eqn.(2.8)).

Note that here, the term $\bar{T}$ will always be zero and δ will always be one, but they have been retained in the formulation of the problem as related computer programs are general and require the input of such parameters.

Eqs.(2.11) and (2.12) constitute the expression of the longitudinal force balance.

2.3-2: Lateral force balance - beam element

The cylinders are slender, and treated as Euler-Bernoulli beams.* Referring to Fig. 2, the moment balance yields

$$Q + \frac{\partial M}{\partial x} = 0 \text{ ,} \tag{2.16}$$

since, as $\delta x \to 0$, circumferential surface (pressure and longitudinal shear) and body (inertial) forces tend to zero. Q is the lateral shear force and M is the bending moment.†

---

* See Timoshenko and Young [68] for an illustration of the effect of neglecting shear deformations and rotary inertia.

† Note that conventions for positive shear and moments may vary from author to author.

The lateral force balance yields (the approach is similar to that in Appendix A)

$$\frac{\partial Q}{\partial x}+\frac{\partial}{\partial x}\left[T\frac{\partial y}{\partial x}\right]+F_L\frac{\partial y}{\partial x}+F_P-m\frac{\partial^2 y}{\partial t^2}-(F_A+F_N)+F_T=0\ , \tag{2.17}$$

where y is the lateral deflection of the cylinder and t the time, F_P is the net lateral (normal) surface static pressure force (per unit length), F_A and F_N are, respectively, the inviscid and "viscous" hydrodynamic forces per unit length, and F_T is the turbulent boundary layer normal pressure force (per unit length).

Note that beam material damping forces will appear in the $\partial Q/\partial x$ term and that fluid coupling effects will arise in the term F_A, F_N and F_T: the former two depend on the motion of all cylinders in the bundle, and the latter on their presence. This shall become clear as we proceed.

As the equations of motion take significantly different forms depending on the nature of the response, we shall need to take two separate approaches, (i) the first pertaining to the effects of the mean flow alone ($F_T = 0$ in eqn.(2.17)) and where the response y is assumed to be periodic and exponentially decaying (or amplified, in the case of flutter - to be discussed in Ch. 2), and (ii) the second encompassing both the mean flow and turbulent boundary layer pressure fluctuations ($F_T \neq 0$) and where the response is assumed to be random in nature.

Note that, were it not for the presence of hysteretic damping in the beam, we could have proceeded further with the analysis without yet having to assume the form of the response y (details can be found in Appendix D).

2.4: MEAN FLOW MODEL

The bending moment for a beam with both viscous and hysteretic damping is, referring to Appendix D,

$$M = EI\frac{\partial^2 y}{\partial x^2}+\mu I\frac{\partial^3 y}{\partial x^2\partial t}+\lambda I\frac{\partial^3}{\partial x^2\partial t}\sum_{r=1}^{\infty}\frac{y_r}{|rf_0|}\ , \tag{2.18}$$

where

$$y = y(x,t) = \sum_{r=1}^{\infty} y_r(x,t) \quad , \tag{2.19}$$

and

$$y_r(x,t) = \sum_{q=1}^{\infty} Y_q(x) \left[P_{qr}\, e^{j\Omega_r t} + P_{qr}^{*}\, e^{-j\Omega_r^{*} t} \right] \quad , \quad r = 1,2,\ldots,\infty \, . \tag{2.20}$$

Note that modal analysis is used here: the response (y) is expanded in terms of (i) natural beam modes (Y_q), in this case comparison functions* (satisfying both geometric and natural boundary conditions, and fully differentiable (in x), and (ii) the latter are "modulated" by (exponentially decaying) harmonic functions, sometimes labelled generalized coordinates.

Ω_r is the complex frequency for the r^{th} harmonic (and Ω_r^{*} is its complex conjugate),

$$\Omega_r = f_r + d_r j \quad , \quad r = 1,2,\ldots,\infty \, , \tag{2.21}$$

f_r is the frequency of oscillation, with

$$f_r = r f_1 \quad , \quad r = 1,2,\ldots,\infty \, , \qquad \text{(see eqn.(2.25))} \tag{2.22}$$

and d_r is a damping parameter.

f_1 is the fundamental frequency of oscillation. We have introduced the following beam (cylinder) parameters: the modulus of elasticity E, the second moment of area I, and the viscous and hysteretic damping coefficients μ and λ. $Y_q(x)$ is the q^{th} natural mode (undamped free vibration) of the beam, for the boundary conditions of interest. Since amplitude information can be found in the P_{qr} coefficients, the $Y_q(x)$ can be normalized arbitrarily. When using dimensionless parameters later on, it will prove useful to have set

$$\int_0^L Y_q^2(x)\, dx = L^3 \quad , \quad q = 1,2,\ldots,\infty \, . \tag{2.23}$$

---

* See Meirovitch [69], P.140.

Finally, the P_{qr} are complex amplitudes, corresponding to the q^{th} beam mode and r^{th} harmonic (and P^{*}_{qr} are their complex conjugates).

Now, combining eqs.(2.16), (2.17) (with $F_T = 0$), and (2.18), we obtain the equation of motion

$$m \frac{\partial^2 y}{\partial t^2} + \mu I \frac{\partial^5 y}{\partial x^4 \partial t} + \lambda I \frac{\partial^5}{\partial x^4 \partial t} \sum_{r=1}^{\infty} \frac{y_r}{|Re(\Omega_r)|} + EI \frac{\partial^4 y}{\partial x^4} - \frac{\partial}{\partial x} \left[T \frac{\partial y}{\partial x} \right] - F_L \frac{\partial y}{\partial x}$$

$$- F_P + (F_A + F_N) = 0 . \qquad (2.24)$$

Note

In eqn.(2.24), the term rf_1 has been replaced by $Re(\Omega_r) = f_r = rf_1$. Since all harmonics need not be present in a periodic signal, we will, from now on, consider Ω_r to be the r^{th} frequency found in the signal; this then alters eqn.(2.22) to read

$$f_r = m_r f_1 , \qquad (m_r \geq r) \qquad (2.25)$$
$$r = 1, 2, \ldots, \infty .$$

(i.e. all harmonics not necessarily present). In our case, the values of m_r and of f_1 are of no interest; only the Ω_r (f_r and d_r) are.

At this point, three lateral force terms have yet to be determined, namely F_P, F_A, and F_N. We recall that F_P is the net lateral force (per unit length) due to (normal) static pressure forces on an element of the beam. Fig. 6 illustrates an element of the beam completely immersed in fluid, including the end faces (following Paidoussis' approach, e.g. see Ref. [43]); this allows us to easily find the contribution of static pressure forces on the circumferential surface of the (bent) element. The lateral force balance is

$$F_P \, \delta x - \frac{\partial}{\partial x} \left[pA \frac{\partial y}{\partial x} \right] \delta x = 0 ,$$

yielding

$$F_P = \frac{\partial}{\partial x} \left[pA \frac{\partial y}{\partial x} \right] . \qquad (2.26)$$

F_A also stems from normal pressure forces at the surface of the cylinder, this time from the fluid lateral acceleration field. For a single (solitary) cylinder in unbounded (no channel) still fluid, the force (per unit length) can be found by considering changes in the fluid kinetic energy due to a change in the cylinder velocity; the velocity field in the fluid is found from potential flow theory. One finds

$$F_A = -\rho A \frac{\partial^2 y}{\partial t^2} \quad ,$$

i.e. there is an apparent (added or virtual) mass (per unit length) "attached" to the accelerating cylinder (equal to ρA here).

In the case of a cylinder in a bundle positioned within a bounding channel and subjected to longitudinally flowing fluid, the force, say in direction y, on cylinder k, labelled $F_{A(y)k}$, is found to depend on the motion of all cylinders in the bundle, in the z- as well as in the y-direction. Derivations are found in Appendix E, following Chen's [44] approach. Results are:

(a) for the z-direction

$$F_{A(z)k} = -\rho A_k \sum_{i=1}^{K} \left(\varepsilon_{ki} \frac{D^2 w_i}{Dt^2} + e_{ki} \frac{D^2 v_i}{Dt^2} \right) \quad , \quad k = 1,2,\ldots,K \, , \tag{2.27}$$

(b) and for the y-direction

$$F_{A(y)k} = -\rho A_k \sum_{i=1}^{K} \left(\kappa_{ki} \frac{D^2 w_i}{Dt^2} + k_{ki} \frac{D^2 v_i}{Dt^2} \right) \quad , \quad k = 1,2,\ldots,K \, . \tag{2.28}$$

In the latter equations, A_k is the cross-sectional area of cylinder k, κ_{ki}, k_{ki}, ε_{ki} and e_{ki}, $k,i = 1,2,\ldots,K$, are dimensionless coefficients dependent on bundle geometrical parameters, namely cylinder radii, their location within the cluster, and the channel radius. D/Dt is the total (or substantial) derivative, and w_i and v_i are the z- and y-direction lateral displacement coordinates respectively, for cylinder i (see Fig. 7).

Equations (2.27) and (2.28) now indicate fluid coupling between the motion of the cylinders in the bundle, namely inviscid hydrodynamic coupling.

Paidoussis and Suss [50] assumed fluid viscosity not to be negligible in the immediate vicinity of any cylinder, where velocity gradients are likely to be the highest; lateral drag forces dependent on the (inviscid) fluid velocity field at the cylinder surface were postulated to exist, resulting in so-called "viscous coupling" between cylinders. One obtains expressions similar to those for inertial (inviscid) forces, namely (see Appendix F for details),

(a) for the z-direction

$$F_{N(z)k} = \frac{1}{2}\rho D_k U C_f \sum_{i=1}^{K}\left(\zeta_{ki}\frac{Dw_i}{Dt} + g_{ki}\frac{Dv_i}{Dt}\right)$$

$$+\frac{1}{2}\rho D_k C_D \cdot \sum_{i=1}^{K}\left(\zeta_{ki}\frac{\partial w_i}{\partial t} + g_{ki}\frac{\partial v_i}{\partial t}\right), \quad k=1,2,\ldots,K, \tag{2.29}$$

(b) and for the y-direction

$$F_{N(y)k} = \frac{1}{2}\rho D_k U C_f \sum_{i=1}^{K}\left(\sigma_{ki}\frac{Dw_i}{Dt} + s_{ki}\frac{Dv_i}{Dt}\right)$$

$$+\frac{1}{2}\rho D_k C_D \cdot \sum_{i=1}^{K}\left(\sigma_{ki}\frac{\partial w_i}{\partial t} + s_{ki}\frac{\partial v_i}{\partial t}\right), \quad k=1,2,\ldots,K. \tag{2.30}$$

The coupled system requires two equations per cylinder, one for each (orthogonal) direction y and z. Consequently, we must use subscripts in previously derived equations (which were for a single cylinder, in one plane of motion). These are equations (2.2), (2.9), (2.11), (2.12), (2.13), (2.19), (2.20), (2.21), (2.24), and (2.26). We now have, in multi-cylinder terminology,

$$F_{L_k} = \frac{1}{2}\rho D_k U^2 C_f, \quad k=1,2,\ldots,K, \tag{2.31}$$

$$D_h = \frac{2\left(R_c^2 - \sum_{k=1}^{K} R_k^2\right)}{\left(R_c + \sum_{k=1}^{K} R_k\right)} \quad , \tag{2.32}$$

$$T_k + pA_k = \left[(m_k - \rho A_k)g + \frac{1}{2}\rho D_k U^2 C_f \left(1 + \frac{D_k}{D_h}\right)\right](L - x) + (T_k + pA_k)\Big|_{x=L} \quad , \tag{2.33}$$

$$k = 1,2,\ldots,K \, ,$$

$$(T_k + pA_k)\Big|_{x=L} = \delta\left[W_k + \bar{T}_k + (1 - 2\nu_k)\bar{p}\,A_k + \frac{1}{2}\rho A_k g L - \frac{1}{2}\rho D_k U^2 C_f \frac{L}{2}\left(1 + \frac{D_k}{D_h}\right)\right]$$

$$+ (1 - \delta)\left[W_k - \rho A_k g L_{w_k} + \frac{1}{2}\rho D_k^2 U^2 C_{b_k} + \frac{1}{2}\rho D_k U^2 C_f \left(L_1 + L_{w_k}\frac{D_k}{D_h}\right)\right] \quad , \tag{2.34}$$

$$k = 1,2,\ldots,K \, ,$$

with

$$L_{w_k} = L_1 + L_2 \frac{A_{2_k}}{A_k} \quad , \qquad k = 1,2,\ldots,K \, , \tag{2.35}$$

and for the z-direction, we have

$$w_k = w_k(x,t) = \sum_{r=1}^{\infty} w_{rk}(x,t) \quad , \qquad k = 1,2,\ldots,K \, , \tag{2.36}$$

$$w_{rk}(x,t) = \sum_{q=1}^{\infty} Y_q(x)\left[P_{qrk}\, e^{j\Omega_r t} + P_{qrk}^{*}\, e^{-j\Omega_r^{*} t}\right] \quad , \qquad \begin{matrix} r = 1,2,\ldots,\infty \, , \\ k = 1,2,\ldots,K \, , \end{matrix} \tag{2.37}$$

where Ω_r is given by eqn.(2.21). Note that the frequency has not been labelled Ω_{rk} but rather Ω_r, since, for a given inter-cylinder coupling mode (to be explained in detail in a later chapter), the frequency is common to all cylinders. Proceeding, we have

$$F_{P(z)k} = \frac{\partial}{\partial x}\left(pA_k \frac{\partial w_k}{\partial x}\right) \quad , \qquad k = 1,2,\ldots,K \, . \tag{2.38}$$

Similarly, for the y-direction (eqs.(2.36), (2.37), and (2.38)), we have

$$v_k = v_k(x,t) = \sum_{r=1}^{\infty} v_{rk}(x,t) \quad , \qquad k = 1,2,\ldots,K \, , \tag{2.39}$$

$$v_{rk}(x,t) = \sum_{q=1}^{\infty} Y_q(x)\left[P_{qr(k+K)}\, e^{j\Omega_r t} + P^*_{qr(k+K)}\, e^{-j\Omega_r^* t} \right] , \qquad \begin{matrix} r = 1,2,\ldots,\infty , \\ k = 1,2,\ldots,K , \end{matrix} \tag{2.40}$$

and

$$F_{P(y)k} = \frac{\partial}{\partial x}\left(pA_k \frac{\partial v_k}{\partial x} \right) , \qquad k = 1,2,\ldots,K . \tag{2.41}$$

Finally, the z-direction equation of motion reads

$$m_k \frac{\partial^2 w_k}{\partial t^2} + \mu_k I_k \frac{\partial^5 w_k}{\partial x^4 \partial t} + \lambda_k I_k \frac{\partial^5}{\partial x^4 \partial t} \sum_{r=1}^{\infty} \frac{w_{rk}}{|\mathrm{Re}(\Omega_r)|} + E_k I_k \frac{\partial^4 w_k}{\partial x^4}$$

$$- \frac{\partial}{\partial x}\left(T_k \frac{\partial w_k}{\partial x} \right) - F_{L_k} \frac{\partial w_k}{\partial x} - F_{P(z)k} + \left(F_{A(z)k} + F_{N(z)k} \right) = 0 , \qquad k = 1,2,\ldots,K , \tag{2.42}$$

and for the y-direction,

$$m_k \frac{\partial^2 v_k}{\partial t^2} + \mu_k I_k \frac{\partial^5 v_k}{\partial x^4 \partial t} + \lambda_k I_k \frac{\partial^5}{\partial x^4 \partial t} \sum_{r=1}^{\infty} \frac{v_{rk}}{|\mathrm{Re}(\Omega_r)|} + E_k I_k \frac{\partial^4 v_k}{\partial x^4}$$

$$- \frac{\partial}{\partial x}\left(T_k \frac{\partial v_k}{\partial x} \right) - F_{L_k} \frac{\partial v_k}{\partial x} - F_{P(y)k} + \left(F_{A(y)k} + F_{N(y)k} \right) = 0 , \qquad k = 1,2,\ldots,K . \tag{2.43}$$

Note that "longitudinal" quantities are common to all cylinders. These are the coordinate x, the lengths L, L_1 and L_2 (see Fig. 3), the beam modes $Y_q(x)$, and the downstream clamping parameter δ. Furthermore, the fluid parameters that apply everywhere are the density ρ, friction coefficient C_f, static pressure p (hence mean static pressure $\bar{p}$ also), and flow velocity U (taken as uniform). Finally, the time t, the drag coefficient C_D, the acceleration due to gravity g, and the hydraulic diameter D_h, are likewise common parameters.

Remarks

Although the experimental work to be presented later applies to cylinders which are geometrically identical (D, L) and the flow velocity (U) is assumed uniformly distributed, the parameters I, F_L, $F_{P(z)}$, and $F_{P(y)}$, dependent on the above variables, will be left subscripted to keep the analysis general.

Now, using eqn.(2.38), we may write

$$\frac{\partial}{\partial x}\left[T_k \frac{\partial w_k}{\partial x}\right] + F_{P(z)k} - \frac{\partial}{\partial x}\left[(T_k + pA_k)\frac{\partial w_k}{\partial x}\right] \quad , \qquad k = 1,2,\ldots,K \, , \tag{2.44}$$

and similarly, for the y-direction.

Substituting eqs.(2.29), (2.30), (2.31), and (2.44) into eqn.(2.42), and also making use of eqs.(2.33) and (2.34), we obtain the equation of motion,

(a) for the z-direction:

$$m_k \frac{\partial^2 w_k}{\partial t^2} + \mu_k I_k \frac{\partial^5 w_k}{\partial x^4 \partial t} + \lambda_k I_k \frac{\partial^5}{\partial x^4 \partial t} \sum_{r=1}^{\infty} \frac{w_{rk}}{|\mathrm{Re}(\Omega_r)|} + E_k I_k \frac{\partial^4 w_k}{\partial x^4}$$

$$+\left[(m_k - \rho A_k)g + \frac{1}{2}\rho D_k U^2 C_f \left(1 + \frac{D_k}{D_h}\right)\right] x \frac{\partial^2 w_k}{\partial x^2} - \left\{ W_k + m_k gL + \delta\left[\bar{T}_k + (1 - 2\nu_k)\bar{p} A_k\right]\right.$$

$$+ \frac{1}{2}\rho D_k^2 U^2 C_{b_k}(1 - \delta) + \frac{1}{2}\rho D_k U^2 C_f \left[(2 - \delta)\left(1 + \frac{D_k}{D_h}\right)\frac{L}{2} + (1 - \delta)\left(L_1 + L_{w_k}\frac{D_k}{D_h}\right)\right]$$

$$\left. - \rho A_k g\left[(2 - \delta)\frac{L}{2} + (1 - \delta) L_{w_k}\right]\right\}\frac{\partial^2 w_k}{\partial x^2} + \left[(m_k - \rho A_k)g + \frac{1}{2}\rho D_k U^2 C_f \frac{D_k}{D_h}\right]\frac{\partial w_k}{\partial x}$$

$$- \rho A_k \sum_{i=1}^{K}\left(\varepsilon_{ki}\frac{D^2 w_i}{Dt^2} + e_{ki}\frac{D^2 v_i}{Dt^2}\right) + \frac{1}{2}\rho D_k U C_f \sum_{i=1}^{K}\left(\zeta_{ki}\frac{Dw_i}{Dt} + g_{ki}\frac{Dv_i}{Dt}\right)$$

$$+ \frac{1}{2}\rho D_k C_D \sum_{i=1}^{K}\left(\zeta_{ki}\frac{\partial w_i}{\partial t} + g_{ki}\frac{\partial v_i}{\partial t}\right) = 0 \, , \qquad k = 1,2,\ldots,K \, , \tag{2.45}$$

and, proceeding similarly,

(b) for the y-direction:

$$m_k \frac{\partial^2 v_k}{\partial t^2} + \mu_k I_k \frac{\partial^5 v_k}{\partial x^4 \partial t} + \lambda_k I_k \frac{\partial^5}{\partial x^4 \partial t} \sum_{r=1}^{\infty} \frac{v_{rk}}{|\mathrm{Re}(\Omega_r)|} + E_k I_k \frac{\partial^4 v_k}{\partial x^4}$$

$$+\left[(m_k - \rho A_k)g + \frac{1}{2}\rho D_k U^2 C_f \left(1 + \frac{D_k}{D_h}\right)\right] x \frac{\partial^2 v_k}{\partial x^2} - \left\{ W_k + m_k gL + \delta\left[\bar{T}_k + (1 - 2\nu_k)\bar{p} A_k\right]\right.$$

$$+ \frac{1}{2}\rho D_k^2 U^2 C_{b_k}(1-\delta) + \frac{1}{2}\rho D_k U^2 C_f \left[(2-\delta)\left(1+\frac{D_k}{D_h}\right)\frac{L}{2} + (1-\delta)\left(L_1 + L_{w_k}\frac{D_k}{D_h}\right)\right]$$

$$- \rho A_k g \left[(2-\delta)\frac{L}{2} + (1-\delta) L_{w_k} \right] \Big\} \frac{\partial^2 v_k}{\partial x^2} + \left[(m_k - \rho A_k) g + \frac{1}{2}\rho D_k U^2 C_f \frac{D_k}{D_h} \right] \frac{\partial v_k}{\partial x}$$

$$- \rho A_k \sum_{i=1}^{K} \left(\kappa_{ki} \frac{D^2 w_i}{Dt^2} + k_{ki} \frac{D^2 v_i}{Dt^2} \right) + \frac{1}{2}\rho D_k U C_f \sum_{i=1}^{K} \left(\sigma_{ki} \frac{Dw_i}{Dt} + s_{ki} \frac{Dv_i}{Dt} \right)$$

$$+ \frac{1}{2}\rho D_k C_D \sum_{i=1}^{K} \left(\sigma_{ki} \frac{\partial w_i}{\partial t} + s_{ki} \frac{\partial v_i}{\partial t} \right) = 0 \ , \qquad k = 1,2,\ldots,K \ . \tag{2.46}$$

For convenience, equations shall be non-dimensionalized; the following (dimensionless) parameters render the equations of motion (eqs.(2.45) and (2.46)) dimensionless;* we define

(i) the longitudinal dimensionless coordinate as

$$\xi = \frac{x}{L} \ , \tag{2.47}$$

(ii) the lateral dimensionless coordinate as

$$\eta_k = \begin{cases} w_k/L \ , & k = 1,2,\ldots,K \ , \\ v_{k-K}/L \ , & k = K+1, K+2 \ldots, 2K \ , \end{cases} \tag{2.48}$$

(iii) the dimensionless time as

$$\tau = \left(\frac{E_0 I_0}{m_0 + \rho A_0} \right)^{1/2} \frac{t}{L^2} \ , \tag{2.49}$$

(iv) and conversely, the dimensionless frequency as

$$\omega = \left(\frac{m_0 + \rho A_0}{E_0 I_0} \right)^{1/2} L^2 \Omega \ , \tag{2.50}$$

(v) the dimensionless flow velocity as

(continued)

---

* After post-multiplication by $L^3/E_0 I_0$.

$$u = \left(\frac{\rho A_0}{E_0 I_0} \right)^{1/2} UL \quad , \tag{2.51}$$

(vi) and finally, the various system parameters are:

$$\varepsilon = \frac{L}{D_0} \quad , \qquad h = \frac{D_0}{D_h} \quad ,$$

$$\alpha = \left[\frac{I_0}{E_0 (m_0 + \rho A_0)} \right]^{1/2} \frac{\mu_0}{L^2} \quad , \qquad T = \frac{\lambda_0}{E_0} \quad ,$$

$$\beta = \frac{\rho A_0}{m_0 + \rho A_0} \quad , \qquad \gamma = \frac{(m_0 - \rho A_0) g L^3}{E_0 I_0} \quad , \tag{2.52}$$

$$\Gamma = \frac{\bar{T}_0 L^2}{E_0 I_0} \quad , \qquad \pi = \frac{\bar{p} A_0 L^2}{E_0 I_0} \quad ,$$

$$c_f = \frac{4}{\pi} C_f \quad , \qquad c_{b_0} = \frac{4}{\pi} C_{b_0} \quad ,$$

$$c = \frac{4}{\pi} C_D L \left(\frac{\rho A_0}{E_0 I_0} \right)^{1/2} \quad ,$$

which also include lower attachment (see Figs. 3, 4, and 5) parameters:

$$\varepsilon_W = \frac{L_W}{D_0} \quad , \qquad \varepsilon_1 = \frac{L_1}{D_0} \quad ,$$

$$\Gamma_A = \frac{W_0 L^2}{E_0 I_0} \quad ; \tag{2.53}$$

finally, we shall require

$$\gamma_C = \frac{m_0 g L^3}{E_0 I_0} \quad , \qquad \gamma_F = \frac{\rho A_0 g L^3}{E_0 I_0} \quad ; \tag{2.54}$$

where it is noted that

$$\gamma = \gamma_C - \gamma_F \quad . \tag{2.55}$$

The parameters D_0, A_0 and I_0 (geometric), E_0, m_0, μ_0 and λ_0 (material properties), L_W, L_1, W_0, $\bar{T}_0$ and C_{b_0} (lower attachment parameters) are those of a reference (typical) cylinder in the cluster. Other parameters are fixed, namely L, D_h, g, ρ, $\bar{p}$, C_f and C_D.

Recall that x and t are independent variables, w_k and v_k ($k = 1,2,\ldots,K$) are dependent variables, and U (the flow velocity) is a variable parameter. Finally, Ω, a generally complex frequency, will be obtained from the calculated (dimensionless) ω.

The resulting dimensionless equations of motion are:

(a) for the z-direction

$$\frac{m_k}{m_0}(1-\beta)\frac{\partial^2\eta_k}{\partial\tau^2} + \frac{I_k}{I_0}\frac{\mu_k}{\mu_0}\alpha\frac{\partial^5\eta_k}{\partial\xi^4\partial\tau} + \frac{I_k}{I_0}\frac{\lambda_k}{\lambda_0}T\frac{\partial^5}{\partial\xi^4\partial\tau}\sum_{r=1}^{\infty}\frac{\eta_{rk}}{|Re(\omega_r)|}$$

$$+ \frac{E_k}{E_0}\frac{I_k}{I_0}\frac{\partial^4\eta_k}{\partial\xi^4} + \left[\frac{m_k}{m_0}\gamma_C - \frac{A_k}{A_0}\gamma_F + \frac{1}{2}\frac{D_k}{D_0}\varepsilon c_f\left(1+\frac{D_k}{D_0}h\right)u^2\right]\xi\frac{\partial^2\eta_k}{\partial\xi^2}$$

$$- \left\{\frac{W_k}{W_0}\Gamma_A + \frac{m_k}{m_0}\gamma_C + \delta\left[\frac{\bar{T}_k}{\bar{T}_0}\Gamma + (1-2\nu_k)\frac{A_k}{A_0}\pi\right] + \frac{(1-\delta)}{2}\frac{A_k}{A_0}\frac{C_{b_k}}{C_{b_0}}c_{b_0}u^2\right.$$

$$+ \frac{1}{2}\frac{D_k}{D_0}c_f u^2\left[\frac{(2-\delta)}{2}\left(1+\frac{D_k}{D_0}h\right)\varepsilon + (1-\delta)\left(\varepsilon_1 + \frac{D_k}{D_0}\frac{L_{W_k}}{L_W}\varepsilon_W h\right)\right]$$

$$\left. - \gamma_F\frac{A_k}{A_0}\left[\frac{(2-\delta)}{2} + (1-\delta)\frac{L_{W_k}}{L_W}\frac{\varepsilon_W}{\varepsilon}\right]\right\}\frac{\partial^2\eta_k}{\partial\xi^2} + \left[\frac{m_k}{m_0}\gamma_C - \frac{A_k}{A_0}\gamma_F + \frac{1}{2}\frac{A_k}{A_0}\right.$$

$$\left.\cdot\,\varepsilon c_f h u^2\right]\frac{\partial\eta_k}{\partial\xi} + \sum_{i=1}^{K}\left\{-\frac{A_k}{A_0}\beta\left(\varepsilon_{ki}\frac{D^2\eta_i}{D\tau^2} + e_{ki}\frac{D^2\eta_{i+K}}{D\tau^2}\right) + \frac{1}{2}\frac{D_k}{D_0}\varepsilon c_f\sqrt{\beta}\,u\right.$$

$$\left.\cdot\left(\zeta_{ki}\frac{D\eta_i}{D\tau} + g_{ki}\frac{D\eta_{i+K}}{D\tau}\right) + \frac{1}{2}\frac{D_k}{D_0}\varepsilon c\sqrt{\beta}\left(\zeta_{ki}\frac{\partial\eta_i}{\partial\tau} + g_{ki}\frac{\partial\eta_{i+K}}{\partial\tau}\right)\right\} = 0 \quad , \qquad (2.56)$$

$$k = 1,2,\ldots,K \, ,$$

(b) and for the y-direction

$$\frac{m_{k-K}}{m_0}(1-\beta)\frac{\partial^2\eta_k}{\partial\tau^2} + \frac{I_{k-K}}{I_0}\frac{\mu_{k-K}}{\mu_0}\alpha\frac{\partial^5\eta_k}{\partial\xi^4\partial\tau} + \frac{I_{k-K}}{I_0}\frac{\lambda_{k-K}}{\lambda_0}T\frac{\partial^5}{\partial\xi^4\partial\tau}\sum_{r=1}^{\infty}\frac{\eta_{rk}}{|Re(\omega_r)|}$$

$$+ \frac{E_{k-K}}{E_0}\frac{I_{k-K}}{I_0}\frac{\partial^4\eta_k}{\partial\xi^4} + \left[\frac{m_{k-K}}{m_0}\gamma_C - \frac{A_{k-K}}{A_0}\gamma_F + \frac{1}{2}\frac{D_{k-K}}{D_0}\varepsilon c_f\left(1+\frac{D_{k-K}}{D_0}h\right)u^2\right]\xi\frac{\partial^2\eta_k}{\partial\xi^2}$$

$$- \left\{ \frac{W_{k-K}}{W_0} \Gamma_A + \frac{m_{k-K}}{m_0} \gamma_C + \delta \left[\frac{\bar{T}_{k-K}}{\bar{T}_0} \Gamma + (1 - 2\nu_k) \frac{A_{k-K}}{A_0} \pi \right] + \frac{(1-\delta)}{2} \frac{A_{k-K}}{A_0} \frac{C_{b_{k-K}}}{C_{b_0}} c_{b_0} u^2 \right.$$

$$\left. + \frac{1}{2} \frac{D_{k-K}}{D_0} c_f u^2 \left[\frac{(2-\delta)}{2} \left(1 + \frac{D_{k-K}}{D_0} h \right) \varepsilon + (1-\delta) \left(\varepsilon_1 + \frac{D_{k-K}}{D_0} \frac{L_{W_{k-K}}}{L_W} \varepsilon_W h \right) \right] \right.$$

$$\left. - \gamma_F \frac{A_{k-K}}{A_0} \left[\frac{(2-\delta)}{2} + (1-\delta) \frac{L_{W_{k-K}}}{L_W} \frac{\varepsilon_W}{\varepsilon} \right] \right\} \frac{\partial^2 \eta_k}{\partial \xi^2} + \left[\frac{m_{k-K}}{m_0} \gamma_C - \frac{A_{k-K}}{A_0} \gamma_F + \frac{1}{2} \frac{A_{k-K}}{A_0} \right.$$

$$\left. \cdot \varepsilon c_f h u^2 \right] \frac{\partial \eta_k}{\partial \xi} + \sum_{i=1}^{K} \left\{ - \frac{A_{k-K}}{A_0} \beta \left(\kappa_{ki} \frac{D^2 \eta_i}{D\tau^2} + k_{ki} \frac{D^2 \eta_{i+K}}{D\tau^2} \right) + \frac{1}{2} \frac{D_{k-K}}{D_0} \varepsilon c_f \sqrt{\beta} u \right.$$

$$\left. \cdot \left(\sigma_{ki} \frac{D\eta_i}{D\tau} + s_{ki} \frac{D\eta_{i+K}}{D\tau} \right) + \frac{1}{2} \frac{D_{k-K}}{D_0} \varepsilon c \sqrt{\beta} \left(\sigma_{ki} \frac{\partial \eta_i}{\partial \tau} + s_{ki} \frac{\partial \eta_{i+K}}{\partial \tau} \right) \right\} = 0 \quad , \qquad (2.57)$$

$$k = K+1, K+2, \ldots, 2K \, .$$

By analogy to eqs.(2.36) and (2.37) (and also (2.39) and (2.40)), and recalling eqn.(2.48), we have

$$\eta_k(x,t) = \sum_{r=1}^{\infty} \eta_{rk}(x,t) \quad , \qquad k = 1,2,\ldots,2K \, , \qquad (2.58)$$

where

$$\eta_{rk}(x,t) = \sum_{q=1}^{\infty} \frac{Y_q(x)}{L} \left[P_{qrk} \, e^{j\Omega_r t} + P^*_{qrk} \, e^{-j\Omega_r^* t} \right] \, , \qquad \begin{matrix} r = 1,2,\ldots,\infty \, , \\ k = 1,2,\ldots,2K \, . \end{matrix} \qquad (2.59)$$

The dimensionless beam modes are defined as

$$\phi_q(\xi) = \frac{Y_q(L\xi)}{L} \quad , \qquad q = 1,2,\ldots,\infty \, , \qquad (2.60)$$

and, from eqn.(2.23), the $\phi_q(\xi)$ normalization reads

$$\int_0^1 \phi_q^2(\xi) \, d\xi = 1 \, , \qquad q = 1,2,\ldots,\infty \, . \qquad (2.61)$$

Also, from eqs.(2.49) and (2.50), we may write

$$\Omega_r t = \omega_r \tau \, , \qquad r = 1,2,\ldots,\infty \, , \qquad (2.62)$$

hence the latter, together with eqs.(2.59) and (2.60), yield

$$\eta_{rk}(\xi,\tau) = \sum_{q=1}^{\infty} \phi_q(\xi)\left[P_{qrk}\, e^{j\omega_r \tau} + P^{*}_{qrk}\, e^{-j\omega^{*}_r \tau} \right] \quad , \quad \begin{matrix} r = 1,2,\ldots,\infty \, , \\ k = 1,2,\ldots,2K \, . \end{matrix} \tag{2.63}$$

In order that equations may be written in more compact form, we define the following parameters:

$$a_k = \frac{m_k}{m_0}\gamma_C - \frac{A_k}{A_0}\gamma_F + \frac{1}{2}\frac{D_k}{D_0}\varepsilon c_f\left(1+\frac{D_k}{D_0}h\right)u^2 \quad , \quad k = 1,2,\ldots,K \, , \tag{2.64}$$

$$b_k = \frac{W_k}{W_0}\Gamma_A + \frac{m_k}{m_0}\gamma_C + \delta\left[\frac{\bar{T}_k}{\bar{T}_0}\Gamma + (1-2\nu_k)\frac{A_k}{A_0}\pi\right] + \frac{(1-\delta)}{2}\frac{A_k}{A_0}\frac{C_{b_k}}{C_{b_0}}c_{b_0}u^2$$

$$+ \frac{1}{2}\frac{D_k}{D_0}c_f u^2\left[\frac{(2-\delta)}{2}\left(1+\frac{D_k}{D_0}h\right)\varepsilon + (1-\delta)\left(\varepsilon_1 + \frac{D_k}{D_0}\frac{L_{W_k}}{L_W}\varepsilon_W h\right)\right]$$

$$- \gamma_F\frac{A_k}{A_0}\left[\frac{(2-\delta)}{2} + (1-\delta)\frac{L_{W_k}}{L_W}\frac{\varepsilon_W}{\varepsilon}\right] \quad , \quad k = 1,2,\ldots,K \, , \tag{2.65}$$

and

$$c_k = \frac{m_k}{m_0}\gamma_C - \frac{A_k}{A_0}\left(\gamma_F - \frac{1}{2}\varepsilon c_f h u^2\right) \quad , \quad k = 1,2,\ldots,K \, . \tag{2.66}$$

Now, equations of motion (2.56) and (2.57) apply not only to the total response η_k, defined by eqn.(2.58), but also to each component η_{rk} separately (at each frequency ω_r, see Appendix D). Hence, eqn.(2.56) is written in terms of η_{rk} and expanded using the relation*

$$\frac{D}{D\tau} = \frac{\partial}{\partial\tau} + \frac{u}{\sqrt{\beta}}\frac{\partial}{\partial\xi} \quad , \tag{2.67}$$

together with eqs.(2.64), (2.65), and (2.66) ,yielding for the z-direction

$$\frac{m_k}{m_0}(1-\beta)\frac{\partial^2\eta_{rk}}{\partial\tau^2} + \frac{I_k}{I_0}\frac{\mu_k}{\mu_0}\alpha\frac{\partial^5\eta_{rk}}{\partial\xi^4\partial\tau} + \frac{I_k}{I_0}\frac{\lambda_k}{\lambda_0}T\frac{\partial^5}{\partial\xi^4\partial\tau}\frac{\eta_{rk}}{|\mathrm{Re}(\omega_r)|}$$

$$+ \frac{E_k}{E_0}\frac{I_k}{I_0}\frac{\partial^4\eta_{rk}}{\partial\xi^4} + a_k\xi\frac{\partial^2\eta_{rk}}{\partial\xi^2} - b_k\frac{\partial^2\eta_{rk}}{\partial\xi^2} + c_k\frac{\partial\eta_{rk}}{\partial\xi} + \sum_{i=1}^{K}\left\{ - \frac{A_k}{A_0}\left[\beta\left(\varepsilon_{ki}\frac{\partial^2\eta_{ri}}{\partial\tau^2}\right.\right.\right.$$

---

* Dimensionless form of the total derivative $\frac{D}{Dt} = \frac{\partial}{\partial t} + U\frac{\partial}{\partial x}$.

$$+ e_{ki} \frac{\partial^2 \eta_{r(i+K)}}{\partial \tau^2} \Big] + 2\sqrt{\beta}\, u \Big[\varepsilon_{ki} \frac{\partial^2 \eta_{ri}}{\partial \xi \partial \tau} + e_{ki} \frac{\partial^2 \eta_{r(i+K)}}{\partial \xi \partial \tau} \Big] + u^2 \Big[\varepsilon_{ki} \frac{\partial^2 \eta_{ri}}{\partial \xi^2}$$

$$+ e_{ki} \frac{\partial^2 \eta_{r(i+K)}}{\partial \xi^2} \Big] \Big] + \frac{1}{2} \frac{D_k}{D_0} \varepsilon \Big[\sqrt{\beta}\, (c_f u + c) \Big[\zeta_{ki} \frac{\partial \eta_{ri}}{\partial \tau} + g_{ki} \frac{\partial \eta_{r(i+K)}}{\partial \tau} \Big]$$

$$+ c_f u^2 \Big[\zeta_{ki} \frac{\partial \eta_{ri}}{\partial \xi} + g_{ki} \frac{\partial \eta_{r(i+K)}}{\partial \xi} \Big] \Big] \Big\} = 0, \qquad \begin{matrix} r = 1,2,\ldots,\infty, \\ k = 1,2,\ldots,K, \end{matrix} \tag{2.68}$$

with a similar expression for the y-direction. Note that eqs.(2.64), (2.65), and (2.66) have been used.

It will prove easier to work with phasors (see Appendix D for proof that phasors can be used here) in the process of finding a solution to the equations of motion. Corresponding to eqn.(2.63), we define the phasor

$$\eta_{rk}(\xi,\tau) = \sum_{q=1}^{\infty} \phi_q(\xi)\, P_{qrk}\, e^{j\omega_r \tau}, \qquad \begin{matrix} r = 1,2,\ldots,\infty, \\ k = 1,2,\ldots 2K. \end{matrix} \tag{2.69}$$

Let

$$\eta_{rk}(\xi,\tau) \Rightarrow \eta_{rk}(\xi,\tau), \qquad \begin{matrix} r = 1,2,\ldots,\infty, \\ k = 1,2,\ldots 2K, \end{matrix} \tag{2.70}$$

in eqn.(2.68), which yields the phasor equation(s) of motion (z-direction)

$$\sum_{q=1}^{\infty} \Bigg[\Big\{ \frac{m_k}{m_0} (1-\beta) \phi_q(\xi) \frac{d^2}{d\tau^2} + \frac{I_k}{I_0} \frac{\mu_k}{\mu_0} \alpha \frac{d^4 \phi_q(\xi)}{d\xi^4} \frac{d}{d\tau} + \frac{I_k}{I_0} \frac{\lambda_k}{\lambda_0} T \frac{d^4 \phi_q(\xi)}{d\xi^4} \frac{1}{|\mathrm{Re}(\omega_r)|}$$

$$\cdot \frac{d}{d\tau} + \frac{E_k}{E_0} \frac{I_k}{I_0} \frac{d^4 \phi_q(\xi)}{d\xi^4} + a_k \xi \frac{d^2 \phi_q(\xi)}{d\xi^2} - b_k \frac{d^2 \phi_q(\xi)}{d\xi^2} + c_k \frac{d\phi_q(\xi)}{d\xi} \Big\} P_{qrk}\, e^{j\omega_r \tau}$$

$$+ \sum_{i=1}^{K} \Big\{ - \frac{A_k}{A_0} \Big[\beta \phi_q(\xi) \frac{d^2}{d\tau^2} + 2\sqrt{\beta}\, u \frac{d\phi_q(\xi)}{d\xi} \frac{d}{d\tau} + u^2 \frac{d^2 \phi_q(\xi)}{d\xi^2} \Big] \Big(\varepsilon_{ki} P_{qri} + e_{ki} P_{qr(i+K)} \Big)$$

$$+ \frac{1}{2} \frac{D_k}{D_0} \varepsilon \Big[\sqrt{\beta}\, (c_f u + c) \phi_q(\xi) \frac{d}{d\tau} + c_f u^2 \frac{d\phi_q(\xi)}{d\xi} \Big] \Big(\zeta_{ki} P_{qri} + g_{ki} P_{qr(i+K)} \Big) \Big\} \Bigg]$$

(continued)

$$\cdot\ e^{j\omega_r\tau} = 0, \qquad \begin{matrix} r = 1,2,\ldots,\infty\,, \\ k = 1,2,\ldots,K\,, \end{matrix} \tag{2.71}$$

with a similar expression for the y-direction.

Two simplifying assumptions are made, namely:

(i) damping is taken as light, so that

$\mathrm{Im}(\omega_r) \ll \mathrm{Re}(\omega_r)$, that is

$$\frac{\omega_r}{|\mathrm{Re}(\omega_r)|} \approx 1\ , \qquad r = 1,2,\ldots,\infty\,, \tag{2.72}$$

where it should be noted that, since phasors are used, ω_r is always positive (see eqn.(2.69)), and

(ii) a finite number of beam modes is sufficient to represent the vibrating cylinder. Truncation to N terms shall be used, and it will be shown later that N of the order of 10 is adequate for our purposes. Hence,

$$q_{max} = N\ . \tag{2.73}$$

Note that truncation (from ∞) to N limits the number of roots r to 4KN; this is because the system consists in K cylinders vibrating in two directions and in N beam modes, and obeying a second order differential equation. Hence,

$$r_{max} = 4KN\ . \tag{2.74}$$

Applying eqn.(2.72), we may write

$$\frac{1}{|\mathrm{Re}(\omega_r)|}\ \frac{d}{d\tau}\ P_{qrk}\ e^{j\omega_r\tau} = j\ P_{qrk}\ e^{j\omega_r\tau}\ , \qquad \begin{matrix} q = 1,2,\ldots,N\,, \\ r = 1,2,\ldots,4KN\,, \\ k = 1,2,\ldots,2K\,, \end{matrix} \tag{2.75}$$

where eqs.(2.73) and (2.74) have been taken into account.

Substituting eqn.(2.75) into eqn.(2.71) (and using eqs.(2.73) and (2.74)), we obtain

(a) for the z-direction

$$\sum_{q=1}^{N} \left[\left\{ \frac{m_k}{m_0}(1-\beta)\phi_q(\xi)\frac{d^2}{d\tau^2} + \frac{I_k}{I_0}\frac{\mu_k}{\mu_0}\alpha\frac{d^4\phi_q(\xi)}{d\xi^4}\frac{d}{d\tau} + \frac{I_k}{I_0}\frac{d^4\phi_q(\xi)}{d\xi^4} \right.\right.$$

$$\cdot \left(\frac{E_k}{E_0} + j\,\frac{\lambda_k}{\lambda_0}\,T \right) + a_k\xi\frac{d^2\phi_q(\xi)}{d\xi^2} - b_k\frac{d^2\phi_q(\xi)}{d\xi^2} + c_k\frac{d\phi_q(\xi)}{d\xi} \Big\}\, P_{qrk}$$

$$+ \sum_{i=1}^{K} \left\{ -\frac{A_k}{A_0}\left[\beta\phi_q(\xi)\frac{d^2}{d\tau^2} + 2\sqrt{\beta}\,u\frac{d\phi_q(\xi)}{d\xi}\frac{d}{d\tau} + u^2\frac{d^2\phi_q(\xi)}{d\xi^2} \right] \left(\varepsilon_{ki}\, P_{qri} \right.\right.$$

$$\left.\left. + e_{ki}\, P_{qr(i+K)} \right) + \frac{1}{2}\frac{D_k}{D_0}\,\varepsilon\left[\sqrt{\beta}\,(c_f u + c)\phi_q(\xi)\frac{d}{d\tau} + c_f u^2\frac{d\phi_q(\xi)}{d\xi} \right]$$

$$\left.\left. \cdot \left(\zeta_{ki}\, P_{qri} + g_{ki}\, P_{qr(i+K)} \right) \right\} \right] e^{j\omega_r\tau} = 0, \qquad \begin{matrix} r = 1,2,\ldots,4KN\,, \\ k = 1,2,\ldots,K\,; \end{matrix} \tag{2.76}$$

and since equations of motion will be put in matrix form, we also write out, for visualization purposes,

(b) the y-direction equations of motion:

$$\sum_{q=1}^{N} \left[\left\{ \frac{m_{k-K}}{m_0}(1-\beta)\phi_q(\xi)\frac{d^2}{d\tau^2} + \frac{I_{k-K}}{I_0}\frac{\mu_{k-K}}{\mu_0}\alpha\frac{d^4\phi_q(\xi)}{d\xi^4}\frac{d}{d\tau} + \frac{I_{k-K}}{I_0}\frac{d^4\phi_q(\xi)}{d\xi^4} \right.\right.$$

$$\cdot \left(\frac{E_{k-K}}{E_0} + j\,\frac{\lambda_{k-K}}{\lambda_0}\,T \right) + a_{k-K}\,\xi\frac{d^2\phi_q(\xi)}{d\xi^2} - b_{k-K}\frac{d^2\phi_q(\xi)}{d\xi^2} + c_{k-K}\frac{d\phi_q(\xi)}{d\xi} \Big\}\, P_{qrk}$$

$$+ \sum_{i=1}^{K} \left\{ -\frac{A_{k-K}}{A_0}\left[\beta\phi_q(\xi)\frac{d^2}{d\tau^2} + 2\sqrt{\beta}\,u\frac{d\phi_q(\xi)}{d\xi}\frac{d}{d\tau} + u^2\frac{d^2\phi_q(\xi)}{d\xi^2} \right] \left(\kappa_{(k-K)i}\, P_{qri} \right.\right.$$

$$\left.\left. + k_{(k-K)i}\, P_{qr(i+K)} \right) + \frac{1}{2}\frac{D_{k-K}}{D_0}\,\varepsilon\left[\sqrt{\beta}\,(c_f u + c)\phi_q(\xi)\frac{d}{d\tau} + c_f u^2\frac{d\phi_q(\xi)}{d\xi} \right]$$

$$\left.\left. \left(\sigma_{(k-K)i}\, P_{qri} + s_{(k-K)i}\, P_{qr(i+K)} \right) \right\} \right] e^{j\omega_r\tau} = 0, \qquad \begin{matrix} r = 1,2,\ldots,4KN\,, \\ k = K+1,K+2,\ldots,2K\,. \end{matrix} \tag{2.77}$$

Now, we define

$$\left\{P(\tau)\right\}_{qr} = \begin{Bmatrix} P_{qr1} \\ P_{qr2} \\ \cdot \\ \cdot \\ P_{qr(2K)} \end{Bmatrix} e^{j\omega_r \tau} \quad , \qquad \begin{matrix} q = 1,2,\ldots,N \, , \\ r = 1,2,\ldots,4KN \, , \end{matrix} \tag{2.78}$$

a (2K x 1) vector.

Then, eqs.(2.76) and (2.77) can be written in matrix form as

$$\sum_{q=1}^{N} \Bigg[\Big[M\Big] \phi_q(\xi) \frac{d^2}{d\tau^2} + \Big[C\Big] \frac{d^4\phi_q(\xi)}{d\xi^4} \frac{d}{d\tau} + \Big(\Big[K_1\Big] + j\Big[K_2\Big]\Big) \frac{d^4\phi_q(\xi)}{d\xi^4}$$

$$+ \Big[F\Big] \xi \frac{d^2\phi_q(\xi)}{d\xi^2} + \Big[E\Big] \frac{d^2\phi_q(\xi)}{d\xi^2} + \Big[G\Big] \frac{d\phi_q(\xi)}{d\xi} + \Big(\Big[R\Big] \phi_q(\xi) \frac{d^2}{d\tau^2}$$

$$+ \Big[S\Big] \frac{d\phi_q(\xi)}{d\xi} \frac{d}{d\tau} + \Big[T\Big] \frac{d^2\phi_q(\xi)}{d\xi^2}\Big) \Big[M_V\Big] + \Big(\Big[X\Big] \phi_q(\xi) \frac{d}{d\tau} + \Big[Y\Big] \frac{d\phi_q(\xi)}{d\xi}\Big)$$

$$\cdot \Big[C_V\Big]\Bigg] \Big\{P(\tau)\Big\}_{qr} = \Big\{0\Big\} \quad , \qquad r = 1,2,\ldots,4KN \, ,$$

which may be rewritten more concisely as

$$\sum_{q=1}^{N} \Bigg[\Big(\Big[M\Big] + \Big[R\Big]\Big[M_V\Big]\Big) \phi_q(\xi) \frac{d^2}{d\tau^2} + \Big(\Big[C\Big] \frac{d^4\phi_q(\xi)}{d\xi^4} + \Big[S\Big]\Big[M_V\Big] \frac{d\phi_q(\xi)}{d\xi}$$

$$+ \Big[X\Big]\Big[C_V\Big] \phi_q(\xi)\Big) \frac{d}{d\tau} + \Big(\Big(\Big[K_1\Big] + j\Big[K_2\Big]\Big) \frac{d^4\phi_q(\xi)}{d\xi^4} + \Big[F\Big] \xi \frac{d^2\phi_q(\xi)}{d\xi^2}$$

$$+ \Big(\Big[E\Big] + \Big[T\Big]\Big[M_V\Big]\Big) \frac{d^2\phi_q(\xi)}{d\xi^2} + \Big(\Big[G\Big] + \Big[Y\Big]\Big[C_V\Big]\Big) \frac{d\phi_q(\xi)}{d\xi}\Big)\Bigg] \Big\{P(\tau)\Big\}_{qr} = \Big\{0\Big\}, \tag{2.79}$$

$$r = 1,2,\ldots,4KN \, ,$$

where eqs.(2.64), (2.65), and (2.66) have been used and where the various matrices are defined as follows:

- First, "ratio" matrices, which are diagonal, will be defined:

$$\left[R_m\right] = \left[\begin{array}{ccc:ccc} m_1/m_0 & m_2/m_0 & \cdots & m_K/m_0 & 0 & \\ \hdashline 0 & & & & m_1/m_0 & \cdots \quad m_K/m_0 \end{array}\right] ,$$

$$\left[R_\mu\right] = \left[\begin{array}{ccc:ccc} \mu_1/\mu_0 & \mu_2/\mu_0 & \cdots & \mu_K/\mu_0 & 0 & \\ \hdashline 0 & & & & \mu_1/\mu_0 & \cdots \quad \mu_K/\mu_0 \end{array}\right] , \tag{2.80}$$

and similarly defined matrices

$$\left[R_E\right], \left[R_\lambda\right], \left[R_D\right], \left[R_W\right], \left[R_T\right], \left[R_\nu\right], \left[R_{C_b}\right] \text{ and } \left[R_{L_W}\right] .$$

Note that we will be using the relations

$$\begin{aligned} \left[R_A\right] &= \left[R_D\right]^2 , \\ \left[R_I\right] &= \left[R_D\right]^4 , \end{aligned} \tag{2.81}$$

which stem from the facts that A (area) $\propto D^2$ (diameter squared) and I (the second moment of area) $\propto D^4$.

- Furthermore, we have the following definitions:

$$\left[M\right] = (1 - \beta)\left[R_m\right] ,$$

$$\left[C\right] = \alpha\left[R_I\right]\left[R_\mu\right] ,$$

$$\left[K_1\right] = \left[R_E\right]\left[R_I\right] ,$$

$$\left[K_2\right] = T\left[R_I\right]\left[R_\lambda\right] ,$$

$$\left[F\right] = \gamma_C\left[R_m\right] - \gamma_F\left[R_A\right] + \frac{1}{2}\varepsilon c_f u^2\left[R_D\right]\left(\left[I\right] + h\left[R_D\right]\right) ,$$

$$\left[E\right] = -\left\{\Gamma_A\left[R_W\right] + \gamma_C\left[R_m\right] + \delta\left(\Gamma\left[R_T\right] + \left(\left[I\right] - 2\nu\left[R_\nu\right]\right)\cdot\pi\left[R_A\right]\right)\right.$$

(continued)

$$+ \frac{(1-\delta)}{2}\left[R_A\right]\left[R_{C_b}\right]c_{b_0}u^2 + \frac{1}{2}\left[R_D\right]c_f u^2\left\{\frac{(2-\delta)}{2}\left(\left[I\right]+\left[R_D\right]h\right)\varepsilon + (1-\delta)\right.$$

$$\left.\cdot\left(\varepsilon_1\left[I\right]+\left[R_D\right]\left[R_{L_W}\right]\varepsilon_W h\right)\right\} - \frac{1}{2}\gamma_F\left[R_A\right]\left\{(2-\delta)\left[I\right]+(1-\delta)\left[R_{L_W}\right]\frac{\varepsilon_W}{\varepsilon}\right\},$$

$$\left[G\right] = \gamma_C\left[R_m\right] - \left(\gamma_F - \frac{1}{2}\varepsilon c_f h u^2\right)\left[R_A\right], \tag{2.82}$$

$$\left[R\right] = -\beta\left[R_A\right],$$

$$\left[S\right] = -2\sqrt{\beta}\,u\left[R_A\right],$$

$$\left[T\right] = -u^2\left[R_A\right],$$

$$\left[X\right] = \frac{1}{2}\varepsilon\sqrt{\beta}\,(c_f u + c)\left[R_D\right],$$

$$\left[Y\right] = \frac{1}{2}\varepsilon c_f u^2\left[R_D\right],$$

where $\left[I\right]$ is the identity matrix.

Finally, we have

$$\left[M_V\right] = \left[\begin{array}{c|c}\left[\varepsilon\right] & \left[e\right] \\ \hline \left[\kappa\right] & \left[k\right]\end{array}\right], \qquad \left[C_V\right] = \left[\begin{array}{c|c}\left[\zeta\right] & \left[g\right] \\ \hline \left[\sigma\right] & \left[s\right]\end{array}\right], \tag{2.83}$$

where $\left[\varepsilon\right]$ has elements ε_{mn}, $m,n = 1,2,\ldots,K$, and so on, and where the subscript V denotes "virtual" (mass and damping) matrices.

The orthogonality properties of the beam modes can be utilized to eliminate the spatial variable ξ from eqn.(2.79). We recall (from Appendix G) the normalized* beam modes for clamped-clamped boundary conditions:

---

* Per eqn.(2.61).

$$\phi_q(\xi) = \cos(\lambda_q\xi) - \cosh(\lambda_q\xi) - \sigma_q\left[\sin(\lambda_q\xi) - \sinh(\lambda_q\xi)\right] \quad , \quad q = 1,2,\ldots,\infty \, , \tag{2.84}$$

where we will actually consider only the first N modes. λ_q and σ_q are characteristic constants evaluated by imposing relevant displacement, slope, and/or bending moment conditions at the ends of the beam under analysis. Values can be found in Appendix H. We find (see Appendix G)

$$\begin{aligned}
&\int_0^1 \phi_q(\xi)\cdot\phi_s(\xi)\cdot d\xi = \delta_{sq} \quad , \\
&\int_0^1 \frac{d\phi_q(\xi)}{d\xi}\cdot\phi_s(\xi)\cdot d\xi = a_{sq} \quad , \\
&\int_0^1 \frac{d^2\phi_q(\xi)}{d\xi^2}\cdot\phi_s(\xi)\cdot d\xi = b_{sq} \quad , \\
&\int_0^1 \frac{d^4\phi_q(\xi)}{d\xi^4}\cdot\phi_s(\xi)\cdot d\xi = c_{sq} \quad , \\
&\int_0^1 \frac{d^2\phi_q(\xi)}{d\xi^2}\cdot\xi\cdot\phi_s(\xi)\cdot d\xi = d_{sq} \quad , \qquad s,q = 1,2,\ldots,\infty \, ,
\end{aligned} \tag{2.85}$$

where again, we shall use only N modes.

In the above equations, δ_{sq} is the Kronecker delta, i.e.

$$\delta_{sq} = \begin{cases} 1 & , \ s = q, \\ 0 & , \ s \neq q, \end{cases} \tag{2.86}$$

and we have (see Appendix G)

$$a_{sq} = \begin{cases} 0 & , \ s = q, \\ \dfrac{4\lambda_q^2\lambda_s^2}{\lambda_q^4 - \lambda_s^4}\left[(-1)^{q+s} - 1\right] & , \ s \neq q, \end{cases}$$

$$b_{sq} = \begin{cases} \lambda_q\sigma_q(2 - \lambda_q\sigma_q) & , \ s = q, \\ \dfrac{4\lambda_q^2\lambda_s^2}{\lambda_q^4 - \lambda_s^4}\left[(-1)^{q+s} + 1\right](\lambda_q\sigma_q - \lambda_s\sigma_s) & , \ s \neq q, \end{cases} \tag{2.87}$$

(continued)

$$c_{sq} = \delta_{sq}\lambda_q^4 \ ,$$

$$d_{sq} = \begin{cases} b_{qq}/2 & , \ s = q, \\ \dfrac{4\lambda_s^2\lambda_q^2}{\lambda_q^4 - \lambda_s^4}\left[(-1)^{s+q}\left[\lambda_q\sigma_q - \lambda_s\sigma_s\right] - \dfrac{(3\lambda_q^4 + \lambda_s^4)\left[(-1)^{s+q} - 1\right]}{(\lambda_q^4 - \lambda_s^4)}\right] & , \ s \neq q, \end{cases}$$

$$s,q = 1,2,\ldots,\infty \ .$$

Multiplying eqn.(2.79) by $\phi_s(\xi)$ and integrating over ξ in (0,1), and making use of eqn.(2.85), we obtain the matrix phasor equations of motion, now solely functions of time (as the independent parameter):

$$\left\{\left(\left[M\right] + \left[R\right]\left[M_V\right]\right)\frac{d}{d\tau^2} + \left(\lambda_s^4\left[C\right] + \left[X\right]\left[C_V\right]\right)\frac{d}{d\tau} + \lambda_s^4\left(\left[K_1\right] + j\left[K_2\right]\right)\right\}$$

$$\left\{P\right\}_{sr} + \sum_{q=1}^{N}\left\{d_{sq}\left[F\right] + b_{sq}\left(\left[E\right] + \left[T\right]\left[M_V\right]\right) + a_{sq}\left(\left[G\right] + \left[Y\right]\left[C_V\right]\right)\right.$$

$$\left. + a_{sq}\left[S\right]\left[M_V\right]\frac{d}{d\tau}\right\}\left\{P\right\}_{qr} = \left\{0\right\} \ , \qquad (2.88)$$

$$s = 1,2,\ldots,N \ ,$$
$$r = 1,2,\ldots,4KN \ .$$

The latter N matrix equations of motion can be assembled into a single (higher dimension) matrix equation, by defining global matrices, as follows:

Let

$$\left\{P(\tau)\right\}_r = \begin{Bmatrix} (P(\tau))_{1r} \\ (P(\tau))_{2r} \\ \cdot \\ \cdot \\ (P(\tau))_{Nr} \end{Bmatrix} \ , \quad r = 1,2,\ldots,4KN \ , \qquad (2.89)$$

a (2KN x 1) vector (each component vector is (2K x 1); see eqn.(2.78)), and

$$\left[M_G\right] = \begin{bmatrix} \left[M\right] + \left[R\right]\left[M_V\right] & \left[0\right] & \cdots & \\ \left[0\right] & \left[M\right] + \left[R\right]\left[M_V\right] & & \\ \vdots & & \ddots & \\ & & & \left[M\right] + \left[R\right]\left[M_V\right] \end{bmatrix} \ ,$$

$$
\left[C_G\right] = \begin{bmatrix} \lambda_1^4\left[C\right]+\left[X\right]\left[C_V\right] & \left[0\right] & \cdots & \\ \left[0\right] & \lambda_2^4\left[C\right]+\left[X\right]\left[C_V\right] & \cdots & \\ \vdots & & & \\ & & & \lambda_N^4\left[C\right]+\left[X\right]\left[C_V\right] \end{bmatrix}
$$

$$
+ \begin{bmatrix} a_{11}\left[S\right]\left[M_V\right] & a_{12}\left[S\right]\left[M_V\right] & \cdots & a_{1N}\left[S\right]\left[M_V\right] \\ a_{21}\left[S\right]\left[M_V\right] & a_{22}\left[S\right]\left[M_V\right] & \cdots & a_{2N}\left[S\right]\left[M_V\right] \\ \vdots & \vdots & & \vdots \\ a_{N1}\left[S\right]\left[M_V\right] & a_{N2}\left[S\right]\left[M_V\right] & \cdots & a_{NN}\left[S\right]\left[M_V\right] \end{bmatrix}, \tag{2.90}
$$

and

$$
\left[K_G\right] = \begin{bmatrix} \lambda_1^4\left(\left[K_1\right]+j\left[K_2\right]\right) & \left[0\right] & \cdots & \\ \left[0\right] & \lambda_2^4\left(\left[K_1\right]+j\left[K_2\right]\right) & \cdots & \\ \vdots & & & \\ & & & \lambda_N^4\left(\left[K_1\right]+j\left[K_2\right]\right) \end{bmatrix}
$$

$$
+ \begin{bmatrix} d_{11}\left[F\right] & d_{12}\left[F\right] & \cdots & d_{1N}\left[F\right] \\ d_{21}\left[F\right] & d_{22}\left[F\right] & \cdots & d_{2N}\left[F\right] \\ \vdots & \vdots & & \vdots \\ d_{N1}\left[F\right] & d_{N2}\left[F\right] & \cdots & d_{NN}\left[F\right] \end{bmatrix}
$$

$$
+ \begin{bmatrix} b_{11}\left(\left[E\right]+\left[T\right]\left[M_V\right]\right) & b_{12}\left(\left[E\right]+\left[T\right]\left[M_V\right]\right) & \cdots & b_{1N}\left(\left[E\right]+\left[T\right]\left[M_V\right]\right) \\ b_{21}\left(\left[E\right]+\left[T\right]\left[M_V\right]\right) & b_{22}\left(\left[E\right]+\left[T\right]\left[M_V\right]\right) & \cdots & b_{2N}\left(\left[E\right]+\left[T\right]\left[M_V\right]\right) \\ \vdots & \vdots & & \vdots \\ b_{N1}\left(\left[E\right]+\left[T\right]\left[M_V\right]\right) & b_{N2}\left(\left[E\right]+\left[T\right]\left[M_V\right]\right) & \cdots & b_{NN}\left(\left[E\right]+\left[T\right]\left[M_V\right]\right) \end{bmatrix}
$$

(continued)

$$+\left[\begin{array}{c|c|c|c} a_{11}\left(\left[G\right]+\left[Y\right]\left[C_V\right]\right) & a_{12}\left(\left[G\right]+\left[Y\right]\left[C_V\right]\right) & \cdots & a_{1N}\left(\left[G\right]+\left[Y\right]\left[C_V\right]\right) \\ \hline a_{21}\left(\left[G\right]+\left[Y\right]\left[C_V\right]\right) & a_{22}\left(\left[G\right]+\left[Y\right]\left[C_V\right]\right) & \cdots & a_{2N}\left(\left[G\right]+\left[Y\right]\left[C_V\right]\right) \\ \hline \vdots & \vdots & & \vdots \\ \hline a_{N1}\left(\left[G\right]+\left[Y\right]\left[C_V\right]\right) & a_{N2}\left(\left[G\right]+\left[Y\right]\left[C_V\right]\right) & \cdots & a_{NN}\left(\left[G\right]+\left[Y\right]\left[C_V\right]\right) \end{array}\right] ,$$

where $\left[0\right]$ is the null matrix. The global matrices are of dimension (2KN x 2KN). Note that $\left[K_G\right]$ is complex.

Using eqs.(2.89) and (2.90), we can write eqn.(2.88) as

$$\left[M_G\right]\left\{\ddot{P}(\tau)\right\}_r + \left[C_G\right]\left\{\dot{P}(\tau)\right\}_r + \left[K_G\right]\left\{P(\tau)\right\}_r = \left\{0\right\} \quad , \qquad r = 1,2,\ldots,4KN , \tag{2.91}$$

where dots denote time derivatives.

Finally, a solution is facilitated by a reduction of order of eqn.(2.91) (a standard procedure), by using the vector

$$\left\{a(\tau)\right\}_r = \left\{\begin{array}{c} \{\dot{P}(\tau)\}_r \\ \{P(\tau)\}_r \end{array}\right\} , \qquad r = 1,2,\ldots,4KN , \tag{2.92}$$

so that eqn.(2.91) may be transformed to read

$$\left\{\dot{a}(\tau)\right\}_r - \left[A\right]\left\{a(\tau)\right\}_r = \left\{0\right\} \quad , \qquad r = 1,2,\ldots,4KN . \tag{2.93}$$

We find that

$$\left[A\right] = \left[\begin{array}{c|c} -\left[M_G\right]^{-1}\left[C_G\right] & -\left[M_G\right]^{-1}\left[K_G\right] \\ \hline \left[I\right] & \left[0\right] \end{array}\right] , \tag{2.94}$$

a square matrix of dimension (4KN x 4KN).

Now, from eqs.(2.92), (2.89), and (2.78), we see that

$$\left\{\dot{a}(\tau)\right\}_r = j\omega_r \left\{a(\tau)\right\}_r , \qquad r = 1,2,\ldots,4KN , \tag{2.95}$$

hence, eqn.(2.93) can be rewritten as an eigenvalue problem, namely

$$\left[j\omega_r \left[I \right] - \left[A \right] \right] \left\{ a(\tau) \right\}_r = \left\{ 0 \right\} \quad , \qquad r = 1,2,\ldots,4KN \, . \tag{2.96}$$

The solution of eqn.(2.96) yields

(i) The 4KN complex frequencies ω_r, the real and imaginary parts of which represents the frequency of oscillation and the damping, respectively (see eqs.(2.62), (2.50), and (2.21)); note that the eigenvalues are $j\omega_r$, i.e. $\omega_r = -j(\text{eigenvalue})_r$.

(ii) The components of the eigenvector(s) $\left\{ a \right\}_r$, which yield the components of $\left\{ P \right\}_r$, namely P_{qrk}, $q = 1,2,\ldots,N$ and $k = 1,2,\ldots,2K$ (for each r).

The response of any cylinder k, corresponding to the r^{th} frequency ω_r, is then given by η_{rk}, from eqn.(2.63), and the total response for that cylinder is η_k, given by eqn.(2.58).

To assist in visualizing how to use the eigenvalues and eigenvectors, we define the following variables:

$$T_{qrk}(\tau) = P_{qrk}\, e^{j\omega_r \tau} + P^*_{qrk}\, e^{-j\omega^*_r \tau} \quad , \qquad \begin{array}{l} q = 1,2,\ldots,N \, , \\ r = 1,2,\ldots,4KN \, , \\ k = 1,2,\ldots,2K \, , \end{array} \tag{2.97}$$

and

$$\omega_r = f_r + jd_r \quad , \qquad r = 1,2,\ldots,4KN \, , \tag{2.98}$$

and

$$P_{qrk} = u_{qrk} + jv_{qrk} \quad , \qquad \begin{array}{l} q = 1,2,\ldots,N \, , \\ r = 1,2,\ldots,4KN \, , \\ k = 1,2,\ldots,2K \, , \end{array} \tag{2.99}$$

Eqs.(2.97), (2.98), and (2.99) may be put in the form

$$T_{qrk}(\tau) = A_{qrk}\, e^{-d_r \tau} \cos(f_r \tau + \phi_{qrk}) \quad , \qquad \begin{matrix} q = 1,2,\ldots,N \, , \\ r = 1,2,\ldots,4KN \, , \\ k = 1,2,\ldots,2K \, , \end{matrix} \tag{2.100}$$

where

$$A_{qrk} = 2\left(u_{qrk}^2 + v_{qrk}^2\right)^{1/2} \quad , \tag{2.101}$$

$$\phi_{qrk} = \arctan\left(\frac{v_{qrk}}{u_{qrk}}\right) \quad , \qquad \begin{matrix} q = 1,2,\ldots,N \, , \\ r = 1,2,\ldots,4KN \, , \\ k = 1,2,\ldots,2K \, . \end{matrix}$$

Using eqn.(2.97) in eqn.(2.63) yields, limiting the response to the first N beam modes (see eqn.(2.73)),

$$\eta_{rk}(\xi,\tau) = \sum_{q=1}^{N} \phi_q(\xi) \cdot T_{qrk}(\tau) \quad , \qquad \begin{matrix} r = 1,2,\ldots,4KN \, , \\ k = 1,2,\ldots,2K \, . \end{matrix} \tag{2.102}$$

Note that r is now limited to 4KN (see eqn.(2.74)).

Each cylinder k has a total response given by eqn.(2.58), limited to the first N beam modes (hence limiting r), namely

$$\eta_k(\xi,\tau) = \sum_{r=1}^{4KN} \eta_{rk}(\xi,\tau) \quad , \qquad k = 1,2,\ldots,2K \, . \tag{2.103}$$

The mean flow model provides the following information about the system (note that theoretical results presented in this Thesis are obtained from the random model, to be derived shortly):

(i) Vibration frequencies and damping; as the system's equations can be reduced to the form of eqn.(2.91), the response is that of a freely vibrating coupled damped system.

(ii) For each characteristic frequency ω_r, the relative motion of cylinders with respect to each other, in the y-z plane. These will be called cross-sectional modes, and stem from the eigenvectors (and natural beam modes (see eqn.(2.97))).

(iii) Finally, for each characteristic frequency ω_r, the beam deflection modes can be computed, from eigenvectors and natural beam modes. These will be called axial modes, and occur in y-x and z-x planes.

2.5: RANDOM MODEL

2.5-1: Vibration response to net lateral forces

When $F_T \neq 0$ in eqn.(2.17) and using eqn.(2.21), the equation of motion (2.24) takes the form

$$m \frac{\partial^2 y}{\partial t^2} + \mu I \frac{\partial^5 y}{\partial x^4 \partial t} + \lambda I \frac{\partial^5}{\partial x^4 \partial t} \sum_{r=1}^{\infty} \frac{y_r}{|f_r|} + EI \frac{\partial^4 y}{\partial x^4} - \frac{\partial}{\partial x}\left[T \frac{\partial y}{\partial x} \right] - F_L \frac{\partial y}{\partial x}$$

$$- F_P + (F_A + F_N) = F_T \quad , \tag{2.104}$$

where F_T is the force per unit length acting on the beam (cylinder), due to the random normal pressure fluctuations in the boundary layer, where

$$F_T = F_T(x,t) . \tag{2.105}$$

It should be pointed out that random excitation and response will be obtained further on, as a limit of the periodic case, when the period tends to infinity (see Appendix D); this allows handling with ease the special form of the hysteretic damping term.

Having introduced a (periodic) force term that is independent of cylinder motion, namely F_T, we are now dealing with a classical case of forced vibration. The response y is assumed to be of the form

$$y(x,t) = \sum_{r=-\infty}^{\infty} y_r(x,t) \quad , \tag{2.106}$$

where

$$y_r(x,t) = \sum_{q=1}^{\infty} Y_q(x) \cdot P_{qr} \, e^{jf_r t} \quad , \qquad r = 0, \pm 1, \pm 2, \ldots, \pm\infty . \tag{2.107}$$

Note that the condition of steady state excitation and response is assumed here (classical forced vibration problem). Also, unlike eqs.(2.19) and (2.20), the summation over r is extended to negative values so as to yield, in the limiting case, Fourier transforms.

There is no DC (zero frequency) component to the forcing function (no average cross-flow), so we may write

$$P_{q0} = 0 \ , \qquad q = 1,2,\ldots,\infty \ . \tag{2.108}$$

Furthermore, eqs.(2.106) and (2.107) are a form of Fourier series with complex coefficients, hence, we must have (since y is real)

$$P_{q(-r)} = P_{qr}^{*} \ , \qquad \begin{array}{l} q = 1,2,\ldots,\infty \ , \\ r = 0,\pm 1,\pm 2,\ldots,\pm\infty \ , \end{array} \tag{2.109}$$

and (the f_r are real)

$$f_{-r} = -f_r \ , \qquad r = 0,\pm 1,\pm 2,\ldots,\pm\infty \ . \tag{2.110}$$

Note that

$$f_0 = 0 \ . \tag{2.111}$$

Following an approach similar to that for the Mean Flow Model, we let, for multi-cylinder systems

$$\begin{aligned} w_k(x,t) &= \sum_{r=-\infty}^{\infty} w_{rk}(x,t) \ , \\ v_k(x,t) &= \sum_{r=-\infty}^{\infty} v_{rk}(x,t) \ , \qquad k = 1,2,\ldots,K \ , \end{aligned} \tag{2.112}$$

where

$$\begin{aligned} w_{rk}(x,t) &= \sum_{q=1}^{\infty} Y_q(x) \cdot P_{qrk}\, e^{jf_r t} \ , \\ v_{rk}(x,t) &= \sum_{q=1}^{\infty} Y_q(x) \cdot P_{qr(k+K)}\, e^{jf_r t} \ , \qquad \begin{array}{l} r = 0,\pm 1,\pm 2,\ldots,\pm\infty \ , \\ k = 1,2,\ldots,K \ . \end{array} \end{aligned} \tag{2.113}$$

Similarly to the single cylinder case (see eqs.(2.108) and (2.109)), we have

$$P_{q0k} = 0 \ , \qquad \begin{array}{l} q = 1,2,\ldots,\infty \ , \\ k = 1,2,\ldots,2K \ , \end{array} \tag{2.114}$$

and

$$P_{q(-r)k} = P^{*}_{qrk} \quad , \qquad \begin{matrix} q = 1,2,\ldots,,\infty \, , \\ r = 0,\pm 1,\pm 2,\ldots,\pm\infty \, , \\ k = 1,2,\ldots,2K \, . \end{matrix} \tag{2.115}$$

We obtain equations of motion similar to eqs.(2.45) and (2.46), but with two differences:

(i) The hysteretic term now reads (dimensional, z-direction)

$$\lambda_k I_k \frac{\partial^5}{\partial x^4 \partial t} \sum_{r=-\infty}^{\infty} \frac{w_{rk}}{|f_r|} \quad ,$$

and

(ii) there is a forcing term

$$F_{T(z)k} \quad ;$$

and likewise for the y-direction.

The new terms $F_{T(z)k}$ and $F_{T(y)k}$ are the lateral forces per unit length on cylinder k and in directions z and y respectively, due to random pressure fluctuations in the boundary layer. These forces are assumed independent of cylinder motion.

Non-dimensionalization is effected as before (see eqs.(2.47) to (2.55) inclusively), and additionally, the dimensionless force (per unit length) reads

$$\Phi_k = \begin{cases} \left(L^3/E_0 I_0\right) \cdot F_{T(z)k} \, , & k = 1,2,\ldots,K \, , \\ \left(L^3/E_0 I_0\right) \cdot F_{T(y)(k-K)} \, , & k = K+1,K+2,\ldots,2K \, . \end{cases} \tag{2.116}$$

The dimensionless deflection now reads (steady state response)

$$\eta_k(\xi,\tau) = \sum_{r=-\infty}^{\infty} \eta_{rk}(\xi,\tau) \, , \qquad k = 1,2,\ldots,2K \, , \tag{2.117}$$

where

$$\eta_{rk}(\xi,\tau) = \sum_{q=1}^{\infty} \phi_q(\xi) \cdot P_{qrk}\, e^{j\omega_r \tau} \quad , \qquad \begin{matrix} r = 0,\pm1,\pm2,\ldots,\pm\infty \, , \\ k = 1,2,\ldots,2K \, . \end{matrix} \tag{2.118}$$

Eqn.(2.104) develops into a form similar to (2.71), but with a different hysteretic damping term and with an additional forcing term (see eqn. (2.116)):

$$\sum_{r=-\infty}^{\infty} \sum_{q=1}^{\infty} \left[\left\{ \frac{m_k}{m_0}(1-\beta)\,\phi_q(\xi)\frac{d^2}{d\tau^2} + \frac{I_k}{I_0}\frac{\mu_k}{\mu_0}\,\alpha\,\frac{d^4\phi_q(\xi)}{d\xi^4}\frac{d}{d\tau} + \frac{I_k}{I_0}\frac{\lambda_k}{\lambda_0}\,\Upsilon\,\frac{d^4\phi_q(\xi)}{d\xi^4} \right.\right.$$

$$\left. \cdot\, j\,\mathrm{sgn}(\omega_r) + \frac{E_k}{E_0}\frac{I_k}{I_0}\frac{d^4\phi_q(\xi)}{d\xi^4} + a_k\xi\,\frac{d^2\phi_q(\xi)}{d\xi^2} - b_k\,\frac{d^2\phi_q(\xi)}{d\xi^2} + c_k\,\frac{d\phi_q(\xi)}{d\xi} \right\} P_{qrk}$$

$$+ \sum_{l=1}^{K} \left\{ -\frac{A_k}{A_0} \left[\beta\phi_q(\xi)\frac{d^2}{d\tau^2} + 2\sqrt{\beta}\,u\,\frac{d\phi_q(\xi)}{d\xi}\frac{d}{d\tau} + u^2\,\frac{d^2\phi_q(\xi)}{d\xi^2} \right] \cdot \left[\varepsilon_{kl}\,P_{qrl} + e_{kl}\,P_{qr(l+K)} \right] \right.$$

$$\left. \left. + \frac{1}{2}\frac{D_k}{D_0}\,\varepsilon \left[\sqrt{\beta}\,(c_f u + c)\,\phi_q(\xi)\frac{d}{d\tau} + c_f u^2\,\frac{d\phi_q(\xi)}{d\xi} \right] \cdot \left[\zeta_{kl}\,P_{qrl} + g_{kl}\,P_{qr(l+K)} \right] \right\} \right] e^{j\omega_r\tau}$$

$$= \Phi_k(\xi,\tau) \quad , \qquad k = 1,2,\ldots,K \, , \tag{2.119}$$

and similarly for the y-direction (k = K+1,K+2,...,2K). Recall that a_k, b_k, and c_k are given by eqs.(2.64), (2.65) and (2.66), respectively.

Note that eqn.(2.50) has been used to define the (real) dimensionless frequency ω_r, namely

$$\omega_r = \left(\frac{m_0 + \rho A_0}{E_0 I_0} \right)^{1/2} L^2 f_r \quad , \qquad r = 0,\pm1,\pm2,\ldots,\pm\infty \, , \tag{2.120}$$

and the sign function has been used in the expression

$$\frac{1}{|\omega_r|}\frac{d}{d\tau}\, e^{j\omega_r\tau} = j \cdot \mathrm{sgn}(\omega_r) \cdot e^{j\omega_r\tau} \, . \tag{2.121}$$

As for the Mean Flow Model, the equations of motion can be written in matrix form; we obtain

$$\sum_{r=-\infty}^{\infty} \sum_{q=1}^{\infty} \left\{ \left[M \right] \phi_q(\xi)\frac{d^2}{d\tau^2} + \left[C \right] \frac{d^4\phi_q(\xi)}{d\xi^4}\frac{d}{d\tau} + \left(\left[K_1 \right] + j \cdot \mathrm{sgn}(\omega_r) \left[K_2 \right] \right) \right.$$

$$\cdot \frac{d^4\phi_q(\xi)}{d\xi^4} + \left[F\right]\xi\,\frac{d^2\phi_q(\xi)}{d\xi^2} + \left[E\right]\frac{d^2\phi_q(\xi)}{d\xi^2} + \left[G\right]\frac{d\phi_q(\xi)}{d\xi} + \left(\left[R\right]\phi_q(\xi)\,\frac{d^2}{d\tau^2}$$

$$+ \left[S\right]\frac{d\phi_q(\xi)}{d\xi}\,\frac{d}{d\tau} + \left[T\right]\frac{d^2\phi_q(\xi)}{d\xi^2}\right)\left[M_V\right] + \left(\left[X\right]\phi_q(\xi)\,\frac{d}{d\tau} + \left[Y\right]\frac{d\phi_q(\xi)}{d\xi}\right)$$

$$\cdot \left[C_V\right]\Big\} \cdot \left\{p(\tau)\right\}_{qr} = \left\{\Phi(\xi,\tau)\right\} \quad , \tag{2.122}$$

where matrices $\left[M\right]$, $\left[C\right]$,..., $\left[Y\right]$ are defined by eqs.(2.82) and (2.83), and where

$$\left\{p(\tau)\right\}_{qr} = \begin{Bmatrix} P_{qr1} \\ P_{qr2} \\ \cdot \\ \cdot \\ P_{qr(2K)} \end{Bmatrix} e^{j\omega_r\tau} \quad , \qquad \begin{matrix} q = 1,2,\ldots,\infty\,, \\ r = 0,\pm1,\pm2,\ldots,\pm\infty\,, \end{matrix} \tag{2.123}$$

and

$$\left\{\Phi(\xi,\tau)\right\} = \begin{Bmatrix} \Phi_1(\xi,\tau) \\ \Phi_2(\xi,\tau) \\ \cdot \\ \cdot \\ \Phi_{2K}(\xi,\tau) \end{Bmatrix} \quad . \tag{2.124}$$

As done previously, the space variable ξ may be eliminated from the equation(s) of motion by multiplying by $\phi_s(\xi)$, and integrating over ξ in (0,1). Eqn.(2.122) therefore takes the form

$$\sum_{r=-\infty}^{\infty}\Bigg[\Big\{\Big(\left[M\right]+\left[R\right]\left[M_V\right]\Big)\frac{d^2}{d\tau^2} + \Big(\lambda_s^4\left[C\right]+\left[X\right]\left[C_V\right]\Big)\frac{d}{d\tau} + \lambda_s^4\Big(\left[K_1\right]$$

$$+ j\cdot \mathrm{sgn}(\omega_r)\left[K_2\right]\Big)\Big\}\left\{p(\tau)\right\}_{sr} + \sum_{q=1}^{\infty}\Big\{d_{sq}\left[F\right] + b_{sq}\Big(\left[E\right]+\left[T\right]\left[M_V\right]\Big) + a_{sq}$$

$$\cdot\Big(\left[G\right]+\left[Y\right]\left[C_V\right]\Big) + a_{sq}\left[S\right]\left[M_V\right]\frac{d}{d\tau}\Big\}\left\{p(\tau)\right\}_{qr}\Bigg] = \left\{\Phi(\tau)\right\}_s \quad , \qquad \begin{matrix} \\ s = 1,2,\ldots,\infty\,, \end{matrix} \tag{2.125}$$

where

$$\left\{\Phi(\tau)\right\}_s = \int_0^1 \left\{\Phi(\xi,\tau)\right\}\cdot\phi_s(\xi)\cdot d\xi \quad , \qquad s = 1,2,\ldots,\infty\,. \tag{2.126}$$

To convert the problem from periodic to random, we use the procedure for obtaining Fourier integrals as a limiting case of Fourier series.

Firstly, we define $\{\Phi\}_s$ as a periodic quantity, represented by a Fourier series with complex coefficients:

$$\{\Phi(\tau)\}_s = \sum_{r=-\infty}^{\infty} \{Q\}_{sr} e^{j\omega_r \tau} \quad , \qquad s = 1,2,\ldots,\infty \, , \tag{2.127}$$

where the coefficients are found from the usual expression

$$\{Q\}_{sr} = \frac{1}{\tau_1} \cdot \int_{-\tau_1/2}^{+\tau_1/2} \{\Phi(\tau)\}_s \, e^{-j\omega_r \tau} \, d\tau \quad , \qquad \begin{matrix} s = 1,2,\ldots,\infty \, , \\ r = 0,\pm 1,\pm 2,\ldots,\pm\infty \, . \end{matrix} \tag{2.128}$$

Secondly, we define the dimensionless displacement vector

$$\{\eta(\xi,\tau)\} = \begin{Bmatrix} \eta_1(\xi,\tau) \\ \eta_2(\xi,\tau) \\ \cdot \\ \cdot \\ \eta_{2K}(\xi,\tau) \end{Bmatrix} \quad , \tag{2.129}$$

which may be written as

$$\{\eta(\xi,\tau)\} = \sum_{r=-\infty}^{\infty} \sum_{q=1}^{\infty} \phi_q(\xi) \{p(\tau)\}_{qr} \quad , \tag{2.130}$$

having used eqs.(2.117), (2.118), and (2.123).

Now, similarly to (2.126), let

$$\{\eta(\tau)\}_s = \int_0^1 \{\eta(\xi,\tau)\} \cdot \phi_s(\xi) \cdot d\xi \quad , \qquad s = 1,2,\ldots,\infty \, , \tag{2.131}$$

and by analogy to eqn.(2.127), we let

$$\{\eta(\tau)\}_s = \sum_{r=-\infty}^{\infty} \{P\}_{sr} e^{j\omega_r \tau} \quad , \qquad s = 1,2,\ldots,\infty \, , \tag{2.132}$$

where it can be shown (eqs.(2.117), (2.118), (2.85), (2.131), and (2.123)) that

$$\left\{P\right\}_{sr} = \begin{Bmatrix} P_{sr1} \\ P_{sr2} \\ \cdot \\ \cdot \\ P_{sr(2K)} \end{Bmatrix} , \qquad \begin{matrix} s = 1,2,\ldots,\infty , \\ r = 0,\pm 1,\pm 2,\ldots,\pm\infty . \end{matrix} \tag{2.133}$$

The Fourier coefficients in eqn.(2.132) are found simply from

$$\left\{P\right\}_{sr} = \frac{1}{\tau_1} \cdot \int_{-\tau_1/2}^{+\tau_1/2} \left\{\eta(\tau)\right\}_s e^{-j\omega_r \tau} \, d\tau , \qquad \begin{matrix} s = 1,2,\ldots,\infty , \\ r = 0,\pm 1,\pm 2,\ldots,\pm\infty . \end{matrix} \tag{2.134}$$

Note that, from eqs.(2.123) and (2.133), we may write

$$\left\{p(\tau)\right\}_{sr} = \left\{P\right\}_{sr} e^{j\omega_r \tau} , \qquad \begin{matrix} s = 1,2,\ldots,\infty , \\ r = 0,\pm 1,\pm 2,\ldots,\pm\infty . \end{matrix} \tag{2.135}$$

We now substitute eqs.(2.135) and (2.127) into the equation of motion (2.125). We get

$$\sum_{r=-\infty}^{\infty} \left[\left\{ \left(\left[M\right] + \left[R\right]\left[M_V\right] \right) \frac{d^2}{d\tau^2} + \left(\lambda_s^4 \left[C\right] + \left[X\right]\left[C_V\right] \right) \frac{d}{d\tau} + \lambda_s^4 \left(\left[K_1\right] + j \cdot \mathrm{sgn}(\omega_r) \left[K_2\right] \right) \right\} \left\{P\right\}_{sr} e^{j\omega_r \tau} + \sum_{q=1}^{\infty} \left\{ d_{sq} \left[F\right] + b_{sq} \left(\left[E\right] + \left[T\right]\left[M_V\right] \right) + a_{sq} \left(\left[G\right] + \left[Y\right]\left[C_V\right] \right) + a_{sq} \left[S\right]\left[M_V\right] \frac{d}{d\tau} \right\} \left\{P\right\}_{qr} e^{j\omega_r \tau} \right] = \sum_{r=-\infty}^{\infty} \left\{Q\right\}_{sr} e^{j\omega_r \tau} , \tag{2.136}$$

$$s = 1,2,\ldots,\infty .$$

Substitution of eqs.(2.134) and (2.128) into (2.136) yields

$$\sum_{r=-\infty}^{\infty} \left[\left\{ \left(\left[M\right] + \left[R\right]\left[M_V\right] \right) \frac{d^2}{d\tau^2} + \left(\lambda_s^4 \left[C\right] + \left[X\right]\left[C_V\right] \right) \frac{d}{d\tau} + \lambda_s^4 \left(\left[K_1\right] + j \cdot \mathrm{sgn}(\omega_r) \left[K_2\right] \right) \right\} e^{j\omega_r \tau} \cdot \frac{1}{\tau_1} \cdot \int_{-\tau_1/2}^{+\tau_1/2} \left\{\eta(\tau)\right\}_s e^{-j\omega_r \tau} \cdot d\tau + \sum_{q=1}^{\infty} \left\{ d_{sq} \left[F\right] + b_{sq} \left[E\right] + \left[T\right]\left[M_V\right] \right) + a_{sq} \left(\left[G\right] + \left[Y\right]\left[C_V\right] \right) + a_{sq} \left[S\right]\left[M_V\right] \frac{d}{d\tau} \right\} e^{j\omega_r \tau}$$

$$\cdot \frac{1}{\tau_1} \cdot \int_{-\tau_1/2}^{+\tau_1/2} \left\{\eta(\tau)\right\}_q e^{-j\omega_r \tau} \cdot d\tau \Big] = \sum_{r=-\infty}^{\infty} e^{j\omega_r \tau} \cdot \frac{1}{\tau_1} \cdot \int_{-\tau_1/2}^{+\tau_1/2} \left\{\Phi(\tau)\right\}_s e^{-j\omega_r \tau} \cdot d\tau \,, \tag{2.137}$$

$$s = 1,2,\ldots,\infty \,.$$

Note that, for the general periodic signal represented by either eqn. (2.132) or (2.127), we have

$$\omega_r = r\,\omega_1 \quad , \qquad r = 1,2,\ldots,\infty \,, \tag{2.138}$$

where ω_1 is the fundamental frequency and is related to the fundamental period by

$$\omega_1 = \frac{2\pi}{\tau_1} \quad . \tag{2.139}$$

Remark

The latter equation implies that the product of dimensionless time and frequency is in radians (hence the 2π (radians per cycle) factor), so that units used must conform to that requirement. Subsequent derivations assume that same condition.

Now, the limiting process is initiated by letting (see eqn.(2.138))

$$\Delta\omega_r = (r+1)\,\omega_1 - r\,\omega_1 = \omega_1 \quad , \tag{2.140}$$

and consequently (see eqn.(2.139)),

$$\Delta\omega_r = \frac{2\pi}{\tau_1} \quad , \qquad r = 0,\pm1,\pm2,\ldots,\pm\infty \,. \tag{2.141}$$

Using this last equation into eqn.(2.137) yields

$$\sum_{r=-\infty}^{\infty} \left[\left\{ \left(\left[M\right] + \left[R\right]\left[M_V\right] \right) \frac{d^2}{d\tau^2} + \left(\lambda_s^4 \left[C\right] + \left[X\right]\left[C_V\right] \right) \frac{d}{d\tau} + \lambda_s^4 \left(\left[K_1\right] \right.\right.\right.$$

$$\left.\left.\left. + j \cdot \mathrm{sgn}(\omega_r) \left[K_2\right] \right) \right\} e^{j\omega_r \tau} \cdot \Delta\omega_r \cdot \frac{1}{2\pi} \cdot \int_{-\tau_1/2}^{+\tau_1/2} \left\{\eta(\tau)\right\}_s e^{-j\omega_r \tau} \cdot d\tau + \sum_{q=1}^{\infty} \left\{ d_{sq} \left[F\right] \right.\right.$$

$$+ b_{sq}\left[E\right] + \left[T\right]\left[M_V\right]\Big) + a_{sq}\Big(\left[G\right] + \left[Y\right]\left[C_V\right]\Big) + a_{sq}\left[S\right]\left[M_V\right]\frac{d}{d\tau}\Big\} e^{j\omega_r\tau}$$

$$\cdot \Delta\omega_r \cdot \frac{1}{2\pi} \cdot \int_{-\tau_1/2}^{+\tau_1/2} \left\{\eta(\tau)\right\}_q e^{-j\omega_r\tau} \cdot d\tau \Bigg] = \sum_{r=-\infty}^{\infty} e^{j\omega_r\tau} \cdot \Delta\omega_r \cdot \frac{1}{2\pi}$$

$$\cdot \int_{-\tau_1/2}^{+\tau_1/2} \left\{\Phi(\tau)\right\}_s e^{-j\omega_r\tau} \cdot d\tau \,, \qquad s = 1,2,\ldots,\infty \,. \tag{2.142}$$

Now we let

$$\tau_1 \to \infty \,, \tag{2.143}$$

i.e. $\omega_1 \to 0$ $(\omega_1\tau_1 = 2\pi = \text{constant})$, and

$$\omega_r \to \omega \,,$$
$$\Delta\omega_r \to d\omega \,, \tag{2.144}$$

hence, in view of (2.142) and (2.144), the limiting case when the period τ_1 tends to infinity, becomes,

$$\int_{-\infty}^{+\infty} \Bigg[\Bigg\{\Big(\left[M\right] + \left[R\right]\left[M_V\right]\Big)\frac{d^2}{d\tau^2} + \Big(\lambda_s^4\left[C\right] + \left[X\right]\left[C_V\right]\Big)\frac{d}{d\tau} + \lambda_s^4\Big(\left[K_1\right]$$

$$+ j\cdot \mathrm{sgn}(\omega)\left[K_2\right]\Big)\Bigg\} e^{j\omega\tau} \cdot d\omega \cdot \frac{1}{2\pi} \cdot \int_{-\infty}^{+\infty} \left\{\eta(\tau)\right\}_s e^{-j\omega\tau} \cdot d\tau + \sum_{q=1}^{\infty}\Big\{d_{sq}\left[F\right]$$

$$+ b_{sq}\left[E\right] + \left[T\right]\left[M_V\right]\Big) + a_{sq}\Big(\left[G\right] + \left[Y\right]\left[C_V\right]\Big) + a_{sq}\left[S\right]\left[M_V\right]\frac{d}{d\tau}\Big\} e^{j\omega\tau}$$

$$\cdot d\omega \cdot \frac{1}{2\pi} \cdot \int_{-\infty}^{\infty} \left\{\eta(\tau)\right\}_q e^{-j\omega\tau} \cdot d\tau \Bigg] = \int_{-\infty}^{+\infty} e^{j\omega\tau} \cdot d\omega \cdot \frac{1}{2\pi} \cdot \int_{-\infty}^{+\infty} \left\{\Phi(\tau)\right\}_s e^{-j\omega\tau} \cdot d\tau \,, \tag{2.145}$$

$$s = 1,2,\ldots,\infty \,.$$

In the above equation, we recognize Fourier transforms, which are defined as

$$\left\{\eta(\omega)\right\}_s = \frac{1}{2\pi} \cdot \int_{-\infty}^{+\infty} \left\{\eta(\tau)\right\}_s e^{-j\omega\tau} \cdot d\tau \quad , \qquad s = 1,2,\ldots,\infty \, . \tag{2.146}$$

and

$$\left\{\Phi(\omega)\right\}_s = \frac{1}{2\pi} \cdot \int_{-\infty}^{+\infty} \left\{\Phi(\tau)\right\}_s e^{-j\omega\tau} \cdot d\tau \quad , \qquad s = 1,2,\ldots,\infty \, , \tag{2.147}$$

Using eqs.(2.146) and (2.147) into (2.145) now results in the equation

$$\left[\left\{\left(\left[M\right] + \left[R\right]\left[M_V\right]\right)\frac{d^2}{d\tau^2} + \left(\lambda_s^4\left[C\right] + \left[X\right]\left[C_V\right]\right)\frac{d}{d\tau} + \lambda_s^4\left[K_1\right]\right\}\right.$$

$$\cdot \int_{-\infty}^{+\infty} \left\{\eta(\omega)\right\}_s e^{j\omega\tau} \cdot d\omega + \lambda_s^4\left[K_2\right] \cdot \left.\int_{-\infty}^{+\infty} j \cdot \mathrm{sgn}(\omega) \cdot \left\{\eta(\omega)\right\}_s e^{j\omega\tau} \cdot d\omega\right]$$

$$+ \sum_{q=1}^{\infty} \left[d_{sq}\left[F\right] + b_{sq}\left(\left[E\right] + \left[T\right]\left[M_V\right]\right) + a_{sq}\left(\left[G\right] + \left[Y\right]\left[C_V\right]\right)\right.$$

$$\left. + a_{sq}\left[S\right]\left[M_V\right]\frac{d}{d\tau}\right] \cdot \int_{-\infty}^{+\infty} \left\{\eta(\omega)\right\}_q e^{j\omega\tau} \cdot d\omega = \int_{-\infty}^{+\infty} \left\{\Phi(\omega)\right\}_s e^{j\omega\tau} \cdot d\omega \quad , \tag{2.148}$$

$$s = 1,2,\ldots,\infty \, .$$

Equation (2.148) contains inverse Fourier transforms, namely the converse of eqs.(2.146) and (2.147),

$$\left\{\eta(\tau)\right\}_s = \int_{-\infty}^{+\infty} \left\{\eta(\omega)\right\}_s e^{j\omega\tau} \cdot d\omega \quad , \qquad s = 1,2,\ldots,\infty \, , \tag{2.149}$$

and

$$\left\{\Phi(\tau)\right\}_s = \int_{-\infty}^{+\infty} \left\{\Phi(\omega)\right\}_s e^{j\omega\tau} \cdot d\omega \quad , \qquad s = 1,2,\ldots,\infty \, , \tag{2.150}$$

respectively, and a Hilbert transform

$$\left\{\eta_H(\tau)\right\}_s = \int_{-\infty}^{+\infty} -j \cdot \mathrm{sgn}(\omega) \cdot \left\{\eta(\omega)\right\}_s e^{j\omega\tau} \cdot d\omega \quad , \qquad s = 1,2,\ldots,\infty \, . \tag{2.151}$$

Remark

For correct units (when dimensional forms are recomputed), Fourier transform pairs must appear as in eqs.(2.146) and (2.149). See Appendix I for more details.

As shown in Appendix D, even in the presence of Hilbert transforms (stemming from the modelling of hysteretic damping), eqn.(2.148) can be written in transfer function form, namely

$$\left(-\omega^2 \left(\left[M \right] + \left[R \right] \left[M_V \right] \right) + j\omega \left(\lambda_s^4 \left[C \right] + \left[X \right] \left[C_V \right] \right) + \lambda_s^4 \left(\left[K_1 \right] + j \left[K_2 \right] \right) \right)$$

$$\cdot \left\{ \eta(\omega) \right\}_s + \sum_{q=1}^{N} \left(j\omega \cdot a_{sq} \left[S \right] \left[M_V \right] + d_{sq} \left[F \right] + b_{sq} \left(\left[E \right] + \left[T \right] \left[M_V \right] \right) \right.$$

$$\left. + a_{sq} \left(\left[G \right] + \left[Y \right] \left[C_V \right] \right) \right) \cdot \left\{ \eta(\omega) \right\}_q = \left\{ \Phi(\omega) \right\}_s \quad , \begin{array}{l} (\omega \geq 0) \\ s = 1,2,\ldots,N \end{array} , \tag{2.152}$$

where the number of beam modes has been truncated to N (the q and s indices above).

The summation (over q) in eqn.(2.152) can be dispensed with by assembly into a larger dimension matrix equation, yielding

$$\left(-\omega^2 \left[M_G \right] + j\omega \left[C_G \right] + \left[K_G \right] \right) \cdot \left\{ \eta(\omega)_G \right\} = \left\{ \Phi(\omega)_G \right\} \quad , \tag{2.153}$$

where $\left[M_G \right]$, $\left[C_G \right]$ and $\left[K_G \right]$ are the "global" matrices defined by eqn. (2.90), and where we have used the "global" vectors

$$\left\{ \eta(\omega)_G \right\} = \begin{Bmatrix} \{\eta(\omega)\}_1 \\ \{\eta(\omega)\}_2 \\ \cdot \\ \cdot \\ \{\eta(\omega)\}_N \end{Bmatrix} \quad , \tag{2.154}$$

and

$$\left\{ \Phi(\omega)_G \right\} = \begin{Bmatrix} \{\Phi(\omega)\}_1 \\ \{\Phi(\omega)\}_2 \\ \cdot \\ \cdot \\ \{\Phi(\omega)\}_N \end{Bmatrix} \quad . \tag{2.155}$$

Now, eqn.(2.153) may be written in standard form as

$$\left\{\eta(\omega)_G\right\} = \left[H(\omega)\right]\left\{\Phi(\omega)_G\right\} \quad , \tag{2.156}$$

where

$$\left[H(\omega)\right] = \frac{1}{-\omega^2[M_G] + j\omega[C_G] + [K_G]} \quad . \tag{2.157}$$

Noting that $\left\{\eta(\omega)_G\right\}$ and $\left\{\Phi(\omega)_G\right\}$ are (2KN x 1) and $\left[H(\omega)\right]$ is (2KN x 2KN), we may write eqn.(2.156) in components form as

$$\begin{Bmatrix} \eta_{11}(\omega) \\ \vdots \\ \eta_{1(2K)}(\omega) \\ \eta_{21}(\omega) \\ \vdots \\ \eta_{2(2K)}(\omega) \\ \eta_{31}(\omega) \\ \vdots \\ \eta_{N(2K)}(\omega) \end{Bmatrix} = \begin{bmatrix} H_{11}(\omega) & H_{12}(\omega) & \cdots & H_{1(2KN)}(\omega) \\ H_{21}(\omega) & H_{22}(\omega) & \cdots & H_{2(2KN)}(\omega) \\ H_{31}(\omega) & H_{32}(\omega) & \cdots & H_{3(2KN)}(\omega) \\ \vdots & \vdots & & \vdots \\ H_{(2KN)1}(\omega) & H_{(2KN)2}(\omega) & \cdots & H_{(2KN)(2KN)}(\omega) \end{bmatrix}$$

$$\cdot \begin{Bmatrix} \Phi_{11}(\omega) \\ \vdots \\ \Phi_{1(2K)}(\omega) \\ \Phi_{21}(\omega) \\ \vdots \\ \Phi_{2(2K)}(\omega) \\ \Phi_{31}(\omega) \\ \vdots \\ \Phi_{N(2K)}(\omega) \end{Bmatrix} \quad , \tag{2.158}$$

where, from eqs.(2.154), (2.146), (2.131), and (2.129), we see that

$$\eta_{mn}(\omega) = \frac{1}{2\pi} \cdot \int_{-\infty}^{+\infty} \cdot \int_{0}^{1} \eta_n(\xi,\tau) \cdot \phi_m(\xi) \cdot d\xi \cdot e^{-j\omega\tau}\, d\tau \quad , \qquad \begin{matrix} m = 1,2,\ldots,N \, , \\ n = 1,2,\ldots,2K \, , \end{matrix} \tag{2.159}$$

and, similarly (from eqs.(2.155), (2.147), (2.126), and (2.124))

$$\Phi_{mn}(\omega) = \frac{1}{2\pi} \cdot \int_{-\infty}^{+\infty} \cdot \int_{0}^{1} \Phi_n(\xi,\tau) \cdot \phi_m(\xi) \cdot d\xi \cdot e^{-j\omega\tau}\, d\tau \quad , \qquad \begin{matrix} m = 1,2,\ldots,N \, , \\ n = 1,2,\ldots,2K \, . \end{matrix} \tag{2.160}$$

The components of $\left[H(\omega)\right]$ are apparent from eqn.(2.153). Eqn.(2.158) can be written out in components form, using index functions; by inspection, for given indices m and n of $\left\{\eta(\omega)_G\right\}$, the corresponding row index of $\left[H(\omega)\right]$ is

$$\beta(m,n) = n + 2K(m-1) \quad , \qquad \begin{matrix} m = 1,2,\ldots,N \, , \\ n = 1,2,\ldots,2K \, , \end{matrix} \tag{2.161}$$

and, for a given column index r of $\left[H(\omega)\right]$, the corresponding indices of $\left\{\phi(\omega)_G\right\}$ are

$$a(r) = \text{int}\left[(r + 2K - 1)/2K\right] \quad ,$$

and (2.162)

$$b(r) = r - 2K\left[a(r) - 1\right] \quad , \qquad r = 1,2,\ldots,2KN \, ,$$

where Curling's [70] terminology has been used. Now we can rewrite eqn. (2.158) as

$$\eta_{mn}(\omega) = \sum_{r=1}^{2KN} H_{\beta(m,n)_r}(\omega) \cdot \Phi_{a(r)b(r)}(\omega) \quad , \qquad \begin{matrix} m = 1,2,\ldots,N \, , \\ n = 1,2,\ldots,2K \, . \end{matrix} \tag{2.163}$$

Rather than using the more rigorous approach of Curling [70] for the derivation of spectral densities, a more concise method has been developed here, based on classical random vibration theory.

We start by back (Fourier) transforming eqn.(2.163), to yield

$$\eta_{mn}(\tau) = \sum_{r=1}^{2KN} \cdot \int_{-\infty}^{+\infty} \psi_{\beta(m,n)_r}(\omega) \cdot e^{j\omega\tau} \cdot d\omega \quad , \qquad \begin{matrix} m = 1,2,\ldots,N \, , \\ n = 1,2,\ldots,2K \, , \end{matrix} \tag{2.164}$$

where also

$$\eta_{mn}(\tau) = \int_{-\infty}^{+\infty} \eta_{mn}(\omega) \cdot e^{j\omega\tau} \cdot d\omega \quad , \qquad \begin{matrix} m = 1,2,\ldots,N \, , \\ n = 1,2,\ldots,2K \, , \end{matrix} \tag{2.165}$$

and where we have defined

$$\psi_{\beta(m,n)_r}(\omega) = H_{\beta(m,n)_r}(\omega)\cdot\Phi_{a(r)b(r)}(\omega) \quad , \qquad \begin{matrix} m=1,2,\ldots,N\,, \\ n=1,2,\ldots,2K\,, \\ r=1,2,\ldots,2KN\,. \end{matrix} \tag{2.166}$$

Now, eqn.(2.164) can be written as

$$\eta_{mn}(\tau) = \sum_{r=1}^{2KN} \psi_{\beta(m,n)_r}(\tau) \quad , \qquad \begin{matrix} m=1,2,\ldots,N\,, \\ n=1,2,\ldots,2K\,, \end{matrix} \tag{2.167}$$

where

$$\psi_{\beta(m,n)_r}(\tau) = \int_{-\infty}^{+\infty} \psi_{\beta(m,n)_r}(\omega)\cdot e^{j\omega\tau}\cdot d\omega \quad , \qquad \begin{matrix} m=1,2,\ldots,N\,, \\ n=1,2,\ldots,2K\,, \\ r=1,2,\ldots,2KN\,. \end{matrix} \tag{2.168}$$

We recall that, given a transfer function relatonship of the form

$$\psi(\omega) = H(\omega)\cdot\Phi(\omega) \quad ,$$

the Fourier transform of $\psi(\omega)$, namely $\psi(\tau)$, may be found from the convolution integral (see Appendix I for information on units ($1/2\pi$ factor))

$$\psi(\tau) = \frac{1}{2\pi}\cdot\int_{-\infty}^{+\infty} h(\tau_1)\cdot\Phi(\tau-\tau_1)\cdot d\tau_1 \quad ,$$

where $h(\tau_1)$ is the Fourier transform of the transfer function, called the impulsive response function and $\Phi(\tau)$ is the Fourier transform of $\Phi(\omega)$. In view of this, eqn.(2.166) yields

$$\psi_{\beta(m,n)_r}(\tau) = \frac{1}{2\pi}\cdot\int_{-\infty}^{+\infty} h_{\beta(m,n)_r}(\tau_1)\cdot\Phi_{a(r)b(r)}(\tau-\tau_1)\cdot d\tau_1 \quad , \qquad \begin{matrix} m=1,2,\ldots,N\,, \\ n=1,2,\ldots,2K\,, \\ r=1,2,\ldots,2KN\,, \end{matrix} \tag{2.169}$$

where

$$h_{\beta(m,n)_r}(\tau) = \int_{-\infty}^{+\infty} H_{\beta(m,n)_r}(\omega)\cdot e^{j\omega\tau}\cdot d\omega \quad , \qquad \begin{matrix} m=1,2,\ldots,N\,, \\ n=1,2,\ldots,2K\,, \\ r=1,2,\ldots,2KN\,, \end{matrix} \tag{2.170}$$

and

$$\Phi_{a(r)b(r)}(\tau) = \int_{-\infty}^{+\infty} \Phi_{a(r)b(r)}(\omega) \cdot e^{j\omega\tau} \cdot d\omega \quad , \qquad r = 1,2,\ldots,2KN \, . \tag{2.171}$$

Then, eqs.(2.167) and (2.169) yield

$$\eta_{mn}(\tau) = \frac{1}{2\pi} \sum_{r=1}^{2KN} \cdot \int_{-\infty}^{+\infty} h_{\beta(m,n)r}(\tau_1) \cdot \Phi_{a(r)b(r)}(\tau - \tau_1) \cdot d\tau_1 \quad , \tag{2.172}$$

$$m = 1,2,\ldots,N \, ,$$
$$n = 1,2,\ldots,2K \, .$$

The system's behaviour in random vibration will be characterized by cross- and auto-spectral density functions, from which information such as relative phase between cylinder motions (versus frequency) and amplitudes of vibration (in selected frequency bands) will be obtained.

We proceed by deriving the response cross-correlation, as a function of the displacement components given by eqn.(2.172). By definition, the (response) cross-correlation function is

$$R_{\eta_i \eta_j}(\xi,\xi',\tau) = \lim_{\tau_1 \to \infty} \frac{1}{\tau_1} \cdot \int_{-\tau_1/2}^{+\tau_1/2} \eta_i(\xi,\tau_0) \cdot \eta_j(\xi',\tau+\tau_0) \cdot d\tau_0 \quad , \tag{2.173}$$

$$i,j = 1,2,\ldots,2K \, ,$$

where $\eta_i(\xi,\tau)$ is the i^{th} (dimensionless) displacement coordinate at (dimensionless) longitudinal location ξ, and at (dimensionless) time τ, and similarly for $\eta_j(\xi',\tau+\tau_0)$. But we note that, from eqs.(2.130), (2.134), and (2.135), we have

$$\left\{\eta(\xi,\tau)\right\} = \sum_{q=1}^{\infty} \phi_q(\xi) \sum_{r=-\infty}^{\infty} \frac{1}{\tau_1} \cdot \int_{-\tau_1/2}^{+\tau_1/2} \left\{\eta(\tau)\right\}_q e^{-j\omega_r\tau} \cdot d\tau \cdot e^{j\omega_r\tau} \quad ,$$

which in the limit (see eqs.(2.141), (2.143), and (2.144)) yields

$$\left\{\eta(\xi,\tau)\right\} = \sum_{q=1}^{\infty} \phi_q(\xi) \int_{-\infty}^{+\infty} \cdot \frac{1}{2\pi} \int_{-\infty}^{+\infty} \left\{\eta(\tau)\right\}_q e^{-j\omega\tau} \cdot d\tau \cdot e^{j\omega\tau} \cdot d\omega \quad .$$

But this equation becomes, in view of eqs.(2.146) and (2.149), and after truncating the number of beam modes (index q) to N,

$$\left\{\eta(\xi,\tau)\right\} = \sum_{q=1}^{N} \phi_q(\xi)\left\{\eta(\tau)\right\}_q \quad . \tag{2.174}$$

Now, we note that the components form of $\left\{\eta(\omega)_G\right\}$, given by eqn.(2.158), are such that (see eqn.(2.154))

$$\left\{\eta_{mn}(\omega)\right\} \longrightarrow n^{th} \text{ component of vector } \left\{\eta(\omega)\right\}_m \ , \qquad \begin{matrix} m = 1,2,\ldots,N \ , \\ n = 1,2,\ldots,2K \ , \end{matrix}$$

and similarly for $\eta_{mn}(\tau)$. Hence, in components form, eqn.(2.174) reads

$$\eta_i(\xi,\tau) = \sum_{q=1}^{N} \phi_q(\xi)\cdot\eta_{qi}(\tau) \quad , \qquad i = 1,2,\ldots,2K \ , \tag{2.175}$$

where we recall that $\eta_i(\xi,\tau)$ are the components of $\left\{\eta(\xi,\tau)\right\}$ (see eqn.(2.129)).

Utilizing eqn.(2.175) into eqn.(2.173), we get for the cross-correlation function

$$R_{\eta_i\eta_j}(\xi,\xi',\tau) = \lim_{\tau_1\to\infty}\frac{1}{\tau_1} \cdot \int_{-\tau_1/2}^{+\tau_1/2} \left(\sum_{q=1}^{N} \phi_q(\xi)\cdot\eta_{qi}(\tau_0)\right)$$

$$\cdot\left(\sum_{s=1}^{N} \phi_s(\xi')\cdot\eta_{sj}(\tau+\tau_0)\right)\cdot d\tau_0 \quad , \qquad i,j = 1,2,\ldots,2K \ . \tag{2.176}$$

At this point, we may use eqn.(2.172) in the latter equation, yielding

$$R_{\eta_i\eta_j}(\xi,\xi',\tau) = \frac{1}{(2\pi)^2}\lim_{\tau_1\to\infty}\frac{1}{\tau_1} \cdot \int_{-\tau_1/2}^{+\tau_1/2} \left(\sum_{q=1}^{N} \phi_q(\xi)\cdot\sum_{r=1}^{2KN}\cdot\int_{-\infty}^{+\infty} h_{\beta(q,i)_r}(\tau_0)\right.$$

$$\left.\cdot\Phi_{a(r)b(r)}(\tau_3-\tau_0)\cdot d\tau_0\right)\cdot\left(\sum_{s=1}^{N} \phi_s(\xi')\cdot\sum_{v=1}^{2KN}\cdot\int_{-\infty}^{+\infty} h_{\beta(s,j)_v}(\tau_2)\right.$$

$$\left.\cdot\Phi_{a(v)b(v)}(\tau+\tau_3-\tau_2)\cdot d\tau_2\right)\cdot d\tau_3 \quad , \qquad i,j = 1,2,\ldots,2K \ . \tag{2.177}$$

The latter equation can be rewritten in the form

$$R_{\eta_i \eta_j}(\xi,\xi',\tau) = \frac{1}{(2\pi)^2} \sum_{q=1}^{N} \sum_{s=1}^{N} \phi_q(\xi)\cdot\phi_s(\xi') \sum_{r=1}^{2KN} \sum_{v=1}^{2KN} \cdot \int_{-\infty}^{+\infty} d\tau_0 \cdot h_{\beta(q,i)_r}(\tau_0)$$

$$\cdot \int_{-\infty}^{+\infty} d\tau_2 \cdot h_{\beta(s,j)_v}(\tau_2) \cdot \lim_{\tau_1\to\infty} \frac{1}{\tau_1} \cdot \int_{-\tau_1/2}^{+\tau_1/2} \Phi_{a(r)b(r)}(\tau_3 - \tau_0)\, \Phi_{a(v)b(v)}(\tau + \tau_3 - \tau_2)\cdot d\tau_3 \quad , \tag{2.178}$$

$$i,j = 1,2,\ldots 2K \, ,$$

and since for an ergodic process (assumed here)

$$\lim_{\tau_1\to\infty} \frac{1}{\tau_1} \cdot \int_{-\tau_1/2}^{+\tau_1/2} \Phi_{a(r)b(r)}(\tau_3 - \tau_0)\cdot\Phi_{a(v)b(v)}(\tau + \tau_3 - \tau_2)\cdot d\tau_3 =$$

$$\lim_{\tau_1\to\infty} \frac{1}{\tau_1} \cdot \int_{-\tau_1/2}^{+\tau_1/2} \Phi_{a(r)b(r)}(\tau_3)\cdot\Phi_{a(v)b(v)}(\tau + \tau_3 + \tau_0 - \tau_2)\cdot d\tau_3 \quad ,$$

eqn.(2.178) may be written as

$$R_{\eta_i \eta_j}(\xi,\xi',\tau) = \frac{1}{(2\pi)^2} \sum_{q=1}^{N} \sum_{s=1}^{N} \phi_q(\xi)\cdot\phi_s(\xi') \sum_{r=1}^{2KN} \sum_{v=1}^{2KN} \cdot \int_{-\infty}^{+\infty} d\tau_0 \cdot h_{\beta(q,i)_r}(\tau_0)$$

$$\cdot \int_{-\infty}^{+\infty} d\tau_2 \cdot h_{\beta(s,j)_v}(\tau_2) \cdot R_{\Phi_{a(r)b(r)}\Phi_{a(v)b(v)}}(\tau + \tau_0 - \tau_2) \quad , \tag{2.179}$$

$$i,j = 1,2,\ldots 2K \, ,$$

where

$$R_{\Phi_{a(r)b(r)}\Phi_{a(v)b(v)}}(\tau + \tau_0 - \tau_2) = \lim_{\tau_1\to\infty} \frac{1}{\tau_1} \cdot \int_{-\tau_1/2}^{+\tau_1/2} \Phi_{a(r)b(r)}(\tau_3)$$

$$\cdot\Phi_{a(v)b(v)}(\tau + \tau_3 + \tau_0 - \tau_2)\cdot d\tau_3 \quad , \tag{2.180}$$

$$r,v = 1,2,\ldots,2KN \, .$$

Furthermore, the cross-correlation function is also the inverse Fourier transform of the cross-spectral density function, namely

$$R_{\Phi_{a(r)b(r)}\,\Phi_{a(v)b(v)}}(\tau+\tau_0-\tau_2)=\int_{-\infty}^{+\infty} S_{\Phi_{a(r)b(r)}\,\Phi_{a(v)b(v)}}(\omega)$$

$$\cdot e^{j\omega(\tau+\tau_0-\tau_2)}\cdot d\omega\,, \qquad r,v=1,2,\ldots,2KN\,. \tag{2.181}$$

Consequently, eqs.(2.179) and (2.181) yield, for the response cross-correlation function

$$R_{\eta_i\eta_j}(\xi,\xi',\tau)=\frac{1}{(2\pi)^2}\sum_{q=1}^{N}\sum_{s=1}^{N}\phi_q(\xi)\cdot\phi_s(\xi')\sum_{r=1}^{2KN}\sum_{v=1}^{2KN}\cdot\int_{-\infty}^{+\infty}d\tau_0\cdot h_{\beta(q,i)r}(\tau_0)$$

$$\cdot\int_{-\infty}^{+\infty}d\tau_2\cdot h_{\beta(s,j)v}(\tau_2)\cdot\int_{-\infty}^{+\infty}S_{\Phi_{a(r)b(r)}\,\Phi_{a(v)b(v)}}(\omega)\cdot e^{j\omega(\tau+\tau_0-\tau_2)}\cdot d\omega\,,$$

that is

$$R_{\eta_i\eta_j}(\xi,\xi',\tau)=\sum_{q=1}^{N}\sum_{s=1}^{N}\phi_q(\xi)\cdot\phi_s(\xi')\sum_{r=1}^{2KN}\sum_{v=1}^{2KN}\cdot\int_{-\infty}^{+\infty}\Big[\frac{1}{2\pi}\cdot\int_{-\infty}^{+\infty}h_{\beta(q,i)r}(\tau_0)$$

$$\cdot e^{j\omega\tau_0}\cdot d\tau_0\cdot\frac{1}{2\pi}\cdot\int_{-\infty}^{+\infty}h_{\beta(s,j)v}(\tau_2)\cdot e^{-j\omega\tau_2}\cdot d\tau_2\Big]\cdot S_{\Phi_{a(r)b(r)}\,\Phi_{a(v)b(v)}}(\omega)$$

$$\cdot e^{j\omega\tau}\cdot d\omega\,, \qquad i,j=1,2,\ldots,2K\,. \tag{2.182}$$

Now, we note that the Fourier transform corresponding to eqn.(2.170) is

$$H_{\beta(m,n)r}(\omega)=\frac{1}{2\pi}\int_{-\infty}^{+\infty}h_{\beta(m,n)r}(\tau)\cdot e^{-j\omega\tau}\cdot d\tau\,, \qquad \begin{matrix} m=1,2,\ldots,N\,,\\ n=1,2,\ldots,2K\,,\\ r=1,2,\ldots,2KN\,, \end{matrix} \tag{2.183}$$

which, when used in eqn.(2.182), finally results in the following form for the cross-correlation function

$$R_{\eta_i\eta_j}(\xi,\xi',\tau)=\sum_{q=1}^{N}\sum_{s=1}^{N}\phi_q(\xi)\cdot\phi_s(\xi')\sum_{r=1}^{2KN}\sum_{v=1}^{2KN}\cdot\int_{-\infty}^{+\infty}H^{*}_{\beta(q,i)r}(\omega)$$

$$\cdot H_{\beta(s,j)_v}(\omega) \cdot S_{\Phi_{a(r)b(r)}\Phi_{a(v)b(v)}}(\omega) \cdot e^{j\omega\tau} \cdot d\omega \quad , \qquad i,j = 1,2,\ldots,2K . \tag{2.184}$$

Now, noting that

$$R_{\eta_i\eta_j}(\xi,\xi',\tau) = \int_{-\infty}^{+\infty} S_{\eta_i\eta_j}(\xi,\xi',\omega) \cdot e^{j\omega\tau} \cdot d\omega \quad , \qquad i,j = 1,,2,\ldots,2K , \tag{2.185}$$

we conclude from eqn.(2.184) that

$$S_{\eta_i\eta_j}(\xi,\xi',\omega) = \sum_{q=1}^{N} \sum_{s=1}^{N} \phi_q(\xi)\cdot\phi_s(\xi') \sum_{r=1}^{2KN} \sum_{v=1}^{2KN} H^{*}_{\beta(q,i)_r}(\omega) \cdot H_{\beta(s,j)_v}(\omega)$$

$$\cdot S_{\Phi_{a(r)b(r)}\Phi_{a(v)b(v)}}(\omega) \quad , \qquad i,j = 1,2,\ldots,2K . \tag{2.186}$$

Furthermore, we wish to expand the term $S_{\Phi_{a(r)b(r)}\Phi_{a(v)b(v)}}(\omega)$. We have

$$S_{\Phi_{a(r)b(r)}\Phi_{a(v)b(v)}}(\omega) = \frac{1}{2\pi} \int_{-\infty}^{+\infty} R_{\Phi_{a(r)b(r)}\Phi_{a(v)b(v)}}(\tau) \cdot e^{-j\omega\tau} \cdot d\tau \quad , \tag{2.187}$$

$$r,v = 1,2,\ldots,2KN ,$$

which is the inverse of eqn.(2.181), and where (see eqn.(2.180))

$$R_{\Phi_{a(r)b(r)}\Phi_{a(v)b(v)}}(\tau) = \lim_{\tau_1\to\infty} \frac{1}{\tau_1} \cdot \int_{-\tau_1/2}^{+\tau_1/2} \Phi_{a(r)b(r)}(\tau_0)\cdot\Phi_{a(v)b(v)}(\tau+\tau_0)\cdot d\tau_0 \quad , \tag{2.188}$$

$$r,v = 1,2,\ldots,2KN .$$

Now, by inspection of indices of eqs.(2.155) and (2.158), and from (2.124) and (2.126), we have, in components form

$$\Phi_{mn}(\tau) = \int_0^1 \phi_m(\xi) \cdot \Phi_n(\xi,\tau) \cdot d\xi \quad , \qquad \begin{matrix} m = 1,2,\ldots,N , \\ n = 1,2,\ldots,2K , \end{matrix} \tag{2.189}$$

which, when used in eqn.(2.188) yields

$$R_{\Phi_{a(r)b(r)}\Phi_{a(v)b(v)}}(\tau) = \lim_{\tau_1\to\infty} \frac{1}{\tau_1} \cdot \int_{-\tau_1/2}^{+\tau_1/2} \cdot \int_0^1 \phi_{a(r)}(\xi_1) \cdot \Phi_{b(r)}(\xi_1,\tau_0) \cdot d\xi_1$$

$$\cdot \int_0^1 \phi_{a(v)}(\xi_2) \cdot \Phi_{b(v)}(\xi_2, \tau + \tau_0) \cdot d\xi_2 \cdot d\tau_0 = \int_0^1 d\xi_1 \cdot \int_0^1 d\xi_2 \cdot \phi_{a(r)}(\xi_1) \cdot \phi_{a(v)}(\xi_2)$$

$$\cdot \lim_{\tau_1 \to \infty} \frac{1}{\tau_1} \cdot \int_{-\tau_1/2}^{+\tau_1/2} \Phi_{b(r)}(\xi_1, \tau_0) \cdot \Phi_{b(v)}(\xi_2, \tau + \tau_0) \cdot d\tau_0 \quad ,$$

that is

$$R_{\Phi_{a(r)b(r)}\Phi_{a(v)b(v)}}(\tau) = \int_0^1 d\xi_1 \cdot \int_0^1 d\xi_2 \cdot \phi_{a(r)}(\xi_1) \cdot \phi_{a(v)}(\xi_2) \cdot$$

$$\cdot R_{\Phi_{b(r)}\Phi_{b(v)}}(\xi_1, \xi_2, \tau) \quad , \qquad r, v = 1, 2, \ldots, 2KN \, . \tag{2.190}$$

Fourier transforming the latter equation, we obtain

$$S_{\Phi_{a(r)b(r)}\Phi_{a(v)b(v)}}(\omega) = \frac{1}{2\pi} \int_{-\infty}^{+\infty} \int_0^1 d\xi_1 \cdot \int_0^1 d\xi_2 \cdot \phi_{a(r)}(\xi_1) \cdot \phi_{a(v)}(\xi_2)$$

$$\cdot R_{\Phi_{b(r)}\Phi_{b(v)}}(\xi_1, \xi_2, \tau) \cdot e^{-j\omega\tau} \cdot d\tau \quad ,$$

that is

$$S_{\Phi_{a(r)b(r)}\Phi_{a(v)b(v)}}(\omega) = \int_0^1 d\xi_1 \cdot \int_0^1 d\xi_2 \cdot \phi_{a(r)}(\xi_1) \cdot \phi_{a(v)}(\xi_2)$$

$$\cdot S_{\Phi_{b(r)}\Phi_{b(v)}}(\xi_1, \xi_2, \omega) \quad , \qquad r, v = 1, 2, \ldots, 2KN \, . \tag{2.191}$$

Then, at last, eqn.(2.191) may be substituted into eqn.(2.186), to get the cross-spectral density of the response, i.e.

$$S_{\eta_i \eta_j}(\xi, \xi', \omega) = \sum_{q=1}^{N} \sum_{s=1}^{N} \phi_q(\xi) \cdot \phi_s(\xi') \sum_{r=1}^{2KN} \sum_{v=1}^{2KN} H^*_{\beta(q,i)r}(\omega) \cdot H_{\beta(s,j)v}(\omega)$$

(continued)

$$\cdot \int_0^1 d\xi_1 \cdot \int_0^1 d\xi_2 \cdot \phi_{a(r)}(\xi_1) \cdot \phi_{a(v)}(\xi_2) \cdot S_{\Phi_{b(r)}\Phi_{b(v)}}(\xi_1,\xi_2,\omega) \ , \qquad (2.192)$$

$$i,j = 1,2,\ldots,2K \ .$$

2.5-2: Pressure forces and resulting response

The one quantity left to be determined so that the latter equation may be used to compute the response cross-spectral density $S_{\eta_i\eta_j}(\xi,\xi',\omega)$, is the cross-spectral density of the random normal pressure forces, namely the term

$S_{\Phi_{b(r)}\Phi_{b(v)}}(\xi_1,\xi_2,\omega)$.

Remark

. Curling [61] used empirical data by Bakewell [26,25] to model pressure force characteristics, in a cluster of equal radius cylinders; as that model is only an interim measure pending in situ measurements, and since vibration tests were also performed on bundles of equi-radius cylinders, we will keep the pressure force analysis in its present form, i.e. based on cylinders all of radius R (and length L).

We first examine the pressure characteristics of flow over an isolated cylinder (multi-cylinder cases are an extension of the individual cylinder one and are treated more easily by defining an alternative coordinate system, as shown later).

2.5-2a: Individual cylinders

Let the instantaneous normal pressure on cylinder i be $p_i(x,\theta,t)$. The instantaneous net lateral force per unit length is simply found by integrating the pressure forces around the circumference, hence,

$$F_{T(z)i}(x,t) = \int_0^{2\pi} -p_i(x,\theta,t)\cdot R_i\cdot\cos\theta\cdot d\theta \ ,$$

$$F_{T(y)i}(x,t) = \int_0^{2\pi} -p_i(x,\theta,t)\cdot R_i\cdot\sin\theta\cdot d\theta \ , \qquad (2.193)$$

$$i = 1,2,\ldots,K \ .$$

The negative sign stems from the fact that the force is taken as positive in the z- and y-directions respectively, whereas the pressure force is negative (at $\theta = 0^o$ and 90^o). The dimensionless lateral force per unit length is found by making use of eqn.(2.116), together with the above equation, yielding

(i) for the z-direction

$$\Phi_i(\xi,\tau) = -\frac{2}{\pi}\frac{R_i}{R_0}\varepsilon \cdot \int_0^{2\pi} p_i(\xi,\theta,\tau)\cdot\cos\theta\cdot d\theta \,, \qquad i = 1,2,\ldots,K \,,$$

(ii) and for the y-direction

$$\Phi_i(\xi,\tau) = -\frac{2}{\pi}\frac{R_{i-K}}{R_0}\varepsilon \cdot \int_0^{2\pi} p_{i-K}(\xi,\theta,\tau)\cdot\sin\theta\cdot d\theta \,, \qquad i = K+1,K+2,\ldots,2K \,, \tag{2.194}$$

in which we have defined the dimensionless pressure by

$$p_i(\xi,\theta,\tau) = \frac{L^2 A_0}{E_0 I_0}\, p_i(\xi,\theta,\tau) \,, \qquad i = 1,2,\ldots,K \,, \tag{2.195}$$

where of course the function $p_i(\xi,\theta,\tau)$ is found from $p_i(x,\theta,t)$, and x and t are related to ξ and τ by eqs.(2.47) and (2.49).

Now, by definition,

$$R_{\Phi_i\Phi_j}(\xi_1,\xi_2,\tau) = \lim_{\tau_1\to\infty}\frac{1}{\tau_1}\cdot\int_{-\tau_1/2}^{+\tau_1/2}\frac{2}{\pi}\frac{R_{r(i)}}{R_0}\varepsilon\cdot\int_0^{2\pi} p_{r(i)}(\xi_1,\theta_1,\tau_0)\cdot\mathrm{trig}_i(\theta_1)\cdot d\theta_1$$

$$\cdot\frac{2}{\pi}\frac{R_{r(j)}}{R_0}\varepsilon\cdot\int_0^{2\pi} p_{r(j)}(\xi_2,\theta_2,\tau+\tau_0)\cdot\mathrm{trig}_j(\theta_2)\cdot d\theta_2\cdot d\tau_0 \,, \qquad \begin{matrix} i,j = 1,2,\ldots,2K \,, \\ |i-j| = 0 \text{ or } K, \end{matrix} \tag{2.196}$$

where the last statement restricts the equation to individual cylinders, and where, following Curling's [61] terminology,

$$r(i) = \begin{cases} i & , \; i \le K \,, \\ i-K & , \; i > K \,, \end{cases} \tag{2.197}$$

an index function which selects the cylinder corresponding to the value i ($i = 1,2,\ldots,K$ for z-axes and $i = K+1,K+2,\ldots,2K$ for y-axes), and

$$\mathrm{trig}_i(\theta) = \begin{cases} \cos\theta & , \ i \le K \ , \\ \sin\theta & , \ i > K \ . \end{cases} \tag{2.198}$$

The cross-spectral density is obtained by Fourier transforming eqn. (2.196); we get

$$S_{\Phi_i \Phi_j}(\xi_1,\xi_2,\omega) = \left(\frac{2}{\pi}\frac{\varepsilon}{R_0}\right)^2 R_{r(i)} \cdot R_{r(j)} \cdot \int_0^{2\pi} d\theta_1 \cdot \int_0^{2\pi} d\theta_2 \cdot S_{p_{r(i)} p_{r(j)}}(\xi_1,\xi_2,\theta_1,\theta_2,\omega)$$

$$\cdot \mathrm{trig}_i(\theta_1) \cdot \mathrm{trig}_j(\theta_2) \ , \qquad i,j = 1,2,\ldots,2K \ , \quad r(i) = r(j) \ , \tag{2.199}$$

where the last statement, which is equivalent to $|i - j| = 0$ or K (see eqn. (2.197)), again restricts the equation to individual cylinders, and where the dimensionless pressure cross spectral density relates to the dimensional one by (see eqs.(2.195) and (2.49))

$$S_{p_i p_j}(\Delta\xi,\Delta\theta,\omega) = \frac{32\sqrt{\pi}\,\varepsilon^2}{\sqrt{E_0^3\,(m_0 + \rho A_0)}}\, S_{p_i p_j}(\Delta\xi,\Delta\theta,\omega) \ , \qquad i,j = 1,2,\ldots,K \ , \tag{2.200}$$

and

$$S_{p_{r(i)} p_{r(j)}}(\xi_1,\xi_2,\theta_1,\theta_2,\omega) = \frac{1}{2\pi} \int_{-\infty}^{+\infty} R_{p_{r(i)} p_{r(j)}}(\xi_1,\xi_2,\theta_1,\theta_2,\tau) \cdot e^{-j\omega\tau} \cdot d\tau \ , \tag{2.201}$$

$$i,j = 1,2,\ldots,2K \ .$$

Of course,

$$R_{p_{r(i)} p_{r(j)}}(\xi_1,\xi_2,\theta_1,\theta_2,\tau) = \lim_{\tau_1 \to \infty} \frac{1}{\tau_1} \cdot \int_{-\tau_1/2}^{+\tau_1/2} p_{r(i)}(\xi_1,\theta_1,\tau_0)$$

$$\cdot p_{r(j)}(\xi_2,\theta_2,\tau+\tau_0) \cdot d\tau_0 \ , \qquad i,j = 1,2,\ldots,2K \ . \tag{2.202}$$

So as to be able to determine $S_{\Phi_i \Phi_j}(\xi_1,\xi_2,\omega)$ in eqn.(2.199) (single cylinder), we must know $S_{p_m p_m}(\xi_1,\xi_2,\theta_1,\theta_2,\omega)$, where $m = r(i) = r(j)$. The random pressure fluctuations being assumed to arise solely from turbulence in

the boundary layer at the cylinder, and independently of cylinder deflection or motion, we may state, for fully developed flow, that

$$S_{p_m p_n}(\xi_1, \xi_2, \theta_1, \theta_2, \omega) = S_{p_m p_n}(\Delta\xi, \Delta\theta, \omega) \quad , \qquad m = n = 1, 2, \ldots, K \, , \tag{2.203}$$

that is, the cross-spectral density depends only on the separation between the pressure points, and not on their absolute (longitudinal and lateral) locations. Note that

$$\left.\begin{aligned} \Delta\xi &= \xi_2 - \xi_1 \quad , \\ \Delta\theta &= \theta_2 - \theta_1 \quad . \end{aligned}\right\} \tag{2.204}$$

Remark

The case where $m \neq n$ (pressure points on different cylinders) will be examined later, at which time an equivalent $\Delta\theta$ ($\Delta\theta_{eq}$) shall be defined.

No theory exists to predict analytically $S_{p_m p_m}(\Delta\xi, \Delta\theta, \omega)$, given the cylinders' geometry and the system's physical properties. Furthermore, in situ measurements for the bundles used in vibration testing are not yet available (although power spectral density measurements were made at the wall of the test channel and will be used in "theoretical" computations). Consequently, Curling [61] finalized his theoretical model by using empirical data for the pressure characteristics; Lakis and Paidoussis' [70] approach of using Bakewell's [26] measurements of pressure characteristics of airflow in pipes was utilized. Note that the applicability of the latter work to water flow over the outer surface of a cylinder was supported in a later study, also by Bakewell [33].

Before proceeding to examine Bakewell's work and its application to the problem at hand, it should be pointed out that the work was originally deemed to apply only to single cylinders, and has been expanded to the general case where $m \neq n$ (see eqn.(2.203)) by Curling [61], whose assumptions shall be reviewed shortly.

Now, Bakewell [26] defined a (dimensionless) normalized cross-correlation function

$$R_{pp'}(\Delta\xi,\Delta\theta,\tau) = \frac{R_{pp'}(\Delta\xi,\Delta\theta,\tau)}{R_{pp'}(0,0,0)} \quad , \tag{2.205}$$

where

$$R_{pp'}(\Delta\xi,\Delta\theta,\tau) = \lim_{\tau_1\to\infty} \frac{1}{\tau_1} \cdot \int_{-\tau_1/2}^{+\tau_1/2} p(\xi_1,\theta_1,\tau_0)\cdot p(\xi_2,\theta_2,\tau+\tau_0)\cdot d\tau_0 \quad . \tag{2.206}$$

For convenience, we have used the dimensionless parameters ξ and τ instead of the original x and t, as well as utilizing $\Delta\theta$ instead of the circumferential distance originally used in Reference [26].

Bakewell actually measured bandpass filtered pressure signals, for a range of Reynolds numbers (based on pipe I.D.) from 100,000 to 300,000, to obtain

$$R_{pp'[\omega,\Delta\omega]}(\Delta\xi,\Delta\theta,\tau) = \frac{R_{pp'[\omega,\Delta\omega]}(\Delta\xi,\Delta\theta,\tau)}{R_{pp'[\omega,\Delta\omega]}(0,0,0)} \quad , \tag{2.207}$$

Note that in eqs.(2.205) and (2.207), there is the inherent assumption that the pressure field is homogeneous, as the zero time delay autocorrelation function

$$R_{pp'[\omega,\Delta\omega]}(0,0,0) = \lim_{\tau_1\to\infty} \frac{1}{\tau_1} \cdot \int_{-\tau_1/2}^{+\tau_1/2} p^2_{[\omega,\Delta\omega]}(\xi,\theta,\tau)\cdot d\tau \quad . \tag{2.208}$$

is not deemed dependent on the coordinates ξ and θ.

Following Corcos' [28] model, Bakewell assumed that the longitudinal and lateral (circumferential) correlations are independent of one another. The latter obtained two empirical expressions for zero time delay normalized bandpass filtered correlations, namely [25]

$$R_{pp'[\omega,\Delta\omega]}(\Delta\xi,0,0) = e^{-b|S_\xi|}\cdot\cos(2\pi S_\xi) \quad , \tag{2.209}$$

for the longitudinal case, and from earlier measurements [26],

$$R_{pp'[\omega,\Delta\omega]}(0,\Delta\theta,0) = \frac{1}{(1+cS_\theta^2)\,(2-e^{-dS_\theta^2})} \quad , \tag{2.210}$$

for the lateral (circumferential) case, where the Strouhal numbers

$$S_\xi = \frac{(x_2 - x_1)(\Omega/2\pi)}{U_c} = \sqrt{\beta}\,\frac{(\xi_2 - \xi_1)(\omega/2\pi)}{u_c} \quad , \tag{2.211}$$

and

$$S_{\theta_{r(i)}} = \frac{R_{r(i)}\,(\theta_2 - \theta_1)(\Omega/2\pi)}{U_c} = \frac{1}{2}\,\frac{\sqrt{\beta}}{\varepsilon}\,\frac{(\theta_2 - \theta_1)(\omega/2\pi)}{u_c}\,\frac{R_{r(i)}}{R_0} \quad , \tag{2.212}$$

are used, and where b, c, and d are constants:

$$\left.\begin{array}{l} b = 0.7 \ , \qquad \text{(from [25])} \\ \left.\begin{array}{l} c = 10 \ , \\ d = 80 \ . \end{array}\right\} \ \text{(from [26])} \end{array}\right\} \tag{2.213}$$

The dimensionless quantities (ξ, ω, u_c $\{U = U_c\}$) are defined in terms of dimensional ones in eqs.(2.47), (2.50), and (2.51) respectively (see also eqn.(2.52) for the definition of ε and β).

Note that the data for longitudinal correlations [25] is more recent and provides better resolution than that for lateral correlations [26] (bandwidths were 30 Hz instead of octave bands (the minimum of which was about 200 Hz)).

For fully developed flows, Willmarth and Yang [71] (referred to by Curling [61]) found that $U_c \simeq 0.8$ x (free stream velocity), but Bakewell's [26] data indicates that at lower frequencies ($\Omega = 300$ Hz), the convection and mean velocities are essentially the same. Hence, we shall set

$$u_c \simeq u \quad , \tag{2.214}$$

where we recall that u is the (dimensionless) bulk velocity within the array.

Now, the assumption of independent longitudinal and lateral correlations takes the form (see Lakis and Paidoussis [70])

$$R_{pp'[\omega,\Delta\omega]}(\Delta\xi,\Delta\theta,0) = R_{pp'[\omega,\Delta\omega]}(\Delta\xi,0,0)\cdot R_{pp'[\omega,\Delta\omega]}(0,\Delta\theta,0) \quad , \tag{2.215}$$

which yields, using eqs.(2.209) and (2.210):

$$R_{pp'[\omega,\Delta\omega]}(\Delta\xi,\Delta\theta,0)_i = \frac{e^{-b|S_\xi|}\cdot\cos(2\pi S_\xi)}{(1+cS_{\theta_i}^2)(2-e^{-dS_{\theta_i}^2})} \quad , \quad i=1,2,\ldots,K \, . \tag{2.216}$$

Curling [61] had also used a curve fit of Bakewell's [26] data, developed by Lakis and Paidoussis [70], on the pressure power spectral densities; we shall use instead in situ measured tunnel wall pressure power spectral density data, to be presented in detail later.

At this point, we wish to "extract" information from the empirically determined zero delay normalized band-limited autocorrelation function, given by eqn.(2.216). First, corresponding to eqn.(2.208), we have

$$R_{pp'[\omega,\Delta\omega]}(0,0,0) = \int_{-(\omega+\Delta\omega)}^{-\omega} S_{pp'}(0,0,\omega)\cdot d\omega + \int_{\omega}^{(\omega+\Delta\omega)} S_{pp'}(0,0,\omega)\cdot d\omega \, , \tag{2.217}$$

where $S_{pp'}(0,0,\omega)$ is the double-sided power spectral density (a real, even function) of the pressure, i.e. eqn.(2.217) is the bandpass filtered power.

For $\Delta\omega$ small enough to consider $S_{pp'}(0,0,\omega)$ constant over the range $(\omega,\omega+\Delta\omega)$, we may write

$$R_{pp'[\omega,\Delta\omega]}(0,0,0) = 2\cdot S_{pp'}(0,0,\omega)\cdot\Delta\omega \, . \tag{2.218}$$

Then, from basic definition,

$$S_{pp'}(\Delta\xi,\Delta\theta,\omega) = \frac{1}{2\pi}\cdot\int_{-\infty}^{+\infty} R_{pp'[\omega,\Delta\omega]}(\Delta\xi,\Delta\theta,\tau)\cdot e^{-j\omega\tau}\cdot d\tau \, , \quad (\omega\le|\omega|\le\omega+\Delta\omega) \tag{2.219}$$

where it should be noted that when computed by the latter equation, $S_{pp'}(\Delta\xi,\Delta\theta,\omega) = 0$ outside the range $\pm(\omega,\omega+\Delta\omega)$, since the signal has been filtered out. The latter function is, in general, complex, i.e. we have

$$S_{pp'}(\Delta\xi,\Delta\theta,\omega) = U_{pp'}(\Delta\xi,\Delta\theta,\omega) - j\cdot V_{pp'}(\Delta\xi,\Delta\theta,\omega) \, , \tag{2.220}$$

where by inspection of eqn.(2.219), we obtain

$$U_{pp'}(\Delta\xi,\Delta\theta,\omega) = \frac{1}{2\pi}\cdot\int_{-\infty}^{+\infty} R_{pp'[\omega,\Delta\omega]}(\Delta\xi,\Delta\theta,\tau)\cdot\cos(\omega\tau)\cdot d\tau \, ,$$

and,

(continued...)

$$V_{pp'}(\Delta\xi,\Delta\theta,\omega) = \frac{1}{2\pi} \cdot \int_{-\infty}^{+\infty} R_{pp'\,[\omega,\Delta\omega]}(\Delta\xi,\Delta\theta,\tau)\cdot\sin(\omega\tau)\cdot d\tau \quad , \qquad (\omega \le |\omega| \le \omega+\Delta\omega) \tag{2.221}$$

hence, from the latter equation, we see that $U_{pp'}(\Delta\xi,\Delta\theta,\omega)$ and $V_{pp'}(\Delta\xi,\Delta\theta,\omega)$ are even and odd functions of ω respectively.

Now, from basic definition,

$$R_{pp'\,[\omega,\Delta\omega]}(\Delta\xi,\Delta\theta,\tau) = \int_{-(\omega+\Delta\omega)}^{-\omega} S_{pp'}(\Delta\xi,\Delta\theta,\omega)\cdot e^{j\omega\tau}\cdot d\omega + \int_{\omega}^{(\omega+\Delta\omega)} S_{pp'}(\Delta\omega,\Delta\theta,\omega)$$

$$\cdot e^{j\omega\tau}\cdot d\omega \quad , \tag{2.222}$$

which yields, after substitution of eqn.(2.220) and making use of the even and odd properties of the functions involved,

$$R_{pp'\,[\omega,\Delta\omega]}(\Delta\xi,\Delta\theta,\tau) = \int_{-(\omega+\Delta\omega)}^{-\omega} \left[U_{pp'}(\Delta\xi,\Delta\theta,\omega)\cdot\cos(\omega\tau) + V_{pp'}(\Delta\xi,\Delta\theta,\omega)\right.$$

$$\left.\cdot\sin(\omega\tau)\right]\cdot d\omega + \int_{\omega}^{(\omega+\Delta\omega)} \left[U_{pp'}(\Delta\xi,\Delta\theta,\omega)\cdot\cos(\omega\tau) + V_{pp'}(\Delta\xi,\Delta\theta,\omega)\cdot\sin(\omega\tau)\right]\cdot d\omega. \tag{2.223}$$

For $\Delta\omega$ sufficiently small (for the functions $U_{pp'}$ and $V_{pp'}$ to be relatively constant over the interval), and since the integrand is even, we may write

$$R_{pp'\,[\omega,\Delta\omega]}(\Delta\xi,\Delta\theta,\tau) = 2\cdot\left[U_{pp'}(\Delta\xi,\Delta\theta,\omega)\cdot\cos(\omega\tau) + V_{pp'}(\Delta\xi,\Delta\theta,\omega)\cdot\sin(\omega\tau)\right]\cdot\Delta\omega. \tag{2.224}$$

It will prove convenient to rewrite eqn.(2.220) as

$$S_{pp'}(\Delta\xi,\Delta\theta,\omega) = \left|S_{pp'}(\Delta\xi,\Delta\theta,\omega)\right|\cdot e^{-j\beta_{pp'}(\Delta\xi,\Delta\theta,\omega)} \quad , \tag{2.225}$$

where

$$\left.\begin{aligned} &\left|S_{pp'}(\Delta\xi,\Delta\theta,\omega)\right| = \left[U^2_{pp'}(\Delta\xi,\Delta\theta,\omega) + V^2_{pp'}(\Delta\xi,\Delta\theta,\omega)\right]^{1/2}, \\ &\text{and} \\ &\beta_{pp'}(\Delta\xi,\Delta\theta,\omega) = \arctan\left[V_{pp'}(\Delta\xi,\Delta\theta,\omega)/U_{pp'}(\Delta\xi,\Delta\theta,\omega)\right] \quad , \end{aligned}\right\} \tag{2.226}$$

and eqn.(2.224) can be written as

$$R_{pp'\,[\omega,\Delta\omega]}(\Delta\xi,\Delta\theta,\tau) = 2\cdot\left|S_{pp'}(\Delta\xi,\Delta\theta,\omega)\right|\cdot\cos\left[\omega\tau - \beta_{pp'}(\Delta\xi,\Delta\theta,\omega)\right]\cdot\Delta\omega \ . \tag{2.227}$$

Now, from eqn.(2.218), and eqs.(2.207) and (2.227) with $\tau = 0$, we get

$$R_{pp'\,[\omega,\Delta\omega]}(\Delta\xi,\Delta\theta,0) = \frac{\left|S_{pp'}(\Delta\xi,\Delta\theta,\omega)\right|\cdot\cos\left[\beta_{pp'}(\Delta\xi,\Delta\theta,\omega)\right]}{S_{pp'}(0,0,\omega)} \ . \tag{2.228}$$

Finally, using eqn.(2.228) into eqn.(2.216), we get

$$\frac{\left|S_{pp'}(\Delta\xi,\Delta\theta,\omega)\right|\cdot\cos\left[\beta_{pp'}(\Delta\xi,\Delta\theta,\omega)\right]}{S_{pp'}(0,0,\omega)} = \frac{e^{-b|S_\xi|}\cdot\cos(2\pi S_\xi)}{(1+cS_\theta^2)\,(2-e^{-dS_\theta^2})} \ . \tag{2.229}$$

On the average, disturbances are being convected downstream at a velocity u_c; hence, in the longitudinal direction, we may consider that the time delay between signals is simply*

$$\tau_\xi = \sqrt{\beta}\,\frac{\xi_2 - \xi_1}{u_c} \ , \tag{2.230}$$

which can be converted to a phase angle, corresponding to a frequency ω:

$\beta_\xi = \omega\cdot\tau_\xi$, i.e. (using eqn.(2.230))

$$\beta_\xi = \sqrt{\beta}\cdot\omega\,\frac{\xi_2 - \xi_1}{u_c} \ ,$$

which can be written as (see eqn.(2.211))

$$\beta_\xi(\Delta\xi,\omega) = 2\pi\cdot S_\xi \ . \tag{2.231}$$

Bakewell [26] found virtually no lateral convection of disturbances and did find a strong longitudinal one, yielding the term $\cos(2\pi\cdot S_\xi)$ in eqn.(2.229); hence, the phase of $S_{pp'}$ (i.e. $\beta_{pp'}$) is not dependent on $\Delta\theta$, i.e.

$$\beta_{pp'}(\Delta\xi,\Delta\theta,\omega) = \beta_{pp'}(\Delta\xi,\omega) = 2\pi\cdot S_\xi \ , \tag{2.232}$$

where eqn.(2.231) has been used.

From eqs.(2.229) and (2.232), we obtain

---

* Dimensionless form of $t_x = \dfrac{x_2 - x_1}{U_c}$.

$$|S_{pp'}(\Delta\xi,\Delta\theta.\omega)|_i = \frac{e^{-b|S_\xi|}\cdot S_{pp'}(0,0,\omega)}{(1+cS_{\theta_i}^2)(2-e^{-dS_{\theta_i}^2})} \quad , \qquad i=1,2,\ldots,K\,. \tag{2.233}$$

Equation (2.232) and (2.233), stemming from simplified empirical relationships, together with eqs.(2.211) and (2.212), now define $S_{pp'}(\Delta\xi,\Delta\theta,\omega)$.

Using the above two equations, eqn.(2.225) becomes

$$S_{pp'}(\Delta\xi,\Delta\theta,\omega)_i = \frac{e^{-b|S_\xi|}\cdot e^{-j2\pi\cdot S_\xi}}{(1+cS_{\theta_i}^2)(2-e^{-dS_{\theta_i}^2})}\, S_{p_m p_m}(0,0,\omega) \quad , \qquad i=1,2,\ldots,K\,, \tag{2.234}$$

where it should be noted that $S_{p_m p_m}(0,0,\omega)$ is the same as $S_{pp'}(0,0,\omega)$.

By virtue of the latter equation and eqn.(2.203), we can write eqn. (2.199) in the (single cylinder) form

$$S_{\Phi_i\Phi_j}(\xi_1,\xi_2,\omega) = \left[\frac{2}{\pi}\frac{\varepsilon}{R_0}\right]^2 R_{r(i)}\cdot R_{r(j)}\cdot\int_0^{2\pi} d\theta_1\cdot\int_0^{2\pi} d\theta_2\cdot \mathrm{trig}_i(\theta_1)\cdot\mathrm{trig}_j(\theta_2)$$

$$\cdot\frac{e^{-b|S_\xi|}\cdot e^{-j2\pi\cdot S_\xi}}{(1+cS_{\theta_l}^2)(2-e^{-dS_{\theta_l}^2})}\, S_{p_m p_m}(0,0,\omega) \quad , \qquad \begin{matrix} i,j=1,2,\ldots,2K\,, \\ l=r(i)=r(j)\,, \end{matrix} \tag{2.235}$$

which may be rewritten as

$$S_{\Phi_i\Phi_j}(\xi_1,\xi_2,\omega) = e^{-b|S_\xi|}\cdot e^{-j2\pi\cdot S_\xi}\cdot\left[\frac{2}{\pi}\frac{\varepsilon}{R_0}\right]^2 R_{r(i)}\cdot R_{r(j)}$$

$$\cdot S_{p_m p_m}(0,0,\omega)\cdot K_{ij,\theta}(\omega) \quad , \qquad \begin{matrix} i,j=1,2,\ldots,2K\,, \\ r(i)=r(j)\,, \end{matrix} \tag{2.236}$$

where we have defined a new function,

$$K_{ij,\theta}(\omega) = \int_0^{2\pi} d\theta_1\cdot\int_0^{2\pi} d\theta_2\cdot\frac{\mathrm{trig}_i(\theta_1)\cdot\mathrm{trig}_j(\theta_2)}{(1+cS_{\theta_l}^2)(2-e^{-dS_{\theta_l}^2})} \quad , \qquad \begin{matrix} i,j=1,2,\ldots,2K\,, \\ l=r(i)=r(j)\,. \end{matrix} \tag{2.237}$$

Remark

Curling [61] initially defines the latter function as being also dependent on ξ, because the convection velocity U_c (found in the expression for S_θ) has been found to vary with the longitudinal spatial separation (attributed to a more rapid decay of smaller pressure producing eddies [71]). This dependence is later dropped to simplify the analysis (this shall be discussed after having extensively reviewed the experimental data).

Equation (2.237) was integrated numerically for a set of values for ω; the resulting data points were curve fitted to yield (see Reference [61] for details)

$$\left.\begin{aligned} K_{ij,\theta}(\omega) &= \frac{a_1 \cdot |S_{R_1}|}{(1 + a_2 \cdot S_{R_1}^2)} \left(1 + e^{-a_3 |S_{R_1}|}\right), \quad i = j, \quad -50 \le S_{R_1} \le +50, \\ K_{ij,\theta}(\omega) &= 0, \quad i \ne j, \quad i,j = 1,2,\ldots,2K, \quad l = r(i) - r(j), \end{aligned}\right\} \tag{2.238}$$

where

$$S_{R_1} = \frac{R_1 (\Omega/2\pi)}{U_C} = \frac{1}{2} \frac{\sqrt{\beta}}{\varepsilon} \frac{(\omega/2\pi)}{u_c} \frac{R_1}{R_0}, \quad l = 1,2,\ldots,K, \tag{2.239}$$

and where a_1, a_2 and a_3 are constants:

$$\left.\begin{aligned} a_1 &= 38.344, \\ a_2 &= 40.611, \\ a_3 &= 19.091. \end{aligned}\right\} \tag{2.240}$$

Notes

(i) The constants in eqn.(2.240) are computed from those derived by Curling [61], which were applicable to "radian" Strouhal numbers of the form $S = R\Omega/U_C$.

(ii) In accordance with minimum lateral fluid distances between pressure points, and also consistent with Bakewell's results, S_θ (see eqn.(2.212)) in eqn.(2.237) is defined from the minimum angle between points at θ_1 and θ_2 (note that the integration limits are 0 and 2π).

2.5-2b: Multi-cylinder (clusters)

$S_{pp'}(\Delta\xi,\Delta\theta,\omega)$ of eqn.(2.234) is the same as $S_{p_m p_m}(\Delta\xi,\Delta\theta,\omega)$ of eqn. (2.203) , i.e. for an individual cylinder. Lacking better information, Curling [61] assumed that the current expressions for $S_{p_m p_n}(\Delta\xi,\Delta\theta,\omega)\Big|_{n=m}$ could also be applied to cases where $n \neq m$, by considering fluid "paths", as illustrated below.

Both the single (i.e. individual) and multi-cylinder lateral distances, l_S and l_M, are of minimum length; to simplify the calculation of $l_M = l_M(m,n,\theta_1,\theta_2)$, Curling [61] assumed that the path is not altered by the presence of one or more neighbouring cylinders blocking it (this can affect results significantly only if correlations remain high at such distances, and will be discussed in Chapter 6).

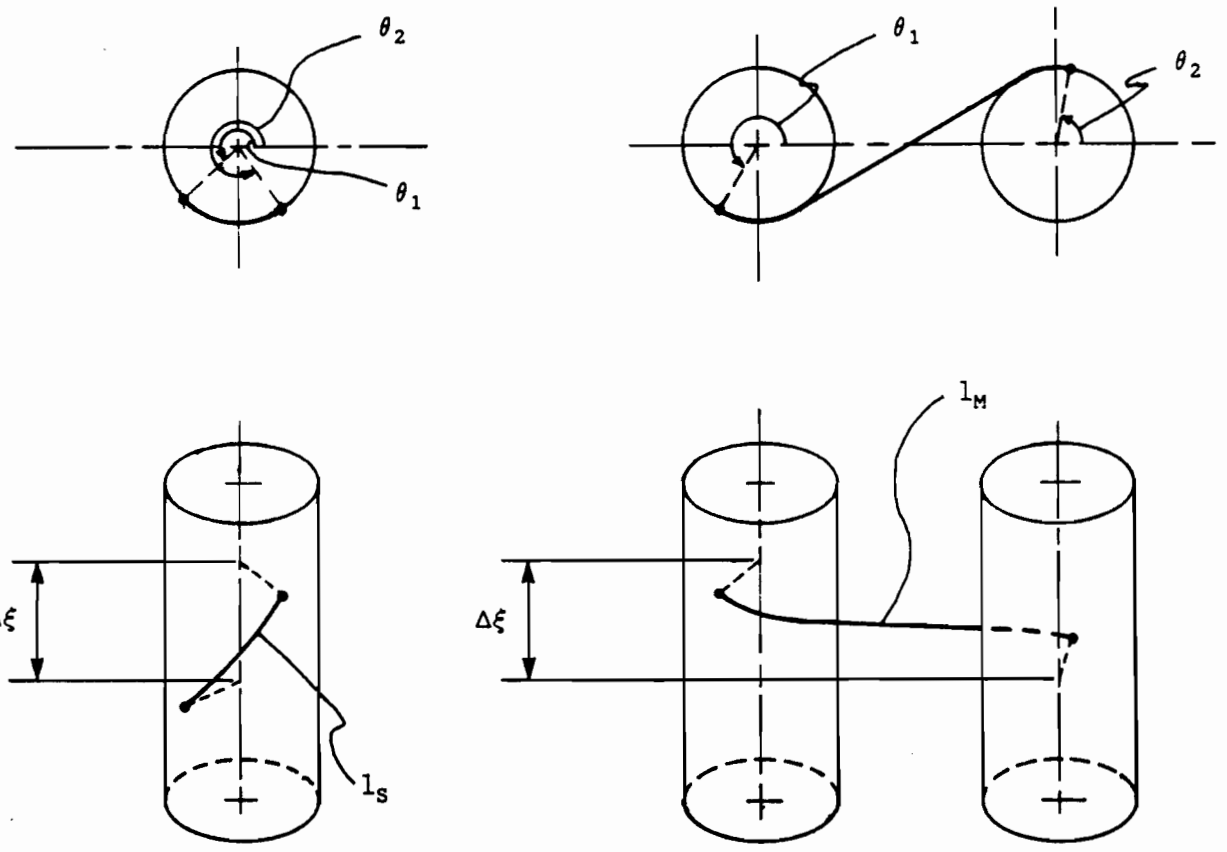

Curling [61] makes two additional assumptions so as to be able to apply the empirical relation for $S_{pp'}(\Delta\xi,\Delta\theta,\omega)$, namely eqn.(2.234), to cylinder pairs:

(i) The longitudinal correlation for a cylinder pair is the same as that for the single cylinder; this implies that S_ξ in eqn.(2.234) can still be computed from eqn.(2.211), where ξ_1 and ξ_2 are now on different cylinders.

(ii) The lateral correlation for a cylinder pair can be obtained by setting

$$S_\theta = \frac{l_M(\Omega/2\pi)}{U_c} \quad , \tag{2.241}$$

that is, using

$$\Delta\theta_{eq} = \frac{l_M}{R_0} \tag{2.242}$$

in eqn.(2.212).

The minimum path length $l_M = l_M(m,n,\theta_1,\theta_2)$ is calculated more easily in a coordinate system parallel to a line joining the centers of the cylinder pairs, as shown below.

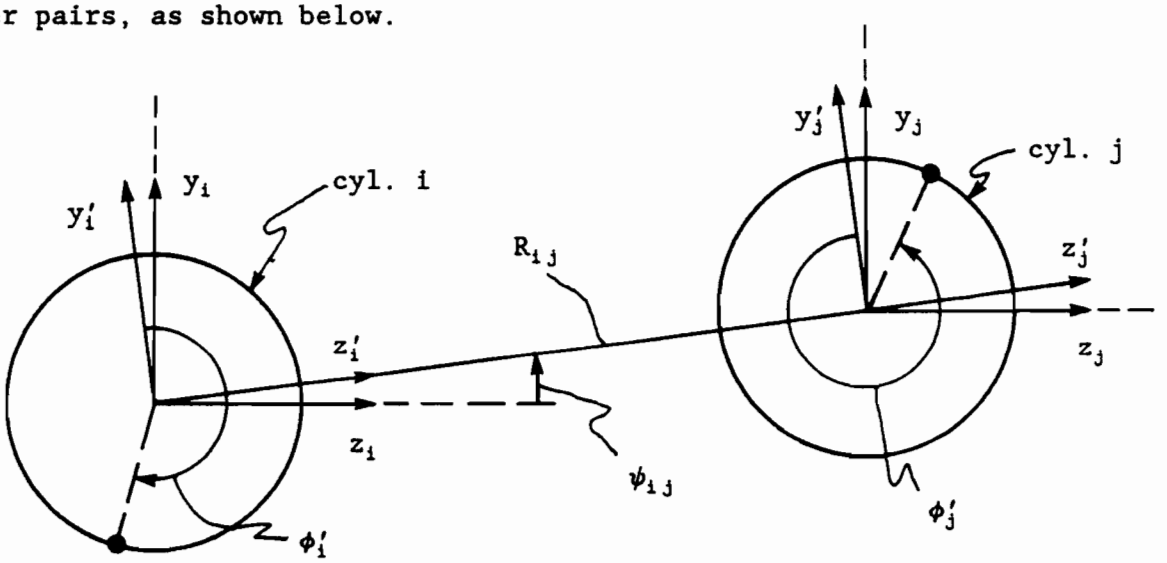

Note that the unusual convention for angles ϕ_i' and ϕ_j' stems from the derivation technique for the algorithm to compute l_M.

Now, corresponding to eqn.(2.194), we have,

(i) for the z'-directions

$$\left.\begin{aligned}\Phi'_i(\xi,\tau) &= \frac{2}{\pi}\frac{R_i}{R_0}\,\varepsilon\cdot\int_0^{2\pi} p'_i(\xi,\phi'_i,\tau)\cdot\sin\phi'_i\cdot d\phi'_i\,, \qquad i=1,2,\ldots,K\,,\\ \text{and}\\ \Phi'_j(\xi,\tau) &= \frac{2}{\pi}\frac{R_j}{R_0}\,\varepsilon\cdot\int_0^{2\pi} p'_j(\xi,\phi'_j,\tau)\cdot(-\sin\phi'_j)\cdot d\phi'_j\,, \qquad j=1,2,\ldots,K\,,\end{aligned}\right\} \tag{2.243}$$

(ii) and for the y'-directions

$$\left.\begin{aligned}\Phi'_i(\xi,\tau) &= \frac{2}{\pi}\frac{R_{i-K}}{R_0}\,\varepsilon\cdot\int_0^{2\pi} p'_{i-K}(\xi,\phi'_i,\tau)\cdot\cos\phi'_i\cdot d\phi'_i\,, \qquad i=K+1,K+2,\ldots,2K\,,\\ \text{and}\\ \Phi'_j(\xi,\tau) &= \frac{2}{\pi}\frac{R_{j-K}}{R_0}\,\varepsilon\cdot\int_0^{2\pi} p'_{j-K}(\xi,\phi'_j,\tau)\cdot\cos\phi'_j\cdot d\phi'_j\,, \qquad j=K+1,K+2,\ldots,2K\,.\end{aligned}\right\} \tag{2.244}$$

By definition (similar to eqn.(2.196)), we have

$$\begin{aligned}R_{\Phi_i\Phi'_j}(\xi_1,\xi_2,\tau) = \lim_{\tau_1\to\infty}\frac{1}{\tau_1}\cdot\int_{-\tau_1/2}^{+\tau_1/2}&\frac{2}{\pi}\frac{R_{r(i)}}{R_0}\,\varepsilon\int_0^{2\pi} p'_{r(i)}(\xi_1,\phi'_i,\tau_0)\cdot trig_{1i}(\phi'_i)\cdot d\phi'_i\\ \cdot\frac{2}{\pi}\frac{R_{r(j)}}{R_0}\,\varepsilon&\int_0^{2\pi} p'_{r(j)}(\xi_2,\phi'_j,\tau+\tau_0)\cdot trig_{2j}(\phi'_j)\cdot d\phi'_j\cdot d\tau_0\,,\end{aligned} \qquad \begin{aligned}&i,j=1,2,\ldots,2K\,,\\ &r(i)\neq r(j)\,,\end{aligned} \tag{2.245}$$

where the last statement restricts the equation to cylinder pairs, and where

$$\left.\begin{aligned}trig_{1i}(\phi'_i) &= \begin{cases}\sin\phi'_i & , i\le K\,,\\ \cos\phi'_i & , i>K\,,\end{cases}\\ trig_{2i}(\phi'_i) &= \begin{cases}-\sin\phi'_i & , i\le K\,,\\ \cos\phi'_i & , i>K\,.\end{cases}\end{aligned}\right\} \tag{2.246}$$

Note that the index function of eqn.(2.197) has been used in eqn. (2.245).

$$K_{ij,\phi'}(\omega) = \int_0^{2\pi} d\phi_i' \cdot \int_0^{2\pi} d\phi_j' \cdot \frac{trig_{1i}(\phi_i') \cdot trig_{2j}(\phi_j')}{(1 + cS_\theta^2)\,(2 - e^{-dS_\theta^2})} \quad , \qquad \begin{matrix} i,j = 1,2,\ldots,2K \, , \\ r(i) \neq r(j) \, . \end{matrix} \tag{2.251}$$

Curling [61] shows that

$$K_{ij,\phi'}(\omega) = K_{ji,\phi'}(\omega) \, , \qquad \begin{matrix} i,j = 1,2,\ldots,2K \, , \\ i \leq K \text{ and } j \leq K \quad \text{or} \quad i > K \text{ and } j > K \, , \\ r(i) \neq r(j) \, , \end{matrix} \tag{2.252}$$

which means that, referring to the earlier primed coordinates figure, the $z_i'z_j'$ and $z_j'z_i'$ are equal, as well as the $y_i'y_j'$ and $y_j'y_i'$; also, by inspection of eqn.(2.253) to follow, the $z_i'y_j'$ and $y_i'z_j'$ correlations are zero.

The non zero part of eqn.(2.251) has been approximated utilizing a technique similar to that used for $K_{ij,\theta}(\omega)$ of eqn.(2.237), yielding (see Ref.[61]), (the following equation now restricts all cylinders to be of <u>equal radii</u>; should it be required, an equivalent expression for cylinders of arbitrary radii could be easily derived)

$$\left.\begin{aligned} K_{ij,\phi'}(\omega) &\simeq \frac{b_1 \cdot \epsilon_{r(i)r(j)}^{c_1} \cdot |S_R|}{(1 + b_2 \cdot \epsilon_{r(i)r(j)}^{c_2} \cdot S_R^2)} \left(1 + e^{-b_3 |S_R|}\right) \, , \\ & \qquad\qquad\qquad\qquad\qquad\qquad i,j \leq K \quad \text{or} \quad i,j > K \, , \\ & \qquad\qquad\qquad\qquad\qquad\qquad -50 \leq S_R \leq +50 \, , \\ & \qquad\qquad\qquad\qquad\qquad\qquad 2 \leq \epsilon \leq 6 \, , \\ K_{ij,\phi'}(\omega) &= 0 \, , \qquad i \leq K \text{ and } j > K \quad \text{or} \quad i > K \text{ and } j \leq K \, , \\ & \qquad\qquad\qquad\qquad\qquad\qquad i,j = 1,2,\ldots,2K \, , \\ & \qquad\qquad\qquad\qquad\qquad\qquad r(i) \neq r(j) \, , \quad R_{r(i)} = R_{r(j)} \, , \end{aligned}\right\} \tag{2.253}$$

where

$$\epsilon_{ij} = \frac{R_{ij}}{R_0} \quad \text{(see Fig.7)} \, , \qquad i,j = 1,2,\ldots,K \, ; \tag{2.254}$$

in eqn. (2.253), ϵ_{ij} is raised to powers c_1 and c_2.

There are two sets of constants:

$$\left.\begin{aligned} b_1 &= -33.795 \, , \\ b_2 &= 44.342 \, , \\ b_3 &= 0.06283 \, , \\ c_1 &= -1.7348 \, , \\ c_2 &= 0.62895 \, , \end{aligned}\right\} \quad (i,j \leq K) \tag{2.255}$$

and

$$\left.\begin{aligned} b_1 &= 52.183\,, \\ b_2 &= 140.666\,, \\ b_3 &= 0.03942\,, \\ c_1 &= -1.3449\,, \\ c_2 &= 1.2100\,. \end{aligned}\right\} \quad (i,j > K) \tag{2.256}$$

Note that, as in the single cylinder case (see eqn.(2.238)), the constants in eqs.(2.255) and (2.256) are derived from those of Curling [61] (the latter uses "radian" instead of "cycle" Strouhal numbers).

Finally, a coordinate transformation must be used on the cross-spectra in the primed coordinate system, namely on $S_{\Phi_i'\Phi_j'}(\xi_1,\xi_2,\omega)$ of eqn.(2.250), to yield the cross-spectra in the main coordinate system. This is readily accomplished by resolving the "primed" forces into the unprimed (main) coordinate system, as follows:

$$\left.\begin{aligned} \Phi_i(\xi,\tau) &= \Phi_i'(\xi,\tau)\cdot\cos\psi_{ij} - \Phi_{i+K}'(\xi,\tau)\cdot\sin\psi_{ij}\,, \\ \Phi_{i+K}(\xi,\tau) &= \Phi_i'(\xi,\tau)\cdot\sin\psi_{ij} + \Phi_{i+K}'(\xi,\tau)\cdot\cos\psi_{ij}\,, \end{aligned}\right\} \quad \begin{matrix} i = 1,2,\ldots,K\,, \\ (j = 1,2,\ldots,K)\,, \end{matrix} \tag{2.257}$$

and similarly for cylinder j.

Starting from the basic definition of the (dimensionless) cross-correlation function (see eqs.(2.194) and (2.196)), and utilizing the latter equation (and its cylinder j equivalent), we obtain

$$\begin{aligned} R_{\Phi_i\Phi_j}(\xi_1,\xi_2,\tau) &= \cos^2\psi_{ij}\cdot R_{\Phi_i'\Phi_j'}(\xi_1,\xi_2,\tau) + \sin^2\psi_{ij}\cdot R_{\Phi_{i+K}'\Phi_{j+K}'}(\xi_1,\xi_2,\tau) \\ &- \sin\psi_{ij}\cdot\cos\psi_{ij}\cdot\left[R_{\Phi_i'\Phi_{j+K}'}(\xi_1,\xi_2,\tau) + R_{\Phi_{i+K}'\Phi_j'}(\xi_1,\xi_2,\tau)\right], \end{aligned} \tag{2.258}$$

$$\begin{matrix} i,j = 1,2,\ldots,K\,, \\ (i \le K \text{ and } j \le K)\,, \\ i \ne j\,. \end{matrix}$$

Similar equations are obtained for the cases

$$\left.\begin{aligned} &i \le K \text{ and } j > K\,, \\ &i > K \text{ and } j \le K\,, \\ &i > K \text{ and } j > K\,. \end{aligned}\right\} \tag{2.259}$$

Fourier transforming eqn.(2.258), we get

$$S_{\Phi_i\Phi_j}(\xi_1,\xi_2,\omega) = \cos^2\psi_{ij}\cdot S_{\Phi'_i\Phi'_j}(\xi_1,\xi_2,\omega) + \sin^2\psi_{ij}\cdot S_{\Phi'_{i+K}\Phi'_{j+K}}(\xi_1,\xi_2,\omega)$$
$$- \sin\psi_{ij}\cdot\cos\psi_{ij}\cdot\left[S_{\Phi'_i\Phi'_{j+K}}(\xi_1,\xi_2,\omega) + S_{\Phi'_{i+K}\Phi'_j}(\xi_1,\xi_2,\omega)\right], \qquad (2.260)$$
$$i,j = 1,2,\ldots,K,\ (i\le K \text{ and } j\le K),\ i\ne j,$$

with similar equations for the three other cases (see eqn.(2.259)).

Now, after inspection of eqs.(2.252) and (2.250), we may rewrite eqn. (2.260) in the reduced form

$$S_{\Phi_i\Phi_j}(\xi_1,\xi_2,\omega) = \cos^2\psi_{ij}\cdot S_{\Phi'_i\Phi'_j}(\xi_1,\xi_2,\omega) + \sin^2\psi_{ij}\cdot S_{\Phi'_{i+K}\Phi'_{j+K}}(\xi_1,\xi_2,\omega), \qquad (2.261)$$
$$i,j = 1,2,\ldots,K,\ (i\le K \text{ and } j\le K),\ i\ne j,$$

again with similarly reduced forms for the other three cases. All four cases can be combined to yield the two cylinder form of eqn.(2.236):

$$S_{\Phi_i\Phi_j}(\xi_1,\xi_2,\omega) = M_{ij}(\psi_{r(i)r(j)})\cdot S_{\Phi'_{r(i)}\Phi'_{r(j)}}(\xi_1,\xi_2,\omega) + \left[N_{ij} - M_{ij}(\psi_{r(i)r(j)})\right]\cdot S_{\Phi'_{r(i)+K}\Phi'_{r(j)+K}}(\xi_1,\xi_2,\omega), \qquad (2.262)$$
$$i,j = 1,2,\ldots,2K,\ r(i)\ne r(j),$$

where we recall that the primed coordinate system cross-spectra are defined by eqn.(2.250), and where

$$M_{ij}(\psi_{r(i)r(j)}) = \text{trig}_i(\psi_{r(i)r(j)})\cdot\text{trig}_j(\psi_{r(i)r(j)}), \qquad (2.263)$$
$$i,j = 1,2,\ldots,2K,$$

the trig_i function having been previously defined in eqn.(2.198), and

$$N_{ij} = \begin{cases} 1 & \text{, if } i,j\le K \text{ or } i,j>K, \\ 0 & \text{, otherwise.} \end{cases} \qquad i,j = 1,2,\ldots,2K, \qquad (2.264)$$

Note that Curling [61] utilizes a 4 x 4 matrix of trigonometric functions instead of the ones defined in eqs.(2.263) and (2.264); his equation, corresponding to eqn.(2.262) above, also contains summations. The latter equation is of a simpler form and is utilized in the FORTRAN computer program listed in Appendix K.

At this point, we have both the single cylinder and cylinder pair form of the cross-spectral densities $S_{\Phi_i \Phi_j}(\xi_1, \xi_2, \omega)$, namely eqn.(2.236) (when $r(i) = r(j)$) and eqn.(2.262) (when $r(i) \neq r(j)$), which completes the pressure forces characterization and allows us to finalize the expression for the response cross-spectral density defined by eqn.(2.192). Hence, from the latter three equations we obtain

$$S_{\eta_i \eta_j}(\xi, \xi', \omega) = \left[\frac{2}{\pi}\frac{\varepsilon}{R_0}\right]^2 R_{r(i)} \cdot R_{r(j)} \cdot S_{p_m p_m}(0,0,\omega) \cdot \sum_{q=1}^{N} \sum_{s=1}^{N} \phi_q(\xi) \cdot \phi_s(\xi')$$

$$\cdot \sum_{r=1}^{2KN} \sum_{v=1}^{2KN} H^{*}_{\beta(q,i)_r}(\omega) \cdot H_{\beta(s,j)_v}(\omega) \cdot K_{a(r)a(v),\xi}(\omega) \cdot F_{b(r)b(v)}(\omega), \qquad (2.265)$$

$$i,j = 1,2,\ldots,2K,$$

where we have defined two functions, namely

$$K_{ij,\xi}(\omega) = \int_0^1 d\xi_1 \cdot \int_0^1 d\xi_2 \cdot \phi_i(\xi_1) \cdot \phi_j(\xi_2) \cdot e^{-b|S_\xi|} \cdot e^{-j2\pi \cdot S_\xi}, \qquad (2.266)$$

$$i,j = 1,2,\ldots,N,$$

and

$$F_{ij}(\omega) = \begin{cases} K_{ij,\theta}(\omega), & \text{if } r(i) = r(j) \quad \text{[single cylinder]}, \\ M_{ij}(\psi_{r(i)r(j)}) \cdot K_{r(i)r(j),\phi'}(\omega) + \left[N_{ij} - M_{ij}(\psi_{r(i)r(j)})\right] \\ \quad \cdot K_{(r(i)+K)(r(j)+K),\phi'}(\omega), & \text{if } r(i) \neq r(j) \quad \text{[cylinder pair]}, \end{cases} \qquad (2.267)$$

$$i,j = 1,2,\ldots,2K.$$

Theoretical results, namely eqn.(2.265), predict the double-sided CSD's of lateral cylinder displacements/length, at longitudinal locations x_i/L and x_j/L respectively, for cylinder pair i,j (see eqs.(2.47) and (2.48)). For comparisons with experimental results, computer codes were written to calculate <u>one-sided</u> CSD's of lateral displacements/<u>diameter</u>, at the longitudinal location $x_i/L = x_j/L = 0.4186$. The latter value was chosen so that, at least, the first three (clamped-clamped) beam modes would be included in the response (see Fig.8). Based on eqn.(2.265), we may write

$$G_{d_i d_j}(\xi_0, \xi_0, \omega) = \left[\frac{2}{\pi}\frac{\varepsilon^2}{R_0}\right]^2 R_{r(i)} \cdot R_{r(j)} \cdot G_{p_m p_m}(0,0,\omega) \cdot \sum_{q=1}^{N} \sum_{s=1}^{N} \phi_q(\xi_0) \cdot \phi_s(\xi_0)$$

(continued)

$$\cdot \sum_{r=1}^{2KN} \sum_{v=1}^{2KN} H^{*}_{\beta(q,i)_r}(\omega) \cdot H_{\beta(s,j)_v}(\omega) \cdot K_{a(r)a(v),\xi}(\omega) \cdot F_{b(r)b(v)}(\omega) , \qquad (2.268)$$

$$i,j = 1,2,\ldots,2K ,$$

where

$$\xi_0 = 0.4186 , \qquad (2.269)$$

and where lateral dimensionless coordinates are now

$$d_k = \begin{cases} w_k/D , & k = 1,2,\ldots,K , \\ v_{k-K}/D , & k = K+1,K+2..,2K . \end{cases} \qquad (2.270)$$

Note that we now have ε^4 in eqn.(2.268), instead of ε^2 (eqn.(2.265)). Both FORTRAN and BASIC computer coding was used, the former for the bulk of numerical calculations, and the latter for files handling, scaling and plotting the results. The FORTRAN program calculates the following "transfer function factors":

$$g_{d_i d_j}(\xi_0,\xi_0,\omega) = \sum_{q=1}^{N} \sum_{s=1}^{N} \phi_q(\xi_0) \cdot \phi_s(\xi_0) \cdot \sum_{r=1}^{2KN} \sum_{v=1}^{2KN} H^{*}_{\beta(q,i)_r}(\omega) \cdot H_{\beta(s,j)_v}(\omega)$$

$$\cdot K_{a(r)a(v),\xi}(\omega) \cdot F_{b(r)b(v)}(\omega) , \qquad (2.271)$$

$$i,j = 1,2,\ldots,2K .$$

From eqs.(2.268) and (2.271), the (dimensionless) response CSD's can be written as

$$G_{d_i d_j}(\xi_0,\xi_0,\omega) = \left[\frac{2}{\pi}\frac{\varepsilon^2}{R_0}\right]^2 R_{r(i)} \cdot R_{r(j)} \cdot G_{p_m p_m}(0,0,\omega) \cdot g_{d_i d_j}(\xi_0,\xi_0,\omega) , \qquad (2.272)$$

$$i,j = 1,2,\ldots,2K .$$

Using eqn.(2.200), the one-sided dimensionless pressure PSD's may be written as

$$G_{p_m p_m}(0,0,\omega) = \frac{32\sqrt{\pi}\,\varepsilon^2}{\sqrt{E_0^3\,(m_0+\rho A_0)}}\, G_{p_m p_m}(0,0,\omega) , \qquad m = 1,2,\ldots,K , \qquad (2.273)$$

where $G_{p_m p_m}(0,0,\omega)$ are the dimensional pressure PSD's.

Concluding remarks

(i) The term $S_{p_m p_m}(0,0,\omega)$ has yet to be defined in eqn.(2.265). Curling [61] had used a curve fit by Lakis and Paidoussis [70], of Bakewell [26] data on power spectral densities at the wall of a smooth pipe conveying air. We shall use instead in situ measured wall pressure data to determine pressure PSD's; the methods utilized to interpret measurements are presented in Section 2.5-3 below.

(ii) The function $K_{ij,\xi}(\omega)$ of eqn.(2.266) is derived in Appendix J, for clamped-clamped boundary conditions (Curling's [61] version was for pinned-pinned beams).

(iii) As the function $K_{ij,\phi'}(\omega)$, partly defining $F_{ij}(\omega)$ in eqn. (2.267), applies only to cylinders of equal radii, and since all experimental data pertains to such cylinders, all of the FORTRAN coding relates to such systems (see Appendix K for listings).

(iv) Curling [61] computer programs were very general (not straightforward to use) and furthermore, did not incorporate ratio matrices (see eqn.(2.80)); hence, new Fortran coding was developed for the computations specifically required here and structured for minimum execution time.

2.5-3: Theoretical considerations - pressure measurements

One parameter is left to be determined to permit the computation of the response cross-spectral density $S_{\eta_i \eta_j}(\xi,\xi',\omega)$ of eqn.(2.265), specifically the normal pressure PSD, $S_{p_m p_m}(0,0,\omega)$. Availability of a theoretical model would be ideal, not only to predict $S_{p_m p_m}(0,0,\omega)$, but also to determine $S_{p_m p_n}(\Delta\xi,\Delta\theta_{eq},\omega)$ (for both the $m = n$ and $m \neq n$ cases). Unfortunately, such models do not presently exist (as far as this author is aware of), hence, it was decided to resort to empirical approaches.

The in situ measurement of pressure characteristics within the bundle is a major endeavour, being the subject of a research effort by another member of the flow-induced-vibration group at McGill (L.R. Curling). Nevertheless, it was felt that at least, pressure PSD's had to be measured in situ, albeit only at the channel wall (since "instrumenting" cylinders

within the bundle requires much development work: the cylinders are only 2.5 cm in diameter and immersed in water). This course of action was considered a minimum requirement, since upstream turbulators had to be designed so as to render the flow uniform, to obtain symmetry in the response (from one cylinder to another in the bundle). Because of the difficulties involved, and since in-bundle tests (which include inter-cylinder cases) are planned (Curling), channel wall cross-correlations were not measured, and the empirical ones presented in the previous section will be used. Note that pressure as well as velocity (profile), and turbulence (scale and intensity) measurements also serve to characterize the test facilities.

The pressure fluctuations in the boundary layer are extremely small compared to the static pressure and its fluctuations (due to the circulating pump, etc...); these latter pressures do not result in net forces on cylinders, being uniformly distributed around the circumference. One obvious method for eliminating such unwanted pressure signals that are either constant (mean static pressure), or varying evenly around a cylinder, is to make differential pressure measurements across a diametrical line (as an indication of net forces). Significant error is possible in this latter method, should the pressure transducers sensitivity be even slightly mismatched (to be analysed below). Furthermore, other effects such as channel lateral motion (e.g. due to pump motor transmitted vibration) can induce spurious signals, which would be read as net differential pressures (but in this case, this effect was found to be small). Here it should be noted that the effect of channel lateral accelerations on cylinder motion depends on the relative densities of fluid and cylinder material: no net cylinder motion (relative to their end supports) will result if densities are equal, whether cylinders will deflect in the positive/negative direction of the acceleration if the fluid is more/less dense than the cylinders.

We shall examine the various pressure signals present at the channel wall, whose characteristics will be assumed to represent those existing at the cylinders (in terms of PSD's). The experimental setup is illustrated schematically on the next page.

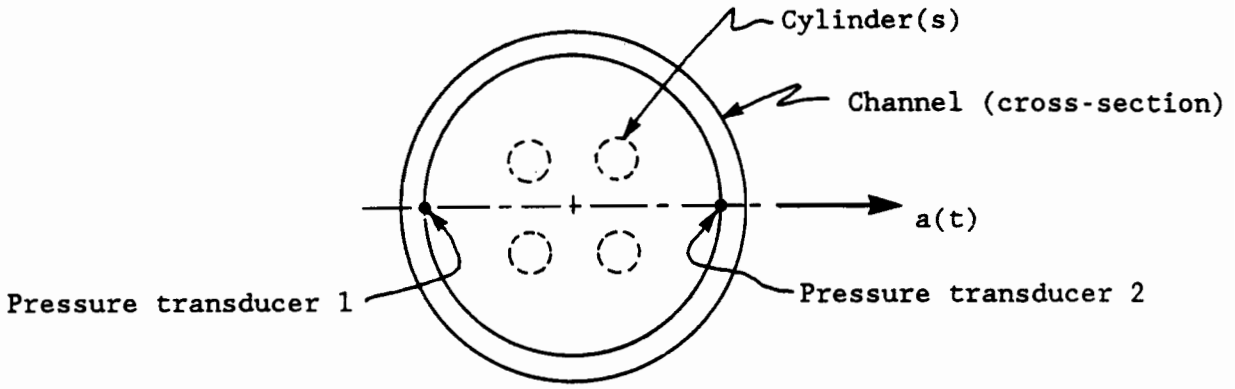

The two point pressures are labelled $p_1(t)$ and $p_2(t)$, and $a(t)$ is the lateral (bulk) channel acceleration (shell mode deformations were found to be negligible). The measured pressures are defined as

$$p_{M_n}(t) = G_n \cdot p_n(t) , \qquad n = 1,2 , \tag{2.274}$$

where the gains G_n are such that

$$G_1 \simeq G_2 \simeq 1 , \tag{2.275}$$

and represent slight error in matching pressure transducers' sensitivities. Note that tests reveal a frequency response that is flat over the range of interest and the match between transducer pairs is excellent; little would have been be gained by making G_1 and G_2 functions of Ω - the nature of measurement errors is well illustrated by the usage of constant gains.

Now, the pressures $p_1(t)$ and $p_2(t)$ are considered to stem from:

(i) the (mean) static pressure, p;

(ii) the static pressure fluctuations, $p_S(t)$;

(iii) acoustically propagated flow disturbances, $p_A(t)$; in the cases where those are (essentially) plane waves travelling along the channel axis, they can be lumped with $p_S(t)$;

(iv) (turbulent) boundary layer pressure fluctuations, labelled $p_{T_1}(t)$ and $p_{T_2}(t)$; they are the quantities of interest here, and their spectral densities are required as inputs in the theoretical model;

(v) channel acceleration induced pressure, $p_a(t)$: it is positive at point 1 and negative at point 2; this potentially yields spurious signals, both for point (absolute) and differential pressures.

Hence, we can write

$$\left.\begin{aligned} p_1(t) &= p + p_S(t) + p_{A_1}(t) + p_a(t) + p_{T_1}(t) \,, \\ p_2(t) &= p + p_S(t) + p_{A_2}(t) - p_a(t) + p_{T_2}(t) \,. \end{aligned}\right\} \tag{2.276}$$

Using eqs.(2.274) and (2.276), we get the measured pressures

$$\left.\begin{aligned} p_{M_1}(t) &= G_1 \left[p + p_S(t) + p_{A_1}(t) + p_a(t) + p_{T_1}(t) \right] , \\ p_{M_2}(t) &= G_2 \left[p + p_S(t) + p_{A_2}(t) - p_a(t) + p_{T_2}(t) \right] . \end{aligned}\right\} \tag{2.277}$$

The true differential pressure is

$$p_d(t) = p_2(t) - p_1(t) \,, \tag{2.278}$$

which, using eqn.(2.276), yields

$$p_d(t) = \left[p_{A_2}(t) - p_{A_1}(t) \right] + \left[p_{T_2}(t) - p_{T_1}(t) \right] - 2 \cdot p_a(t) \,. \tag{2.279}$$

The only term in the last equation that stems purely from boundary layer effects, is $\left[p_{T_2}(t) - p_{T_1}(t) \right]$. The other two are "extraneous", and are deemed not to affect cylinder motion, for the following reasons: The term $\left[p_{A_2}(t) - p_{A_1}(t) \right]$ stems from acoustic pressure, which may be assumed to propagate predominantly along the channel axis (i.e. plane wave) for sources far enough with respect to channel diameter, making that last term vanish. The effect of the acceleration induced pressure, $-2 \cdot p_a(t)$, depends on the relative density of the fluid and the cylinder material; for example, if the cylinder is neutrally buoyant, lateral tunnel accelerations would not result in net cylinder motion, relative to the channel (the cylinder would accelerate as a whole, in phase with the channel). In actual fact, cylinders are about 15 % more dense than the fluid, so that tunnel acceleration induced pressures will affect their motion to some extent, but because the latter have been found to be small (see Appendix N), the effects of $p_a(t)$ (on cylinder) motion may be considered negligible. Hence, the desired pressure is

$$p_d(t) = p_{T_2}(t) - p_{T_1}(t) \,. \tag{2.280}$$

The measured differential pressure is simply

$$p_{d_M}(t) = p_{M_2}(t) - p_{M_1}(t) \,, \tag{2.281}$$

which, making use of eqn.(2.277), becomes

$$p_{d_M}(t) = \Delta G \cdot p + \Delta G \cdot p_S(t) + \left[G_2 \cdot p_{A_2}(t) - G_1 \cdot p_{A_1}(t) \right] - \left[G_1 + G_2 \right] \cdot p_a(t)$$
$$+ \left[G_2 \cdot p_{T_2}(t) - G_1 \cdot p_{T_1}(t) \right] , \tag{2.282}$$

where

$$\Delta G = G_2 - G_1 \,. \tag{2.283}$$

The term $\Delta G \cdot p$ represents a DC offset which, although potentially large (in "DC coupled" pressure transducers), is basically of no concern here, having no effect on motion. As discussed above, the acoustically propagated pressures $p_{A_1}(t)$ and $p_{A_2}(t)$ are deemed equal and in phase (plane waves) and lumped with the static pressure fluctuations term $p_S(t)$. Therefore, eqn. (2.282) takes the reduced form (excludes $\Omega = 0$, i.e. DC signals)

$$p_{d_M}(t) \simeq \Delta G \cdot p_S(t) - \left[G_1 + G_2 \right] \cdot p_a(t) + \left[G_2 \cdot p_{T_2}(t) - G_1 \cdot p_{T_1}(t) \right] , \quad (\Omega > 0) \,. \tag{2.284}$$

In spite of the gains being nearly equal (see eqn.(2.275)), there is potential for significant error in differential pressure measurements, owing to the term $\Delta G \cdot p_S(t)$ in the latest equation. This is because we have $p_S(t) \gg p_{T_n}(t)$ $(n = 1,2)$. Furthermore, the elimination of the acceleration induced pressure, in eqn. (2.284), calls for the measurement of the channel acceleration, together with the measurement of the coherence between the latter and the differential pressure (see Appendix N).

Consequently, to relax requirements for close sensitivity match between transducers, and to eliminate the need for tunnel acceleration measurements, a method based on single point (as opposed to differential) pressures and the corresponding coherence, was developed.

The point pressures $p_{M_1}(t)$ and $p_{M_2}(t)$, given by eqn.(2.277), were measured either using (i) hydrophones, which are "AC coupled", or (ii) a

pair of differential "DC coupled" pressure transducers, one side of each of which was kept pneumatically at pressure p by a specially developed mean tunnel pressure follower (a necessary accessory to prevent not only over-ranges on the transducers, but also irreversible damage; see Fig.9). Hence, in both cases, the mean pressure p was not measured. Also, as discussed above, the acoustically propagated pressures $p_{A_1}(t)$ and $p_{A_2}(t)$ are lumped with the static pressure fluctuations, $p_S(t)$. Consequently, eqn.(2.277) takes the form

$$p_{M_n}(t) = G_n \left[p_S(t) + p_{T_n}(t) \right] + (3 - 2\cdot n)\cdot G_n \cdot p_a(t) \,, \quad n = 1,2. \tag{2.285}$$

*

The terms $G_n \cdot p_S(t) + (3 - 2\cdot n)\cdot G_n \cdot p_a(t)$ may be lumped into two fully correlated pressures, to be shown at once: let

$$p_{C_n}(t) = G_n \left[p_S(t) + (3 - 2\cdot n)\cdot p_a(t) \right] , \quad n = 1,2 . \tag{2.286}$$

For convenience, we rewrite the above as

$$p_{C_n}(t) = s_n(t) + a_n(t) , \quad n = 1,2 , \tag{2.287}$$

where, of course,

$$\left.\begin{aligned} s_n(t) &= G_n \cdot p_S(t) , \\ a_n(t) &= G_n \cdot (3 - 2\cdot n)\cdot p_a(t) , \end{aligned}\right\} \quad n = 1,2 . \tag{2.288}$$

We shall make use of the coherence function, defined by

$$\gamma^2_{p_{C_1} p_{C_2}}(\Omega) = \frac{\left| S_{p_{C_1} p_{C_2}}(\Omega) \right|^2}{S_{p_{C_1}}(\Omega) \cdot S_{p_{C_2}}(\Omega)} \,. \tag{2.289}$$

Now, we assume that the static (and acoustic) pressures and the acceleration induced pressures are fully independent of one another, i.e., we may write

$$S_{s_1 a_1}(\Omega) = S_{s_1 a_2}(\Omega) = S_{s_2 a_1}(\Omega) = S_{s_2 a_2}(\Omega) = 0 , \tag{2.290}$$

which allows us to write

$$S_{p_{C_1} p_{C_2}}(\Omega) = S_{s_1 s_2}(\Omega) + S_{a_1 a_2}(\Omega) , \tag{2.291}$$

---

* The term $(3 - 2\cdot n)$ determines the sign of the last term.

and

$$S_{p_{c_n}}(\Omega) = S_{s_n}(\Omega) + S_{a_n}(\Omega), \qquad n = 1,2 . \tag{2.292}$$

The CSD's are, in general, complex, that is

$$\left.\begin{aligned} S_{s_1 s_2}(\Omega) &= R_{s_1 s_2}(\Omega) + j \cdot I_{s_1 s_2}(\Omega) , \\ S_{a_1 a_2}(\Omega) &= R_{a_1 a_2}(\Omega) + j \cdot I_{a_1 a_2}(\Omega) , \end{aligned}\right\} \tag{2.293}$$

but, in this case, since the signals $s_1(t)$ and $s_2(t)$ are in phase, and the signals $a_1(t)$ and $a_2(t)$ are "out of phase" (180°), their imaginary parts are zero, hence, both $S_{s_1 s_2}(\Omega)$ and $S_{a_1 a_2}(\Omega)$ are <u>real</u>, i.e.

$$I_{s_1 s_2}(\Omega) = I_{a_1 a_2}(\Omega) = 0 . \tag{2.294}$$

Therefore, eqn.(2.291) may be written in the form

$$|S_{p_{c_1} p_{c_2}}(\Omega)|^2 = |S_{s_1 s_2}(\Omega) + S_{a_1 a_2}(\Omega)|^2 = (S_{s_1 s_2}(\Omega) + S_{a_1 a_2}(\Omega))^2 . \tag{2.295}$$

From eqs.(2.289), (2.292), and (2.295), we obtain

$$\gamma^2_{p_{c_1} p_{c_2}}(\Omega) = \frac{(S_{s_1 s_2}(\Omega) + S_{a_1 a_2}(\Omega))^2}{(S_{s_1}(\Omega) + S_{a_1}(\Omega)) \cdot (S_{s_2}(\Omega) + S_{a_2}(\Omega))} . \tag{2.296}$$

The assumptions on $s_n(t)$ and $a_n(t)$ $(n = 1,2)$ are such that their respective coherences are unity, and since their CSD's are real, we may write

$$\left.\begin{aligned} S^2_{s_1 s_2}(\Omega) &= S_{s_1}(\Omega) \cdot S_{s_2}(\Omega) , \\ S^2_{a_1 a_2}(\Omega) &= S_{a_1}(\Omega) \cdot S_{a_2}(\Omega) , \end{aligned}\right\} \tag{2.297}$$

which, after substitution eqn.(2.296), yields

$$\gamma^2_{p_{c_1} p_{c_2}}(\Omega) = \frac{S_{s_1}(\Omega) \cdot S_{s_2}(\Omega) + S_{a_1}(\Omega) \cdot S_{a_2}(\Omega) + 2 \cdot \sqrt{S_{s_1}(\Omega) \cdot S_{s_2}(\Omega) \cdot S_{a_1}(\Omega) \cdot S_{a_2}(\Omega)}}{S_{s_1}(\Omega) \cdot S_{s_2}(\Omega) + S_{s_1}(\Omega) \cdot S_{a_2}(\Omega) + S_{s_2}(\Omega) \cdot S_{a_1}(\Omega) + S_{a_1}(\Omega) \cdot S_{a_2}(\Omega)} . \tag{2.298}$$

The PSD's are assumed symmetrical, namely

$$\left.\begin{aligned} S_{s_1}(\Omega) &= S_{s_2}(\Omega) , \\ S_{a_1}(\Omega) &= S_{a_2}(\Omega) , \end{aligned}\right\} \tag{2.299}$$

and, finally, combining eqs.(2.296) and (2.297), we get

$$\gamma^2_{p_{c_1} p_{c_2}}(\Omega) = 1 . \tag{2.300}$$

Now that the full coherence of static (including acoustic disturbances) and acceleration-induced pressures has been established, we may resume the development of the single point pressure method.

By the nature of the pressure signals, we may state that $G_n \cdot p_{T_n}(t)$ $(n=1,2)$ are totally uncorrelated to $p_{C_m}(t)$ $(m=1,2)$, i.e.

$$\gamma^2_{(p_{C_m})(G_n \cdot p_{T_n})}(\Omega) = 0 \,, \qquad m,n=1,2 \,. \tag{2.301}$$

Also, based on measured turbulence scales, which are about two orders of magnitude less than the test tunnel diameter, we assume no correlation between boundary layer pressures at points 1 and 2 (see P. 85), i.e.

$$\gamma^2_{(G_1 \cdot p_{T_1})(G_2 \cdot p_{T_2})}(\Omega) = 0 \,. \tag{2.302}$$

Remark

Equations (2.300), (2.301) and (2.302) would hold even had we used frequency dependent gains, i.e. $G_n = G_n(\Omega)$, $n=1,2$.

For more compact terminology, we rewrite eqn.(2.285) in the form

$$p_{M_n}(t) = p_{C_n}(t) + p_{U_n}(t) \,, \qquad n=1,2, \tag{2.303}$$

where $p_{C_n}(t)$ is defined by eqn.(2.286), and where

$$p_{U_n}(t) = G_n \cdot p_{T_n}(t) \,, \qquad n=1,2 \,, \tag{2.304}$$

the fully uncorrelated pressures.

Now, from basic definition,

$$R_{p_{M_1} p_{M_2}}(t) = \lim_{\tau_1 \to \infty} \frac{1}{\tau_1} \cdot \int_{-\tau_1/2}^{+\tau_1/2} p_{M_1}(\tau) \cdot p_{M_2}(\tau + t) \cdot d\tau \,,$$

which, making use of eqn.(2.303), reads

$$R_{p_{M_1} p_{M_2}}(t) = R_{p_{C_1} p_{C_2}}(t) + R_{p_{C_1} p_{U_2}}(t) + R_{p_{U_1} p_{C_2}}(t) + R_{p_{U_1} p_{U_2}}(t) \,. \tag{2.305}$$

After inspection of eqs.(2.301), (2.302), (2.286), and (2.304), and Fourier transforming the resulting reduced equation, we get

$$S_{p_{M_1} p_{M_2}}(\Omega) = S_{p_{C_1} p_{C_2}}(\Omega) \ . \tag{2.306}$$

By definition,

$$\gamma^2_{p_{M_1} p_{M_2}}(\Omega) = \frac{\left| S_{p_{M_1} p_{M_2}}(\Omega) \right|^2}{S_{p_{M_1}}(\Omega) \cdot S_{p_{M_2}}(\Omega)} \ , \tag{2.307}$$

and similarly for $\gamma^2_{p_{C_1} p_{C_2}}(\Omega)$. From eqs.(2.300) and (2.289), we obtain

$$\left| S_{p_{C_1} p_{C_2}}(\Omega) \right|^2 = S_{p_{C_1}}(\Omega) \cdot S_{p_{C_2}}(\Omega) \ , \tag{2.308}$$

and using this latter equation together with eqs.(2.306) and (2.307) results in

$$\gamma^2_{p_{M_1} p_{M_2}}(\Omega) = \frac{S_{p_{C_1}}(\Omega) \cdot S_{p_{C_2}}(\Omega)}{S_{p_{M_1}}(\Omega) \cdot S_{p_{M_2}}(\Omega)} \ . \tag{2.309}$$

From symmetry, we set

$$S_{p_{T_1}}(\Omega) = S_{p_{T_2}}(\Omega) \ , \tag{2.310}$$

which, when used in eqn.(2.304), results in the relation

$$G_2^2 \cdot S_{p_{U_1}}(\Omega) = G_1^2 \cdot S_{p_{U_2}}(\Omega) \ . \tag{2.311}$$

By inspection, eqs.(2.300) and (2.303), we get

$$S_{p_{M_n}}(\Omega) = S_{p_{C_n}}(\Omega) + S_{p_{U_n}}(\Omega) \ , \qquad n = 1,2 \ , \tag{2.312}$$

which, combined with eqn.(2.311), yields

$$G_2^2 \cdot \left[S_{p_{M_1}}(\Omega) - S_{p_{C_1}}(\Omega) \right] = G_1^2 \cdot \left[S_{p_{M_2}}(\Omega) - S_{p_{C_2}}(\Omega) \right] \ ,$$

which can be rearranged to read

$$\frac{S_{p_{C_2}}(\Omega)}{S_{p_{M_2}}(\Omega)} - \frac{S_{p_{C_1}}(\Omega) \cdot S_{p_{C_2}}(\Omega)}{S_{p_{M_1}}(\Omega) \cdot S_{p_{M_2}}(\Omega)} = \left[\frac{G_1}{G_2} \right]^2 \cdot \frac{S_{p_{M_2}}(\Omega)}{S_{p_{M_1}}(\Omega)} \cdot \frac{S_{p_{C_2}}(\Omega)}{S_{p_{M_2}}(\Omega)} \left[1 - \frac{S_{p_{C_2}}(\Omega)}{S_{p_{M_2}}(\Omega)} \right] . \tag{2.313}$$

Now, we define

$$P(\Omega) = \frac{S_{p_{M_2}}(\Omega)}{S_{p_{M_1}}(\Omega)} \quad , \tag{2.314}$$

a quantity to be experimentally obtained, and

$$R(\Omega) = \frac{S_{p_{C_2}}(\Omega)}{S_{p_{M_2}}(\Omega)} \quad , \tag{2.315}$$

a ratio to be computed, as shown below.

Substituting eqs.(2.314), (2.315), as well as eqn.(2.309), into eqn. (2.313), yields

$$R(\Omega) - \gamma^2_{p_{M_1}p_{M_2}}(\Omega) = \left[\frac{G_1}{G_2}\right]^2 \cdot P(\Omega)\cdot R(\Omega) \cdot \Big[\, 1 - R(\Omega) \,\Big] \, ,$$

which is a quadratic equation in $R(\Omega)$, namely

$$\left[\frac{G_1}{G_2}\right]^2 \cdot P(\Omega)\cdot R^2(\Omega) + \left[\, 1 - \left[\frac{G_1}{G_2}\right]^2 \cdot P(\Omega) \,\right] R(\Omega) - \gamma^2_{p_{M_1}p_{M_2}}(\Omega) = 0. \tag{2.316}$$

Since none of the four quantities $(G_1/G_2)^2$, $P(\Omega)$, $\gamma^2_{p_{M_1}p_{M_2}}(\Omega)$, or $R(\Omega)$ can be negative, the solution to eqn.(2.303) reads

$$R(\Omega) = \frac{-B(\Omega) + \sqrt{B^2(\Omega) - 4\cdot A(\Omega)\cdot C(\Omega)}}{2\cdot A(\Omega)} \quad , \tag{2.317}$$

where

$$\left.\begin{aligned} A(\Omega) &= \left[\frac{G_1}{G_2}\right]^2 \cdot P(\Omega) \, , \\ B(\Omega) &= \left[\, 1 - \left[\frac{G_1}{G_2}\right]^2 \cdot P(\Omega) \,\right] \, , \\ C(\Omega) &= - \gamma^2_{p_{M_1}p_{M_2}}(\Omega) \, . \end{aligned}\right\} \tag{2.318}$$

Note that the coherence function, $\gamma^2_{p_{M_1}p_{M_2}}(\Omega)$, is determined experimentally.

Finally, from eqs.(2.312) and (2.315), we obtain

$$R(\Omega) = 1 - \frac{S_{p_{U_2}}(\Omega)}{S_{p_{M_2}}(\Omega)} \, , \tag{2.319}$$

but, from eqn.(2.304), we get

$$S_{p_{U_2}}(\Omega) = G_2^2 \cdot S_{p_{T_2}}(\Omega) \ , \tag{2.320}$$

hence, the latter two equations lead to

$$S_{p_{T_n}}(\Omega) = \frac{1 - R(\Omega)}{G_2^2} S_{p_{M_2}}(\Omega) \ , \qquad n = 1,2 \ , \tag{2.321}$$

where eqn.(2.310) has been taken into account.

We shall prove that the factor $(1 - R(\Omega))$, in the last equation, has variations of the same order of magnitude as either (G_1/G_2), or $P(\Omega)$; this is to verify that the method developed above, resulting in eqn.(2.321), does not require accurate match of pressure transducer gains, and is not overly dependent on point pressure PSD's symmetry.

For convenience, we let

$$Q = (G_1/G_2)^2 \ , \tag{2.322}$$

Eqn.(2.318) may therefore be rewritten as

$$\left.\begin{aligned} A &= Q \cdot P \ , \\ B &= (1 - Q \cdot P) \ , \\ C &= -\gamma^2_{p_{M_1} p_{M_2}} \ , \end{aligned}\right\} \tag{2.323}$$

where independent variable Ω has been omitted for convenience. We note that the parameters Q and P only occur in the form of the product $(Q \cdot P)$: this allows us to seek only a single partial derivative; from eqs.(2.317) and (2.323), we find

$$\frac{\partial(1 - R)}{\partial P} = \frac{PQ(2\gamma^2 - 1) + 1 - S}{2P^2 QS} \ , \tag{2.324}$$

where we have defined

$$S = [P^2 Q^2 + 2PQ(2\gamma^2 - 1) + 1]^{1/2} . \tag{2.325}$$

---

* For simplicity, the "subscript" has been omitted for the coherence (γ).

Of course, we may write (interchanging P and Q in eqs.(2.324) and (2.325))

$$\frac{\partial(1 - R)}{\partial Q} = \frac{PQ(2\gamma^2 - 1) + 1 - S}{4PQ^2 S} , \tag{2.326}$$

We actually want the quantities $\frac{\partial(1 - R)/(1 - R)}{\partial P/P}$, and $\frac{\partial(1 - R)/(1 - R)}{\partial(G_1/G_2)/(G_1/G_2)}$, that is the rate of change of $(1 - R)$ with respect of the rates of change of P and (G_1/G_2) respectively. First, we note that

$$\frac{\partial(1 - R)/(1 - R)}{\partial P/P} = \frac{\partial(1 - R)}{\partial P} \cdot \frac{P}{1 - R} ,$$

which, after making use of eqs.(2.317), (2.323), and (2.324), yields

$$\frac{\partial(1 - R)/(1 - R)}{\partial P/P} = \frac{PQ(2\gamma^2 - 1) + 1 - S}{S\,(PQ + 1 - S)} . \tag{2.327}$$

From eqn.(2.322), we note that

$\frac{\partial Q}{Q} = 2\,\frac{\partial(G_1/G_2)}{(G_1/G_2)}$, and proceeding as above, we obtain

$$\frac{\partial(1 - R)/(1 - R)}{\partial(G_1/G_2)/(G_1/G_2)} = 2\,\frac{PQ(2\gamma^2 - 1) + 1 - S}{S\,(PQ + 1 - S)} . \tag{2.328}$$

We wish to evaluate the rates of change about the nominal conditions, which are $P = P(\Omega) = 1$ (symmetry of point pressure PSD's), and $Q = 1$ (equality of pressure transducer gains). Eqs.(2.327) and (2.328) yield

$$\left.\frac{\partial(1 - R)/(1 - R)}{\partial P/P}\right|_{P=Q=1} = -\frac{1}{2} , \tag{2.329}$$

and

$$\left.\frac{\partial(1 - R)/(1 - R)}{\partial(G_1/G_2)/(G_1/G_2)}\right|_{P=Q=1} = -1 . \tag{2.330}$$

We see that the error in "measurement" of $R(\Omega)$ is of the same order of magnitude as the degree of deviation of point pressure PSD's from symmetry (see eqn.(2.314)), and likewise on the error in gain matching (ratio, see eqn.(2.322)); as PSD symmetry has been found to be excellent, and as the gain ratio is easily set very close to unity, the error in $R(\Omega)$ may be considered negligible.

Gains G_1 and G_2 can be adjusted, easily to within 1% (i.e. the maximum deviation of the gain ratio), hence we let

$$\frac{G_1}{G_2} = 1 \ , \tag{2.331}$$

in eqn.(2.318), yielding for eqn.(2.317),

$$R(\Omega) = \frac{\left[P(\Omega) - 1 \right] + \left[\left[P(\Omega) - 1 \right]^2 + 4 \cdot P(\Omega) \cdot \gamma^2_{p_{M_1} p_{M_2}}(\Omega) \right]^{1/2}}{2 \cdot P(\Omega)} \ , \tag{2.332}$$

and for eqn.(2.321),

$$S_{p_{T_n}}(\Omega) = \left[1 - R(\Omega) \right] \cdot S_{p_{M_2}}(\Omega) \ , \qquad n = 1,2 \ . \tag{2.333}$$

Note that the special case where we have perfect symmetry, i.e. $G_1 = G_2 = 1$, and $P(\Omega) = 1$ (for all Ω), then eqs.(2.317) and (2.318) reduce to

$$R(\Omega) = \gamma_{p_{M_1} p_{M_2}}(\Omega) \ . \tag{2.334}$$

In summary, the method utilized to compute the boundary layer point pressure fluctuations, from point pressure measurements, is as follows:

(i) measurement of the point pressure PSD's, $S_{p_{M_1}}(\Omega)$ and $S_{p_{M_2}}(\Omega)$, is effected (at points 1 and 2), as well as the corresponding coherence function $\gamma^2_{p_{M_1} p_{M_2}}(\Omega)$;

(ii) the function $P(\Omega)$, given by eqn.(2.314), is calculated;

(iii) the function $R(\Omega)$ is computed from eqn.(2.332); and finally

(iv) the boundary layer (point) pressure PSD, $S_{p_{T_n}}(\Omega)$ $(n = 1,2)$, is calculated, from eqn.(2.333).

Note that, because of eqs.(2.310) and (2.301), eqn.(2.280) yields

$$S_{p_d}(\Omega) = 2 \cdot S_{p_{T_n}}(\Omega) \ , \quad (n = 1,2) \ . \tag{2.335}$$

The direct method of measurement yields, using eqn.(2.284) (autocorrelation, Fourier transformed), subject to eqs.(2.301) and (2.302),

$$S_{p_{d_M}}(\Omega) \simeq (\Delta G)^2 \cdot S_{p_S}(\Omega) + G_1^2 \cdot S_{p_{T_1}}(\Omega) + G_2^2 \cdot S_{p_{T_2}}(\Omega) \ ,$$

which can be rewritten, with little loss in accuracy,

$$S_{p_{d_M}}(\Omega) = (\Delta G)^2 \cdot S_{p_S}(\Omega) + 2 \cdot S_{p_{T_n}}(\Omega) \ , \quad (n = 1,2) \ . \tag{2.336}$$

When gains are matched, eqs.(2.333), (2.335), and (2.336) yield

$$2 \left[1 - R(\Omega) \right] \cdot S_{p_{M_2}}(\Omega) \simeq S_{p_{d_M}}(\Omega) \ . \tag{2.337}$$

The latter relationship was used to compare the direct method of measurement (RHS of eqn.(2.337)) to the computational one (LHS of eqn.(2.337)) - with excellent agreement (see Appendix N).

Remarks

(i) The measured PSD's are single-sided ($\Omega \geq 0$) rather than the double-sided ones presented in the theoretical models (which arise naturally from one of the frequency limits being $-\infty$). Recall that

$$G(\Omega) = 2 \cdot S(\Omega) \ , \qquad \Omega \geq 0 \ , \tag{2.338}$$

since $S(\Omega)$ is always an even function of Ω.

(ii) Experimental data was processed using the single-sided form of eqn. (2.337), namely

$$G_{p_{d_M}}(\Omega) \simeq 2 \left[1 - R(\Omega) \right] \cdot G_{p_{M_2}}(\Omega) \ . \tag{2.339}$$

The latter results were later converted to single point pressure PSD's, by using the single-sided form of eqn.(2.335):

$$G_{p_T}(\Omega) = \frac{1}{2} \cdot G_{p_d}(\Omega) \ , \tag{2.340}$$

and then non-dimensionalized, yielding $G_{p_m p_m}(0,0,\omega)$ [see eqn.(2.273)], for input to the theoretical model.

3. TEST EQUIPMENT

3.1: WATER TUNNEL

Tests were conducted in a closed loop stainless steel water tunnel, a schematic of which is shown in Fig. 10.; cylinder bundles were mounted inside a 74 cm (29 in) long vertical sub-section of the tunnel, which is a 20.5 cm (8.06 in) diameter acrylic (plexiglas) channel, illustrated in Fig. 1. The latter (picture) also shows the two access windows, with the upper one holding a static pressure control transducer (see text below), a cluster of four aluminium cylinders together with their lower brass support (the upper one is barely visible), and a pair of wall mounted pressure transducers. Water was circulated by a centrifugal pump* driven by an SCR controlled 40 hp motor§, allowing average bulk velocities of up to about 6 m/s (20 ft/sec); continuous deaeration under partial vacuum (about 1/3 below atmospheric) was used to keep the water free of air bubbles and a heat exchanger utilized to keep the temperature relatively constant ($\pm 1^{\circ}C$) [necessary because of thermal expansion in the rubber, yielding a change in tension]; the water static pressure was kept at 55.2±2.0 KPa (8.0±0.3 psi), by an automatic feedback system which controlled the position of the heat exchanger water flowthrough valve (average flow rate through the exchanger could be varied by adjusting its outlet valve).

Average (bulk) velocity in the bundle was calculated from the water volumetric flow rate and the net cross-sectional area in the channel (taking into account the presence of the cylinders); a Venturi insert nozzle† together with a mercury manometer were used to measure volume flow rates. Flow in the test section was downward. Especially because of the relatively close proximity of turning vanes (see Fig. 10), flow characteristics in the test section were not sufficiently uniform to yield acceptable symmetry in the vibration response (tests with bundles of four cylinders). Consequently, a turbulator had to be designed to improve conditions: the basic aim was to obtain adequate symmetry of response while maintaining vibration levels to

---

* Ingersol-Rand, Centurion type S.

§ Beel Controls Ltd.; speed regulation 0.1% @ 95% load change.

† BIF model 131.

a minimum. The two stage turbulator illustrated in Fig. 11 fulfilled such criteria: the first stage is meant to create larger scale turbulence to promote mixing, while the purpose of the second one is to reduce both turbulence level and scale. The latter stage was located 32.5 cm (12.8 in) upstream from (top of) cylinders.

The basic measurements made pertained to cylinder vibration characteristics. Tests were also conducted on water pressure spectra at the channel wall, and fluid velocity profiles together with turbulence intensity and scale were measured so as to characterize the tunnel (see Appendix L).

3.2: PRESSURE - TRANSDUCERS

Pressures were measured at the tunnel wall, at diametrically opposite points, located 23.3 cm (9.2 in) downstream from the cylinders top (almost exactly mid-point along the cluster). Holes, 0.16 cm (1/16 in) dia., were drilled directly in the channel wall, and hydrophones were mounted at the outer surface of the wall, as shown in Fig. 12. The latter transducers were PCB microphones, model 106B; their frequency range is 0.5 Hz (-5%) to 60 KHz (resonance), and linearity is 1.0 %. To investigate pressure characteristics at very low frequencies, some measurements were also conducted with unbonded strain gages differential pressure transducers, STATHAM model PM5TC, the frequency range being 0 to 12 Hz (resonance*) and linearity 0.5% of full scale; the latter measurements are presented in Appendix N.§ It should be noted that the response of hydrophones, mounted as shown in Fig. 12, has a lower resonant frequency, but in this case, owing to the very high stiffness of the PCB microphones (calculated in Appendix N), that limit is much higher than the range of interest.

Note that to obtain differential pressures, one of two techniques is used, namely (i) subtraction of the two analog signals (voltages), or (ii)

---

* Tested in water, see Appendix N.

§ PCB measurements were smoothed and low frequency extrapolation utilized: the latter was based on STATHAM tests.

processing of the frequency domain information (PSD's together with the coherence, see Section 2.5-3).

3.3: VIBRATION - INSTRUMENTED CYLINDERS

Vibration experiments were conducted with 47.0 cm (18.5 in) long and 2.53 cm (0.996 in) diameter flexible silicone (Dow Corning Silastic E) rubber cylinders, some of which were instrumented with strain gages. Mounting in the test section was effected: (i) for clusters of four or less, with ogival supports at the upstream end and cylindrical supports at the downstream end; supports themselves were fixed to fins arranged in a cross and supported at the channel wall; [Fig. 13 depicts a typical bundle (in the picture, aluminium cylinders were used to make the assembly rigid); recall that cylinder mounting is also shown in Fig. 3]; (ii) for clusters of 28 (of which only four were flexible), with machined support plates, the top one being shown schematically in Fig. 14. It should be noted that, as the rubber cylinders have a very low modulus of elasticity and the mountings are metal and firmly anchored to the tunnel wall, the upper and lower boundary conditions can truly be said to be clamped. Furthermore, flexibility easily allowed reaching high dimensionless velocities, up to and above the first beam mode critical buckling (divergence type instability) point [55].

The cylinders that were instrumented had been cast with embedded strain gages, shown schematically in Fig. 15: each of two orthogonal deflection planes of motion was sensed by a pair of gages. The latter were mounted relatively close to the outer surface, and in a longitudinal location that yielded almost equal response to unit amplitude deflections in the first three (free lateral vibration, clamped-clamped) beam modes; see Appendix H for details on the determination of that location, and Appendix M of Ref. [75] for the manufacturing technique.

Details on the electronics used (strain gage bridge balancing and amplification circuits, etc.) are found in Ref. [75]; Amplifiers* had a zero to

---

* Analog Devices 606L instrumentation amplifiers (powered by Analog Devices 902 power supply).

10 KHz bandwidth, and excellent linearity (0.002%).

Calibration of the instrumented cylinders was necessary, mostly since the gages themselves are stiffer than the silicone rubber, thereby resisting deformation; the measured strain is lower than that which would occur should the gages have a flexibility equal to that of the rubber. Fortunately, the response was found to be repeatable and linear (albeit about 12 times lower than strain levels calculated from beam geometry), in two sets of tests utilizing different beam deflection modes, the first for a clamped-free beam being deflected at the (free) end, and the second for a clamped-clamped beam being deflected at its mid-length (see Appendix M for details). None of the latter modes is identical to that of a freely vibrating beam, although the second is closer; to confirm the validity of the calibration results without the burden of a dynamic test, an instrumented cylinder was tested under static deflection (due to gravity) in a horizontal position (the latter mode is almost identical to a dynamic mode) and the strain gage bridge output was within 2% of the value predicted from the previous calibration results.

For comparisons with theory, we wish to convert the voltage output from the strain gage circuits, to the dimensionless displacement at $\xi_0 = 0.4186$ (see eqn.(2.269)). Although strain gage outputs reflect about equally <u>maximum</u> deflections in the first three natural beam modes (which occur at different values of ξ, see Appendix H), they <u>do not</u> reflect equal deflection amplitudes at ξ_0. For later reference, strain gage outputs represent the following relative deflection amplitudes at ξ_0, found by considering normalized deflections and their second derivative (see Figs. 8 and H.1):

$$\begin{aligned} (d)_1 &= 1.000\,, \qquad \text{(reference)} \\ (d)_2 &= 0.563\,, \\ (d)_3 &= 0.586\,. \end{aligned} \tag{3.1}$$

The actual dimensionless deflection $(d)_1$ is obtained as follows. The true strain at $\xi = 0.1047$ (gage location) can be calculated, for a first natural beam mode deflection, from the amplifier output voltage e_0, by using eqn.(M.27), namely

$$\varepsilon_t = 2 \cdot c_0 \cdot \frac{e_0}{G} , \tag{3.2}$$

where we recall (Appendix M) that c_0 is a calibrated "gage coefficient", G is the amplifier gain, and ε_t is the (theoretical) strain (at $\xi = 0.1047$, for a first natural beam mode deflection).

Now, from eqs.(H.1) and (H.7), we may write

$$[\phi_1(\xi)]_{meas} = A_1 \{\cos(\lambda_1 \xi) - \cosh(\lambda_1 \xi) - \sigma_1 [\sin(\lambda_1 \xi) - \sinh(\lambda_1 \xi)]\} , \tag{3.3}$$

and

$$\frac{d^2 [\phi_1(\xi)]_{meas}}{d\xi^2} = \frac{L^2}{aD} \varepsilon_t = -A_1 \lambda_1^2 \{\cos(\lambda_1 \xi) + \cosh(\lambda_1 \xi) - \sigma_1 [\sin(\lambda_1 \xi) + \sinh(\lambda_1 \xi)]\} \Big|_{\xi = 0.1047} , \quad \text{(at gage location)} \tag{3.4}$$

where we note that a new constant A_1 has been used, since the beam mode $[\phi_1(\xi)]_{meas}$ now represents the measured dimensionless deflection (corresponding to the first (natural beam) mode), where the non-dimensionalization is with respect to diameter (rather than length, as in Appendix M), that is

$$[\phi_1(\xi)]_{meas} = \frac{1}{D} [Y_1(x = L\xi)]_{meas} , \quad \text{(subject to eqn.(2.47))} \tag{3.5}$$

which results in

$$\frac{d^2 [\phi_1(\xi)]_{meas}}{d\xi^2} = \frac{L^2}{D} \frac{d^2 [Y_1(x)]_{meas}}{dx^2} . \tag{3.6}$$

From eqs.(3.2), (3.3), and (3.4), we obtain

$$[\phi_1(\xi)]_{meas} = \frac{1}{\cos(\lambda_1 \xi) + \cosh(\lambda_1 \xi) - \sigma_1 [\sin(\lambda_1 \xi) + \sinh(\lambda_1 \xi)] \Big|_{\xi = 0.1047}} \cdot \frac{-2 L^2 c_0 e_0}{a D G \lambda_1^2} \{\cos(\lambda_1 \xi) - \cosh(\lambda_1 \xi) - \sigma_1 [\sin(\lambda_1 \xi) - \sinh(\lambda_1 \xi)]\} . \tag{3.7}$$

Recalling various system constants, namely

$$\left.\begin{aligned} &\lambda_1 \simeq 4.730040745 \,, \\ &\sigma_1 \simeq 0.982502215 \,, \\ &L = 47.0 \text{ cm} \,, \\ &D = 2.53 \text{ cm} \,, \\ &a = 1.00 \text{ cm} \,, \end{aligned}\right\} \quad \text{(see Fig. 14)} \tag{3.8}$$

we obtain

$$[\phi_1(\xi)]_{meas} \simeq -75.675 \ \frac{c_0 \, e_0}{G} \ \{\cos(\lambda_1 \xi) - \cosh(\lambda_1 \xi) - \sigma_1 [\sin(\lambda_1 \xi) - \sinh(\lambda_1 \xi)]\} \,. \tag{3.9}$$

Three more parameters are constant in the experiments, specifically, the "gage coefficient" c_0 (but we have slightly different values for each of the two instrumented cylinders), the amplifier gain G, and the longitudinal location $\xi = \xi_0$, at which we wish to compute the measured displacement(s) [assuming a first beam mode deflection; this shall be discussed in the next Chapter, when examining the results]:

- from Appendix M (eqn.M.26)),

$$\begin{aligned} &(c_0)_{cyl\ 1} \simeq 1.11 \ (\text{volts})^{-1} \,, \\ &(c_0)_{cyl\ 2} \simeq 1.18 \ (\text{volts})^{-1} \,; \end{aligned} \tag{3.10}$$

- the amplifier gain was set (to obtain output voltages in the range required by signal processing instrumentation) to

$$G = 5000 \,; \tag{3.11}$$

- and, as established earlier (see eqn.(2.269)),

$$\xi_0 = 0.4186 \,. \tag{3.12}$$

Finally, from eqs.(3.9) to (3.12), we get

$$[\phi_1(\xi_0)]_{meas} \simeq C_n \cdot e_0 \,, \quad n = 1,2 \,, \tag{3.13}$$

where

$$C_n = \begin{cases} 25.2 \times 10^{-3} \,, & n = 1 \,, \\ 26.8 \times 10^{-3} \,, & n = 2 \,, \end{cases} \tag{3.14}$$

which are calibration factors to be utilized with the two instrumented cylinders.

Remark

Calibration factors for $\xi_0 = 0.5$ had been used in the processing of vibration signals (HP 5420A Spectrum Analyzer) in tunnel tests, namely $C_1 = 26.9 \times 10^{-3}$ and $C_2 = 28.5 \times 10^{-3}$. The results were later rescaled to yield values at $\xi_0 = 0.4186$, for comparisons with theory.

PSD's and CSD's obtained from processing cylinder vibration voltages are still not dimensionless, since the frequency axis (HP5420A) is in Hz, thereby yielding units of Hz^{-1} for the density axis; final non-dimensionalization is effected by making use of eqn.(2.49), as follows.

Let a measured CSD (PSD) be labelled $G(\ell)_{meas}$, with units of $(-)^2/Hz$, and where the numerator represents "power" in dimensionless vibration amplitudes. Therefore, the fully dimensionless CSD (PSD) reads

$$G(\omega)_{meas} = G(\ell)_{meas} \left[\frac{(-)^2\ s}{\text{cycle}}\right] \cdot \frac{\Omega}{\omega} \left[\frac{\text{rad}}{s}\right] \cdot \left\{\frac{\text{cycle}}{2\pi\ \text{rad}}\right\} ,$$

which takes the form (see eqn.(2.49))

$$G(\omega)_{meas} = \frac{1}{2\pi} \cdot \left[\frac{E_0\ I_0}{m_0 + \rho A_0}\right]^{1/2} \cdot \frac{1}{L^2} \cdot G(\ell)_{meas} . \tag{3.15}$$

The system constants are:

$$\begin{aligned} E_0 &\simeq 2780\ \text{KPa}\ (403\ \text{lbf/in}^2) , \\ I_0 &\simeq 2.011\ \text{cm}^4\ (0.0483\ \text{in}^4) , \\ m_0 &\simeq 0.577\ \text{Kgm/m}\ (0.388\ \text{lbm/ft}) , \\ \rho &\simeq 1.00\ \text{gm/cm}^3\ (62.4\ \text{lbm/ft}^3) , \\ A_0 &\simeq 5.03\ \text{cm}^2\ (0.779\ \text{in}^2) , \\ L &\simeq 47.0\ \text{cm}\ (18.5\ \text{in}) . \end{aligned} \tag{3.16}$$

Eqs.(3.15) and (3.16) yield

$$G(\omega)_{meas} \simeq 0.1639 \cdot G(\ell)_{meas} . \tag{3.17}$$

Note that the terms of the latter equation have the following units:

$G(\omega)_{meas}$: -

0.1639 : Hz/rad

$G(\ell)_{meas}$: Hz^{-1}

4. EXPERIMENTAL AND THEORETICAL RESULTS

In order to compute theoretical vibration data, pressure PSD's had to be measured in situ (test channel; recall that pressure correlations are assumed to be the same as those for pipe flow); hence, pressure measurements are covered first, to be followed by theoretical and experimental vibration results.

Dimensionless flow velocity will be used throughout, hence its relationship to the dimensional one is given now: eqn.(2.51), together with the system physical constants (see Section 4.2, to follow), yield

$$U\ [\text{m/sec}] = 0.709 \cdot u\ [-]\ , \tag{4.1}$$

where U and u are the dimensional and dimensionless velocities, respectively, and the factor 0.709 m/sec stems from the term $\frac{1}{L}\left[\frac{E_0 I_0}{\rho A_0}\right]^{1/2}$.

4.1: PRESSURE MEASUREMENTS

4.1-1: Units - pressure data

Before presenting the experimental data, it will prove helpful to discuss scaling from the dimensional measured PSD's, to the dimensionless ones. The latter are the ones used as input to the theoretical model, and are defined by eqn.(2.273), which reads

$$G_{p_m p_m}(0,0,\omega) = \frac{32\sqrt{\pi}\,\varepsilon^2}{\sqrt{E_0^3\,(m_0+\rho A_0)}}\; G_{p_m p_m}(0,0,\omega)\ , \qquad m = 1,2,\ldots,K\ ,$$

where $G_{p_m p_m}(0,0,\omega)$ and $G_{p_m p_m}(0,0,\omega)$ are the dimensionless and dimensional pressure PSD's respectively.

Remark

The frequency argument in density functions, e.g. ω in $G_{p_m p_m}(0,0,\omega)$ above, does not necessarily set the frequency units of the function itself; for example $G_{p_m p_m}(0,0,\omega)$ could have units of $(\text{KPa})^2/\text{Hz}$: when plotted versus ω, and integrated, the resulting units of power would be $(\text{KPa})^2 \cdot (-)/\text{Hz}$,

where (-) are the "units" of the dimensionless frequency ω. This is equivalent to stating a length in, for example, m^2/cm, but is nevertheless valid. The units for pressure power could be made "proper" by multiplication by the factor 0.1639 Hz/rad, discussed at the end of the last Chapter, yielding $(KPa)^2$. This remark is simply to stress that $G_{p_m p_m}(0,0,\omega)$ in the above equation could have been written as $G_{p_m p_m}(0,0,\Omega)$.

Pressure data shall be presented in one of two forms; these are (i) in dimensionless form, i.e. $G_{p_m p_m}(0,0,\omega)$ versus ω, and (ii) in dimensional form, i.e. $G_{p_m p_m}(0,0,\ell)$ versus ℓ, with density units as $(KPa)^2/Hz$, and frequency units as Hz.

Dimensional pressure PSD's may be obtained from dimensionless ones by multiplication by the factor

$$\frac{\sqrt{E_0^3\,(m_0 + \rho A_0)}}{32\sqrt{\pi}\,\varepsilon^2} \quad \text{(see above equation)},$$

which yields (see physical constants, in Section 4.2 to follow)

$$G_{pp}(\ell)\ [(KPa)^2/Hz] = 1.545 \cdot G_{pp}(\omega)\ [-]\ . \tag{4.2}$$

The frequency axis scaling is simply effected with the factor (see eqn. (2.50))

$$\frac{1}{L^2}\cdot\left[\frac{E_0 I_0}{m_0 + \rho A_0}\right]^{1/2} \quad \text{(together with } 2\pi \text{ rad/(Hz·sec)) yielding}$$

$$\ell\ [Hz] = 0.1639 \cdot \omega\ [-]\ . \tag{4.3}$$

4.1-2: Pressure - results

Processing of the measured data points may yield either differential or single point pressure PSD's (which are related by eqn.(2.340)). For example, in one-sided PSD terminology and with Hz as the frequency units, eqn. (2.333) reads

$$G_{p_T}(\ell) = \left[1 - R(\ell)\right] \cdot G_{p_{M2}}(\ell)\ , \tag{4.4}$$

where $G_{p_{M_2}}(\ell)$ is the measured (transducer no.2) single point PSD, and $G_{p_T}(\ell)$ is the single point turbulent boundary layer pressure fluctuation PSD, and

where $R(\ell)$ is found from (see eqn.(2.310))

$$R(\ell) = \frac{\left[P(\ell) - 1\right] + \left[\left[P(\ell) - 1\right]^2 + 4 \cdot P(\ell) \cdot \gamma^2_{p_1 p_2}(\ell)\right]^{1/2}}{2 \cdot P(\ell)} \quad . \tag{4.5}$$

$P(\ell)$ reads (see eqn.(2.314))

$$P(\ell) = \frac{G_{p_{M_2}}(\ell)}{G_{p_{M_1}}(\ell)} \quad . \tag{4.6}$$

To obtain differential pressure PSD's, eqn.(2.335) is used; it may be rewritten as

$$G_{p_d}(\ell) = 2 \cdot G_{p_T}(\ell) \quad . \tag{4.7}$$

Since the theoretical model is set to utilize single point pressure PSD's, that form (as opposed to differential pressure PSD's, i.e. using eqn.(4.7)) shall be used here. It should be noted that

$$G_{p_T}(\ell) = G_{pp}(\ell) = G_{p_m p_m}(0,0,\omega(\ell)) \quad .$$

Pressure data was gathered for three different tunnel configurations, namely (i) $K = 0$ (no cylinders in channel), (ii) $K = 4$, $G_c = 0.75$, and (iii) $K = 28$, $G_c = 0.75$. In the latter two cases, the cylinders were rigid.* The $K = 4$ case yielded results very similar to the $K = 0$ case, hence, the former results shall not be presented. The calculated (eqs.(4.4) to (4.6) above) single point pressure PSD's, were utilized as input data for theoretical computations. The $K = 0$ data was used in all theoretical calculations, except for $K = 28$ cases (where the $K = 28$ pressure data was used). The reasoning behind this was that in $K = 1$, 2, and 4 cases, the "outside" of the centrally located bundles was exposed to "unconfined" fluid, whereas the reverse was true for the $K = 28$ bundles (see Fig. 14). Recall also that, prior to being used as input data (for the theoretical model), pressure PSD's were smoothed by digital filtering (see Appendix O): this was mainly to render calculated PSD's smooth, so as to facilitate comparisons to experimental data. Note

---

* Note that tests conducted with flexible cylinders, in the $K = 4$, $G_c = 0.75$ setup, yielded no correlation between cylinder motion and wall pressure (cylinders-wall separation too large).

that it is expected that both vibration and pressure measurements would yield "smooth" results (no rapid changes in PSD levels, from one frequency point to the next), were it not for various sources of experimental error (e.g. electrical noise); nevertheless, in the case of vibration data, it was deemed preferable to present the "raw" data, as interpretation of the data would not have been made easier, and as smoothing itself would have been more involved, especially for phase data.

Figs. 16 and 17 illustrate measured point pressure PSD's and corresponding coherence functions, at flow velocities $u = 1$, 3, and 5, for the $K = 0$ and $K = 28$ cases, respectively. The PSD levels are generally two to three orders of magnitude higher than the corresponding calculated turbulent boundary layer (single point) pressure PSD's; evidently, system disturbances emanating upstream and convected downstream account for most of the observed single point pressure fluctuations. This may be seen by comparing the $u = 3$ data of Figs. 16 to the boundary layer pressure PSD depicted in Fig. 18, where the latter has been computed from the two measured point pressure PSD's and their corresponding coherence, using eqs.(4.4) to (4.6) inclusively. To help the reader visualize the actual physical magnitude of the results, Fig. 18 has dual dimensionless/dimensional axes. Note that there is no direct relation between the PSD's of measured single point and boundary layer pressures; a convincing example of this may be seen in Figs. 19a and 19b, where two significantly different measured single point pressure PSD's and respective coherences (Fig. 19a), yield essentially "identical" boundary layer pressure PSD's (Fig. 19b). Note that in the top graph of Fig. 19a, the solid traces correspond to the main scale (1.5×10^{-3}), which has been set high enough to show the very high peaks at $\omega \simeq 54$; the dotted traces have been expanded twenty times, i.e. plotted on a scale of 7.5×10^{-5}, which is 160 times lower than the scale for the bottom part of Fig. 19a. The difference in the measured point pressure PSD's stems from the use of two different Venturi insert nozzles, for the measurement of the total volume flow rate of water in the tunnel (see Fig. 10); in the course of testing the match in calibration of Venturi insert nozzles, earlier vibration testing revealed that (vibration) PSD's were unaffected by the choice of either one of the two nozzles (one for low ranges and the other for higher ranges), so

it was only natural to verify excitation pressures as well. Note that the expectation of smooth PSD's is supported by the data in Fig. 19b, in the sense that the trace corresponding to the least "noisy" (i.e. high power level) measured single point PSD (in Fig. 19a) is smoothest.

There is some similarity between measured point pressures, at all flow velocities and for both the K = 0 and K = 28 cases, viz. peaks near dimensionless frequencies 15 and 50 (Figs. 16 and 17), which reflect flow-independent "tunnel noise" characteristics. Structural acceleration-induced point pressure PSD peaks may also be seen, for example at dimensionless frequencies 27 and 54 (first and second harmonics), at u = 1, in Fig. 16: these peaks stem from a slight unbalance in the main pump-motor assembly, which rotated at the dimensionless frequency of 27 (265 rpm).

Figs. 20a illustrates boundary layer pressure PSD's for the full range of flow velocities (u = 0.5 to 5.0), for the K = 0 case, in the dimensionless frequency range of 0-75. Fig. 20b is for the larger frequency range of 0-150. The former range is sufficient to yield vibration results (from the theoretical model) covering the first two beam mode groups (of vibration),* and the latter is meant to be utilized for a handful of calculations for the investigation the third beam mode group. The PSD's are relatively flat throughout, except for a very broad "hump" with a "center frequency" which appears to be roughly proportional to flow velocity.

The K = 28 boundary layer pressure PSD's are shown in Fig. 21a, in the dimensionless frequency range 0-75, again for the full range of flow velocities. At lower frequencies (from about 0-20 at u = 5 to 0-5 at u = 0.5), the levels are roughly double those at K = 0, which can be seen more clearly in Fig. 21b (a replot of Fig. 21a with double the PSD scales of Fig. 20a); beyond those frequencies, these levels rise significantly to about ten times those of the K = 0 case. As before, we find a very broad "hump", whose "center frequency" is roughly proportional to the flow velocity. As the third

---

* To be covered in detail shortly.

vibration mode group was never studied in the K = 28 case, the extended dimensionless frequency range of 0-150 was not investigated.

Digitally smoothed PSD's (see Appendix O for details on the technique used) were utilized as inputs to the theoretical model; typical results at u = 1, 3, and 5, are depicted in Figs. 22a and 22b for the K = 0 case, and Fig. 23 for the K = 28 case. The original (unsmoothed) PSD's are also shown, to indicate the extent of smoothing. In the K = 0 case, both the 0-75 and 0-150 bandwidths are illustrated; The latter were analyzed separately (HP5420A analyzer)*, and then smoothed individually. Each bandwidth has 256 data points. The digital filter parameters were set to retain the "general trends" ("waviness") in the PSD's, and to reflect the fact that, near zero, levels were found to be nominally flat, from measurements with DC coupled STATHAM pressure transducers (see Appendix N). Note that the unsmoothed PSD's of Figs. 22a and 22b, and Fig. 23 are not reliable near zero, as the PCB pressure transducers are AC coupled, (-5% at 0.5 Hz).

* In bandwidth of 12.5 Hz and 25.0 Hz respectively.

4.2: VIBRATION, SUB-CRITICAL - PREAMBLE

4.2-1: General characteristics - system dynamics

The basic dynamical characteristics, with increasing velocities, of a cylinder cluster subjected to axial flow, may be obtained by neglecting random pressure fluctuations, that is by using the "mean flow model" described at the beginning of Chapter 2. One finds three basic régimes, as the flow velocity increases, depicted in Fig. 24 (the real part represents frequency of oscillation and the imaginary part the damping).

(i) At low flow velocities, we have damped subcritical vibration; a system with initial displacements, and subjected to a mean flow velocity u ($0 \leq u < u_{crit}$), vibrates at discrete frequencies, numbering 2K,* with exponentially decreasing amplitudes (i.e. as a damped freely vibrating multi-degree of freedom system). Note that with increasing mean flow velocity, frequencies are reduced, and bandwidth (the difference between the highest and lowest frequencies) is increased.

(ii) As the flow velocity is increased further, the first frequency reaches zero (see Fig. 24); a critical velocity (u_{crit}), signifying the onset of divergence (buckling), is reached when the imaginary part of one of the roots becomes negative (see "*", in Figs. 24 and 25) - a zero frequency coupled with negative damping yields a static instability (divergence).

(iii) With further increase in mean flow velocity, the "mean flow model" predicts flutter, which occurs when non-zero frequencies reappear, and damping is negative (see Fig. 25).

Régimes (i) and (ii) were both observed experimentally, and the predicted u_{crit} has been found to be in good agreement (10-15% low) with measurements [75]. Because divergence and flutter régimes are intermixed (at least in theory), and also because of the unstable nature of flutter, régime (iii) has not been studied extensively - but see Refs. [55] and [75].

---

* Two pairs of frequencies are repeated in Fig. 24, namely ω_3 & ω_4 (not labelled), and ω_5 & ω_6 (labelled, at top).

The behaviour described above is that of a first group of 2K frequencies, amongst N such groups, where N is the number of comparison functions used in the beam mode expansion (see eqs. (2.73) and (2.63)). At each frequency (in each group), cylinders in the cluster move with respect to their neighbours in in a definite pattern, resulting in so-called "cross-sectional" modes, which recur for subsequent frequency groups (see next Section); these "cross-sectional mode groups" also exist in the random model, and shall be discussed later.

4.2-2: Test programme - general objectives

Whereas the study of régime (ii) above was part of an earlier study [75], the test programme in this Thesis was designed to study subcritical vibration, i.e. régime (i) above; primarily, we wish to study fluid coupling between cylinders in a cluster, the main effect of which is to produce "cross-sectional" inter-cylinder vibration modes. Fig. 26 illustrates typical theoretical modes, for a bundle of four cylinders (K = 4), at the discrete frequencies predicted by the mean flow theory. For example, at the lowest frequency cylinders move "radially" in an "imploding-exploding" pattern, at the highest frequency cylinders move "tangentially" in a twisting pattern, and so on. Note that, unlike the mean flow theory, the theoretical random model predicts vibration at all frequencies. The correspondence between the two is illustrated in Fig. 27, for three flow velocities: it can be seen that the random model PSD's tend to peak in the vicinity* of mean flow (discrete) frequency values, indicating a propensity for the system to vibrate at its natural (more specifically damped) frequencies (assuming a pressure excitation with relatively uniform power distribution).

Remark

The terms "Radial" and "Tangential" directions shall be used extensively when discussing experimental and theoretical results: these directions are

---

* The PSD's do not reach a maximum exactly at the discrete frequencies. For example, in a single degree of freedom second order system, the damped frequency is $\sqrt{4\,mk - c^2}/2\,m$ versus $\sqrt{4\,mk - 2\,c^2}/2\,m$ for the transfer function maximum.

with respect to an imaginary circle with its center at the geometric center of the bundle (this is the test channel center when the bundle is located symmetrically). For example (K = 4), these directions correspond to Planes 1 and 2 in Fig. 28, when $\theta = 45°$. Likewise, "Edge" directions occur when $\theta = 0°$. Occasionally, the short forms "R", "T", and "E" will be used.

4.2-3: Investigated clusters - description

Two "types" of clusters were tested, the first with all cylinders flexible (Dow Corning Silastic E silicone rubber) and the second with a combination of flexible and rigid (aluminium and/or acetal*) cylinders.

Remark

For conciseness, flexible cylinders shall be identified by an "F", and rigid ones by an "R".§ Furthermore, when applicable, the positions of the cylinders within the bundle will be given in brackets following the cylinder type. For example, 1F(1)/3R(2,3,4) represents a four-cylinder cluster with a flexible cylinder in position 1, and rigid ones in positions 2, 3, and 4. The position numbering convention used for the latter case is simply the quadrant number in which the cylinder(s) lie. This convention shall also be utilized to identify positions in all other clusters, except for "28-cylinder" bundles; numbering in this case is depicted in Fig. 29.

Any given setup may be instrumented in a variety of ways, in terms of which positions are occupied by strain gages equipped cylinders, and in which angular directions the latter are oriented. Fig. 30 illustrates four typical measurement setups. When referring to any one of the experimental systems (to be listed shortly), the positions of instrumented cylinders as well as their respective orientation (which is always that of Plane 1 versus dir. 1, as in Fig. 28) shall be given. As an example, case (iii) of Fig. 30 would be described as Pos.1 @ 0° and Pos.2 @ 90° (the latter angle is that of measuring direction "1" with respect to dir. 1 in Fig. 28, i.e. $\theta = 90°$).

---

* Also known by the registered trade name of DELRIN (Cadillac Plastic).

§ The meaning of "R", whether Radial or Rigid, will be obvious from the context.

The main ("Reference") cluster consisted of four flexible cylinders located centrally within the test channel, and with a minimum inter-cylinder gap of three quarters of a (cylinder) radius, i.e. with the parameter G_c = 0.75. This setup is illustrated in Fig. 28. To investigate the behaviour of smaller bundles, a two-cylinder as well as a one-cylinder cluster were tested. Finally, experiments were conducted with a number of combination (flexible-rigid cylinders) bundles, to study the effect of the presence (rigid cylinders) versus presence and motion (flexible cylinders) of neighbouring cylinders. The various systems tested are tabulated below, together with a brief description of the test objectives.

Ref. No.	K & G_c	Combination & Directions	Location in channel	Purpose/Remarks
1	4 0.75	4F(1,2,3,4) 45°(1) & 225°(3)	Symmetrical, about center.	Main cluster, diagonal instrumented pair, R & T.
2	4 0.75	4F(1,2,3,4) 0°(1) & 180°(3)	Symmetrical, about center.	Main cluster, diagonal instrumented pair, E & E.
3	4 0.75	4F(1,2,3,4) 45°(1) & 135°(2)	Symmetrical, about center.	Main cluster, adjacent instrumented pair, R & T.
4	4 1.00	4F(1,2,3,4) 45°(1) & 225°(3)	Symmetrical, about center.	Main cluster, reduced coupling (see Ref. No. 1).
5	4 1.50	4F(1,2,3,4) 45°(1) & 225°(3)	Symmetrical, about center.	Main cluster, reduced coupling (see Ref. No. 1).
6	2 1.89	2F(1,3) 45° & 225°	Symmetrical, about center.	Absence of other diagonal pair, in Ref. No. 1 (this results in the $G_c = 1.89$).
7	1 -	1F 45°	Near the center (slightly offset).	No coupling (neglecting effect of channel).
8	4 0.75	1F(1)/3R(2,3,4) 45°	Symmetrical, about center.	Coupling to rigid cylinders (see Ref. No. 1).
9	4 0.75	2F(1,3)/2R(2,4) 45° & 225°	Symmetrical, about center.	Two rigid diagonal cylinders out of four, R & T.
10	4 0.75	2F(1,2)/2R(3,4) 45° & 135°	Symmetrical, about center.	Two rigid adjacent cylinders out of four, R & T.
11	28 0.75	4F(1,2,3,4)/24R* 45°(1) & 225°(3)	Central in K = 28 bundle.	Study behaviour when part of large cluster.
12	28 0.75	4F(6,7,2,1)/24R* 135°(7) & 315°(1)	Parallel offset in K = 28 bundle.	Study behaviour when part of large cluster.
13	28 0.75	4F(5,6,1,16)/24R* 45°(5) & 225°(1)	Diagonal offset in K = 28 bundle.	Study behaviour when part of large cluster.

* All other positions occupied by rigid cylinders.

Note

The "28-cylinder" bundle is actually composed of 24 full cylinders (of which 4 are flexible and 20 rigid), and 8 half-cylinders. The latter are not numbered (see Fig. 29).

4.2-4: System physical constants

The system geometry was described in Chapter 3. We have

- Flexible cylinder(s) radius; $R = 1.265$ cm (0.498 in*),
- Test channel radius; $R_c = 10.24$ cm (4.03 in).

Note

The rigid cylinders were actually 1.000 inches in diameter (stock size), but for simplicity, in theoretical computations, rigid cylinders were assumed to have a diameter equal to that of the flexible ones (i.e. 0.996 in).

The usual frequency analysis bandwidth utilized was 12.5 Hz. This range encompassed the first two "cross-sectional mode groups"; this is more than adequate as most of the (vibration) power occurs in the first group, and as inter-cylinder phase relationships (i.e. cross-sectional coupling modes - see Fig. 26) do not change from one group to another (at least in theory).

It was decided to generate theoretical data at frequency points equal to those obtained experimentally, for direct comparisons, and with the same (frequency) resolution. Measurement data (HP5420A signal analyzer) were available at 256 discrete points, starting with zero, and ending at $\ell_{MAX} = (255 \cdot \Delta\ell)$, where

$$\Delta\ell = \frac{\ell_{BW}}{256} \ ,$$

and where ℓ_{BW} is the analysis bandwidth. In the case where

$$\ell_{BW} = 12.5 \text{ Hz},$$

---

* The manufacturing mould was 0.500 in. in radius, but the silicone rubber was subject to some shrinkage upon vulcanization.

$$\Delta f = \frac{12.5}{256} \text{ Hz}.$$

Now, $\Delta\Omega = \Delta f \cdot 2\pi$, and, using eqn.(2.50) [see below for physical constants], and rounding to four decimal places, we get

$\Delta\omega = 0.2979$, and

$\omega_{MAX} = 255 \cdot \Delta\omega = 75.9645$.

The above high (dimensionless) frequency point was used for all cases, except when investigating the third mode group ($\omega_{MAX} = 2 \times 75.9645$ in that latter case).

We are left with the description of the physical properties of the flexible and rigid cylinders, and those of the fluid (water).

(i) Cylinders:

(a) Fixed geometrical, and lower attachment parameters:

$L = 47.0$ cm (18.5 in),
$D = D_0 = 2.53$ cm (0.996 in),*

$L_0 = 1.37$ cm (0.54 in),
$L_1 = 1.09$ cm (0.43 in),
$W_0 = 0.34$ N (0.077 lbf),
$\delta = 1$ (lower end clamped),
$\bar{T}_0 = 0$ (no pre-tensioning).

(b) Physical properties:

$m_0 = 0.577$ Kgm/m (0.388 lbm/ft),§ for Silastic E,
$m = 0.717$ Kgm/m (0.482 lbm/ft),§ for acetal,
$m = 1.339$ Kgm/m (0.900 lbm/ft),§ for aluminium,

---

* All cylinders (i.e. including the reference one) are of equal diameter. Also, as pointed out earlier, rigid cylinder diameters (1.000 in stock) are assumed to be the same as that of the flexible ones.

§ Based of D_0 given above.

$E_0 = 2779$ KPa (403 lbf/in^2), for Silastic E,
$E = 3.59 \times 10^6$ KPa (5.2×10^5 lbf/in^2), for acetal,
$E = 6.89 \times 10^7$ KPa (10.0×10^6 lbf/in^2), for aluminium,

$\nu_0 = 0.47$, for Silastic E,
$\nu =$ N.A., for acetal,
$\nu = 0.33$, for aluminium, } (ν_0 used*)

$\mu_0 = 8.5 \times 10^{-4}$ sec, for Silastic E,
$\mu =$ N.A., for acetal,
$\mu =$ N.A., for aluminium, } (μ_0 used*)

$\lambda_0 = 61.2$ KPa (8.87 blf/in^2), for Silastic E,
$\lambda =$ N.A., for acetal,
$\lambda =$ N.A., for aluminium, } (λ_0 used*)

(ii) Fluid:

$\rho = 1000$ Kgm/m^3 (62.4 lbm/ft^3),
$\bar{p} = 55.2$ KPa (8.0 lbf/in^2),
$C_f = 0.013$ [yields $c_f \simeq 0.016$],
$C_{b_0} = 0$ (not used),
$C_D = 2.17$ cm/sec (0.85 in/sec) [yields $c \simeq 0.039$].

The value of C_{b_0} is irrelevant, since the parameter δ is always equal to 1 (full clamping at the lower end). The values for C_f and C_D were estimated as follows.

4.2-4a: Longitudinal friction, C_f

The friction coefficient C_f is available empirically, and values were gathered from a few sources so as to obtain an estimate. The applicable equation is always of the general form

$$F_L = \frac{1}{2} \rho D U^2 C_f \qquad \text{(i.e., as eqn.(2.2))}, \tag{4.8}$$

---

* As shall be proven later, since E for acetal and aluminium are so much larger than that for Silastic E, other parameters are of little import.

with minor local variations. Three publications have been used, and the corresponding values are discussed below.

(1) A.P. DOWLING 1988, Journal of Fluid Mechanics 187, 507-532. "The Dynamics of Towed Flexible Cylinders Part 1. Neutrally Buoyant Elements".

The equation used here is

$$F_T = \rho_0 \pi a_A U^2 C_T \ , \qquad (4.8a)$$

where F_T and C_T are tangential force per unit length and friction coefficient respectively, ρ_0 is the fluid density, a_A is the cylinder radius, and U is the (cylinder) towing speed. Eqs.(4.8) and (4.8a) simply yield

$$C_f = \pi \cdot C_T \ .$$

Dowling utilizes the value $C_T = 0.0025$* (from a private communication), which results in

$$C_f \simeq 0.01 \ .$$

(2) C.C. NI and R.J. HANSEN 1978, Journal of Fluids Engineering 100, 389-394. "An Experimental Study of the Flow-Induced Motions of a Flexible Cylinder in Axial Flow".

The relationship utilized here is

$$C_D = \frac{\text{Total drag}}{\rho U_M^2 \pi a L} \ ,$$

where C_D is the <u>longitudinal</u> drag coefficient, ρ and U_M are the fluid density and <u>maximum</u> velocity respectively, and a and L are the cylinder radius and length. Ni and Hansen refer back to empirical work by J.N. Knudsen and D.L. Katz for the ratio

$$\frac{U_M}{U} \simeq 1.14 \ ,$$

---

* Dowling does not give Reynolds number values, but because the phenomenon studied is towed sonar arrays, we can presume values of the order of those occuring here.

where U is the bulk velocity. The total drag is simply

Total drag = (Force per unit length) x (Length), hence we may write

$$(F_L) = \rho \pi a U^2 (1.14)^2 C_D \ . \qquad (4.8b)$$

We obtain, from eqs.(4.8) and (4.8b),

$$C_f = \pi (1.14)^2 \cdot C_D \ .$$

Ni and Hansen present measured* values of drag coefficient, versus Reynolds number, as well as results from analytical models for infinite mediums and for annular flows. The test values center approximately around the infinite medium value, which is approximately constant at 3.0×10^{-3}. This latter value is used here, yielding (see the last equation):

$$C_f \simeq 0.012 \ .$$

(3) M. HANNOYER, Ref.[72].

In his PhD Thesis, in Appendix G, Hannoyer uses the equation

$$q_{et} = \frac{1}{2} \rho_e U_e^2 D_e \pi c_f' \ , \qquad (4.8c)$$

where q_{et} is the force per unit length, ρ_e and U_e are the fluid density and velocity respectively, D_e is the cylinder diameter, and c_f' is a friction coefficient. From eqs.(4.8) and (4.8c), we get

$$C_f = \pi \cdot c_f' \ .$$

Hannoyer uses the value $c_f' = 4 \times 10^{-3}$, stemming from elementary boundary layer analysis: The momentum thickness is assumed to remain small compared to the cylinder diameter, and the "Prandtl-Schlichting" skin friction formula provides an estimate for the average friction coefficient for flat plates (labelled c_f in Hannoyer's Thesis). For Reynolds numbers of interest (2×10^6), Hannoyer argues that a corrective factor proposed by Hoerner for turbulent flow over a cylinder, is negligible, hence allowing the assumption that c_f' (flat plate) $\simeq c_f$ (cylinder). The latter coefficient is evaluated as 4×10^{-3} (skin friction formula), which yields

---

* Test section 19.05 cm in diameter with a single cylinder 1.59 cm in diameter and 7.92 cm length, located at the center.

$C_f \simeq 0.013$.

The maximum of the three will be chosen (in any case differences are relatively small), that is we use

$$C_f = 0.013 \ . \tag{4.9}$$

4.2-4b: Lateral "drag", C_D

The coefficient C_D is a linearized drag coefficient; the usual expression

$$\text{Lateral drag} = \frac{1}{2}\,\rho DV^2 (C_D)_{classical}$$

is assumed to reduce to

$$\text{Lateral drag} = \frac{1}{2}\,\rho DVC_D \ .$$

The latter equation is given, in cylinder cluster form, by eqs.(2.29) and (2.30). Details are found in Appendix F.

The "drag" coefficient C_D is analyzed in some detail in Ref. [42] (Added Mass and Damping of a Vibrating Rod in Confined Viscous Fluids, by Chen et al.), both in theory and experimentally. A short review is made here, leading to an estimated value for the constant.

Lateral vibration of a rigid rod submerged in a viscous fluid enclosed in a concentric rigid shell, is modelled by the equation

$$(m + C_M \cdot \rho A) \cdot \frac{d^2y}{dt^2} + C_v \cdot \frac{dy}{dt} + K \cdot y = 0 \ ,$$

where m is the mass per unit length of the cylinder, C_M is an added mass coefficient, ρ is the fluid density, A is the cylinder cross-sectional area, C_v is a lateral friction ("drag") coefficient, K is the lateral stiffness, y is the lateral displacement of the cylinder, and t is the time. Note that the K is a pseudo stiffness, as the modelling applies to a cylinder forced to oscillate harmonically (K is never used directly in the analysis, nor is the forcing function). The fluid is modelled by a simplified vorticity transport equation, namely

$$\nabla^4 \psi - \frac{1}{\nu} \frac{\partial}{\partial t} \nabla^2 \psi = 0 ,$$

where ψ is a stream function, and ν is the fluid kinematic viscosity. A family of theoretical curves are generated for (i) C_M versus D/d, and for (ii) $C_v/\rho A\omega$ versus D/d, for a set of values of a parameter S, where D and d are the channel (not to be confused with this Thesis cylinder diameter, D) and cylinder diameters respectively, ω is the frequency of (forced) oscillation, and

$$S = \frac{\omega d^2}{\nu} .$$

Experimental values are generated to cover a significant portion of the theoretical range of values, with good agreement. In our case, the value of C_D shall be evaluated from Chen's et al. C_v, by computing the theoretical value for a single cylinder ($K = 1$), in infinite fluid. Note that, in this Thesis, effects of confinement or presence of other cylinders form an integral part of the theory, i.e. we essentially wish to obtain the C_D for an isolated cylinder in fluid, or $D/d \to \infty$.

A value for ω had to be chosen to determine the parameter S: a value of 4 Hz (about 25 rad/sec) is representative of test results in this Thesis. Furthermore, we have $\nu \simeq 1 \times 10^{-6}$ m^2/sec (water at 20°C). We obtain

$$S \simeq 16085 .$$

The values obtained from Chen et al. are

$C_M \simeq 1$, (effect of confinement negligible)

and

$$\frac{C_v}{\rho A\omega} \simeq 0.0218 .$$

The relationship between C_v and C_D may be deduced from

$$\text{Force per unit length} = C_v \cdot \frac{dy}{dt} = \frac{1}{2} \rho D C_D \cdot \frac{\partial y}{\partial t} ,$$ *

---

* Now D represents the cylinder diameter (i.e. not D, the channel diameter in Chen et al. nomenclature).

where the first part stems from Chen's et al. equation of motion (see above), and the second part is an equivalent single cylinder equation, based on eqn. (F.7) [see Appendix F]. Hence,

$$C_D = \frac{2 \cdot C_v}{\rho \cdot D} ,$$

which may be rewritten as

$$C_D = \frac{\pi}{2} \omega D \left(\frac{C_v}{\rho A \omega} \right) . \qquad (4.10)$$

Substitution of the various values finally yield

$C_D \simeq 0.0217$ m/sec.

4.2-5: Input data for theoretical computations

Computer programs for calculating theoretical response (see Appendix K) are run in the following sequence:

(i) Inter-cylinder coupling coefficients (mass and viscosity), corresponding to eqs.(2.27) to (2.30) inclusively, are computed. The required input parameters are basically the "cross-sectional" geometrical dimensions of the system, namely:

- -the number of cylinders in the bundle (K),
- -for each cylinder, its radius and position in the channel (in polar coordinates, relative to the channel center*); all cylinders are of equal radii, R, and typical positions are given below,
- -for the channel, its radius, R_c.

Cylinder positions, of course, depend on the parameter G_c, and on the radius R (= 0.498 inches - see next Section). As a typical example, we take the case of K = 4, and G_c = 0.75; the resulting positions are (polar coordinates):

(0.96874,45)
(0.96874,135)
(0.96874,225)
(0.96874,315),

---

* The angle is with respect to "dir.1", as in Fig. 28.

where the radial distances are in inches (as used originally for input data), and the angle in degrees.

Note

Length inputs to the computer program (CPL.f, see Appendix K) may be in any units, but the latter must be the same for all data. Angle inputs must be in degrees.

In addition to the above inputs, the program requires the number of cylinders at the center of the channel (always = 0 here), the value of G_c (used only as reference, for printout), truncation variables "mm" and "mp" (see Ref. [73] for details; values of 15 and 11 have been found to yield adequate accuracy; always used here), and finally, a flag to include/exclude computation of viscosity coefficients (1, for include, always used here).

(ii) The "normalized" CSD's of eqn.(2.271) are computed, in "Cartesian" directions (viz. dir. 1 and dir. 2 of Fig. 28), for either a single cylinder or a pair of cylinders. Both cases are illustrated below.

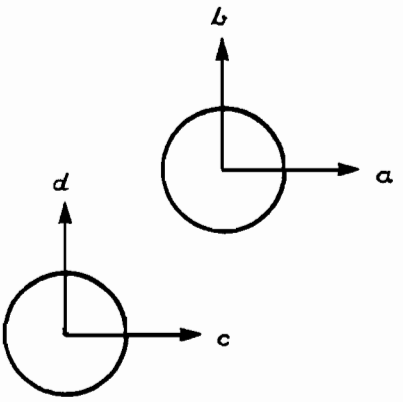

In single cylinder cases, $G_{aa}(\omega)$, $G_{bb}(\omega)$, and $G_{ab}(\omega)$ are computed, and, in cylinder pair cases, $G_{ac}(\omega)$, $G_{ad}(\omega)$, $G_{bc}(\omega)$, and $G_{bd}(\omega)$. Note that, in general, $G_{ab}(\omega) = G^*_{ba}(\omega)$ [single cylinder or a pair].

Input data required by the program is stored in three separate types of data files; a fourth file, the "RUN.data" file (see Appendix K), controls (i) the number of runs to be effected, and for each run, (ii) the dimensionless flow velocity and (iii) the corresponding three files to be read by the program, which are:

(a) The "CPLdata-" file, holding the following data:

- -the coupling coefficients calculated above [used to assemble matrices that define the frequency response function, see eqs. (2.157), (2.90) and (2.83)],
- -the cylinder(s) and channel radii, R and R_c,
- -the number of cylinders, K,
- -the parameter G_c (for reference only - not used in calculations),
- -a file identifier (for reference only - not used in calculations).

(b) The "CSDdata1-" file, holding the following data:

- -the ratio (diagonal) matrices (see eqn.(2.80)), which are unity matrices when all cylinders are identical (i.e. all flexible).

Two types of flags are used to indicate whether ratio matrices are unity or not: (i) a global flag (second line in the file, after a reference identification number) - if zero, all ratio matrices are initialized to unity in the main program (the file contains no data); if not the flag is equal to K, signifying that at least one matrix is not unity. In the latter case, secondary flags are made use of; there is one (secondary) flag per matrix (a total of ten), with zero indicating a unity matrix (no data to be read), and one signifying a non-unity matrix, i.e. data is to be read.

In addition to the above data, there is a file identification number (for reference only).

(c) The "CSDdata2-" file, holding the following data:

- -the number of comparison functions to be utilized in the beam modes expansion, N; the value N = 3 was found to be sufficient to model the first two "cross-sectional mode groups" (see Section 4.3-1c).

-values for the system physical constants (see preceeding Section),
-the convection velocity ratio [this parameter was always set at 1 (see eqn.(2.214)],
-the longitudinal offset (from $\xi = 0.5$) for the location at which displacements are to be computed ($\Delta\xi = 0.4186 - 0.5 = -0.0814$; recall that $\xi_0 = 0.4186$ was chosen earlier [Chapter 3]),
-the (dimensionless) frequency limits for calculations, as well as the number of points (at regular frequency intervals) at which computations are to be performed (256 points were always chosen here, to emulate the HP5420A signal analyzer; the low frequency point was always chosen as 0, and the high frequency point usually fixed at the dimensionless equivalent of 12.5 Hz),
-the number of inter-cylinder pairs for which calculations are to be effected, followed by the chosen pairs; here, a repeated pair specify a single cylinder, otherwise a cylinder pair is indicated. Examples will clarify the ensuing computations:

Example 1; Pair: i i ($i = 1,2,\ldots,K$).

In this case, the following are computed:
$G_{ii}(\omega)$, a "z-direction" PSD,
$G_{(i+K)(i+K)}(\omega)$, a "y-direction" PSD,
$G_{i(i+K)}(\omega)$, a z-y directions CSD.

Typically, $i = j = 1$, and $K = 4$, hence
$G_{11}(\omega)$, $G_{55}(\omega)$, and $G_{15}(\omega)$ are computed, or
two PSD's and one CSD [note that $G_{51}(\omega) = G_{15}^{*}(\omega)$].

Example 2; Pair: i j ($i,j = 1,2,\ldots,K$), and $i \neq j$.

In this case, the following are computed:
$G_{ij}(\omega)$, a "z-z direction" CSD,
$G_{(i+K)(j+K)}(\omega)$, a "y-y direction" CSD,
$G_{i(j+K)}(\omega)$, a z-y directions CSD,
$G_{(i+K)j}(\omega)$, a y-z directions CSD.

Typically, i = 1 and j = 3, and K = 4, hence
$G_{13}(\omega)$, $G_{58}(\omega)$, $G_{18}(\omega)$, and $G_{53}(\omega)$ are computed,
i.e. four CSD's.

(iii) The "normalized CSD's computed in (ii) are to be resolved in arbitrary directions. Computations to this point were carried out in FORTRAN, being time consuming;* from now on, calculations are to be effected in BASIC, and most of the input-output handled through data files, the latter compatible with a "utility" program§ used to examine (graphics display) and plot the data.

The previously calculated CSD's may readily be resolved in arbitrary directions; the technique is illustrated here: consider the cylinder pair shown below, with "Cartesian" directions a and b for the first cylinder, and c and d for the second one.

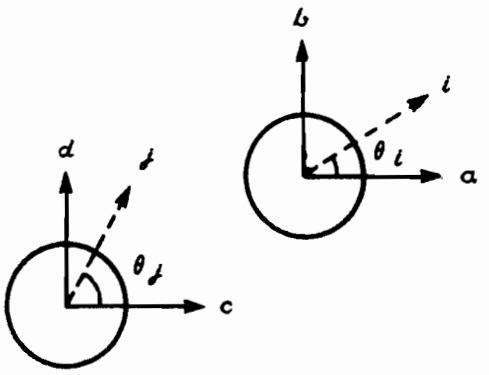

The quantities $G_{ac}(\omega)$, $G_{ad}(\omega)$, $G_{bc}(\omega)$, and $G_{bd}(\omega)$ are known. We wish to compute $G_{ij}(\omega)$. From basic definition,

$$R_{ij}(\tau) = \lim_{\tau_1 \to \infty} \frac{1}{\tau_1} \cdot \int_{-\tau_1/2}^{+\tau_1/2} i(\tau_0) \cdot j(\tau + \tau_0) \cdot d\tau_0 \quad , \tag{4.11}$$

---

* On the HP9000 computer, FORTRAN was found to be approximately three times faster than BASIC (V).

§ Not listed as it basically does not perform any calculations (and would have unduly added to the length of this Thesis, being about 5000 lines of coding).

where $i(\tau)$ and $j(\tau)$ are the time dependent motions in the i- and j- directions respectively. The latter may be resolved in terms of signals $a(\tau)$, $b(\tau)$, $c(\tau)$, and $d(\tau)$, as

$$i(\tau) = \cos\theta_i \cdot a(\tau) + \sin\theta_i \cdot b(\tau) \ , \tag{4.12}$$

and

$$j(\tau) = \cos\theta_j \cdot c(\tau) + \sin\theta_j \cdot d(\tau) \ . \tag{4.13}$$

The above equations simply yield

$$R_{ij}(\tau) = \lim_{\tau_1 \to \infty} \frac{1}{\tau_1} \cdot \int_{-\tau_1/2}^{+\tau_1/2} [\cos\theta_i \cdot a(\tau_0) + \sin\theta_i \cdot b(\tau_0)] \cdot [\cos\theta_j \cdot c(\tau+\tau_0) + \sin\theta_j \cdot d(\tau+\tau_0)] \cdot d\tau_0 \ ,$$

which results in the relationship

$$R_{ij}(\tau) = \cos\theta_i \cdot \cos\theta_j \cdot R_{ac}(\tau) + \sin\theta_i \cdot \sin\theta_j \cdot R_{bd}(\tau) + \cos\theta_i \cdot \sin\theta_j \cdot R_{ad}(\tau) + \sin\theta_i \cdot \cos\theta_j \cdot R_{bc}(\tau) \ . \tag{4.14}$$

Fourier transforming eqn.(4.13), we obtain

$$G_{ij}(\omega) = \cos\theta_i \cdot \cos\theta_j \cdot G_{ac}(\omega) + \sin\theta_i \cdot \sin\theta_j \cdot G_{bd}(\omega) + \cos\theta_i \cdot \sin\theta_j \cdot G_{ad}(\omega) + \sin\theta_i \cdot \cos\theta_j \cdot G_{bc}(\omega) \ . \tag{4.15}$$

In single cylinder cases (for example, cylinder "i" above), we are given (previously computed) $G_{aa}(\omega)$, $G_{bb}(\omega)$, and $G_{ab}(\omega)$; $G_{ii}(\omega)$ may be derived in a manner similar to one utilized above. We get

$$G_{ii}(\omega) = \cos^2\theta_i \cdot G_{aa}(\omega) + \sin^2\theta_i \cdot G_{bb}(\omega) + \sin\theta_i \cdot \cos\theta_i \cdot [G_{ab}(\omega) + G^*_{ab}(\omega)] \ , \tag{4.16}$$

where the relationship $G_{ba}(\omega) = G^*_{ab}(\omega)$ was used.

Eqs.(4.15) and (4.16) are the basic relationships used to compute PSD's and CSD's, in the (BASIC) program CSD_comp (see Appendix K).

Other (BASIC) programs used are: (i) THEOR_CALC, for implementing eqn. (2.272), namely multiplying the "normalized" CSD's (computed by CSD_comp) by the appropriate (user chosen) pressure PSD, and non-dimensionalizing. Also, (ii) COH_CALC is used to compute coherence (see Appendix K).

4.2-6: Units - vibration data

Vibration data shall be presented in dimensionless form. For both the theoretical* and experimental cases, (i) the dimensionless amplitude is with respect to the (reference) cylinder diameter D (see eqn.(2.270)), and (ii) the dimensionless frequency is defined by eqn.(2.50).

Dimensional vibration PSD's (CSD's) may be computed simply by multiplying the dimensionless ones by $D^2\omega/\Omega$, i.e., from eqn.(2.50), by the factor $8 \cdot L^2 \cdot \left[\frac{m_0 + \rho A_0}{\pi E_0} \right]^{1/2}$. Hence, we may write (see also eqs.(2.47) and (2.269))

$$G_{yy}(\ell)\Big|_{x/L = 0.4186} = 8 \cdot L^2 \cdot \left[\frac{m_0 + \rho A_0}{\pi E_0} \right]^{1/2} \cdot G_{dd}(\xi_0, \xi_0, \omega) , \qquad (4.17)$$

where $G_{yy}(\ell)$ is the dimensional PSD, and ℓ is the frequency in Hz (see eqn.(4.3)). Note that the diameter has been cancelled out, as it appears equally in the amplitude and frequency terms. For the particular values of the parameters of the system under analysis, the factor becomes 39.0 cm^2/Hz, i.e., eqn.(4.17) becomes

$$G_{yy}(\ell)\Big|_{x = 19.67 \text{ cm}} [cm^2/Hz] = 39.0 \cdot G_{dd}(\xi_0, \xi_0, \omega) . \qquad (4.18)$$

---

* Note that the original derivation is in terms of η (see eqn.(2.48)), and later modified to be in terms of d (eqn.(2.270)).

4.3: VIBRATION - RESULTS (THEORY AND EXPERIMENTS)

Theoretical results have been presented along with experimental ones, to allow comparisons as we proceed, and to minimize the required number of plots. The experimentally investigated clusters were described earlier (Section 4.2-3), and theoretical computations have been effected for each case, at selected velocity points (usually $u = 1,3,5$).

Data for each of the thirteen tested clusters is presented in a standard format, which shall now be described in the course of reviewing the basic "Reference" tests, namely the $K = 4$, $G_c = 0.75$, 4F, diagonally opposite pair, Radial-Tangential case (see "Ref. 1", in Section 4.2-3).

4.3-1: $K = 4$, $G_c = 0.75$, 4F, R-T (1,3) - "Reference" test

4.3-1a: Basic results

The $K = 4$, 4F configuration was chosen as the "reference" one, for the following reasons:

(i) it was desirable to investigate a bundle with a large enough number of cross-sectional coupling modes, which number 2K (see Fig. 26); it was felt that $K = 2$ was too small, although $K = 3$ might have provided an adequate number;

(ii) mounting of four cylinders, calling for support fins arranged as a cross, was considered much easier than three, which made that last option undesirable;

(iii) investigating $K > 4$ (as a reference test, which calls for further comparison experiments), would have required considerably more computer time to generate theoretical data;

(iv) four cylinders provided conveniently orthogonal symmmetry angles (Radial, Tangential, and Edge, described earlier); this is also true for the sub-case of $K = 2$.

Both experimental and theoretical data for this case will now be examined; Fig. 31 depicts power spectral densities (PSD's), in both the Radial and Tangential directions, for cylinder Position 1 (see Fig. 28), at the

values of the dimensionless velocity u = 1, 3, and 5. Note that the latter value is close to the critical velocity, hence the range 0-5 (for u) covers basically the whole range of sub-critical vibration.* Solid lines correspond to the PSD scale, whereas the dotted ones are an expansion of those (solid) lines, to permit visualization of lower power levels. The dimensionless frequency range was chosen to encompass both the first and second beam mode groups: recall that, theoretically (mean-flow or random models), it is predicted that motion occurs in subsequent frequency groups, each group corresponding approximately to motion in a dominant lateral beam deflection mode, the first such group corresponding, of course, to the lowest beam mode (least number of nodes), and so on. Experimental second mode group powers are already significantly lower than first group ones (by a factor of approximately 500 for u = 1, 300 for u = 3, and 50 for u = 5): for that reason, we shall (shortly) show only one case where the third mode group was detected, and show none for higher mode groups (fourth and on). Note that the assumption of a dominant n^{th} beam mode for the n^{th} mode group has been made here, for computation of powers: for example, in estimating powers, say for u = 1, the integrated PSD in the frequency range of 0 to about 45 is taken as first group power, and the integrated PSD in the frequency range of 45 to 75, weighed by the factor $(0.563)^2$ [see eqn. (3.1)], is taken as the second mode group power. The justification for choosing frequency ranges as done here will become obvious shortly, after comparisons have been made between theoretical and experimental mode groups.

In Fig. 31, one may see both the first and second mode groups, at each velocity, the latter albeit at much lower power levels. Individual "peaks", corresponding to mean flow discrete frequencies (see Fig. 27), are not always present in the experimental PSD's. With increasing velocity, (i) we observe a general decrease of frequencies, accompanied with a slow increase in bandwidth (the high limit frequency does also go down with velocity), (ii) there is an increase in power (i.e. in rms vibration amplitudes). The PSD shapes (power distribution) remain relatively constant (except for

---

* Critical velocity is covered to some extent in Ref. [75].

power levels and bandwidth), and so does the relation between radial and tangential motion: there appear to be two dominant peaks in the radial directions, and two to three in the tangential one. When the latter (measured) PSD's are plotted together with the theoretical ones, it will be possible to infer much more about the behaviour of the system, especially when supplemented by coherence and phase comparisons (experiments vs theory).

To illustrate the correspondence between dimensional and dimensionless quantities (frequencies and PSD's), the $u = 3$ case of Fig. 31 has been replotted in Fig. 32, with dual scales. For reference, the total (vibration) power for the latter PSD's (about the same in both radial and tangential directions) is of the order of 130μ cm^2 (0.11 mm (0.004 in) rms amplitude). Note that the latter Figure is not part of the "standard presentation format" mentioned earlier.

System characteristics are easier to visualize by inspection of Figs. 33a and 33b, which illustrate in more detail behaviour of the system with increasing* velocity, covering the range $u = 0.5$ to 5.0, in 0.5 increments: The very slow decrease of the upper frequency limits (both radial and tangential) are obvious here (around $\omega = 30$), and so is the faster decrease of the lower limit (see Fig. 24 for the analogous behaviour of the mean flow model frequencies).

Total powers (integrated areas under the PSD curves§) are plotted versus flow velocity, in Fig. 34: there is exponential increase at first, but this trend is not preserved at higher velocities (most cases will be found to behave exponentially, and this aspect will be discussed in more detail in Chapter 5). Note that, as mentioned in the last paragraph, the $u = 3$ point (about 20μ) represents an rms amplitude of 0.11 mm.

---

* Note that lowest velocities are depicted <u>at the bottom</u> of the page, in Figs. 33a and 33b.

§ The lower bound used is $\omega = 1$, to cut off the effect of large DC offsets near zero. The upper bound is $\omega = 75$ (factor of eqn. (3.1) not used here: effect negligible).

Figs. 35a and 35b depict both experimental and theoretical PSD's, at three flow velocities, for the Radial and Tangential directions respectively. Separate density scales were required, as measured and predicted power (density) levels differ by more than one order of magnitude; the left-hand side scales apply to the experimental data (RED traces), and the right-hand side ones to the theoretical data (GREEN traces). The dotted traces are expansions of the solid ones, to allow visualization of the second beam mode groups, and scales are given in the captions. Note that theoretical scales had to be expanded more than experimental ones, signifying that the ratio of theoretical to experimental power (densities) is not the same for first and second mode groups; it is lower in the latter case, for all three velocities.

In both Radial and Tangential directions, there is remarkable agreement between theory and experiment, in terms of PSD shapes (relative power distribution, versus frequency), except for the following items: (i) There is (relatively) more power, at $u = 1$, at low frequencies (0-15), in both directions (Radial and Tangential). (ii) There is a tendency for closely spaced theoretical "peaks" (e.g. $\omega = 26$ and 28 in Fig. 35a, at $u = 1$) to not be reproduced experimentally (although we do find such peaks in the $u = 1$ case, for the tangential direction). (iii) Damping in the measured data seems to correspond to that modelled in the theory only at the lowest velocity ($u = 1$); otherwise it appears that actual (experimental) damping goes up (relative to the theory) with flow velocity (broadness of PSD's). (iv) Second mode group PSD shapes are not as well matched as the first group ones, and theoretically predicted frequencies are underestimated to some extent. The second mode group $u = 1$ data, in the tangential direction (Fig. 35b), has "peaks" not predicted by theory, at $\omega \simeq 38$ and 49 (the measured peaks corresponding to theory are at $\omega \simeq 60$ and 66 respectively). The above discrepancies will be discussed in Chapter 5.

Powers do not compare well: the theoretical results consistently overestimate power levels, by a factor of 10 to 26 (i.e. amplitudes by a factor of 3 to 5) for the first frequency group [e.g. $\omega = 0$ to about 40 at $u = 3$],

and by a factor of 3 to 7 for the second mode group. Discussion of power levels is postponed until Chapter 5.

Inter-cylinder coupling characteristics are revealed by coherence and phase measurements; the present "Reference" test was conducted with an instrumented cylinder pair located diagonally opposite within the bundle, with the measurement planes oriented in radial and tangential directions. Case (iv) in Fig. 30 depicts such a setup. There are two non-zero inter-cylinder cross-spectra* in that particular setup, namely the Radial-Radial and Tangential-Tangential cases. Figs. 36a to 36f inclusively depict data for the three flow velocities $u = 1$, 3, and 5; the R-R (1,3)§ case at $u = 1$ is shown in Fig. 36a: Agreement can be said to be excellent, considering the relative complexity of the system. We note the same theoretical under-valuation of frequencies in the second mode group (found for PSD's), i.e. around $\omega = 54$ and 66. Furthermore, corresponding to the "noise" in PSD power found at low frequencies (Fig. 35a, at $u = 1$, in $\omega = 0$ to 15), we find the coherence is higher than predicted. Although the experimental and theoretical coherences of Fig. 36a do not match "perfectly", a review of the "large" number of cases investigated will reveal a close similarity between the two. The T-T (1,3), $u = 1$ case is depicted in Fig. 36b, followed by the $u = 3$ and $u = 5$ cases (for Radial and Tangential directions, Figs. 36c to 36 f). Experimental and theoretical phases are basically indentical, except where the measured coherence is low; Starting from $\omega = 0$, the phase sequence of 0°-180°-0° is found in both theory and experiments. The measured phase jumps to basically 180° at $\omega \simeq 30$, and the discrepancy persists until $\omega \simeq 35$ (at low levels of measured coherences). The next region of disagreement starts at $\omega \simeq 45$, again corresponding to low levels of measured coherence. Inspection of all phase results will show that theoretical and experimental phases always match, unless the measured coherence is low, which occurs mainly when the theoretical one is low as well (recall that, in general, coherences do match). Coherence and phase results will be much easier to interpret from global results (all cases), but nevertheless, more information can be ex-

---

* It can be seen by symmetry that R Pos.1 and T Pos.3 should be uncorrelated.

§ Abbreviated terminology for Radial-Radial (directions), Positions 1 and 3.

tracted from Fig. 36 (a to f): (i) The measured phase tends to have the value of 180° or fluctuate "wildly", whenever coherence is low, (ii) the coherence shapes are generally the same: some examples are in the vicinity $\omega = 26$ in Fig. 36a, at $\omega \simeq 50$ in Fig. 36c, all of Fig. 36d, and so on. An important feature in the correspondence between measured and calculated coherences is that when a match does not exist, the relative shapes do compare, albeit at different levels; for example, Fig. 36c at $\omega \simeq 23$, and Fig. 36f at $\omega \simeq 10$. There are discrepancies in terms of coherence "peaks bandwidth": Fig. 36a at $\omega > 60$ and Fig. 36b at $\omega > 62$ indicate wider experimental coherences, while Fig. 36b at $\omega \simeq 29$ suggests the reverse.

Additionallly, we note that (iii) there is a one to one correspondence between the "discrete" phase sequence of the mean flow model, and the related values of the random model; for example, R-R "discrete" phases and frequencies are, at $u = 3$, from Figs. 26 and 27, 0° at $\omega \simeq 16$, 180° at $\omega \simeq 23$, and 0° at $\omega \simeq 26$ (note the measurement directions of instrumented cylinders, in Fig. 30). The random model phases are identical (at those frequencies), as seen in Fig. 36c. Note that this discrete sequence is repeated for higher mode groups, in both the random and mean flow models. By inspection, the T-T "discrete" phases also have a correspondence with the random case (i.e. 0° at $\omega \simeq 19$, 180° at $\omega \simeq 21$, and 0° at $\omega \simeq 28$). Of course, the random model does yield phase information at all frequencies; this yields additional phase information, for example 180°, for T-T, at low frequencies (see Figs. 36b and 36d). In connection with the latter observation, we note that, with the downward shift of frequencies with flow velocity, this 180° T-T phase has dissapeared at $u = 5$ (see Fig. 36f), which means that (iv) the random model phase sequence (with increasing frequency) is not necessarily the same for each beam mode group, although it tends to be. Another example of "irregular" sequence can be seen for the $u = 1$, R-R case (Fig. 36a), at $\omega \simeq 39$, where the phase is 180° instead of the value of 0° found at the other two velocities (Figs.36c and 36e), although the corresponding coherence is extremely low (so that this "irregularity" is not meaningful).

In summary, we may tentatively list the following salient features of the $K = 4$, $G_c = 0.75$, 4F system:

-In terms of PSD's:

(1) Motion tends to occur in (frequency) groups, the n^{th} group corresponding to the n^{th} beam lateral deflection mode.

(2) Most power lies in the first mode group.

(3) The theoretically predicted PSD shapes are indeed reproduced experimentally, most accurately at low flow velocities.

(4) Relative to the theory, experimental damping gets progressively higher, with increasing flow velocity.

(5) The theory underestimates the second mode group frequencies, more so at higher flow velocities, by up to about 15%.

(6) Theoretically predicted power levels are high by more than one order of magnitude (i.e. amplitudes by more than 1/2 order of magnitude).

(7) Power increases exponentially with flow velocity, at least in the lower velocity range.

-In terms of CSD's:

(1) Experimental and theoretical coherences are generally similar, with a number of exceptions in levels (values), but with generally very similar shapes.

(2) Phases (theory and experiments) are essentially identical, with the exception that where coherences are low, the measured ones tend to either fluctuate "wildly" or hover around 180°; as for PSD's, the second mode group theoretical frequencies are slightly low.

(3) The mean flow model "discrete" phase sequences are a subset of the "continuous" ones of the random model, and the latter tend to recur in (frequency domain) groups.

Comparisons with other systems (e.g. with larger $G_c = 1.00$), and more detailed discussions will be presented later.

The following sections (4.3-1b to 4.3-1f inclusively) deal with selected topics which require discussion, and which were investigated using the same bundle ("Reference" - K = 4, $G_c = 0.75$, 4F). The sequence in which the foregoing information has been reviewed constitutes the so-called "standard" format (mentioned earlier).

4.3-1b: Third beam mode group

In 4.3-1a, we discussed only the first two beam mode groups, that is results in a frequency range corresponding only to the first two beam lateral deflection modes. To verify that signal power does decrease as we proceed to higher mode groups, and to ascertain the existence of at least a third mode group, data was analyzed in a wider frequency band, namely in the ω range of 0-150 (instead of the usual 0-75). Fig. 37 illustrates both experimental and theoretical* PSD's, at u = 3, in Radial and Tangential directions. The left and right hand scales apply to the solid RED and GREEN curves respectively, and both the dotted and dashed traces have undergone a scale expansion. The experimental data is believed to represent the third mode group, but agreement with theory is rather poor: in the Radial direction, the experimental peak at $\omega \simeq 130$ could represent the theoretical peak at $\omega \simeq 100$, and similarly, the (experimental) tangential peak at $\omega \simeq 130$ would correspond to the (theoretical) peak at $\omega \simeq 110$ (the measured peak at $\omega \simeq 100$ is thought to correspond to the "stray" power found in the u = 1 second mode group tangential case (see Fig. 35b, at $\omega \simeq 38$). Powers for both experimental and theoretical data are more than one order of magnitude lower than the second mode group, and (third mode) experimental data is about three orders of magnitude lower than the first mode group data.

Coherence and phase data can be interpreted fairly easily by keeping in mind the idea that the theory underestimates third mode frequencies by about 20% (see Fig. 37). The u = 3, R-R (1,3) and T-T (1,3) cases, are depicted in Figs. 38a and 38b respectively: The experimental R-R coherence

---

* With N = 5. Note that the theoretical data is from an earlier run: different values of the constants c and c_f ($c = 0$, $c_f = 0.027$) were used at that time; this does not change the results in any major way (see 4.3-1d below).

"peak" at $\omega \simeq 130$ would represent the theoretical peak at $\omega \simeq 100$, and the measured T-T coherence "peak" at $\omega \simeq 130$ would correspond to the theory's $\omega \simeq 120$ (the $\omega \simeq 117$ measured peak would stem from the "stray" power mentioned above). As usual, phases do basically agree, where the measured data has a high enough coherence to yield reliable data.

Note that the third mode was investigated mostly to support conclusions about the second mode, but given the very low signal strengths involved (rms amplitudes of about 0.2×10^{-3} in. [5×10^{-3} mm]), could not have been said to generate "independently reliable" data.

4.3-1c: Choice of N

The number of comparison functions utilized for theoretical computations was three (N = 3), in most cases (for example, an exception is the analysis of the third beam mode in 4.3-1b above, where N = 5). We wish to determine the minimum value of N, so as to obtain reasonable accuracy for the frequency range of 0-75, which encompasses the second beam mode group.

Theoretical radial and tangential direction PSD's, at u = 3, are shown in Fig. 39, for the three values N = 5, 3, and 2. The second mode groups are shown as dotted traces, and the third ones as dashed traces (as before, density scale expansions were necessary here). We see that the radial and tangential direction results behave in a similar way. Any effects of N (5, 3, or 2) on the first group PSD's are not apparent here, and we may safely state that N = 2 is sufficient for the first group. The difference between second mode group PSD's, for N = 5 (RED) and N = 3 (GREEN) is very small and hence, N = 3 is in fact sufficient to model second mode group PSD's. We note that some error exists in the third mode group when N = 3 (GREEN), and considerable error (virtual absence of power) occurs when N = 2 (BLUE).

The above conclusions also apply to the computations of coherence and phase; compare the N = 5 (RED) and N = 3 (GREEN) data in Fig. 40a [R-R (1,3)], Fig. 40b [T-T (1,3)], Fig. 40c [R-R (1,2)], and Fig. 40d [T-T (1,2)].

Unless otherwise noted, the value of N used for theoretical calculations will have been 3.

4.3-1d: Effect of c and c_f

The only two system constants that have a relatively high degree of uncertainty are the "linearized drag coefficient" c, and the longitudinal (fluid) friction coefficient c_f (see eqn. (2.52)). Approximate (dimensional) values have been established in Chapter 4 (Section 4.2-4). The corresponding dimensionless values, used in Appendix K, are $c = 0.039$ and $c_f = 0.016$.

Theoretical computations were effected with the values $c = 0.00$, 0.01, 0.02, and 0.03,* and similarly for c_f; the "Reference" system, that is $K = 4$, $G_c = 0.75$, 4F, was utilized. Since the Edge (as compared to Radial or Tangential) direction PSD's contain "peaks" at all frequencies, this direction was chosen for comparisons. The mid-range velocity $u = 3$ was chosen. The effect of varying c is shown in the top part of Fig. 41: We see that PSD's are relatively insensitive to changes of c (integrated power level changes are minimal). The middle part of the same Figure depicts the effect of varying c_f: In this case, the resulting PSD's are affected to a greater extent, but only in terms of the height of the "peaks"; the overall power varies to a lesser extent. The effect of varying both coefficients simultaneously is illustrated in the bottom plot of Fig. 41. The trends resemble those found for c_f, with slightly more accentuated effects. In summary, the dominant effect is for the PSD "peaks" to be reduced in height with increasing c_f.

The effect of simultaneous variations in c and c_f on the coherence function can be seen in Figs. 42a and 42b, for position pairs 1,3 (diagonally opposite cylinders) and 1,2 (adjacent cylinders) respectively. It should be noted that the second peak, dominant in the T-T case, is affected signifi-

---

* At the time when calculations were performed, the values commonly used for c and c_f were 0.00 and 0.027 respectively: hence the range of trial values was set at 0.03 (rather than 0.04).

cantly, reaching a fairly low level when $c = c_f = 0.03$ (this could be a plausible explanation for coherence level discrepancies between theory and experiments).

Phases can be said to be essentially unaffected by c and c_f (see Figs. 42a and 42b).

4.3-1e: Symmetry

Most of the thirteen systems tested are inherently symmetrical; for example, the "Reference" $K = 4$, $G_c = 0.75$, 4F system should possess identical PSD's in all four Radial directions, all four Tangential directions, and all eight Edge directions (see Fig. 28). The experimental system response was not originally symmetrical, and the problem was eventually corrected with the development of the two-stage turbulator depicted in Fig. 11. Every experimental run involved symmetry checks, as verification for cylinder alignment, orientation of strain gage measurement planes, etc. Symmetry was comparable in all cases, therefore only one system will be presented; the "Reference" case shall be used, especially since it is the only one for which Edge direction measurements are available, in addition to the Radial and Tangential ones.

Figs. 43a, 43b, and 43c illustrate symmetry for the flow velocities $u = 1$, 3, and 5, in the Radial and Tangential directions, and Fig. 44 depicts symmetry for the same velocities, but for the four Edge directions (of the two instrumented cylinders). In general, it can be seen that symmetry is excellent; we notice a few isolated exceptions, namely low frequency "stray" power (Fig. 43a in the Radial direction, Fig. 44), and additional power "peaks" (Fig. 43a in the Tangential direction, Fig. 44 at $u = 1$ in two of the Edge directions [$\omega \simeq 38$]).

We may say that symmetry is more than adequate, and includes at least the second mode group (in spite of much reduced power levels).

4.3-1f: Repeatability

Another important criterion is experimental repeatability. Given the consistently observed symmetry of the various systems tested, it was felt that a single repeatability test, performed on the "Reference" system, would be adequate. PSD's, coherence functions, and phases were measured for the $K = 4$, $G_c = 0.75$, 4F system, at $u = 1$, 3, and 5, in the Radial and Tangential directions. Repeatability testing was effected by running two independent experiments with the same setup; for each setup, the whole assembly was taken fully apart, then reassembled and relocated in the test channel. This procedure included operations such as resetting the radial position of cylinder support ogives (see Fig. 13) and angular positioning of the strain gage measurement planes. Figs. 45a, 45b, and 45c depict Radial and Tangential PSD's, at the three flow velocities tested, and Figs. 46a, 46b, 46c, and 46d illustrate coherences and phases, for cylinder Positions 1 and 3 (diagonally opposite).

Repeatability is generally very good at all velocities, and in both directions; the worst discrepancy may be seen if Fig. 45b, in the Radial direction, at $\omega \simeq 16$. The largest phase discrepancy is for the $u = 1$, T-T (1,3) case, in the low frequency range: this is of no concern (and normal), however, since the corresponding coherence is low.

The next system to be examined is the same as the "Reference" system discussed earlier, but with vibration measurements in Edge directions (e.g. case (i), Dir. 1, in Fig. 30) instead of the Radial and Tangential ones.

4.3-2: K = 4, G_c = 0.75, 4F, E-E (1,3)

Following the presentation format introduced in Section 4.3-1a for the "Reference" test, we begin by examining PSD's at u = 1, 3, and 5: Fig. 47 illustrates the two Edge direction PSD's, for the cylinder in Position 1. As should be the case by symmetry, the PSD's are basically the same, for both the first and second mode groups (the latter, as usual, requiring a scale expansion). Note that this Figure is the Edge equivalent to Radial and Tangential of Fig. 31; in the case of the Edge direction(s), all inter-cylinder coupling mode frequencies (see Fig. 26) are present, as both Radial and Tangential directions have components in the Edge direction(s). This yields the more uniform PSD shapes of Fig. 47. Otherwise, the observed trends (i.e. dominant frequencies and power versus flow velocity) are the same as those for Radial and Tangential directions. Fig. 48 represents the data of Fig. 47 ($\theta = 0°$ Edge direction only) versus flow velocity, for easier visualization of these trends.

Total power, integrated from the data of Fig. 48, is shown versus flow velocity, in Fig. 49; it is comparable to those computed for the Radial and Tangential directions (see Fig. 34). Nevertheless, the u = 5 Edge power is about 15% lower than expected from Radial and Tangential power data: the latter read 76μ and 88μ respectively, yielding an expected 82μ* for the Edge direction, versus the value of 69μ of Fig. 49.

Comparisons of the experimental to the theoretical PSD's is made in Fig. 50, at the three flow velocity values of u = 1, 3, and 5. It can be seen that, similarly to the Radial and Tangential cases, closely separated theoretical peaks are not resolved in the measurements (assuming that they do indeed exist). Again we find some stray power at u = 1, at low frequency and at $\omega \simeq 38$. The second mode group results do not appear to compare as well as they did in the Radial and Tangential cases (see Figs. 35a and 35b), but are nevertheless acceptable.

---

* The R-T CSD is zero (by symmetry, theoretically, and also measured), hence $P_E = (P_R + P_T)/2$, where P is power.

Coherence function and phase, both experimental and theoretical, are depicted in Fig. 51 (a to f), for u = 1, 3, and 5. Two cases are examined, namely, E (1) @ 0° versus E (3) @ 180°, and E (1) @ 90° versus E (3) @ 270°. Theoretically, these two cases are identical (symmetry), and it can be seen from Figs. 51a and 51b (u = 1), Figs. 51c and 51d (u = 3), and Figs. 51e and 51f (u = 5), that the same is basically true of the measured data. Coherence functions generally compare well, with some particularly good instances, for example at $\omega \simeq 23$ for u = 1 (Figs. 51a and 51b, see also phases), and some rather poor comparisons, for example at $\omega \simeq 53$, at u = 1, for the 0°-180° case (Fig. 51a). Phases generally compare very well, except as before, in cases of low coherence. But there are coherence and phase discrepancies: at $\omega \simeq 39$, at u = 1, for the 0°-180° case (Fig. 51a) there is a coherence "peak" not present in the theory; the corresponding phase is 180° rather than the 0° value predicted in theory. An analogous situation exists for the 90°-270° case (Fig. 51b). The cause for this appears to be the stray power mentioned above (see Fig. 50). Furthermore, for $\omega < 12$, at u = 5 (Figs. 51e and 51f), coherences basically do not agree (although phases do). This is believed to be due to the underestimation of damping, in the theory (see Fig. 50, at u = 5); a more detailed discussion of that problem shall be presented in Chapter 5.

We proceed to examine a variant of the basic system (K = 4, G_c = 0.75, 4F, R-T (1,3)), namely the same system, but Positions 1 and 2.

4.3-3: K = 4, G_c = 0.75, 4F, R-T (1,2)

Since this is a variant of the "Reference" test of Section 4.3-1, no PSD's will be presented here (refer instead to Figs. 31, 33a and 33b, and 35a and 35b), and we consider only the inter-cylinder quantities of coherence function and (CSD) phase.

The usual R-R and T-T combinations have been chosen, and Positions are 1 and 2 (see Fig. 28). Coherences and phases are illustrated in Figs. 52a and 52b (u = 1), 52c and 52d (u = 3), and 52e and 52f (u = 5). Coherence compare remarkably well in both the R-R and T-T cases, at all flow velocities. The "usual" theoretical underestimation of frequencies, for the second mode group, is again seen here. Whenever coherences are high enough, the experimental and theoretical phases fully agree; one could presume that the closer proximity of adjacent cylinders results in stronger coupling, but a comparison of coherence functions for this (1,2) case, with those of the (1,3) case [Fig.36 (a to f)] reveal that the latter are not any smaller in magnitude.

This case provides strong reinforcement in terms of agreement between experimental and theoretical inter-cylinder data.

The next two cases to be reviewed involve again variants of the "Reference" system (K = 4, G_c = 0.75, 4F, R-T (1,3)), but for larger inter-cylinder spacing, namely G_c = 1.00 (next Section) and G_c = 1.50.

4.3-4: K = 4, G_c = 1.00, 4F, R-T (1,3)

One important variable in the study of fluid coupling is inter-cylinder spacing. Results are now reviewed for this G_c = 1.00 bundle, for eventual comparison with the (G_c = 0.75) "Reference" cluster, and also with the G_c = 1.50 bundle, to be presented next.

Measured Radial and Tangential PSD's are depicted in Fig. 53. Comparing this Figure with Fig. 31 (G_c = 0.75), we see that power (density) levels are slightly lower, PSD's are not as broad, and dominant frequencies are about the same; differences are not obvious, unless direct graphical comparisons are used; this will be done in Chapter 5.

Figs. 54a and 54b illustrate Radial and Tangential direction PSD's versus flow velocity, and Fig. 55 shows the corresponding integrated powers, also versus flow velocity: no new characteristics can be detected here.

The comparison between experimental and theoretical PSD's is made in Figs. 56a (Radial) and 56b (Tangential): the key feature here is that the lower dominant "peaks"* (as compared to the G_c = 0.75 case - see Figs. 35a and 35b) in the measured PSD's are also found in the theoretically computed ones: this lends support to the theoretical model, in terms of relative trends (recall that power levels do not agree, hence the use of separate experimental and theoretical scales in Figs. 56a and 56b).

The effect of increasing inter-cylinder spacing on coherence and phase may be seen by comparing Figs. 57a to 57f (G_c = 1.00), to Figs. 36a to 36f (G_c = 0.75): both experimental and theoretical coherences and phases, in R-R and T-T cases, and at u = 1, 3, and 5, are virtually the same, except for slightly narrower coherence "peaks" and corresponding phase "cycle". For example, in the R-R case at u = 1, and $\omega \simeq 25$, the G_c = 1.00 (Fig. 36a) data (coherence and 180° phase) is "wider" than the corresponding G_c = 1.00 data (Fig. 57a). Effects of G_c will be reviewed in more detail in Chapter 5 (and will include, of course, the G_c = 1.50 case to follow).

---

* Ratio of "crests" to "valleys".

4.3-5: K = 4, G_c = 1.50, 4F, R-T (1,3)

To supplement the G_c = 0.75 and G_c = 1.00 cases, experimental and theoretical data was generated for the G_c = 1.50 case; comparatively to the former two cases, the measured PSD's for this latter case, illustrated in Fig. 58 do not exhibit trends easy to detect, other than a more pronounced tendency for the first two Tangential "peaks" ($\omega \simeq 24$, 22, 16, corresponding to u = 1, 3, and 5 respectively) to merge. Comparison plots, in Chapter 5, will confirm that the system does indeed behave as predicted in theory, in the sense of narrowing of PSD's with increasing G_c; for example, the third Tangential "peak", at u = 1, is found at $\omega \simeq 29$ in the G_c = 0.75 case (Fig. 31, at top), and $\omega \simeq 28$ in the G_c = 1.00 case (Fig. 53, at top), whereas this "peak" is at $\omega \simeq 27$ in the G_c = 1.50 case (Fig. 58, at top).

Figs. 59a and 59b show the variation of Radial and Tangential direction PSD's with flow velocity: the behaviour of the system is basically the same as that for the G_c = 1.00 (Figs. 54a and 54b) case.

Total powers are depicted in Fig. 60, and are found to be slightly higher than those for G_c = 1.00 (Fig. 55), and as for the latter case, Radial and Tangential powers are of almost equal magnitude, with the Radial being the highest of the two. The power versus velocity plots for the three G_c's (0.75, 1.00, 1.50) all suggest an "exponential" increase of power, with flow velocity (see Figs. 34, 55, and 60).

As for closer spacings, this latter case compares well with theory, in terms of PSD shapes, as seen in Fig. 61a (Radial) and Fig. 61b (Tangential). As before, the u = 1 cases compare remarkably well (in the first mode group).

The further "narrowing" of coherences and phases (with increasing inter-cylinder spacing) is obvious, when comparing Figs. 62a to 62f (G_c = 1.50), to Figs. 57a to 57f (G_c = 1.00). Furthermore, coherences have lowered noticeably in this latter case (G_c = 1.50), both theoretically and experimentally, in comparison to the earlier cases (G_c = 1.00 and 0.75). This indicates a reduction in fluid coupling, owing to an increase in inter-cylinder distances. Note that even when experimental and theoretical coherence magni-

tudes disagree, the lowering trend is nevertheless consistent: for example, the $u = 1$, R-R (1,3) cases, at $\omega > 60$, in Figs. 57a and 62a.

We now proceed to examine the various cases where the number (K) and combination of Flexible and Rigid cylinders were varied. The next two cases involve two flexible (K = 2, 2F) cylinders, and a single flexible (K = 1, 1F) cylinder, respectively.

4.3-6: $K = 2$, $G_c = 1.89$, 2F, R-T (1,3)

The purpose of investigating this cluster is twofold: (i) to study the characteristics of a $K = 2$ system, as compared to the "Reference" ($K = 4$) system, where the former system is obtained from the latter, after two diagonal cylinders have been removed (which results in the $G_c = 1.89$ value), (ii) to provide a reference system, for comparisons with $G_c = 0.75$, 2F/2R systems (to follow), for later investigation of the relative effects of (flexible) cylinder motion versus (rigid) cylinder "presence", in the study of fluid coupling. At this point, results shall only be discussed in relation to item (i) above; comparisons of this $G_c = 1.89$, 2F system (and $G_c = 0.75$, 4F system), with the ($G_c = 0.75$) 2F/2R systems shall be effected only after reviewing the latter (Chapter 5).

This $K = 2$, $G_c = 1.89$ system is "widely" spaced; this can be seen by inspecting Fig. 28, Positions 1 and 3 only (i.e. Positions 2 and 4 cylinders removed). The resulting measured Radial and Tangential PSD's are almost the same, as shown in Fig. 63; little distinction remains between the two measurement directions, since fluid coupling is weak, owing to the relatively large inter-cylinder spacing. For the $u = 1$ case, we can distinguish two "peaks", in both directions; this is not as obvious at $u = 3$ and $u = 5$. The power (density) levels of the second beam mode group PSD's are similar to those found in the cases reviewed previously. We again note the "stray peak" at $u = 1$, in the Tangential direction, at $\omega \simeq 38$. As expected, the combination of a reduction in the number of cylinders and a fairly large inter-cylinder spacing yields PSD's which converge towards those for a single isolated cylinder, although in this case, $G_c = 1.89$ is still low enough to retain typical two-cylinder characteristics (see below).

The variations of Radial and Tangential measured PSD's with flow velocity is illustrated in Figs. 64a and 64b. Note that the slower downward shift in frequencies with increasing flow velocity is simply due to a higher critical velocity (for divergence) than that for four flexible cylinders.

The integrated total powers are depicted, versus flow velocity, in Fig. 65. Again, approximately exponential curves are obtained, and power levels in Radial and Tangential directions are similar.

Experimental and theoretical PSD's compare very well, as may be seen in Figs. 66a (Radial) and 66b (Tangential). As in earlier cases, the best agreement occurs at $u = 1$, and it appears that actual (measured) damping is, as before, higher than theoretically predicted (to be discussed in Chapter 5). The theory underestimates to some extent the second mode group frequencies.

Figs. 67a to 67f depict experimental and theoretical coherences and phases, for the R-R (1,3) and T-T (1,3) cases, at $u = 1$, 3, and 5 (usual format). In theory, there are four (2K) cross-sectional coupling modes, which are (as in the mean flow model) flow velocity invariant: for example ($u = 1$), at $\omega \simeq 24$ (Figs. 67a and 67b), the Radial and Tangential direction motions are in and out of (180°) phase respectively, and at $\omega \simeq 26$, the reverse (180° and 0°) occurs. The measured coherences and phases compare with the theoretical ones in the same fashion as before, i.e. whenever the experimental coherence is high, phases do agree, with the usual undervaluation of second mode group frequencies. There is, however, an apparent discrepancy, for the T-T (1,3) case, at $u = 1$ (Fig. 67b): coherence for $30 < \omega < 55$ does not behave in the same manner as the theoretical one - there appears to be some coherent power in that frequency range, not predicted in theory; this occurs to a slighter extent at $u = 3$ (Fig. 67d), and basically not at all at $u = 5$ (Fig. 67f). At this point, no explanation can be found for this; the plausible cause of "stray power" is not even present here (see Fig. 63), but this problem can be considered secondary, as it pertains to the second mode group, where signal levels are quite low (resulting in higher possibilities of experimental error).

We may now proceed to the single cylinder case.

4.3-7: K = 1, 1F

The single cylinder was located near the center of the channel, which makes this case essentially that of an isolated cylinder in "infinite" fluid ($G_W \simeq 5.1^*$). Mounting in the channel was slightly offset from the center (less than one diameter), hence the use of "Radial" and "Tangential" to identify the two mutually perpendicular measurement directions (the theoretical calculations were for a cylinder with the same offset).

Measured PSD's, in the "Radial" and "Tangential" directions, are shown in Fig. 68, for u = 1, 3, and 5. As they should, these PSD's are essentially identical. It should be noted that higher density scales than usual were required, as the PSD's are relatively sharply "peaked". The dominant frequencies decrease more slowly than for the K = 2 and K = 4 cases reviewed previously; this is to be expected, since the critical flow velocity for the K = 1 is the highest of all.† It is interesting to note that there is again "stray" power near $\omega = 37$, in the "Tangential" direction (normal to the longitudinal axis of the support fins), at u = 1. This suggests that this particular "noise" stems from the test setup itself (e.g. mountings), and is not inherently part of the systems under analysis. We also note some difference in powers near $\omega = 67$ (but not a harmonic of the "stray" power).

The variation of PSD's, with flow velocity, is illustrated in Fig. 69a ("Radial") and Fig. 69b ("Tangential").

Total powers are shown in Fig. 70; an exponential trend is strongly apparent.

Theory and experiments are compared in Figs. 71a ("Radial") and 71b ("Tangential"): The PSD's compare well, and as before the best agreement is at u = 1, the theory underestimating damping§ at higher flow velocities. Again,

---

* Spacing to wall; this value would have been 7.1 had the cylinder been located exactly at the center of the channel.

† See Ref. [75] for more details on stability.

§ Note that the theoretical damping model itself may not be valid.

the second mode group frequencies are lower in theory than in the measurements.

Of course, no inter-cylinder measurements apply here.

This ends the review of systems composed entirely of flexible cylinders. We are left with "combination systems", i.e. with mixed Rigid/Flexible cylinders. In all cases to follow, the inter-cylinder spacing is constant, namely $G_c = 0.75$, and the systems are either $K = 4$ or $K = 28$.

Specifically, the cases left to be reviewed are the following: a 1F/3R system, two 2F/2R systems (diagonal and adjacent flexible cylinders), and three 4F/24R systems (central, parallel offset, and diagonal offset 4F subclusters).

4.3-8: $K = 4$, $G_c = 0.75$, 1F(1)/3R(2,3,4)

This test forms an integral part of fluid coupling testing; comparisons will be made with the 1F case to study the effect of the presence of the three rigid cylinders near the flexible one.

The measured Radial and Tangential directions PSD's are depicted in Fig. 72. In comparison with the 1F case (see Fig. 68), shapes are similar, but power levels are generally higher; also, dominant frequencies are lower (comparison plots will be presented in Chapter 5). Furthermore, Radial and Tangential power levels are not always the same (viz. $u = 1$ and $u = 5$). Finally, as found for earlier cases, first mode group characteristics extend to the second mode group, powers for the latter being of the usual order of magnitude (see expansion scales in Fig. 72), and $u = 1$ low frequency "stray" power and $\omega \simeq 38$ Tangential "peak" are also present. Tentatively, we may presume that the main effects of the presence of the three rigid cylinders in the 1F/3R case are to slightly increase the virtual mass of the flexible one, and to modify the boundary layer pressure field characteristics.

System behaviour with increasing flow velocity is illustrated in Fig. 73a for the Radial direction, and Fig. 73b for the Tangential one. The corresponding integrated powers are shown in Fig. 74: results suggest that powers in the two directions are not proportional to each other, as was the case for the other systems investigated (this can also be inferred from data of Fig. 72).

Comparisons with theory are very similar to those for the 1F case; see Figs. 75a and 75b (R and T, for 1F/3R), versus Figs. 71a and 71b ("R" and "T", for 1F).

The next two combination systems involve 2F/2R cases.

4.3-9: K = 4, G_c = 0.75, 2F(1,3)/2R(2,4)

We recall that the "Reference" system is composed of four flexible cylinders; the two flexible cylinders system of Section 4.3-6 (G_c = 1.89) stems from the "Reference" system, after two diagonally opposite cylinders have been removed. The case to be reviewed here is obtained by making the latter diagonal pair rigid instead, to provide additional insight into fluid coupling. (Note that the next case to be presented will involve making two adjacent rather than two diagonal cylinders, rigid.)

Experimental Radial and Tangential direction PSD's are depicted in Fig. 76: this may be compared to Fig. 31 (K = 4, 4F, G_c = 0.75), and to Fig. 63 (K = 2, 2F, G_c = 1.89). All three systems have different characteristics, and this will later (Chapter 5) assist in discovering basic features of inter-cylinder fluid coupling. We note the constant presence of Tangential u = 1 "stray" power ($\omega \simeq 38$), and the usual similarity and relative power levels of second to first mode PSD's.

Figs. 77a and 77b illustrate PSD's versus flow velocity: we see that Radial power density levels decrease more gradually than Tangential ones, a fact confirmed in the plot of total powers (versus flow velocity), in Fig. 78. The latter Figure again suggests an exponential increase with flow.

Experimental and theoretical PSD's are illustrated in Figs. 79a (Radial) and 79b (Tangential). As was the case previously, the best comparisons are at u = 1 (rather than higher values of u = 3 and 5), with the theory still underestimating damping at higher flow velocities, as well as second mode group frequencies.

No unusual features are found, when comparing theoretical and experimental coherences and phases, depicted in Figs. 80a to f, except for a generally better agreement of R-R coherences (versus the T-T ones).

Another 2F/2R setup was also investigated, this time with two adjacent rigid (and two adjacent flexible) cylinders, to follow.

4.3-10: K = 4, $G_c = 0.75$, 2F(1,2)/2R(3,4)

This system in meant to complement the previous one, by considering adjacent instead of diagonal pairs of (flexible and rigid) cylinders. Apparently due to a combination of few flexible cylinders (two) and their proximity ($G_c = 0.75$*), this case will be seen to yield the best results of all, in terms of agreement between theory and experiments.

An interesting feature here is that Radial and Tangential PSD's are very similar to one another: this may be seen in Fig. 81. The usual peculiarities of Tangential u = 1 "stray" power at $\omega \simeq 38$ and $\omega = 0$ to 15 "noise" are still present.

Radial and Tangential PSD's and the corresponding total powers are shown, versus flow velocity, in Figs. 82a and 82b, and Fig. 83. Note the somewhat lower Radial power.

Comparisons of measured and theoretical PSD's follow prior trends, as illustrated in Figs. 84a (Radial) and 84b (Tangential).

Where results are exceptionally good are for coherences and phases, which may be seen by inspection of Figs. 85a to f. Other than areas of phase disagreement where measured coherence is low, and other than underestimation of second mode group frequencies by the theory, agreement is generally excellent; there are a few instances where the experimental coherence amplitudes are lower than theoretically predicted, but (coherence function) shapes are nevertheless correct, for example in $\omega = 0$ to 15, at u = 5, in both Radial and Tangential directions (Figs. 85e and 85f).

The above data will be further discussed in Chapter 5. We are left to review data for the three 4F/24R systems.

---

* Note that the other two flexible cylinder systems, i.e. those of Sections 4.3-6 and 4.3-9, have an inter-flexible-cylinder G_c of 1.89.

4.3-11: K = 28, G_c = 0.75, 4F(1,2,3,4)/24R(rest)

This is the first of three 28-cylinder test clusters; the four flexible cylinders are located centrally within the test channel, namely Positions 1, 2, 3, and 4, in Fig. 29, and the twenty full cylinders and eight half cylinders (counted as four cylinders, hence the use of K = 28) are rigid. The two other systems to be studied are a parallel offset one (Positions 6, 7, 2, 1 in Fig. 29), and a diagonally offset one (Positions 5, 6, 1, 16 in Fig. 29).

Because 28-cylinder theoretical calculations require large amounts of computer memory and time, it was decided to approximate the K = 28 system(s) by smaller clusters, and to use only two comparison functions (N = 2); the one used here is discussed next.

4.3-11a: Reduced size theoretical equivalent, K = 12, R_c = 8.00 cm

The first "equivalent" reduced system, for representing the 4F(1,2,3,4) /24R(rest) case, was chosen as follows: (i) The eight rigid cylinders closest to the four central ones were retained (viz. Positions 6, 7, 9, 10, 12, 13, 15, and 16 in Fig. 29), and (ii) the enclosing channel diameter was reduced, so as to "simulate" the presence of peripheral cylinders, inclusive of half cylinders and the original channel wall. The choice of the new R_c (reduced channel radius) was based on the matching of hydrodynamic coupling coefficients, as described below. The resulting equivalent system, with K = 12 and R_c = 8.00 cm, is illustrated in Fig. 86.

Note that in terms of fluid coupling, the system dynamics is dominated by the hydrodynamic, rather than by the "viscous" part; for example, setting the coefficients c and c_f (dimensionless form of C_f and C_D of eqs.(2.29) and (2.30)) to zero did not alter the theoretical PSD, coherence function, and phase of the "Reference" system very much (see Figs. 41, 42a, and 42b), compared say, to the difference between the latter system, and a single cylinder (no hydrodynamic coupling* - see Fig. 71a, at u = 3).

---

* In the single cylinder case, we have equal Radial, Tangential, and Edge PSD's.

The following discussion pertains to equations (2.27) and (2.28), i.e. hydrodynamic fluid coupling forces (per unit length) on cylinders, induced by acceleration of others. The structure of these equations implies that:

$-\rho A_k \varepsilon_{ki}$ is the force per unit length on cylinder k, in the z-direction, due to a unit acceleration of cylinder i, in the z-direction (see Fig. 7 for "cross-sectional" directions).

In short tabular form,

Coefficient	Force per unit length: Cylinder	Force per unit length: Direction	Due to acceleration: Cylinder	Due to acceleration: Direction
ε_{ki}	k	z	i	z
e_{ki}	k	z	i	y
κ_{ki}	k	y	i	z
k_{ki}	k	y	i	y

The "square" array geometry possesses a number of planes of symmetry: Fig. 87 depicts typical symmetry examples for the four cylinders of the central bundle (Positions 1, 2, 3, and 4). In part (a) of the Figure, we consider coupling between motion of cylinder 1 in the z-direction, and cylinder 3 in the y-direction; first symmetry results in the relation

$e_{13} = \kappa_{31}$, that is, the force (per unit length) induced on cylinder 1 in the z-direction, due to a unit acceleration of cylinder 3 in the y- direction, is equal to the force (per unit length) induced on cylinder 3 in the y-direction, due to a unit acceleration of cylinder 1 in the z-direction. A 90° counterclockwise rotation of selected vectors yields, again by symmetry, and equivalent pair (dashed vectors): hence, we may also state

$-\kappa_{24} = -e_{42} = e_{13} = \kappa_{31}$. Yet another symmetry situation is obtained by pivoting the original vectors about the diagonal line through cylinders 1 and 3 (dotted vectors), resulting in additional matched coefficients

$$\kappa_{13} = e_{31} = -\kappa_{24} = -e_{42} = e_{13} = \kappa_{31} .$$

Similar operations in part (b) of the Figure yield

$$\varepsilon_{13} = \varepsilon_{31} = k_{24} = k_{42} = k_{13} = k_{31} .$$

By inspection, we see that symmetry dictates a total of seven (out of 64) independent hydrodynamic coupling coefficients, representing the following inter-cylinder motion:

$\varepsilon_{11} = \varepsilon_{22} = \varepsilon_{33} = \varepsilon_{44} = k_{11} = k_{22} = k_{33} = k_{44}$: single cylinder(s);
z- (y-) direction force (per unit length), due to
its z- (y-) direction acceleration.

$e_{11} = -e_{22} = e_{33} = -e_{44} = \kappa_{11} = -\kappa_{22} = \kappa_{33} = -\kappa_{44}$: single cylinder(s);
z- (y-) direction force (per unit length), due to
its y- (z-) direction acceleration.

$\varepsilon_{12} = \varepsilon_{21} = \varepsilon_{34} = \varepsilon_{43} = k_{23} = k_{32} = k_{41} = k_{14}$: adjacent cylinder pair(s);
z-direction force (per unit length) on first cylinder, due to
the z-direction acceleration of the other.

$\varepsilon_{23} = \varepsilon_{32} = \varepsilon_{41} = \varepsilon_{14} = k_{12} = k_{21} = k_{34} = k_{43}$: adjacent cylinder pair(s);
y-direction force (per unit length) on first cylinder, due to
the y-direction acceleration of the other.

$e_{12} = -e_{21} = e_{23} = -e_{32} = e_{34} = -e_{43} = e_{41} = -e_{14} =$
$-\kappa_{12} = \kappa_{21} = -\kappa_{23} = \kappa_{32} = -\kappa_{34} = \kappa_{43} = -\kappa_{41} = \kappa_{14}$: adjacent cylinder pair(s);
z- (y-) direction force (per unit length) on first cylinder, due to
the y- (z-) direction acceleration of the other.

$\varepsilon_{13} = \varepsilon_{31} = \varepsilon_{24} = \varepsilon_{42} = k_{13} = k_{31} = k_{24} = k_{42}$: diagonal cylinder pair(s);
z- (y-) direction force (per unit length) on first cylinder, due to
the z- (y-) direction acceleration of the other.

$e_{13} = e_{31} = -e_{24} = -e_{42} = \kappa_{13} = \kappa_{31} = -\kappa_{24} = -\kappa_{42}$: diagonal cylinder pair(s);
z- (y-) direction force (per unit length) on first cylinder, due to
the y- (z-) direction acceleration of the other.

Identical groupings exist for "viscous" coupling, where $\varepsilon \rightarrow \zeta$, $e \rightarrow g$, $\kappa \rightarrow \sigma$, $k \rightarrow s$.

The four central cylinder coefficients, for the reduced $K = 12$ cluster, were compared to those for the $K = 28$ cluster (actually a $K = 24$ bundle, as the half-cylinders were absent), and an "optimum" R_c found by trial and error. For $R_c = 8.00$ cm (3.154 in), results are:

Parameter	K = 28 values	K = 12 values
ε_{11}	-1.359	-1.361
ε_{12}	0.230	0.227
ε_{13}	0.00265	-0.00095
ε_{14}	-0.418	-0.422
e_{11}	-0.00327	-0.00080
e_{12}	0.00399	0.00374
e_{13}	0.158	0.158

We note that not all coefficients are well matched, some even reversing in sign (ε_{13}), but the poorly matched coefficients are small compared to the dominant ones, namely ε_{11}, e_{11}, and e_{12}, versus ε_{11}, ε_{12}, ε_{14}, and e_{13}.

It is interesting to note that in this case, the "viscous" coupling coefficients end up well matched as well; the $R_c = 8.00$ cm values are:

Parameter	K = 28 values	K = 12 values
ζ_{11}	1.000	1.000
ζ_{12}	-0.0976	-0.0962
ζ_{13}	-0.00101	0.00046
ζ_{14}	0.177	0.179
g_{11}	0.000	0.000
g_{12}	-0.00182	-0.00158
g_{13}	-0.0668	-0.0667

Again, the poorly matched coefficients are relatively small (compared to the magnitude of the matched ones).

Theoretical PSD and CSD computations are then effected, using the above K = 12 coupling coefficients as input to the FORTRAN program CSD.f (see Appendix K).

4.3-11b: Modulus of elasticity, rigid cylinders

The rigid cylinders were made of one of two materials, namely aluminium, or acetal (plastic), with moduli of elasticity of 6.89×10^7 KPa (10.0×10^6 psi) and 3.59×10^6 KPa (5.2×10^5 psi) respectively. In test bundles such as this K = 28 one, both types of rigid cylinders were utilized simultaneously; we wish to show that both types can be considered equally rigid, relative to the flexible, Silastic E rubber cylinders, whose modulus of elasticity is only 2779 KPa (403 psi).

Figs. 88, 89a, and 89b illustrate the fact that whether the modulus of elasticity (ratio matrix for E [eqn.(2.80)]) used in theoretical computations is that for aluminium, or that for acetal (DELRIN), results are essentially identical, in terms of PSD's, coherence functions, and phases. This confirms the validity of using E for acetal in all K = 28 computations, to represent either aluminium or acetal cylinders, and indicates that we may indeed consider both types of cylinders "rigid".

4.3-11c: Basic results

Now that parameters pertaining to the theoretical calculations have been established, we shall review experimental and theoretical results for this case (K = 28, G_c = 0.75, central K = 4 flexible sub-cluster).

The main purpose for this test, in addition to studying fluid coupling (presence of peripheral rigid cylinders, about the 4F cylinders), is the investigation of the response of the sub-bundle, subjected to the different boundary layer pressure field that exists in the closely spaced K = 28 bundle (as compared to the "open" K = 4 case); recall that pressure PSD's were different, for the K = 0 and K = 28 cases (Figs. 20 and 21).

Fig. 90 depicts measured Radial and Tangential PSD's, at three flow velocities; note that the maximum is u = 4, since divergence was present as early as u = 4.5. The usual low frequency (ω = 0 to 15) "noise" is observed, but this time, the u = 1 Tangential "stray" power (was at $\omega \simeq 38$ before) is absent: this latter observation strongly indicates a support structure induced vibration, when the 90° cross of Fig. 13 is positioned in the channel, either mechanically transmitted or in interaction with the flow (e.g. a Strouhal frequency). The cross was used in all tests except the (three) K = 28 systems, the latter utilizing a support machined from a 0.95 cm (3/8 in) thick solid brass plate (see Fig. 14).

Radial direction PSD's are shown, versus flow velocity, in Fig. 91a; note that the maximum u depicted is 4 (rather than the usual 5). Compared to the K = 4, G_c = 0.75, 4F case (see Fig. 33a), we note similar power levels, in spite of higher boundary layer pressure PSD's (K = 28 data versus K = 0 data),

although it should be kept in mind that the two systems do not have the same transfer function matrices (see comparisons with theory below). Another difference is the absence of the first Radial "peak" in this K = 28 case, at least at the higher flow velocities. Tangential direction data, shown in Fig. 91b, is quite similar to the K = 4 data.

Total Radial and Tangential direction powers are plotted in Fig. 92, versus flow velocity. As found for a number of other systems, both powers are about equal, and the power increase with flow velocity is basically exponential. Note that this system has become divergent at u = 4.5, hence there are no available PSD's at u = 4.5 and 5.0.

Comparisons of theoretical and experimental PSD's, shown in Figs. 93a and 93b, reveal a few aspects that differ from those found previously: (i) The Radial direction discrepancies are more pronounced, at higher flow velocities (u = 3, and 4), specifically the absence of a clear first "peak". (ii) The theory overestimates power levels even more than before (compare scales with those of Figs. 35a and 35b, which are for the "Reference" K = 4 test). (iii) The u = 4 PSD's (Radial and Tangential) do not suggest that the critical flow velocity is being approached, although experimentally reached at u = 4.5; note the u = 5 PSD's of the "Reference" case (Figs. 35a and 35b). As a check the theoretical u = 4.5 and 5.0 Radial and Tangential PSD's, for this K = 28 case, have been plotted in Fig. 94, to confirm that divergence was in fact not (theoretically) imminent at u = 4. (iv) The Tangential direction theoretical "peak" preceeding the last one (first mode group) is not found experimentally. Recall that second mode group comparisons cannot be made here, as corresponding theoretical data is not reliable (N = 2 used in the computations).

In terms of coherence and phase, the u = 1 results compare fairly well, but already with some exceptions: (i) Referring to the R-R (1,3) case, in Fig. 95a, it can be seen that the theoretically predicted coherence "peak", at $\omega \simeq 27$, is very small in the measured data; nevertheless, the tendency of the corresponding phase ($\omega \simeq 27$) to go to zero would suggest that the very

small amount of coherence represents the particular cross-sectional coupling mode predicted in theory (this is rejected below). (ii) An analogous situation is found in the T-T (1,3) case as well; in Fig. 95b, the coherence "peak" at $\omega \simeq 21$ (theory) is not found in the measured data, although one could have interpreted the rapid local change in phase ($\omega \simeq 21$) towards zero to signify detection of the predicted coupling mode. The coherence function shapes do not agree, in the T-T (1,3) case (Fig. 95b), near $\omega = 24$: the experimental data is basically "single peaked", whether the theoretical data is "double peaked"; nevertheless, corresponding phases do agree.

It will prove easier to discuss the remaining two ($u = 3$ and $u = 4$) cases for Radial and Tangential directions separately, each versus the corresponding $u = 1$ data. Radial coherence and phase comparisons get progressively worse: (i) the $\omega \simeq 27$ "peak" of the $u = 1$ data is now, in theory, at $\omega \simeq 24$ for $u = 3$ (Fig. 95c), and $\omega \simeq 22$ for $u = 4$ (Fig. 95e); in the $u = 3$ case, we may state that neither the coherence nor the phase are detected experimentally, and at $u = 4$, we may say that the phase alone <u>appears</u> to be present, as in the $u = 1$ case, but in itself, the measured phase is meaningless without some coherent power. Hence, we can state that that particular theoretical mode has not been measured. (ii) The first (R-R) coherence "peak", found both in theory and experimentally for the $u = 1$ case, at $\omega \simeq 20$, is barely present at $u = 3$ (Fig. 95c), at $\omega \simeq 14$ (note that the phase tends to zero in both cases also), and basically absent at $u = 4$ (theory at $\omega \simeq 11$, in Fig. 95e).

Tangential coherence and phase comparisons fare better than Radial ones (as did the PSD's). The first coherence "peak" and corresponding 0° phase, in theory at $\omega \simeq 17$ for $u = 3$ (Fig. 95d) and at $\omega \simeq 12$ for $u = 4$ (Fig. 95f), is still not present in the measured data - this particular theoretical coupling mode has not been detected experimentally, at any velocity.

Overall for this system ($K = 28$), theory and experiments do not agree very well, and possible explanations for this shall be discussed in Chapter 5, after reviewing the other two $K = 28$ systems.

4.3-12: K = 28, G_c = 0.75, 4F(6,7,1,2)/24R(rest)

The second 28-cylinder cluster is a variant of the first, where the sub-bundle of 4F cylinders is moved in the y-direction: the purpose is to test the uniformity of the flow and pressure field in the water tunnel, as well as providing an additional test case versus the theory. As in Section 4.3-11, a reduced cluster is used for theoretical computations, described below.

4.3-12a: Reduced size theoretical equivalent, K = 12, R_c = 8.00 cm

Since in the case of a central bundle (Section 4.3-11), the additional peripheral cylinders are best simulated by a reduced channel radius of 8.00 cm, it is to be expected that this parallel offset case of four cylinders (see Fig. 29) will be represented well by the same reduced system (i.e. same R_c). The following comparison (coefficients of Section 4.3-11a, but for translated cylinders) bears this out.

Parameter	K = 28 values	K = 12 values
ε_{66}	-1.416	-1.405
ε_{67}	0.209	0.208
ε_{62}	-0.00994	-0.0159
ε_{61}	-0.438	-0.453
e_{66}	-0.00578	0.0277
e_{67}	0.0309	0.0455
e_{62}	0.170	0.178

Note that the only poorly matched coefficients are relatively small. In this latter case, there are more than 7 independent coefficients (the number is 19), since symmetry is now only about a single axis (y), rather than the two axes (x and y) of the central cluster case, for the two cylinders in Positions 6 and 7. The remaining coefficients are tabulated below.

Parameter	K = 28 values	K = 12 values
ε_{11}	-1.359	-1.361
ε_{12}	0.230	0.227
e_{11}	-0.00327	-0.00080
e_{12}	0.00399	0.00374
e_{16}	-0.00466	-0.00777
e_{17}	-0.146	-0.144
e_{61}	-0.00855	-0.00129
k_{12}	-0.418	-0.422

(continued)

k_{16}	0.228	0.207
k_{26}	0.00444	-0.00830
k_{66}	-1.363	-1.351
k_{67}	-0.416	-0.426

We see that all dominant coefficients are well matched.

As was the case in the previous Section, the K = 12 coefficients are used as input data for the computation of theoretical PSD's and CSD's.

4.3-12b: Basic results

The parallel offset sub-cluster, namely Positions 6, 7, 2, and 1, may be seen in Fig. 29. We note that, in terms of fluid coupling, this situation is very similar to that for the case of 4F(1,2,3,4)/24R (Section 4.3-11 above)*: In the latter system, four flexible cylinders in Positions 1, 2, 3, and 4, are coupled mostly to immediately "surrounding" rigid cylinders, in Positions 5 to 16 inclusively. Similarly, in the present system, the four flexible cylinders in Positions 6, 7, 2, and 1, are coupled to the rigid cylinders in Positions 17, 18, 8, 9, 10, 3, 4, 15, 16, and 5, as well as to (unnumbered) half-cylinders adjacent to Positions 17 and 18 respectively (including the channel wall at R_c = 10.24 cm [the outer diameter in Fig. 29]). Differences between the two systems are expected to stem chiefly from non-uniformity in flow through the test channel, the latter brought mostly by the presence of the channel wall (both within and upstream from the bundle).

The usual format for data presentation will not be followed exactly here, as a symmetry investigation will be made. We start by comparing measured Radial and Tangential PSD's, in Positions 7 and 1, to evaluate the extent of asymmetry in the tunnel: Figs. 96a, 96b and 96c illustrate experimental PSD's, at u = 1, 3, and 4§, in Positions 7 and 1: the Tangential direction data exhibits little asymmetry, at any flow velocity, but this is not the case for the Radial direction, where we observe both power and, to a lesser

---

* At least in theory, to be shown below.

§ As in the previous K = 28 system, instability occured at u > 4.

extent, PSD shape differences, getting progressively worse with increasing flow velocity. There is one exception in the Tangential direction, specifically, at u = 4, in the second mode group (Fig. 96c), where power levels and distribution (i.e. shapes) do not compare well (in the two Positions). Globally, this indicates flow field asymmetry, principally in gaps such as "8-18-7" ("surrounding" Positions - see Fig. 29), rather than gaps such as "18-17-6-7". This shall be discussed in Chapter 5, after having reviewed the third K = 28 system (Section 4.3-13 to follow shortly).

Fig. 97a depicts measured Radial and Tangential PSD's for Position 7, at u = 1, 3, and 4 and Fig. 97b shows similar data for Position 1. As for the previous K = 28 system, the u = 1 Tangential "stray" power (was at $\omega \simeq$ 38 in other cases) is absent, in either position, reinforcing the concept of the 90° cross (Fig. 13) being the source of "stray" motion of the cylinder. Moreover, it is interesting to note that the (ω = 0-15) low frequency "noise" is stronger is Position 7 (closer to the channel wall) than it is in Position 1, the level in the latter case basically remaining the same as the one found (in that position) for the central 4F/24R case; this provides new data to provide insight into the ("noise") problem and shall be discussed in Chapter 5.

PSD's are plotted versus flow velocity, in Figs. 98a (Rad., Pos. 7), 98b (Rad., Pos.1), 98c (Tan., Pos.7), and 98d (Tan., Pos.1); other than the previously noted Radial direction power level differences with cylinder position, the only unusual characteristic is the sudden increase in low frequency ($\omega < 15$) power in the Position 1 Radial PSD, from u = 3.5 to u = 4.0: this may very well indicate that instability occurs first in centrally located cylinders (Positions 1 and 2), possibly because of a relatively higher average flow velocity there. However, a contradiction of sorts exists here, since we normally expect higher total powers (integrated PSD's) when flow velocities are themselves higher; but Position 1 Radial PSD's have lower power levels than those in Position 7!. Again, we postpone detailed discussion to Chapter 5, where all available data shall be utilized for analysis.

Total powers versus flow velocity are depicted in Fig. 99, for both cylinder positions, and for the Radial and Tangential directions; trends are still basically exponential, and we note that rates of change of power with velocity are similar, except for the case of Tan., Pos. 1, which is lower.

The concept of the central and parallel offset K = 28 systems being basically equivalent (fluid coupling to "surrounding" cylinders, discussed above), is supported in theory, as shown in Figs. 100a, 100b and 100c for Radial and Tangential PSD's (at u = 1, 3, and 4), and Figs. 101a to 101f, for corresponding coherences and phases, where Position 1 (and 3) of the central sub-cluster is compared to both Positions 7 and 1 of the parallel offset system (the latter two positions are not truly symmetrical, on account of the offset). Note that phase "spikes", e.g. the GREEN trace in Fig. 101a, at $\omega \simeq 33$, simply mean that the phase is going down "gradually" towards -180°: All plots had been formatted to interpret a zero real part for the CSD's, as 180°, rather than -180°, which is valid in cases of "instantaneous" phase changes, but not in the latter case, where indications are for a -180° phase instead. However, the usual format has been retained for convenience, and to facilitate comparisons. We note slight departures from the usual 0° or 180° phases, in the theory; for example, in Fig. 101c at $\omega \simeq 32$: this is due to numerical error, stemming from very small real and imaginary parts of the CSD used to calculate coherence. This is of no real concern here, as phase for essentially non-coherent signals is meaningless.

We may now compare experimental and theoretical results. Figs. 102a and 102b illustrate Radial PSD's, for Positions 7 and 1 respectively, and Figs. 102c and 102d depict the same information, for the Tangential direction. In all but one case, first mode group frequency* ranges are in agreement, but power distribution within these ranges (shapes of PSD's) are not always the same; the one (frequency range) exception is Radial, Position 1, u = 4 (Fig. 102b), where higher theoretical power levels near $\omega = 11$ and $\omega = 14$, do not

---

* Recall that theoretical results are not reliable for the second mode group, as N = 2 (comparison functions) was used.

materialize experimentally. As before, better agreement is found at the lowest velocity (u = 1). Theoretical to experimental power ratios are comparable to those for the central K = 28 case (see Fig. 93).

Experimental and theoretical coherences and phases are illustrated in Figs. 103a to 103f (cylinder Positions 7 and 1): comparisons with data for the central K = 28 cluster reveals that, in all cases (Radial and Tangential, u = 1, 3, and 4), coherences are quite similar, but for two obvious exceptions; (i) the R-R u = 3 measurement, in the $\omega = 0$ to 9 range, where the central sub-bundle displays a higher (not theoretically predicted) magnitude than found the present parallel offset system (Fig. 95c versus Fig. 103c), and (ii) the R-R u = 4 data, at $\omega \simeq 22$, where some coherence is in evidence (in agreement with theory), not present earlier in the central cluster case (see Figs. 103e and 95e).

Where measured coherences are high, theoretical and experimental phases are for the most part equal, with the difference that phase changes are occasionally more gradual in this (parallel offset) system, but to a greater extent than theoretically predicted: for example, the R-R case, at u = 3 (Fig. 103c) and u = 4 (Fig. 103e), near $\omega = 25$ and 23 respectively. Note that measured R-R phase at u = 4, in the range $\omega \simeq 37$ to 50 (Fig. 103e), reads about -30°, which might be indicative of an experimental error; however, the matter will not be pursued further, since second mode group comparisons are not being made here (N = 2 only in the theory).

The last K = 28 system, this time with a diagonal offset, will now be reviewed; this will end the presentation of experimental and theoretical data, and shall be followed by "Discussion and Conclusions" (Chapter 5).

4.3-13: K = 28, G_c = 0.75, 4F(5,6,1,16)/24R(rest)

This third and last 28-cylinder bundle is also a variant of the central one of Section 4.3-11: the 4F sub-bundle is moved diagonally, i.e. in the z- and y-directions simultaneously, to provide further testing on the water tunnel pressure field uniformity, and a last case for comparison with theory.

In the case of this diagonally offset sub-bundle, a reduced K = 12 cluster is not sufficient for modelling, since the cylinder in Position 5 would be missing (see Figs. 86 and 29). Hence, a larger K = 16 reduced cluster was utilized to represent the diagonally offset case, illustrated in Fig. 104. It is described next.

4.3-13a: Reduced size theoretical equivalent, K = 16, R_c = 9.40 cm

The coefficients matching (with the K = 28 cluster) procedure used in the above Section (4.3-11a) was also made use of here. This latter case exhibits only "diagonal" symmetry, resulting in 20 independent coefficients, which are listed below, for the "optimized" channel radius of R_c = 9.40 cm (3.700 in), versus the true (K = 28) values.

Parameter	K = 28 values	K = 16 values
ε_{11}	-1.359	-1.344
ε_{51}	-0.00502	-0.0220
ε_{55}	-1.344	-1.472
ε_{66}	-1.416	-1.283
ε_{56}	0.201	0.209
$\varepsilon_{5\,16}$	-0.431	-0.470
ε_{61}	-0.438	-0.395
$\varepsilon_{6\,16}$	-0.0140	0.00939
$\varepsilon_{16\,1}$	0.228	0.231
$\varepsilon_{16\,16}$	-1.363	-1.351
e_{11}	-0.00327	0.00305
e_{16}	-0.00466	0.0126
e_{51}	0.146	0.178
e_{55}	0.0175	0.0612
e_{56}	-0.00222	0.0500
e_{61}	-0.00855	-0.00065
e_{65}	-0.0373	0.00449
e_{66}	-0.00578	0.00308
$e_{6\,16}$	-0.193	-0.152
$e_{16\,6}$	-0.157	-0.129

The agreement for the most dominant coefficients is more than acceptable, viz. ε_{11} (-1.344 instead of -1.359), ε_{55} (-1.472 instead of -1.344), ε_{66} (- 1.283 instead of -1.416), and $\varepsilon_{16\,16}$ (-1.351 rather than -1.363); similarly for "secondary" coefficients (e.g. $\varepsilon_{5\,16}$ at -0.470 versus -0.431).

4.3-13b: Basic results

This diagonally offset sub-bundle (flexible cylinders) may be visualized in Fig. 29, viz. Positions 5, 6, 1, and 16. Were it not for the cylinder in Position 5, this system would be very similar to the last two K = 28 cases, the latter consisting essentially in four flexible cylinders "surrounded" by rigid ones. Nevertheless, the Position 5 cylinder is located near two adjacent half-cylinders and the channel wall, approximating two full cylinders (and no wall between them). Experimental data for this system will be compared to data for the previous two K = 28 cases (central and parallel offset).

As in Section 4.3-12b (Basic results for the parallel offset system), the usual presentation format will not be followed to the letter here. Figs. 105a, 105b, and 105c depict Radial and Tangential directions PSD's, at the flow velocities u = 1, 3, and 5 (note that divergence has not occured here, contrary to the two other cases), and in Positions 5 and 1. Given the two potential sources of asymmetry present in this case, namely the different fluid coupling environment of the cylinder in Position 5, and possible non-uniformity in the fluid flow field (e.g. due to the presence of the channel wall), results are surprisingly symmetrical: this suggests one of two possibilities, namely (i) tunnel flow is uniform within the bundle and fluid coupling of the flexible to the rigid cylinders is similar in both Positions 5 and 1, or (ii) one effect (tunnel flow non-uniformities) compensates for the other (coupling environment).

Fig. 106a illustrates Radial and Tangential directions PSD's, at u = 1, 3, and 5, for Position 5; Fig. 106b depicts the same infomation for Position 1. Trends found earlier occur again here, namely (i) the absence of u = 1 Tangential "stray" power, which confirms the 90° cross as being the source of noise at $\omega \simeq 38$, and (ii) the low frequency "noise" (ω = 0-15) is stronger

in the offset Position 5, than it is in Position 1 (similar to previous case).

The measured PSD's are plotted versus flow velocity, in Figs. 107a (Rad., Pos. 5), 107b (Rad., Pos. 1), 107c (Tan., Pos.5), and 107d (Tan., Pos.1): A sudden increase of low frequency power from u = 4.5 to u = 5.0, indicating incipient divergence, occurs in all four cases at once for this diagonally offset system, rather than being restricted to the Radial direction in Position 1, as was found for the parallel offset system. This contradicts the presumption of higher average flow velocities in the central part of the tunnel, made in the previous Section (to explain why the parallel offset system should buckle in a central Position first); Chapter 5 shall deal with this subject.

Fig. 108 depicts measured total powers, versus flow velocity (as before, obtained from integration of PSD's, namely those in Fig. 107): An exponential increase is again found here, and powers vary with cylinder position, in a fairly consistent manner (Rad., Pos. 5 being dominant and so on).

PSD comparisons between Position 1 of the central sub-cluster (Section 4.3-11), and each of Positions 5 and 1 of the diagonal offset sub-cluster, are made in Figs. 109a, 109b, and 109c, for the flow velocities u = 1, 3, and 5 respectively, and in both the Radial and Tangential directions. Relative to the comparisons made with respect to the parallel offset system (Figs. 100a, 100b, and 100c), we find that the Radial direction PSD's still match fairly well, but that this does not occur to the same extent in the Tangential direction: comparisons get progressively worse in this latter case, and at u = 5, only frequency ranges still agree. Inspection of Figs. 29 and 104 does suggest a much poorer fluid coupling equivalence, in Position 5 Tangential direction, between the K = 28 system and the reduced K = 16 system (used for the diagonal offset system), the latter having no close solid (wall or cylinder) surface (Tan. direction); furthermore, because Position 1 is not only coupled to "adjacent" Rigid and Flexible cylinders, but also to the (Flexible) cylinder in Position 5, its PSD is also "adversely" affected (see BLUE as well as GREEN traces in Fig. 109c). We can infer that the reduced

$K = 16$, $R_c = 9.40$ cm system models the full $K = 28$ system only poorly in the Tangential direction; consequently, in this case, more emphasis should be put on the measured PSD's, and not so much on the theoretical ones.

The situation is similar for coherences and phases, although the Tangential direction comparisons are now better: Figs. 110a to 110f illustrate comparisons between theoretical results for the central versus the diagonally offset sub-bundles; Radial direction coherences and phases compare well, and Tangential direction ones are fairly similar, except for coherences corresponding to the first tangential coupling mode within a mode group, for example, at $\omega \simeq 20$ and $u = 1$ (Fig. 110b), with coherences being underestimated in the diagonal offset case.

Experimental and theoretical PSD's are depicted in Figs. 111a and 111b for Position 5, and Figs. 111c and 111d for Position 1, for the three flow velocities of $u = 1$, 3, and 5. In the theoretically more reliable Radial direction, PSD shapes agree well only at $u = 1$ (Figs. 111a and 111c); otherwise (at $u = 3$ and 5), measured PSD's suggest higher damping (no "sharp peaks"). In terms of frequency ranges (e.g. $\omega \simeq 18$-25, at $u = 1$), agreement is always very good. In the Tangential direction, experimental PSD's indicate (even at $u = 1$) less sharply peaked power distributions, which is to be expected from the previous theoretical comparisons of Fig. 109. Frequency ranges compare very well, as did those in Fig. 109. Experimental and theoretical coherence functions compare very poorly in the R-R case, but reasonably well in the T-T case, as seen in Figs. 112b, 112d, and 112f). Note that in the latter case, there is nevertheless an obvious discrepancy, namely the double peaked coherence (e.g., at $\omega \simeq 21$-26 for $u = 1$, Fig. 112b) found in theory do not repeat experimentally. The reason for the above poor coherence comparisons may be inferred from phase results: the usual good correspondence between experimental and theoretical phases (neglecting regions of low coherence) is also present here, indicating that the inter-cylinder coupling modes are indeed detected in the measurements; more gradual phase changes, together with less "peaked" PSD's and coherences, in the experiments, suggest much higher damping than predicted in theory, which can explain the

poor match of coherences and "flatter" PSD's (see Figs. 42a and 42b for effect of varying c and c_f, on coherences).

This (diagonal offset) system will provide mostly experimental data for comparisons with the previous central and parallel offset systems, in the Chapter to follow, although we have had some reinforcing evidence that theoretical results for offset combination (Rigid-Flexible cylinders) systems are meaningfull, except for a strong underestimation of damping (or possibly other causes such as nonlinearities, etc.).

Having reviewed all systems, we may now proceed to the last Chapter, "Discussion and Conclusions".

5. DISCUSSION AND CONCLUSIONS

This last Chapter is structured as follows.

Part 1 will consist of comparisons between different types of systems, to investigate effects of varying selected system parameters, for example varying the inter-cylinder spacing G_c. This shall include the discussion of inter-cylinder fluid coupling, as the relevant systems are examined.

Part 2 shall review and discuss discrepancies between theory and experiments, and propose explanations where possible.

Part 3 will discuss characteristics that are common to both experiments and theory: for example, the lowering of frequencies with increasing flow velocity; this will form a set of what may be termed major system characteristics. Finally, overall conclusions and recommendations for future research shall be provided.

5.1: INTER-SYSTEM COMPARISONS

In this Section, the effect of varying selected system parameters will be examined so as to establish major system characteristics, and investigate inter-cylinder fluid coupling. Note that power levels will be discussed separately later, in Section 5.2. The first comparison deals with the effect of inter-cylinder spacing.

5.1-1: Effect of G_c

Inter-cylinder spacing was tested on the K = 4, 4F bundle, and involves data of Sections 4.3-1 ($G_c = 0.75$), 4.3-4 ($G_c = 1.00$), and 4.3-5 ($G_c = 1.50$); the latter data is for position pair 1,3. The interpretation of the effect of G_c is intimately linked to the understanding of inter-cylinder coupling modes, hence, for this K = 4 case, data for the position pair 1,2 (Section 4.3-3, for $G_c = 0.75$) is also important. Because theoretical computations were found to be in agreement with measured data, and since the former are much easier to "read", they have been utilized to deduce basic system characteristics. The theoretical behaviour of the system is illustrated in Fig. 113, at u = 3, for both the Radial and Tangential directions, and for the values of G_c of 0.75, 1.00, and 1.50. The dominant effect is that of a nar-

rowing of the bandwidth with increasing G_c, i.e. the frequencies corresponding to the mean flow cross-sectional coupling modes depicted in Fig. 26 are closer to one another. The frequencies corresponding to repeated (mean flow roots) tend to remain constant, in both the Radial and Tangential directions, with $\omega \simeq 23$ and 21 respectively, in Fig. 113, and other frequencies about those values move in, fastest where differences are greatest; for example, the lowest Radial frequency ($\omega \simeq 16$ at $G_c = 0.75$) moves in the fastest. This behaviour is also similar in the second mode group, and furthermore is found at all flow velocities, as shown in Figs. 114a and 114b (u = 1, 3, and 5). It should be noted that a coupling mode is considered dominant when we have a local maximum in coherent power, the latter being the product of the PSD of interest (e.g. Radial) and the corresponding coherence function; the latter is found to peak smoothly at frequencies very close to those of the PSD's (maxima), which themselves usually peak sharply; consequently, the frequency values corresponding to given coupling modes are determined from the PSD's (to avoid having to compute coherent power, which from the foregoing argument, peaks at basically the same frequency).

Note that, in general, mean-flow-model repeated frequencies do not necessarily exist (for example, not found in the K = 2 case), and are not proven to have values which are relatively insensitive to variations in G_c (slight variations may be seen, in the Tangential direction [highest peak] - see Fig. 114b). Rather, the reasons for system characteristics will be interpreted physically, and the resulting "rules" shall allow general conclusions to be drawn. First, the random vibration model cross-sectional coupling modes will be investigated by inspecting coherence and phase plots, at u = 3, for Radial and Tangential directions; in Figs. 115a and 115b, data for position pair 1,3, and $G_c = 0.75$, 1.00, and 1.50, is depicted; in Figs. 116a and 116b, data is shown for position pair 1,3 versus pair 1,2, for $G_c = 0.75$. Coupling modes are determined as follows: for example, the (random model) coupling mode, in the Radial direction at $\omega \simeq 23$ and $G_c = 0.75$, has a phase of 180° for both pairs 1,3 and 1,2 (Fig. 116a), which indeed agrees* with

---

* Recall the convention for measurement and computation (theory) directions: Radial positive outward and Tangential positive counterclockwise (Fig. 30).

the mean flow model mode depicted in Fig. 26 (ω_5, ω_6). We have additional information from the random model data, which indicates that (Radial direction) cylinder motion of pairs 1,3 and 2,4 are essentially independent of one another: this is because the pair 1,2 coherence is basically zero at the frequency of interest ($\omega \simeq 23$). Note that other coupling modes involve all four cylinders simultaneously, for example the Radial mode at the lowest frequency ($\omega \simeq 15$ [$G_c = 0.75$], in Fig. 116a), where phases are 0° and coherences basically unity (see Fig. 26, the ω_1 mode). We may now infer why the $\omega \simeq 23$ frequency is relatively unchanging with inter-cylinder spacing: cylinders 1,2 move in unison, with the result that the added mass due to "surrounding fluid" is very insensitive to the spacing of those cylinders, the "entrained fluid mass" being relatively constant. We also note that the total added mass is about twice that for an unconfined single cylinder, which is why the dominant frequency for that particular coupling mode is very close to the one for a single cylinder.

A similar situation is seen to occur in the Tangential direction, at $\omega \simeq 21$ ($G_c = 0.75$, $u = 3$, see Fig. 116b): pairs 1,3 and 2,4 move essentially independently of one another, and each pair again moves in unison (see the "ω_3, ω_4" case, in Fig. 26), and the fluid "entrained" by both cylinders is about twice that for a single cylinder.

Furthermore, R-T coherences and phases for position pairs 1,3 and 1,2, see Fig. 117, reveals an interesting additional (random model) feature: in the frequency range ($\omega \simeq 20$-25) were both Positions 1,2 R-R and T-T coherences vanish, we find some coherence between the Radial and Tangential directions, for position pair 1,2. Note that, by symmetry, we cannot have any R-T coherence between positions 1 and 3. The phases (0° and 180°) corresponding to the two "peaks" (Fig. 117), indicate that both the "ω_3, ω_4" and "ω_5, ω_6" modes of Fig. 26 exist simultaneously; note that this indication, together with the $G_c = 0.75$ PSD's of Fig. 113, point to a gradual change from a Tangential direction dominated "dual" (Radial-Tangential) mode to one that is Radially dominated (as frequency goes from $\omega \simeq 21$ to $\omega \simeq 23$).

Conversely, in a coupling mode such as the lowest frequency Radial (see ω_1 in Fig. 26), cylinders move in opposite directions, with the result that proximity significantly increase the influence of motion of one cylinder on that of the (three) others, "entrained" fluid regions opposing each other. It should be noted that G_c does not alter the coupling modes themselves, but predominantly their corresponding dominant frequencies. Another "type" of situation may be illustrated using a Tangential direction coupling mode: at $u = 3$, and $G_c = 0.75$, Fig. 116b reveals that ($\omega \simeq 28$) all four cylinders execute a twisting motion (see Fig. 26, the ω_8 case) - the corresponding higher (than single cylinder) frequency can be explained by the fact that "entrained" fluid is common to all cylinders, i.e. reducing the effective added mass on each cylinder, to a value below that for a single cylinder.

In terms of dominant frequencies, Figs. 115a and 115b indicate a trend similar to that found for the PSD's.

It should be noted that the random model predicts simultaneous motion in Radial and Tangential directions at all frequencies, that is, a dominant R-R coupling mode does not preclude T-T modes at the given frequency, and vice versa: for example, the $G_c = 0.75$, $u = 3$ data, at $\omega \simeq 15$, shown in Fig. 116a, is a dominant R-R mode which coexists with a T-T mode, shown (at $\omega \simeq 15$) in Fig. 116b (position pair 1,2).

As would be expected, as inter-cylinder spacing is increased beyond certain values, the cylinders may be considered to behave independently, as individual single cylinders. This effect is depicted, in theory, in Figs. 118 (PSD's), 119a and 119b (coherences and phases), where data is for $G_c =$ 1.00, 1.50, 2.00, and 2.50: both Radial and Tangential direction PSD's converge with increasing G_c to that of a single cylinder (see Figs. 71a, 71b), and coherences tend to zero (although not as quickly as PSD's would suggest).

We may generalize the above theoretical results in a few rules: with increasing G_c, in a given mode group, in an arbitrary direction (e.g. Radial), as follows.

(1) The frequency band remains centered on a constant "center" frequency, corresponding to that of a single cylinder.

(2) The frequency bandwidth is progressively decreased, resulting in gradual coalescing of various frequencies, until in the limit, only the single cylinder PSD remains.

(3) The cross-sectional coupling modes remain unchanged, and the coherence function decreases, eventually reaching zero in the limiting case.

Typical experimental data is shown in Figs. 120a and 120b for PSD's, and Figs. 121a and 121b for coherences and phases; behaviour is essentially the same as predicted in theory and as summarized in the foregoing.

5.1-2: Effect of K

As was the case for the effect of G_c (Section 5.1-1 above), agreement between theory and experiments was found to be good enough to warrant using (more easily interpreted) theoretical results, for discussing the effect of K (the number of cylinders in an all-flexible bundle).

Theoretical Radial and Tangential direction PSD's, at $u = 3$, are illustrated in Fig. 122, for $K = 1$, 2, 4, and 12*. The $K > 1$ systems have a G_c of 0.75. We recall that a total of 2K "peaks" are expected for a K flexible§ cylinder cluster, unless (mean flow model) repeated frequencies are present; note that the 2K total occurs in any two orthogonal measurement directions, e.g. Radial and Tangential, as utilized for $K = 4$ (in which case there were six distinct frequencies, with two mutually exclusive sets of three in the Radial and Tangential directions, and two "repeated" frequencies). These individual dominant frequencies are easily seen in Fig. 122, namely (i) for $K = 1$, one independent and one repeated (resulting in a single frequency, for both the Radial and Tangential directions), (ii) for $K = 2$, four independent, with two in each direction, (iii) for $K = 4$, six independent, with three in

---

* Position 1 in the cluster; other Positions are similar.

§ Or more correctly, "equally flexible".

each direction, and two "repeated" frequencies, as described above, and (iv) for K = 12, a not easily counted series of "peaks" (a mix of distinct and repeated frequencies).

Based on the discussion of fluid coupling in Section 5.1-1 above, we may presume that some "in unison" coupling modes will result in frequencies close to that of a single cylinder, some "in opposition" modes generating lower frequencies, and some "common entrained fluid" resulting in higher frequencies. This, together with the evidence of Fig. 122, suggest that K > 1 systems will manifest some dominant frequencies both above and below that of the K = 1 (single cylinder) system.

Theory predicts that the effect of varying K is basically flow independent, for the K = 1, 2, and 4* systems shown in Figs. 123a (Radial direction) and 123b (Tangential direction), for u = 1, 3, and 5. Note that the second mode group behaves in a fashion similar to that of the first group. It is important to note that increasing the number of cylinders (K) does destabilize the system: this is obvious from Figs. 123a and 123b, where PSD shifts toward a zero frequency is much faster for the K = 4 system than the other two (and the K = 12 system is already divergent at u = 5), and faster for the K = 2 than the K = 1 one (this latter may be seen by observing the increasing difference between the single cylinder "peak", and the lowest Radial and Tangential "peaks" of the two-cylinder system, as flow velocity goes up.

In summary, we may state that increasing K will increase the number of dominant frequencies, while broadening the corresponding bandwidth, "about" the single cylinder frequency; the latter appears to occur faster at the low end (e.g., in Fig. 122, the difference between the K = 1 frequency and the lowest dominant K = 12 value [$\omega \simeq 23$ and 15] is larger than the difference between the K = 12 highest dominant frequency and that for the K = 1 [$\omega \simeq 27$ and 23]. As evidenced by data in Figs. 122 and 123a, an increase in K also severely destabilizes the system, the lowest dominant frequencies

---

* The K = 12 system is already divergent at u = 5, hence was not included in the Figure.

for larger (K) systems reaching zero much faster; however, it should be kept in mind that experimental high velocity PSD's exhibit power distributions that basically match those in theory, only in terms of frequency bands and to a much lesser extent, in terms of shapes; for example, the $K = 4$, $G_c = 0.75$, 4F Radial PSD's, in Fig. 35a (theoretical data is the same, in the latter Figure and in Fig. 123a). Nevertheless, in spite of PSD shape differences, theory and experiments still agree fairly closely in terms of critical flow velocities, which makes the above conclusion about destabilization essentially correct.

Note that, should fluid coupling be absent, each cylinder in a bundle would "behave" as a single cylinder (neglecting the effect of adjacent cylinders on the flow field characteristics).

The available experimental evidence supports the foregoing theoretical conclusions, as shown in Figs. 124a and 124b. Note that the $K = 2$ data is for the larger value of $G_c = 1.89$; the corresponding $G_c = 0.75$ system would have broader PSD's, because of the closer spacing.

5.1-3: Effect of neighbouring rigid cylinders

A third variant (other than inter-cylinder spacing G_c, and the number of cylinders K) was utilized to study fluid coupling, namely the substitution of some of the flexible cylinders in the "Reference" $K = 4$, $G_c = 0.75$, 4F cluster, by essentially rigid ones: we recall that the systems tested were (i) 1F(1)/3R(2,3,4), i.e. three flexible cylinders replaced by rigid ones, (ii) 2F(1,3)/2R(2,4), where two diagonal flexible cylinders have been replaced by rigid ones, and (iii) 2F(1,2)/2R(3,4), which is similar to the previous case, but where adjacent cylinders have been changed.

The effect of surrounding the "Reference" system by rigid cylinders was also studied, namely the 4F(1,2,3,4)/24R(rest) system; finally, tunnel flow field symmetry was investigated by testing variants of the latter system: a 4F(6,7,1,2)/24R(rest) parallel offset system, and a 4F(5,6,1,16)/24R(rest) diagonal offset system.

5.1-3a: 1F(1)/3R(2,3,4) and related cases

In addition to making comparisons between the K = 4, 4F and K = 4, 1F(1)/3R(2,3,4) systems (both with $G_c = 0.75$), results for the K = 1, 1F system will also be used. Fig. 125 depicts theoretical Radial and Tangential PSD's, at u = 3, for the three types of systems, and Fig. 126 is the corresponding experimental data (where damping is seen to be higher): the similarity between the 1F and 1F/3R systems is obvious, signifying that the substitution of three flexible cylinders by rigid ones virtually eliminates any "coupling" effect that was present when all cylinders were flexible. However, the three rigid cylinders do increase the added mass of the flexible one, the result of which is a slightly lower dominant frequency for the latter cylinder, as compared to that of a single (flexible) cylinder.

Note that the pressure excitation PSD used for theoretical computations was the "K = 0" one, for all cases in Fig. 125; this is of course only an approximation, as we expect the flow field to be affected, if only by the presence (motion itself could also change the excitation field) of one or more adjacent cylinders. The relative power levels, between systems, is not as different in theory (Fig. 125) as in the experiments (Fig. 126), and we see clearly (experimentally) that the presence of three rigid cylinders, in the 1F/3R case, has resulted in an increase of the response, relative to the 1F case (see the BLUE and RED traces, in Fig. 126). Power level considerations will be discussed shortly.

We continue with an examination of the first 2F/2R system.

5.1-3b: 2F(1,3)/2R(2,4) and related cases

Again, three types of systems will be compared, namely two K = 4 systems, the 2F(1,3)/2R(2,4) and the 4F systems, and the K = 2, 2F system. As before, since theory and experiments compared well in Chapter 4, we shall analyze the various effects by inspecting theoretical data first; Radial and Tangential PSD's are illustrated in Fig. 127, for u = 3, and for the three systems described above. The RED traces apply to the K = 2, 2F system ($G_c = 1.89$); if two more (diagonal) cylinders are added, we obtain the K = 4, 4F ($G_c = 0.75$) system, shown as GREEN traces in the Figure, and if the added cylinders

are made rigid, we obtain the 2F(1,3)/2R(2,4) ($G_c = 0.75$) system, plotted in BLUE. We wish to examine coupling modes, in addition to the latter PSD's; Figs. 128a and 128b depict theoretical coherences and phases for the above three systems, at $u = 3$, in both the Radial and Tangential directions, for position pairs 1,3 (pair 1,2 data for the 4F case is shown in Figs. 116a and 116b).

The 2F inter-cylinder coupling modes are first inferred; there are four distinct dominant frequencies, namely $\omega \simeq 21.2$ (T-T), 21.6 (R-R), 23.4 (R-R), and 23.8 (T-T), associated to phase angles of 180°, 0°, 180°, and 0° respectively. The coupling modes are shown in part (a) of Fig. 129. The corresponding coupling modes for the 2F(1,3)/2R(2,4) system is, at $\omega \simeq 19.9$, 20.8, 22.6, and 23.3, 0° (R-R), 180° (T-T), 0° (T-T), and 180° (R-R); we note that frequency shifts, due to the presence of the diagonal rigid cylinders, have occurred, as may be seen in Fig. 129: the frequency sequence has now changed to ω_2, ω_1, ω_4, and ω_3 (part (b)). In a similar way, the coupling modes for the $K = 4$, 4F case are obtained and shown in part (c) of Fig. 129; the dominant frequencies are $\omega_1 \simeq 15.8$, $\omega_2 \simeq 18.9$, $\omega_3 = \omega_4 \simeq 20.8$, $\omega_5 = \omega_6 \simeq 23.2$, $\omega_7 \simeq 25.8$, and $\omega_8 \simeq 27.7$. The corresponding modes, between systems, are shown in each of the four columns in Fig. 129. Note that eight 4F coupling modes have been shown (rather than the six depicted in Fig. 26); this format was utilized to illustrate two "additional" coupling modes that may be obtained by symmetry, simply by mirror imaging on a diagonal line,* the modes corresponding to the mean flow repeated frequencies, namely the first and third columns of part (c) of Fig. 129. We proceed by comparing frequencies of each of the three systems shown in Fig. 129, columnwise:

	System dominant frequency		
Column	2F	2F/2R	4F
1	21.2	20.8	20.8
2	21.6	19.9	15.8, 25.8
3	23.4	23.3	23.2
4	23.8	22.6	18.9, 27.7

* These modes simply correspond to the original ones, after having been rotated 90°, clockwise (column 1) and counterclockwise (column 3).

We first examine the coupling modes of column 1, that is the first (T-T) mode of the 2F system, and the corresponding ones of the other two systems (2F/2R and 4F): going from the 2F to the 2F/2R system, we see only a slight lowering of the dominant frequency (from $\omega \simeq 21.2$ to $\omega \simeq 20.8$), due to the presence of the additional two rigid cylinders - the "entrained fluid" mass is relatively constant, as the rigid cylinders are not directly in its "path". Furthermore, we find the 2F/2R and 4F systems to possess basically equal dominant frequencies (20.8); having made the two additional cylinders rigid has altered the dynamics very little, i.e. the cylinders in positions 2 and 4 are "seen" by those in positions 1 and 3, almost as if they were rigid, each pair moving at right angle with respect to the other (note that in the theoretical model, boundary conditions are imposed at the position of rest of cylinders - motion amplitudes have no effect on system dynamics). Note that Tangential direction forces on, say Position 1 cylinder, due to potential flow induced pressure changes from Tangential motion of Position 4 cylinder, would be cancelled by motion of Position 2 cylinder; the reason why the 4F dominant frequency is slightly higher than the 2F/2R one (see Fig. 128b, at $\omega \simeq 20.8$) is found in Fig. 117: there is some coherence between the Radial direction motion of Position 1 cylinder in the Radial direction and Position 2 cylinder in the Tangential direction which, by symmetry, implies the converse. The phase is 180°, i.e., referring to part (c) of Fig. 129, while cylinder 1 moves tangentially "counterclockwise", cylinder 2 has a (non-dominant) motion in the opposite direction, i.e. radially inward (and similarly for the other cylinders).

A very analogous situation is found in column 3 (see the above table), i.e. in relation to the "in unison" Radial direction motion of cylinders; this includes some R-T coherence, in the 4F case (see Fig. 117).*

The modes illustrated in columns 2 and 4 of Fig. 129 involve cylinders moving "in opposition", rather than "in unison" as was the case for columns 1 and 3 above. Comparing the 2F and 2F/2R cases, in column 2, reveals

---

* Radial and Tangential direction motions still oppose each other, and the 0° phase (instead of the former 180°) stems from direction conventions).

some reduction in frequency with the addition of two rigid cylinders, specifically from $\omega \simeq 21.6$ (2F) to $\omega \simeq 19.9$ (2F/2R); the presence of the two rigid cylinders in the latter case, results in a change in "cross-sectional flow pattern", where outward/inward motion of the two flexible cylinders require fluid to flow inward/outward, through interstitial gaps between cylinders - this increases the added mass seen by the moving cylinders. Inspection of the two 4F coupling modes (column 2) and their corresponding dominant frequencies ($\omega \simeq 15.8$ and 25.8), indicate an increase (four cylinders instead of two moving in phase) and a decrease respectively, of that "choking" effect.

The Tangential direction modes of column 4 are very similar to those of column 2, and need not be discussed.

Experimental data is behaved basically as predicted in theory: typical $u = 3$ data is shown in Fig. 130 (PSD's) and Figs. 131a and 131b (coherences and phases); so, the foregoing analysis is supported by experiment.

The previous qualitative explanations shall be reinforced by a similar review of inter-cylinder coupling modes for "adjacent" pairs.

5.1-3c: 2F(1,2)/2R(3,4) and related cases

In Section 5.1-3b above, our attention was focused on cylinder Positions 1 and 3 ("diagonal" pair); we now supplement that data with results for Position pair 1,2 ("adjacent" cylinders), namely the 2F(1,2)/2R(3,4) case. The latter system shall be compared to the 4F one.

Theoretical data will again be presented first, starting with Radial and Tangential direction PSD's, shown in Fig. 132, for the 4F (RED traces) and 2F(1,2)/2R(3,4) (GREEN traces) systems (at $u = 3$). Inter-cylinder coupling modes may be obtained from the usual coherence and phase plots: Figs. 133a (R-R) and 133b (T-T) depict that data, for the two systems of interest (at $u = 3$). We recall that the data for the 4F system pair 1,2, necessary to

fully determine coupling modes,* is shown in Figs. 116a and 116b. The corresponding cross-sectional coupling modes are illustrated in Fig. 134, and dominant frequencies are $\omega_1 \simeq 19.0$, $\omega_2 \simeq 19.9$, $\omega_3 \simeq 23.8$, and $\omega_4 \simeq 24.5$, for the 2F/2R system, and (as listed in the previous Section), $\omega_1 \simeq 15.8$, $\omega_2 \simeq 18.9$, $\omega_3 = \omega_4 \simeq 20.8$, $\omega_5 = \omega_6 \simeq 23.2$, $\omega_7 \simeq 25.8$, and $\omega_8 \simeq 27.7$, for the 4F system. Note that the 4F modes depicted in Figs. 134 and 129 are the same, but they are not plotted in the same order (since comparisons are to different systems).

Following the format used in the previous Section, we tabulate frequencies, columnwise.

	System dominant frequency	
Column	2F/2R	4F
1	19.0	15.8, 23.2
2	19.9	20.8, 18.9
3	23.8	20.8, 27.7
4	24.5	25.8, 23.2

In the light of the discussion on fluid coupling in Section 5.1-3b above, it shall not prove necessary to discuss data of Fig. 134 in detail. Suffice it to say that, when the two (adjacent) rigid cylinders of the 2F/2R system are replaced by flexible ones, the resulting (4F system) frequency will be lower or higher than the 2F/2R one, depending on whether the (replacement) flexible cylinders tend to "displace" fluid in the same or in the opposite direction to the original (flexible) cylinders; for example, in column 1 (Fig. 134), the 4F coupling mode at ω_1 has cylinders in positions 3 and 4 moving "in opposition" to those in positions 1 and 2, thereby lowering the dominant frequency associated with that mode, whereas the reverse occurs with the "ω_5-ω_6" coupling mode (frequency increases). This behaviour confirms the interpretation given in Section 5.1-3b.

Experimental data follows theoretically predicted trends, as seen in Fig. 135 (PSD's) and Figs. 136a and 136b (coherences and phases).

---

* Done in the previous Section (see Fig. 129).

5.1-3d: 4F(1,2,3,4)/24R(rest) and related cases

Two sets of comparisons shall be effected here: (i) the 4F(1,2,3,4)/24R and the [K = 4] 4F(1,2,3,4) systems, and (ii) the three K = 28 systems, i.e. 4F(1,2,3,4)/24R, 4F(6,7,1,2)/24R, and 4F(5,6,1,16)/24R systems. The usual u = 3.0 flow velocity used for comparisons is now too close to the experimental critical velocity (close to 4.0); hence, data at u = 1.0 will be utilized instead, for all 4F/24R cases.

Recall that to minimize computer time requirements, all 4F/24R theoretical calculations were effected with N = 2 (comparison functions), making these results valid only for the first mode group (see Section 4.3-1c); therefore, (theoretical) PSD plots do not illustrate the second mode group.

(a) K = 28 versus K = 4, with 4F(1,2,3,4)

We wish to investigate the effect of "surrounding" the four Flexible cylinders, in the 4F case, by Rigid cylinders, i.e. the 4F/24R case. Theory is again used to discuss trends (since good agreement with experiments* has previously been found). Radial and Tangential PSD's, at u = 1, are depicted in Fig. 137. As is expected from single cylinder results (Section 5.1-3a), we observe a general lowering of frequencies, when Rigid cylinders are present (GREEN traces). We also note that, relative to the Tangential direction, there is an increase in Radial direction power, specifically at $\omega \simeq 22.3$ (GREEN trace); the corresponding power in the 4F system was "negligible", as seen at $\omega \simeq 23.9$ (RED trace).§ A similar situation exists for the Tangential direction power (relative to the Radial one), at $\omega \simeq 24.8$ (GREEN trace), corresponding to the (previously negligible) 4F system power at $\omega \simeq 26.3$ (RED trace§). Coherences and phases for both systems are illustrated, for u = 1, for the R-R and T-T cases and for both Position pairs 1,3 and 1,2, in Figs. 138a, 138b, 138c, and 138d, and furthermore, the R-T data for Position pairs 1,3 and 1,2 is shown in Fig. 139. The 4F/24R dominant inter-cylinder coupling

---

* At least at low flow velocities.

§ Barely visible at u = 1; see Fig. 35 for PSD's at u = 3, and 5.

modes are the same as those illustrated in Fig. 26, except that "$\omega_5 = \omega_6$" modes are now also significant at "$\omega_3 = \omega_4$" and vice versa.*

We may conclude that, theoretically, the presence of the neighbouring rigid cylinders has not only depressed frequencies (as occurs in the case of the single cylinder), but has also brought about some alteration of the system transfer function matrix (see eqn. 2.157), since the (relatively flat) excitation pressure power yields different characteristic responses (see Fig. 137). It should be noted that the pressure PSD's used for computation of the theoretical responses is not the same, in the 4F and 4F/24R cases, being the so-called K = 0 PSD's (see Figs. 20a and 22a) and K = 28 PSD's (see Figs. 21a and 23) respectively; this mostly accounts for the power level differences found in Fig. 137 (note separate PSD scales). Inter-cylinder coupling modes are identical, except that associated powers (PSD's) may differ (due to the changes in transfer function matrix).

These effects have been observed experimentally, but with some exceptions; we shall examine the measured data in some detail, to verify to what extent the theory is supported experimentally. The theoretically predicted lowering of frequencies (with the presence of surrounding Rigid cylinders) is indeed observed in measurements: a comparison of Figs. 137 (theory) and 140 (experiments) reveals much similarity in terms of frequency shifting; the Radial frequency downward shift occurs mostly at the high end, whereas the reverse is true for the Tangential direction. In terms of coherence and phase, u = 1 measurements for Position pair 1,3,§ for the R-R and T-T cases, shown in Figs. 141a and 141b, exhibit frequency shifts much like those predicted in theory: for example, the Fig. 141a R-R downward shift of the 0°-180°-0° phase sequence, from 22.0, 27.0 (RED trace) to 20.9, 26.2 (GREEN trace), and the Fig. 141b T-T low end (0°-180°) downward shift of the 0°-180°-0° phase sequence, from 22.2 to 21.3. Unfortunately, experimental phase sequences, which have compared very well for other systems (K < 28),

---

* These theoretical modes do exist in the 4F case, except that the associated power is relatively low.

§ Measurements for Position pair 1,2 were never made.

do so only to a limited extent here, as was previously discussed (Section 4.3-13b). Nevertheless, we may state that downward frequency shifts are present in the measurements, supporting the theory.

Note that second mode group comparisons are not made, as theoretical computations were effected with $N = 2$.

We recall that another theoretically predicted effect of the presence of Rigid surrounding cylinders is an increase, at specific frequencies, of Radial (relative to Tangential) power, and vice versa: the (theoretical) frequencies $\omega \simeq 22.3$ (Radial) and $\omega \simeq 24.8$ (Tangential), and with corresponding new "peaks" may be seen in Fig. 137 (GREEN traces); this effect was experimentally found, with certainty, only in the Radial direction, as seen at $\omega \simeq 21.9$, in Fig. 140 (GREEN trace), and moreover with the correct corresponding phase and similar coherence (see Fig. 138a for theory and 141a for experiment). Note that there is some indication that the Tangential direction data exhibits a relative increase in power: this can be seen in Fig. 93b (RED trace, at top, at $\omega \simeq 24.7$), where a slight inflection in the PSD exists; again, the corresponding phase corresponds to the theoretical one (Figs. 141b and 138b). Hence, experimental evidence does provide some support for the theory, in this latter respect.

In summary, there is only limited experimental evidence to support the theoretical effects of surrounding four Flexible cylinders by Rigid ones, although it must be stressed that some of these effects are quite small (e.g. relative increase of Radial power), and their very detection could be said to be surprising in the first place. The latter results provide some support as well as casting some doubt, in terms of the soundness of the theoretical model, and/or the correctness of the pressure PSD's and pressure correlations used. Discussion of discrepancies shall be deferred to Section 5.2.

(b) Three K = 28 systems

Experimental PSD's for the 4F(1,2,3,4)/24R (central), 4F(6,7,1,2)/24R (parallel offset), and 4F(5,6,1,16)/24R (diagonal offset) systems, will be compared, in an attempt to establish the uniformity of the test tunnel characteristics. Differences* may be attributed to one or a combination of two causes, both related to the 4F location of the cylinders within the 24R ones: (i) inherent differences between systems, which will be evaluated from theoretical data, and (ii) differences due to non-uniformity in the flow field within the test tunnel.

The common (to all three systems) cylinder Position 1 shall be examined. In theory, the first of the above causes proves to be negligible, as seen in Figs. 100 and 109, that is, in spite of the existence of inter-cylinder fluid coupling (which is to adjacent cylinders possessing slightly different PSD's, depending on which of the three systems we are looking at), the PSD's (Radial and Tangential) of the cylinder in Position 1 remains basically the the same. Note that this can be explained by the fact that the immediate surrounding of Position 1 cylinders is the same in all systems, namely five Rigid cylinders and three Flexible ones (e.g., in the central case, Positions 7,6,5,16,15 and 4,3,2 respectively - see Fig. 29), where the surroundings of the other three cylinders themselves is not radically different from one system to another.

Measured Radial and Tangential direction PSD's, for the cylinder in Position 1, are depicted in Figs. 142a and 142b respectively, for u = 1, 3, and 4: except for the Radial direction, at u = 4, PSD's have basically the same bandwidths, but with some differences in PSD shapes; this author can think of only one explanation for this, namely test channel flow asymmetries, which would alter the response of "off-central" (i.e. not Positions 1 to 4 incl.) cylinders, affecting Position 1 through fluid coupling. However, experimental data contradicts this, as follows: the "off-center" responses (PSD's), coupled with their corresponding coherences, result in

---

* Other than experimental error, assumed negligible since repeatability was found to be very good.

even less influence on Position 1 cylinder(s) than theoretically predicted (with the latter resulting in almost equal PSD's, as discussed above). This is because the experimental PSD's are less "peaked" than their theoretical counterparts (see Figs. 102 and 111), and their corresponding (measured) coherences are usually lower than in theory (see Figs. 103 and 112). At this stage, it has to be said that the PSD shape differences found in the three 4F/24R systems remain unexplained.

Power levels tend to be lowest in the central sub-bundle case; this suggests that the bulk flow velocity in the central portion of the tunnel is not higher than that at the "periphery", implying a fairly even velocity distribution in the test channel. This is not unexpected, given the regularity and density of cylinders in K = 28 clusters (see Fig. 29).

Discrepancies between theory and experiments are discussed next.

5.2: EXPERIMENTS & THEORY, DISCREPANCIES

We proceed with a discussion of discrepancies between measurements and theoretical computations. We shall deal with (i) PSD levels (powers), (ii) PSD shapes (power distributions), (iii) dominant frequencies, (iv) phases, and (v) coherence functions, in that order.

5.2-1: PSD levels

The greatest discrepancy between theory and experiments lies with power levels; for example, for the "Reference" system ($K = 4$, $G_c = 0.75$, 4F), the ratios of theoretical to experimental scales are approximately 24* ($u = 1$), 13 ($u = 3$), and 27 ($u = 5$) respectively, as seen in Fig. 35 (a, b); this corresponds to rms amplitudes about five times higher in theory than in experiments. As tabulated below, we see that the (theoretical/experimental) scale ratios do not, in general, vary significantly with the system tested (note that all theoretical computations for these systems were effected using the $K = 0$ pressure PSD's), but do vary with the mode group.

			First mode group scale ratios, at			Second mode group scale ratios,§ at		
K	G_c	System	u = 1	3	5	1	3	5
4	0.75	4F	24	13	27	19	8	13
4	1.00	4F	40	13	27	21	9	11
4	1.50	4F	32	13	27	21	8	11
2	1.89	2F	32	11	20	16	8	8
1	-	1F	31	13	31	13	8	7
4	0.75	1F(1)/3R	25	13	33	16	5	5
4	0.75	2F(1,3)/2R	32	15	27	21	9	12
4	0.75	2F(1,2)/2R	32	15	27	21	9	12

Scale ratios for the systems utilizing $K = 28$ pressure PSD's are as follows:

			First mode group scale ratios, at			Second mode group scale ratios
K	G_c	System	u = 1	3	4	
28	0.75	4F(1,2,3,4)/24R	200	120	53	Not available: theoretical data for N = 2 only.
28	0.75	4F(6,7,1,2)/24R	150	43	25	
28	0.75	4F(5,6,1,16)/24R	180	42	10 (u = 5)	

* Equal to 1.2/0.05.

§ Experimental second beam mode integrated powers were corrected by the factor $1/(0.563)^2$ - see eqn. (3.1).

Scale ratio changes are the greatest for (i) $K \neq 28$ versus $K = 28$ systems (note that different pressure PSD's are used for the two categories of systems), (ii) the second versus the first mode group, and (iii) different flow velocities. To verify if some trend exists for the last item, data at $u = 0.5$, 1.5, 2.0, 2.5, 3.5, 4.0, and 4.5 is plotted in Figs. 143a to 143g inclusively, for the "Reference" system, and the corresponding scale ratios tabulated below, together with the previous data at $u = 1.0$, 3.0, and 5.0.

Mode group	u = 0.5	1.0	1.5	2.0	2.5	3.0	3.5	4.0	4.5	5.0
1	60	24	9	8	12	13	13	15	17	27
2	76	19	9	8	7	8	6	6	9	13

Similar data for the "central" $K = 28$ case follows, corresponding to Fig. 93 (a, b), and Figs. 144a to 144e inclusively.

Mode group	u = 0.5	1.0	1.5	2.0	2.5	3.0	3.5	4.0
1	55	200	240	330	200	120	80	53
2	Not available, theoretical data is for N = 2 only.							

The tabulated $K = 4$ and $K = 28$ scale ratios are shown in graphical form in Fig. 145. The two $K = 4$ mode groups behave in a very similar way, namely higher scale ratios at low and high flow velocities, with a "dip" in the mid-range. Interestingly, the behaviour for the $K = 28$ system in basically the reverse, and with greater variations (minimum to maximum).

5.2-1a: Excitation pressure characteristics

A general discussion of pressure excitation forces is in order at this point. Fig. 1 illustrates a typical four-cylinder bundle ($K = 4$, $G_c = 0.75$) in the test channel; a longitudinal view, representing schematically that system "hydraulic configuration" is shown to scale, in Fig. 146. We recall that flow is downward, with the two stage turbulator upstream. The ogives are fixed to streamlined fins (not shown here - see Fig. 13), and so are the lower supports, with the flexible cylinders mounted in between.

Strategic longitudinal points are marked in Fig. 146; they are (1) the region immediately downstream from the lower stage of the turbulator, (2)

the leading tip of the support ogives, (3) the top level of the flexible cylinders, (4) the level at which pressure PSD's were measured (basically at the mid-point of the cylinders), and (5) the bottom level of the flexible cylinders.

Level (1) corresponds to what may be termed upstream conditions, where flow has a relatively high level of turbulence and the velocity distribution is uniform (see Appendix L for details on turbulence characteristics, measured at level (4)). Level (2) is approximately where flow conditions start changing, due to the presence of the cluster, and level (3) represents "upstream" flow characteristics, as seen by the cylinders. Level (4) is where pressure (and turbulence - see Appendix L) data has been gathered, and also represents "mid-way" conditions as seen by the cylinders. Finally, level (5) corresponds to "downstream" flow conditions as seen by the cylinders.

Ideal test conditions would have required, as a minimum, very long (several hydraulic diameters) top support ogives, so that fully developed flow conditions could exist at level (3), resulting in pressure PSD's and CSD's which are independent of the longitudinal location (of measurement points, along the cylinders); practical limitations did not allow this, and tests had to be carried out under the "less than ideal" conditions, shown in Fig. 146.

The various parameters thought to influence excitation pressure characteristics (hence cylinder vibration) in the system depicted in Fig. 146, are the following: (i) fluid properties, namely density and viscosity, (ii) upstream flow characteristics, which may possibly be defined* by bulk velocity, velocity profile, and turbulence intensity and scale at level (1), (iii) the distances between levels (1), (2), (3), and (5), (iv) the channel diameter, and the geometry of the bundle (cylinder diameter, number [K], and positions in the channel); furthermore, (v) channel and cylinder surface roughness could be relevant, and of course so could be (vi) the very motion

---

* Assumed here; the listing of relevant system parameters is not necessarily exhaustive, but serve to illustrate the complexity of the problem.

of the cylinders. The latter two items will be ignored, for they would be amongst the last causes to ever be investigated, after other effects have either been ruled out or thoroughly understood.

Note that item (ii) has been included here, in spite of previous indications that upstream turbulence is not convected very deep in a bundle [53], because (a) the $K \neq 28$ bundles are sparsely populated, in the sense that the tunnel cross-section remains mostly free of cylinders (see Fig. 28), and (b) the original turbulator-free vibration experiments (none were performed with $K = 28$) yielded power levels about seven times lower than those with turbulator. It should be stressed that item (ii) is more likely to be negligible in the $K = 28$ cases, because of the smaller hydraulic diameter ($\simeq 2.8$ cm).

The above items alone cannot determine pressure PSD's and CSD's, as the latter should also be dependent on (a) the chosen cylinders ($K = 28$ bundles only, as other clusters of interest here have symmetry such that one cylinder is equivalent to another), and (b) the longitudinal and circumferential position of the chosen reference point(s) (PSD or CSD) on the cylinder(s). The pressure CSD may be written in general form as

$$S_{p_m p_n} = \text{function}\,([\text{items (i) to (iv) incl.}],(\xi_m,\theta_m),(\xi_n,\theta_n),m,n), \qquad (A)$$

where the first (reference) point has longitudinal and lateral coordinates (ξ_m,θ_m), on cylinder m, and the second point coordinates (ξ_n,θ_n), on cylinder n. Note that (A) includes the case $m = n$ (isolated cylinder).

With the condition of fully developed flow (sufficiently long top support ogives), form (A) may be written as

$$S_{p_m p_n} = \text{function}\,([\text{items (i) and (iv)}],u,\theta_m,\theta_n,\xi_n-\xi_m,m,n), \qquad (B)$$

where the pressure CSD no longer depends on upstream conditions (item (ii)) or on distances between levels (1), (2), (3), and (5) (see Fig. 146) (item (iii)), or on the absolute longitudinal location of measurement points; dependence is retained on (a) fluid properties, (b) system geometry, (c) angular position of measurement points, and (d) which cylinder pair is under consideration (m,n).

It should be noted that form (B) [developed flows] is still of considerable complexity, especially due to the dependency on system geometry and, to a lesser extent (because of the lower magnitude of correlations), on the chosen cylinder pair; it will prove sufficient to discuss the "Reference" K = 4 system and the "central" K = 28 one, for qualitative understanding of factors which influence PSD's and CSD's. Note that we may divide the latter spectral densities into three "categories": (i) PSD's, which are measured on a single cylinder, (ii) CSD's on a single cylinder (a function of longitudinal and lateral (angular) separation, and (iii) CSD's between a pair of cylinders (also a function of the cylinders chosen).

5.2-1b: K = 4 system (developed flows)

Even where m = n (correlations on one cylinder), we would generally retain a dependence on which cylinder, within a bundle, is chosen. In the case of either very small clusters or very large ones, symmetry conditions lead to some simplifications.

By inspection of Fig. 28 (K = 4), we see that because of symmetry, (a) the dependence on which cylinder is chosen dissapears,* i.e. form (B) reduces to

$$S_{p_m p_m} = \text{function}\ ([\text{items (i) and (iv)}], u, \theta_1, \theta_2, \xi_1 - \xi_2),$$

where (ξ_1, θ_1) and (ξ_2, θ_2) are two points selected on cylinder m (m = 1, 2, 3, or 4).

Another feature of this particular (K = 4) system is (b) a lateral symmetry about "diagonal" lines, such that if a family of (single cylinder) CSD's (i.e. a range of $[\xi_1 - \xi_2]$ and $[\theta_2 - \theta_1]$) were to be measured, e.g. for Position 1 cylinder, the range $\theta_1 = 45°$ to 225° would be sufficient to cover all possible cases. As an example, assume that m = 2, $\theta_1 = 90°$, $\theta_2 = 180°$, and $\xi_2 - \xi_1 = \Delta\xi$; the particular CSD, namely $S_{p_2 p_2}(u, 90°, 180°, \Delta\xi)$, is simply equal to $S_{p_1 p_1}(u, 90°, 0°, \Delta\xi)$. Note that, in this case, $\Delta\theta = 90°$ for cylinder 2, and -90° for cylinder 1. In general, for the K = 4 system, we may write

---

* Note the same situation would also arise when chosing a cylinder within a very large cluster.

$$S_{p_m p_m}(u,\theta_1,\theta_2,\Delta\xi) = S_{p_1 p_1}(u,f_1(\theta_1),f_2(\theta_2-\theta_1),\Delta\xi)\ , \qquad m=2,3,4\ , \tag{C}$$

where f_1 and f_2 are simple functions to define equivalent angles. Note also that the PSD, namely $S_{p_m p_m}(u,\theta_1,\theta_1,0)$, has a "cycle" of 180°, with the previous range of $\theta_1 = 45°$ to 225°.

The CSD's on a selected cylinder in a bundle, that is form (C) above, would still require considerable amounts of data, as an interdependence between longitudinal and lateral coordinates is implied; hence, for each θ_1 selected, one would have to cover the full range of interest for $\Delta\xi$, for each value of θ_2 (i.e. $\Delta\theta$). Inter-cylinder CSD's are even more data intensive, in that some dependence is retained on which cylinder pair is chosen: with four cylinders, two types of choice are possible, namely adjacent or diagonal pair. For inter-cylinder CSD's, form (C) may be rewritten as

$$S_{p_m p_n}(u,\theta_1,\theta_2,\Delta\xi) = S_{p_1 p_{L(m,n)}}(u,h_1(\theta_1,m,n),h_2(\theta_2-\theta_1,m,n),\Delta\xi)\ , \qquad m,n=1,2,3,4\ , \tag{D}$$

where h_1 and h_2 are functions similar to f_1 and f_2, with the difference that equivalent angle selection also depends on m and n; L(m,n) is a logical (binary) function, to select either the adjacent or diagonal pair CSD, with the cylinder in Position 1 as reference (e.g. L(4,2) = 3, since 4,2 is a diagonal pair, equivalent to pair 1 (reference cylinder),3).

5.2-1c: Central K = 28 system (developed flows)

The "central" K = 28 system has different symmetry conditions than those of the K = 4 one. If we consider the central sub-cluster, that is Positions 1, 2, 3, and 4 in Fig. 29, and assume that conditions in the central portion of the channel are the ones for an "infinite" size cluster, then the following symmetry conditions will apply: (a) there is no dependence on the chosen cylinder, and the "cycle" of symmetry now spans only 45°* (versus 180° for the K = 4 case), with for example a range of $\theta_1 = 0°$ to 45°. As for the K = 4

---

* Preliminary results of recent tests, by L.R. Curling of the Fluid-Structure Interaction research group here at McGill, suggest such a behaviour.

case, one could obtain CSD's (and PSD's) for a given cylinder, from data on say the cylinder in Position 1 alone,

$$S_{p_m p_m}(u,\theta_1,\theta_2,\Delta\xi) = S_{p_1 p_1}(u,g_1(\theta_1),g_2(\theta_2 - \theta_1),\Delta\xi)\ , \qquad m = 2,3,4\ , \tag{E}$$

where g_1 and g_2 are functions similar to f_1 and f_2 in (C).

In both Sections 5.2-1b and 5.2-1c, in spite of reductions in the forms for PSD's and CSD's, the required data would nevertheless still be quite voluminous. Additional assumptions are necessary if further simplification of PSD and CSD expressions is desired. Bakewell [25], following Corcos' [28] model, assumed that longitudinal and lateral correlations were independent of each other, for flow inside a smooth pipe, which in terms of symmetry, is equivalent to an isolated cylinder (not part of a bundle, but in a "large" channel). For lack of data, Curling [61] used Bakewell's measurements, both for (a) single cylinders (in a cluster) PSD's and CSD's, and (b) inter-cylinder CSD's, where the concept of the "least fluid paths" was used for lateral correlations (see Section 2.5-2b), implying the following assumptions: (i) correlations measured for (low velocity) air flow in a pipe are applicable to (axial) water flow over an isolated cylinder, (ii) these correlations may be used for a single cylinder that is part of a bundle, and (iii) the "least fluid distance" scheme may be utilized to extend correlations to pairs of cylinders within a cluster.

As a set, the latter assumptions are most probably not justifiable, and even the present state of knowledge confirms this: as a simple example, PSD's for an isolated cylinder are measurement-angle independent (by symmetry), but such is not the case for a single cylinder within a bundle. The situation for CSD's has briefly been discussed above, and does also indicate the implausibility of these assumptions, especially (ii) and (iii). Finally, the much reduced form for CSD's, including inter-cylinder cases and PSD's (when $\Delta\xi = \Delta\theta = 0$), is

$$S_{p_m p_n}(u,\xi_1,\xi_2,\theta_1,\theta_2,\omega) = C_{long}(u,\Delta\xi,\omega) \cdot C_{lat}(u,\Delta\theta_{eq},\omega) \cdot S_{pp}(u,\omega)\ , \qquad m,n = 1,2,\ldots,2K\ , \tag{F}$$

where C_{long} and C_{lat} are normalized longitudinal and lateral correlations,

S_{pp} is a cylinder-wall PSD, and where $\Delta\theta_{eq}$ is used for cylinder pairs (see eqn. (2.242)).

Unfortunately, this is the best that could be done at this time, no other data being available; an intermediate measure was taken to slightly improve accuracy of theoretical computations, namely pressure PSD's were measured in situ, but at the channel wall, (a) in the cylinder-free channel (K = 0), reflecting "open space" excitation (i.e. the outer region of small bundles located at the center of the channel), and (b) in the fully populated channel, reflecting the excitation within K = 28 clusters and in the inner region of smaller bundles (i.e. in between cylinders).

We recall that so-called K = 0 pressure PSD's were used for all but K = 28 clusters, as input data for theoretical calculations, and K = 28 pressure PSD's for K = 28 bundles. Although a certain source of error, it seems unlikely to be the main cause of power scale ratios of up to about 300 (see Fig. 145). Nevertheless, this subject calls for some discussion, before turning our attention to CSD's.

5.2-1d: Pressure PSD's as sources of discrepancies

There are two main sources of potential discrepancies between the pressure PSD's used in the calculations (K = 0 and K = 28 channel wall PSD's), and what actually exists within the various bundles tested: namely, (i) longitudinal variations along a particular cylinder, and (ii) lateral variations either (a) on a specific cylinder (angular orientation of the measurement points), or (b) due to the location of the selected cylinder in the bundle.

Longitudinal variations are expected to exist here, because of inadequate distances between (i) the downstream end of the turbulator and the leading tip of the top support ogives (levels (1) and (2) in Fig. 146), and (ii) the latter level and the leading end (top) of the cylinders themselves (levels (2) and (3) in Fig. 146). Furthermore, the decay of upstream turbulence depends on the hydraulic diameter, and so does the very generation of turbulence within an array. In situ measurements of PSD's (for various bulk flow velocities) were made only at the mid-cylinder level of the channel

wall (labelled (4) in Fig. 146): the K = 0 tests, yielding virtually the same results as a separate K = 4 experiment with aluminium cylinders, may be indicative of turbulence generation in "open spaces", provided upstream turbulence has already decayed at that longitudinal location. The K = 28 tests likely reflect turbulence generation in "closed spaces", that is within clusters, as we expect upstream turbulence to decay rapidly owing to the relatively small hydraulic diameter ($\simeq$ 2.8 cm) of that cluster. It should be pointed out that, as pressure PSD's for the K = 28 case are higher than those for the K = 0 case (see Figs. 20a and 21b), we expect the turbulence generated within the K = 28 array to actually exceed upstream (level (3) in Fig. 146) values. Note that in both cases (K = 0 and K = 28), we would expect the pressure PSD's at level (3) (see Fig. 146) and at a given bulk velocity, to be different from those actually measured at level (4); specifically, pressure PSD's should not have attained steady state at level (3), although we would expect that condition to occur fairly rapidly in the K = 28 system.

One consideration reduces the importance of longitudinal variations in PSD's, should they exist (plausible in the K = 4 case): in terms of vibration response in the first beam mode, PSD values in the mid-length region of the cylinder(s) have a dominant effect, as the system "admittance" is lowest there, and the measured PSD's would represent more of less the average excitation in that mid-length region. In any case, the K = 4 cluster is subjected to both "open space" and "closed space" PSD's (K = 0 and K = 28 measurements respectively), the latter expected to reach steady state fairly quickly.

In summary, it is not expected that longitudinal fluctuations in pressure PSD's are the major cause of vibration level discrepancies between theory and experiments; in particular, the K = 28 pressure PSD's should exhibit relatively little change longitudinally, although this is where the largest discrepancies occur.

Lateral variations in pressure PSD's have been discussed qualitatively in Sections 5.2-1b and 5.2-1c; as stated there, we would expect "symmetry cycles" of 45° and 180° for the K = 4 and K = 28 systems respectively. Refer-

ring to Fig. 28, we may infer "close space" (K = 28) PSD's in the inner portion between cylinders, and "open space" (K = 0) PSD's in the outer region around the cylinders; in retrospect, it might have been more realistic to utilize an average between K = 0 and K = 28 pressure PSD's for the K ≠ 28 clusters, and although this would have raised scale ratios, it would have reduced the difference between the K = 4 and K = 28 systems (see Fig. 146). Referring to Fig. 29, and recalling that K = 28 pressure PSD's were measured at the channel wall, specifically between cylinder pairs 19,20 and 23,24; those measured PSD's (various velocities) are not in the "symmetry region" presumed to exist in the central region of the cluster. Preliminary experimental data obtained by Curling* suggests a five-to-one ratio between low frequency band (10 to 50 Hz) integrated pressure signal power, at 0° and 45° measurement angles respectively (see Position 1 cylinder, in Fig. 29); whether the K = 28 PSD's are within that range of power or not is not known. Consequently, we can only presume that the measured K = 28 PSD's are of the same order of magnitude, with similar power distributions (frequency content), as what could be termed net effective PSD's, stemming from the "symmetry region" PSD's.

In conclusion, although "effective" K = 0 or K = 28 pressure PSD's are not known with certainty, it would be rather surprising if their magnitudes were anywhere up to ≃ 300 times less than measured wall PSD's (assuming that the theory yields correct results given accurate PSD's, and that currently used correlations are valid): hence, we may safely conclude that lateral variations in PSD's would not result, by themselves, in the scale ratio depicted in Fig. 145.

We are left to discuss CSD's, which are thought to be the main cause of vibration power level discrepancies between measurements and theoretical computations.

5.2-1e: Pressure CSD's as sources of discrepancies

A lenghty discussion of CSD's, either on single cylinders (in a bundle) on cylinder pairs, will not be required here, as the subject was quite

---

* Of the Fluid-Structure Interaction group, here at McGill.

thoroughly reviewed in Section 5.2-1a. Of the various assumptions made to reduce the general form of CSD's, from form (A) to form (F), three are very major, namely isolated cylinder CSD's (a) are the same as those for a pipe with internal flow, (b) these same CSD's apply to any selected cylinder in a cluster, and (c) they may be extented to apply to cylinder pairs. These are very strong assumptions indeed, and can really be justified only by in situ measurement of pressure characteristics. To this author's knowledge, very limited data is available on the influence of system geometry on pressure correlations, which leads to the conclusion that excitation pressure CSD's are the weakest link in the overall theoretical results. Note that in addition to the likelihood of dependence on system geometry, correlations would have to vary with flow velocity as well, so as to result in the scale ratios found in Fig. 145 (no other cause seems likely to result in such wide variations of scale ratios).

5.2-1f: Causes of vibration PSD level discrepancies

In the light of the foregoing discussion, the first plausible dominant source of vibration power level dsicrepancies between theory and experiments is excitation pressure CSD's (PSD's are likely to be of the right order of magnitude). Another source of power discrepancies is likely to be weaknesses in the theoretical model, at least in terms of system damping; from PSD shape comparisons (see Section 5.2-2 below), the system damping appears to be progressively underestimated, theoretically; this effect by itself would tend to make the scale ratios of Fig. 145 go up gradually with flow velocity, which would alter the data of Fig. 145 quantitatively, but not qualitatively (i.e. it cannot explain by itself the discrepancies found).

5.2-2: PSD shapes (power distributions)

Other than for "finer detail", it can be said that experimental and theoretical PSD's essentially agree, in terms of power distribution, at lower flow velocities (e.g. $u = 1$). This may be seen, for all systems tested, in Figs. 35, 50, 56, 61, 66, 71, 75, 79, 84, 93, 102 and 111. However, in all cases, the low velocity measurements indicate low frequency "noise" ($\omega = 0$ to 15), the level of which does not appear to change much with flow velocity, as evidenced by its absence at higher velocities. Industrial systems usually operate at velocities far from critical (u_{crit}), meaning that the

"noise" in question could be of practical interest, since its power levels are of the same order of magnitude as the "predicted" signal; for example, in Fig. 35a ($u = 1$), the "noise" power is about equal to that for the characteristic Radial PSD ($\omega \simeq 17$ to 30).

The investigation of sources of that "noise" should proceed in the same direction as that for power levels, as discussed in Section 5.2-1. In situ measurement of pressure characteristics (PSD's and CSD's) might reveal peculiarities, especially in terms of longitudinal or lateral correlations, that would explain the overall system response, and truly confirm the validity of the random model. Alternately, weaknesses in the model could be revealed.

It is important to note that, whatever the causes of the low frequency "noise" might be, it is certainly extremely sensitive to cylinder position in the channel, as shown in Fig. 43a, for the Radial direction; we see that, although symmetry for the "predicted" signal is excellent, such is not the case for the "noise" level (but this is less pronounced in the Tangential direction).

Where discrepancies become significant, in terms of PSD shapes, is at higher flow velocities and for the second mode group, as may be seen by inspection of the Figures listed at the beginning of this Section. For the "Reference" system ($K = 4$, 4F, $G_c = 0.75$), Fig. 35(a, b) and Fig. 143(a to g inclusively) suggest that discrepancies become significant at about $u = 3.5$. Theoretical data on the effect of varying the fluid damping coefficients c and c_f, at $u = 5.0$, and up to high values,* are depicted in Figs. 147a (c_f only), 147b (c only), and 147c (c and c_f together, including experimental data): It can be seen that altering the values of these coefficients is not sufficient to model measured data adequately, and it is suspected that the damping mechanism utilized in the theory fails for the higher range of flow velocities; this could stem from the adaptation of G.I. Taylor's [20] mod-

---

* Recall that variations about low values, and at $u = 3$, were examined in Section 4.3-1d.

elling (see Appendix F) for flow about long cylinders inclined to the flow, and/or the linearization procedure for lateral viscous forces (following Paidoussis, see Appendix F). In the latter procedure, a dependence on U^2 is dropped, which may lead to unacceptable error for larger values of U.

Note that frequencies that are closely spaced in theory, are not usually resolved in the measurements, for example, at $u = 1$ in Fig. 35a, at $\omega \simeq 26$ and 28: Higher experimental damping is strongly suspected as being the cause for this phenomenon.

5.2-3: Dominant frequencies

It can be said that agreement between theory and experiments, in terms of dominant frequencies, is generally excellent for the first beam mode group, and good for the second group, but with theory consistently underestimating frequencies in this latter case; typical results may be seen in Figs. 35 (K = 4, 4F), 66 (K = 2, 2F), and 71 (K = 1, 1F).

One could argue that the second and higher deflection modes should be modelled by a Timoshenko beam rather than a Bernoulli-Euler one; unfortunately, the net effect of doing this, which results in rotary inertia and shear deformations to be taken into account, would be to even further depress theoretical frequencies, hence this is not a plausible explanation for higher experimental values.

On another front, PSD shapes suggest that damping is underestimated in theory; however, further increases of theoretical damping would increase the gap between measured and calculated values even more, therefore, damping does not provide an explanation for frequency discrepancies.

Another potential effect was tension induced by the deflection of the cylinders, which are fixed at both ends; because of higher curvatures in the second beam mode as compared to the first, this (time variant) tension should affect second mode frequencies more than the first (i.e. a plausible explanation for second mode group frequency discrepancies). However, a brief examination of data indicates that, even for the higher theoretical vibra-

tion amplitudes, induced tensions are orders of magnitude less than for example, longitudinal fluid friction forces, hence negligible.

Rather, it would appear that the modelling of mean flow (as distinguished from random boundary layer pressure) fluid forces has deficiencies, in cylinder deflection modes with smaller radii of curvature (although theoretical frequency underestimation has not been demonstrated conclusively for the third beam mode group (Section 4.3-1b)). The model for inter-cylinder coupling is not suspected to be at fault, since second mode group theoretical frequencies are also lower in the case of an isolated (single) cylinder (Figs. 71a and 71b), by basically the same amount as other systems. Although the following observation does not presently improve our understanding of the problem, it might eventually prove useful to note the following (approximate) features of the frequency discrepancy, (i) $\Delta\omega \propto \sqrt{u}$, and (ii) $\Delta\omega \propto \omega$; this may be seen to occur for various systems, although the amount of shifting does vary with the system under consideration. For example, if we let

$$\Delta\omega = C_\Delta \cdot \sqrt{u} \cdot \omega_{exper} ,$$

then we find: $C_\Delta \simeq 0.03$ for the K = 1, 1F system, and $\simeq 0.04$ for the K = 4, 4F ($G_c = 0.75$) system.

If one presently assumes that mean flow fluid forces may be adequately represented by a quasi-static model, then measurement of components of forces on immobile bent elements of cylinders, in nominally axial flow, could very well provide guidance on how to improve the current modelling.

It should be noted that dominant frequency discrepancies become "significant" only in the second mode group, where power levels are relatively quite low: this makes potential improvements more an academic than a practical interest.

5.2-4: Phases

In comparisons between theoretical and experimental phases, whenever the magnitude of the corresponding coherence function was "high enough" (approximately 0.10), the agreement has been excellent. The reason for this may be inferred from Fig. 42(a, b) and Fig. 148(a, b), which depict the effect of

varying fluid damping parameters on theoretical phases; it can be seen that, unlike coherence (and PSD's - see Fig. 147), phases are very insensitive to variations in (fluid) damping, which can be said to be the least "established" mechanism of all. Consequently, it is not surprising that agreement of measured phases with theory be so consistent, and this provides very strong support for at least inertial inter-cylinder fluid coupling (note phases for $c = c_f = 0$, in Fig. 42).

5.2-5: Coherence functions

In the two systems where the cylinder pair utilized for coherence function measurement was closest, namely the adjacent pair 1,2, agreement with theory has been found to excellent. The first such system is the 2F(1,2)/2R(3,4), whose coherence functions are shown in Fig. 85 (a to f incl.), and the second is the K = 4, 4F, $G_c = 0.75$, with Position pair 1,2 instrumented, the coherence data for which is depicted in Fig. 52 (a to f incl.). In all other systems, the instrumented cylinder pair was a diagonal one, with correspondingly greater separation ("fluid distance"); for these latter systems, the general agreement between theory and experiments, in terms of coherence function, has not been as good, although the larger discrepancies tend to be confined to specific coupling modes, as will be discussed shortly.

At this point, we can at least conclude that the fluid coupling mechanisms incorporated in the theory do dominate at small distances, but become increasingly inadequate as cylinder separation increases; three such mechanisms are utilized, namely (i) inertial coupling, where cylinder accelerations are considered interdependent, determined from potential flow theory, (ii) so-called viscous coupling, where normal (to cylinder axis) fluid friction forces on cylinders are deemed altered, by the potential flow velocity field (item (i) above) at the cylinder boundary, and (iii) lateral correlations in the turbulent boundary layer pressure fluctuations, using the "shortest lateral fluid distance" scheme. Note that mechanisms (i) and (ii) depend on potential flow theory, where the fluid is assumed incompressible, which implies instantaneous propagation of the acceleration of a given cylinder, through the fluid; this is a valid approximation, as the speed of sound in water is much larger than any system velocity. Mechanism (iii) stems from statistical properties of the fluid flow, and is also "instanta-

neous", being obtained from simultaneous measurements at two points of interest.

No investigation of theoretical dependence of coherence on pressure correlations has been done, but because inter-cylinder distances (center to center) are of the order of cylinder half-circumference (maximum correlation length), it is expected that mechanism (iii) does not alter coherences very significantly. Inertial coupling dominates, but "viscous coupling" does alter somewhat coherence functions, as seen in Fig. 42(a, b) and Fig. 148(a, b), where it should be kept in mind that the latter Figure covers a very wide range of damping parameter values. We now proceed to review some specific cases, where we shall restrict ourselves to $u = 1$ as PSD comparisons were best at low velocities, and to the first beam mode group as power levels are quite low in the second.

Starting with the simplest cases, we examine two-cylinder (flexible) systems, which number three: the $K = 2$, 2F system, and two $K = 4$ systems, the 2F(1,3)/2R(2,4) and the 2F(1,2)/2R(3,4) cases.

Coherences for the $K = 2$, 2F ($G_c = 1.89$) system are illustrated in Figs. 67a and 67b. The worst agreement involves the first Radial and second Tangential "peaks"; referring to Fig. 129 (part a), we see that these modes involve the highest interaction between cylinders (the other two modes approach the situation of two cylinders moving independently of each other), which is bound to yield more error, should fluid forces on the cylinders not be modelled accurately; poor matching in theoretical and experimental coherences indicates an inadequacy in modelling fluid forces, for cylinders not spaced "very" closely (recall excellent matching for the two tested $G_c = 0.75$ systems with adjacent cylinders).

Data for the $K = 4$ ($G_c = 0.75$), 2F(1,3)/2R(2,4) system is depicted in Figs. 80a and 80b, and the corresponding cross-sectional coupling modes shown in Fig. 129 (part b). Somehow, it seems that the presence of the two rigid cylinders (at least at $u = 1$; see Fig. 80c) alters the flow field such that agreement is good for the first Radial "peak", unlike the 2F system,

but as for the latter case, agreement is poor for the second Tangential "peak". The better agreement for the first Radial "peak" might stem from an effect which is not part of the theory at all, namely a requirement for the "outflow"/"inflow" of fluid from the central region between cylinders, due to the inward/outward motion of the moving cylinders, resulting in an increase of coherent fluid forces on cylinders; the presence of the two rigid cylinders would increase such action, raising the experimental value over that for the 2F case, but having limited potential effect on the theoretical value, as it is already near one.*

Results for the K = 4 ($G_c = 0.75$), 2F(1,2)/2R(3,4) system show excellent agreement between theory and experiments (Figs. 85a and 85b), which suggests that, at close proximity, the theory models the system adequately, as far as coherence is concerned. Should the "outflow"/"inflow" mechanism mentioned above have any significance, it would not necessarily alter coherences notably, when those are already at a high level. Note that comparisons are still very good at higher flow velocities, as evidenced by Figs. 85c to 85f inclusively.

We shall examine the three K = 4, 4F systems with varying G_c, to verify that the data supports previous inferences.

For the most closely spaced system, i.e. with G = 0.75, we have data for both pairs 1,3 and 1,2. Data for pair 1,3 is shown in Figs. 36a and 36b, and coupling modes illustrated in Fig. 129 (part c). As for the 2F(1,3)/2R(2,4) system and contrary to the 2F system, agreement for the first Radial mode (ω_1 in Fig. 129) is very good; this is again assumed to result from the "outflow"/"inflow" mechanism, which raises measured coherences to levels of the theory (already high and therefore plausibly insensitive to the latter mechanism). The second Radial "peak" (ω_5, ω_6 in Fig. 129) shows good agreement; as before, the low interaction between cylinders may explain why this is so. The third Radial "peak" (ω_7 in Fig. 129) compares less well,

---

* Note that adding coherent power to a signal will produce higher percentage changes in originally smaller coherences.

which is consistent with previous explanations, in that there is interaction between diagonal (hence farther apart) cylinders, but no "outflow"/"inflow". In the Tangential (i.e. T-T) case, the first "peak" (ω_2 in Fig. 129) agreement is poor; here the explanation might be more indirect, in the sense that motion of the diagonal pair can be said to be correlated (T-T), mostly because each of those cylinders (Positions 1 and 3) is itself fairly strongly correlated, at least in theory, to its immediate neighbours (Positions 2 and 4), as shown in Fig. 52b. The lower experimental coherence in the latter case would explain the poor agreement found here (first T-T/1,3 "peak", K = 4, 4F system), to be discussed shortly. The second Tangential "peak" of Fig. 36b (ω_3,ω_4 in Fig. 129) has excellent agreement (experiment versus theory), and corresponds to an "in unison", minimum inter-cylinder fluid forces situation, as discussed above. The comparison for the third Tangential "peak" (ω_8 in Fig. 129) is poor; as for the second "peak", there is an indirect dependence on pair 1,2 coherence, to be discussed next.

Pair 1,2 of the latter K = 4, 4F ($G_c = 0.75$) system will now be examined. Coherence data is found in Figs. 52a and 52b and, as for the 1,3 case, coupling modes are illustrated in Fig. 129 (part c): again, we have very good agreement for the first Radial "peak" (Fig. 52a), which corresponds to the ω_1 mode in Fig. 129 (part c), as expected since we are dealing with an adjacent pair. The agreement is also very good for the second Radial "peak" of Fig. 52a (ω_7 in Fig. 129), for the same reason. In terms of Tangential coherences, we have a lower than expected experimental coherence at the first "peak" in Fig. 52b (ω_2 in Fig. 129); here the fact that cylinders of interest are adjacent does not result in the predicted good agreement: this constitutes an exception to earlier observations, and is very unlikely to stem from experimental error (misalignment,etc...), as the same "poor" agreement has also been found for the 1,3 pair, the latter being a completely separate test. The second Tangential "peak" (ω_8 in Fig. 129) follows predicted trends in that agreement is good.

We turn our attention to K = 4, 4F bundles, with increased spacing: comparisons of $G_c = 1.00$ and $G_c = 1.50$ cases to the $G_c = 0.75$ one reveal the same system behaviour, as seen from Figs. 36a, 57a, and 62a for the R-R coher-

ences, and Figs. 36b, 57b, and 62b for the T-T ones. The greater inter-cylinder distances result in slightly lower experimental coherences (versus theory), as expected.

The effect of increased flow velocity degrades comparisons significantly for diagonal pairs, but surprisingly very little for adjacent pairs. The former may be seen by inspection of Fig. 36 (a, b), (c, d) and (e, f), for $u = 1$, 3 and 5, respectively, for the $K = 4$, 4F ($G_c = 0.75$) system; the same applies to a lesser extent, for the $K = 2$, 2F ($G_c = 1.89$), as depicted in Fig. 67 (a to f incl.) and in Fig. 80 (a to f incl.), for the $K = 4$, 2F(1,3)/2R(2,4) ($G_c = 0.75$) system. Adjacent cylinder setups are shown in Fig. 52 (a to f incl.) for the $K = 4$, 4F ($G_c = 0.75$) system, and Fig. 85 (a to f incl.) for the $K = 4$, 2F(1,2)/2R(3,4) ($G_c = 0.75$) system.

5.2-6: Miscellaneous

In the light of previous discussions, it is apparent that, for items such as the low frequency experimental "noise" ($\omega \simeq 0$-15, e.g. see Fig. 35a) and the $K = 28$ systems asymmetries, for example PSD power level differences with cylinder Position in the parallel case (see Radial direction, in Fig. 96), cannot really be explained without knowing more about excitation pressure characteristics, at which point it would be possible to verify whether the present theory predicts the measured vibration data.

5.3: CONCLUSIONS

Finally, we may draw general conclusions about axial (parallel) flow over cylinder clusters.

5.3-1: System characteristics

For symmetric systems with a cluster of K flexible cylinders, surrounded or not (i.e unbounded fluid) by a channel and/or rigid cylinders, we find the following experimental and theoretical characteristics.

(1) Motion tends to occur in (frequency) groups, the n^{th} group corresponding to the n^{th} beam lateral deflection mode (the number of groups is truncated to N in the theory); this is basically due to the system transfer function which tends to peak in regions corresponding to natural frequencies of cylinders in fluid.

(2) In each group, motion tends to occur (see items (3) and (4) below) according to definite inter-cylinder (fluid) coupling modes, predominantly in either "radial" or a "tangential" directions (the latter stemming from symmetry considerations); a dominant frequency is associated with each mode, and there are up to 2K such frequencies (some of which will be "repeated", whenever a given coupling mode possesses symmetric equivalents, e.g. see Fig. 129); the system simply behaves as a multi-degree of freedom m,c,k system, with characteristic frequencies and modes.

(3) In each mode group, PSD power distribution tends to peak at the dominant frequencies associated with coupling modes.

(4) In each mode group, the coherence function tends to peak at the dominant frequencies associated with coupling modes, which reflects the tendency of the system to extract energy from the flow at its characteristic frequencies and in the corresponding modes.

(5) Most power lies in the first mode group.

(6) Dominant system frequencies are lowered and the power distribution broadens (lower frequencies go down faster than higher ones), as the flow velocity increases; this is mostly due to a decrease of system stiffness, owing to "centrifugal forces" proportional to u^2. This

eventually leads to divergence (instability), as effective stiffness reaches zero and "damping" (imaginary part of the complex mean-flow model frequency) becomes negative.

(7) The system damping increases with flow velocity, due to longitudinal fluid friction forces.

(8) Overall system response is due to a combination of effects of the mean flow, which is velocity and deflection dependent, and effects of random pressure fluctuations in the boundary layer, where the latter depends on flow velocity, upstream turbulence, and the geometry of the system, as well as other parameters.

5.3-2: Weaknesses in the theory

(1) Because the theory consistently underestimates second mode group frequencies, it is felt that the modelling of the longitudinal fluid forces has weaknesses, for lower radii of beam curvature.

(2) From coherence function investigation, it appears that the modelling of lateral fluid friction forces is inadequate for cylinders interspaced to $G_c \simeq 1$ or more. Furthermore, it appears that a geometry and coupling mode dependent "outward/inward" flow mechanism (fluid displaced out/in of a region because of cylinder motion) may be at work, a phenomenon not taken into account in the present theoretical model.

(3) Flow velocity dependent damping is progressively underestimated, as velocity gets higher; this may be seen by PSD shapes comparisons.

At this point, the principal discrepancy between theory and experiments, namely power levels, cannot be concluded to stem from a flaw in the theory: the pressure field correlations used as input data to the theory are most probably not indicative of the situation existing in the clusters tested. Hence, this discrepancy is likely mainly due to the inadequate and inappropriate empirical input into the theoretical model, which is nevertheless the best available at present.

5.3-3: Recommendations

In order of importance, the following research could eventually provide data leading to a definitive evaluation of the theoretical model:

(1) In situ experimental data on pressure characteristics should be gathered, or alternatively similar applicable data should be used, as input to the theoretical model. This is mostly to confirm that power level discrepancies are due to having used improper correlations.

(2) Data should be gathered on flow velocity dependent friction forces on (a) deflected cylinders in nominally axial flow, in both the lateral and longitudinal directions, and (b) a moving (first beam mode) cylinder in still flow, to evaluate lateral forces. This is to shed light on the theoretical undervaluation of second mode group frequencies as well as undervaluation of damping at higher flow velocities, and on the inadequacy of modelling of fluid forces at larger separations, as evidenced by coherence measurements.

(3) It may prove useful to include the "outward/inward" flow mechanism in the model, should comparisons using new data and possibly modified fluid damping mechanisms still result in coherence discrepancies, as discussed in Section 5.2-5.

REFERENCES

1. F.-J. BOURRIÈRES 1939, Publications Scientifiques et Techniques du Ministère de l'Air, No. 147. " Sur un phénomène d'oscillation auto-entretenue en mécanique des fluides réels ".

2. H. ASHLEY and G. HAVILAND 1950, Journal of Applied Mechanics 17, 229-232. " Bending vibrations of a pipeline containing flowing fluid ".

3. V.P. FEODOS'EV 1951, Inzhenernyi Sbornik 10, 169-170. " Vibrations and stability of a pipe when liquid flows through it ".

4. G.W. HOUSNER 1952, Journal of Applied Mechanics 19(2), 205-208. " Bending vibrations of a pipe line containing flowing fluid ".

5. F.I. NIORDSON 1953, Kungliga Tekniska Hogskolans Handlingar, No.73. " Vibrations of a cylindrical tube containing flowing fluid ".

6. M.P. PAIDOUSSIS and N.T. ISSID 1974, Journal of Sound and Vibration 33, 267-294. " Dynamic stability of pipes conveying fluid ".

7. D. BURGREEN, J.J. BYRNES and B. BENFORADO 1958, Trans. ASME 80(5), 991-1003. " Vibration of rods induced by water in parallel flow ".

8. C.M. SHIELDS 1960, U.S. Atomic Energy Commission Report GEAP-3583. " N.-S. Savannah fuel design and development program - fuel rod vibration ".

9. E.P. QUINN 1962, U.S. Atomic Energy Commission Report GEAP-4059. " Vibration of fuel rods in parallel flow ".

10. E.P. QUINN 1965, U.S. Atomic Energy Commission Report GEAP-4966. " Vibration of SEFOR fuel rods in parallel flow ".

11. P.G. AVANZINI 1971, 1st Int'l Conf. on Structural Mechanics in Reactor Technology, Paper no. E3/5, Berlin, Germany. " Self-sustained vibrations of rods in parallel flow ".

12. M.P. PAIDOUSSIS 1974, ASME Journal of Engineering for Industry 96, 547-552. " Vibration of cylindrical structures induced by axial flow ".

13. Anonymous 1962, Société Grenobloise d'Etudes et Applications Hydrauliques Special Report No. 3, EURAEC-288. " Study of vibrations and load losses in tubular clusters ".

14. K.G. ROSTRÖM and N. ANDERSSON 1964, Report R 4-327, RPL-724, Aktiebolaget Atomenergi, Stockholm. " Boiler element for Marviken, vibration tests with one rod ".

15. K.G. ROSTRÖM and N. ANDERSSON 1964, Report R 4-328, RPL-725, Aktiebolaget Atomenergi, Stockholm. " Superheater element for Marviken, vibration tests with one rod ".

16. K.G. ROSTRÖM 1964, Report R 4-341, RPL-726, Aktiebolaget Atomenergi, Stockholm. " Seven-rod fuel element - vibration test ".

17. M.P. PAIDOUSSIS 1965, Atomic Energy of Canada Report AECL-2225, Chalk River, Ontario, Canada. " The amplitude of fluid-induced vibration of cylinders in axial flow ".

18. M.P. PAIDOUSSIS 1969, Nuclear Science and Engineering 35, 127-138. " An experimental study of vibration of flexible cylinders induced by nominally axial flow ".

19. M.P. PAIDOUSSIS 1965, Proc. Institution of Mechanical Engineers, 180(3J), 1-11. " Vibration of flexible cylinders with supported ends, induced by axial flow ".

20. G.I. TAYLOR 1952, Proceedings of the Royal Society, London 214(A), 158-183. " Analysis of the swimming of long and narrow animals ".

21. M.J. LIGHTHILL 1960, Journal of Fluid Mechanics 9, 305-317. " Note on the swimming of slender fish ".

22. M.P. PAIDOUSSIS 1966, Journal of Fluid Mechanics 26, 717-751. " Dynamics of flexible slender cylinders in axial flow. Part 1: Theory, Part 2: Experiments ".

23. J.R. REAVIS 1967, Trans. of the American Nuclear Society 10, 369-371. " WVI-Westinghouse vibration correlation for maximum fuel-element displacement in parallel turbulent flow ".

24. J.R. REAVIS 1969, Nuclear Science and Engineering 38, 63-69. " Vibration correlation for maximum fuel-element displacement in parallel turbulent flow ".

25. H.P. BAKEWELL Jr. 1964, Journal of the Acoustical Society of America 36(1), 146-148. " Narrow-band investigations of the longitudinal space-time correlation function in turbulent airflow ".

26. H.P. BAKEWELL Jr. et al. 1962, Naval Underwater Sound Laboratory, AD-283683. " Wall pressure correlations in turbulent pipe flow ".

27. M.Y el BAROUDI et al. 1963, Advisory Group for Aeronautical Research and Development, Paris (April 1963), AGARD-465. " An experimental investigation of turbulence-excited panel vibration and noise (boundary-layer noise) ".

28. G.M. CORCOS 1962, Univ. Calif. Institute of Engineering Research Rept., Ser. 183, Issue 2. " Pressure fluctuations in shear flows ".

29. D.J. GORMAN 1969, Atomic Energy of Canada Report AECL-3371, Chalk River, Ontario, Canada. " The role of turbulence in the vibration of reactor fuel elements in liquid flow ".

30. D.J. GORMAN 1971, Nuclear Science and Engineering 44, 277-290. " Analytical and experimental investigation of the vibration of cylindrical reactor fuel elements in two-phase parallel flow ".

31. R.M. KANAZAWA and A.P. BORESI 1970, Proc. Conf. on Flow-Induced Vibration in Reactor System Components, Argonne, Ill., ANL-7685, p. 47-63. " Calculation of the response of rods to boundary layer pressure fluctuations ".

32. S.S. CHEN and M.W. WAMBSGANSS 1970, Proc. Conf. on Flow-Induced Vibration in Reactor System Components, Argonne, Ill., ANL-7685, p. 5-31. " Response of a flexible rod to nearfield noise ".

33. H.P. BAKEWELL Jr. 1968, Journal of the Acoustical Society of America 43(6), 1358-1363. " Turbulent wall-pressure fluctuations on a body of revolution ".

34. Y.N. CHEN 1970, Flow-Induced Vibration in Heat Exchangers (D.D. Reiff, ed.), p. 57-66, New York :ASME. " Turbulence-induced vibration in heat exchangers with cross and parallel flow. Part 1: parallel flow ".

35. S.S. CHEN and M.W. WANBSGANSS 1972, Nuclear Engineering and Design 18, 253-278. " Parallel flow-induced vibration of fuel rods ".

36. S.S. CHEN 1975, Journal of Engineering for Industry 97, 1212-1217. " Vibrations of a row of circular cylinders in a liquid ".

37. V.Y. MAZUR 1970, Izvestiya Akademi Nauk SSSR, Mekhanika Zhiakostii Gaza 6, 80-84. " Motion of two circular cylinders in an ideal fluid ".

38. T. SHIMOGO and T. INUI 1971, Proc. 21st Japan Natl. Cong. for Applied Mechanics, p. 495-505. " Coupled vibration of many elastic circular bars in water ".

39. M.W. WAMBSGANSS and P.L. ZALESKI 1970, Proc. Conf. Flow Induced Vibrations in Reactor Components, Argonne, Ill., ANL-7685, p. 112-137. " Measurement, interpretation and characterization of near field flow noise ".

40. S.S. CHEN 1972, Journal of Sound and Vibration 21, 387-398. " Free vibration of a coupled fluid/structural system ".

41. S.S. CHEN 1975, ASME Journal of Pressure Vessel Technology 97, 78-83. " Dynamic responses of two parallel circular cylinders in a liquid ".

42. S.S. CHEN, M.W. WAMBSGANSS and J.A. JENDRZEJCZYK 1976, Journal of Applied Mechanics 43, 325-329. " Added mass and damping of a vibrating rod in confined viscous fluids ".

43. M.P. PAIDOUSSIS 1973, Journal of Sound and Vibration 29, 365-385. " Dynamics of cylindrical structures subjected to axial flow ".

44. S.S. CHEN 1975, Nuclear Engineering and Design 35, 399-422. " Vibration of nuclear fuel bundles ".

45. S.S. CHEN 1976, Journal of Fluids Engineering 98, 462-469. " Dynamics of heat exchanger tube banks ".

46. T.T. YEH and S.S. CHEN, Argonne Tech. Mem. ANL-CT-77-24. " The effect of fluid viscosity on coupled tube/fluid vibrations ".

47. B.T. LUBIN, K.H. HASLINGER, A. PURI and J. GOLDBERG 1977, ASME Joint Applied Mechanics, Fluids Engineering & Bioengineering Conf., New Haven, Connecticut (June 1977). " Experimental data on the natural frequency of a tubular array ".

48. S.S. CHEN and J.A. JENDRZEJCZYK 1978, ASME Journal of Mechanical Design 100, 540-548. " Experiments on fluidelastic vibration of cantilevered tube bundles ".

49. S.S. CHEN, J.A. JENDRZEJCZYK and M.W. WAMBSGANSS 1977, ASME: Fluid-Structure Interaction Phenomena in Pressure Vessels and Piping Systems (Au-Yang & Brown, eds) p. 19-36. " An experimental and theoretical investigation of coupled vibration of tube banks ".

50. M.P. PAIDOUSSIS and S. SUSS 1977, ASME Journal of Applied Mechanics 44, 401-408. " Stability of a cluster of flexible cylinders in bounded axial flow ".

51. M.P. PAIDOUSSIS, S. SUSS and M. PUSTEJOVSKY 1977, Journal of Sound and Vibration 55, 443-459. " Free vibration of cylinders in liquid-filled channels ".

52. T.M. MULCAHY, T.T. YEH and A.J. MISKEVICS 1980, Journal of Sound and Vibration 69, 59-69. " Turbulence and rod vibrations in an annular region with upstream disturbances ".

53. W.H. LIN, M.W. WAMBSGANSS and J.A. JENDRZEJCZYK 1981, General Electric Report GEAP-24375, San Jose, California. " Wall pressure fluctuations within a seven-rod array ".

54. M.P. PAIDOUSSIS 1979, Journal of Sound and Vibration 65, 391-417. " The dynamics of clusters of flexible cylinders in axial flow: theory and experiments ".

55. M.P. PAIDOUSSIS, L.R. CURLING and J.O. GAGNON 1982, ASME Journal of Fluids Engineering 104, 342-347. " Experiments on fluidelastic instability of cylinder clusters in axial flow ".

56. M.P. PAIDOUSSIS and J.O. GAGNON 1982, Intl. Conf. on Vibration in Nuclear Plants, Keswick (May 1982), U.K., paper 1.3., p. 50-60. " Experiments on the dynamics of cylinder clusters in axial flow ".

57. M.P. PAIDOUSSIS and J.O. GAGNON 1984, Journal of Sound and Vibration 96, 341-352. " Experiments on vibration of clusters of cylinders in axial flow: modal and spectral characteristics ".

58. M.P. PAIDOUSSIS, J.O.GAGNON and C. CHEN 1983, IAHR, 20th Cong., Moscow, USSR, vol. 4, p. 358-367. " Fluid coupling characteristics of clustered cylinders in still or axially flowing liquid ".

59. M.P. PAIDOUSSIS and L.R. CURLING 1985, Journal of Sound and Vibration 98, 493-517. " An analytical model for vibration of clusters of flexible cylinders in turbulent axial flow ".

60. L.R. CURLING and J.O. GAGNON 1984, ASME: Symposium on Flow-Induced Vibrations, New Orleans, vol.4, p. 105-115. " A theoretical model for vibration analysis of cylinders in axial flow ".

61. L.R. CURLING 1982, M. Eng. Thesis, McGill Univ., " Theory of vibration of clusters of cylinders in axial flow ".

62. M.P. PAIDOUSSIS 1987, Applied Mechanics Reviews 40(2), 163-175. " Flow-induced instabilities of cylindrical structures ".

63. M.P. PAIDOUSSIS 1981, Journal of Sound and Vibration 76, 329-360. " Fluidelastic vibration of cylinder arrays in axial and cross flow: State of the art ".

64. M.P. PAIDOUSSIS 1979, Practical Experiences with Flow-Induced Vibrations (Naudascher & Rockwell, eds), Springer-Verlag, p. 1-81. " Flow-induced vibrations in nuclear reactors and heat exchangers: Practical experiences and state of knowledge ".

65. M.J. PETTIGREW 1981, Power Industry Research 1, 97-133. " Flow-induced vibration phenomena in nuclear power: Station components ".

66. S.S. CHEN 1974, Shock and Vibration Digest 6, 1-11. " Parallel flow-induced vibrations and instabilities of cylindrical structures ".

67. S.S. CHEN 1977, Shock and Vibration Digest 9, 25-38. " Flow-induced vibrations of circular cylindrical structures, part 1: stationary fluids and parallel flow ".

68. S. TIMOSHENKO and D.H. YOUNG, Vibration Problems in Engineering (Van Nostrand, 1966).

69. L.MEIROVITCH, Analytical Methods in Vibrations (Macmillan, 1967).

70. A.A. LAKIS and M.P. PAIDOUSSIS 1972, Journal of Sound and Vibration 25, 1-27. "Prediction of the response of a cylindrical shell to arbitrary or boundary-layer-induced random pressure fields".

71. W.W. WILLMARTH and C.S. YANG 1970, Journal of Fluid Mechanics 41, part 1, 47-80. "Wall pressure fluctuations beneath turbulent boundary layers on a flat plate and a cylinder".

72. M. HANNOYER 1977, PhD Thesis, McGill Univ., "Instabilities of Tubular Beams Induced by Axial Flows".

73. S. SUSS 1977, M. Eng. Thesis, McGill Univ., "Dynamics of Clusters of Flexible Cylinders in Bounded Axial Fluid Flows".

74. R.E. BISHOP and D.C. JOHNSON, The Mechanics of Vibration (Cambridge University Press, 1979).

75. J.O. GAGNON 1982, M. Eng. Thesis, McGill Univ., "Flow-Induced Vibration of Cylinder Cluster in Incompressible Confined Axial Flow".

76. J.S. BENDAT and A.G. PIERSOL, Random Data: Analysis and Measurement Procedures (Wiley-Interscience, 1971).

77. H. CHUNG and S.S. CHEN 1977, Journal of Applied Mechanics 44, 213-217. "Vibration of a Group of Circular Cylinders in a Confined Fluid".

Appendix A

Static circumferential pressure forces and moments

We wish to examine net forces and moments arising from static pressure acting on the circumferential surface of an element of cylinder. The task is facilitated by considering the element fully immersed in fluid (see Paidoussis [43]) and making use of the overall buoyancy force and forces at the ends of the element, as shown below.

Consider an element of cylinder, immersed in fluid:

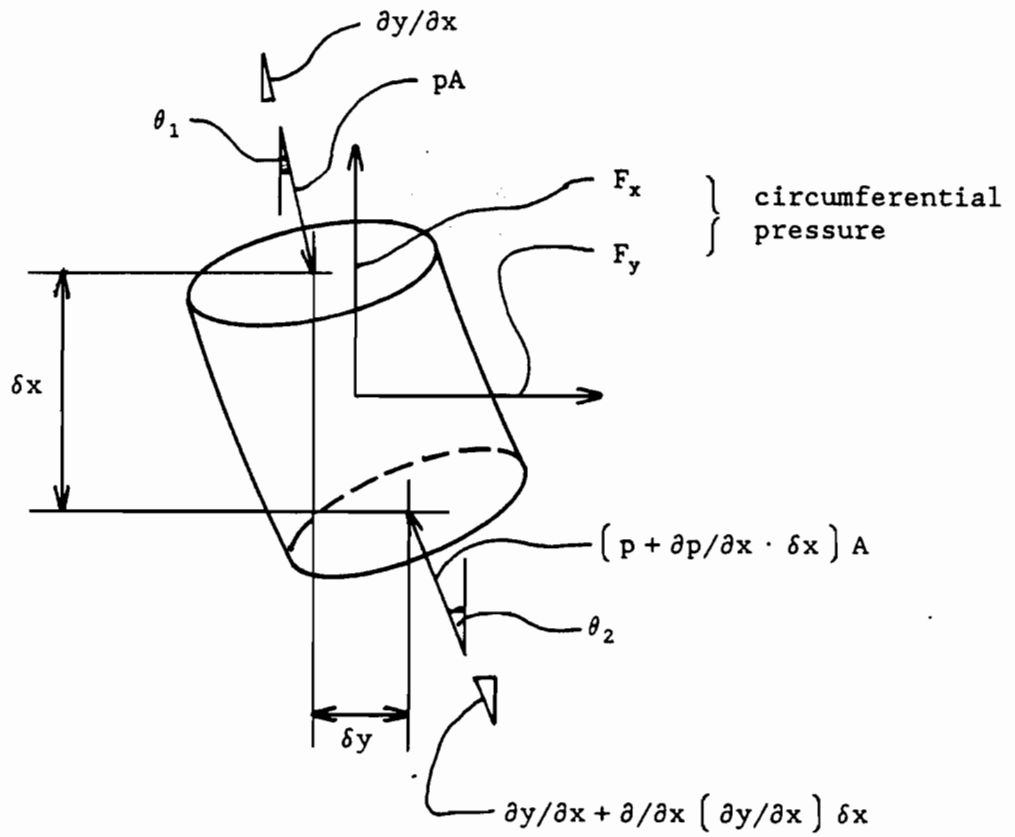

The net (upward) buoyancy force is

$$F_1 = \frac{\partial p}{\partial x} (A \cdot \delta x) \ . \qquad (A.1)$$

The upward force due to the end faces is

$$F_2 = \left(p + \frac{\partial p}{\partial x} \delta x \right) A \cdot \cos \theta_2 - pA \cdot \cos \theta_1 \ . \qquad (A.2)$$

Hence, the net upward force due to the circumferential pressure is $F_x = F_1 - F_2$, i.e. we have

$$F_x - pA\left(\cos\theta_1 - \cos\theta_2\right) - \frac{\partial p}{\partial x}\,\delta x \cdot A\left(1 - \cos\theta_2\right) = 0 \ . \tag{A.3}$$

The lateral force F_y is opposed by end face forces, so that

$$F_y + pA \cdot \sin\theta_1 - \left(p + \frac{\partial p}{\partial x}\,\delta x\right) A \cdot \sin\theta_2 = 0 \ . \tag{A.4}$$

Now, we approximate the trigonometric functions in terms of slopes:

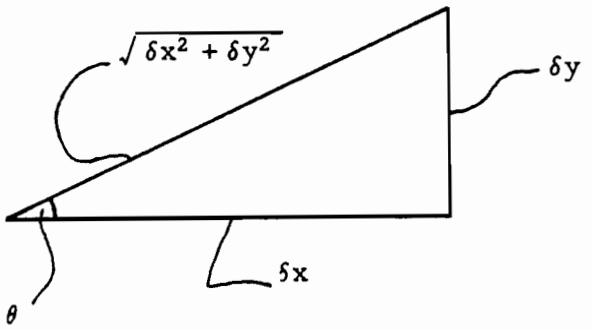

$\delta y / \delta x \ll 1$.

$$\cos\theta = \frac{\delta x}{\sqrt{\delta x^2 + \delta y^2}} = \frac{1}{\sqrt{1 + (\delta y / \delta x)^2}} \simeq \frac{1}{1 + 1/2 \cdot (\delta y / \delta x)^2} \ ,$$

$$\cos\theta \simeq \frac{2}{2 + (\partial y / \partial x)^2} \ , \tag{A.5}$$

and, we also have

$$\sin\theta \simeq \frac{2 \cdot \partial y/\partial x}{2 + (\partial y / \partial x)^2} \ . \tag{A.6}$$

Consequently, we can write

$$\cos\theta_1 - \cos\theta_2 \simeq \frac{2}{2 + \left(\frac{\partial y}{\partial x}\right)^2} - \frac{2}{2 + \left[\frac{\partial y}{\partial x} + \frac{\partial}{\partial x}\left(\frac{\partial y}{\partial x}\right)\delta x\right]^2} \ ,$$

$$\simeq \frac{2}{2 + \left(\frac{\partial y}{\partial x}\right)^2} - \frac{2}{2 + \left(\frac{\partial y}{\partial x}\right)^2 + 2\,\frac{\partial y}{\partial x}\,\frac{\partial^2 y}{\partial x^2}\,\delta x + \left[\frac{\partial}{\partial x}\left(\frac{\partial y}{\partial x}\right)\delta x\right]^2} \ ,$$

and dropping the last term in the second denominator, we get

$$\cos\theta_1 - \cos\theta_2 \simeq \frac{4\,\frac{\partial y}{\partial x}\,\frac{\partial^2 y}{\partial x^2}\,\delta x}{\left[2+\left(\frac{\partial y}{\partial x}\right)^2\right]\left[2+\left(\frac{\partial y}{\partial x}\right)^2+2\,\frac{\partial y}{\partial x}\,\frac{\partial^2 y}{\partial x^2}\,\delta x\right]} \quad , \text{ i.e.}$$

$$\cos\theta_1 - \cos\theta_2 \simeq \frac{\partial y}{\partial x}\,\frac{\partial^2 y}{\partial x^2}\,\delta x \ . \tag{A.7}$$

Similarly,

$$1 - \cos\theta_2 \simeq \frac{1}{2}\left(\frac{\partial y}{\partial x}\right)^2 + \frac{\partial y}{\partial x}\,\frac{\partial^2 y}{\partial x^2}\,\delta x \ , \tag{A.8}$$

and (see (A.6))

$$\sin\theta_1 \simeq \frac{2\cdot\frac{\partial y}{\partial x}}{2+\left(\frac{\partial y}{\partial x}\right)^2} \quad , \tag{A.9}$$

$$\sin\theta_2 \simeq \frac{2\cdot\left[\frac{\partial y}{\partial x}+\frac{\partial}{\partial x}\left(\frac{\partial y}{\partial x}\right)\delta x\right]}{2+\left[\frac{\partial y}{\partial x}+\frac{\partial}{\partial x}\left(\frac{\partial y}{\partial x}\right)\delta x\right]^2} \quad , \tag{A.10}$$

Using (A.7) to (A.10) inclusively, in eqs.(A.3) and (A.4) yields

$$F_x - A\cdot\delta x\left[p\,\frac{\partial y}{\partial x}\,\frac{\partial^2 y}{\partial x^2}+\frac{1}{2}\,\frac{\partial p}{\partial x}\left(\frac{\partial y}{\partial x}\right)^2+\frac{\partial p}{\partial x}\,\frac{\partial y}{\partial x}\,\frac{\partial^2 y}{\partial x^2}\,\delta x\right] = 0 \ ,$$

i.e.

$$F_x \simeq 0 \ , \tag{A.11}$$

$$\text{for } \frac{\partial y}{\partial x} \text{ and } \frac{\partial^2 y}{\partial x^2} \ll 1 \ ,$$

and (fourth order terms neglected in numerator)

$$F_y = \frac{4A\cdot\delta x\left(p\,\frac{\partial^2 y}{\partial x^2}+\frac{\partial p}{\partial x}\,\frac{\partial y}{\partial x}\right)}{\left[2+\left(\frac{\partial y}{\partial x}\right)^2\right]\left[2+\left(\frac{\partial y}{\partial x}+\frac{\partial}{\partial x}\left(\frac{\partial y}{\partial x}\right)\delta x\right)^2\right]}$$

which reduces to

$$F_y = A\cdot\delta x\,\frac{\partial}{\partial x}\left(p\,\frac{\partial y}{\partial x}\right) \ . \tag{A.12}$$

To investigate moments, it will prove sufficient to consider that F_y acts at $\delta x/2$; ignoring end faces we get, for the fluid forces,

$$M = \frac{\delta x}{2} F_y = \frac{A}{2} (\delta x)^2 \frac{\partial}{\partial x} \left[p \frac{\partial y}{\partial x} \right] ,$$

$$\text{i.e. } M \simeq 0 , \qquad \text{(A.13)}$$

which is to be expected for distributed forces (as compared, for example, to lateral shear).

Appendix B

Axial stresses induced by fluid pressure

The axial compressive force induced in the cylinder, due to the static fluid pressure is examined here. As is shown below, it is a special case of Lamé's problem.*

An initially unstressed thick tube is bound at its ends, by two planar surfaces. It is then subjected to uniform internal and external pressures p_1 and p_2. The cross-sectional view below illustrates the problem:

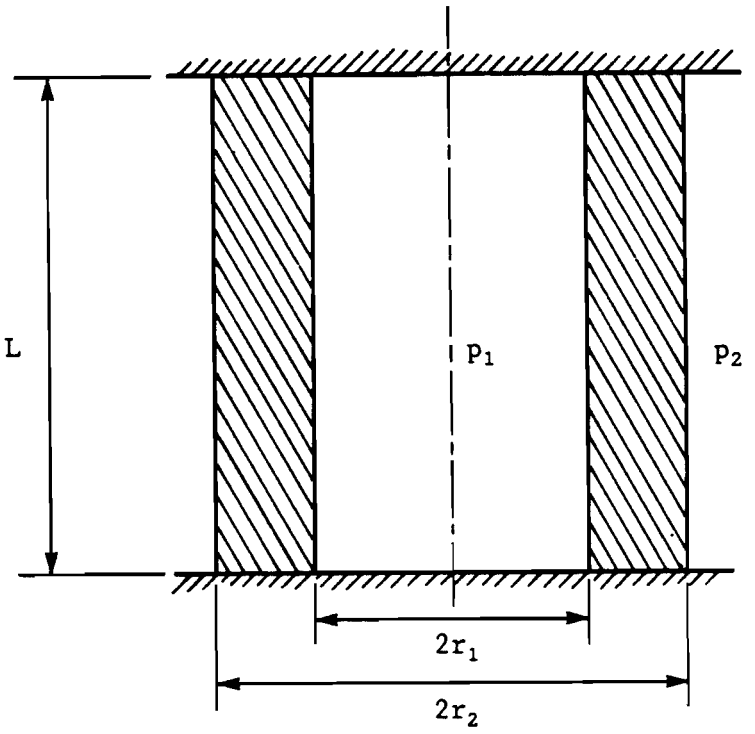

where L is the (fixed) tube length, and r_1 and r_2 are the (unstressed) tube inner and outer radii respectively.

---

* See: *Advanced Strength of Materials* (1971) by E. Volterra & J.H. Gaines, ch.3.

A solution is found by assuming a state of plane strain. Recall the basic relationships for stresses, strains and displacements for bodies at rest, with no body forces:

(a) Equations of equilibrium:

$$\frac{\partial \sigma_x}{\partial x} + \frac{\partial \tau_{xy}}{\partial y} + \frac{\partial \tau_{xz}}{\partial z} = 0,$$

$$\frac{\partial \tau_{yx}}{\partial x} + \frac{\partial \sigma_y}{\partial y} + \frac{\partial \tau_{yz}}{\partial z} = 0, \qquad \text{(B.1)}$$

$$\frac{\partial \tau_{zx}}{\partial x} + \frac{\partial \tau_{zy}}{\partial y} + \frac{\partial \sigma_z}{\partial z} = 0.$$

(b) Strain-displacement relationships:

$$\varepsilon_x = \frac{\partial u}{\partial x}, \qquad \varepsilon_y = \frac{\partial v}{\partial y}, \qquad \varepsilon_z = \frac{\partial w}{\partial z},$$

$$\gamma_{xy} = \frac{\partial u}{\partial y} + \frac{\partial v}{\partial x}, \qquad \gamma_{yz} = \frac{\partial v}{\partial z} + \frac{\partial w}{\partial y}, \qquad \gamma_{zx} = \frac{\partial w}{\partial x} + \frac{\partial u}{\partial z}. \qquad \text{(B.2)}$$

(c) Compatibility equations:

$$\frac{\partial^2 \varepsilon_x}{\partial y^2} + \frac{\partial^2 \varepsilon_y}{\partial x^2} = \frac{\partial^2 \gamma_{xy}}{\partial x \partial y},$$

$$\frac{\partial^2 \varepsilon_y}{\partial z^2} + \frac{\partial^2 \varepsilon_z}{\partial y^2} = \frac{\partial^2 \gamma_{yz}}{\partial y \partial z}, \qquad \text{(B.3)}$$

$$\frac{\partial^2 \varepsilon_z}{\partial x^2} + \frac{\partial^2 \varepsilon_x}{\partial z^2} = \frac{\partial^2 \gamma_{zx}}{\partial z \partial x}.$$

Note that (B.3) follows from (B.2).

(d) Stress-strain relationships:

$$\varepsilon_x = \frac{1}{E}\left[\sigma_x - \nu(\sigma_y + \sigma_z)\right],$$

$$\varepsilon_y = \frac{1}{E}\left[\sigma_y - \nu(\sigma_z + \sigma_x)\right],$$

(continued)

$$\varepsilon_z = \frac{1}{E}\left[\sigma_z - \nu(\sigma_x + \sigma_y)\right] ,$$

and

$$\left.\begin{aligned} \tau_{xy} &= \tau_{yz} = G\,\gamma_{xy} = G\,\gamma_{yx} \ , \\ \tau_{yz} &= \tau_{zy} = G\,\gamma_{yz} = G\,\gamma_{zy} \ , \\ \tau_{zx} &= \tau_{xz} = G\,\gamma_{zx} = G\,\gamma_{xz} \ . \end{aligned}\right\} \qquad (B.4)$$

Note that the above equations use standard terminology.

We take the plane normal to the tube axis as the (y,z)-plane. A state of plane strain exists in that plane, if the displacements obey the following relations

$$\left.\begin{aligned} u &= 0 \ , * \\ v &= v(y,z) \ , \\ w &= w(y,z) \ . \end{aligned}\right\} \qquad (B.5)$$

From (B.5) and (B.2), we get

$$\left.\begin{aligned} \varepsilon_x &= \frac{\partial u}{\partial x} \equiv 0 \ , \\ \gamma_{xy} &= \frac{\partial u}{\partial y} + \frac{\partial v}{\partial x} \equiv 0 \ , \\ \gamma_{zx} &= \frac{\partial w}{\partial x} + \frac{\partial u}{\partial z} \equiv 0 \ . \end{aligned}\right\} \qquad (B.6)$$

Eqn.(B.1), making use of shear relations in (B.4) and (B.6), yields

$$\left.\begin{aligned} \frac{\partial \sigma_x}{\partial x} &= 0 \ , \\ \frac{\partial \sigma_y}{\partial y} + \frac{\partial \tau_{yz}}{\partial z} &= 0 \ , \\ \frac{\partial \sigma_z}{\partial z} + \frac{\partial \tau_{zy}}{\partial y} &= 0 \ . \end{aligned}\right\} \qquad (B.7)$$

---

* The statement $\equiv 0$ means identically zero, i.e. all derivatives are also zero.

Substituting the normal strain relation ($\varepsilon_x = 0$) of (B.6) into (B.4), we get

$$\sigma_x = \nu(\sigma_y + \sigma_z) \ . \tag{B.8}$$

The other two normal strain relations of (B.4) become, upon substitution of (B.8),

$$\varepsilon_y = \frac{1+\nu}{E} \left[(1-\nu)\sigma_y - \nu\sigma_z\right] \ ,$$

$$\varepsilon_z = \frac{1+\nu}{E} \left[(1-\nu)\sigma_z - \nu\sigma_y\right] \ . \tag{B.9}$$

Using the fact that $\tau_{yz} = \tau_{zy}$, the last two equations of (B.7) can be lumped, after differentiation yielding

$$\frac{\partial^2\sigma_y}{\partial y^2} + \frac{\partial^2\sigma_z}{\partial z^2} + 2\,\frac{\partial\tau_{yz}}{\partial y\partial z} = 0 \ . \tag{B.10}$$

Now, recall the fundamental relation

$$G = \frac{E}{2(1+\nu)} \ . \tag{B.11}$$

Making use of the (shear) stress-strain relation of (B.4), and using (B.11), eqn.(B.10) becomes

$$\frac{\partial^2\sigma_y}{\partial y^2} + \frac{\partial^2\sigma_z}{\partial z^2} + \frac{E}{(1+\nu)}\,\frac{\partial^2\gamma_{yz}}{\partial y\partial z} = 0 \ ,$$

and using (B.3), the above equation becomes

$$\frac{\partial^2\sigma_y}{\partial y^2} + \frac{\partial^2\sigma_z}{\partial z^2} + \frac{E}{(1+\nu)}\left[\frac{\partial^2\varepsilon_y}{\partial z^2} + \frac{\partial^2\varepsilon_z}{\partial y^2}\right] = 0 \ . \tag{B.12}$$

From eqs.(B.9) and (B.12), we get

$$\frac{\partial^2\sigma_y}{\partial y^2} + \frac{\partial^2\sigma_y}{\partial z^2} + \frac{\partial^2\sigma_z}{\partial y^2} + \frac{\partial^2\sigma_z}{\partial z^2} = 0 \ ,$$

which is rewritten

$$\left(\frac{\partial^2}{\partial y^2} + \frac{\partial^2}{\partial z^2} \right) (\sigma_y + \sigma_z) = 0 \ . \tag{B.13}$$

To solve (B.7) and (B.13), Airy's stress function is used, namely

$$\Psi = \Psi(y,z) \ , \tag{B.14}$$

such that

$$\left.\begin{aligned} \sigma_y &= \frac{\partial^2 \Psi}{\partial z^2} \ , \\ \sigma_z &= \frac{\partial^2 \Psi}{\partial y^2} \ , \\ \text{and} \\ \tau_{yz} &= \frac{-\partial^2 \Psi}{\partial y \partial z} \ . \end{aligned}\right\} \tag{B.15}$$

Note that, by (B.15), the last two equations of (B.7) are satisfied.

Substituting the normal stress relations of (B.15) into (B.13) yields

$$\left(\frac{\partial^2}{\partial y^2} + \frac{\partial^2}{\partial z^2} \right) \left(\frac{\partial^2 \Psi}{\partial z^2} + \frac{\partial^2 \Psi}{\partial y^2} \right) = 0 \ . \tag{B.16}$$

In polar coordinates (r,θ)*, eqn.(B.16) becomes

$$\left(\frac{\partial^2}{\partial r^2} + \frac{1}{r}\frac{\partial}{\partial r} + \frac{1}{r^2}\frac{\partial^2}{\partial \theta^2} \right) \left(\frac{\partial^2 \Psi}{\partial r^2} + \frac{1}{r}\frac{\partial \Psi}{\partial r} + \frac{1}{r^2}\frac{\partial^2 \Psi}{\partial \theta^2} \right) = 0 \ . \tag{B.17}$$

Furthermore, recall the rules for two-dimensional partial derivatives:

$$\left.\begin{aligned} \frac{\partial^2}{\partial y^2} &= \cos^2\theta \frac{\partial^2}{\partial r^2} - \frac{\sin 2\theta}{r}\frac{\partial^2}{\partial r \partial \theta} + \frac{\sin^2\theta}{r^2}\frac{\partial^2}{\partial \theta^2} + \frac{\sin^2\theta}{r}\frac{\partial}{\partial r} + \frac{\sin 2\theta}{r^2}\frac{\partial}{\partial \theta} \ , \\ \frac{\partial^2}{\partial z^2} &= \sin^2\theta \frac{\partial^2}{\partial r^2} + \frac{\sin 2\theta}{r}\frac{\partial^2}{\partial r \partial \theta} + \frac{\cos^2\theta}{r^2}\frac{\partial^2}{\partial \theta^2} + \frac{\cos^2\theta}{r}\frac{\partial}{\partial r} - \frac{\sin 2\theta}{r^2}\frac{\partial}{\partial \theta} \ , \\ \frac{\partial^2}{\partial y \partial z} &= \frac{\sin 2\theta}{2}\frac{\partial^2}{\partial r^2} + \frac{\cos 2\theta}{r}\frac{\partial^2}{\partial r \partial \theta} - \frac{\sin 2\theta}{2r^2}\frac{\partial^2}{\partial \theta^2} - \frac{\sin 2\theta}{2r}\frac{\partial}{\partial r} - \frac{\cos 2\theta}{r^2}\frac{\partial}{\partial \theta} \ . \end{aligned}\right\} \tag{B.18}$$

---

* $\theta = 0$ being along the positive y-axis (unlike the convention in the main body of the Thesis.

The problem is simplified by making use of the fact that we have symmetry with respect to θ.

We have (at $\theta = 0$):

$$\left.\begin{aligned} &\sigma_y\big|_{\theta=0} = \sigma_r\big|_{\theta=0} \ , \\ &\sigma_z\big|_{\theta=0} = \sigma_\theta\big|_{\theta=0} \ , \\ &\varepsilon_y\big|_{\theta=0} = \varepsilon_r\big|_{\theta=0} \ , \\ &\varepsilon_z\big|_{\theta=0} = \varepsilon_\theta\big|_{\theta=0} \ , \\ &\tau_{yz}\big|_{\theta=0} = \tau_{r\theta}\big|_{\theta=0} \ . \end{aligned}\right\} \qquad \text{(B.19)}$$

From (B.19) and (B.8), we can write

$$\sigma_x\big|_{\theta=0} = \nu\left(\sigma_r\big|_{\theta=0} + \sigma_\theta\big|_{\theta=0}\right) \ ,$$

but, by symmetry, we can say

$$\sigma_x = \nu(\sigma_r + \sigma_\theta) \ . \qquad \text{(B.20)}$$

Similarly, (B.9) can be written in the form

$$\left.\begin{aligned} &\varepsilon_r = \frac{1+\nu}{E}\left[(1-\nu)\sigma_r - \nu\sigma_\theta\right] \ , \\ &\varepsilon_\theta = \frac{1+\nu}{E}\left[(1-\nu)\sigma_\theta - \nu\sigma_r\right] \ . \end{aligned}\right\} \qquad \text{(B.21)}$$

Likewise, using (B.19), (B.15) and (B.18) yields

$$\sigma_r\big|_{\theta=0} = \frac{1}{r^2}\frac{\partial^2\Psi}{\partial\theta^2} + \frac{1}{r}\frac{\partial\Psi}{\partial r} \ ,$$

$$\sigma_\theta\big|_{\theta=0} = \frac{\partial^2\Psi}{\partial r^2} \ ,$$

$$\tau_{r\theta}\big|_{\theta=0} = -\frac{\partial}{\partial r}\left(\frac{1}{r}\frac{\partial\Psi}{\partial\theta}\right) \ ,$$

but since we have no variations with θ, we have

$$\sigma_r = \frac{1}{r}\frac{d\Psi}{dr} ,$$

$$\sigma_\theta = \frac{d^2\Psi}{dr^2} , \qquad (B.22)$$

$$\tau_{r\theta} = 0.$$

Lastly, eqn.(B.17) takes the form

$$\left(\frac{d^2}{dr^2} + \frac{1}{r}\frac{d}{dr}\right)\left(\frac{d^2\Psi}{dr^2} + \frac{1}{r}\frac{d\Psi}{dr}\right) = 0 , \qquad (B.23)$$

the general solution of which is

$$\Psi(r) = A\cdot\ln(r/R) + Br^2\cdot\ln(r/R) + Cr^2 + D , \qquad (B.24)$$

where A, B, C, D and R are arbitrary constants.

Substitution of eqn.(B.24) into (B.22) yields

$$\left.\begin{aligned} \sigma_r &= \frac{A}{r^2} + B[1 + 2\ \ln(r/R)] + 2C , \\ \sigma_\theta &= -\frac{A}{r^2} + B[3 + 2\ \ln(r/R)] + 2C , \end{aligned}\right\} \qquad (B.25)$$

and, as before,

$$\tau_{r\theta} = 0 .$$

Recall the basic plane strain relations

$$\left.\begin{aligned} &\varepsilon_r = \frac{da}{dr} , \qquad \varepsilon_\theta = \frac{a}{r} , \\ &\gamma_{r\theta} = \frac{1}{r}\frac{\partial a}{\partial\theta} + \frac{\partial b}{\partial r} - \frac{b}{r} , \end{aligned}\right\} \qquad (B.26)$$

where a and b are the radial and circumferential displacements respectively.

Again by symmetry, a does not depend on θ, and $v = 0$; therefore, from (B.26), we get

$$\gamma_{r\theta} = 0 ,$$

which is in agreement with $\tau_{r\theta} = 0$ of (B.22).

Substituting the normal stresses of (B.25) into (B.21), and using the resulting normal strain equations in (B.26), we obtain

$$\frac{da}{dr} = \frac{1}{E}\left[(1-\nu^2)\left\{\frac{A}{r^2} + B[1 + 2\ \ln(r/R)] + 2C\right\} - \nu(1+\nu)\left\{\frac{-A}{r^2} + B[3 + 2\ \ln(r/R)] + 2C\right\}\right] , \tag{B.27}$$

and

$$a = \frac{r}{E}\left[(1-\nu^2)\left\{\frac{-A}{r^2} + B[3 + 2\ \ln(r/R)] + 2C\right\} - \nu(1+\nu)\left\{\frac{A}{r^2} + B[1 + 2\ \ln(r/R)] + 2C\right\}\right] . \tag{B.28}$$

Differentiating eqn.(B.28) with respect to r and using the resulting equation in (B.27), we get

$4(1-\nu)B = 0$, i.e.

$$B = 0 . \tag{B.29}$$

From (B.29) and (B.25), we have

$$\sigma_r = \frac{A}{r^2} + 2C ,$$
$$\sigma_\theta = \frac{-A}{r^2} + 2C . \tag{B.30}$$

The boundary conditions on σ_r are

$$\sigma_r\Big|_{r=r_1} = -p_1 ,$$
$$\sigma_r\Big|_{r=r_2} = -p_2 , \tag{B.31}$$

hence, from (B.31) and (B.30), we find the constants A and C, and consequently

$$\sigma_r = \frac{1}{r_2^2 - r_1^2}\left[\frac{r_1^2 r_2^2 (p_2 - p_1)}{r^2} + (r_1^2 p_1 - r_2^2 p_2)\right] , \tag{B.32}$$

$$\sigma_\theta = \frac{1}{r_2^2 - r_1^2} \left[\frac{- r_1^2 r_2^2 (p_2 - p_1)}{r^2} + (r_1^2 p_1 - r_2^2 p_2) \right] .$$

Finally, we substitute (B.32) into eqn.(B.20) to get the stress in the axial direction

$$\sigma_x = \frac{2\nu (r_1^2 p_1 - r_2^2 p_2)}{r_2^2 - r_1^2} . \qquad (B.33)$$

The case of interest here is that of a solid rod immersed in a fluid with static pressure p. Therefore let

$$\sigma = \lim_{r_1, p_1 \to 0} \sigma_x \Big|_{p_2 = p} , \qquad (B.34)$$

From eqs.(B.34) and (B.33), we obtain

$$\sigma = -2\nu p . \qquad (B.35)$$

Note that, in the actual experimental set-up, the static pressure varies (linearly) along the x-axis. For a longitudinal force balance on an arbitrary element* of the cylinder, we must have a constant tension§ throughout. This occurs by a longitudinal stress redistribution through a varying strain. The pressure gradient in the fluid is relatively small, hence, the assumption of plane strain is still valid.

From eqn.(B.35), we have

$$T(x) = A\, \sigma(x) , \qquad (B.36)$$

where A is the cross-sectional area of the cylinder. $\sigma(x)$ is given by (B.35) with $p = p(x)$.

The average (through stress redistribution) tension is

$$T = \frac{1}{L} \int_0^L T(\chi)\, d\chi , \qquad (B.37)$$

---

* The fluid static pressure is the sole effect considered here.

§ In our case, the tension is negative.

where L is the cylinder length.

From (B.35), (B.36), and (B.37), we have

$$T = -2\nu\bar{p}A\,, \tag{B.38}$$

where

$$\bar{p} = \frac{1}{L}\int_0^L p(x)\,dx\,,$$

the average static pressure.

Appendix C

Downstream boundary conditions

New boundary conditions, reflecting the actual experimental set-up, are derived here. This involves the term $(T + pA)|_{x=L}$ of eqn.(2.11).

The flexible rubber cylinders are mounted (see Fig. 3) in the test channel using glued-on rigid end attachments. The upstream (upper) ends are clamped in all tests. The "clamped" downstream (lower) ends may have one of two "status", specified by the parameter δ:

$$\delta = \begin{cases} 0, \text{ for free axial sliding, but no rotation,} \\ 1, \text{ for full clamping.} \end{cases} \tag{C.1}$$

We first establish the boundary conditions in the case of $\delta = 0$.

(a) Free Axial Sliding (no Rotation)

The test channel set-up is made in the following sequence:

(1) The cylinders are hung vertically, being clamped on top and "supporting" the sliding lower attachment(s) (weight) at the bottom;
(2) The water tunnel is filled;
(3) A downward velocity U is imposed on the fluid, keeping the static pressure constant.

A force balance (see Fig. 5) on the lower attachment yields

$$T\Big|_{x=L+\delta L} = F_L L_1 + W - p_{b_1} A_1 - p_{b_2} A_2 \ , \tag{C.2}$$

for the tension at the lower end of the cylinder.

The base pressures p_{b_1} and p_{b_2} are assumed to result from the static pressure (at $U = 0$), reduced by a form drag effect, i.e.

$$p_{b_1} A_1 = A_1 p\Big|_{x=L+\delta L+L_1} - \frac{1}{2}\rho D^2 U^2 C_{b_1} \ , \tag{C.3}$$

and

$$p_{b_2} A_2 = A_2 p\Big|_{x=L+\delta L+L_1+L_2} - \frac{1}{2}\rho D^2 U^2 C_{b_2} \ , \tag{C.4}$$

where C_{b_1} and C_{b_2} are base drag coefficients similar to that used by Paidoussis [43].

Note that in (C.2), (C.3), and (C.4), δL is the elongation of the cylinders at $x = L$, due to longitudinal forces. It is shown below (see table in subsection after eqn.(C.8)) that $\delta L/L \ll 1$.

Using (2.2) and (2.8), together with (C.2), (C.3) and (C.4), we get

$$T\Big|_{x=L+\delta L} = W - \rho A g L_0 + \frac{1}{2}\rho D^2 U^2 C_b + \frac{1}{2}\rho D U^2 C_f \left[L_1 + L_0 \frac{D}{D_h}\right] - Ap\Big|_{x=L+\delta L} , \qquad (C.5)$$

where

$$C_b = C_{b_1} + C_{b_2} , \qquad (C.6)$$

and

$$L_0 = L_1 + L_2 \frac{A_2}{A} . \qquad (C.7)$$

It is shown below that, for typical experimental data, $\delta L/L$ is much smaller than 1, hence we rewrite (C.5) as

$$(T + pA)\Big|_{x=L} = W - \rho A g L_0 + \frac{1}{2}\rho D^2 U^2 C_b + \frac{1}{2}\rho D U^2 C_f \left[L_1 + L_0 \frac{D}{D_h}\right] . \qquad (C.8)$$

Typical cylinder elongation

We consider the following diagram:

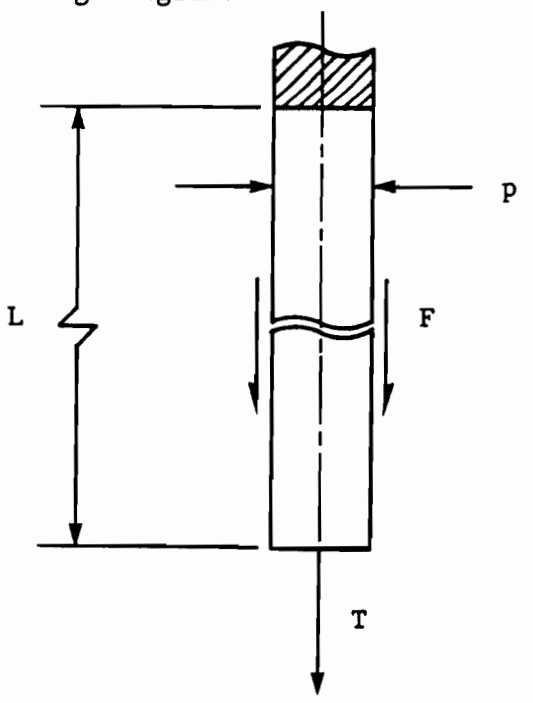

where,

L is the original (unstressed) length,

p is the static pressure (circumferential),

F is the overall force per unit length, resulting from the cylinder weight and from fluid longitudinal frictional forces, and

T is the lower end tension.

We take the total elongation δL as a linear combination of:

(1) δL_1, due to T,

(2) δL_2, due to F, and

(3) δL_3, due to p,

that is

$$\delta L = \delta L_1 + \delta L_2 + \delta L_3 \ . \tag{C.9}$$

Assuming $\delta L/L \ll 1$,* we can write (C.5) as

$$T = T\Big|_{x=L} = W - \rho A g L_0 + \frac{1}{2}\rho D^2 U^2 C_b + \frac{1}{2}\rho D U^2 C_f \left(L_1 + L_0 \ \frac{D}{D_h}\right) - Ap\Big|_{x=L} .$$

But, we have

$$p\Big|_{x=L} = \bar{p} + \frac{\partial p}{\partial x}\ \frac{L}{2} \ ;\S$$

therefore, from the above two equations and (2.8), we obtain

$$T = W - A\bar{p} - \rho A g\left(L_0 + \frac{L}{2}\right) + \frac{1}{2}\rho D^2 U^2 C_b + \frac{1}{2}\rho D U^2 C_f \left[\ L_1 + \frac{D}{D_h}\left(L_0 + \frac{L}{2}\right)\right] . \tag{C.10}$$

Also, from fundamental stress-strain relationships, we have

$$\frac{\delta L_1}{L} = \frac{T}{AE} \ . \tag{C.11}$$

Substituting (C.10) into (C.11), we get

$$\delta L_1 = \frac{L}{AE}\left\{W - A\bar{p} - \rho A g\left(L_0 + \frac{L}{2}\right) + \frac{1}{2}\rho D^2 U^2 C_b + \frac{1}{2}\rho D U^2 C_f \left[L_1 + \frac{D}{D_h}\left(L_0 + \frac{L}{2}\right)\right]\right\} . \tag{C.12}$$

---

* To be proven below.

§ $\bar{p} = \frac{1}{L}\int_0^L p\ d\chi = p|_{x=L/2}$, since $\partial p/\partial x$ is constant.

Now, we have (see Appendix B of Ref. [75])

$$F = mg + \frac{1}{2}\rho DU^2 C_f \ , \tag{C.13}$$

and furthermore,*

$$\frac{\delta L_2}{L} = \frac{\rho_e g L}{2E} \ , \tag{C.14}$$

where ρ_e is an "equivalent" density:

$$\rho_e = \frac{m}{A} + \frac{1}{2}\frac{\rho DU^2 C_f}{gA} \ . \tag{C.15}$$

Consequently, from (C.13), (C.14), and (C.15),

$$\delta L_2 = \frac{L^2}{2AE}\left(mg + \frac{1}{2}\rho DU^2 C_f\right) \ . \tag{C.16}$$

Finally, if L were fixed, the static pressure would induce a compressive axial force of (see Appendix B)

$$C = 2\nu \bar{p} A \ . \tag{C.17}$$

Hence, taking the elongation required for "compression relief" as δL_3, with

$$\frac{\delta L_3}{L} = \frac{C}{AE} \ , \tag{C.18}$$

then substitution of (C.17) into (C.18) yields

$$\delta L_3 = \frac{2\nu \bar{p}}{E} \ . \tag{C.19}$$

Using (C.12), (C.16), and (C.19) in (C.9) yields

$$\frac{\delta L}{L} = \frac{1}{AE}\left\{W + \frac{mgL}{2} - (1 - 2\nu)\bar{p}A - \rho Ag\left(L_0 + \frac{L}{2}\right) + \frac{1}{2}\rho D^2 U^2 C_b + \frac{1}{2}\rho DU^2 C_f\left[\left(L_1 + \frac{L}{2}\right) + \frac{D}{D_h} \cdot \left(L_0 + \frac{L}{2}\right)\right]\right\} \ . \tag{C.20}$$

For numerical computation of a typical $\delta L/L$, we will use (C.7), (C.20), and eqn.(2.6), which reads

---

* See *Theory of Elasticity* (1961) by S.P. Timoshenko & J.N. Goodier, Ch.9.

$$A_N = \pi(R_c^2 - KR^2) \ ,$$

and (alternate form of eqn.(2.9))

$$D_h = \frac{2}{\pi} \frac{A_N}{(R_c + KR)} \ .$$

The following typical (experimental) data is used:

(i) Test channel and cylinders:

$D \simeq 2.53$ cm (0.996 in).

$A = \frac{\pi}{4} D^2 \simeq 5.03$ cm^2 (0.779 in^2).

$R = \frac{D}{2} \simeq 1.27$ cm (0.498 in).

$K = 4$.

$L = 47.0$ cm (18.5 in).

$R_c \simeq 10.24$ cm (4.03 in).

$D_h \simeq 12.85$ cm (5.06 in).

(ii) Fluid:

$\bar{p} \simeq 69$ KPa (10 lbf/in^2).

$\rho \simeq 1.00$ gm/cm^3 (62.4 lbm/ft^3).

$U \simeq 6.1$ m/s [max.] (20 ft/sec).

(iii) Cylinder material (Dow Corning Silastic E rubber, lot # QL 119778):

$E \simeq 2780$ KPa (403 lbf/in^2).

$m \simeq 0.577$ Kgm/m (0.388 lbm/ft).

$\nu \simeq 0.47$.

(iv) Lower attachment:

$W \simeq 0.34$ N (0.077 lbf).

$L_1 \simeq 1.09$ cm (0.43 in).

$L_2 \simeq 5.08$ cm (2.00 in).

$$A_2 = \frac{\pi}{4} D_2^2 \Big|_{D_2 \simeq 0.60 \text{ cm}} .$$

$L_0 \simeq 1.37$ cm (0.54 in).

Finally, we determine the base drag and friction coefficients:

Recall, from (2.52),

$$C_b = \frac{\pi}{4} c_b ,$$

and

$$C_f = \frac{\pi}{4} c_f .$$

A reasonable value for c_b is 0.20 (experimental value; see Appendix H of [72]). Hence, we take

$C_b \simeq 0.16$.

For $\varepsilon = L/D \simeq 20$, a reasonable value of εc_f is 0.30 (see Ch. 5 for details). Hence, we take

$C_f \simeq 0.013$.

Computations were made for a number of values of U. They are tabulated below.

U		$\delta L_1/L$	$\delta L_2/L$	$\delta L_3/L$	$\delta L/L$
(m/s)	(ft/sec)	due to T	due to F	due to P	overall
0	0	-0.0237	0.0010	0.0233	0.0006
0.9	3	-0.0237	0.0010	0.0233	0.0006
1.8	6	-0.0236	0.0010	"	0.0007
2.7	9	-0.0234	0.0011	"	0.0010
3.7	12	-0.0231	0.0013	"	0.0015
4.6	15	-0.0228	0.0015	"	0.0020
5.5	18	-0.0224	0.0018	"	0.0027

We see that $\delta L/L < 0.3\%$, hence, δL is negligible. Note that the two dominant factors, the tension T^* and the static pressure p, essentially cancel each other. Hence, eqn.(C.8) is correct.

We next examine the case of $\delta = 1$.

(b) Full Clamping

In this case, the test channel set-up is made in the following sequence:

(1) The cylinders are hung vertically, being clamped on top and "supporting" the sliding lower attachment(s) (weight) at the bottom.
(2) Pre-tensioning is imposed (if any) by hanging a weight $\bar{T}$ to the lower attachment(s).
(3) Lower attachments are locked in place with set-screws and the pre-tensioning weights are removed.
(4) The water tunnel is filled.
(5) A downward velocity U is imposed on the fluid, keeping the static pressure in the tunnel constant.

Hence, before locking the lower attachment (i.e. clamping), the tension at the downstream (lower) end of the cylinder is

$$T_0\Big|_{x=-L+\delta L} = W + \bar{T} \ . \tag{C.21}$$

After clamping and filling the tunnel, the static pressure p acts on the circumferential surface and induces an axial compressive load along the cylinder(s), yielding (see Appendix B) a change in tension

$$\Delta T_1\Big|_{x=-L+\delta L} = -2\nu\bar{p}A \ , \tag{C.22}$$

where

$$\bar{p} = \frac{1}{L}\int_0^L p\cdot d\chi = p\Big|_{x=-L/2} . \S \tag{C.23}$$

---

* Negative because of buoyancy effects.

§ Inspection of eqn.(2.8) reveals that $\partial p/\partial x$ is independent of x.

It should be noted that the flexible cylinder is bonded directly to its top and bottom rigid supports; consequently, the stresses at the cylinder -support interface(s) are not affected by buoyancy forces.

Imposing the velocity U on the fluid causes a longitudinal friction force $F_L L$ to act on the cylinder. By symmetry, half the force appears as a compressive load at the lower end, causing the change in tension

$$\Delta T_2 \Big|_{x=-L+\delta L} = -F_L \frac{L}{2} .$$

From the above equation and (2.2), we get

$$\Delta T_2 \Big|_{x=-L+\delta L} = \frac{1}{2}\rho D U^2 C_f \frac{L}{2} . \tag{C.24}$$

Consequently, the lower end tension is

$$T\Big|_{x=-L+\delta L} = T_0 \Big|_{x=-L+\delta L} + \Delta T_1 \Big|_{x=-L+\delta L} + \Delta T_2 \Big|_{x=-L+\delta L} . \tag{C.25}$$

Substituting (C.21), (C.22), and (C.24) into (C.25) yields

$$T\Big|_{x=-L+\delta L} = W + \bar{T} - 2\nu \bar{p} A - \frac{1}{2}\rho D U^2 C_f \frac{L}{2} ; \tag{C.26}$$

but, we can write

$$p\Big|_{x=-L+\delta L} = \bar{p} + \frac{\partial p}{\partial x}\left(\frac{L}{2} + \delta L\right) ,$$

or, multiplying the above equation by the area A and using eqn.(2.8) for the $A(\partial p/\partial x)$ term, we get

$$Ap\Big|_{x=-L+\delta L} = \bar{p}A + \rho A g \frac{L}{2} - \frac{1}{2}\rho D U^2 C_f \frac{D}{D_h}\frac{L}{2} + \delta L\left(\rho A g - \frac{1}{2}\rho D U^2 C_f \frac{D}{D_h}\right) . \tag{C.27}$$

Adding $Ap\Big|_{x=-L+\delta L}$ to both sides of (C.26), and using (C.27), we obtain

$$(T + pA)\Big|_{x=-L+\delta L} = W + \bar{T} + (1 - 2\nu)\bar{p}A + \rho A g \frac{L}{2} - \frac{1}{2}\rho D U^2 C_f \frac{L}{2}\left(1 + \frac{D}{D_h}\right) + \delta L\left(\rho A g - \frac{1}{2}\rho D U^2 C_f \frac{D}{D_h}\right) . \tag{C.28}$$

It is shown below that, for typical experimental data, $\delta L/L$ is much smaller than 1, hence we rewrite (C.28) as

$$(T + pA)\Big|_{x=L} = W + \tilde{T} + (1 - 2\nu)\bar{p}A + \rho Ag\,\frac{L}{2} - \frac{1}{2}\rho DU^2 C_f\,\frac{L}{2}\left(1 + \frac{D}{D_h}\right) . \qquad (C.29)$$

Typical cylinder elongation

Consider the following diagram:

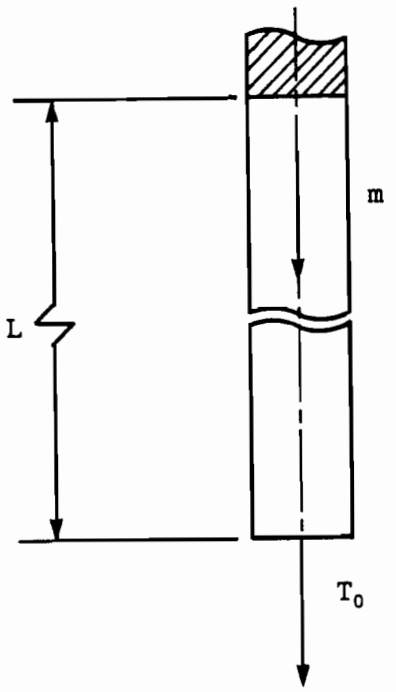

where

L is the original (unstressed) length,

m is the mass per unit length of cylinder, and

T_0 is the lower end tension, before the lower end is locked (clamped).

We take the total elongation δL as a linear combination of

(1) δL_1, due to T_0,

(2) δL_2, due to m,

that is,

$$\delta L = \delta L_1 + \delta L_2 . \qquad (C.30)$$

Assuming $\delta L/L \ll 1$ (proven shortly), we can write (C.21) as

$$T_0\Big|_{x=L} = T_0 = W + \tilde{T} . \qquad (C.31)$$

Using (C.11) and (C.31), we get

$$\frac{\delta L_1}{L} = \frac{W + \bar{T}}{AE} \quad . \tag{C.32}$$

For elongation of bars under distributed loading, we have*

$$\frac{\delta L_2}{L} = \frac{mgL}{2AE} \quad . \tag{C.33}$$

From (C.30), (C.32), and (C.33), we obtain

$$\frac{\delta L}{L} = \frac{1}{AE}\left(W + \bar{T} + \frac{mgL}{2}\right) \quad . \tag{C.34}$$

We use the experimental data listed previously in this Appendix, together with

$\bar{T} = 2.30$ N (0.516 lbf).

We obtain,

$$\frac{\delta L}{L} \simeq 0.0029 \ ,$$

of which $\simeq 0.0016$ is due to $\bar{T}$, and $\simeq 0.0013$ is due to W and m.

We see that $\delta L/L < 0.3\%$, hence negligible.

(c) Downstream Boundary Conditions - General Case

The two different boundary conditions (free axial sliding, but no rotation, and full clamping) are lumped into one $(T + pA)\big|_{x=L}$ term by using the "status" parameter δ, that is, from (C.1), (C.8), and (C.29); we can write

$$(T + pA)\Big|_{x=L} = \delta\left[W + \bar{T} + (1 - 2\nu)\bar{p}A + \rho Ag\,\frac{L}{2} - \frac{1}{2}\rho DU^2C_f\left(1 + \frac{D}{D_h}\right)\frac{L}{2}\right] + (1 - \delta)$$

$$\cdot\left[W - \rho AgL_0 + \frac{1}{2}\rho D^2U^2C_b + \frac{1}{2}\rho DU^2C_f\left(L_1 + L_0\,\frac{D}{D_h}\right)\right] \quad . \tag{C.35}$$

---

* See *Theory of Elasticity* (1961) by S.P. Timoshenko & J.N. Goodier, Ch.9.

Appendix D

Visco-hysteretic damping--mathematical model

Since we are interested in beam dynamics (a continuous system), rather than the "usual" mass-spring-damper system, we shall examine the former.

(a) Viscoelastically damped beam in free vibration

The lateral force balance on a freely vibrating beam is a reduced form of eqn.(2.17), namely

$$\frac{\partial Q}{\partial x} - m \frac{\partial^2 y}{\partial t^2} = 0 \ , \tag{D.1}$$

where Q is the lateral shear force, m the mass per unit length, y the lateral deflection of the beam, x the longitudinal beam coordinate, and t the time.

From classical beam theory, the bending moment for a Bernoulli-Euler beam with viscoelastic damping of the Kelvin-Voigt type is

$$M = EI \frac{\partial^2 y}{\partial x^2} + \mu I \frac{\partial}{\partial t}\left[\frac{\partial^2 y}{\partial x^2}\right] \ , \tag{D.2}$$

where M is the bending moment, E is the modulus of elasticity, I is the second moment of area, and μ is the viscoelastic damping coefficient.

Also, recall eqn.(2.16):

$$Q + \frac{\partial M}{\partial x} = 0 \ . \tag{D.3}$$

Combining eqs.(D.1), (D.2), and (D.3), we get the equation of motion

$$m \frac{\partial^2 y}{\partial t^2} + \mu I \frac{\partial}{\partial t}\left[\frac{\partial^4 y}{\partial x^4}\right] + EI \frac{\partial^4 y}{\partial x^4} = 0 \ . \tag{D.4}$$

Now, $y = y(x,t)$ may be expanded in terms of the natural (undamped) modes of vibration of a beam with the boundary condition of interest, i.e.

$$y = \sum_{n=1}^{\infty} y_n \ , \tag{D.5}$$

with

$$y_n = Y_n(x)\left[P_n e^{j\Omega_n t} + P_n^* e^{-j\Omega_n^* t}\right] , \quad n=1,2,\ldots,\infty , \tag{D.6}$$

where $Y_n(x)$ is the n^{th} natural beam deflection mode, P_n are complex coefficients, and Ω_n are complex frequencies whose real part represent the frequency of oscillation and imaginary part the rate of exponential attenuation of the vibration amplitude. Note that eqn.(D.6) is real, as it should be.

As shown later, we will need the energy dissipated per cycle of vibration. We shall investigate the (arbitrary) n^{th} mode. Now, the energy dissipated per unit length is

$$E_n(x) = \int_{\text{cycle}} f_n(x,t) \cdot \frac{\partial y_n(x,t)}{\partial t}\, dt , \quad n=1,2,\ldots,\infty , \tag{D.7}$$

where $f_n(x,t)$ is the viscoelastic damping force per unit length which reads, from eqn.(D.4),

$$f_n = \mu I \frac{\partial}{\partial t}\left(\frac{\partial^4 y_n}{\partial x^4}\right) , \quad n=1,2,\ldots,\infty , \tag{D.8}$$

and where $[\partial y_n(x,t)/\partial t]\cdot dt$ represents the distance travelled owing to the (lateral) motion of the beam. Hence, eqn.(D.7) is an integral of the work performed (per unit length), over a cycle of motion, by the viscoelastic forces. Eqs.(D.6), (D.7), and (D.8) yield

$$E_n(x) = -\mu I \cdot Y_n(x) \frac{d^4 Y_n(x)}{dx^4} \cdot \int_0^{2\pi/\mathrm{Re}(\Omega_n)} \left[\Omega_n P_n e^{j\Omega_n t} - \Omega_n^* P_n^* e^{-j\Omega_n^* t}\right]^2 \cdot dt , \quad n=1,2,\ldots,\infty , \tag{D.9}$$

where the period is given by $2\pi/\mathrm{Re}(\Omega_n)$, the latter denominator being the real part of Ω_n (i.e. the frequency of oscillation).

It will shortly prove useful to "decompose" Ω_n and P_n; let

$$\Omega_n = F_n + D_n j , \quad n=1,2,\ldots,\infty , \tag{D.10}$$

and

$$P_n = a_n + b_n j \quad , \qquad n = 1,2,\ldots,\infty \, . \tag{D.11}$$

Note that, from eqn.(D.10),

$$\mathrm{Re}(\Omega_n) = F_n \quad , \qquad n = 1,2,\ldots,\infty \, . \tag{D.12}$$

Using eqn.(D.12) in (D.9), and expanding, we get

$$E_n(x) = -\mu I \cdot Y_n(x) \frac{d^4 Y_n(x)}{dx^4} \left\{ \Omega_n^2 P_n^2 \cdot \int_0^{2\pi/F_n} e^{2j\Omega_n t}\, dt + \Omega_n^{*2} P_n^{*2} \cdot \int_0^{2\pi/F_n} e^{-2j\Omega_n^* t}\, dt \right.$$

$$\left. - 2\,\Omega_n \Omega_n^* P_n P_n^* \cdot \int_0^{2\pi/F_n} e^{j(\Omega_n - \Omega_n^*)t}\, dt \right\} \quad , \qquad n = 1,2,\ldots,\infty \, .$$

Making use of eqs.(D.10) and (D.11), the above equation can be integrated to yield

$$E_n(x) = \mu I \cdot Y_n(x) \frac{d^4 Y_n(x)}{dx^4} \left[1 - e^{-4\pi D_n/F_n} \right] \cdot \left\{ \frac{\Omega_n \Omega_n^* P_n P_n^*}{D_n} + \left[2\, a_n b_n F_n \right. \right.$$

$$\left. \left. + \left(a_n^2 - b_n^2 \right) D_n \right] \right\} \quad , \qquad n = 1,2,\ldots,\infty \, . \tag{D.13}$$

In eqn.(D.13), it will prove more physically meaningful to use the amplitude and phase of y rather than its complex amplitude P_n, i.e. a_n and b_n; eqn.(D.6) can alternatively be written as

$$y_n = Y_n(x) \cdot A_n e^{-D_n t} \cos\left(F_n t + \phi_n\right) \quad , \qquad n = 1,2,..,\infty \, , \tag{D.14}$$

where it is readily shown that

$$A_n^2 = 4 \left(a_n^2 + b_n^2 \right)$$

$$= 4\, P_n P_n^* \quad , \text{ and} \tag{D.15}$$

$$\phi_n = \arctan\left(b_n / a_n\right) \quad , \qquad n = 1,2,\ldots,\infty \, ,$$

or conversely,

$$a_n = \frac{A_n}{2} \cos\left(\phi_n\right) \quad , \tag{D.16}$$

$$b_n = \frac{A_n}{2} \sin(\phi_n) , \qquad n = 1,2,\ldots,\infty .$$

Making use of eqs.(D.15) and (D.16), together with eqs.(D.10) and (D.11), into eqn.(D.13) yields

$$E_n(x) = \mu I \cdot Y_n(x) \frac{d^4 Y_n(x)}{dx^4} \frac{A_n^2}{4} \left(1 - e^{-4\pi D_n/F_n}\right) \cdot \left\{ \frac{F_n^2 + D_n^2}{D_n} + F_n \sin(2\phi_n) + D_n \cos(2\phi_n) \right\} , \qquad n = 1,2,\ldots,\infty . \tag{D.17}$$

The total energy dissipated along the beam is simply

$$E_n = \int_0^L E_n(x) \cdot dx , \tag{D.18}$$

where L is the length of the beam. From eqs.(D.17) and (D.18), we obtain

$$E_n = \frac{\mu I \beta_n^4 L^3 A_n^2}{4} \left(1 - e^{-4\pi D_n/F_n}\right) \cdot \left\{ \frac{F_n^2 + D_n^2}{D_n} + F_n \sin(2\phi_n) + D_n \cos(2\phi_n) \right\} , \tag{D.19}$$

$$n = 1,2,\ldots,\infty ,$$

where

$$\beta_n^4 = \frac{1}{L^3} \int_0^L Y_n(x) \frac{d^4 Y_n(x)}{dx^4} dx , \qquad n = 1,2,\ldots,\infty . \tag{D.20}$$

For the boundary conditions of interest here, that is clamped-clamped, we have (see Appendix G):

$$\beta_n = \frac{\rho_0 A}{EI} F_n^2 , \qquad n = 1,2,\ldots,\infty , \tag{D.21}$$

where ρ_0 is the beam density, A its cross-sectional area, E its modulus of elasticity, and I its second moment of area. F_n is the n^{th} natural frequency of the (undamped) beam vibrating in vacuo.

As is, equation (D.19) would not be easy to apply to cases of hysteretic damping (using the equivalent viscoelastic damping concepts illustrated in the next section). But, we note the following:

As $D_n/F_n \to 0$, we get

$$\lim_{D_n/F_n \to 0} E_n = \frac{\mu I \beta_n^4 L^3 A_n^2}{4} \left\{ \lim_{D_n/F_n \to 0} F_n \left[1 + \left(\frac{D_n}{F_n} \right)^2 \right] \frac{1 - e^{-4\pi D_n/F_n}}{D_n/F_n} \right.$$

$$\left. + \lim_{D_n/F_n \to 0} F_n \left(1 - e^{-4\pi D_n/F_n} \right) \left(\sin (2\phi_n) + \frac{D_n}{F_n} \cos (2\phi_n) \right) \right\} , \quad n = 1,2,\ldots,\infty .$$

By l'Hospital's rule,

$$\lim_{D_n/F_n \to 0} \frac{1 - e^{-4\pi D_n/F_n}}{D_n/F_n} = \lim_{D_n/F_n \to 0} \frac{(4\pi)\, e^{-\pi D_n/F_n}}{1} = 4\pi , \quad n = 1,2,\ldots,\infty ,$$

and furthermore,

$$\lim_{D_n/F_n \to 0} \left(1 - e^{-4\pi D_n/F_n} \right) = 0 , \quad n = 1,2,\ldots,\infty .$$

Applying the above results, we get

$$\lim_{D_n/F_n \to 0} E_n = \pi \mu I \beta_n^4 L^3 A_n^2 F_n , \quad n = 1,2,\ldots,\infty . \tag{D.22}$$

This equation shall shortly be shown to correspond to the case of steady state forced harmonic oscillation (as expected).

We now examine the "behaviour" of eqn.(D.19) for typical (measured) values of frequency of oscillation (F_n) and viscoelastic damping coefficients (D_n). For convenience, the equation can be rewritten as

$$E_n = \frac{\mu I \beta_n^4 L^3 A_n^2}{4} \left(1 - e^{-4\pi D_n/F_n} \right) \left(\frac{F_n^2 + D_n^2}{D_n} \right) \left[1 + \frac{D_n}{\sqrt{F_n^2 + D_n^2}} \sin (2\phi_n + \theta_n) \right] , \tag{D.23}$$

$$n = 1,2,\ldots,\infty ,$$

where

$$\theta_n = \arctan (D_n/F_n) , \quad n = 1,2,\ldots,\infty . \tag{D.24}$$

We see that E_n has a constant average value, $\bar{E}_n$, which is "modulated" sinusoidally by a function of the phase angle, $E_n(\phi_n)$. We can write

$$\frac{|E_n(\phi_n)|}{\bar{E}_n} = \frac{D_n}{\sqrt{F_n^2 + D_n^2}} \quad , \quad n = 1,2,\ldots,\infty \, . \tag{D.25}$$

The material properties of the cylinders used in water tunnel testing were measured (see Appendix R of Ref.[75]), and for a vertically hanging cantilever first beam mode. Typical values are

$$\begin{aligned} F_1 &\simeq 1.2 \text{ Hz} \simeq 7.54 \text{ rad/sec} \, , \\ \delta_1 &\simeq 0.038 \text{ (logarithmic decrement)}, \end{aligned} \tag{D.26}$$

so we find

$$D_1 \simeq 0.0456 \text{ (rad/sec)} \, ,$$

since

$$\delta_1 = 2\pi \frac{D_1}{F_1} \, . \tag{D.27}$$

Remark

Part of the energy dissipation was found to be due to hysteretic damping (see Appendix R of Ref.[75]); it is assumed here that δ_1 is entirely due to viscoelastic damping, which yields conservative results as D_1 is then overestimated.

The values in eqn.(D.26) yield, for eqn.(D.25):

$$\frac{|E_n(\phi_n)|}{\bar{E}_n} \simeq 0.6 \ \% \, , \tag{D.28}$$

i.e. the signal phase ϕ_1 can be ignored, at least for a first cantilever beam mode. The same is assumed here for the first clamped-clamped beam mode, and since the latter was found to be dominant in water tunnel tests, eqn.(D.28) will be considered applicable for higher modes as well, eventually allowing the general use of "equivalent" viscoelastic damping, for hysteretically damped systems.

Equation (D.23) (see also (D.19)) takes the reduced form

$$E_n = \frac{\mu I \beta_n^4 L^3 A_n^2}{4} \left(1 - e^{-4\pi D_n/F_n}\right) \left(\frac{F_n^2 + D_n^2}{D_n}\right) \, , \quad n = 1,2,\ldots,\infty \, , \tag{D.29}$$

no longer a function of ϕ_n .

Now, from eqs.(D.29) and (D.22), we find

$$\frac{E_n}{\lim_{D_n/F_n \to 0} E_n} = \frac{1 - e^{-4\pi D_n/F_n}}{4\pi F_n} \left[\frac{F_n^2 + D_n^2}{D_n}\right] , \quad n = 1,2,\ldots,\infty . \tag{D.30}$$

For the values of F_1 and D_1 given by eqn.(D.26), we obtain

$$\frac{E_1}{\lim_{D_1/F_1 \to 0} E_1} \simeq 0.96 . \tag{D.31}$$

Hence, for a typical case, the energy dissipated per cycle, in free vibration (first beam mode), is about 4% less than that for steady state vibration; consequently, the error in using an "equivalent" viscoelastic damping coefficient, as shown below, to apply to free vibration cases, will certainly be acceptable.

(b) Equivalent viscoelastic damping - hysteretic systems

For forced vibration of a viscoelastically damped Bernoulli-Euler beam, eqn.(D.4) takes the form

$$m \frac{\partial^2 y}{\partial t^2} + \mu I \frac{\partial}{\partial t}\left[\frac{\partial^4 y}{\partial x^4}\right] + EI \frac{\partial^4 y}{\partial x^4} = f , \tag{D.32}$$

where $f = f(x,t)$ is the force per unit length acting on the beam.

We wish to investigate the special case where f forces the beam to oscillate harmonically at constant amplitude, and in its n^{th} natural deflection mode. Generally, for the latter condition to occur, f cannot be fully separable in x and t, but nevertheless can take the simple form

$$f_n(x,t) = C_n(x)\, e^{jFt} + C_n^*(x)\, e^{-jFt} , \quad n = 1,2,\ldots,\infty , \tag{D.33}$$

where

$$C_n(x) = u_n(x) + j\, v_n(x) , \quad n = 1,2,\ldots,\infty . \tag{D.34}$$

Now, as desired, we let the response be

$$y_n = Y_n(x)\left[P_n e^{jFt} + P_n^* e^{-jFt}\right] , \qquad n = 1,2,\ldots,\infty , \tag{D.35}$$

i.e. constant amplitude harmonic oscillation in the n^{th} deflection mode, at the excitation frequency F.

The solution of eqn.(D.32), subject to eqs.(D.33), (D.34), and (D.35), simply yields, for the functions $u_n(x)$ and $v_n(x)$

$$\begin{aligned} u_n(x) &= \left[EI\,\frac{d^4Y_n(x)}{dx^4} - mF^2\,Y_n(x)\right]a_n - \mu IF\,\frac{d^4Y_n(x)}{dx^4}\,b_n , \\ v_n(x) &= \left[EI\,\frac{d^4Y_n(x)}{dx^4} - mF^2\,Y_n(x)\right]b_n + \mu IF\,\frac{d^4Y_n(x)}{dx^4}\,a_n , \end{aligned} \tag{D.36}$$

where $Y_n(x)$ is the desired deflection mode, a_n and b_n, i.e. P_n (see eqn. (D.11)), can be determined from the desired amplitude and phase of y_n (see eqn.(D.16)). F is the frequency of oscillation and E, I, m, and μ are properties of the beam.

Similarly to eqn.(D.7), the energy per unit length dissipated per cycle of oscillation is

$$E_n(x) = \int_{\text{cycle}} f_{V_n}(x,t)\cdot\frac{\partial y_n(x,t)}{\partial t}\,dt , \qquad n = 1,2,\ldots,\infty , \tag{D.37}$$

where $f_{V_n}(x,t)$ is the viscoelastic damping force (per unit length).

Proceeding as for the case of free vibration (preceding section), we obtain

$$E_n(x) = 4\pi\mu I Y_n(x)\,\frac{d^4Y_n(x)}{dx^4}\,P_n P_n^*\,F , \qquad n = 1,2,\ldots,\infty , \tag{D.38}$$

and applying eqn.(D.18) to (D.38), we get

$$E_n = (\pi I\beta_n^4 L^3)\mu A_n^2 F , \qquad n = 1,2,\ldots,\infty . \tag{D.39}$$

Recall that β_n is given by eqn.(D.20) and note that the first part of eqn. (D.15) has been used.

As pointed out in the last section, the energy (per cycle) for steady state vibration, eqn.(D.39) above, is the same as the energy for free vibration, when the exponential decay* tends to zero, viz. eqn.(D.22).

As shown by eqn.(D.39), the modal energy dissipated per cycle of oscillation, for a viscoelastically damped beam, is proportional to the viscoelastic damping coefficient μ, to the square of the amplitude A_n, and to the frequency of oscillation F.

When damping is hysteretic, the energy dissipated per cycle of vibration is still dependent on the square of the amplitude, but is no longer a function of frequency. It is still proportional to a damping factor (to be discussed below). The classical approach is to assume that motion (of the hysteretically damped system) is still harmonic, which allows the use of an "equivalent" viscoelastic damping coefficient as shown shortly. Note that the assumption of harmonic motion implies that either the hysteretic damping force is itself harmonic (and its amplitude varies with frequency so as to keep E constant), or that it is so small that other (harmonic) forces dominate. Moreover, note that the applicability of "equivalent" viscoelastic damping to periodic and to random motion will be discussed later.

Now, for hysteretic damping, the energy dissipated (per cycle of oscillation) can be written as eqn.(D.39), but without the frequency dependence and with a proportionality (hysteretic damping) coefficient:

$$E_n = (\pi I \beta_n^4 L^3) \lambda A_n^2 \quad , \qquad n = 1,2,\ldots,\infty \, , \tag{D.40}$$

where λ is the hysteretic damping coefficient. Equating energies, namely eqs.(D.39) and (D.40), we obtain an equivalent viscoelastic damping coefficient,

$$(\mu)_{eq} = \frac{\lambda}{|F|} \quad , \tag{D.41}$$

where the absolute value of F is required whenever negative frequencies are to be used in the mathematical representation of the deflection y (since $(\mu)_{eq}$ must always be positive).

---

* Eqn.(D.22) applies either to $D_n \to 0$ or $D_n/F_n \to 0$.

The use of eqn.(D.41) into eqn.(D.32) yields the equation of motion

$$m \frac{\partial^2 y}{\partial t^2} + \frac{\lambda}{|F|} I \frac{\partial}{\partial t}\left[\frac{\partial^4 y}{\partial x^4}\right] + EI \frac{\partial^4 y}{\partial x^4} = f \ . \tag{D.42}$$

Equation (D.42) is valid only for an harmonic f of frequency F. Note that F is arbitrary and the energy dissipated per cycle of oscillation obeys the correct equation, that is (D.40).

(c) Visco-hysteretic systems - harmonic excitation

A combination visco-hysteretically damped system can be represented by an equation of the form

$$m \frac{\partial^2 y}{\partial t^2} + \left(\mu + \frac{\lambda}{|F|}\right) I \frac{\partial}{\partial t}\left[\frac{\partial^4 y}{\partial x^4}\right] + EI \frac{\partial^4 y}{\partial x^4} = f \ , \tag{D.43}$$

again valid only for harmonic f (of frequency F).

(d) Visco-hysteretic systems - periodic excitation

Let f be periodic, i.e.

$$f(x,t) = \sum_{p=1}^{\infty} f_p(x,t) \ , \tag{D.44}$$

where

$$f_p(x,t) = C_p(x)\, e^{jF_p t} + C_p^*(x)\, e^{-jF_p t} \ , \qquad p = 1,2,\ldots,\infty \ , \tag{D.45}$$

corresponding to eqn.(D.33). By analogy to eqn.(D.34), we have

$$C_p(x) = u_p(x) + j\, v_p(x) \ , \qquad p = 1,2,\ldots,\infty \ . \tag{D.46}$$

Similarly (see eqn.(D.35))

$$y_p(x,t) = \sum_{q=1}^{\infty} Y_q(x) \left[P_{qp}\, e^{jF_p t} + P_{qp}^*\, e^{-jF_p t} \right] \ , \qquad p = 1,2,\ldots,\infty \ , \tag{D.47}$$

where we no longer have restricted the response in only one (previously the n^{th}) beam mode (for a given frequency $F = F_p$). Furthermore, similarly to eqn.(D.11),

$$P_{qp} = a_{qp} + b_{qp}\, j \ , \qquad p,q = 1,2,\ldots,\infty \ . \tag{D.48}$$

For an arbitrary p, we can apply eqn.(D.43), yielding

$$m \frac{\partial^2 y_p}{\partial t^2} + \left[\mu + \frac{\lambda}{|F_p|} \right] I \frac{\partial}{\partial t} \left[\frac{\partial^4 y_p}{\partial x^4} \right] + EI \frac{\partial^4 y_p}{\partial x^4} = f_p \quad . \tag{D.49}$$

From eqs.(D.45) to (D.49) inclusively, we obtain the functions $u_p(x)$ and $v_p(x)$, for multi-mode response at F_p:

$$u_p(x) = \sum_{q=1}^{\infty} \left\{ \left[EI \frac{d^4 Y_q(x)}{dx^4} - mF_p^2 Y_q(x) \right] a_{qp} - \left[\mu F_p + \lambda \right] I \frac{d^4 Y_q(x)}{dx^4} b_{qp} \right\} ,$$

$$v_p(x) = \sum_{q=1}^{\infty} \left\{ \left[EI \frac{d^4 Y_q(x)}{dx^4} - mF_p^2 Y_q(x) \right] b_{qp} + \left[\mu F_p + \lambda \right] I \frac{d^4 Y_q(x)}{dx^4} a_{qp} \right\} ,$$

(D.50)

$p = 1,2,\ldots,\infty$,
$(F_p \geq 0)$.

Note that eqn.(D.50) is equivalent to (D.36), but now includes multi-beam deflection modes response (for the single frequency F_p), and hysteretic damping.

Equation (D.49) is valid for an arbitrary p. If we sum the equations in (D.49), we get

$$\sum_{p=1}^{\infty} \left\{ m \frac{\partial^2 y_p}{\partial t^2} + \left[\mu + \frac{\lambda}{|F_p|} \right] I \frac{\partial}{\partial t} \left[\frac{\partial^4 y_p}{\partial x^4} \right] + EI \frac{\partial^4 y_p}{\partial x^4} \right\} = f ,$$

and if we define

$$y(x,t) = \sum_{p=1}^{\infty} y_p(x,t) \quad , \tag{D.51}$$

we can write

$$m \frac{\partial^2 y}{\partial t^2} + \mu I \frac{\partial}{\partial t} \left[\frac{\partial^4 y}{\partial x^4} \right] + \lambda I \frac{\partial^5}{\partial t \partial x^4} \sum_{p=1}^{\infty} \frac{y_p}{|F_p|} + EI \frac{\partial^4 y}{\partial x^4} = f \quad . \tag{D.52}$$

Equation (D.49) has the form $\mathfrak{L}(y_p) = f_p$, where $\mathfrak{L}$ is an operator. Now, in the case where $\lambda = 0$,

$\sum_{p=1}^{\infty} \mathfrak{L}(y_p) = \sum_{p=1}^{\infty} f_p$ reduces to

$$\mathfrak{L} \sum_{p=1}^{\infty} y_p = \mathfrak{L}(y) = f \ .$$

The above form does not apply when there is hysteretic damping, which slightly complicates the equation of motion (see eqn.(D.52)). However, the use of phasors yields qualitatively similar results; hysteretic damping brings about the existence of a complex stiffness, as shown below.

For an arbitrary p, from substitution of eqs.(D.45) and (D.47) into eqn.(D.49), we get two equations, one corresponding to $e^{jF_p t}$ and the other to $e^{-jF_p t}$:

$$\sum_{q=1}^{\infty} \left\{ \left[EI \frac{d^4 Y_q(x)}{dx^4} - mF_p^2 Y_q(x) \right] + j I \left(\mu F_p + \frac{F_p}{|F_p|} \lambda \right) \frac{d^4 Y_q(x)}{dx^4} \right\} P_{qp} = C_p(x) \ , * \quad (F_p \geq 0), \tag{D.53}$$

and

$$\sum_{q=1}^{\infty} \left\{ \left[EI \frac{d^4 Y_q(x)}{dx^4} - mF_p^2 Y_q(x) \right] - j I \left(\mu F_p + \frac{F_p}{|F_p|} \lambda \right) \frac{d^4 Y_q(x)}{dx^4} \right\} P^*_{qp} = C_p^*(x) \ , \quad (F_p \geq 0),$$

the latter equation being the complex conjugate of eqn.(D.53), that is, all the information about the dynamics of the system is contained in one of the equations, allowing the use of phasors:

$$\langle f_p \rangle \rightarrow C_p(x) \, e^{jF_p t} \ , \tag{D.54}$$

$$\langle y_p \rangle \rightarrow \sum_{q=1}^{\infty} Y_q(x) \, P_{qp} \, e^{jF_p t} \ .$$

Now, the classical complex frequency response function is defined as the ratio of response and force phasors, i.e.

$$H_p(F_p) = \frac{\langle y_p \rangle}{\langle f_p \rangle} \tag{D.55}$$

---

* Using eqs.(D.46) and (D.48) into (D.53) will yield eqn.(D.50).

$$= \frac{\sum_{q=1}^{\infty} Y_q(x)\, P_{qp}\, e^{jF_p t}}{C_p(x)\, e^{jF_p t}}$$

$$= \frac{\sum_{q=1}^{\infty} Y_q(x)\, P_{qp}}{C_p(x)} \quad ,$$

which becomes, using eqn.(D.53)

$$H_p(F_p) = \frac{\sum_{q=1}^{\infty} Y_q(x)\, P_{qp}}{\sum_{q=1}^{\infty} \left\{ -mF_p^2\, Y_q(x) + j\,\mu I F_p \frac{d^4 Y_q(x)}{dx^4} + I\,(E+\lambda j) \frac{d^4 Y_q(x)}{dx^4} \right\} P_{qp}} \quad ,$$

$$(F_p \geq 0) .$$

The P_{qp} may be set arbitrarily, hence

$$H_p(F_p) = \sum_{q=1}^{\infty} H_{qp}(F_p) \quad , \tag{D.56}$$

where

$$H_{qp}(F_p) = \frac{Y_q(x)}{-mF_p^2\, Y_q(x) + j\,\mu I F_p \frac{d^4 Y_q(x)}{dx^4} + I\,(E+\lambda j) \frac{d^4 Y_q(x)}{dx^4}} \quad . \tag{D.57}$$

We have introduced the complex stiffness

$$E_c = E + \lambda j \quad . \tag{D.58}$$

It should be noted that the complex stiffness arises in conjunction with the use of phasors, and cannot be used <u>directly</u> in a real equation of motion, i.e. it must be used in a <u>phasor</u> equation of motion. The following form is valid: from eqn.(D.55), we may write

$\langle y_p \rangle = H_p(F_p) \cdot \langle f_p \rangle$, which yields

$y_p = H_p(F_p) \langle f_p \rangle + H_p^*(F_p) \langle f_p \rangle^*$, that is

$$y_p(x,t) = H_p(F_p) \cdot C_p(x) \cdot e^{jF_p t} + H_p^*(F_p) \cdot C_p^*(x) \cdot e^{-jF_p t} \quad . \tag{D.59}$$

From eqs.(D.51) and (D.59), we get

$$y(x,t) = \sum_{p=1}^{\infty} \left[H_p(F_p) \cdot C_p(x) \cdot e^{jF_p t} + H_p^*(F_p) \cdot C_p^*(x) \cdot e^{-jF_p t} \right] \quad . \tag{D.60}$$

(e) Visco-hysteretic systems - random excitation

An approach similar to that used in Appendix I, i.e. obtaining the Fourier transform as a limiting case of Fourier series, is used here.

First, the forcing function can be written as a Fourier series with complex coefficients: eqs.(D.44) and (D.45) take the form

$$f(x,t) = \sum_{r=-\infty}^{\infty} C_r(x)\, e^{jF_r t} \quad , \tag{D.61}$$

with

$$\left.\begin{aligned} &C_0(x) = 0 \quad \text{(zero DC component)} \\ &\text{and} \\ &C_{-r}(x) = C_r^*(x) \quad . \end{aligned}\right\} \tag{D.62}$$

Similarly, eqs.(D.51) and (D.47) can be written as

$$y(x,t) = \sum_{q=1}^{\infty} Y_q(x) \sum_{r=-\infty}^{\infty} P_{qr}\, e^{jF_r t} \quad , \tag{D.63}$$

where

$$\left.\begin{aligned} &P_{q0} = 0 \quad , \qquad q = 1,2,\ldots,\infty \, , \\ &\text{and} \\ &P_{q(-r)} = P_{qr}^* \quad , \qquad q,r = 1,2,\ldots,\infty \, . \end{aligned}\right\} \tag{D.64}$$

Note that we may write

$$Y_r = \sum_{q=1}^{\infty} Y_q(x) \cdot P_{qr}\, e^{jF_r t} \quad , \qquad r = 0,\pm 1,\pm 2,\ldots,\pm\infty \quad (Y_0 = 0) \tag{D.65}$$

and

$$y_p = Y_p + Y_{-p} \quad , \qquad p = 1,2,\ldots,\infty \, . \tag{D.66}$$

Also, we note that

$$F_{-r} = -F_r \quad , \qquad r = 1,2,\ldots,\infty \, . \tag{D.67}$$

Substituting eqs.(D.63), (D.66), and (D.61) into the equation of motion for periodically excited systems, namely eqn.(D.52), we get

$$\sum_{q=1}^{\infty} \sum_{r=-\infty}^{\infty} \left\{ \left[m \frac{\partial^2}{\partial t^2} + \mu I \frac{\partial^5}{\partial x^4 \partial t} + EI \frac{\partial^4}{\partial x^4} \right] Y_q(x) P_{qr} e^{jF_r t} + \lambda I \frac{\partial^5}{\partial x^4 \partial t} \right.$$

$$\left. \cdot \frac{Y_q(x) P_{qr} e^{jF_r t}}{|F_r|} \right\} = \sum_{r=-\infty}^{\infty} C_r(x) e^{jF_r t} \, . \tag{D.68}$$

Now, we note that, for the excitation to be truly periodic, we must have (F_r/F_s) rational, for all values of r and s (otherwise, the fundamental period tends to infinity and the excitation is no longer periodic). Hence, there is no loss of generality in setting

$$F_r = r \cdot F_1 \quad , \qquad r = 0,\pm 1,\pm 2,\ldots,\pm\infty \, , \tag{D.69}$$

where F_1 is the fundamental frequency. Note that eqn.(D.69) satisfies eqn. (D.67).

From eqs.(D.69) and (D.68), we get the equation of motion

$$\sum_{q=1}^{\infty} \sum_{r=-\infty}^{\infty} \left\{ \left[m \frac{\partial^2}{\partial t^2} + \mu I \frac{\partial^5}{\partial x^4 \partial t} + EI \frac{\partial^4}{\partial x^4} \right] Y_q(x) P_{qr} e^{jrF_1 t} + \lambda I \frac{\partial^5}{\partial x^4 \partial t} \right.$$

$$\left. \cdot \frac{Y_q(x) P_{qr} e^{jrF_1 t}}{|rF_1|} \right\} = \sum_{r=-\infty}^{\infty} C_r(x) e^{jrF_1 t} \, . \tag{D.70}$$

Similarly, eqs.(D.61) and (D.63) can be rewritten as

$$f(x,t) = \sum_{r=-\infty}^{\infty} C_r(x) e^{jrF_1 t} \quad , \tag{D.71}$$

and

$$y(x,t) = \sum_{r=-\infty}^{\infty} \left[\sum_{q=1}^{\infty} Y_q(x) P_{qr} \right] e^{jrF_1 t} \, . \tag{D.72}$$

Now, from Fourier series relationships, we may write the Fourier coefficients as

$$C_r(x) = \frac{1}{T_1} \cdot \int_{-T_1/2}^{+T_1/2} f(x,t) \cdot e^{-jrF_1 t} \cdot dt \qquad (D.73)$$

for the force (per unit length) f, and

$$\sum_{q=1}^{\infty} Y_q(x)\, P_{qr} = \frac{1}{T_1} \cdot \int_{-T_1/2}^{+T_1/2} y(x,t) \cdot e^{-jrF_1 t} \cdot dt \quad , \qquad (D.74)$$

for the displacement y, where T_1 is the fundamental period, i.e.

$$T_1 = \frac{2\pi}{F_1} \quad .* \qquad (D.75)$$

Using eqs.(D.73) and (D.74) in (D.70) yields

$$\sum_{r=-\infty}^{\infty} \left(m \frac{\partial^2}{\partial t^2} + \mu I \frac{\partial^5}{\partial x^4 \partial t} + EI \frac{\partial^4}{\partial x^4} \right) e^{jrF_1 t} \cdot \frac{1}{T_1} \cdot \int_{-T_1/2}^{+T_1/2} y(x,t) \cdot e^{-jrF_1 t} \cdot dt$$

$$+ \sum_{r=-\infty}^{\infty} \lambda I \frac{\partial^5}{\partial x^4 \partial t} \frac{e^{jrF_1 t}}{|rF_1|} \cdot \frac{1}{T_1} \cdot \int_{-T_1/2}^{+T_1/2} y(x,t) \cdot e^{-jrF_1 t} \cdot dt = \sum_{r=-\infty}^{\infty} e^{jrF_1 t}$$

$$\cdot \frac{1}{T_1} \cdot \int_{-T_1/2}^{+T_1/2} f(x,t) \cdot e^{-jrF_1 t} \cdot dt \quad . \qquad (D.76)$$

Let

$$\Delta F_r = (r+1)F_1 - rF_1 = F_1 \quad , \qquad (D.77)$$

and using eqn.(D.75) in (D.77), we can write

$$\frac{1}{T_1} = \frac{\Delta F_1}{2\pi} \quad . \qquad (D.78)$$

Substituting eqn.(D.78) into (D.76), and also using (D.69), we obtain

---

* Note that the 2π factor applies when F_1 is in rad/(unit time) and T_1 is (unit time).

$$\sum_{r=-\infty}^{\infty} \left(m \frac{\partial^2}{\partial t^2} + \mu I \frac{\partial^5}{\partial x^4 \partial t} + EI \frac{\partial^4}{\partial x^4} \right) e^{jF_r t} \cdot \Delta F_r \cdot \frac{1}{2\pi} \cdot \int_{-T_1/2}^{+T_1/2} y(x,t) \cdot e^{-jF_r t} \cdot dt$$

$$+ \sum_{r=-\infty}^{\infty} \lambda I \frac{\partial^5}{\partial x^4 \partial t} \frac{e^{jF_r t}}{|F_r|} \cdot \Delta F_r \cdot \frac{1}{2\pi} \cdot \int_{-T_1/2}^{+T_1/2} y(x,t) \cdot e^{-jF_r t} \cdot dt = \sum_{r=-\infty}^{\infty} e^{jF_r t}$$

$$\cdot \Delta F_r \cdot \frac{1}{2\pi} \cdot \int_{-T_1/2}^{+T_1/2} f(x,t) \cdot e^{-jF_r t} \cdot dt \ . \qquad (D.79)$$

We have, in the limiting case

$T_1 \to \infty, \quad F_1 \to 0$,

$F_r \to F, \quad \Delta F_r \to dF$,

which, when used in eqn.(D.79), yields

$$\int_{-\infty}^{+\infty} \left(m \frac{\partial^2}{\partial t^2} + \mu I \frac{\partial^5}{\partial x^4 \partial t} + EI \frac{\partial^4}{\partial x^4} \right) e^{jFt} \cdot dF \cdot \frac{1}{2\pi} \int_{-\infty}^{+\infty} y(x,t) \cdot e^{-jFt} \cdot dt$$

$$+ \int_{-\infty}^{+\infty} \lambda I \frac{\partial^5}{\partial x^4 \partial t} \frac{e^{jFt}}{|F|} \cdot dF \cdot \frac{1}{2\pi} \int_{-\infty}^{+\infty} y(x,t) \cdot e^{-jFt} \cdot dt = \int_{-\infty}^{+\infty} e^{jFt} \cdot dF$$

$$\cdot \frac{1}{2\pi} \int_{-\infty}^{+\infty} f(x,t) \cdot e^{-jFt} \cdot dt \ . \qquad (D.80)$$

We have two new Fourier transforms, namely

$$\bar{y}(x,F) = \frac{1}{2\pi} \int_{-\infty}^{+\infty} y(x,t) \cdot e^{-jFt} \cdot dt \ , \qquad (D.81)$$

and

$$\bar{f}(x,F) = \frac{1}{2\pi} \int_{-\infty}^{+\infty} f(x,t) \cdot e^{-jFt} \cdot dt \ . \qquad (D.82)$$

Eqs.(D.81) and (D.82), used in (D.80), yield

$$\left(m \frac{\partial^2}{\partial t^2} + \mu I \frac{\partial^5}{\partial x^4 \partial t} + EI \frac{\partial^4}{\partial x^4} \right) \cdot \int_{-\infty}^{+\infty} \bar{y}(x,F) \cdot e^{jFt} \cdot dF + \lambda I \frac{\partial^5}{\partial x^4 \partial t}$$

$$\cdot \int_{-\infty}^{+\infty} \frac{\bar{y}(x,F)}{|F|} \cdot e^{jFt} \cdot dF = \int_{-\infty}^{+\infty} \bar{f}(x,F) \cdot e^{jFt} \cdot dF \ . \qquad (D.83)$$

The term associated with hysteretic damping can be written in an alternate form, as

$$\frac{\partial^5}{\partial x^4 \partial t} \cdot \int_{-\infty}^{+\infty} \frac{\bar{y}(x,F)}{|F|} \cdot e^{jFt} \cdot dF = \frac{\partial^4}{\partial x^4} \cdot \int_{-\infty}^{+\infty} j F \frac{\bar{y}(x,F)}{|F|} \cdot e^{jFt} \cdot dF \ , \text{ or}$$

$$\frac{\partial^5}{\partial x^4 \partial t} \cdot \int_{-\infty}^{+\infty} \frac{\bar{y}(x,F)}{|F|} \cdot e^{jFt} \cdot dF = \frac{\partial^4}{\partial x^4} \cdot \int_{-\infty}^{+\infty} j \, \mathrm{sgn}(F) \cdot \bar{y}(x,F) \cdot e^{jFt} \cdot dF \ , \qquad (D.84)$$

where sgn(F) is the sign function.

We recall the Hilbert transform, which can be defined in terms of the Fourier transform as

$$\bar{\bar{y}}(x,F) = -j \, \mathrm{sgn}(F) \cdot \bar{y}(x,F) \ . \qquad (D.85)$$

Hence, eqs.(D.85) and (D.84) may be used in (D.83), to yield

$$\left(m \frac{\partial^2}{\partial t^2} + \mu I \frac{\partial^5}{\partial x^4 \partial t} + EI \frac{\partial^4}{\partial x^4} \right) \cdot \int_{-\infty}^{+\infty} \bar{y}(x,F) \cdot e^{jFt} \cdot dF - \lambda I \frac{\partial^5}{\partial x^4 \partial t}$$

$$\cdot \int_{-\infty}^{+\infty} \bar{\bar{y}}(x,F) \cdot e^{jFt} \cdot dF = \int_{-\infty}^{+\infty} \bar{f}(x,F) \cdot e^{jFt} \cdot dF \ . \qquad (D.86)$$

As shown below, the phasor form of the (real) equation of motion need not require the use of Hilbert transforms.

Equation (D.83) must hold in an arbitrary frequency band, say F_1, $F_1 + \delta F_1$. In this case, the integration limits are $-(F_1 + \delta F_1)$ to $-F_1$ and F_1 to

$(F_1+\delta F_1)$. As $\delta F_1 \to 0$, the integrands in eqn.(D.83) must obey the relation

$$\left[m \frac{\partial^2}{\partial t^2} + \mu I \frac{\partial^5}{\partial x^4 \partial t} + EI \frac{\partial^4}{\partial x^4} \right] \left[\bar{y}(x,F) \cdot e^{jFt} + \bar{y}(x,-F) \cdot e^{-jFt} \right] + \lambda I \frac{\partial^5}{\partial x^4 \partial t}$$

$$\cdot \left[\frac{\bar{y}(x,F)}{|F|} \cdot e^{jFt} + \frac{\bar{y}(x,-F)}{|-F|} \cdot e^{-jFt} \right] = \left[\bar{f}(x,F) \cdot e^{jFt} + \bar{f}(x,-F) \cdot e^{-jFt} \right] , \quad (D.87)$$
$$(F \geq 0).$$

Note that, as the equation is symmetrical, we can impose the condition that F be positive.

By inspection of (D.82) and (D.81), we see that

$$\left.\begin{aligned} &\bar{y}(x,-F) = \bar{y}^*(x,F) \\ &\text{and} \\ &\bar{f}(x,-F) = \bar{f}^*(x,F) \ ; \end{aligned}\right\} \quad (D.88)$$

hence, using (D.88) in (D.87), and the condition that $F \geq 0$, we may write

$$\left[-mF^2 + j\mu IF \frac{\partial^4}{\partial x^4} + I(E + j\lambda) \frac{\partial^4}{\partial x^4} \right] \bar{y}(x,F)\, e^{jFt} + \left[-mF^2 - j\mu IF \frac{\partial^4}{\partial x^4} \right.$$

$$\left. + I(E - j\lambda) \frac{\partial^4}{\partial x^4} \right] \bar{y}^*(x,F)\, e^{-jFt} = \bar{f}(x,F)\, e^{jFt} + \bar{f}^*(x,F)\, e^{-jFt} , \quad (D.89)$$
$$(F \geq 0).$$

The above equation has the form

$$A(x,F) \cdot \bar{y}(x,F) \cdot e^{jFt} + A^*(x,F) \cdot \bar{y}^*(x,F) \cdot e^{-jFt} = \bar{f}(x,F) \cdot e^{jFt} + \bar{f}^*(x,F)$$

$$\cdot e^{-jFt} ,$$

which may be split into two equations, namely

$$\left.\begin{aligned} &A(x,F) \cdot \bar{y}(x,F) \cdot e^{jFt} = \bar{f}(x,F) \cdot e^{jFt} \\ &\text{and} \\ &A^*(x,F) \cdot \bar{y}^*(x,F) \cdot e^{-jFt} = \bar{f}^*(x,F) \cdot e^{-jFt} , \end{aligned}\right\} \quad (D.90)$$

where

$$A(x,F) = -mF^2 + j\,\mu IF\,\frac{\partial^4}{\partial x^4} + I(E + j\,\lambda)\,\frac{\partial^4}{\partial x^4} \quad , \tag{D.91}$$

a complex operator.

Since both equations in (D.90) are equivalent, either one can be used. We then obtain

$$\bar{y}(x,F) = H(x,F) \cdot \bar{f}(x,F) \quad , \qquad (F \geq 0) \tag{D.92}$$

a phasor equation of motion, where

$$H(x,F) = \frac{1}{-mF^2 + j\,\mu IF\,\frac{\partial}{\partial x^4} + I(E + j\,\lambda)\,\frac{\partial^4}{\partial x^4}} \quad , \tag{D.93}$$

an "operator" (in x) transfer function.

Note that eqn.(D.93) again involves the complex stiffness, defined by eqn.(D.58).

Appendix E

Inviscid hydrodynamic coupling

Cylinder bundles immersed in an incompressible frictionless fluid may exhibit inviscid hydrodynamic coupling: pressure forces on a given cylinder may be induced by the motion of others, through fluid coupling.

A detailed review of Chen's [44] theory, extended by Suss [73] to take into account effects of the mean flow,* is made here. The method essentially consists in deriving a two-dimensional fluid velocity potential, for any arbitrary cross-section in the (y,z)-plane, by imposing velocity boundary conditions at the cylinder§ and channel† walls. Lighthill's (see Appendix F, in Ref.[75]) slender body theory is then used to determine pressure forces on the cylinders, for a flowing fluid.

Note that all cylinders are taken as identical and with the same boundary conditions. The coordinate system for clusters of cylinders is illustrated in Fig. 7.

The fluid being assumed inviscid, its velocity potential must satisfy

$$\nabla^2 \phi(y,z) = 0 \,. \tag{E.1}$$

(The boundary layers for both longitudinal and lateral directions are assumed to be small, potential flow existing everywhere else in the fluid.)

The general solution to eqn.(E.1) is, in polar coordinates,

$$\phi(r,\theta) = \sum_{n=1}^{\infty} \left[A_n r^n \cos(n\theta) + B_n r^n \sin(n\theta) + C_n r^{-n} \cos(n\theta) + D_n r^{-n} \sin(n\theta) \right] , \tag{E.2}$$

where A_n, B_n, C_n, and D_n are constants (determined from the boundary conditions). It should be noted that n takes integer values only, because of the

---

* The presence of a confining channel is treated in both [77] and [73].

§ Small motions are assumed. Hence, the cylinder positions are taken as fixed.

† The channel wall is taken as rigid.

periodicity of the boundary conditions (period of 2π in θ).

Following Chen's [36] approach, the total potential is taken as the sum of the K potentials due to the presence of each cylinder in the channel.

In its local coordinate system, each cylinder has the potential

$$\phi_j(r_j,\theta_j) = \sum_{n=1}^{\infty}\left[A_{nj}r_j^n\cos(n\theta_j) + B_{nj}r_j^n\sin(n\theta_j) + C_{nj}r_j^{-n}\cos(n\theta_j) + D_{nj}r_j^{-n}\sin(n\theta_j)\right], \quad j=1,2,\ldots,K, \tag{E.3}$$

where A_{nj}, B_{nj}, C_{nj}, and D_{nj} are to be determined from the boundary conditions.

As seen from Fig. 7, the coordinate transformation from one cylinder to another is, in complex form:

$$r_j\, e^{j\theta_j} = r_i\, e^{j\theta_i} - R_{ij}\, e^{j\psi_{ij}},$$

or,

$$r_j^{\pm n}\cdot e^{\pm jn\theta_j} = \left[r_i\cdot e^{j\theta_i} - R_{ij}\cdot e^{j\psi_{ij}}\right]^{\pm n}. \tag{E.4}$$

Taylor series* expansion of (E.4), for both positive and negative exponent (n), yield the coordinate transformation equations (after separating the real and imaginary components):

$$r_j^n\begin{Bmatrix}\cos(n\theta_j)\\ \sin(n\theta_j)\end{Bmatrix} = \sum_{m=0}^{n}\frac{(-1)^{n-m}\,n!\,R_{ij}^{n-m}\,r_j^m}{m!\,(n-m)!}\begin{Bmatrix}\cos[m\theta_i+(n-m)\psi_{ij}]\\ \sin[m\theta_i+(n-m)\psi_{ij}]\end{Bmatrix}\ \S, \quad n=1,2,\ldots,\infty,\ i,j=1,2,\ldots,K, \tag{E.5}$$

and, for $r_i < R_{ij}$,

$$r_j^{-n}\begin{Bmatrix}\cos(n\theta_j)\\ \sin(n\theta_j)\end{Bmatrix} = \sum_{m=0}^{\infty}\frac{(-1)^{n}\,(n+m-1)!\,r_i^m}{m!\,(n-1)!\,R_{ij}^{n+m}}\begin{Bmatrix}\cos[m\theta_i-(n+m)\psi_{ij}]\\ -\sin[m\theta_i-(n+m)\psi_{ij}]\end{Bmatrix}, \quad n=1,2,\ldots\infty,\ i,j=1,2,\ldots,K, \tag{E.6}$$

---

* Binomial theorems, for positive and negative exponents, can also be used.

§ In this case, the brackets $\begin{Bmatrix}\ \\ \ \end{Bmatrix}$ represent a vector.

or, for $r_i > R_{ij}$,

$$r_j^{-n}\begin{Bmatrix}\cos(n\theta_j)\\ \sin(n\theta_j)\end{Bmatrix} = \sum_{m=n}^{\infty} \frac{(m-1)!\ R_{ij}^{m-n}}{(n-1)!\ (m-n)!\ r_i^m} \begin{Bmatrix}\cos[m\theta_i - (m-n)\psi_{ij}]\\ \sin[m\theta_i - (m-n)\psi_{ij}]\end{Bmatrix}, \quad \begin{matrix} n = 1,2,..,\infty, \\ i,j = 1,2,\ldots,K. \end{matrix} \tag{E.7}$$

Recall (ref. [73]) that,

ϕ_j is the potential of cylinder j, expressed in its own coordinates, (r_j, θ_j),

$\phi_{(i)j}$ is the potential of cylinder j, expressed in terms of cylinder i local coordinates, (r_i, ϕ_i), and

$\phi_{(t)i}$ is the total potential, expressed in terms of cylinder i local coordinates, (r_i, ϕ_i).

It should also be noted that subscripts "c" refer to the coordinate system centered on the channel, (r_c, θ_c).

The total potential is (in coordinates (r_i, θ_i))

$$\phi_{(t)i} = \phi_i + \sum_{j=1}^{K}{}^{*} \phi_{(i)j}, \qquad i = 1,2,\ldots,K, \tag{E.8}$$

where the starred summation excludes $j = i$.

The first boundary condition on each of the cylinder potentials is that, at the channel wall

$$\text{I:}\ \left.\frac{\partial \phi_{(c)j}}{\partial r_c}\right|_{r_c = R_c} = 0, \qquad j = 1,2,\ldots,K, \tag{E.9}$$

that is, velocity components normal to the wall are zero.

The other boundary condition on the total potential is, at each cylinder

$$\text{II:}\ \left.\frac{\partial \phi_{(t)i}}{\partial r_i}\right|_{r_i = R_i} = \frac{Dw_i}{Dt}\cos\theta_i + \frac{Dv_i}{Dt}\sin\theta_i, \qquad i = 1,2,\ldots,K, \tag{E.10}$$

where

$$\frac{D}{Dt} = \frac{\partial}{\partial t} + U\frac{\partial}{\partial x}, \tag{E.11}$$

the total* derivative.

The use of the total derivative can be easily visualized by considering a direction vector $\vec{a}$, in the (y,z)-plane, with angle θ_i (relative to the w_i axis). We examine a cross-section of cylinder i, in the (a,x) plane:

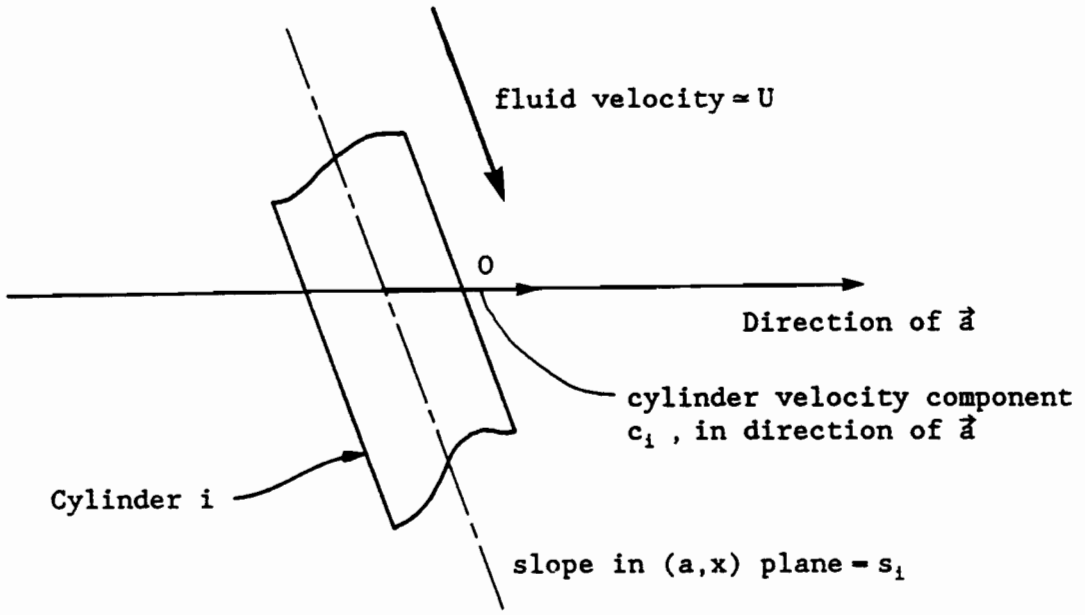

We have

$$s_i = \frac{\partial w_i}{\partial x} \cos \theta_i + \frac{\partial v_i}{\partial x} \sin \theta_i \ , \text{ and}$$

$$c_i = \frac{\partial w_i}{\partial t} \cos \theta_i + \frac{\partial v_i}{\partial t} \sin \theta_i \ .$$

At point 0, the fluid velocity is

$$\left.\frac{\partial \phi_{(t)i}}{\partial r_i}\right|_{r_i = R_i} = c_i + U \cdot s_i \ ,$$

which yields eqn.(E.10).

We now impose the boundary conditions I and II, which will yield sets of equations for the coefficients A_{nj}, B_{nj}, C_{nj}, and D_{nj} of eqn.(E.3).

---

* Also labelled "substantial" or "material".

(a) Imposing Boundary Condition I

(i) Special case of a cylinder positioned at the center of the channel

This case is labelled with the index $j = q$.

Since $\phi_{(c)q} = \phi_q$, we can rewrite (E.9) as

$$\left.\frac{\partial \phi_q}{\partial r_q}\right|_{r_q = R_c} = 0 . \tag{E.12}$$

Substituting eqn.(E.3) with $j = q$ in (E.12), and making use of the fact that $\sin(\theta_q)$ and $\cos(\theta_q)$ are linearly independent, we obtain

$$\begin{Bmatrix} A_{nq} \\ B_{nq} \end{Bmatrix} R_c^{n-1} = \begin{Bmatrix} C_{nq} \\ D_{nq} \end{Bmatrix} \frac{1}{R_c^{n+1}} , \quad n = 1,2,\ldots,\infty . \tag{E.13}$$

(ii) General case ($j \neq q$)

The expression for $\phi_{(c)j}$ is obtained by using the coordinate transformations (E.5) and (E.7) with $i = c$, in eqn.(E.3). Imposing the boundary condition (E.9) on the latter expression for $\phi_{(c)j}$ yields*

$$\sum_{n=1}^{\infty}\left[\sum_{m=1}^{\infty}\left(\frac{(-1)^{n-m}\, n!\, R_{cj}^{n-m}\, R_c^{m-1}}{(m-1)!\,(n-m)!}\right)\left(A_{nj}\cos[m\theta_c + (n-m)\psi_{cj}] + B_{nj}\sin[m\theta_c + (n-m)\psi_{cj}]\right) + \sum_{m=n}^{\infty}\left(\frac{(-1)\, m!\, R_{cj}^{m-n}}{(n-1)!\,(m-n)!\, R_c^{m+1}}\right)\cdot\left(C_{nj}\cos[m\theta_c - (m-n)\psi_{cj}] + D_{nj}\cdot\sin[m\theta_c - (m-n)\psi_{cj}]\right)\right] = 0 , \tag{E.14}$$

§ $j \neq q$, $j = 1,2,\ldots,K$.

Using trigonometric identities for $\sin(a \pm b)$ and $\cos(a \pm b)$, and using the fact that $\sin(m\theta_c)$ and $\cos(m\theta_c)$ are linearly independent, eqn.(E.14) can be be split into two, resulting in

---

* Note that we have $r_c = R_c$ here.

§ Note that the sum $m = 0$ to n has become $m = 1$ to n, as $\partial(r_c^m)/\partial r_c \Big|_{m=0} = 0$.

$$\sum_{n=1}^{\infty}\left[\sum_{m=1}^{n}\left(\frac{(-1)^{n-m}\, n!\, R_{c_j}^{n-m}\, R_c^{m-1}}{(m-1)!\ (n-m)!}\right)\left(A_{n_j}\cos[(n-m)\psi_{c_j}] + B_{n_j}\sin[(n-m)\psi_{c_j}]\right)\right.$$

$$\cdot\cos(m\theta_c) + \sum_{m=n}^{\infty}\left(\frac{(-1)\, m!\, R_{c_j}^{m-n}}{(n-1)!\ (m-n)!\ R_c^{m+1}}\right)\left(C_{n_j}\cos[(m-n)\psi_{c_j}] - D_{n_j}\sin[(m-n)\psi_{c_j}]\right)$$

$$\left.\cdot\cos(m\theta_c)\right] = 0\ ,$$

and (E.15)

$$\sum_{n=1}^{\infty}\left[\sum_{m=1}^{n}\left(\frac{(-1)^{n-m}\, n!\, R_{c_j}^{n-m}\, R_c^{m-1}}{(m-1)!\ (n-m)!}\right)\left(-A_{n_j}\sin[(n-m)\psi_{c_j}] + B_{n_j}\cos[(n-m)\psi_{c_j}]\right)\right.$$

$$\cdot\sin(m\theta_c) + \sum_{m=n}^{\infty}\left(\frac{(-1)\, m!\, R_{c_j}^{m-n}}{(n-1)!\ (m-n)!\ R_c^{m+1}}\right)\cdot\left(C_{n_j}\sin[(m-n)\psi_{c_j}] + D_{n_j}\cos[(m-n)\psi_{c_j}]\right)$$

$$\left.\cdot\sin(m\theta_c)\right] = 0\ ,$$

$$j \neq q\ ,$$
$$j = 1,2,\ldots,K\ .$$

The $\sin(m\theta_c)$ and $\cos(m\theta_c)$ terms can be isolated, in (E.15), by using the identities*

$$\sum_{n=1}^{\infty}\sum_{m=1}^{n} P_{mn}\ Q_m = \sum_{m=1}^{\infty} Q_m \sum_{n=m}^{\infty} P_{mn}\ ,$$

and

$$\sum_{n=1}^{\infty}\sum_{m=n}^{\infty} P_{mn}\ Q_m = \sum_{m=1}^{\infty} Q_m \sum_{n=1}^{m} P_{mn}\ .$$

Furthermore, by virtue of the linear independence of the $\sin(m\theta_c)$ terms and the $\cos(m\theta_c)$ terms, the resulting homogeneous equations have ($\sin(m\theta_c)$) coefficients equal to zero, i.e.

$$\sum_{n=m}^{\infty}\left(\frac{(-1)^{n-m}\, n!\, R_{c_j}^{n-m}\, R_c^{m-1}}{(m-1)!\ (n-m)!}\right)\left[\begin{Bmatrix} A_{n_j} \\ B_{n_j} \end{Bmatrix}\cos[(n-m)\psi_{c_j}] + \begin{Bmatrix} B_{n_j} \\ -A_{n_j} \end{Bmatrix}\sin[(n-m)\psi_{c_j}]\right]$$

(continued)

---

* Proven by expanding and rearranging terms.

$$-\sum_{n=1}^{m}\left[\frac{m!\ R_{c_j}^{m-n}}{(n-1)!\ (m-n)!\ R_c^{m+1}}\right]\cdot\left[\begin{Bmatrix}C_{nj}\\D_{nj}\end{Bmatrix}\cos[(m-n)\psi_{cj}]+\begin{Bmatrix}-D_{nj}\\C_{nj}\end{Bmatrix}\sin[(m-n)\psi_{cj}]\right]$$

$$=\begin{Bmatrix}0\\0\end{Bmatrix}, \qquad (E.16)$$

$j \neq q$,
$j = 1,2,\ldots,K$.
$m = 1,2,\ldots,\infty$.

(b) Imposing Boundary Condition II

Note that the case of $j = q$ need not be treated separately here.

The expression for $\phi_{(t)j}$ is obtained by using the coordinate transformations (E.5) and (E.6) in eqn.(E.3). Imposing the boundary condition (E.10) on the latter expression for $\phi_{(t)j}$ yields*

$$\sum_{n=1}^{\infty}\left[nR_i^{n-1}\ [A_{ni}\cos(n\theta_i)+B_{ni}\sin(n\theta_i)]-nR_i^{-(n+1)}\ [C_{ni}\cos(n\theta_i)+D_{ni}\right.$$

$$\left.\cdot\sin(n\theta_i)]\right]+\sum_{j=1}^{K}{}^{*}\sum_{n=1}^{\infty}\left[\sum_{m=1}^{n}\left[\frac{(-1)\,n!\,R_{ij}^{n-m}\,R_i^{m-1}}{(m-1)!\,(n-m)!}\right]\cdot\left(A_{nj}\cos[m\theta_i+(n-m)\psi_{ij}]+B_{nj}\right.\right.$$

$$\left.\cdot\sin[m\theta_i+(n-m)\psi_{ij}]\right)+\sum_{m=1}^{\infty}\left[\frac{(-1)^n\,(n+m-1)!\,R_i^{m-1}}{(m-1)!\,(n-1)!\,R_{ij}^{n+m}}\right]\left(C_{nj}\cos[m\theta_i-(n+m)\psi_{ij}]\right.$$

$$\left.\left.-D_{nj}\sin[m\theta_i-(n+m)\psi_{ij}]\right)\right]=\frac{Dw_i}{Dt}\cos\theta_i+\frac{Dv_i}{Dt}\sin\theta_i, \qquad (E.17)$$

$i = 1,2,\ldots,K$.

Proceeding as for boundary condition I, using the additional identity

$$\sum_{n=1}^{\infty}\sum_{m=1}^{\infty}P_{mm}\,Q_m=\sum_{m=1}^{\infty}Q_m\sum_{n=1}^{\infty}P_{mm},$$

we get

$$\sum_{n=1}^{\infty}\left[n\begin{Bmatrix}\cos(n\theta_i)\\\sin(n\theta_i)\end{Bmatrix}\left(\begin{Bmatrix}A_{ni}\\B_{ni}\end{Bmatrix}R_i^{n-1}-\begin{Bmatrix}C_{ni}\\D_{ni}\end{Bmatrix}\frac{1}{R_i^{n+1}}\right)\right]+\sum_{j=1}^{K}{}^{*}\left[\sum_{m=1}^{\infty}\begin{Bmatrix}\cos(m\theta_i)\\\sin(m\theta_i)\end{Bmatrix}\right.$$

$$\left.\cdot\left[\sum_{n=m}^{\infty}\left[\frac{(-1)^{n-m}\,n!\,R_{ij}^{n-m}\,R_i^{m-1}}{(m-1)!\,(n-m)!}\right]\cdot\left(\begin{Bmatrix}A_{nj}\\B_{nj}\end{Bmatrix}\cos[(n-m)\psi_{ij}]+\begin{Bmatrix}B_{nj}\\-A_{nj}\end{Bmatrix}\sin[(n-m)\psi_{ij}]\right)\right.\right.$$

---

* Note that we have $r_i = R_i$ here.

$$+\sum_{n=1}^{\infty}\left[\frac{(-1)^n\,(n+m-1)!\,R_i^{m-1}}{(m-1)!\,(n-1)!\,R_{ij}^{n+m}}\right]\left[\left\{\begin{matrix}C_{nj}\\-D_{nj}\end{matrix}\right\}\cos[(n+m)\psi_{ij}]+\left\{\begin{matrix}D_{nj}\\C_{nj}\end{matrix}\right\}\sin[(n+m)\psi_{ij}]\right]\Bigg]$$

$$=\left\{\begin{matrix}(Dw_i/Dt)\cos\theta_i\\(Dv_i/Dt)\sin\theta_i\end{matrix}\right\},\qquad i=1,2,\ldots,K. \tag{E.18}$$

Again using the fact that the $\sin(m\theta_i)$ terms and the $\cos(m\theta_i)$ terms are linearly independent, eqn.(E.18) becomes

$$\sum_{j=1}^{K}{}^{*}\left[\sum_{n=m}^{\infty}\left[\frac{(-1)^{n-m}\,n!\,R_{ij}^{n-m}\,R_i^{m-1}}{(m-1)!\,(n-m)!}\right]\left[\left\{\begin{matrix}A_{nj}\\B_{nj}\end{matrix}\right\}\cos[(n-m)\psi_{ij}]+\left\{\begin{matrix}B_{nj}\\-A_{nj}\end{matrix}\right\}\right.\right.$$

$$\left.\cdot\sin[(n-m)\psi_{ij}]\right]+\sum_{n=1}^{\infty}\left[\frac{(-1)^n\,(n+m-1)!\,R_i^{m-1}}{(m-1)!\,(n-1)!\,R_{ij}^{n+m}}\right]\cdot\left[\left\{\begin{matrix}C_{nj}\\-D_{nj}\end{matrix}\right\}\cos[(n+m)\psi_{ij}]\right.$$

$$\left.\left.+\left\{\begin{matrix}D_{nj}\\C_{nj}\end{matrix}\right\}\sin[(n+m)\psi_{ij}]\right]\right]+\left\{\begin{matrix}A_{mi}\\B_{mi}\end{matrix}\right\}mR_i^{m-1}-\left\{\begin{matrix}C_{mi}\\D_{mi}\end{matrix}\right\}\frac{m}{R_i^{m+1}}=\delta_{im}\left\{\begin{matrix}Dw_i/Dt\\Dv_i/Dt\end{matrix}\right\}, \tag{E.19}$$

$$i=1,2,\ldots,K,\quad m=1,2,\ldots,\infty,$$

where δ_{ij} is the Kronecker delta.

(c) Final Boundary Condition Equations Using Dimensionless Constants

Inspection of eqn.(E.19) reveals that the coefficients A_{nj}, B_{nj}, C_{nj}, and D_{nj} are linear functions of Dw_i/Dt and Dv_i/Dt ($i=1,2,\ldots,K$). Furthermore, the units of ϕ_j being L^2/T^*, and those of r_j being L, we see from eqn.(E.3) that the above coefficients have the following units:

L^{2-n}/T for A_{nj} and B_{nj}, and

L^{2+n}/T for C_{nj} and D_{nj}.

Consequently, the following linear relationships can be written

$$\left.\left\{\begin{matrix}A_{nj}\\B_{nj}\end{matrix}\right\}=R_j^{1-n}\sum_{\ell=1}^{K}\left[\left\{\begin{matrix}\alpha_{nj\ell}\\\beta_{nj\ell}\end{matrix}\right\}\frac{Dw_\ell}{Dt}+\left\{\begin{matrix}a_{nj\ell}\\b_{nj\ell}\end{matrix}\right\}\frac{Dv_\ell}{Dt}\right],\right\} \tag{E.20}$$

and

---

* L: length and T: time.

(eqn.(E.20) continued)

$$\begin{Bmatrix} C_{n\mathscr{j}} \\ D_{n\mathscr{j}} \end{Bmatrix} = R_{\mathscr{j}}^{1+n} \sum_{\ell=1}^{K} \left(\begin{Bmatrix} \gamma_{n\mathscr{j}\ell} \\ \delta_{n\mathscr{j}\ell} \end{Bmatrix} \frac{Dw_\ell}{Dt} + \begin{Bmatrix} c_{n\mathscr{j}\ell} \\ d_{n\mathscr{j}\ell} \end{Bmatrix} \frac{Dv_\ell}{Dt} \right), \quad \begin{matrix} n = 1,2,..,\infty, \\ \mathscr{j} = 1,2,\ldots,K, \end{matrix}$$

where $\alpha_{n\mathscr{j}\ell}$, $\beta_{n\mathscr{j}\ell}$, etc. are dimensionless constants, dependent on (fixed) geometric conditions: namely, the channel and cylinder radii, and the number and location of the cylinders in the channel. The cylinder radii, $R_{\mathscr{j}}$, are used* to render the constants ($A_{n\mathscr{j}}$, etc.) non-dimensional.

The final sets of linear equations, for the determination of the latter dimensionless constants, are found by substituting eqn.(E.20) into the boundary condition equations (E.13), (E.16), and (E.19), yielding, after isolating the Dw_i/Dt and Dv_i/Dt terms,

(1) for boundary condition I and $\mathscr{j} = q$:

$$\left(\frac{R_c}{R_q}\right)^{n-1} \begin{Bmatrix} \alpha_{nq\ell} \\ a_{nq\ell} \\ \beta_{nq\ell} \\ b_{nq\ell} \end{Bmatrix} - \left(\frac{R_q}{R_c}\right)^{n+1} \begin{Bmatrix} \gamma_{nq\ell} \\ c_{nq\ell} \\ \delta_{nq\ell} \\ d_{nq\ell} \end{Bmatrix} = \begin{Bmatrix} 0 \\ 0 \\ 0 \\ 0 \end{Bmatrix}, \quad \begin{matrix} n = 1,2,\ldots,\infty, \\ \ell = 1,2,\ldots,K. \end{matrix} \tag{E.21}$$

(2) for boundary condition I and $\mathscr{j} \neq q$:

$$\sum_{n=m}^{\infty} \frac{(-1)^{n-m}\, n!\, R_{c\mathscr{j}}^{n-m}\, R_c^{m-1}}{(m-1)!\,(n-m)!\, R_{\mathscr{j}}^{n-1}} \left[\begin{Bmatrix} \alpha_{n\mathscr{j}\ell} \\ a_{n\mathscr{j}\ell} \\ -\beta_{n\mathscr{j}\ell} \\ -b_{n\mathscr{j}\ell} \end{Bmatrix} \cos[(n-m)\psi_{c\mathscr{j}}] + \begin{Bmatrix} \beta_{n\mathscr{j}\ell} \\ b_{n\mathscr{j}\ell} \\ \alpha_{n\mathscr{j}\ell} \\ a_{n\mathscr{j}\ell} \end{Bmatrix} \sin[(n-m)\psi_{c\mathscr{j}}] \right]$$

$$- \sum_{n=1}^{m} \frac{m!\, R_{c\mathscr{j}}^{m-n}\, R_{\mathscr{j}}^{n+1}}{(n-1)!\,(m-n)!\, R_c^{m+1}} \left[\begin{Bmatrix} \gamma_{n\mathscr{j}\ell} \\ c_{n\mathscr{j}\ell} \\ -\delta_{n\mathscr{j}\ell} \\ -d_{n\mathscr{j}\ell} \end{Bmatrix} \cos[(m-n)\psi_{c\mathscr{j}}] - \begin{Bmatrix} \delta_{n\mathscr{j}\ell} \\ d_{n\mathscr{j}\ell} \\ \gamma_{n\mathscr{j}\ell} \\ c_{n\mathscr{j}\ell} \end{Bmatrix} \sin[(m-n)\psi_{c\mathscr{j}}] \right]$$

$$= \begin{Bmatrix} 0 \\ 0 \\ 0 \\ 0 \end{Bmatrix}, \quad \begin{matrix} m = 1,2,..,\infty, \\ \mathscr{j},\ell = 1,2,\ldots,K. \end{matrix} \tag{E.22}$$

---

* Any fixed parameter with units of length could have been used.

Note that the signs of all coefficients in the 3rd and 4th parts (rows) of the above equation have been changed (allowable since RHS = 0) to get the same form of equation found in [50].

(3) for boundary condition II:

$$\sum_{j=1}^{K} * \left[\sum_{n=m}^{\infty} \frac{(-1)^{n-m}\, n!\, R_{ij}^{n-m}\, R_i^{m-1}}{(m-1)!\,(n-m)!\, R_j^{n-1}} \left[\begin{Bmatrix} \beta_{nj\ell} \\ b_{nj\ell} \\ -\alpha_{nj\ell} \\ -a_{nj\ell} \end{Bmatrix} \sin[(n-m)\psi_{ij}] + \begin{Bmatrix} \alpha_{nj\ell} \\ a_{nj\ell} \\ \beta_{nj\ell} \\ b_{nj\ell} \end{Bmatrix} \right.\right.$$

$$\left.\cdot \cos[(n-m)\psi_{ij}] \right] + \sum_{n=1}^{\infty} \frac{(-1)^{n}\, (n+m-1)!\, R_i^{m-1}\, R_j^{n+1}}{(n-1)!\,(m-1)!\, R_{ij}^{n+m}} \left[\begin{Bmatrix} \delta_{nj\ell} \\ d_{nj\ell} \\ \gamma_{nj\ell} \\ c_{nj\ell} \end{Bmatrix} \sin[(n+m)\psi_{ij}] \right.$$

$$\left.\left. + \begin{Bmatrix} \gamma_{nj\ell} \\ c_{nj\ell} \\ -\delta_{nj\ell} \\ -d_{nj\ell} \end{Bmatrix} \cos[(n+m)\psi_{ij}] \right] \right] + m \begin{Bmatrix} \alpha_{mi\ell} \\ a_{mi\ell} \\ \beta_{mi\ell} \\ b_{mi\ell} \end{Bmatrix} - m \begin{Bmatrix} \gamma_{mi\ell} \\ c_{mi\ell} \\ \delta_{mi\ell} \\ d_{mi\ell} \end{Bmatrix} = \begin{Bmatrix} \delta_{1m}\ \delta_{i\ell} \\ 0 \\ 0 \\ \delta_{1m}\ \delta_{i\ell} \end{Bmatrix}, \qquad \text{(E.23)}$$

$$m = 1,2,\ldots,\infty,$$
$$i,\ell = 1,2,\ldots,K.$$

The solution of the above equations,* namely (E.21), (E.22), and (E.23) is found in reference [73].

The potentials for the cylinders are found by substituting eqn.(E.20) into (E.3), yielding

$$\phi_j(r_j,\theta_j) = \sum_{n=1}^{\infty} \sum_{\ell=1}^{K} \left[R_j^{1-n}\ r_j^{n} \left[\left(\alpha_{nj\ell} \frac{Dw_\ell}{Dt} + a_{nj\ell} \frac{Dv_\ell}{Dt} \right) \cos(n\theta_j) + \left(\beta_{nj\ell} \frac{Dw_\ell}{Dt} \right.\right.\right.$$

$$\left. + b_{nj\ell} \frac{Dv_\ell}{Dt} \right) \sin(n\theta_j) \Big] + R_j^{1+n}\ r_j^{-n} \left[\left(\gamma_{nj\ell} \frac{Dw_\ell}{Dt} + c_{nj\ell} \frac{Dv_\ell}{Dt} \right) \cos(n\theta_j) + \left(\delta_{nj\ell} \frac{Dw_\ell}{Dt} \right.\right.$$

$$\left.\left.\left. + d_{nj\ell} \frac{Dv_\ell}{Dt} \right) \sin(n\theta_j) \right] \right], \qquad j = 1,2,\ldots,K. \qquad \text{(E.24)}$$

---

* Truncated to $m = 1,2,\ldots,N$.

Finally, to obtain the total velocity potential $\phi_{(t)j}$, one substitutes eqn. (E.24), i.e. ϕ_j, and the equation resulting from the use of coordinate transformations (E.5) and (E.6) in (E.24), i.e. $\phi_{(i)j}$, into eqn.(E.8). The resulting equation, in matrix (vector) form, reads

$$\phi_{(t)i} = \sum_{\ell=1}^{K} \left[\left\{ \frac{Dw_\ell}{Dt} \quad \frac{Dv_\ell}{Dt} \right\} \left(\sum_{n=1}^{\infty} \sum_{j=1}^{K} * \left[\frac{R_j^{1-n} \; r_i^n}{(K-1)} \left(\left\{ \begin{matrix} \alpha_{nil} \\ a_{nil} \end{matrix} \right\} \cos(n\theta_i) + \left\{ \begin{matrix} \beta_{nil} \\ b_{nil} \end{matrix} \right\} \right.\right.\right.$$

$$\left.\left.\left. \cdot \sin(n\theta_i) \right) + \frac{R_i^{1+n} \; r_i^{-n}}{(K-1)} \left(\left\{ \begin{matrix} \gamma_{nil} \\ c_{nil} \end{matrix} \right\} \cos(n\theta_i) + \left\{ \begin{matrix} \delta_{nil} \\ d_{nil} \end{matrix} \right\} \sin(n\theta_i) \right) + R_j^{1-n} \sum_{m=0}^{n} \right.\right.$$

$$\left.\left. \cdot \frac{(-1)^{n-m} \, n! \, R_{ij}^{n-m} \, r_i^m}{m! \; (n-m)!} \left(\left\{ \begin{matrix} \alpha_{njl} \\ a_{njl} \end{matrix} \right\} \cos[m\theta_i + (n-m)\psi_{ij}] + \left\{ \begin{matrix} \beta_{njl} \\ b_{njl} \end{matrix} \right\} \sin[m\theta_i + (n-m)\psi_{ij}] \right) \right.$$

$$\left. + R_j^{1+n} \sum_{m=0}^{\infty} \frac{(-1)^n \, (n+m-1)! \, r_i^m}{m! \; (n-1)! \; R_{ij}^{n+m}} \left(\left\{ \begin{matrix} \gamma_{njl} \\ c_{njl} \end{matrix} \right\} \cos[m\theta_i - (n+m)\psi_{ij}] - \left\{ \begin{matrix} \delta_{njl} \\ d_{njl} \end{matrix} \right\} \right.\right.$$

$$\left.\left. \cdot \sin[m\theta_i - (n+m)\psi_{ij}] \right) \right] \Bigg] , \qquad i = 1,2,\ldots,K . \tag{E.25}$$

Equation (E.25) completely defines the total velocity potential which is seen to depend linearly on Dw_ℓ/Dt and Dv_ℓ/Dt ($\ell = 1,2,\ldots,K$), the other parameters depending on fixed geometric conditions.

(d) Inviscid Force(s) per Unit Length

Slender body theory is used to evaluate pressure forces (normal to the wall) induced on cylinders. Following Lighthill (see Appendix F of Ref. [75]), we write the inviscid hydrodynamic forces per unit length as follows:

(i) in the y-direction, on cylinder k

$$F_{A(y)k} = -\rho \cdot \int_0^{2\pi} \left(\frac{\partial}{\partial t} + U \frac{\partial}{\partial x} \right) \phi_{(t)k}(r_k, \theta_k) \cdot R_k \cdot \sin\theta_k \cdot d\theta_k , \qquad k = 1,2,\ldots,K . \tag{E.26}$$

(ii) in the z-direction, on cylinder k

$$F_{A(z)k} = -\rho \cdot \int_0^{2\pi} \left(\frac{\partial}{\partial t} + U \frac{\partial}{\partial x} \right) \phi_{(t)k}(r_k, \theta_k) \cdot R_k \cdot \cos\theta_k \cdot d\theta_k , \qquad k = 1,2,\ldots,K .$$

Only the derivations for $F_{A(y)k}$ are carried out here, the procedure for $F_{A(z)k}$ being analogous.

Note that the (inviscid) hydrodynamic coupling effect is present in the total potential $\phi_{(t)k}$.

Since R_k is constant and θ_k does not depend on x or t, we can write* (E.26) as

$$F_{A(y)k} = -\rho R_k \cdot \frac{D}{Dt} \int_0^{2\pi} \phi_{(t)k} \cdot \sin\theta_k \cdot d\theta_k , \qquad k = 1,2,\ldots,K . \tag{E.27}$$

Substituting eqn.(E.25) with $i = k$ into (E.27), making use of

$$\int_0^{2\pi} \sin(n\theta)\cdot\sin\theta\cdot d\theta = \delta_{1n}\cdot\pi , \qquad n = 1,2,\ldots,\infty ,$$

and

$$\int_0^{2\pi} \cos(n\theta)\cdot\sin\theta\cdot d\theta = 0 , \qquad n = 1,2,..,\infty ,$$

and noting that the integral is at the cylinder wall, i.e. $r_k = R_k$ ($k = 1,2,\ldots,K$), we obtain

$$F_{A(y)k} = -\pi\rho R_k^2 \sum_{\ell=1}^{K} \left[\left\{ \frac{D^2 w_\ell}{Dt^2} \quad \frac{D^2 w_\ell}{Dt^2} \right\} \left(\begin{Bmatrix} \beta_{1k\ell}+\delta_{1k\ell} \\ b_{1k\ell}+d_{1k\ell} \end{Bmatrix} + \sum_{j=1}^{K} {}^{*} \sum_{n=1}^{\infty} (-1)^n \, n \right.\right.$$

$$\left[\left(\frac{R_{kj}}{R_j}\right)^{n-1} \left(\begin{Bmatrix} \alpha_{njl} \\ a_{njl} \end{Bmatrix} \sin[(n-1)\psi_{kj}] - \begin{Bmatrix} \beta_{njl} \\ b_{njl} \end{Bmatrix} \cos[(n-1)\psi_{kj}] \right) + \left(\frac{R_j}{R_{kj}}\right)^{n+1} \left(\begin{Bmatrix} \gamma_{njl} \\ c_{njl} \end{Bmatrix} \right.\right.$$

$$\left.\left.\left.\left.\cdot\sin[(n+1)\psi_{kj}] - \begin{Bmatrix} \delta_{njl} \\ d_{njl} \end{Bmatrix} \cos[(n+1)\psi_{kj}] \right)\right]\right)\right] , \qquad k = 1,2,\ldots,K . \tag{E.28}$$

The problem is simplified by defining the following dimensionless constants:

---

* Leibnitz' rule.

$$\begin{Bmatrix}\kappa_{k\ell}\\ k_{k\ell}\end{Bmatrix} - \begin{Bmatrix}\beta_{1\,k\ell}+\delta_{1\,k\ell}\\ b_{1\,k\ell}+d_{1\,k\ell}\end{Bmatrix} + \sum_{j=1}^{K}{}^{*}\sum_{n=1}^{\infty}(-1)^n\, n \left[\left(\frac{R_{kj}}{R_j}\right)^{n-1}\left(\begin{Bmatrix}\alpha_{nj\ell}\\ a_{nj\ell}\end{Bmatrix}\cdot \sin[(n-1)\psi_{kj}]\right.\right.$$

$$\left.\left. - \begin{Bmatrix}\beta_{nj\ell}\\ b_{nj\ell}\end{Bmatrix}\cos[(n-1)\psi_{kj}]\right) + \left(\frac{R_j}{R_{kj}}\right)^{n+1}\left(\begin{Bmatrix}\gamma_{nj\ell}\\ c_{nj\ell}\end{Bmatrix}\cdot \sin[(n+1)\psi_{kj}] - \begin{Bmatrix}\delta_{nj\ell}\\ d_{nj\ell}\end{Bmatrix}\right.\right.$$

$$\left.\left.\cdot\cos[(n+1)\psi_{kj}]\right)\right], \qquad k=1,2,\ldots,K. \tag{E.29}*$$

From eqs.(E.29) and (E.28), we obtain

$$F_{A(y)k} = -\pi\rho R_k^2 \sum_{\ell=1}^{K}\left[\begin{Bmatrix}\frac{D^2w_\ell}{Dt^2} & \frac{D^2v_\ell}{Dt^2}\end{Bmatrix}\begin{Bmatrix}\kappa_{k\ell}\\ k_{k\ell}\end{Bmatrix}\right], \qquad k=1,2,\ldots,K.$$

But, in our case, all cylinder radii R_k are the same and equal to R. Hence we have

$$F_{A(y)k} = -\rho A \sum_{\ell=1}^{K}\left[\kappa_{k\ell}\frac{D^2w_\ell}{Dt^2} + k_{k\ell}\frac{D^2v_\ell}{Dt^2}\right], \qquad k=1,2,\ldots,K. \tag{E.30}$$

Finally, the last two equations of (E.23), with m = 1, are

$$\begin{Bmatrix}0\\ \delta_{i\ell}\end{Bmatrix} - \begin{Bmatrix}\beta_{1\,i\ell}-\delta_{1\,i\ell}\\ b_{1\,i\ell}-d_{1\,i\ell}\end{Bmatrix} + \sum_{j=1}^{K}{}^{*}\sum_{n=1}^{\infty}(-1)^n\, n\left[\left(\frac{R_{ij}}{R_j}\right)^{n-1}\cdot\left(\begin{Bmatrix}\alpha_{nj\ell}\\ a_{nj\ell}\end{Bmatrix}\sin[(n-1)\psi_{ij}]\right.\right.$$

$$\left.\left. - \begin{Bmatrix}\beta_{nj\ell}\\ b_{nj\ell}\end{Bmatrix}\cos[(n-1)\psi_{ij}]\right) + \left(\frac{R_j}{R_{ij}}\right)^{n+1}\left(\begin{Bmatrix}\gamma_{nj\ell}\\ c_{nj\ell}\end{Bmatrix}\sin[(n+1)\psi_{ij}] - \begin{Bmatrix}\delta_{nj\ell}\\ d_{nj\ell}\end{Bmatrix}\right.\right.$$

$$\left.\left.\cdot\cos[(n+1)\psi_{ij}]\right)\right], \qquad i=1,2,\ldots,K. \tag{E.31}$$

Subtracting (E.31), with $i=k$, from (E.29), we obtain

$$\begin{aligned}\kappa_{k\ell} &= 2\delta_{1\,k\ell},\\ k_{k\ell} &= \delta_{k\ell} + 2d_{1\,k\ell},\end{aligned} \qquad k,\ell=1,2,\ldots,K. \tag{E.32}$$

Similar results hold for $F_{A(z)k}$. They are found in reference [73].

---

* Note that there is a sign error in Suss' [73] eqn.(3.30).

Appendix F

"Viscous" hydrodynamic coupling

At any arbitrary (y,z)-plane cross-section, there are two kinds of fluid forces* acting on a cylinder: namely, normal pressure forces and tangential friction forces. The boundary layer is assumed infinitesimally small,§ hence all forces are assumed to act at the surface of the cylinder. The normal pressure forces are treated in Appendix E, and the tangential friction forces are examined here, following Suss' [73] approach.

The forces of interest here lie in the (y,z)-plane and arise because of relative fluid-cylinder velocities. A viscous fluid friction model, adopted by Paidoussis [22]† is used.

A coupling effect exists because the velocity field in any (y,z)-plane is dependent on the motion of all cylinders, as established in Appendix E.

Recall eqn.(B.12) of Ref.[75] (Appendix B):

$$F_N = \frac{1}{2}\rho D U^2 (C_{D_p} \cdot \sin^2\psi + C_f \cdot \sin\psi), \qquad (F.1)$$

for the normal force per unit length on a cylinder inclined to the flow, at an angle ψ.

Let us consider an (x,y)-plane cross-section of an element of cylinder k, shown on the next page, where:
$(\Omega_k)_y$ is the angle of incidence (ψ), for cylinder k, in the "y-direction", and
$(V_y)_k$ is the fluid velocity component, in the y-direction, due to the motion of all other (K-1) cylinders of the bundle (excluding cylinder k):

---

* Per unit length of cylinder.

§ It is also assumed that there is no flow separation.

† Paidoussis found an error in his paper [22] and subsequently corrected it in [43].

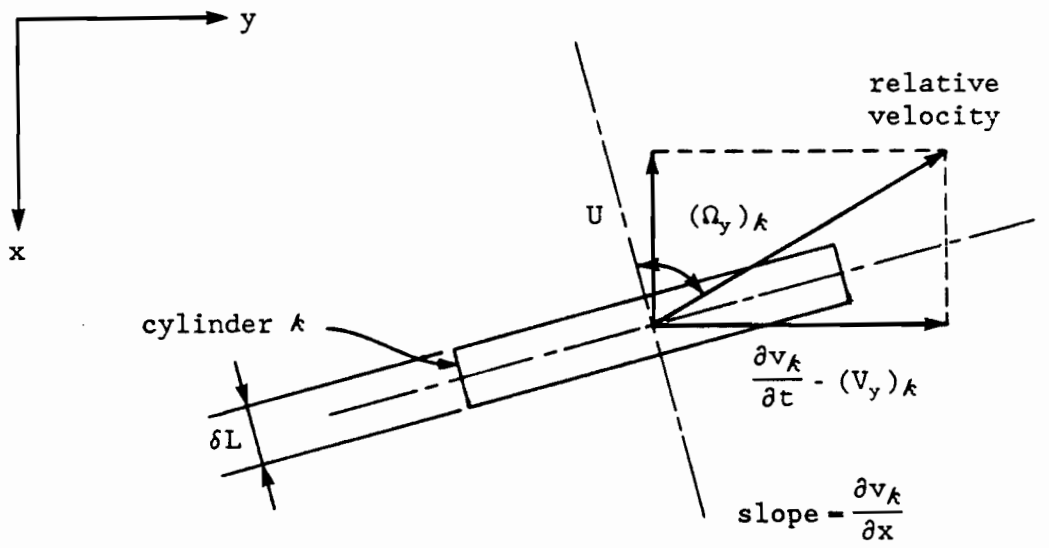

By inspection of the above diagram, we can write

$$(\Omega_y)_k = \arctan\left[\frac{\partial v_k}{\partial x}\right] + \arctan\left[\frac{1}{U}\left[\frac{\partial v_k}{\partial t} - (V_y)_k\right]\right], \quad k = 1,2,\ldots,K. \tag{F.2}$$

From (F.1), using multi-cylinder terminology, we get

$$F_{N(y)k} = \frac{1}{2}\rho DU^2\left[C_{D_p}\cdot\sin^2[(\Omega_y)_k] + C_f\cdot\sin[(\Omega_y)_k]\right], \quad k = 1,2,\ldots,K, \tag{F.3}$$

where $F_{N(y)k}$ is the normal viscous force per unit length, acting on cylinder k, in the y-direction. Note that, since we consider only small motion, i.e. small angle(s) of incidence, the y- and x-direction components of the normal force (per unit length) are taken as $F_{N(y)k}$ and zero respectively.

Hydrodynamic coupling appears in the term $(V_y)_k$ of eqn.(F.2), which alters the angle of incidence $(\Omega_y)_k$, and therefore, from (F.3), the force per unit length $F_{N(y)k}$. Hence the label "viscous" hydrodynamic coupling.

The force(s) $F_{N(z)k}$ is not derived here, the procedure being exactly the same as for $F_{N(y)k}$.

Substitution of eqn.(F.2) into (F.3) yields, for $(\Omega_y)_k \ll 1$:

$$F_{N(y)k} = \frac{1}{2}\rho DUC_f\left[U\frac{\partial v_k}{\partial x}+\frac{\partial v_k}{\partial t} - (V_y)_k\right] + \frac{1}{2}\rho DC_{D_p}\left[U\frac{\partial v_k}{\partial x}+\frac{\partial v_k}{\partial t} - (V_y)_k\right]^2, \qquad (F.4)$$

$$k = 1,2,\ldots,K .$$

To avoid powers of derivatives in the final equation(s) of motion of the cylinders, which would make it non-linear, Paidoussis has linearized the quadratic viscous forces at $U = 0$. Note that this amounts to assuming that lateral drag (viscous damping) forces are proportional to velocity rather than velocity squared. (Chen et al. [43] has measured such damping coefficients, which have been used in this Thesis in FORTRAN programs for theoretical computations.) The linearization procedure, involving the second term of eqn.(F.4) is illustrated here.

As $U \to 0$, eqn.(F.4) becomes

$$F_{N(y)k}\Big|_{U\to 0} = \frac{1}{2}\rho DC_{D_p}\left[\frac{\partial v_k}{\partial t} - (V_{y,0})_k\right]^2, \qquad k = 1,2,\ldots,K, \qquad (F.5)$$

where

$$(V_{y,0}) = (V_y)_k\Big|_{U\to 0}, \qquad \text{(for conciseness)} \quad k = 1,2,\ldots,K, \qquad (F.6)$$

or,

$$\frac{F_{N(y)k}\Big|_{U\to 0}}{1/2(\rho D)} = C_{D_p}\left[\frac{\partial v_k}{\partial t} - (V_{y,0})_k\right]^2, \qquad k = 1,2,\ldots,K .$$

This expression is linearized by using the approximation

$$\frac{F_{N(y)k}\Big|_{U\to 0}}{1/2(\rho D)} \simeq C_D\left[\frac{\partial v_k}{\partial t} - (V_{y,0})_k\right], \qquad k = 1,2,\ldots,K, \qquad (F.7)$$

illustrated graphically below.

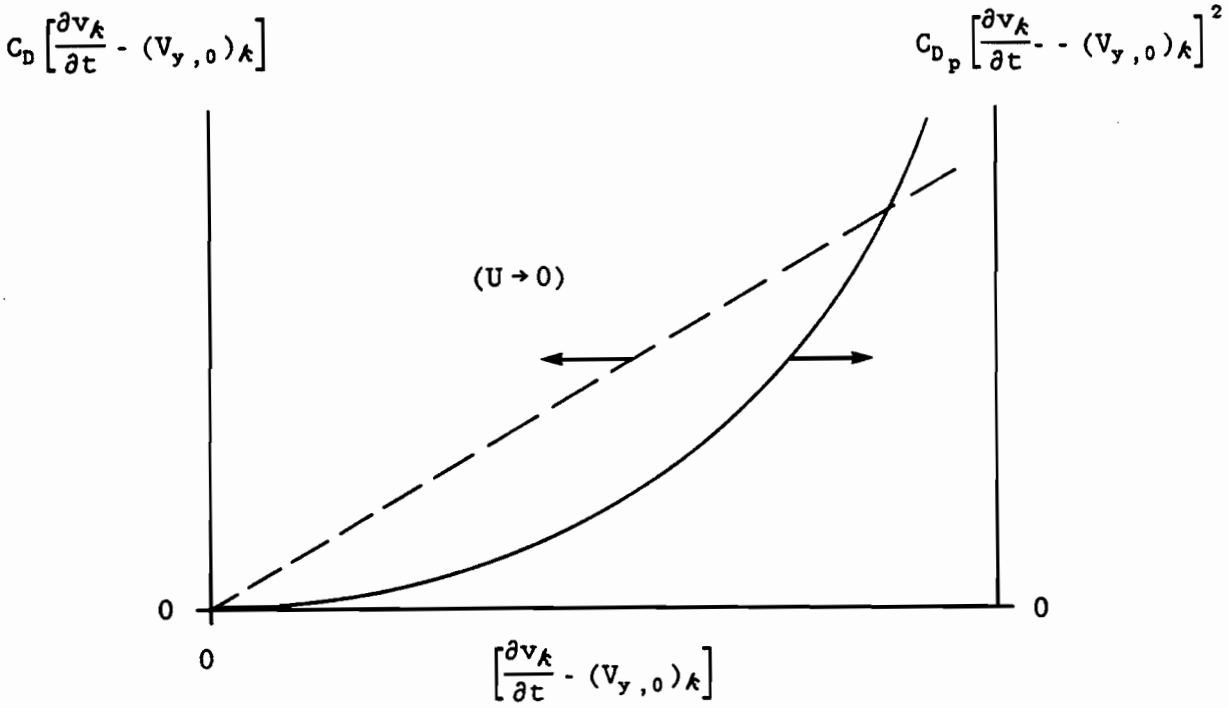

Note that C_D has dimensions L/T.

Eqn.(F.7) is retained as the new second term of (F.4), hence

$$F_{N(y)k} = \frac{1}{2}\rho DUC_f\left[U\,\frac{\partial v_k}{\partial x} + \frac{\partial v_k}{\partial t} - (V_y)_k\right] + \frac{1}{2}\rho DC_D\left[\frac{\partial v_k}{\partial t} - (V_{y,0})_k\right], \qquad k = 1,2,\ldots,K. \tag{F.8}$$

We obtain $(V_y)_k$ from the total velocity potential $\phi_{(t)k}$, less the potential of cylinder k, ϕ_k. From eqn.(E.8) of Appendix E, we have

$$\phi_{(t)k} - \phi_k = \sum_{i=1}^{K}{}^{*}\,\phi_{(k)i}\,, \qquad k = 1,2,\ldots,K, \tag{F.9}$$

the starred summation excluding $i = k$.

The fluid velocity component in the y-direction, resulting from the velocity potential $(\phi_{(t)k} - \phi_k)$ is,

$$v_y(r_k,\theta_k) = \frac{\partial(\phi_{(t)k} - \phi_k)}{\partial y} ,$$

or

$$v_y(r_k,\theta_k) = \frac{\partial(\phi_{(t)k} - \phi_k)}{\partial r_k} \sin\theta_k + \frac{1}{r_k}\frac{\partial(\phi_{(t)k} - \phi_k)}{\partial\theta_k} \cos\theta_k , \qquad k = 1,2,\ldots,K . \tag{F.10}$$

To estimate $(V_y)_k$, Suss [73] takes an average of v_y, around the circumference of cylinder k, that is

$$(V_y)_k = \frac{1}{2\pi}\int_0^{2\pi} v_y(r_k,\theta_k)\, d\theta_k , \qquad k = 1,2,\ldots,K . \tag{F.11}$$

Using (F.10) in (F.11), we get

$$(V_y)_k = \frac{1}{2\pi}\int_0^{2\pi}\left[\frac{\partial(\phi_{(t)k} - \phi_k))}{\partial r_k} \sin\theta_k + \frac{1}{r_k}\frac{\partial(\phi_{(t)k} - \phi_k)}{\partial\theta_k} \cos\theta_k\right] d\theta_k , \qquad k = 1,2,\ldots,K . \tag{F.12}$$

Using eqn.(F.9) in eqn.(F.12), and carrying the integration as done in Appendix E, we obtain

$$(V_y)_k = \sum_{\ell=1}^{K}{}^{*}\left(\bar{\nu}_{k\ell}\frac{Dw_\ell}{Dt} + \bar{n}_{k\ell}\frac{Dv_\ell}{Dt}\right) , \qquad k = 1,2,\ldots,K , \tag{F.13}$$

the starred summation excluding $\ell = k$, and where

$$\begin{Bmatrix}\bar{\nu}_{k\ell}\\ \bar{\eta}_{k\ell}\end{Bmatrix} = \sum_{\delta=1}^{K}{}^{*}\sum_{n=1}^{\infty}\left[(-1)^{n-1}\, n\left(\frac{R_{k\delta}}{R_\delta}\right)^{n-1}\left(\begin{Bmatrix}\beta_{n\delta\ell}\\ b_{n\delta\ell}\end{Bmatrix}\cos[(n-1)\psi_{k\delta}] + \begin{Bmatrix}-\alpha_{n\delta\ell}\\ -a_{n\delta\ell}\end{Bmatrix}\right.\right.$$
$$\left.\cdot\sin[(n-1)\psi_{k\delta}]\right) + (-1)^n\, n\left(\frac{R_\delta}{R_{k\delta}}\right)^{n+1}\left(\begin{Bmatrix}-\delta_{n\delta\ell}\\ -d_{n\delta\ell}\end{Bmatrix}\cos[(n+1)\psi_{k\delta}] + \begin{Bmatrix}\gamma_{n\delta\ell}\\ c_{n\delta\ell}\end{Bmatrix}\right.$$
$$\left.\left.\cdot\sin[(n+1)\psi_{k\delta}]\right)\right] , \qquad k = 1,2,\ldots,K , \tag{F.14}$$

the starred summation excluding $\delta = k$.

Note that the dimensionless constants $\bar{\nu}_{k\ell}$ and $\bar{\eta}_{k\ell}$ depend on parameters which are themselves geometric (e.g. R_δ) or dependent on the geometry of the system (e.g. $\alpha_{n\delta\ell}$) (see Appendix E).

From (F.6) and (F.13), we have

$$(V_{y,0})_k = \sum_{\ell=1}^{K}{}^{*} \left[\bar{\nu}_{k\ell} \frac{\partial w_\ell}{\partial t} + \bar{\eta}_{k\ell} \frac{\partial v_\ell}{\partial t}\right], \quad k = 1,2,\ldots,K. \tag{F.15}$$

Substituting eqn.(F.13) and (F.15) into (F.8) we get

$$F_{n(y)k} = \frac{1}{2}\rho DUC_f \left[\frac{\partial v_k}{\partial t} + U \frac{\partial v_k}{\partial x} - \sum_{\ell=1}^{K}{}^{*} \left[\bar{\nu}_{k\ell} \frac{Dw_\ell}{Dt} + \bar{\eta}_{k\ell} \frac{Dv_\ell}{Dt}\right]\right] + \frac{1}{2}\rho DC_D \left[\frac{\partial v_k}{\partial t} - \sum_{\ell=1}^{K}{}^{*} \left[\bar{\nu}_{k\ell} \frac{\partial w_\ell}{\partial t} + \bar{\eta}_{k\ell} \frac{\partial v_\ell}{\partial t}\right]\right], \quad k = 1,2,\ldots,K. \tag{F.16}$$

The format of the above equation is simplified by defining

$$\left.\begin{aligned} \sigma_{k\ell} &= \begin{cases} -\bar{\nu}_{k\ell} & , \text{ if } \ell \neq k \\ 0 & , \text{ if } \ell = k \end{cases} \\ \text{and} \\ s_{k\ell} &= \begin{cases} -\bar{\eta}_{k\ell} & , \text{ if } \ell \neq k \\ 1 & , \text{ if } \ell = k \end{cases} \end{aligned}\right\} \quad k = 1,2,\ldots,K. \tag{F.17}$$

Finally, from (F.16) and (F.17), we can write

$$F_{N(y)k} = \frac{1}{2}\rho DUC_f \sum_{\ell=1}^{K} \left[\sigma_{k\ell} \frac{Dw_\ell}{Dt} + s_{k\ell} \frac{Dv_\ell}{Dt}\right] + \frac{1}{2}\rho DC_D \sum_{\ell=1}^{K} \left[\sigma_{k\ell} \frac{\partial w_\ell}{\partial t} + s_{k\ell} \frac{\partial v_\ell}{\partial t}\right], \quad k = 1,2,\ldots,K. \tag{F.18}$$

Appendix G

Freely vibrating beam modes

We consider the free lateral vibration of a clamped-clamped* beam. Bernoulli-Euler beam theory is used, for which the following assumptions apply:

(i) Any lateral beam cross-section remains plane during motion (or static displacements),

(ii) The motion (displacements) can be analyzed in a plane (going through the beam longitudinal axis), that is, the problem is two-dimensional,

(iii) The radius of curvature of the (deflected) beam longitudinal axis is, at any point, much larger than the beam width, i.e. displacements are much smaller than the beam width,

(iv) The shear deformation effects are negligible,

(v) The rotational inertia (in the plane of motion) is negligible, and

(vi) All properties are constant and homogeneous.

The resulting equation of motion is§

$$\frac{\partial^2 y}{\partial t^2} + \frac{EI}{\rho A}\frac{\partial^4 y}{\partial x^4} = 0 \ , \qquad (G.1)$$

where

E is the modulus of elasticity,

I is the second moment of area,

ρ is the density,

A is the cross-sectional area,

t is the time, and

x,y are the axial coordinate and beam deflection, respectively.

Using separation of variables to solve eqn.(G.1), i.e. letting

$$y = Y(x) \cdot F(t) \ , \qquad (G.2)$$

one obtains

---

* A clamped but axially sliding (with no rotation) beam has the same modes.

§ See Bishop and Johnson [74].

$$\frac{d^2F(t)}{dt^2} = -\omega_n^2 F(t) \ , \tag{G.3}$$

where F(t) was assumed harmonic, and

$$\frac{d^4Y(x)}{dx^4} - \beta_n^4 Y(x) = 0 \ , \tag{G.4}$$

where

$$\beta_n^4 = \frac{\rho A}{EI} \omega_n^2 \ . \tag{G.5}$$

The general solution to the above eigenvalue problem, eqn.(G.4), is given by

$$Y_n(x) = C_{1n} \sin(\beta_n x) + C_{2n} \cos(\beta_n x) + C_{3n} \sinh(\beta_n x) + C_{4n} \cosh(\beta_n x) \ , \tag{G.6}$$
$$n = 1,2,\ldots,\infty \ ,$$

where

C_{nn} ,
$n = 1,2,3,4$,
$n = 1,2,\ldots,\infty$,

are arbitrary constants.

Imposing the boundary conditions (clamped-clamped) on (G.6), one obtains the characteristic equation

$$\cos(\beta_n L) \cdot \cosh(\beta_n L) = 1 \ , \tag{G.7}$$
$$n = 1,2,\ldots,\infty \ ,$$

where L is the length of the beam, and the modal beam shapes $Y_n(x)$, corresponding, in free vibration, to harmonics of frequency ω_n,

$$Y_n(x) = C_n\{\cos(\beta_n x) - \cosh(\beta_n x) - \sigma_n[\sin(\beta_n x) - \sinh(\beta_n x)]\} \ , \tag{G.8}$$
$$n = 1,2,\ldots,\infty \ ,$$

where the C_n are arbitrary constants, and where

$$\sigma_n = \frac{\cos(\beta_n L) - \cosh(\beta_n L)}{\sin(\beta_n L) - \sinh(\beta_n L)} \ , \tag{G.9}$$
$$n = 1,2,\ldots,\infty \ .$$

Before examining the orthogonality properties of the eigenfunctions, we non-dimensionalize and normalize them as follows:

(i) Let the beam dimensionless longitudinal coordinate be

$$\xi = x/L \, . \tag{G.10}$$

(ii) Let the normalized dimensionless modal shapes be $\phi_r(\xi)$, such that

$$\int_0^1 [\phi_r(\xi)]^2 \, d\xi = 1 \, , \qquad r = 1,2,\ldots,\infty \, . \tag{G.11}$$

Since we must have $\beta_r x = \lambda_r \xi$, where λ_r are the dimensionless eigenvalues,

$$\lambda_r = \beta_r L \, , \qquad r = 1,2,\ldots,\infty \, . \tag{G.12}$$

Using (G.12) in (G.7) and (G.9) respectively, we get

$$\cos \lambda_r \cdot \cosh \lambda_r = 1 \, , \qquad r = 1,2,\ldots,\infty \, , \tag{G.13}$$

and

$$\sigma_r = \frac{\cos \lambda_r - \cosh \lambda_r}{\sin \lambda_r - \sinh \lambda_r} \, , \qquad r = 1,2,\ldots,\infty \, . \tag{G.14}$$

It can be shown that

$$\phi_r(\xi) = \cos(\lambda_r \xi) - \cosh(\lambda_r \xi) - \sigma_r[\sin(\lambda_r \xi) - \sinh(\lambda_r \xi)] \, , \qquad r = 1,2,\ldots,\infty \, , \tag{G.15}$$

together with eqn.(G.13), satisfy (G.11).

In Chapter 2, eqn.(2.88) results from (2.79) by using the following modal shape integrals:

$$\left.\begin{aligned} a_{mn} &= \int_0^1 \frac{d\phi_n}{d\xi} \, \phi_m \, d\xi \, , \\ b_{mn} &= \int_0^1 \frac{d^2\phi_n}{d\xi^2} \, \phi_m \, d\xi \, , \\ d_{mn} &= \int_0^1 \xi \, \frac{d^2\phi_n}{d\xi^2} \, \phi_m \, d\xi \, , \end{aligned}\right\} \qquad m,n = 1,2,\ldots,N \, , \tag{G.16}$$

and

$$\int_0^1 \frac{d^4\phi_n}{d\xi^4}\,\phi_m\,d\xi = \lambda_n^4\,\delta_{mn}\,, \qquad m,n = 1,2,\ldots,N\,;^{*}$$

where δ_{mn} is the Kronecker delta.

The latter equation results from the fact that

$$\frac{d^4\phi_n}{d\xi^4} = \lambda_n^4\,\phi_n\,, \tag{G.17}$$

which can be seen by inspection of eqn.(G.15), and also because

$$\int_0^1 \phi_n\,\phi_m\,d\xi = \delta_{mn}\,,$$

the basic orthonormality property of the normalized modal shapes.

The procedure to obtain the constants of (G.16) is illustrated with the derivation for a_{mn}.

From eqn.(G.17) we have

$$\frac{d^5\phi_n}{d\xi^5} = \lambda_n^4\,\frac{d\phi_n}{d\xi}\,.^{\S}$$

Consequently, we can write

$$\left(\frac{d^4\phi_m}{d\xi^4}\right)\frac{d\phi_n}{d\xi} = (\lambda_m^4\,\phi_m)\,\frac{d\phi_n}{d\xi}\,, \tag{G.18}$$

and

$$\left(\frac{d^5\phi_n}{d\xi^5}\right)\phi_m = \left(\lambda_n^4\,\frac{d\phi_n}{d\xi}\right)\phi_m\,. \tag{G.19}$$

Combining eqs.(G.18) and (G.19), we get

---

* N is the number of comparison functions used in the solution (see Chapter 2).

§ The range of the indices m and n, always $1,2,\ldots,\infty$, is omitted for the sake of conciseness.

$$(\lambda_n^4 - \lambda_m^4)\int_0^1 \frac{d\phi_n}{d\xi}\,\phi_m\,d\xi = \int_0^1 \frac{d^5\phi_n}{d\xi^5}\,\phi_m\,d\xi - \int_0^1 \frac{d^4\phi_m}{d\xi^4}\,\frac{d\phi_n}{d\xi}\,d\xi\ .$$

Using integration by parts, the above equation can be written as

$$(\lambda_n^4 - \lambda_m^4)\int_0^1 \frac{d\phi_n}{d\xi}\,\phi_m\,d\xi = \left[\phi_m\,\frac{d^4\phi_n}{d\xi^4}\,\Big|_0^1 - \frac{d\phi_m}{d\xi}\,\frac{d^3\phi_n}{d\xi^3}\,\Big|_0^1 + \int_0^1 \frac{d^2\phi_m}{d\xi^2}\,\frac{d^3\phi_n}{d\xi^3}\,d\xi\right]$$

$$-\left[\frac{d^3\phi_m}{d\xi^3}\,\frac{d\phi_n}{d\xi}\,\Big|_0^1 - \frac{d^2\phi_m}{d\xi^2}\,\frac{d^2\phi_n}{d\xi^2}\Big|_0^1 + \int_0^1 \frac{d^2\phi_m}{d\xi^2}\,\frac{d^3\phi_n}{d\xi^3}\,d\xi\right],$$

which becomes

$$(\lambda_n^4 - \lambda_m^4)\int_0^1 \frac{d\phi_n}{d\xi}\,\phi_m\,d\xi = \left[\phi_m\,\frac{d^4\phi_n}{d\xi^4} - \frac{d\phi_m}{d\xi}\,\frac{d^3\phi_n}{d\xi^3} - \frac{d^3\phi_m}{d\xi^3}\,\frac{d\phi_n}{d\xi} + \frac{d^2\phi_m}{d\xi^2}\,\frac{d^2\phi_n}{d\xi^2}\right]\Bigg|_0^1 . \quad (G.20)$$

But, from eqn.(G.15), we see that

$$\phi_n\Big|_{\xi=0} = \phi_n\Big|_{\xi=1} = 0\ , \quad (G.21)$$

and

$$\frac{d\phi_n}{d\xi}\Big|_{\xi=0} = \frac{d\phi_n}{d\xi}\Big|_{\xi=1} = 0\ . \quad (G.22)$$

Using (G.21) and (G.22) in (G.20), we obtain

$$(\lambda_n^4 - \lambda_m^4)\int_0^1 \frac{d\phi_n}{d\xi}\,\phi_m\,d\xi = -\frac{d^2\phi_m}{d\xi^2}\,\frac{d^2\phi_n}{d\xi^2}\,\Big|_0^1\ . \quad (G.23)$$

Also, using eqn.(G.15), we get

$$\frac{d^2\phi_n}{d\xi^2}\Big|_{\xi=0} = -2\lambda_n^2\ , \quad (G.24)$$

and

$$\frac{d^2\phi_n}{d\xi^2}\Big|_{\xi=0} = -\frac{2\lambda_n^2(\cos\lambda_n\cdot\sinh\lambda_n - \sin\lambda_n\cdot\cosh\lambda_n)}{\sin\lambda_n - \sinh\lambda_n}\ . \quad (G.25)$$

Consequently, from (G.24), (G.25), and (G.23),

$$(\lambda_n^4 - \lambda_m^4)\int_0^1 \frac{d\phi_n}{d\xi}\,\phi_m\,d\xi = 4\lambda_n^2\,\lambda_m^2(F_nF_m - 1), \quad (G.26)$$

where

$$F_n = \frac{\cos\lambda_n\cdot\sinh\lambda_n - \sin\lambda_n\cdot\cosh\lambda_n}{\sin\lambda_n - \sinh\lambda_n}\ . \quad (G.27)$$

The terms F_n and F_m of eqn.(G.21) can be considerably simplified as follows: From eqn.(G.27), we have

$$F_n = \frac{\cos^2\lambda_n \cdot \sinh^2\lambda_n + \sin^2\lambda_n \cdot \cosh^2\lambda_n - 2\sin\lambda_n \cdot \cos\lambda_n \cdot \sinh\lambda_n \cdot \cosh\lambda_n}{\sin^2\lambda_n + \sinh^2\lambda_n - 2\sin\lambda_n \cdot \sinh\lambda_n} ,$$

which becomes, using eqn.(G.13),*

$$F_n^2 = 1 . \qquad (G.28)$$

The sign of F_n is obtained from the fact that, for all roots λ_n of eqn. (G.13), the following holds:

$\cos\lambda_n \ll 1$,

$\sinh\lambda_n \gg 1$,

$\cosh\lambda_n \simeq \sinh\lambda_n$, and

$\sin\lambda_n \simeq (-1)^n$.

The latter stems from the fact that the roots $\lambda_n \simeq (2n+1)\pi/2$.

Therefore, using above and (G.27), we get

$$F_n \simeq \frac{0 - (-1)^n \cosh\lambda_n}{-\cosh\lambda_n} , \quad \text{or}$$

$$F_n \simeq (-1)^n ,$$

which, by virtue of eqn.(G.28), becomes

$$F_n = (-1)^n . \qquad (G.29)$$

Finally, substituting eqn.(G.29) into (G.26), making use of the first part of (G.16), we get

$$\left.\begin{aligned} a_{mn} &= \frac{4\lambda_n^2\lambda_m^2}{\lambda_n^4 - \lambda_m^4}\left[(-1)^{m+n} - 1\right] , \\ \text{which, for } m &= n, \text{ reduces to} \\ a_{mn} &= 0 . \end{aligned}\right\} \qquad (G.30)$$

---

* Together with sin, cos, sinh, and cosh identities.

Similarly, one obtains

$$b_{mn} = \left\{ \begin{array}{l} [(-1)^{m+n} + 1](\lambda_n \sigma_n - \lambda_m \sigma_m) \dfrac{4 \lambda_n^2 \lambda_m^2}{\lambda_n^4 - \lambda_m^4} \text{ , if } m \neq n \text{ ,} \\ \lambda_n \sigma_n (2 - \lambda_n \sigma_n) \text{ , if } m = n \text{ ,} \end{array} \right\} \tag{G.31}$$

and

$$d_{mn} = \left\{ \begin{array}{l} \dfrac{4 \lambda_n^2 \lambda_m^2}{\lambda_n^4 - \lambda_m^4} \left[(-1)^{m+n} [\lambda_n \sigma_n - \lambda_m \sigma_m] - [(-1)^{m+n} - 1] \dfrac{3 \lambda_n^4 + \lambda_m^4}{\lambda_n^4 - \lambda_m^4} \right] \text{ , if } m \neq n \text{ ,} \\ \dfrac{b_{nn}}{2} \text{ , if } m = n \text{ .} \end{array} \right. \tag{G.32}$$

Numerical values for the λ_n and σ_n are found in Appendix H, for the lowest values of n.

Appendix H

Longitudinal location of strain gages

The location of strain gages is shown diagrammatically in Fig. 13. The radial location was made to be as close as possible to the cylinder surface, mostly constrained in this respect, by the manufacturing procedure (see Appendix M of Ref. [75]). The criterion for the longitudinal location of the gages follows.

The dimensionless modal shapes for clamped-clamped beams are obtained from eqs.(G.8), (G.10), and (G.12), namely,

$$\phi_r(\xi) = A_r\{\cos(\lambda_r\xi) - \cosh(\lambda_r\xi) - \sigma_r[\sin(\lambda_r\xi) - \sinh(\lambda_r\xi)]\}\,, \qquad r = 1,2,\ldots\infty\,, \tag{H.1}$$

where the A_r are arbitrary (dimensionless) constants* and where (eqn.(G.14))

$$\sigma_r = \frac{\cos\lambda_r - \cosh\lambda_r}{\sin\lambda_r - \sinh\lambda_r}\,, \qquad r = 1,2,\ldots\infty\,. \tag{H.2}$$

Let the $\phi_r(\xi)$ be "normalized"§ such that

$$|\phi_r(\xi)|_{max} = 1\,, \qquad r = 1,2,\ldots\infty\,. \tag{H.3}$$

Letting the first derivative(s) of $\phi_r(\xi)$ go to zero, we get

$$\sin(\lambda_r\xi) + \sinh(\lambda_r\xi) + \sigma_r[\cos(\lambda_r\xi) - \cosh(\lambda_r\xi)] = 0\,, \qquad r = 1,2,\ldots\infty\,. \tag{H.4}$$

For each r, one of the roots of eqn.(H.4), called ξ_M will yield a maximum for $|\phi_r(\xi)|$. Hence, we let

$$A_r = \{\cos(\lambda_r\xi_M) - \cosh(\lambda_r\xi_M) - \sigma_r[\sin(\lambda_r\xi_M) - \sinh(\lambda_r\xi_M)]\}^{-1}\,, \qquad r = 1,2,\ldots,\infty\,. \tag{H.5}$$

Now, for large radii of curvature, we have the elementary relationship

---

* Equal to C_r/L.

§ Scheme local to this Appendix (see eqn.(2.61) for alternate scheme).

$$\varepsilon_r = \frac{a}{L}\frac{d^2\phi_r(\xi)}{d\xi^2}\ ^{*}, \qquad r = 1,2,\ldots\infty, \tag{H.6}$$

where ε_r is the (fiber) strain,
a is the radial distance from the neutral axis,
L is the beam length.

From eqs.(H.6) and (H.1), we can write,

$$\frac{d^2\phi_r(\xi)}{d\xi^2} = \frac{L}{a}\varepsilon_r = -A_r\lambda_r^2\{\cos(\lambda_r\xi) + \cosh(\lambda_r\xi) - \sigma_r[\sin(\lambda_r\xi) + \sinh(\lambda_r\xi)]\}, \tag{H.7}$$
$$r = 1,2,\ldots\infty.$$

Numerical values for the first four modes are tabulated here, to about six significant digits (λ_r and σ_r are from [74], p. 376).

r	λ_r	σ_r	ξ_M	A_r
1	4.73005	0.982502	0.5	-0.629665
2	7.85320	1.000777	0.290426§	-0.662592
3	10.9956	0.999966	0.207742§	-0.661138
4	14.1372	1.000001	0.161567§	-0.661201

Using the constants λ_r, σ_r, and A_r of the above Table, the second derivative, eqn.(H.7), is plotted in the interval $0 \le \xi \le 1$ (for the first four modes). The dotted lines are the negatives of the solid lines. The second plot depicts an expanded portion of the first one.

Fig. H-1 illustrates that the first three beam modes, for a unit maximum displacement, have approximately equal second derivatives (absolute values); hence, by eqn.(H.6), approximately equal (fiber) strains exist, at

---

* The L appears because of non-dimensionalization, i.e., $d^2Y_r(x)/dx^2 = (1/L)\cdot d^2\phi_r(\xi)/d\xi^2$.

§ There are two symmetrical roots in this case (one at each beam end).

$$r - \xi\Big|_{(gage)} - \frac{x}{L}\Big|_{(gage)} \simeq 0.1047 \, . \tag{H.8}$$

This criterion has been used for longitudinally locating the strain gages.

Appendix M of Ref. [75] discusses the radial location of the strain gages.

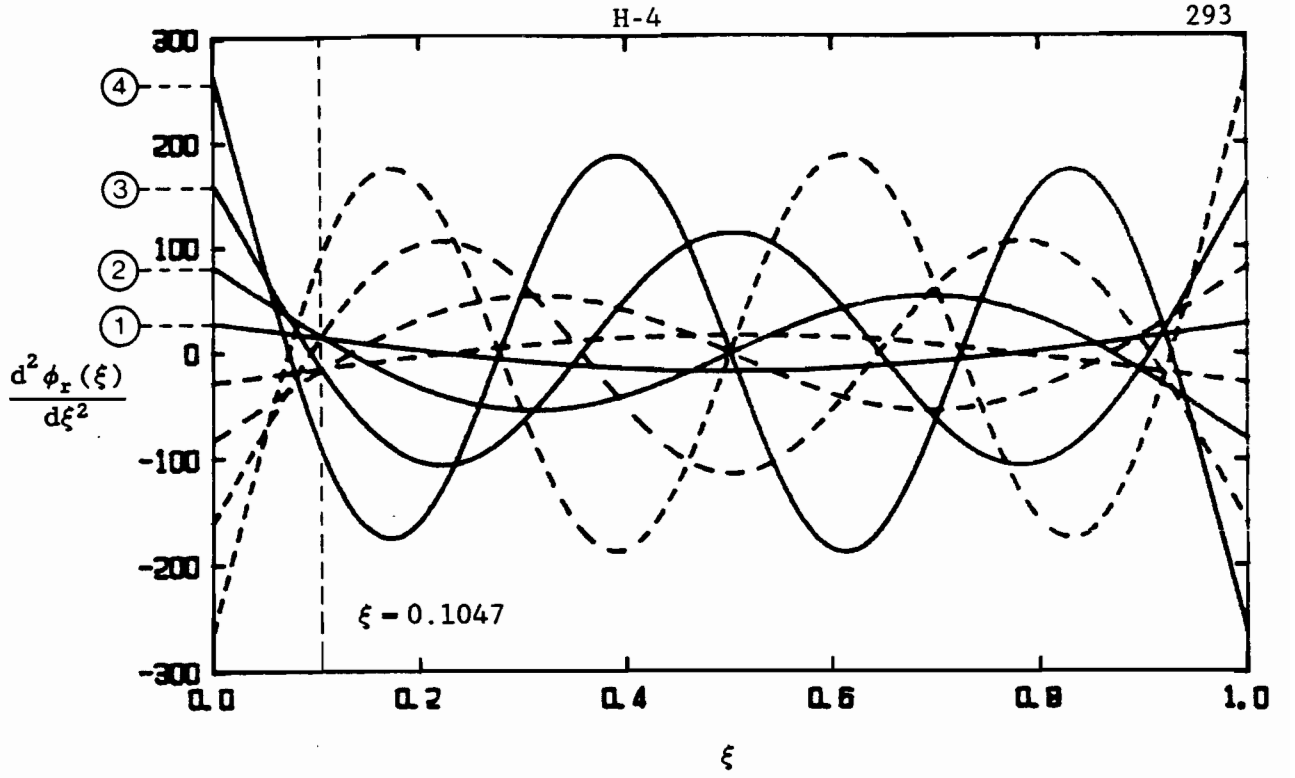

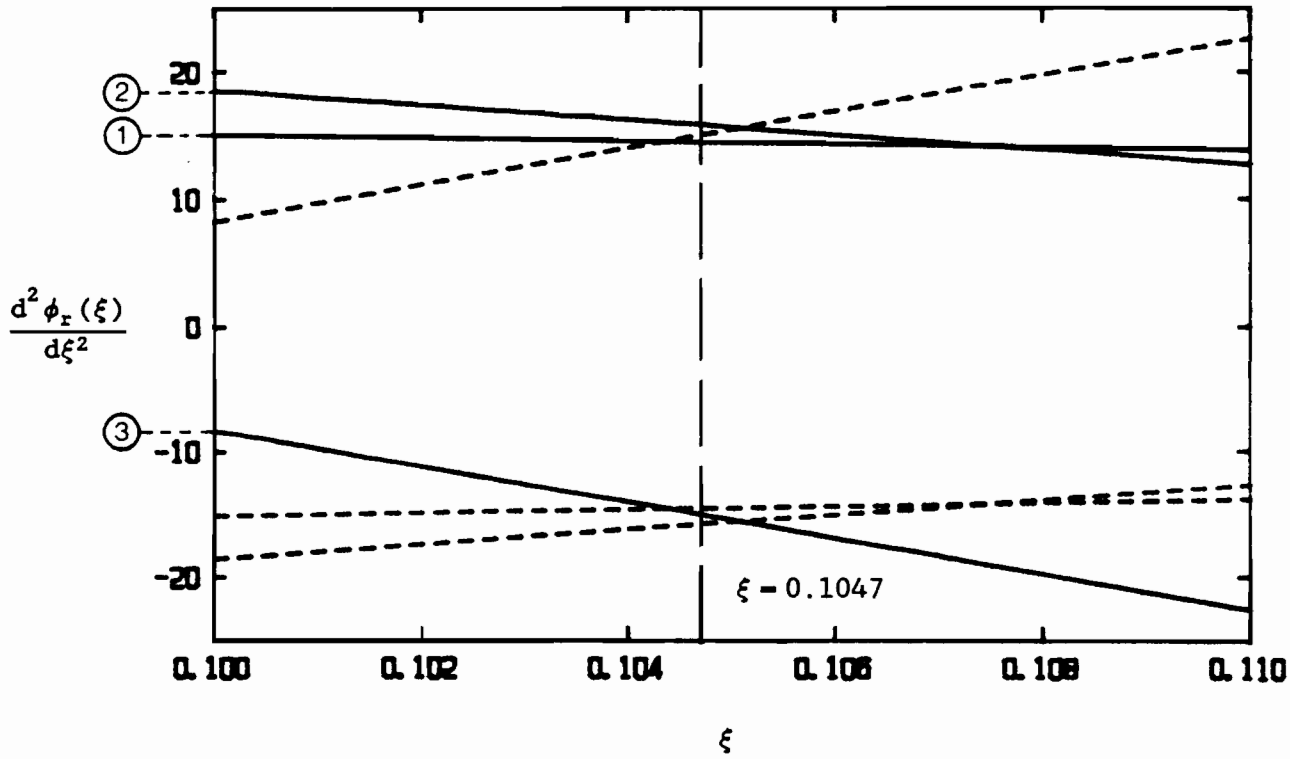

Fig. H-1: Second derivatives of beam modes. Note: The circled digits identify modes.

Appendix I

Units--Fourier Transforms and convolution integrals

(a) Fourier Transforms

Fourier transform pairs are defined in the literature as

$$f(t) = c_1 \int_{-\infty}^{+\infty} F(\omega)\, e^{j\omega t}\, d\omega \ , \tag{I.1}$$

and

$$F(\omega) = c_2 \int_{-\infty}^{+\infty} f(t)\, e^{-j\omega t}\, dt \ . \tag{I.2}$$

The values assigned to the constants c_1 and c_2 depend:

(i) On the units of ω and t.

For example, if the product ωt is in radians, yielding 2π (radians) per cycle, then we find (various authors)

$$c_1 c_2 = \frac{1}{2\pi} \ . \tag{I.3}$$

(ii) On the author.

In the example given in (i), common values found for c_1 and c_2 are

(a) $c_1 = \frac{1}{2\pi}$, $c_2 = 1$,

e.g. A. PAPOULIS, The Fourier Integral and its Applications, McGraw Hill, 1962, p.7,

(b) $c_1 = \frac{1}{\sqrt{2\pi}}$, $c_2 = \frac{1}{\sqrt{2\pi}}$,

e.g. KORN, G.A. and KORN, T.M., Mathematical Handbook for Scientists and Engineers, McGraw Hill, 2nd ed., p.139,

(c) $c_1 = 1$, $c_2 = \frac{1}{2\pi}$,

e.g. C.R. WYLIE, Advanced Engineering Mathematics, McGraw Hill, 1975, p.244.

Often, units are chosen such that $\omega t = 1$ (e.g. ω in Hz, t in sec), and $c_1 = c_2 = 1$ is used, which will be shown to lead to correct units for PSD's (power spectral densities).

Before proceeding, we should note that the units of the complex exponent of e, namely $j\omega t$, may be considered arbitrary, as long as they are compatible with the trigonometric functions (sin and cos) used, as

$$e^{j\omega t} = \cos(\omega t) + j \sin(\omega t);$$

for example, ωt may have to be in degrees. Alternatively, if the infinite series expansion is used for $e^{j\omega t}$, then we require ωt to be in radians. We shall adopt the latter units.

The proper values for c_1 and c_2 (such that a PSD from an autocorrelation function has the correct power) will be found by considering the limiting case of Fourier series, yielding Fourier integrals.

Recall the complex form of Fourier series:

$$f(t) = \sum_{n=-\infty}^{\infty} A_n e^{jnc\omega_1 t}, \qquad (I.4)$$

where ω_1 is the fundamental frequency, A_n the complex amplitudes, and c a units scaling factor to make the product $c\omega_1 t$ in radians (assumed above).

The units of ω_1 and t are taken as arbitrary, and the units of T_1, the fundamental period, are taken as those for t. We have

$$c\omega_1 T_1 = 2\pi . \qquad (I.5)$$

Note that, in general, c has "units", e.g. (rad · min/deg · sec). Now, let the units of f(t) be U_f (e.g. U_f could be L^2, M/L, etc...). Hence, the A_n also have units of U_f; $e^{jnc\omega_1 t}$ is (always) dimensionless.

The coefficients A_n in eqn.(I.4) are given by

$$A_n = \frac{1}{T_1} \cdot \int_{-T_1/2}^{+T_1/2} f(t)\, e^{-jnc\omega_1 t} \cdot dt \quad . \tag{I.6}$$

Note that units are correct in the above equation, A_n and $f(t)$ having units U_f, and the units of T_1 cancelling those of dt.

Substituting eqn.(I.6) into (I.4), we get

$$f(t) = \sum_{n=-\infty}^{\infty} \left[\frac{1}{T_1} \cdot \int_{-T_1/2}^{+T_1/2} f(t)\, e^{-jnc\omega_1 t} \cdot dt \right] e^{jnc\omega_1 t} \quad ,$$

which can be rewritten as

$$f(t) = \sum_{n=-\infty}^{\infty} \frac{1}{\omega_1 T_1} \cdot \omega_1 \cdot \int_{-T_1/2}^{+T_1/2} f(t)\, e^{-jnc\omega_1 t} \cdot dt \cdot e^{jnc\omega_1 t} \quad . \tag{I.7}$$

Now, we define

$$\left.\begin{aligned} \omega_n &= n\omega_1 \quad , \\ \Delta\omega_n &= (n+1)\omega_1 - n\omega_1 = \omega_1 \quad , \end{aligned}\right\} \tag{I.8}$$

which substituted into eqn.(I.7), yields

$$f(t) = \sum_{n=-\infty}^{\infty} \frac{e^{-jc\omega_n t}}{\omega_1 T_1} \cdot \int_{-T_1/2}^{+T_1/2} f(t)\, e^{-jc\omega_n t} \cdot dt \cdot \Delta\omega_n \quad . \tag{I.9}$$

In eqn.(I.9), we may define

$$F(\omega_n) = \frac{1}{\omega_1 T_1} \cdot \int_{-T_1/2}^{+T_1/2} f(t)\, e^{-jc\omega_n t} \cdot dt \quad . \tag{I.10}$$

Note that the factor $1/\omega_1 T_1$ has been "arbitrarily" assigned to the function $F(\omega_n)$; the correctness of so doing will be proven below, when considering units of PSD's versus the autocorrelation function.

By inspection of the above equation, we see that the units of $F(\omega_n)$ are U_f/U_w, where U_w are the units of ω_1 (e.g. deg/min). Combining eqs.(I.9) and (I.10), we obtain

$$f(t) = \sum_{n=-\infty}^{\infty} F(\omega_n)\, e^{jc\omega_1 t} \cdot \Delta\omega_n \quad . \tag{I.11}$$

Note that correct units are still maintained. Pursuing the standard procedure for obtaining Fourier integrals from Fourier series, we let

$$\left.\begin{aligned} &T_1 \to \infty \ , \ \omega_1 \to 0 \quad (\omega_1 T_1 \text{ constant}), \\ &\text{and} \quad \omega_n \to \omega \ , \ \Delta\omega_n \to d\omega \ , \end{aligned}\right\} \tag{I.12}$$

which, when used in eqs.(I.10) and (I.11), results in the expressions

$$F(\omega) = \frac{1}{\omega_1 T_1} \cdot \int_{-\infty}^{+\infty} f(t)\, e^{-jc\omega t} \cdot dt \ , \tag{I.13}$$

and

$$f(t) = \int_{-\infty}^{+\infty} F(\omega)\, e^{jc\omega t} \cdot d\omega \ . \tag{I.14}$$

In terms of units, we note,

(a) for eqn.(I.13):

$$\frac{U_f}{U_w} : \frac{1}{U_w U_t}\, U_f \ (-)\ U_t \ ,$$

where U_t are (time) units of T_1 and dt, and (-) means dimensionless. Hence

$$\frac{U_f}{U_w} : \frac{U_f}{U_w} \quad , \text{ which is correct.}$$

(b) for eqn.(I.15):

$$U_f : \frac{U_f}{U_w}\ (-)\ U_w$$

i.e. $U_f : U_f$, which is also correct.

Equations (I.13) and (I.14) indicate that, for correct units for the Fourier transform pair of eqs.(I.1) and (I.2), we must have

$$\left.\begin{aligned} c_1 &= 1 \ , \\ c_2 &= \frac{1}{\omega_1 T_1} \ . \end{aligned}\right\} \tag{I.15}$$

For example, if ω_1 is in rad/sec and t (T_1) in sec, then $\omega_1 T_1 = 2\pi$ rad and

$$c_1 = 1 \quad , \quad c_2 = \frac{1}{2\pi} \ .$$

Note that, to be more general, the factor c may be used in the exponent of e (eqs.(I.1) and (I.2)).

Applying eqs.(I.13) and (I.14) to PSD's is straightforward. The auto-correlation function is the Fourier transform of the PSD, i.e. by analogy to eqn.(I.14), we have

$$R_f(t) = \int_{-\infty}^{+\infty} S_f(\omega)\, e^{jc\omega t}\, d\omega \ . \tag{I.16}$$

Now, we have (from its basic definition)

$$P_f = R_f(0) \ , \tag{I.17}$$

where P_f is the total power in the function f(t). From eqs.(I.16) and (I.17), we get

$$P_f = \int_{-\infty}^{+\infty} S_f(\omega)\, d\omega \ , \tag{I.18}$$

which is true for the (double-sided) PSD ,$S_f(\omega)$. In terms of units, we have the form

$$U_p \ : \ \frac{U_p}{U_w}\, U_w \quad , \text{ i.e. } U_p \ : \ U_p \ ,$$

where U_p are units of "power", in the sense that $U_p = U_f^2$ (recall that U_f are units of f(t)). Conversely, from eqn.(I.13), we may write

$$S_f(\omega) = \frac{1}{\omega_1 T_1} \cdot \int_{-\infty}^{+\infty} R_f(t)\, e^{-jc\omega t} \cdot dt \ , \tag{I.19}$$

where the autocorrelation is, by definition

$$R_f(t) = \lim_{T \to \infty} \frac{1}{T} \cdot \int_{-T/2}^{+T/2} f(\tau) \cdot f(\tau + t) \cdot d\tau \ , \tag{I.20}$$

and, can be seen to have units of U_f^2 (as expected since $R_f(0) = P_f$).

In terms of units, we see in eqn.(I.19) that

$$\frac{U_f^2}{U_w} : \frac{1}{U_w U_t} U_f^2 \ (\text{-}) \ U_t \ , \ \text{i.e.} \ \frac{U_f^2}{U_w} : \frac{U_f^2}{U_w} = \frac{U_p}{U_w} \ ,$$

which confirms eqn.(I.15) as the correct values for c_1 and c_2 in the transform pair of eqs.(I.1) and (I.2).

In the particular case where the product ωt is in radians (i.e. $\omega_1 T_1 = 2\pi$), the correct Fourier transform pair reads (see eqs.(I.13) and (I.14))

$$\left.\begin{aligned} F(\omega) &= \frac{1}{2\pi} \cdot \int_{-\infty}^{+\infty} f(t)\, e^{-j\omega t} \cdot dt \ , \\ f(t) &= \int_{-\infty}^{+\infty} F(\omega)\, e^{j\omega t} \cdot d\omega \ . \end{aligned}\right\} \tag{I.21}$$

Note that in the above case, $c = 1$.

(b) Convolution integral

In addition to the functions defined in eqn.(I.21), we consider

$$\left.\begin{aligned} X(\omega) &= \frac{1}{2\pi} \cdot \int_{-\infty}^{+\infty} x(t)\, e^{-j\omega t} \cdot dt \ , \\ \text{and} \\ x(t) &= \int_{-\infty}^{+\infty} X(\omega)\, e^{j\omega t} \cdot d\omega \ . \end{aligned}\right\} \qquad (I.22)$$

Furthermore, we assume that $X(\omega)$ and $F(\omega)$ are related by a transfer function. i.e.

$$X(\omega) = F(\omega) \cdot H(\omega) \ . \qquad (I.23)$$

Now, as done earlier, the units of f(t) are taken as U_f and those of time and frequency as U_t and U_w respectively. The units of x(t) are assumed to be U_x. The first part of eqn.(I.22) is, units-wise,

$$\frac{U_x}{U_w} : \frac{1}{U_w U_t}\, U_x \ (\text{-})\ U_t \quad ,$$

and in the second part of the equation, $F(\omega)$ has units of U_f/U_w, as before. Consequently, we must have U_x/U_f for the units of $H(\omega)$, by eqn.(I.23).

The impulse response function is the Fourier Transform of the transfer function:

$$\left.\begin{aligned} h(t) &= \int_{-\infty}^{+\infty} H(\omega)\, e^{j\omega t} \cdot d\omega \ , \\ \text{and conversely,} \\ H(\omega) &= \frac{1}{2\pi} \cdot \int_{-\infty}^{+\infty} h(t)\, e^{-j\omega t} \cdot dt \ . \end{aligned}\right\} \qquad (I.24)$$

By inspection, the units of h(t) are $U_x U_w / U_f$.

Finally, we recall the convolution integral corresponding to eqn. (I.23)

$$x(t) = \frac{1}{2\pi} \cdot \int_{-\infty}^{+\infty} h(\tau) \cdot f(t - \tau) \cdot d\tau \ , \qquad \text{(I.25)}$$

where we see that units are balanced, as

$$U_x \ : \ \frac{1}{U_w U_t} \ \frac{U_x U_w}{U_f} \ U_f \ U_t \ ,$$

which shows that the factor $1/2\pi$ is required in eqn.(I.25) (note that $U_w U_t$ is assumed to be in radians here). The general form of the convolution integral is

$$x(t) = \frac{1}{\omega_1 T_1} \cdot \int_{-\infty}^{+\infty} h(\tau) \cdot f(t - \tau) \cdot d\tau \ , \qquad \text{(I.26)}$$

where the product $\omega_1 T_1$ is for a cycle and based on units of U_w and U_t (as before).

Appendix J

Derivation, longitudinal correlation function

Recall eqn. (2.266):

$$K_{ij,\xi}(\omega) = \int_0^1 d\xi_1 \cdot \int_0^1 d\xi_2 \cdot \phi_i(\xi_1) \cdot \phi_j(\xi_2) \cdot e^{-b|S_\xi|} \cdot e^{-j2\pi \cdot S_\xi} \quad , \quad i,j = 1,2,\ldots,N . \tag{J.1}$$

We wish to integrate the above function, for clamped-clamped boundary conditions, that is, when

$$\phi_i(\xi) = \cos(\lambda_i \xi) - \cosh(\lambda_i \xi) - \sigma_i [\sin(\lambda_i \xi) - \sinh(\lambda_i \xi)] \quad , \quad i = 1,2,\ldots,\infty , \tag{J.2}$$

the normalized (dimensionless) beam modes, and where

$$\sigma_i = \frac{\cos \lambda_i - \cosh \lambda_i}{\sin \lambda_i - \sinh \lambda_i} \quad , \quad i = 1,2,\ldots,\infty . \tag{J.3}$$

Recall (Appendix G) that the λ_i above are obtained from the characteristic equation

$$\cos \lambda_i \cdot \cosh \lambda_i = 1 \quad , \quad i = 1,2,\ldots,\infty . \tag{J.4}$$

Also recall that b is a constant (see eqn.(2.213)) and, from eqn. (2.211),

$$S_\xi = \sqrt{\beta}\, \frac{(\xi_2 - \xi_1)(\omega/2\pi)}{u_c} \quad , \tag{J.5}$$

a "cycle" (versus "radian") Strouhal number.

Substituting eqn.(J.5) into (J.1), and breaking up the second integral in the latter equation, we may write

$$K_{ij,\xi}(\omega) = \int_0^1 d\xi_1 \cdot \phi_i(\xi_1) \left\{ \int_0^{\xi_1} d\xi_2 \cdot \phi_j(\xi_2) \cdot e^{-\frac{b}{2\pi} \frac{\sqrt{\beta}\,\omega}{u_c} (\xi_1 - \xi_2)} \right.$$

$$\left. \cdot e^{-j \frac{\sqrt{\beta}\,\omega}{u_c} (\xi_2 - \xi_1)} + \int_{\xi_1}^1 d\xi_2 \cdot \phi_j(\xi_2) \cdot e^{-\frac{b}{2\pi} \frac{\sqrt{\beta}\,\omega}{u_c} (\xi_2 - \xi_1)} \cdot e^{-j \frac{\sqrt{\beta}\,\omega}{u_c} (\xi_2 - \xi_1)} \right\} ,$$

$$(\omega \geq 0) \qquad i,j = 1,2,\ldots,N ,$$

where the frequency ω has been restricted to positive values (experimental work and computer programs do not consider negative frequencies). The above equation is rewritten as

$$K_{ij,\xi}(\omega) = \int_0^1 d\xi_1 \cdot \phi_i(\xi_1) \left\{ \int_0^{\xi_1} d\xi_2 \cdot \phi_j(\xi_2) \cdot e^{Z^*(\xi_2 - \xi_1)} + \int_{\xi_1}^1 d\xi_2 \cdot \phi_j(\xi_2) \cdot e^{-Z(\xi_2 - \xi_1)} \right\}, \quad \begin{matrix}(\omega \geq 0) \\ i,j = 1,2,\ldots,N,\end{matrix}$$

or more concisely as

$$K_{ij,\xi}(\omega) = \int_0^1 d\xi_1 \cdot \phi_i(\xi_1) \left\{ \cdot e^{-Z^* \xi_1} \cdot \int_0^{\xi_1} d\xi_2 \cdot \phi_j(\xi_2) \cdot e^{Z^* \xi_2} + e^{Z \xi_1} \cdot \int_{\xi_1}^1 d\xi_2 \cdot \phi_j(\xi_2) \cdot e^{-Z \xi_2} \right\}, \quad \begin{matrix}(\omega \geq 0) \\ i,j = 1,2,\ldots,N,\end{matrix} \tag{J.6}$$

where

$$Z = \frac{\sqrt{\beta}\omega}{u_c} \left(\frac{b}{2\pi} + j\right) . \tag{J.7}$$

Equation (J.6) is reduced, for two separate cases, namely (i) $\omega > 0$, and (ii) $\omega = 0$.

Case (i): $\omega > 0$

Both integrals in eqn. (J.6) have the form

$$X_i(Z,a,b) = \int_a^b \phi_i(\xi) \cdot e^{Z\xi} \cdot d\xi , \quad i = 1,2,\ldots,N . \tag{J.8}$$

Using integration by parts, we obtain

$$X_i(Z,a,b) = \frac{e^{Z\xi}}{Z} \phi_i(\xi) \Big|_a^b - \int_a^b \frac{e^{Z\xi}}{Z} \cdot \frac{d\phi_i(\xi)}{d\xi} d\xi ,$$

and continuing the process, leads to

$$X_i(Z,a,b) = \left[e^{Z\xi} \left(\frac{1}{Z} \phi_i(\xi) - \frac{1}{Z^2} \frac{d\phi_i(\xi)}{d\xi} + \frac{1}{Z^3} \frac{d^2\phi_i(\xi)}{d\xi^2} - \frac{1}{Z^4} \frac{d^3\phi_i(\xi)}{d\xi^3} \right) \right] \Big|_a^b$$

(continued)

$$+ \int_a^b \frac{e^{Z\xi}}{Z^4} \cdot \frac{d^4\phi_i(\xi)}{d\xi^4} \cdot d\xi \,, \qquad i = 1,2,\ldots,N \,. \tag{J.9}$$

We can use a property of the modes $\phi_i(\xi)$ for clamped-clamped beams, namely (see Appendix G)

$$\frac{d^4\phi_i(\xi)}{d\xi^4} = \lambda_i^4 \cdot \phi_i(\xi) \,, \qquad i = 1,2,\ldots,\infty \,, \tag{J.10}$$

which, after substitution into eqn.(J.9), yields an explicit expression for $X_i(Z,a,b)$:

$$X_i(Z,a,b) = \frac{Z^4 e^{Z\xi}}{Z^4 - \lambda_i^4} \cdot I_i(Z,\xi)\Big|_{\xi=a}^{b} \,, \qquad i = 1,2,\ldots N \,, \tag{J.11}$$

where we have defined the new function

$$I_i(Z,\xi) = \frac{1}{Z}\,\phi_i(\xi) - \frac{1}{Z^2}\,\frac{d\phi_i(\xi)}{d\xi} + \frac{1}{Z^3}\,\frac{d^2\phi_i(\xi)}{d\xi^2} - \frac{1}{Z^4}\,\frac{d^3\phi_i(\xi)}{d\xi^3} \,, \qquad i = 1,2,\ldots,N \,. \tag{J.12}$$

Using eqs.(J.8) and (J.11) in eqn.(J.6) yields

$$K_{ij,\xi}(\omega) = \int_0^1 d\xi_1 \cdot \phi_i(\xi_1) \left\{ \frac{(Z^*)^4 e^{-Z^*\xi_1}}{(Z^*)^4 - \lambda_j^4} \left[e^{Z^*\xi_1} \cdot I_j(Z^*,\xi_1) - I_j(Z^*,0) \right] \right.$$

$$\left. + \frac{Z^4 e^{Z\xi_1}}{Z^4 - \lambda_j^4} \left[e^{-Z} \cdot I_j(-Z,1) - e^{-Z\xi_1} \cdot I_j(-Z,\xi_1) \right] \right\} \,, \quad \begin{matrix}(\omega \geq 0)\\ i,j = 1,2,\ldots,N \,,\end{matrix}$$

which can be expanded to read

$$K_{ij,\xi}(\omega) = \frac{(Z^*)^4}{(Z^*)^4 - \lambda_j^4} \left[Y_{ij}(Z^*,0,1) - X_i(-Z^*,0,1) \cdot I_j(Z^*,0) \right] + \frac{Z^4}{Z^4 - \lambda_j^4}$$

$$\cdot \left[e^{-Z} \cdot X_i(Z,0,1) \cdot I_j(-Z,1) - Y_{ij}(-Z,0,1) \right] \,, \quad \begin{matrix}(\omega \geq 0)\\ i,j = 1,2,\ldots,N \,,\end{matrix} \tag{J.13}$$

where

$$Y_{ij}(Z,a,b) = \int_a^b \phi_i(\xi) \cdot I_j(Z,\xi) \cdot d\xi \,, \qquad i,j = 1,2,\ldots,N \,. \tag{J.14}$$

Note that eqn.(J.13) contains terms of the form $X_i(Z,0,1)$ and $Y_{ij}(Z,0,1)$. From eqn.(J.11), we get

$$X_i(Z,0,1) = \frac{Z^4 \left[e^Z \cdot I_i(Z,1) - I_i(Z,0) \right]}{Z^4 - \lambda_i^4} , \qquad i,j = 1,2,\ldots,N , \tag{J.15}$$

and from eqs.(J.14) and (J.12), we obtain

$$Y_{ij}(Z,0,1) = \int_0^1 \phi_i(\xi) \left[\frac{1}{Z}\,\phi_j(\xi) - \frac{1}{Z^2}\,\frac{d\phi_j(\xi)}{d\xi} + \frac{1}{Z^3}\,\frac{d^2\phi_j(\xi)}{d\xi^2} - \frac{1}{Z^4}\,\frac{d^3\phi_j(\xi)}{d\xi^3} \right] d\xi , \qquad i,j = 1,2,\ldots,N ,$$

that is

$$Y_{ij}(Z,0,1) = \frac{\delta_{ij}}{Z} - \frac{a_{ij}}{Z^2} + \frac{b_{ij}}{Z^3} - \frac{c_{ij}}{Z^4} , \qquad i,j = 1,2,\ldots,N , \tag{J.16}$$

where

$$\left.\begin{aligned} \delta_{ij} &= \int_0^1 \phi_i(\xi)\cdot\phi_j(\xi)\cdot d\xi , \qquad \text{(Kronecker delta)} \\ a_{ij} &= \int_0^1 \phi_i(\xi) \cdot \frac{d\phi_j(\xi)}{d\xi}\, d\xi , \\ b_{ij} &= \int_0^1 \phi_i(\xi) \cdot \frac{d^2\phi_j(\xi)}{d\xi^2}\, d\xi , \qquad i,j = 1,2,\ldots,N , \end{aligned}\right\} \tag{J.17}$$

which are evaluated in Appendix G, and where

$$q_{ij} = \int_0^1 \phi_i(\xi) \cdot \frac{d^3\phi_j(\xi)}{d\xi^3}\, d\xi , \qquad i,j = 1,2,\ldots,N . \tag{J.18}$$

We need only evaluate this latest coefficient; the techniques of Appendix G are utilized. From eqn.(J.10), we can write

$$\frac{d^7\phi_i(\xi)}{d\xi^7} = \lambda_i^4 \cdot \frac{d^3\phi_i(\xi)}{d\xi^3} , \qquad i,j = 1,2,\ldots,\infty ,$$

which may be combined with eqn.(J.10), to yield

$$\frac{d^4\phi_i(\xi)}{d\xi^4} \cdot \frac{d^3\phi_j(\xi)}{d\xi^3} = \lambda_i^4 \cdot \phi_i(\xi) \cdot \frac{d^3\phi_j(\xi)}{d\xi^3} ,$$

and

$$\frac{d^7\phi_i(\xi)}{d\xi^7} \cdot \phi_j(\xi) = \lambda_j^4 \cdot \frac{d^3\phi_j(\xi)}{d\xi^3} \cdot \phi_i(\xi) .$$

Explicit expressions are derived for q_{ij}, separately for the cases $i \neq j$ and $i = j$. When $i \neq j$, the latter two equations can be subtracted, resulting in

$$(\lambda_j^4 - \lambda_i^4) \cdot \phi_i(\xi) \cdot \frac{d^3\phi_j(\xi)}{d\xi^3} = \phi_i(\xi) \cdot \frac{d^7\phi_j(\xi)}{d\xi^7} - \frac{d^4\phi_i(\xi)}{d\xi^4} \cdot \frac{d^3\phi_j(\xi)}{d\xi^3}, \quad \begin{matrix} i \neq j \\ i,j = 1,2,\ldots,N. \end{matrix} \tag{J.19}$$

Integrating eqn.(J.19) over ξ, in the range (0,1), we obtain

$$q_{ij} = \frac{1}{\lambda_j^4 - \lambda_i^4} \left[\int_0^1 \phi_i(\xi) \cdot \frac{d^7\phi_j(\xi)}{d\xi^7}\, d\xi - \int_0^1 \frac{d^4\phi_i(\xi)}{d\xi^4} \cdot \frac{d^3\phi_j(\xi)}{d\xi^3}\, d\xi \right], \quad \begin{matrix} i \neq j \\ i,j = 1,2,\ldots,N. \end{matrix} \tag{J.20}$$

Integration by parts yields

$$q_{ij} = \frac{1}{\lambda_j^4 - \lambda_i^4} \left[\phi_i(\xi) \cdot \frac{d^6\phi_j(\xi)}{d\xi^6} \Bigg|_0^1 - \int_0^1 \frac{d\phi_i(\xi)}{d\xi} \cdot \frac{d^6\phi_j(\xi)}{d\xi^6}\, d\xi - \frac{d^3\phi_i(\xi)}{d\xi^3} \cdot \frac{d^3\phi_j(\xi)}{d\xi^3} \Bigg|_0^1 + \int_0^1 \frac{d^3\phi_i(\xi)}{d\xi^3} \cdot \frac{d^4\phi_j(\xi)}{d\xi^4}\, d\xi \right], \quad \begin{matrix} i \neq j \\ i,j = 1,2,\ldots,N, \end{matrix}$$

and by inspection, the first term in the brackets is zero (no displacements at the ends). Again using integration by parts, we may write

$$q_{ij} = \frac{1}{\lambda_j^4 - \lambda_i^4} \left[- \frac{d\phi_i(\xi)}{d\xi} \cdot \frac{d^5\phi_j(\xi)}{d\xi^5} \Bigg|_0^1 + \int_0^1 \frac{d^2\phi_i(\xi)}{d\xi^2} \cdot \frac{d^5\phi_j(\xi)}{d\xi^5}\, d\xi - \frac{d^3\phi_i(\xi)}{d\xi^3} \cdot \frac{d^3\phi_j(\xi)}{d\xi^3} \Bigg|_0^1 + \frac{d^2\phi_i(\xi)}{d\xi^2} \cdot \frac{d^4\phi_j(\xi)}{d\xi^4} \Bigg|_0^1 - \int_0^1 \frac{d^2\phi_i(\xi)}{d\xi^2} \cdot \frac{d^5\phi_j(\xi)}{d\xi^5}\, d\xi \right], \quad \begin{matrix} i \neq j \\ i,j = 1,2,\ldots,N. \end{matrix}$$

The first term in the brackets is zero (slopes are zero at the ends), and the second and fifth terms cancel out. Making use of eqn.(J.10) in the latter equation, we get

$$q_{ij} = \frac{1}{\lambda_j^4 - \lambda_i^4} \left[- \frac{d^3\phi_i(\xi)}{d\xi^3} \cdot \frac{d^3\phi_j(\xi)}{d\xi^3} \Bigg|_0^1 + \lambda_j^4 \cdot \frac{d^2\phi_i(\xi)}{d\xi^2} \phi_j(\xi) \Bigg|_0^1 \right], \quad \begin{matrix} i \neq j \\ i,j = 1,2,\ldots,N, \end{matrix}$$

which reduces to (the last term is zero)

$$q_{ij} = \frac{1}{\lambda_j^4 - \lambda_i^4}\left[-\frac{d^3\phi_i(\xi)}{d\xi^3}\cdot\frac{d^3\phi_j(\xi)}{d\xi^3}\Bigg|_0^1\right], \quad \begin{matrix} i \neq j \\ i,j = 1,2,\ldots,N. \end{matrix} \tag{J.21}$$

Now, from eqn.(J.2), we may write

$$\frac{d^3\phi_i(\xi)}{d\xi^3} = \lambda_i^3\left\{\sin(\lambda_i\xi) - \sinh(\lambda_i\xi) + \sigma_i[\cos(\lambda_i\xi) + \cosh(\lambda_i\xi)]\right\}, \quad i = 1,2,\ldots,\infty. \tag{J.22}$$

Hence, we obtain

$$\frac{d^3\phi_i(\xi)}{d\xi^3}\Bigg|_{\xi=0} = 2\sigma_i\lambda_i^3, \quad i = 1,2,\ldots,\infty, \tag{J.23}$$

and

$$\frac{d^3\phi_i(\xi)}{d\xi^3}\Bigg|_{\xi=1} = \lambda_i^3\left\{\sin\lambda_i - \sinh\lambda_i + \sigma_i[\cos\lambda_i + \cosh\lambda_i]\right\}, \quad i = 1,2,\ldots,\infty.$$

Making use of eqn.(J.3) in the latter, we get

$$\frac{d^3\phi_i(\xi)}{d\xi^3}\Bigg|_{\xi=1} = \frac{-2\lambda_i^3\cdot\sin\lambda_i\cdot\sinh\lambda_i}{\sin\lambda_i - \sinh\lambda_i}, \quad i = 1,2,\ldots,\infty. \tag{J.24}$$

Furthermore, we may write

$$(\cos\lambda_i - \cosh\lambda_i)^2 = \sin^2\lambda_i\cdot\sinh^2\lambda_i, \quad i = 1,2,\ldots,\infty, \tag{J.25}$$

where eqn.(J.4) has been used. Now, for all λ_i, we have (see Appendix G)

$\sinh\lambda_i \simeq \cosh\lambda_i \gg 1$, and

$\cos\lambda_i \leq 1$.

Consequently,

$\cos\lambda_i - \cosh\lambda_i < 0$, and since

$\sinh\lambda_i > 0$ (for all i), we have:

$$\begin{aligned} &\text{if } \sin\lambda_i > 0,\ \cos\lambda_i - \cosh\lambda_i = -\sin\lambda_i\cdot\sinh\lambda_i, \\ &\text{if } \sin\lambda_i < 0,\ \cos\lambda_i - \cosh\lambda_i = +\sin\lambda_i\cdot\sinh\lambda_i, \end{aligned} \tag{J.26}$$

for all i.

From Appendix G, the sign of $\sin\lambda_i$ is

$$\operatorname{sgn}(\sin\lambda_i) = (-1)^i \ , \tag{J.27}$$

for all i, hence, from eqs.(J.25), (J.26), and (J.27), we may write

$$\sin\lambda_i \cdot \sinh\lambda_i = (-1)^{i+1} \left[\cos\lambda_i - \cosh\lambda_i\right] \ , \qquad i = 1,2,\ldots,\infty \ . \tag{J.28}$$

Substitution of eqn.(J.28) into (J.24) results in the relation

$$\left.\frac{d^3\phi_i(\xi)}{d\xi^3}\right|_{\xi=-1} = \frac{-2\lambda_i^3(-1)^{i+1}\left[\cos\lambda_i - \cosh\lambda_i\right]}{\sin\lambda_i - \sinh\lambda_i} \ , \qquad i = 1,2,\ldots,\infty \ ,$$

which reduces to, after making use of eqn.(J.3):

$$\left.\frac{d^3\phi_i(\xi)}{d\xi^3}\right|_{\xi=-1} = 2(-1)^i \cdot \sigma_i \cdot \lambda_i^3 \ , \qquad i = 1,2,\ldots,\infty \ . \tag{J.29}$$

Now, combining eqs.(J.23), (J.29), and (J.21), we obtain

$$q_{ij} = \frac{4\sigma_i \cdot \sigma_j \cdot \lambda_i^3 \cdot \lambda_j^3}{\lambda_i^4 - \lambda_j^4} \ , \qquad \begin{matrix} i \neq j \\ i,j = 1,2,\ldots,N \ . \end{matrix} \tag{J.30}$$

When $i = j$, eqn. (J.18) takes the form

$$q_{ii} = \int_0^1 \phi_i(\xi)\,\frac{d^3\phi_i(\xi)}{d\xi^3}\,d\xi \ , \qquad i = 1,2,\ldots,N \ ,$$

and again utilizing integration by parts, we may write

$$q_{ii} = \phi_i(\xi)\cdot\frac{d^2\phi_i(\xi)}{d\xi^2}\Bigg|_0^1 - \int_0^1 \frac{d^2\phi_i(\xi)}{d\xi^2}\cdot\frac{d\phi_i(\xi)}{d\xi}\cdot d\xi \ , \qquad i = 1,2,\ldots,N \ .$$

The first term vanishes, and q_{ii} is further expanded to read

$$q_{ii} = -\frac{d\phi_i(\xi)}{d\xi}\cdot\frac{d\phi_i(\xi)}{d\xi}\Bigg|_0^1 + \int_0^1 \frac{d\phi_i(\xi)}{d\xi}\cdot\frac{d^2\phi_i(\xi)}{d\xi^2}\cdot d\xi \ , \qquad i = 1,2,\ldots,N \ .$$

Finally, the last term is written as (the first term again vanishes)

$$q_{ii} = -\int_0^1 \frac{d^2\phi_i(\xi)}{d\xi^2} \cdot \frac{d\phi_i(\xi)}{d\xi} \cdot d\xi + \int_0^1 \frac{d\phi_i(\xi)}{d\xi} \cdot \frac{d^2\phi_i(\xi)}{d\xi^2} \cdot d\xi \,, \qquad i = 1,2,\ldots,N \,,$$

that is,

$$q_{ij} = 0 \,, \qquad \begin{matrix} i \neq j \\ i,j = 1,2,\ldots,N \,. \end{matrix} \tag{J.31}$$

Finally, eqn.(J.13) may be written in the compact form

$$K_{ij,\xi}(\omega) = A_{ij}(Z) - A_{ij}(-Z^*) + e^{-Z} \cdot B_{ij}(Z) \cdot I_j(-Z,1) - B_{ij}(-Z^*) \cdot I_j(Z^*,0) \,,$$

$$(\omega \geq 0) \qquad \begin{matrix} \\ i,j = 1,2,\ldots,N \,, \end{matrix} \tag{J.32}$$

where we have defined

$$\left.\begin{aligned} A_{ij}(Z) &= \frac{-Z^4}{Z^4 - \lambda_j^4} \cdot Y_{ij}(-Z,0,1) \,, \\ B_{ij}(Z) &= \frac{Z^4}{Z^4 - \lambda_j^4} \cdot X_i(Z,0,1) \,, \end{aligned}\right\} \qquad i,j = 1,2,\ldots,N \,. \tag{J.33}$$

This completes the $\omega > 0$ case.

Case (ii): $\omega = 0$

In this case, we have (see eqn.(J.7)) $Z = 0$, which alters eqn.(J.1) to read

$$K_{ij,\xi}(0) = \int_0^1 d\xi_1 \cdot \phi_i(\xi_1) \cdot \int_0^1 d\xi_2 \cdot \phi_j(\xi_2) \,, \qquad i,j = 1,2,\ldots,N \,. \tag{J.34}$$

We simply require an explicit expression for an integral of the form

$$C_i = \int_0^1 d\xi \cdot \phi_i(\xi) \,, \qquad i = 1,2,\ldots,\infty \,, \tag{J.35}$$

where the ∞ limit just signifies that the results will be applicable over the full range of i.

Substituting eqn.(J.2) into (J.35), we obtain,

$$C_i = \int_0^1 \{\cos(\lambda_i \xi) - \cosh(\lambda_i \xi) - \sigma_i [\sin(\lambda_i \xi) - \sinh(\lambda_i \xi)]\} d\xi \,, \qquad i = 1,2,\ldots,\infty \,,$$

which reduces to

$$C_i = \frac{1}{\lambda_i} [\sin \lambda_i - \sinh \lambda_i + \sigma_i (\cos \lambda_i + \cosh \lambda_i - 2)] \,, \qquad i = 1,2,\ldots,\infty \,.$$

Using eqn.(J.3) in the latter equation, and manipulating the resulting expression, we get

$$C_i = \frac{-2 (\sin \lambda_i \cdot \sinh \lambda_i + \cos \lambda_i - \cosh \lambda_i)}{\lambda_i (\sin \lambda_i - \sinh \lambda_i)} \,, \qquad i = 1,2,\ldots,\infty \,.$$

Making use of eqn.(J.28) in the above equation, we obtain

$$C_i = -2 [(-1)^{i+1} + 1] \frac{(\cos \lambda_i - \cosh \lambda_i)}{\lambda_i (\sin \lambda_i - \sinh \lambda_i)} \,, \qquad i = 1,2,\ldots,\infty \,,$$

which simply reduces to, using eqn.(J.3),

$$C_i = -2 \frac{\sigma_i}{\lambda_i} [(-1)^{i+1} + 1] \,, \qquad i = 1,2,\ldots,\infty \,. \tag{J.36}$$

In view of eqs.(J.35) and (J.36), we can rewrite eqn.(J.34) as

$$K_{ij,\xi}(0) = \frac{4\sigma_i \sigma_j}{\lambda_i \lambda_j} [(-1)^{i+1} + 1][(-1)^{j+1} + 1] \,, \qquad i,j = 1,2,\ldots,N \,. \tag{J.37}$$

By inspection, we may write eqn.(J.37) as

$$K_{ij,\xi}(0) = \left\{ \begin{array}{ll} \dfrac{16 \sigma_i \sigma_j}{\lambda_i \lambda_j} \,, & \text{if i and j odd} \,, \\ 0 \,, & \text{if i or j even} \,, \end{array} \right\} \qquad i,j = 1,2,\ldots,N \,. \tag{J.38}$$

Appendix K

Computer programs-listings and users instructions

Time consuming computations were effected in FORTRAN 77, and others, inclusive of plotting, were carried out in BASIC V (for convenience, flexibility and expediency [particularly for the development of a "general" plotting program: FORTRAN compiling is very slow]). The steps leading to theoretically computed results are the following.

(1) FORTRAN 77 program for the computation of the coefficients of eqs. (2.27) to (2.30) inclusively. This program called "CPL.f", is that of [73], modified to eliminate input data redundancies (which became a major inconvenience for larger systems).

(2) FORTRAN 77 program to calculate the "normalized" CSD's of eqn.(2.271). Computations are in "Cartesian" directions only, namely in the z- and y-directions; the program in (3) can then resolve CSD's in arbitrary directions. This program is called "CSD.f".

(3) A BASIC V program to resolve PSD's, single cylinder CSD's, and inter-cylinder CSD's, as desired, from data generated in (2). Its name is "CSD_comp".

(3) A BASIC V program to calculate the non-dimensional CSD's (PSD's) of eqn.(2.272), from data generated in (2). Its name is "THEOR_CALC".

(4) A BASIC V program to calculate coherence, from either theoretical or experimental data. The program is called "COH_CALC".

(5) Finally, a program to display (colour monitor), scale and format data, for plotting. Because of its large size and since no computations are involved, this program, called "DISK_RDPL", shall not be listed and its usage not covered here.

Remark

Other programs, such as one for bulk non-dimensionalization of the experimental data, are omitted. Likewise, operational details, such as integer format storage of real variables (as used in the HP5420A spectrum analyzer) for space economizing, are not presented.

1. CPL.f

This program is taken from Ref.[73]; it has been modified so that inter-cylinder distances and angles are computed by the program, rather than having to be input as data (a redundancy anyway).

(a) Listing

This listing is FORTRAN 77 compatible.

```
      implicit integer*2 (i-n)
      implicit real*8 (a-h,o-z)
      dimension a(15,15,4),b(15,15,4)
      dimension w1(15,15),w2(15,15),w3(15,15),w4(15,15)
      dimension g(88,88),w5(88,8),w6(88)
      dimension ch(4,4),r(4,4),ri(4),ra(4),c1(4)
      dimension a1(15),a2(15),a3(2,66),a4(2,6)
      dimension vc(8,8),xc(4),yc(4)
      dimension s(31),co(31),f(30),r1(32),r2(32),r3(31)
      dimension am(10,10)
      character*9  file1
      character*8  file2
      character*2  num
c
      open (1,FILE='CPLinp')
      open (4,FILE='/dev/console')
      file1='CPLprint-'
      file2='CPLdata-'
      ioff=48
c
      write (4,31)
      read (4,*)  id
      j1=id/10
      j2=id-10*j1
      num(1:1)=char(j1+ioff)
      num(2:2)=char(j2+ioff)
      open (2,FILE=file1//num)
      open (3,FILE=file2//num)
c
      read (1,11)  k,mn
      if (k.eq.4)  go to 80
      write (2,32)
   32 format ('ERROR: k not equal to 4')
      close (1)
      close (2)
      close (3)
      close (4)
      stop
   80 read (1,26)  gc
      read (1,11)  mm,mp
      read (1,27)  idea
```

```
c     read ri ('length'), cl (degrees) and ra ('length')
      read (1,24)  (ri(i),cl(i),ra(i),i=1,k)
      read (1,26)  ro
      close (1)
c
      ff=3.1415926535898d0/180.d0
      rfac=1.0d03
      zro1=ra(1)*1.0d-06
      zro2=1.0d-02
      do 10  i=1,k
      x=rfac*ra(i)*dcos(ff*cl(i))
      y=rfac*ra(i)*dsin(ff*cl(i))
      ix=idnint(x)
      iy=idnint(y)
      xc(i)=dble(ix)/rfac
      yc(i)=dble(iy)/rfac
      do 10  j=1,k
      if (i.ne.j)  go to 15
 30   ch(i,j)=0.0d00
      r(i,j)=0.0d00
      go to 10
 15   x=ra(j)*dcos(ff*cl(j))-ra(i)*dcos(ff*cl(i))
      y=ra(j)*dsin(ff*cl(j))-ra(i)*dsin(ff*cl(i))
      r(i,j)=dsqrt(x**2+y**2)
      if (dabs(x).lt.zro1)  go to 20
      if (dabs(y).lt.zro1)  go to 25
      fi=datan(y/x)/ff
      if (dabs(fi).lt.zro2)  fi=0.0d00
      sa=dsign(1.0d00,x)
      sb=dsign(1.0d00,y)
      ch(i,j)=fi+(2.0d00-sb*(1.0d00+sa))*90.0d00
      if (dabs(360.0d00-ch(i,j)).lt.zro2)  ch(i,j)=0.0d00
      go to 10
 20   if (dabs(y).lt.zro1)  go to 30
      ch(i,j)=90.0d00
      if (y.lt.0.0d00)  ch(i,j)=270.0d00
      go to 10
 25   ch(i,j)=0.0d00
      if (x.lt.0.0d00)  ch(i,j)=180.0d00
 10   continue
c
      write (2,19)  k,mm,mn,mp
      write (2,21)
      write (2,12)  ((ch(i,j),j=1,k),i=1,k)
      write (2,22)
      write (2,12)  ((r(i,j),j=1,k),i=1,k)
      write (2,17)
      write (2,18)  (i,ri(i),ra(i),cl(i),i=1,k)
c     Degrees to radians
      do 35  i=1,k
      cl(i)=cl(i)*ff
      do 35  j=1,k
      ch(i,j)=ch(i,j)*ff
```

```
35  continue
    call fact(mm,mp,f)
    ml=2*mp*k
    call fixup(mm,k,a,b,w1,w2,w3,w4,ro,mn,r1,r2,r3,ri,ra,cl,s,co,f)
    if (idea.eq.0)  go to 40
    do 50  idea=1,k
    kk=2*(k-1)
    call fixup2(mm,mp,k,kk,ml,a,b,w1,w2,w3,w4,ch,r,ri,r1,r2,r3,s
   *,co,f,g,w5,w6,idea)
    call viscou(mp,mm,k,idea,ml,s,co,r,ch,r1,ri,a1,a2,a3,a4,w5,a,b)
    ix=idea+k
    jx=0
    kk=2*k
    do 45  j=1,kk
    if(j.eq.idea.or.j.eq.ix)  go to 45
    jx=jx+1
    vc(idea,j)=-a4(1,jx)
    vc(ix,j)=-a4(2,jx)
45  continue
    vc(idea,idea)=1.0d0
    vc(ix,ix)=1.d0
    vc(idea,ix)=0.d0
    vc(ix,idea)=0.d0
50  continue
    write (2,16)  ro
    write (2,12)  ((vc(i,j),j=1,k),i=1,kk)
    k1=k+1
    write (2,16)  ro
    write (2,12)  ((vc(i,j),j=k1,kk),i=1,kk)
    idea=0
40  kk=2*k
    call fixup2(mm,mp,k,kk,ml,a,b,w1,w2,w3,w4,ch,r,ri,r1,r2,r3,s
   *,co,f,g,w5,w6,idea)
    ix=1
    k2=k+2
    do 55  i=1,ml,mp
    ix=ix+1
    do 60  j=1,kk
    jx=j+1
    if(j.gt.k)jx=j+2
    if(ix.eq.k2)ix=ix+1
    am(ix,jx)=2.d0*w5(i,j)
    w5(i,j)=2.0d0*w5(i,j)
60  continue
    j=(i-1+mp)/mp
    am(ix,ix)=1.0d0+am(ix,ix)
    w5(i,j)=1.0d0+w5(i,j)
55  continue
    k1=k+2
    am(1,1)=-1.0d0
    am(1,k1)=0.0d0
    am(k1,1)=0.0d0
    am(k1,k1)=-1.0d0
```

```
      do 65  j=1,k
      jx=j+1
      jp=jx+k+1
      ff=(ri(j)/ro)**2
      am(1,jx)=ff
      am(1,jp)=0.0d0
      am(kl,jx)=0.0d0
      am(kl,jp)=ff
      am(jx,1)=1.0d0
      am(jp,1)=0.0d0
      am(jx,kl)=0.0d0
      am(jp,kl)=1.0d0
      do 70  i=1,k
      ix=i+1
      ip=ix+k+1
      fg=(ri(i)/ro)**2
      am(1,jx)=am(1,jx)-fg*am(ix,jx)
      am(1,jp)=am(1,jp)-fg*am(ix,jp)
      am(kl,jx)=am(kl,jx)-fg*am(ip,jx)
      am(kl,jp)=am(kl,jp)-fg*am(ip,jp)
      am(jx,1)=am(jx,1)-am(jx,ix)
      am(jp,1)=am(jp,1)-am(jp,ix)
      am(jx,kl)=am(jx,kl)-am(jx,ip)
      am(jp,kl)=am(jp,kl)-am(jp,ip)
 70   continue
      am(1,1)=am(1,1)-am(1,jx)
      am(1,kl)=am(1,kl)-am(1,jp)
      am(kl,1)=am(kl,1)-am(kl,jx)
      am(kl,kl)=am(kl,kl)-am(kl,jp)
 65   continue
      kl=kk+2
      write (2,14)  ro
      write (2,13)  ((am(i,j),j=1,kl),i=1,kl)
      ix=0
      close (2)
c
c**********
c     File 3 is ONLY valid for equi-radii cylinders
c**********
      write (3,27)  id
      write (3,28)  k,gc
      write (3,29)  ri(1),ro
      write (3,23)  (xc(i),yc(i),i=1,k)
      do 75  i=1,ml,mp
      ix=ix+1
      write (3,23)  (w5(i,j),vc(ix,j),j=1,kk)
 75   continue
      close (3)
      close (4)
c
      stop
 11   format (2i3)
 12   format (4d12.5)
```

```
   13  format (5d12.5)
   14  format (/,10x,'The mass matrix with enclosing '
      *,'cylinder at',/,'ro=',f10.5,/)
   16  format (/,10x,'The viscosity matrix with enclosing '
      *,'cylinder at',/,'ro=',f10.5,/)
   17  format (/,5x,'i',7x,'r(i)',10x,'r(0,i)',4x,'ch(0,i) in deg',/)
   18  format (3x,i3,3f14.7)
   19  format (5x,'k=',i2,'  mm=',i2,'  cylinder at centre of array',i
      *2,'  mp=',i2,/)
   21  format (/,'The matrix defining ch(i,j) in degrees:',/)
   22  format (/,'The matrix defining r(i,j):',/)
   23  format (2f10.5)
   24  format (f10.5,f7.2,f10.5)
   26  format (f10.5)
   27  format (i3)
   28  format (i2,f8.3)
   29  format (2f10.3)
   31  format ('Enter run no.:')
       end
c
c
       subroutine  fact(mm,mp,f)
c      Generate factorials such that f(j+1)=j factorial
       integer*2  mm,mp,mt,mtt,i,ip
       real*8  f(1)
       mtt=2*mp
       mt=mm+1
       if (mtt.gt.mt)  mt=mtt
       f(1)=1.0d00
       do 10  i=2,mt
       ip=i-1
       f(i)=dble(ip)*f(ip)
   10  continue
       return
       end
c
c
       subroutine  gen(ch,m,s,c)
c      Generate c(i) and s(i) such that,
c      c(i+1)=dcos(i*ch) and s(i+1)=dsin(i*ch)
       implicit real*8  (a-h,o-z)
       integer*2  m,i
       dimension  c(1),s(1)
       c(1)=1.0d00
       s(1)=0.0d00
       do 10  i=2,m
       h=dble(i-1)*ch
       c(i)=dcos(h)
       if (dabs(c(i)).lt.1.0d-10)  c(i)=0.0d00
       s(i)=dsin(h)
       if (dabs(s(i)).lt.1.0d-10)  s(i)=0.0d00
   10  continue
       return
```

```
      end
c
c
      subroutine  cont(r1,m,a)
c     Generate a(i) such that a(i+1)=r1**i
      integer*2  m,i,ip
      real*8  a(1),r1
      a(1)=1.0d00
      do 10  i=2,m
      ip=i-1
      a(i)=r1*a(ip)
 10   continue
      return
      end
c
c
      subroutine  tmult(m,a,b,c)
c     Multiplies two upper triangular matrices, c=a*b
      integer*2  m,i,j,l
      real*8  a(m,l),b(m,l),c(m,l)
      do 10  i=1,m
      do 10  j=1,m
      c(i,j)=0.0d00
 10   continue
      do 15  i=1,m
      do 15  j=i,m
      do 15  l=i,j
      c(i,j)=c(i,j)+a(i,l)*b(l,j)
 15   continue
      return
      end
c
c
      subroutine  tinv(m,a,b)
c     Inverts an upper diagonal matrix
      integer*2  m,i,j,n,jj,ip,ig,l
      real*8  a(m,l),b(m,l)
      do 10  i=1,m
      do 15  j=1,m
      b(i,j)=0.0d00
 15   continue
      b(i,i)=1.0d00/a(i,i)
 10   continue
      n=m-1
      do 20  i=1,n
      ip=m-i
      do 25  j=1,i
      jj=m+1-j
      ig=ip+1
      do 30  l=ig,jj
      b(ip,jj)=b(ip,jj)-a(ip,l)*b(l,jj)
 30   continue
      b(ip,jj)=b(ip,jj)/a(ip,ip)
```

```
   25  continue
   20  continue
       return
       end
c
c
       subroutine  dmult(m,a,b,c)
c      Multiplies matrices, c=a*b
       integer*2  m,i,j,l
       real*8  a(m,l),b(m,l),c(m,l)
       do 10  i=1,m
       do 10  j=1,m
       c(i,j)=0.0d00
       do 15  l=1,m
       c(i,j)=c(i,j)+a(i,l)*b(l,j)
   15  continue
   10  continue
       return
       end
c
c
       subroutine  add(m,a,b,c)
c      Adds two matrices, c=a+b
       integer*2  m,i,j
       real*8  a(m,l),b(m,l),c(m,l)
       do 10  i=1,m
       do 10  j=1,m
       c(i,j)=a(i,j)+b(i,j)
   10  continue
       return
       end
c
c
       subroutine  cmult(m,x,a)
c      Multiplies a matrix by a constant
       integer*2  m,i,j
       real*8  a(m,l),x
       do 10  i=1,m
       do 10  j=1,m
       a(i,j)=x*a(i,j)
   10  continue
       return
       end
c
c
       subroutine  ripl(m,x,y,wl,w2,a,b)
c      Computes the sums x*a-y*b and x*b+y*a,
c      and stores them in wl and w2 respectively
       integer*2  m
       real*8  x(m,l),y(m,l),wl(m,l),w2(m,l),a(m,l),b(m,l),u
       u=-1.0d00
       call  dmult(m,x,a,wl)
       call  dmult(m,y,b,w2)
```

```
      call  cmult(m,u,w2)
      call  add(m,w1,w2,w1)
      call  dmult(m,x,b,w2)
      call  dmult(m,y,a,x)
      call  add(m,w2,x,w2)
      return
      end
c
c
      subroutine  repl(m,a,b,c,d,w1,w2)
c     Computes (b*ainv*b+a)inv*(b*ainv*c-d), and stores it in b,
c     and, -(b*ainv*b+a)inv*(b*ainv*d+c), and stores it in a
      integer*2  m
      real*8  a(m,1),b(m,1),c(m,1),d(m,1),w1(m,1),w2(m,1),u
      u=-1.0d00
      call  tinv(m,a,w1)
      call  tmult(m,b,w1,w2)
      call  tmult(m,w2,b,w1)
      call  add(m,w1,a,a)
      call  tinv(m,a,w1)
      call  dmult(m,w2,c,b)
      call  dmult(m,w2,d,a)
      call  cmult(m,u,d)
      call  add(m,b,d,d)
      call  dmult(m,w1,d,b)
      call  add(m,a,c,c)
      call  dmult(m,w1,c,a)
      call  cmult(m,u,a)
      return
      end
c
c
      subroutine  diag(m,a,b,w1,w2)
c     (not commented)
      integer*2  m,i,j
      real*8  a(m,1),b(m,1),w1(m,1),w2(m,1),di
      do 10  i=1,m
      di=dble(i)
      do 15  j=1,m
      w1(i,j)=di*a(i,j)
      w2(i,j)=di*b(i,j)
  15  continue
      w1(i,i)=w1(i,i)-di
  10  continue
      return
      end
c
c
      subroutine  viscou(m,mm,k,idea,ml,s,c,r,ch,rl,ri,w1,w2,w3,w4,w5
     *,a,b)
c     Calculates the viscous coupling coefficients on cylinder "idea"
      implicit integer*2  (i-n)
      implicit real*8  (a-h,o-z)
```

```
      dimension  s(1),c(1),r1(1),ri(1),w1(1),w2(1)
      dimension  r(k,1),ch(k,1)
      dimension  w5(m1,1),a(mm,mm,1),b(mm,mm,1)
      dimension  w3(2,1),w4(2,1)
      u=-1.0d00
      m2=2*m*(k-1)
      iz=m*(k-1)
      m3=m+2
      if (mm.gt.m3)  m3=mm
      jx=0
      do 10  j=1,k
      if (j.eq.idea)  go to 10
      jx=jx+1
      r4=r(idea,j)/ri(j)
      r6=1.0d00/r4
      call  cont(r4,mm,r1)
      call  gen(ch(idea,j),m3,s,c)
      do 15  n=1,mm
      n1=n-1
      r5=u**n1*r1(n)*dble(n)
      w1(n)=r5*c(n)
      w2(n)=r5*s(n)
   15 continue
      call  cont(r6,m3,r1)
      do 20  l=1,m
      ii=(jx-1)*m+l
      n1=l+2
      ip=ii+iz
      r4=0.0d00
      r5=0.0d00
      r6=0.0d00
      r7=0.0d00
      do 25  n=1,mm
      r2=a(n,1,j)
      r3=b(n,1,j)
      r4=r4+w1(n)*r2
      r5=r5+w1(n)*r3
      r6=r6+w2(n)*r2
      r7=r7+w2(n)*r3
   25 continue
      r8=u**l*r1(n1)*dble(l)
      r9=r8*c(n1)
      r10=r8*s(n1)
      w3(1,ii)=r9+r4-r7
      w3(1,ip)=r10+r5+r6
      w3(2,ii)=r10-r5-r6
      w3(2,ip)=r4-r7-r9
   20 continue
   10 continue
      k1=2*(k-1)
      do 30  i=1,2
      do 30  j=1,k1
      w4(i,j)=0.0d00
```

```
      do 30  l=1,m2
      w4(i,j)=w4(i,j)+w3(i,l)*w5(l,j)
   30 continue
      return
      end
c
c
      subroutine  fixup(mm,k,a,b,w1,w2,w3,w4,ro,mn,r1,r2,r3,ri,ra,c1
     *,s,co,f)
c     (not commented)
      implicit integer*2  (i-n)
      implicit real*8  (a-h,o-z)
      dimension  a(mm,mm,1),b(mm,mm,1)
      dimension  w1(mm,1),w2(mm,1),w3(mm,1),w4(mm,1)
      dimension  ri(1),ra(1),c1(1),s(1),co(1),f(1),r1(1),r2(1),r3(1)
      u=-1.0d00
      mv=mm+2
      do 10  l=1,k
      do 10  i=1,mm
      do 10  j=1,mm
      a(j,i,l)=0.0d00
      b(j,i,l)=0.0d00
   10 continue
      call  cont(ro,mv,r1)
      do 15  j=1,k
      if (j.eq.mn)  go to 45
      do 20  m=1,mm
      do 20  n=1,mm
      w3(m,n)=0.0d00
      w4(m,n)=0.0d00
   20 continue
      call  gen(c1(j),mm,s,co)
      call  cont(ri(j),mv,r2)
      call  cont(ra(j),mm,r3)
      do 25  m=1,mm
      r4=r1(m)/f(m)
      n4=m+1
      n5=m+2
      r6=f(n4)/r1(n5)
      do 30  n=m,mm
      n1=n-m
      n2=n1+1
      n3=n+1
      r5=u**n1*f(n3)*r3(n2)*r4/r2(n)/f(n2)
      a(m,n,j)=r5*co(n2)
      b(m,n,j)=r5*s(n2)
   30 continue
      do 35  n=1,m
      n1=m-n+1
      n3=n+2
      r5=r6*r3(n1)*r2(n3)/f(n)/f(n1)
      w3(m,n)=u*r5*co(n1)
      w4(m,n)=r5*s(n1)
```

```
   35  continue
   25  continue
       call  repl(mm,a(1,1,j),b(1,1,j),w3,w4,w1,w2)
       go to 15
   45  r6=(ri(mn)/ro)**2
       r5=r6
       do 40  m=1,mm
       a(m,m,mn)=r6
       r6=r6*r5
   40  continue
   15  continue
       return
       end
c
c
       subroutine  fixup2(mm,mp,k,kk,ml,a,b,w1,w2,w3,w4,ch,r,ri
      *,r1,r2,r3,s,co,f,g,w5,w6,idea)
c      (not commented)
       implicit integer*2  (i-n)
       implicit real*8  (a-h,o-z)
       integer*4  kk_4,mt_4,ml_4,id_4,ier_4
       dimension  a(mm,mm,1),b(mm,mm,1)
       dimension  w1(mm,1),w2(mm,1),w3(mm,1),w4(mm,1)
       dimension  w6(1),ri(1),s(1),co(1),f(1)
       dimension  r1(1),r2(1),r3(1)
       dimension  ch(k,1),r(k,1),g(ml,1),w5(ml,1)
       u=-1.0d00
       ms=2*mp+1
       if (ms.lt.mm)  ms=mm
       mw=mm+2
       mq=mp*k
       if (idea.ne.0)  mq=mp*(k-1)
       ix=0
       do 10  i=1,k
       if (i.eq.idea)  go to 10
       ix=ix+1
       call  cont(ri(i),mm,r1)
       jx=0
       do 15  j=1,k
       if (j.eq.idea)  go to 15
       jx=jx+1
       if (i.eq.j)  go to 45
       call  cont(ri(j),mw,r2)
       call  cont(r(i,j),ms,r3)
       do 20  m=1,mm
       do 20  n=1,mm
       w3(m,n)=0.0d00
       w4(m,n)=0.0d00
   20  continue
       call  gen(ch(i,j),ms,s,co)
       do 25  m=1,mm
       r4=r1(m)/f(m)
       do 30  n=m,mm
```

```
      nl=n-m
      n2=nl+1
      n3=n+1
      r5=u**nl*f(n3)*r3(n2)*r4/r2(n)/f(n2)
      w3(m,n)=r5*co(n2)
      w4(m,n)=r5*s(n2)
   30 continue
   25 continue
      call  ripl(mm,w3,w4,wl,w2,a(1,1,j),b(1,1,j))
      do 35  m=1,mp
      ii=(ix-1)*mp+m
      ip=ii+mq
      r4=rl(m)/f(m)
      do 40  n=1,mp
      jj=(jx-1)*mp+n
      jp=jj+mq
      nl=n+m+1
      n2=n+2
      n3=n+m
      r5=u**n*f(n3)*r4*r2(n2)/f(n)/r3(nl)
      r6=r5*co(nl)
      ff=r5*s(nl)
      r5=wl(m,n)
      r7=w2(m,n)
      g(ii,jj)=r5+r6
      g(ip,jp)=r5-r6
      g(ii,jp)=r7+ff
      g(ip,jj)=ff-r7
   40 continue
   35 continue
      go to 15
   45 call  diag(mm,a(1,1,i),b(1,1,i),wl,w2)
      do 50  m=1,mp
      ii=(jx-1)*mp+m
      ip=ii+mq
      do 55  n=1,mp
      jj=(jx-1)*mp+n
      jp=jj+mq
      r6=wl(m,n)
      ff=w2(m,n)
      g(ii,jj)=r6
      g(ii,jp)=ff
      g(ip,jj)=u*ff
      g(ip,jp)=r6
   55 continue
   50 continue
   15 continue
   10 continue
c     (to solve the equations)
      mt=2*mp*k
      if (idea.ne.0)  mt=2*mp*(k-1)
      id=0
      do 60  j=1,kk
```

```
      do 60  i=1,mt
      w5(i,j)=0.0d00
      ii=(j-1)*mp+1
      w5(ii,j)=1.0d00
60    continue
      kk_4=kk
      mt_4=mt
      ml_4=ml
      id_4=id
      call  leqtlf(g,kk_4,mt_4,ml_4,w5,id_4,w6,ier_4)
      ier=ier_4
      return
      end
```

(b) Dimensions

The above program is dimensioned for a four cylinder cluster (k = 4), and for specific values for the truncation constants mm and mp, namely mm = 15 and mp = 11. The latter values have been minimized to yield adequately accurate results with reasonably fast computation times (see [73] for details), and have not been changed.

Parameter(s)	Dimension
a,b	mm,mm,k
w1,w2,w3,w4	mm,mm
g	$2\cdot mp\cdot k, 2\cdot mp\cdot k$
w5	$2\cdot mp\cdot k, 2\cdot k$
vc	$2\cdot k, 2\cdot k$
ch,r	k,k
am	$2\cdot(k+1), 2\cdot(k+1)$
a3	$2, 2\cdot mp\cdot(k-1)$
a4	$2, 2\cdot(k-1)$
w6	$2\cdot mp\cdot k$
r1,r2	$2\cdot mm+2$
s,co,r3	$2\cdot mm+1$
f	$2\cdot mm$
a1,a2	mm
ri,ra,c1,xc,yc	k

(c) Data

A typical input data file is listed below, together with explanatory comments (right hand side). This particular data set is for a four cylinder bundle with $G_c = 0.75$, positioned in a square pattern at the center of the channel (R = 0.498 in and $R_c = 4.03$ in; note that units are unimportant here,

as the program works with dimensionless ratios).

```
 4  0                                   no. of cyl. & no. of cyl. at center
    75000                                   Gc
15 11                                       mm & mp
 1                                  1,0: viscous coupling coefs. desired or not
    49800   4500     96874      }
    49800  13500     96874      } cylinder radii, position angles and
    49800  22500     96874      } radii (relative to channel center)
    49800  31500     96874      }
   403000                                   channel radius
```

(d) Output

Data is output to two different files: (i) A "CPLprint-" file, which consists in (a) an echo of input parameters, (b) the calculated inter-cylinder distances and angles, and (c) the computed viscosity and mass matrices (printed four and five columns at a time, respectively, in the above example). (ii) A "CPLdata-" file, which contains (i) a file identifier (input manually at run time), (ii) the values for K and G_c, (iii) the cylinder(s) and channel radii, (iv) the z-y cylinders positions, and (v) the computed mass and viscosity coefficients (in a convenient two columns format). The "CPLprint-" file is listed below, with added comments on the right-hand side where required; the "CPLdata-" file is identical to the one used for input to the program CSD.f, listed later.

CPLprint- file:

```
     k= 4  mm=15  cylinder at centre of array 0  mp=11

The matrix defining r(i,j):

  .00000D+00  .13700D+01  .19375D+01  .13700D+01
  .13700D+01  .00000D+00  .13700D+01  .19375D+01
  .19375D+01  .13700D+01  .00000D+00  .13700D+01
  .13700D+01  .19375D+01  .13700D+01  .00000D+00

The matrix defining ch(i,j) in degrees:

  .00000D+00  .18000D+03  .22500D+03  .27000D+03
  .00000D+00  .00000D+00  .27000D+03  .31500D+03
  .45000D+02  .90000D+02  .00000D+00  .00000D+00
  .90000D+02  .13500D+03  .18000D+03  .00000D+00
```

i	r(i)	r(0,i)	ch(0,i) in deg
1	.4980000	.9687400	45.0000000
2	.4980000	.9687400	135.0000000
3	.4980000	.9687400	225.0000000
4	.4980000	.9687400	315.0000000

The viscosity matrix with enclosing cylinder at
ro= 4.03000

.10000D+01	-.12536D+00	-.21311D-01	.14985D+00	ζ_{11} ζ_{12} ζ_{13} ζ_{14}
-.12536D+00	.10000D+01	.14985D+00	-.21311D-01	ζ_{21} ζ_{22} ζ_{23} ζ_{24}
-.21311D-01	.14985D+00	.10000D+01	-.12536D+00	ζ_{31} ζ_{32} ζ_{33} ζ_{34}
.14985D+00	-.21311D-01	-.12536D+00	.10000D+01	ζ_{41} ζ_{42} ζ_{43} ζ_{44}
.00000D+00	-.20665D-01	-.73436D-01	.18338D-01	σ_{11} σ_{12} σ_{13} σ_{14}
.20665D-01	.00000D+00	-.18338D-01	.73436D-01	σ_{21} σ_{22} σ_{23} σ_{24}
-.73436D-01	.18338D-01	.00000D+00	-.20665D-01	σ_{31} σ_{32} σ_{33} σ_{34}
-.18338D-01	.73436D-01	.20665D-01	.00000D+00	σ_{41} σ_{42} σ_{43} σ_{44}

The viscosity matrix with enclosing cylinder at
ro= 4.03000

.00000D+00	.18338D-01	-.73436D-01	-.20665D-01	g_{11} g_{12} g_{13} g_{14}
-.18338D-01	.00000D+00	.20665D-01	.73436D-01	g_{21} g_{22} g_{23} g_{24}
-.73436D-01	-.20665D-01	.00000D+00	.18338D-01	g_{31} g_{32} g_{33} g_{34}
.20665D-01	.73436D-01	-.18338D-01	.00000D+00	g_{41} g_{42} g_{43} g_{44}
.10000D+01	.14985D+00	-.21311D-01	-.12536D+00	s_{11} s_{12} s_{13} s_{14}
.14985D+00	.10000D+01	-.12536D+00	-.21311D-01	s_{21} s_{22} s_{23} s_{24}
-.21311D-01	-.12536D+00	.10000D+01	.14985D+00	s_{31} s_{32} s_{33} s_{34}
-.12536D+00	-.21311D-01	.14985D+00	.10000D+01	s_{41} s_{42} s_{43} s_{44}

The mass matrix with enclosing cylinder at
ro= 4.03000

-.11319D+01	.32975D-01	.32975D-01	.32975D-01	.32975D-01	(see variables
.86736D-18	-.22201D-02	.22201D-02	-.22201D-02	.22201D-02	list below)
.21594D+01	-.11532D+01	.27214D+00	.48093D-01	-.32637D+00	
-.14539D+00	-.14473D-01	-.45022D-01	.15986D+00	.45022D-01	
.21594D+01	.27214D+00	-.11532D+01	-.32637D+00	.48093D-01	
.14539D+00	.45022D-01	.14473D-01	-.45022D-01	-.15986D+00	
.21594D+01	.48093D-01	-.32637D+00	-.11532D+01	.27214D+00	
-.14539D+00	.15986D+00	.45022D-01	-.14473D-01	-.45022D-01	
.21594D+01	-.32637D+00	.48093D-01	.27214D+00	-.11532D+01	
.14539D+00	-.45022D-01	-.15986D+00	.45022D-01	.14473D-01	
-.43368D-18	-.22201D-02	.22201D-02	-.22201D-02	.22201D-02	
-.11319D+01	.32975D-01	.32975D-01	.32975D-01	.32975D-01	
-.14539D+00	-.14473D-01	.45022D-01	.15986D+00	-.45022D-01	
.21594D+01	-.11532D+01	-.32637D+00	.48093D-01	.27214D+00	
.14539D+00	-.45022D-01	.14473D-01	.45022D-01	-.15986D+00	
.21594D+01	-.32637D+00	-.11532D+01	.27214D+00	.48093D-01	
-.14539D+00	.15986D+00	-.45022D-01	-.14473D-01	.45022D-01	
.21594D+01	.48093D-01	.27214D+00	-.11532D+01	-.32637D+00	
.14539D+00	.45022D-01	-.15986D+00	-.45022D-01	.14473D-01	
.21594D+01	.27214D+00	.48093D-01	-.32637D+00	-.11532D+01	

Note: Because of lack of space above, the added mass coefficients are identified here.

$$
\begin{array}{ccccc}
\varepsilon_{00} & \varepsilon_{01} & \varepsilon_{02} & \varepsilon_{03} & \varepsilon_{04} \\
e_{00} & e_{01} & e_{02} & e_{03} & e_{04} \\
\varepsilon_{10} & \varepsilon_{11} & \varepsilon_{12} & \varepsilon_{13} & \varepsilon_{14} \\
e_{10} & e_{11} & e_{12} & e_{13} & e_{14} \\
\varepsilon_{20} & \varepsilon_{21} & \varepsilon_{22} & \varepsilon_{23} & \varepsilon_{24} \\
e_{20} & e_{21} & e_{22} & e_{23} & e_{24} \\
\varepsilon_{30} & \varepsilon_{31} & \varepsilon_{32} & \varepsilon_{33} & \varepsilon_{34} \\
e_{30} & e_{31} & e_{32} & e_{33} & e_{34} \\
\varepsilon_{40} & \varepsilon_{41} & \varepsilon_{42} & \varepsilon_{43} & \varepsilon_{44} \\
e_{40} & e_{41} & e_{42} & e_{43} & e_{44} \\
\kappa_{00} & \kappa_{01} & \kappa_{02} & \kappa_{03} & \kappa_{04} \\
k_{00} & k_{01} & k_{02} & k_{03} & k_{04} \\
\kappa_{10} & \kappa_{11} & \kappa_{12} & \kappa_{13} & \kappa_{14} \\
k_{10} & k_{11} & k_{12} & k_{13} & k_{14} \\
\kappa_{20} & \kappa_{21} & \kappa_{22} & \kappa_{23} & \kappa_{24} \\
k_{20} & k_{21} & k_{22} & k_{23} & k_{24} \\
\kappa_{30} & \kappa_{31} & \kappa_{32} & \kappa_{33} & \kappa_{34} \\
k_{30} & k_{31} & k_{32} & k_{33} & k_{34} \\
\kappa_{40} & \kappa_{41} & \kappa_{42} & \kappa_{43} & \kappa_{44} \\
k_{40} & k_{41} & k_{42} & k_{43} & k_{44}
\end{array}
$$

Remark: The zero index above represents a channel wall which is free to move. These are not printed to the "CPLdata-" file: the channel is always considered rigid here.

2. CSD.f

This program has been written for computing normalized CSD's and PSD's, in the orthogonal z- and y-directions. Note that part of the program is designed to handle execution interruptions (multi-users time sharing of the computer) which does not relate in any way to the computations.

(a) Listing

This listing is FORTRAN 77 compatible.

```
c
c     VERSION 9 (09 Nov. 1988)
c
      implicit integer*2 (i-n)
      implicit real*8 (a-h,o-z)
c
      complex*16  kg(24,24),h(24,24),hi(24,24)
      complex*16  kxst(3,3),kx,vlp,snv,z,cdumy,hco
      complex*16  dcmplx,dconjg
      real*8  mg(24,24),cg(24,24),wv(24)
      real*8  mv(8,8),cv(8,8),kfpst(8,8),ktst(8,8),mst(8,8),fst(8,8)
      real*8  wm1(8,8),wm2(8,8),wm3(8,8),wm4(8,8),wm5(8,8)
      real*8  m(8),r(8),c(8),s(8),x(8),k1(8),k2(8),f(8),e(8)
      real*8  t(8),g(8),y(8)
      real*8  rm(8),ru(8),re(8),rb(8),rd(8),rw(8),rt(8),rn(8)
      real*8  rc(8),rl(8),ra(8),ri(8)
c
      real*8  xc(4),yc(4),param(16)
      real*8  rrs(4,4),frs(4,4),cosf(4,4),sinf(4,4)
      real*8  lam(8),sig(8)
      real*8  am(3,3),bm(3,3),cm(3,3),dm(3,3),bmst(3)
      real*8  snst(4,256,28)
      real*8  nu,kt,kfp,kfnc,mf,nij
      real*8  uv(25),rk2
      integer*4  leq1,leq2,itst,itst1,itst2,itst3,lop4,lpr4
      integer*2  dim1,dim2,dim3,dim4,dim5
      integer*2  cr(16),cs(16),rv(8),adx(24),bdx(24)
      integer*2  bfst(3,8),igst(4,4),ist(16,4),jst(16,4),mdst(4)
      integer*2  cofs,nv(25),runlop,flg,wflg,pflg,tintv
      character*70  line
      character*22  unffile
      character*19  datdir
      character*12  datf(3,25)
c
      common  /BLK1/alp,ups,beta,gamc,gamf,gama,gam,del,eps
     *,epsw,epsl,pie,cd,nu,cf,cb,rr,rch,u
      common /BLK2/a1,a2,a3
      common /BLK3/ba1,ba2,ba3,ca1,ca2,bb1,bb2,bb3,cb1,cb2,rrblk3
      common /BLK4/zo
```

```
      equivalence  (param(1),alp)
c
      open (1,FILE='/dev/console')
      open (8,FILE='/users/Jean/CNTRL/STOP.data',FORM='unformatted')
      open (9,FILE='/users/Jean/CNTRL/INDX.data',FORM='unformatted')
c
c     GENERAL CONSTANTS
      pflg=0
      cofs=48
      unffile(1:19)='/users/Jean/CSDunf-'
      datdir='/users/Jean/INPDTA/'
      pi=3.14159265359d00
      dim1=16
      dim2=24
      dim3=8
      dim4=4
      dim5=3
c
c     CONSTANTS FOR MAIN PROGRAM
      bz=0.7d00
c
c     CONSTANTS FOR ROUTINES
      zo=1.0d-07
      a1=38.344d00
      a2=40.611d00
      a3=19.091d00
      ba1=-33.795d00
      ba2=44.342d00
      ba3=0.06283d00
      ca1=-1.7348d00
      ca2=0.62895d00
      bb1=52.183d00
      bb2=140.666d00
      bb3=0.03942d00
      cb1=-1.3449d00
      cb2=1.2100d00
c
c     BEAM MODES CONSTANTS, CLAMPED-CLAMPED
      lam(1)=4.730040744864d00
      lam(2)=7.853204624096d00
      lam(3)=10.995607838002d00
      lam(4)=14.137165491257d00
      lam(5)=17.278759657399d00
      lam(6)=20.420352245626d00
      lam(7)=23.561944902040d00
      lam(8)=26.703537555508d00
      sig(1)=0.982502214576d00
      sig(2)=1.000777311907d00
      sig(3)=0.999966450125d00
      sig(4)=1.000001449898d00
      sig(5)=0.999999937344d00
      sig(6)=1.000000002708d00
      sig(7)=0.999999999883d00
```

```
      sig(8)=1.000000000005d00
c
c     INITIALIZE RATIO MATRICES
      do 10  i=1,dim3
      rm(i)=1.0d00
      ru(i)=1.0d00
      re(i)=1.0d00
      rb(i)=1.0d00
      rd(i)=1.0d00
      rw(i)=1.0d00
      rt(i)=1.0d00
      rn(i)=1.0d00
      rc(i)=1.0d00
      rl(i)=1.0d00
  10  continue
c
c     READ IN TIME DELTA AND INITIALIZE STOP FLAG FILE
      read (8)  flg,tintv
      rewind 8
      flg=0
      write (8)  flg,tintv
c
c     PARAMETERS INPUT FROM "RUN.data" AND data FILES
      open (5,FILE='/users/Jean/CNTRL/RUN.data')
      read (5,*)  nrun
      if (nrun.ne.0)  go to 260
      write (1,32)
  32  format ('ERROR: no run(s) requested',/,"$")
      close (5)
      go to 300
 260  if (nrun.gt.0.and.nrun.le.25) go to 225
      write (1,1)
   1  format ('ERROR: too many subsequent runs',/,"$")
      close (5)
      go to 300
 225  do 220  i=1,nrun
      read (5,*)  nv(i),uv(i),datf(1,i),datf(2,i),datf(3,i)
 220  continue
      ncnt=nrun
      do 230  i=nrun+1,25
      read (5,*,END=235)  nv(i),uv(i),datf(1,i),datf(2,i),datf(3,i)
      ncnt=ncnt+1
 230  continue
 235  close (5)
c
c     READ CURRENT LOOP INDICES
      read (9)  llop,llpr
      rewind 9
      lops=llop+1
      lprs=llpr+1
      ltst=llop+llpr
      if (ltst.eq.0)  go to 280
c
```

```
c     ECHO RUN (CONTINUATION) INSTRUCTION
c     (delete last two lines from 'STAT.data')
      open (7,FILE='/users/Jean/CNTRL/STAT.data')
 305  read (7,33,END=310)  line
      go to 305
 310  backspace 7
      backspace 7
      endfile 7
      close (7)
      wflg=1
c     (echo...)
      write (1,38)
  38  format ('Background run continued',/,"$")
c
c     READ COMPUTED DATA FROM FILE (CONTINUATIONS ONLY)
      open (10,FILE='/users/Jean/CSDtemp',FORM='unformatted')
      read (10)  igmx
      read (10)  (((snst(i,j,1),l=1,igmx),j=1,lops),i=1,4)
      close (10)
      go to 285
c
c     ECHO RUN (STARTING) INSTRUCTION
 280  wflg=0
      write (1,34)
  34  format ('Background run started',/,"$")
c
 285  do 240  runlop=1,nrun
      irun=nv(runlop)
      u=uv(runlop)
      if (wflg.eq.1)  go to 350
      open (7,FILE='/users/Jean/CNTRL/STAT.data')
      if (ltst.eq.0)  go to 270
 265  read (7,33,END=270)  line
      go to 265
 270  write (7,22) irun
  22  format ('RUN NO.:',i5)
      write (7,23) u
  23  format ('u (-):',f8.2)
      close (7)
c
 350  open (2,FILE=datdir//datf(1,runlop))
      read (2,5)  id0
   5  format (i3)
      read (2,6) k,gc
   6  format (i2,f8.3)
      if (k.le.dim4)  go to 15
      write (1,7)
   7  format ('ERROR: K too large',/,"$")
      close (2)
      go to 300
  15  nrd=2*k
      rk2=dble(k**2)
      read(2,8) rr,rch
```

```
    8  format (2f10.3)
       rrblk3=rr
       read (2,9) (xc(i),yc(i),i=1,k)
       read (2,9) ((mv(i,j),cv(i,j),j=1,nrd),i=1,nrd)
    9  format (2f10.5)
       close (2)
c
       open (3,FILE=datdir//datf(2,runlop))
       read (3,5)  id1
       read (3,11) kts
   11  format (i3)
       if (kts.eq.k.or.kts.eq.0) go to 65
       write (1,12)
   12  format ('ERROR: ratio matrices K does not match',/,"$")
       close (3)
       go to 300
   65  call  vecrd(nrd,rm)
       call  vecrd(nrd,ru)
       call  vecrd(nrd,re)
       call  vecrd(nrd,rb)
       call  vecrd(nrd,rd)
       call  vecrd(nrd,rw)
       call  vecrd(nrd,rt)
       call  vecrd(nrd,rn)
       call  vecrd(nrd,rc)
       call  vecrd(nrd,rl)
       close (3)
c
c      CALCULATE RATIO MATRICES (actually vectors of diagonal
c      elements) Ra and Ri
c
       do 60  i=1,dim3
       ra(i)=rd(i)**2
       ri(i)=rd(i)**4
   60  continue
c
       open (4,FILE=datdir//datf(3,runlop))
       read (4,5)  id2
       read (4,6) n
       if (n.le.dim5) go to 20
       write (1,13)
   13  format ('ERROR: N too large',/,"$")
       close (4)
       go to 300
   20  read (4,14) param
   14  format (8f8.6)
       read (4,16) cvr,dxsi
   16  format (2f10.3)
       read (4,17)  wmin,wmax,nw
   17  format (2f10.4,i5)
       if (nw.eq.1)  go to 200
       dw=(wmax-wmin)/dble(nw-1)
       go to 205
```

```
 200  dw=0.0d00
 205  read (4,5) npair
      if (npair.le.dim1)  go to 55
      write (1,18)
  18  format ('ERROR: npair too large',/,"$")
      close (4)
      go to 300
  55  read (4,19) (cr(i),cs(i),i=1,npair)
  19  format (2i3)
      close (4)
c
      if (wflg.eq.1)  go to 290
      open (7,FILE='/users/Jean/CNTRL/STAT.data')
 380  read (7,33,END=385)  line
      go to 380
 385  write (7,31)  id0,id1,id2
  31  format ("Data files ID's:  ",3i4,/)
      close (7)
c
c     ADDITIONAL PROGRAM CONSTANTS
 290  kk=2*k
      kn2=2*k*n
      zr1=rr*1.0d-06
      zr2=1.0d-07
c
c     SETTING INDEX VECTOR r(2K)
      do 85  i=1,kk
      if (i.gt.k) then
      rv(i)=i-k
      else
      rv(i)=i
      endif
  85  continue
c
c     COMPUTATION OF INTER-CYLINDER DISTANCES AND ANGLES
c     AND TRIG FUNCTIONS ON ANGLES
c
      do 25  i=1,k
      do 25  j=1,k
      dx=xc(j)-xc(i)
      dy=yc(j)-yc(i)
      dmg=dx**2+dy**2
      dumy=dsqrt(dmg)
      rrs(i,j)=dumy
      if (i.ne.j) go to 30
  35  frs(i,j)=0.0d00
      go to 90
  30  if (dabs(dx).lt.zr1) go to 40
      if (dabs(dy).lt.zr1) go to 45
      fval=datan(dy/dx)
      if (dabs(fval).lt.zr2) fval=0.0d00
      sx=dsign(1.0d00,dx)
      sy=dsign(1.0d00,dy)
```

```
      frs(i,j)=fval+(2.0d00-sy*(1.0d00+sx))*pi/2.0d00
      if (dabs(2.0d00*pi-frs(i,j)).lt.zr2) frs(i,j)=0.0d00
      go to 90
   40 frs(i,j)=pi/2.0d00
      if (dy.lt.0.0d00)  frs(i,j)=1.5d00*pi
      go to 90
   45 frs(i,j)=0.0d00
      if (dx.lt.0.0d00)  frs(i,j)=pi
   90 if (i.le.j)  go to 95
      cosf(i,j)=-cosf(j,i)
      sinf(i,j)=-sinf(j,i)
      go to 25
   95 arg=frs(i,j)
      dumy=dcos(arg)
      cosf(i,j)=dumy
      dumy=dsin(arg)
      sinf(i,j)=dumy
   25 continue
c
c     ASSEMBLE SYSTEM MATRICES
c
      call  mckecc(n,k,dim5,lam,sig,am,bm,cm,dm,dim3,rm,ru,re,rb,rd
     *,rw,rt,rn,rc,rl,ra,ri,mv,cv,m,r,c,s,x,k1,k2,f,e,t,g,y,wm1,wm2
     *,wm3,wm4,wm5,dim2,mg,cg,kg)
c
c     CALCULATE IGST AND RELATED VECTORS
      do 395  ii=1,4
      md=mod(ii,2)
      mdst(ii)=md
      do 170  j=1,4
      igst(ii,j)=0
  170 continue
  395 continue
      np1=0
      np2=0
      igmx=0
      do 210  lpr=1,npair
      ic=cr(lpr)
      jc=cs(lpr)
      if (ic.eq.jc) then
      np1=np1+1
      else
      np2=np2+1
      endif
      igst(ic,jc)=igmx+1
      do 215  ii=1,4
      ieq=1
      if (ic.ne.jc)  go to 80
      if (ii.eq.4)  go to 215
      ieq=0
   80 md=mdst(ii)
      ia=iabs(ii-md-2)/2
      i=ic+k*(1-md)
```

```
      j=jc+k*(1-ia)
      ist(lpr,ii)=i
      jst(lpr,ii)=j
      igmx=igmx+(1-ieq)*ia+ieq*md
 215  continue
 210  continue
      itst1=18*np1+23*np2
      itst2=12+itst1
      itst3=nw*itst2+20*(npair+1)
c
c     COMPUTE VECTOR OF BEAM MODES
      xloc=0.5d00+dxsi
      do 120  i=1,n
      dumy=bmf(lam,sig,i,xloc)
      bmst(i)=dumy
 120  continue
c
c     CALCULATE Mij FUNCTION
      do 125  i=1,kk
      do 125  j=1,kk
      dumy=mf(dim4,cosf,sinf,rv,i,j)
      mst(i,j)=dumy
 125  continue
c
c     CALCULATE BETA INDEX FUNCTION
      do 150  i=1,n
      do 150  j=1,kk
      bfst(i,j)=j+kk*(i-1)
 150  continue
c
c     CALCULATE A AND B INDEX FUNCTIONS
      do 160  i=1,kn2
      adx(i)=(i+kk-1)/kk
      bdx(i)=i-kk*(adx(i)-1)
 160  continue
c
c     (FREQUENCY DEPENDENT CALCULATIONS)
      do 75  lop=lops,nw
      lop4=lop
      llop=lop-1
      w=wmin+dble(lop-1)*dw
      w2=w**2
c
c     CALCULATE FREQUENCY RESPONSE FUNCTION
      do 70  i=1,kn2
      do 70  j=1,kn2
      c1=-w2*mg(i,j)
      c2=w*cg(i,j)
      hi(i,j)=dcmplx(c1,c2)+kg(i,j)
      h(i,j)=dcmplx(0.0d00,0.0d00)
      if (i.eq.j)  h(i,j)=dcmplx(1.0d00,0.0d00)
  70  continue
c
```

```
      rewind 8
      read (8)  flg
      if (flg.eq.1)  go to 275
c
      leq1=kn2
      leq2=dim2
      call  leqt1c(hi,leq1,leq2,h,leq1,leq2,0,wv,ier)
c
c     COMPUTE Kij,xsi FUNCTION
      temp1=bz/(2.0d00*pi)
      z=w*dsqrt(beta)*dcmplx(temp1,1.0d00)/(cvr*u)
      do 100  i=1,n
      do 100  j=1,n
      if (i.le.j)  go to 105
      kxst(i,j)=dconjg(kxst(j,i))
      go to 100
 105  cdumy=kx(lam,sig,dim5,am,bm,i,j,z)
      kxst(i,j)=cdumy
 100  continue
c
c     COMPUTE Kij,teta AND Kij,fi primed FUNCTIONS
      sr=w*dsqrt(beta)/(4.0d00*pi*eps*cvr*u)
      kfnc=kt(sr,1,1)
      do 110  i=1,kk
      do 110  j=1,kk
      if (i.eq.j) then
      ktst(i,j)=kfnc
      else
      ktst(i,j)=0.0d00
      endif
      if (i.le.j)  go to 115
      if (i.gt.k)  then
      if (j.gt.k)  go to 50
      go to 115
      else
      if (j.gt.k)  go to 115
      endif
  50  kfpst(i,j)=kfpst(j,i)
      go to 110
 115  dumy=kfp(dim4,rrs,rv,k,sr,i,j)
      kfpst(i,j)=dumy
 110  continue
c
c     CALCULATE Fij FUNCTION
      do 130  i=1,kk
      do 130  j=1,kk
      ic=rv(i)
      jc=rv(j)
      if (ic.eq.jc)  go to 135
      temp1=mst(i,j)*kfpst(ic,jc)
      nij=0.0d00
      if (i.eq.ic.and.j.eq.jc)  nij=1.0d00
      if (i.ne.ic.and.j.ne.jc)  nij=1.0d00
```

```
      fst(i,j)=temp1+(nij-mst(i,j))*kfpst(ic+k,jc+k)
      go to 130
  135 fst(i,j)=ktst(i,j)
  130 continue
c
c     COMPUTE NORMALIZED CSD's
      do 165  lpr=lprs,npair
      lpr4=lpr
      llpr=lpr-1
c
      rewind 8
      read (8)  flg
      if (flg.eq.1)  go to 275
c
      itst=(itst3-itst2*lop4-20*lpr4)/60
      if ((lpr.eq.lprs).and.(lop.eq.lops)) go to 390
      if (mod(itst,tintv).ne.0)  go to 335
  390 time=dble(itst)+0.1d00
      time=time*rk2/16.0d00
      itime=idint(time)
      imin=mod(itime,60)
      ihr=(itime-imin)/60
c     (round off minutes)
      mod5=mod(imin,5)
      imin=imin-mod5+5*int(mod5/3)
      if (imin.eq.60)  then
      imin=0
      ihr=ihr+1
      endif
      if ((imin+ihr).eq.0)  imin=2
      open (7,FILE='/users/Jean/CNTRL/STAT.data')
  340 read (7,33,END=345)  line
      go to 340
  345 if (pflg.eq.0) then
      pflg=1
      else
      backspace 7
      backspace 7
      endif
      write (7,39)  ihr,imin
   39 format ('Time left (this run), approx. ',i4,' hrs',i4,' min',/)
      close (7)
c
  335 ic=cr(lpr)
      jc=cs(lpr)
      do 140  ii=1,4
      ieq=1
      if (ic.ne.jc)  go to 175
      if (ii.eq.4)  go to 140
      ieq=0
  175 md=mdst(ii)
      i=ist(lpr,ii)
      j=jst(lpr,ii)
```

```
      ig=igst(ic,jc)
      if (ieq.eq.0)  go to 195
      if (ii.gt.2)  ig=ig+1
  195 snv=dcmplx(0.0d00,0.0d00)
      do 145  in=1,n
      do 145  jn=1,n
      vlp=dcmplx(0.0d00,0.0d00)
      do 155  ikn2=1,kn2
      do 155  jkn2=1,kn2
      ia1=adx(ikn2)
      ia2=adx(jkn2)
      ib1=bdx(ikn2)
      ib2=bdx(jkn2)
      ih1=bfst(in,i)
      ih2=bfst(jn,j)
      hco=dconjg(h(ih1,ikn2))
      vlp=vlp+hco*h(ih2,jkn2)*kxst(ia1,ia2)*fst(ib1,ib2)
  155 continue
      snv=snv+bmst(in)*bmst(jn)*vlp
  145 continue
      snvr=dble(snv)
      snvi=dimag(snv)
      if (ieq.ne.0)  go to 180
      if (ii.eq.3)  go to 185
      snst(ii,lop,ig)=snvr
      go to 140
  185 snst(ii,lop,ig)=snvr
      snst(ii+1,lop,ig)=snvi
      go to 140
  180 idx=1+2*(1-md)
      snst(idx,lop,ig)=snvr
      snst(idx+1,lop,ig)=snvi
  140 continue
  165 continue
      llpr=0
      lprs=1
   75 continue
c
c     WRITE COMPUTED DATA TO FILE
c     (set file number)
      j1=(irun/10)*10
      j2=(j1/100)*100
      l1=irun-j1
      l2=(j1-j2)/10
      l3=j2/100
      unffile(20:20)=char(l3+cofs)
      unffile(21:21)=char(l2+cofs)
      unffile(22:22)=char(l1+cofs)
c     (write data)
      open (6,FILE=unffile,FORM='unformatted')
      write (6)  irun,id0,id1,id2,k,gc,u,nw,npair,igmx
      write (6)  (cr(i),i=1,npair),(cs(i),i=1,npair)
      write (6)  ((igst(i,j),j=1,k),i=1,k)
```

```
      write (6)  wmin,wmax
      write (6)  (((snst(i,j,1),l=1,igmx),j=1,nw),i=1,4)
      rewind 6
      close (6)
      go to 295
 275  if ((llop+llpr).ne.0) then
      open (10,FILE='/users/Jean/CSDtemp',FORM='unformatted')
      write (10)  igmx
      write (10)  (((snst(i,j,1),l=1,igmx),j=1,llop+1),i=1,4)
      close (10)
      go to 360
      endif
c
c     EARLY ABORT CONDITION
      write (9)  llop,llpr
c
c     ABORT (EARLY STOP) ECHOED
      open (7,FILE='/users/Jean/CNTRL/STAT.data')
 365  read (7,33,END=375)  line
      go to 365
 375  write (7,41)
  41  format ('Background program aborted early, per request',/)
      close (7)
      write (1,42)
  42  format ('Background program aborted early, per request',/,"$")
      go to 300
c
c     UPDATE "INDX.data" file
 360  write (9)  llop,llpr
c
c     STOP REQUEST ECHOED
      open (7,FILE='/users/Jean/CNTRL/STAT.data')
 325  read (7,33,END=330)  line
      go to 325
 330  if (pflg.eq.0) go to 355
      backspace 7
      backspace 7
 355  write (7,36)
  36  format ('Background program stopped, per request',/)
      close (7)
      write (1,43)
  43  format ('Background program stopped, per request',/,"$")
      go to 300
c
c     UPDATE "INDX.data" AND "RUN.data" FILES
 295  llop=0
      llpr=0
      wflg=0
      ltst=1
      lprs=1
      lops=1
      write (9)  llop,llpr
      rewind 9
```

```
      open (5,FILE='/users/Jean/CNTRL/RUN.data')
      write (5,4)  nrun-runlop
      do 245  i=runlop+1,nrun
      write (5,3)  nv(i),uv(i),datf(1,i),datf(2,i),datf(3,i)
 245  continue
      if (ncnt.eq.nrun)  go to 255
      do 250  i=nrun+1,ncnt
      write (5,3)  nv(i),uv(i),datf(1,i),datf(2,i),datf(3,i)
 250  continue
 255  close (5)
c
c     DELETE "Time left" FROM "STAT.data" FILE
      if (pflg.ne.0) then
      open (7,FILE='/users/Jean/CNTRL/STAT.data')
 400  read (7,33,END=370)  line
      go to 400
 370  backspace 7
      backspace 7
      endfile 7
      close (7)
      pflg=0
      endif
c
c     EMPTY OUT CSDtemp
      open (10,FILE='/users/Jean/CSDtemp',FORM='unformatted')
      rewind 10
      endfile 10
      close (10)
 240  continue
c
c     PROGRAM ENDING ECHOED
      open (7,FILE='/users/Jean/CNTRL/STAT.data')
 315  read (7,33,END=320)  line
      go to 315
 320  write (7,37)
  37  format ('Background program ended, all runs finished',/)
      close (7)
c
 300  close (1)
      close (8)
      close (9)
   3  format (i3,f10.3,3x,"'",a12,"'",3x,"'",a12,"'",3x,"'",a12,"'")
   4  format (i2)
  33  format (70a)
      end
c
c     (09 Nov. 1988)
c
      subroutine vecrd(kk,rat)
      real*8  rat(1)
      integer*2  kk,iflg
      read (3,1)  iflg
      if (iflg.eq.0)  return
```

```
      read (3,2)  (rat(i),i=1,kk)
    1 format (i1)
    2 format (4e10.4)
      return
      end
c
c
      subroutine  mckecc(n,k,d1,lam,sig,am,bm,cm,dm,d2,rm,ru,re,rb,rd
     *,rw,rt,rn,rc,rl,ra,ri,mv,cv,m,r,c,s,x,k1,k2,f,e,t,g,y,wm1,wm2
     *,wm3,wm4,wm5,d3,mg,cg,kg)
      implicit integer*2 (i-n)
      integer*2  d1,d2,d3
      implicit real*8 (a-h,o-z)
      real*8  mv(d2,1),cv(d2,1)
      real*8  wm1(d2,1),wm2(d2,1),wm3(d2,1),wm4(d2,1),wm5(d2,1)
      real*8  rm(1),ru(1),re(1),rb(1),rd(1),rw(1),rt(1),rn(1),rc(1)
     *,rl(1),ra(1),ri(1)
      real*8  m(1),r(1),c(1),s(1),x(1),k1(1),k2(1),f(1),e(1),t(1)
     *,g(1),y(1)
      real*8  mg(d3,1),cg(d3,1)
      complex*16  kg(d3,1),jc,dcmplx
      real*8  lam(1),sig(1),am(d1,1),bm(d1,1),cm(d1,1),dm(d1,1)
      real*8  nu,li2,li4,lj2,lj4
      common /BLK1/alp,ups,beta,gamc,gamf,gama,gam,del,eps
     *,epsw,epsl,pie,cd,nu,cf,cb,rr,rch,u
c
      jc=dcmplx(0.0d00,1.0d00)
      kk=2*k
      rk=dble(k)
      dh=2.0d00*(rch**2-rk*rr**2)/(rch+rk*rr)
      h=2.0d00*rr/dh
      cons=eps*cf*u**2/2.0d00
      sqbt=dsqrt(beta)
c
      do 10  i=1,kk
      m(i)=(1.0d00-beta)*rm(i)
      c(i)=alp*ri(i)*ru(i)
      k1(i)=re(i)*ri(i)
      k2(i)=ups*ri(i)*rb(i)
      f(i)=gamc*rm(i)-gamf*ra(i)+cons*rd(i)*(1.0d00+h*rd(i))
      temp1=del*(gam*rt(i)+(1.0d00-2.0d00*nu*rn(i))*pie*ra(i))
      temp1=temp1+gama*rw(i)+gamc*rm(i)
      temp1=temp1+(1.0d00-del)*ra(i)*rc(i)*cb*u**2/2.0d00
      temp2=(2.0d00-del)*(1.0d00+h*rd(i))*eps/2.0d00
      temp2=temp2+(1.0d00-del)*(epsl+rd(i)*rl(i)*epsw*h)
      temp1=temp1+temp2*rd(i)*cf*u**2/2.0d00
      temp2=2.0d00-del+(1.0d00-del)*rl(i)*epsw/eps
      e(i)=-(temp1-temp2*gamf*ra(i)/2.0d00)
      g(i)=gamc*rm(i)-(gamf-cons*h)*ra(i)
      r(i)=-beta*ra(i)
      s(i)=-2.0d00*sqbt*u*ra(i)
      t(i)=-u**2*ra(i)
      x(i)=eps*sqbt*(cf*u+cd)*rd(i)/2.0d00
```

```
      y(i)=cons*rd(i)
      do 10  j=1,kk
      wm1(i,j)=0.0d00
      wm2(i,j)=0.0d00
      wm3(i,j)=0.0d00
      wm4(i,j)=0.0d00
      wm5(i,j)=0.0d00
   10 continue
c
      do 15  i=1,n
      do 15  j=1,n
      if (i.eq.j)  go to 20
      li2=lam(i)**2
      li4=li2**2
      lj2=lam(j)**2
      lj4=lj2**2
      fac=4.0d00*li2*lj2/(lj4-li4)
      iexp=i+j
      pow1=(-1.0d00)**iexp
      temp1=lam(j)*sig(j)-lam(i)*sig(i)
      am(i,j)=fac*(pow1-1.0d00)
      bm(i,j)=fac*(pow1+1.0d00)*temp1
      cm(i,j)=0.0d00
      dm(i,j)=fac*(pow1*temp1-(3.0d00*lj4+li4)*(pow1-1.0d00)/(lj4-li4))
      go to 15
   20 am(i,j)=0.0d00
      bm(i,j)=lam(i)*sig(i)*(2.0d00-lam(i)*sig(i))
      cm(i,j)=lam(i)**4
      dm(i,j)=bm(i,j)/2.0d00
   15 continue
c
      do 25  i=1,kk
      do 25  j=1,kk
      wm1(i,j)=r(i)*mv(i,j)
      wm2(i,j)=x(i)*cv(i,j)
      wm3(i,j)=s(i)*mv(i,j)
      wm4(i,j)=t(i)*mv(i,j)
      wm5(i,j)=y(i)*cv(i,j)
      if (i.ne.j)  go to 25
      wm1(i,j)=wm1(i,j)+m(i)
      wm4(i,j)=wm4(i,j)+e(i)
      wm5(i,j)=wm5(i,j)+g(i)
   25 continue
c
      do 30  ip=1,n
      do 30  jp=1,n
      if (ip.eq.jp) li4=lam(ip)**4
      do 30  i=1,kk
      do 30  j=1,kk
      idx=kk*(ip-1)+i
      jdx=kk*(jp-1)+j
      mg(idx,jdx)=0.0d00
      cg(idx,jdx)=am(ip,jp)*wm3(i,j)
```

```
      temp1=bm(ip,jp)*wm4(i,j)+am(ip,jp)*wm5(i,j)
      if (i.eq.j) temp1=temp1+dm(ip,jp)*f(i)
      kg(idx,jdx)=dcmplx(temp1,0.0d00)
      if (ip.ne.jp)  go to 30
      mg(idx,jdx)=wm1(i,j)
      cg(idx,jdx)=cg(idx,jdx)+wm2(i,j)
      if (i.ne.j)  go to 30
      cg(idx,jdx)=cg(idx,jdx)+li4*c(i)
      kg(idx,jdx)=kg(idx,jdx)+li4*(k1(i)+jc*k2(i))
   30 continue
      return
      end
c
c     (09 Nov. 1988)
c
      real*8 function bmf(lam,sig,i,xloc)
      integer*2  i
      real*8  lam(1),sig(1)
      real*8  xloc,arg
      real*8  dcos,dsin,dcosh,dsinh
      arg=lam(i)*xloc
      bmf=dcos(arg)-dcosh(arg)-sig(i)*(dsin(arg)-dsinh(arg))
      return
      end
c
c
      complex*16 function kx(lam,sig,ndim,am,bm,m,n,z)
      implicit real*8  (a-h,o-z)
      implicit integer*2 (i-n)
      integer*2  ind(4)
      real*8  fi(2,4)
      real*8  am(ndim,1),bm(ndim,1)
      real*8  lam(1),sig(1)
      complex*16  z,zc,af,bf,if,zexp,dconjg
      common /BLK4/zo
      common /BLK5/fi
      common /BLK6/dmn,amn,bmn,fmn
c
c
      ind(1)=m
      ind(2)=m
      ind(3)=n
      ind(4)=n
c
      if (zabs(z).gt.zo)  go to 10
      kx=16.0d00*sig(m)*sig(n)/(lam(m)*lam(n))
      if (mod(m*n,2).eq.0)  kx=0.0d00
      return
c
   10 amn=am(m,n)
      bmn=bm(m,n)
      if (m.eq.n)  go to 15
      dmn=0.0d00
```

```
      fmn=-amn*lam(m)*lam(n)*sig(m)*sig(n)
      go to 20
   15 dmn=1.0d0
      fmn=0.0d00
c
c     INDEX DIRECTORY FOR fi(i,j)
c       i=1: Second Derivative
c        =2: Third Derivative
c       j=1: Mode m, xsi=0
c        =2:      m,     1
c        =3:      n,     0
c        =4:      n,     1
c
   20 zc=dconjg(z)
      do 25  j=1,4
      k=ind(j)
      arg=0.0d00
      if (mod(j,2).eq.0)  arg=lam(k)
      cs=dcos(arg)
      sn=dsin(arg)
      ep=dexp(arg)
      en=dexp(-arg)
      c1=-lam(k)**2
      c2=lam(k)**3
      f1=(1.0d00-sig(k))*ep/2.0d00
      f2=(1.0d00+sig(k))*en/2.0d00
      fi(1,j)=c1*(cs-sn*sig(k)+f1+f2)
      fi(2,j)=c2*(sn+cs*sig(k)-f1+f2)
   25 continue
      kx=af(lam,z,n)-af(lam,-zc,n)
      ipas=4
      kx=kx+zexp(-z)*bf(lam,z,m,n)*if(-z,ipas)
      ipas=3
      kx=kx-bf(lam,-zc,m,n)*if(zc,ipas)
      return
      end
c
      complex*16  function if(z,j)
      integer*2  j
      complex*16  z
      real*8  fi(2,4)
      common /BLK5/fi
      if=(fi(1,j)-fi(2,j)/z)/(z**3)
      return
      end
c
      complex*16 function af(lam,z,n)
      integer*2  n
      complex*16 z
      real*8  dmn,amn,bmn,fmn
      real*8  lam(1)
      common /BLK6/dmn,amn,bmn,fmn
      af=dmn/z+amn/z**2+bmn/z**3+fmn/z**4
```

```
      af=af/(1.0d00-(lam(n)/z)**4)
      return
      end
c
      complex*16 function bf(lam,z,m,n)
      integer*2  m,n,j1,j2
      complex*16  z,if
      complex*16  zexp
      real*8  lam(1)
      j1=1
      j2=2
      bf=zexp(z)*if(z,j2)-if(z,j1)
      bf=bf/(1.0d00-(lam(m)/z)**4)
      bf=bf/(1.0d00-(lam(n)/z)**4)
      return
      end
c
c
      real*8 function kt(sr,i,j)
      integer*2  i,j
      real*8  sr,a1,a2,a3,x1,x2,x3
      real*8  dabs,dexp
      common /BLK2/a1,a2,a3
      if (i.eq.j)  go to 10
   15 kt=0.0d00
      return
   10 if (dabs(sr).gt.50.0d00)  go to 15
      x1=a1*sr
      x2=1.0d00+dexp(-a3*sr)
      x3=1.0d00+a2*sr**2
      kt=x1*x2/x3
      return
      end
c
c
      real*8 function kfp(kdim,rrs,rv,k,sr,i,j)
      integer*2  kdim,k,i,j,idx,jdx
      integer*2  rv(1)
      real*8  sr,e1,x1,x2,x3
      real*8  dlog,dexp
      real*8  ba1,ba2,ba3,ca1,ca2,bb1,bb2,bb3,cb1,cb2,rr
      real*8 rrs(kdim,1)
      common /BLK3/ba1,ba2,ba3,ca1,ca2,bb1,bb2,bb3,cb1,cb2,rr
      idx=rv(i)
      jdx=rv(j)
      if (idx.ne.jdx)  go to 25
      kfp=0.0d00
      return
   25 e1=dlog(rrs(idx,jdx)/rr)
      if (i.gt.k)  go to 10
      if (j.le.k)  go to 20
      kfp=0.0d00
      return
```

```
   10  if (j.gt.k)  go to 15
       kfp=0.0d00
       return
   20  x1=ba1*dexp(ca1*el)*sr
       x2=1.0d00+dexp(-ba3*sr)
       x3=1.0d00+ba2*dexp(ca2*el)*sr**2
       kfp=x1*x2/x3
       return
   15  x1=bb1*dexp(cb1*el)*sr
       x2=1.0d00+dexp(-bb3*sr)
       x3=1.0d00+bb2*dexp(cb2*el)*sr**2
       kfp=x1*x2/x3
       return
       end
c
c
       real*8 function mf(ndim,cosf,sinf,rv,i,j)
       integer*2  ndim,i,j,ic,jc
       integer*2  rv(1)
       real*8  cosf(ndim,1),sinf(ndim,1)
       real*8  ci,cj
       ic=rv(i)
       jc=rv(j)
       if (i.eq.ic)  go to 10
       ci=sinf(ic,jc)
       go to 15
   10  ci=cosf(ic,jc)
   15  if (j.eq.jc)  go to 20
       cj=sinf(ic,jc)
       go to 25
   20  cj=cosf(ic,jc)
   25  mf=ci*cj
       return
       end
```

(b) Dimensions

The above program is dimensioned for a four cylinder cluster (k = 4), and for three comparison functions (n = 3). Note that the last two dimensions of the vector snst reflect the number of frequency points for which computations are carried out (set to the number used in the HP5420A analyzer, i.e. 256) and the maximum number of independent inter-cylinder combinations for the case under analysis (28 exceed by far the usual number utilized, namely 3).

Parameter(s)	Dimension
snst	4,256,28
ist,jst	16,4
datf	3,25
mg,kg,cg,h,hi	2·k·n,2·k·n
mv,cv,kfpst,ktst,mst,fst wm1,wm2,wm3,wm4,wm5,igst	2·k,2·k
bfst	n,2·k
am,bm,cm,dm,kxst	n,n
xc,yc,rrs,frs,cosf,sinf	k,k
uv,nv	25
cr,cs,param	16
lam,sig	8
mdst	4
wv,adx,bdx	2·k·n
m,r,c,s,x,k1,k2,f,e,t g,y,rm,ru,re,rb,rd,rw rt,rn,rc,rl,ra,ri,rv	2·k
bmst	n

(c) Data

Typical input data files (three required here) are listed below, together with explanatory comments (right hand side). Note that "program execution control" (STOP.data and INDX.data) and "temporary storage" (CSDtemp) files have no bearing on how calculations are effected, and furthermore, are unformatted (binary data): hence they are not listed.

RUN.data: This file controls input data to the program. The first number determines how many sequential runs are to be carried out, in this case, 3. The next three lines furnish information for each of the three runs to be performed; starting from the left column, we have (i) the run number (solely an identification number), (ii) the dimensionless velocity u for that run, (iii) the name of the file holding cylinder cluster geometry data as well as the corresponding coupling coefficients, (iv) the file name for ratio matrices data, and finally, (v) the data file name for the system's parameters (physical properties, etc.), frequency points (band and number of points), and the selected inter-cylinder pairs.

RUN.data file:

```
  3
1       1.000   'CPLdata-1   '   'CSDdata1-13 '   'CSDdata2-23 '
2       3.000   'CPLdata-1   '   'CSDdata1-13 '   'CSDdata2-23 '
3       5.000   'CPLdata-1   '   'CSDdata1-13 '   'CSDdata2-23 '
```

CPL data file ("CPLdata-" file, from CPL.f program):

```
  1                                  identification number
 4   0.750                           number of cylinders and Gc
     0.498     4.030                 cylinder(s) and channel radii
   0.68500   0.68500   }
  -0.68500   0.68500   }
  -0.68500  -0.68500   }  z- and y- coordinates of cylinders
   0.68500  -0.68500   }
  -1.15326   1.00000   virtual mass and viscosity  }      ε11   ζ11
   0.27215  -0.12536   viscosity coefficients      }      ε12   ζ12
   0.04810  -0.02131                                      ε13   ζ13
  -0.32637   0.14985                                      ε14   ζ14
  -0.01448   0.00000                                      e11   g11
  -0.04505   0.01835                                      e12   g12
   0.15995  -0.07347                                      e13   g13
   0.04505  -0.02068                                      e14   g14
   0.27215  -0.12536                                      ε21   ζ21
  -1.15326   1.00000                                      ε22   ζ22
  -0.32637   0.14985                                      ε23   ζ23
   0.04810  -0.02131                                      ε24   ζ24
   0.04505  -0.01835                                      e21   g21
   0.01448   0.00000                                      e22   g22
  -0.04505   0.02068                                      e23   g23
  -0.15995   0.07347                                      e24   g24
   0.04810  -0.02131                                      ε31   ζ31
  -0.32637   0.14985                                      ε32   ζ32
  -1.15326   1.00000                                      ε33   ζ33
   0.27215  -0.12536                                      ε34   ζ34
   0.15995  -0.07347                                      e31   g31
   0.04505  -0.02068                                      e32   g32
  -0.01448   0.00000                                      e33   g33
  -0.04505   0.01835                                      e34   g34
  -0.32637   0.14985                                      ε41   ζ41
   0.04810  -0.02131                                      ε42   ζ42
   0.27215  -0.12536                                      ε43   ζ43
  -1.15326   1.00000                                      ε44   ζ44
  -0.04505   0.02068                                      e41   g41
  -0.15995   0.07347                                      e42   g42
   0.04505  -0.01835                                      e43   g43
   0.01448   0.00000                                      e44   g44
  -0.01448   0.00000                                      κ11   σ11
   0.04505  -0.02068                                      κ12   σ12
   0.15995  -0.07347                                      κ13   σ13
  -0.04505   0.01835                                      κ14   σ14
  -1.15326   1.00000                                      k11   s11
```

-0.32637	0.14985	k_{12} s_{12}
0.04810	-0.02131	k_{13} s_{13}
0.27215	-0.12536	k_{14} s_{14}
-0.04505	0.02068	κ_{21} σ_{21}
0.01448	0.00000	κ_{22} σ_{22}
0.04505	-0.01835	κ_{23} σ_{23}
-0.15995	0.07347	κ_{24} σ_{24}
-0.32637	0.14985	k_{21} s_{21}
-1.15326	1.00000	k_{22} s_{22}
0.27215	-0.12536	k_{23} s_{23}
0.04810	-0.02131	k_{24} s_{24}
0.15995	-0.07347	κ_{31} σ_{31}
-0.04505	0.01835	κ_{32} σ_{32}
-0.01448	0.00000	κ_{33} σ_{33}
0.04505	-0.02068	κ_{34} σ_{34}
0.04810	-0.02131	k_{31} s_{31}
0.27215	-0.12536	k_{32} s_{32}
-1.15326	1.00000	k_{33} s_{33}
-0.32637	0.14985	k_{34} s_{34}
0.04505	-0.01835	κ_{41} σ_{41}
-0.15995	0.07347	κ_{42} σ_{42}
-0.04505	0.02068	κ_{43} σ_{43}
0.01448	0.00000	κ_{44} σ_{44}
0.27215	-0.12536	k_{41} s_{41}
0.04810	-0.02131	k_{42} s_{42}
-0.32637	0.14985	k_{43} s_{43}
-1.15326	1.00000	k_{44} s_{44}

CSDdata1 file:

```
 13                                                identification number
  4                          flag: 0 if all matrices are identity, k otherwise
1                                                   flag set (read ratio matrices)
 1.0000e00 1.2400e00 1.2400e00 1.2400e00  \
 1.0000e00 1.2400e00 1.2400e00 1.2400e00  /  ratio coefficients, mass
1                                                   flag set (read ratio matrices)
 1.0000e00 0.0000e00 0.0000e00 0.0000e00  \  ratio coefficients, viscous
 1.0000e00 0.0000e00 0.0000e00 0.0000e00  /                       damping
1                                                   flag set (read ratio matrices)
 1.0000e00 1.3000e03 1.3000e03 1.3000e03  \
 1.0000e00 1.3000e03 1.3000e03 1.3000e03  /  ratio coefficients, stiffness
1                                                   flag set (read ratio matrices)
 1.0000e00 0.9000e00 0.9000e00 0.9000e00  \  ratio coefficients, hysteretic
 1.0000e00 0.9000e00 0.9000e00 0.9000e00  /                       damping
0                                                   flag reset (diameter ratios)
0                                        flag reset (attachment weight ratios)
0                                                   flag reset (pre-tension ratios)
1                                                   flag set (read ratio matrices)
 1.0000e00 0.7000e00 0.7000e00 0.7000e00  \ ratio coefficients, Poisson
 1.0000e00 0.7000e00 0.7000e00 0.7000e00  /                       ratio
0                                     flag reset (lower end drag coef. ratios)
0                                        flag reset (attachment length ratios)
```

CSDdata2 file:

```
 23                                                identification number
 3                                                  number of comparison functions
0.000865   0.022   0.466   10.52    9.16    1.36     0.0     1.0 \ system
   18.57    0.54    0.43   109.6   0.039    0.47   0.016     0.0 / param.*
    1.000   -0.0814      convection velocity ratio and longitudinal offset
   0.0000   75.9645  256  dimensionless frequency limits and no. of points
 3              number of inter-cylinder pairs
 1  1       \
 1  2        } inter-cylinder pairs
 1  3       /
```

* The (dimensionless) system parameters, defined by eqs.(2.52) to (2.54) inclusively, and by eqn.(2.14), are the following (ν is Poisson ratio [no defining equation]):

α T β γ_C γ_F Γ_A Γ δ ε ε_W ε_1 π c ν c_f c_{b_0}

3. CSD_comp

This program resolves the normalized CSD's and PSD's computed by "CSD.f", in arbitrary directions. The user simply inputs the desired cylinder pair (of course that particular pair has to have been previously selected, when running "CSD.f"), followed by an angle for each of the two cylinders. Note that a PSD is obtained if only one cylinder is selected, and if the two angles are equal (e.g. pair 1-1 and angles 45°-45°).

After computation of the resolved normalized CSD (or PSD), data is stored on (3.5 in) diskette. The printout is for "accounting" purposes only (keeping track of the data).

Remark

Because experimental results originally had Hz for the frequency axis, this program stores the data (diskette) with Hz as the frequency axis unit (note that the so-called normalized CSD's are not densities. They simply are multiplication factors "modulating" the pressure PSD's which are themselves densities). This allowed preliminary comparisons between theory and experiments, without having to make use of pressure PSD's.

(a) Listing

This listing is BASIC V compatible (run on HP9000-300 computer).

```
10    OPTION BASE 1
20    COMPLEX Csd(256,4),Res(256)
30    DIM B$[15],F$[34],A$[3]
40    DIM F(4),Snst(4,256,28)
50    INTEGER Irun,Id0,Id1,Id2,K,Nw,Npair
60    INTEGER Igst(16,16),Cr(16),Cs(16)
70    INTEGER Hi(20),Vi(1024),Rn(2)
80    INTEGER Ic,Jc,I,J,L,V1,V2,V3,V4
90    INTEGER Ig,Igmx,Ieq,Rcnt,Rno,Rflg,Rprt
100   INTEGER Dim1,Dim7,Flg,Dumy(2)
110   INTEGER Aflg,Icv(3),Jcv(3),Icnt,Jcnt,Dflg
120   INTEGER Igdim,Case
130   DIM Trv(3,3),Tsv(3,3)
140   !
150   DEG
160   Flg=0
170   Tr=1.0E+6
180   Ts=1.0E+6
```

```
  Igdim=16
  !
  Icnt=0
  Jcnt=0
  Icv(1)=1
  Icv(2)=1
  Icv(3)=1
  Jcv(1)=1
  Jcv(2)=2
  Jcv(3)=3
  Trv(1,1)=0.
  Trv(1,2)=45.
  Trv(1,3)=135.
  Trv(2,1)=0.
  Trv(2,2)=45.
  Trv(2,3)=135.
  Trv(3,1)=0.
  Trv(3,2)=45.
  Trv(3,3)=135.
  Tsv(1,1)=0.
  Tsv(1,2)=45.
  Tsv(1,3)=135.
  Tsv(2,1)=180.
  Tsv(2,2)=135.
  Tsv(2,3)=225.
  Tsv(3,1)=180.
  Tsv(3,2)=225.
  Tsv(3,3)=315.
  !
  Wfac=12.5/76.2624
  Dim1=16
  Dim7=256
  Hi(8)=0
  Hi(10)=500
  Hi(11)=20971
  Hi(12)=-31239
  Hi(17)=0
  Hi(18)=0
  Hi(19)=2
  Hi(20)=0
  !
Fmt1: IMAGE /,/,"Record no.:",5D,"    Unix file:  ",15A
Fmt2: IMAGE "Run:",4D,"     Data files id's:",3(4D)
Fmt3: IMAGE "K=",3D,"  Gc=",2D.3D,"    u=",2D.D
Fmt4: IMAGE "Nominal band (Hz):",3D.4D,",",3D.4D,"    No. pts.:",4D
Fmt5: IMAGE /,"Cyl. pair:",3D,3D
Fmt6: IMAGE "Angles (deg):",5D.2D,5D.2D,6/
  !
  BEEP
  INPUT "1, 2 or 3, for K= 4, 12, 16:",Case
  SELECT Case
  CASE 1
  REDIM Igst(4,4)
```

```
720   Igdim=4
730   CASE 2
740   REDIM Igst(12,12)
750   Igdim=12
760   CASE 3
770   CASE ELSE
780   GOTO 670
790   END SELECT
800   !
810   BEEP
820   DISP "Put printer on - press Continue..."
830   PAUSE
840   ASSIGN @Printer TO 701
850   OUTPUT @Printer USING "@"
860   WAIT 7
870   BEEP
880   DISP "Align top of page - press Continue..."
890   PAUSE
900   !
910   BEEP
920   DISP "Insert data disk - press Continue..."
930   PAUSE
940   !
950   ASSIGN @Outdir TO "UXDIR:,700,1";FORMAT OFF
960   ASSIGN @Outrec TO "UNIXDTA:,700,1";FORMAT OFF
970   CONTROL @Outdir,5;1
980   ENTER @Outdir;Rn(*)
990   Dflg=0
1000  IF Rn(1)-Rn(2)>1 THEN
1010  BEEP
1020  DISP "Incompatible Rn(2) - press Continue..."
1030  PAUSE
1040  GOTO 3640
1050  END IF
1060  IF Rn(2)<Rn(1)+250 THEN GOTO 1160
1070  Dflg=1
1080  GOTO 1160
1090  ASSIGN @Outdir TO *
1100  ASSIGN @Outrec TO *
1110  BEEP
1120  DISP "Change disk - press Continue..."
1130  PAUSE
1140  GOTO 950
1150  !
1160  BEEP
1170  DISP "Enter UNIX File  (null for stopping)";
1180  B$=""
1190  INPUT B$
1200  IF B$="" THEN GOTO 3640
1210  F$[1,12]="/users/Jean/"
1220  F$[13,27]=B$
1230  F$[28,34]=":,700,0"
1240  ASSIGN @File TO F$;FORMAT OFF
```

```
1250  !
1260  CONTROL @File,5;1
1270  ENTER @File;Dumy(*),Irun,Id0,Id1,Id2,K,Gc,U,Nw,Npair,Igmx,Dumy(*)
1280  IF Nw<=Dim7 THEN GOTO 1320
1290  BEEP
1300  DISP "ERROR: too many frequency points"
1310  STOP
1320  IF Npair<=Dim1 THEN GOTO 1370
1330  BEEP
1340  DISP "ERROR: too many cylinder pairs"
1350  STOP
1360  !
1370  REDIM Cr(Npair),Cs(Npair)
1380  ENTER @File;Dumy(*),Cr(*),Cs(*),Dumy(*)
1390  ENTER @File;Dumy(*),Igst(*),Dumy(*)
1400  ENTER @File;Dumy(*),Wmin,Wmax,Dumy(*)
1410  !
1420  W1=Wmin*Wfac
1430  W2=Wmax*Wfac
1440  Dw=(W2-W1)/(Nw-1)
1450  Nbw=Nw*Dw
1460  CALL Tri(W1,Hi(13),Hi(14))
1470  CALL Tri(Dw,Hi(15),Hi(16))
1480  !
1490  REDIM Snst(4,256,Igmx)
1500  ENTER @File;Dumy(*),Snst(*),Dumy(*)
1510  !
1520  A$="NO"
1530  Rflg=0
1540  BEEP
1550  DISP "Want data replacement (def. NO) ";
1560  INPUT A$
1570  IF A$="YES" THEN
1580  Rflg=1
1590  BEEP
1600  DISP "First record number to be REPLACED ";
1610  INPUT Rno
1620  IF Rno<Rn(1) OR Rno>Rn(2) THEN
1630  BEEP
1640  DISP "ERROR, record number out of range - press Continue..."
1650  PAUSE
1660  GOTO 1520
1670  END IF
1680  ELSE
1690  IF Dflg=1 THEN
1700  BEEP
1710  DISP "ERROR, disk full - press Continue..."
1720  PAUSE
1730  GOTO 1090
1740  END IF
1750  END IF
1760  !
1770  A$="YES"
```

```
1780  BEEP
1790  DISP "Want auto choice (def. YES) [pairs 1-1,1-2,1-3] ";
1800  INPUT A$
1810  IF A$="YES" THEN
1820  Aflg=0
1830  FOR I=1 TO Npair
1840  FOR J=1 TO 3
1850  IF Cr(I)=Icv(J) AND Cs(I)=Jcv(J) THEN GOTO 1920
1860  NEXT J
1870  BEEP
1880  DISP "ERROR: auto pairs not all available - press Continue..."
1890  PAUSE
1900  Aflg=1
1910  GOTO 1970
1920  NEXT I
1930  ELSE
1940  Aflg=1
1950  END IF
1960  !
1970  IF Aflg<>0 THEN
1980  IF Flg<>0 THEN
1990  Flg=0
2000  BEEP
2010  DISP "Advance paper - press Continue..."
2020  PAUSE
2030  ELSE
2040  Flg=1
2050  END IF
2060  !
2070  BEEP
2080  DISP "ID of first cylinder (zero for new UNIX file or STOP) ";
2090  INPUT Ic
2100  IF Ic=0 THEN GOTO 1160
2110  BEEP
2120  DISP "ID of second cylinder (zero for new UNIX file or STOP) ";
2130  INPUT Jc
2140  IF Jc=0 THEN GOTO 1160
2150  IF Ic>Igdim OR Jc>Igdim THEN GOTO 2070
2160  IF Ic<1 OR Jc<1 THEN GOTO 2070
2170  Ig=Igst(Ic,Jc)
2180  IF Ig<>0 THEN GOTO 2390
2190  BEEP
2200  DISP "ERROR: Data not available for this pair - press Continue"
2210  PAUSE
2220  GOTO 2070
2230  ELSE
2240  Icnt=Icnt+1
2250  IF Icnt<4 THEN GOTO 2290
2260  Icnt=0
2270  Jcnt=0
2280  GOTO 1160
2290  Ic=Icv(Icnt)
2300  Jc=Jcv(Icnt)
```

```
2310  Ig=Igst(Ic,Jc)
2320  IF Ig<>0 THEN GOTO 2390
2330  BEEP
2340  DISP "ERROR: Data not available for this pair - press Continue"
2350  PAUSE
2360  GOTO 2070
2370  END IF
2380  !
2390  IF Ic=Jc THEN GOTO 2480
2400  Ieq=1
2410  FOR I=1 TO Nw
2420  Csd(I,1)=CMPLX(Snst(1,I,Ig),Snst(2,I,Ig))
2430  Csd(I,2)=CMPLX(Snst(3,I,Ig),Snst(4,I,Ig))
2440  Csd(I,3)=CMPLX(Snst(1,I,Ig+1),Snst(2,I,Ig+1))
2450  Csd(I,4)=CMPLX(Snst(3,I,Ig+1),Snst(4,I,Ig+1))
2460  NEXT I
2470  GOTO 2560
2480  Ieq=0
2490  FOR I=1 TO Nw
2500  Csd(I,1)=CMPLX(Snst(1,I,Ig),0.)
2510  Csd(I,2)=CMPLX(Snst(2,I,Ig),0.)
2520  Csd(I,3)=CMPLX(Snst(3,I,Ig),Snst(4,I,Ig))
2530  Csd(I,4)=CMPLX(Snst(3,I,Ig),-Snst(4,I,Ig))
2540  NEXT I
2550  !
2560  IF Aflg<>0 THEN
2570  Trst=Tr
2580  Tsst=Ts
2590  BEEP
2600  DISP "Enter ANGLE (deg) at cyl. (no input for new pair) ";Ic;
2610  INPUT Tr
2620  BEEP
2630  DISP "Enter ANGLE (deg) at cyl. (no input for new pair) ";Jc;
2640  INPUT Ts
2650  IF Tr<>Trst THEN GOTO 2780
2660  IF Ts<>Tsst THEN GOTO 2780
2670  GOTO 1970
2680  ELSE
2690  Jcnt=Jcnt+1
2700  IF Jcnt<4 THEN GOTO 2740
2710  Jcnt=0
2720  OUTPUT @Printer USING "@"
2730  GOTO 1970
2740  Tr=Trv(Icnt,Jcnt)
2750  Ts=Tsv(Icnt,Jcnt)
2760  END IF
2770  !
2780  C1=COS(Tr)
2790  C2=COS(Ts)
2800  S1=SIN(Tr)
2810  S2=SIN(Ts)
2820  F(1)=C1*C2
2830  F(2)=S1*S2
```

```
2840  F(3)=C1*S2
2850  F(4)=S1*C2
2860  FOR I=1 TO 256
2870  Res(I)=CMPLX(0.,0.)
2880  FOR J=1 TO 4
2890  Res(I)=Res(I)+F(J)*Csd(I,J)
2900  NEXT J
2910  NEXT I
2920  !
2930  Hi(1)=Id0
2940  Hi(2)=Id1
2950  Hi(4)=Id2
2960  IF Ieq=0 AND Tr=Ts THEN GOTO 3140
2970  Hi(3)=1024
2980  Hi(5)=-30717
2990  Hi(6)=-7
3000  Hi(7)=258
3010  Hi(9)=-27660
3020  FOR I=1 TO 256
3030  L=4*I-3
3040  A=REAL(Res(I))
3050  B=IMAG(Res(I))
3060  CALL Tri(A,V1,V2)
3070  CALL Tri(B,V3,V4)
3080  Vi(L)=V1
3090  Vi(L+1)=V2
3100  Vi(L+2)=V3
3110  Vi(L+3)=V4
3120  NEXT I
3130  GOTO 3270
3140  Hi(3)=512
3150  Hi(5)=-30718
3160  Hi(6)=-3
3170  Hi(7)=256
3180  Hi(9)=-28684
3190  FOR I=1 TO 256
3200  L=2*I-1
3210  A=REAL(Res(I))
3220  CALL Tri(A,V1,V2)
3230  Vi(L)=V1
3240  Vi(L+1)=V2
3250  NEXT I
3260  !
3270  IF Rflg=0 THEN
3280  Rn(2)=Rn(2)+1
3290  IF Rn(2)=Rn(1)+249 THEN Dflg=1
3300  Rprt=Rn(2)
3310  Rcnt=Rn(2) MOD 250
3320  IF Rcnt=0 THEN Rcnt=250
3330  !
3340  CONTROL @Outdir,5;1
3350  CONTROL @Outdir,7;3
3360  OUTPUT @Outdir;Rn(*)
```

```
3370  ELSE
3380  Rcnt=Rno MOD 250
3390  Rprt=Rno
3400  IF Rcnt=0 THEN Rcnt=250
3410  Rno=Rno+1
3420  IF Rno>Rn(2) THEN
3430  Dflg=1
3440  END IF
3450  END IF
3460  !
3470  CONTROL @Outrec,7;251
3480  OUTPUT @Outrec,Rcnt;Hi(*),Vi(*)
3490  !
3500  OUTPUT @Printer USING Fmt1;Rprt,B$
3510  OUTPUT @Printer USING Fmt2;Irun,Id0,Id1,Id2
3520  OUTPUT @Printer USING Fmt3;K,Gc,U
3530  OUTPUT @Printer USING Fmt4;W1,Nbw,Nw
3540  OUTPUT @Printer USING Fmt5;Ic,Jc
3550  OUTPUT @Printer USING Fmt6;Tr,Ts
3560  !
3570  IF Dflg=0 THEN GOTO 2560
3580  ASSIGN @Outdir TO *
3590  ASSIGN @Outrec TO *
3600  BEEP
3610  DISP "Disk now full - insert new disk - press Continue..."
3620  PAUSE
3630  GOTO 950
3640  ASSIGN @Outdir TO *
3650  ASSIGN @Outrec TO *
3660  BEEP
3670  DISP "Finished"
3680  END
3690  !
3700  !
3710  SUB Tri(A,INTEGER I1,I2)
3720  INTEGER I,J,K
3730  Aa=ABS(A)
3740  I1=0
3750  I2=0
3760  IF Aa=0. THEN SUBEXIT
3770  I=FNInt(LOG(Aa)/LOG(2.0))
3780  Aa=Aa/(2.0^I)
3790  IF Aa<1.0 THEN GOTO 3820
3800  Aa=Aa/2.0
3810  I=I+1
3820  FOR J=1 TO 15
3830  Aa=Aa*2.
3840  K=FNInt(Aa)
3850  Aa=FNFract(Aa)
3860  IF K<>0 THEN I1=BINIOR(I1,2^(15-J))
3870  NEXT J
3880  IF Aa=0. THEN GOTO 3990
3890  FOR J=16 TO 22
```

```
3900  Aa=Aa*2.0
3910  K=FNInt(Aa)
3920  Aa=FNFract(Aa)
3930  IF K<>0 THEN I2=BINIOR(I2,2^(23-J))
3940  NEXT J
3950  Aa=Aa*2.0
3960  IF Aa<1.0 THEN Aa=Aa*1.000001
3970  K=FNInt(Aa)
3980  IF K<>0 THEN I2=BINIOR(I2,1)
3990  IF A>0. THEN GOTO 4070
4000  I1=BINCMP(I1)
4010  SELECT I2
4020  CASE 0
4030  I1=I1+1
4040  CASE ELSE
4050  I2=256-I2
4060  END SELECT
4070  I2=SHIFT(I2,-8)
4080  SELECT I
4090  CASE <0
4100  I2=I2+2*(128+I)+1
4110  CASE ELSE
4120  I2=I2+2*I
4130  END SELECT
4140  SUBEND
4150  !
4160 SUB Tir(INTEGER I1,I2,REAL Rw)
4170  INTEGER Sm,Se,M1,M2,E,Cb
4180  IF I1=-32768 THEN
4190  I1=0
4200  I2=0
4210  END IF
4220  Sm=BIT(I1,15)
4230  Se=BIT(I2,0)
4240  M1=I1
4250  M2=I2
4260  M2=SHIFT(M2,8)
4270  IF Sm=0 THEN GOTO 4330
4280  Cb=0
4290  M2=BINCMP(M2)+1
4300  IF M2=0 THEN Cb=1
4310  M1=BINCMP(M1)+Cb
4320  M2=BINAND(255,M2)
4330  E=SHIFT(I2,1)
4340  E=SHIFT(E,-9)
4350  E=SHIFT(E,9)
4360  IF Se=1 THEN E=128-E
4370  Fu=REAL(M1)/32768.0
4380  Fl=REAL(M2)/8388608.0
4390  F=REAL(1-2*Sm)*(Fu+Fl)
4400  Rw=F*2.0^((1-2*Se)*E)
4410  SUBEND
4420  !
```

```
4430  DEF FNInt(A)
4440  B=SGN(A)*INT(ABS(A)*1.0000000001)
4450  RETURN B
4460  FNEND
4470  !
4480  DEF FNFract(A)
4490  B=A-FNInt(A)
4500  IF ABS(B)<1.E-10 THEN B=0.
4510  RETURN B
4520  FNEND
```

4. THEOR_CALC

This program has a triple purpose: firstly it sets the frequency axis units of the computed results to be the same as those of the specified (input data) pressure data files (those may be selected either in Hz or as dimensionless), secondly it multiplies the normalized CSD's obtained previously, by those pressure PSD's, and finally it non-dimensionalizes such that the theoretical CSD's (PSD's) represent lateral displacement divided by cylinder diameter. Here, the user simply inputs the diskette record numbers for both the pressure PSD and for the theoretical (normalized) CSD to be used. Data is then stored on (3.5 in) diskette. The printout is for "accounting" purposes only (keeping track of the data).

Remarks

The parameter "Fac1" (line 70 in the program) stems from the term $\left[\frac{2}{\pi}\frac{\varepsilon^2}{R_0}\right]^2 R_{r(i)}\cdot R_{r(j)}$ in eqn.(2.272), with $R_{r(i)} = R_{r(j)} = R_0$.

Likewise, "Fac2" (line 80 in the program) represents the ratio ω/Ω of eqn.(2.50).

(a) Listing

This listing is BASIC V compatible (run on HP9000-300 computer).

```
10    OPTION BASE 1
20    INTEGER Cnt,I,J,K,L,M,N,Q,Ndsk,Dflg,Rp,Rt,Mt,Rcnt
30    INTEGER Bwn,Ofs,Udsk(6),Kflg,Ofsv(2,2)
40    INTEGER H1(20),V1(1024),H2(20),V2(1024),Rn(2),U(2)
50    DIM Vc(512),Va(256),Vp(256)
60    !
70    Fac1=4.824E+4
80    Fac2=76.2624/12.5
90    Cnt=0
100   Ofsv(1,1)=10
110   Ofsv(2,1)=30
120   Ofsv(1,2)=50
130   Ofsv(2,2)=0  ! Not defined
140   !
150 Fmt1:  IMAGE /,/,"Record numbers","  Theor.:",5D,"  Pres.:",4D,/,16X,"Targe
160   BEEP
170   DISP "Put printer on - press Continue..."
180   PAUSE
190   ASSIGN @Printer TO 701
```

```
200   OUTPUT @Printer USING "@"
210   WAIT 7
220   BEEP
230   DISP "Align top of page - press Continue..."
240   PAUSE
250   !
260   BEEP
270   INPUT "12.5 Hz: 1,  25.0 Hz: 2",Bwn
280   IF Bwn<>1 AND Bwn<>2 THEN GOTO 260
290   !
300   BEEP
310   INPUT "Pres.;   K=0: 1, K=28: 2",Kflg
320   IF Kflg<>1 AND Kflg<>2 THEN GOTO 300
330   !
340   BEEP
350   INPUT "No. of UNIX disks to copy",Ndsk
360   IF Ndsk<7 THEN GOTO 410
370   BEEP
380   DISP "No. of disks too large - press Continue..."
390   PAUSE
400   GOTO 340
410   BEEP
420   SELECT Ndsk
430   CASE 1
440   INPUT "UNIX disk no. ?",Udsk(1)
450   CASE 2
460   INPUT "Two UNIX disk nos. ?",Udsk(1),Udsk(2)
470   CASE 3
480   INPUT "Three UNIX disk nos. ?",Udsk(1),Udsk(2),Udsk(3)
490   CASE 4
500   INPUT "Four UNIX disk nos. ?",Udsk(1),Udsk(2),Udsk(3),Udsk(4)
510   CASE 5
520   INPUT "Five UNIX disk nos. ?",Udsk(1),Udsk(2),Udsk(3),Udsk(4),Udsk(5)
530   CASE 6
540   Udsk(1)=1
550   Udsk(2)=2
560   Udsk(3)=3
570   Udsk(4)=4
580   Udsk(5)=5
590   Udsk(6)=6
600   END SELECT
610   !
620   FOR I=1 TO Ndsk
630   INITIALIZE ":MEMORY,0,"&VAL$(Udsk(I)-1),2200
640   BEEP
650   DISP "Insert disk no. "&VAL$(Udsk(I))&" - press Continue..."
660   PAUSE
670   DISP "COPYING disk no. "&VAL$(Udsk(I))
680   COPY ":,700,1" TO ":,0,"&VAL$(Udsk(I)-1)
690   SELECT Udsk(I)
700   CASE 1
710   ASSIGN @Urec1 TO "UXDIR:,0,0";FORMAT OFF
720   ASSIGN @Unix1 TO "UNIXDTA:,0,0";FORMAT OFF
```

```
730   CASE 2
740   ASSIGN @Urec2 TO "UXDIR:,0,1";FORMAT OFF
750   ASSIGN @Unix2 TO "UNIXDTA:,0,1";FORMAT OFF
760   CASE 3
770   ASSIGN @Urec3 TO "UXDIR:,0,2";FORMAT OFF
780   ASSIGN @Unix3 TO "UNIXDTA:,0,2";FORMAT OFF
790   CASE 4
800   ASSIGN @Urec4 TO "UXDIR:,0,3";FORMAT OFF
810   ASSIGN @Unix4 TO "UNIXDTA:,0,3";FORMAT OFF
820   CASE 5
830   ASSIGN @Urec5 TO "UXDIR:,0,4";FORMAT OFF
840   ASSIGN @Unix5 TO "UNIXDTA:,0,4";FORMAT OFF
850   CASE 6
860   ASSIGN @Urec6 TO "UXDIR:,0,5";FORMAT OFF
870   ASSIGN @Unix6 TO "UNIXDTA:,0,5";FORMAT OFF
880   END SELECT
890   NEXT I
900   !
910   INITIALIZE ":MEMORY,0,6",2200
920   CREATE BDAT "PRES:MEMORY,0,6",10,2088
930   ASSIGN @Pres TO "PRES:MEMORY,0,6";FORMAT OFF
940   BEEP
950   DISP "Insert pressure data disk (no. 37) - press Continue..."
960   PAUSE
970   ASSIGN @Pdta TO "TAPE37:CS80,700,1";FORMAT OFF
980   CONTROL @Pres,5;1
990   CONTROL @Pres,7;11
1000  DISP "Copying dimensionless pressure PSD's"
1010  Ofs=Ofsv(Bwn,Kflg)
1020  FOR I=1 TO 10
1030  ENTER @Pdta,I+Ofs;H2(*),V2(*)
1040  OUTPUT @Pres,I;H2(*),V2(*)
1050  NEXT I
1060  !
1070  ASSIGN @Pdta TO *
1080  BEEP
1090  DISP "Insert target diskette - press Continue..."
1100  PAUSE
1110  ASSIGN @Outdir TO "UXDIR:,700,1";FORMAT OFF
1120  ASSIGN @Outrec TO "UNIXDTA:,700,1";FORMAT OFF
1130  CONTROL @Outdir,5;1
1140  ENTER @Outdir;Rn(*)
1150  Dflg=0
1160  IF Rn(1)-Rn(2)>1 THEN
1170  BEEP
1180  DISP "Incompatible Rn(2) - press Continue..."
1190  PAUSE
1200  ASSIGN @Outdir TO *
1210  ASSIGN @Outrec TO *
1220  GOTO 1080
1230  END IF
1240  IF Rn(2)>=Rn(1)+249 THEN
1250  BEEP
```

```
1260  DISP "Error, target disk full - press Continue..."
1270  PAUSE
1280  GOTO 1200
1290  END IF
1300  !
1310  Rp=0
1320  BEEP
1330  INPUT "Enter record no. (null or, Pres. PSD, Theor. PSD or CSD factor):",
1340  IF Rp<>0 THEN GOTO 1400
1350  ASSIGN @Outdir TO *
1360  ASSIGN @Outrec TO *
1370  BEEP
1380  DISP "Stopped"
1390  STOP
1400  Rp=Rp-Ofs
1410  IF Rp<1 OR Rp>10 THEN GOTO 1310
1420  !
1430  K=FNInt((Rt-1)/250)+1
1440  FOR J=1 TO Ndsk
1450  IF K=Udsk(J) THEN GOTO 1510
1460  NEXT J
1470  BEEP
1480  DISP "Error, record number not available - press Continue..."
1490  PAUSE
1500  GOTO 1310
1510  SELECT K
1520  CASE 1
1530  CONTROL @Urec1,5;1
1540  ENTER @Urec1;U(*)
1550  CASE 2
1560  CONTROL @Urec2,5;1
1570  ENTER @Urec2;U(*)
1580  CASE 3
1590  CONTROL @Urec3,5;1
1600  ENTER @Urec3;U(*)
1610  CASE 4
1620  CONTROL @Urec4,5;1
1630  ENTER @Urec4;U(*)
1640  CASE 5
1650  CONTROL @Urec5,5;1
1660  ENTER @Urec5;U(*)
1670  CASE 6
1680  CONTROL @Urec6,5;1
1690  ENTER @Urec6;U(*)
1700  END SELECT
1710  IF Rt>=U(1) AND Rt<=U(2) THEN GOTO 1760
1720  BEEP
1730  DISP "Error, record number(s) out of range - press Continue..."
1740  PAUSE
1750  GOTO 1310
1760  SELECT K
1770  CASE 1
1780  CONTROL @Unix1,5;1
```

```
1790  ENTER @Unix1,Rt;H1(*),V1(*)
1800  CASE 2
1810  CONTROL @Unix2,5;1
1820  ENTER @Unix2,(Rt-250);H1(*),V1(*)
1830  CASE 3
1840  CONTROL @Unix3,5;1
1850  ENTER @Unix3,(Rt-500);H1(*),V1(*)
1860  CASE 4
1870  CONTROL @Unix4,5;1
1880  ENTER @Unix4,(Rt-750);H1(*),V1(*)
1890  CASE 5
1900  CONTROL @Unix5,5;1
1910  ENTER @Unix5,(Rt-1000);H1(*),V1(*)
1920  CASE 6
1930  CONTROL @Unix6,5;1
1940  ENTER @Unix6,(Rt-1250);H1(*),V1(*)
1950  END SELECT
1960  Q=H1(3)/2
1970  Mt=SHIFT(H1(9),-1)
1980  Mt=SHIFT(Mt,10)
1990  !
2000  CONTROL @Pres,5;1
2010  ENTER @Pres,Rp;H2(*),V2(*)
2020  Q=H2(3)/2
2030  FOR L=1 TO Q
2040  M=2*L-1
2050  CALL Tir(V2(M),V2(M+1),Vp(L))
2060  NEXT L
2070  !
2080  Q=H1(3)/2
2090  SELECT Mt
2100  CASE 7
2110  FOR L=1 TO Q
2120  M=2*L-1
2130  CALL Tir(V1(M),V1(M+1),Va(L))
2140  NEXT L
2150  CASE 9
2160  FOR L=1 TO Q
2170  M=2*L-1
2180  CALL Tir(V1(M),V1(M+1),Vc(L))
2190  NEXT L
2200  CASE ELSE
2210  BEEP
2220  DISP "Error, wrong type of theoretical file - press Continue..."
2230  PAUSE
2240  GOTO 1310
2250  END SELECT
2260  !
2270  Q=H2(3)/2
2280  SELECT Mt
2290  CASE 7
2300  FOR L=1 TO Q
2310  M=2*L-1
```

```
2320  Vr=Va(L)*Fac1*Vp(L)
2330  CALL Tri(Vr,V1(M),V1(M+1))
2340  NEXT L
2350  CASE 9
2360  FOR L=1 TO Q
2370  M=2*L-1
2380  N=2*M-1
2390  Vr=Vc(M)*Fac1*Vp(L)
2400  CALL Tri(Vr,V1(N),V1(N+1))
2410  Vr=Vc(M+1)*Fac1*Vp(L)
2420  CALL Tri(Vr,V1(N+2),V1(N+3))
2430  NEXT L
2440  END SELECT
2450  !
2460  FOR L=12 TO 13
2470  M=2*L-11
2480  CALL Tir(H1(M),H1(M+1),Hr)
2490  Hr=Hr*Fac2
2500  CALL Tri(Hr,H1(M),H1(M+1))
2510  NEXT L
2520  H1(20)=1
2530  !
2540  Rn(2)=Rn(2)+1
2550  IF Rn(2)=Rn(1)+249 THEN Dflg=1
2560  Rcnt=Rn(2) MOD 250
2570  IF Rcnt=0 THEN Rcnt=250
2580  CONTROL @Outdir,5;1
2590  CONTROL @Outdir,7;3
2600  OUTPUT @Outdir;Rn(*)
2610  CONTROL @Outrec,7;251
2620  OUTPUT @Outrec,Rcnt;H1(*),V1(*)
2630  !
2640  OUTPUT @Printer USING Fmt1;Rt,Rp+Ofs,Rn(2)
2650  Cnt=Cnt+1
2660  IF Cnt=14 THEN
2670  Cnt=0
2680  OUTPUT @Printer USING "@"
2690  END IF
2700  !
2710  IF Dflg=0 THEN GOTO 1300
2720  BEEP
2730  DISP "Disk now full - press Continue..."
2740  PAUSE
2750  ASSIGN @Outdir TO *
2760  ASSIGN @Outrec TO *
2770  BEEP
2780  DISP "Insert new target disk - press Continue..."
2790  PAUSE
2800  GOTO 1110
2810  END
2820  !
2830  !
2840  SUB Tri(A,INTEGER I1,I2)
```

```
2850  INTEGER I,J,K
2860  Aa=ABS(A)
2870  I1=0
2880  I2=0
2890  IF Aa=0. THEN SUBEXIT
2900  I=FNInt(LOG(Aa)/LOG(2.0))
2910  Aa=Aa/(2.0^I)
2920  IF Aa<1.0 THEN GOTO 2950
2930  Aa=Aa/2.0
2940  I=I+1
2950  FOR J=1 TO 15
2960  Aa=Aa*2.
2970  K=FNInt(Aa)
2980  Aa=FNFract(Aa)
2990  IF K<>0 THEN I1=BINIOR(I1,2^(15-J))
3000  NEXT J
3010  IF Aa=0. THEN GOTO 3120
3020  FOR J=16 TO 22
3030  Aa=Aa*2.0
3040  K=FNInt(Aa)
3050  Aa=FNFract(Aa)
3060  IF K<>0 THEN I2=BINIOR(I2,2^(23-J))
3070  NEXT J
3080  Aa=Aa*2.0
3090  IF Aa<1.0 THEN Aa=Aa*1.000001
3100  K=FNInt(Aa)
3110  IF K<>0 THEN I2=BINIOR(I2,1)
3120  IF A>0. THEN GOTO 3200
3130  I1=BINCMP(I1)
3140  SELECT I2
3150  CASE 0
3160  I1=I1+1
3170  CASE ELSE
3180  I2=256-I2
3190  END SELECT
3200  I2=SHIFT(I2,-8)
3210  SELECT I
3220  CASE <0
3230  I2=I2+2*(128+I)+1
3240  CASE ELSE
3250  I2=I2+2*I
3260  END SELECT
3270  SUBEND
3280  !
3290 SUB Tir(INTEGER I1,I2,REAL Rw)
3300  INTEGER Sm,Se,M1,M2,E,Cb
3310  IF I1=-32768 THEN
3320  I1=0
3330  I2=0
3340  END IF
3350  Sm=BIT(I1,15)
3360  Se=BIT(I2,0)
3370  M1=I1
```

```
3380  M2=I2
3390  M2=SHIFT(M2,8)
3400  IF Sm=0 THEN GOTO 3460
3410  Cb=0
3420  M2=BINCMP(M2)+1
3430  IF M2=0 THEN Cb=1
3440  M1=BINCMP(M1)+Cb
3450  M2=BINAND(255,M2)
3460  E=SHIFT(I2,1)
3470  E=SHIFT(E,-9)
3480  E=SHIFT(E,9)
3490  IF Se=1 THEN E=128-E
3500  Fu=REAL(M1)/32768.0
3510  Fl=REAL(M2)/8388608.0
3520  F=REAL(1-2*Sm)*(Fu+Fl)
3530  Rw=F*2.0^((1-2*Se)*E)
3540  SUBEND
3550  !
3560  DEF FNInt(A)
3570  B=SGN(A)*INT(ABS(A)*1.0000000001)
3580  RETURN B
3590  FNEND
3600  !
3610  DEF FNFract(A)
3620  B=A-FNInt(A)
3630  IF ABS(B)<1.E-10 THEN B=0.
3640  RETURN B
3650  FNEND
```

5. COH_CALC

This program calculates coherences. The latter were not stored (although measured) during tests, for space economizing (HP5420A magnetic tape cassettes). The calculations of theoretical coherences are also conveniently effected with this program. The user need only input diskette record numbers, for the cross-spectral density (CSD) and the two corresponding power spectral densities (PSD's). In most theoretical cases, because of the problem symmetry, the same record number is repeated twice for the latter two items (PSD). The frequency units are preserved (either Hz or dimensionless).

(a) Listing

This listing is BASIC V compatible (run on HP9000-300 computer).

```
10    OPTION BASE 1
20    INTEGER Cnt,I,J,K,L,M,Q,Ndsk,Dflg,Rcnt,Cflg
30    INTEGER Rn(2),H(20),V(1024),R(3),U(2),Hst(3,20)
40    INTEGER Tno(4,2),Id(2),T(3)
50    INTEGER Udsk(6),Sflg
60    DIM Vc(512),Vp1(256),Vp2(256)
70    DIM T$(2)[6]
80    !
90    T$(1)[1,4]="TAPE"
100   T$(2)[1,4]="TAPE"
110   Cnt=0
120   !
130 Fmt1:  IMAGE /,/,"Record numbers","  CSD:",5D,"  PSD #1:",5D,"  PSD #2:",5D
140 Fmt2:  IMAGE /,/,"Tape numbers","  CSD:",3D,"  PSD #1:",3D,"  PSD #2:",3D
150 Fmt3:  IMAGE "Record numbers","  CSD:",5D,"  PSD #1:",5D,"  PSD #2:",5D,/,1
160   !
170   BEEP
180   DISP "Put printer on - press Continue..."
190   PAUSE
200   ASSIGN @Printer TO 701
210   OUTPUT @Printer USING "@"
220   WAIT 7
230   BEEP
240   DISP "Align top of page - press Continue..."
250   PAUSE
260   !
270   BEEP
280   INPUT "Theor. 1, Exper. 2:",Cflg
290   IF Cflg<>1 AND Cflg<>2 THEN GOTO 270
300   !
310   BEEP
320   IF Cflg=1 THEN
```

```
330   INPUT "No. of UNIX disks to copy",Ndsk
340   IF Ndsk<7 THEN GOTO 450
350   BEEP
360   DISP "No. of disks too large - press Continue..."
370   PAUSE
380   GOTO 310
390   ELSE
400   INPUT "No. of (tape) disks to copy",Ndsk
410   IF Ndsk<7 THEN GOTO 660
420   GOTO 310
430   END IF
440   !
450   BEEP
460   SELECT Ndsk
470   CASE 1
480   INPUT "UNIX disk no. ?",Udsk(1)
490   CASE 2
500   INPUT "Two UNIX disk nos. ?",Udsk(1),Udsk(2)
510   CASE 3
520   INPUT "Three UNIX disk nos. ?",Udsk(1),Udsk(2),Udsk(3)
530   CASE 4
540   INPUT "Four UNIX disk nos. ?",Udsk(1),Udsk(2),Udsk(3),Udsk(4)
550   CASE 5
560   INPUT "Five UNIX disk nos. ?",Udsk(1),Udsk(2),Udsk(3),Udsk(4),Udsk(5)
570   CASE 6
580   Udsk(1)=1
590   Udsk(2)=2
600   Udsk(3)=3
610   Udsk(4)=4
620   Udsk(5)=5
630   Udsk(6)=6
640   END SELECT
650   !
660   FOR I=1 TO Ndsk
670   SELECT Cflg
680   CASE 1
690   INITIALIZE ":MEMORY,0,"&VAL$(Udsk(I)-1),2200
700   BEEP
710   DISP "Insert disk no. "&VAL$(Udsk(I))&" - press Continue..."
720   PAUSE
730   DISP "COPYING disk "&VAL$(Udsk(I))
740   COPY ":,700,1" TO ":,0,"&VAL$(Udsk(I)-1)
750   GOTO 990
760   CASE 2
770   INITIALIZE ":MEMORY,0,"&VAL$(I-1),2200
780   BEEP
790   DISP "Insert disk "&VAL$(I)&" - press Continue..."
800   PAUSE
810   DISP "COPYING disk no. "&VAL$(I)
820   COPY ":,700,1" TO ":,0,"&VAL$(I-1)
830   END SELECT
840   !
850   ASSIGN @Diskfile TO "TPFILES:MEMORY,0,"&VAL$(I-1);FORMAT OFF
```

```
860   ENTER @Diskfile;Id(*)
870   ASSIGN @Diskfile TO *
880   FOR J=1 TO 2
890   Tid=Id(J)
900   Tno(I,J)=Tid
910   IF Tid<10 THEN
920   T$(J)[5,5]="0"
930   T$(J)[6,6]=VAL$(Tid)
940   ELSE
950   T$(J)[5,6]=VAL$(Tid)
960   END IF
970   NEXT J
980   !
990   SELECT Cflg
1000  CASE 1
1010  Sflg=Udsk(I)
1020  CASE 2
1030  Sflg=I
1040  END SELECT
1050  SELECT Sflg
1060  CASE 1
1070  IF Cflg=1 THEN
1080  ASSIGN @Urec1 TO "UXDIR:,0,0";FORMAT OFF
1090  ASSIGN @Unix1 TO "UNIXDTA:,0,0";FORMAT OFF
1100  ELSE
1110  ASSIGN @Tape1 TO T$(1)&":,0,0";FORMAT OFF
1120  ASSIGN @Tape2 TO T$(2)&":,0,0";FORMAT OFF
1130  END IF
1140  CASE 2
1150  IF Cflg=1 THEN
1160  ASSIGN @Urec2 TO "UXDIR:,0,1";FORMAT OFF
1170  ASSIGN @Unix2 TO "UNIXDTA:,0,1";FORMAT OFF
1180  ELSE
1190  ASSIGN @Tape3 TO T$(1)&":,0,1";FORMAT OFF
1200  ASSIGN @Tape4 TO T$(2)&":,0,1";FORMAT OFF
1210  END IF
1220  CASE 3
1230  IF Cflg=1 THEN
1240  ASSIGN @Urec3 TO "UXDIR:,0,2";FORMAT OFF
1250  ASSIGN @Unix3 TO "UNIXDTA:,0,2";FORMAT OFF
1260  ELSE
1270  ASSIGN @Tape5 TO T$(1)&":,0,2";FORMAT OFF
1280  ASSIGN @Tape6 TO T$(2)&":,0,2";FORMAT OFF
1290  END IF
1300  CASE 4
1310  IF Cflg=1 THEN
1320  ASSIGN @Urec4 TO "UXDIR:,0,3";FORMAT OFF
1330  ASSIGN @Unix4 TO "UNIXDTA:,0,3";FORMAT OFF
1340  ELSE
1350  ASSIGN @Tape7 TO T$(1)&":,0,3";FORMAT OFF
1360  ASSIGN @Tape8 TO T$(2)&":,0,3";FORMAT OFF
1370  END IF
1380  CASE 5
```

```
1390  IF Cflg=1 THEN
1400  ASSIGN @Urec5 TO "UXDIR:,0,4";FORMAT OFF
1410  ASSIGN @Unix5 TO "UNIXDTA:,0,4";FORMAT OFF
1420  ELSE
1430  ASSIGN @Tape9 TO T$(1)&":,0,4";FORMAT OFF
1440  ASSIGN @Tape10 TO T$(2)&":,0,4";FORMAT OFF
1450  END IF
1460  CASE 6
1470  IF Cflg=1 THEN
1480  ASSIGN @Urec6 TO "UXDIR:,0,5";FORMAT OFF
1490  ASSIGN @Unix6 TO "UNIXDTA:,0,5";FORMAT OFF
1500  ELSE
1510  ASSIGN @Tape11 TO T$(1)&":,0,5";FORMAT OFF
1520  ASSIGN @Tape12 TO T$(2)&":,0,5";FORMAT OFF
1530  END IF
1540  END SELECT
1550  NEXT I
1560  !
1570  BEEP
1580  DISP "Insert target diskette - press Continue..."
1590  PAUSE
1600  ASSIGN @Outdir TO "UXDIR:,700,1";FORMAT OFF
1610  ASSIGN @Outrec TO "UNIXDTA:,700,1";FORMAT OFF
1620  CONTROL @Outdir,5;1
1630  ENTER @Outdir;Rn(*)
1640  Dflg=0
1650  IF Rn(1)-Rn(2)>1 THEN
1660  BEEP
1670  DISP "Incompatible Rn(2) - press Continue..."
1680  PAUSE
1690  ASSIGN @Outdir TO *
1700  ASSIGN @Outrec TO *
1710  GOTO 1570
1720  END IF
1730  IF Rn(2)>=Rn(1)+249 THEN
1740  BEEP
1750  DISP "Error, target disk full - press Continue..."
1760  PAUSE
1770  GOTO 1690
1780  END IF
1790  !
1800  IF Cflg=1 THEN GOTO 1850
1810  !
1820  BEEP
1830  INPUT "Tape numbers (CSD,PSD1,PSD2)",T(1),T(2),T(3)
1840  !
1850  R(1)=0
1860  BEEP
1870  INPUT "Record numbers [1st: null to stop] (CSD,PSD1,PSD2):",R(1),R(2),R(3
1880  IF R(1)<>0 THEN GOTO 1950
1890  ASSIGN @Outdir TO *
1900  ASSIGN @Outrec TO *
1910  BEEP
```

```
1920  DISP "Stopped"
1930  STOP
1940  !
1950  FOR J=1 TO 3
1960  IF Cflg=1 THEN
1970  K=FNInt((R(J)-1)/250)+1
1980  FOR L=1 TO Ndsk
1990  IF K=Udsk(L) THEN GOTO 2090
2000  NEXT L
2010  BEEP
2020  DISP "Error, record number too large - press Continue..."
2030  PAUSE
2040  GOTO 1800
2050  ELSE
2060  GOTO 2570
2070  END IF
2080  !
2090  SELECT K
2100  CASE 1
2110  CONTROL @Urec1,5;1
2120  ENTER @Urec1;U(*)
2130  CASE 2
2140  CONTROL @Urec2,5;1
2150  ENTER @Urec2;U(*)
2160  CASE 3
2170  CONTROL @Urec3,5;1
2180  ENTER @Urec3;U(*)
2190  CASE 4
2200  CONTROL @Urec4,5;1
2210  ENTER @Urec4;U(*)
2220  CASE 5
2230  CONTROL @Urec5,5;1
2240  ENTER @Urec5;U(*)
2250  CASE 6
2260  CONTROL @Urec6,5;1
2270  ENTER @Urec6;U(*)
2280  END SELECT
2290  IF R(J)>=U(1) AND R(J)<=U(2) THEN GOTO 2350
2300  BEEP
2310  DISP "Error, record number out of range - press Continue..."
2320  PAUSE
2330  GOTO 1800
2340  !
2350  SELECT K
2360  CASE 1
2370  CONTROL @Unix1,5;1
2380  ENTER @Unix1,R(J);H(*),V(*)
2390  CASE 2
2400  CONTROL @Unix2,5;1
2410  ENTER @Unix2,(R(J)-250);H(*),V(*)
2420  CASE 3
2430  CONTROL @Unix3,5;1
2440  ENTER @Unix3,(R(J)-500);H(*),V(*)
```

```
2450  CASE 4
2460  CONTROL @Unix4,5;1
2470  ENTER @Unix4,(R(J)-750);H(*),V(*)
2480  CASE 5
2490  CONTROL @Unix5,5;1
2500  ENTER @Unix5,(R(J)-1000);H(*),V(*)
2510  CASE 6
2520  CONTROL @Unix6,5;1
2530  ENTER @Unix6,(R(J)-1250);H(*),V(*)
2540  END SELECT
2550  GOTO 3170
2560  !
2570  FOR K=1 TO Ndsk
2580  FOR L=1 TO 2
2590  IF Tno(K,L)=T(J) THEN GOTO 2660
2600  NEXT L
2610  NEXT K
2620  BEEP
2630  DISP "Error, tape not found"
2640  STOP
2650  !
2660  SELECT K
2670  CASE 1
2680  IF L=1 THEN
2690  CONTROL @Tape1,5;1
2700  ENTER @Tape1,R(J);H(*),V(*)
2710  ELSE
2720  CONTROL @Tape2,5;1
2730  ENTER @Tape2,R(J);H(*),V(*)
2740  END IF
2750  CASE 2
2760  IF L=1 THEN
2770  CONTROL @Tape3,5;1
2780  ENTER @Tape3,R(J);H(*),V(*)
2790  ELSE
2800  CONTROL @Tape4,5;1
2810  ENTER @Tape4,R(J);H(*),V(*)
2820  END IF
2830  CASE 3
2840  IF L=1 THEN
2850  CONTROL @Tape5,5;1
2860  ENTER @Tape5,R(J);H(*),V(*)
2870  ELSE
2880  CONTROL @Tape6,5;1
2890  ENTER @Tape6,R(J);H(*),V(*)
2900  END IF
2910  CASE 4
2920  IF L=1 THEN
2930  CONTROL @Tape7,5;1
2940  ENTER @Tape7,R(J);H(*),V(*)
2950  ELSE
2960  CONTROL @Tape8,5;1
2970  ENTER @Tape8,R(J);H(*),V(*)
```

```
2980  END IF
2990  CASE 5
3000  IF L=1 THEN
3010  CONTROL @Tape9,5;1
3020  ENTER @Tape9,R(J);H(*),V(*)
3030  ELSE
3040  CONTROL @Tape10,5;1
3050  ENTER @Tape10,R(J);H(*),V(*)
3060  END IF
3070  CASE 6
3080  IF L=1 THEN
3090  CONTROL @Tape11,5;1
3100  ENTER @Tape11,R(J);H(*),V(*)
3110  ELSE
3120  CONTROL @Tape12,5;1
3130  ENTER @Tape12,R(J);H(*),V(*)
3140  END IF
3150  END SELECT
3160  !
3170  FOR L=1 TO 20
3180  Hst(J,L)=H(L)
3190  NEXT L
3200  Q=H(3)/2
3210  SELECT J
3220  CASE 1
3230  FOR L=1 TO Q
3240  M=2*L-1
3250  CALL Tir(V(M),V(M+1),Vc(L))
3260  NEXT L
3270  CASE 2
3280  FOR L=1 TO Q
3290  M=2*L-1
3300  CALL Tir(V(M),V(M+1),Vp1(L))
3310  NEXT L
3320  CASE 3
3330  FOR L=1 TO Q
3340  M=2*L-1
3350  CALL Tir(V(M),V(M+1),Vp2(L))
3360  NEXT L
3370  END SELECT
3380  NEXT J
3390  !
3400  IF Hst(2,3)<>Hst(3,3) OR 2*Hst(2,3)<>Hst(1,3) THEN GOTO 3530
3410  FOR L=10 TO 16
3420  IF Hst(1,L)<>Hst(2,L) OR Hst(2,L)<>Hst(3,L) THEN
3430  IF L=11 OR L=12 THEN
3440  BEEP
3450  DISP "WARNING: H(11) discrepancy !"
3460  WAIT 2
3470  ELSE
3480  GOTO 3530
3490  END IF
3500  END IF
```

```
3510  NEXT L
3520  GOTO 3580
3530  BEEP
3540  DISP "Error, records not matched - press Continue..."
3550  PAUSE
3560  GOTO 1800
3570  !
3580  Q=Hst(2,3)/2
3590  FOR L=1 TO Q
3600  M=2*L-1
3610  Den=Vp1(L)*Vp2(L)
3620  IF Den=0. THEN
3630  Vr=1.0
3640  ELSE
3650  Vr=(Vc(M)^2+Vc(M+1)^2)/Den
3660  END IF
3670  CALL Tri(Vr,V(M),V(M+1))
3680  NEXT L
3690  !
3700  H(1)=-1
3710  H(2)=15215
3720  H(4)=0
3730  H(5)=-32766
3740  H(6)=-7
3750  H(7)=258
3760  H(8)=0
3770  H(9)=-26636
3780  H(17)=0
3790  H(18)=0
3800  H(19)=2
3810  !
3820  H(3)=Hst(2,3)
3830  H(20)=1
3840  FOR L=10 TO 13
3850  H(L)=Hst(1,L)
3860  NEXT L
3870  !
3880  Rn(2)=Rn(2)+1
3890  IF Rn(2)=Rn(1)+249 THEN Dflg=1
3900  Rcnt=Rn(2) MOD 250
3910  IF Rcnt=0 THEN Rcnt=250
3920  CONTROL @Outdir,5;1
3930  CONTROL @Outdir,7;3
3940  OUTPUT @Outdir;Rn(*)
3950  CONTROL @Outrec,7;251
3960  OUTPUT @Outrec,Rcnt;H(*),V(*)
3970  !
3980  SELECT Cflg
3990  CASE 1
4000  OUTPUT @Printer USING Fmt1;R(1),R(2),R(3),Rn(2)
4010  Cnt=Cnt+1
4020  IF Cnt=14 THEN GOTO 4110
4030  CASE 2
```

```
4040  OUTPUT @Printer USING Fmt2;T(1),T(2),T(3)
4050  OUTPUT @Printer USING Fmt3;R(1),R(2),R(3),Rn(2)
4060  Cnt=Cnt+1
4070  IF Cnt=10 THEN GOTO 4110
4080  END SELECT
4090  GOTO 4140
4100  !
4110  Cnt=0
4120  OUTPUT @Printer USING "@"
4130  !
4140  IF Dflg=0 THEN GOTO 1800
4150  BEEP
4160  DISP "Disk now full - press Continue..."
4170  PAUSE
4180  ASSIGN @Outdir TO *
4190  ASSIGN @Outrec TO *
4200  BEEP
4210  DISP "Insert new target disk - press Continue..."
4220  PAUSE
4230  GOTO 1590
4240  END
4250  !
4260  !
4270  SUB Tri(A,INTEGER I1,I2)
4280  INTEGER I,J,K
4290  Aa=ABS(A)
4300  I1=0
4310  I2=0
4320  IF Aa=0. THEN SUBEXIT
4330  I=FNInt(LOG(Aa)/LOG(2.0))
4340  Aa=Aa/(2.0^I)
4350  IF Aa<1.0 THEN GOTO 4380
4360  Aa=Aa/2.0
4370  I=I+1
4380  FOR J=1 TO 15
4390  Aa=Aa*2.
4400  K=FNInt(Aa)
4410  Aa=FNFract(Aa)
4420  IF K<>0 THEN I1=BINIOR(I1,2^(15-J))
4430  NEXT J
4440  IF Aa=0. THEN GOTO 4550
4450  FOR J=16 TO 22
4460  Aa=Aa*2.0
4470  K=FNInt(Aa)
4480  Aa=FNFract(Aa)
4490  IF K<>0 THEN I2=BINIOR(I2,2^(23-J))
4500  NEXT J
4510  Aa=Aa*2.0
4520  IF Aa<1.0 THEN Aa=Aa*1.000001
4530  K=FNInt(Aa)
4540  IF K<>0 THEN I2=BINIOR(I2,1)
4550  IF A>0. THEN GOTO 4630
4560  I1=BINCMP(I1)
```

```
4570  SELECT I2
4580  CASE 0
4590  I1=I1+1
4600  CASE ELSE
4610  I2=256-I2
4620  END SELECT
4630  I2=SHIFT(I2,-8)
4640  SELECT I
4650  CASE <0
4660  I2=I2+2*(128+I)+1
4670  CASE ELSE
4680  I2=I2+2*I
4690  END SELECT
4700  SUBEND
4710  !
4720 SUB Tir(INTEGER I1,I2,REAL Rw)
4730  INTEGER Sm,Se,M1,M2,E,Cb
4740  IF I1=-32768 THEN
4750  I1=0
4760  I2=0
4770  END IF
4780  Sm=BIT(I1,15)
4790  Se=BIT(I2,0)
4800  M1=I1
4810  M2=I2
4820  M2=SHIFT(M2,8)
4830  IF Sm=0 THEN GOTO 4890
4840  Cb=0
4850  M2=BINCMP(M2)+1
4860  IF M2=0 THEN Cb=1
4870  M1=BINCMP(M1)+Cb
4880  M2=BINAND(255,M2)
4890  E=SHIFT(I2,1)
4900  E=SHIFT(E,-9)
4910  E=SHIFT(E,9)
4920  IF Se=1 THEN E=128-E
4930  Fu=REAL(M1)/32768.0
4940  Fl=REAL(M2)/8388608.0
4950  F=REAL(1-2*Sm)*(Fu+Fl)
4960  Rw=F*2.0^((1-2*Se)*E)
4970  SUBEND
4980  !
4990  DEF FNInt(A)
5000  B=SGN(A)*INT(ABS(A)*1.0000000001)
5010  RETURN B
5020  FNEND
5030  !
5040  DEF FNFract(A)
5050  B=A-FNInt(A)
5060  IF ABS(B)<1.E-10 THEN B=0.
5070  RETURN B
5080  FNEND
```

Appendix L

Tunnel - velocity profile and turbulence tests

The test channel has been characterized by measuring velocity profiles along diametrical lines, and by performing turbulence intensity and scale measurements.

(1) Velocity profiles

Data on velocity profiles are available from Ref. [75]. Various bulk velocities were considered, and the tunnel configurations tested were K = 0 (no cylinder in tunnel), (i) in dir.1, and (ii) in dir.2 (see Fig. 19 for directions identification), and K = 4 with (iii) $G_c = 2.0$, (iv) $G_c = 1.5$, and (v) $G_c = 1.0$. It is important to note that these velocity measurements were effected without a turbulator; nevertheless, they do indicate that the velocity distribution is flat in K = 0 cases, and that velocities in the interstitial spaces between cylinders (K = 4) is somewhat reduced. In spite of satisfactory velocity profiles when no turbulator was used, vibration tests exhibited fairly strong asymmetry: hence the need to eventually develop an effective turbulator. It is believed that since the turbulator utilized has solved the symmetry problems (by rendering the flow more uniform), resulting velocity profiles should be even flatter than those presented here.

The Pitot-static tube used is depicted Fig. L-1, together with its support, wall mounting sleeve, connection tubing, and radial positioning slider (top part). The only in-tunnel components are the Pitot-static tube itself and its horizontal support bar. External dimensions are given in Fig. L-1 (bottom part); pressure port diameters are 0.081 cm (0.032 in) for the dynamic one and 0.048 cm (0.019 in) for the six static ones. This probe was custom-made, the main component being the commercially fabricated Pitot-static tube, intended primarily for airflow measurements. It was stiffened by adding the (0.635 cm dia.) support jacket, and a special chamber designed to accommodate hydraulic connections at the output end; furthermore, a slider was incorporated for accurately locating the probe.

The very high hydraulic resistance of that probe (small diameter ports and conduits) required relatively low displacement pressure transducers (to avert very long stabilization delays), precluding the usage of, for example, a mercury manometer. Consequently, unbonded strain gage differential pressure transducers were used: a ±1 psid STATHAM model PM80TC±1-350 for lower velocity ranges and a ±5 psid STATHAM model PM280TC±5-350 for the higher velocity ranges.

The usual expression (Bernoulli's equation)

$$\Delta p = \frac{1}{2}\,\rho \cdot U^2 \tag{L.1}$$

is used, where Δp is the difference between dynamic and static pressures, ρ is the fluid density, and U is the fluid velocity. The average Δp is obtained from low-pass filtered outputs of the aforementioned transducers (signals were also amplified by a factor of 100); we have (from calibration factors, bridge excitation voltage, and the latter amplification factor):

$$\Delta p_n = C_n \cdot e_n \,, \qquad n = 1,2 \,, \tag{L.2}$$

where $n = 1,2$ represent the ±1 psid and ±5 psid transducer respectively, Δp_n and e_n being input(s) and output(s), and where

$$C_n = \begin{cases} 216.1 \text{ KPa/volt } (31.34 \text{ psi/volt}) \,, \\ 1243.0 \text{ KPa/volt } (180.27 \text{ psi/volt}) \,. \end{cases} \tag{L.3}$$

Figs. (L-2) to (L-6) inclusively depict the measurements. Figs. (L-2) and (L-3) show that velocity profiles are nominally flat, in both (orthogonal) dir.1 and dir.2. The boundary layer at the wall is about 1.3 cm (0.5 in) thick. Figs. (L-4) to (L-6) illustrate the gradual reduction of mid-gap (interstitial, between cylinders) velocity, as cylinder spacing is reduced; this indicates the extent to which the assumption of uniform velocity distribution is violated. Note that for the higher flow velocities, it was impossible to gather data all the way across the tunnel, because of cross-flow induced lateral vibration.

(2) Turbulence tests

In this case, tests were conducted both with and without the turbulator* (depicted in Fig. 11). Measurements included PSD's as well as autocorrelations, from which turbulence intensities and integral scales could be calculated, respectively. Of course, conditions "experienced" by the cylinders, in vibration testing, are those with the turbulator in place, hence they define what shall be considered as tunnel characteristics.

Turbulence intensities and scales were measured using a TSI hot film anemometer model 1054B, together with a model 1231W probe. Fig. L-7 shows the probe (vertical) mounted on its holder (horizontal), the latter being a 0.635 cm (0.250 in) diameter bar which slides within a wall mounted sleeve; the probe itself is 0.152 cm (0.060 in) in diameter and 1.270 cm (0.500 in) long, and attached to a horizontal stem 0.318 cm (0.125 in) in diameter and 3.429 cm (1.350 in) in length. The measurement surface (probe tip) is conically shaped, and was located 22.1 cm (8.7 in, slightly upstream from the cluster mid-point) from the top of the cylinders. Turbulence measurements were effected along a diametrical line, at various radial positions, illustrated in Fig. L-8. One set of tests was conducted with a bundle of four rigid cylinders ($G_c = 0.75$), and one set without any cylinder (in the latter case, radial positions were slightly different).

Hot film anemometers work on the same principle as hot wire anemometers, namely an electric current is circulated through the probe, heating it to a temperature above ambient (fluid being measured), and such that its electrical resistance and hence its temperature, remains constant (resistance is temperature dependent); changes in probe resistance are detected by a Wheatstone bridge and fed back to a current control circuit (which changes the current in response to bridge unbalances). The bulk temperature of the fluid is kept constant, and changes in its velocity past the probe result in changes in heat transfer rates (probe to fluid), hence in probe current (for constant probe temperature). The heat transfer rate is a function of

---

* Intermediate tests, carried out during the development of the turbulator itself, will not be presented.

the probe itself and the fluid (fixed parameters), and of the fluid velocity (variable parameter), the latter in a non-linear fashion. In situ calibration is necessary and the details of that procedure, which is standard, will not be covered here. Suffice it to say that, typically, the anemometer was calibrated to read

$$u = 0.6 \cdot e \,, \tag{L.4}$$

where u is the dimensionless flow velocity and e the anemometer output voltage. Note that, by design, such probes are much more sensitive to velocity changes in the direction of the flow, so that fluctuations in the voltage e may be assumed to indicate changes in u only.

We shall review turbulence intensity measurements first, followed by those on turbulence scales.

(a) Turbulence intensity

The intensity (or level) of turbulence may be defined* as

$$I_t = \frac{1}{\bar{u}} \left[\frac{1}{3} \left(\overline{u^2} + \overline{v^2} + \overline{w^2} \right) \right]^{1/2} , \tag{L.5}$$

where $\bar{u}$ is the mean velocity of the flow, and u, v, and w are the three (orthogonal) components of velocity fluctuation (the terms in eqn.(L.5) represent their root mean square (rms)), with u being in the direction of u. When turbulence is isotropic (generally the case, at "a certain distance from screens"*), i.e.

$$\overline{u^2} = \overline{v^2} = \overline{w^2} \,, \tag{L.6}$$

then it is sufficient to restrict oneself to fluctuations in the direction of the flow, that is, from eqs.(L.5) and (L.6),

$$I_t = \frac{1}{\bar{u}} \left[\overline{u^2} \right]^{1/2} . \tag{L.7}$$

---

* *Boundary-Layer Theory*, by H. Schlichting (1979, 7th edition, McGraw Hill), P.475.

For all measurements to be discussed $\bar{u}$ has been taken as the maximum (which is close enough to the average) velocity on a diametrical line; this is at the center of the channel when K = 0 (no cylinder), and at about a radial distance (from the center) of 6.35 cm (2.5 in) when K = 4 (rigid cylinders, $G_c = 0.75$). The fluctuating component u has power at frequencies up to and beyond 1.6 KHz (the maximum bandwidth utilized here*), but with ever diminishing (power) density. Figs. L-9a and L-9b illustrate PSD's for the K = 0 case and $\bar{u} = 3$, at the center of the channel, and with the turbulator in place; various bandwidths are depicted, down to 50 Hz. As we are mostly interested in low frequencies (vibration tests), a bandwidth of 2-50 Hz has been chosen for intensity computation purposes (the low limit was chosen at 2 Hz, to "filter out" DC [average velocity] data).

Experimental turbulence intensities versus flow velocities are shown in Fig. L-10; these measurements are for the K = 4 ($G_c = 0.75$) case, at the radial position (from the center) of 6.35 cm (2.5 in), the latter location chosen because it corresponds to the peak velocity (arbitrary choice). Note that rms velocity fluctuations from which the intensities are calculated, generally tend to increase with flow velocity (intensities here generally decrease because rms values increase more slowly than velocities). As the latter measurements only serve to characterize the tunnel, they are not discussed further.

Fig. L-11 illustrates variations of turbulence intensities with radial position (origin is at the channel center), at $\bar{u} = 3$, for three cases: (i) no turbulator and K = 0, (ii) with turbulator and K = 0, and (iii) with turbulator and K = 4 ($G_c = 0.75$). The no-turbulator intensities are seen to be considerably less than the with-turbulator ones. The uniformity of the former, coupled with flat velocity profiles (presented earlier), nevertheless did yield asymmetrical (with cylinder position in the channel) vibration PSD's: the main reason is believed to be very large (and probably non-uniform) variations in turbulence scale, throughout the test channel, although

---

* Tests at an intermediate stage of turbulator design indicate power up to and beyond 6.4 KHz.

this has not been verified experimentally, since turbulator design was called for in any case (scale values in this case are available only at two points [see below]). Where the turbulator is present, we see that intensities increase gradually as the channel wall is approached. Also, in the K = 4 case, it should be noted that intensity levels are higher in the interstitial space (between cylinders).

(b) Turbulence scale

Single point autocorrelation function measurements were utilized to obtain integral times, from which scales could be computed. The integral time is defined here as*

$$T = \int_0^t R(t) \cdot dt \,, \tag{L.8}$$

where $R(t)$ is the autocorrelation function of the flow velocity at a point (in the channel), t is the time, and t is the time for the first zero crossing of $R(t)$, i.e.

$$R(t) = 0, \quad \text{(the first zero of the function)}. \tag{L.9}$$

The "integral" scale (length) is simply

$$L = \bar{u} \cdot T \,, \tag{L.10}$$

where T is defined in eqn.(L.8), and $\bar{u}$ is the average flow velocity, at the point of interest.

Fig. L-12 depicts a typical measured autocorrelation function (case with turbulator, K = 4, radial position 8.9 cm (3.5 in) - see Fig. L-8); here, the data obtained was:

Zero crossing, $t = 28.2$ m sec,
Integral time, $T = 6.51$ m sec,
Local velocity, $\bar{u} = 2.49$. i.e. 1.72 m/sec (5.64 ft/sec),
Integral length, $L = 1.12$ cm (0.440 in).

---

* See Ref. [52].

Fig. L-13 illustrates turbulence scales, at fixed radial positions and with the turbulator in place, versus (average) flow velocity, for both the K = 0 and K = 4 cases. The radial positions were chosen (arbitrarily) as those corresponding to peak velocities, being at the channel center for the K = 0 case, and 6.35 cm (2.5 in) for the K = 4 test. It can be seen that scales are relatively constant (with velocity); also, it should be noted that, in all cases, the turbulence scales are a fraction of (less than) the cylinder diameter (0.996 in), and conversely, three to nine times greater than the pressure transducers tunnel port (1/16 in).

The variations of turbulence scale with radial position in the channel can be seen in Fig. L-14. The two tests shown were conducted with the turbulator in place, and for $\bar{u} = 3$; note that $\bar{u}$ itself varies with position. It should be kept in mind that, as the anemometer output tended to exhibit some DC drift, thereby yielding some uncertainty in the values of (local) $\bar{u}$, the confidence in the scale values shown in Fig. L-14 is not high; errors of the order of 25 % are not deemed unlikely. Extensive testing, including repeatability, was not thought necessary, as we only wished to evaluate the test channel characteristics. An exploratory test on the turbulence scales in the K = 0, no-turbulator channel yielded scales of the order of 1.0 cm (0.40 in) near the wall, and 7.6 cm (3.0 in) at the center.

From Figs. L-13 and L-14, it appears that the presence of cylinders in the tunnel tends to increase turbulence scales throughout. This increase seemingly also occurs for flow near the channel wall (see Fig. L-14)).

National Library
of Canada

Canadian Theses Service

Bibliothèque nationale
du Canada

Service des thèses canadiennes

NOTICE

AVIS

THE QUALITY OF THIS MICROFICHE IS HEAVILY DEPENDENT UPON THE QUALITY OF THE THESIS SUBMITTED FOR MICROFILMING.

UNFORTUNATELY THE COLOURED ILLUSTRATIONS OF THIS THESIS CAN ONLY YIELD DIFFERENT TONES OF GREY.

LA QUALITE DE CETTE MICROFICHE DEPEND GRANDEMENT DE LA QUALITE DE LA THESE SOUMISE AU MICROFILMAGE.

MALHEUREUSEMENT, LES DIFFERENTES ILLUSTRATIONS EN COULEURS DE CETTE THESE NE PEUVENT DONNER QUE DES TEINTES DE GRIS.

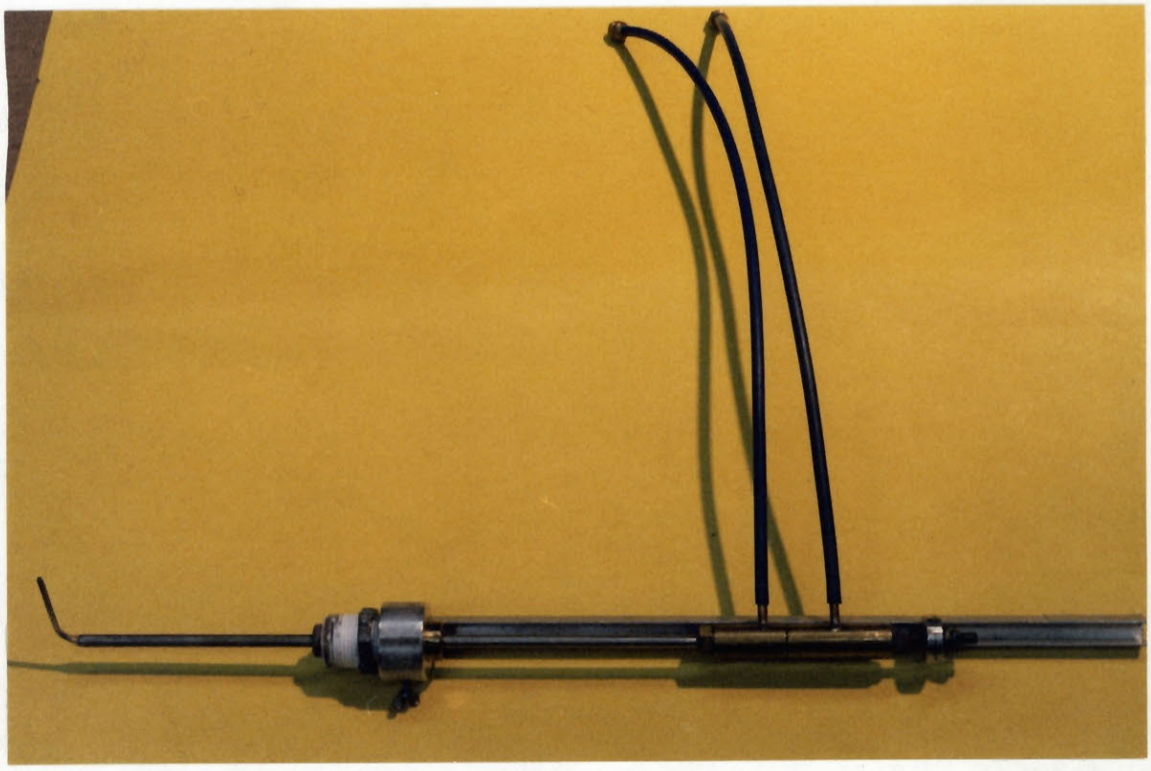

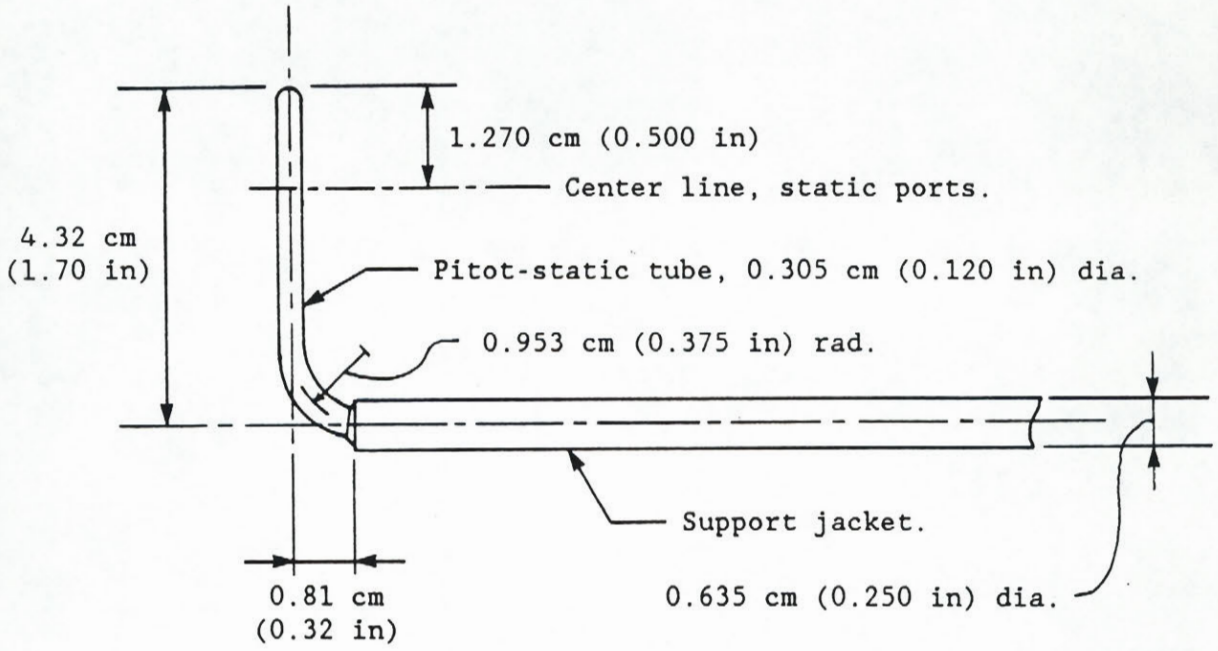

Fig.L-1: Pitot-static tube, with support.

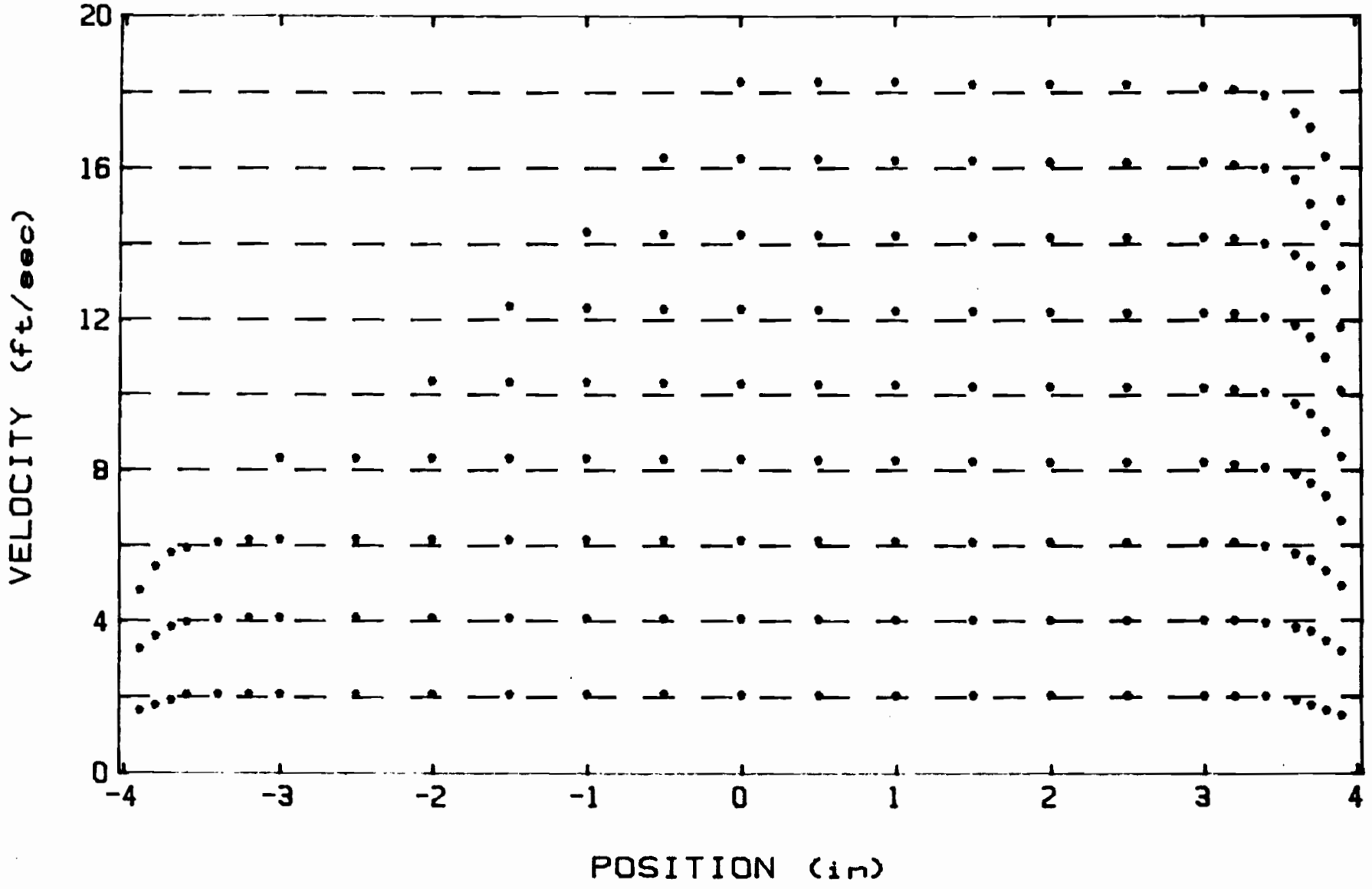

Fig.L-2: Velocity profiles, K = 0, dir.1 [75].
Note: Individual points are measurements and dashed lines bulk velocities.

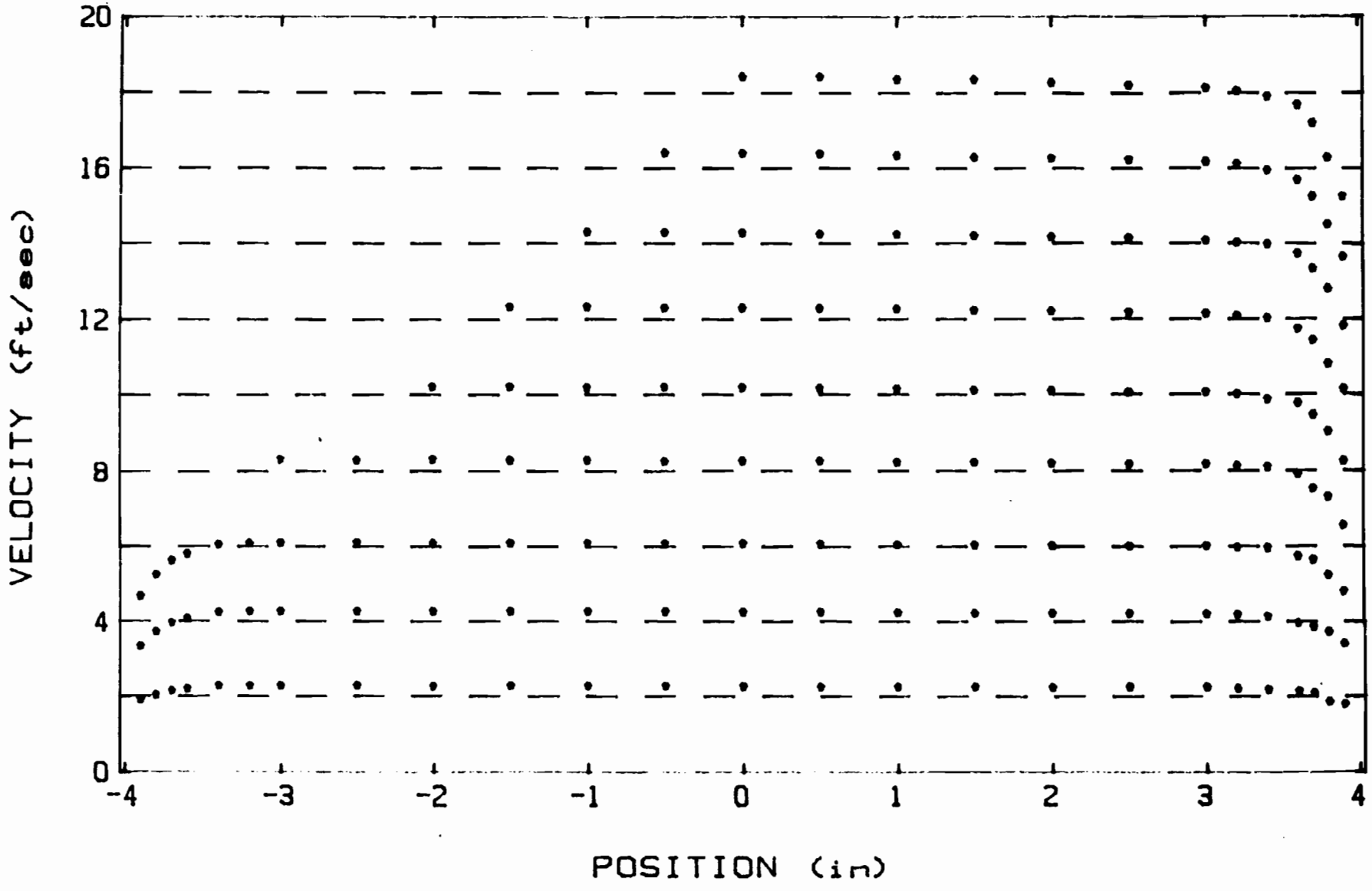

Fig.L-3: Velocity profiles, K = 0, dir.2 [75].
Note: Individual points are measurements and dashed lines bulk velocities.

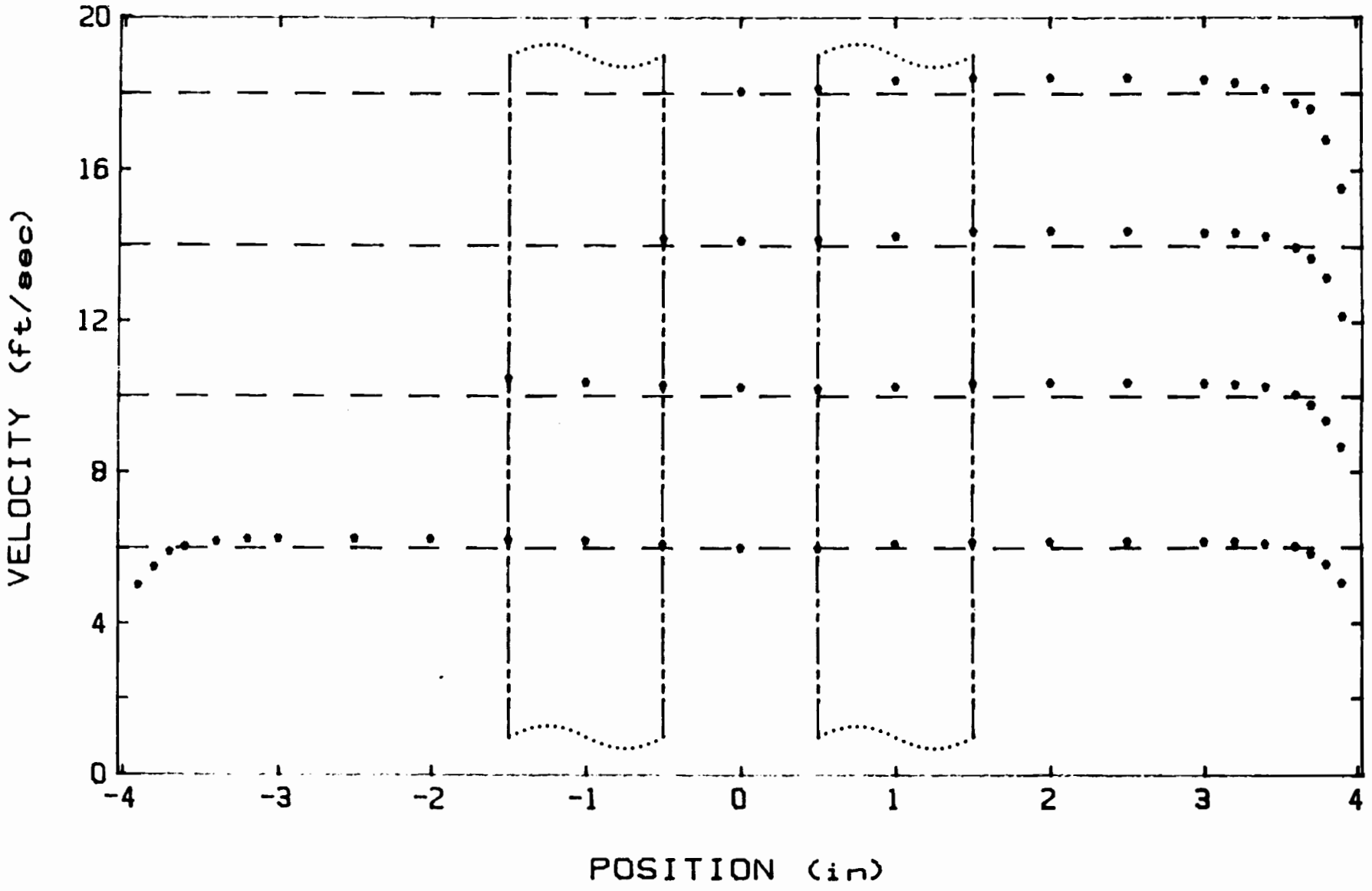

Fig.L-4: Velocity profiles, K = 4, G_c = 2.0, dir.1 [75].
Note: Individual points are measurements and dashed lines bulk velocities.

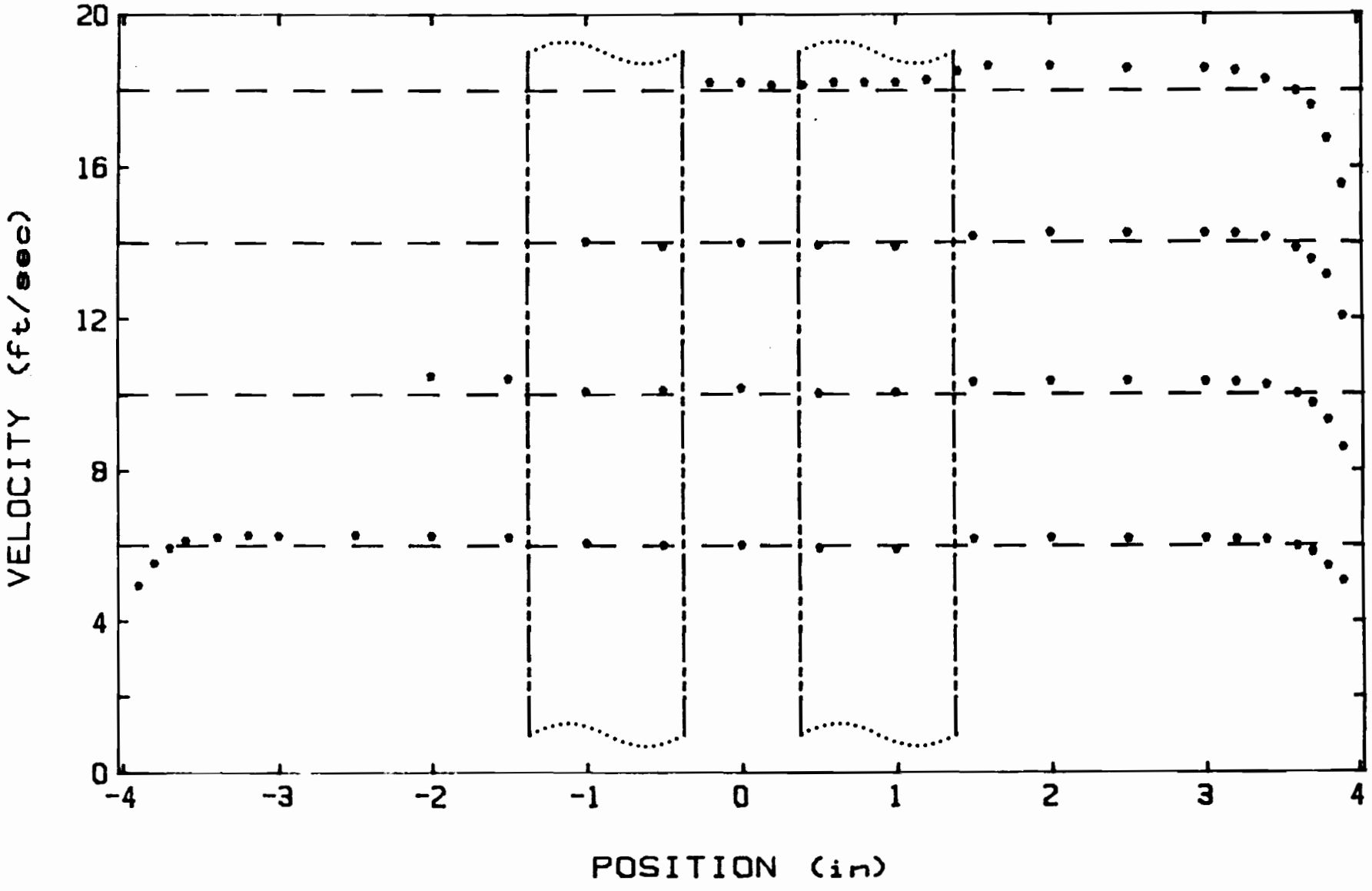

Fig.L-5: Velocity profiles, K = 4, G_c = 1.5, dir.1 [75].
Note: Individual points are measurements and dashed lines bulk velocities.

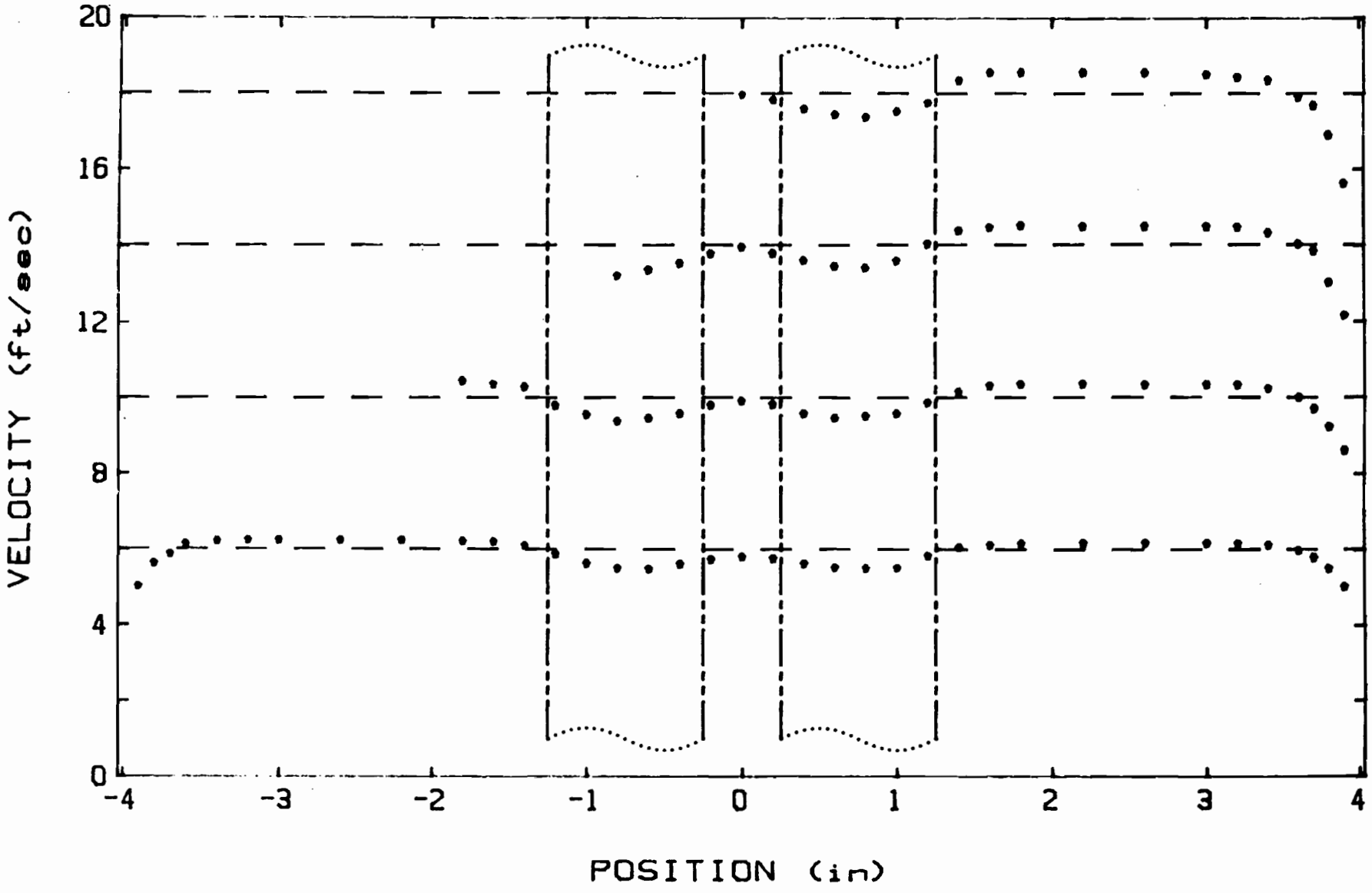

Fig.L-6: Velocity profiles, K = 4, G_c = 1.0, dir.1 [75].
Note: Individual points are measurements and dashed lines bulk velocities.

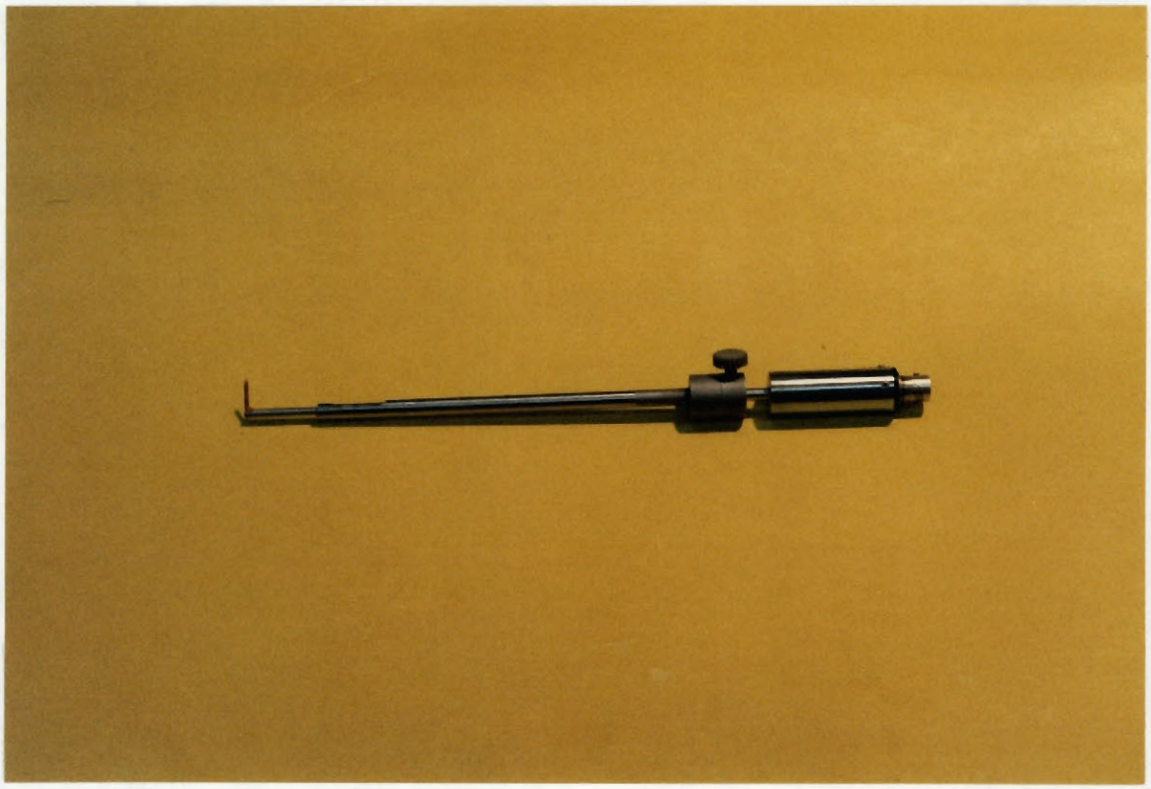

Fig.L-7: Hot film probe and support.

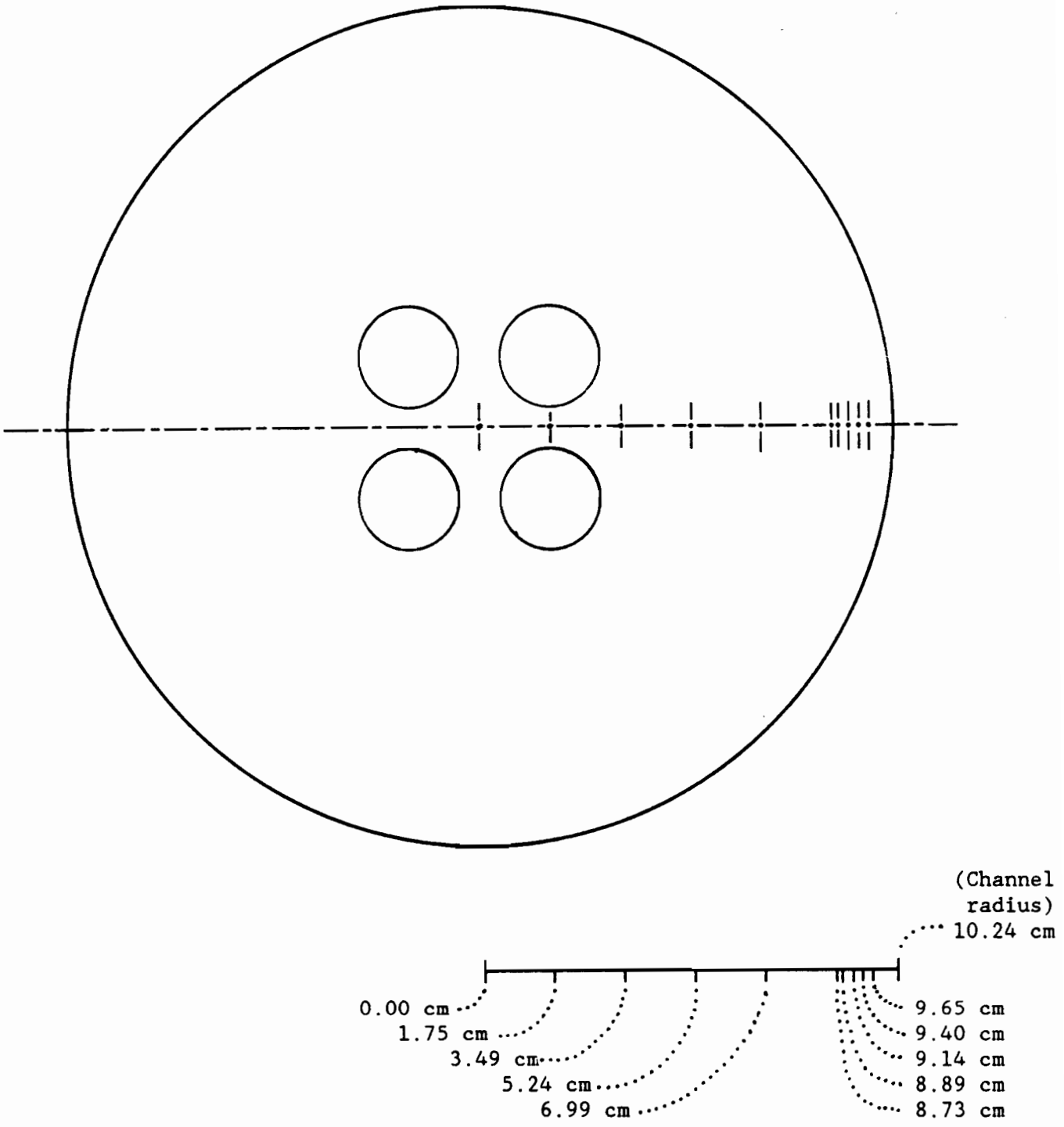

Fig.L-8: Turbulence measurement points ($K = 4$, $G_c = 0.75$).

Note: The values in inches are 0.000, 0.688, 1.375, 2.063, 2.750, 3.438, 3.500, 3.600, 3.700, 3.800, 4.030.

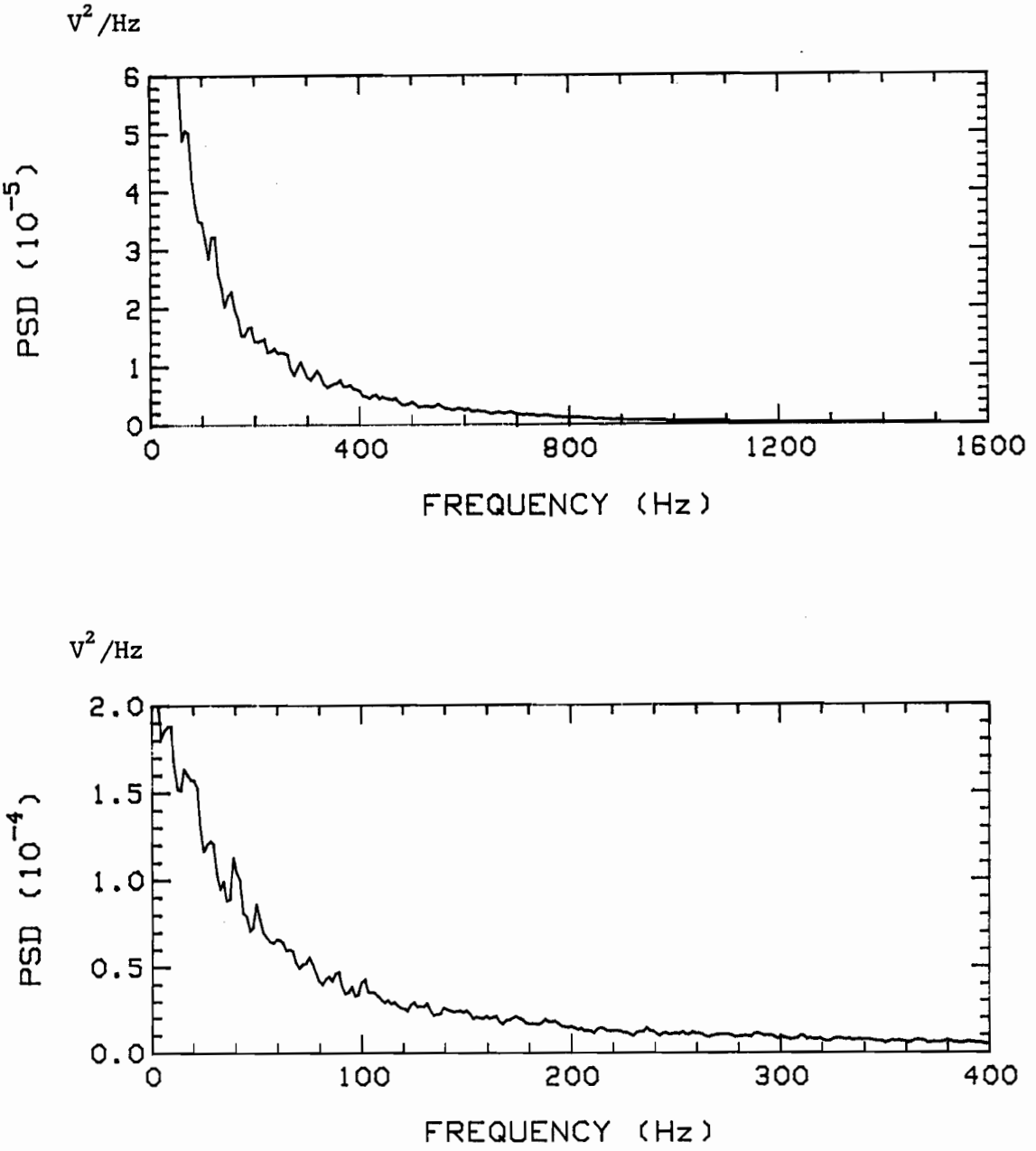

Fig.L-9a: Velocity fluctuations, $K = 0$, $\bar{u} = 3$, center of channel.
Note: PSD scale may be converted in terms of dimensionless velocity by using eqn. (L.4).

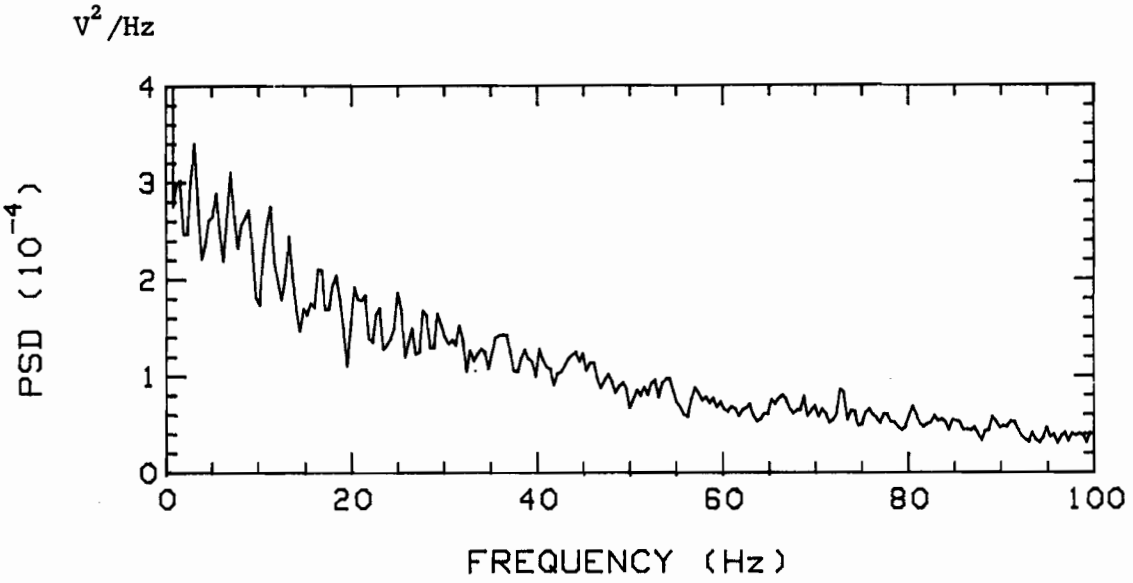

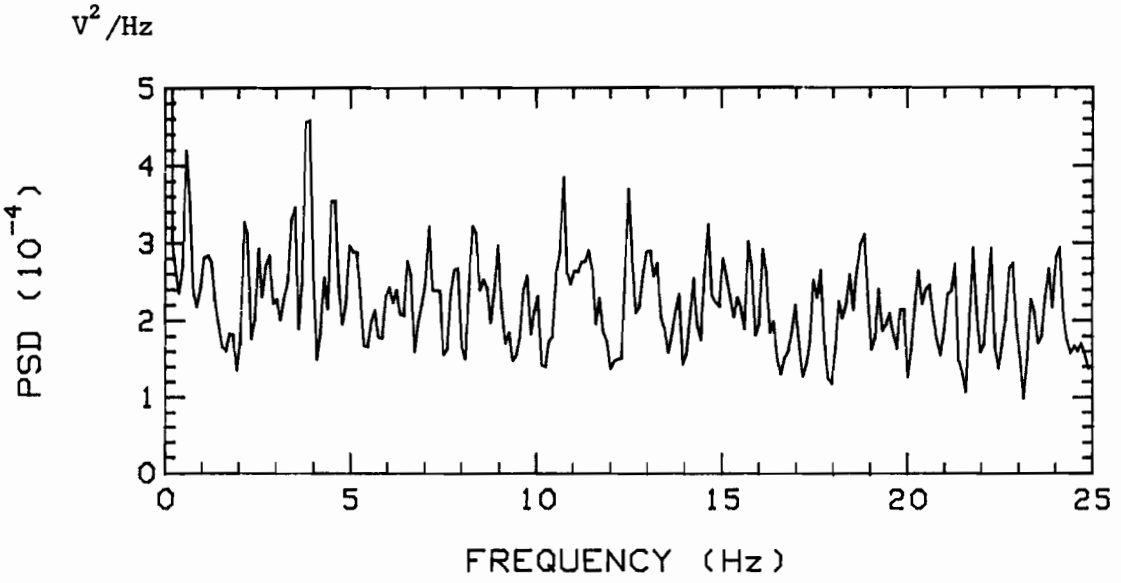

Fig.L-9b: Velocity fluctuations, $K = 0$, $\bar{u} = 3$, center of channel.
Note: PSD scale may be converted in terms of dimensionless velocity by using eqn. (L.4).

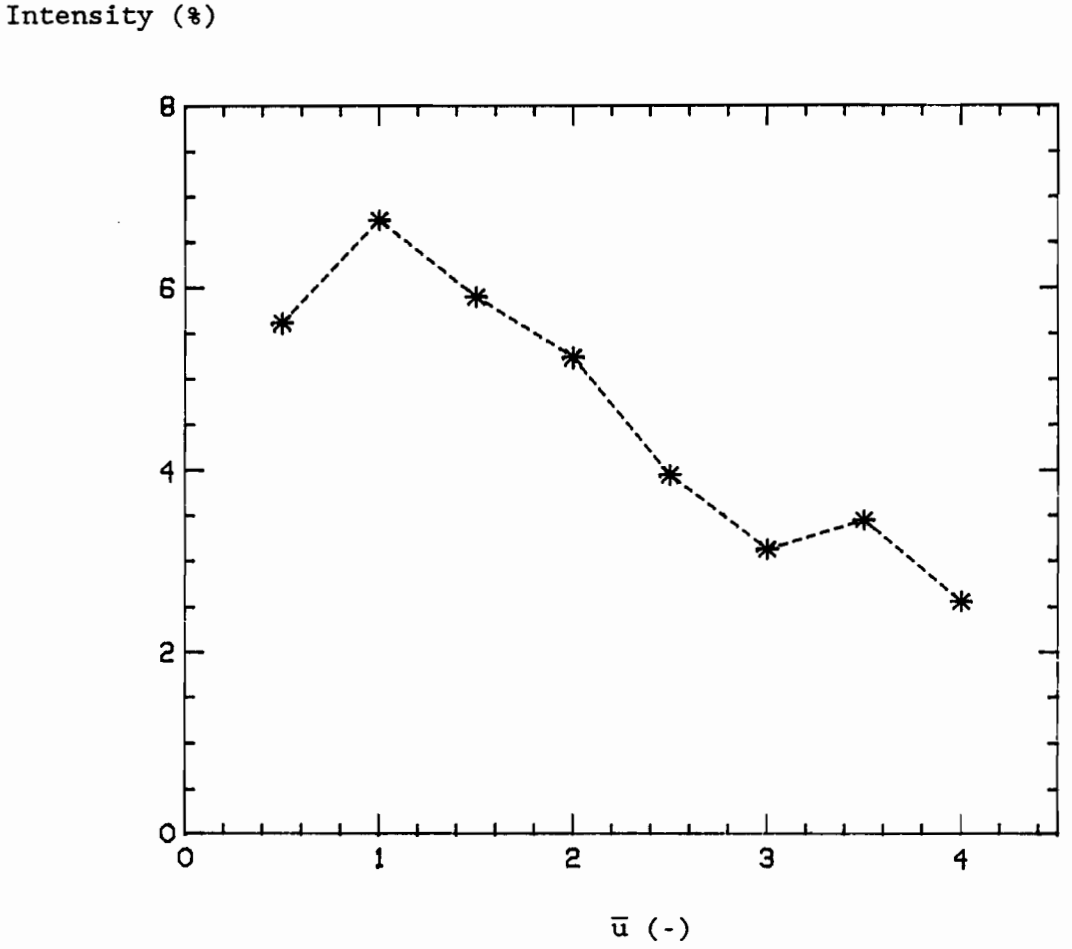

Fig.L-10: Turbulence intensities versus flow velocity, $K = 4$, $G_c = 0.75$, with turbulator, radial position = 2.5 in

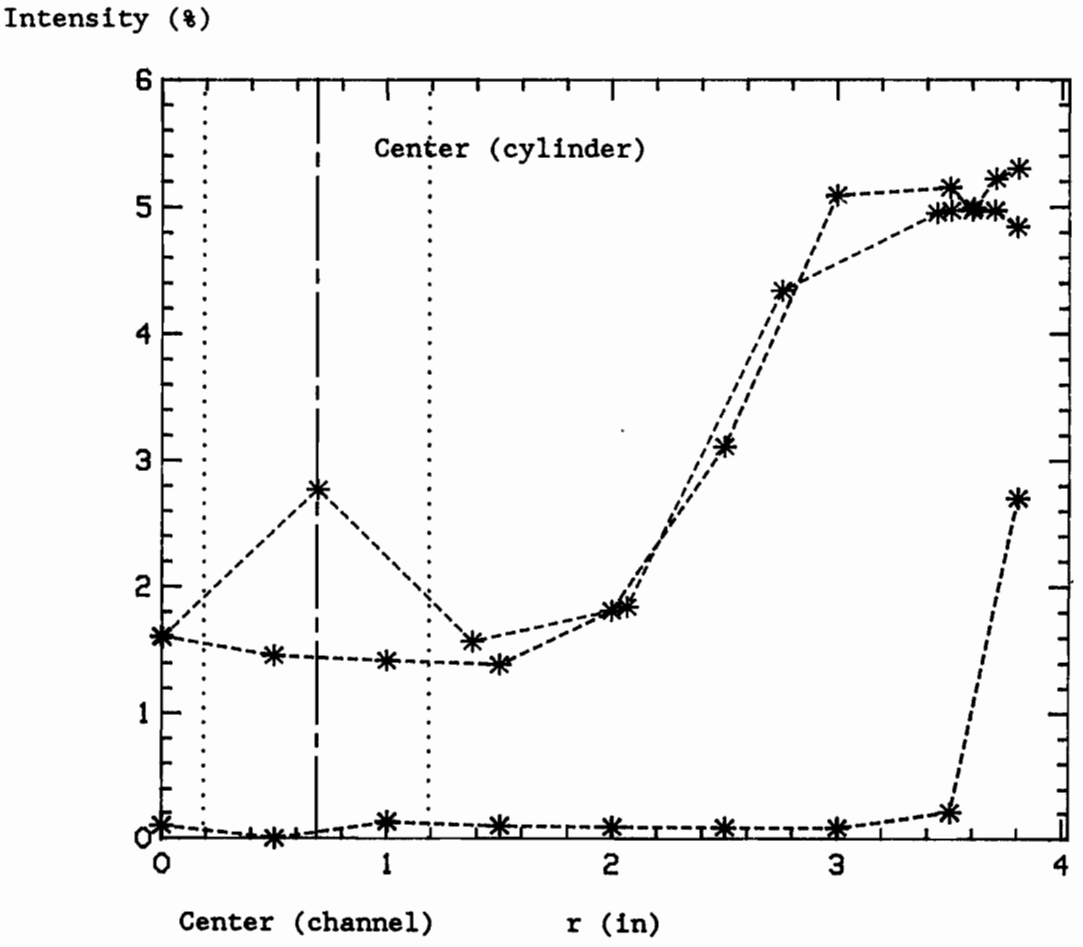

Fig.L-11: Turbulence intensities versus radial position, at $\bar{u} = 3$, (i) no turbulator, K = 0 (RED), (ii) with turbulator, K = 0 (GREEN), (iii) with turbulator, K = 4, $G_c = 0.75$ (BLUE).

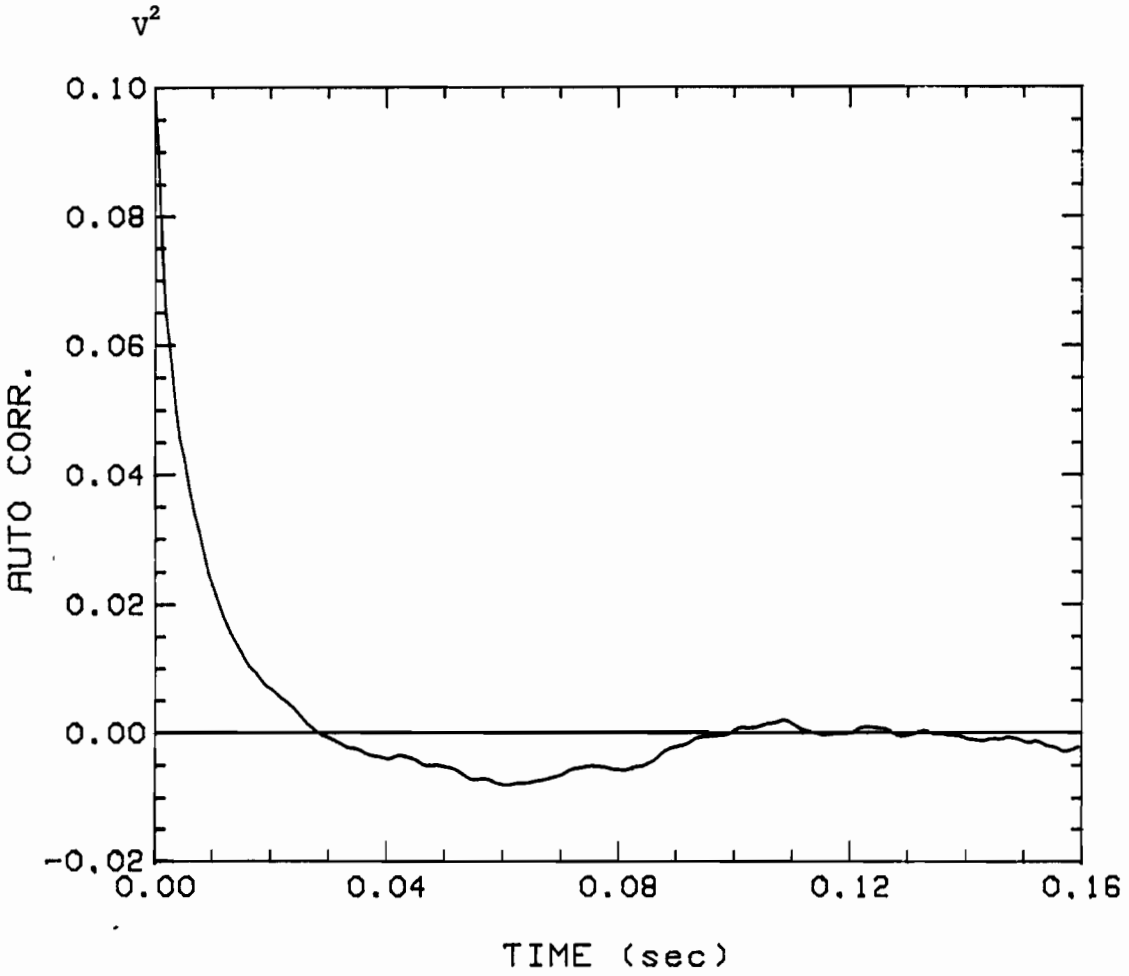

Fig.L-12: Typical autocorrelation function for flow velocity, with turbulator, $\bar{u} = 3$, $K = 4$, $G_c = 0.75$, radial position = 0.688 in.

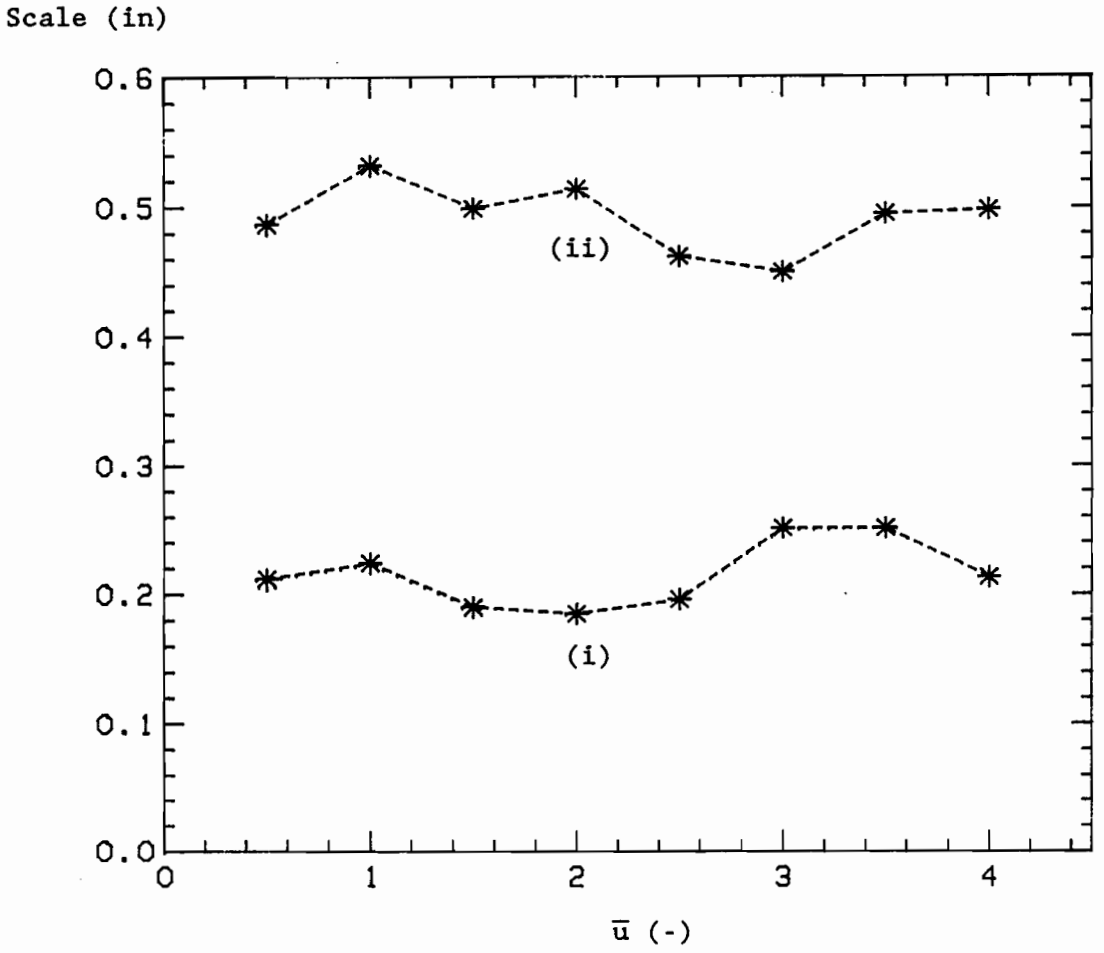

Fig.L-13: Turbulence scales versus flow velocity, with turbulator, (i) K = 0, center of channel, (ii) K = 4, G_c = 0.75, radial position 2.5 in.

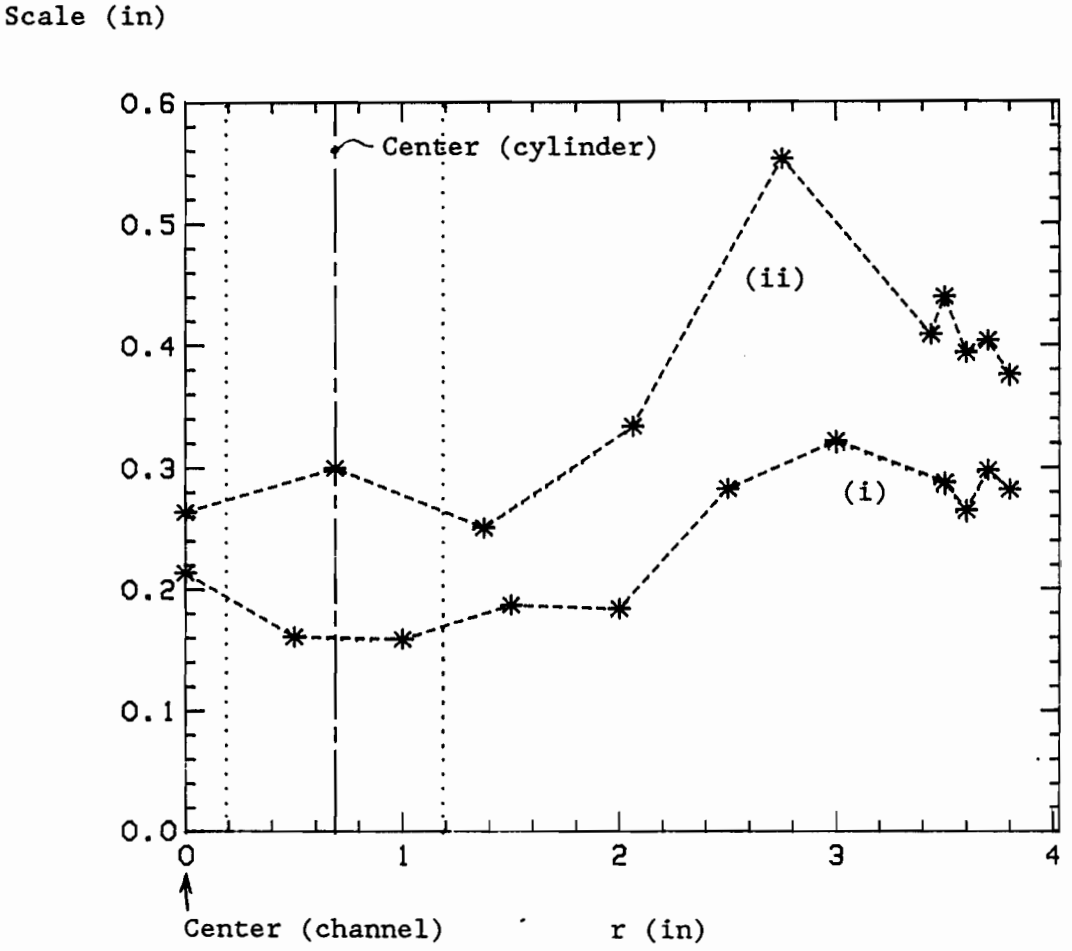

Fig.L-14: Turbulence scales versus radial position, with turbulator, at $\bar{u} = 3$, (i) $K = 0$, (ii) $K = 4$, $G_c = 0.75$.

Appendix M

Instrumented cylinder calibration

Owing to the fact that the embedded strain gages have a higher modulus of elasticity than the surrounding silicone rubber, they resist deformation and consequently, indicate a lower strain than would exist were the gages not present.

This effect, that is, the ratio of the expected (theoretically) to the measured strains, has been evaluated by calibration of the instrumented cylinder(s), as follows.

Given a modal shape and its amplitude, longitudinal strains (induced by bending) can readily be calculated, for any arbitrary point within the cylinder. The calibration procedure used here involves forced static deformations, in two different beam modes (neither of which corresponds exactly to a freely vibrating clamped-clamped cylinder, in each of the two strain gage pair planes (see Fig. 14).

The two different modes were tested to ascertain that the ratio (of theoretical to measured strains) is not modal shape dependent. The two strain gage pair planes were tested to verify that no asymmetry was present (for example, due to a manufacturing defect).

The two deformation configurations used were (1) a vertically hanging cantilevered cylinder with a concentrated lateral load (forced displacement) at the free end, and (2) a vertical clamped-clamped cylinder with a concentrated lateral load (forced displacement) at mid-span (see Fig. M-1). The deflections being relatively small, the effect of gravity was neglected.

Let

$$s = \frac{\varepsilon_t}{\varepsilon_m}, \qquad (M.1)$$

where s is the strain ratio, ε_t is the theoretical (calculated) strain, and ε_m is the measured gages strain.

We recall (see Fig. 14 and also Appendix M of Ref. [75], and Appendix H) that the strain gages are located at a radial distance a from the neutral axis of the cylinder and at a distance r·L from its upstream (upper) end, where r is a constant and L is the cylinder length:

$$a = 1.00 \text{ cm } (3.92 \text{ in}), \text{ and} \tag{M.2}$$

$$r = 0.1047 . \tag{M.3}$$

The strain gage bridge, for one of the two planes of motion, is shown below (exclusive of balancing or amplification circuits*).

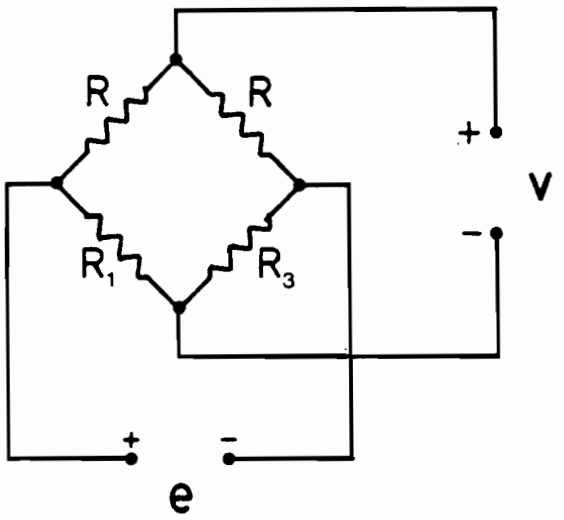

Here, v is the excitation voltage, and e is the bridge output voltage. Resistors R_1 and R_3 are the gages themselves, and R are fixed reference precision resistors.

When the output current of the bridge is negligible,§ we have

---

* See Ref. [75] for details on the electronics.

§ Which is the case here, amplifiers being of high input impedance.

$$\frac{e}{v} = \frac{R\,(R_1 - R_3)}{(R+R_1)\,(R+R_3)} \quad . \tag{M.4}$$

We can write

$$\begin{aligned} R_1 &= R + \delta R \ , \quad \text{and} \\ R_3 &= R - \delta R \ , \end{aligned} \tag{M.5}$$

since the strains will be of opposite sign (note that δR can be negative) and equal. Neglecting second order terms, eqs.(M.4) and (M.5) become

$$\frac{e}{v} = \frac{\delta R}{2 \cdot R} \quad . \tag{M.6}$$

Now recall that,

$$f = \frac{\delta R / R}{\varepsilon_m} \tag{M.7}$$

is the (strain) gage factor, furnished by the manufacturer; ε_m is the measured strain.

If the bridge output is amplified by a factor (gain) of G, then

$$e_0 = G \cdot e \ , \tag{M.8}$$

where e_0 is the amplifier output voltage.

Finally, from eqs.(M.6), (L.7), and (M.8), we may write

$$\varepsilon_m = \frac{2}{fG} \frac{e_0}{v} \ . \tag{M.9}$$

The theoretical strains for the tested deformation modes are as follows:

(a) Vertically hanging cantilevered cylinder

With gravity, including the presence of the lower (light aluminium) cap, neglected, we have*

$$\sigma_M = \frac{W}{Z} \, (L - x) \ , \tag{M.10}$$

where σ_M is the maximum (fiber) stress, W is the concentrated lateral load,

---

* e.g. see *Machinery's Handbook* (19th ed.), by Oberg & Jones, P. 408.

Z is the beam section modulus, L is the beam (cylinder) length, and x is the distance of the point of interest from the fixed end. We also have

$$y = \frac{W \cdot L^3}{3 E I} , \tag{M.11}$$

where y is the free end (lower)lateral deflection, E is the modulus of elasticity, and I is the second moment of area.

Next, recall the definition of section modulus:

$$Z = \frac{I}{c} ; \tag{M.12}$$

here, c is the maximum distance, in the plane of deflection, from the neutral axis. Furthermore, from basic stress-strain relationships,

$$E = \frac{\sigma}{\varepsilon} , \tag{M.13}$$

where σ and ε are fiber stress and strain respectively.

Now, the theoretical stress at a distance a (rather than c) from the neutral axis is

$$\sigma_{t_1} = \sigma \frac{a}{c} , \tag{M.14}$$

and, using eqn.(M.13),

$$\varepsilon_{t_1} = \frac{\sigma_{t_1}}{E} . \tag{M.15}$$

From eqs.(M.10), (M.11), (M.12), (M.14), and (M.15), we obtain

$$\varepsilon_{t_1} = \frac{3 a y (L - r)}{L^3} . \tag{M.16}$$

But, in our case,

$$x = r \cdot L , \tag{M.17}$$

hence, the latter, together with eqn.(M.16), yield

$$\varepsilon_{t_1} = \frac{3 a y (1 - r)}{L^2} . \tag{M.18}$$

(b) Vertical clamped-clamped cylinder

Proceeding in a similar way, we get, for a concentrated load at L/2,

$$\varepsilon_{t_2} = \frac{24\, a\, y\, (1 - 4r)}{L^2} . \qquad (M.19)$$

Calibration procedure

The varied test parameters are y in eqs.(M.18) and (M.19), and e_0 in eqn.(M.9); the other parameters are fixed.

From eqs.(M.1), (M.9), and (M.18), we have

$$s_1 = \frac{3}{2} \frac{a\, f\, Gv\, (1 - r)}{L^2} \frac{y}{e_0} , \qquad (M.20)$$

and from eqs.(M.1), (M.9), and (M.19), we get

$$s_2 = \frac{12\, a\, f\, Gv\, (1 - 4r)}{L^2} \frac{y}{e_0} , \qquad (M.21)$$

where s_1 is the gage ratio based on beam mode 1 testing, and s_2 on mode 2 testing (see Fig. M-1).

Typical calibration data is shown in Tables M-1 and M-2. The values of the fixed parameters were:

a = 1.00 cm (see eqn.(M.2)),
r = 0.1047 (see eqn.(M.3)),
f = 2.085 ,
G = 2000 , *
v = 5.03 volts, and
l = 47.0 cm (18.5 in).

The gage ratios s_1 and s_2 were computed from eqs.(M.20) and (M.21), utilizing mid-range values of e_0; the latter was to minimize errors due to nonlinearity (if high end values of e_0 chosen) and DC offsets (if low end values of e_0 used). In the case of mode 1 results, e_0 averages for positive

* Note that the gain used for vibration testing was 5000.

and negative deflections were taken, for y = 2.54 mm. For mode 2 deflections, the value y = 1.27 mm was used. The computed gage ratios are, respectively

$$s_1 \simeq 11.65 \text{ , and}$$
$$s_2 \simeq 11.67 \text{ .} \qquad \text{(M.22)}$$

The two values are remarkably close and strongly suggest that the ratios are indeed independent of the beam deflection mode. Note that for relatively low radii of curvature at the gage longitudinal location (i.e. high cylinder bending in the vicinity of the gages), for example in combination higher beam modes/deflections, the gages may no longer behave in a linear fashion.* The average gage ratio is, from eqn. (M.22),

$$s = 11.66 \text{ .} \qquad \text{(M.23)}$$

For a given cylinder, the accuracy of s and linearity (small displacements) are estimated to be of the order of 1%.

For completeness, gage ratios were also measured for different cylinder lengths: Fig. M-2 illustrates the variations. The length was varied by cutting the cylinder at the lower end, which was tested solely as a vertically hanging cantilever (mode 1). It should be noted that the ratio r did not remain constant, as the longitudinal distance at the gages from the top was fixed, while the cylinder length was varied; hence results not only reflect variations in cylinder slenderness (L/D), but also the effect of variations of r.

Remark

In the latter tests, the ratio s has different values from that of eqn. (M.22) because both the type of strain gage used and the silicone rubber lot number were different (earlier work on the development of instrumented cylinders).

---

* Such cases do not occur in actual testing in flow (amplitudes are very small.

Given a value for the ratio s, the "theoretical" strain, corresponding to the actual deflection, can be calculated: from eqs.(M.1) and (M.9),we find

$$\varepsilon_t = \frac{2s}{fv} \frac{e_0}{G} . \tag{M.24}$$

For convenience, the known parameters, namely the gage ratio s (calibrated), the gage factor f (gage manufacturer's data), and bridge excitation voltage (fixed power supply) are lumped into a single constant, here called gage coefficient:

$$c_0 = \frac{s}{fv} . \tag{M.25}$$

Two* instrumented cylinders were manufactured and individually calibrated; their gage coefficients were found as

$$\begin{aligned} (c_0)_1 &\simeq 1.11 \text{ (volts)}^{-1} , \\ (c_0)_2 &\simeq 1.18 \text{ (volts)}^{-1} . \end{aligned} \tag{M.26}$$

Finally, from eqs.(M.24) and (M.25), we obtain

$$\varepsilon_t = 2 \cdot c_0 \cdot \frac{e_0}{G} . \tag{M.27}$$

---

* A 52.0 cm (20.5 in) cylinder has also been manufactured, but has not been used here; it had a c_0 value of 1.40 $(\text{volts})^{-1}$.

Deflection plane	y (mm)	y (10^{-3}in)	e_0 (mV)	e_0/y (mV/mm)	e_0/y (mV/0.050 in)
1	0.00	0	0	-	-
	1.27	50	138	108.7	138.0
	2.54	100	279	109.8	139.5
	3.81	150	419	110.0	139.7
	5.08	200	559	110.0	139.8
	0.00	0	-2	-	-
1	0.00	0	0		-
	1.27	50	-133	104.7	133.0
	2.54	100	-273	107.5	136.5
	3.81	150	-411	107.9	137.0
	5.08	200	-549	108.1	137.3
	0.00	0	0	-	-
2	0.00	0	0	-	-
	1.27	50	137	107.9	137.0
	2.54	100	278	109.4	139.0
	3.81	150	417	109.4	139.0
	5.08	200	555	109.3	138.8
	0.00	0	7	-	-
2	0.00	0	0	-	-
	1.27	50	-141	111.0	141.0
	2.54	100	-278	109.4	139.0
	3.81	150	-414	108.7	138.0
	5.08	200	-551	108.5	137.9
	0.00	0	-4	-	-

Table M-1: Strain gage response, deflection mode 1. Silastic E (lot # QL119778), L=47.0 cm (18.5 in).

Deflection plane	y (mm)	y (10^{-3}in)	e_0 (mV)	e_0/y (mV/mm)	e_0/y (mV/0.050 in)
1	0.00	0	0	-	-
	0.64	25	365	570.3	730.0
	1.27	50	730	570.3	730.0
	1.91	75	1089	567.2	726.0
	2.54	100	1447	565.2	723.6
	0.00	0	8	-	-
1	0.00	0	0		-
	0.64	25	-362	565.6	724.0
	1.27	50	-724	565.6	724.0
	1.91	75	-1085	565.1	723.4
	2.54	100	-1442	563.3	721.0
	0.00	0	-8	-	-
2	0.00	0	0	-	-
	0.64	25	356	556.3	712.0
	1.27	50	710	554.7	710.0
	1.91	75	1064	554.2	709.4
	2.54	100	1415	552.7	707.6
	0.00	0	-2	-	-
2	0.00	0	0	-	-
	0.64	25	-351	548.4	702.0
	1.27	50	-706	551.6	706.0
	1.91	75	-1059	551.6	706.0
	2.54	100	-1409	550.4	704.6
	0.00	0	1	-	-

Table M-2: Strain gage response, deflection mode 2. Silastic E (lot # QL119778), L=47.0 cm (18.5 in).

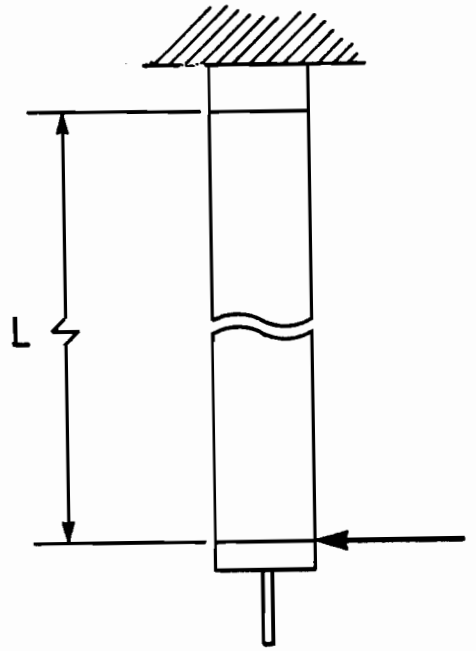

Mode 1

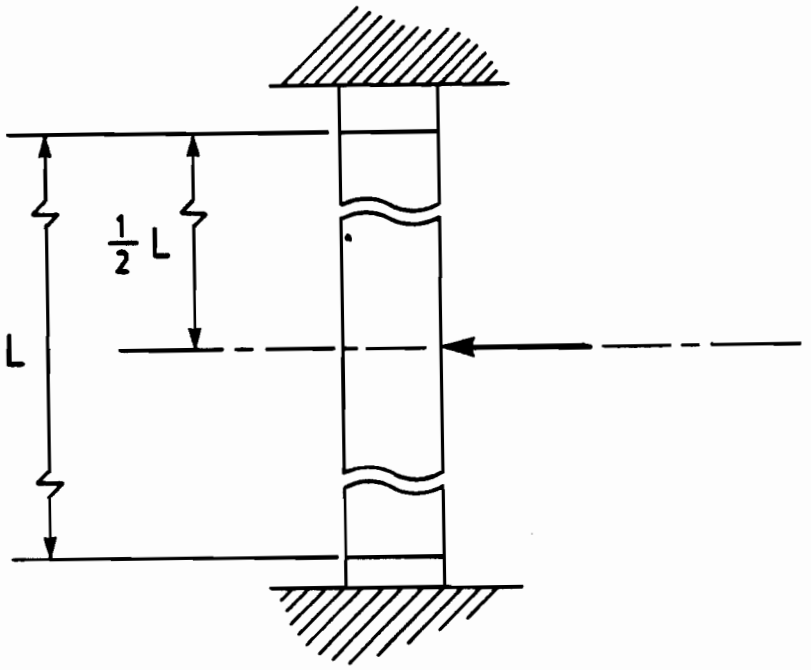

Mode 2

Fig. M-1: Deflection modes (forced displacements) for tests on imbedded strain gage response - instrumented cylinder calibration.

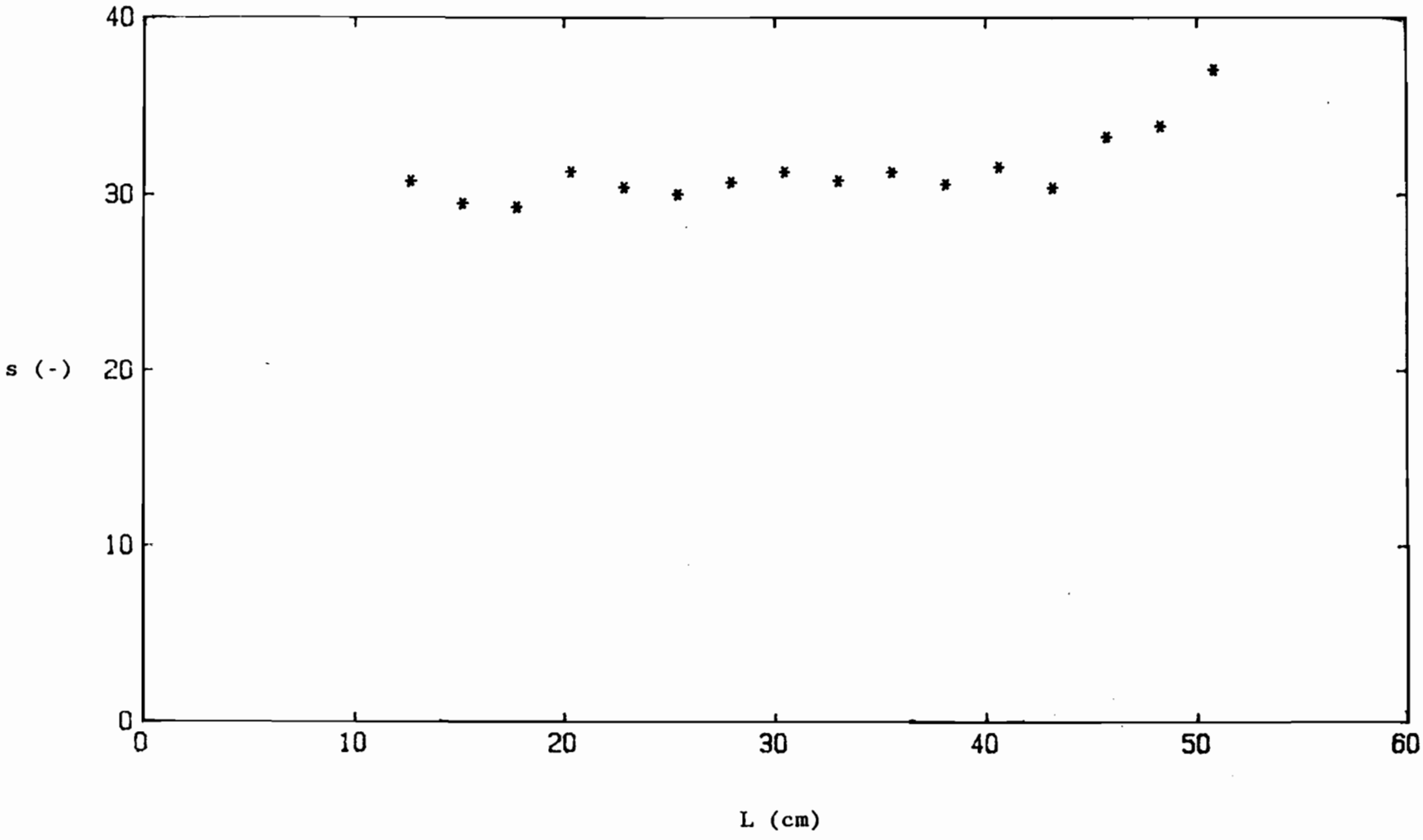

Fig. M-2: Gage ratio versus cylinder length.

Appendix N

Pressure-ancillary measurements

Pressure measurements were made at the wall of the test channel, at two opposite points on a diametrical line. A pair of pressure transducers (in this case, STATHAM model PM5TC) can be seen mounted in Fig. 1, at mid-length. Ideally, DC coupled transducers of high sensitivity and reasonably high bandwidth would have provided measurements covering the complete range (of frequencies) of interest; unfortunately, the available DC coupled transducers (STATHAM unbonded strain gage, model PM5TC) had a fairly low natural frequency (about 40 Hz), and that problem was compounded when measurements were for water (transfer function tests are presented below). Hence, basic pressure tests were conducted with hydrophones (PCB, model 106B), which are AC coupled with a low frequency -5% point of 0.5 Hz; the latter are presented in Chapter 4.

This Appendix shall cover the following: (i) basic theoretical calculations to predict the frequency response of both types of transducers used, (ii) transfer function tests for investigating the effect of reducing the pressure port diameter, inclusive of second order system curve fits, (iii) presentation of tests on tunnel acceleration induced pressures, together with a method for correcting the measured differential pressure PSD, (iv) comparison of the latter method to the one used in the main measurements (single point pressures), and (v) presentation of the pressure measurements made with the STATHAM transducers (to investigate pressure PSD's near zero).

The two hydraulic configurations used (channel wall mounting) are depicted in Figs. N-1 and N-2, for the PCB microphones and the STATHAM transducers, respectively. Both mountings were designed with hydraulic pressure losses minimization in mind. The test chamber used for transfer function measurements is depicted in Fig. N-3; note that its hydraulic configuration at the transducer is very close to that found in the tunnel (when the 0.159 cm dia. "pill" in used). The bleed valve (top chamber port) and pressure source (bottom chamber port), the latter consisting in a diaphragm connected to a shaker, are not shown in this Figure.

(1) Basic theoretical calculations

An estimate of the natural (undamped) frequency of a pressure transducer and attached tube may be estimated from the relationship*

$$\omega_n = \left[\frac{1}{\omega_t^2} + \frac{16\,\rho L\, C_{vp}}{3\,\pi\, d^2} \right]^{-1/2}, \qquad (N.1)$$

where,

ω_n is the natural (undamped) frequency of the transducer/tube system,

ω_t is the transducer's natural frequency (in air),

C_{vp} is the transducer's volume change per unit pressure coefficient,

ρ is the fluid density,

L is the tube length,

d is the tube diameter.

In the case of N cascaded tubes, we shall use the equation

$$\omega_n = \left[\frac{1}{\omega_t^2} + \frac{16\,\rho\, C_{vp}}{3\,\pi} \sum_{j=1}^{N} \frac{L_j}{d_j^2} \right]^{-1/2}, \qquad (N.2)$$

where L_j and d_j are length and diameter of the j^{th} tube.

At this point, we require: (i) The geometry (hydraulic configuration) of the tubing system; this will include the internal pressure chamber in the case of the STATHAM transducer, since its diaphragm is not on the outside (as is the case for the PCB microphone) and since ω_t is measured in air whether the fluid of interest here is water. All pertinent geometrical parameters are illustrated in Figs. N-1, N-2 (water tunnel), and N-3 (test chamber). (ii) The fluid (water) density; its value is 1.0×10^3 Kgm/m^3 (62.4 lbm/ft^3). (iii) The transducer's natural frequency (in air) ω_t; the value for the PCB microphone is given in its specifications, namely 60 KHz, but in the case of the STATHAM transducer, it had to be measured (by observing its response to a step change in air pressure). This latter value was

---

* *Measurement systems-Application and design*, by E.O. Doebelin (1975, McGraw Hill), P.396.

found to be about 40 Hz. (iv) Finally, the volume "swept" by the diaphragm for a unit change of pressure is required; the value being relatively large for the STATHAM transducer, it could be measured directly, using a water filled pipette (and, of course, transducer pressure chamber as well) to record volume changes. Air pressure was varied at the pipette open end and its change measured by the transducer itself. The value (C_{vp}) was found to be 6.2×10^{-8} m^3/KPa (2.6×10^{-2} in^3/psi). In the case of the PCB microphone, calculations had to be performed; the approach makes use of the acceleration sensitivity of the microphone (a parameter given in its specifications), as follows.

We model the pressure transducer (PCB microphone) as a spring-mass system (diaphragm & piezoelectric element assembly), as illustrated below.

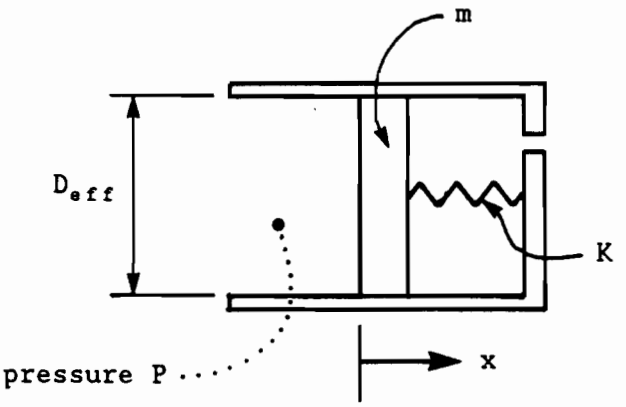

Note that D_{eff} is the effective piston area, where $D_{eff} < D$, the diameter of the diaphragm.

From (PCB) specifications,

$$\left.\begin{aligned} &D = 1.10 \text{ cm } (0.435 \text{ in}), \\ &\omega_t = 60 \text{ KHz}, \\ &C_a = 1.38 \times 10^{-2} \text{ KPa/g } (0.002 \text{ psi/g}), \end{aligned}\right\} \qquad (N.3)$$

the latter coefficient being the transducer's acceleration sensitivity, where g is the acceleration due to gravity (9.8 m/s^2, or 32.2 ft/sec^2).

The d'Alembert force on the "piston", due to an acceleration a, is the apparent pressure divided by the "piston" area, that is

$$f = C_a \cdot a \cdot A_{eff} , \tag{N.4}$$

where A_{eff} is the effective ("piston") area.

That force is also equal to that required to accelerate the "piston", namely

$$f = m \cdot a . \tag{N.5}$$

Equations (N.4) and (N.5) simply yield

$$m = C_a \cdot A_{eff} . \tag{N.6}$$

Recall the elementary relationship

$$K = m \cdot \omega_t^2 , \tag{N.7}$$

which combined with eqn.(N.6), yields

$$K = C_a \cdot A_{eff} \cdot \omega_t^2 . \tag{N.8}$$

The basic definition of the coefficient C_{vp} is simply

$$C_{vp} = \frac{\Delta V}{\Delta P} , \tag{N.9}$$

i.e. the ratio of volume to pressure changes. Therefore,

$$C_{vp} = \frac{A_{eff} \cdot \Delta x}{\Delta P} = A_{eff} \cdot \frac{f}{K} \cdot \frac{A_{eff}}{f} , \text{ or}$$

$$C_{vp} = \frac{A_{eff}^2}{K} . \tag{N.10}$$

Finally, combining eqs.(N.8) and (N.10), we obtain

$$C_{vp} = \frac{A_{eff}}{C_a \cdot \omega_t^2} . \tag{N.11}$$

The only unknown is A_{eff}. The latter must be a fraction of the actual diaphragm area, that is

$$A_{eff} = c \cdot A = c \cdot \frac{\pi}{4} \cdot D^2 , \tag{N.12}$$

where $0 < c < 1$.

As the value of c is unknown, it will be estimated by assuming that the diaphragm (PCB) deflects as a spherical segment, as illustrated below.

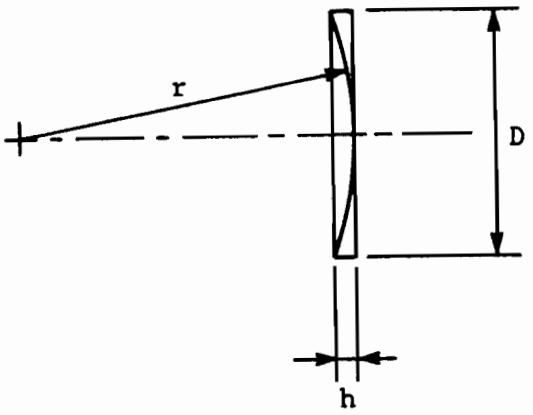

From elementary geometry, as $h/r \to 0$, we find

$$c = 1/2 \, . \qquad \text{(N.13)}$$

Equations (N.3), (N.11), (N.12), and (N.13) yield an estimate for C_{vp} for PCB microphones:

$$C_{vp} \simeq 2.37 \times 10^{-13} \ m^3/KPa \ (1.01 \times 10^{-7} \ in^3/psi). \qquad \text{(N.14)}$$

Note that this is about 260,000 times the value for the STATHAM transducer.

We are now ready to perform the basic estimates for resonant frequencies of transducer (STATHAM or PCB) - "tubing" systems (test chamber or tunnel wall). First, we shall examine the case of the PCB microphone in the test chamber, using the "pill" (see Fig. N-3) with the 0.159 cm (1/16 in) diameter hole (this is later selected as the port size for the tunnel itself). Note that the other diameters used are 0.079 cm, 0.119 cm, 0.238 cm, and 0.318 cm (1/32 in, 3/64 in, 3/32 in, and 1/8 in). The hydraulic configuration of the circuit of interest can be seen in Fig. N-3: we have $L_1 = 0.11$ cm and $d_1 = 1.11$ cm (see Fig. N-1), a tapered section, and $L_2 = 0.269$ cm (see table in Fig. N-3) and $d_2 = 0.159$ cm. Since $L_2/d_2^2 = 10.64 \ cm^{-1}$, is much larger than $L_1/d_1^2 = 0.09 \ cm^{-1}$, we shall neglect the latter, as well as the tapered section. From eqs. (N.2), (N.3), (N.14), and $\rho = 1.0 \times 10^3 \ Kgm/m^3$ (water), we get

$$\omega_n \simeq 7600 \text{ Hz} . \qquad (N.15)$$

Tests conducted in the chamber (to be reviewed shortly), with one PCB microphone as reference (see Fig. N-3), yield a lower value (in this case, about 3100 Hz); this is not unexpected, as eqn. (N.2) is only an approximation, and damping is not taken into account. Furthermore, as shall be seen, some air left in the system can easily degrade response. Nevertheless, the calculated value (eqn. (N.15)) is useful in the sense that it confirms that the value of C_{vp} of eqn. (N.14) is of the right order of magnitude.

Since the hydraulic configurations of both the test chamber and the tunnel wall mounting are similar, and because the frequencies of interest for tunnel pressure measurements are at most a few hundred Hz, calculations for the PCB microphone when mounted at the channel wall will not be carried out.

Now, we proceed by evaluating ω_n for a STATHAM transducer mounted in the test chamber, using a "pill" of 0.159 cm diameter. The purpose served will be similar to that for the PBC. The hydraulic configuration of interest can be obtained by inspection of Figs. N-2 and N-3: $L_1 = 0.38$ cm and $d_1 = 3.81$ cm, $L_2 = 0.38$ cm and $d_2 \simeq 0.6$ cm, $L_3 = 3.98$ cm and $d_3 = 0.48$ cm, $L_4 = 0.11$ cm and $d_4 = 1.11$ cm, and $L_5 = 0.269$ cm and $d_5 = 0.159$ cm* (the fourth and fifth data pair are taken from Fig. N-3).

We obtain

$$\omega_n \simeq 9 \text{ Hz} . \qquad (N.16)$$

The experimentally obtained value is actually higher, at about 13 Hz. One would have expected a lower value since damping is ignored in the calculation; at least, the values are of the same order of magnitude. We shall rely on test chamber calibrated values (but calculations do indicate that the STATHAM characteristics [C_{vp} and ω_t] are roughly correct).

---

* The taper is omitted.

(2) Transfer function measurements

The test chamber depicted in Fig. N-3 was used to perform frequency response measurements on both PCB microphones and STATHAM pressure transducers; as shown, the chamber is set up with the reference transducer on the right-hand side (PCB microphone with no "pill") and a PCB microphone on the left, with a "pill" having a pressure port of 0.159 cm (1/16 in) in diameter. The chamber was designed to allow easy interchange of "pills".

Two series of transfer function tests were conducted, one involving a PCB microphone, the other a STATHAM transducer. In both cases, the reference transducer was a PCB microphone, with no "pill". In each case, transfer function measurements were made with (i) no "pill", and (ii) with a choice of up to five "pills"": the respective sizes of pressure port (see Fig. N-3) diameters were 0.079 cm, 0.119 cm, 0.159 cm, 0.238 cm, and 0.318 cm (in inches, those dimensions are 1/32, 3/64, 1/16, 3/32, and 1/8). Note that Fig. N-3 illustrates the setup for a PCB transducer with an insert of 0.159 cm (1/16 in).

Fig. N-4 illustrates results for a STATHAM transducer. In addition to the no "pill" case, tests were carried out with 0.318 cm, 0.238 cm, 0.159 cm, and 0.079 cm port diameters (it was felt unnecessary to conduct a test with the 0.119 cm "pill"). By inspection, we see that with the 0.159 cm (1/16 in) dia. port, the resonant frequency is already down to about 13.0 Hz, with a fair increase in damping from the no "pill" case. For the 0.079 cm (1/32 in) dia. port, the system is highly damped. To verify the existence of second order behaviour, the test data were curve fitted (theoretical second order system); this is shown in Figs. N-5a to N-5e. To allow utilizing the STATHAM transducers for near zero frequency measurements (recall that the PCB's may be used down to about 0.5 Hz), it was decided to use a 0.159 cm (1/16 in) port (which involved drilling the tunnel wall). Repeatability was adequate, especially considering that the STATHAM measurements are meant to investigate pressures only near zero frequency (in a bandwidth only about a tenth of resonance), and coherence was close to one.

Remarks

(1) Results near DC are not reliable, because the reference PCB microphone is not DC coupled. This is unimportant as we can safely assume that the STATHAM transducer response there is unity (magnitude of 1 and phase of 0).

(2) The no "pill" hydraulic configuration is very similar to the one shown in Fig. N-2; only the pressure port area differs slightly in the test chamber (that configuration is depicted in Fig. N-3).

Measurements of PCB microphone transfer functions proved much more difficult: this is attributed to the considerable effect of even small air bubbles on the microphone side of the pressure port - with no air present, virtually no "flow" is required through the port when pressure changes, owing to the extremely low C_{vp} of the microphone (this effect is much less important for the STATHAM as the required "flow" is much larger; recall the C_{vp} ratio of 260,000) - but the effective C_{vp} can be increased significantly when air is present.

Therefore, only tests to model the chosen port diameter, namely with the 0.159 cm (1/16 in) diameter "pill", are reported here. In any case, the lowest measured resonant frequency is about 2400 Hz (presence of air is suspected), which is much higher than the highest frequencies of interest here (at most a few hundreds of Hz). Fig. N-6a illustrates the rather poor repeatability of the measured transfer function (0.159 cm "pill"), and Fig. N-6b shows the corresponding coherences. The range of lowest resonant frequency is from about 2400 Hz to about 3400 Hz; more air (on the microphone side of the "pill") will lower the resonant frequency, hence we could consider 3400 Hz as a lower limit for the actual resonant frequency of the particular microphone/"pill" combination, were it not for the odd behaviour of the corresponding coherence (which may indicate a problem with the reference transducer). The "blue" coherence being fairly high, we shall consider 3100 Hz as the lowest limit for the resonant frequency (note that air may be present even in this latter case).

We may safely state that the frequency response of PCB microphones, when mounted at the channel wall (0.159 cm pressure port), is flat over the range of interest (<< 3100 Hz).

(3) Acceleration induced pressure

As mentioned in Chapter 2,* differential pressures (across a diametrical line, at the channel wall) will be induced by tunnel accelerations (along the said diametrical line). The tunnel cross-section is illustrated schematically below.

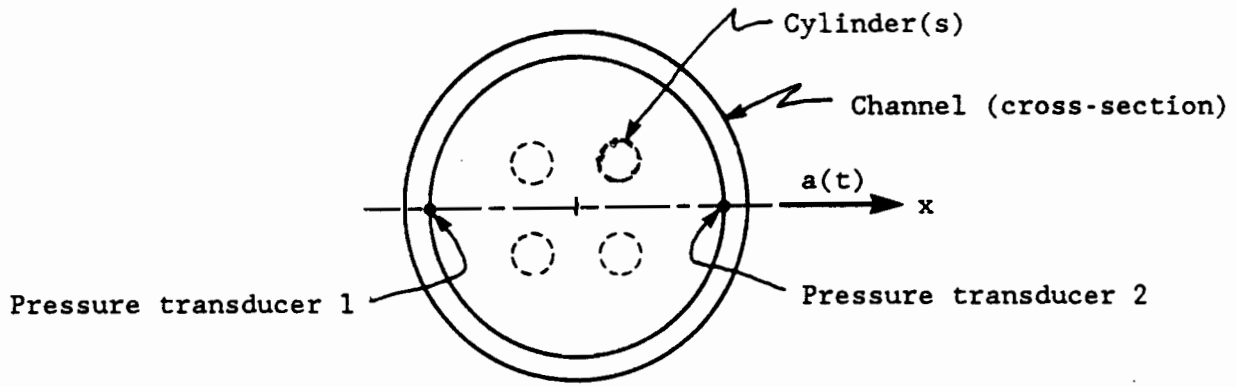

A channel acceleration, a(t), will result in a pressure gradient in the fluid, say $-dp_a(t)/dx$, where $p_a(t)$ is fluid pressure and x the distance along the diameter. The pressure difference between points 1 and 2 (due to the acceleration of the tunnel) is simply

$$p_a(t) = \rho \cdot D_c \cdot a(t) , \qquad (N.17)$$

where ρ is the fluid density and D_c is the channel diameter.

A test was conducted to ascertain that tunnel motion had a negligible effect on measured pressures. A preliminary test confirmed that shell modes were virtually non-existent in the tunnel (i.e. accelerations at points 1 and 2, in the diametrical direction shown, were the same). Hence, the reading from only one accelerometer was retained for analysis. The outputs from

---

* See the end of Section (c).

pressure transducers (PCB microphones) at points 1 and 2 were electrically subtracted, to yield the differential pressure.*

First, the applicability of eqn. (N.17) was confirmed by measuring "background" differential pressure and acceleration, at U = 0 (no flow); the latter condition was chosen so as to obtain high values of coherence. The top part of Fig. N-7 shows PSD's for both (differential) pressure and acceleration; the analysis bandwidth was chosen as 12.5 Hz, which is about 80 dimensionless units (the range most commonly utilized for main vibration data is 75). The density scales are set to correspond to eqn. (N.17). The bottom part depicts the corresponding coherence. It can be seen that, where coherence is near unity (i.e. nearly all of the pressure signal is due to tunnel motion), agreement is excellent.

Next, a technique similar to that described in Chapter 2 may be used to remove the part of the (differential) pressure due to tunnel motion: the relevant equation is§

$$G_d(\Omega) = (1 - \gamma^2_{da}(\Omega)) \cdot G_{meas}(\Omega) \,, \qquad (N.18)$$

where $G_{meas}(\Omega)$ and $G_d(\Omega)$ are the measured and computed (differential) pressures respectively, and $\gamma^2_{da}(\Omega)$ is the coherence function (between the differential pressure and the acceleration). This method is illustrated in Fig. N-8: The earlier U = 0 (u = 0) case is shown on top and a typical case, at u = 2.0, is shown on the bottom (the clipped peak corresponds to the tunnel circulation pump rotation frequency, the latter inducing channel motion).

The technique used in Chapter 2, to compute differential pressures, will automatically remove the acceleration induced pressures, as they are fully correlated, between pressure points 1 and 2.

---

* As these measurements are not part of the main work of this thesis, details on instrumentation are not given.

§ The derivation technique is similar (and simpler) than that used in Chapter 2.

We close with the following remark: Because the cylinder density is different from that of the fluid, some net cylinder motion excitation will occur due to tunnel accelerations (discussed in detail in Chapter 2), but removal from the measured differential pressure is still effected for three reasons: (i) measured accelerations together with cylinder/fluid density differences indicate only small motion excitation due to tunnel acceleration, (ii) channel acceleration PSD's show significant power only a very few (usually only one) discrete frequency points, and (iii) there is no evidence of increased power at those discrete points, in the measured vibration PSD's.

(4) Comparisons - methods of pressure PSD correction

The method used for correcting the measured pressure PSD's, detailed in Chapter 4, is meant to remove not only the acceleration induced pressure part (from the total differential pressure PSD), but also effects of fluctuations of static pressure (which includes plane acoustic waves). Whereas the method described in Section (3) above utilizes the directly measured differential pressure (which, when transducer gains are "perfectly" matched, does not include any effect of fluctuating static pressure), together with the test channel acceleration and corresponding coherence, the "main" method uses the two single point pressures, and corresponding coherence. The latter method has two advantages over the former one: (i) tunnel acceleration need not be measured, and (ii) transducer gains do not require very close matching. Typical results are shown in Fig. 9, and this single comparison will suffice to evaluate both methods. The top part depicts the single point PSD's, together with the corresponding coherence function; this is to illustrate the fact that the level of single point pressure PSD's is much higher than the one for the differential pressures (bottom part), which confirms the need for closely matched gains when differential pressure is obtained directly from the difference between the pressure signals. The bottom part illustrates differential pressure PSD, computed from both methods. It can be seen that results are very similar (especially when one considers the power levels found in the single point pressures), with exceptions near 2 Hz: It appears that the analog (voltage) subtraction of the pressure signals has yielded an error in the resulting differential pres-

sure PSD. Note that the differential pressure PSD stemming from the single point pressures has a more constant value, which is assumed to reflect more accurately the true PSD. A series of such comparisons does suggest that PSD's are indeed flat, which confirms that the single point pressures method is the best one (the alternate method always possesses local peaks). Note that acceleration induced pressures are properly corrected by both methods (i.e. they are absent from the differential PSD's in Fig. 9). The pressure measurements were effected with four* rigid cylinders at $G_c = 0.75$, using the PCB transducers; the mid-range value of $u = 3$ is shown in Fig. 9.

(5) STATHAM measurements

To investigate near-zero frequency behaviour of wall pressure, the DC coupled STATHAM pressure transducers were used. This complements the main measurements which were effected with AC coupled (-5% @ 0.5 Hz) PCB microphones. In each case (STATHAM or PCB), tests were conducted for three different values of K, namely 0 (no cylinder in the test channel), 4, and 28 (rigid cylinders). Each test included ten values of dimensionless flow velocity (u), which were 0.5 to 5.0, in 0.5 increments.

The $K = 0$ and $K = 4$ tests yielded very similar results,§ hence, the $K = 4$ data is not presented here ($K = 0$ data can be compared with pipe flow results available in the literature). Fig. N-10a illustrates differential pressure PSD's computed from measured point pressure† PSD's and corresponding coherence (the method used is detailed in Chapter 2), for the $K = 0$ case (no cylinder in the test channel). Fig. N-10b is the single point pressure dimensionless PSD equivalent (see eqn.(2.340)) of Fig. N-10a, to allow comparisons with PCB transducers data [Chapter 4]. Figs. N-11a and N-11b depict the same information, but for the $K = 28$ case.

---

* Results are almost identical to the $K = 0$ case (for which no tunnel acceleration measurements were made).

§ See Chapter 4 for comparisons of PCB results.

† Single point, as opposed to differential (two-point) pressure.

It should be kept in mind that the STATHAM transducers were used only to investigate pressure PSD's at frequencies near DC, as the PCB microphones are AC coupled. Both tests (K = 0 and K = 28) suggest that PSD's are basically flat at very low frequencies. This information has been utilized, in Chapter 4, to extrapolate the PCB measurements.

Typical point pressure PSD's and coherence are shown, for the u = 3 runs, for both the K = 0 and K = 28 cases, in Figs. N-12 and N-13 respectively. Only the K = 0 case exhibits excellent symmetry and high coherence: this is believed to stem from the absence of "interfering" cylinders between measurement points, which occurs in the K = 28 case.

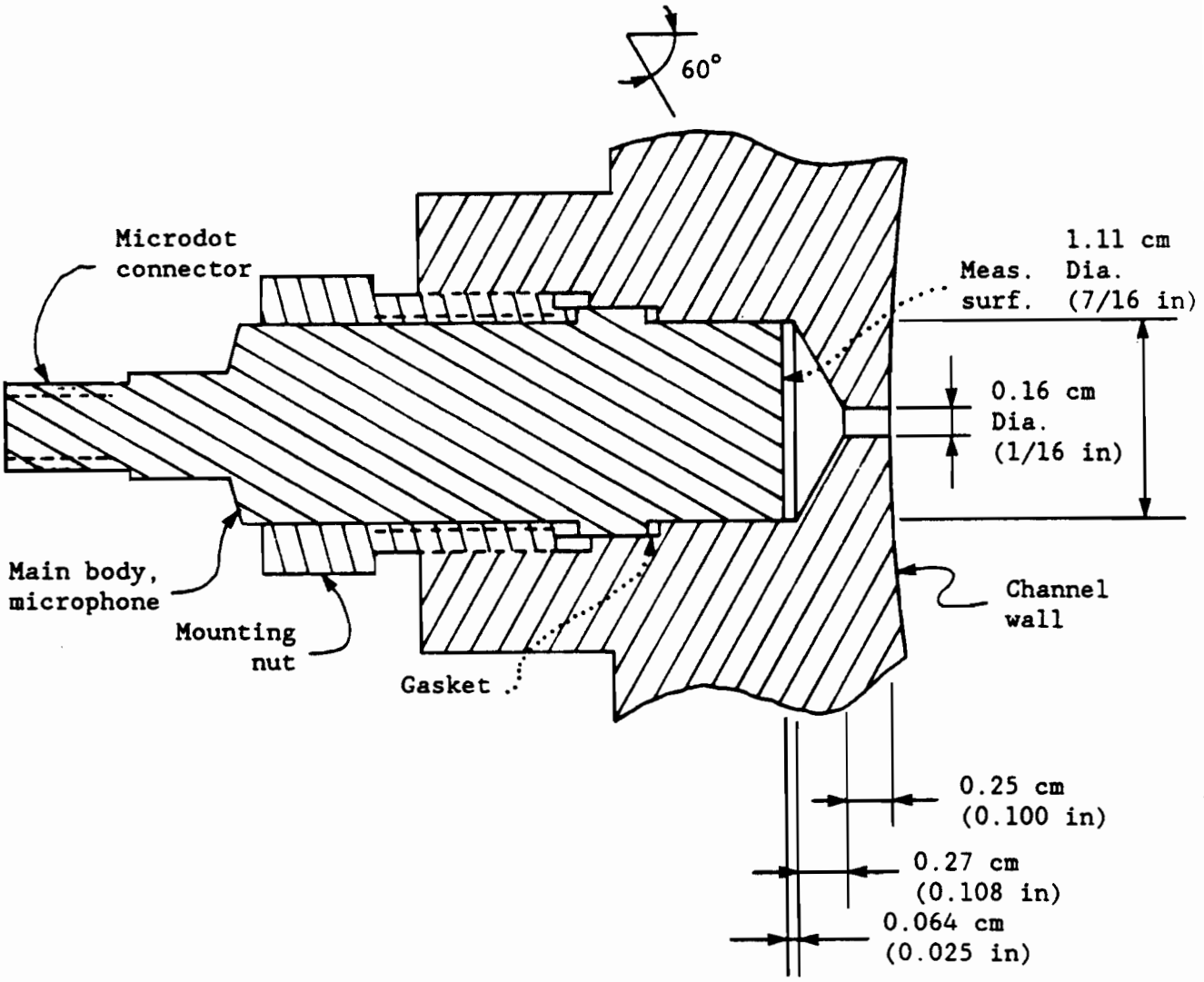

Fig.N-1: Hydraulic configuration, PCB microphone(s).

Note: The water (or air) filled area is not cross-hatched.

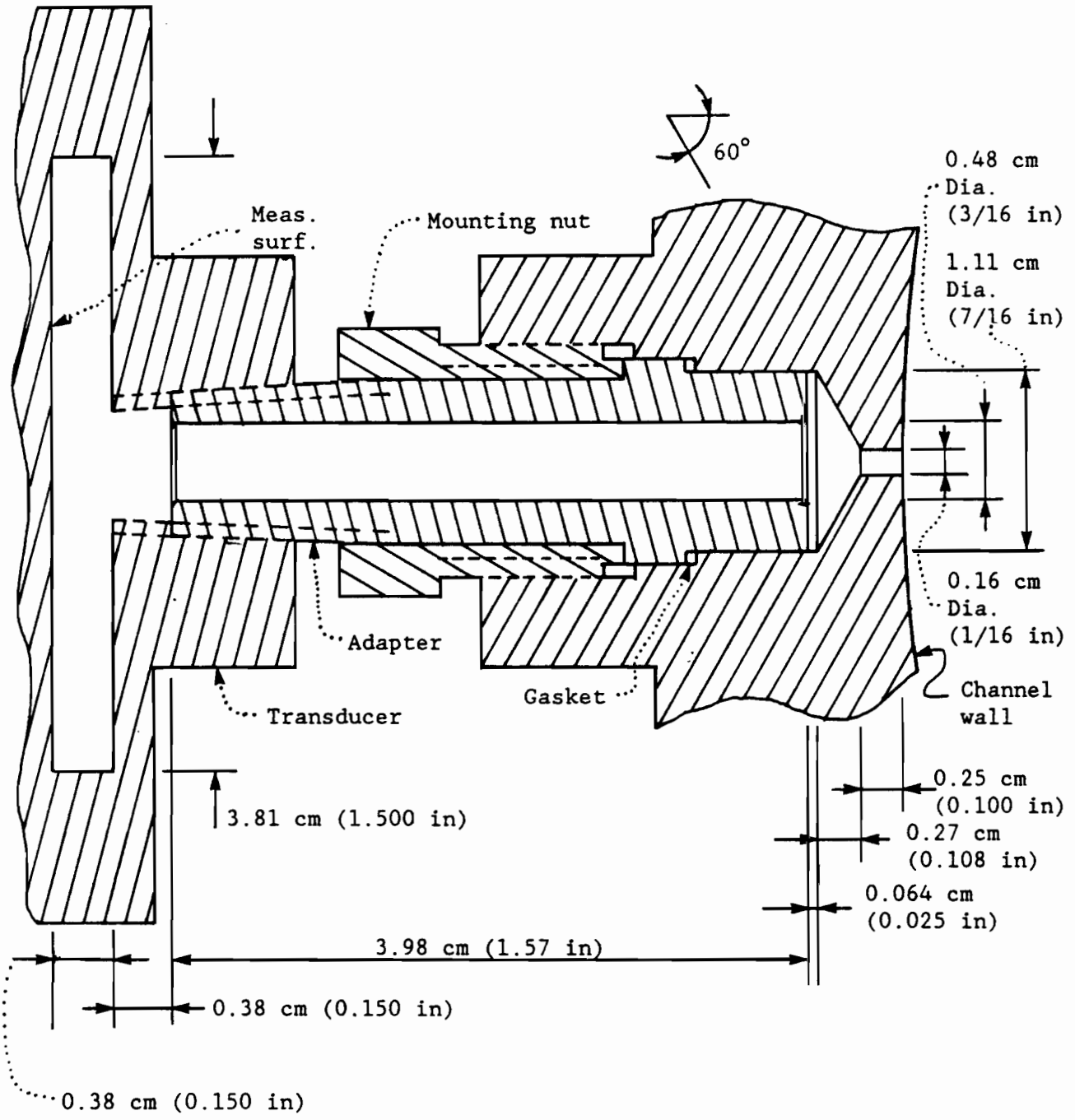

Fig.N-2: Hydraulic configuration, STATHAM transducer(s).

Note: The water (or air) filled area is not cross-hatched.

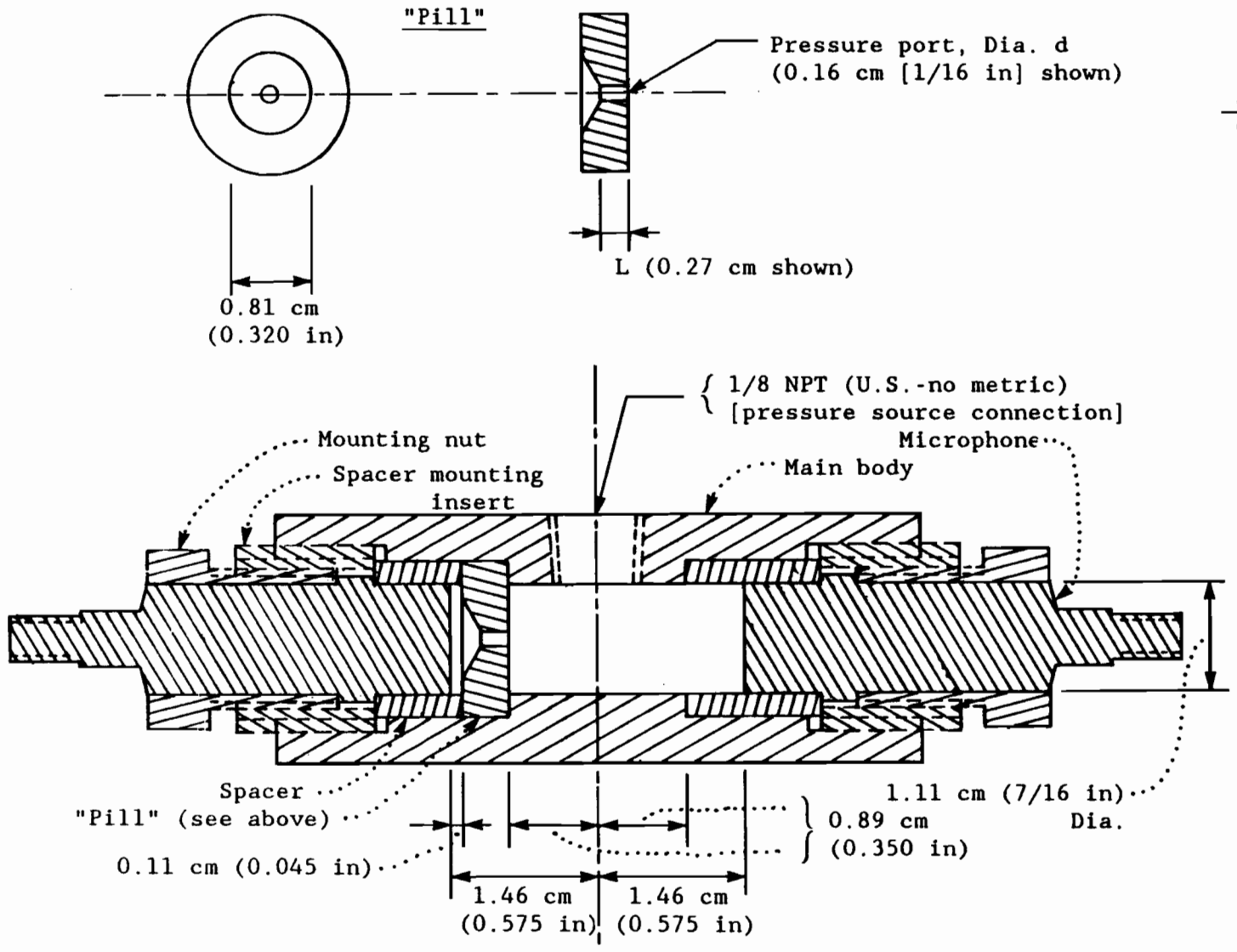

d (cm)	L (cm)
0.079	0.246
0.119	0.257
0.159	0.269
0.238	0.292
0.318	0.315

Fig.N-3: Test chamber (only important dimensions shown).

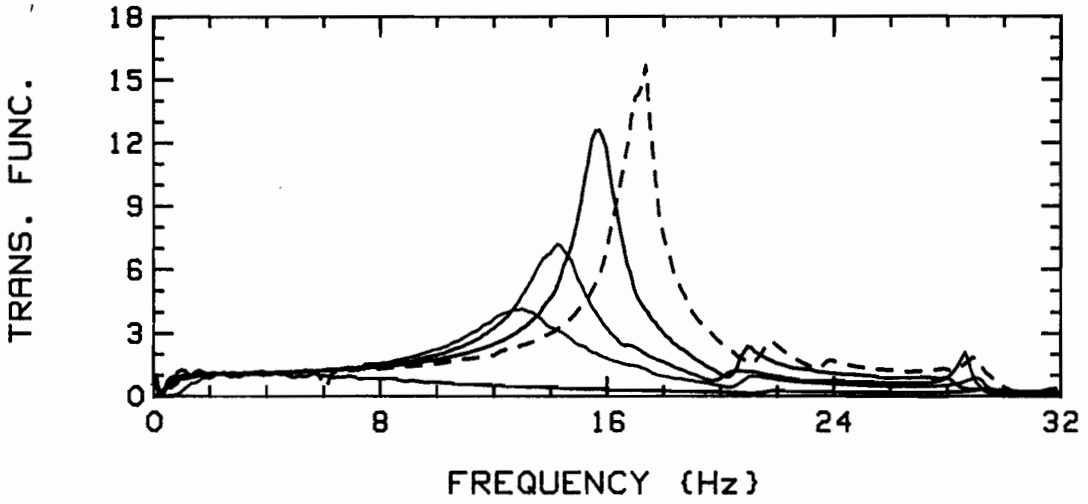

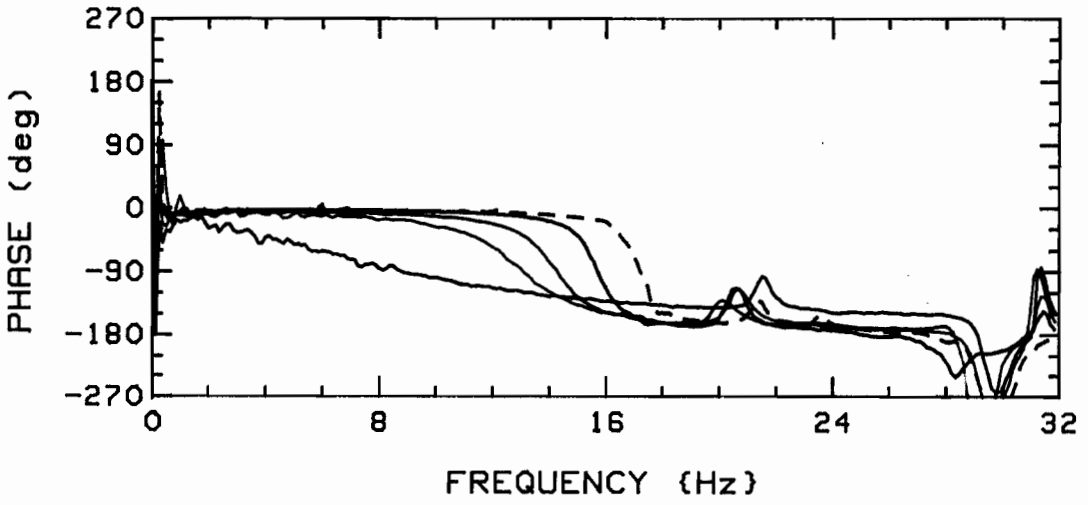

Note: The pressure port diameters were: --- (no "pill"), 0.318 cm, 0.238 cm, 0.159 cm, and 0.079 cm, corresponding to frequencies in descending order.

Fig.N-4: Transfer functions, STATHAM transducer.

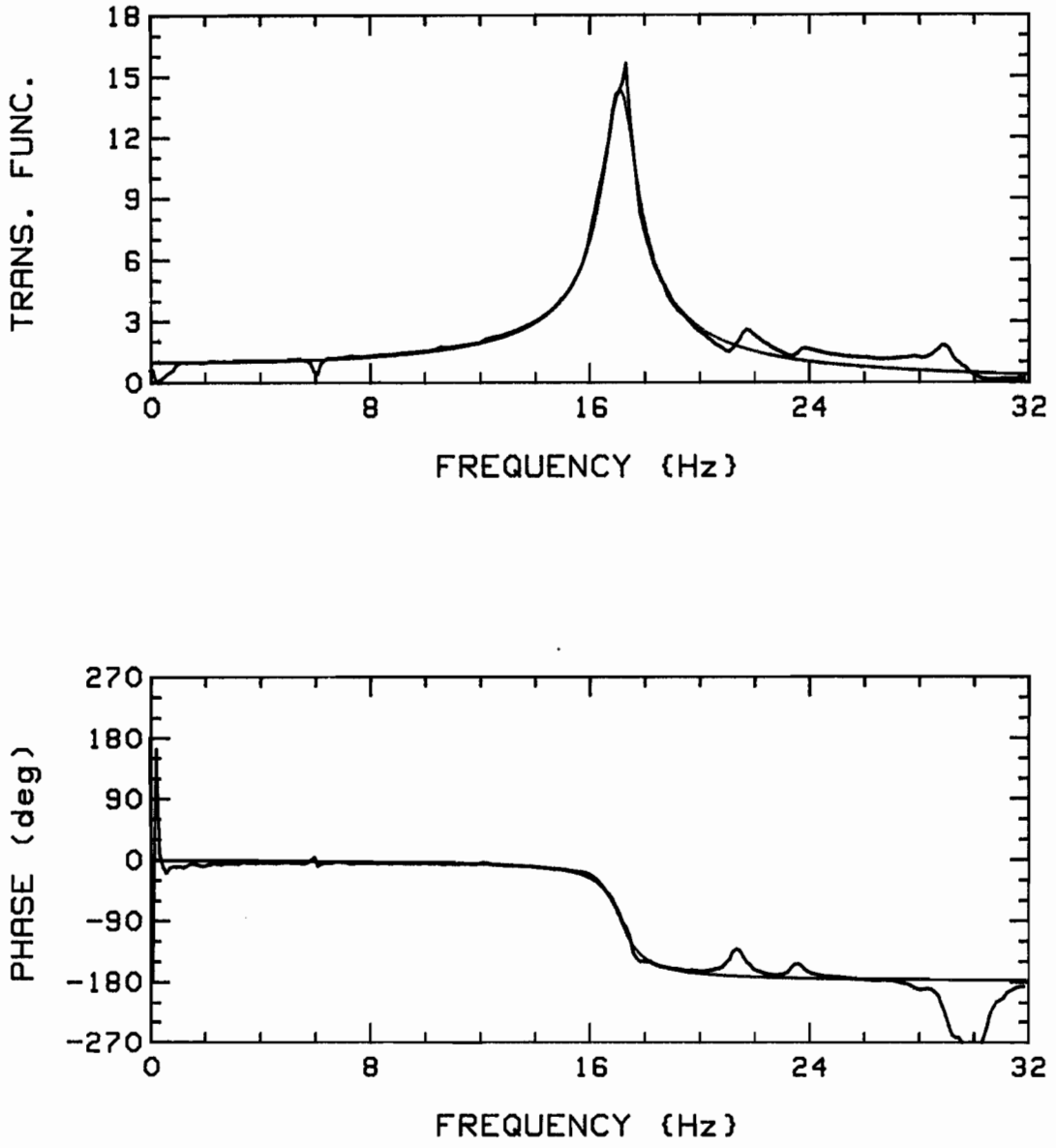

Fig.N-5a: Transfer function curve fit, STATHAM transducer, "no pill".
($f_n \simeq 17.1$ Hz, $\zeta \simeq 3.5$ %).

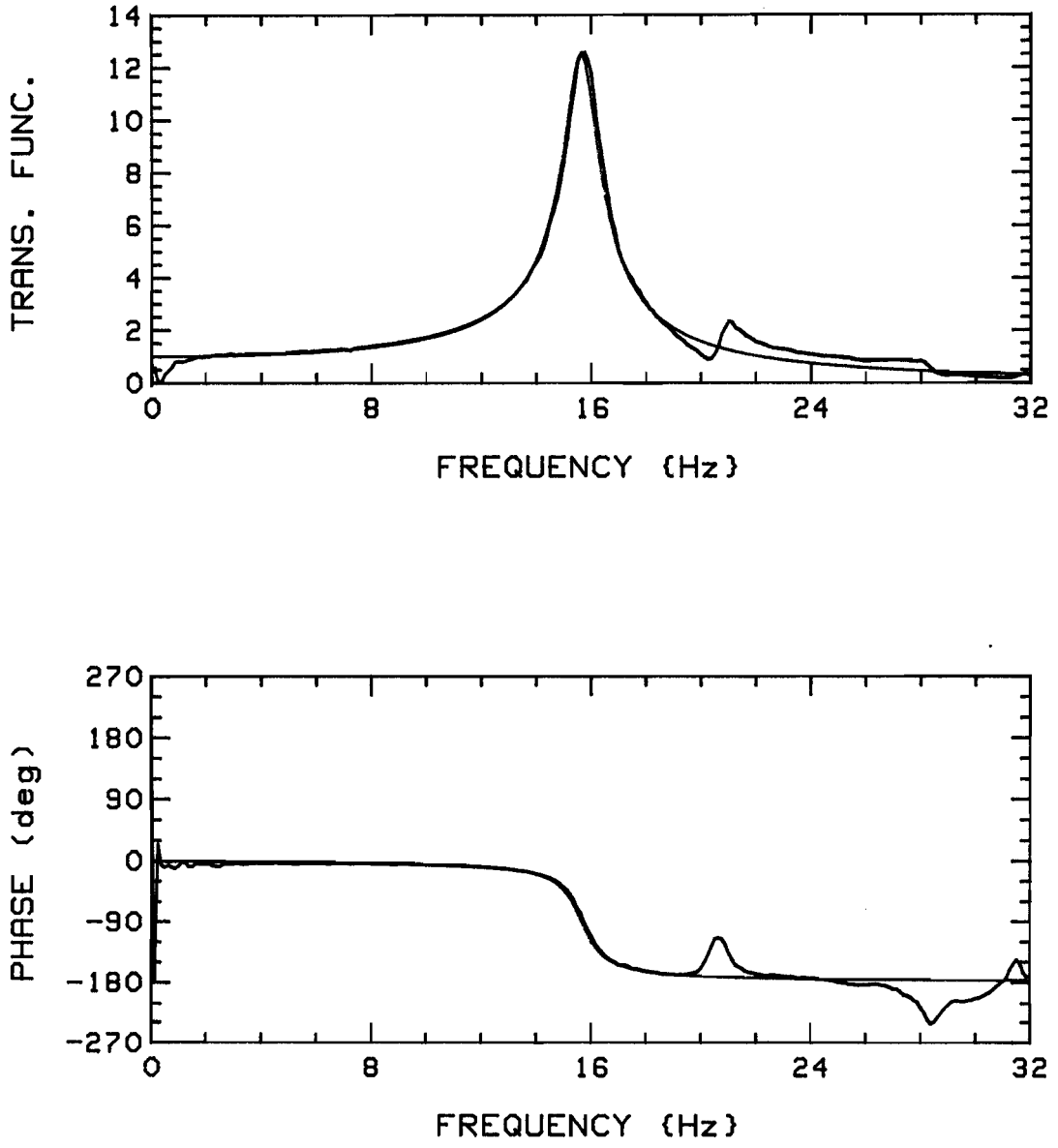

Fig.N-5b: Transfer function curve fit, STATHAM transducer, 0.318 cm dia. port. ($f_n \approx 15.6$ Hz, $\zeta \approx 4.0$ %).

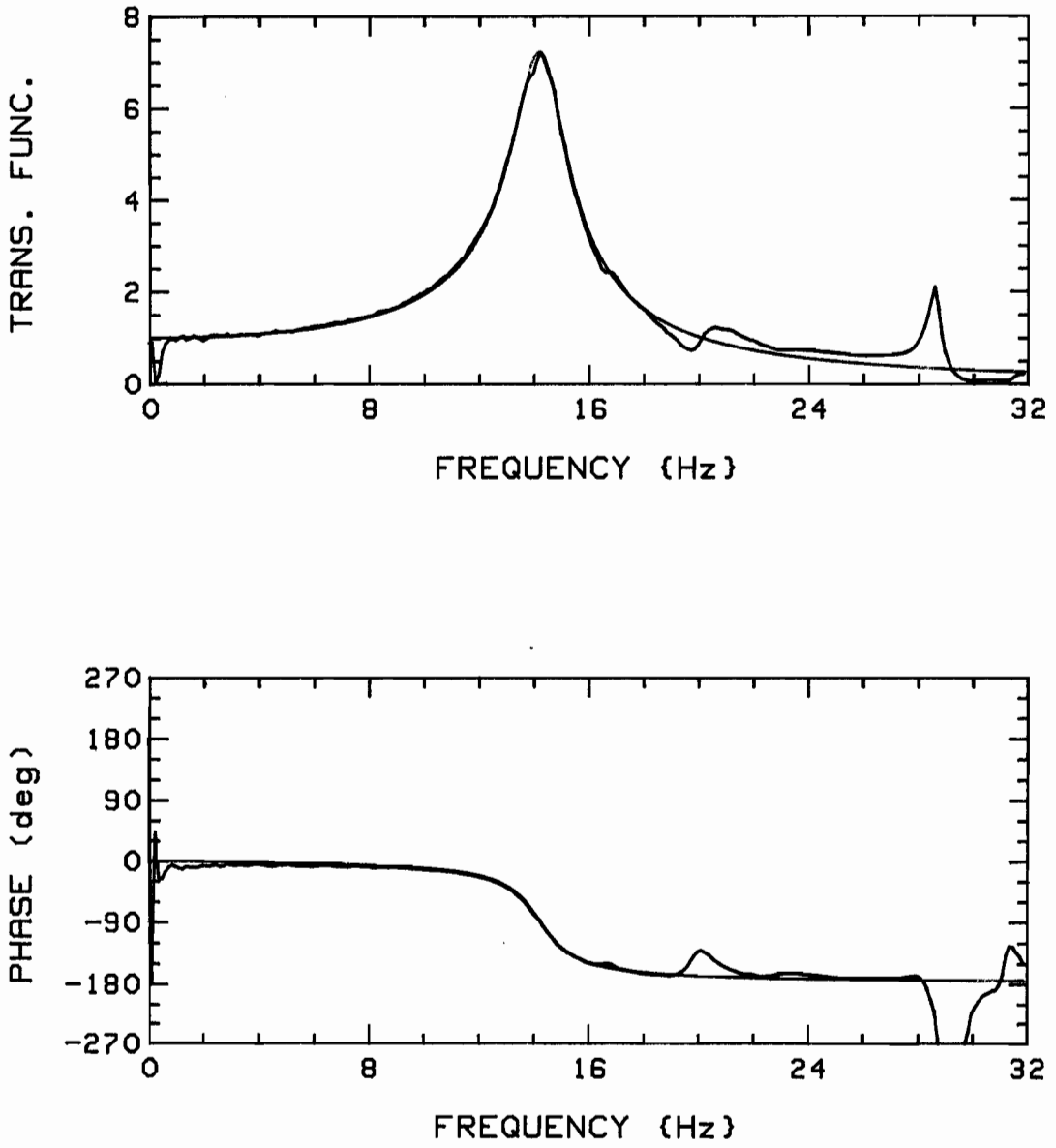

Fig.N-5c: Transfer function curve fit, STATHAM transducer, 0.238 cm dia. port. ($f_n \simeq 14.3$ Hz, $\zeta \simeq 6.9$ %).

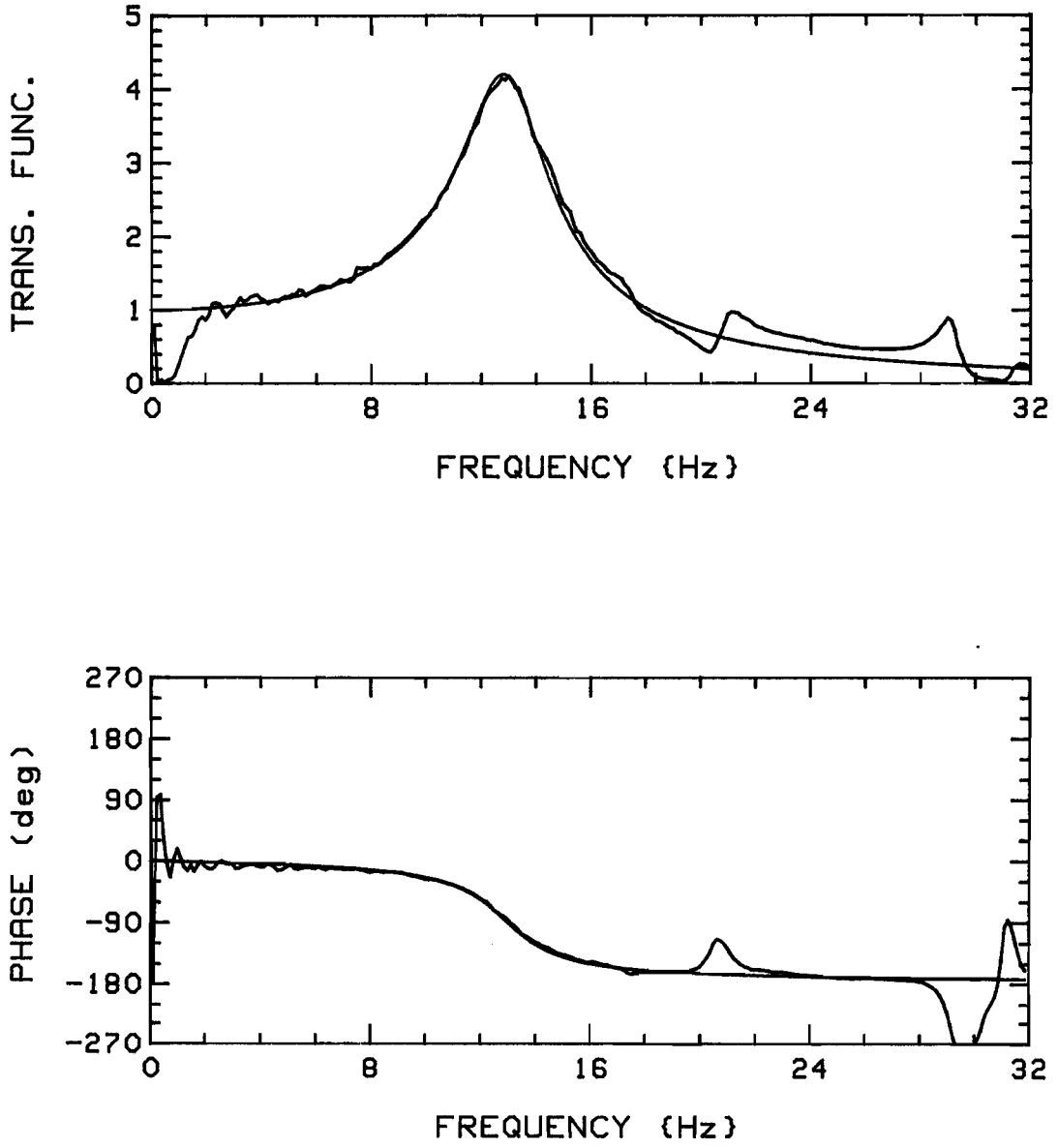

Fig.N-5d: Transfer function curve fit, STATHAM transducer, 0.159 cm dia. port. ($f_n \approx 13.0$ Hz, $\zeta \approx 12.0$ %).

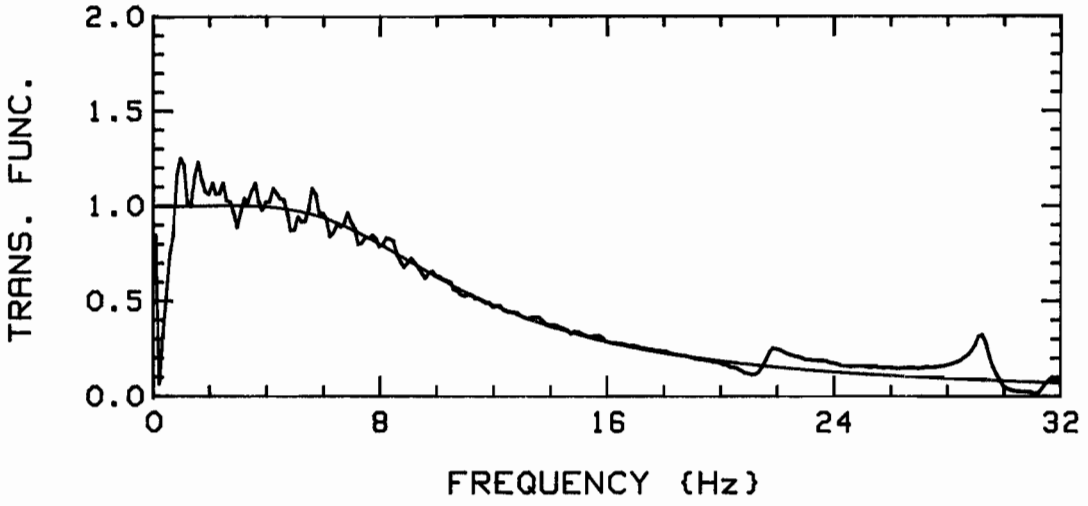

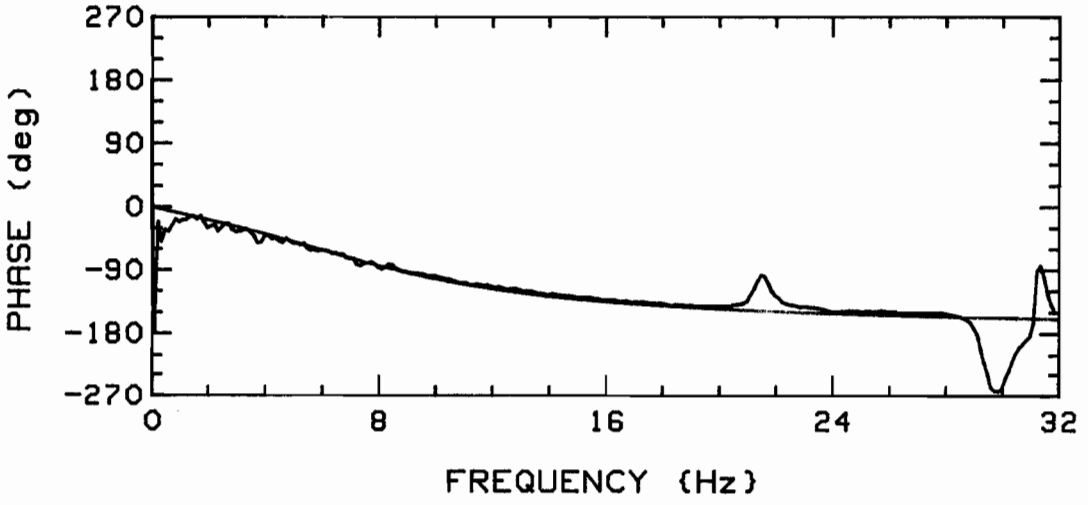

Fig.N-5e: Transfer function curve fit, STATHAM transducer, 0.079 cm dia. port. ($f_n \simeq 8.6$ Hz, $\zeta \simeq 67.1$ %).

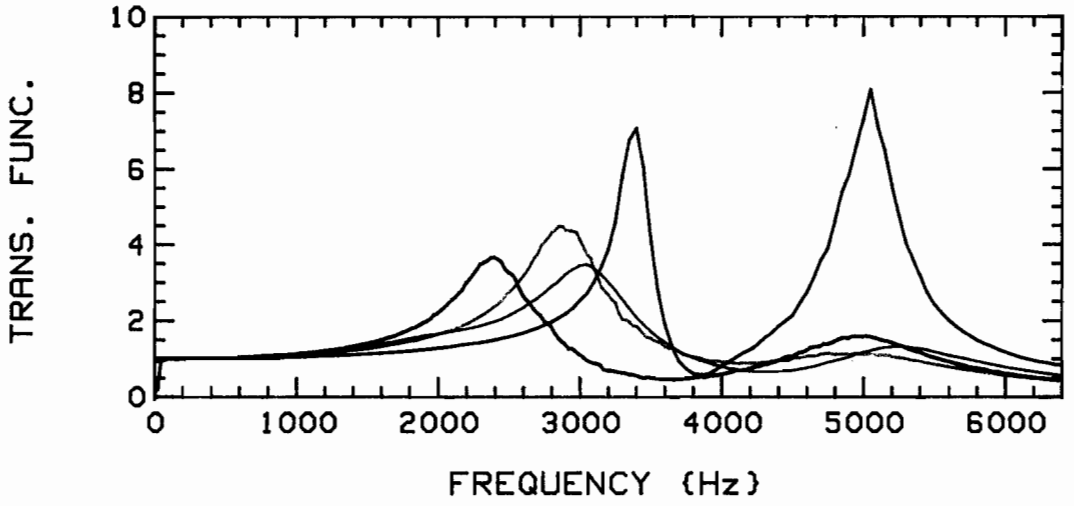

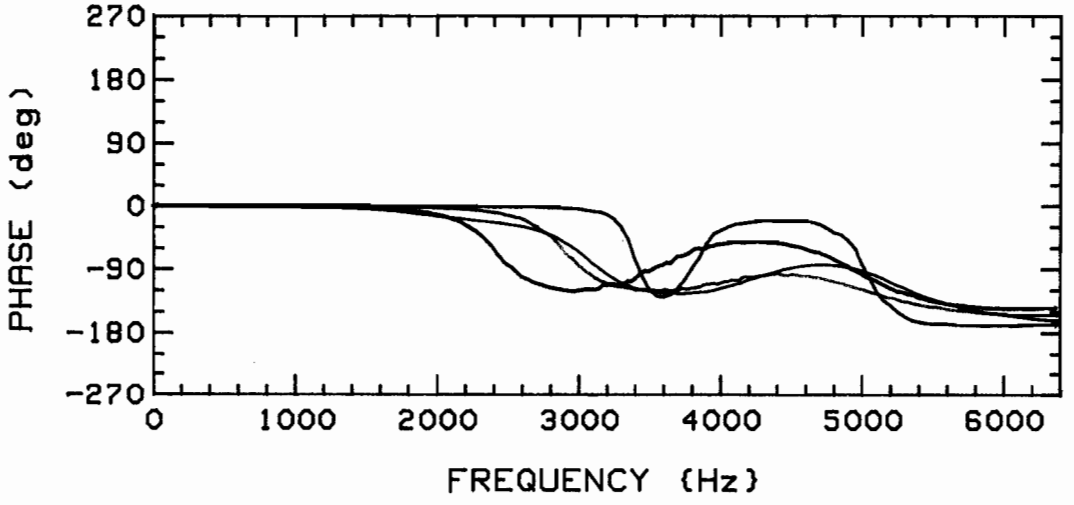

Fig.N-6a: Transfer function repeatability, PCB, 0.159 cm port.

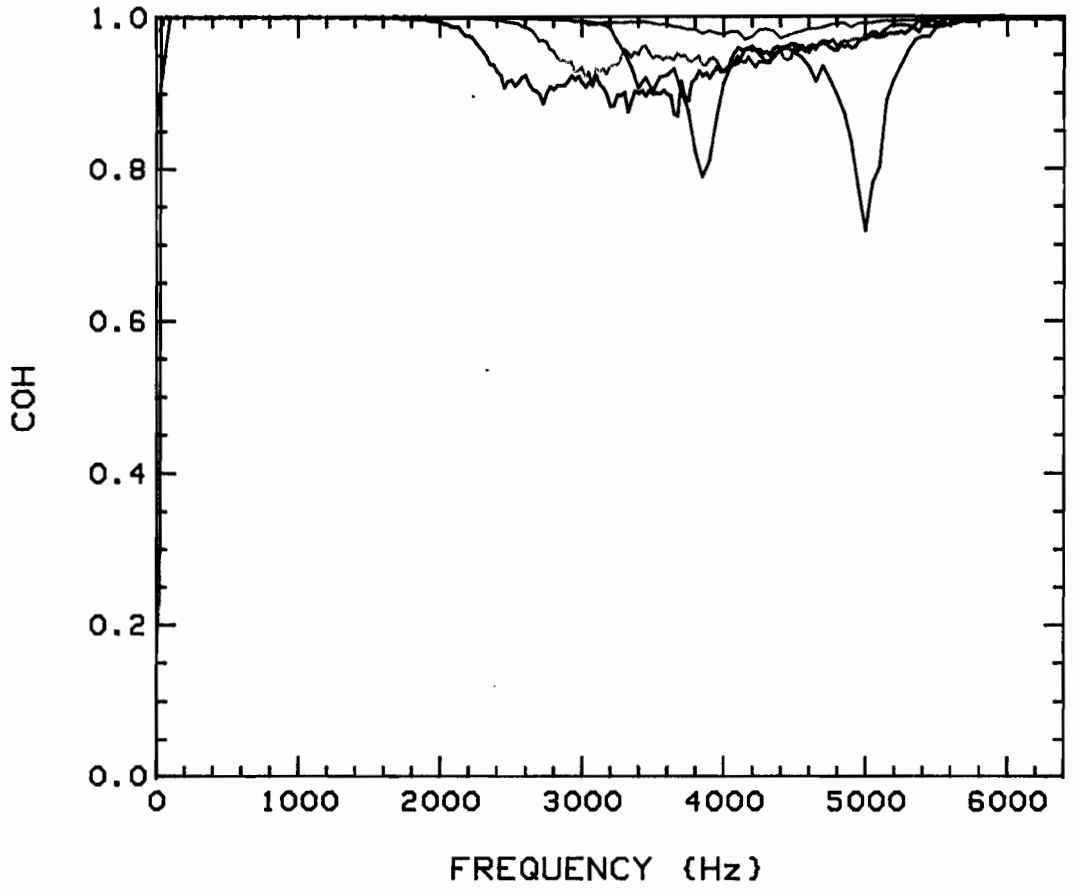

Fig.N-6b: Coherences, corresponding to the traces in Fig. N-6a.

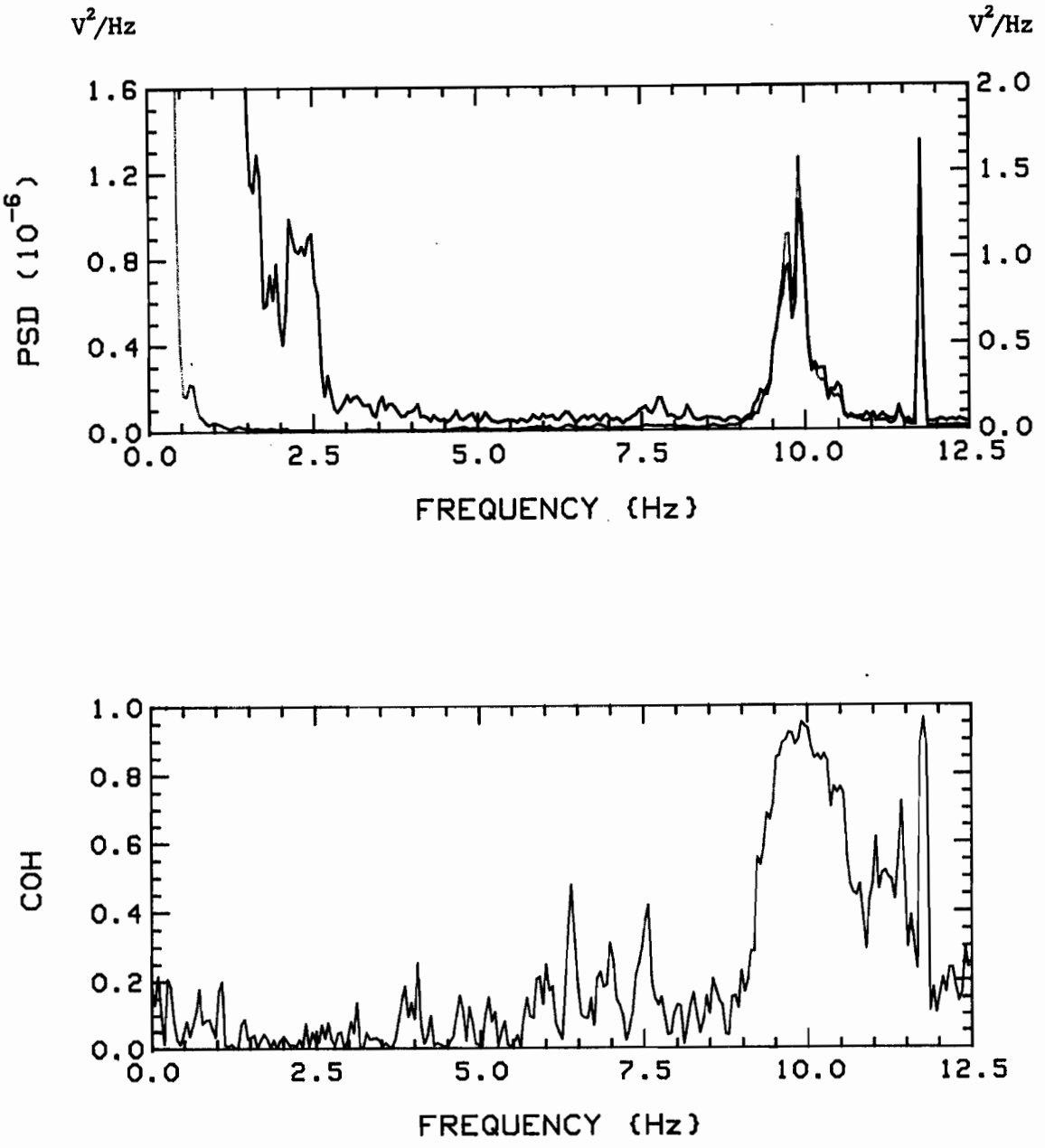

Fig.N-7: PSD's of differential pressure and acceleration, at u = 0, and corresponding coherence.

Note: PSD scales were matched from eqn. (N.17), and transducer calibration factors (inclusive of amplification): 27.59 V/psi and 8.98 V/g.

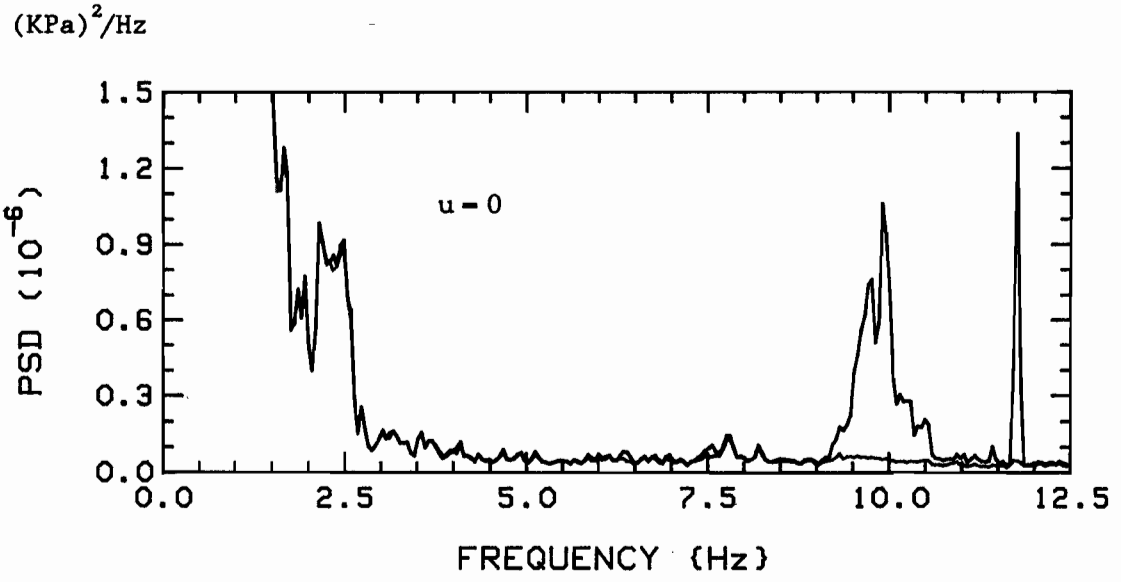

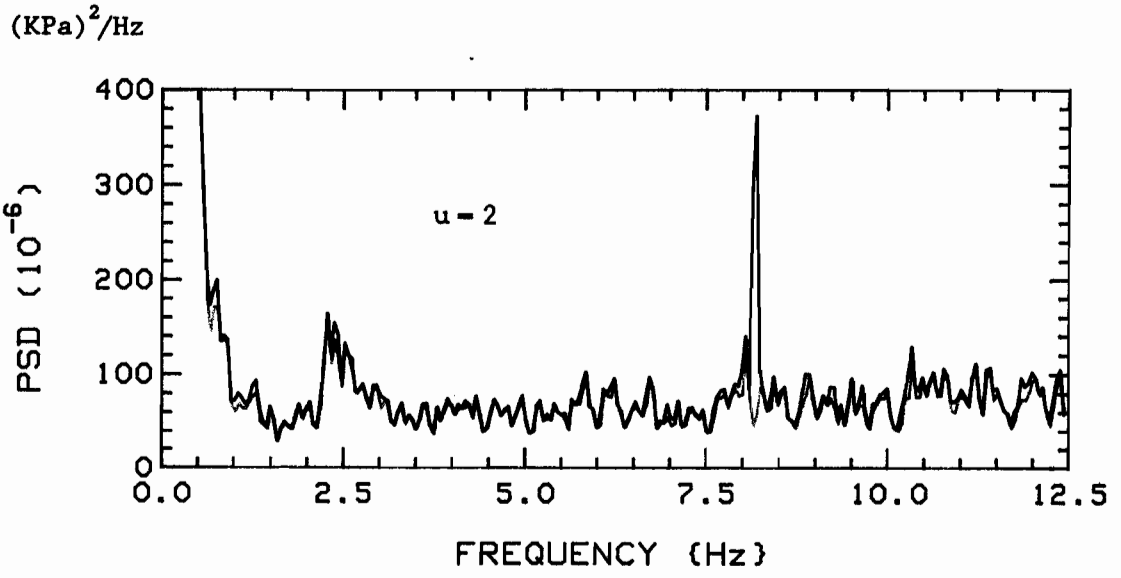

Fig.N-8: Differential pressure PSD's: Original (red) and corrected for acceleration (green).

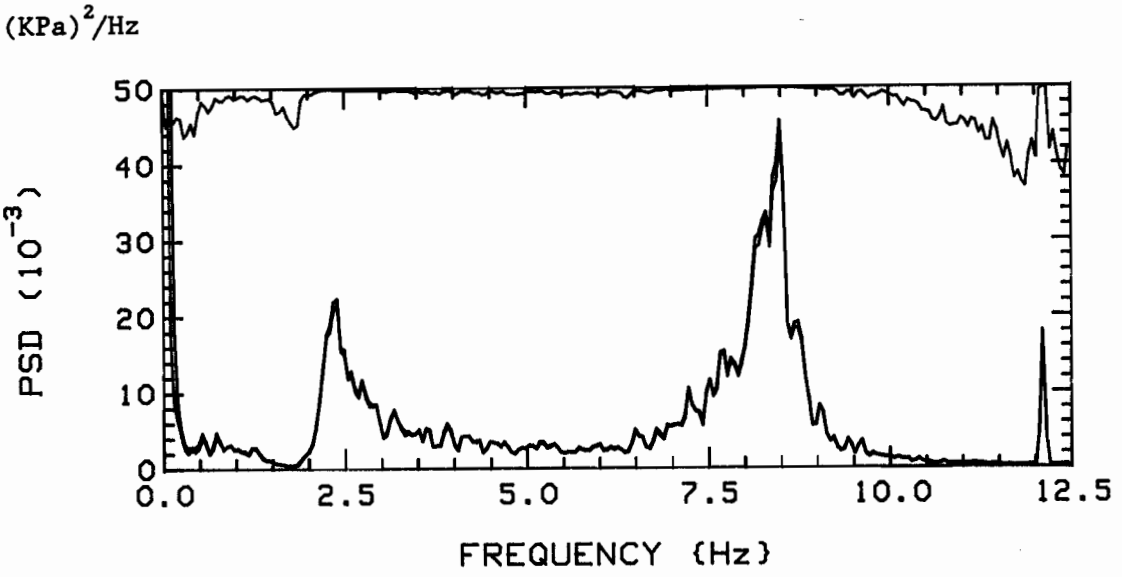

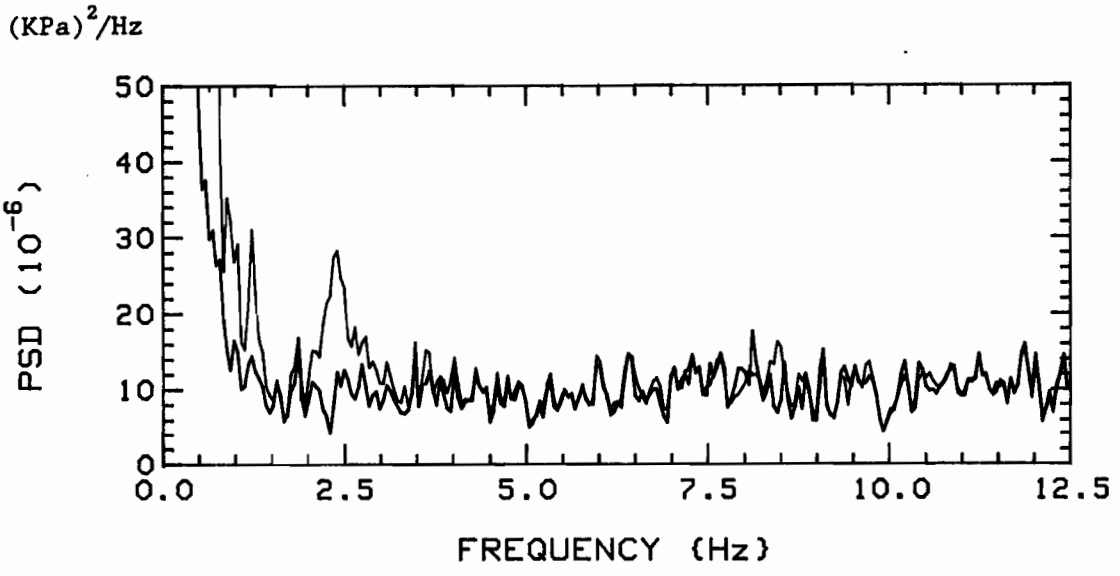

Fig.N-9: Top: Point pressure PSD's (RED and GREEN) and corresponding coherence (BLUE),
Bot.: Corresponding (single point method) differential PSD (RED), and directly measured differential pressure PSD (GREEN) [u = 3].

Note: Coherence scale is 1.

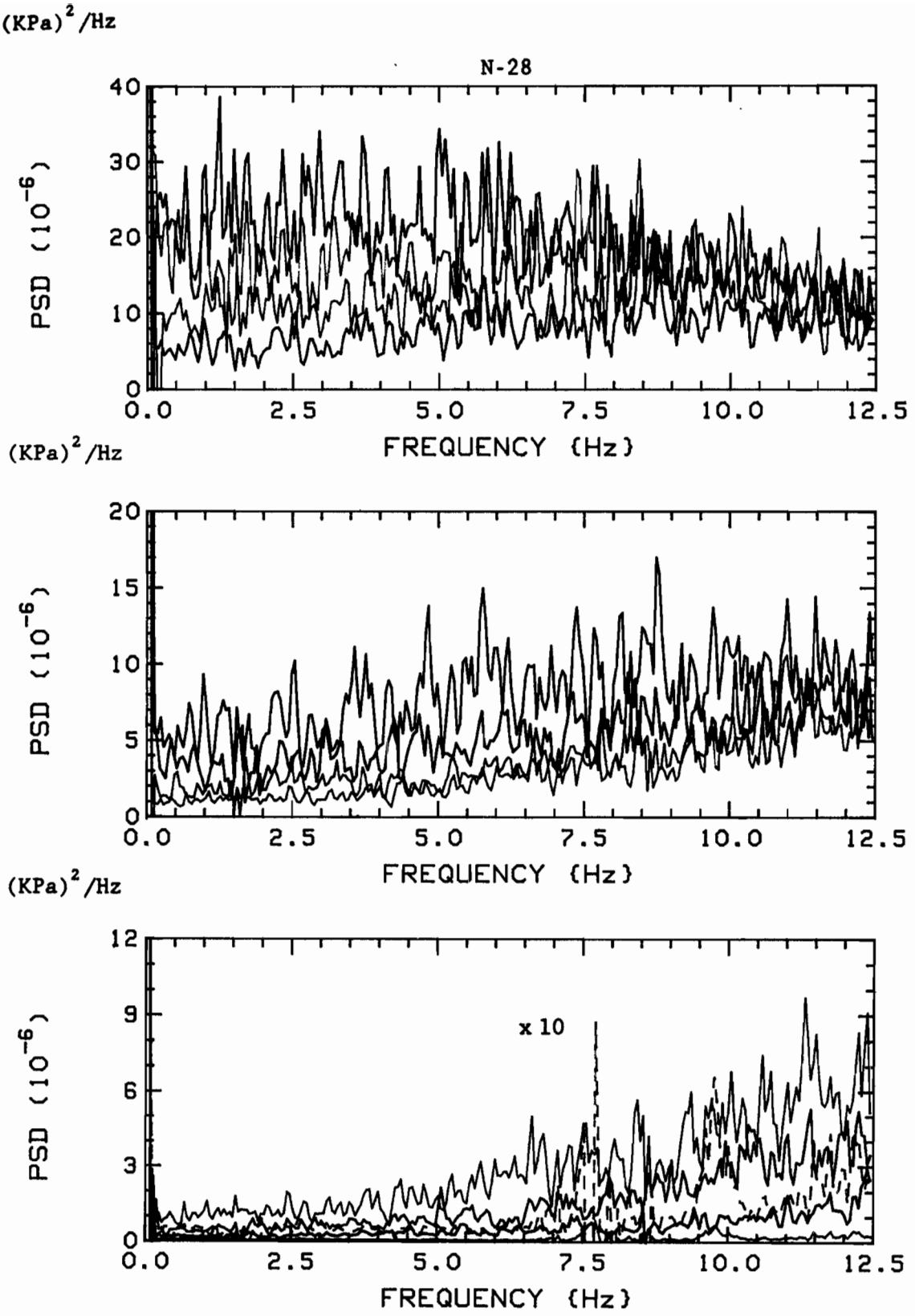

Fig.N-10a: Differential pressure PSD's, for K = 0, versus flow velocity. In descending order, u = 5.0 to 0.5, in steps of 0.5. Colour sequence: RED, GREEN, BLUE, BLACK.

Note: Last trace of each plot is repeated in the next.

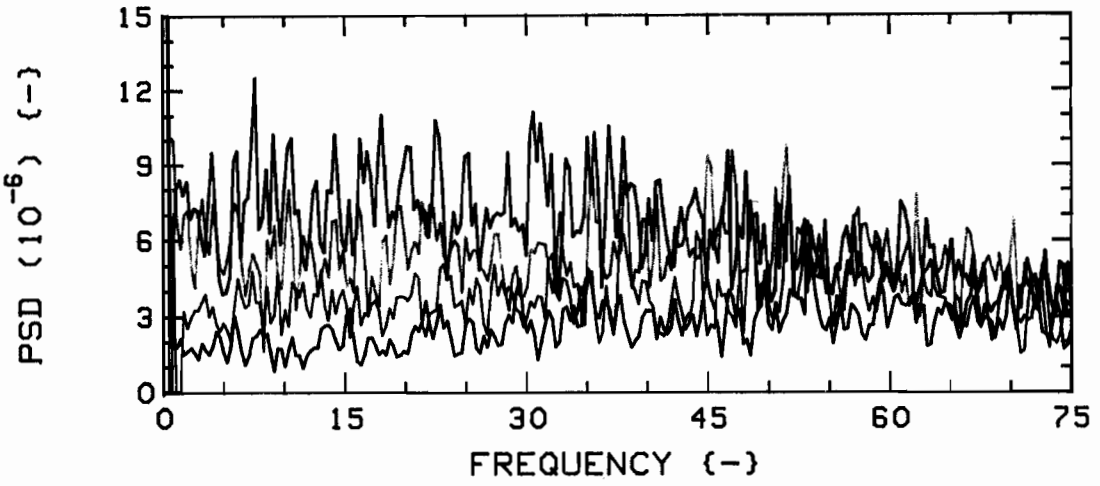

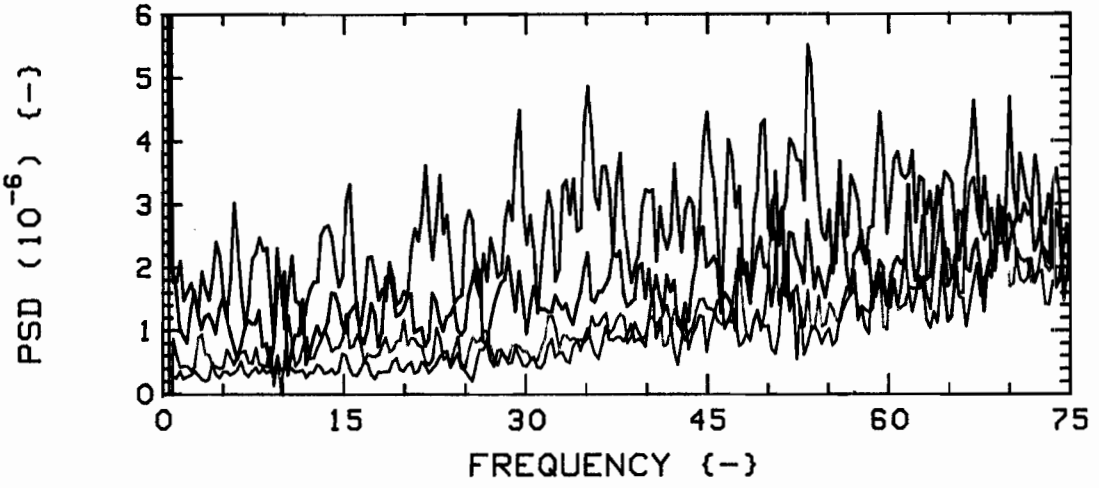

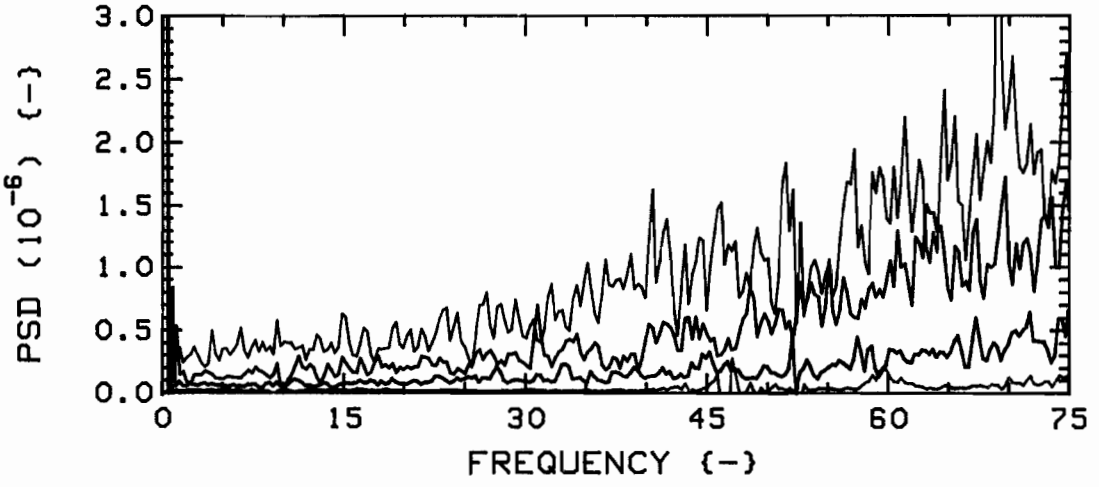

Fig.N-10b: PSD's, dimensionless single point pressure equivalent of Fig. N-10a data.

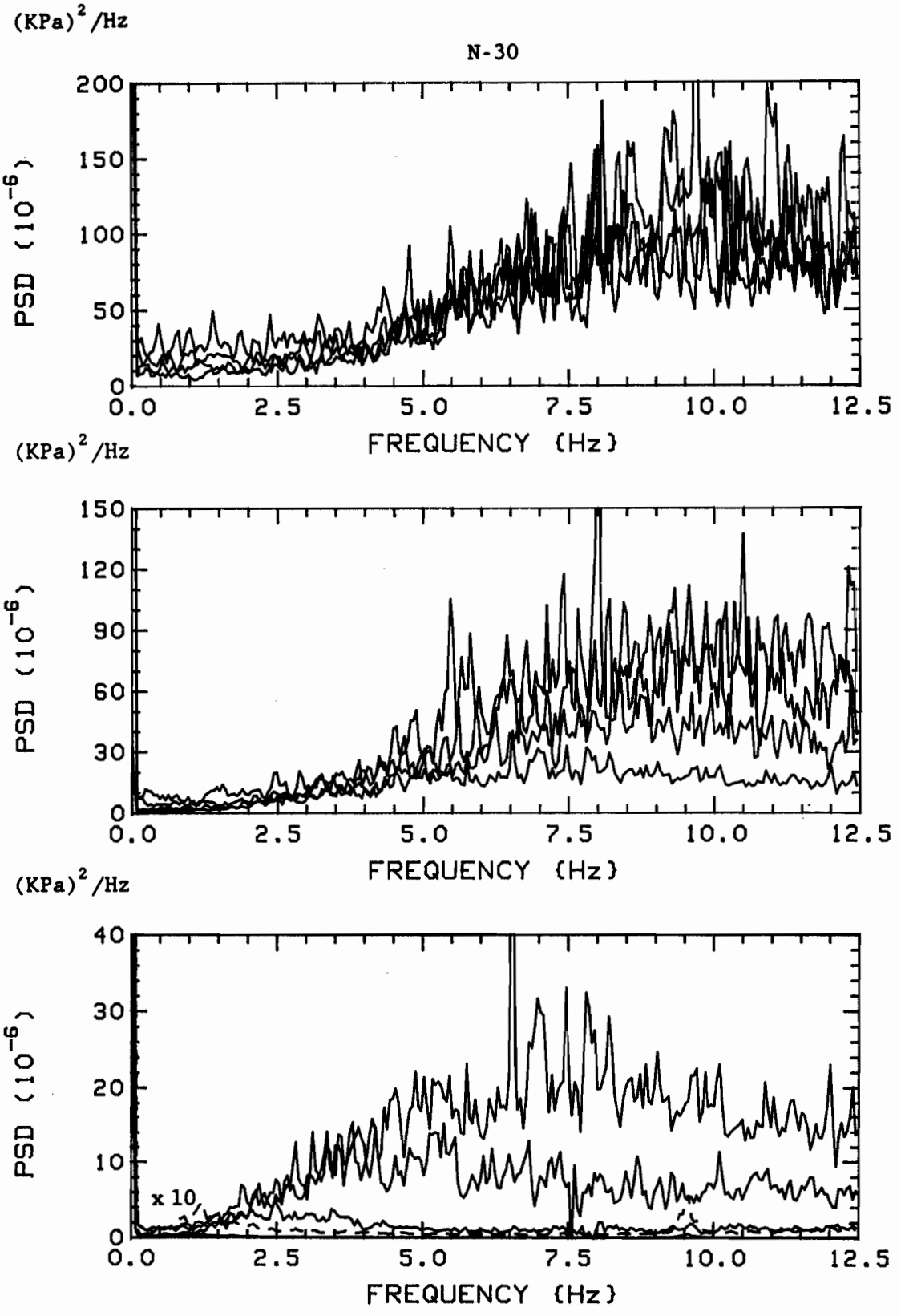

Fig.N-11a: Differential pressure PSD's, for K = 28, versus flow velocity. In descending order, u = 5.0 to 0.5, in steps of 0.5. Colour sequence: RED, GREEN, BLUE, BLACK.

Note: Last trace of each plot is repeated in the next.

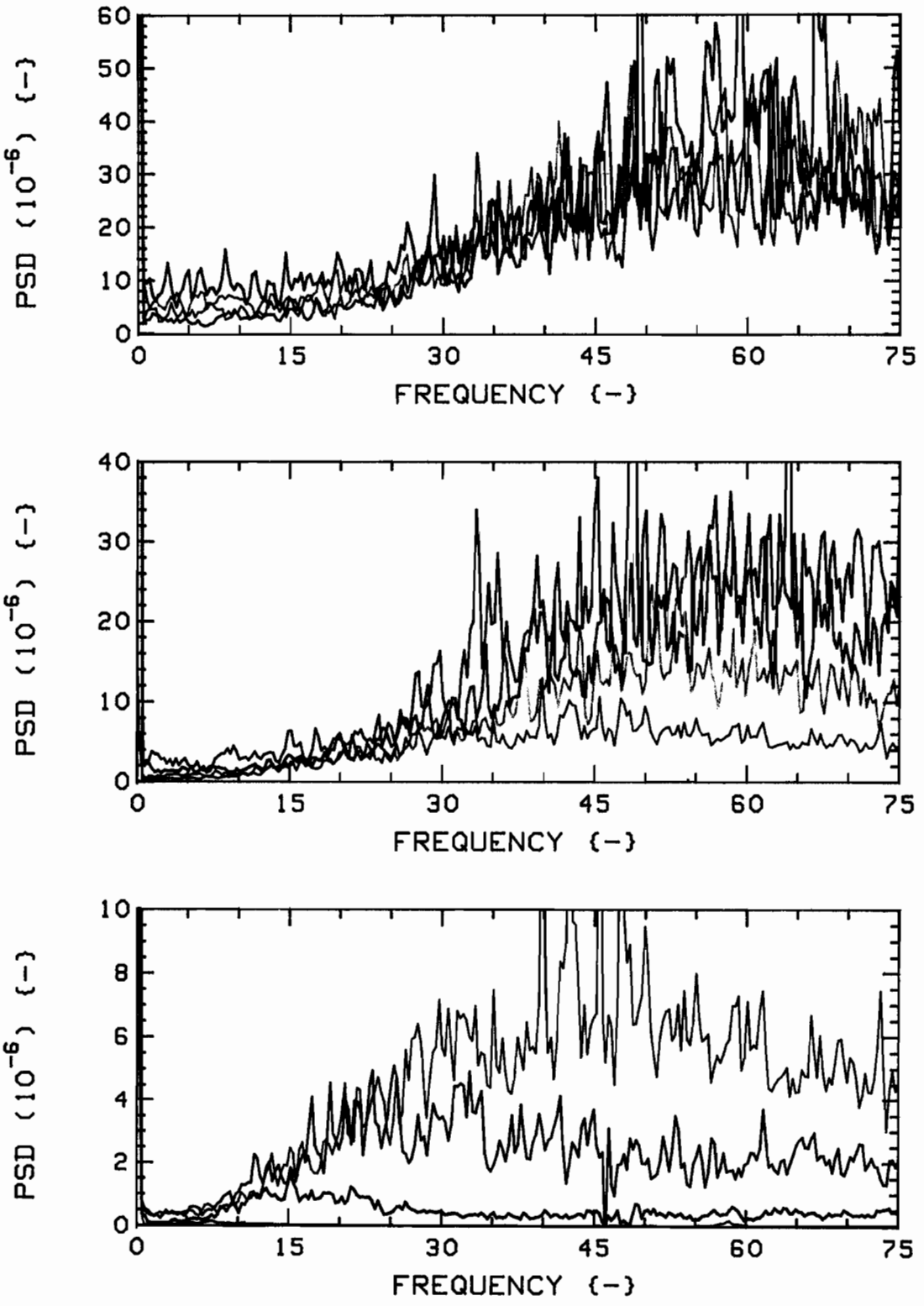

Fig.N-11b: PSD's, dimensionless single point pressure equivalent of Fig. N-11a data.

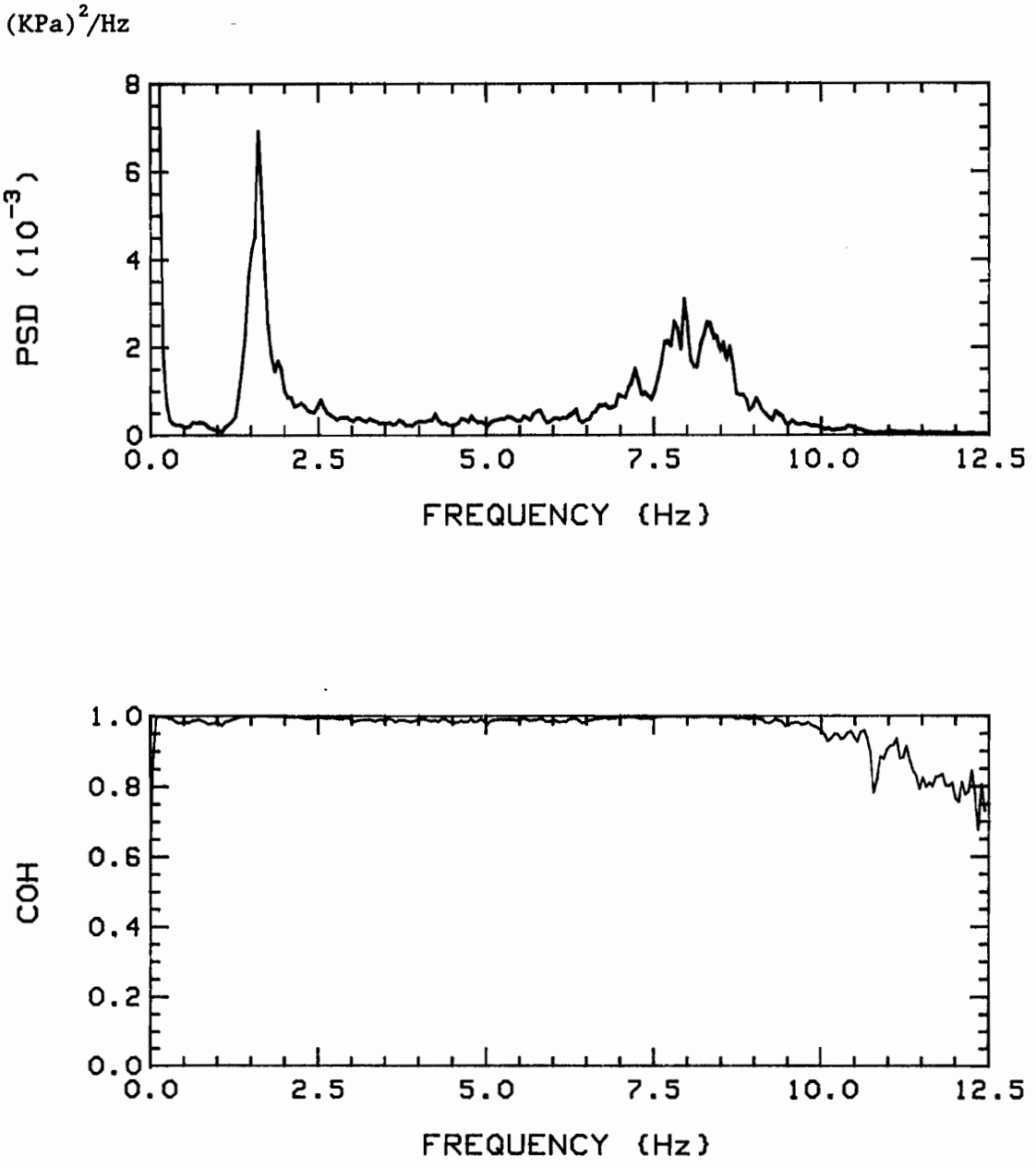

Fig.N-12: Point pressure PSD's (top) and coherence, for u = 3, K = 0.

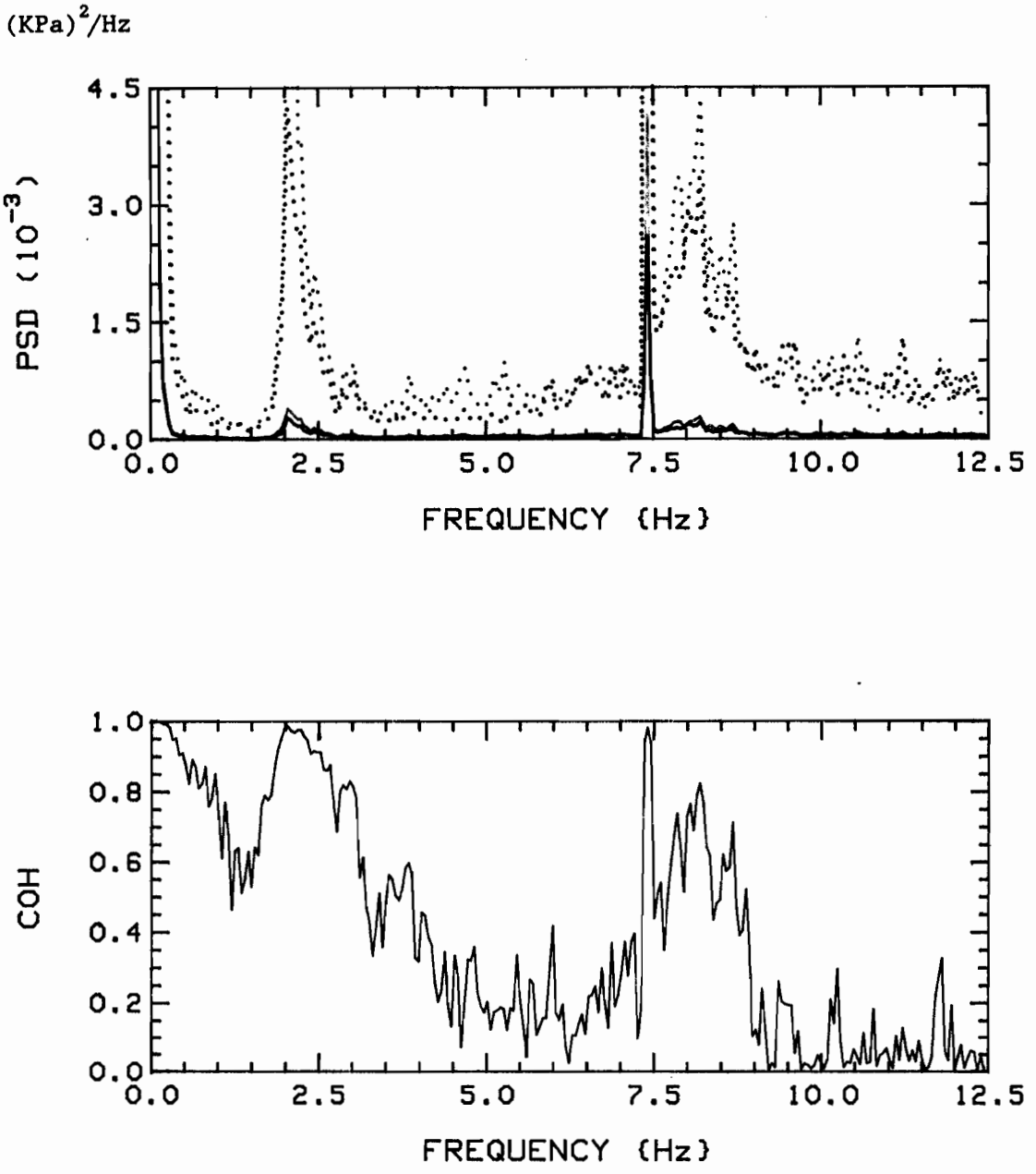

Fig.N-13: Point pressure PSD's (top) and coherence, for u = 3, K = 28.

Note: The dotted traces on top are x 15 expansions of the solid traces.

Appendix O

Pressure measurements - digital filter smoothing

As for vibration PSD's, measured pressure power spectral densities exhibit (non-repeatable) rapid fluctuations about the "mean". These pressure PSD's are to be utilized as empirical inputs to the theoretical model, and to keep the resulting theoretical PSD's "smooth", for easy differentiation with experimental data, those fluctuations were filtered out prior to their use (in the theory). Note that only the "mean" values are of interest here, as fluctuations likely stem from experimental error (in any case, having kept the pressure data intact would have made theoretically computed data more similar to the measured vibration PSD's, albeit more difficult to distinguish from the latter).

As all data was stored in digital form, the most natural way to process the information was by using a digital filter. In fact, techniques such as analog filtering would not have been possible, as they introduce phase shifts in the signal, clearly unacceptable for PSD's. Such problems can be readily compensated for in digital filtering, by following a forward pass by a rearward one (this technique, which may or may not be standard in other fields, was suggested to me by Mr. Bill Mark, of our research group). Following are the details of the particular algorithms used in this case.

In [76], P. 297, the recursive relationship for a low pass RC filter is

$$y_n = (1 - a)\, x_n + a\, y_{n-1} , \tag{O.1}$$

where y_n is the output corresponding to the input x_n (and is also a function of the previous output, y_{n-1}). The parameter a is defined as

$$a = e^{-\Delta t/RC} , \tag{O.2}$$

where Δt is the sample point "time" (in this case frequency) spacing, and RC is a "time" constant. The (dimensionless) parameter a will be assigned a value based on trial and error (to be illustrated graphically shortly).

Multiple (in forward-rearward pairs) passes shall be used, which is the equivalent of a cascaded, hence higher order filter. The number of passes, as for the parameter a, is also determined by trial and error.

Before filtering can be effected on a given PSD trace*, a scheme has to be devised for handling data at both ends: for example, for data point number one (zero frequency in this case), namely x_1, there is no y_{1-1} data. This problem could be circumvented by starting the filtering procedure at point two, in which case $x_1 = y_{2-1} = y_1$ and x_2 are both available to compute y_2, but this produces two problems, specifically (i) the next pass has to start at point three, since there is no new data at point one (and so on for subsequent passes), and (ii) large DC offsets (zero frequency) caused by voltage drifts produce unwanted (nonexistent) signal power at low frequencies. Particularly in view of solving the latter problem, an extrapolation scheme was devised, as detailed below.

First, it must be noted that pressure data obtained from measurements with DC coupled pressure transducers indicate that PSD levels are essentially constant near zero frequency. Moreover, because of superior characteristics, such as higher bandwidth and stiffness, hydrophones were used for final measurements; but the latter, being AC coupled, do not yield data at very low frequencies. Therefore, the extrapolation scheme to be used should tend to produce constant PSD's at low frequencies. Finally, it was found (to be seen graphically shortly) that the same scheme worked well at the upper end also, as the data there usually changes slowly and monotonically.

To recap, the desired trace values near the ends must: (i) have values close to those slightly away from the ends, and (ii) have a slope matching that slightly away from the ends. This can be accomplished fairly effectively by extrapolating as follows:

---

* Exactly the same procedure would apply for a time trace.

Let the original data points vector be X(I), I = 0,N. Let each extrapolated point be such that the generated traces (at each end) are the inverted (pivoted about the end point(s)) mirror image of the main trace, as illustrated below.

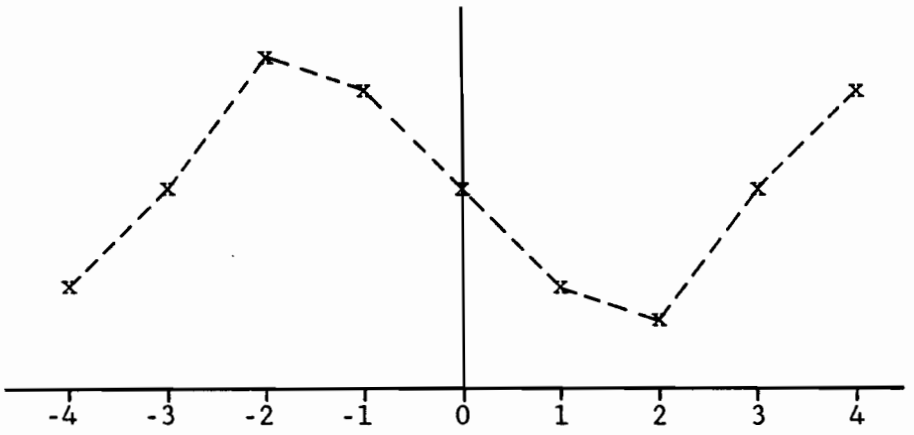

Therefore, we have

$$X(-I) = 2 \cdot X(0) - X(I) , \qquad I = 1,2,\ldots,M , \tag{0.3}$$

for the lower end, and

$$X(N+I) = 2 \cdot X(N) - X(N-I) , \qquad I = 1,2,\ldots,M , \tag{0.4}$$

for the upper end. The constant M represents the number of extrapolated points (taken as equal at both ends).

If we let the number of passes (forward and rearward) be P, we may now summarize the method.

SUMMARY

Given a set of data points X(I), I = 0,1,2,...,N to be filtered.

(i) Set the parameter a (0 < a < 1), which basically determines the low pass cutoff "frequency" (when data is versus "time"),

(ii) Set the number of extrapolated points, M. Recall that this applies at both ends.

(iii) Set the number of passes, P. This is equivalent to cascading filters, yielding sharper cutoffs.

For each pass, the computation procedure is:

(a) New points are defined, at each end, using eqs.(0.3) and (0.4).

(b) Forward filtering is effected, utilizing eqn.(0.1), sequentially, for $n = (-M+1)$ to $n = (M+N)$ [n incremented].

(c) This is followed by rearward filtering, for $n = (M+N-1)$ to $n = (-M)$ [n decremented].

Note that a new set of extrapolated points is generated at each (forward/rearward) pass.

Original and filtered data are presented in Chapter 4, Section (b).

Remark

The data to be smoothed stems from measurements with AC coupled PCB pressure transducers, which yield unreliable low (near zero) frequency data: an extra parameter shall be used to determine the index below which data is to be extrapolated, as follows

$$X(I) = X(B), \quad I = 0,1,2,\ldots,B. \tag{0.5}$$

B is the new low frequency extrapolation parameter. Its value is based on measurements with DC coupled STATHAM pressure transducers (see Appendix N).

FLUID COUPLING AND RESPONSE CHARACTERISTICS OF CYLINDER CLUSTERS IN AXIAL FLOW

by

Jean O. Gagnon
Department of Mechanical Engineering
McGill University, Montreal

July 1989

VOLUME 2: FIGURES

A Thesis submitted to the Faculty of Graduate Studies and Research in partial fulfillment of the requirements for the Degree of Doctor of Philosophy

© Jean O. Gagnon 1989

Table of Contents

Volume 2

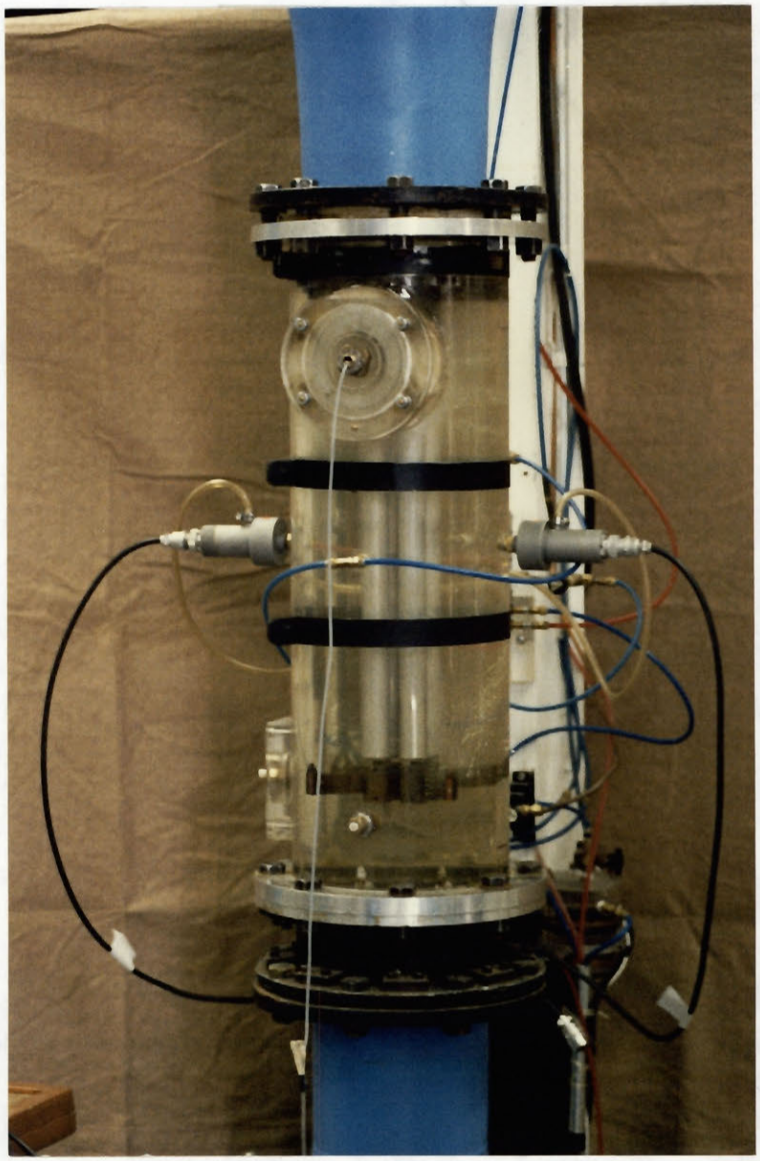

Fig.1: Typical cylinder bundle in test channel.

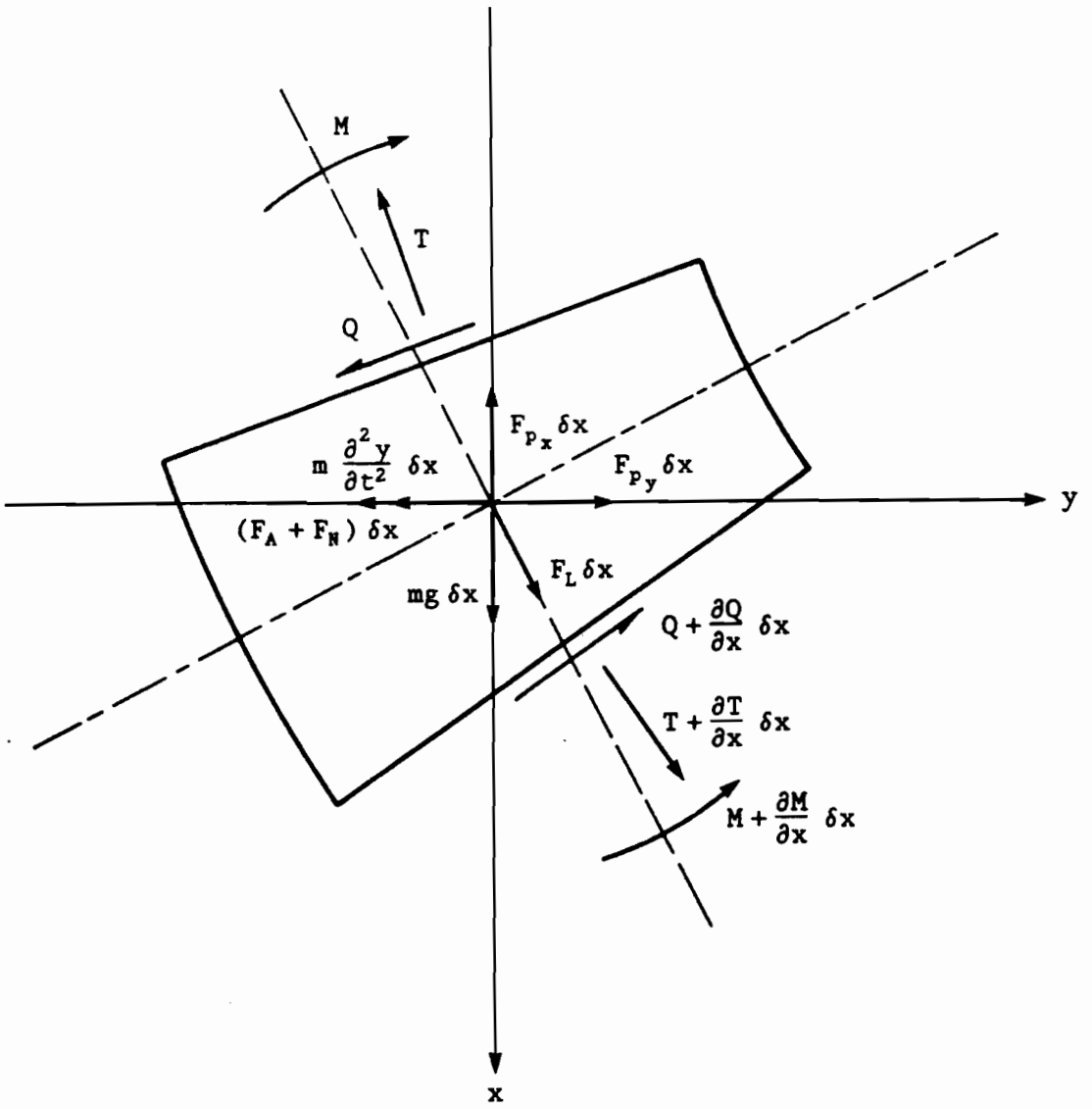

Fig.2: Forces and moments balance on an element of cylinder, in the x-y plane.

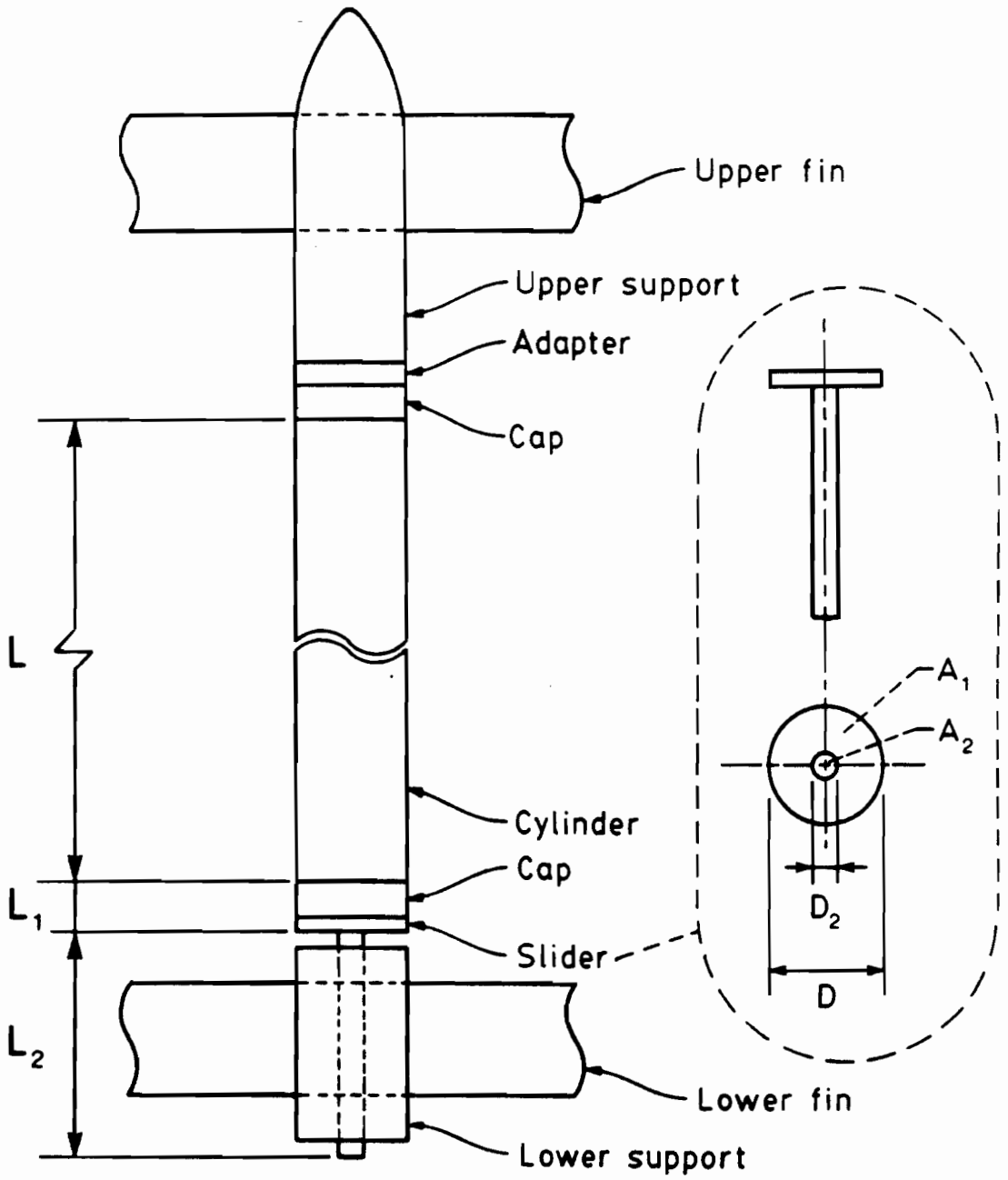

Fig.3: Cylinder mounting.

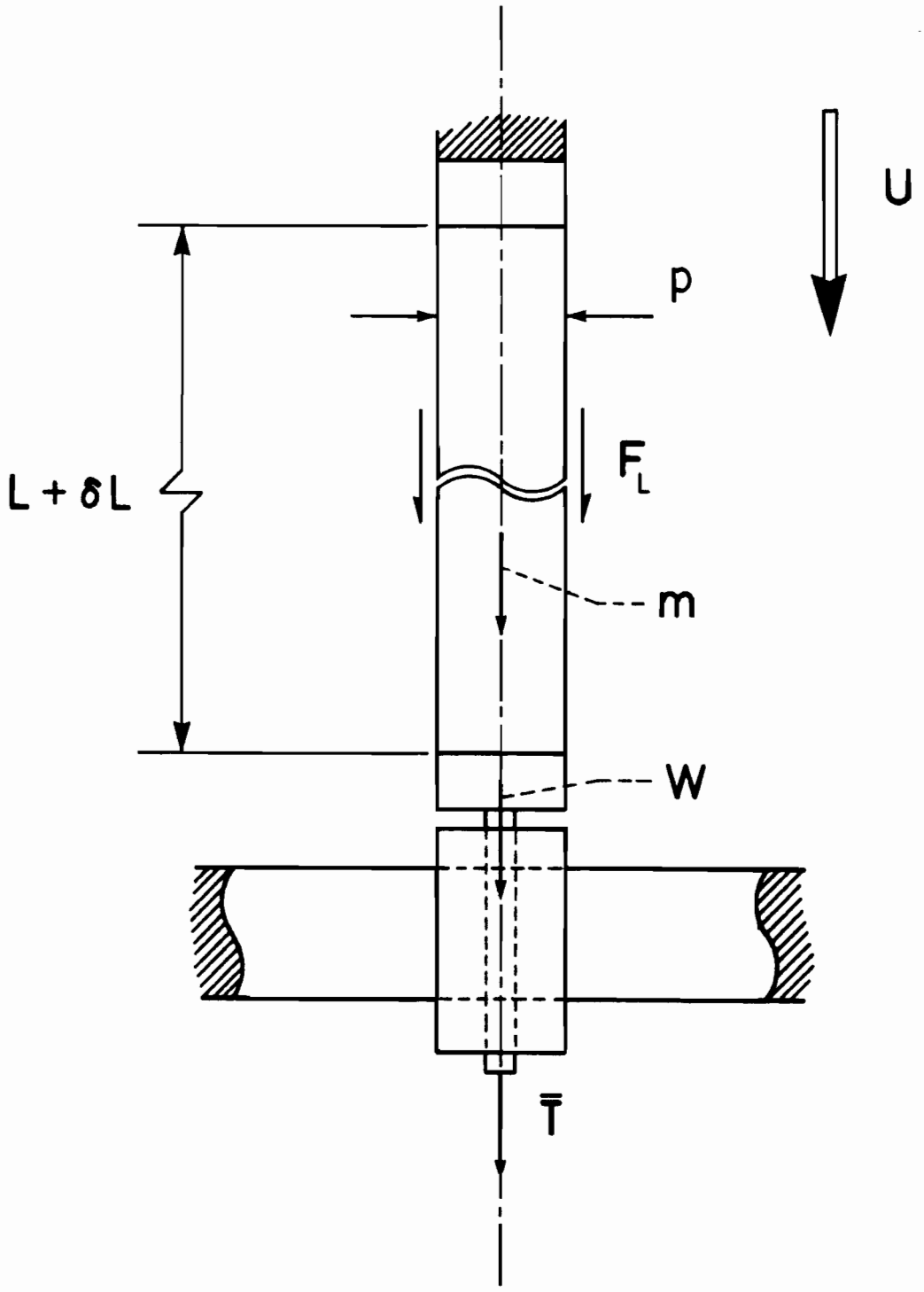

Fig.4: Forces acting at clamped downstream end.

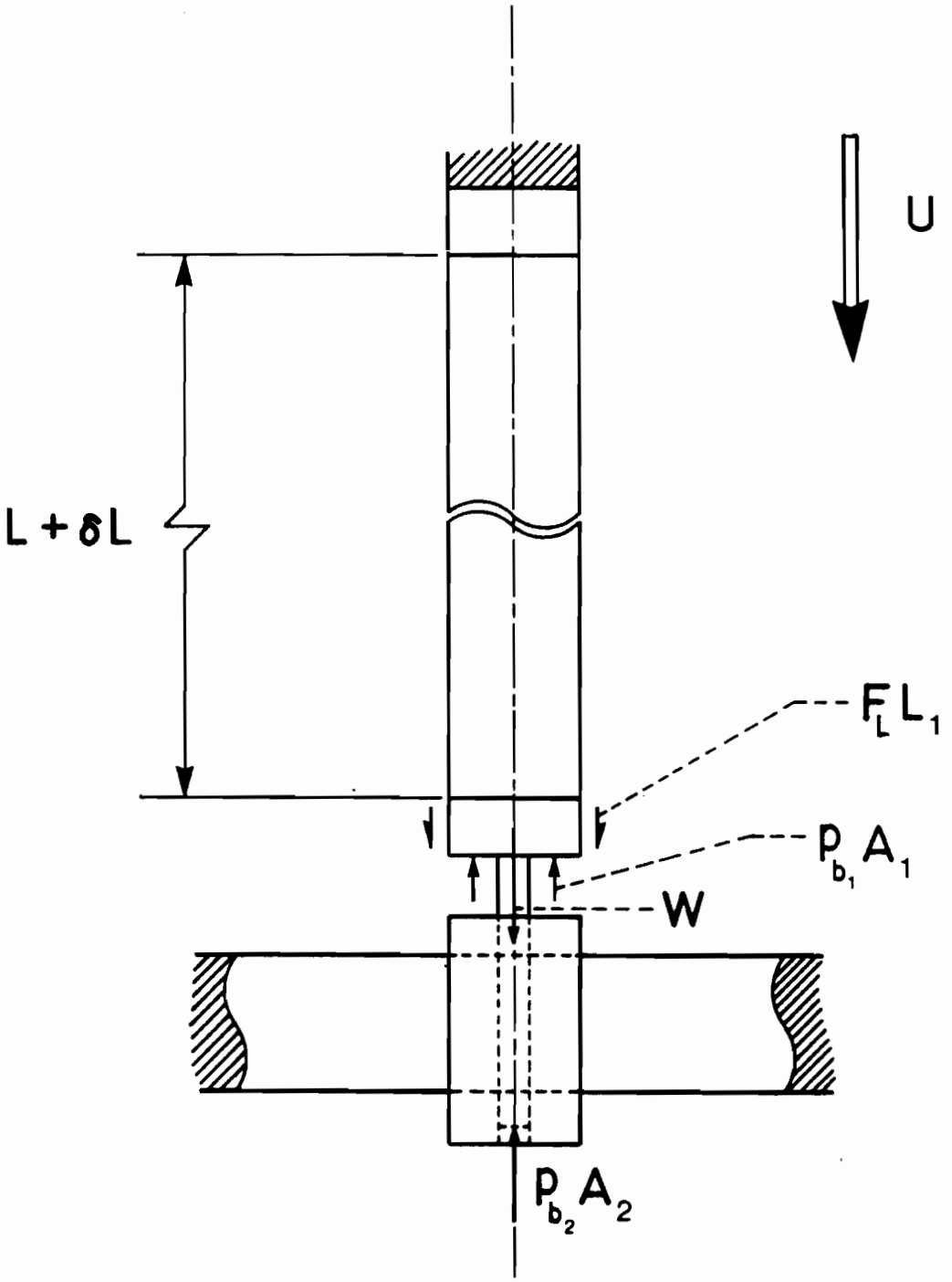

Fig.5: Forces acting at sliding downstream end.

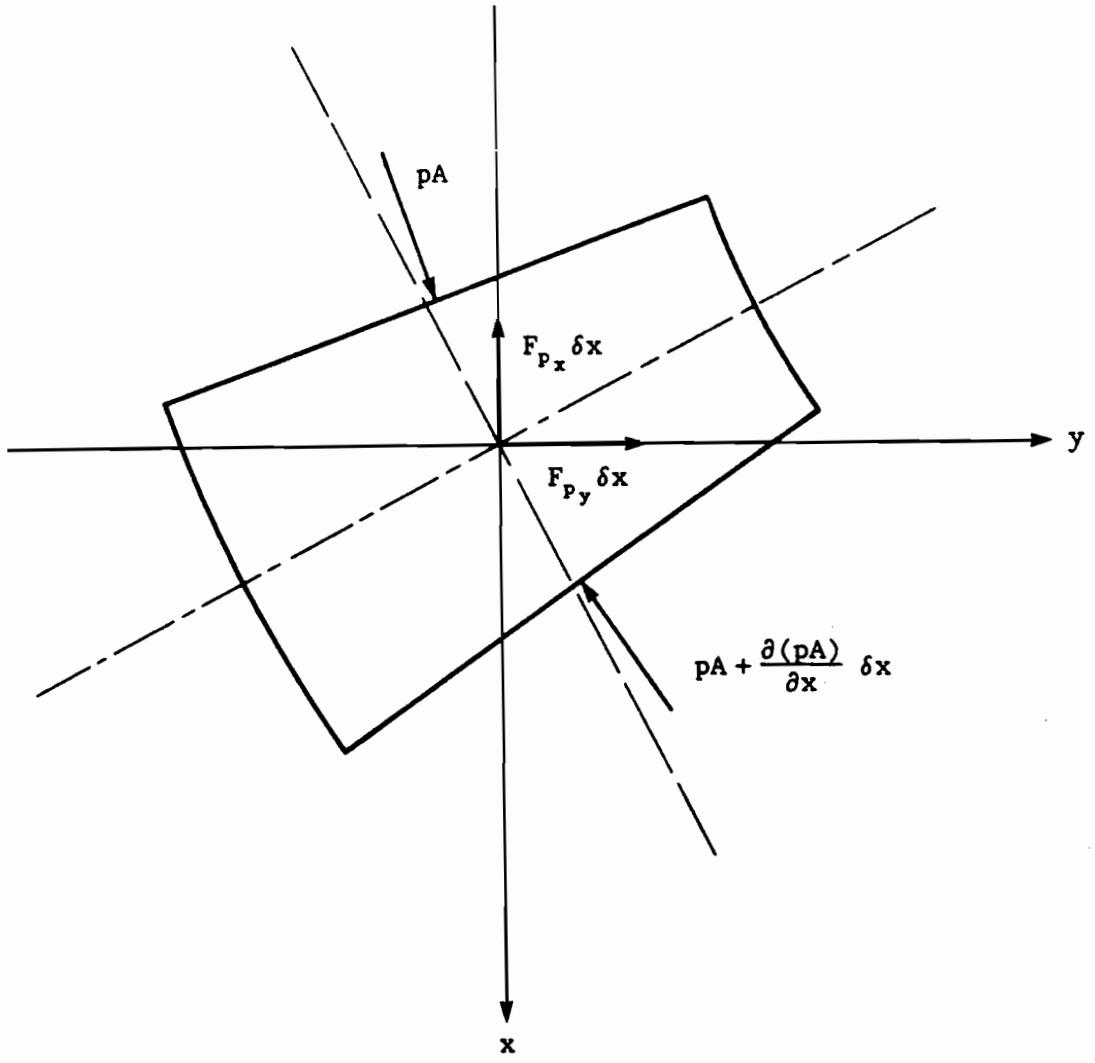

Fig.6: Forces on an immersed element of cylinder.

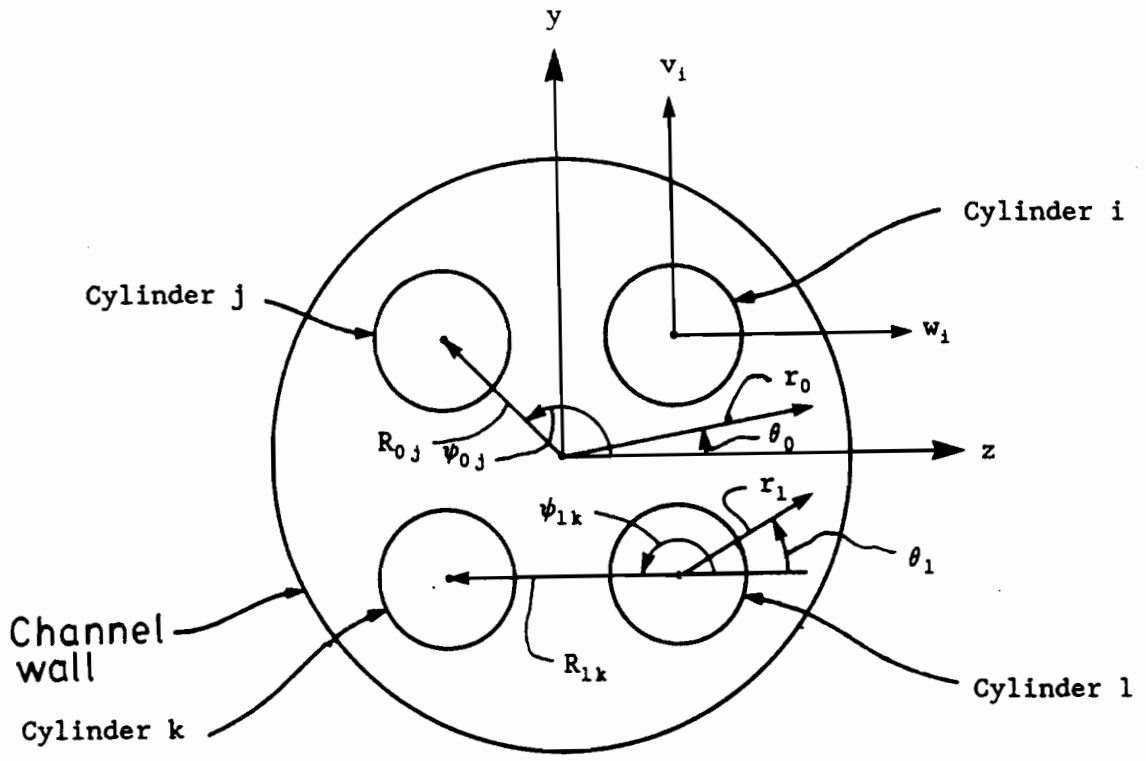

Fig.7: Lateral coordinate system.

Note: the longitudinal system (x-axis) points into the page.

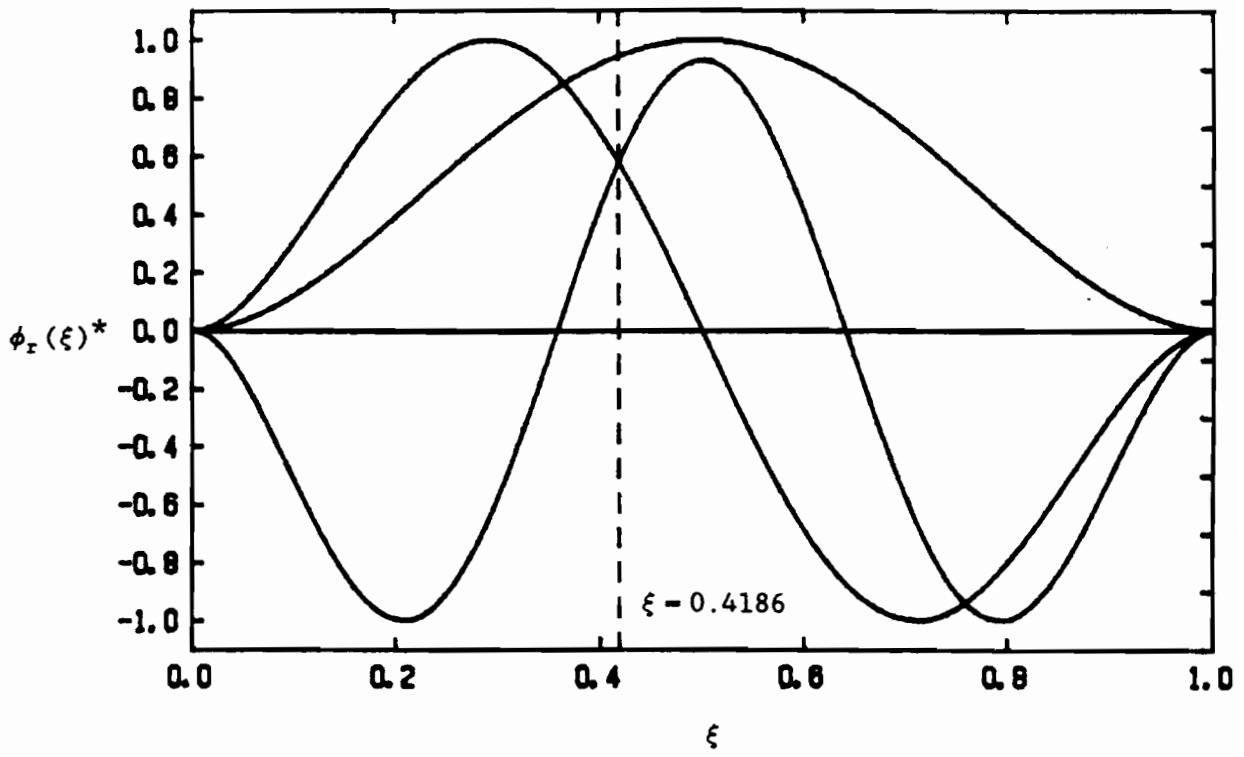

Fig.8: Normalized* natural beam modes.

* Unit maximum amplitude.

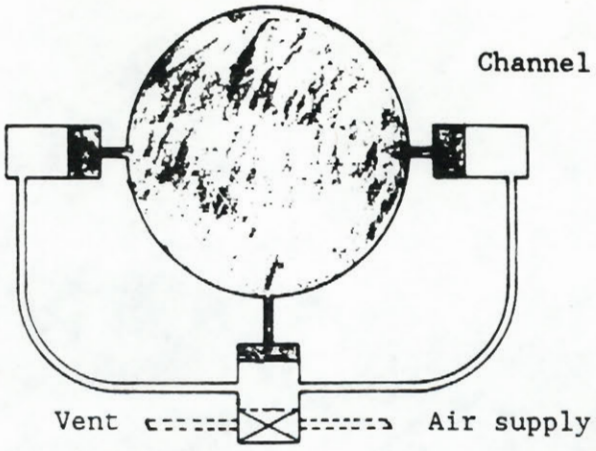

Follower (the bottom part of this schematic represents the control section).

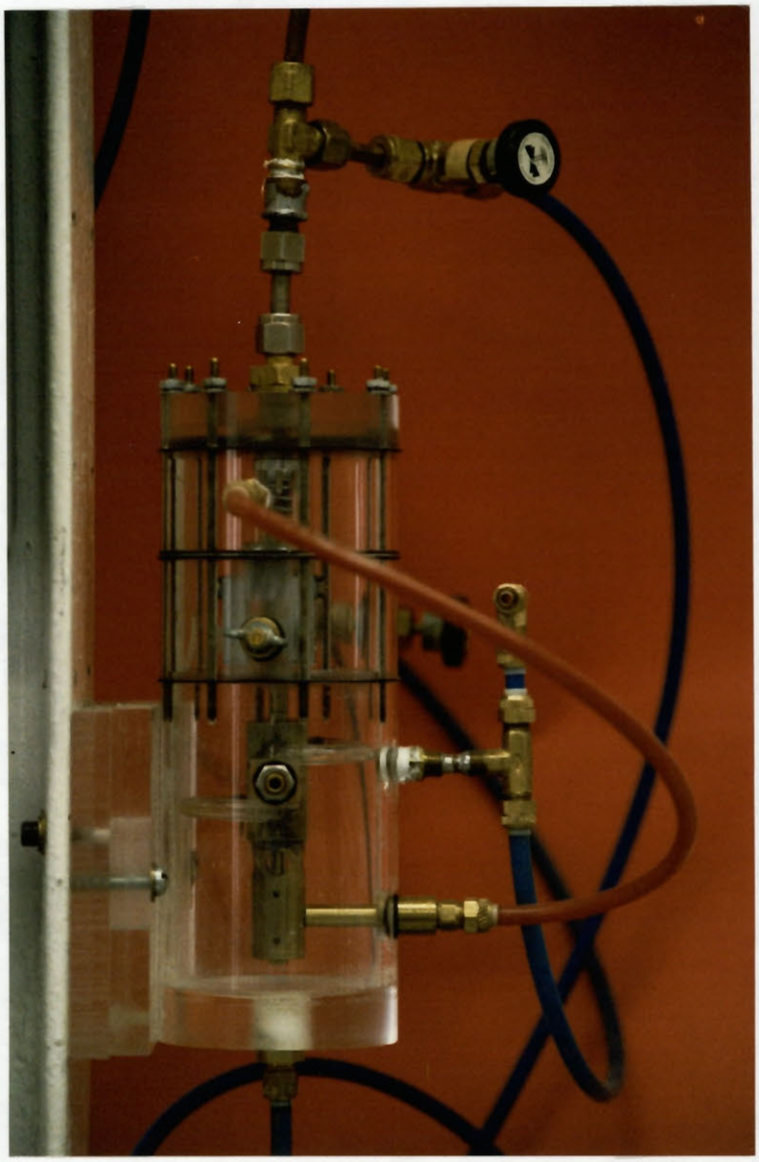

Fig.9: Pressure follower.
Note: The shaded area shows water filled regions.

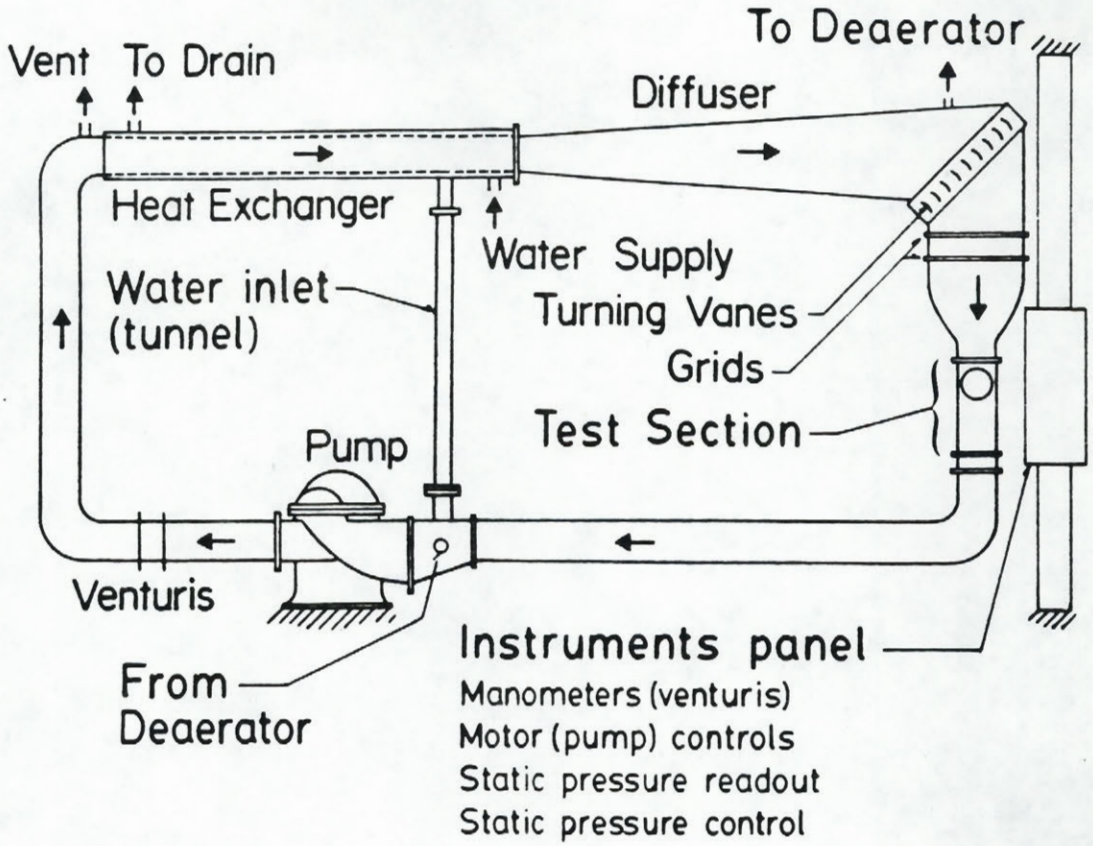

Dimensions, circulation loop: Height, 3.4 m (11 ft)
Width, 7.0 m (23 ft).

Fig.10: Water tunnel circulation loop.

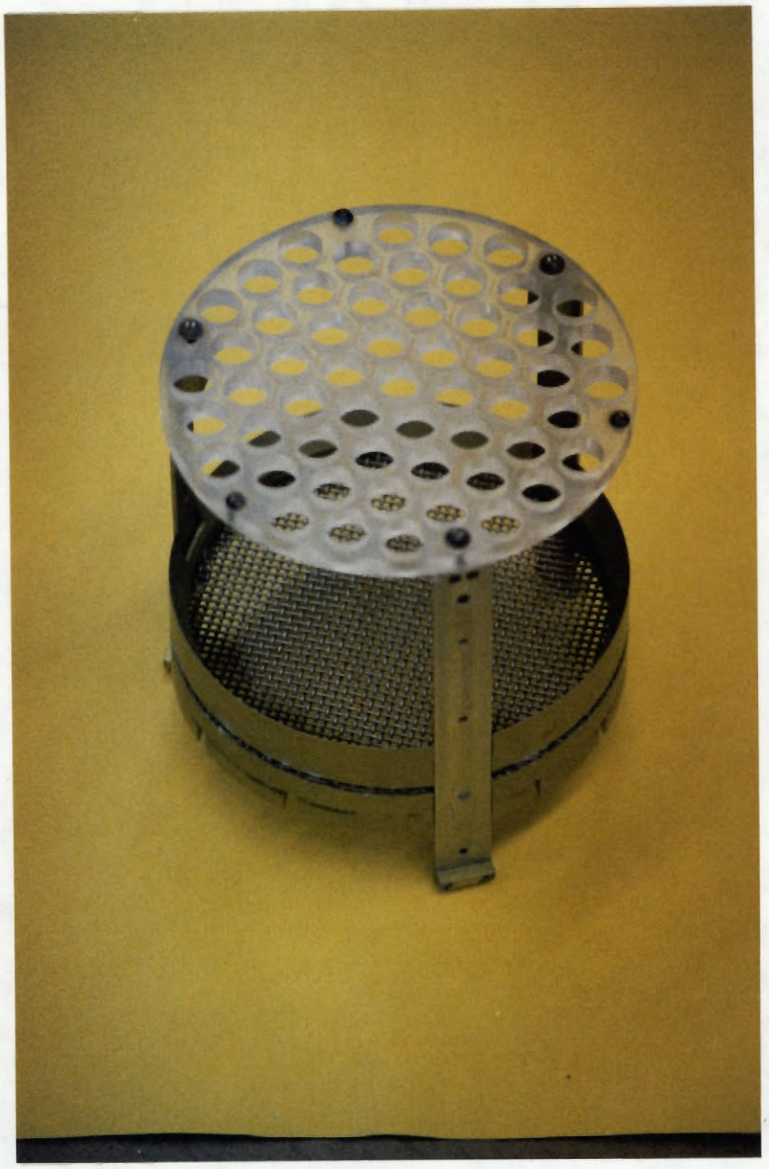

Array (holes in acrylic, top): triangular.
Center to center distance: 3.53 cm (1.39 in).
Holes diameter: 1.59 cm (5/8 in).
Thickness: 0.95 cm (3/8 in).
Major diameter: 20.3 cm (8.0 in).

Mesh pattern: 0.16 cm (1/16 in) wire,
(metallic, bottom) 0.42 cm (0.165 in) spacing,
0.47 cm (0.185 in) weave thickness.

Stages spacing (inner surfaces): 13.8 cm (5.43 in).

Fig.11: Turbulator.

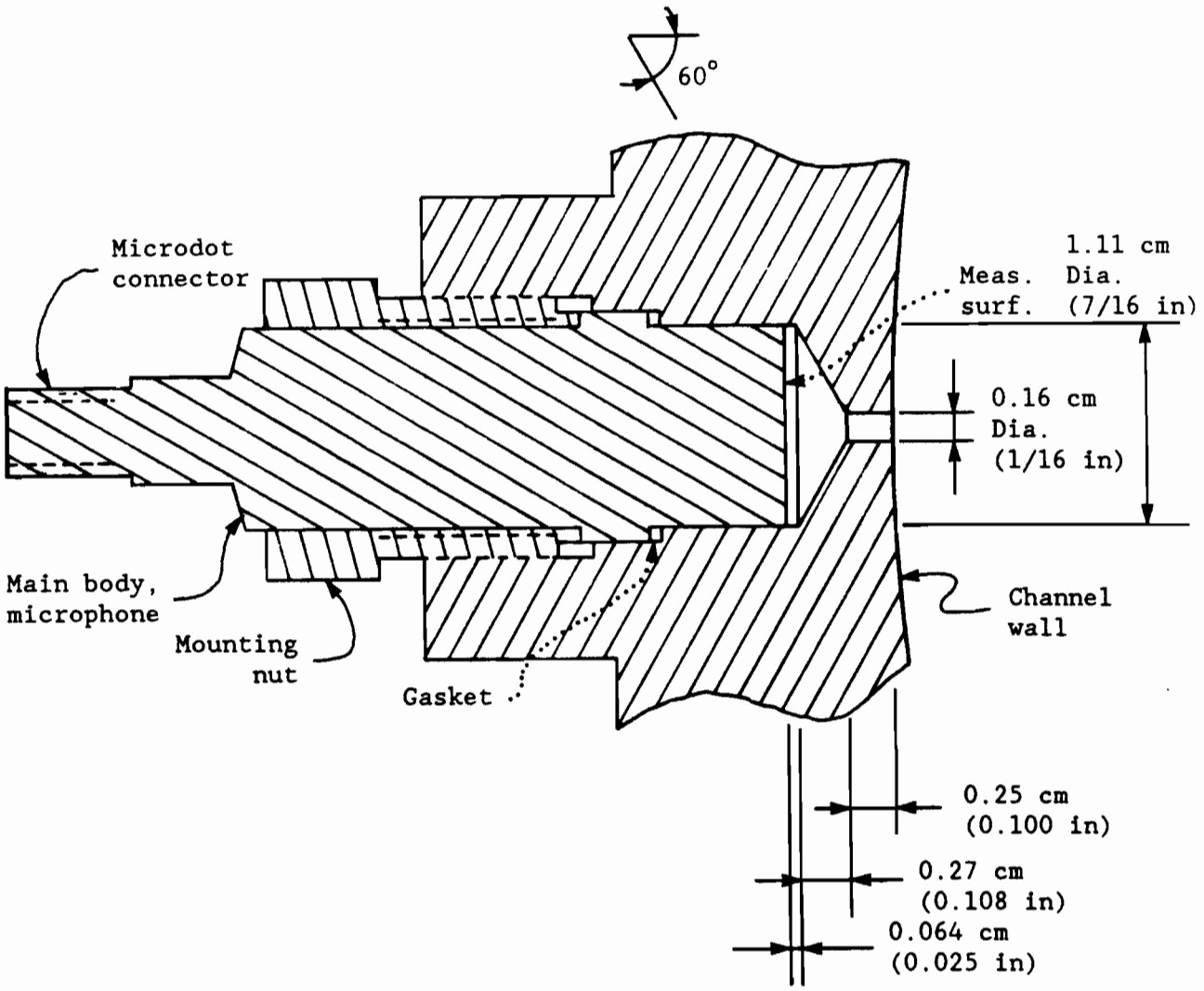

Fig.12: Hydrophones mounting, channel wall.

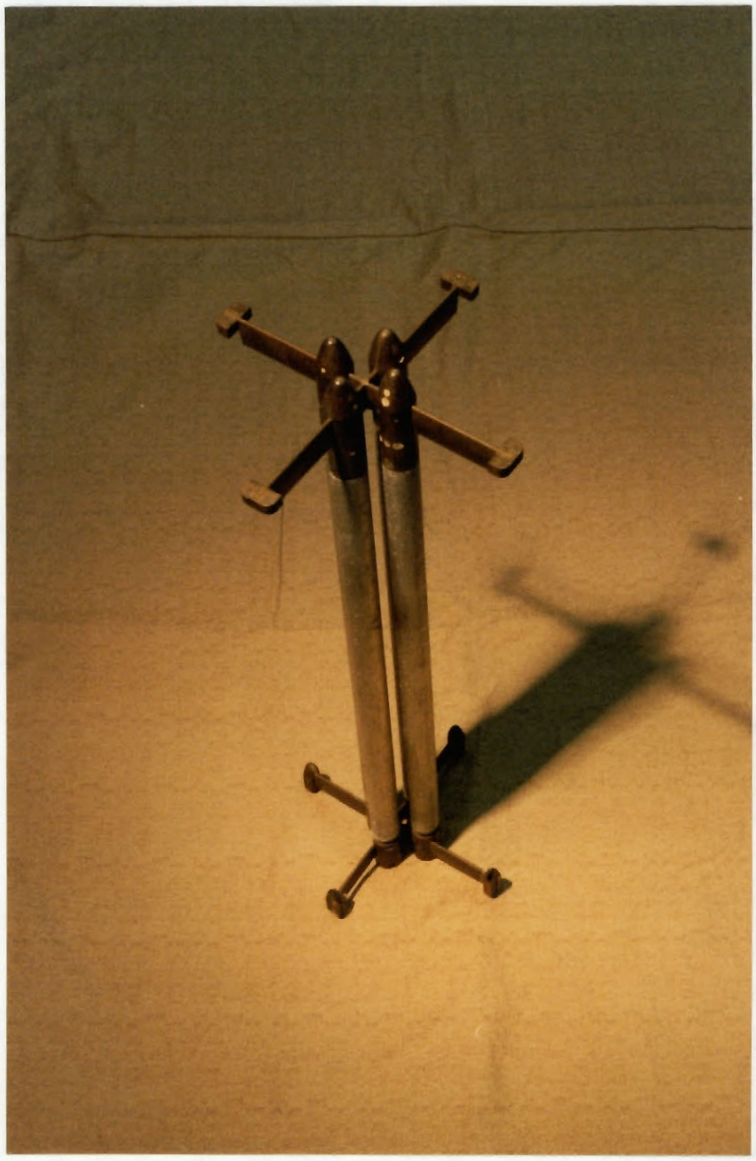

Fig.13: Assembled cylinder cluster.

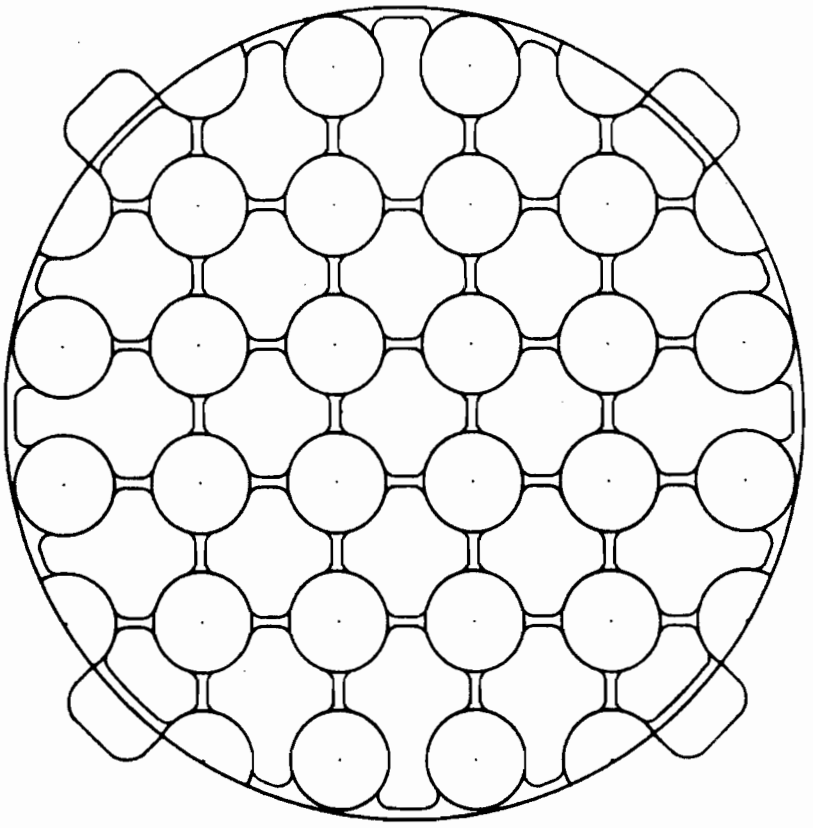

Thickness: 0.95 cm (3/8 in).

O.D.: 20.47 cm (8.06 in).

Fig.14: Top support (brass) for 28-cylinder cluster.

Note: The bottom support is similar.

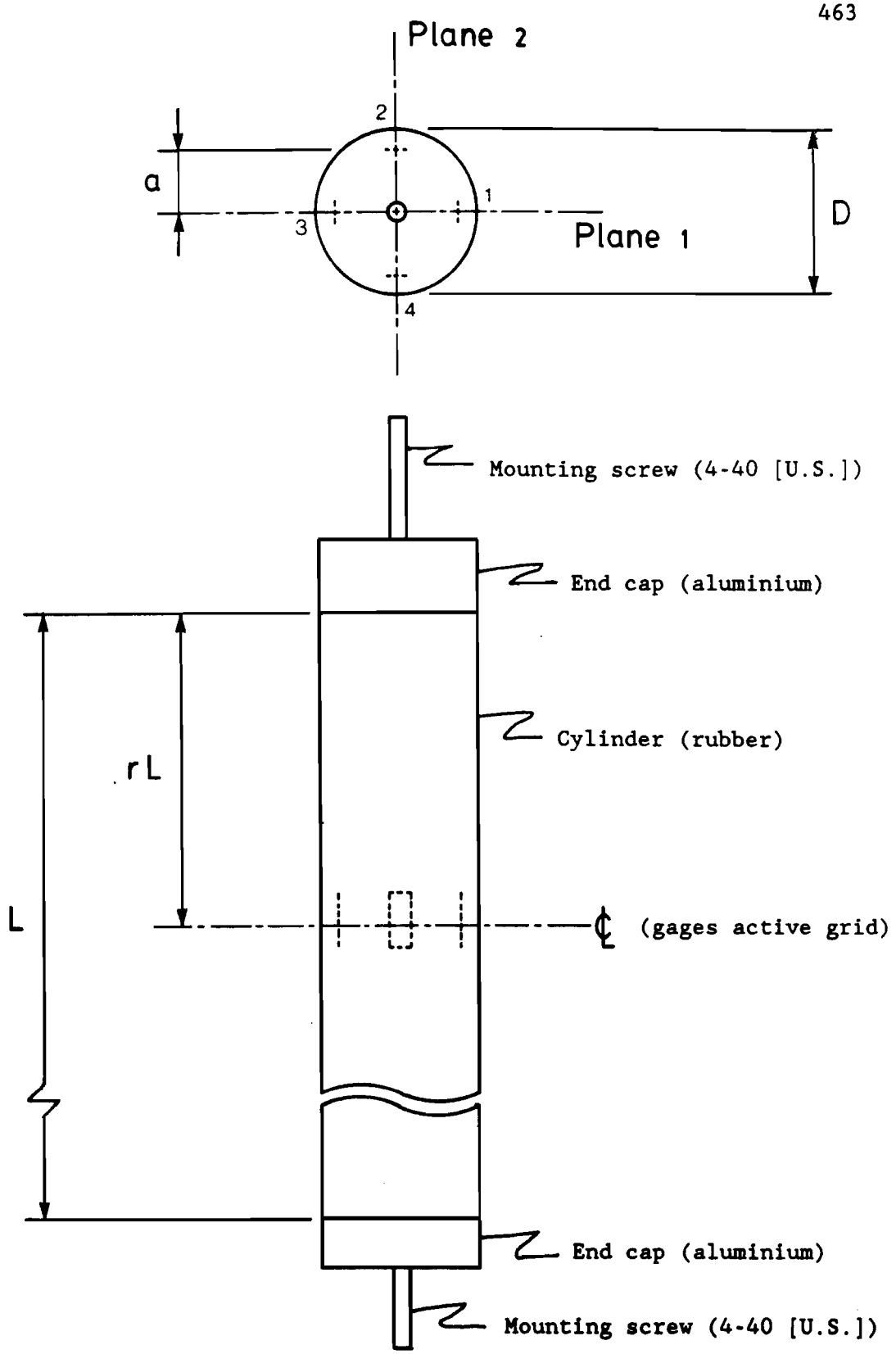

Fig.15: Schematic, instrumented cylinder.

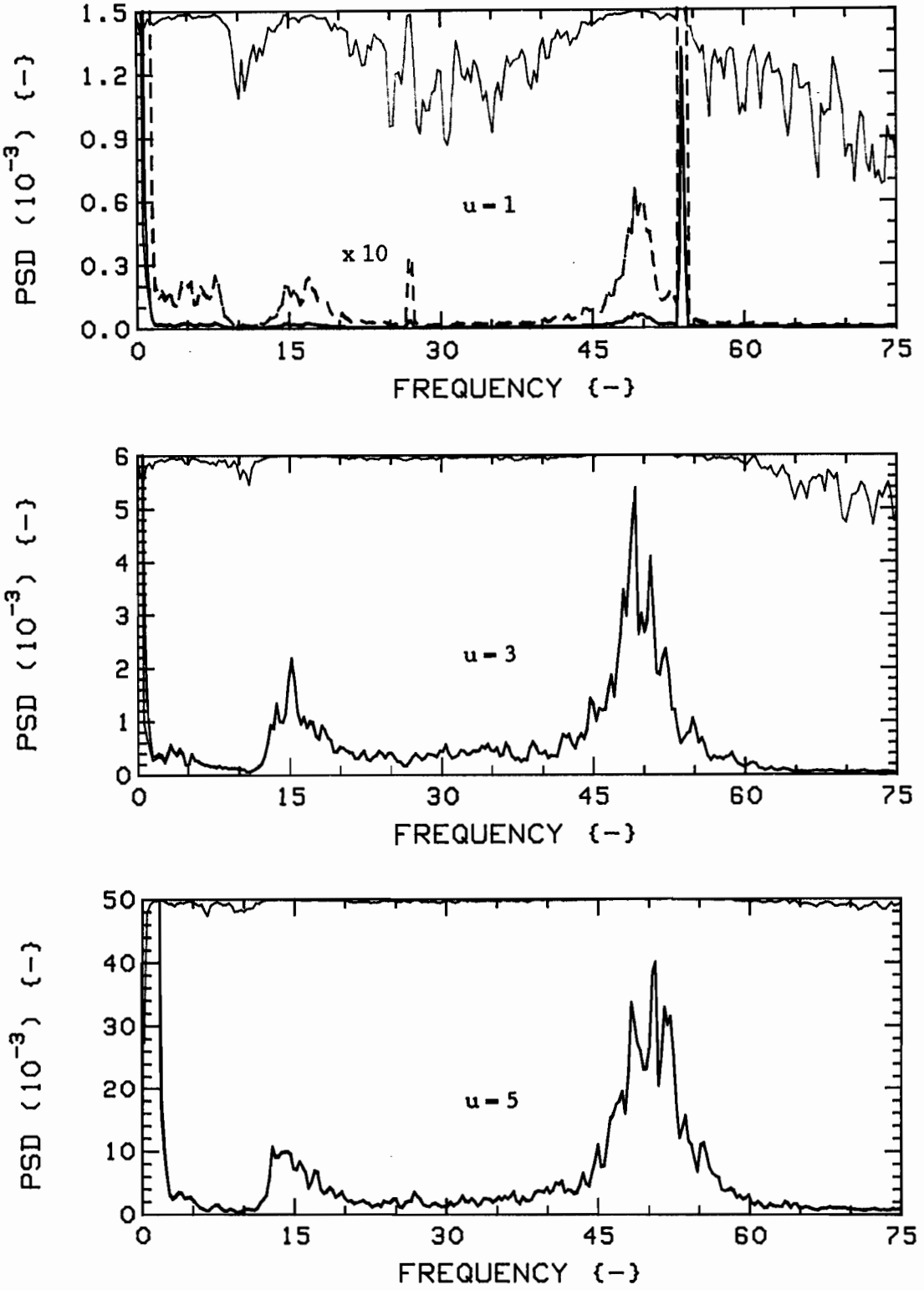

Fig.16: Measured point pressure PSD's (RED, GREEN) and corresponding coherence functions (BLUE), for K = 0.

Note: Coherence scales are 1.

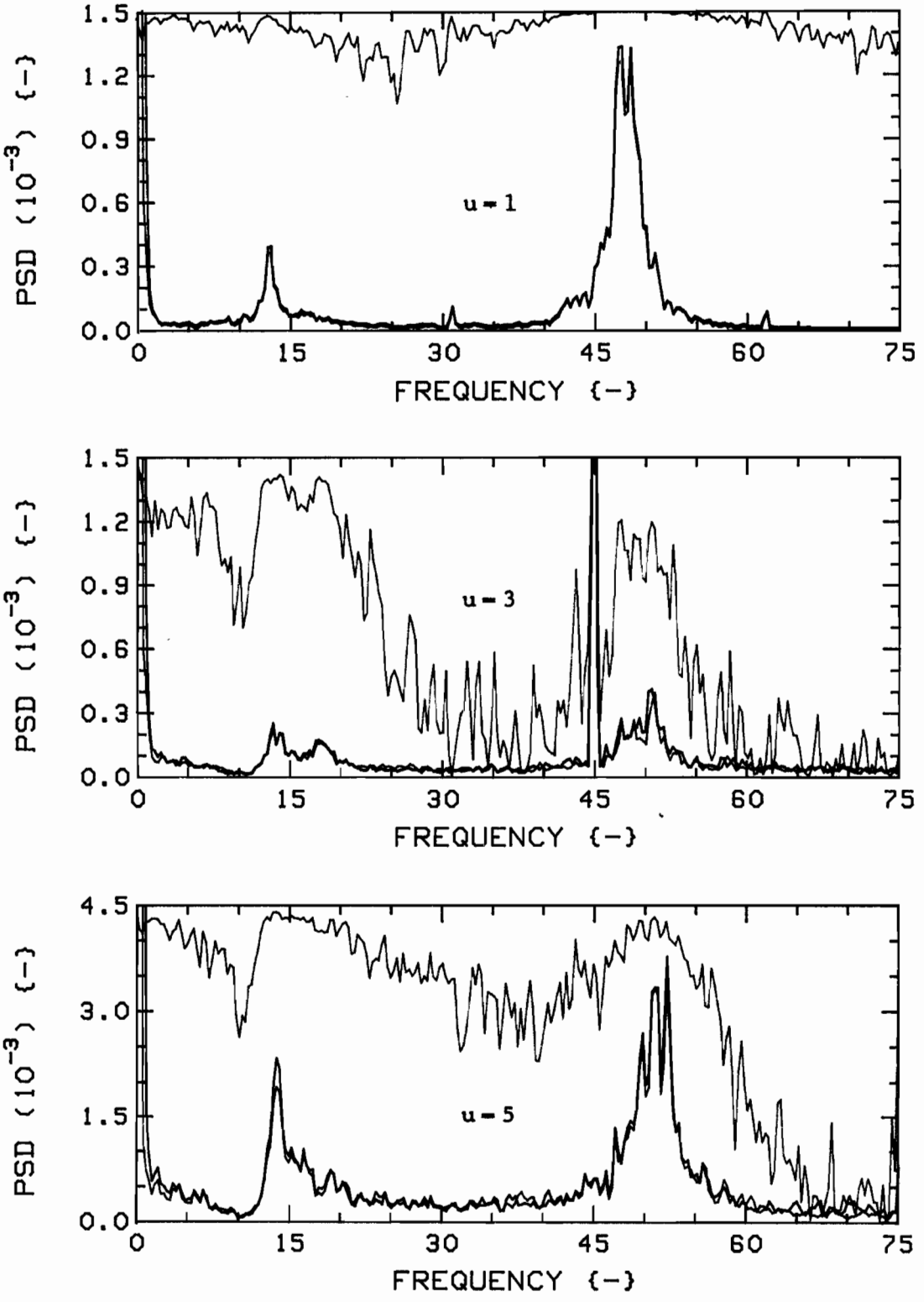

Fig.17: Measured point pressure PSD's (RED, GREEN) and corresponding coherence functions (BLUE), for K = 28.

Note: Coherence scales are 1.

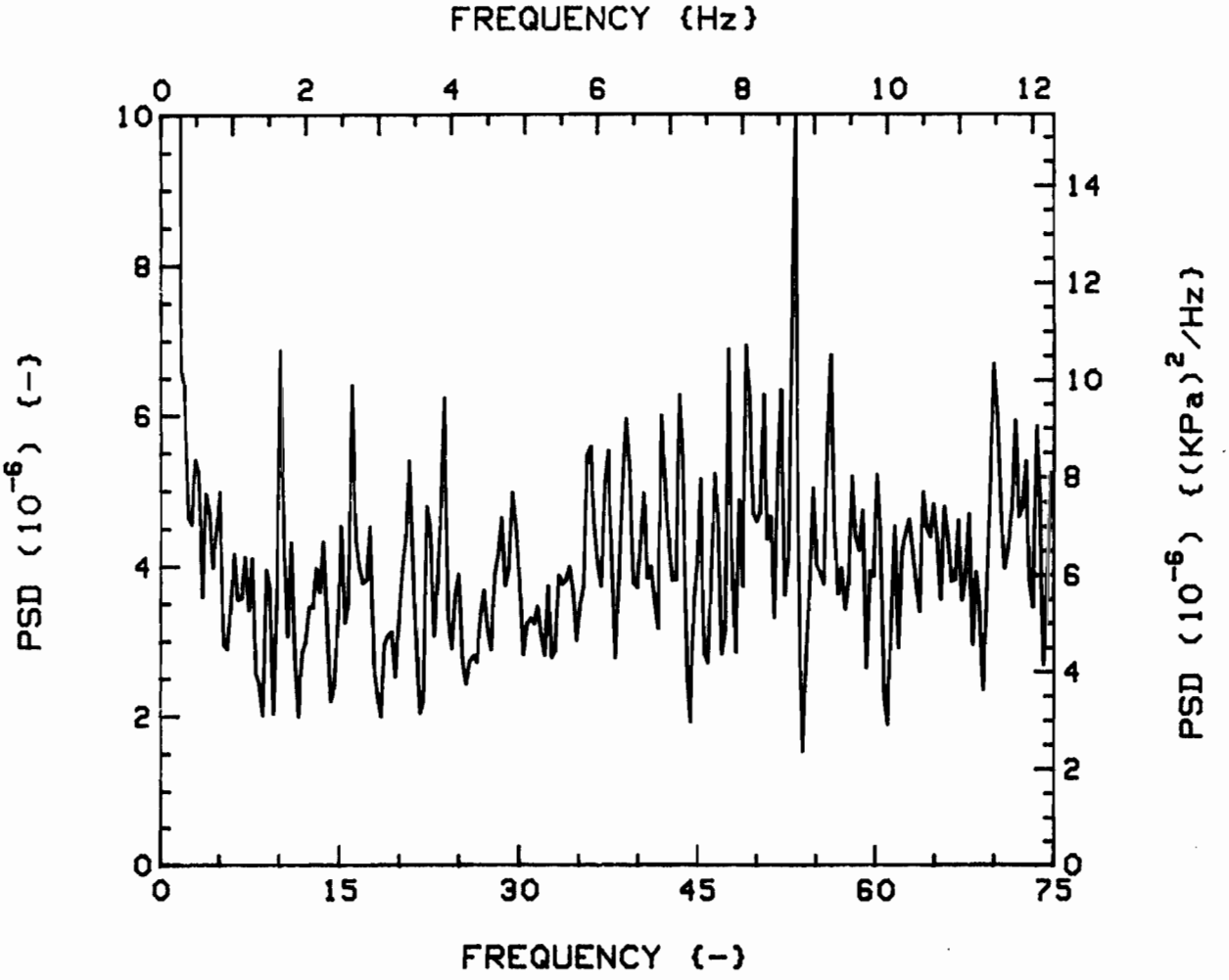

Fig.18: Scales comparison, dimensionless versus dimensional, boundary layer pressure PSD's. The K = 0, u = 3 case is depicted (see Fig. 20a).

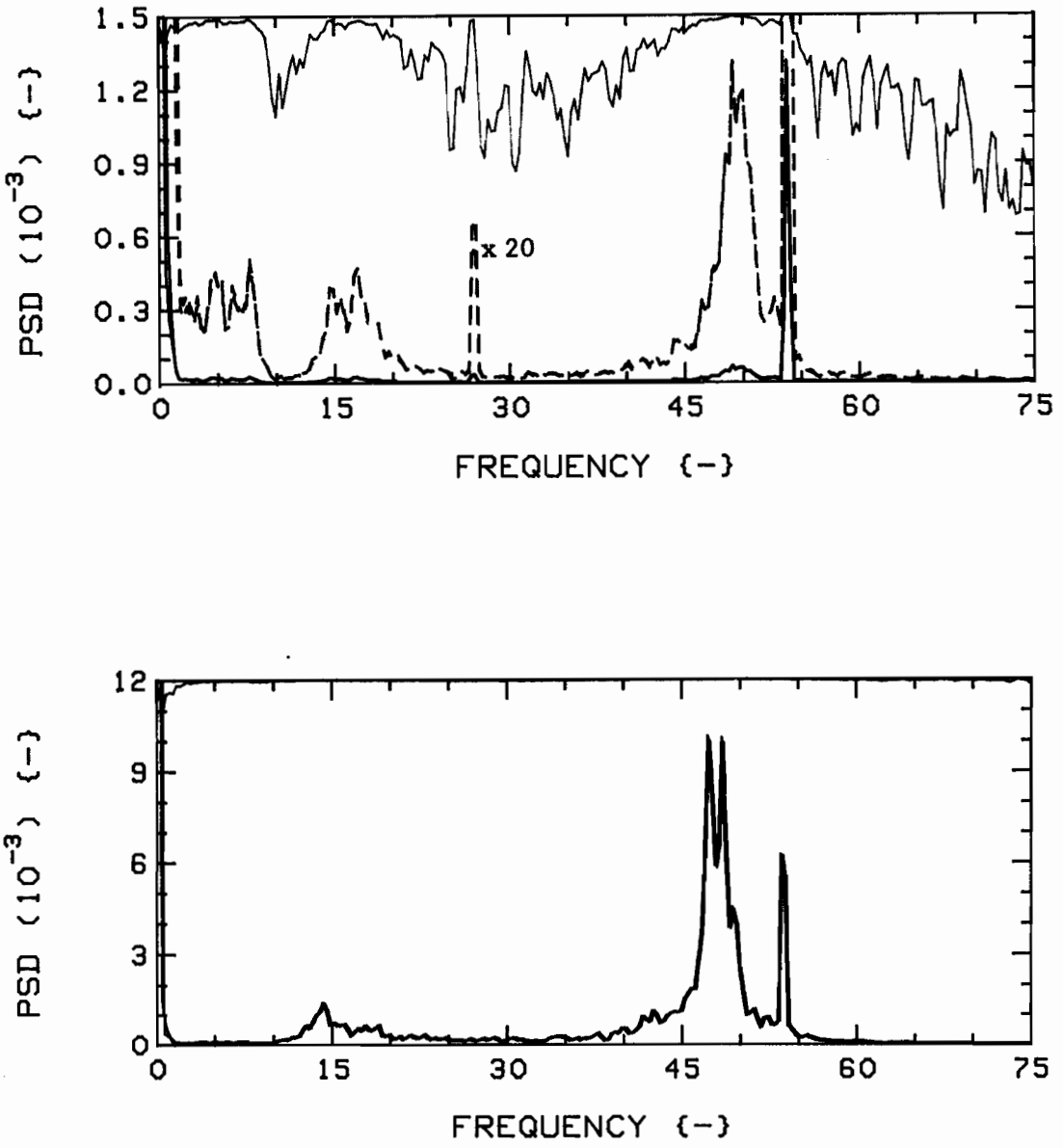

Fig.19a: Measured single point pressure PSD's (RED, GREEN), and corresponding coherences (BLUE), for K = 0, at u = 1.5. Venturi insert nozzle used; Top: large (upper range), Bottom: small (lower range).

Note: Coherence scales are 1.

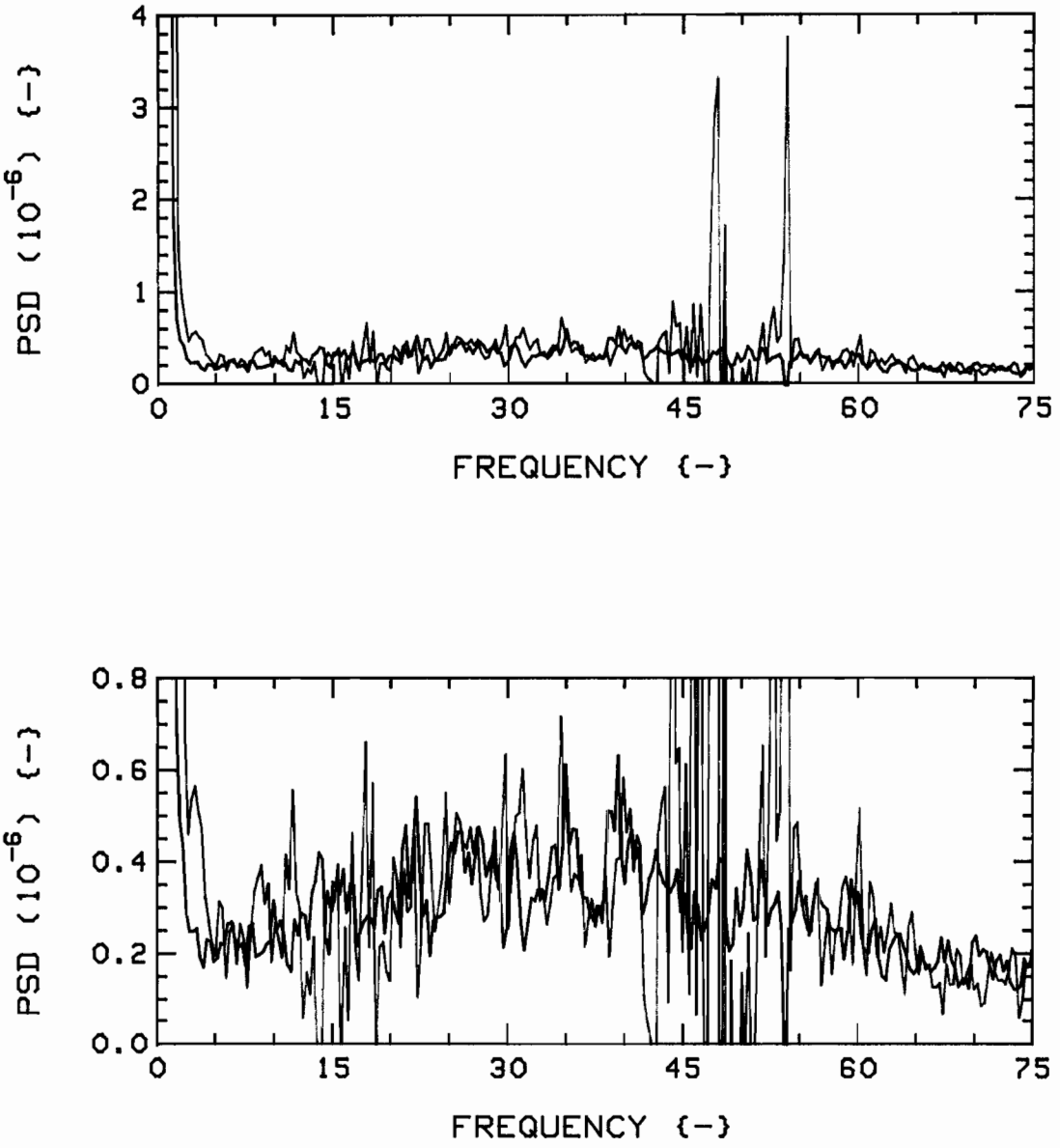

Fig.19b: Boundary layer pressure PSD's, corresponding to point PSD's of Fig. 19a (K = 0, u = 1.5). Venturi insert nozzles: large (RED), small (GREEN). The lower plot has an expanded scale, for easier comparison.

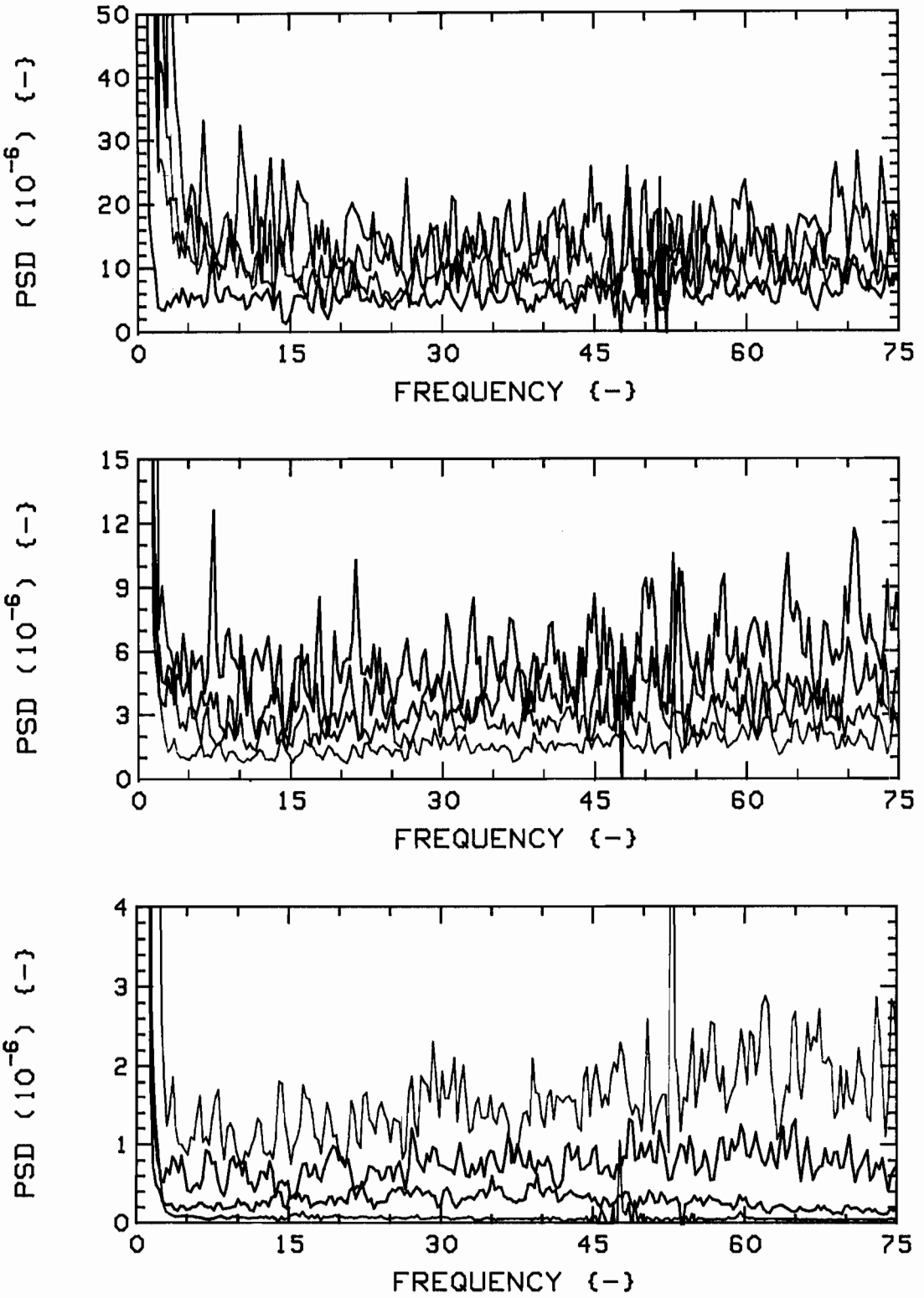

Fig.20a: Boundary layer pressure PSD's, for K = 0, versus flow velocity. In descending order, u = 5.0 to 0.5, in steps of 0.5. Colour sequence: RED, GREEN, BLUE, BLACK (lowest trace of each plot is highest of the next one, e.g. BLACK in top two).

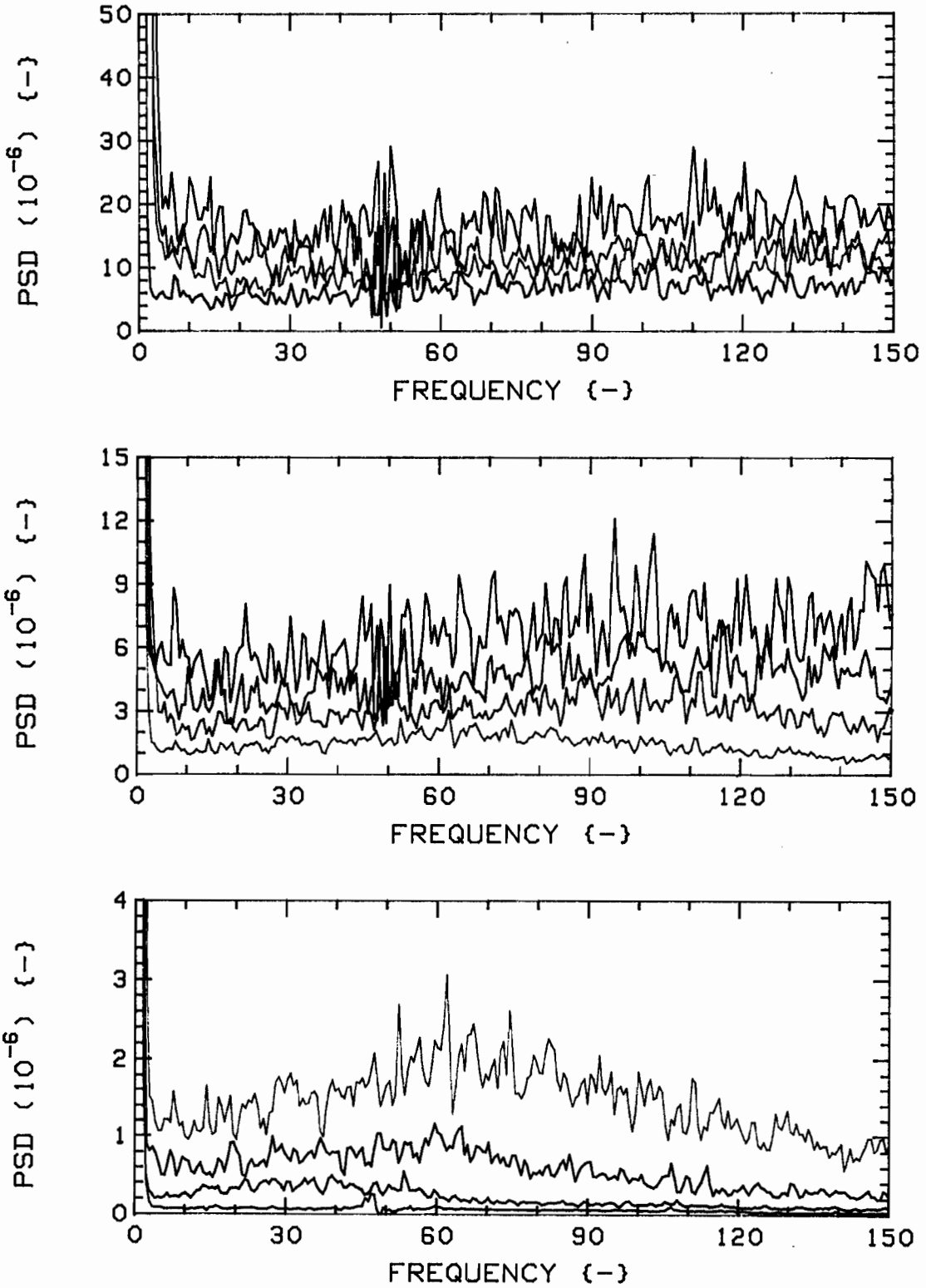

Fig.20b: Boundary layer pressure PSD's, for K = 0, versus flow velocity. In descending order, u = 5.0 to 0.5, in steps of 0.5. Colour sequence: RED, GREEN, BLUE, BLACK (lowest trace of each plot is highest of the next one, e.g. BLACK in top two).

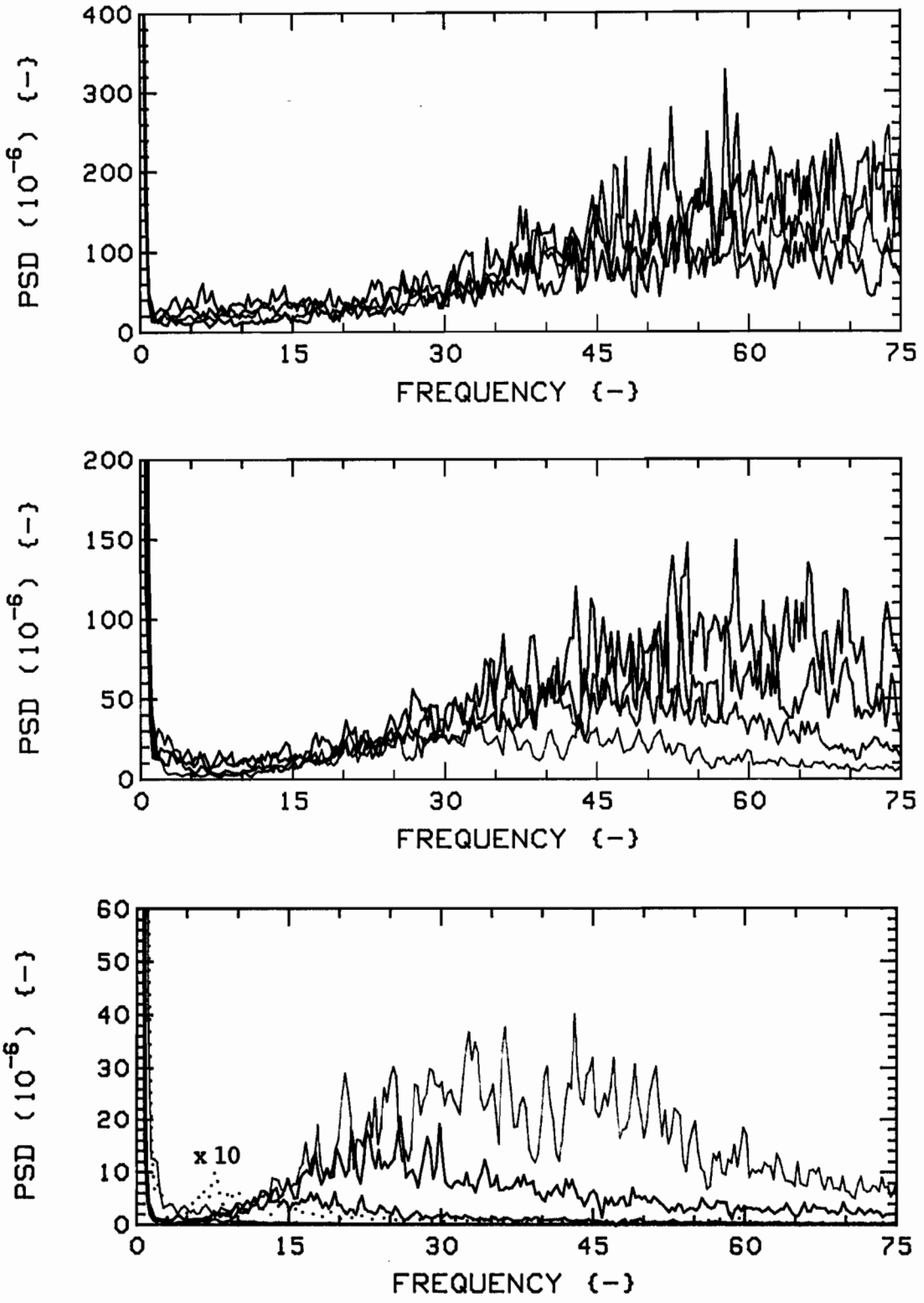

Fig.21a: Boundary layer pressure PSD's, for K = 28, versus flow velocity. In descending order, u = 5.0 to 0.5, in steps of 0.5. Colour sequence: RED, GREEN, BLUE, BLACK (lowest trace of each plot is highest of the next one, e.g. BLACK in top two).

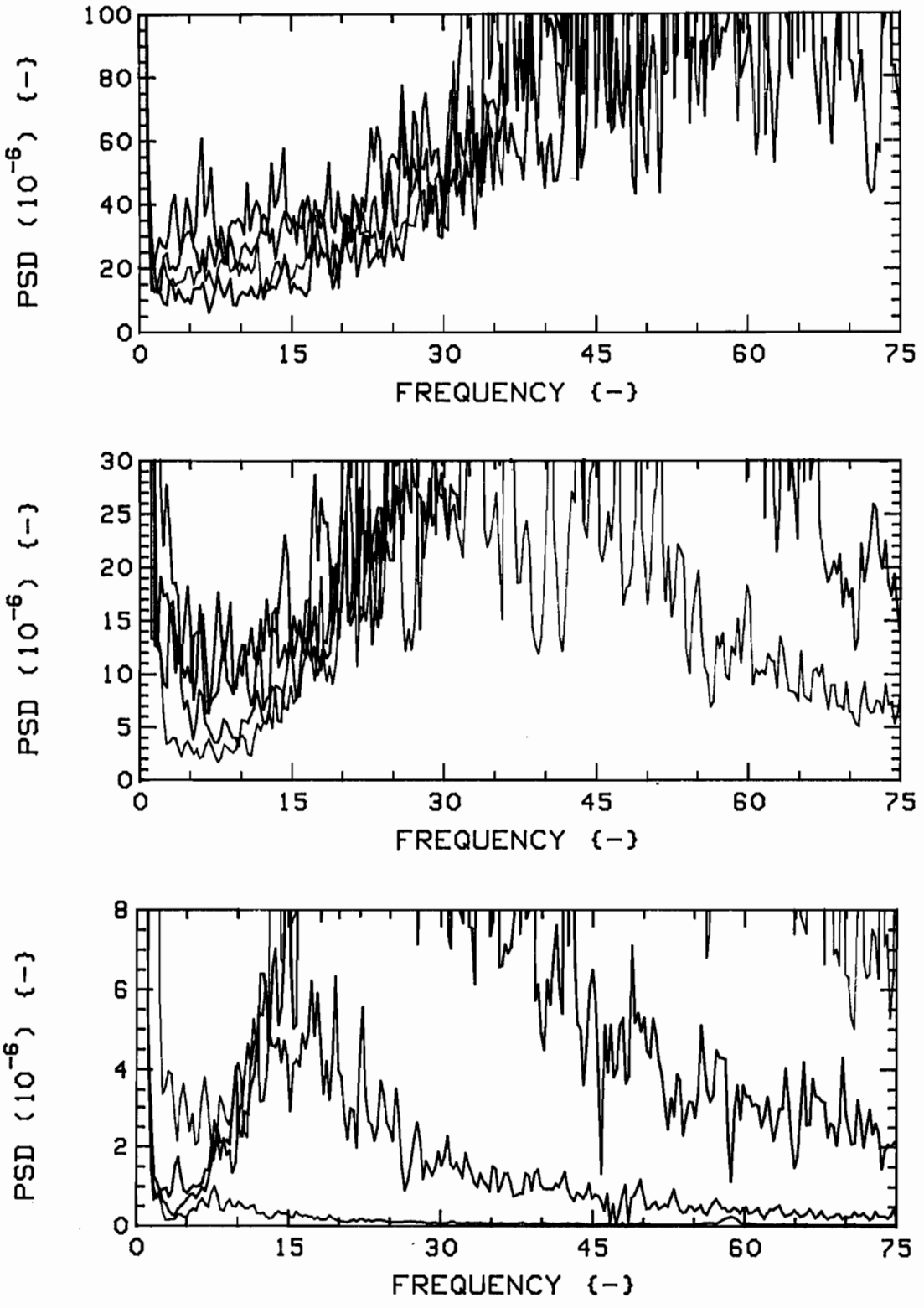

Fig. 21b: Data of Fig. 21a, replotted to double the PSD scale of Fig. 20a, for comparisons (at low frequencies).

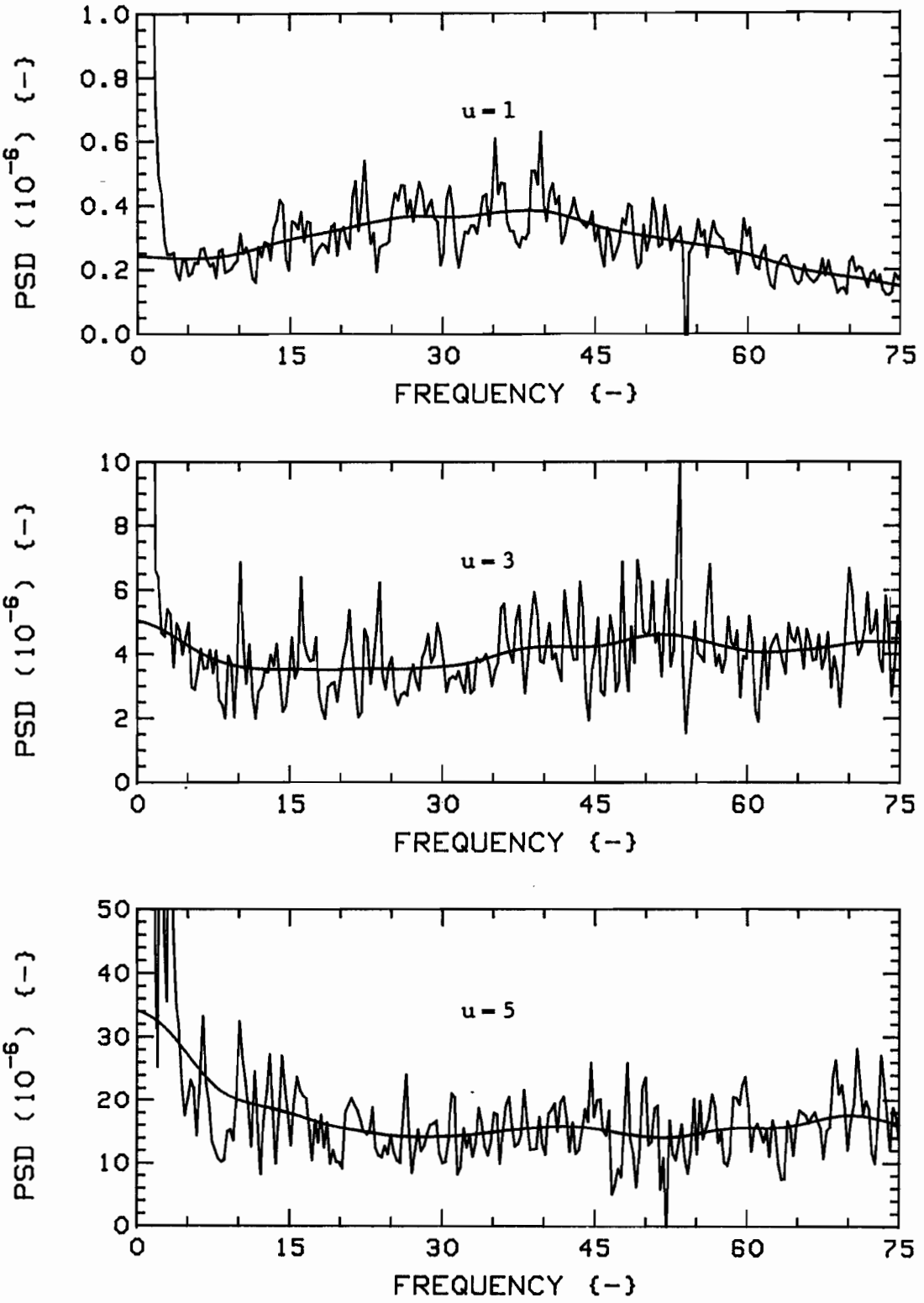

Fig.22a: Original (RED) and smoothed (GREEN) boundary layer pressure PSD's, for K = 0. Filter* parameters: a = 0.8, M = 5, P = 5, B = 10.

* See Appendix O.

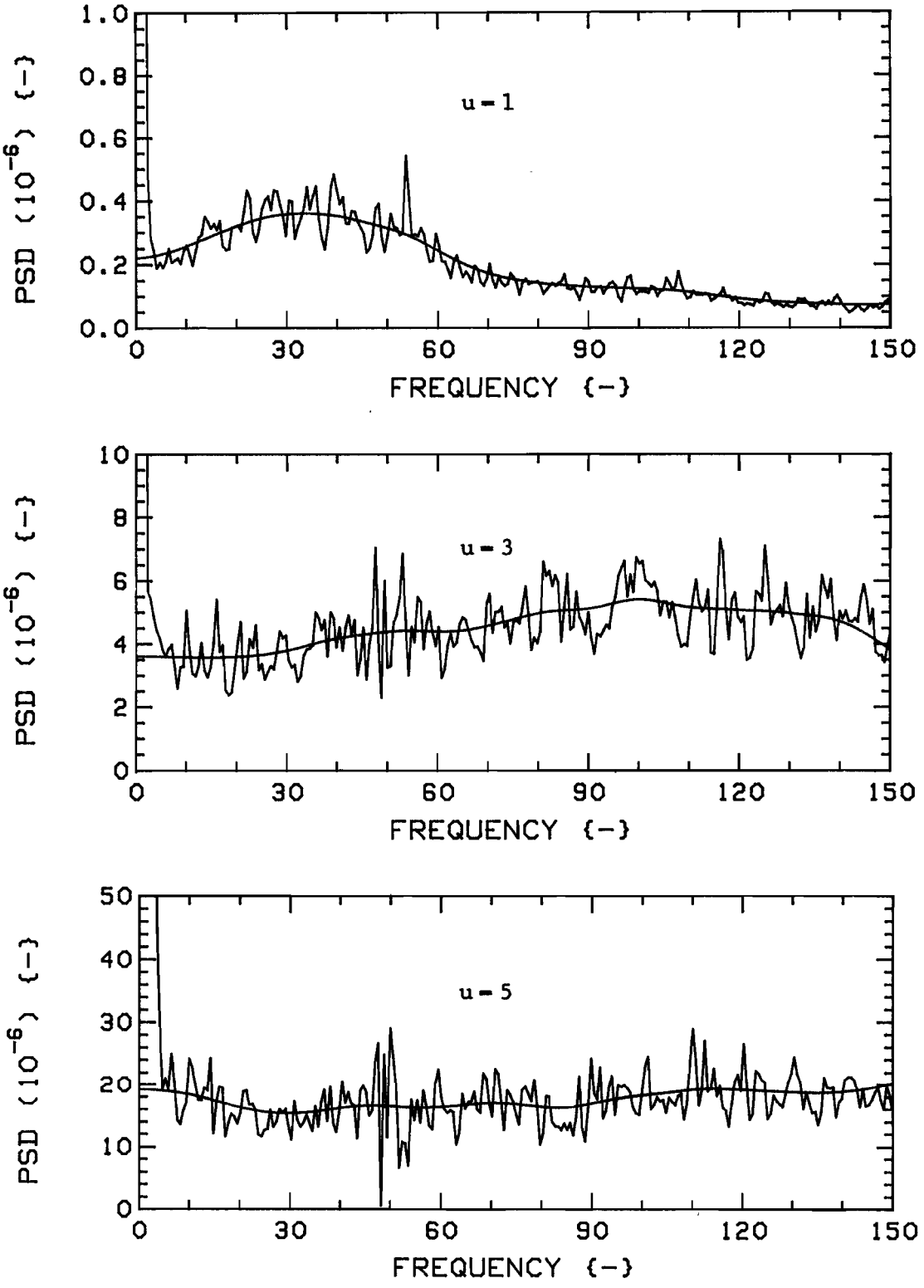

Fig.22b: Original (RED) and smoothed (GREEN) boundary layer pressure PSD's, for K = 0. Filter* parameters: a = 0.8, M = 5, P = 5, B = 10.

* See Appendix O.

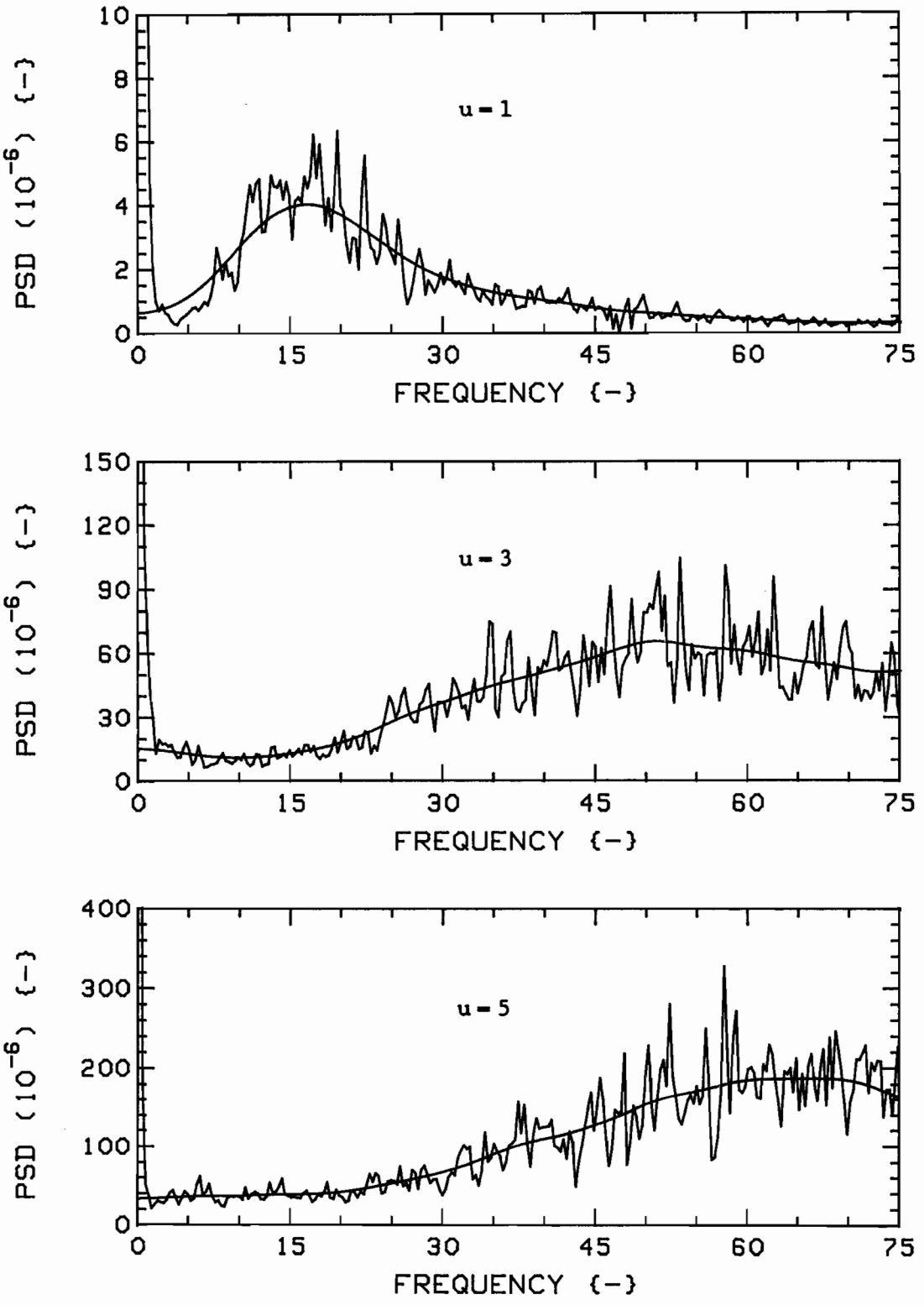

Fig.23: Original (RED) and smoothed (GREEN) boundary layer pressure PSD's, for K = 0. Filter* parameters: a = 0.8, M = 5, P = 5, B = 10.

* See Appendix O.

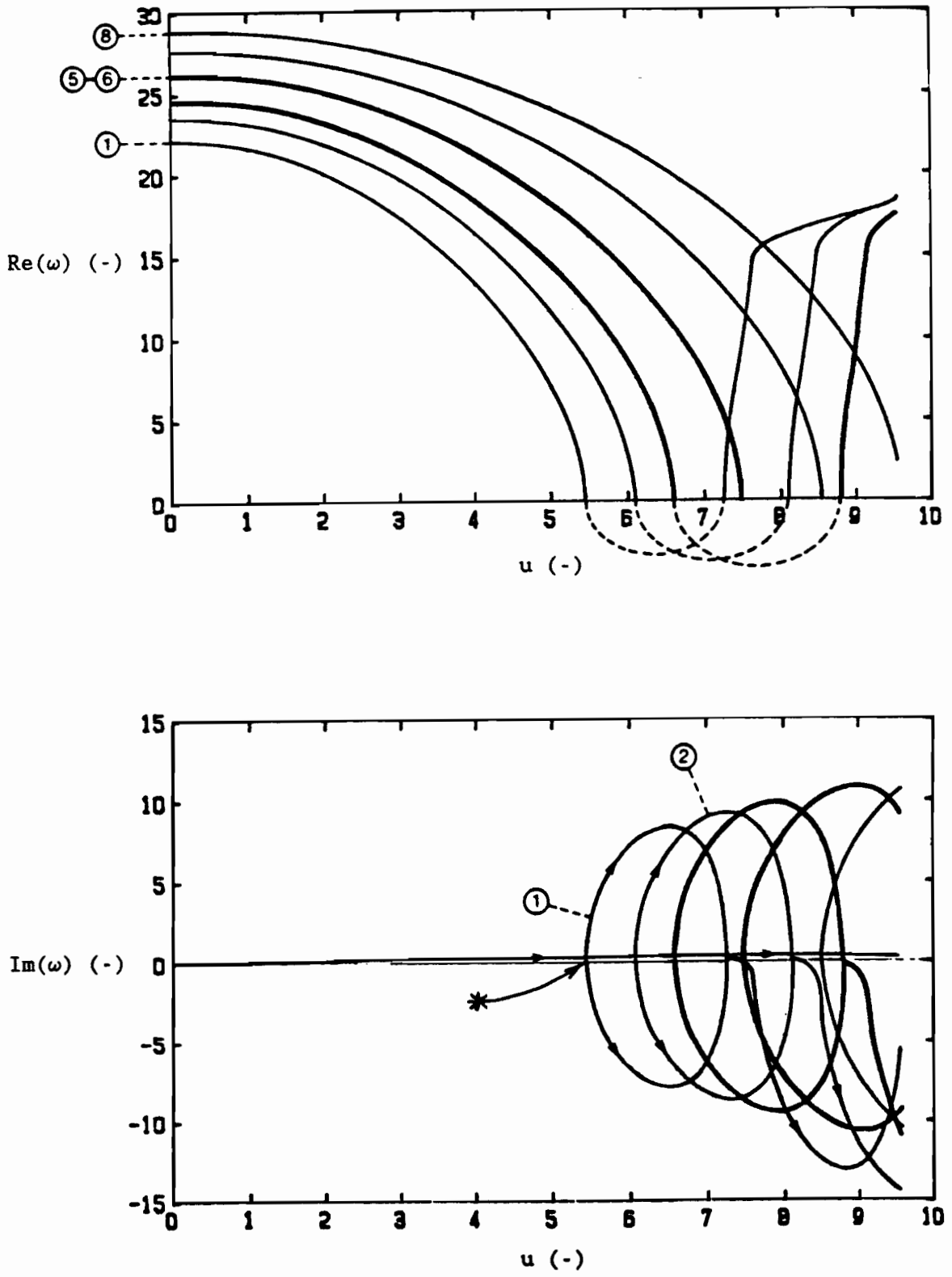

Fig.24: Mean flow model - typical, $K = 4$, $G_c = 0.75$ [75]. Frequency versus flow velocity. Wider lines represent repeated roots, and circled digits identify modes (not all modes shown).

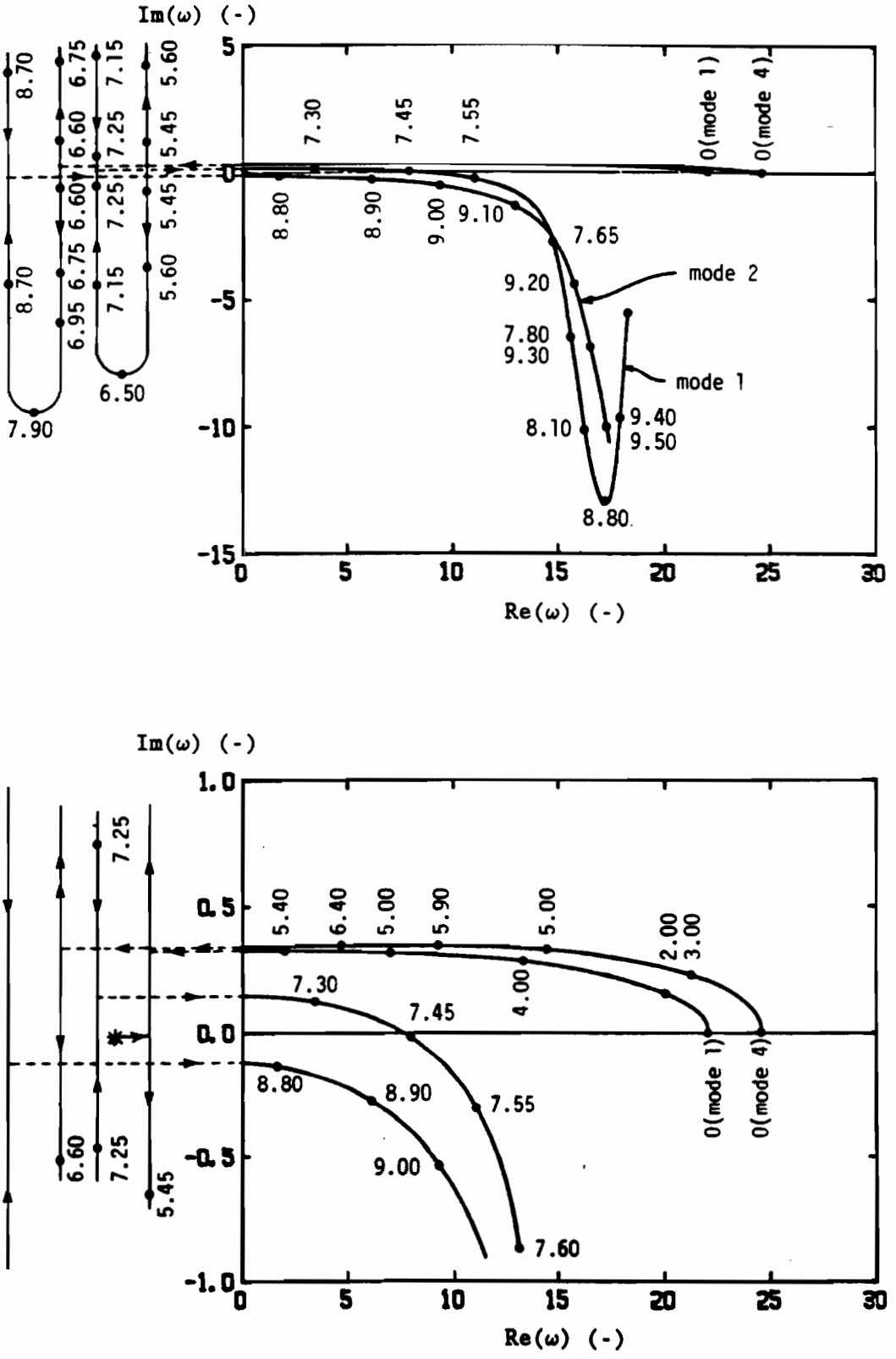

Fig.25: Typical Argand diagram [75], data of Fig. 24. Dots identify (dimensionless) velocity points. Scale is expanded in the lower plot.

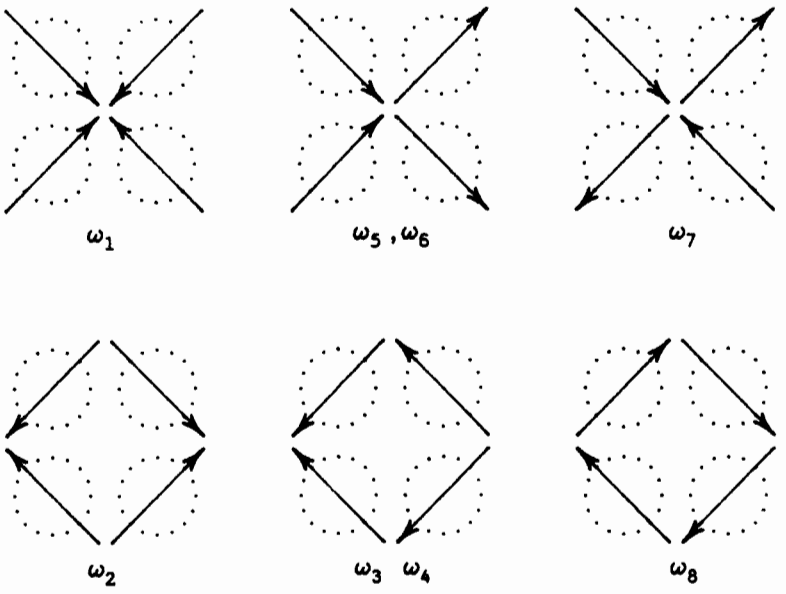

Fig.26: Mean flow model - cross-sectional modes, K = 4.

Note: These also correspond to the dominant modes of the random model.

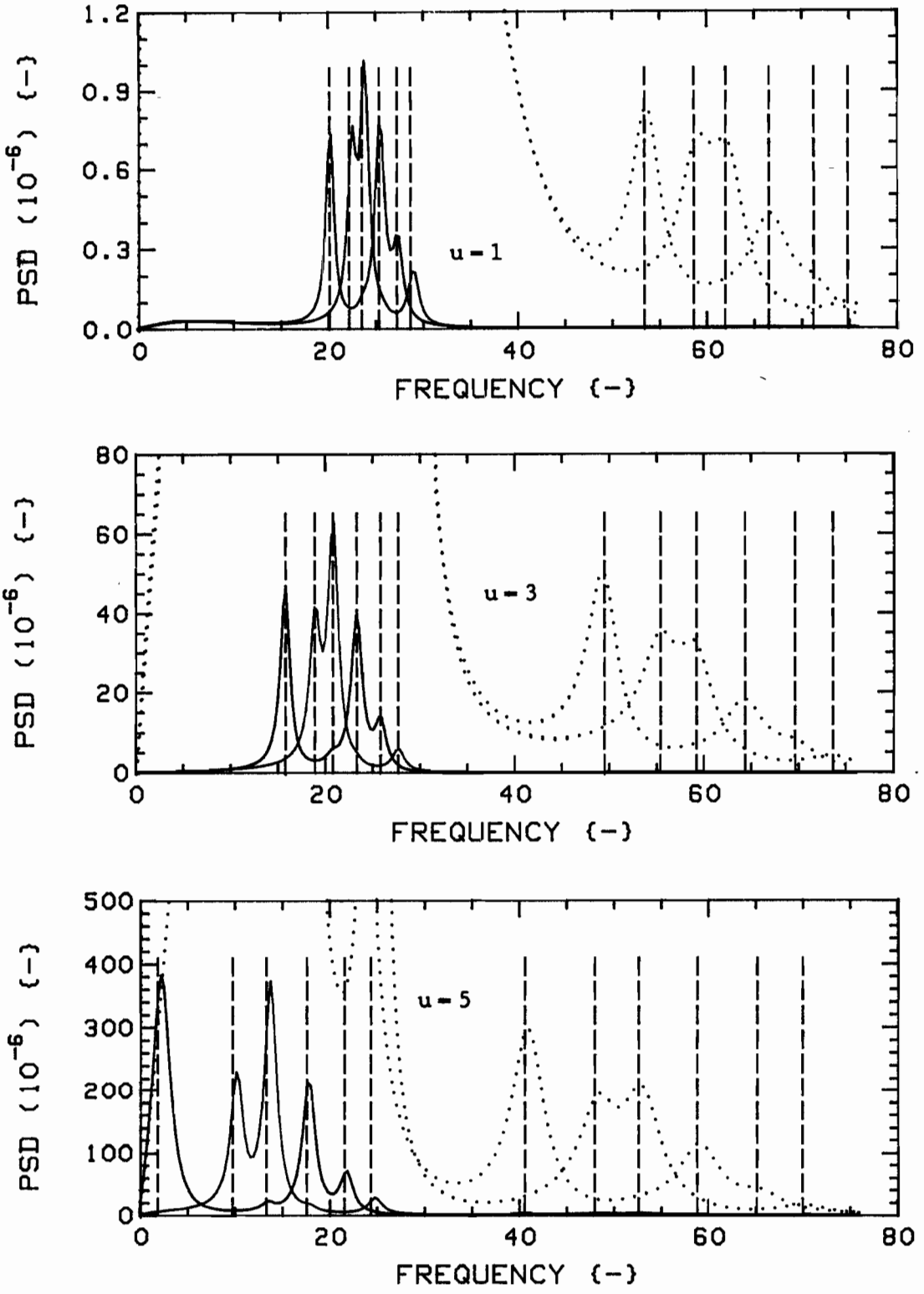

Fig.27: Mean flow model characteristic frequencies (cursors) versus Random model power spectral densities, K = 4, G_c = 0.75: radial (RED) and tangential (GREEN) directions. The dotted traces are expansions of second beam mode group PSD's.

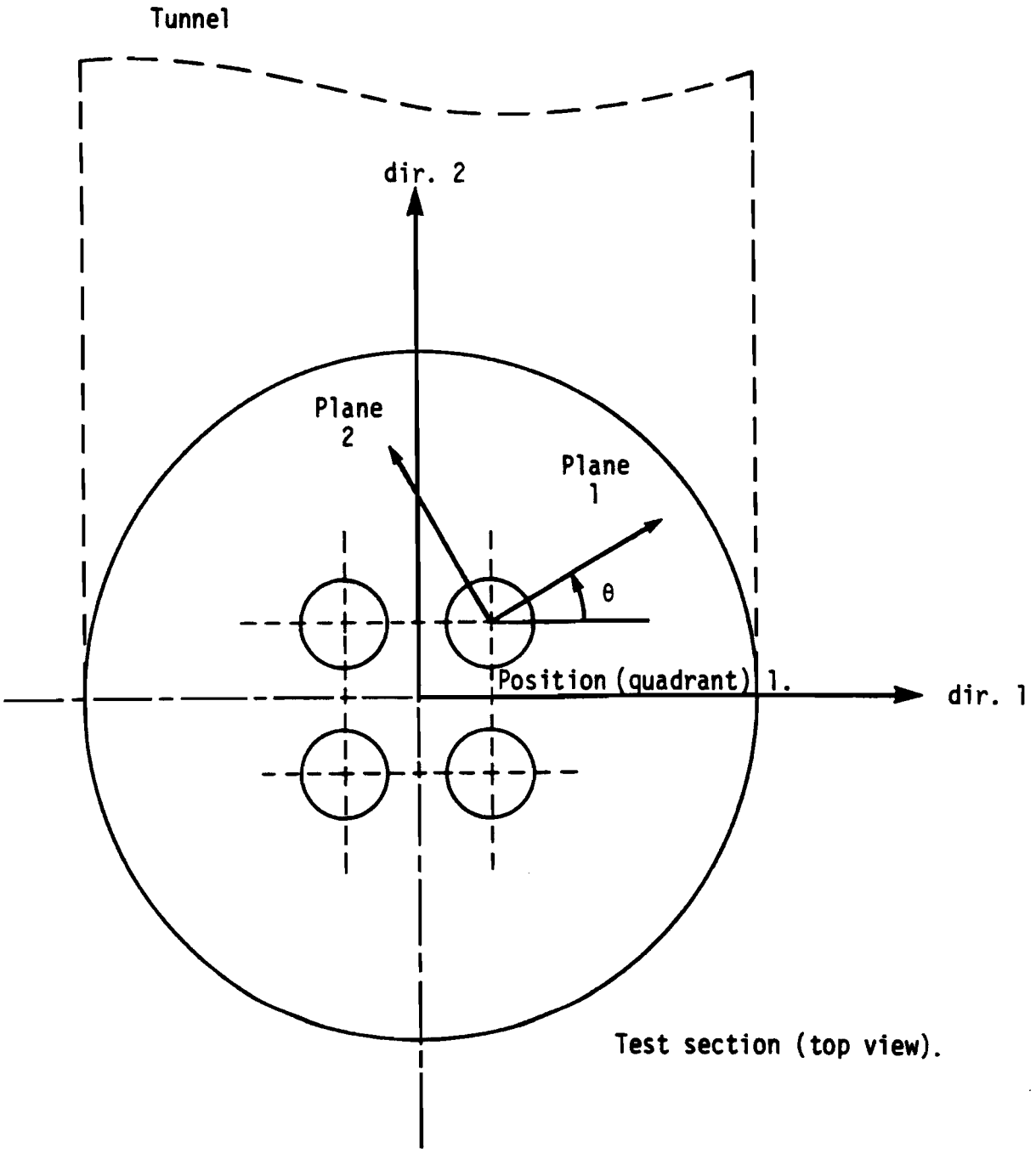

Fig.28: Orientation of K = 4 measurement planes.

Note: Cylinder positions are identified by the quadrants in which they lie.

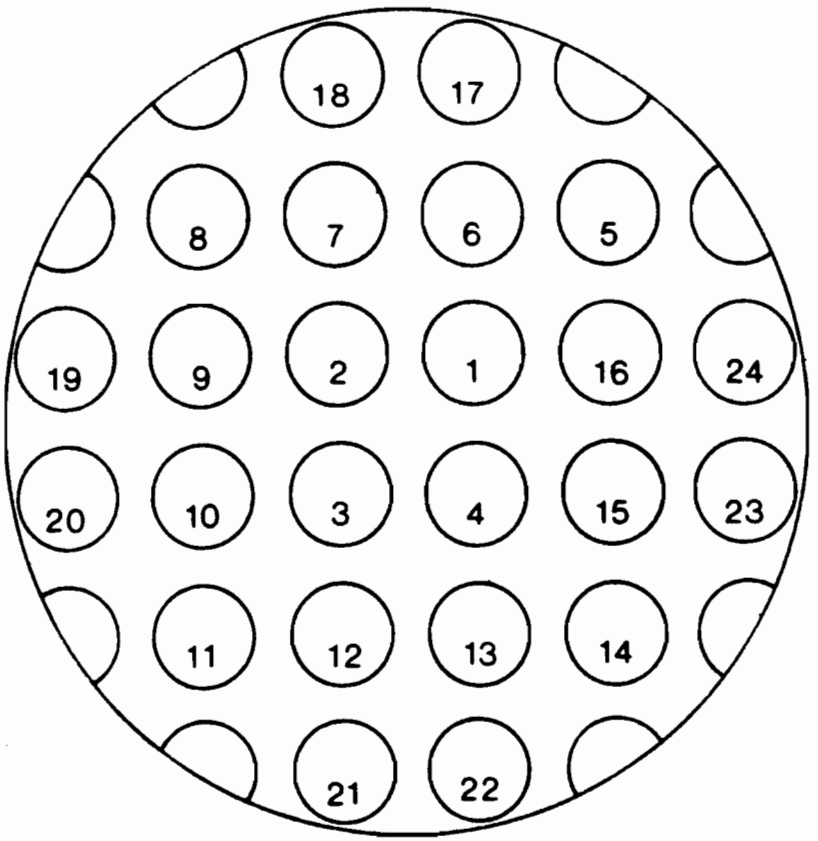

Fig.29: Cylinder positions identification, K = 28.

Note: The eight half-cylinders are not numbered.

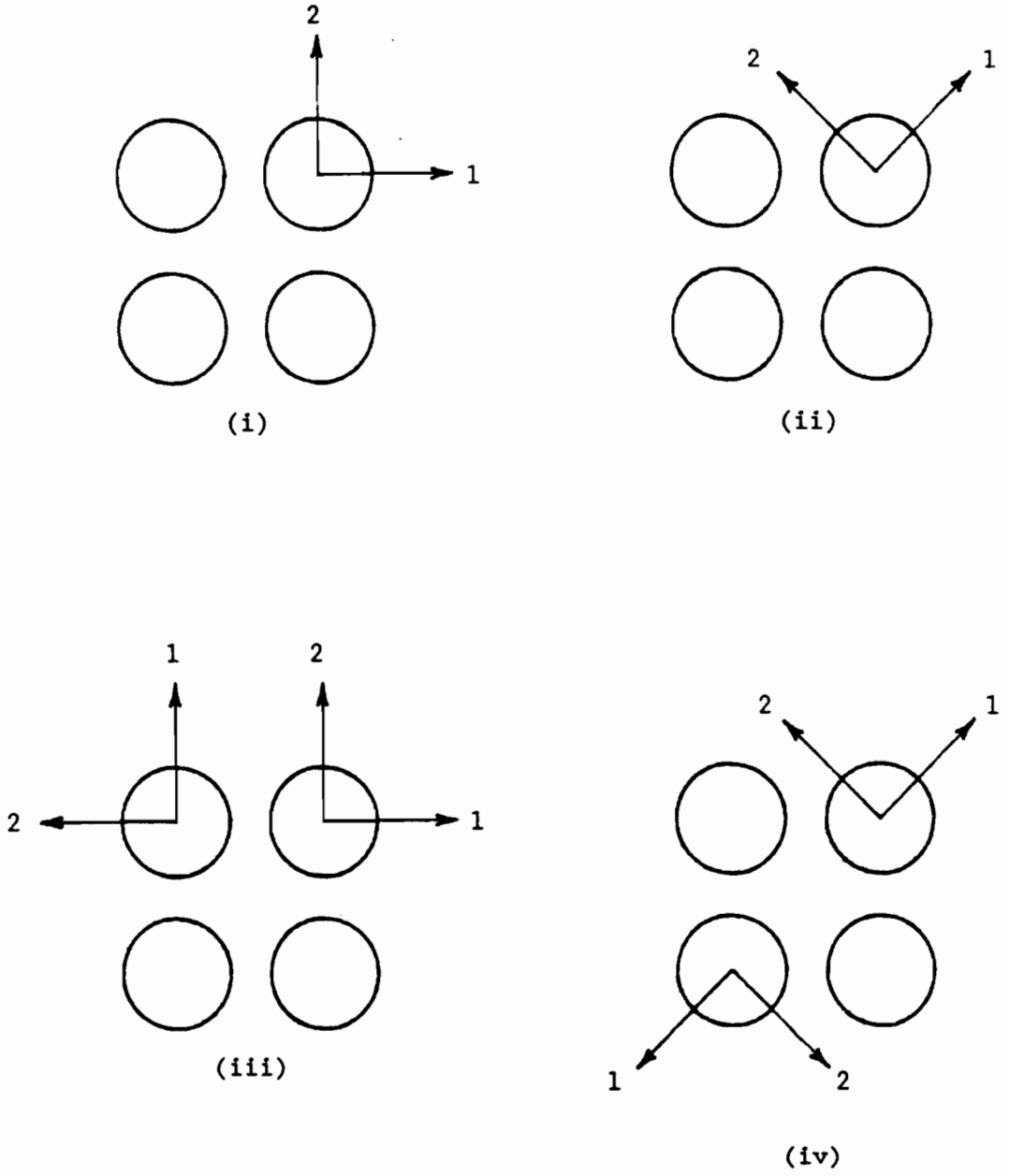

Fig.30: Typical instrumented cylinders measurement setups; (i) 1F/3R, "E" directions, (ii) 1F/3R, "R" and "T" directions, (iii) 4F, "E" directions, adjacent pair, (iv) 4F, "R" and "T" directions, diagonal pair.

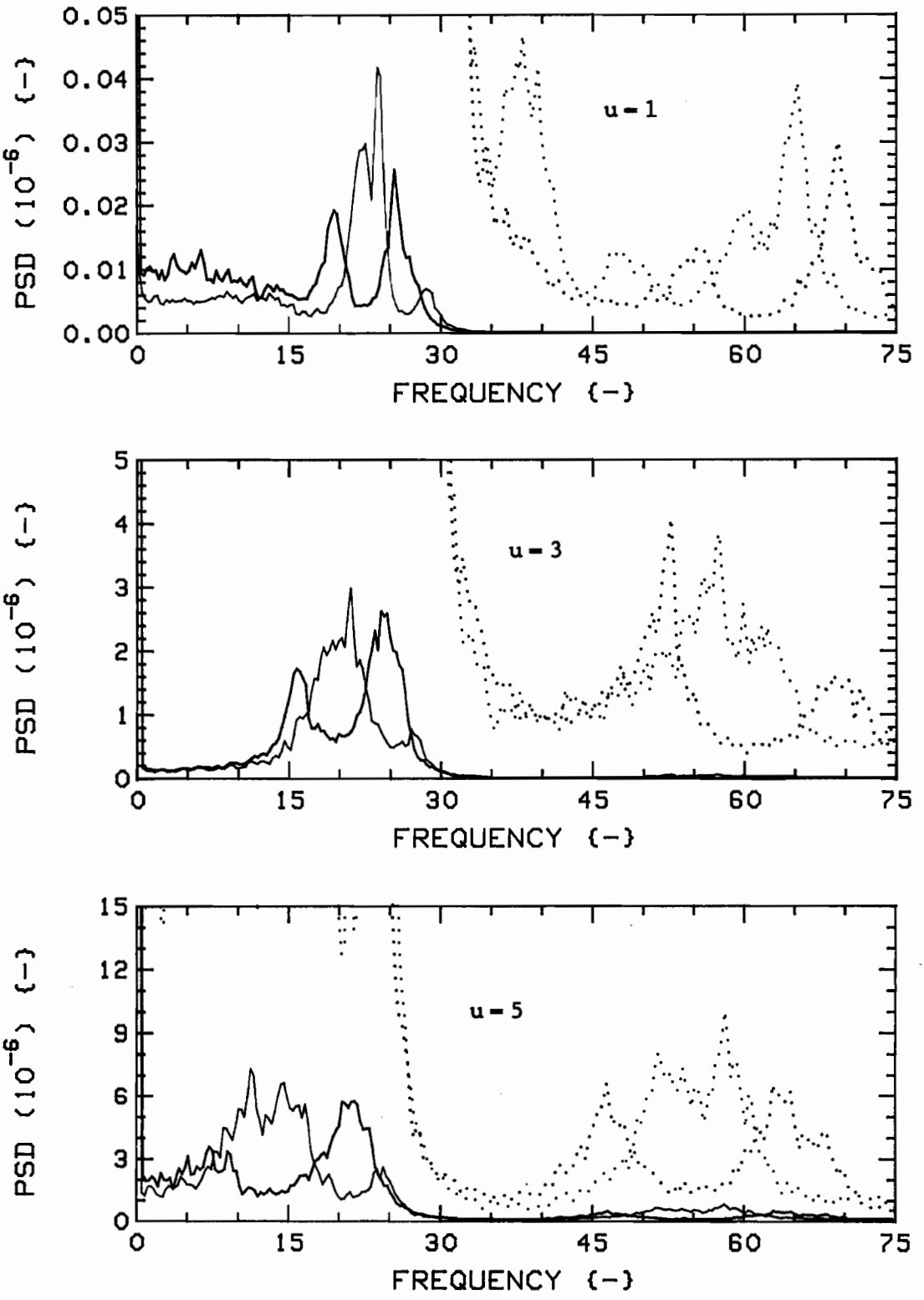

Fig.31: Measured vibration PSD's for K = 4, $G_c = 0.75$, 4F, Radial (RED) and Tangential (BLUE) directions.

The dotted traces are expansions of the solid ones; scales are, from top: 3.0×10^{-10}, 8.0×10^{-8}, 1.2×10^{-6}.

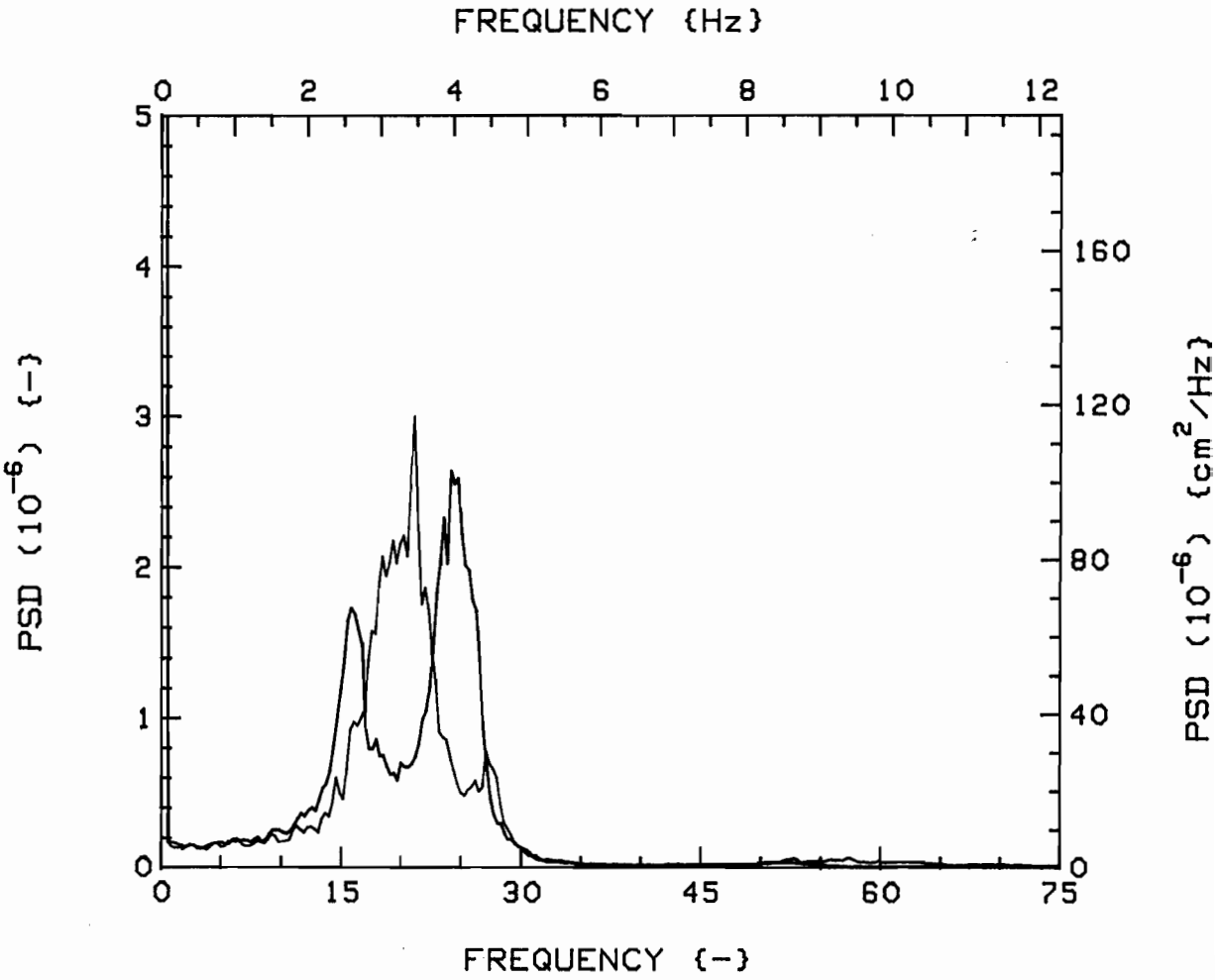

Fig.32: Scales comparison, dimensionless versus dimensional, vibration PSD's of Fig. 31, at u = 3.

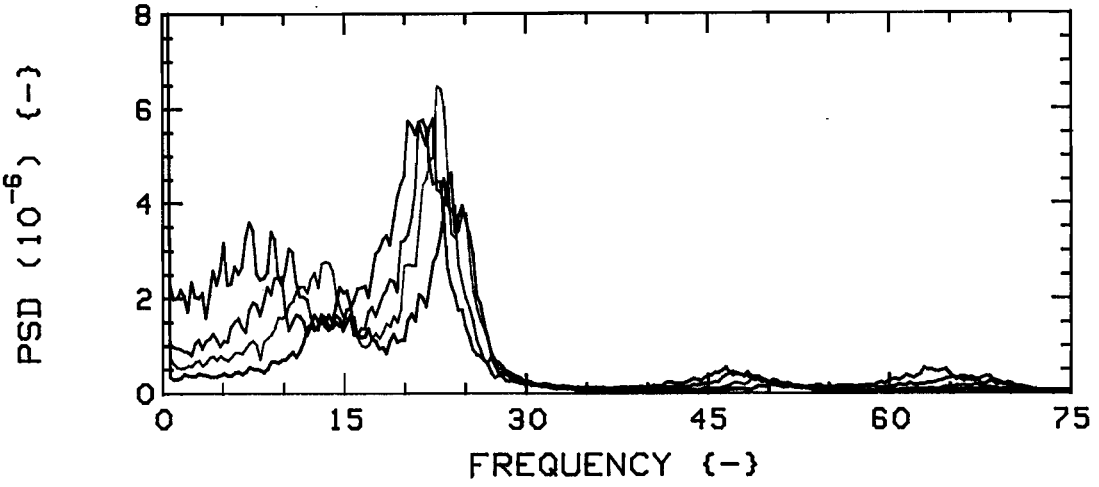

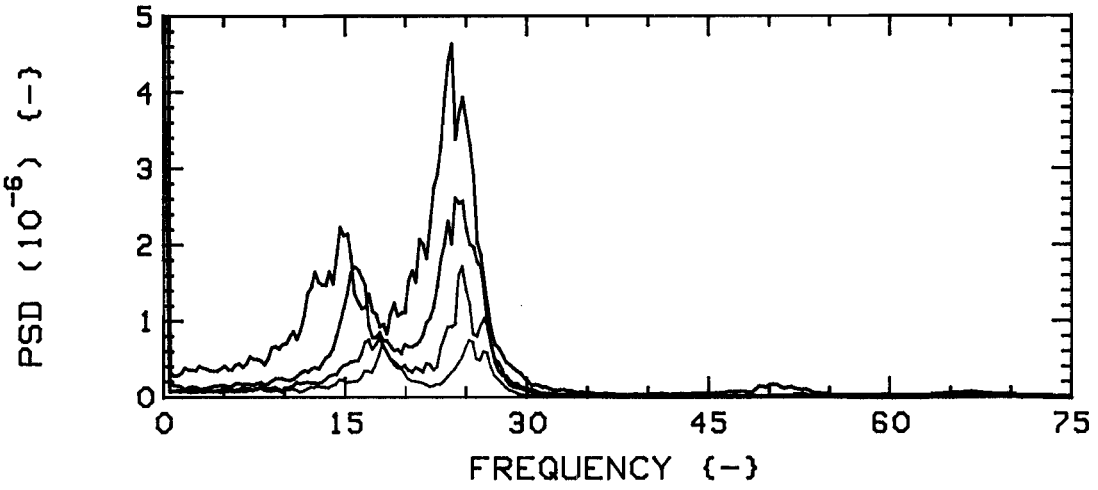

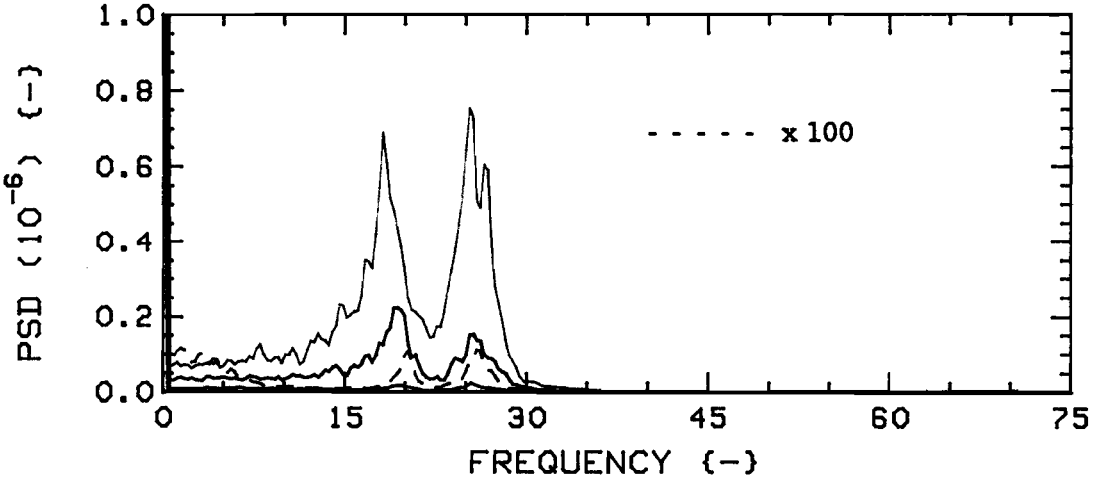

Fig.33a: Measured vibration PSD's for K = 4, G_c = 0.75, 4F, Radial direction, versus flow velocity. In descending order, u = 5.0 to 0.5, in steps of 0.5. Colour sequence: RED, GREEN, BLUE, BLACK (lowest trace of each plot is highest of the next one).

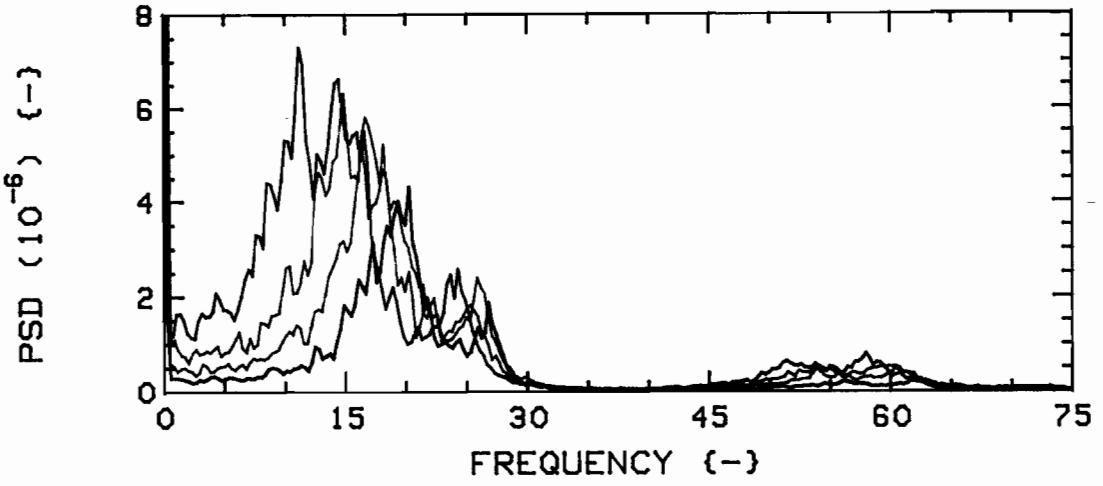

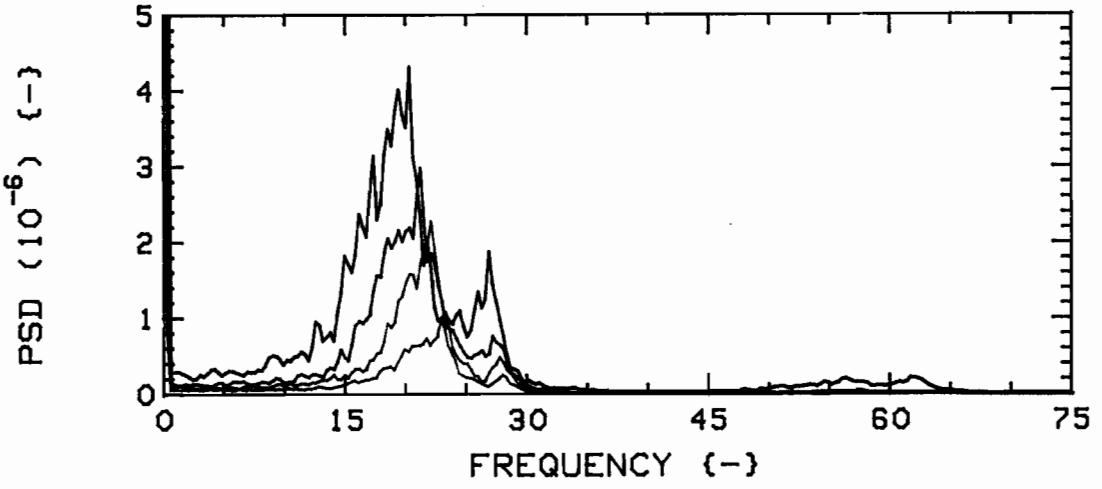

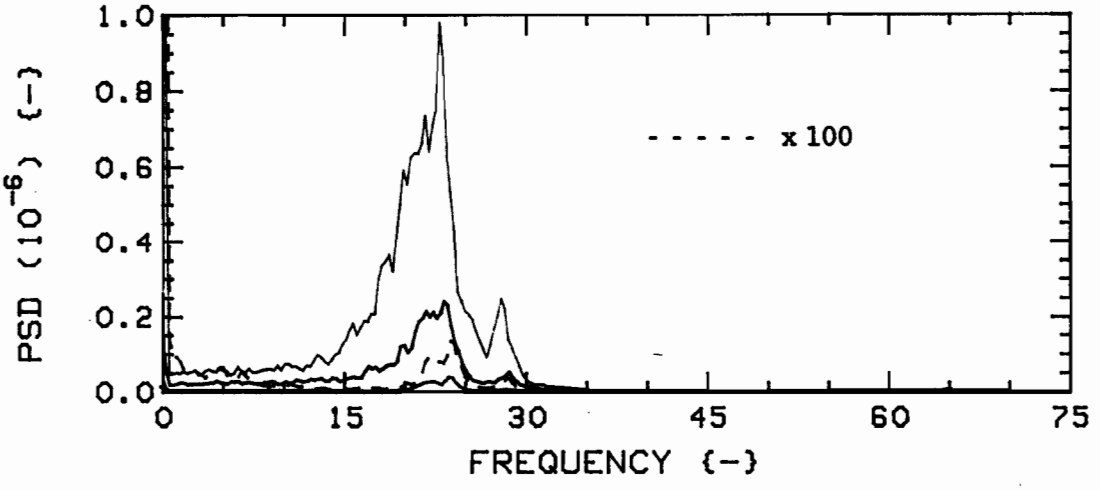

Fig.33b: Measured vibration PSD's for K = 4, G_c = 0.75, 4F, Tangential direction, versus flow velocity. In descending order, u = 5.0 to 0.5, in steps of 0.5. Colour sequence: RED, GREEN, BLUE, BLACK (lowest trace of each plot is highest of the next one).

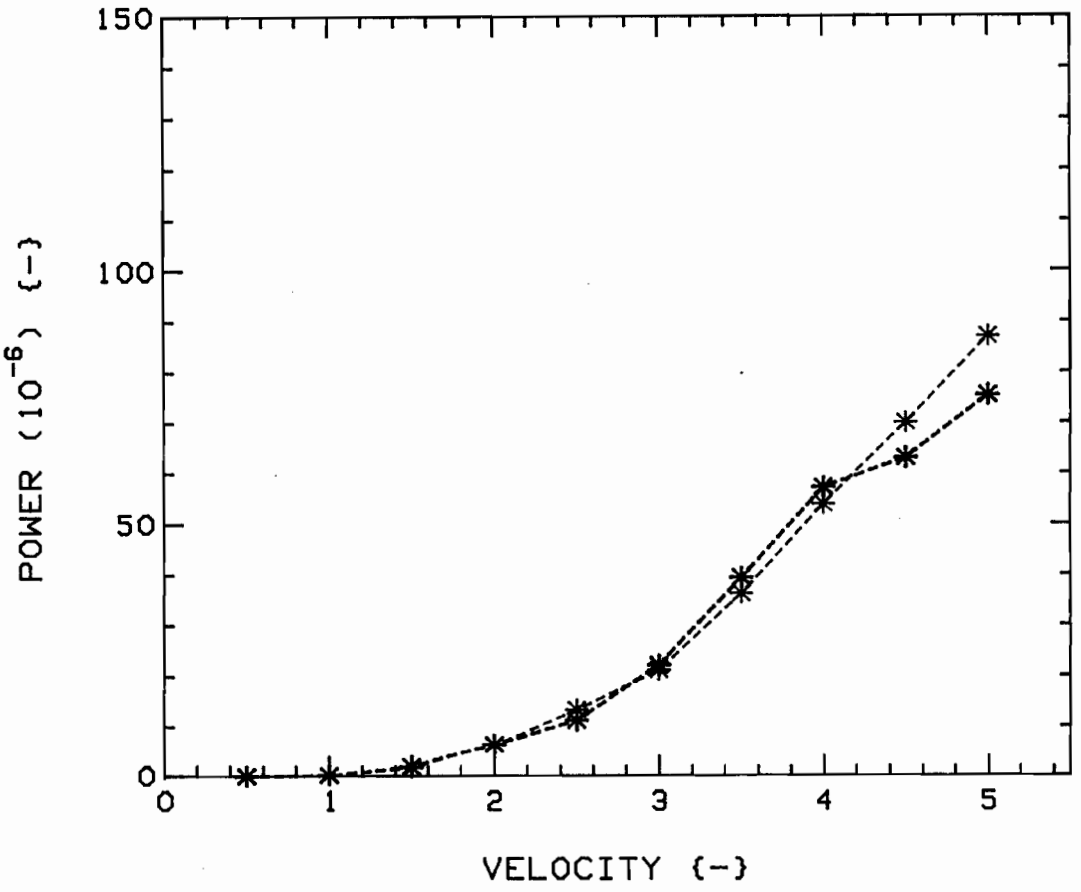

Fig.34: Powers versus flow velocity, for K = 4, G_c = 0.75, 4F, from (integrated) PSD's of Figs. 33a and 33b. Radial (RED) and Tangential (BLUE) directions.

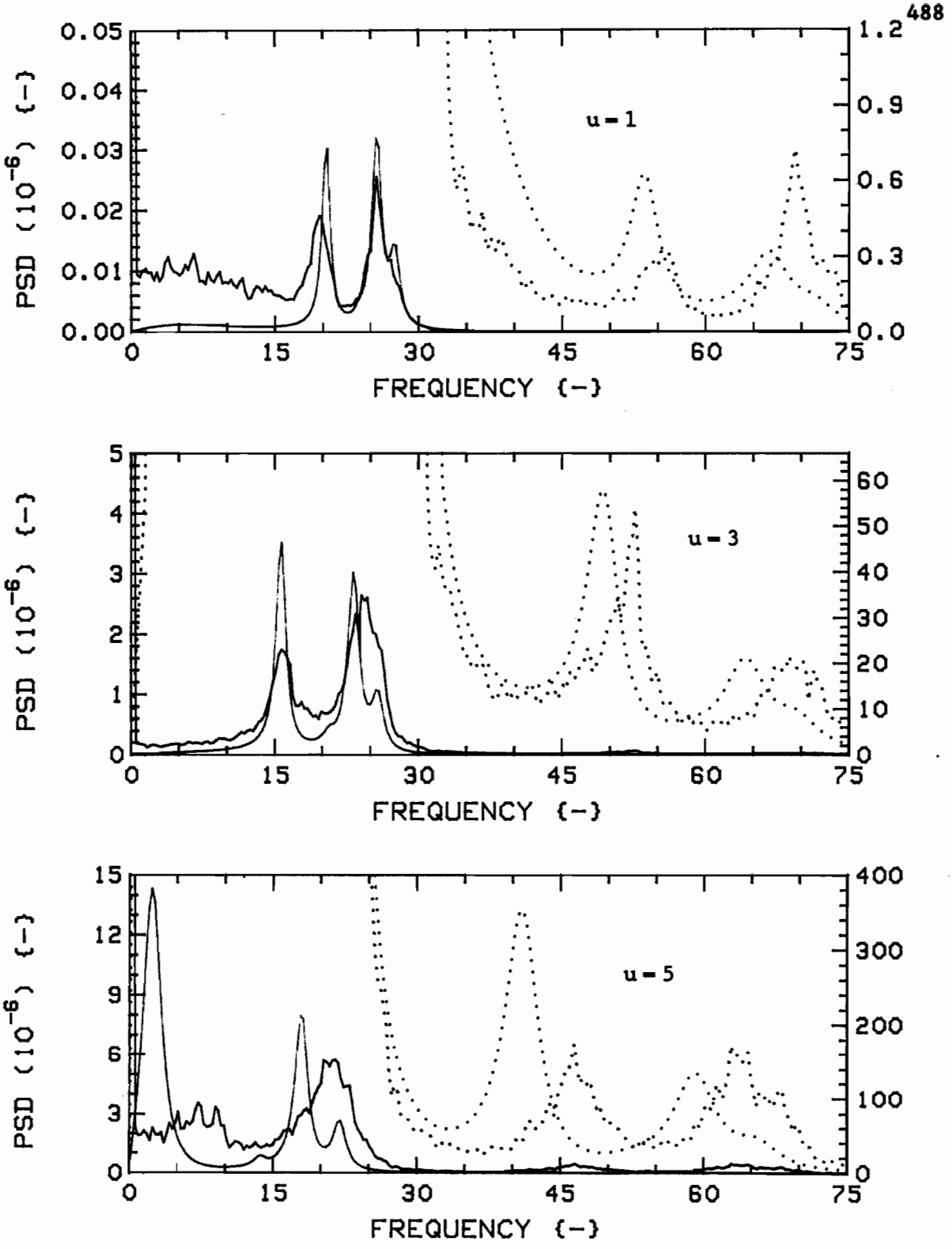

Fig.35a: Measured (RED) and theoretical (GREEN) vibration PSD's for K = 4, G_c = 0.75, 4F, Radial direction.

The dotted traces are expansions of the solid ones; scales are, from top, (RED): 3.0×10^{-10}, 8.0×10^{-8}, 1.2×10^{-6}, (GREEN): 2.0×10^{-8}, 1.8×10^{-7}, 4.0×10^{-6}.

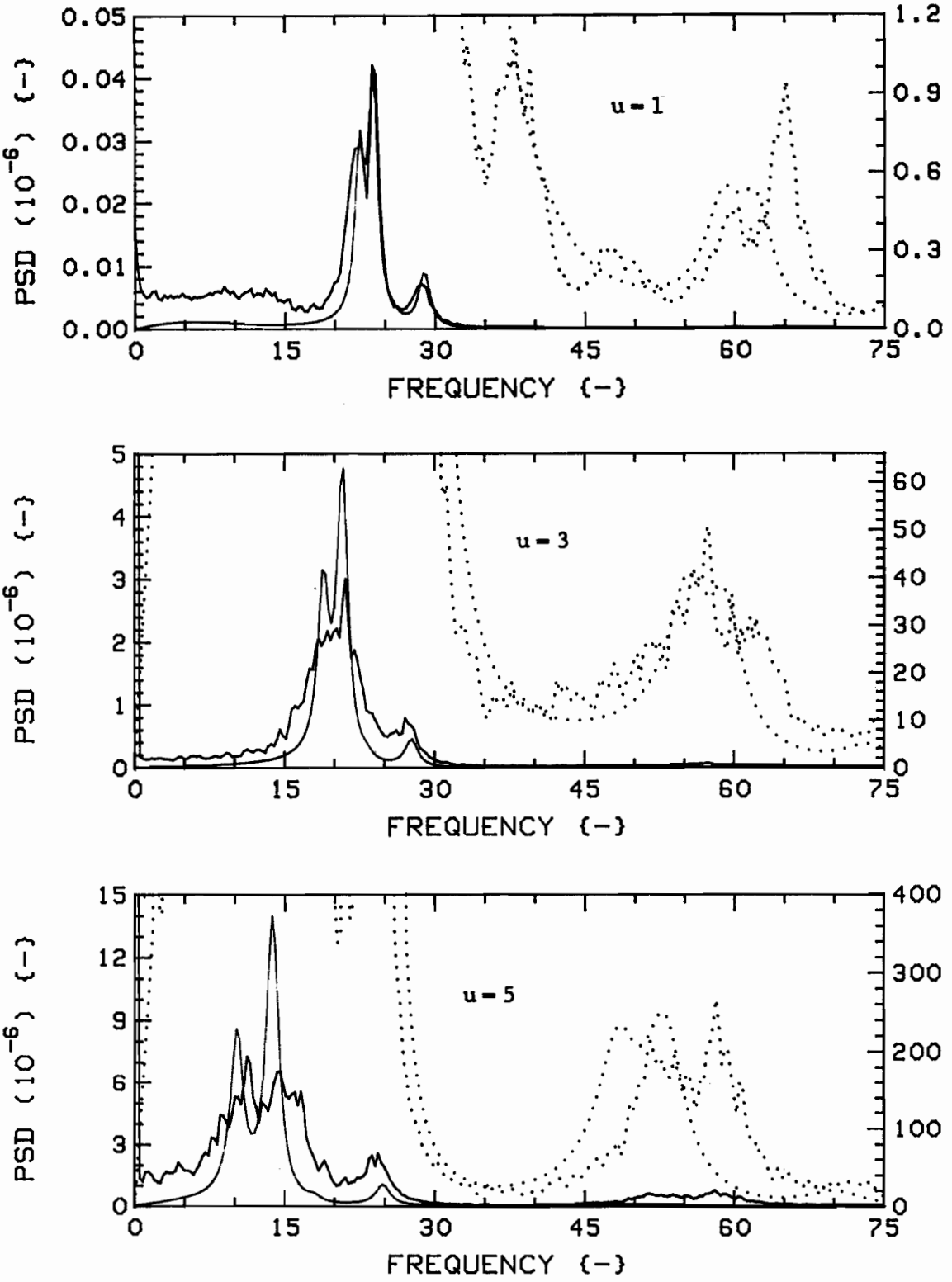

Fig.35b: Measured (RED) and theoretical (GREEN) vibration PSD's for K = 4, $G_c = 0.75$, 4F, Tangential direction.

The dotted traces are expansions of the solid ones; scales are, from top, (RED): 3.0×10^{-10}, 8.0×10^{-8}, 1.2×10^{-6},

(GREEN): 2.0×10^{-9}, 1.8×10^{-7}, 4.0×10^{-6}.

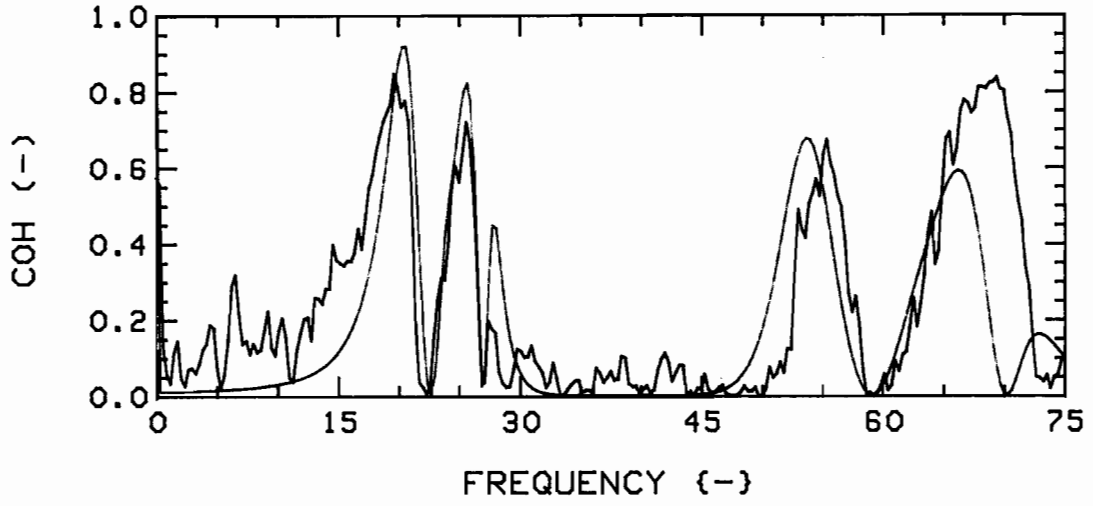

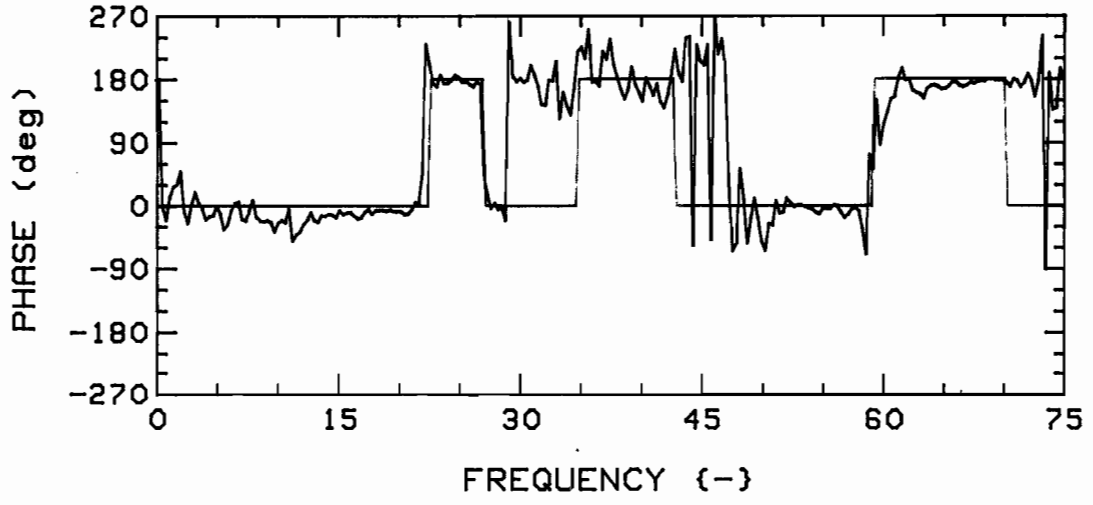

Fig.36a: Measured (RED) and theoretical (GREEN) coherence functions and phases, for K = 4, G_c = 0.75, 4F, R-R (1,3), at u = 1.

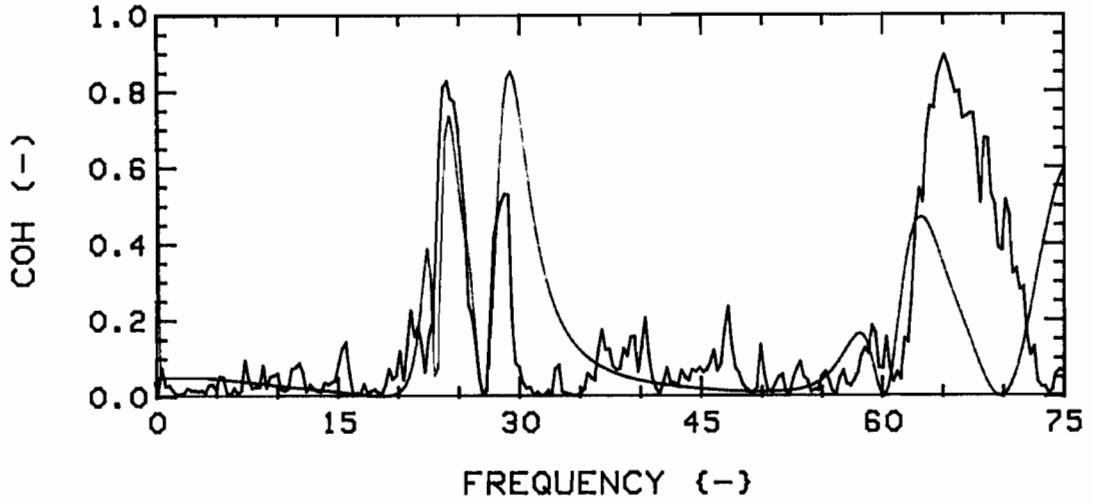

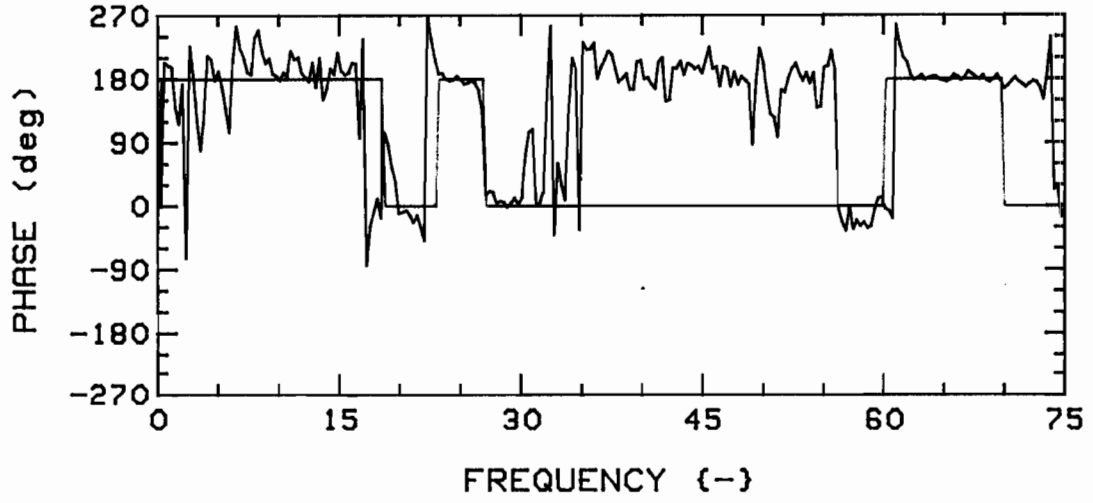

Fig.36b: Measured (RED) and theoretical (GREEN) coherence functions and phases, for K = 4, G_c = 0.75, 4F, T-T (1,3), at u = 1.

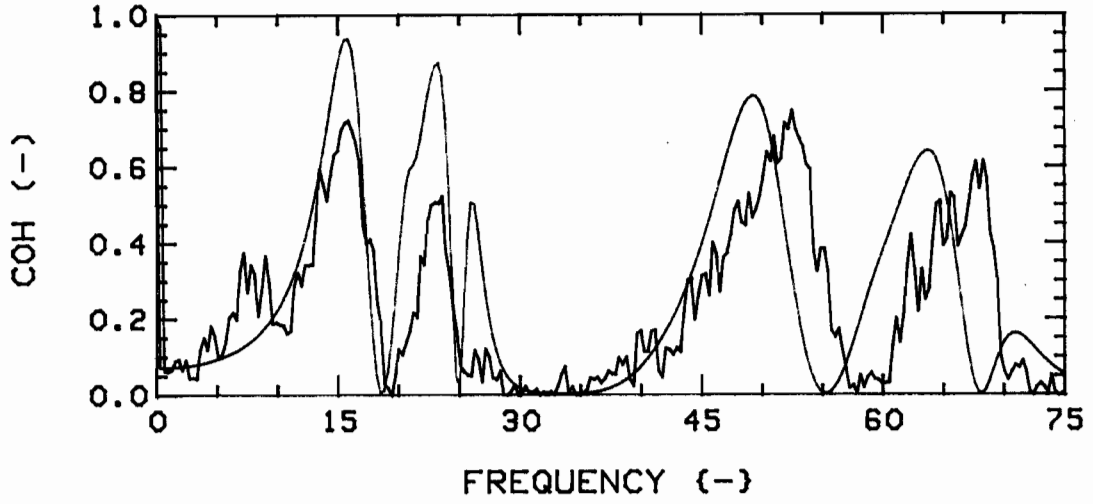

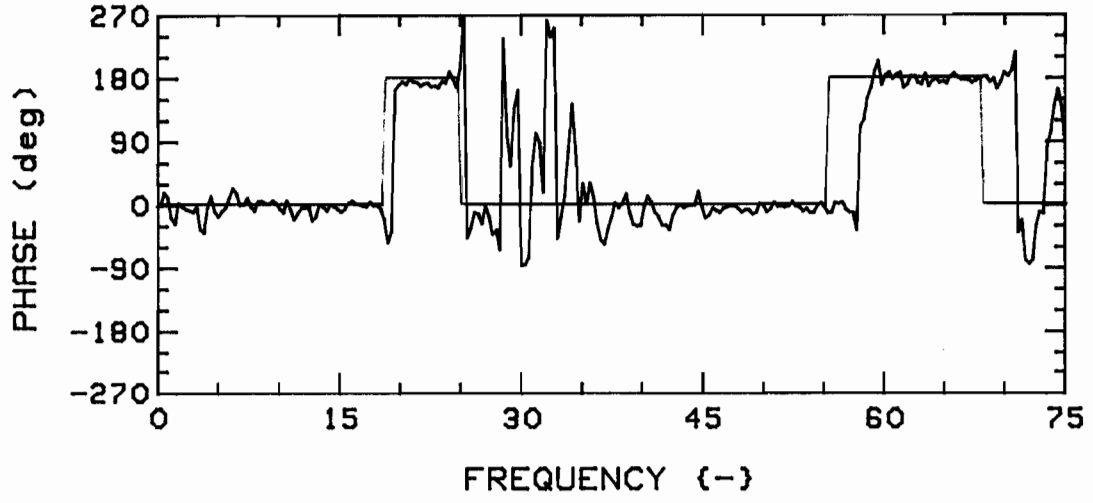

Fig.36c: Measured (RED) and theoretical (GREEN) coherence functions and phases, for K = 4, G_c = 0.75, 4F, R-R (1,3), at u = 3.

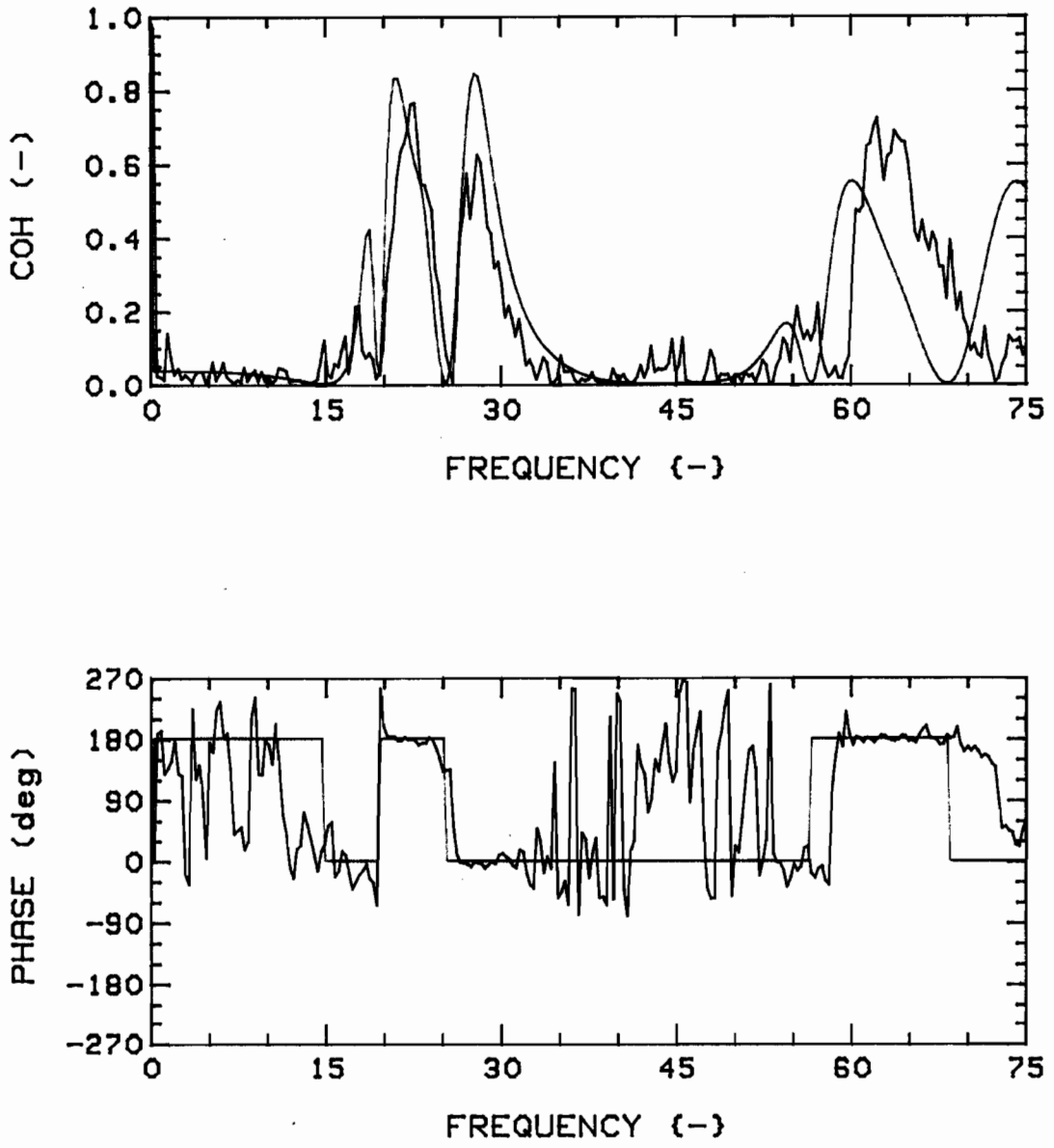

Fig.36d: Measured (RED) and theoretical (GREEN) coherence functions and phases, for K = 4, G_c = 0.75, 4F, T-T (1,3), at u = 3.

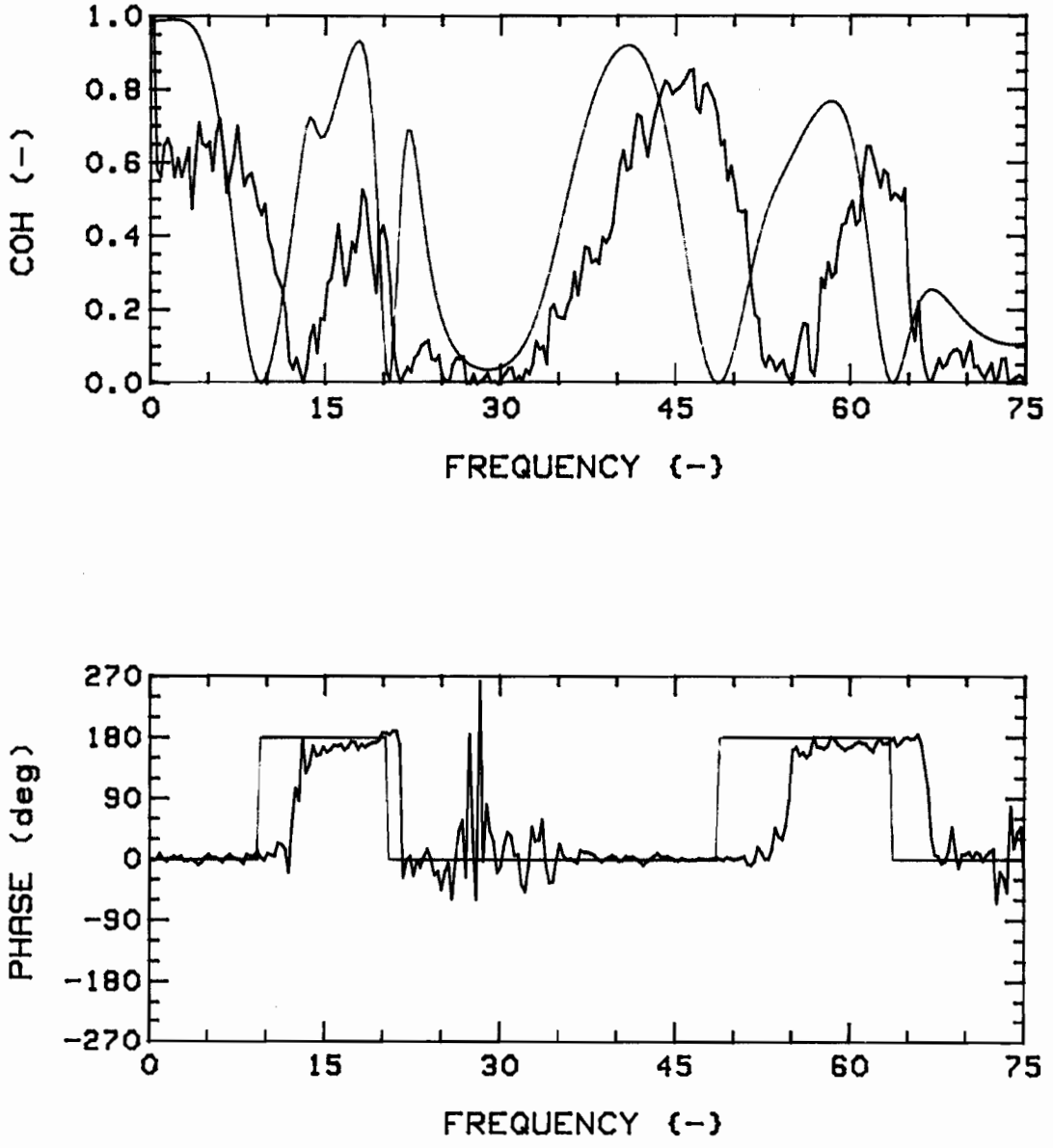

Fig.36e: Measured (RED) and theoretical (GREEN) coherence functions and phases, for K = 4, G_c = 0.75, 4F, R-R (1,3), at u = 5.

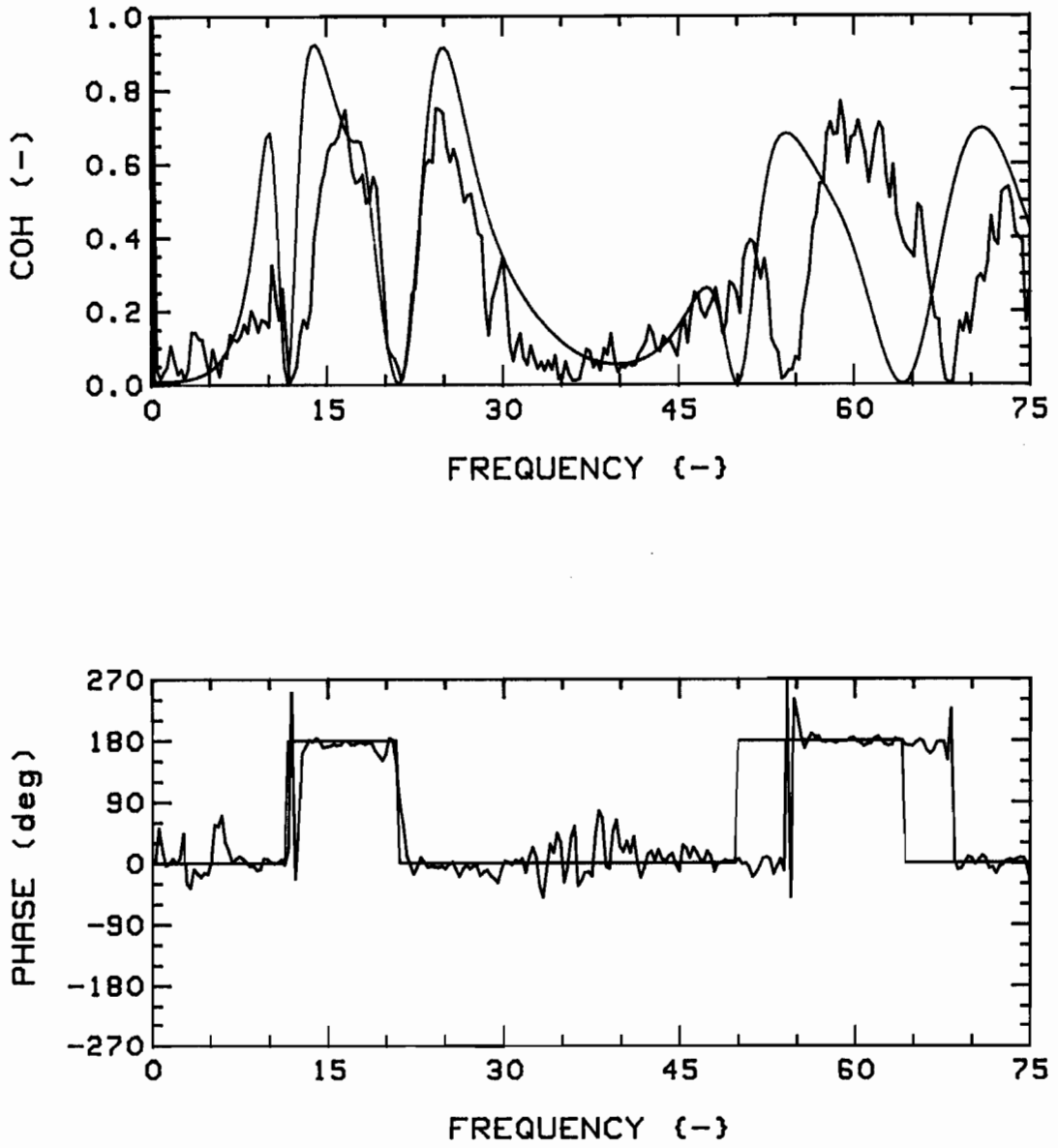

Fig.36f: Measured (RED) and theoretical (GREEN) coherence functions and phases, for K = 4, G_c = 0.75, 4F, T-T (1,3), at u = 5.

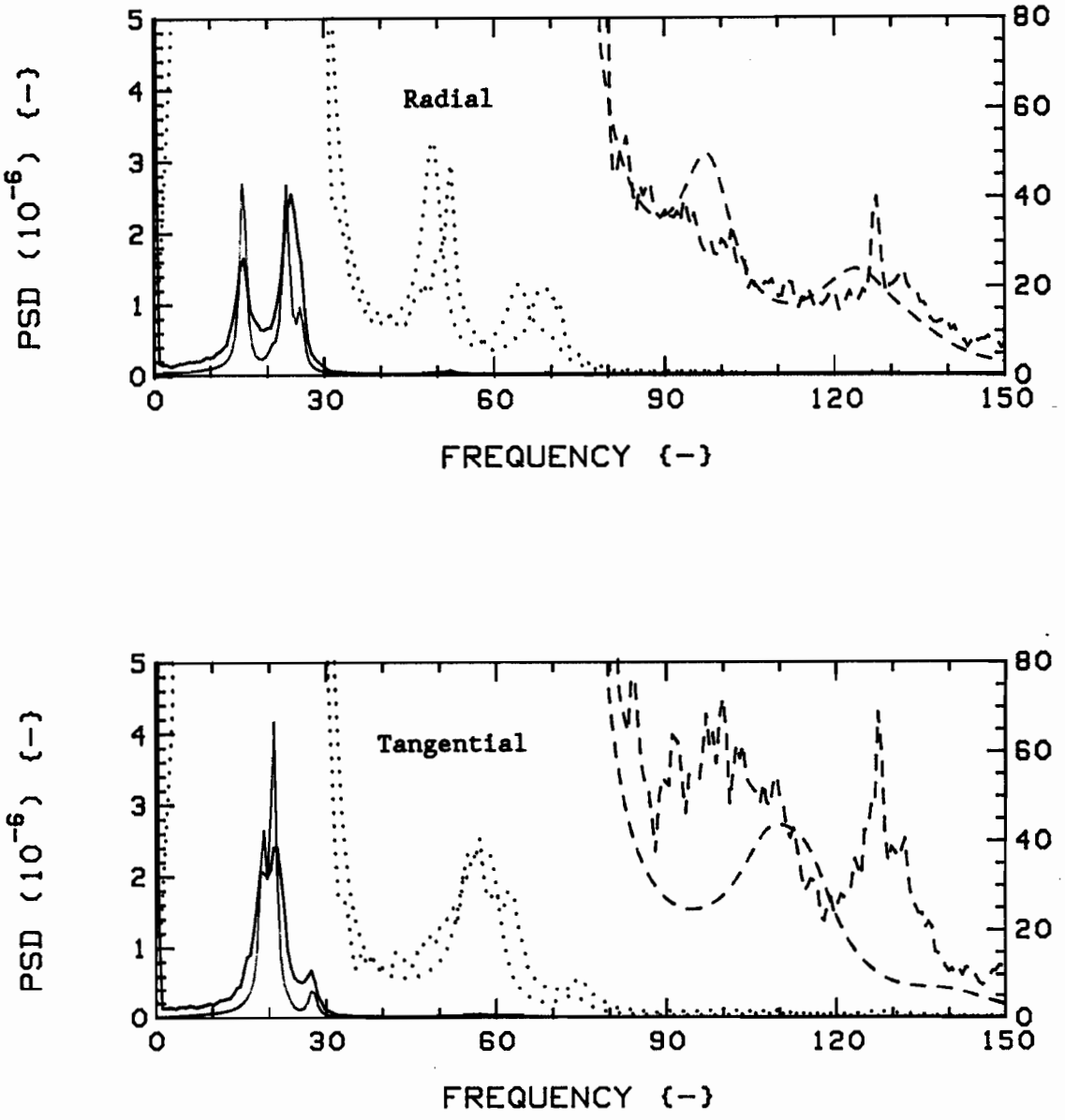

Fig.37: Third beam mode group detection: measured (RED) and theoretical* (GREEN) vibration PSD's for K = 4, $G_c = 0.75$, 4F, and u = 3. Note the higher bandwidth used.

The dotted and dashed traces are expansions of the solid ones; scales are, (RED): 1.0×10^{-7} and 2.5×10^{-9}, (GREEN): 2.5×10^{-7} and 4.0×10^{-9}.

* N = 5, and earlier values of c = 0 and $c_z = 0.027$ used here.

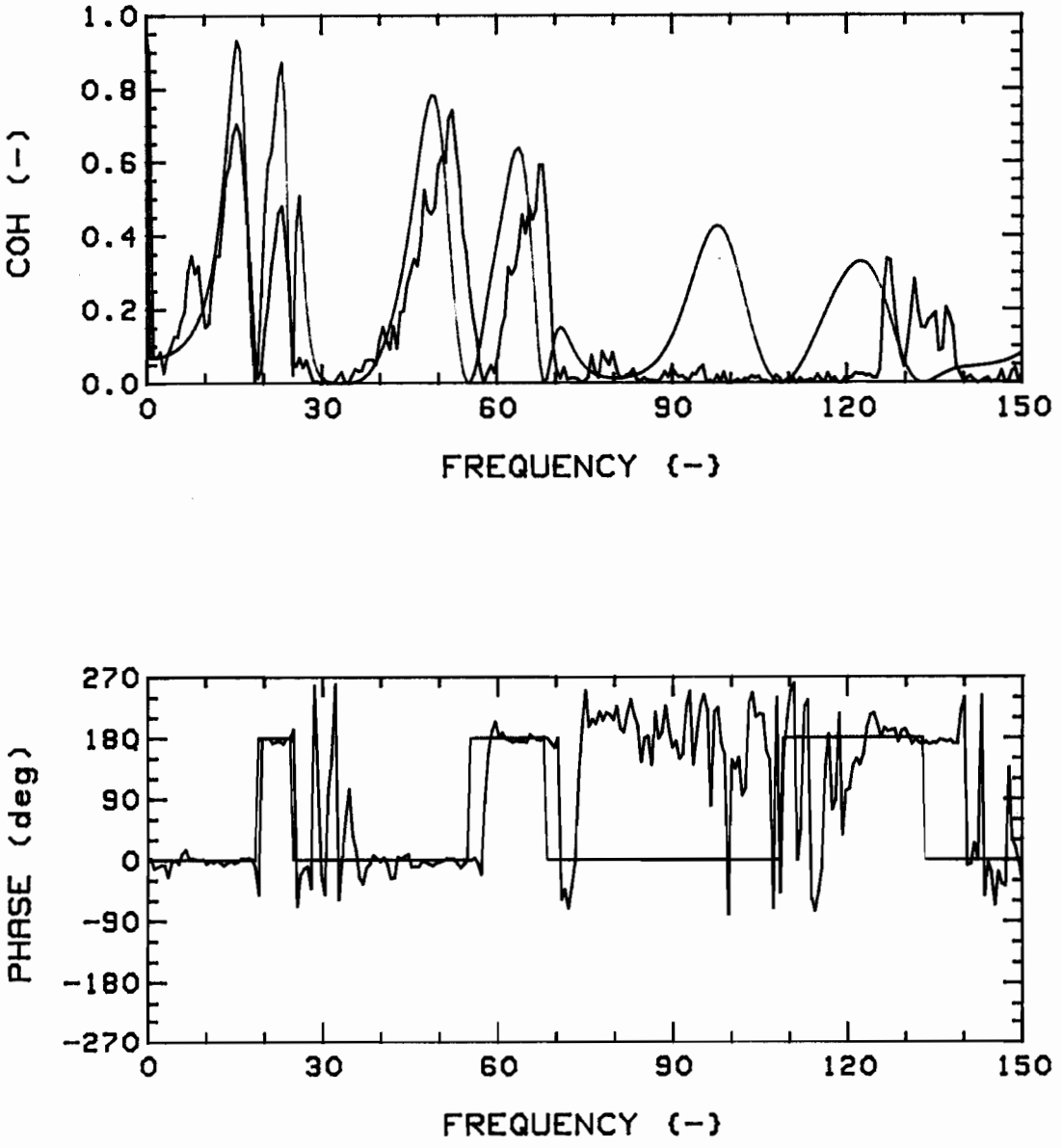

Fig.38a: Third beam mode group detection: measured (RED) and theoretical* (GREEN) coherence functions and phases, for K = 4, $G_c = 0.75$, 4F, R-R (1,3), and u = 3. Note the higher bandwidth used.

* N = 5, and earlier values of c = 0 and $c_f = 0.027$ used here.

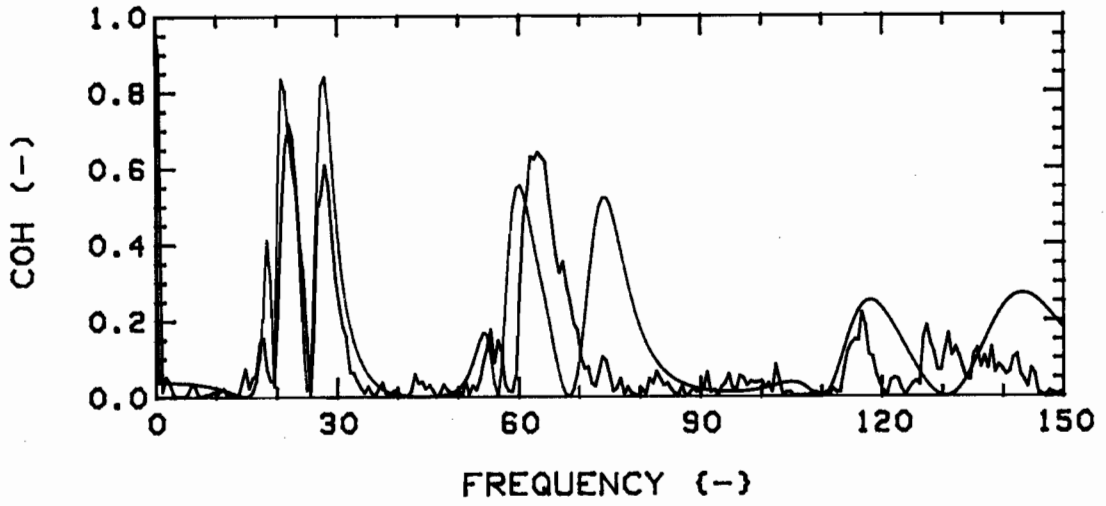

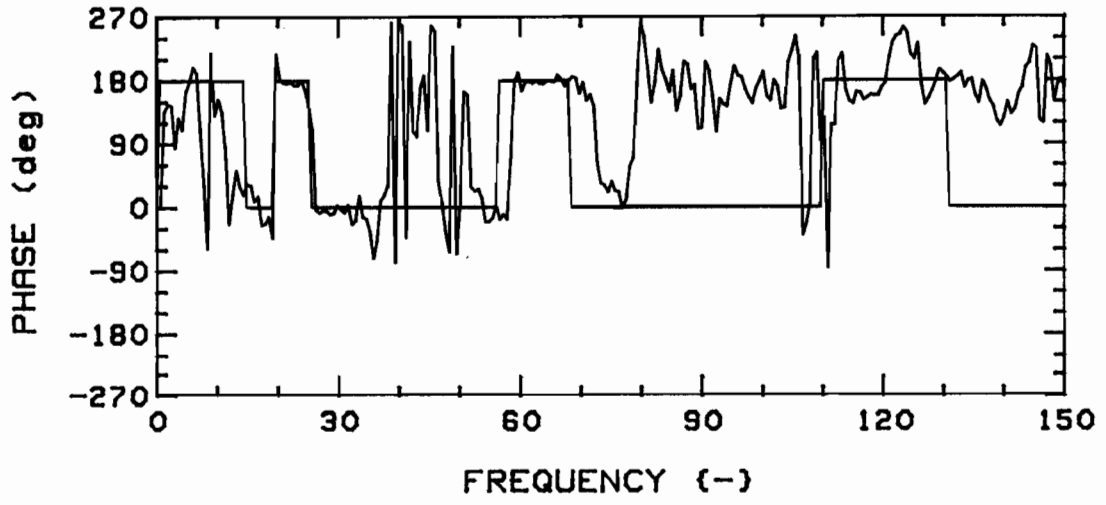

Fig.38b: Third beam mode group detection: measured (RED) and theoretical* (GREEN) coherence functions and phases, for K = 4, $G_c = 0.75$, 4F, T-T (1,3), and u = 3. Note the higher bandwidth used.

* N = 5, and earlier values of c = 0 and $c_z = 0.027$ used here.

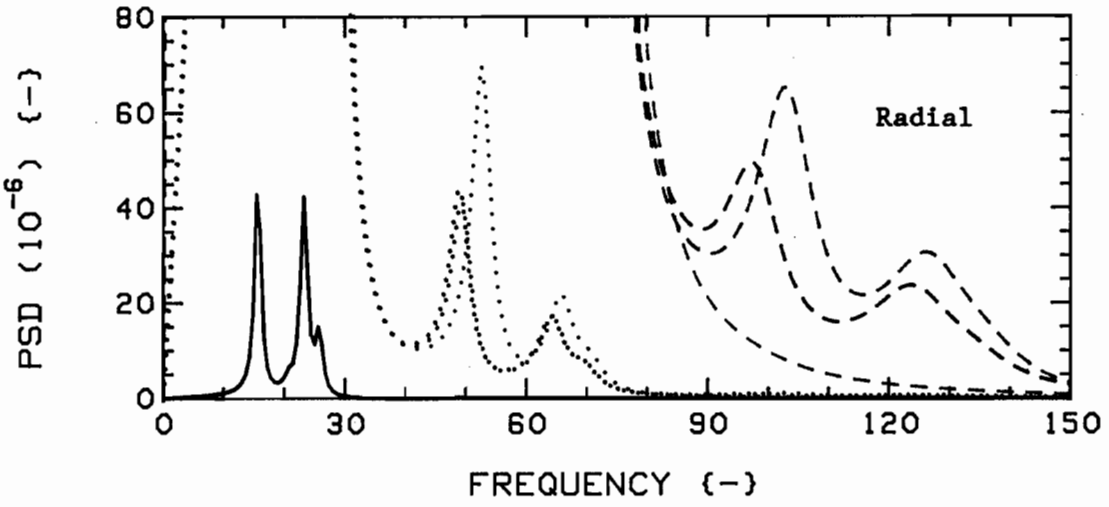

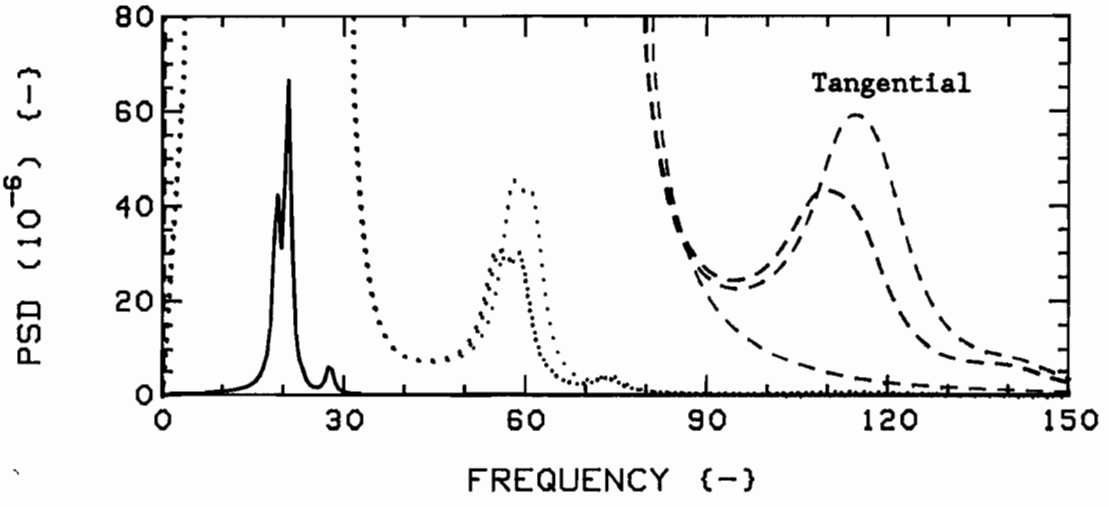

Fig.39: Effect of the number of comparison functions used in the theory,* on vibration PSD's. Test case: K = 4, G_c = 0.75, 4F, u = 3. Note the higher bandwidth used.
Values: N = 5 (RED), 3 (GREEN), 2 (BLUE).

The dotted and dashed traces are expansions of the solid ones; scales are 3.0×10^{-7} and 4.0×10^{-9} respectively.

* Earlier values of c = 0 and c_f = 0.027 used here.

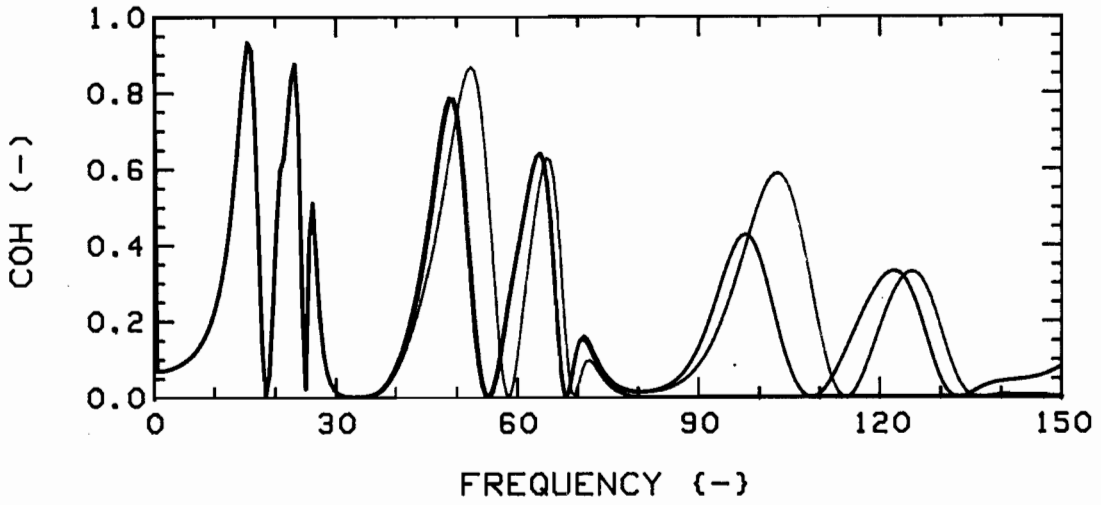

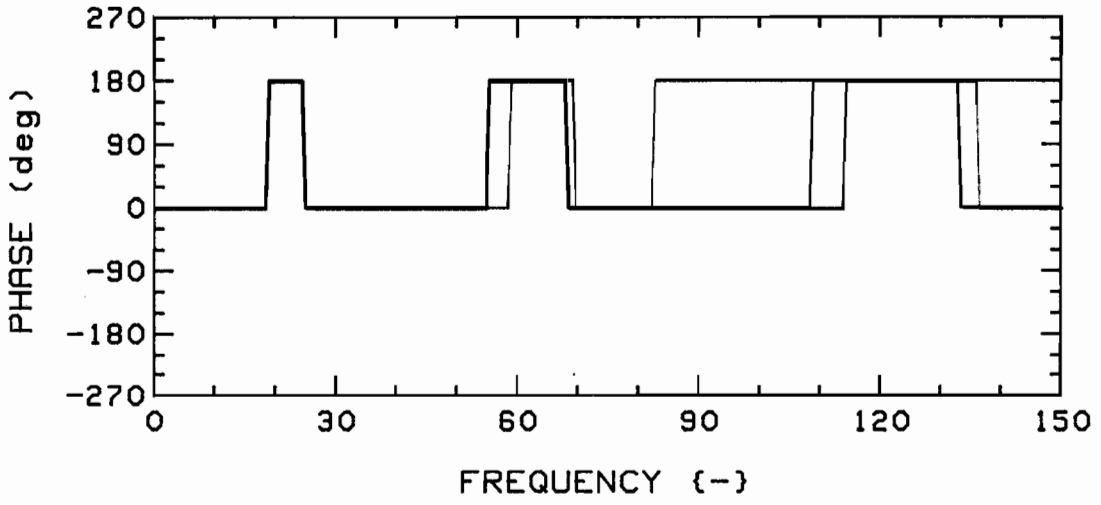

Fig.40a: Effect of the number of comparison functions used in the theory,* on coherence function and phase, R-R (1,3). Test case: K = 4, G_c = 0.75, 4F, u = 3. Note the higher bandwidth used.
Values: N = 5 (RED), 3 (GREEN), 2 (BLUE).

* Earlier values of c = 0 and c_f = 0.027 used here.

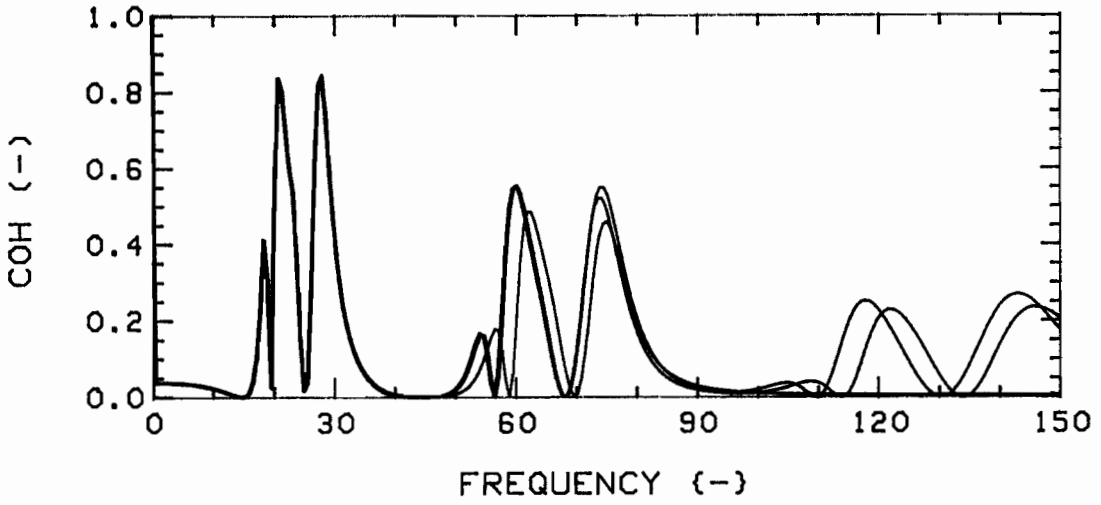

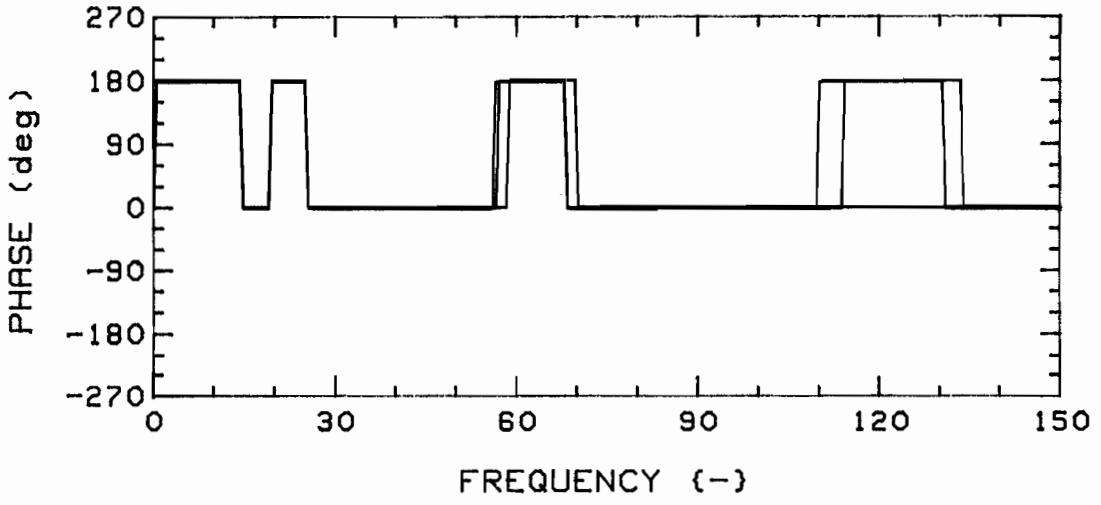

Fig.40b: Effect of the number of comparison functions used in the theory,* on coherence function and phase, T-T (1,3). Test case: K = 4, $G_c = 0.75$, 4F, u = 3. Note the higher bandwidth used.
Values: N = 5 (RED), 3 (GREEN), 2 (BLUE).

* Earlier values of c = 0 and $c_f = 0.027$ used here.

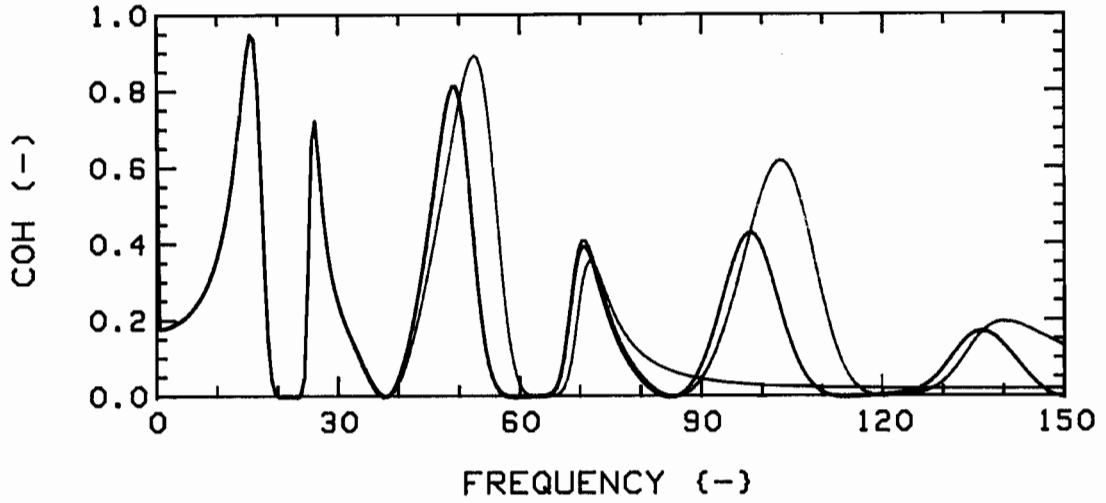

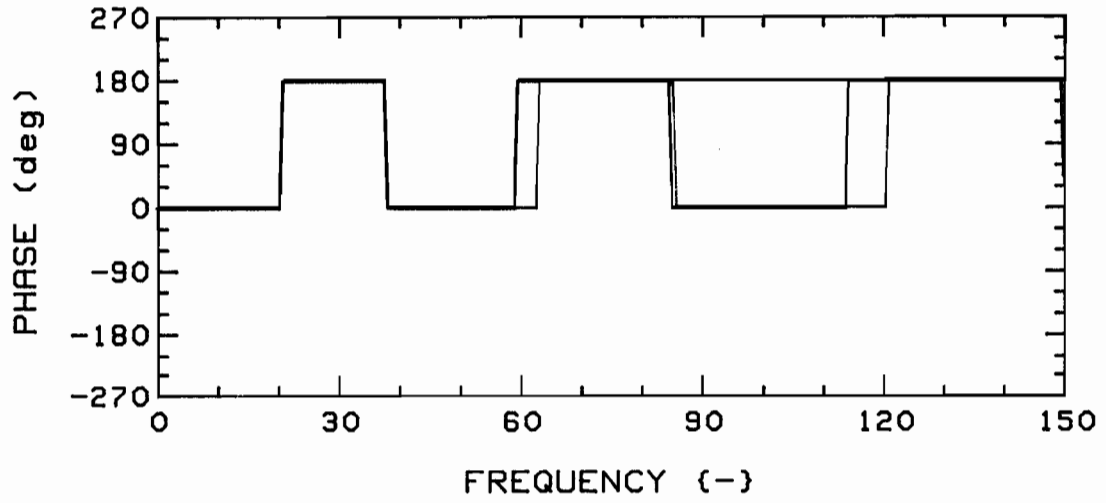

Fig.40c: Effect of the number of comparison functions used in the theory,* on coherence function and phase, R-R (1,2). Test case: K = 4, G_c = 0.75, 4F, u = 3. Note the higher bandwidth used.
Values: N = 5 (RED), 3 (GREEN), 2 (BLUE).

* Earlier values of c = 0 and c_f = 0.027 used here.

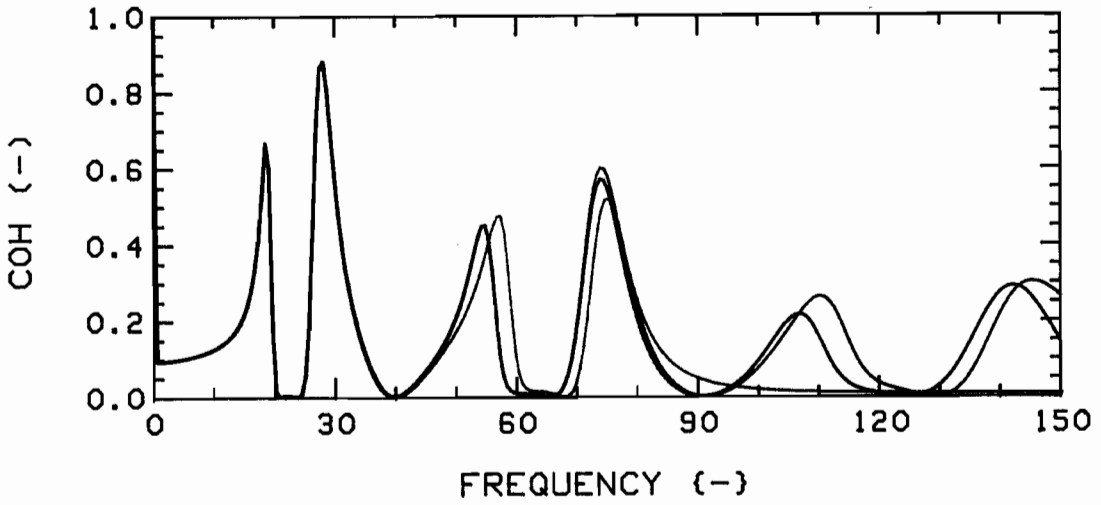

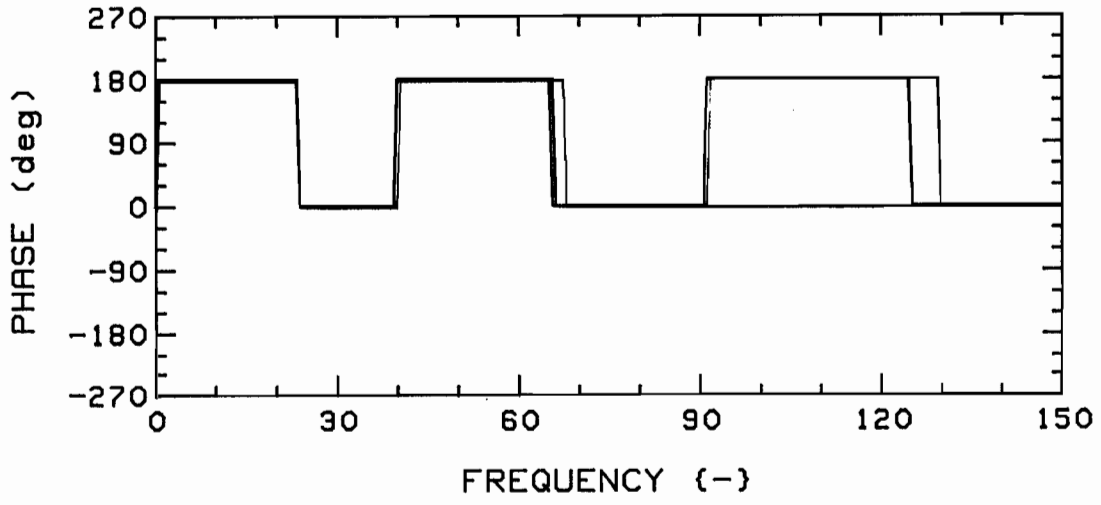

Fig.40d: Effect of the number of comparison functions used in the theory,* on coherence function and phase, T-T (1,2). Test case: K = 4, G_c = 0.75, 4F, u = 3. Note the higher bandwidth used.
Values: N = 5 (RED), 3 (GREEN), 2 (BLUE).

* Earlier values of c = 0 and c_f = 0.027 used here.

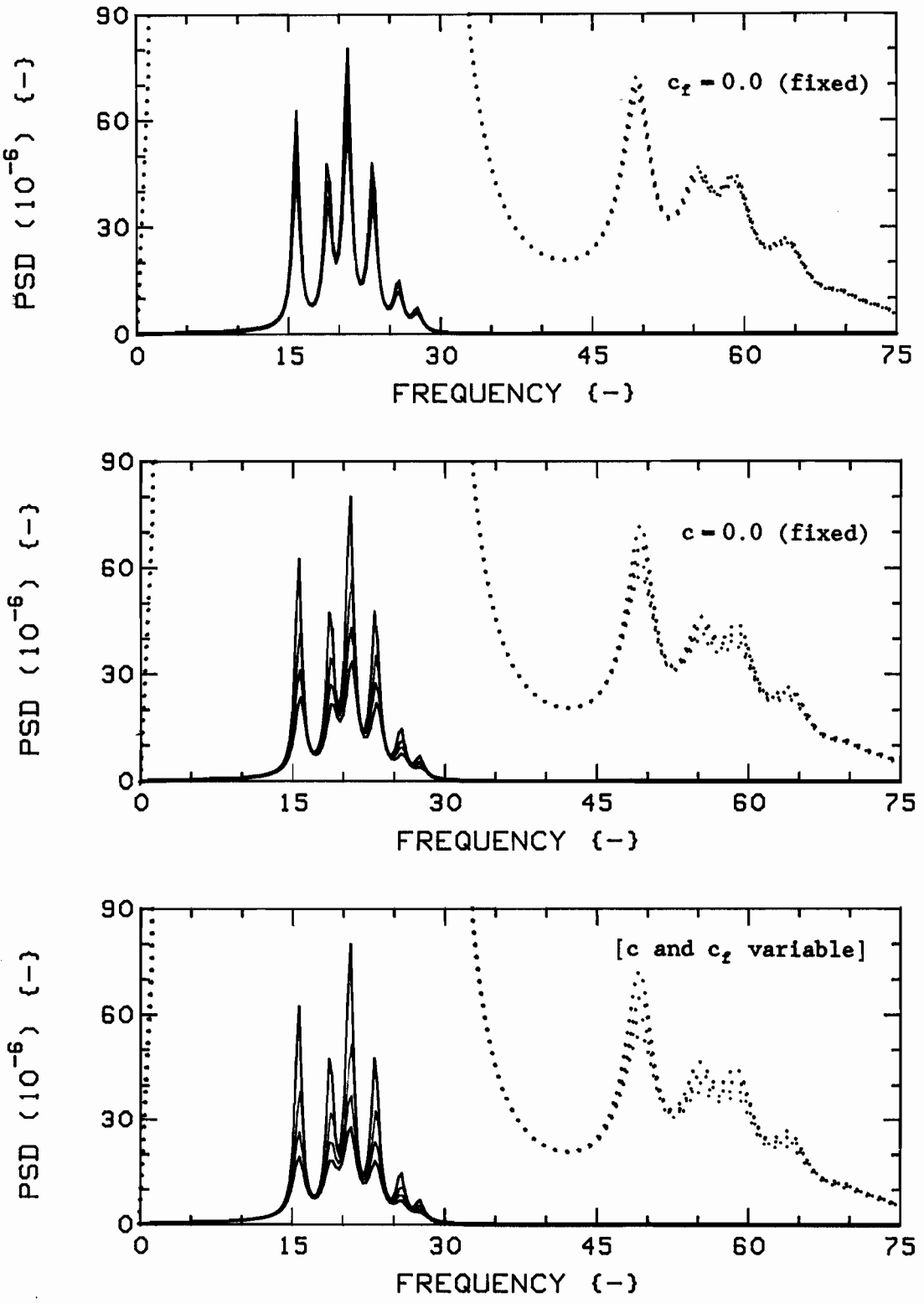

Fig.41: Effect of the values of c and c_f used in the theory, on vibration PSD's. Test case: K = 4, G_c = 0.75, 4F, u = 3. c only (top), c_f only (mid), and both (bottom). Values are 0.00 (RED), 0.01 (GREEN), 0.02 (BLUE), and 0.03 (BLACK). Note that Edge direction PSD's were used here.

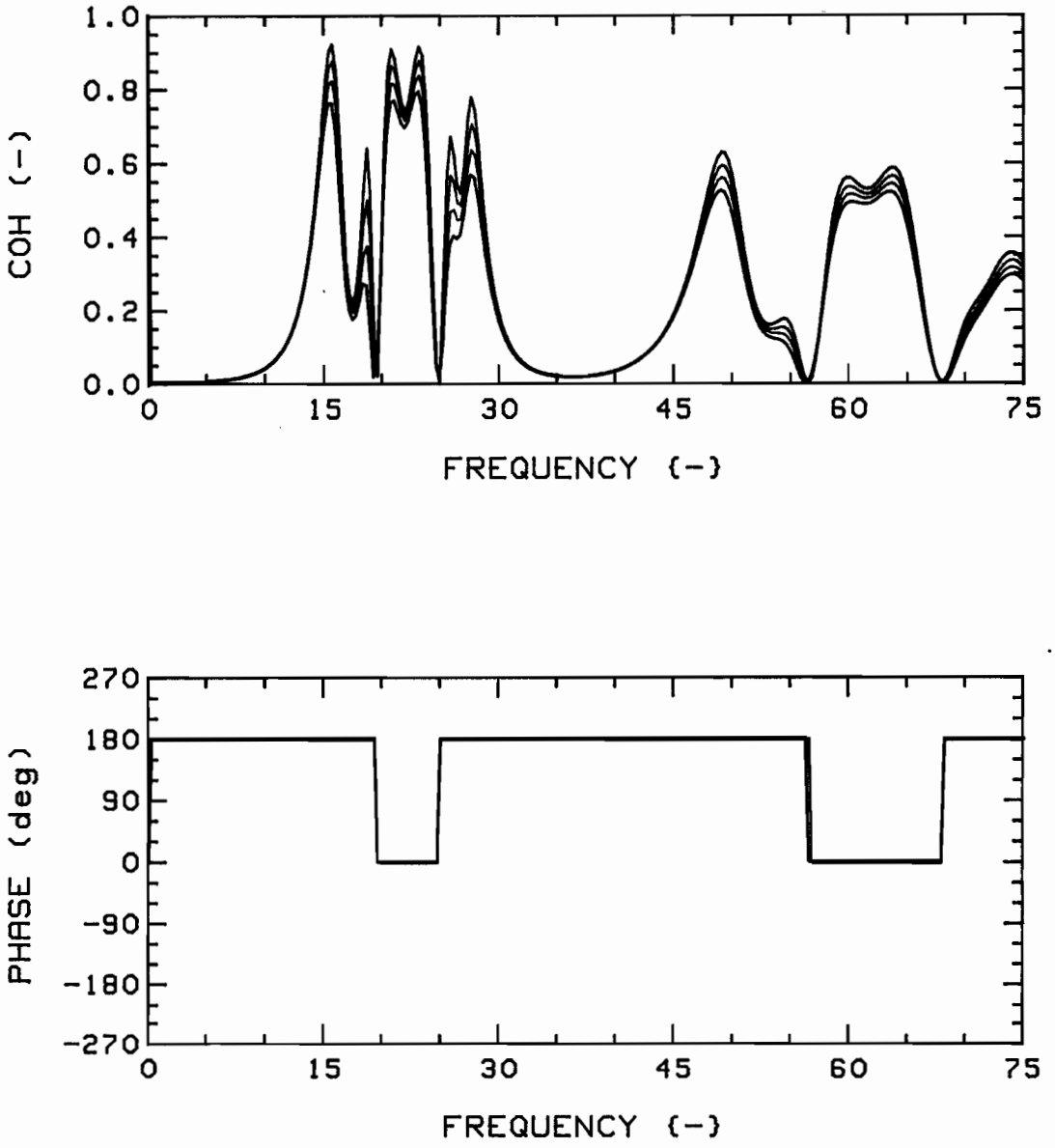

Fig.42a: Effect of the values of c and c_z used in the theory, on coherence function and phase, E-E (1,3). Test case: K = 4, G_c = 0.75, 4F, u = 3. Both c and c_z varied simultaneously. Values are 0.00 (RED), 0.01 (GREEN), 0.02 (BLUE), and 0.03 (BLACK).

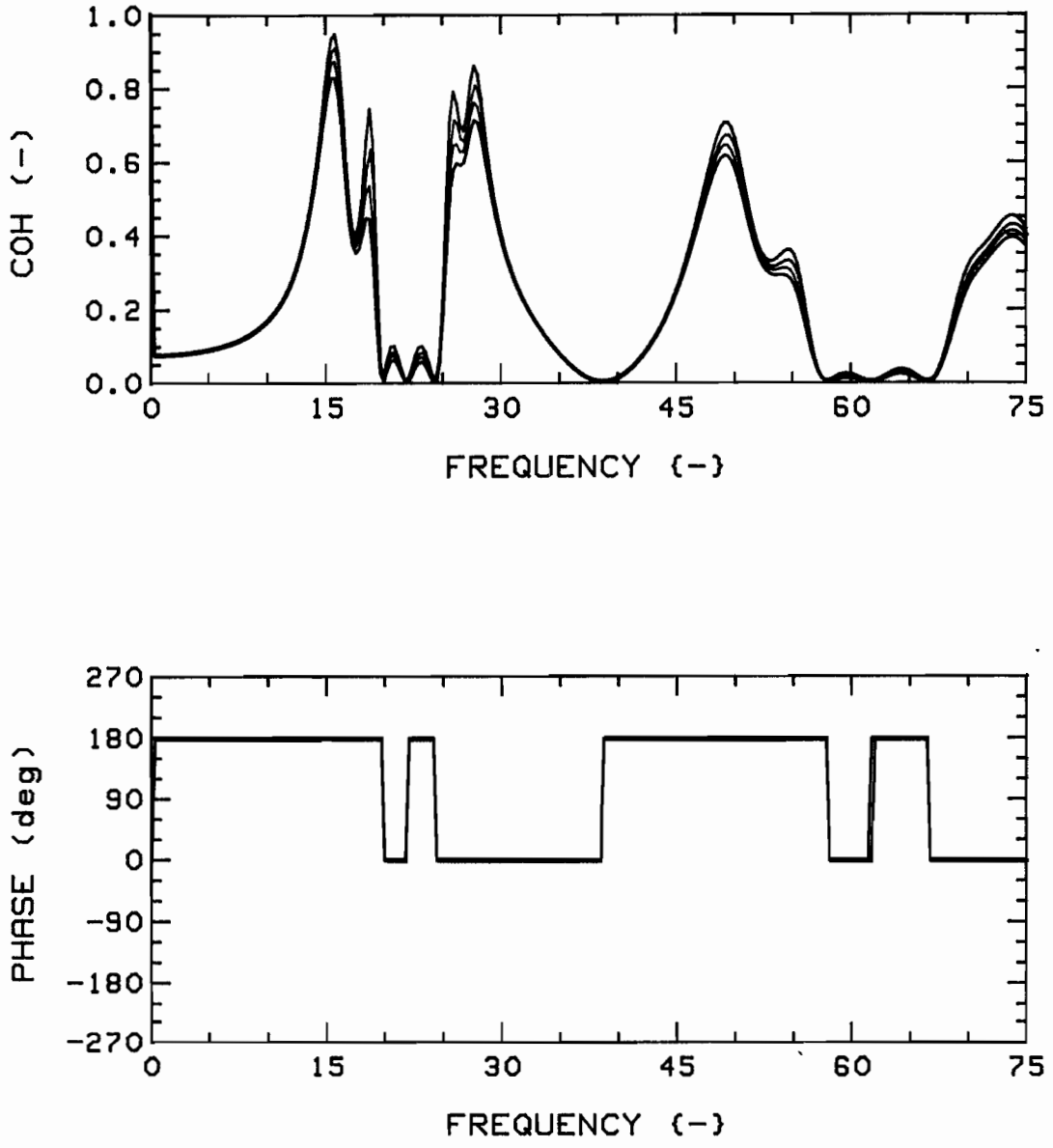

Fig.42b: Effect of the values of c and c_f used in the theory, on coherence function and phase, E-E (1,2). Test case: K = 4, G_c = 0.75, 4F, u = 3. Both c and c_f varied simultaneously. Values are 0.00 (RED), 0.01 (GREEN), 0.02 (BLUE), and 0.03 (BLACK).

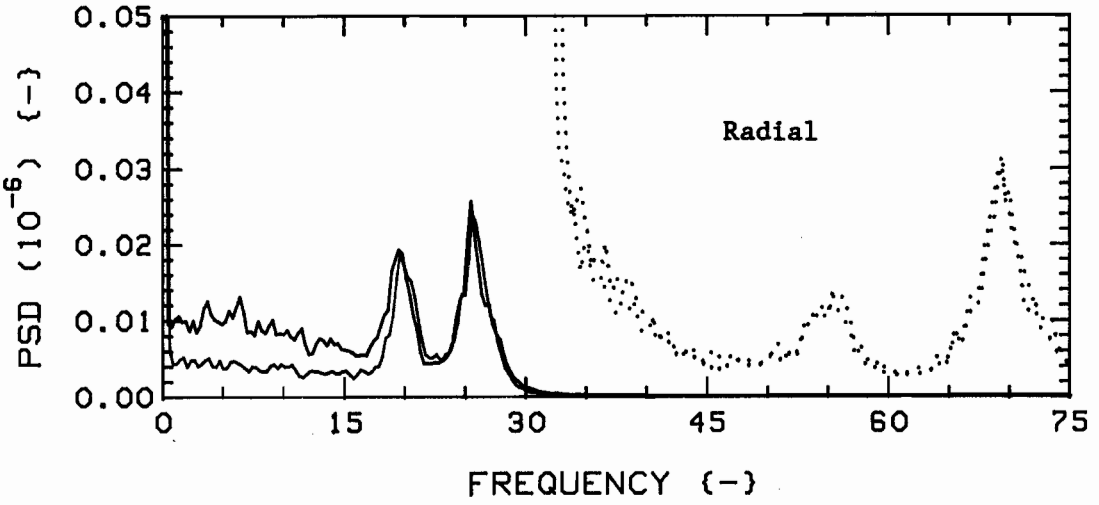

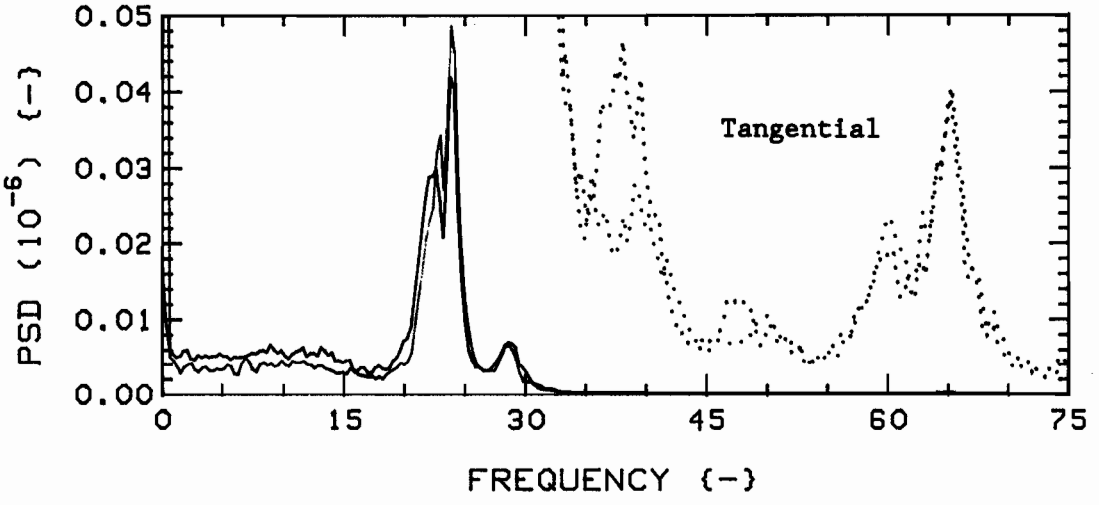

Fig.43a: Positional symmetry, measured vibration PSD's.
Test case: K = 4, G_c = 0.75, 4F, u = 1.
Positions 1 (RED) and 3 (GREEN).

The dotted traces are expansions of the solid ones; scale is 3.0×10^{-10}.

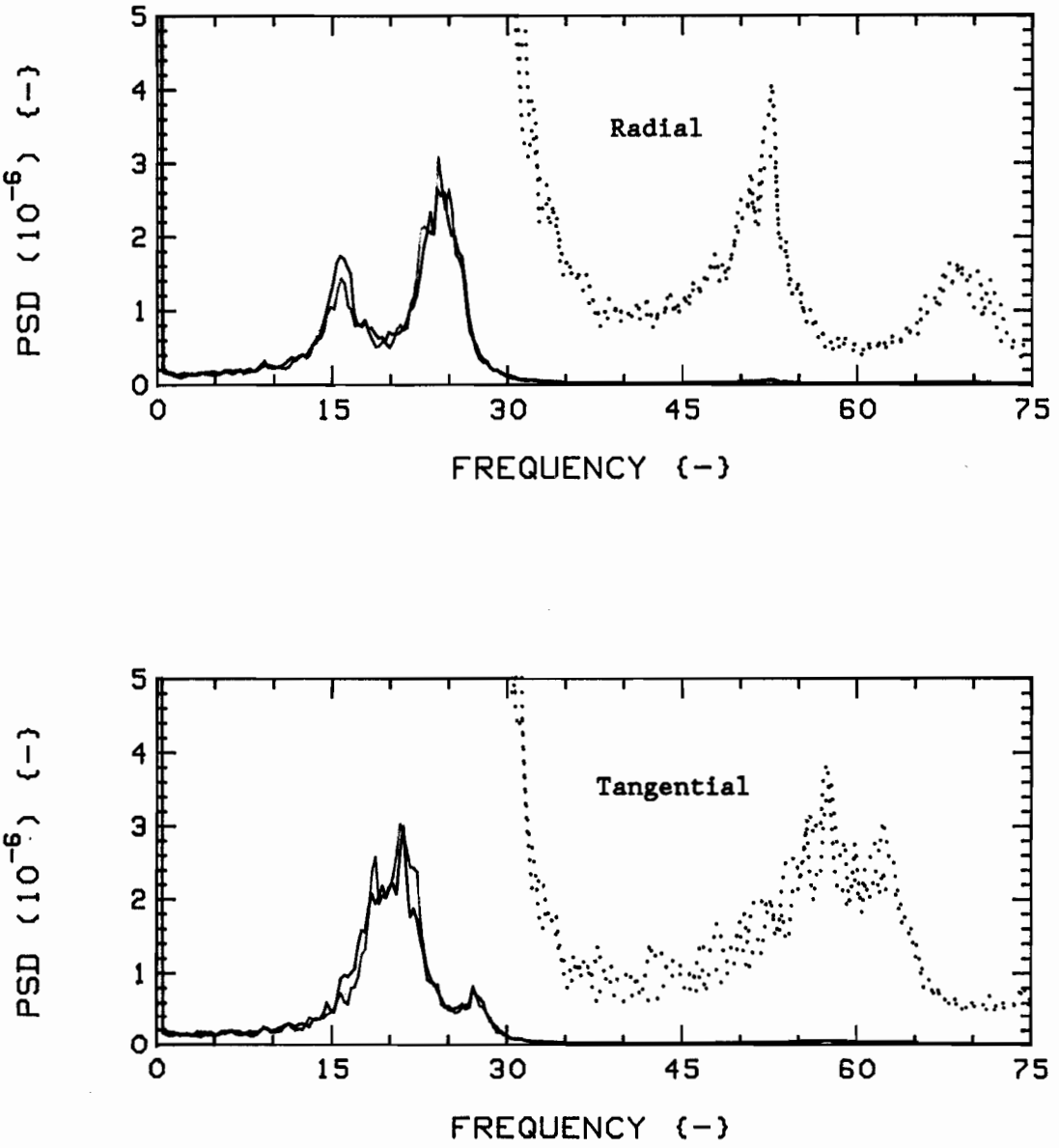

Fig.43b: Positional symmetry, measured vibration PSD's.
Test case: K = 4, G_c = 0.75, 4F, u = 3.
Positions 1 (RED) and 3 (GREEN).

The dotted traces are expansions of the solid ones; scale is 8.0×10^{-8}.

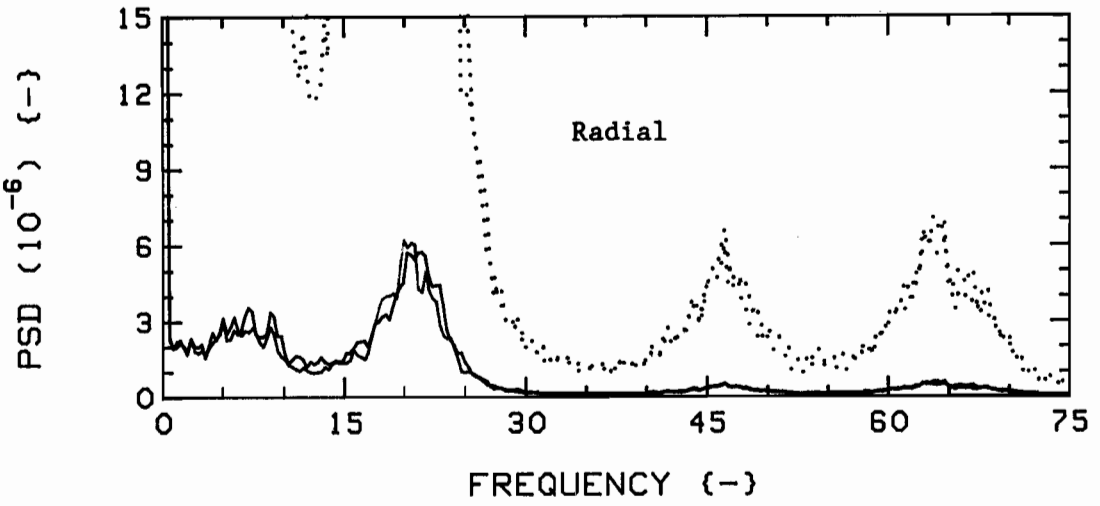

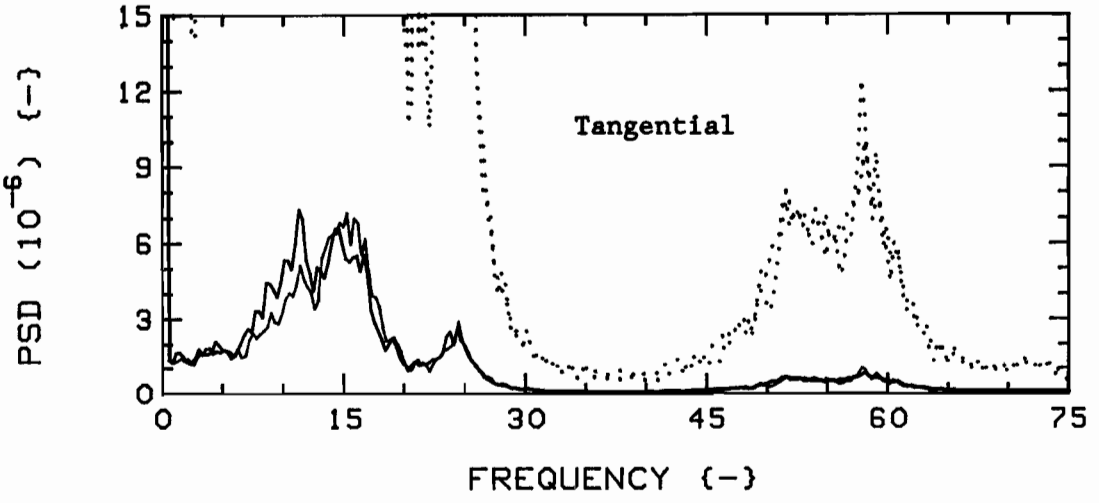

Fig.43c: Positional symmetry, measured vibration PSD's.
Test case: K = 4, G_c = 0.75, 4F, u = 5.
Positions 1 (RED) and 3 (GREEN).

The dotted traces are expansions of the solid ones; scale is 1.2×10^{-6}.

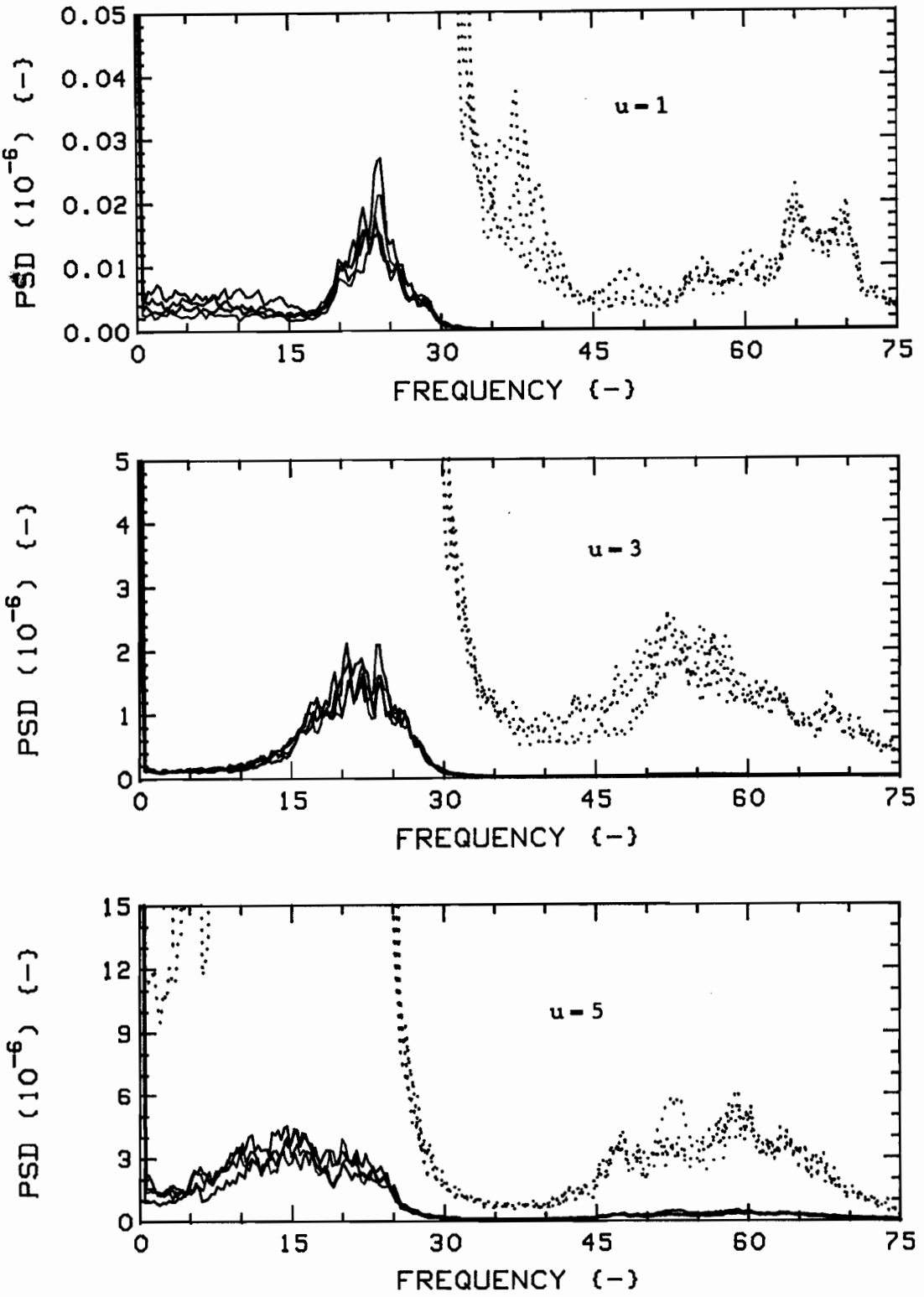

Fig.44: Positional and directional symmetry, measured vibration, Edge directions.
PSD's. Test case: K = 4, G_c = 0.75, 4F.
Pos.1 @ 0° (RED) and @ 90° (GREEN), and
Pos.3 @ 180° (BLUE) and @ 270° (BLACK).

The dotted traces are expansions of the solid ones;

scales are, from top: 3.0×10^{-10}, 8.0×10^{-8}, 1.2×10^{-6}.

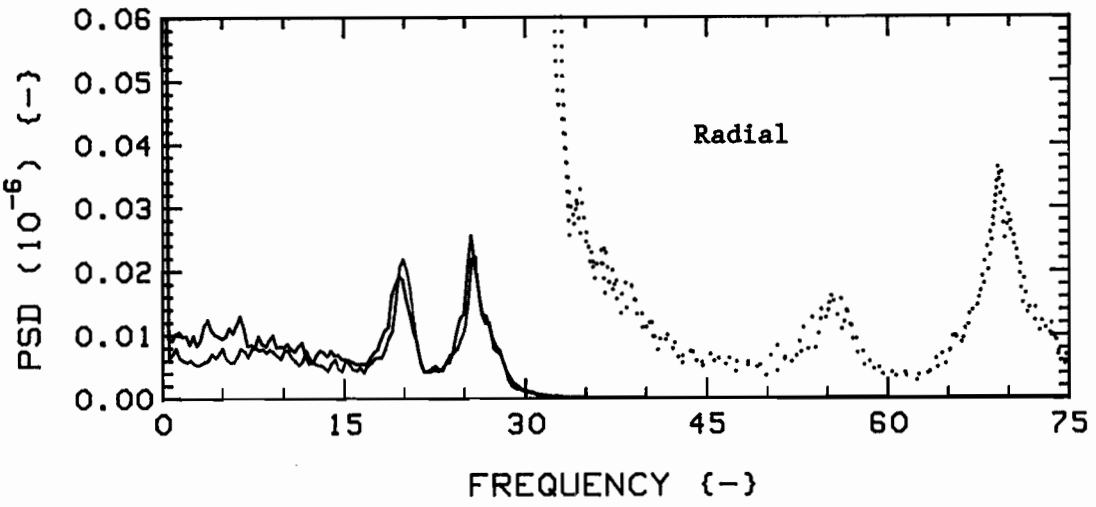

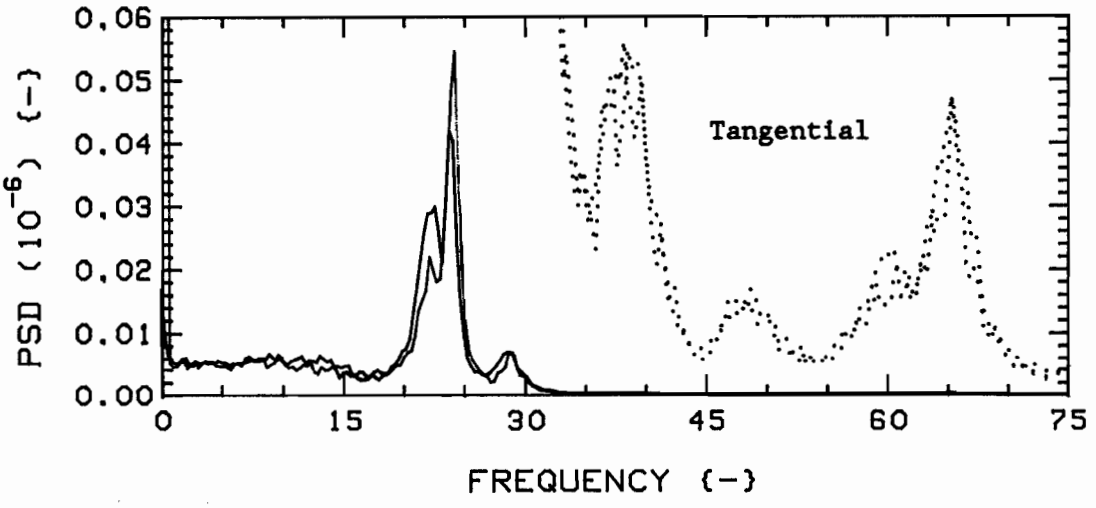

Fig.45a: Repeatability, measured vibration PSD's.
Test case: K = 4, G_c = 0.75, 4F, u = 1.
First (RED) and second (GREEN) tests.

Note: Main PSD scale is 0.06×10^{-6} instead of the usual 0.05×10^{-6}, to show the high Tangential peak (GREEN).

The dotted traces are expansions of the solid ones; scale is 3.0×10^{-10}.

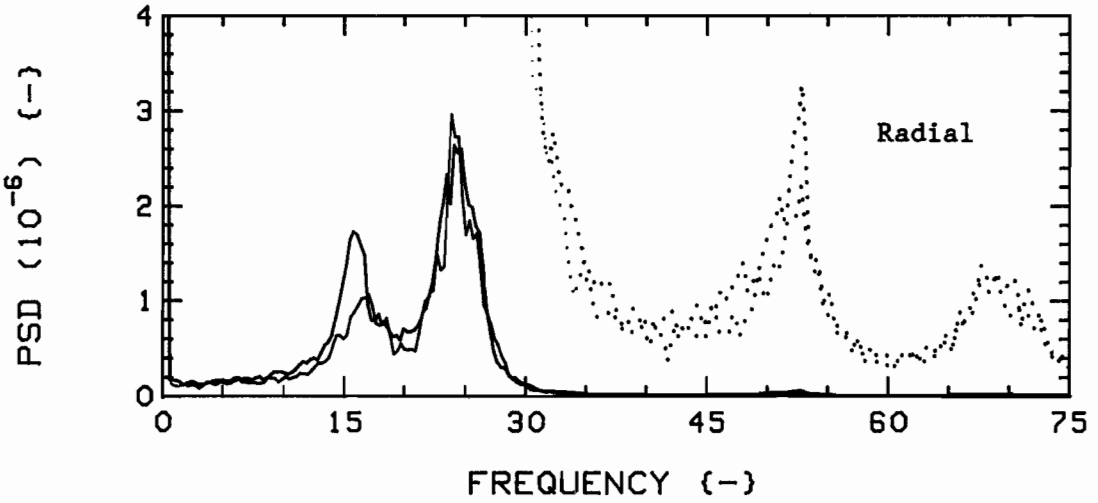

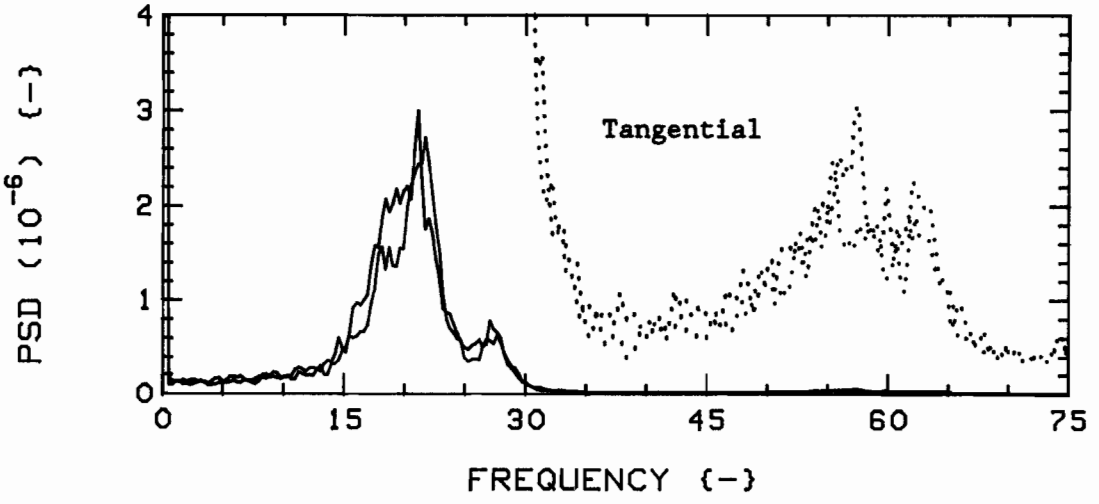

Fig.45b: Repeatability, measured vibration PSD's.
Test case: K = 4, G_c = 0.75, 4F, u = 3.
First (RED) and second (GREEN) tests.

The dotted traces are expansions of the solid ones; scale is 8.0×10^{-8}.

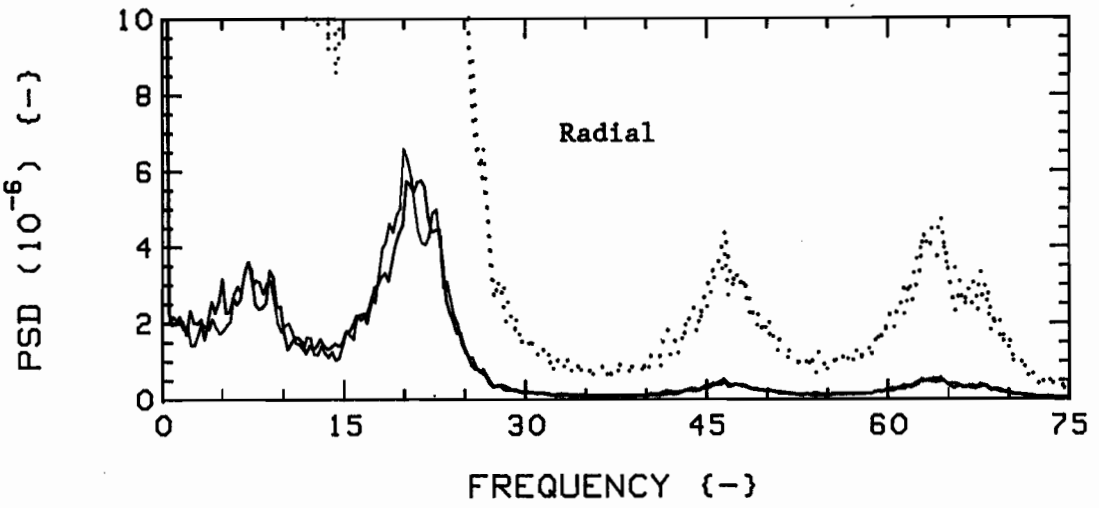

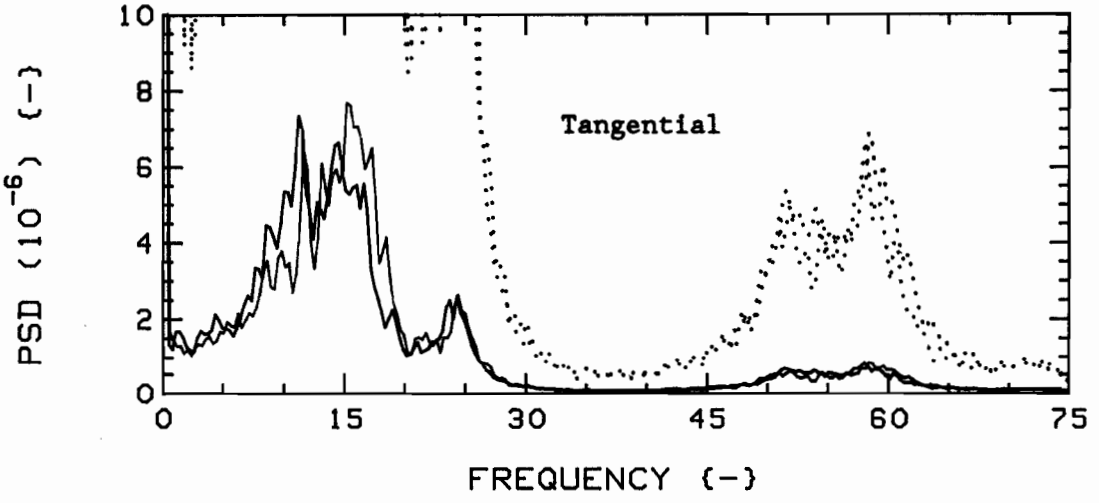

Fig.45c: Repeatability, measured vibration PSD's.
Test case: K = 4, G_c = 0.75, 4F, u = 5.
First (RED) and second (GREEN) tests.

The dotted traces are expansions of the solid ones; scale is 1.2×10^{-6}.

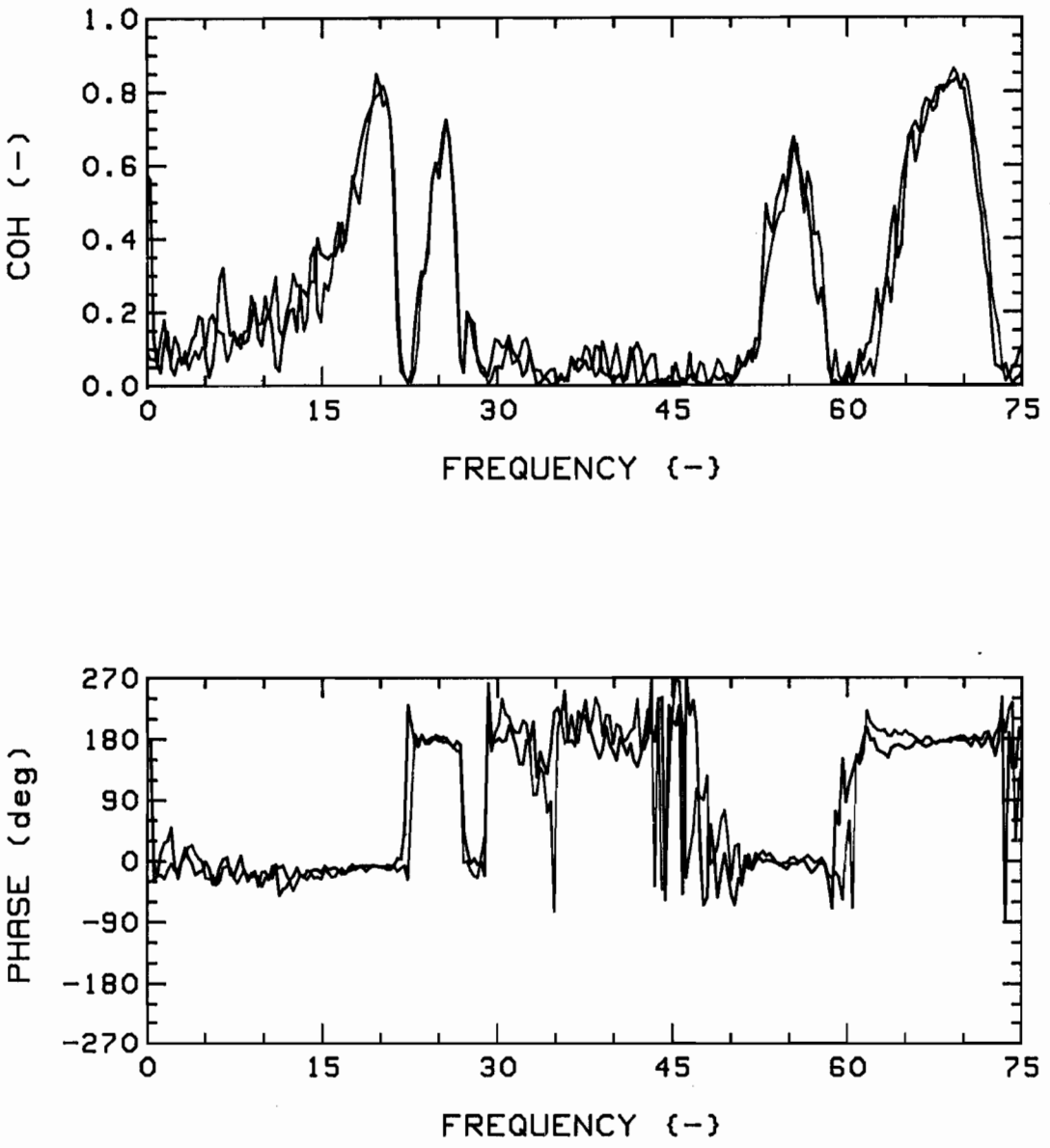

Fig.46a: Repeatability, measured coherence function and phase, R-R (1,3). Test case: K=4, G_c=0.75, 4F, u=1.

First (RED) and second (GREEN) tests.

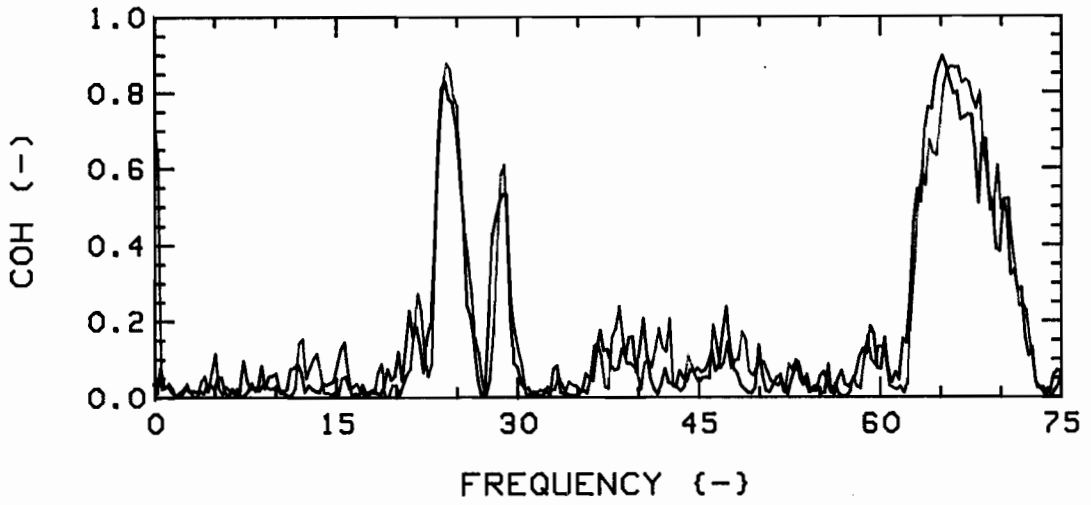

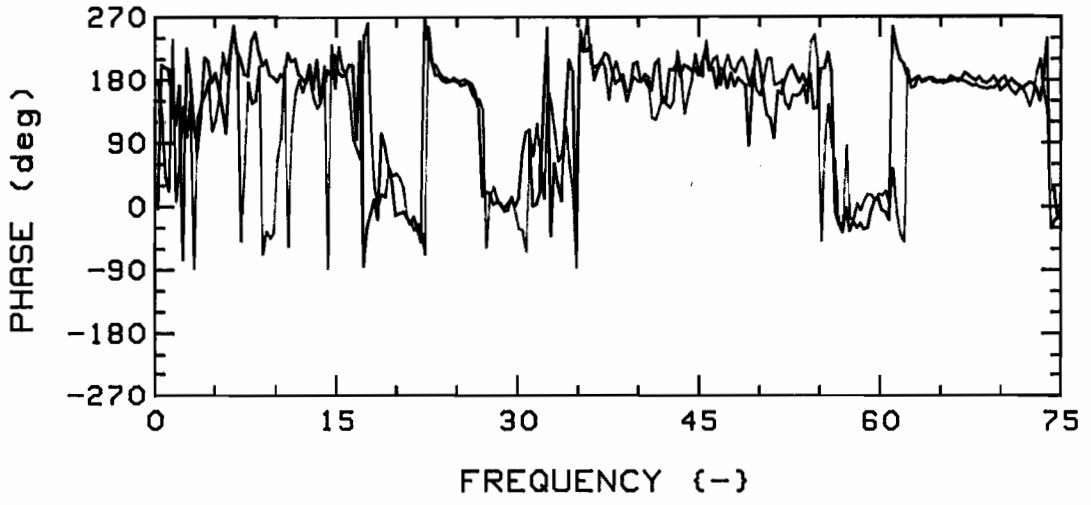

Fig.46b: Repeatability, measured coherence function and phase, T-T (1,3). Test case: K = 4, G_c = 0.75, 4F, u = 1.

First (RED) and second (GREEN) tests.

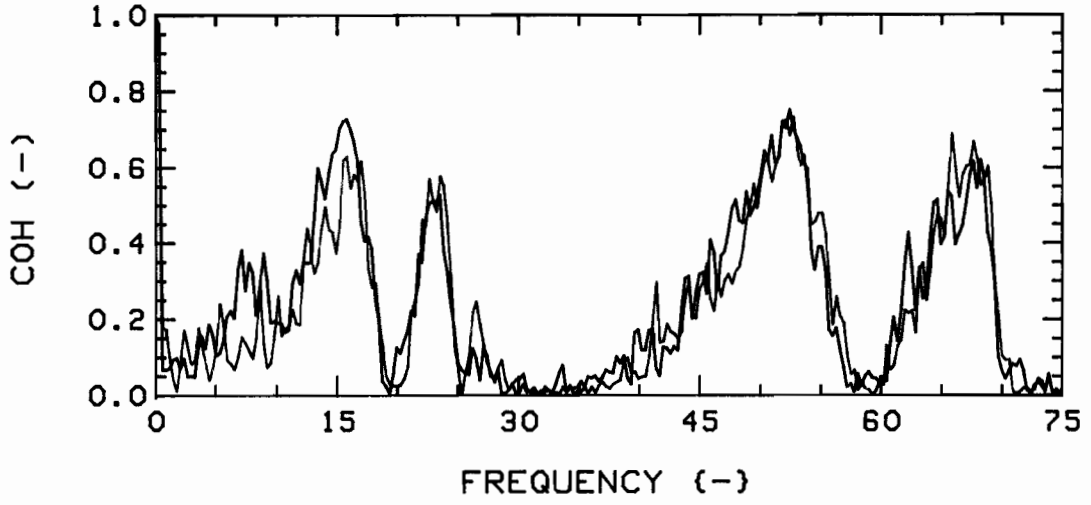

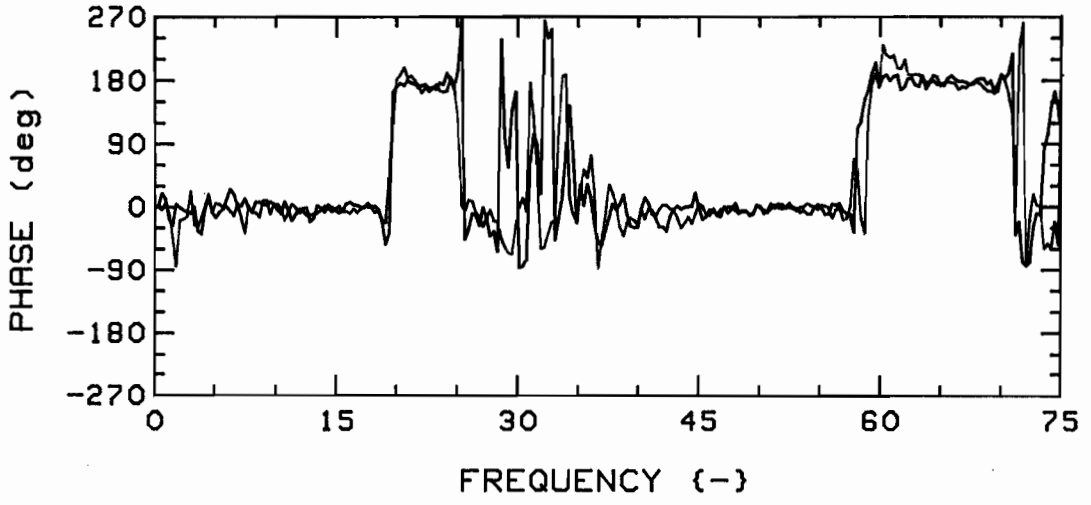

Fig.46c: Repeatability, measured coherence function and phase, R-R (1,3). Test case: K = 4, G_c = 0.75, 4F, u = 3.

First (RED) and second (GREEN) tests.

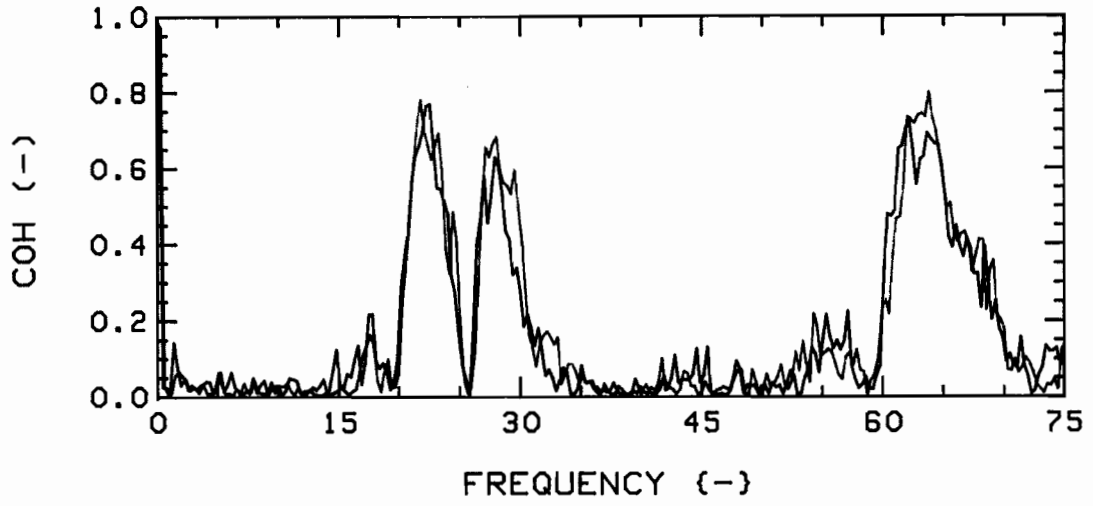

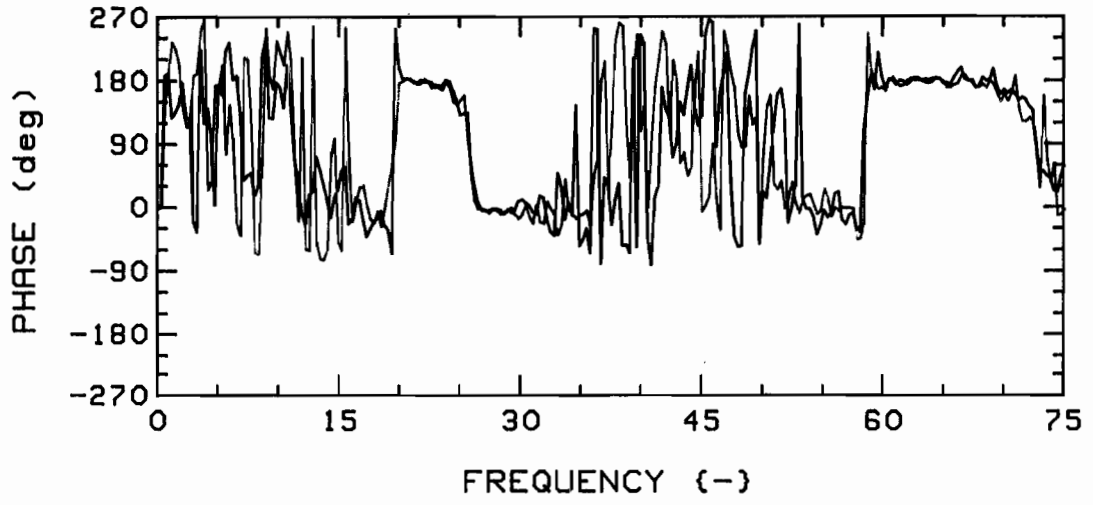

Fig.46d: Repeatability, measured coherence function and phase, T-T (1,3). Test case: K = 4, G_c = 0.75, 4F, u = 3.

First (RED) and second (GREEN) tests.

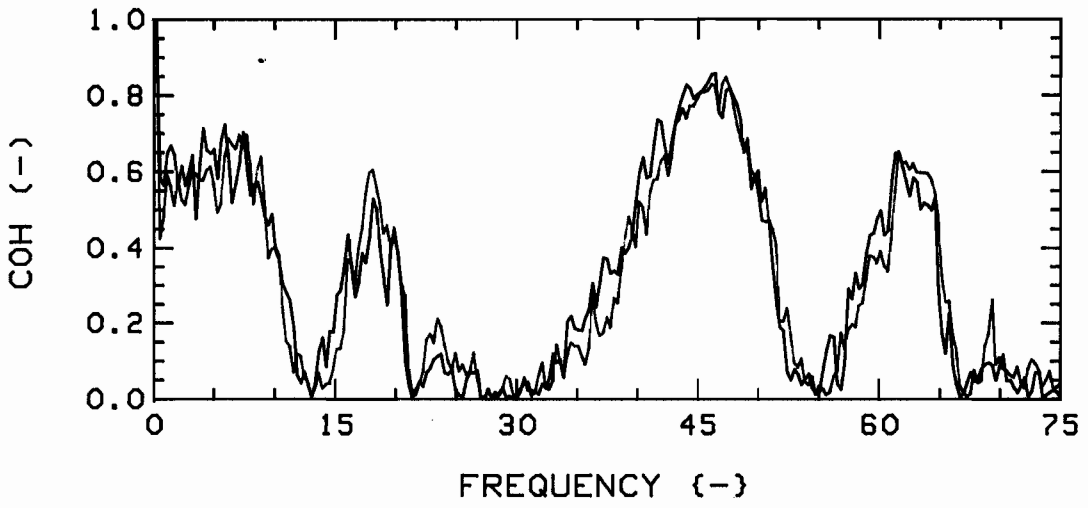

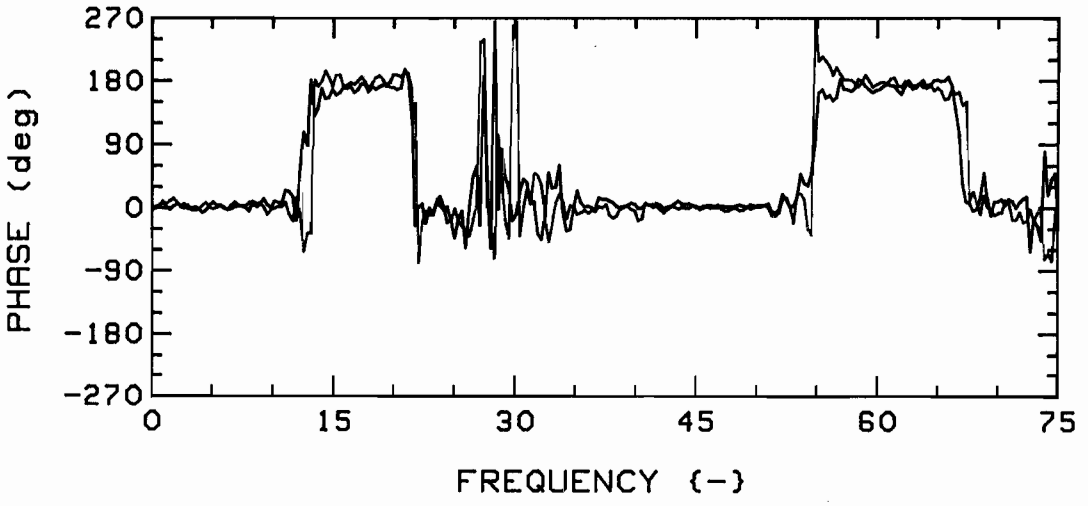

Fig.46e: Repeatability, measured coherence function and phase, R-R (1,3). Test case: K = 4, G_c = 0.75, 4F, u = 5.

First (RED) and second (GREEN) tests.

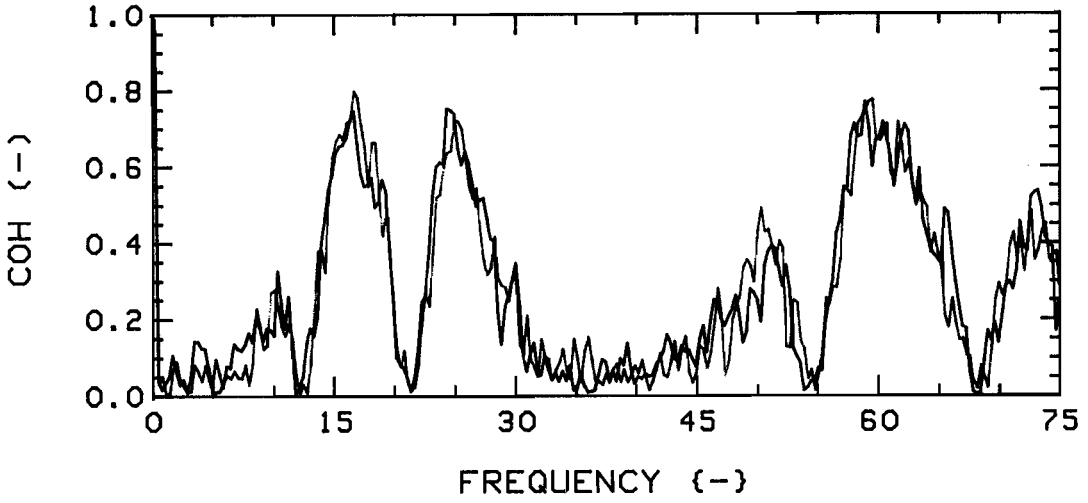

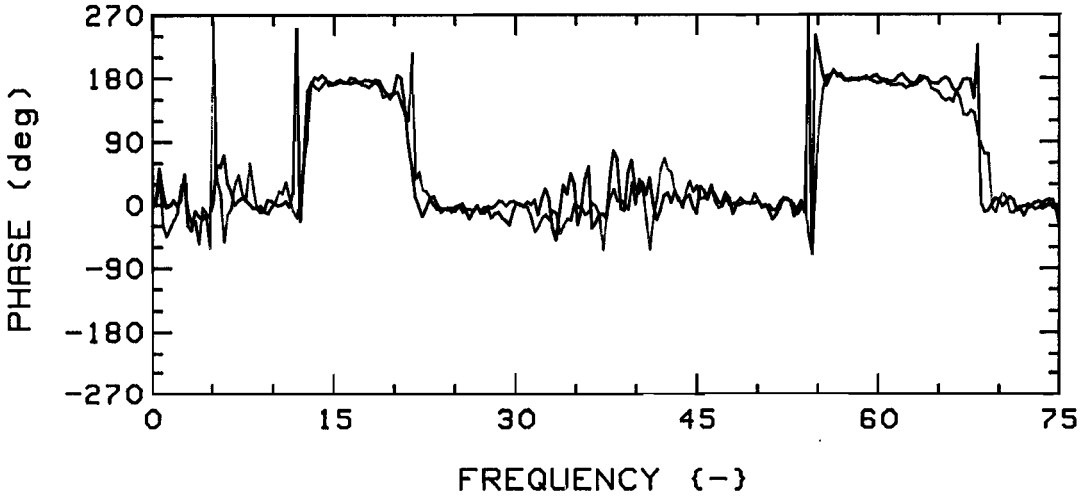

Fig.46f: Repeatability, measured coherence function and phase, T-T (1,3). Test case: K = 4, G_c = 0.75, 4F, u = 5.

First (RED) and second (GREEN) tests.

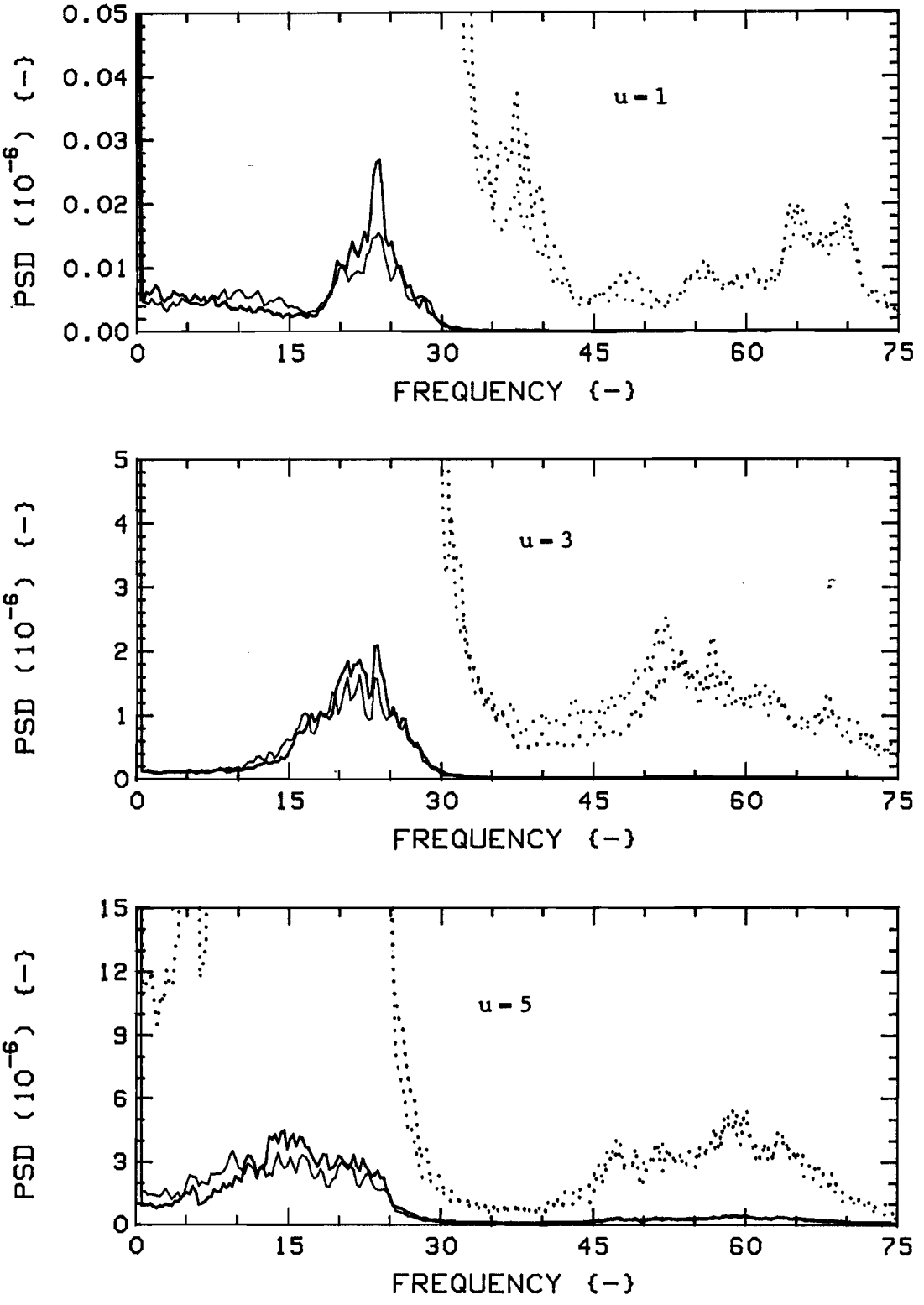

Fig.47: Measured vibration PSD's for K = 4, G_c = 0.75, 4F, Edge directions; Pos. 1 @ 0° (RED) and @ 90° (BLUE). The dotted traces are expansions of the solid ones; scales are, from top: 3.0×10^{-10}, 8.0×10^{-8}, 1.2×10^{-6}.

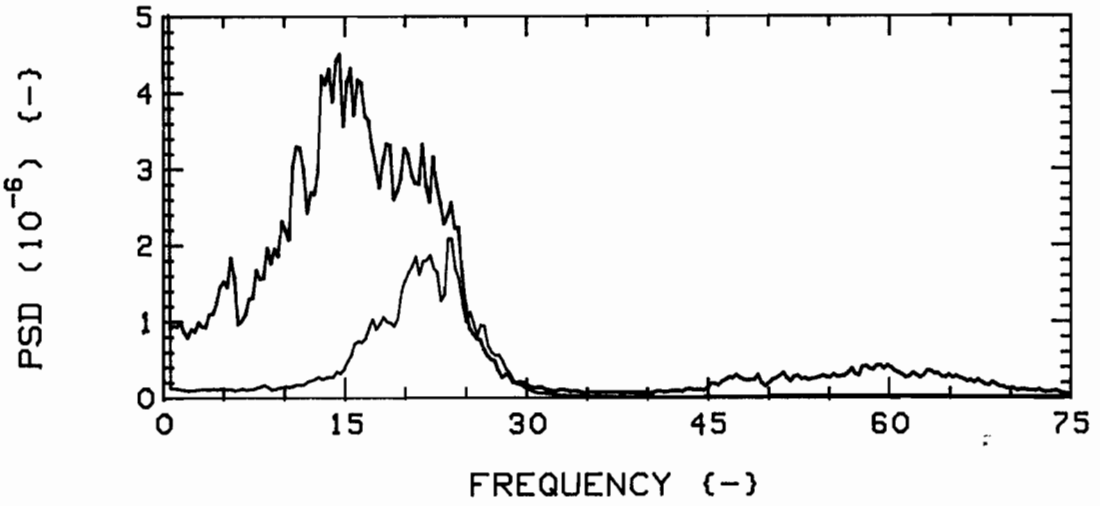

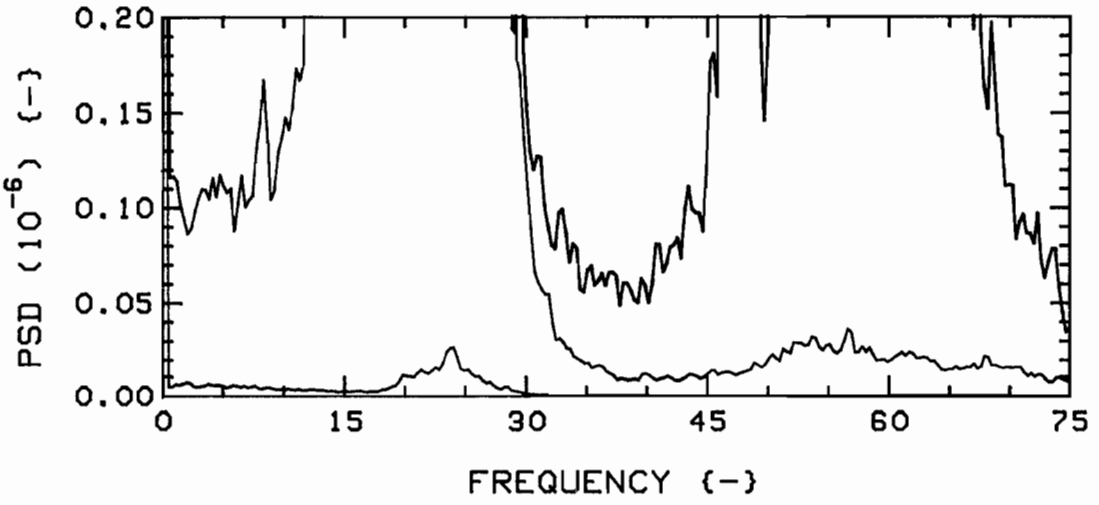

Fig.48: Measured vibration PSD's for K = 4, G_c = 0.75, 4F, Edge direction, versus flow velocity. In descending order, u = 5.0, 3.0, and 1.0. Colour sequence: RED, GREEN, BLUE.

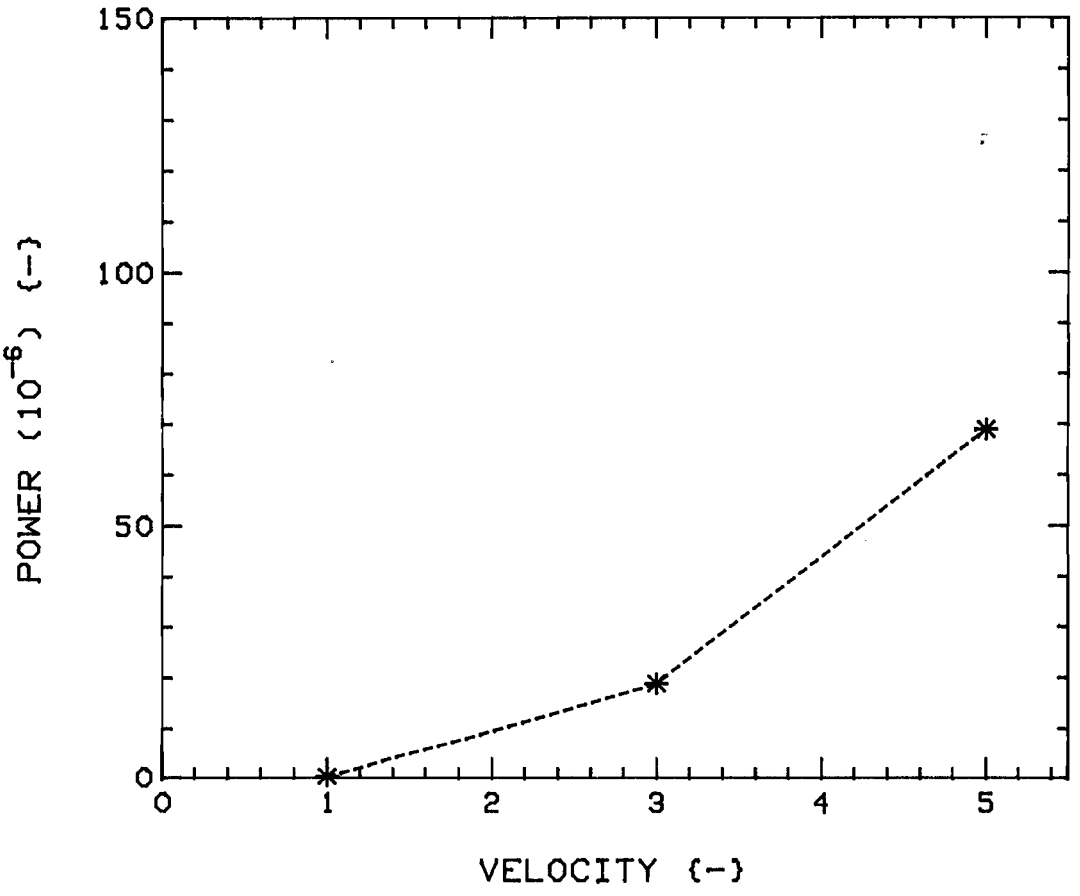

Fig.49: Power versus flow velocity, for K = 4, G_c = 0.75, 4F, from (integrated) PSD's of Fig. 48. Edge direction.

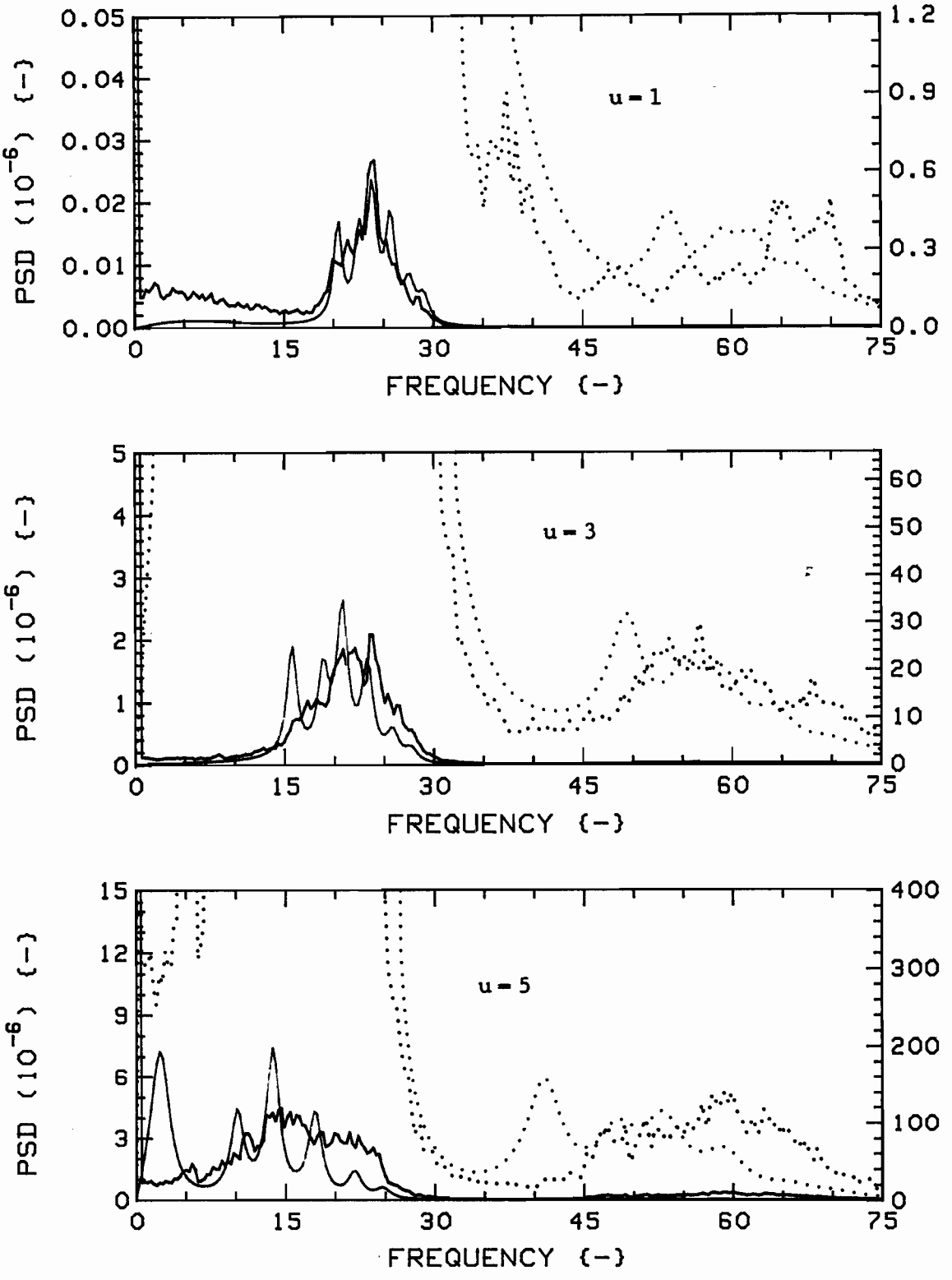

Fig.50: Measured (RED) and theoretical (GREEN) vibration PSD's for K = 4, G_c = 0.75, 4F, Edge direction.

The dotted traces are expansions of the solid ones; scales are, from top, (RED): 3.0×10^{-10}, 8.0×10^{-8}, 1.2×10^{-6},

(GREEN): 2.0×10^{-9}, 1.8×10^{-7}, 4.0×10^{-6}.

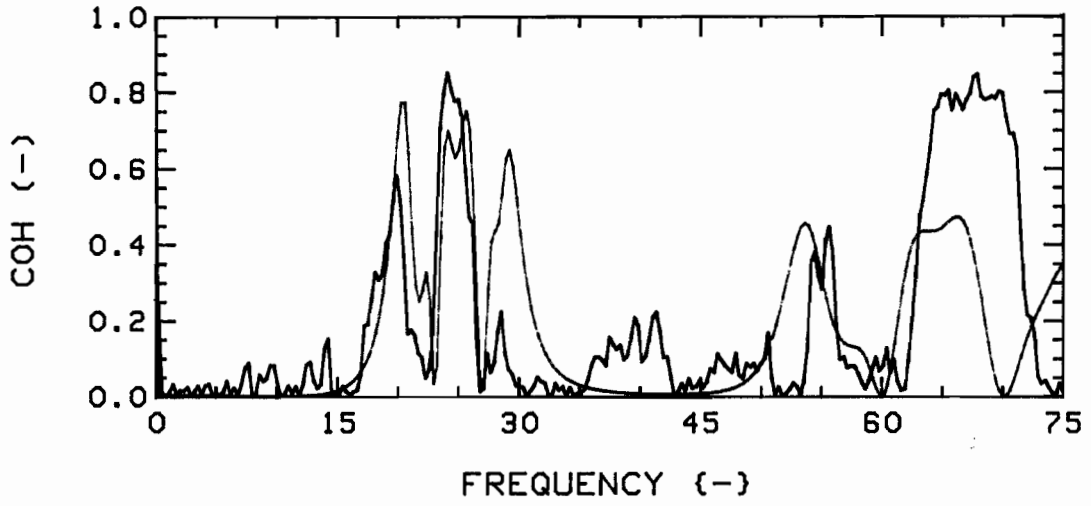

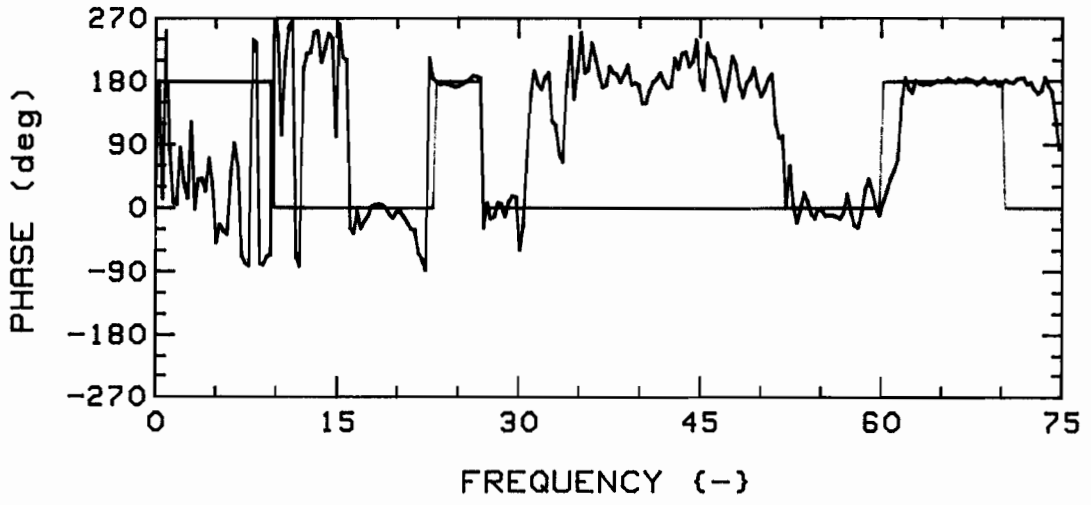

Fig.51a: Measured (RED) and theoretical (GREEN) coherence functions and phases, for K = 4, G_c = 0.75, 4F, E-E (1 @ 0°, 3 @ 180°), at u = 1.

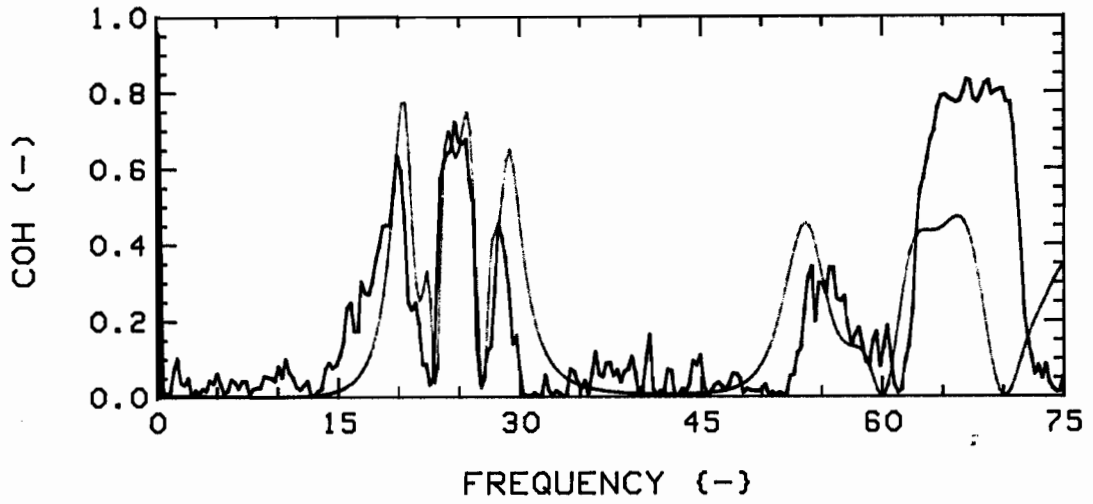

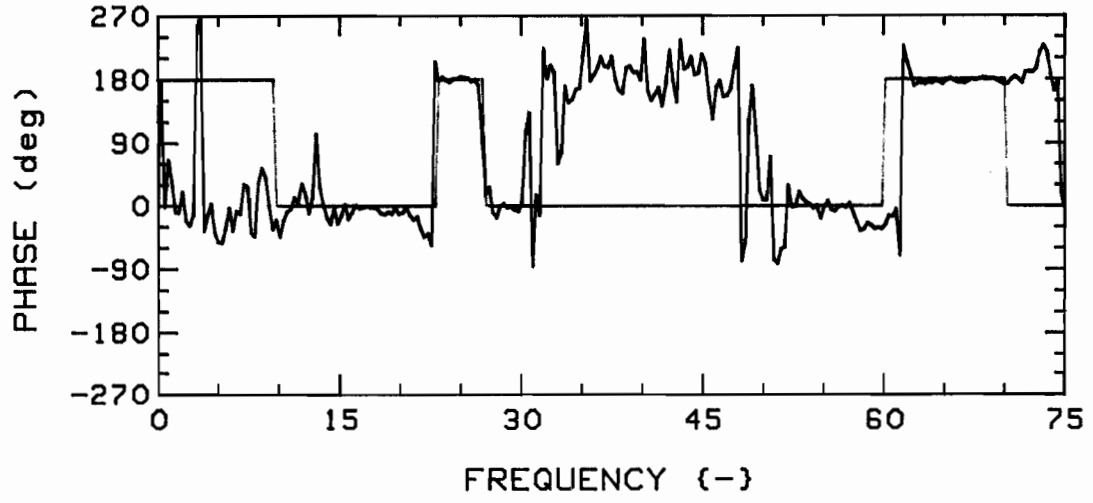

Fig.51b: Measured (RED) and theoretical (GREEN) coherence functions and phases, for K = 4, G_c = 0.75, 4F, E-E (1 @ 90°,3 @ 270°), at u = 1.

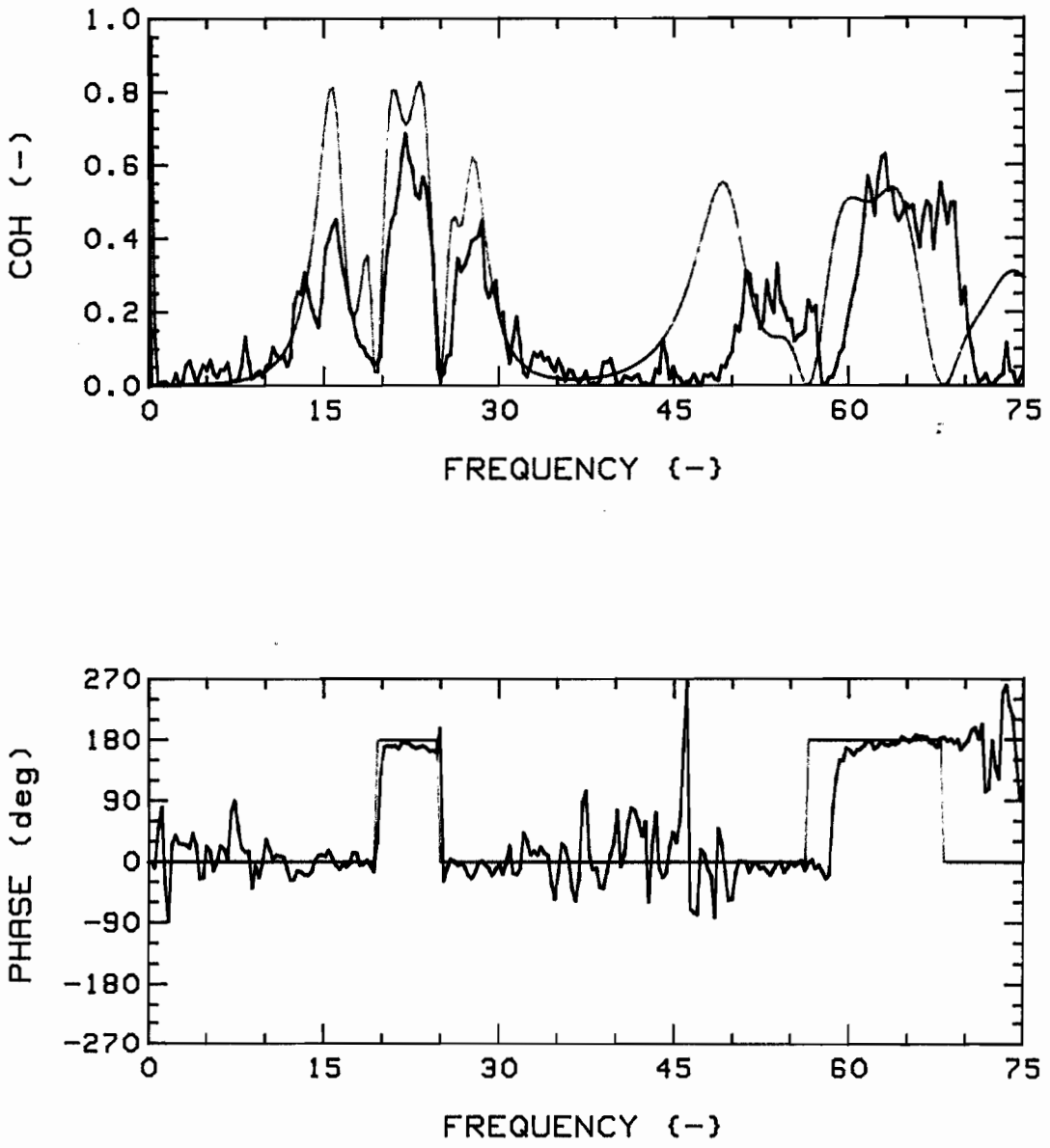

Fig.51c: Measured (RED) and theoretical (GREEN) coherence functions and phases, for K = 4, G_c = 0.75, 4F, E-E (1 @ 0°, 3 @ 180°), at u = 3.

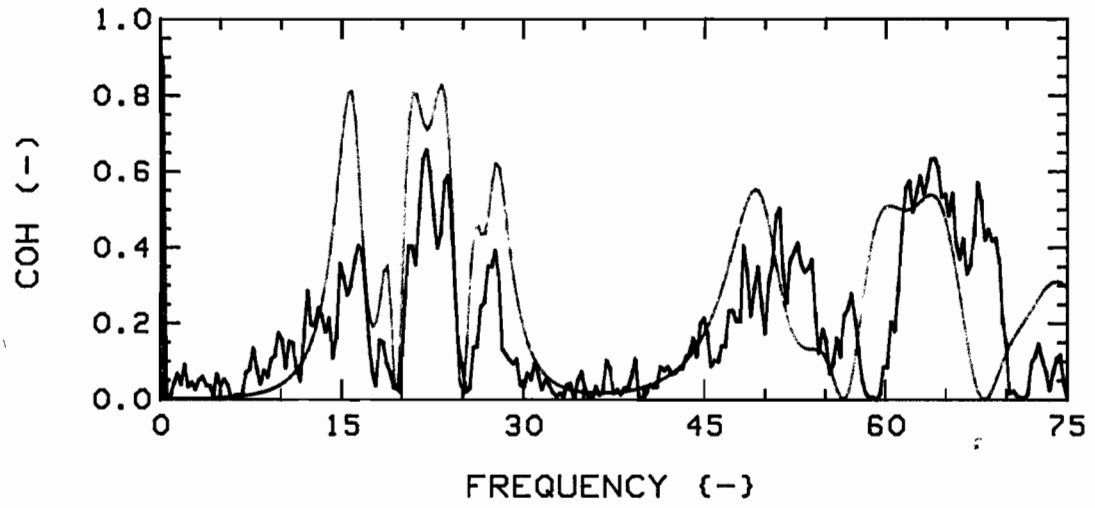

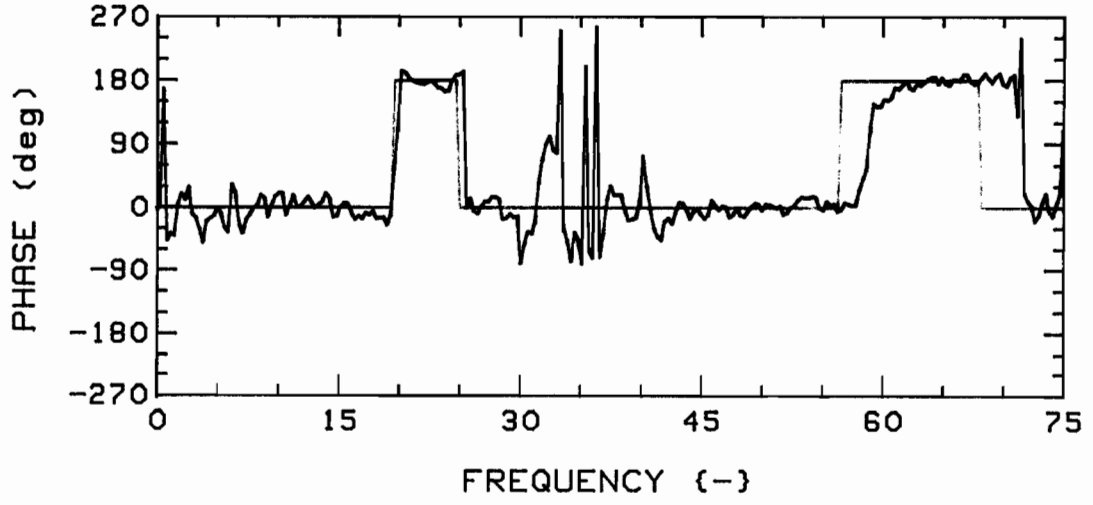

Fig.51d: Measured (RED) and theoretical (GREEN) coherence functions and phases, for K = 4, G_c = 0.75, 4F, E-E (1 @ 90°, 3 @ 270°), at u = 3.

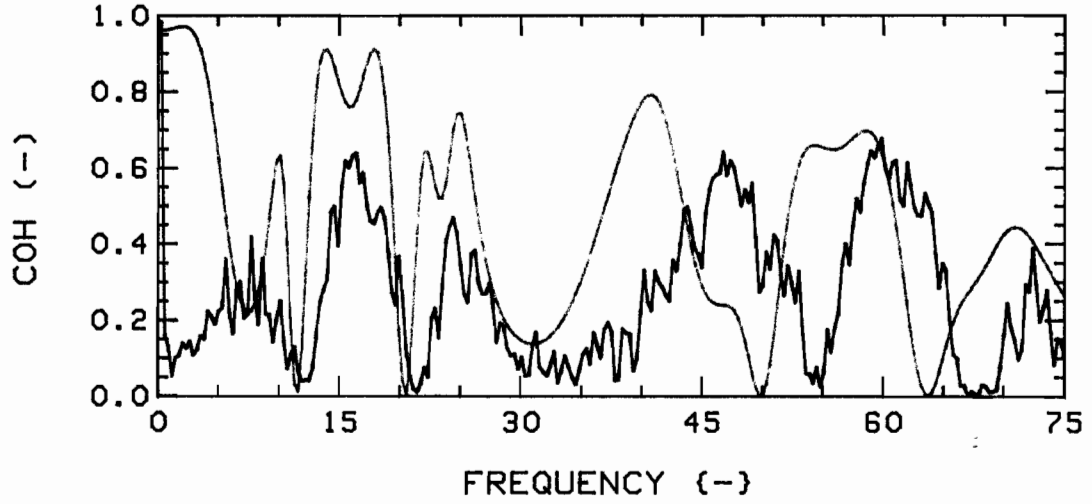

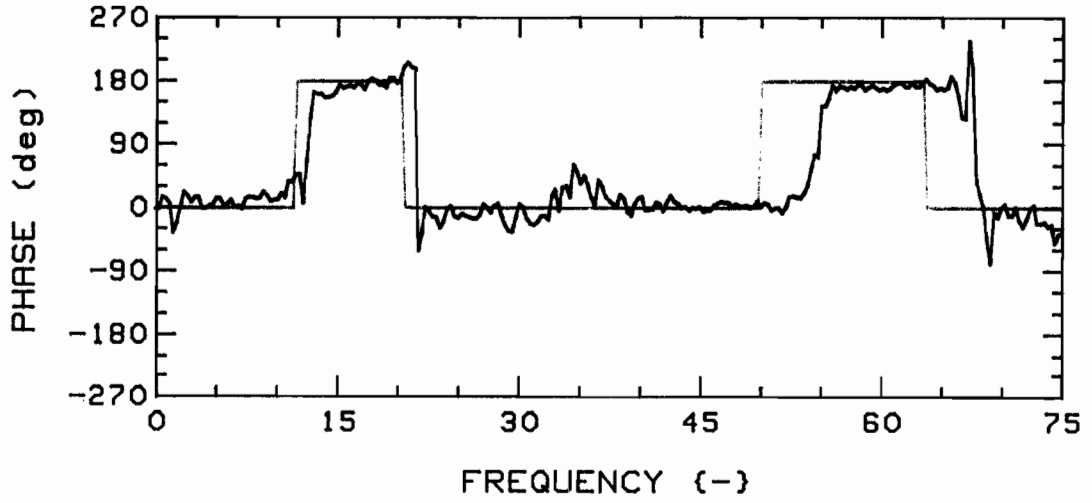

Fig.51e: Measured (RED) and theoretical (GREEN) coherence functions and phases, for K = 4, G_c = 0.75, 4F, E-E (1 @ 0°, 3 @ 180°), at u = 5.

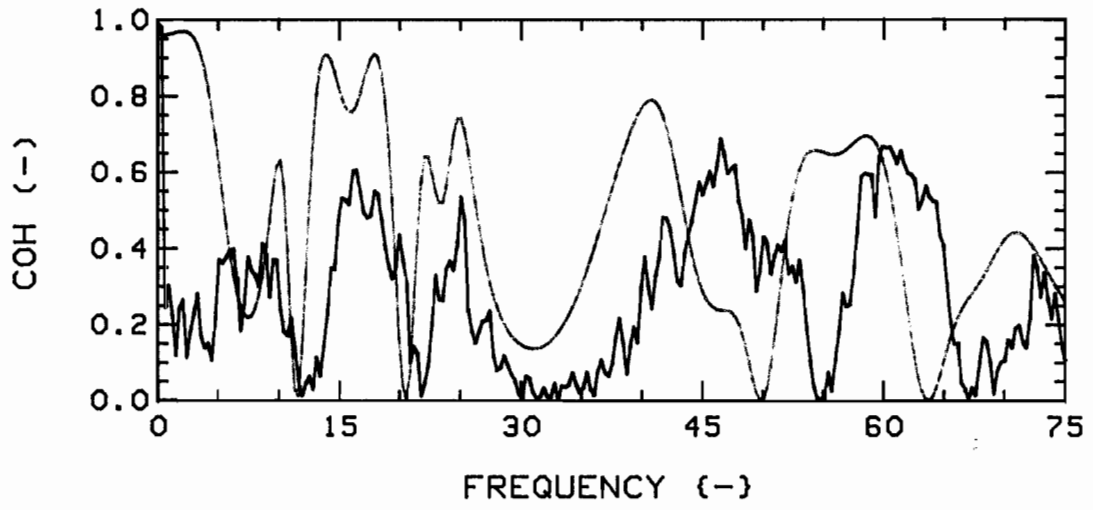

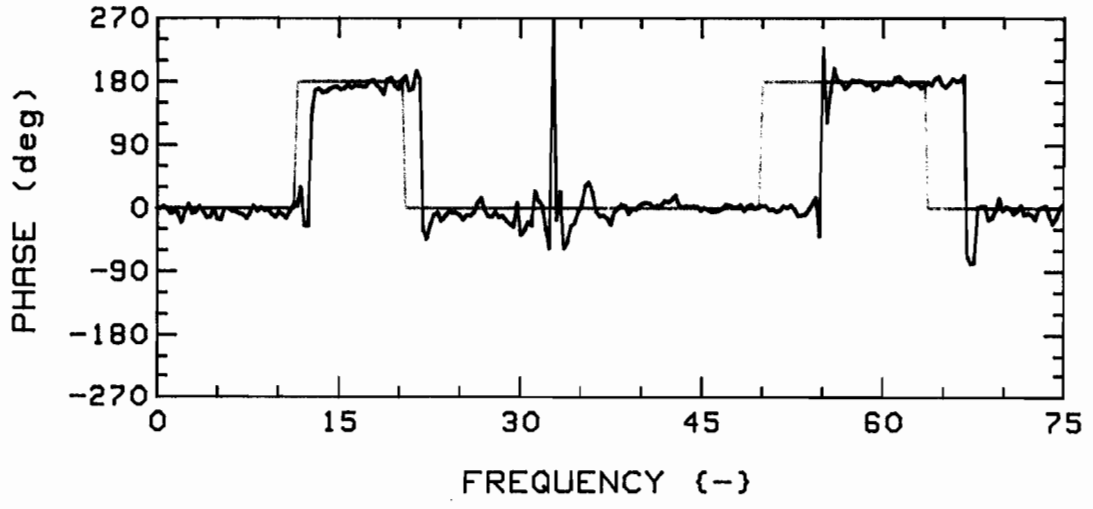

Fig.51f: Measured (RED) and theoretical (GREEN) coherence functions and phases, for K = 4, G_c = 0.75, 4F, E-E (1 @ 90°, 3 @ 270°), at u = 5.

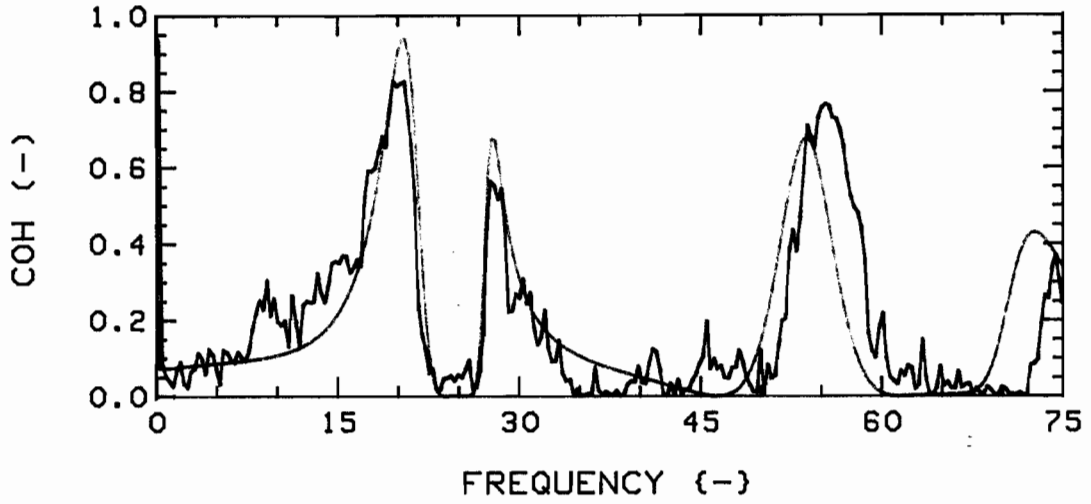

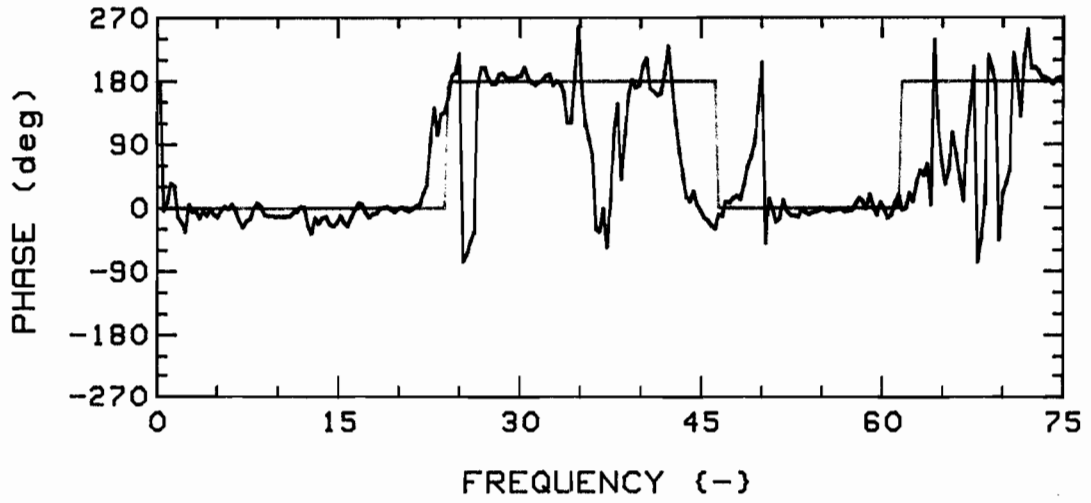

Fig.52a: Measured (RED) and theoretical (GREEN) coherence functions and phases, for K = 4, G_c = 0.75, 4F, R-R (1,2), at u = 1.

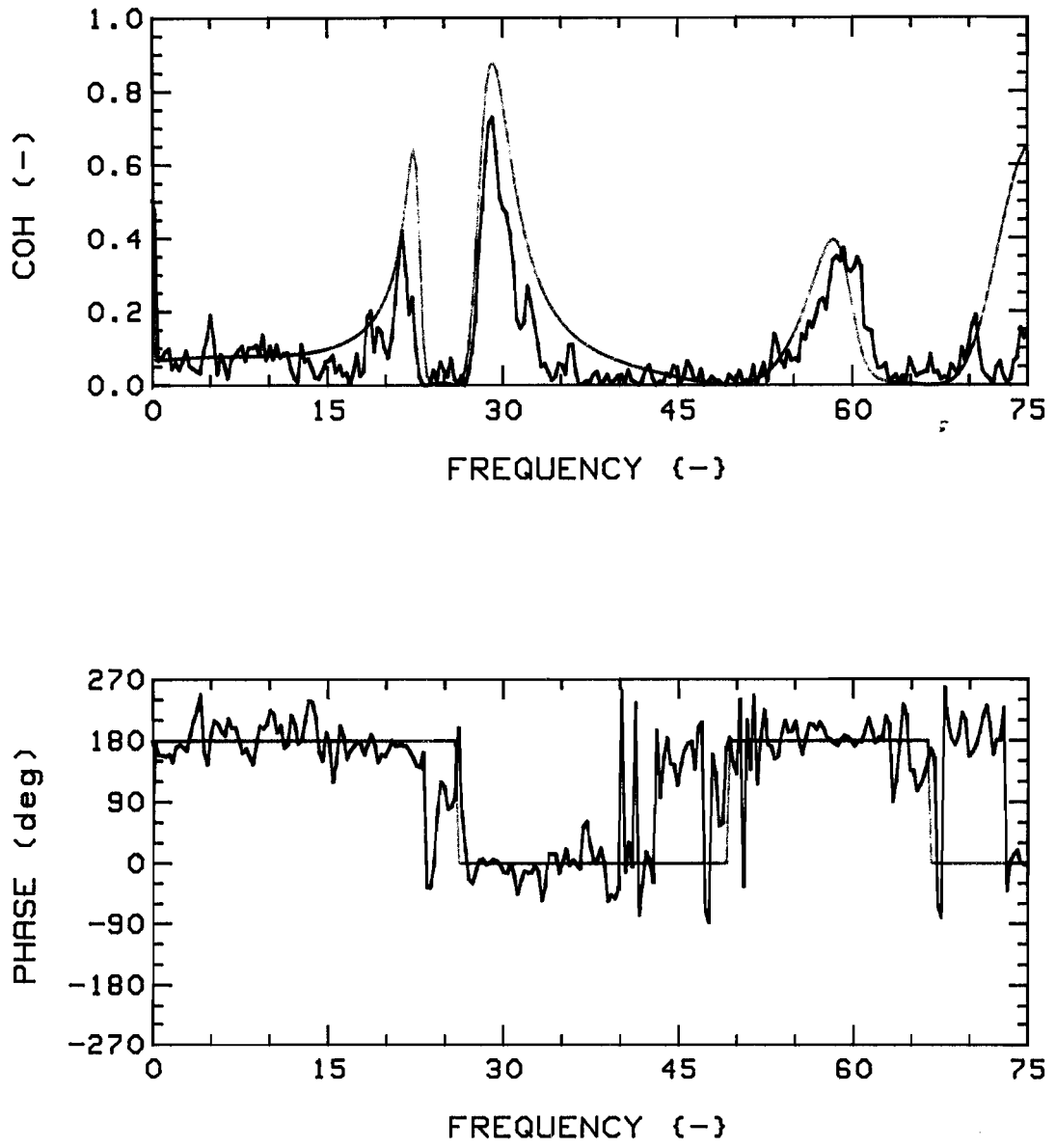

Fig.52b: Measured (RED) and theoretical (GREEN) coherence functions and phases, for K = 4, G_c = 0.75, 4F, T-T (1,2), at u = 1.

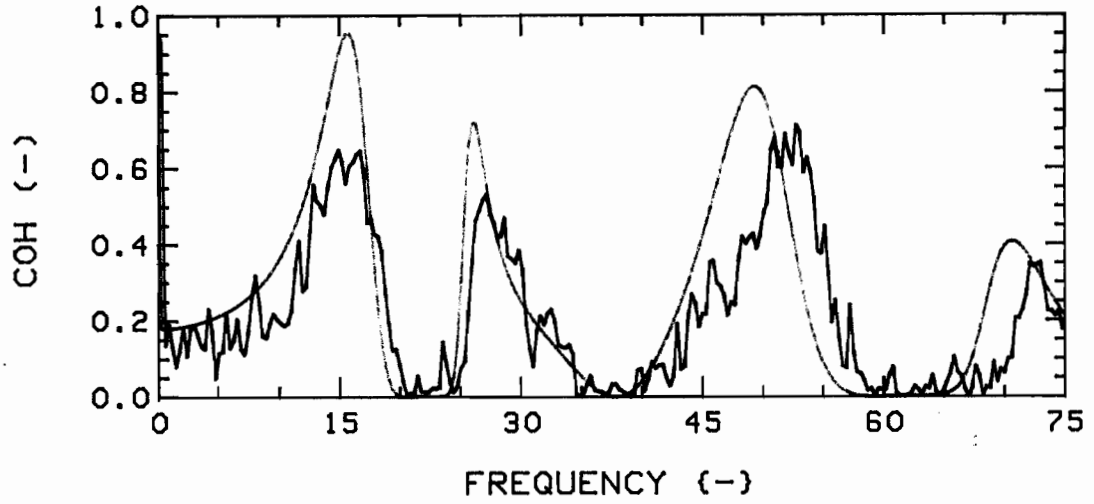

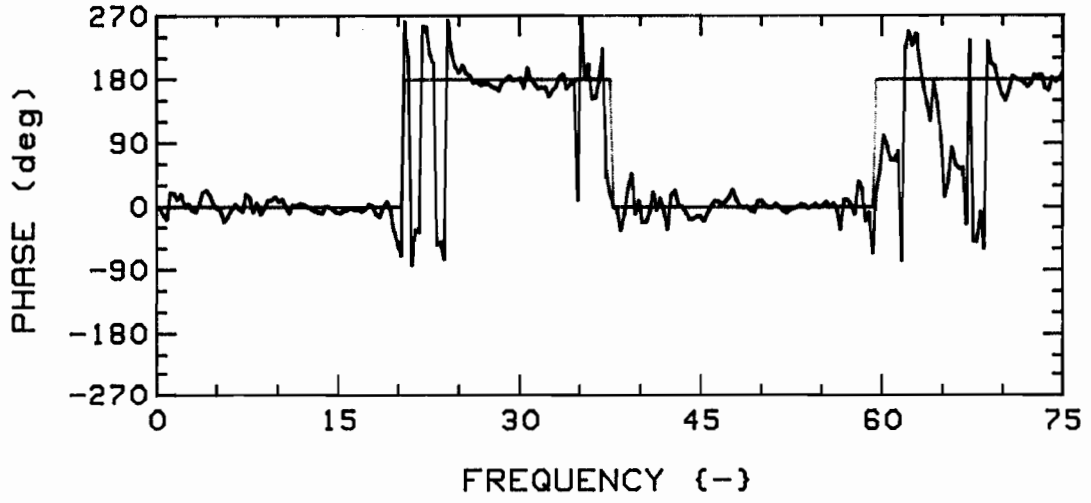

Fig.52c: Measured (RED) and theoretical (GREEN) coherence functions and phases, for K = 4, G_c = 0.75, 4F, R-R (1,2), at u = 3.

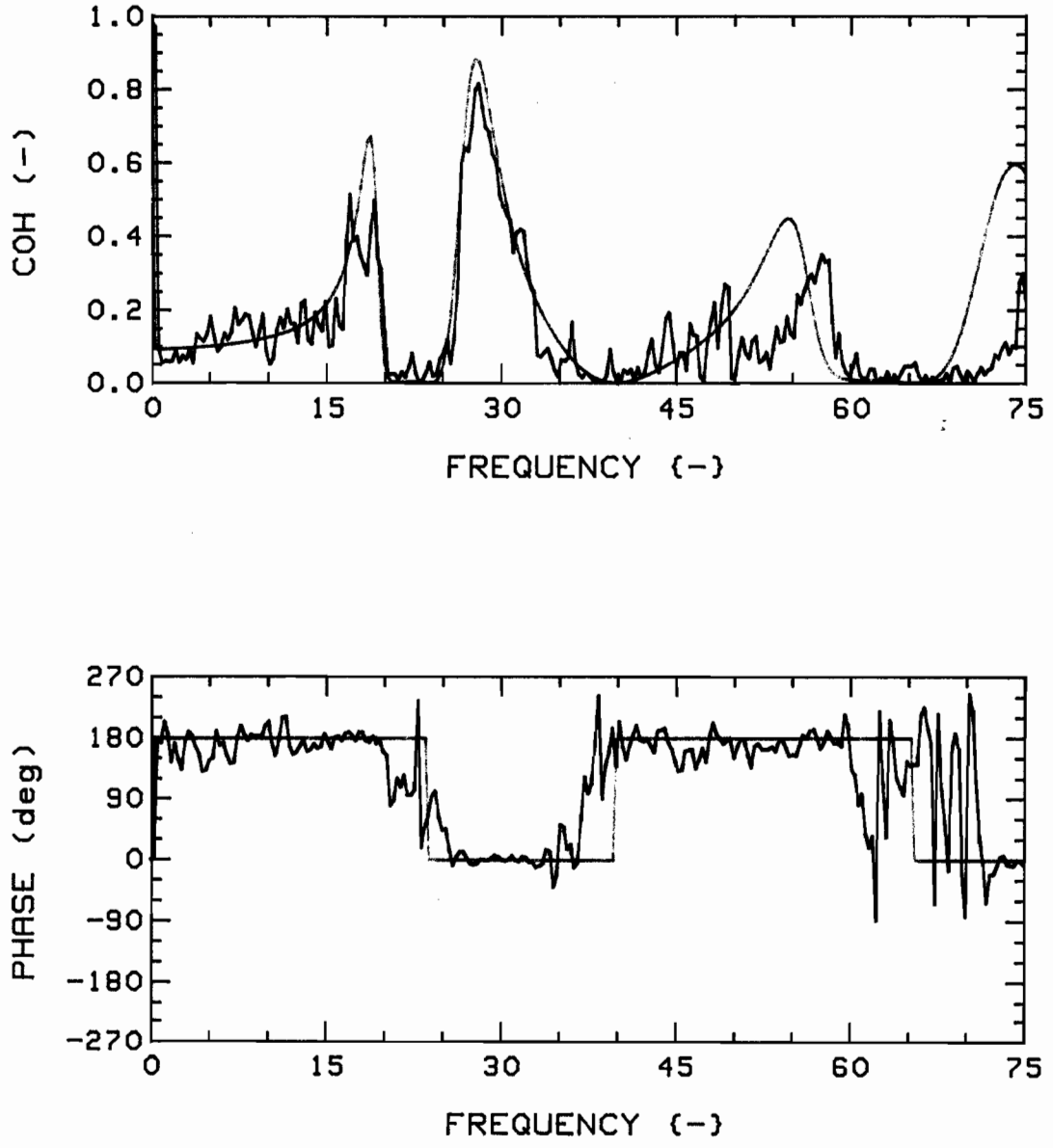

Fig.52d: Measured (RED) and theoretical (GREEN) coherence functions and phases, for K = 4, G_c = 0.75, 4F, T-T (1,2), at u = 3.

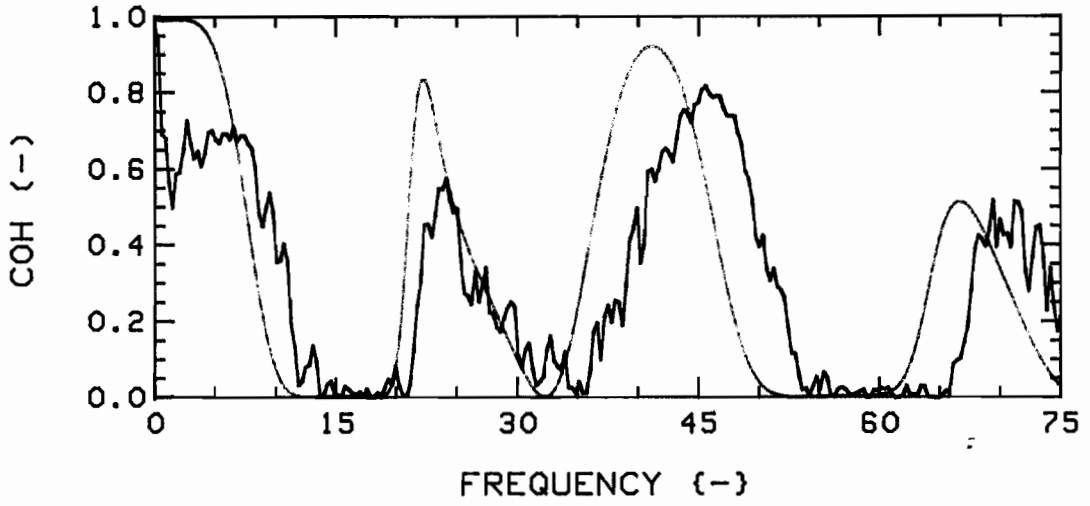

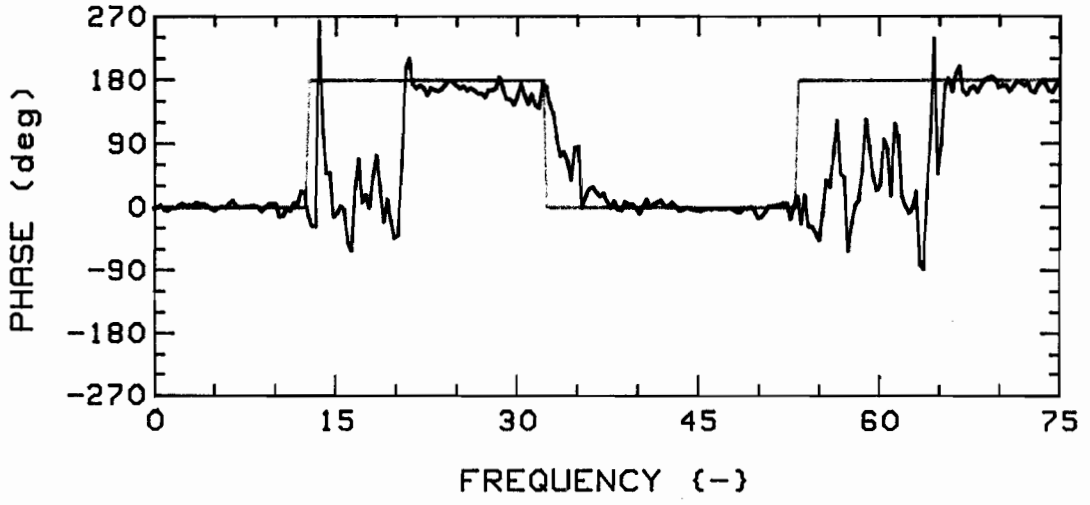

Fig.52e: Measured (RED) and theoretical (GREEN) coherence functions and phases, for K = 4, G_c = 0.75, 4F, R-R (1,2), at u = 5.

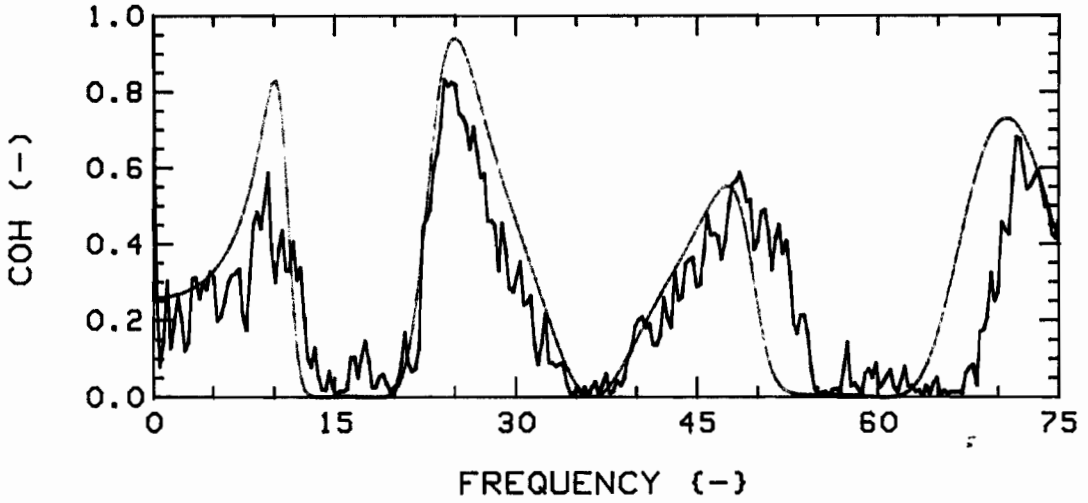

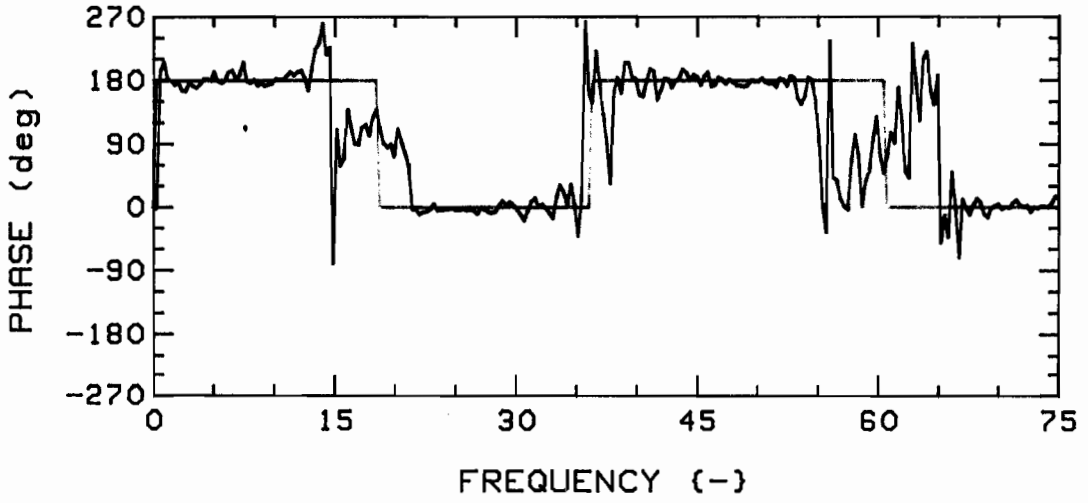

Fig.52f: Measured (RED) and theoretical (GREEN) coherence functions and phases, for K = 4, G_c = 0.75, 4F, T-T (1,2), at u = 5.

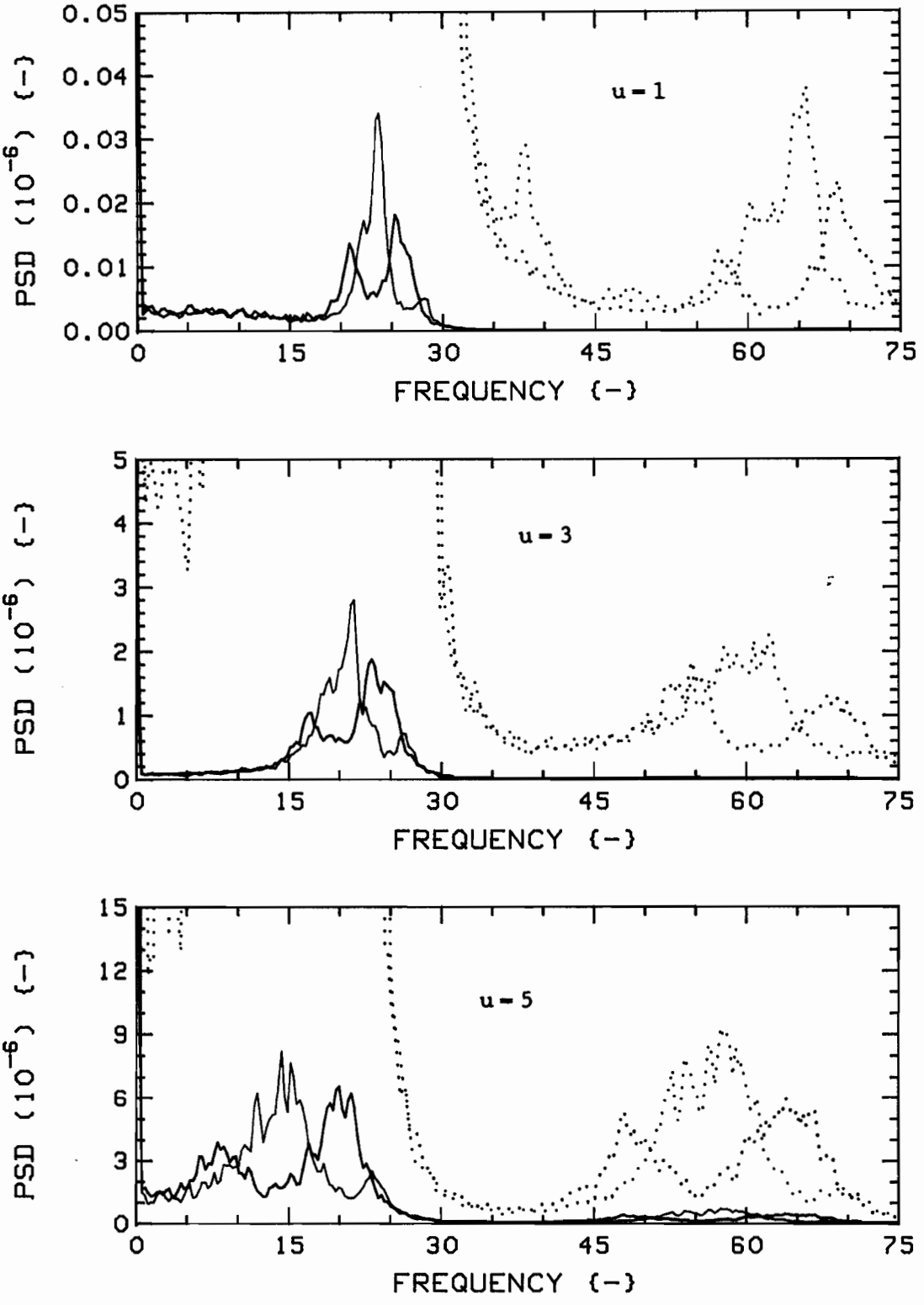

Fig.53: Measured vibration PSD's for K = 4, G_c = 1.00, 4F, Radial (RED) and Tangential (BLUE) directions.

The dotted traces are expansions of the solid ones; scales are, from top: 3.0×10^{-10}, 8.0×10^{-8}, 1.2×10^{-6}.

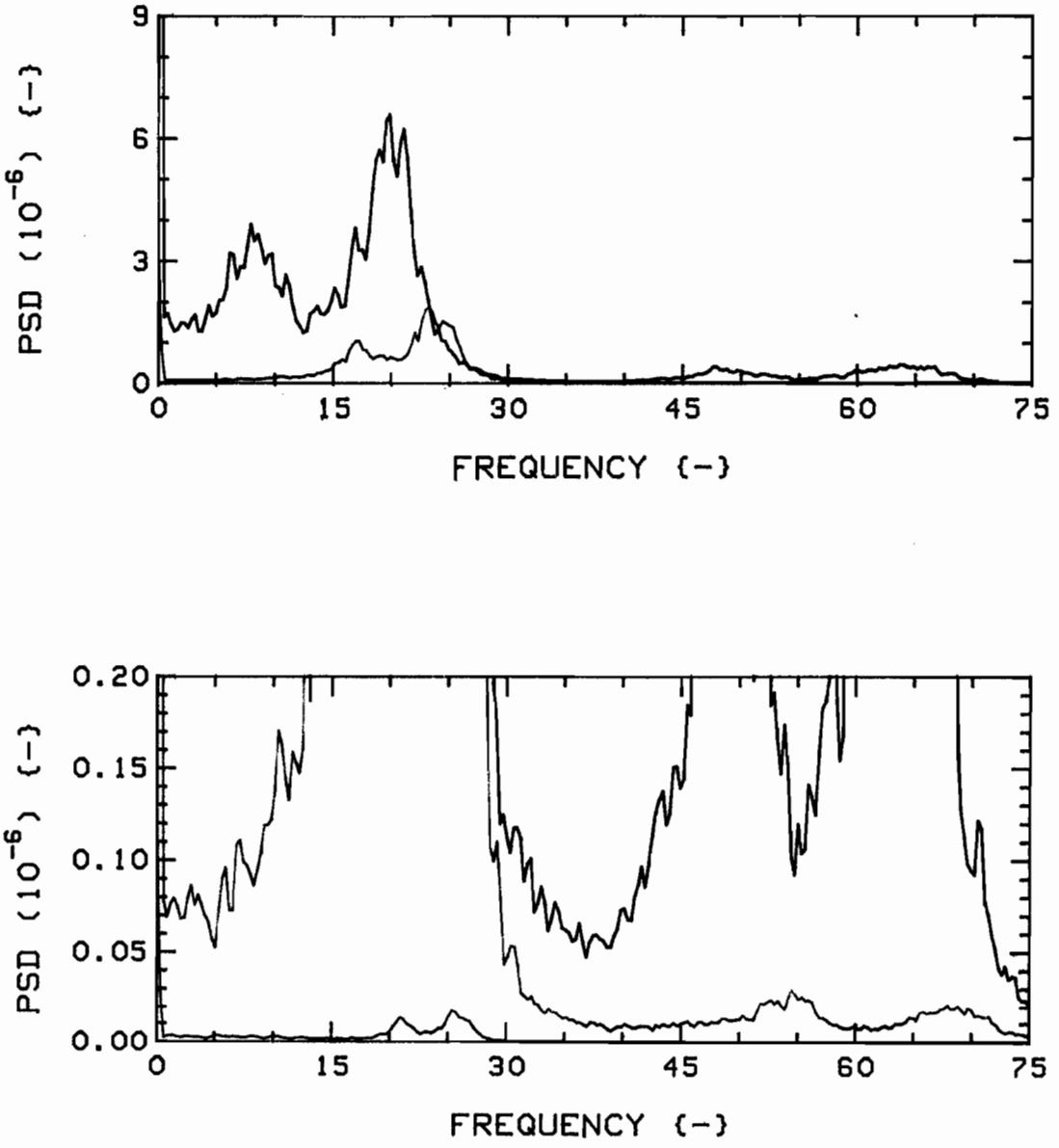

Fig.54a: Measured vibration PSD's for K = 4, G_c = 1.00, 4F, Radial direction, versus flow velocity. In descending order, u = 5.0, 3.0, and 1.0. Colour sequence: RED, GREEN, BLUE.

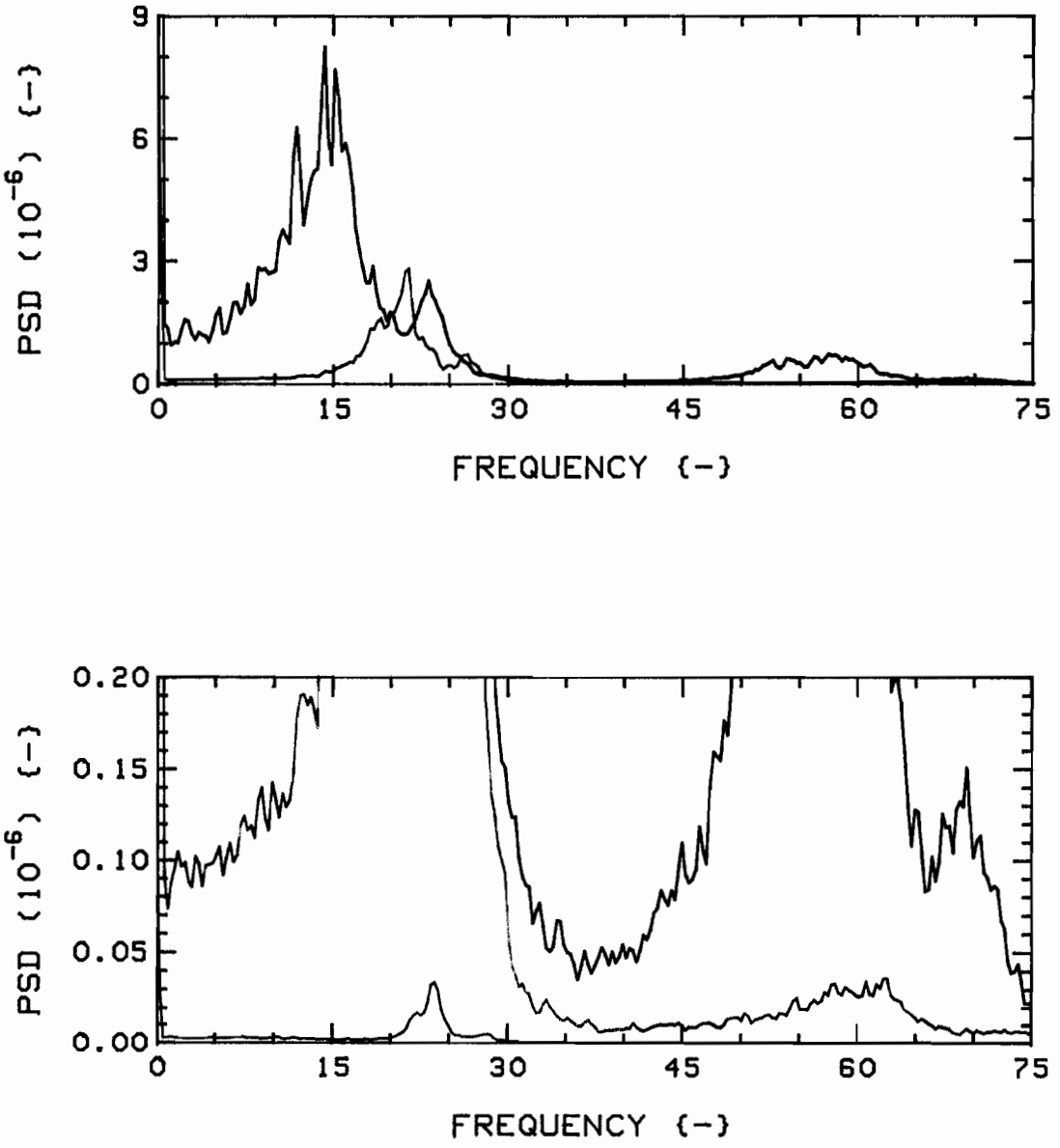

Fig.54b: Measured vibration PSD's for K = 4, G_c = 1.00, 4F, Tangential direction, versus flow velocity. In descending order, u = 5.0, 3.0, and 1.0. Colour sequence: RED, GREEN, BLUE.

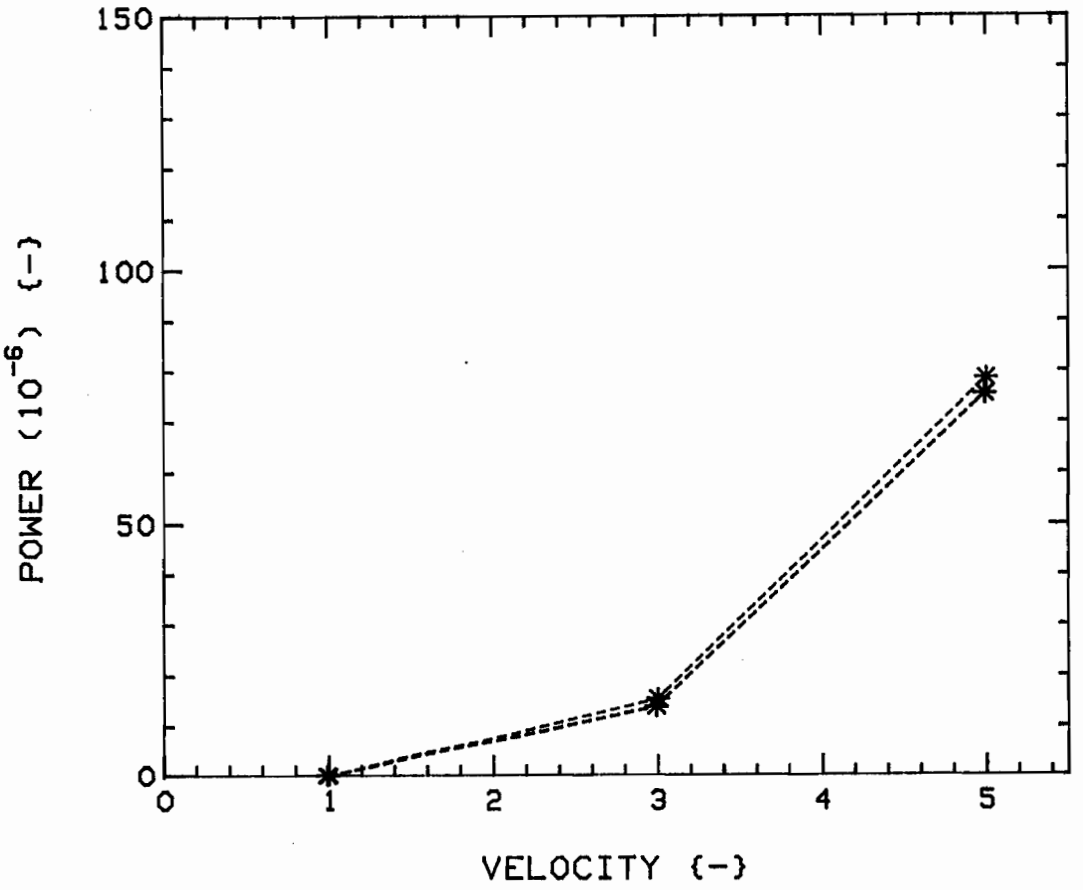

Fig.55: Powers versus flow velocity, for K = 4, G_c = 1.00, 4F, from (integrated) PSD's of Figs. 54a and 54b. Radial (RED) and Tangential (BLUE) directions.

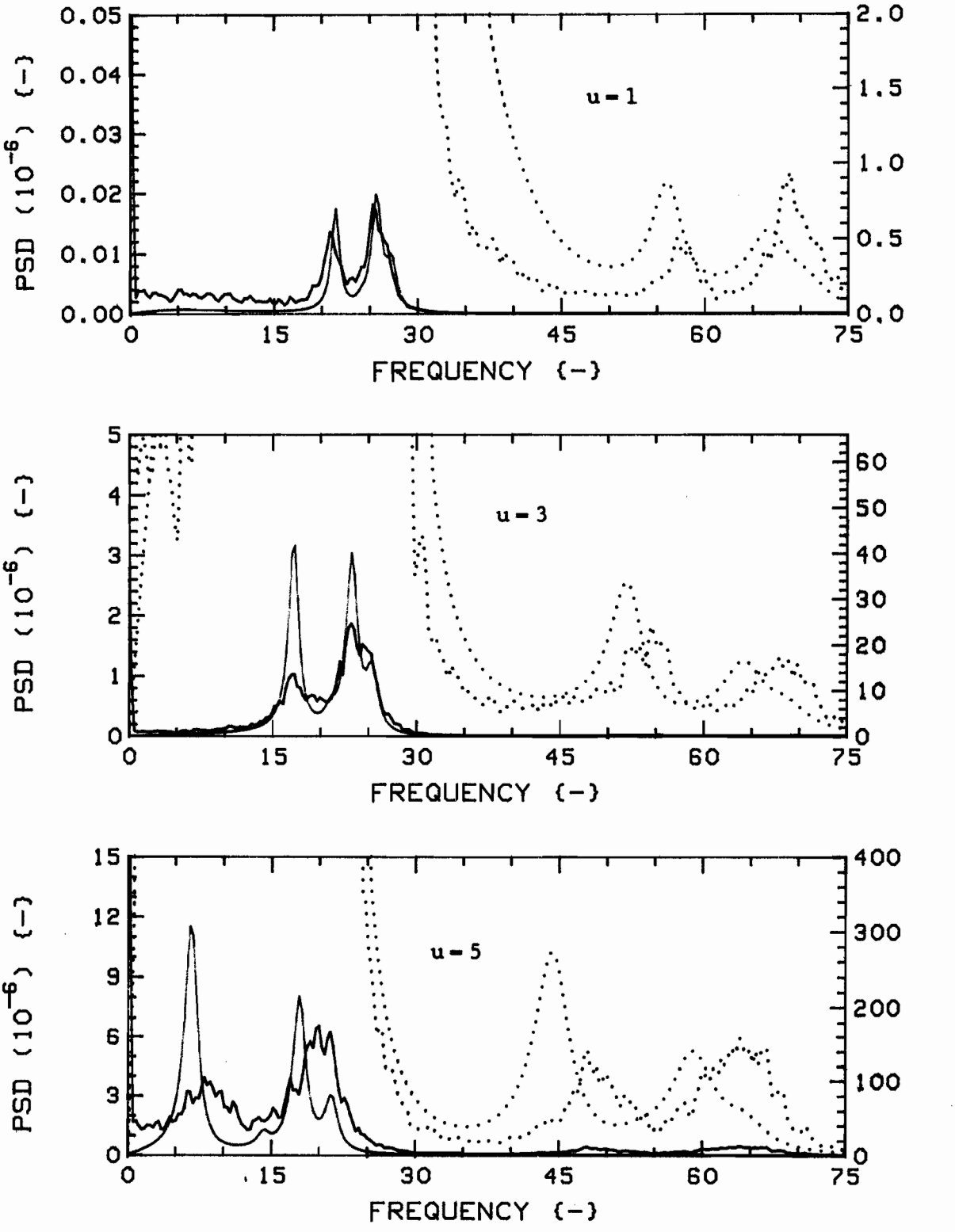

Fig.56a: Measured (RED) and theoretical (GREEN) vibration PSD's for K = 4, G_c = 1.00, 4F, Radial direction.

The dotted traces are expansions of the solid ones; scales are, from top, (RED): 3.0×10^{-10}, 8.0×10^{-8}, 1.2×10^{-6},
(GREEN): 2.0×10^{-9}, 1.8×10^{-7}, 4.0×10^{-6}.

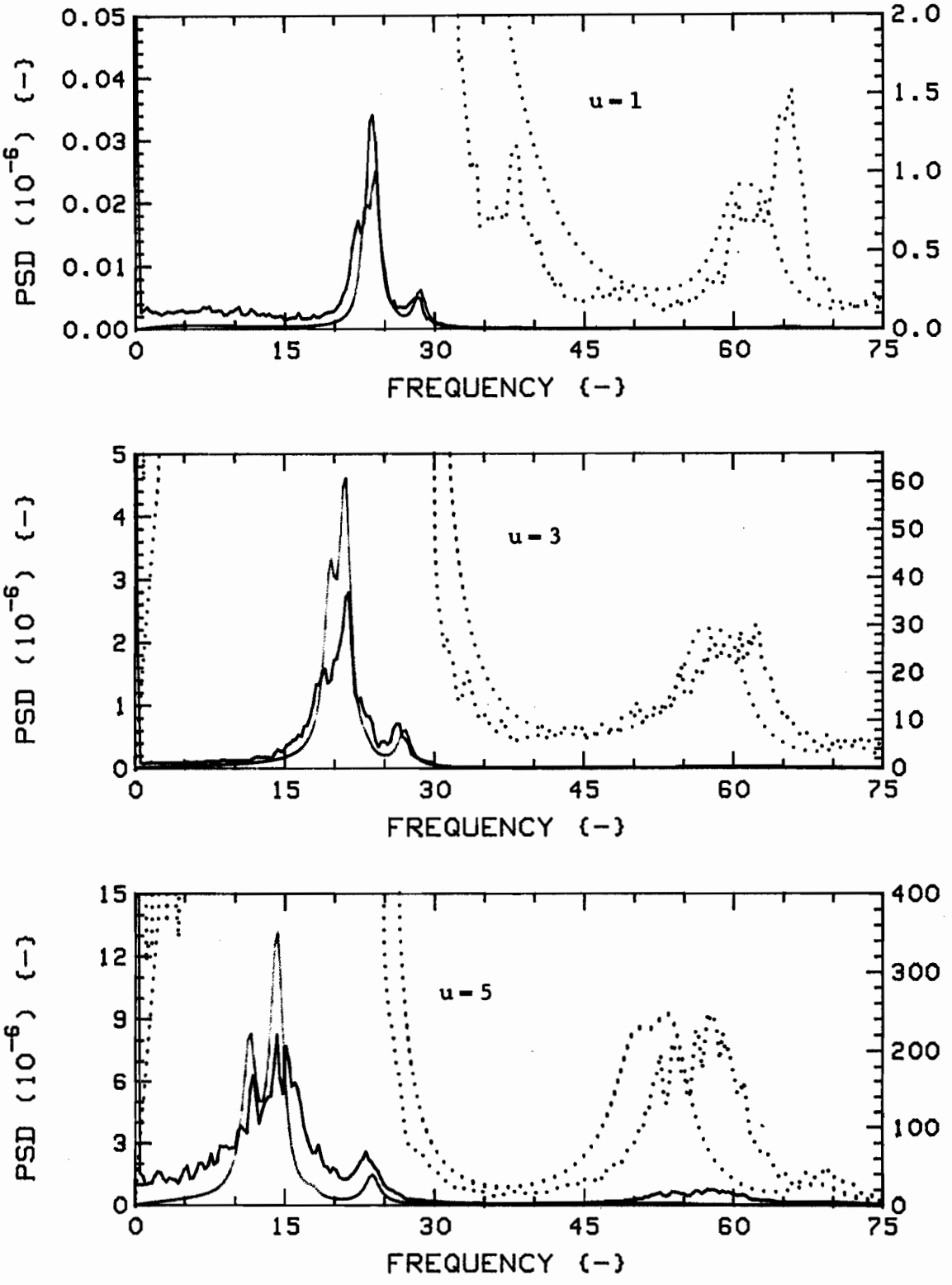

Fig.56b: Measured (RED) and theoretical (GREEN) vibration PSD's for K = 4, G_c = 1.00, 4F, Tangential direction.

The dotted traces are expansions of the solid ones; scales are, from top, (RED): 3.0×10^{-10}, 8.0×10^{-8}, 1.2×10^{-6}, (GREEN): 2.0×10^{-9}, 1.8×10^{-7}, 4.0×10^{-6}.

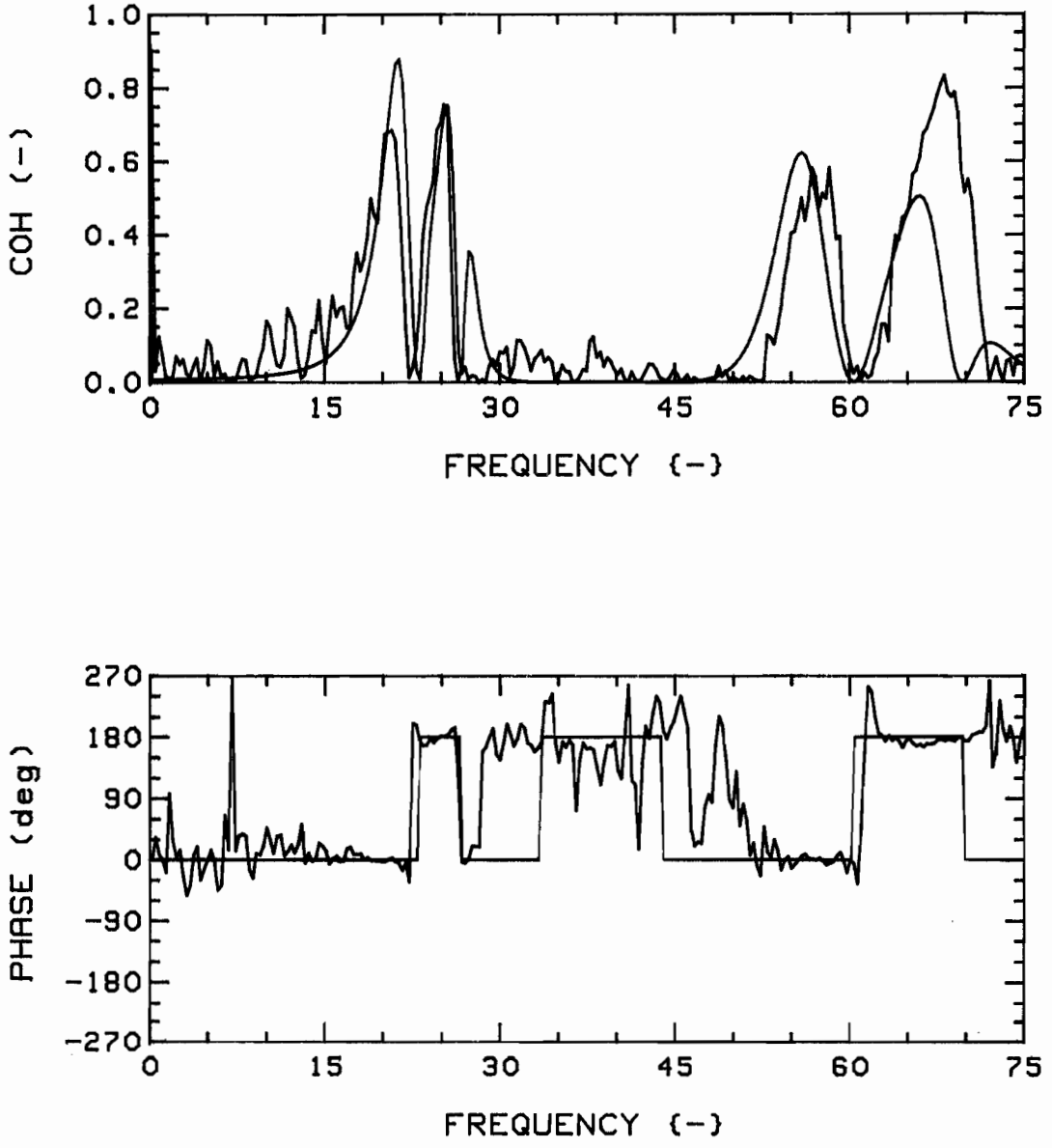

Fig.57a: Measured (RED) and theoretical (GREEN) coherence functions and phases, for K=4, G_c=1.00, 4F, R-R (1,3), at u=1.

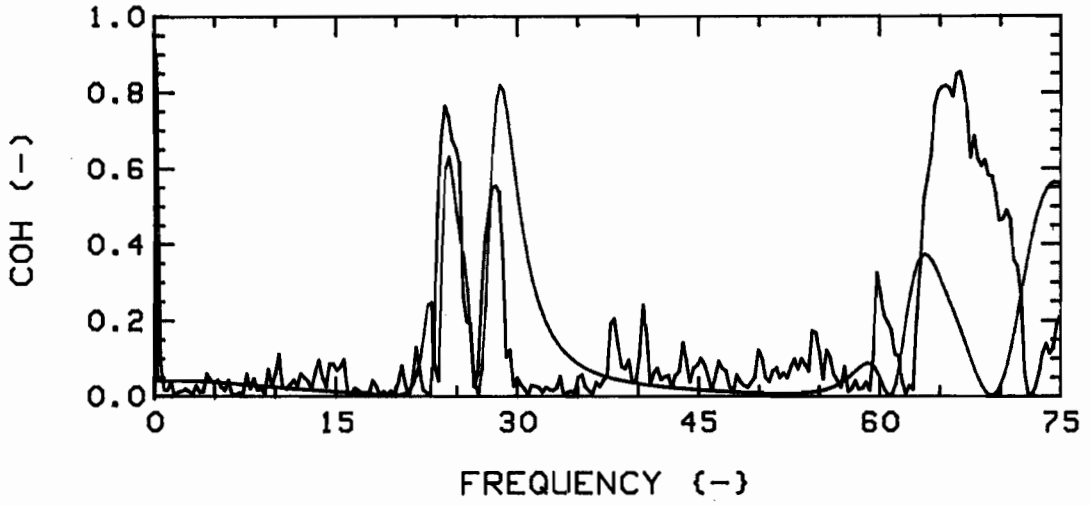

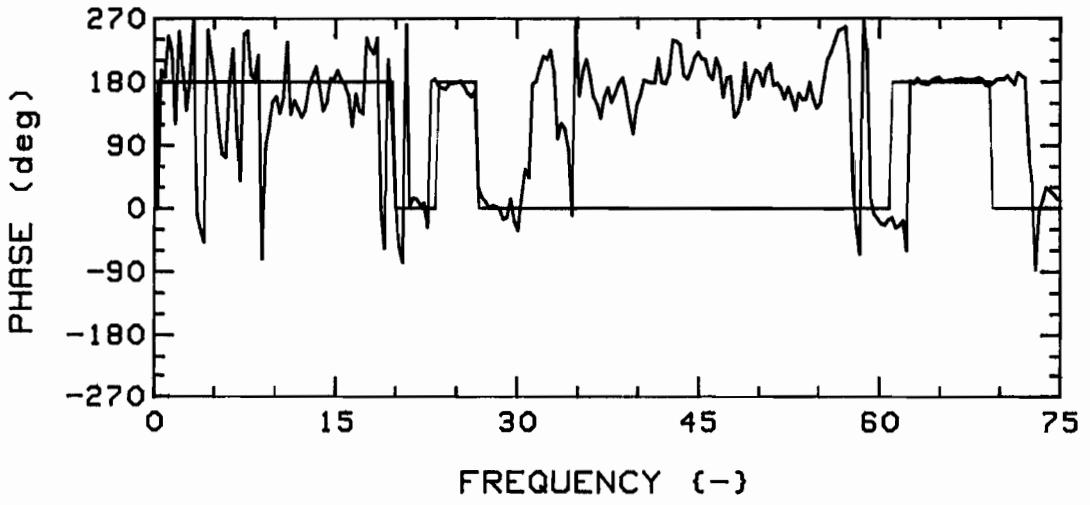

Fig.57b: Measured (RED) and theoretical (GREEN) coherence functions and phases, for K = 4, G_c = 1.00, 4F, T-T (1,3), at u = 1.

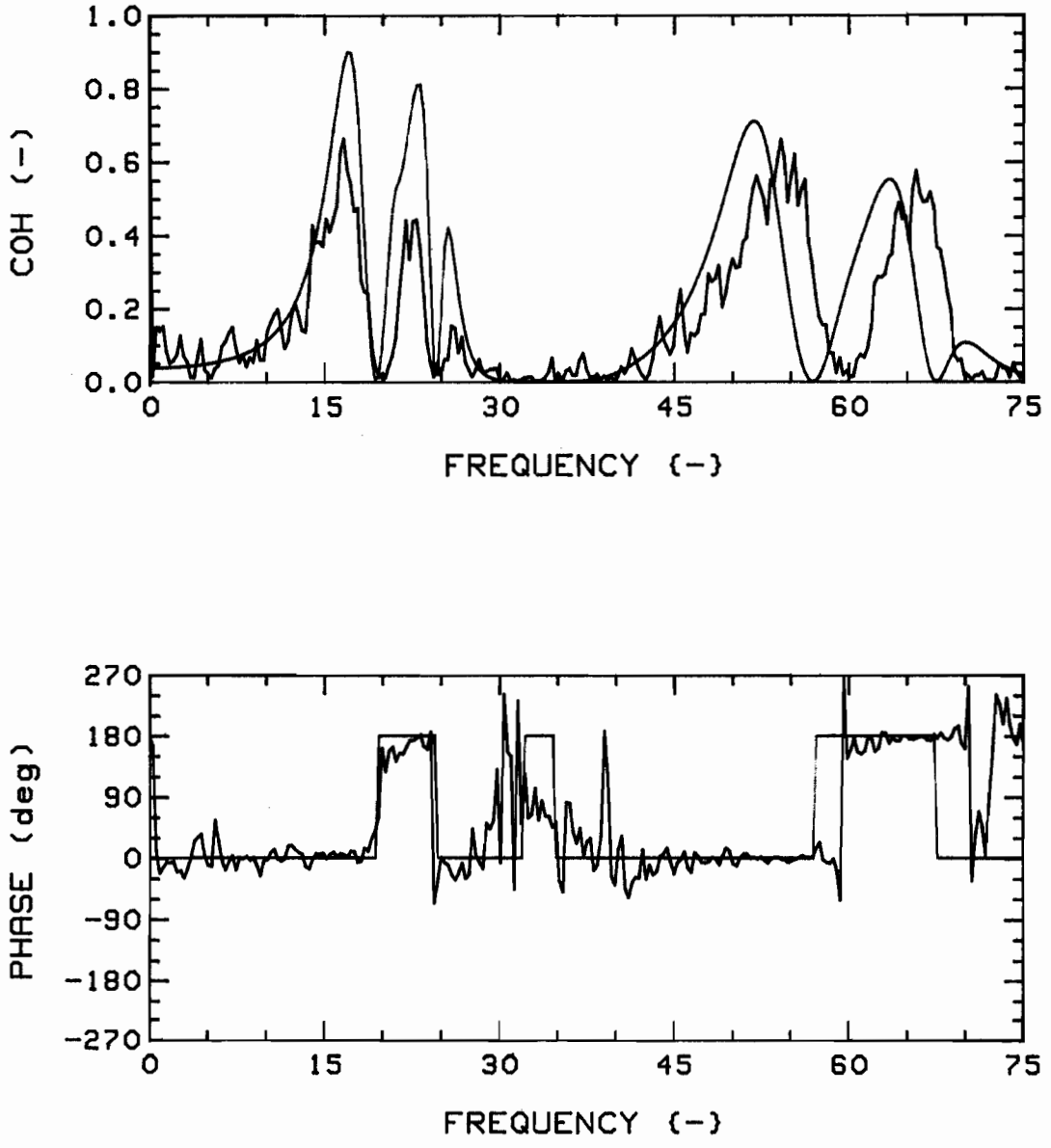

Fig.57c: Measured (RED) and theoretical (GREEN) coherence functions and phases, for K = 4, G_c = 1.00, 4F, R-R (1,3), at u = 3.

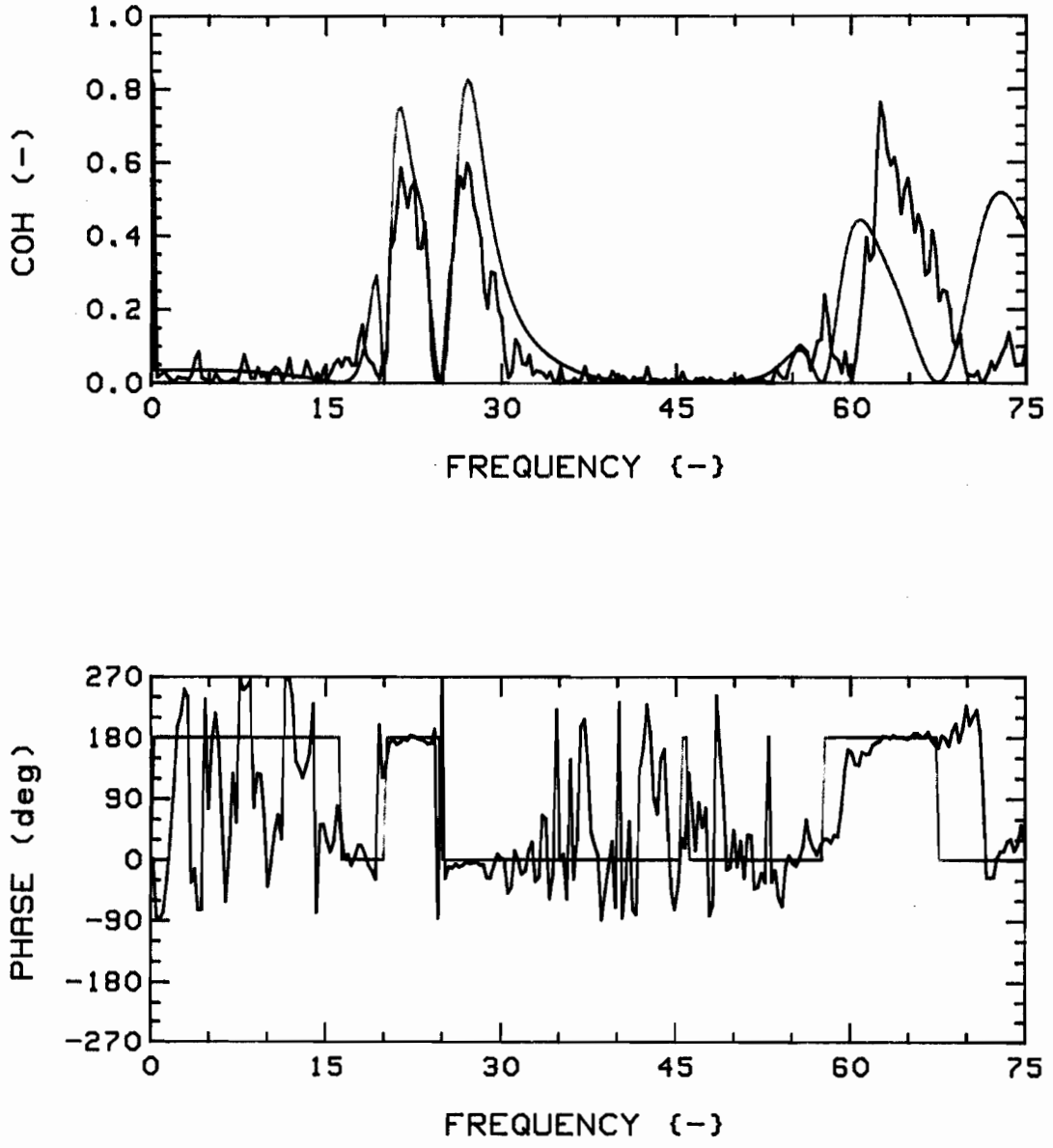

Fig.57d: Measured (RED) and theoretical (GREEN) coherence functions and phases, for K = 4, G_c = 1.00, 4F, T-T (1,3), at u = 3.

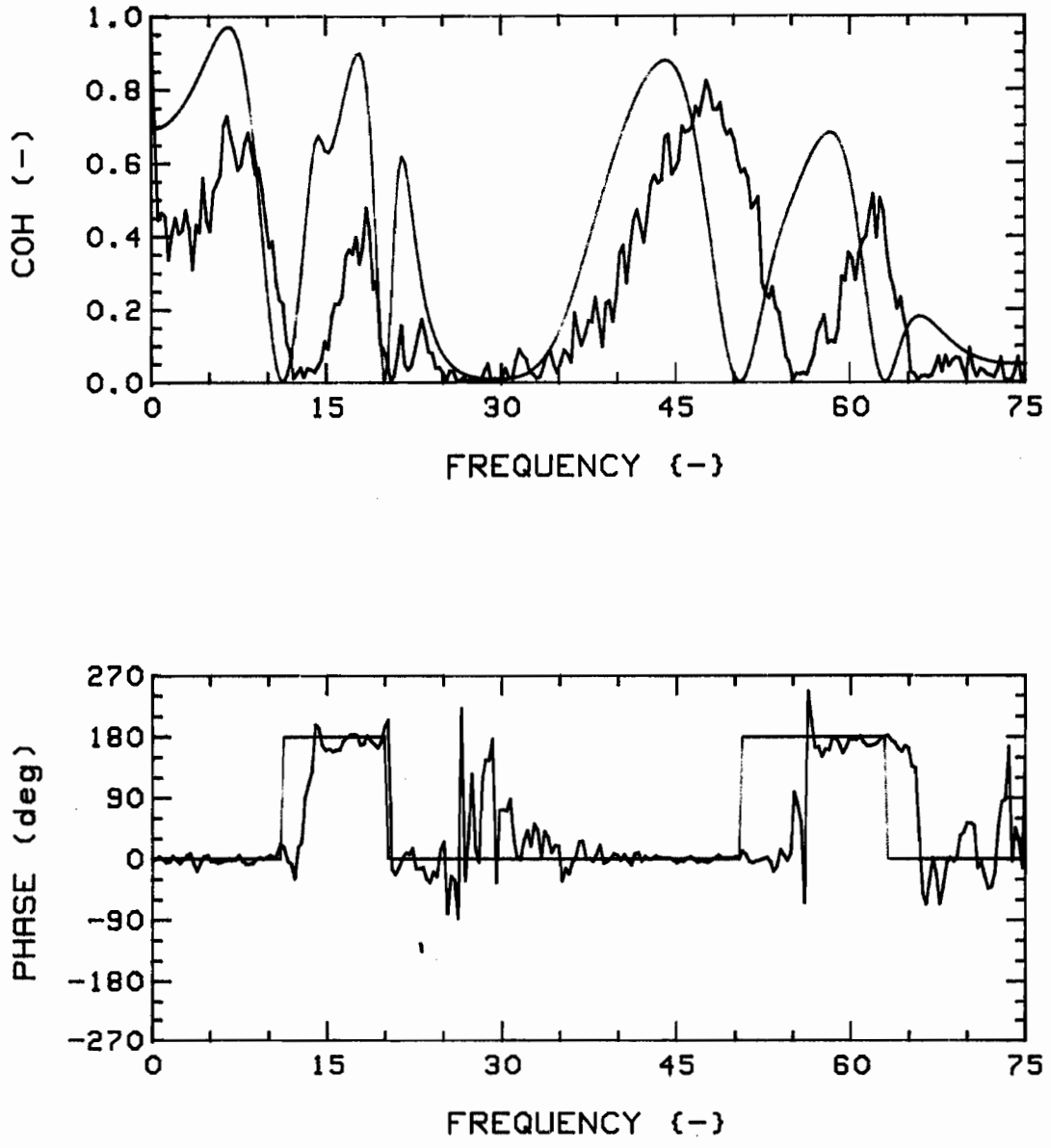

Fig.57e: Measured (RED) and theoretical (GREEN) coherence functions and phases, for K = 4, G_c = 1.00, 4F, R-R (1,3), at u = 5.

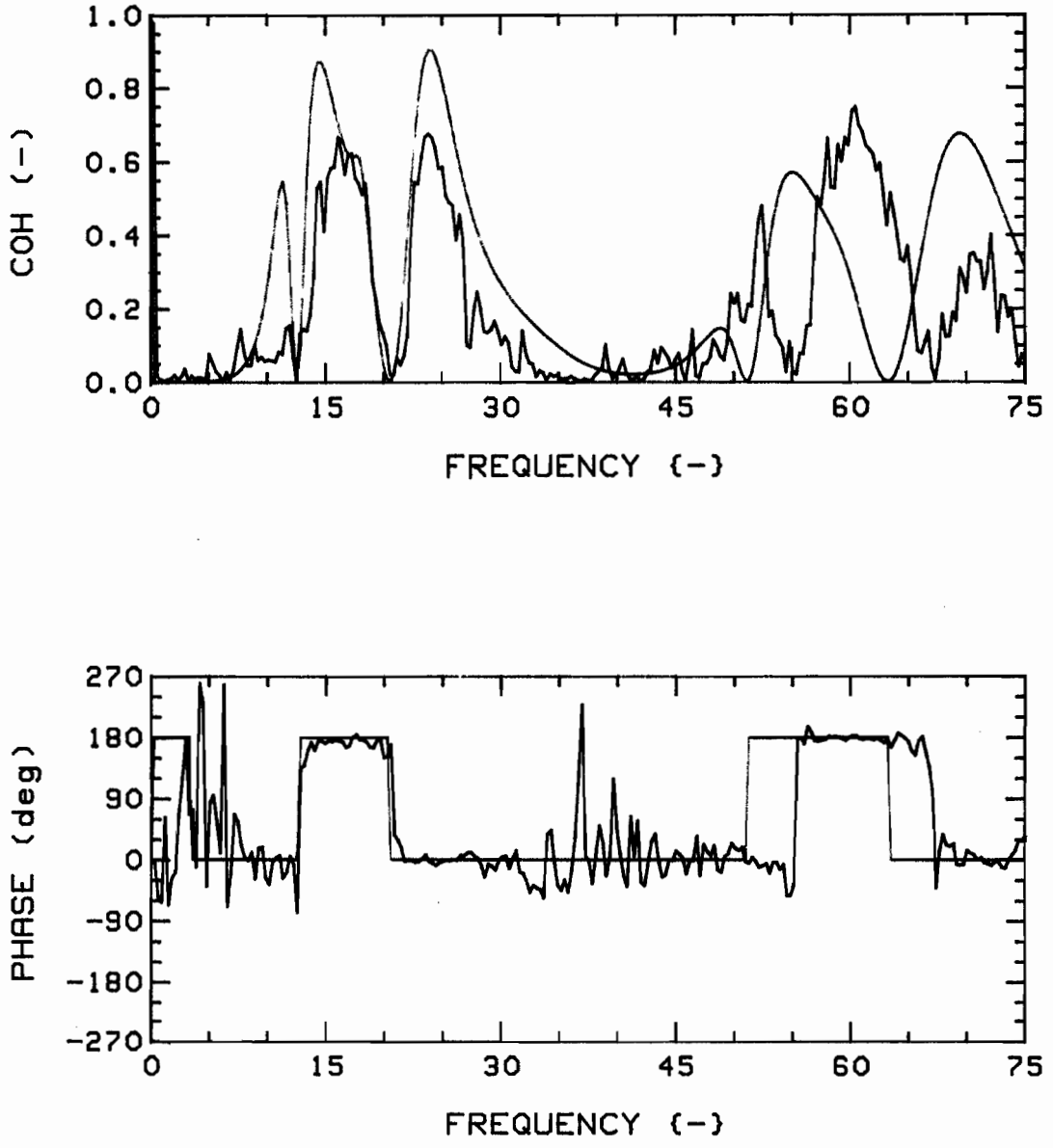

Fig.57f: Measured (RED) and theoretical (GREEN) coherence functions and phases, for K = 4, G_c = 1.00, 4F, T-T (1,3), at u = 5.

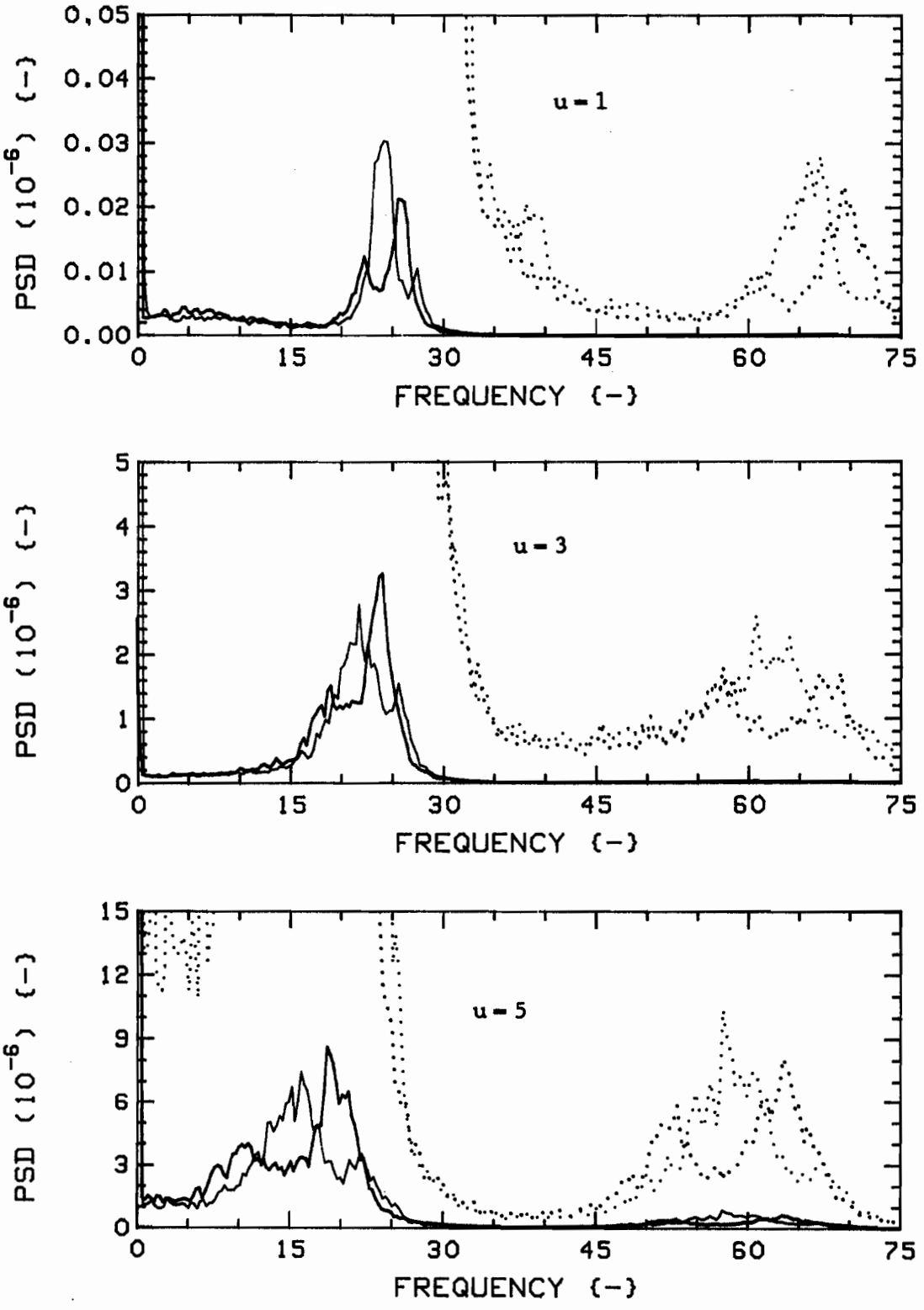

Fig.58: Measured vibration PSD's for K = 4, G_c = 1.50, 4F, Radial (RED) and Tangential (BLUE) directions.

The dotted traces are expansions of the solid ones; scales are, from top: 3.0×10^{-10}, 8.0×10^{-8}, 1.2×10^{-6}.

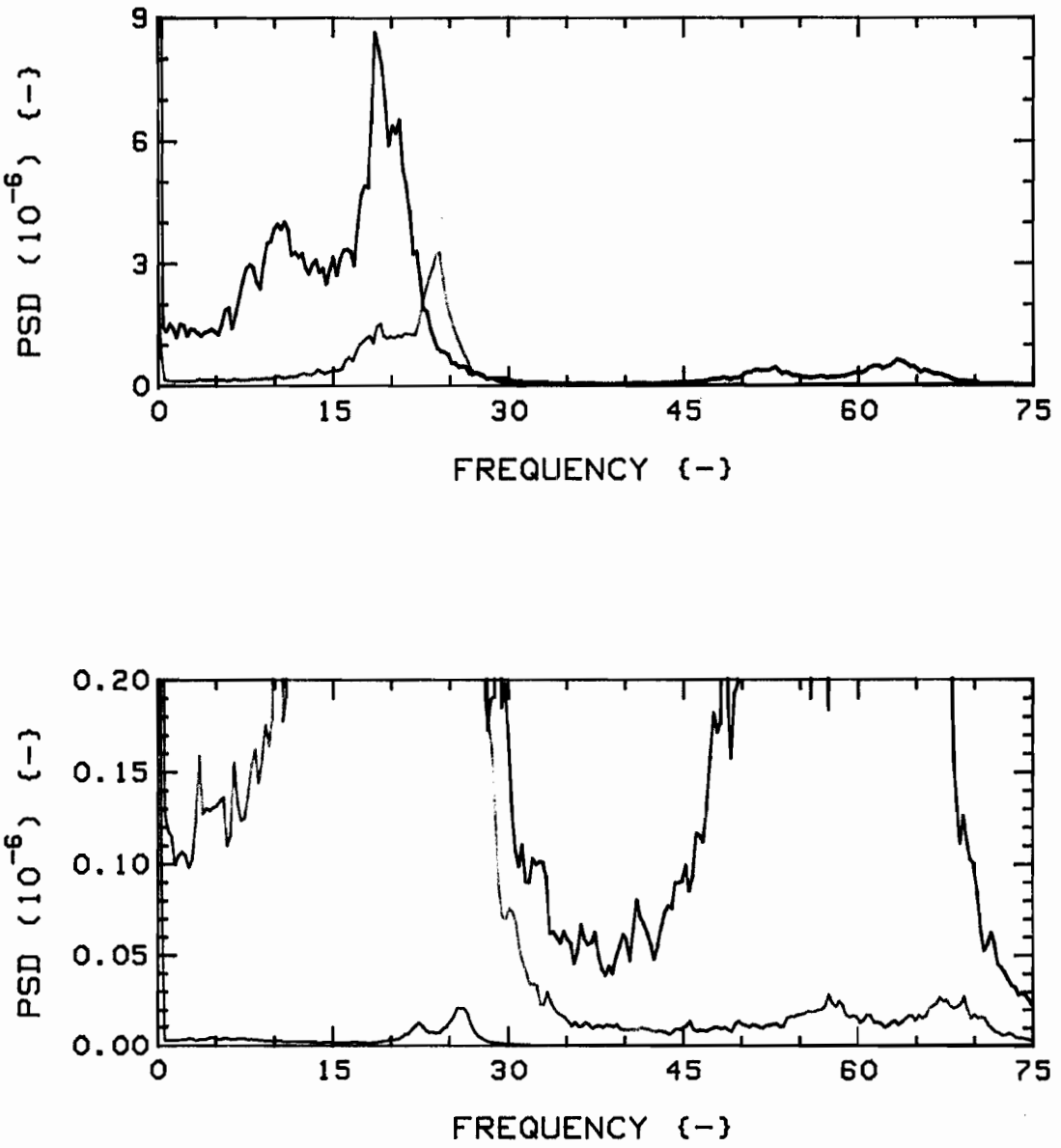

Fig.59a: Measured vibration PSD's for K = 4, G_c = 1.50, 4F, Radial direction, versus flow velocity. In descending order, u = 5.0, 3.0, and 1.0. Colour sequence: RED, GREEN, BLUE.

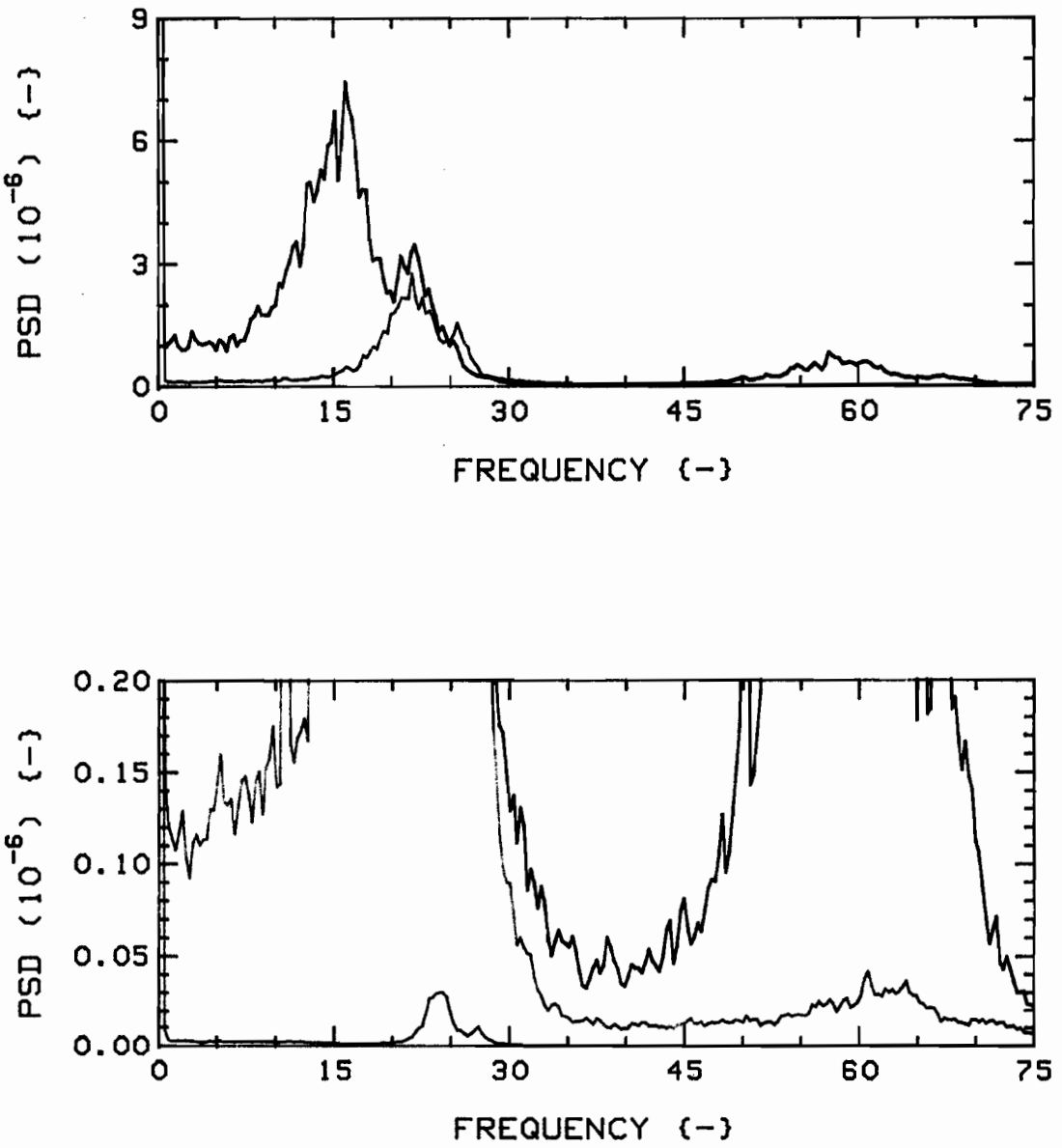

Fig.59b: Measured vibration PSD's for K = 4, G_c = 1.50, 4F, Tangential direction, versus flow velocity. In descending order, u = 5.0, 3.0, and 1.0. Colour sequence: RED, GREEN, BLUE.

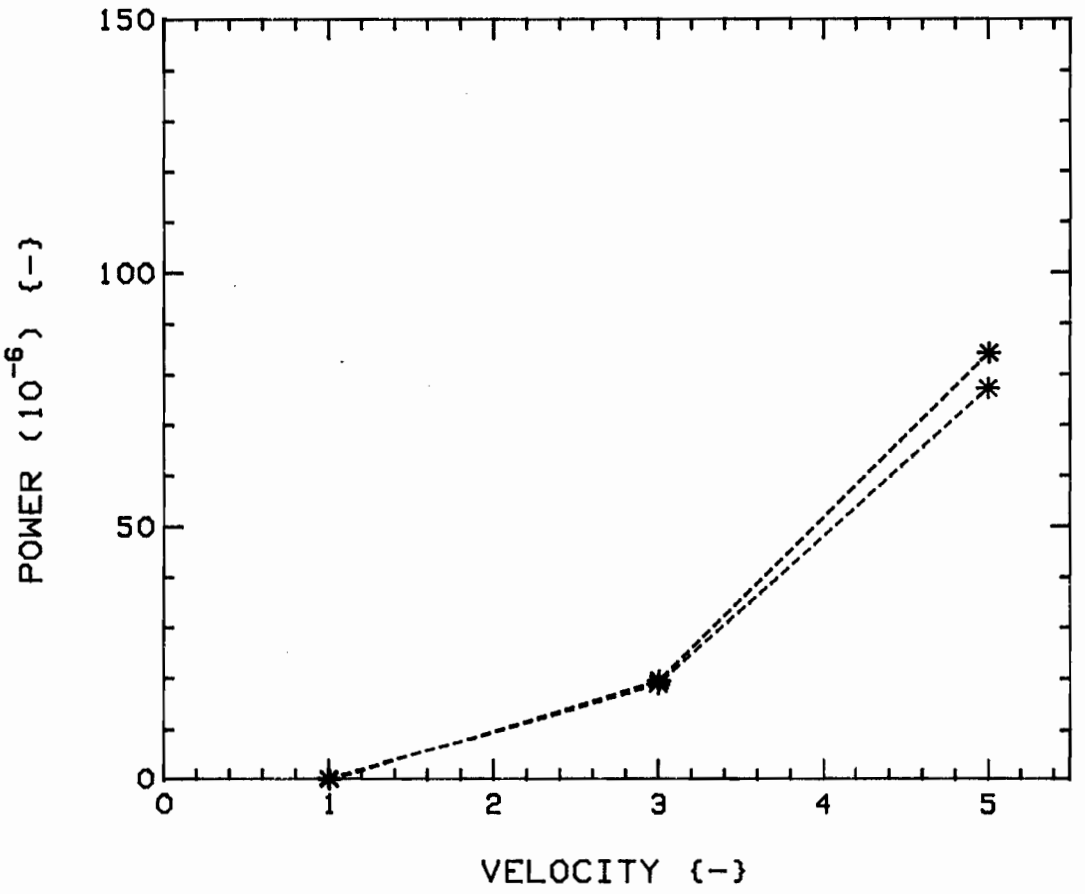

Fig.60: Powers versus flow velocity, for K = 4, G_c = 1.50, 4F, from (integrated) PSD's of Figs. 59a and 59b. Radial (RED) and Tangential (BLUE) directions.

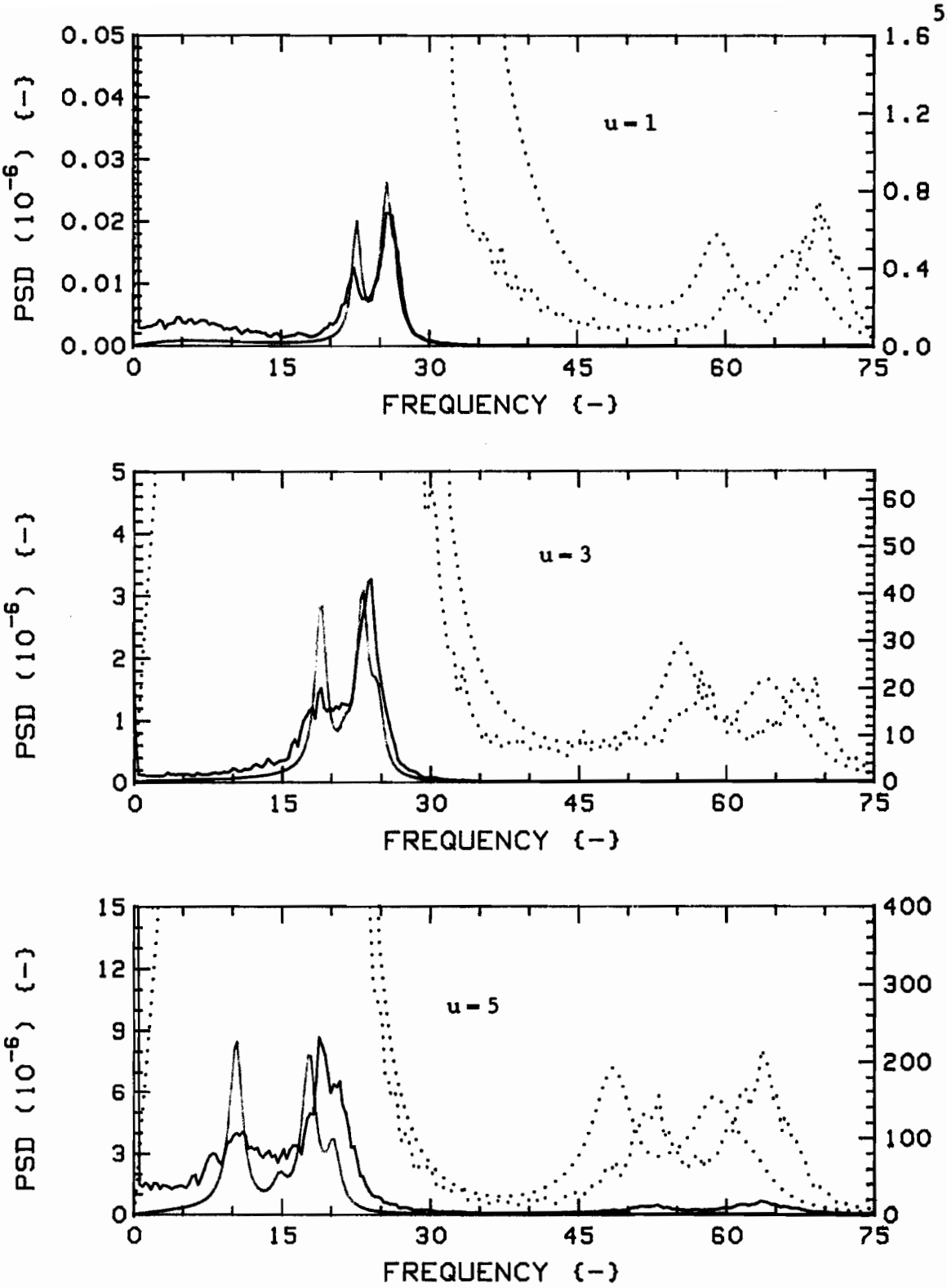

Fig.61a: Measured (RED) and theoretical (GREEN) vibration PSD's for K = 4, G_c = 1.50, 4F, Radial direction.

The dotted traces are expansions of the solid ones; scales are, from top, (RED): 3.0×10^{-10}, 8.0×10^{-8}, 1.2×10^{-6}, (GREEN): 2.0×10^{-9}, 1.8×10^{-7}, 4.0×10^{-6}.

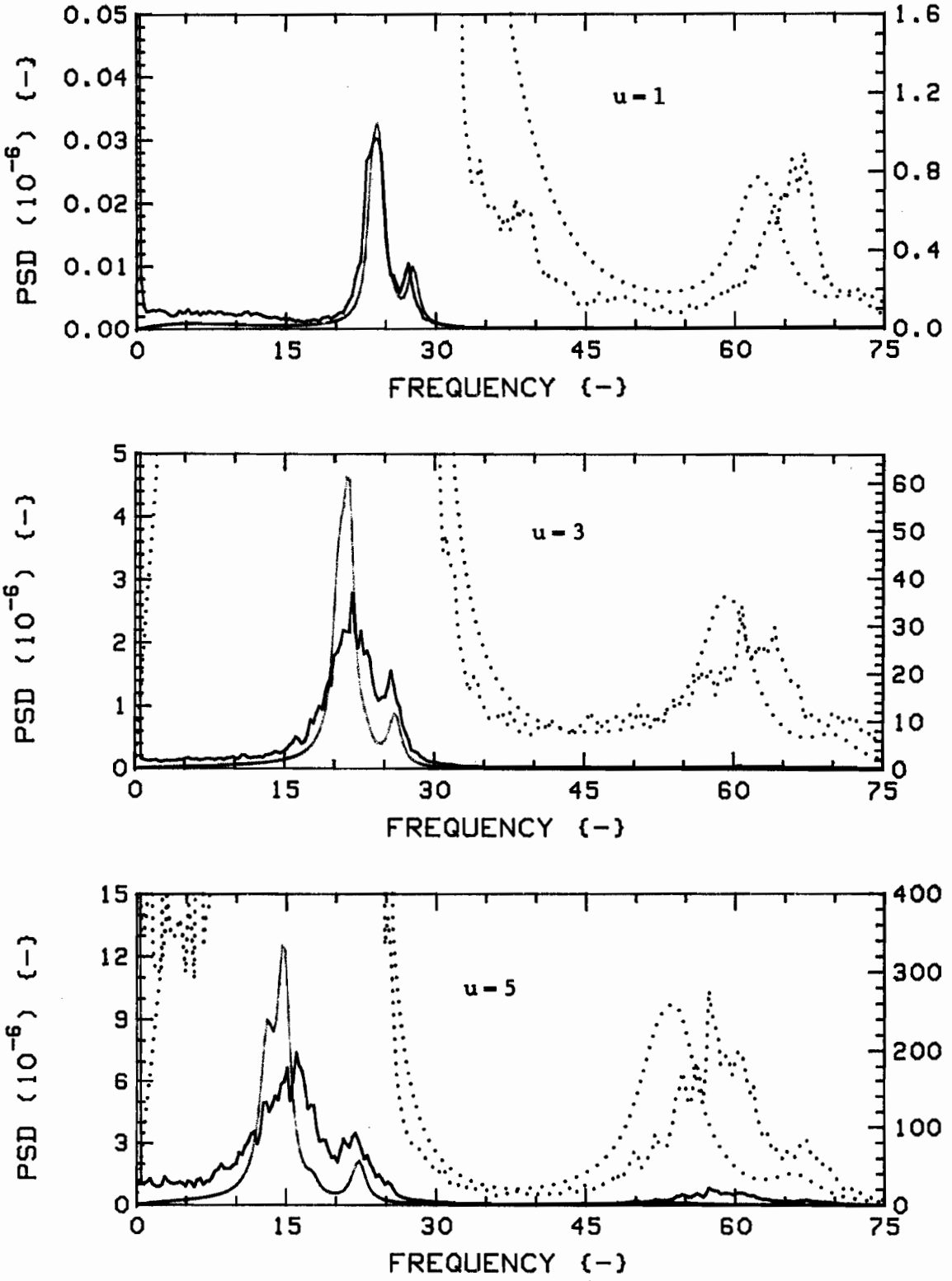

Fig.61b: Measured (RED) and theoretical (GREEN) vibration PSD's for K = 4, G_c = 1.50, 4F, Tangential direction.

The dotted traces are expansions of the solid ones; scales are, from top, (RED): 3.0×10^{-10}, 8.0×10^{-8}, 1.2×10^{-6}, (GREEN): 2.0×10^{-9}, 1.8×10^{-7}, 4.0×10^{-6}.

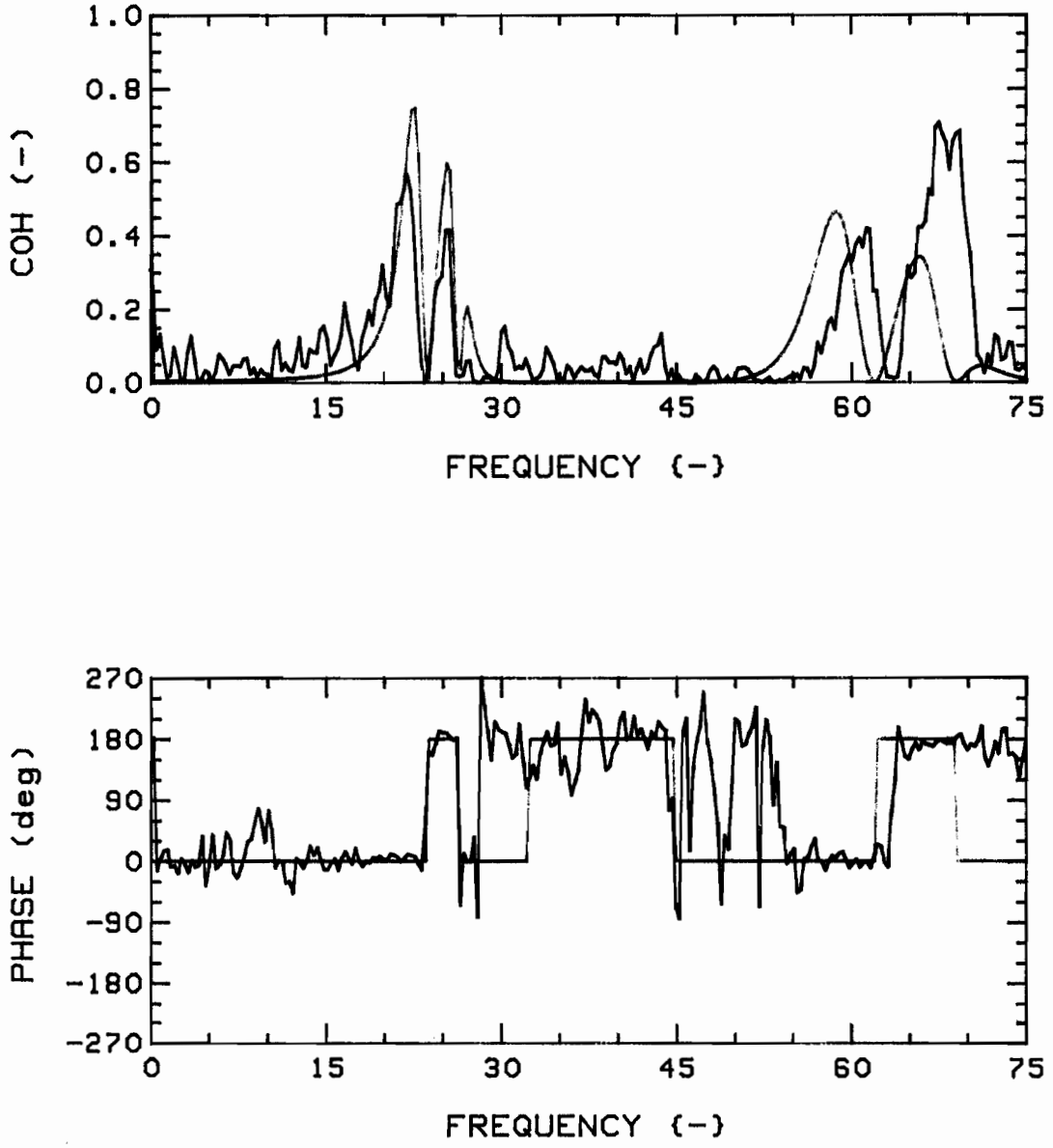

Fig.62a: Measured (RED) and theoretical (GREEN) coherence functions and phases, for K = 4, G_c = 1.50, 4F, R-R (1,3), at u = 1.

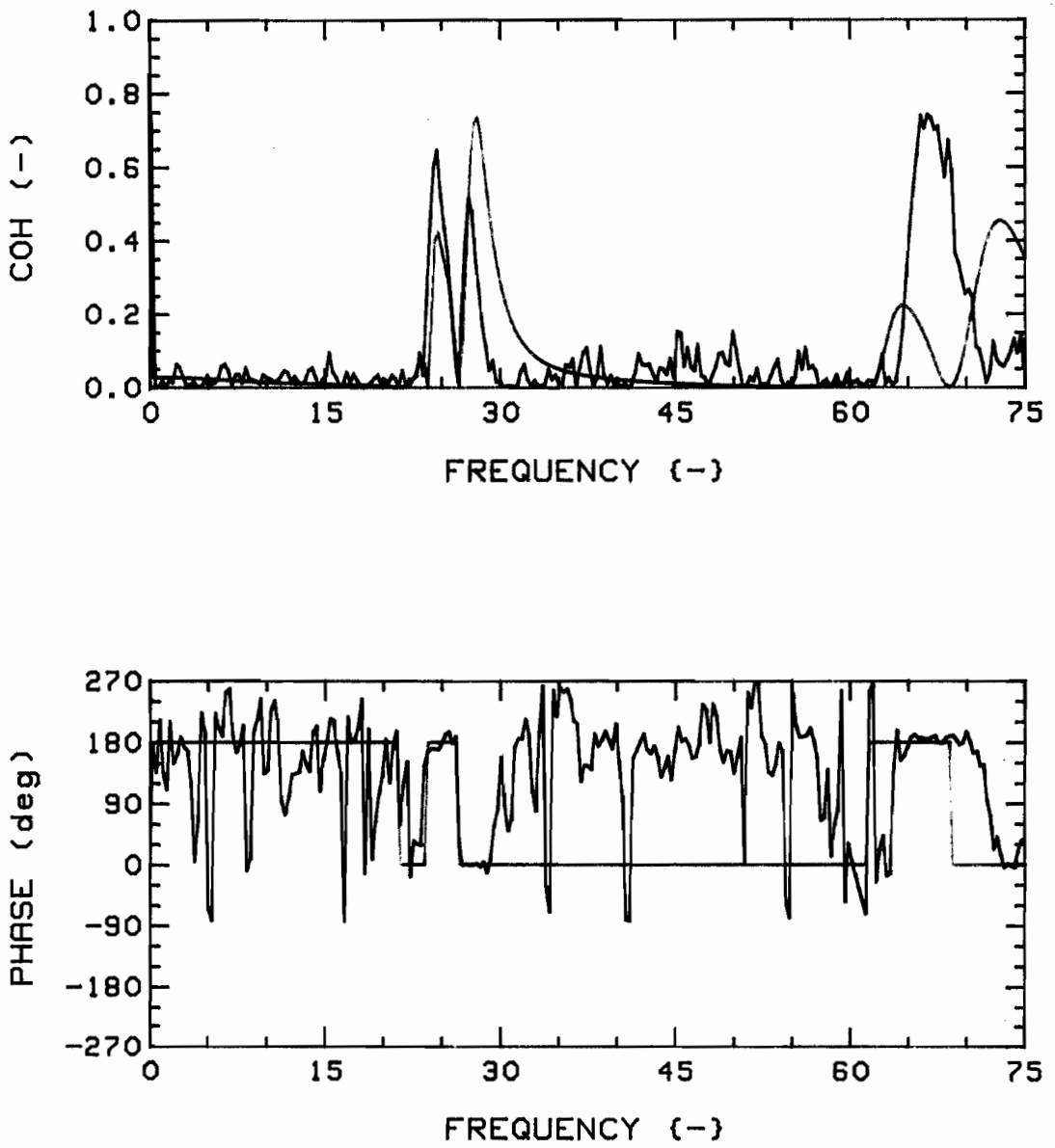

Fig.62b: Measured (RED) and theoretical (GREEN) coherence functions and phases, for K = 4, G_c = 1.50, 4F, T-T (1,3), at u = 1.

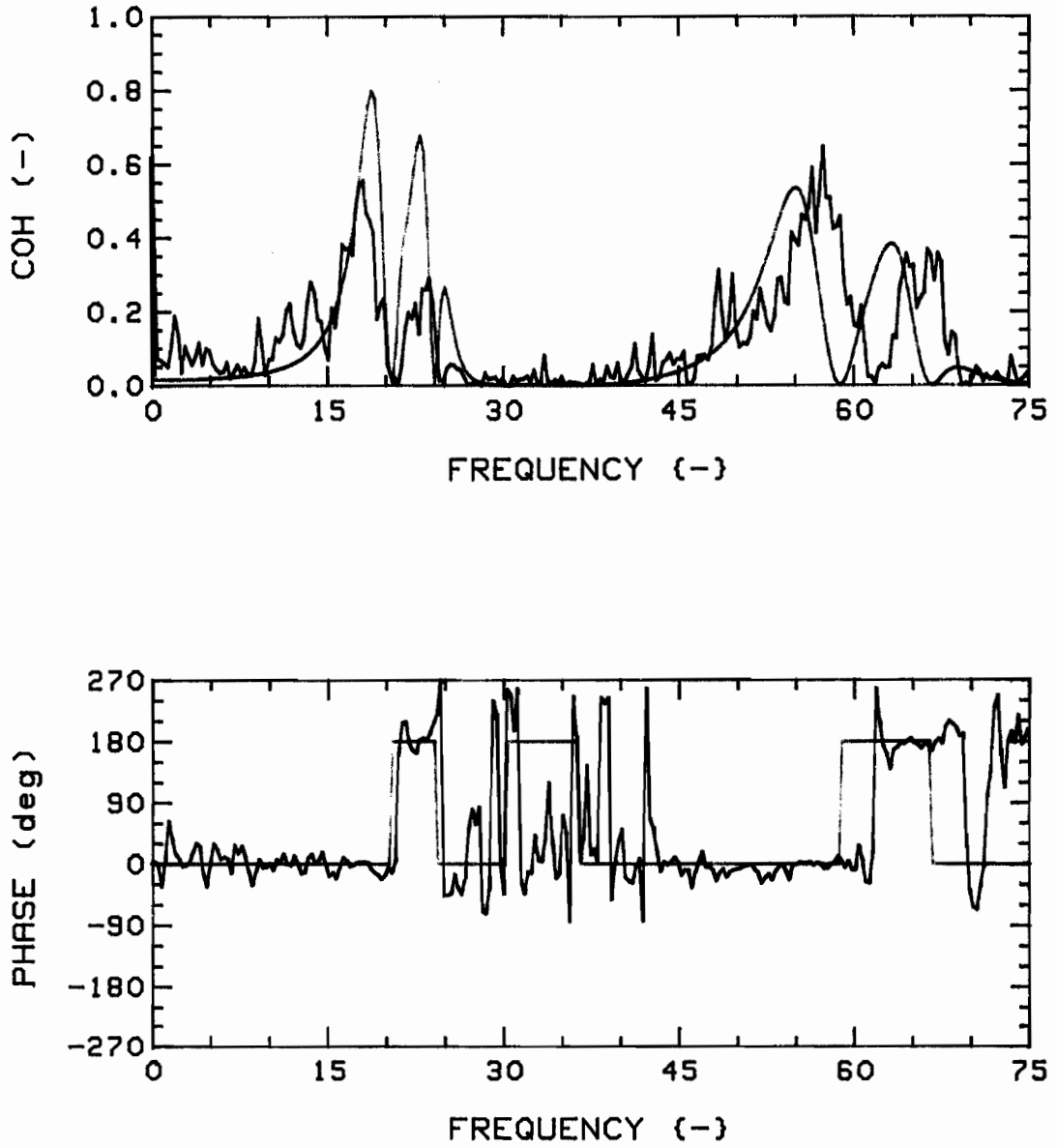

Fig.62c: Measured (RED) and theoretical (GREEN) coherence functions and phases, for K = 4, G_c = 1.50, 4F, R-R (1,3), at u = 3.

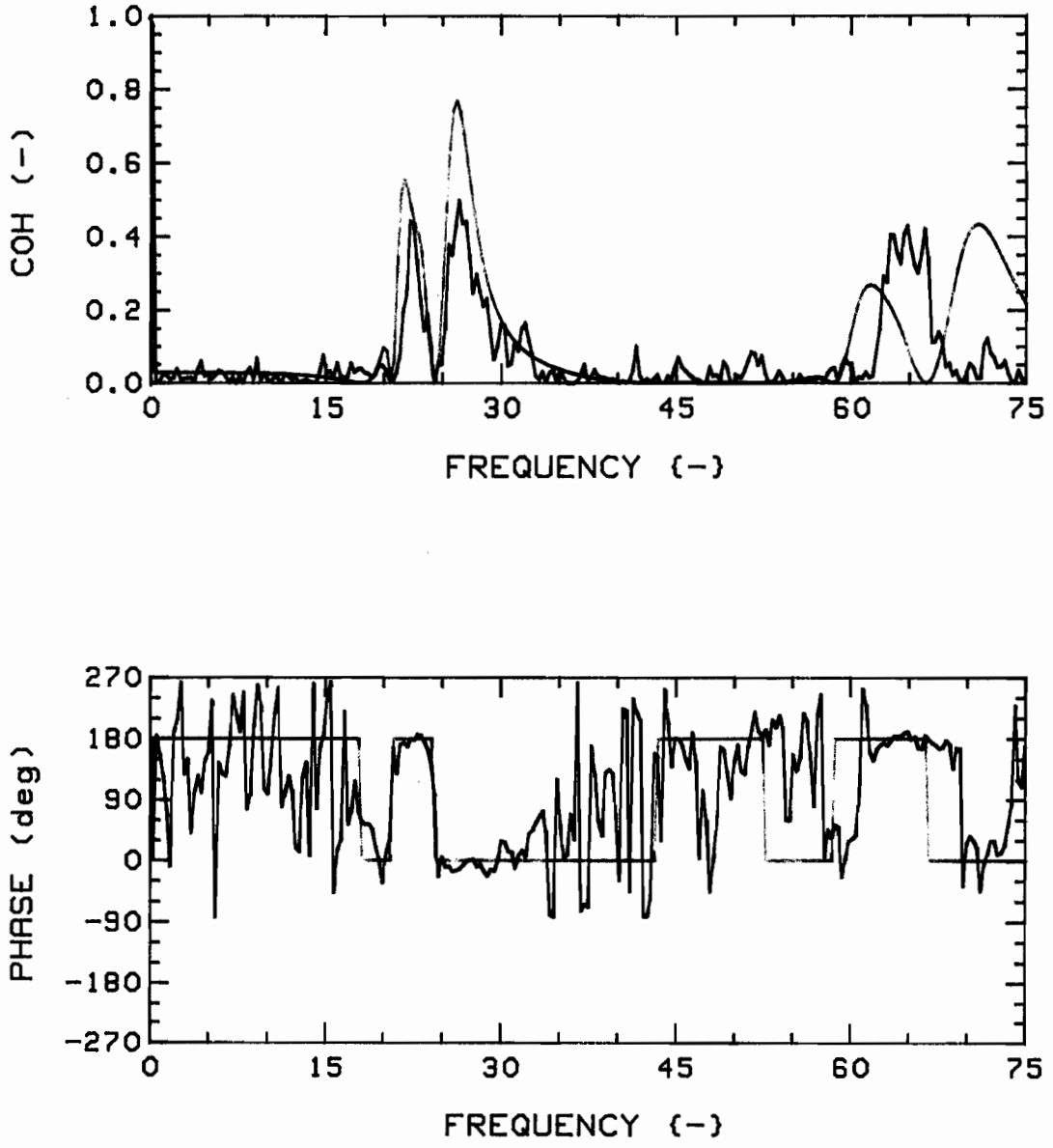

Fig.62d: Measured (RED) and theoretical (GREEN) coherence functions and phases, for K = 4, G_c = 1.50, 4F, T-T (1,3), at u = 3.

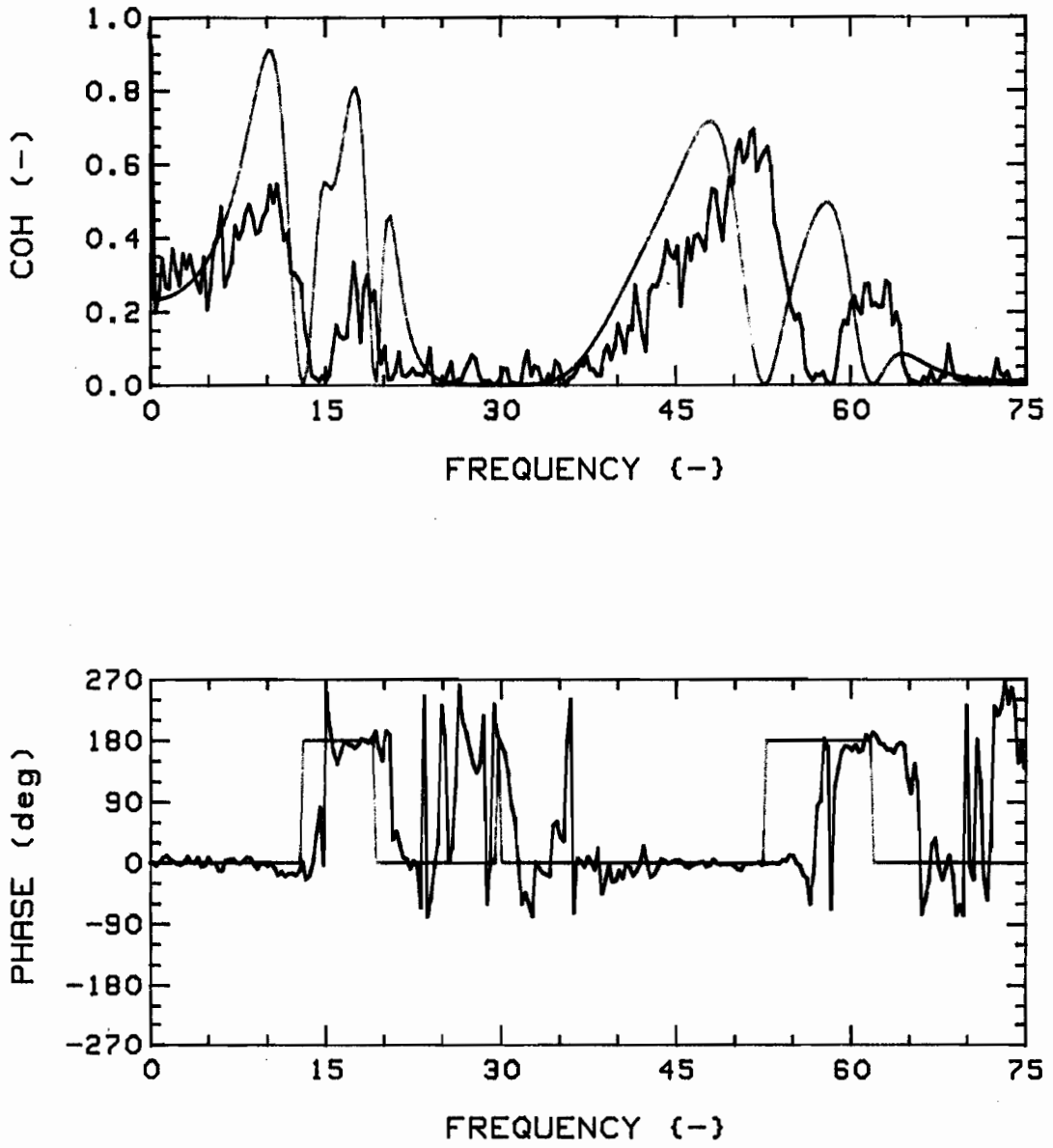

Fig.62e: Measured (RED) and theoretical (GREEN) coherence functions and phases, for K = 4, G_c = 1.50, 4F, R-R (1,3), at u = 5.

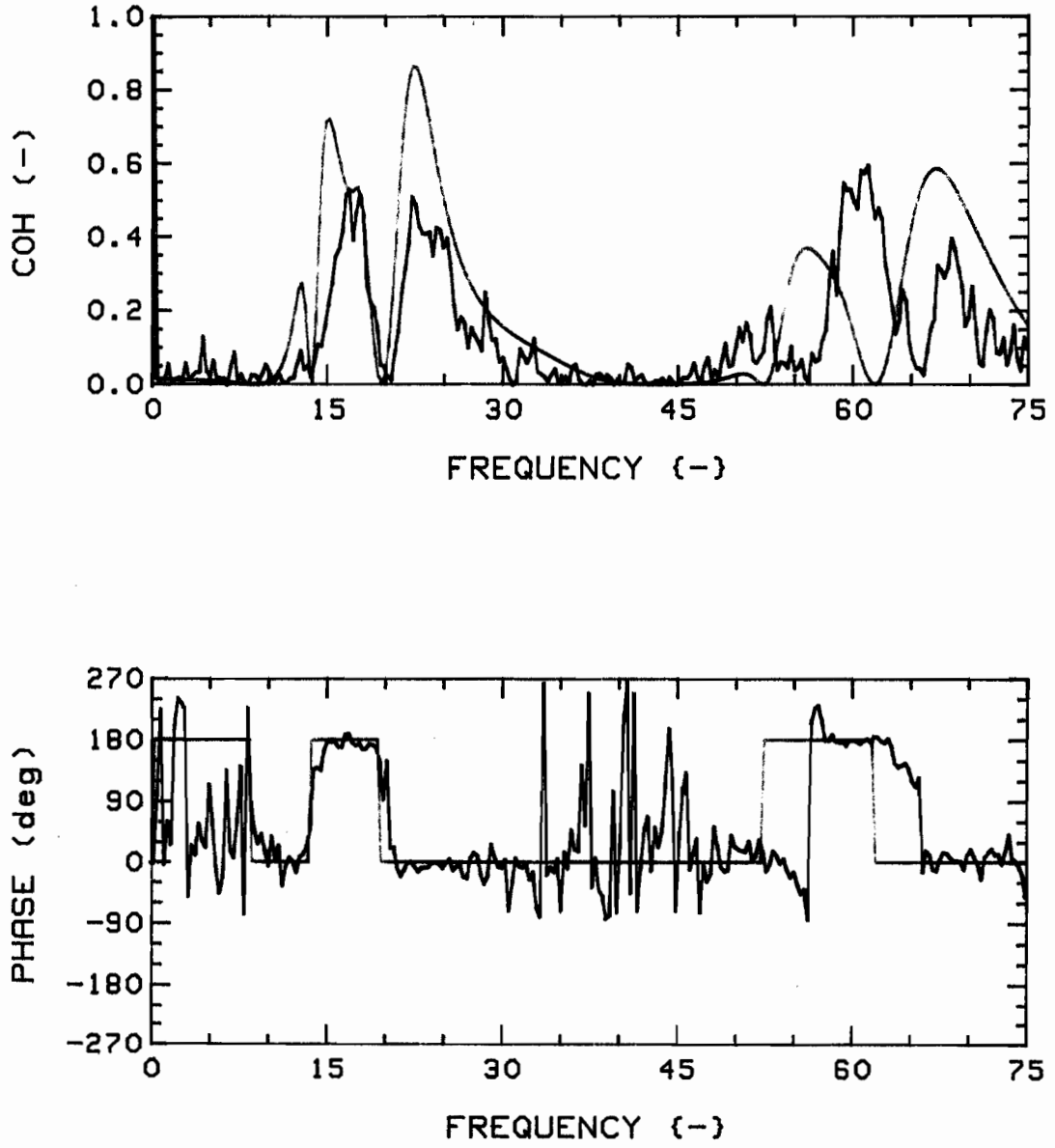

Fig.62f: Measured (RED) and theoretical (GREEN) coherence functions and phases, for K = 4, G_c = 1.50, 4F, T-T (1,3), at u = 5.

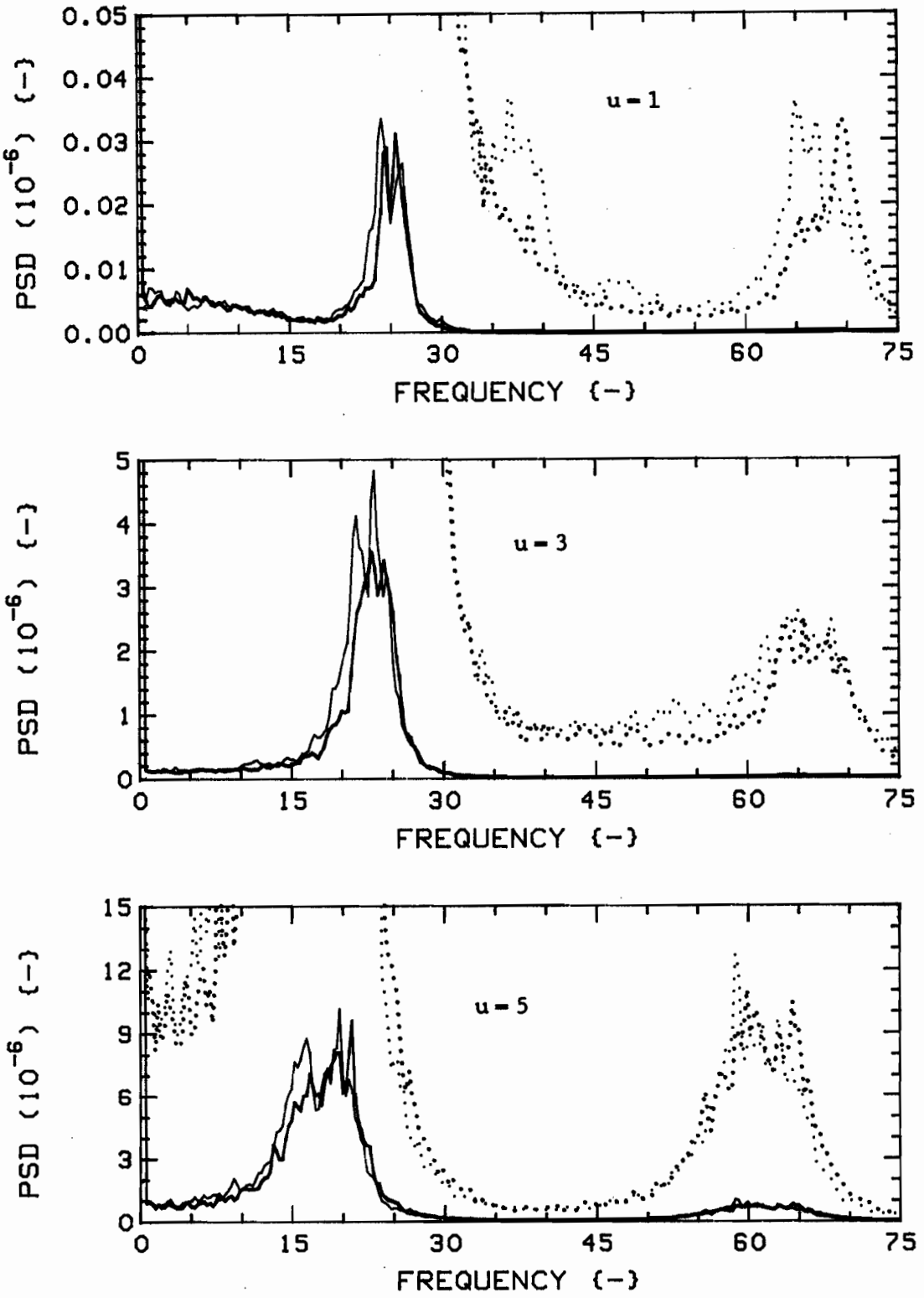

Fig.63: Measured vibration PSD's for K = 2, G_c = 1.89, 2F, Radial (RED) and Tangential (BLUE) directions.

The dotted traces are expansions of the solid ones; scales are, from top: 3.0×10^{-10}, 8.0×10^{-8}, 1.2×10^{-6}.

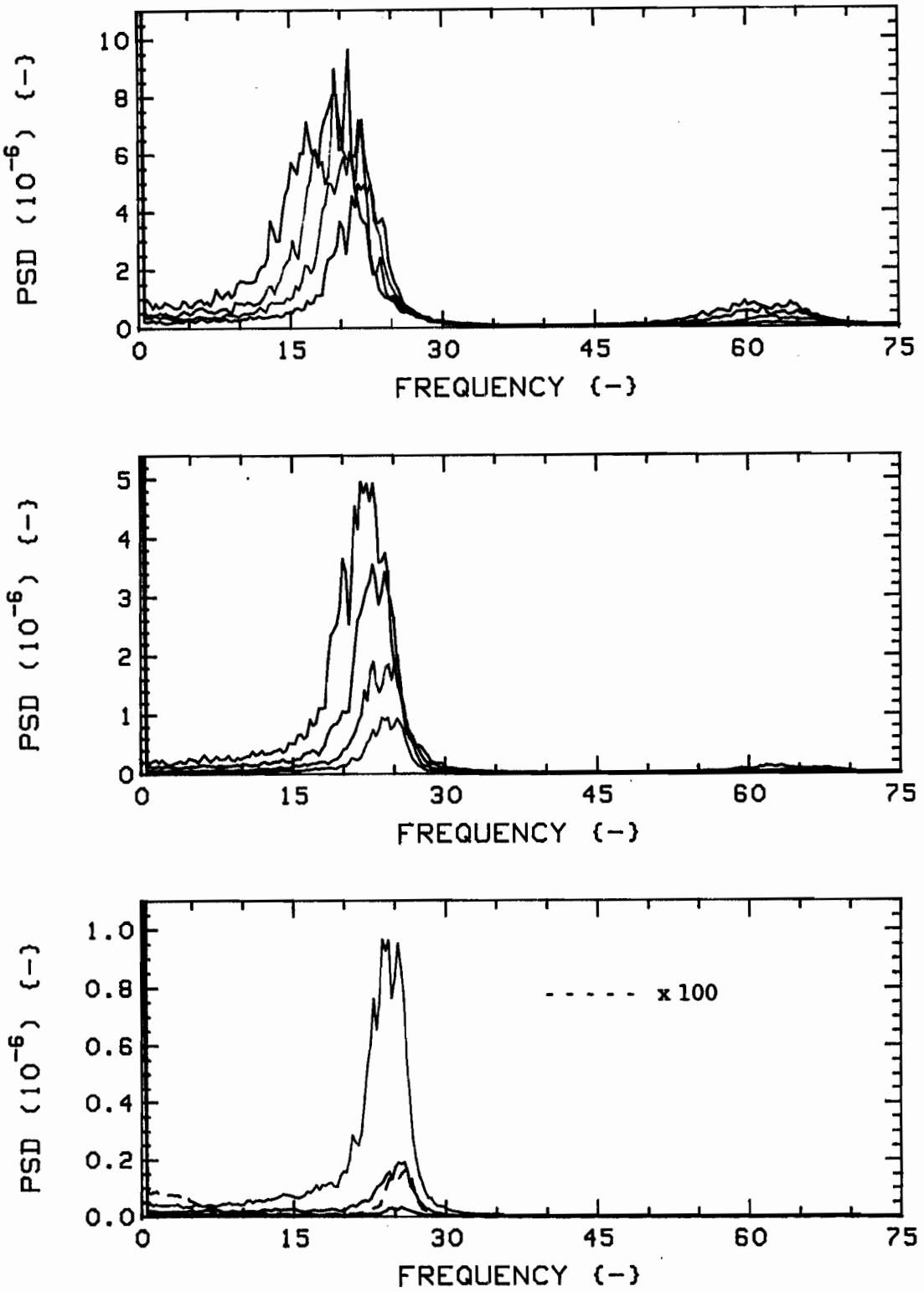

Fig.64a: Measured vibration PSD's for K = 2, G_c = 1.89, 2F, Radial direction, versus flow velocity. In descending order, u = 5.0 to 0.5, in steps of 0.5. Colour sequence: RED, GREEN, BLUE, BLACK (lowest trace of each plot is highest of the next one).

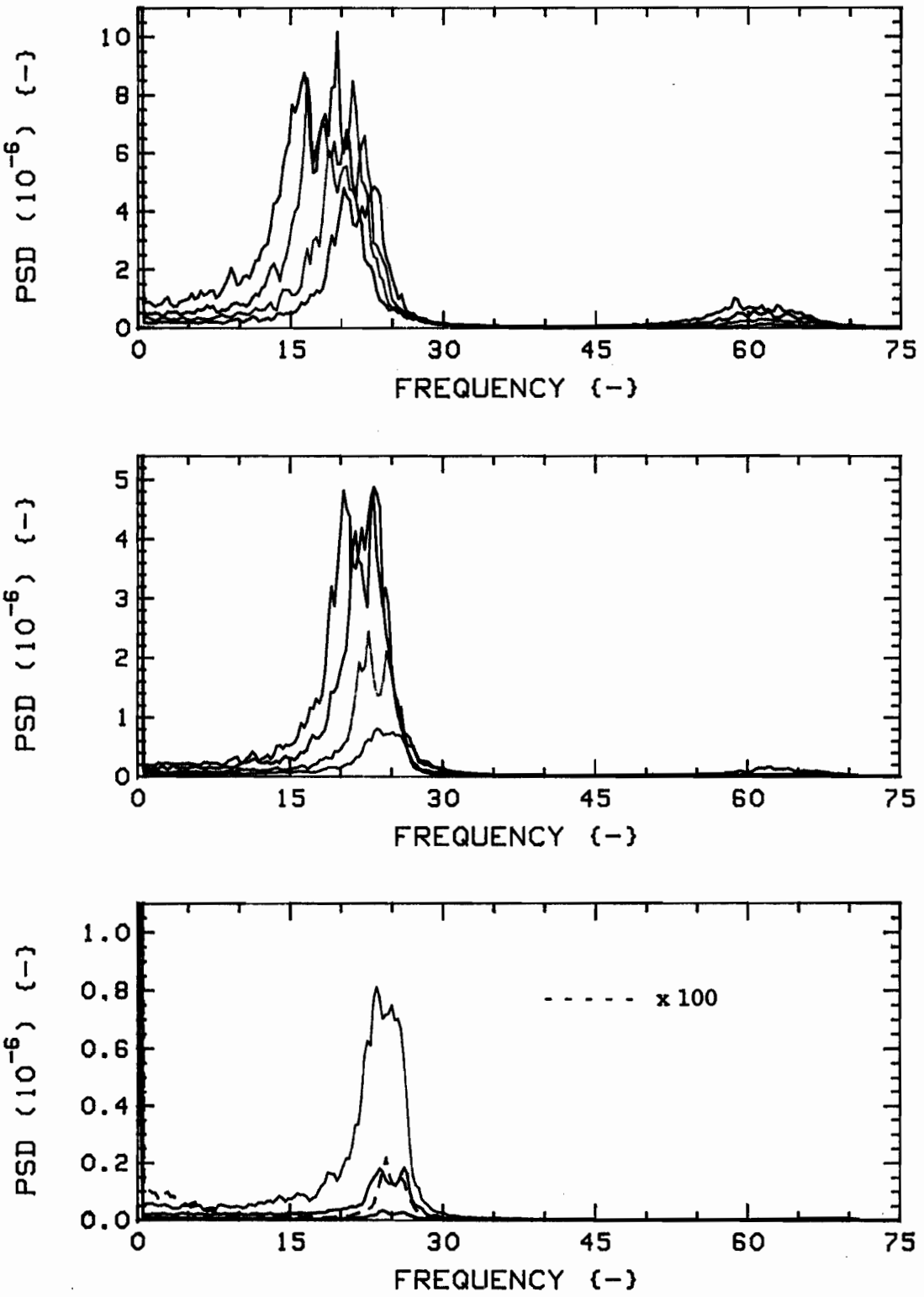

Fig.64b: Measured vibration PSD's for K = 2, G_c = 1.89, 2F, Tangential direction, versus flow velocity. In descending order, u = 5.0 to 0.5, in steps of 0.5. Colour sequence: RED, GREEN, BLUE, BLACK (lowest trace of each plot is highest of the next one).

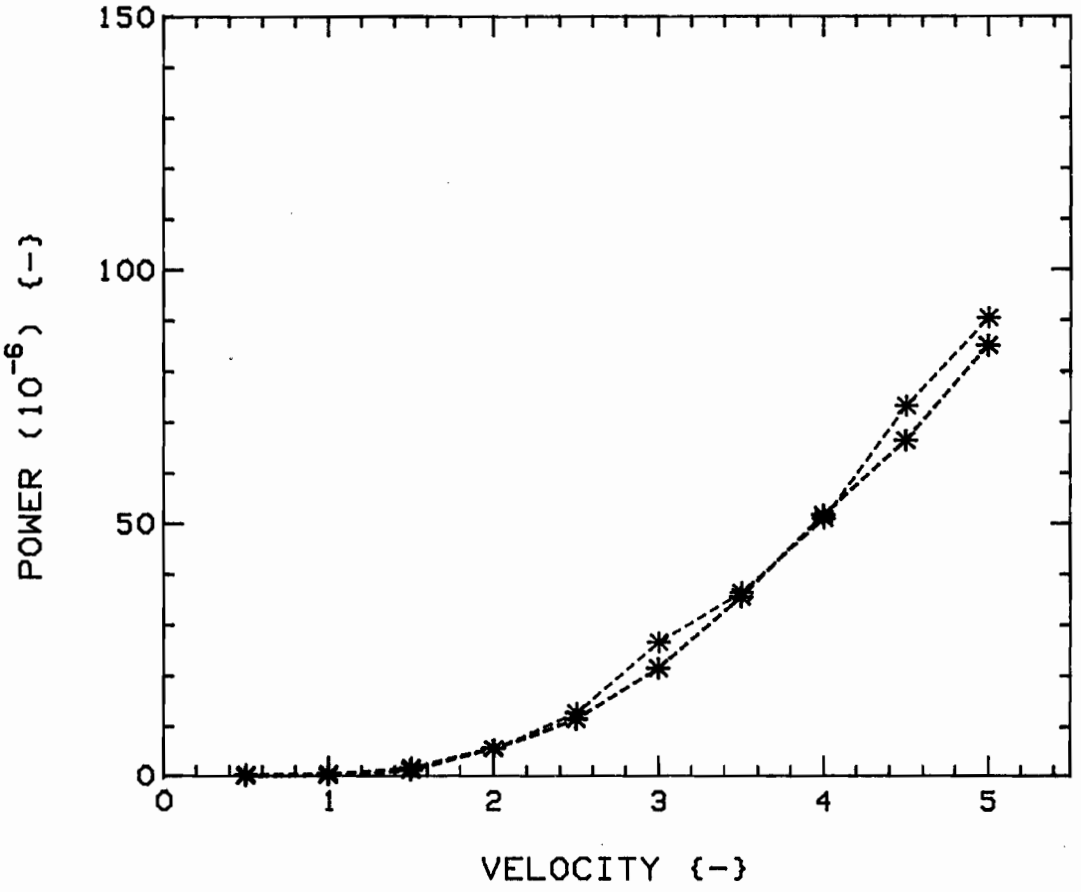

Fig.65: Powers versus flow velocity, for K = 2, G_c = 1.89, 2F, from (integrated) PSD's of Figs. 64a and 64b. Radial (RED) and Tangential (BLUE) directions.

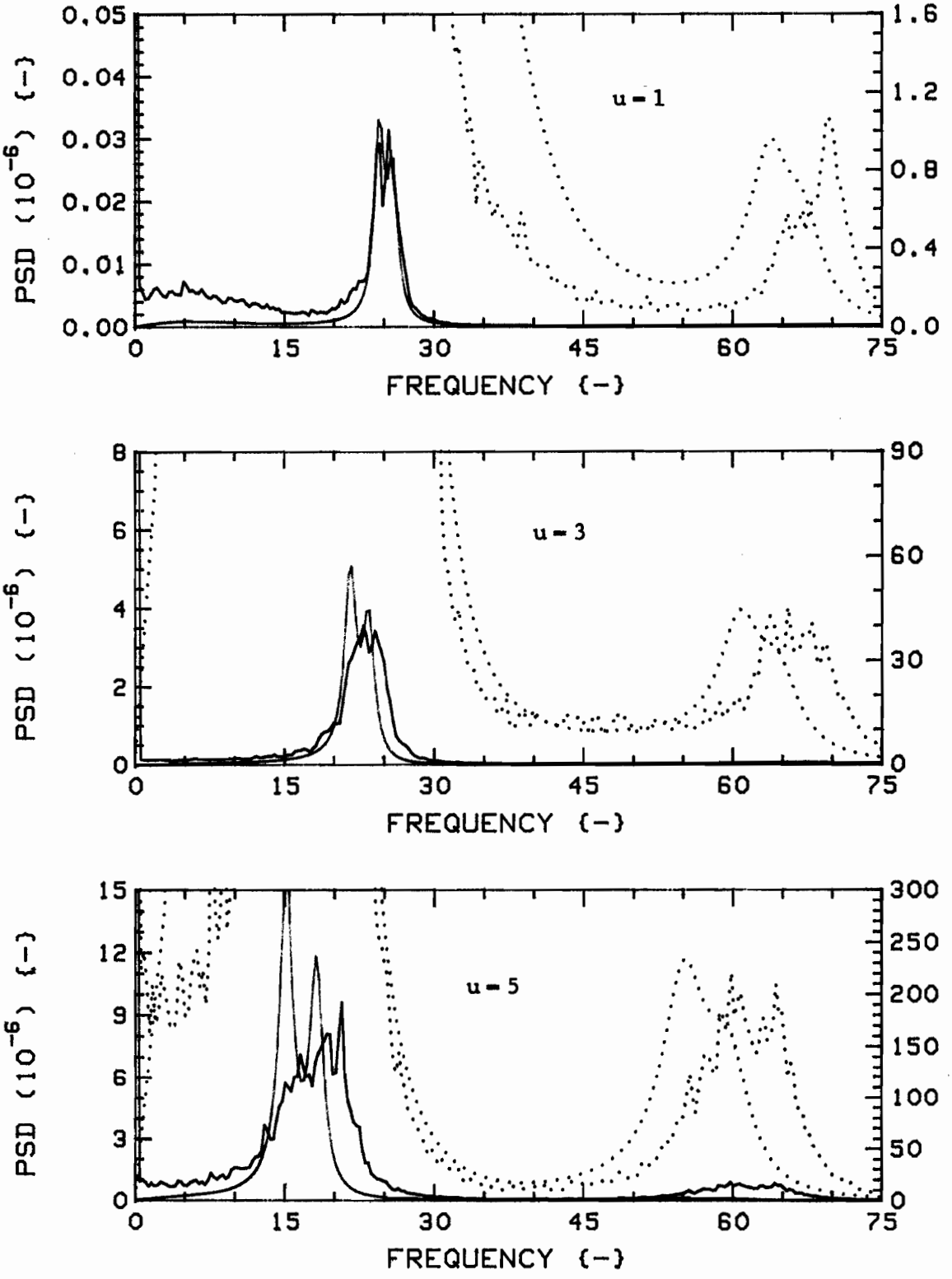

Fig.66a: Measured (RED) and theoretical (GREEN) vibration PSD's for K = 2, G_c = 1.89, 2F, Radial direction.

The dotted traces are expansions of the solid ones; scales are, from top, (RED): 3.0×10^{-10}, 8.0×10^{-8}, 1.2×10^{-6}, (GREEN): 1.5×10^{-9}, 2.0×10^{-7}, 3.0×10^{-6}.

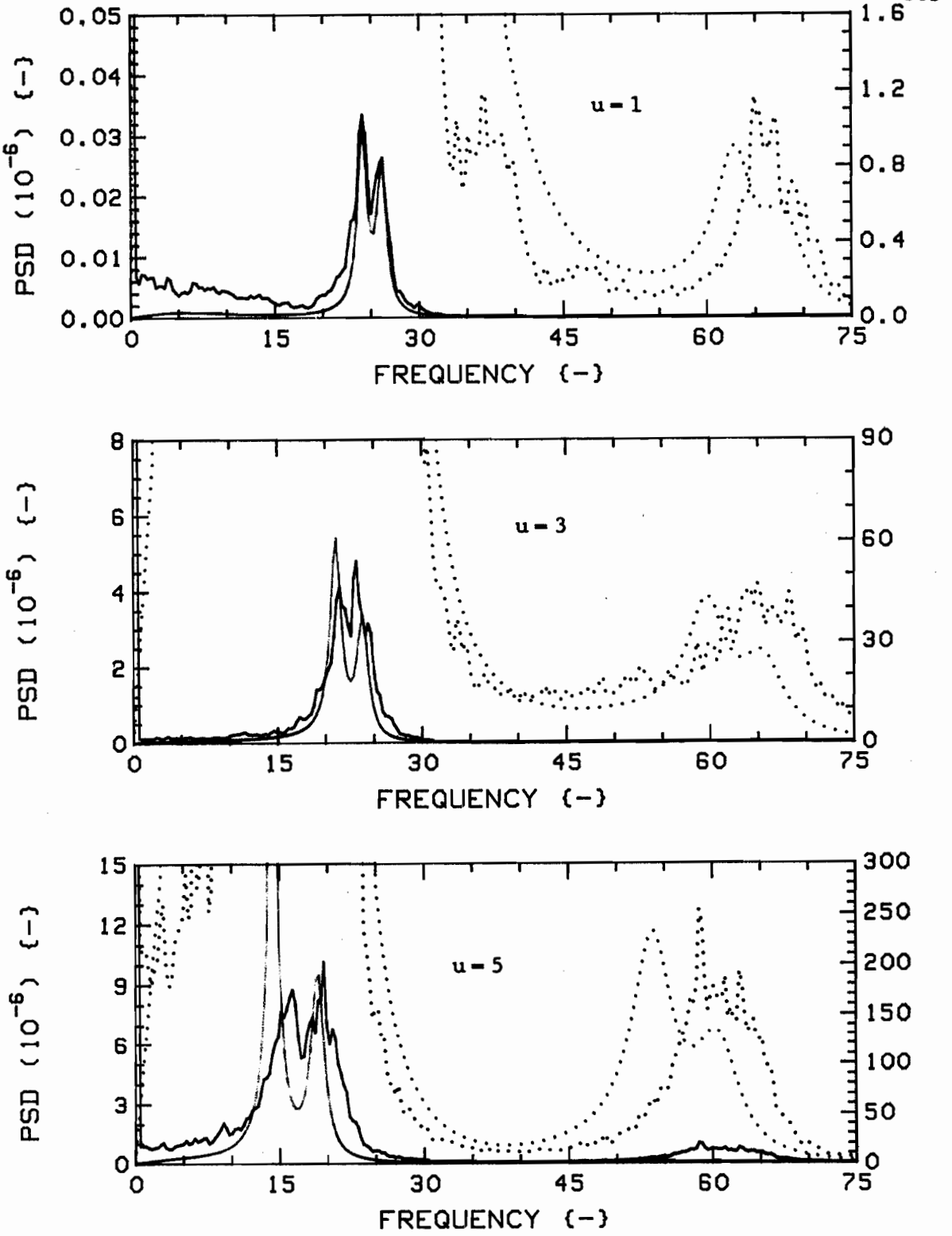

Fig.66b: Measured (RED) and theoretical (GREEN) vibration PSD's for K = 2, G_c = 1.89, 2F, Tangential direction.

The dotted traces are expansions of the solid ones; scales are, from top, (RED): 3.0×10^{-10}, 8.0×10^{-8}, 1.2×10^{-6}, (GREEN): 1.5×10^{-9}, 2.0×10^{-7}, 3.0×10^{-8}.

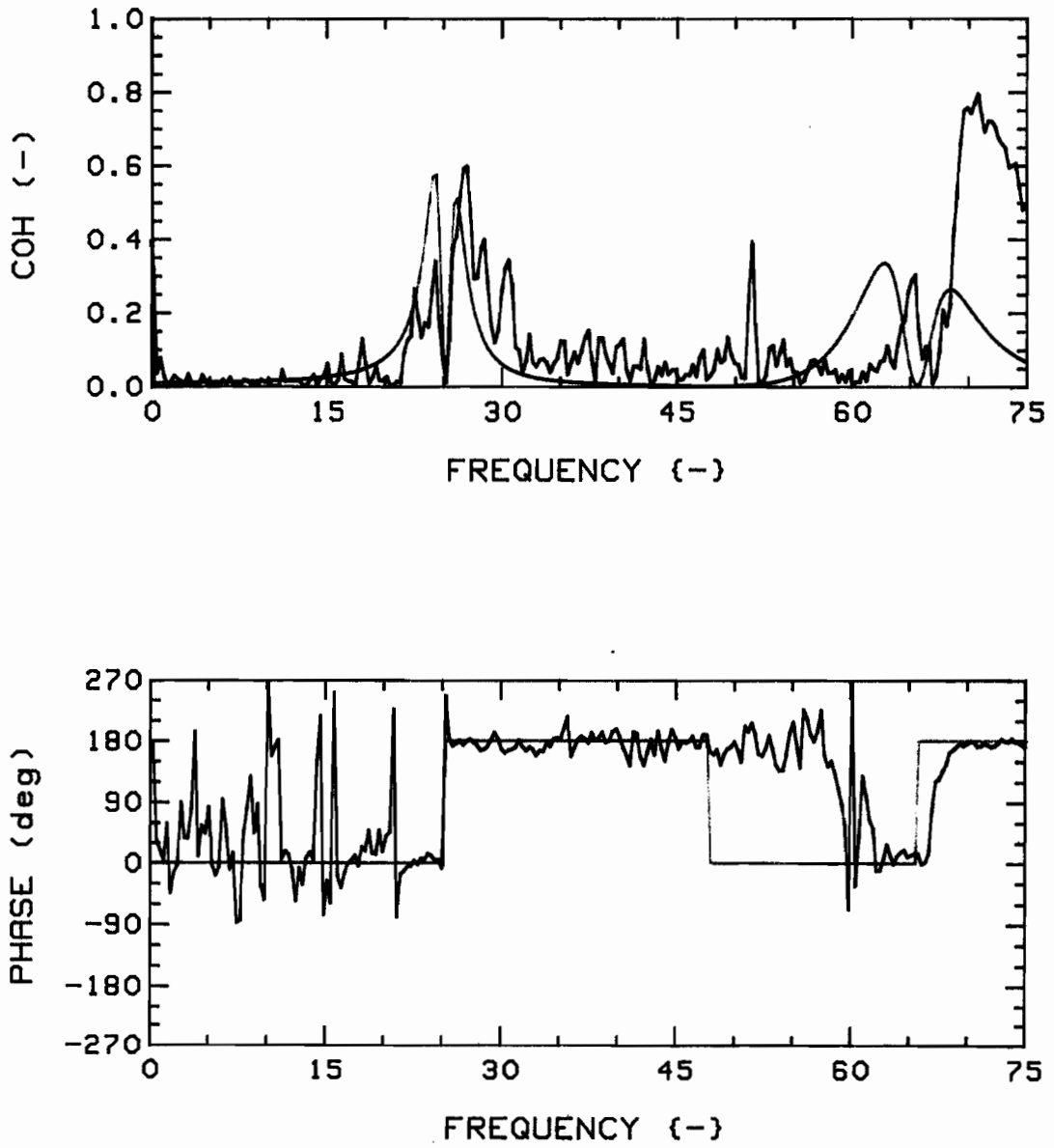

Fig.67a: Measured (RED) and theoretical (GREEN) coherence functions and phases, for K = 2, G_c = 1.89, 2F, R-R (1,3), at u = 1.

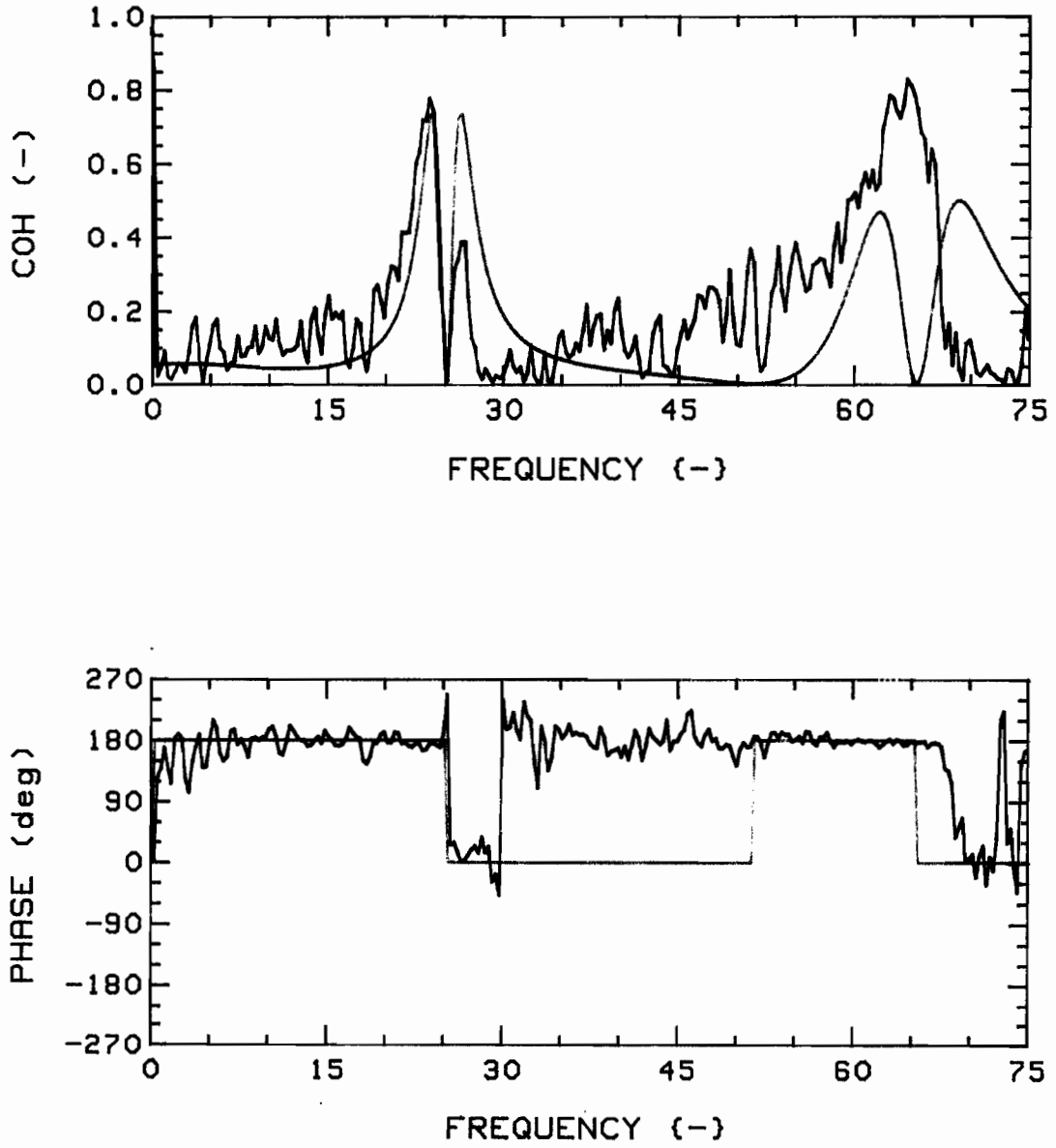

Fig.67b: Measured (RED) and theoretical (GREEN) coherence functions and phases, for K = 2, G_c = 1.89, 2F, T-T (1,3), at u = 1.

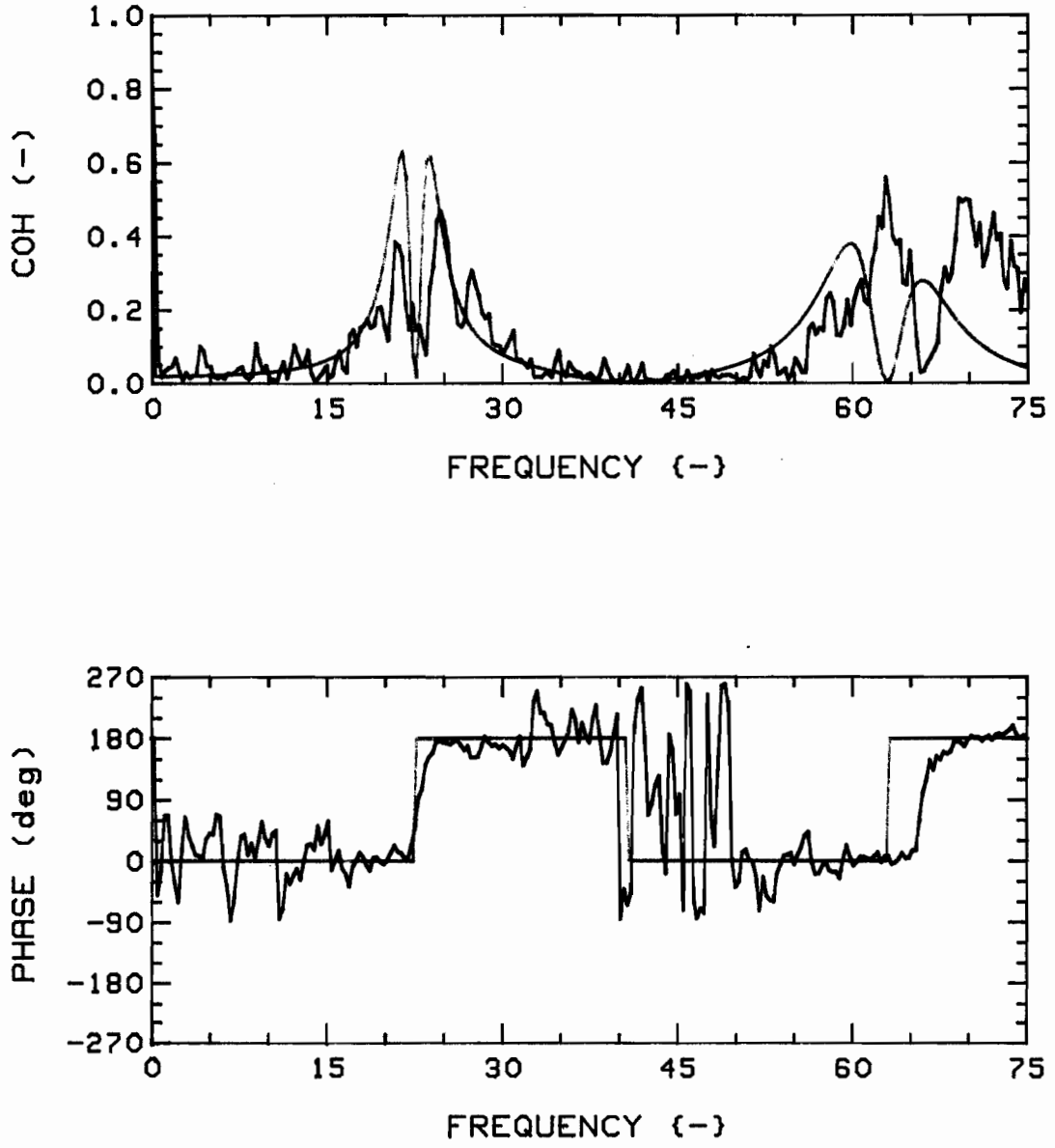

Fig.67c: Measured (RED) and theoretical (GREEN) coherence functions and phases, for K = 2, G_c = 1.89, 2F, R-R (1,3), at u = 3.

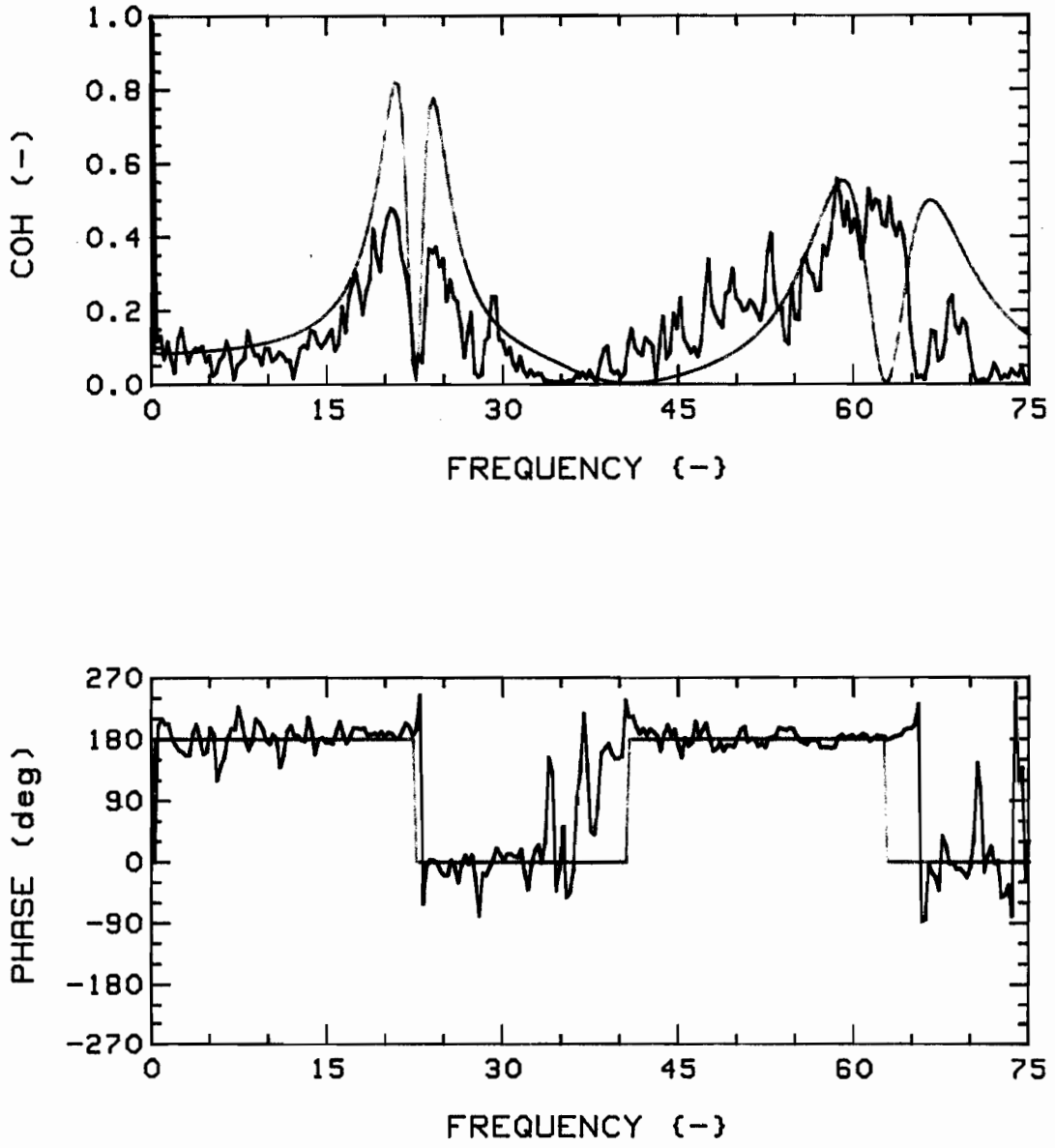

Fig.67d: Measured (RED) and theoretical (GREEN) coherence functions and phases, for K = 2, G_c = 1.89, 2F, T-T (1,3), at u = 3.

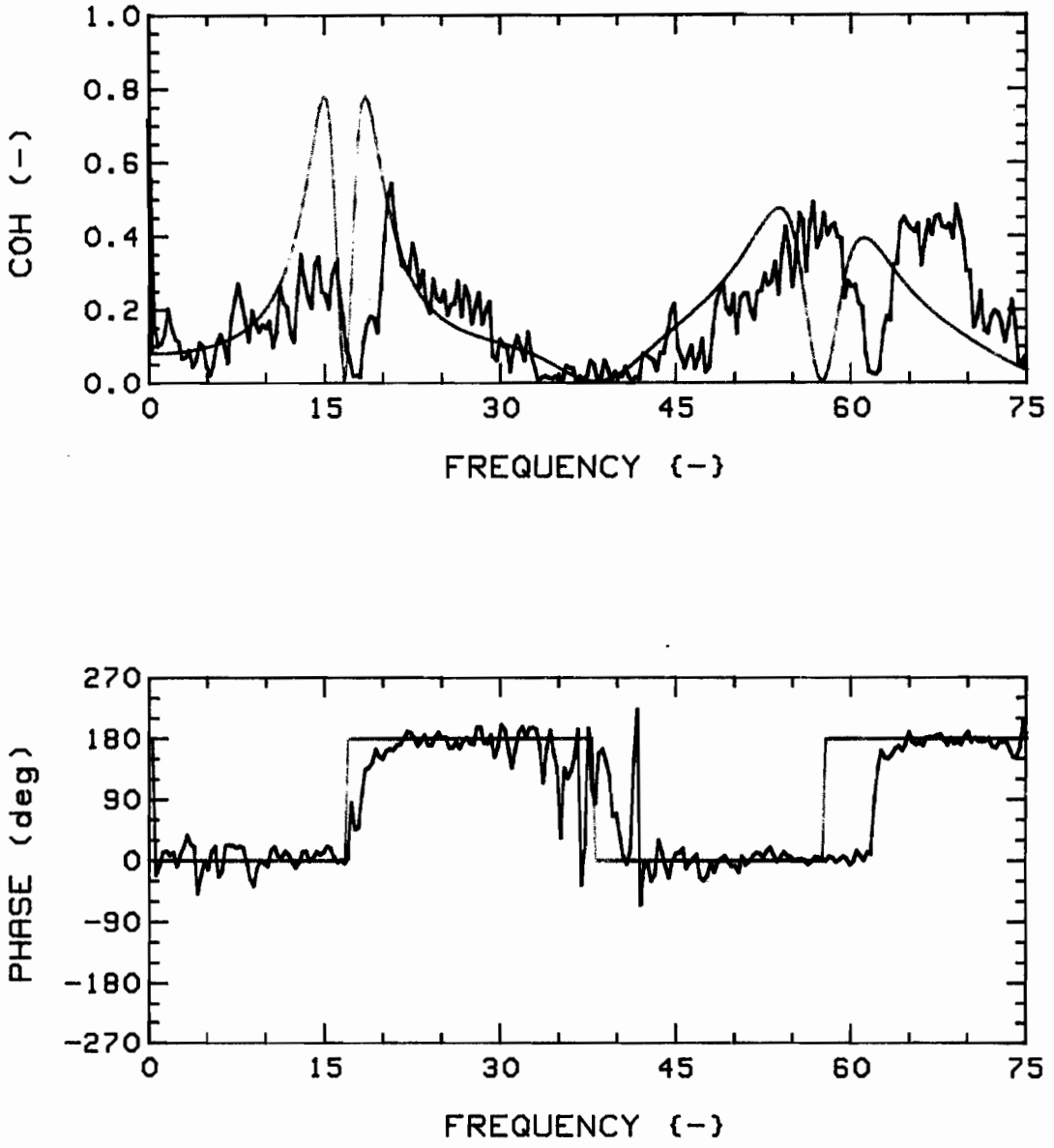

Fig.67e: Measured (RED) and theoretical (GREEN) coherence functions and phases, for K = 2, G_c = 1.89, 2F, R-R (1,3), at u = 5.

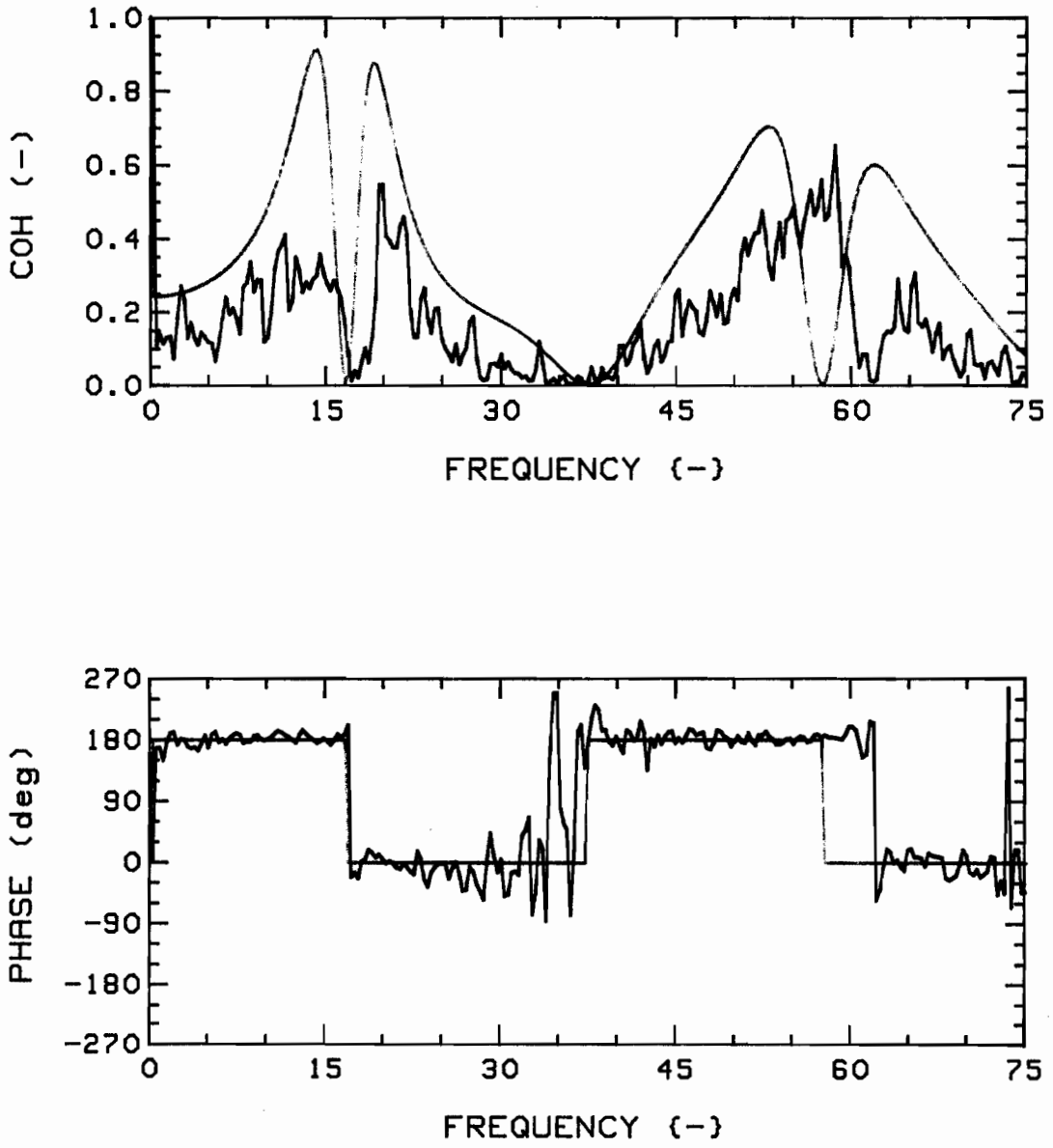

Fig.67f: Measured (RED) and theoretical (GREEN) coherence functions and phases, for K = 2, G_c = 1.89, 2F, T-T (1,3), at u = 5.

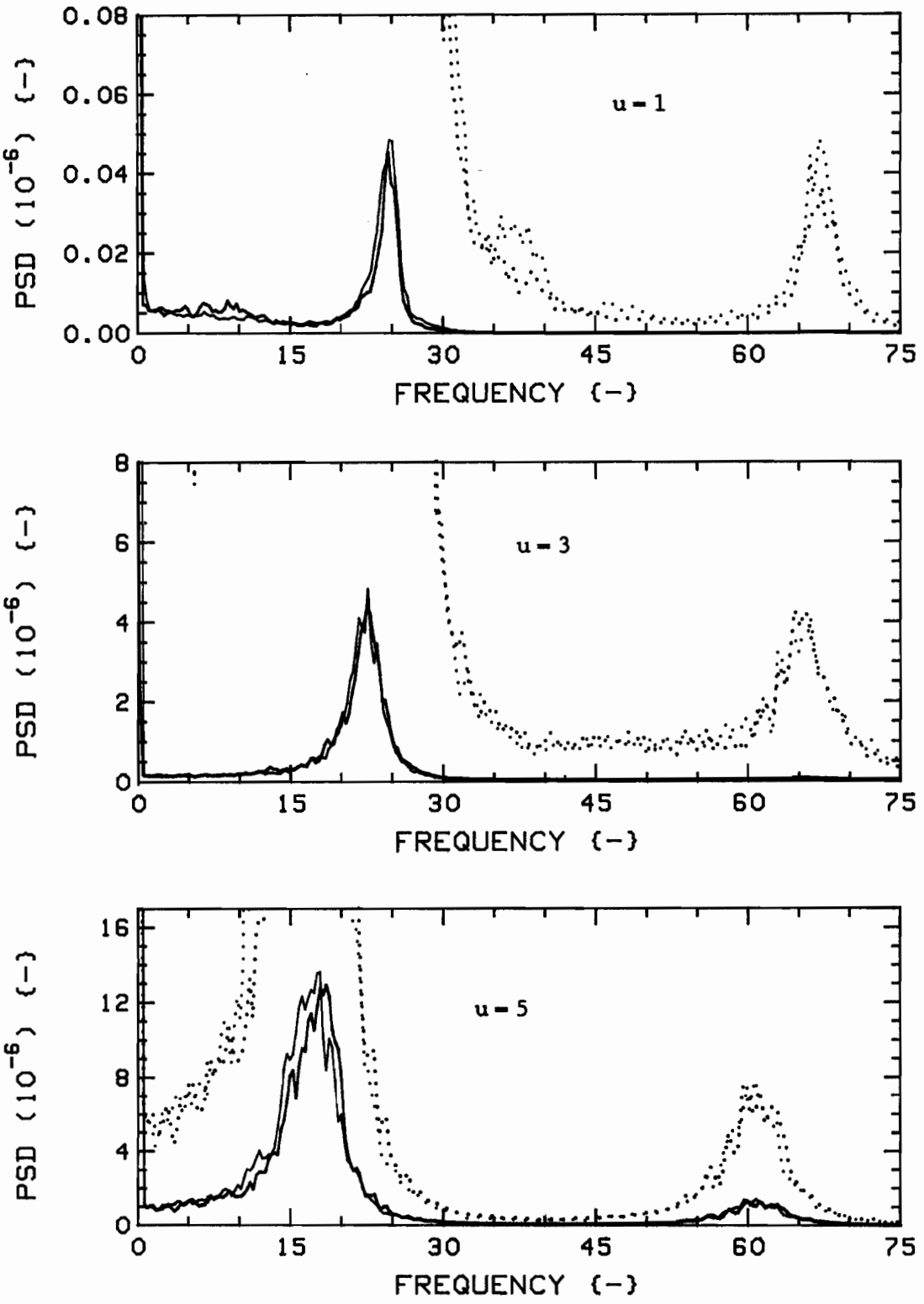

Fig.68: Measured vibration PSD's for K = 1, 1F,
"Radial" (RED) and "Tangential" (BLUE) directions.
The dotted traces are expansions of the solid ones;
scales are, from top: 6.0×10^{-10}, 1.0×10^{-7}, 3.0×10^{-6}.

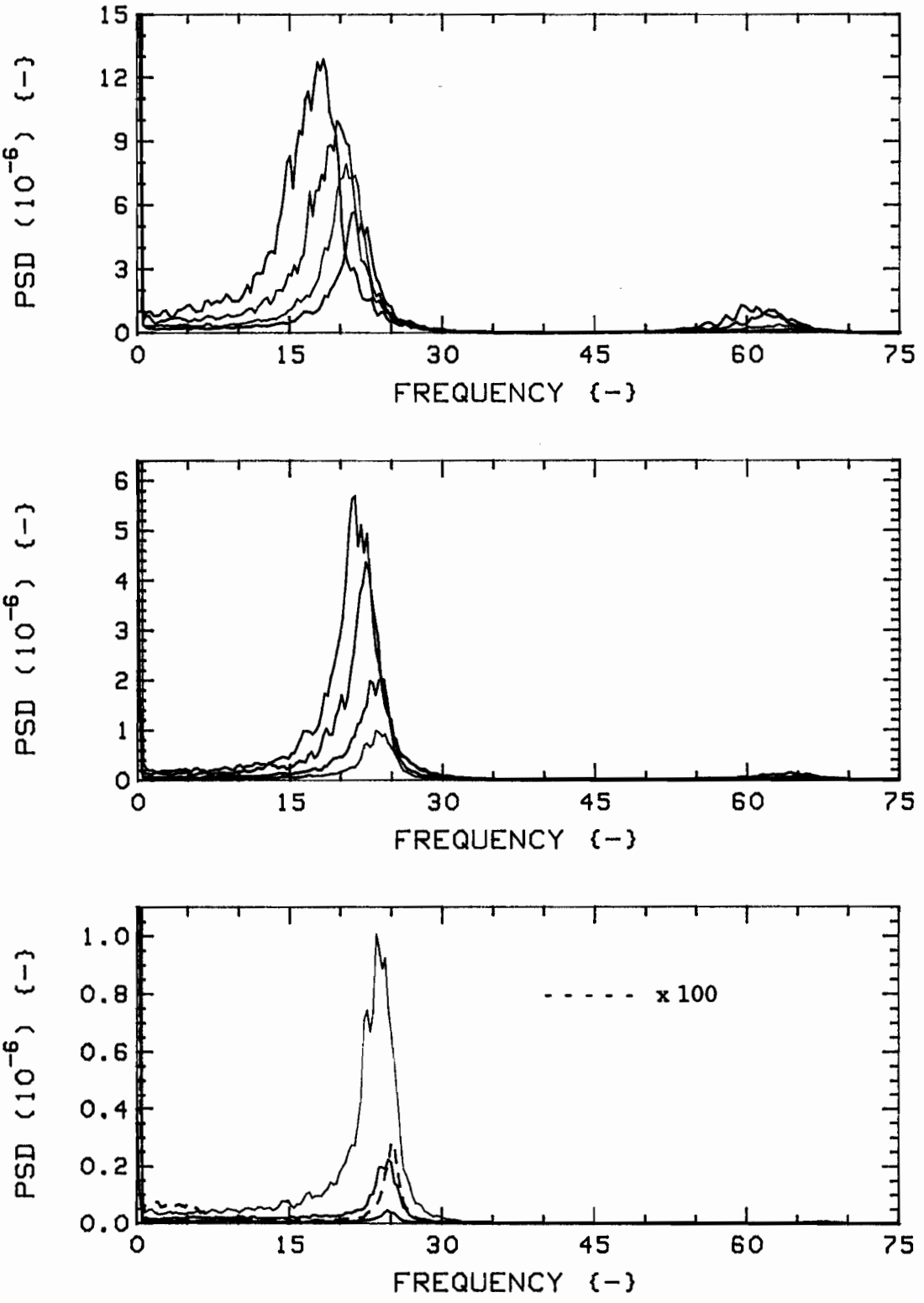

Fig.69a: Measured vibration PSD's for K = 1, 1F, "Radial" direction, versus flow velocity. In descending order, u = 5.0 to 0.5, in steps of 0.5. Colour sequence: RED, GREEN, BLUE, BLACK (lowest trace of each plot is highest of the next one).

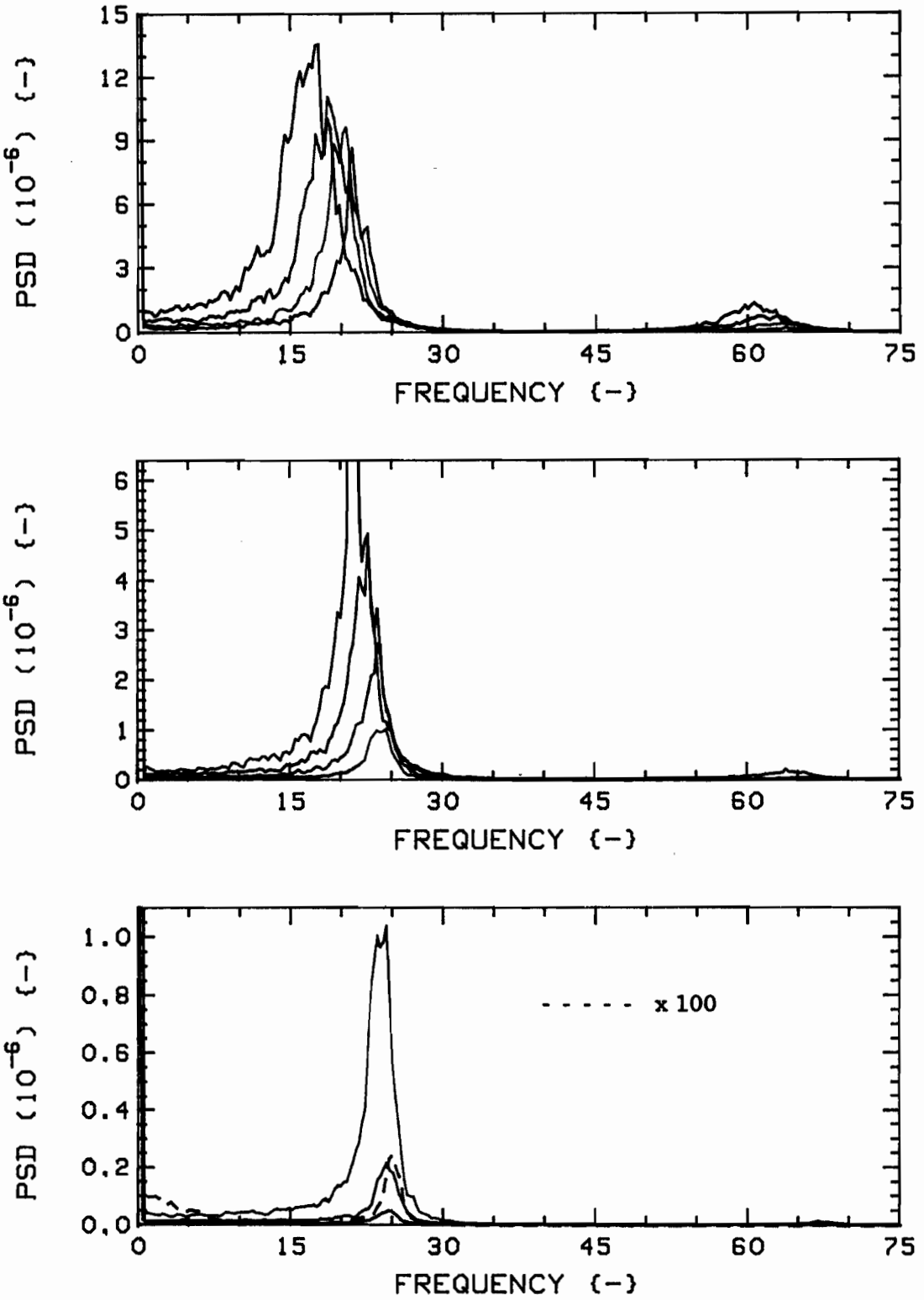

Fig.69b: Measured vibration PSD's for K = 1, 1F, "Tangential" direction, versus flow velocity. In descending order, u = 5.0 to 0.5, in steps of 0.5. Colour sequence: RED, GREEN, BLUE, BLACK (lowest trace of each plot is highest of the next one).

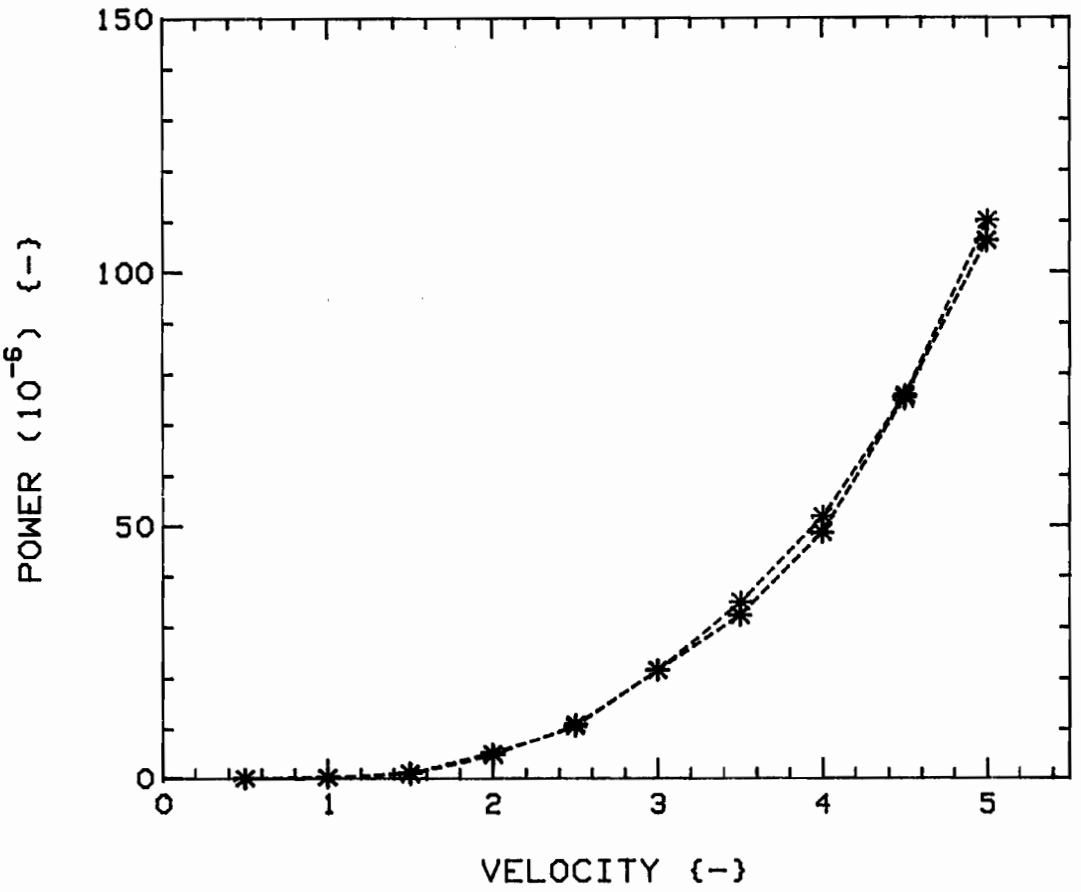

Fig.70: Powers versus flow velocity, for K = 1, 1F,
from (integrated) PSD's of Figs. 69a and 69b.
"Radial" (RED) and "Tangential" (BLUE) directions.

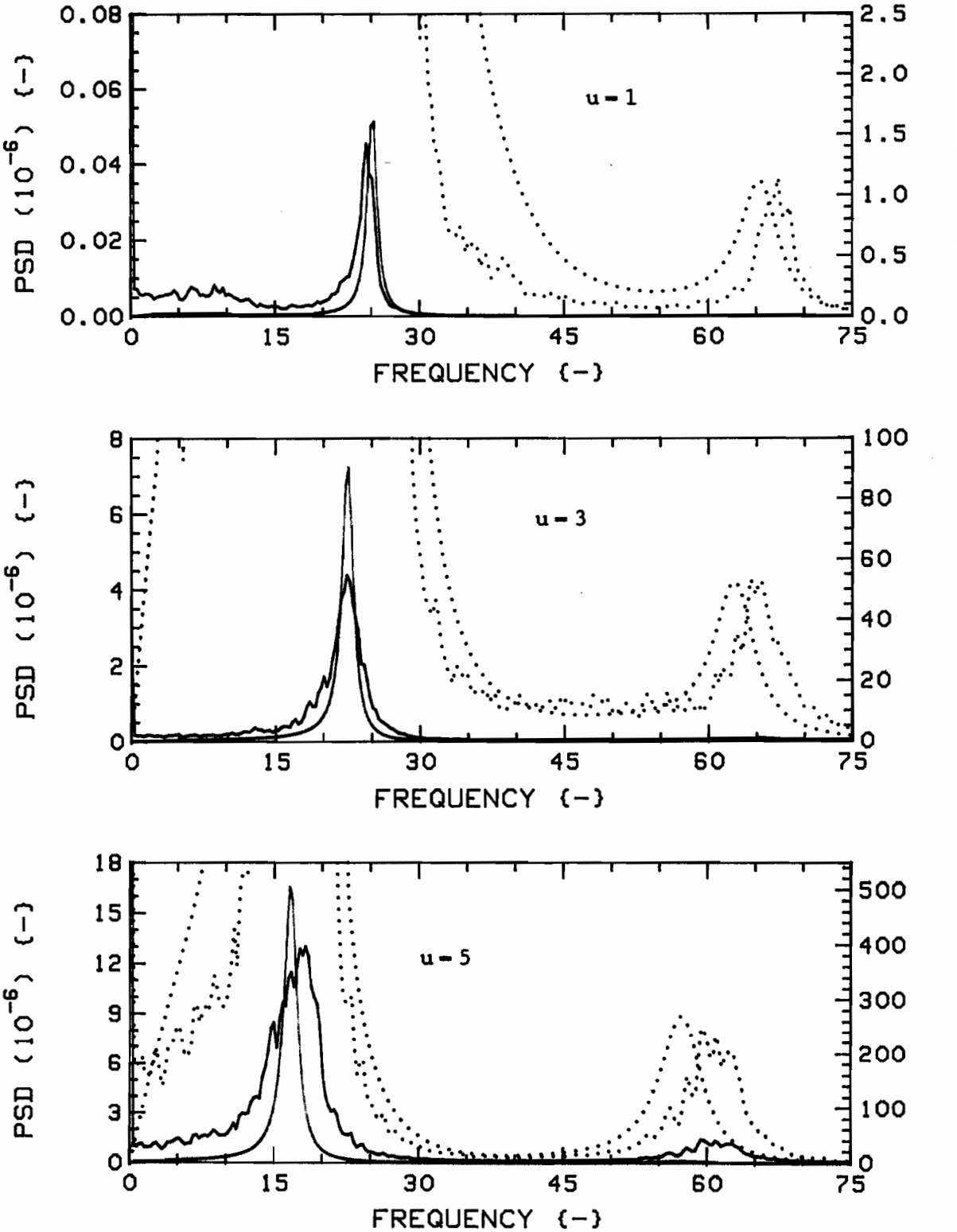

Fig.71a: Measured (RED) and theoretical (GREEN) vibration PSD's for K = 1, 1F, "Radial" direction.

The dotted traces are expansions of the solid ones; scales are, from top, (RED): 6.0×10^{-10}, 1.0×10^{-7}, 3.0×10^{-6},

(GREEN): 2.5×10^{-9}, 2.4×10^{-7}, 6.5×10^{-6}.

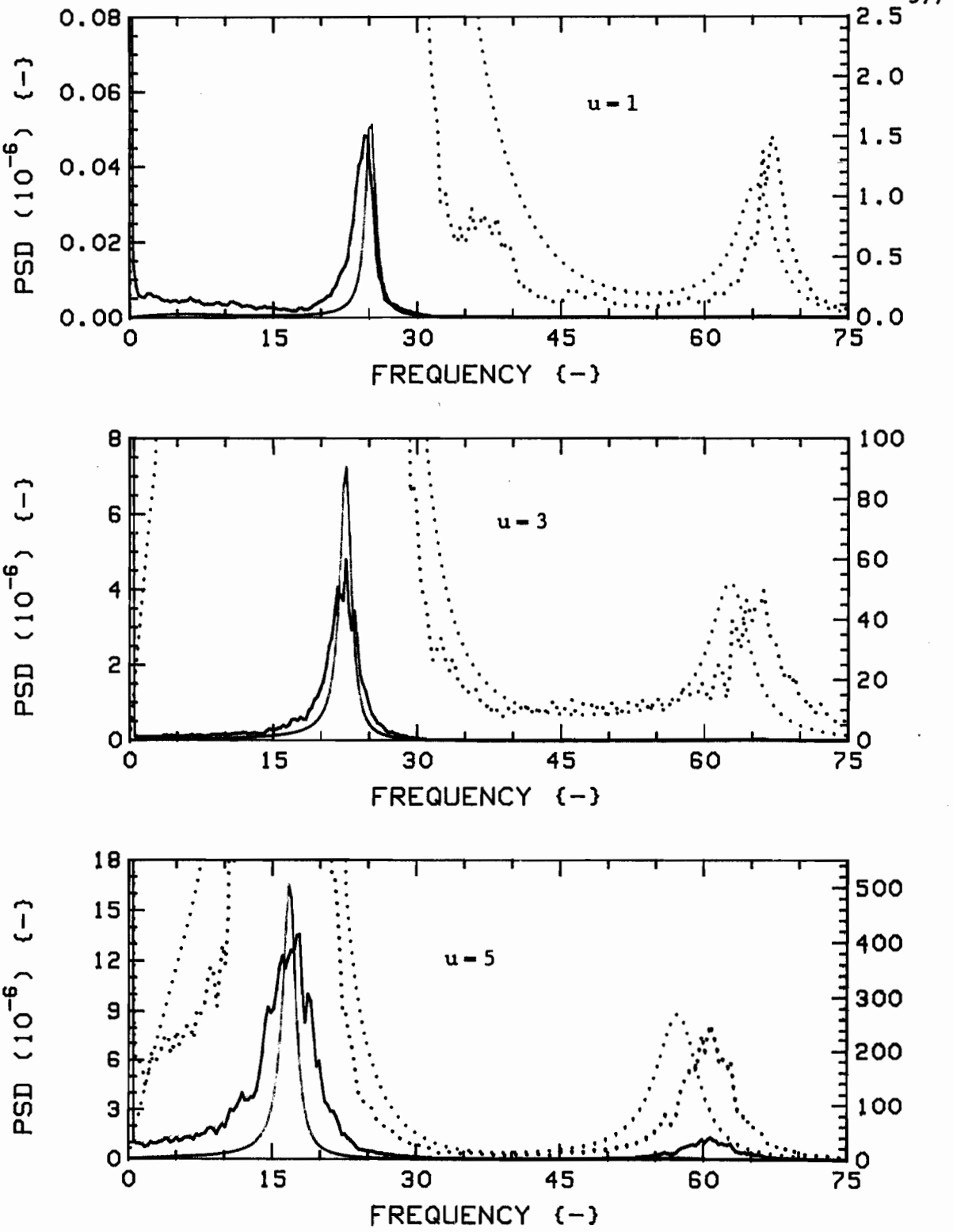

Fig.71b: Measured (RED) and theoretical (GREEN) vibration PSD's for K = 1, 1F, "Tangential" direction.

The dotted traces are expansions of the solid ones; scales are, from top, (RED): 6.0×10^{-10}, 1.0×10^{-7}, 3.0×10^{-6},
(GREEN): 2.5×10^{-9}, 2.4×10^{-7}, 6.5×10^{-6}.

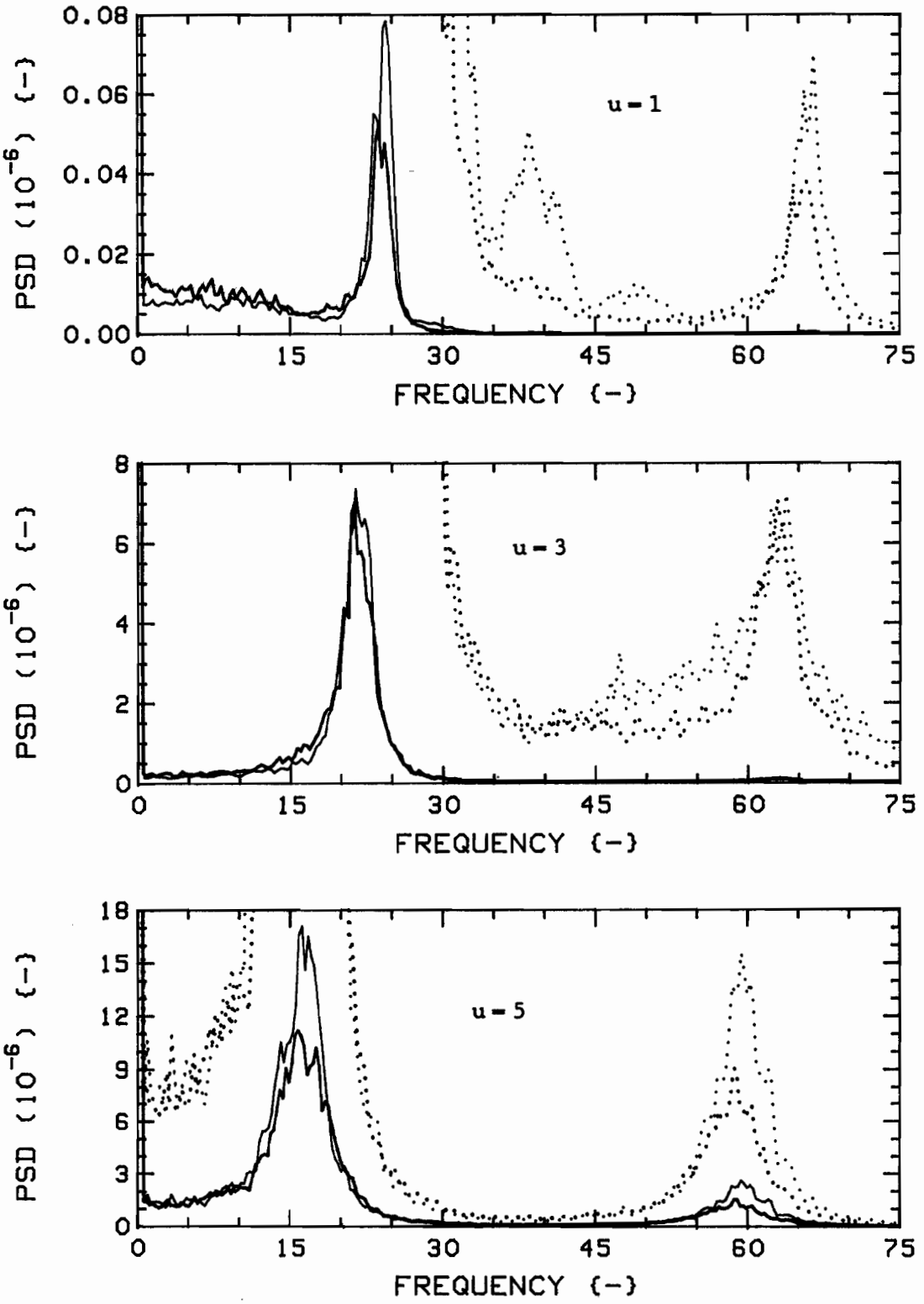

Fig.72: Measured vibration PSD's for K = 4, G_c = 0.75, 1F/3R, Radial (RED) and Tangential (BLUE) directions.

The dotted traces are expansions of the solid ones; scales are, from top: 6.0×10^{-10}, 1.0×10^{-7}, 3.0×10^{-6}.

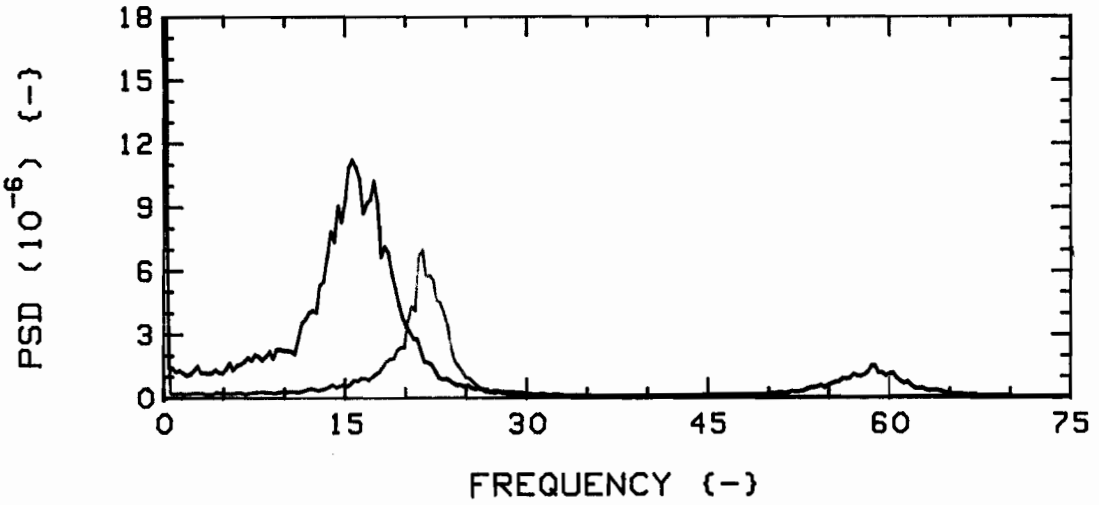

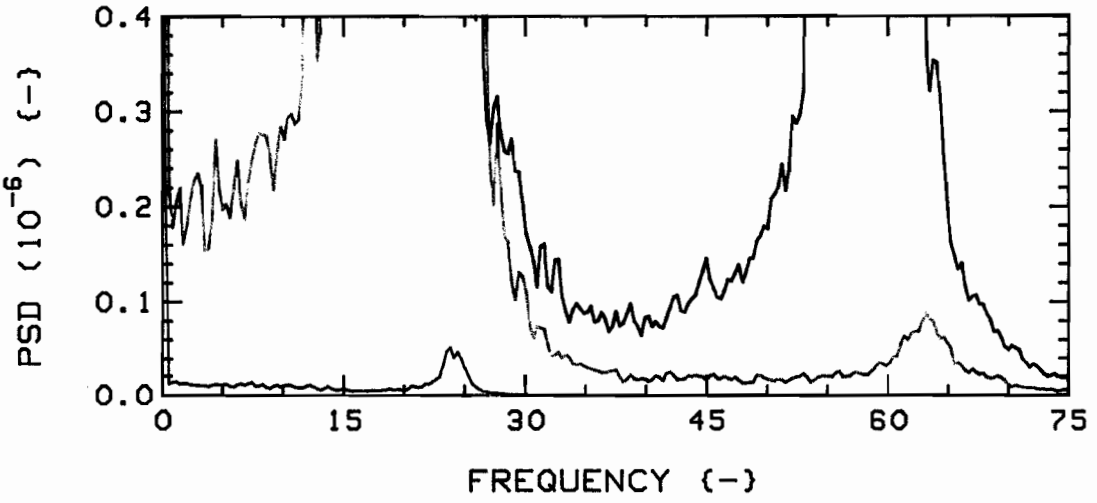

Fig.73a: Measured vibration PSD's for K = 4, G_c = 0.75, 1F/3R, Radial direction, versus flow velocity. In descending order, u = 5.0, 3.0, and 1.0. Colour sequence: RED, GREEN, BLUE.

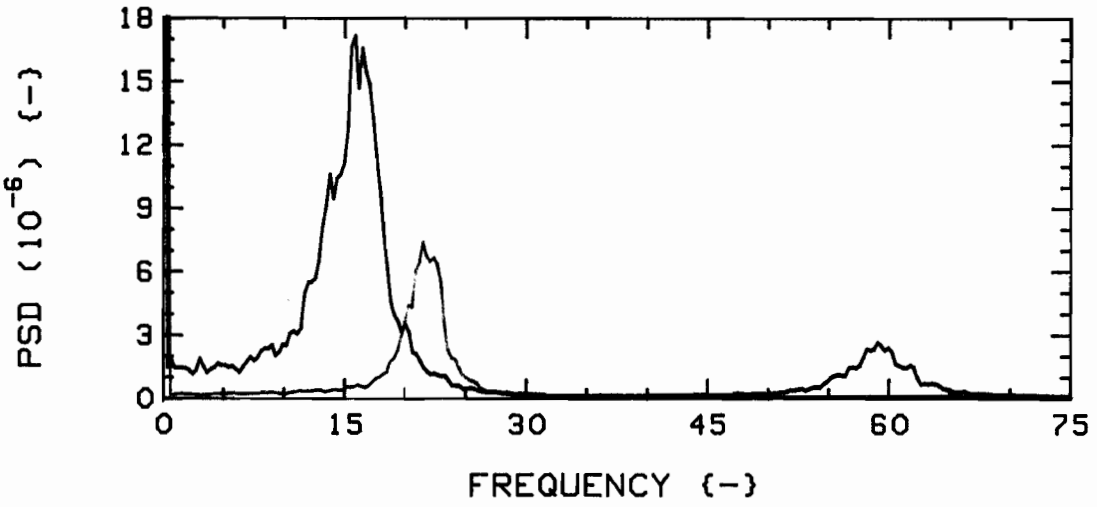

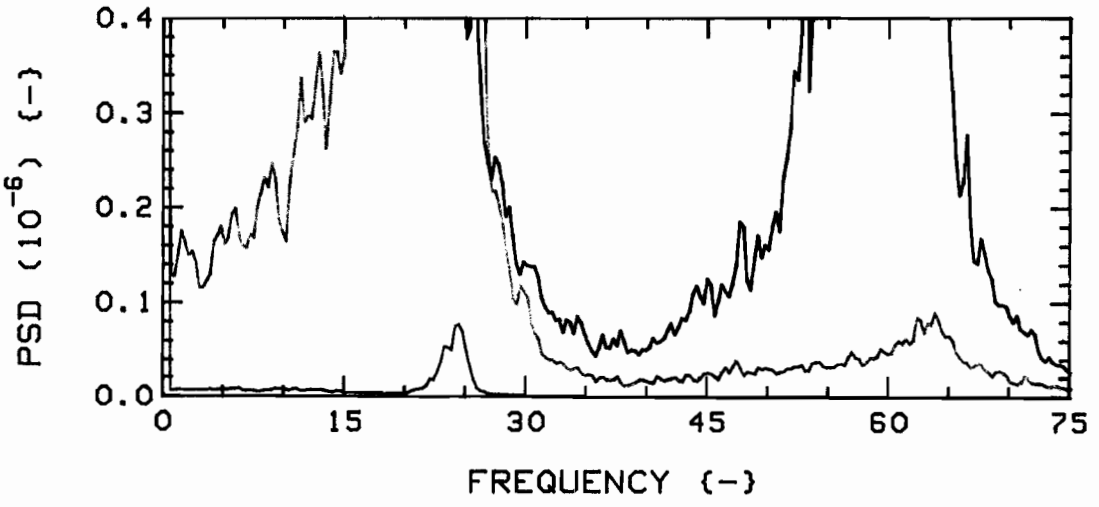

Fig.73b: Measured vibration PSD's for K = 4, G_c = 0.75, 1F/3R, Tangential direction, versus flow velocity. In descending order, u = 5.0, 3.0, and 1.0. Colour sequence: RED, GREEN, BLUE.

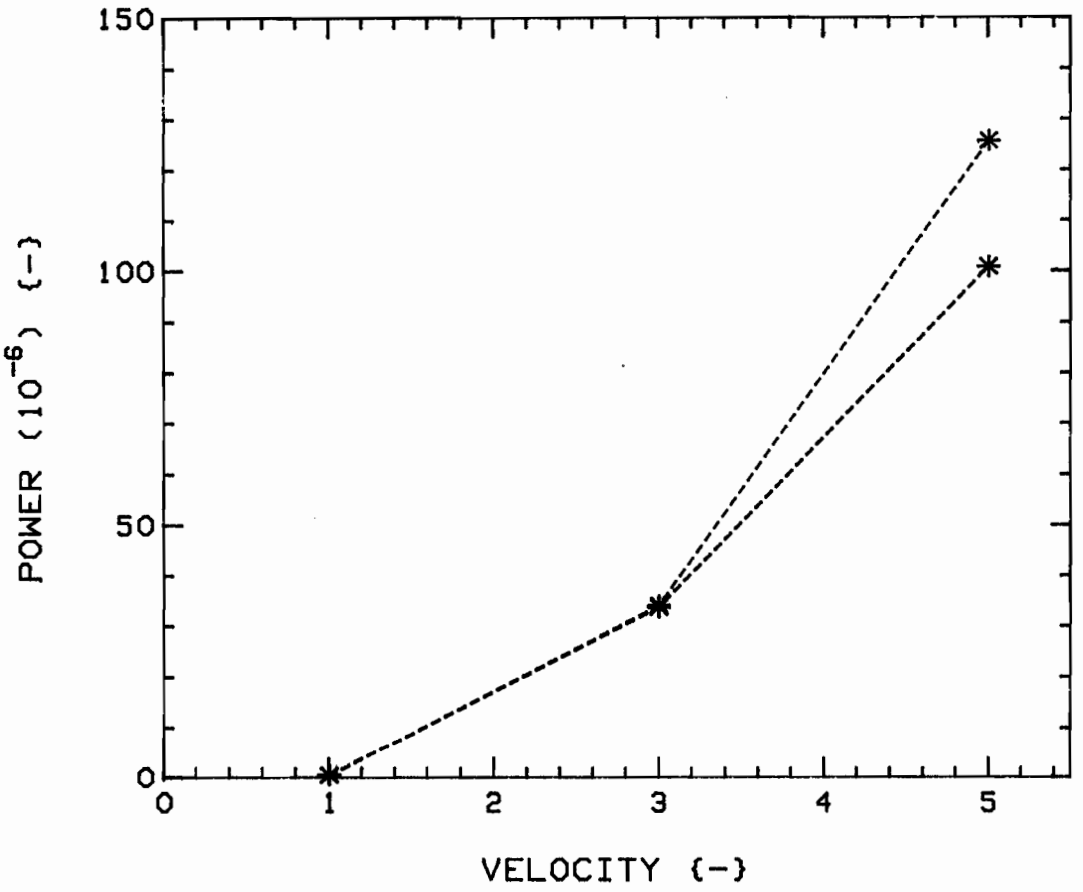

Fig.74: Powers versus flow velocity, for K = 4, G_c = 0.75, 1F/3R, from (integrated) PSD's of Figs. 73a and 73b. Radial (RED) and Tangential (BLUE) directions.

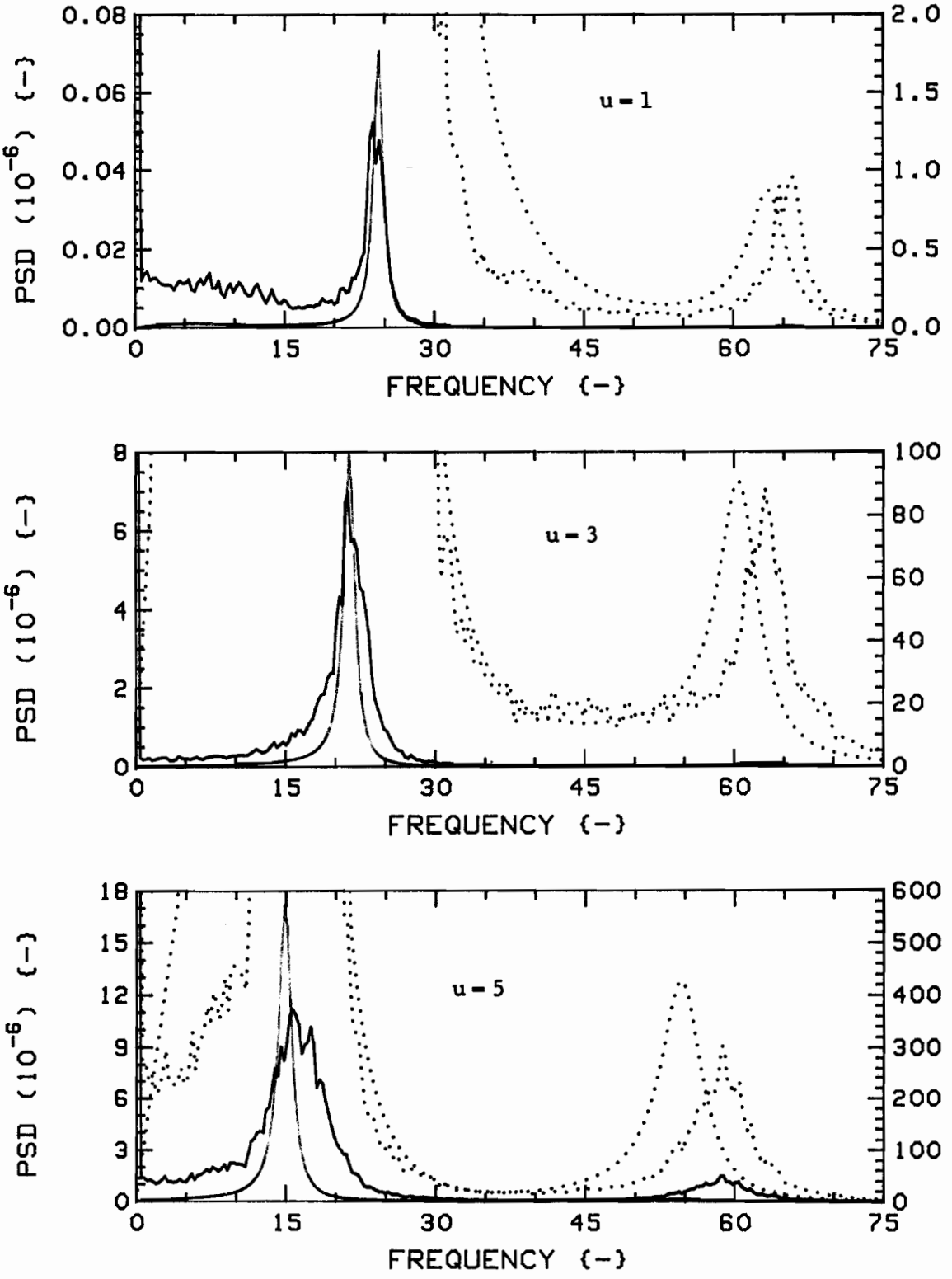

Fig.75a: Measured (RED) and theoretical (GREEN) vibration PSD's for K = 4, G_c = 0.75, 1F/3R, Radial direction.

The dotted traces are expansions of the solid ones; scales are, from top, (RED): 6.0×10^{-10}, 1.0×10^{-7}, 3.0×10^{-6},

(GREEN): 3.0×10^{-9}, 1.6×10^{-7}, 5.0×10^{-6}.

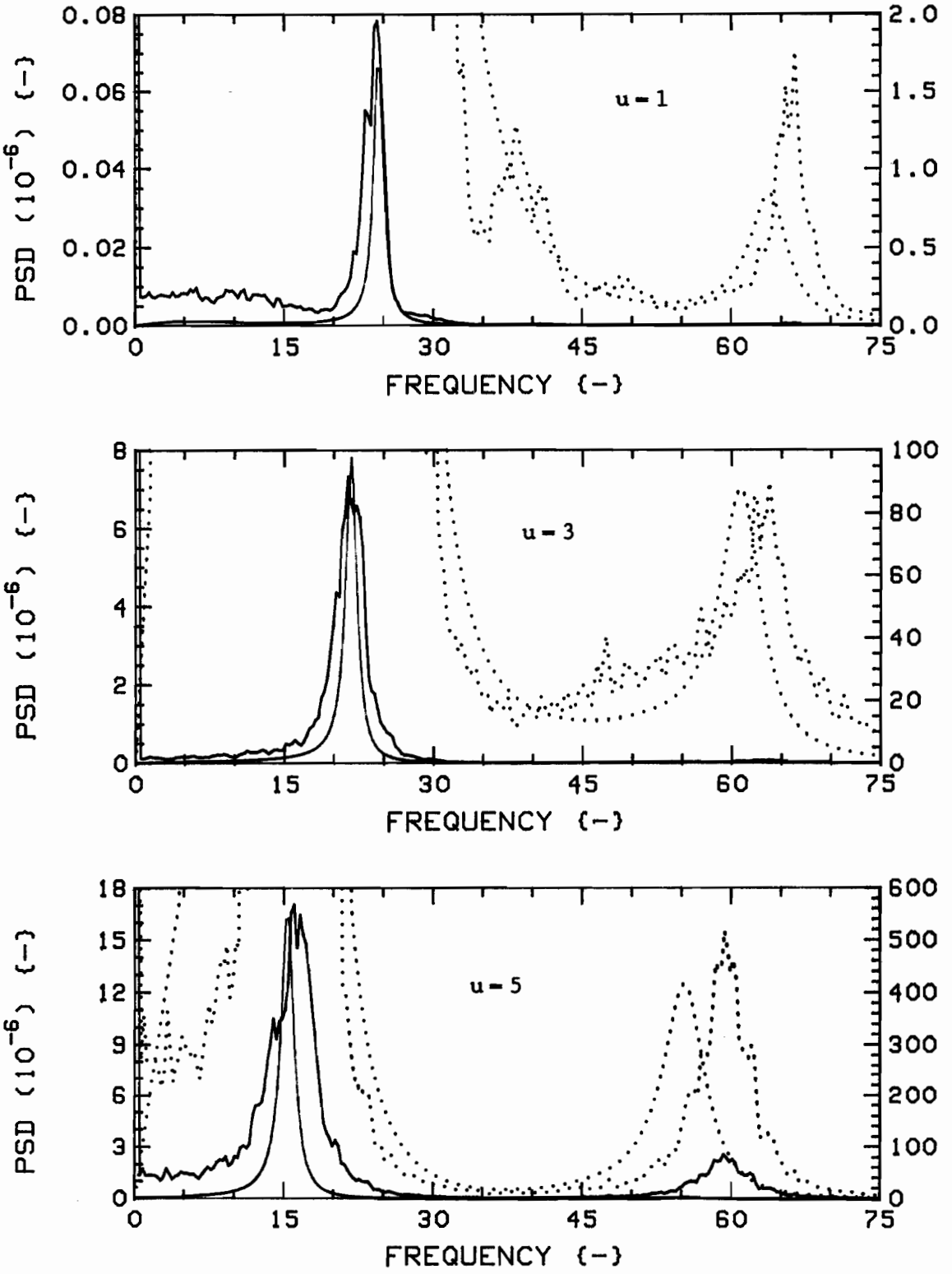

Fig.75b: Measured (RED) and theoretical (GREEN) vibration PSD's for K = 4, $G_c = 0.75$, 1F/3R, Tangential direction.

The dotted traces are expansions of the solid ones; scales are, from top, (RED): 6.0×10^{-10}, 1.0×10^{-7}, 3.0×10^{-6},

(GREEN): 3.0×10^{-9}, 1.6×10^{-7}, 5.0×10^{-6}.

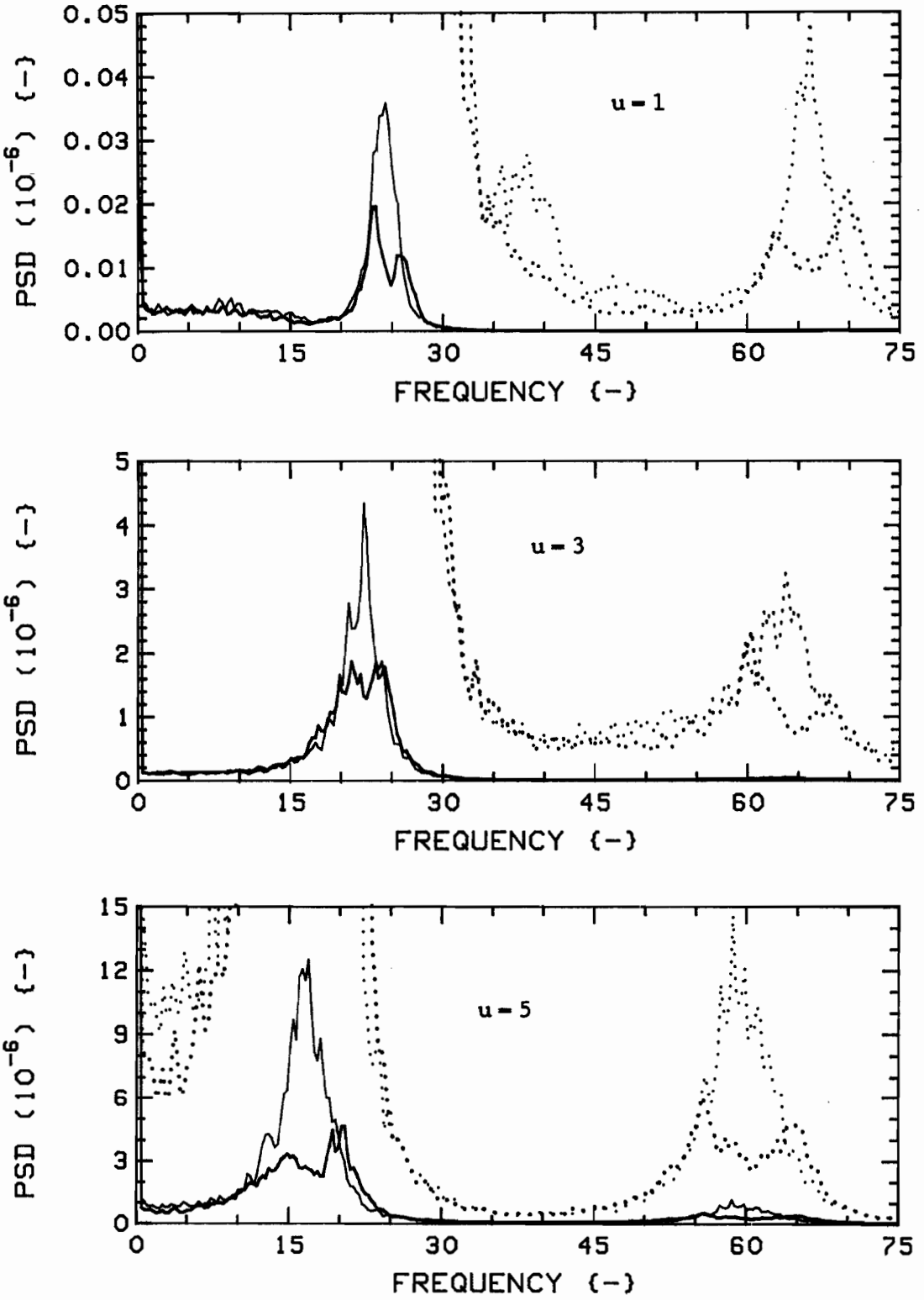

Fig.76: Measured vibration PSD's for K = 4, G_c = 0.75, 2F(1,3)/ 2R(2,4), Radial (RED) and Tangential (BLUE) directions. The dotted traces are expansions of the solid ones; scales are, from top: 3.0×10^{-10}, 8.0×10^{-8}, 1.2×10^{-6}.

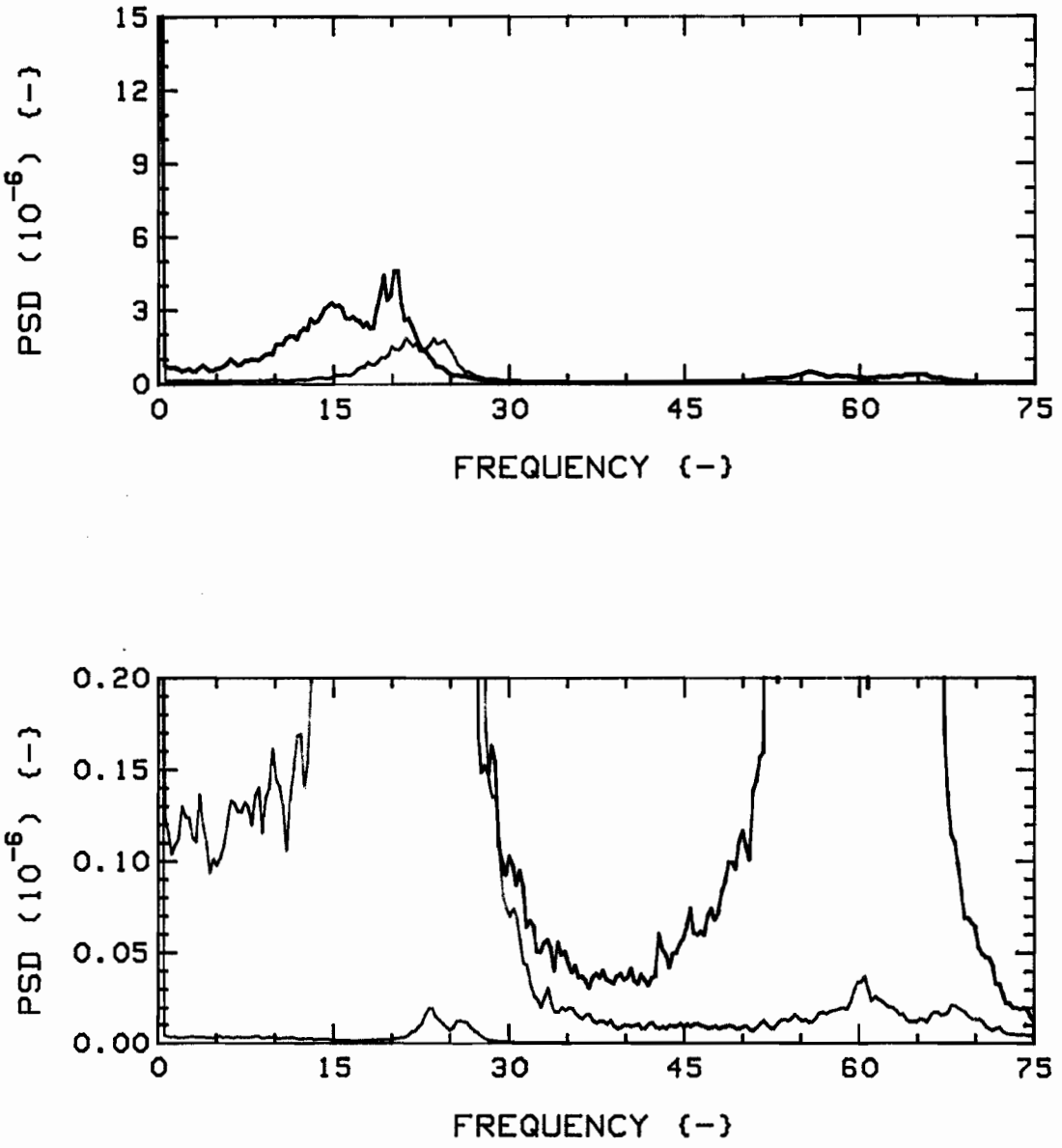

Fig.77a: Measured vibration PSD's for K = 4, G_c = 0.75, 2F(1,3)/2R(2,4), Radial direction, versus flow velocity. In descending order, u = 5.0, 3.0, and 1.0. Colour sequence: RED, GREEN, BLUE.

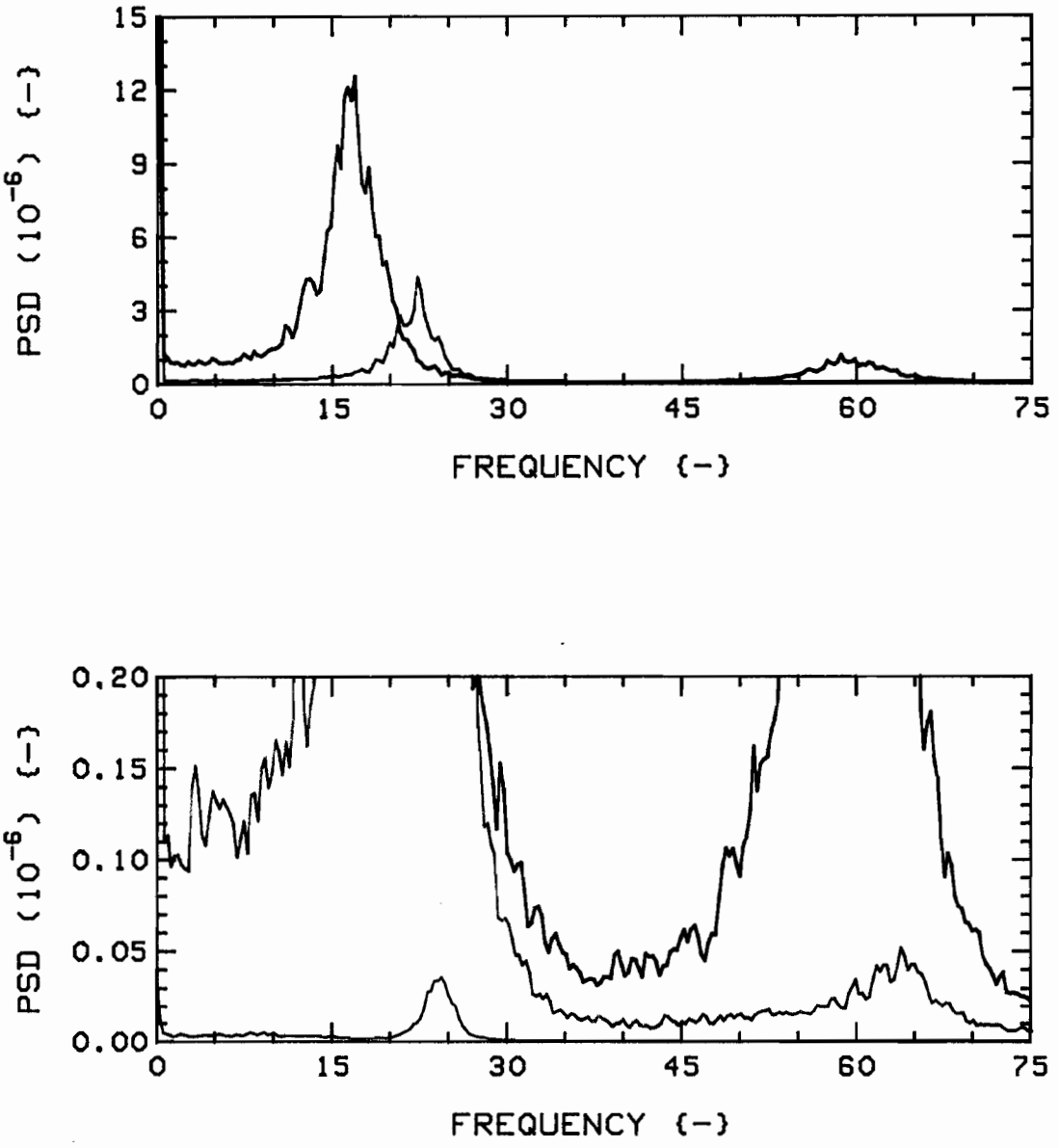

Fig.77b: Measured vibration PSD's for K = 4, G_c = 0.75, 2F(1,3)/2R(2,4), Tangential direction, versus flow velocity. In descending order, u = 5.0, 3.0, and 1.0. Colour sequence: RED, GREEN, BLUE.

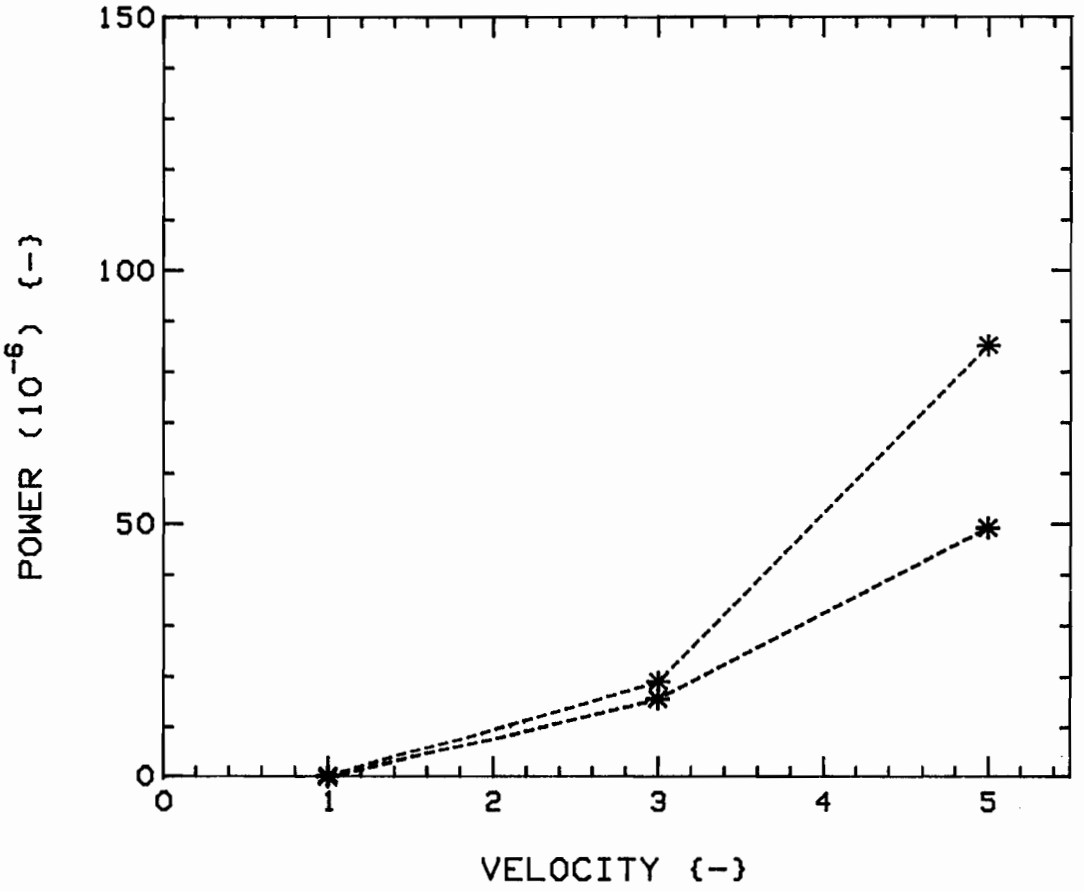

Fig.78: Powers versus flow velocity, for K = 4, G_c = 0.75, 2F(1,3)/2R(2,4), from (integrated) PSD's of Figs. 77a and 77b. Radial (RED) and Tangential (BLUE) directions.

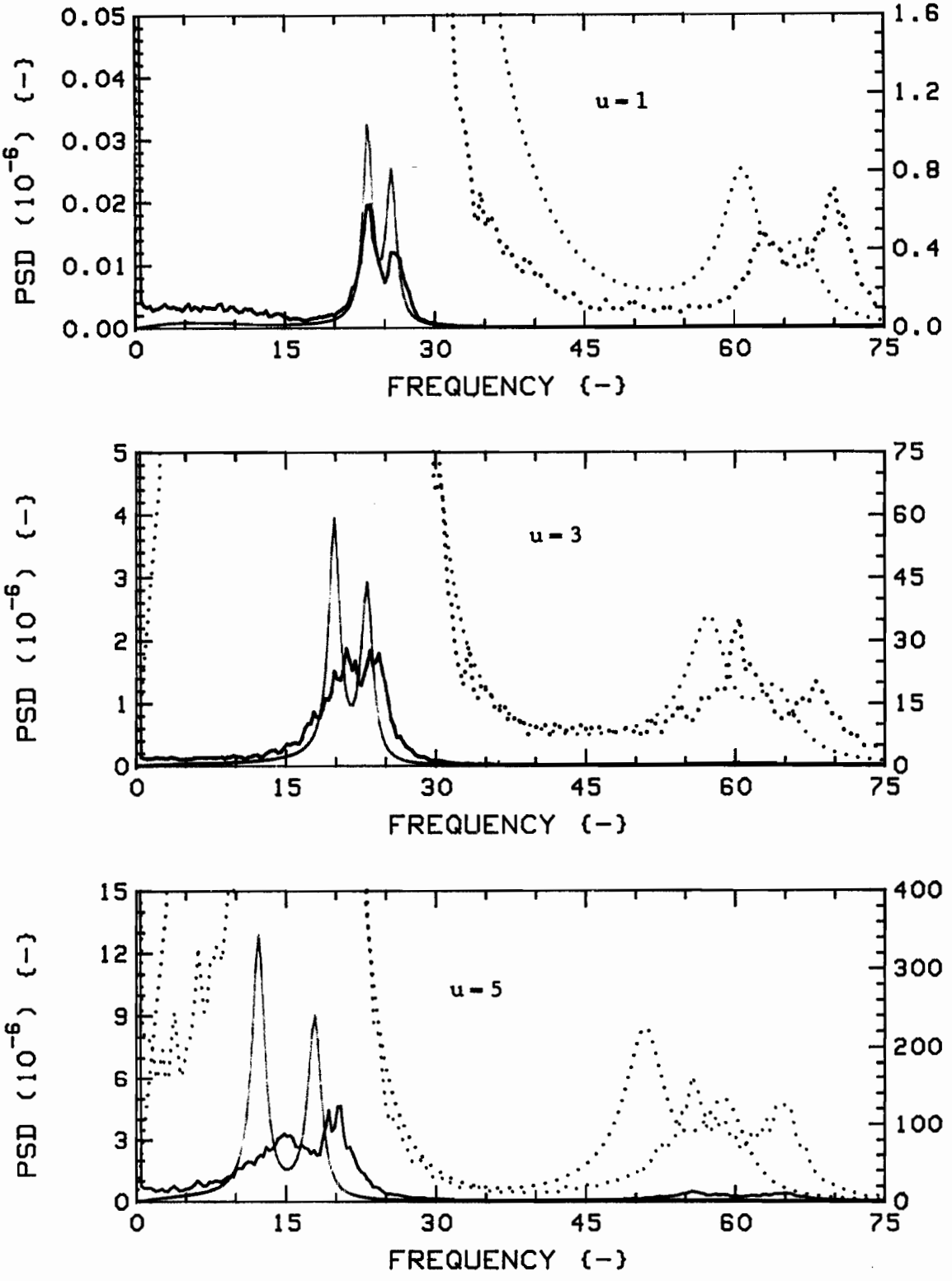

Fig.79a: Measured (RED) and theoretical (GREEN) vibration PSD's for K = 4, $G_c = 0.75$, 2F(1,3)/2R(2,4), Radial direction.

The dotted traces are expansions of the solid ones; scales are, from top, (RED): 3.0×10^{-10}, 8.0×10^{-8}, 1.2×10^{-6},

(GREEN): 2.0×10^{-9}, 2.4×10^{-7}, 4.5×10^{-6}.

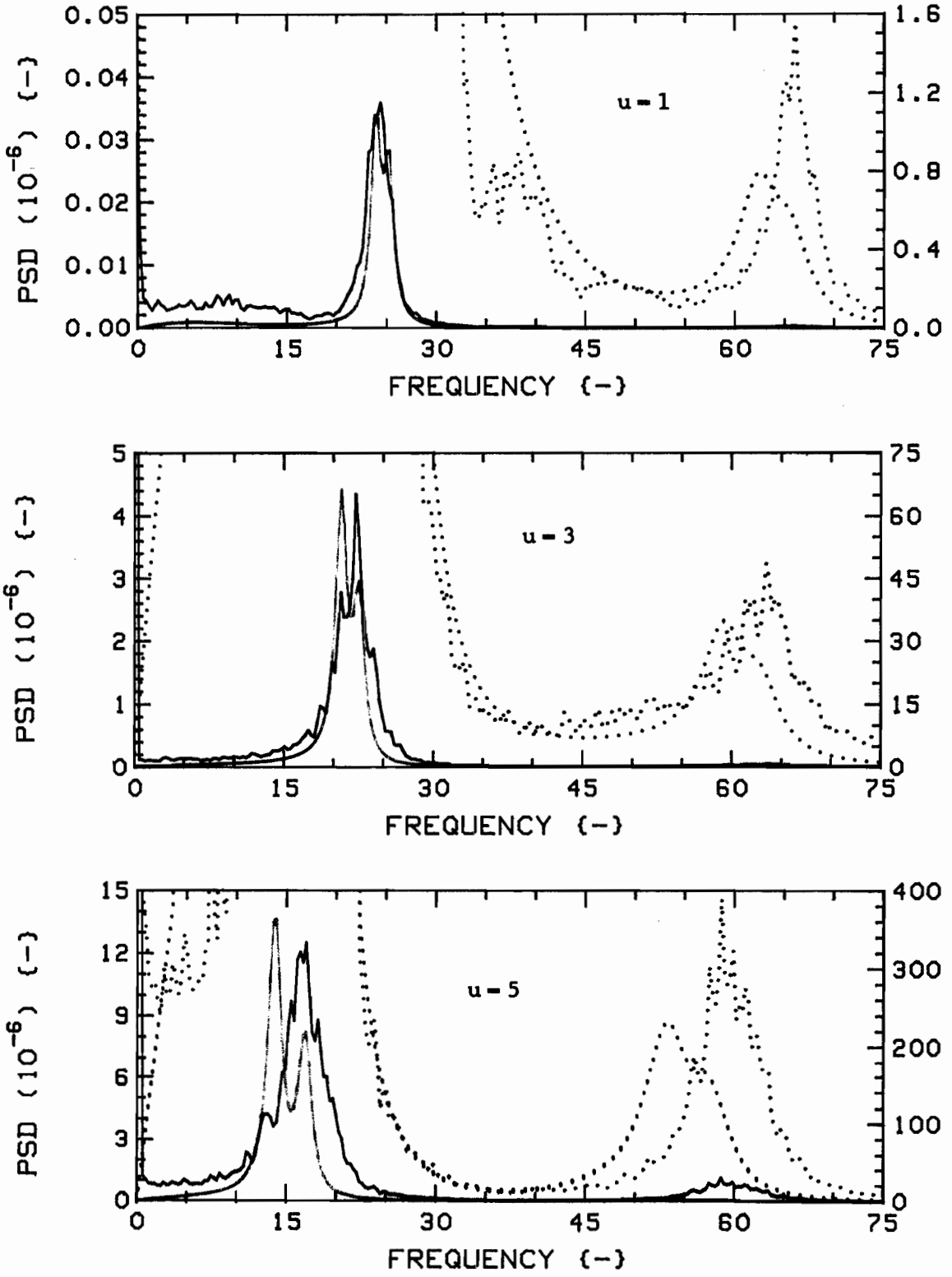

Fig.79b: Measured (RED) and theoretical (GREEN) vibration PSD's for K = 4, $G_c = 0.75$, 2F(1,3)/2R(2,4), Tangential direction.

The dotted traces are expansions of the solid ones; scales are, from top, (RED): 3.0×10^{-10}, 8.0×10^{-8}, 1.2×10^{-6},

(GREEN): 2.0×10^{-9}, 2.4×10^{-7}, 4.5×10^{-6}.

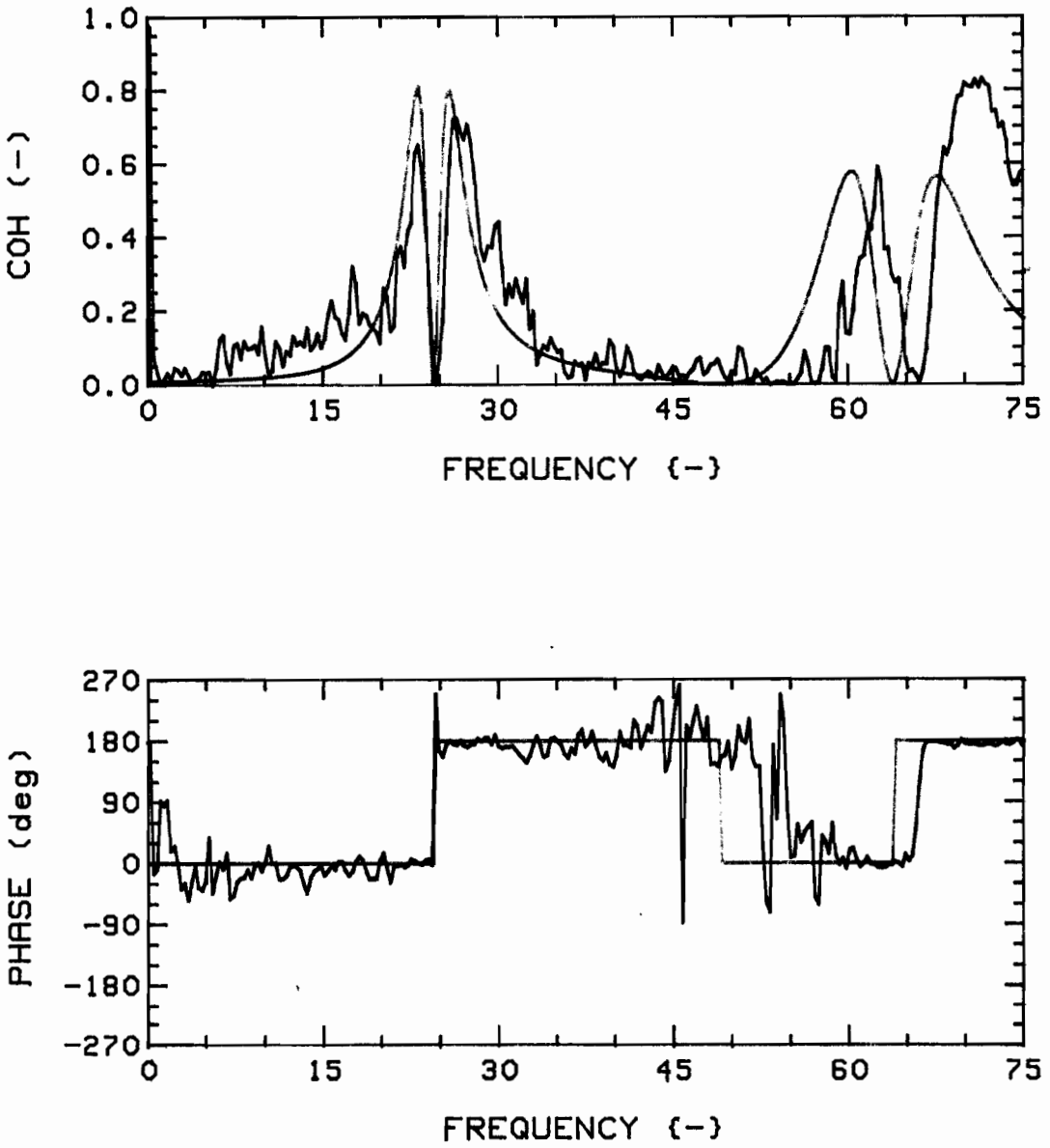

Fig.80a: Measured (RED) and theoretical (GREEN) coherence functions and phases, for K = 4, G_c = 0.75, 2F(1,3)/2R(2,4), R-R (1,3), at u = 1.

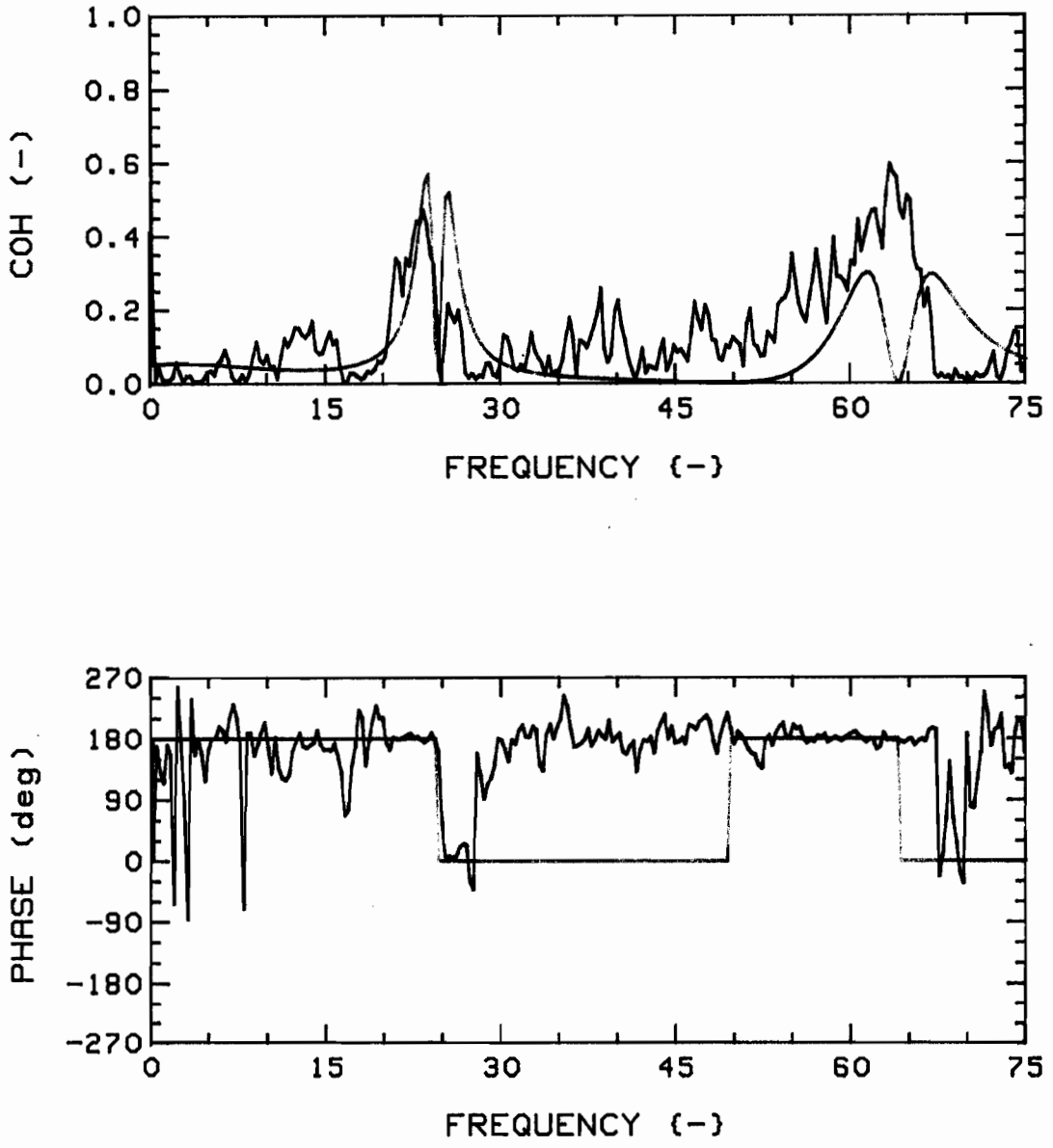

Fig.80b: Measured (RED) and theoretical (GREEN) coherence functions and phases, for K = 4, $G_c = 0.75$, 2F(1,3)/2R(2,4), T-T (1,3), at u = 1.

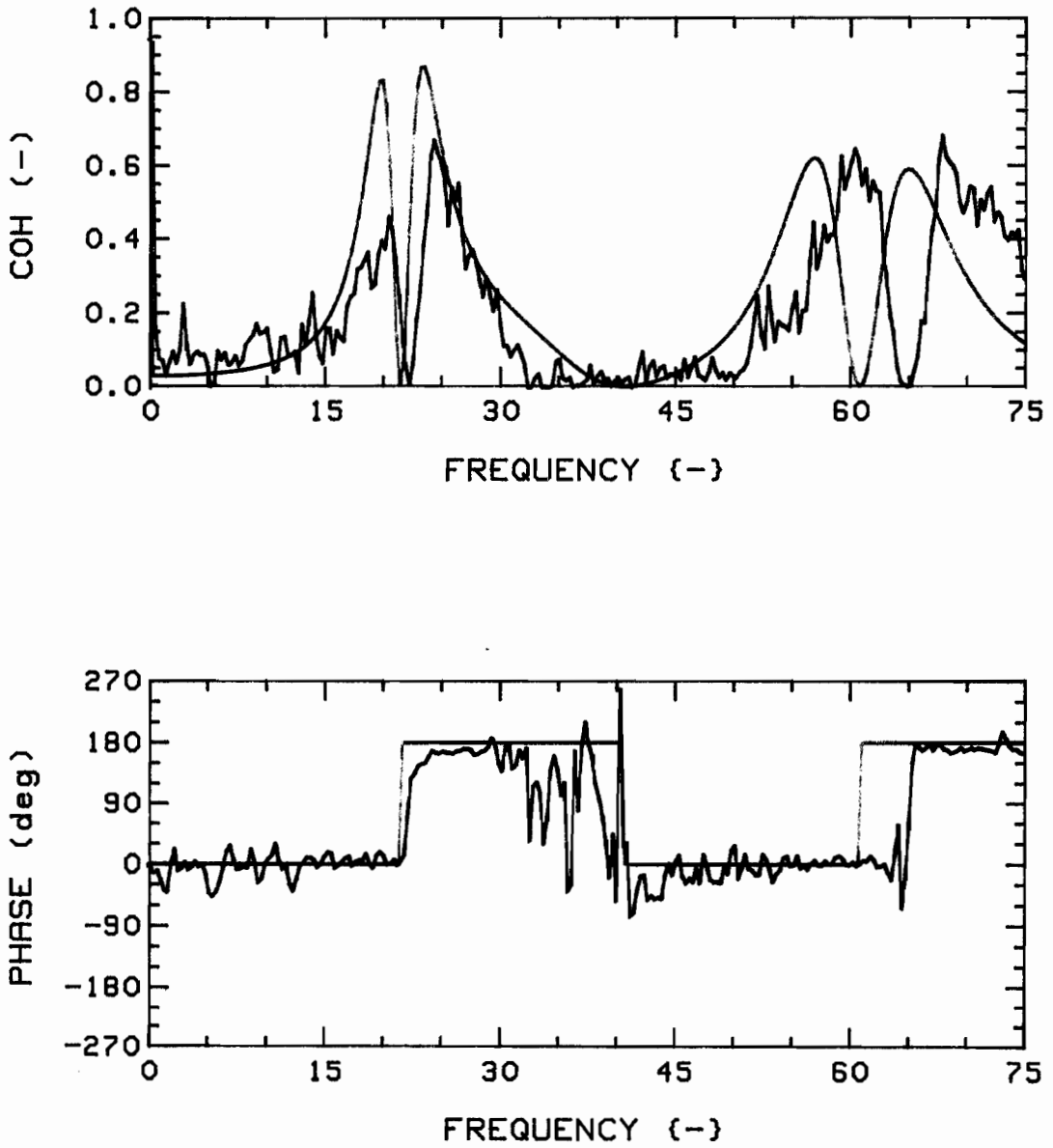

Fig.80c: Measured (RED) and theoretical (GREEN) coherence functions and phases, for K = 4, $G_c = 0.75$, 2F(1,3)/2R(2,4), R-R (1,3), at u = 3.

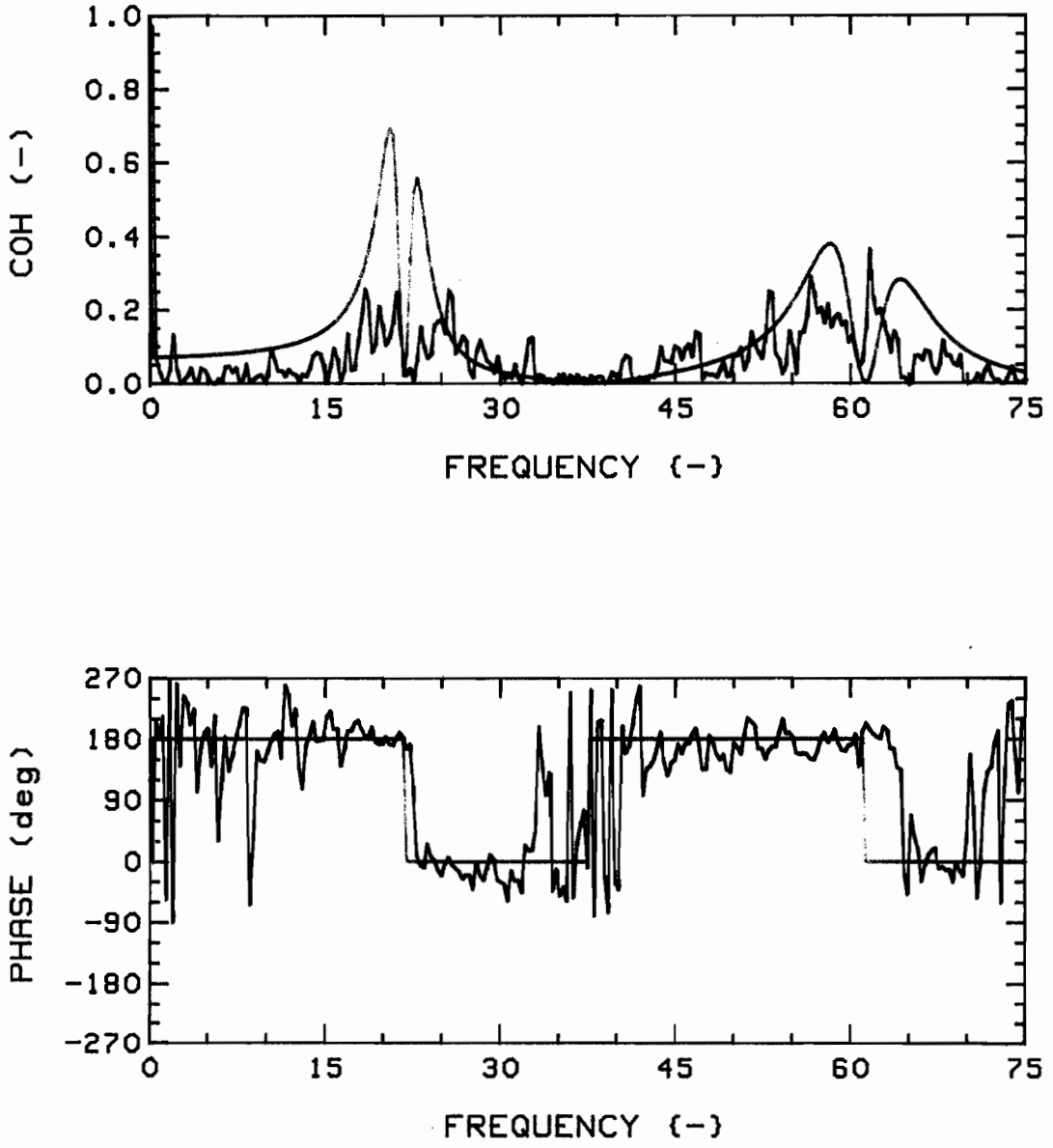

Fig.80d: Measured (RED) and theoretical (GREEN) coherence functions and phases, for K = 4, G_c = 0.75, 2F(1,3)/2R(2,4), T-T (1,3), at u = 3.

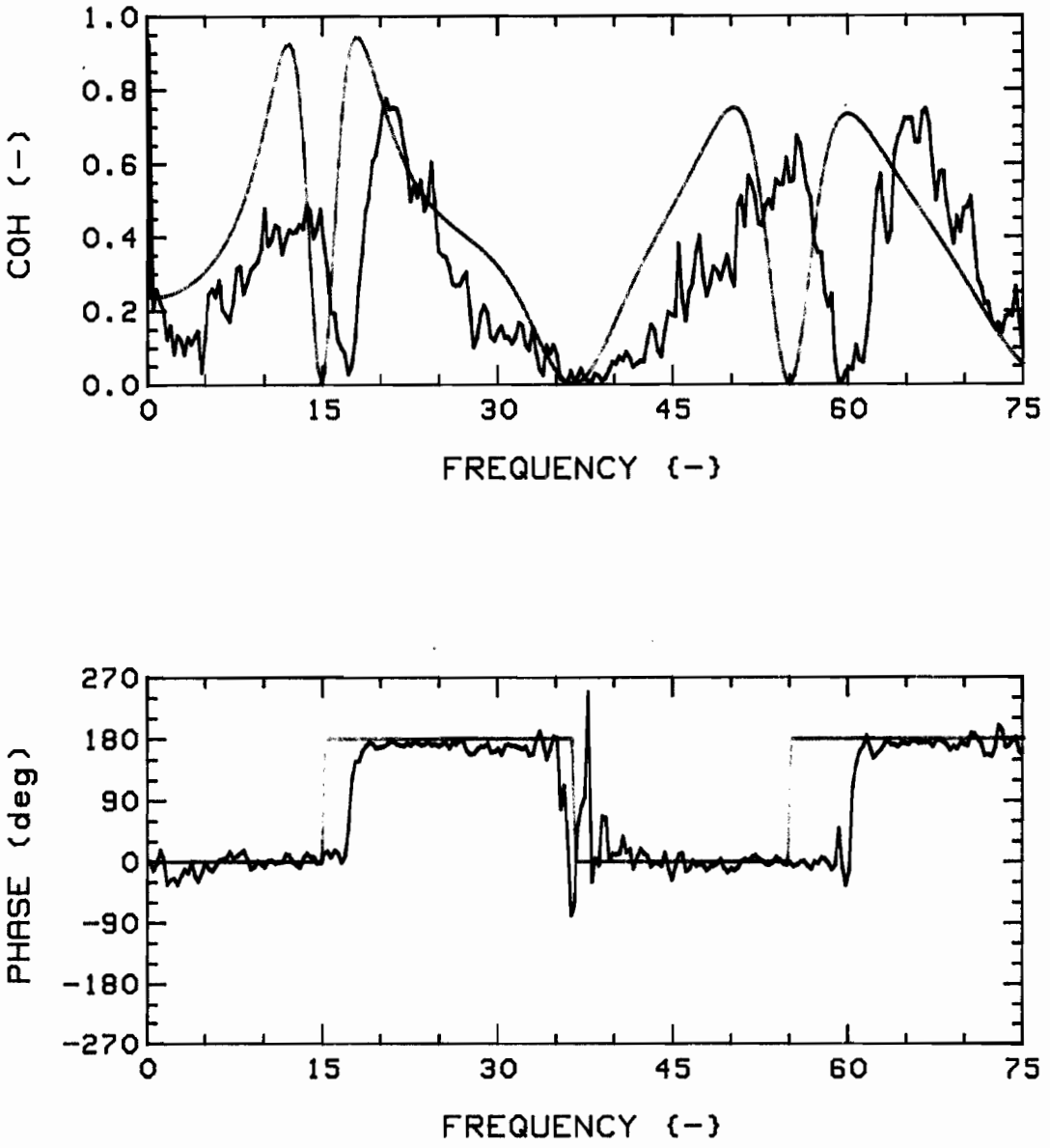

Fig.80e: Measured (RED) and theoretical (GREEN) coherence functions and phases, for K = 4, $G_c = 0.75$, 2F(1,3)/2R(2,4), R-R (1,3), at u = 5.

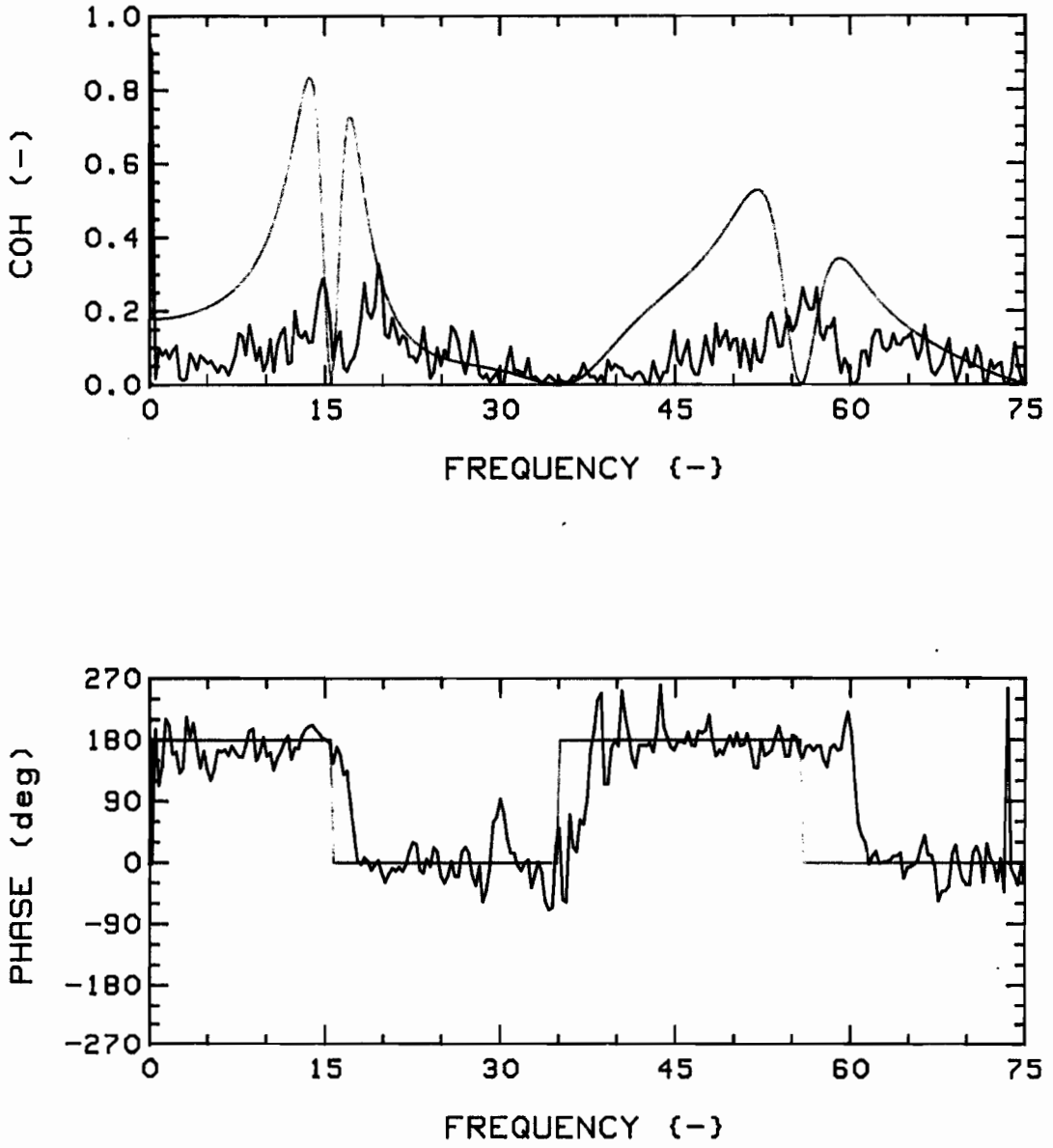

Fig.80f: Measured (RED) and theoretical (GREEN) coherence functions and phases, for K = 4, G_c = 0.75, 2F(1,3)/2R(2,4), T-T (1,3), at u = 5.

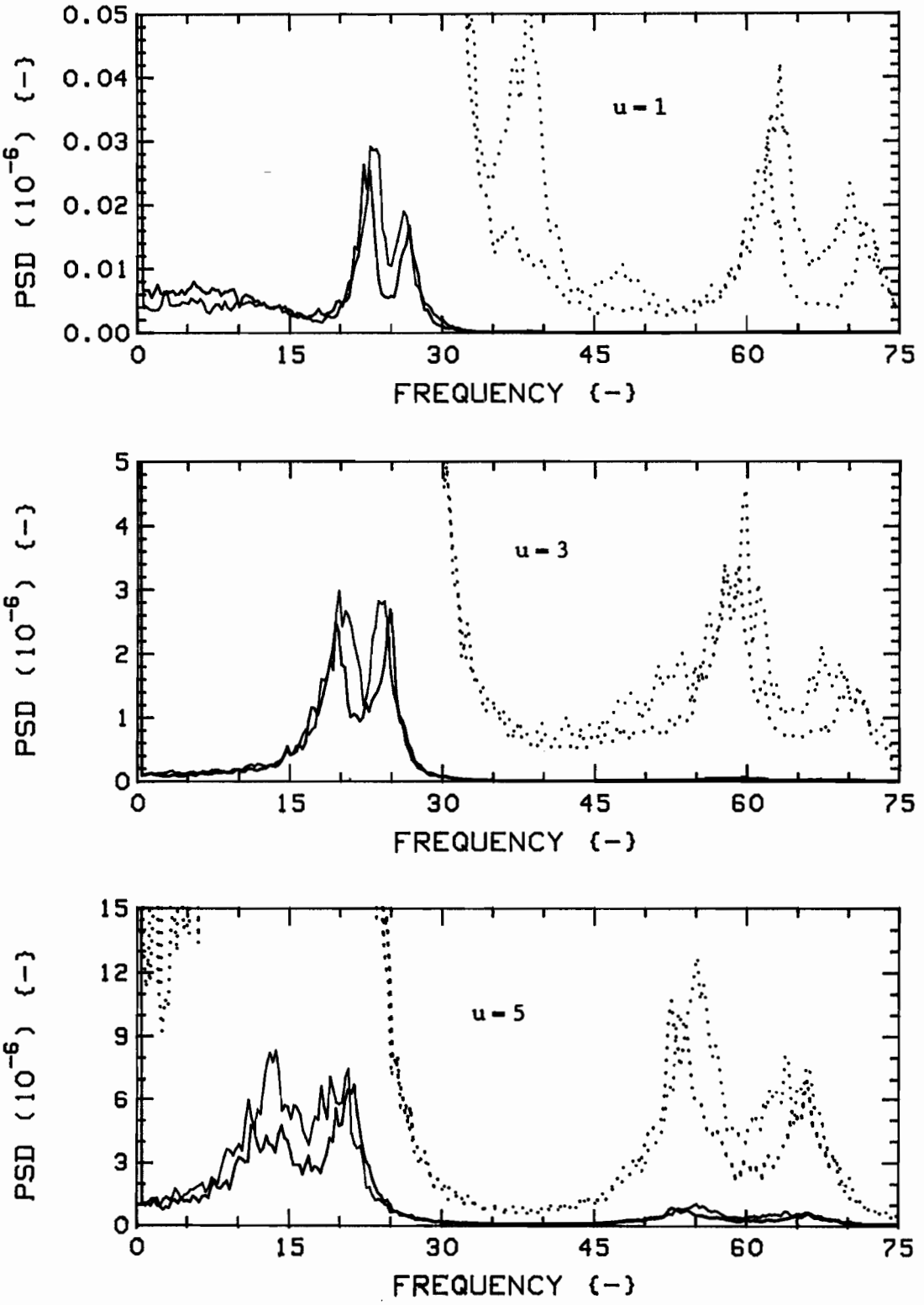

Fig.81: Measured vibration PSD's for K = 4, G_c = 0.75, 2F(1,2)/ 2R(3,4), Radial (RED) and Tangential (BLUE) directions. The dotted traces are expansions of the solid ones; scales are, from top: 3.0×10^{-10}, 8.0×10^{-8}, 1.2×10^{-6}.

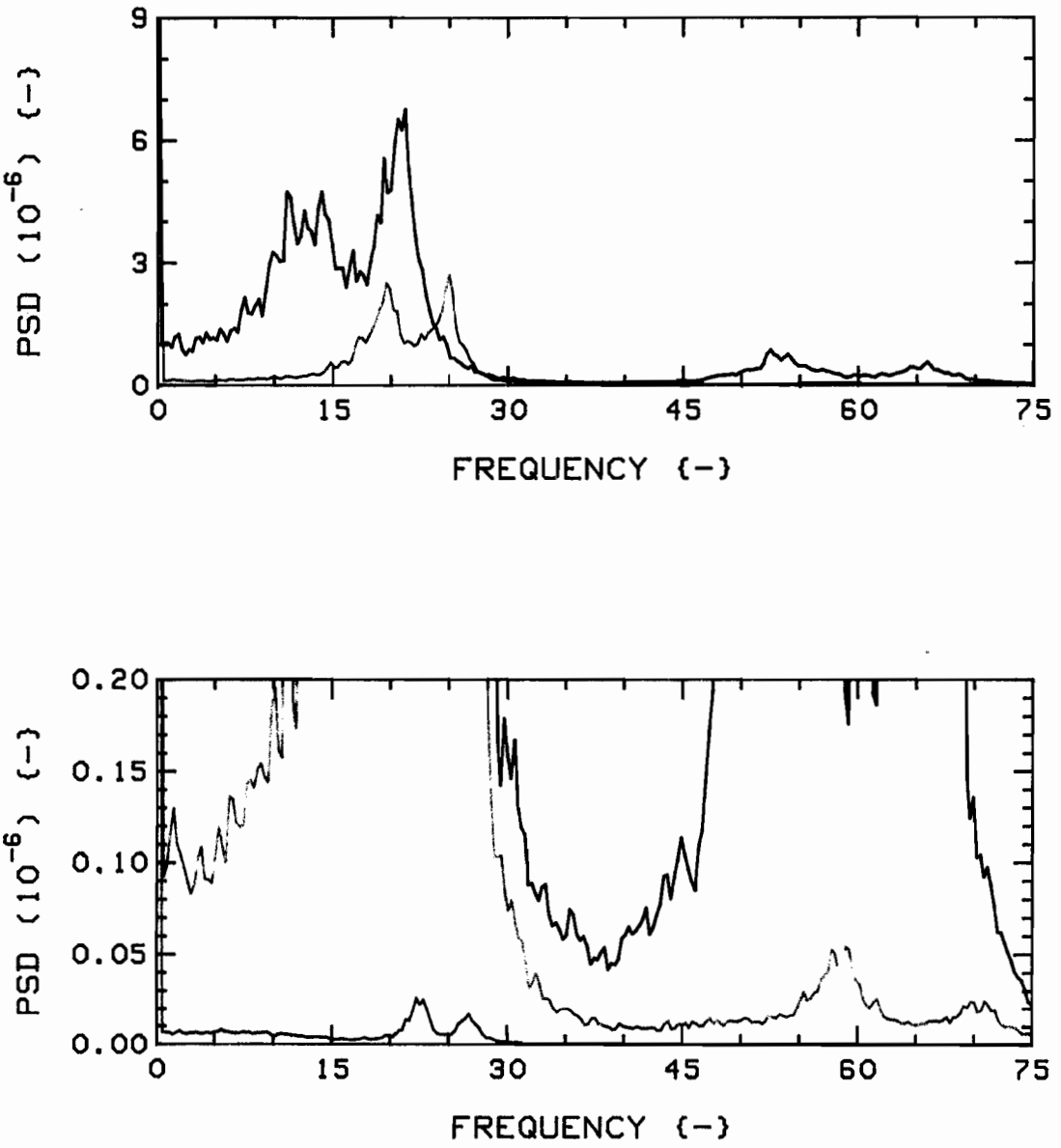

Fig.82a: Measured vibration PSD's for K = 4, G_c = 0.75, 2F(1,2)/2R(3,4), Radial direction, versus flow velocity. In descending order, u = 5.0, 3.0, and 1.0. Colour sequence: RED, GREEN, BLUE.

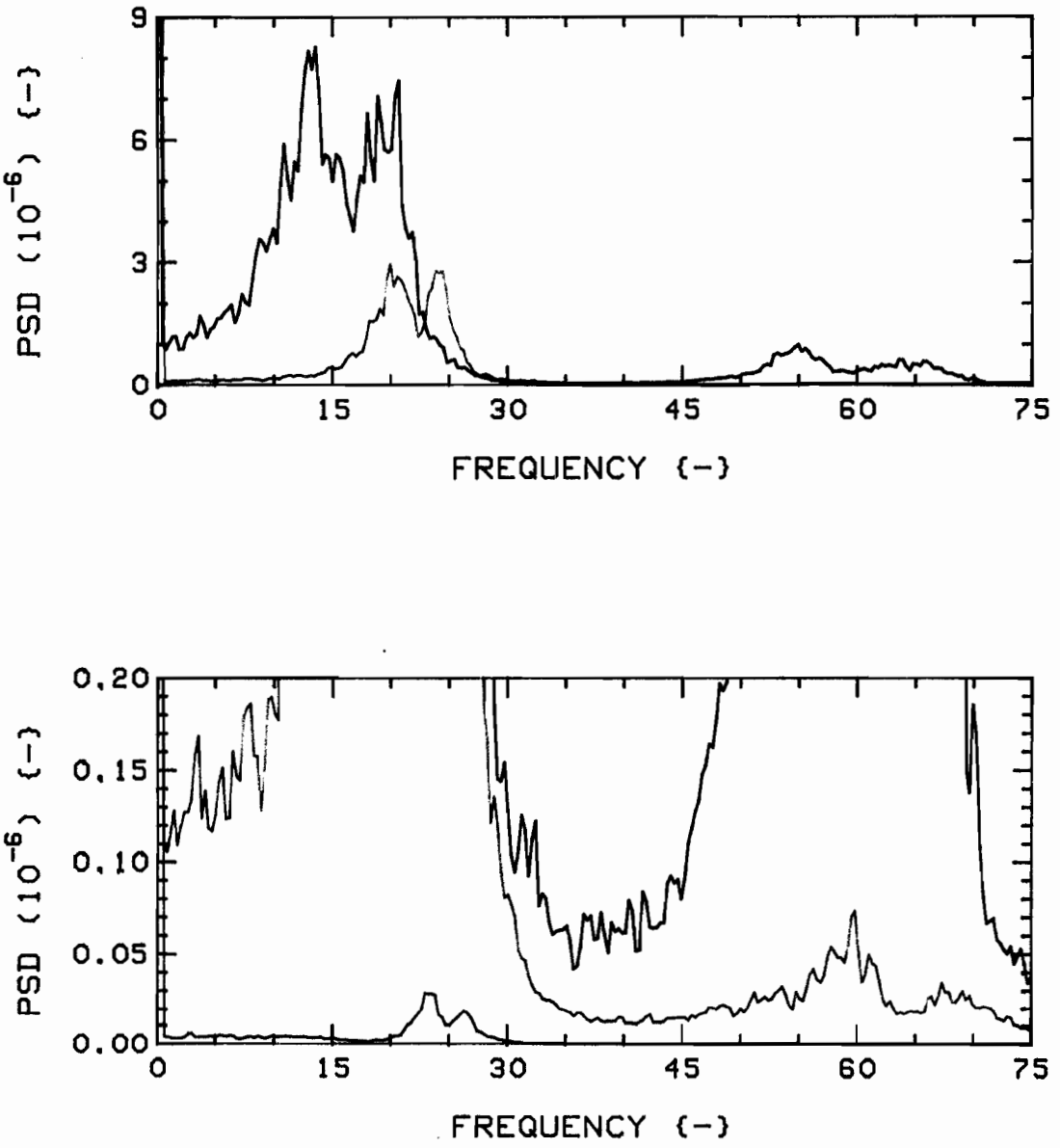

Fig.82b: Measured vibration PSD's for K = 4, G_c = 0.75, 2F(1,2)/2R(3,4), Tangential direction, versus flow velocity. In descending order, u = 5.0, 3.0, and 1.0. Colour sequence: RED, GREEN, BLUE.

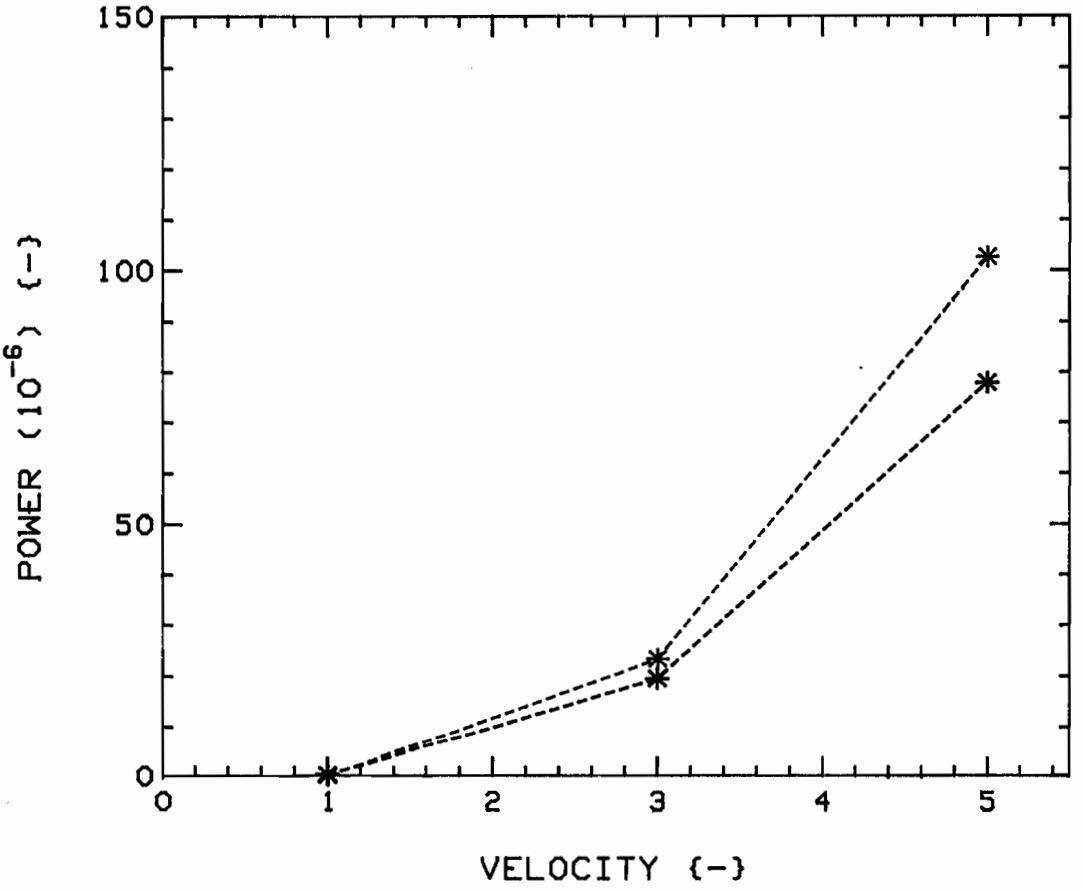

Fig.83: Powers versus flow velocity, for K = 4, G_c = 0.75, 2F(1,2)/2R(3,4), from (integrated) PSD's of Figs. 82a and 82b. Radial (RED) and Tangential (BLUE) directions.

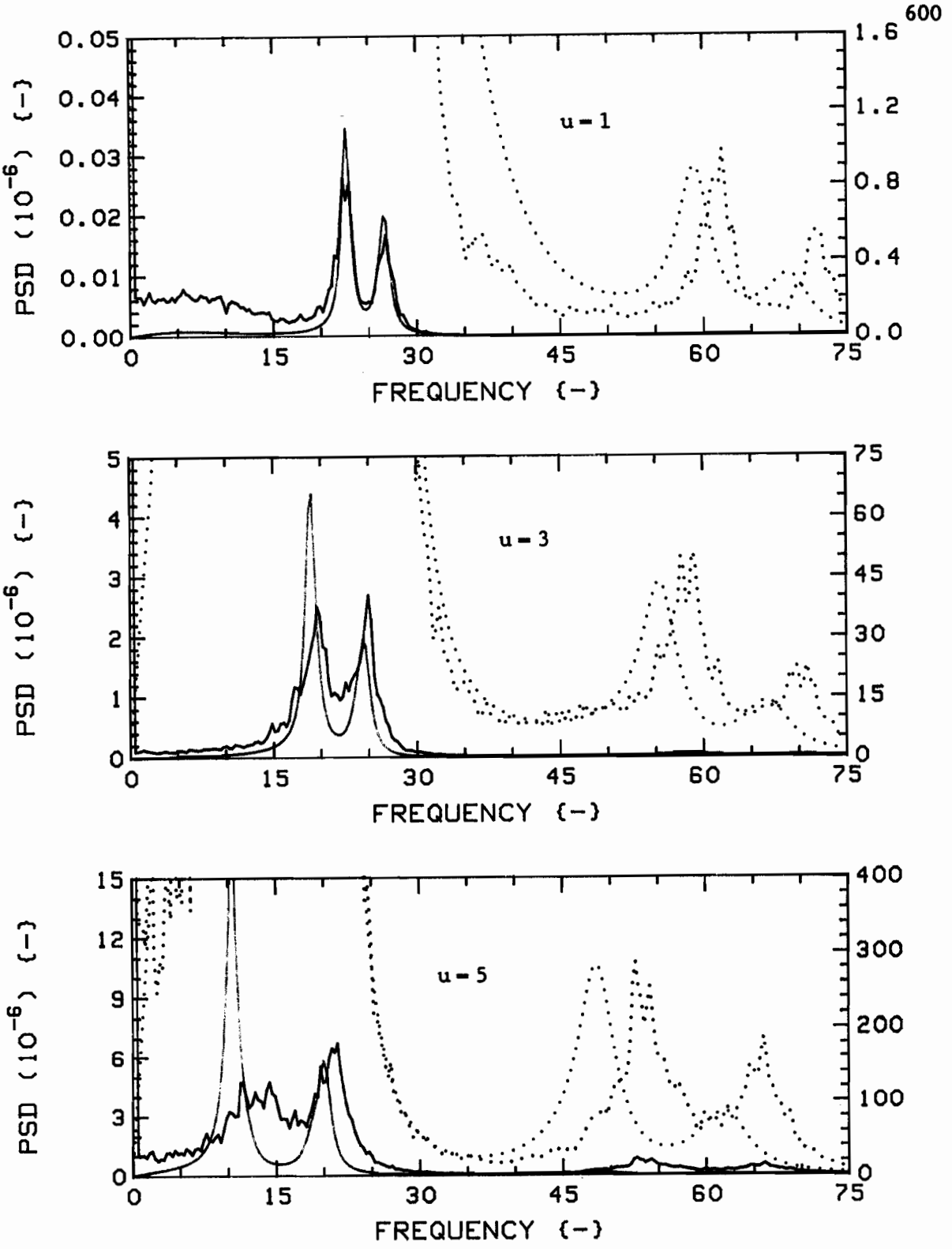

Fig.84a: Measured (RED) and theoretical (GREEN) vibration PSD's for K = 4, $G_c = 0.75$, 2F(1,2)/2R(3,4), Radial direction.

The dotted traces are expansions of the solid ones; scales are, from top, (RED): 3.0×10^{-10}, 8.0×10^{-8}, 1.2×10^{-6},

(GREEN): 2.0×10^{-9}, 2.4×10^{-7}, 4.5×10^{-6}.

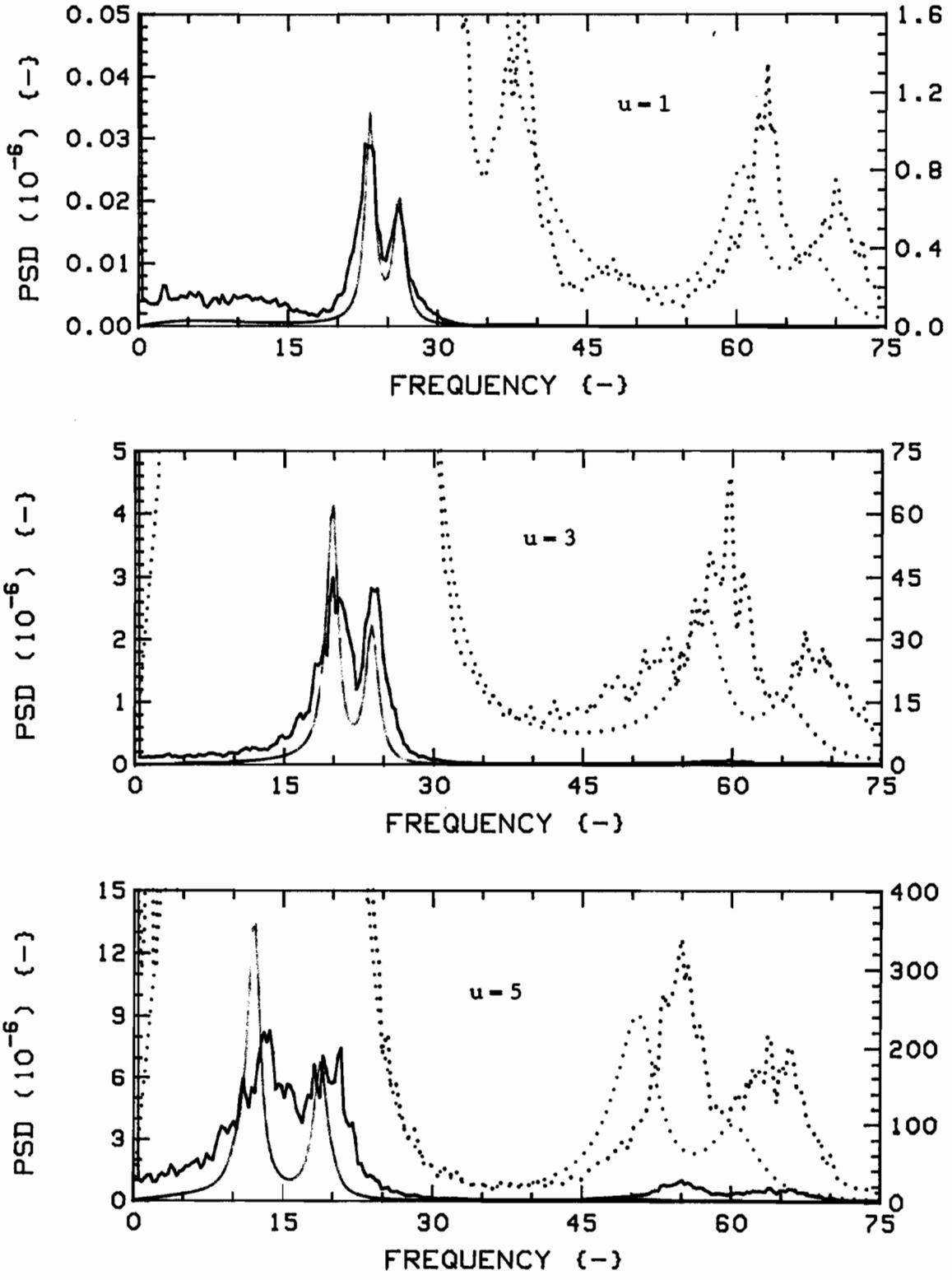

Fig.84b: Measured (RED) and theoretical (GREEN) vibration PSD's for K = 4, G_c = 0.75, 2F(1,2)/2R(3,4), Tangential direction.

The dotted traces are expansions of the solid ones; scales are, from top, (RED): 3.0×10^{-10}, 8.0×10^{-8}, 1.2×10^{-6},

(GREEN): 2.0×10^{-9}, 2.4×10^{-7}, 4.5×10^{-6}.

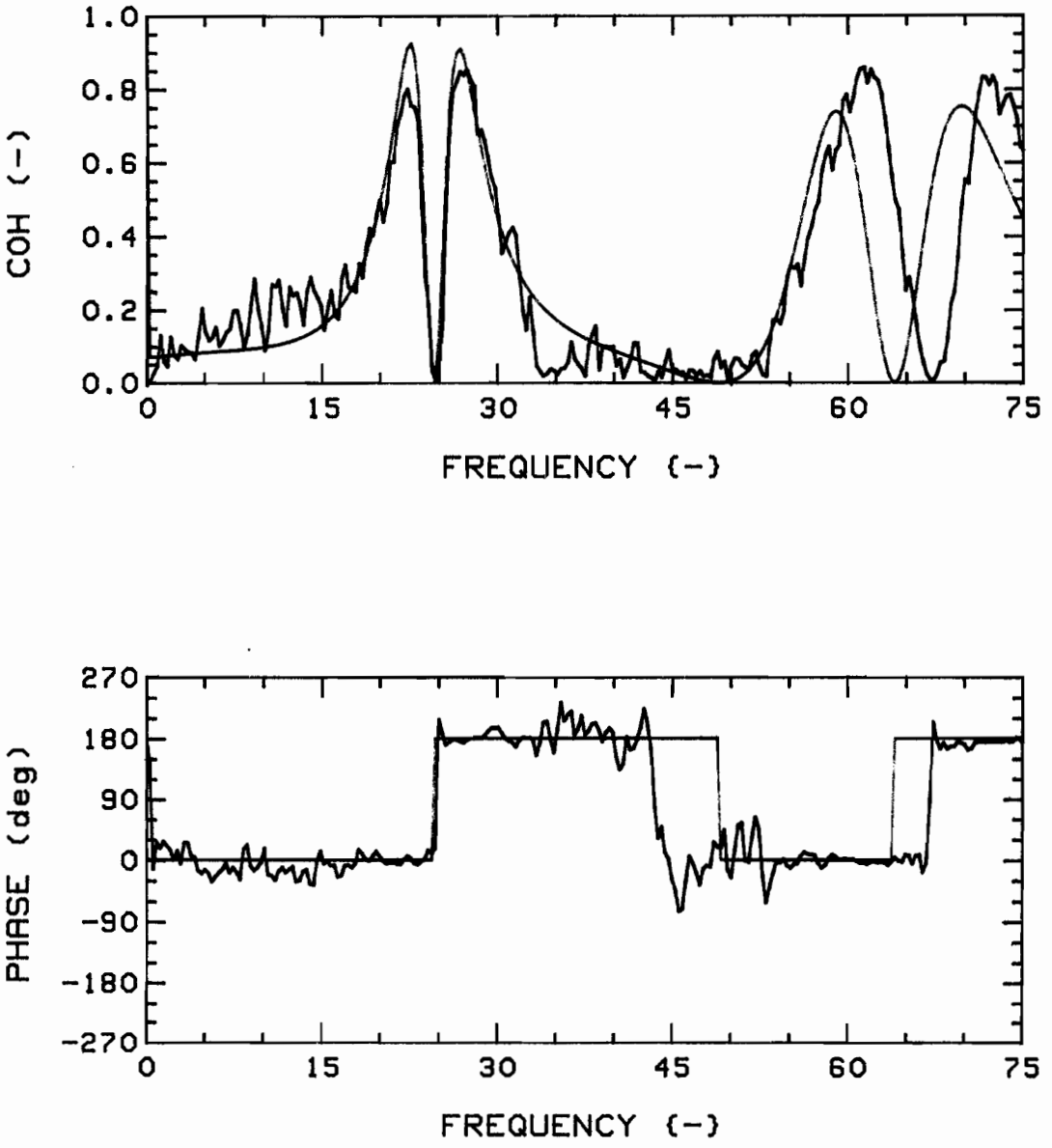

Fig.85a: Measured (RED) and theoretical (GREEN) coherence functions and phases, for K = 4, G_c = 0.75, 2F(1,2)/2R(3,4), R-R (1,3), at u = 1.

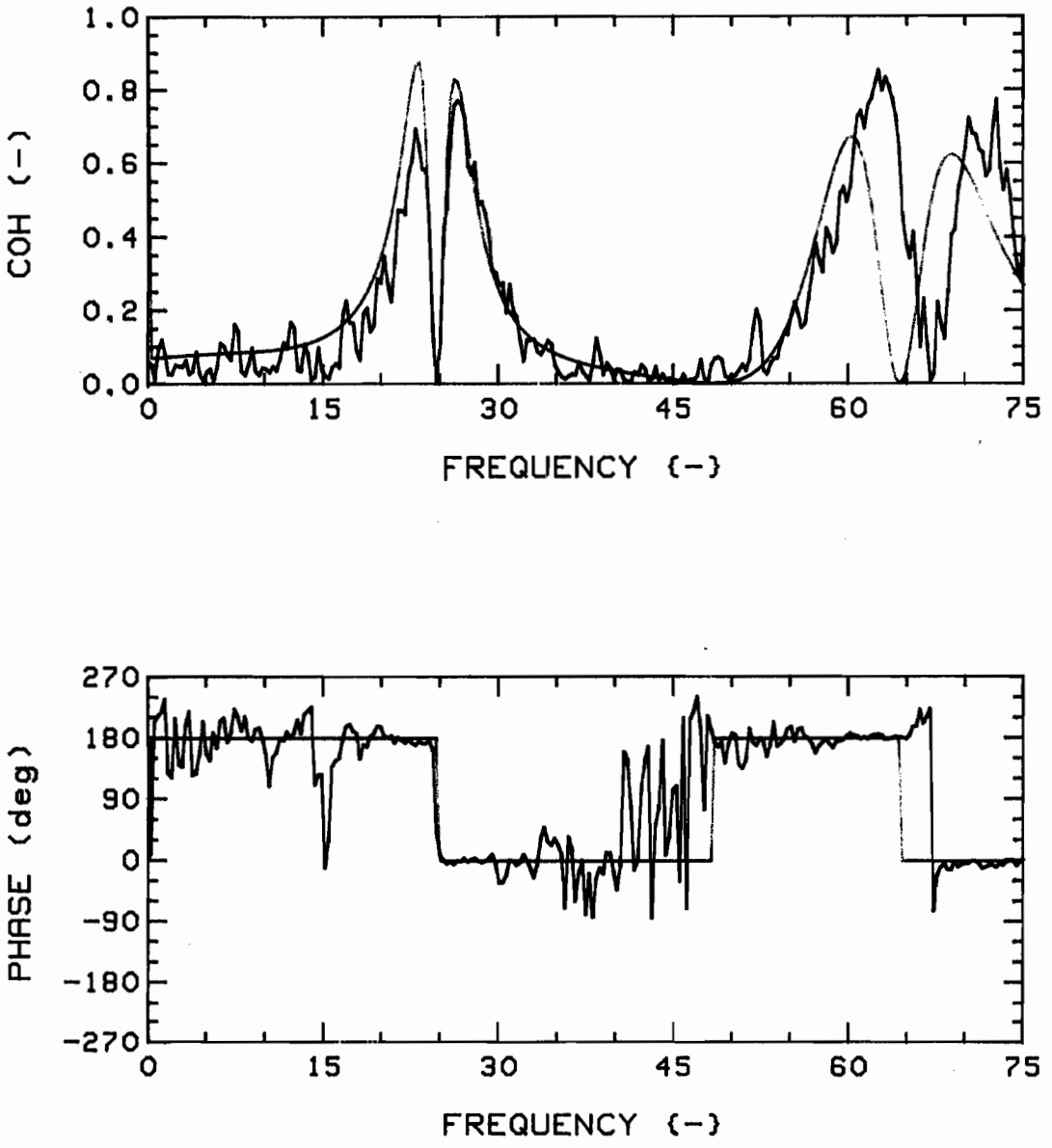

Fig.85b: Measured (RED) and theoretical (GREEN) coherence functions and phases, for K = 4, G_c = 0.75, 2F(1,2)/2R(3,4), T-T (1,3), at u = 1.

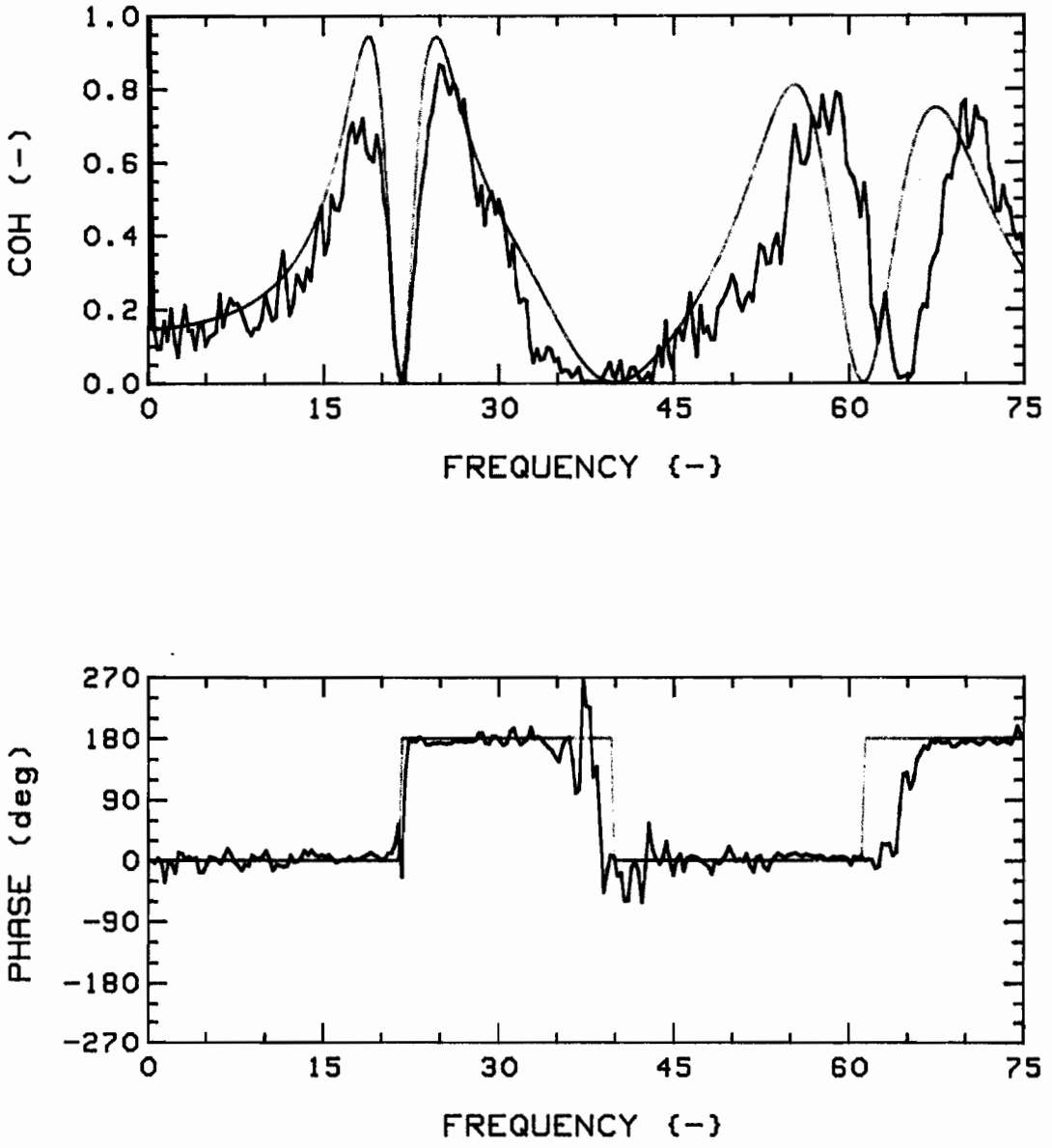

Fig.85c: Measured (RED) and theoretical (GREEN) coherence functions and phases, for K = 4, G_c = 0.75, 2F(1,2)/2R(3,4), R-R (1,3), at u = 3.

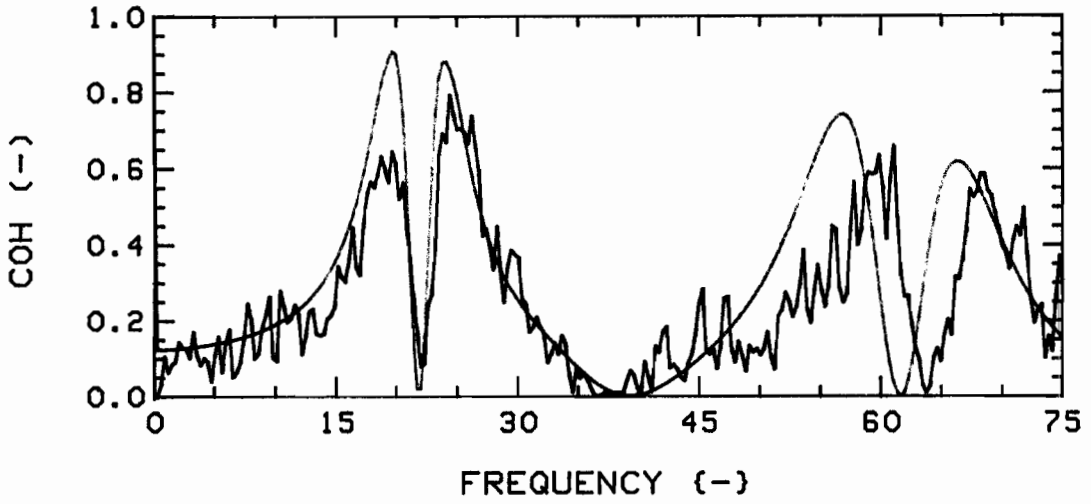

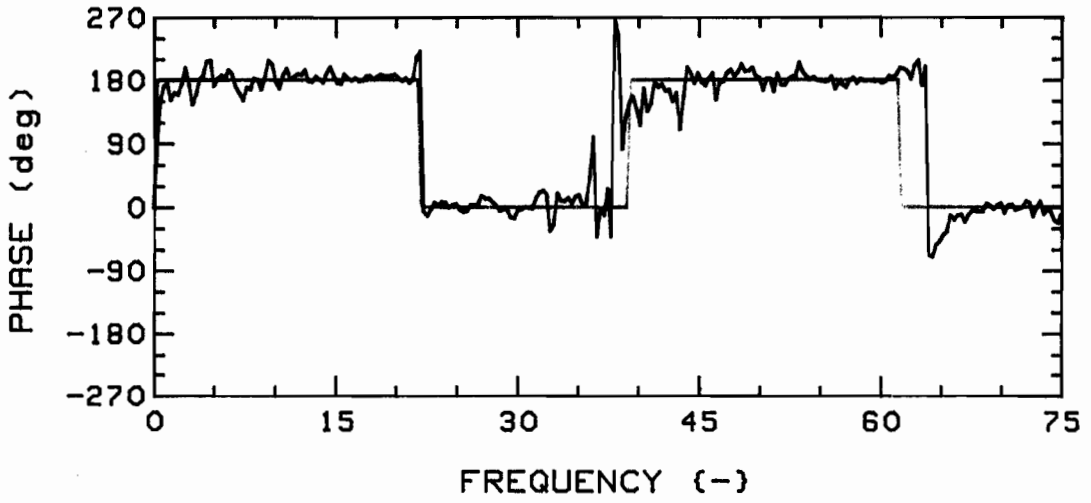

Fig.85d: Measured (RED) and theoretical (GREEN) coherence functions and phases, for K = 4, G_c = 0.75, 2F(1,2)/2R(3,4), T-T (1,3), at u = 3.

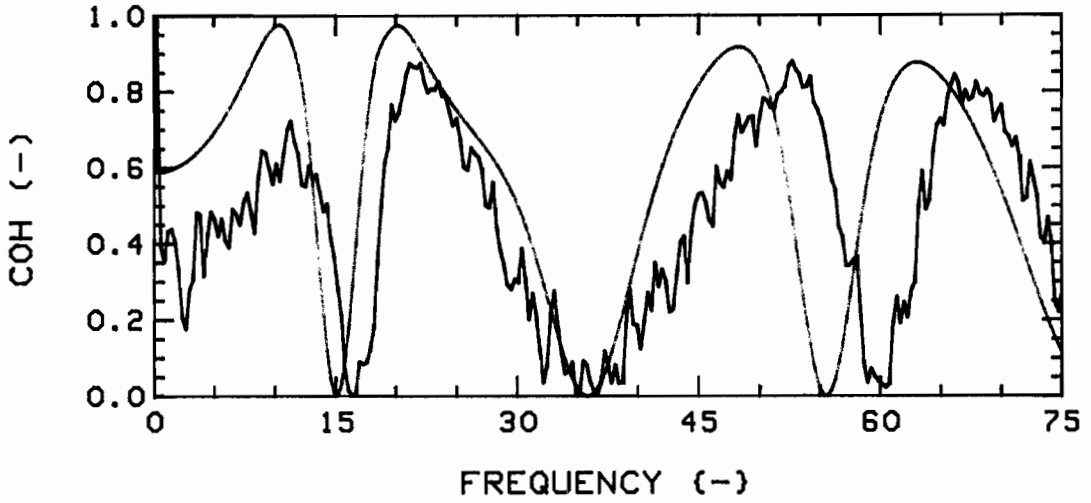

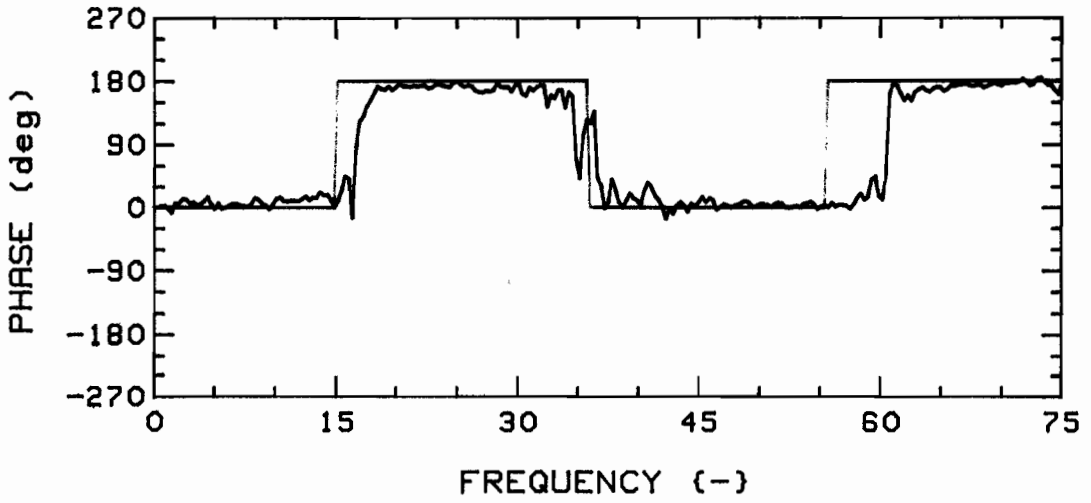

Fig.85e: Measured (RED) and theoretical (GREEN) coherence functions and phases, for K = 4, G_c = 0.75, 2F(1,2)/2R(3,4), R-R (1,3), at u = 5.

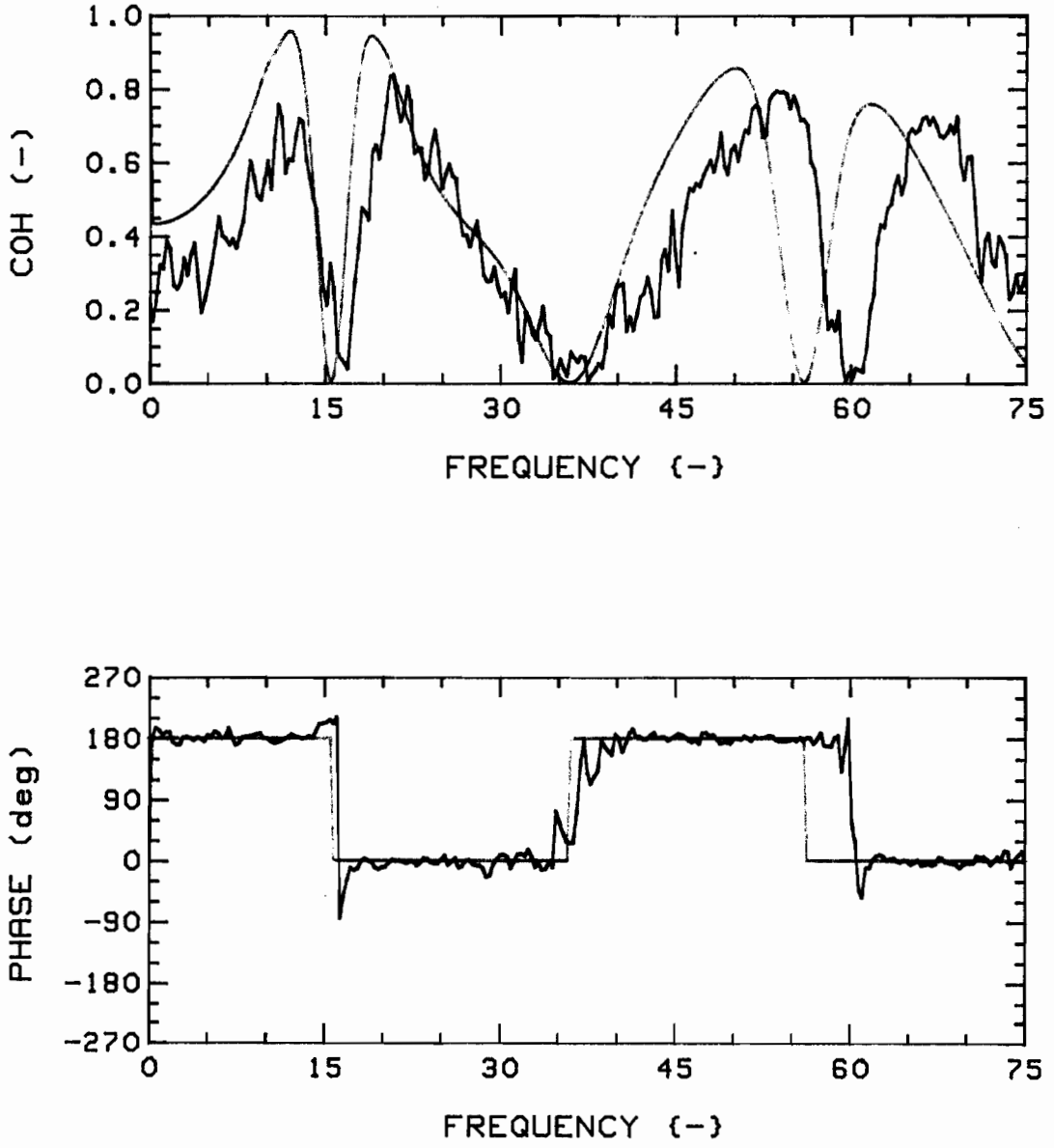

Fig.85f: Measured (RED) and theoretical (GREEN) coherence functions and phases, for K = 4, $G_c = 0.75$, 2F(1,2)/2R(3,4), T-T (1,3), at u = 5.

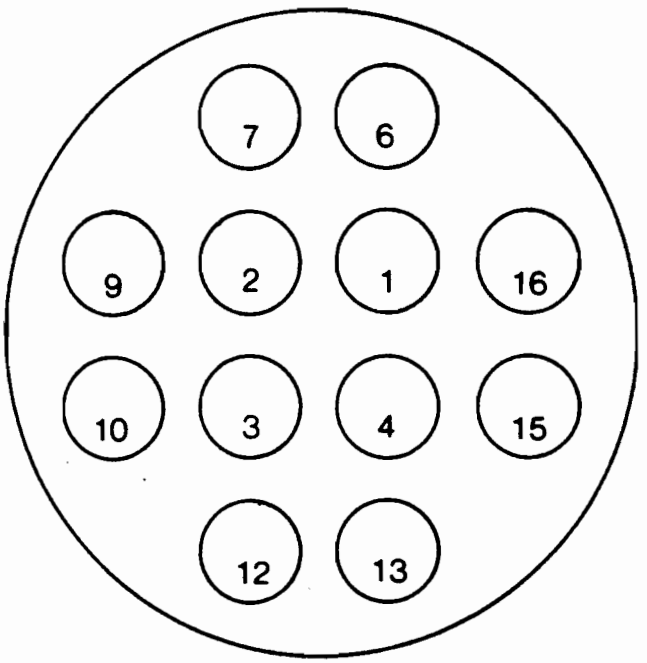

Fig.86: Reduced cluster (K = 12, G_c = 0.75, R_c = 8.00 cm), for 4F(1,2,3,4)/24R(rest) and 4F(1,6,7,2)/24R(rest) theoretical computations.

Note: See Fig. 29 for full cluster.

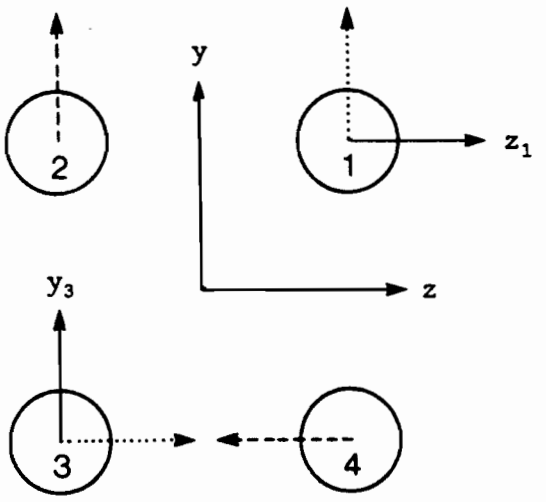

(a)

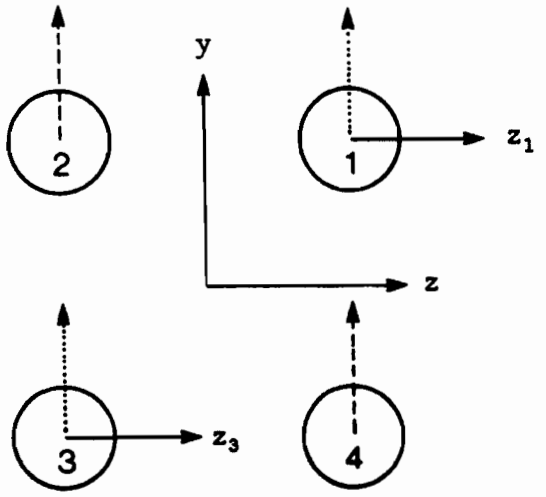

(b)

Fig.87: Cases of symmetry in inter-cylinder fluid coupling.

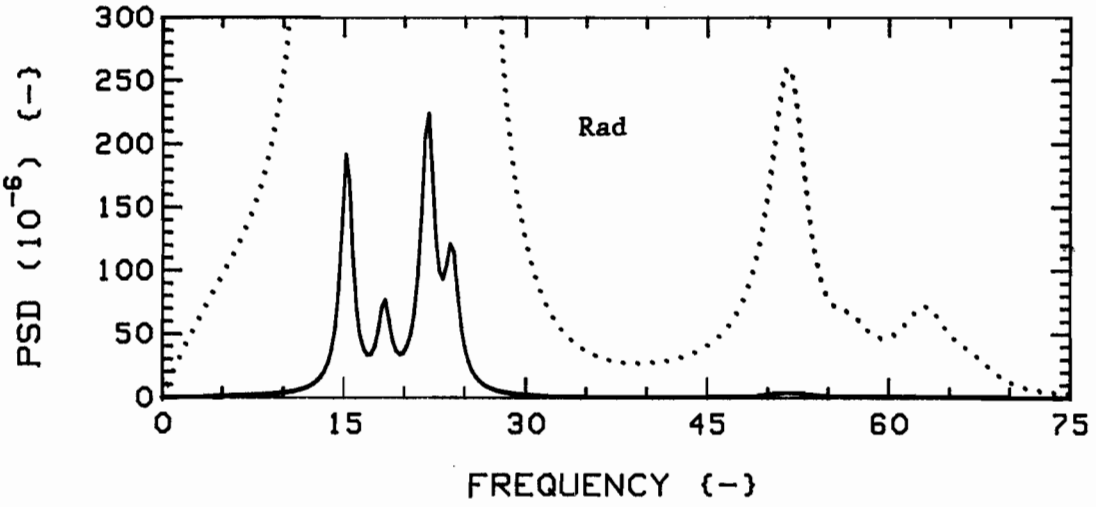

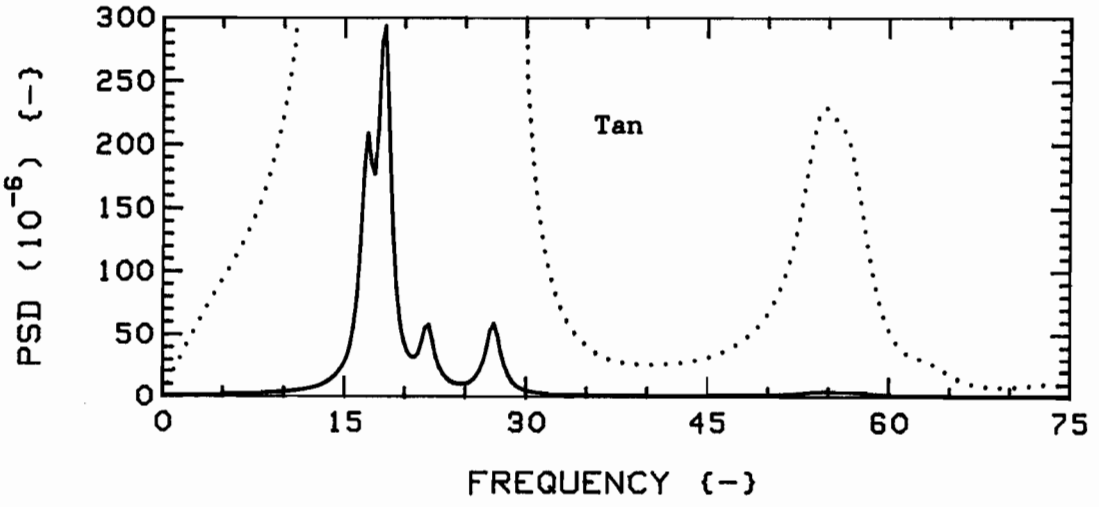

Fig.88: Effect of modulus of elasticity of Rigid cylinders on theoretical vibration PSD's of Flexible ones, for $G_c = 0.75$, 4F(1,2,3,4)/24R system; aluminium (RED) versus acetal (GREEN).

Note: Colors are superposed (identical PSD's).

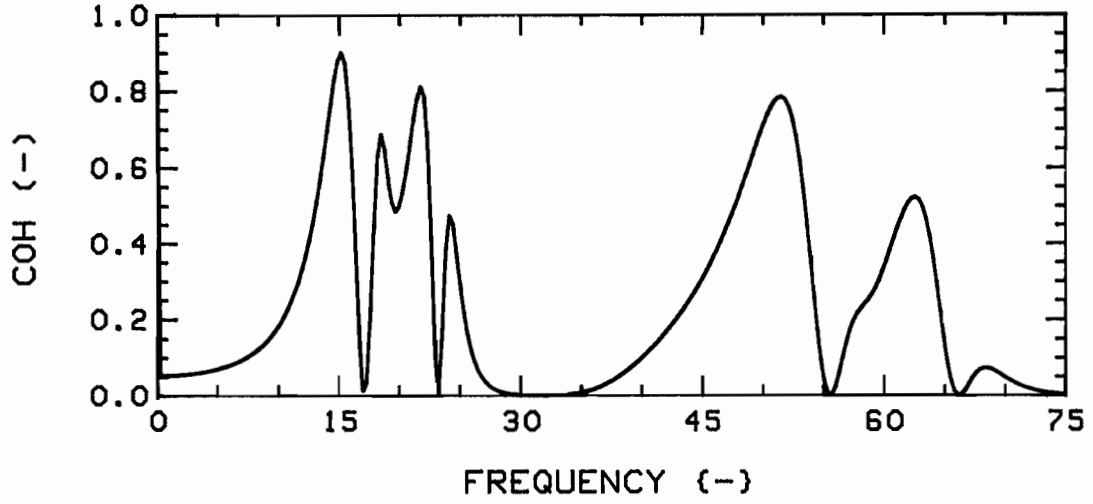

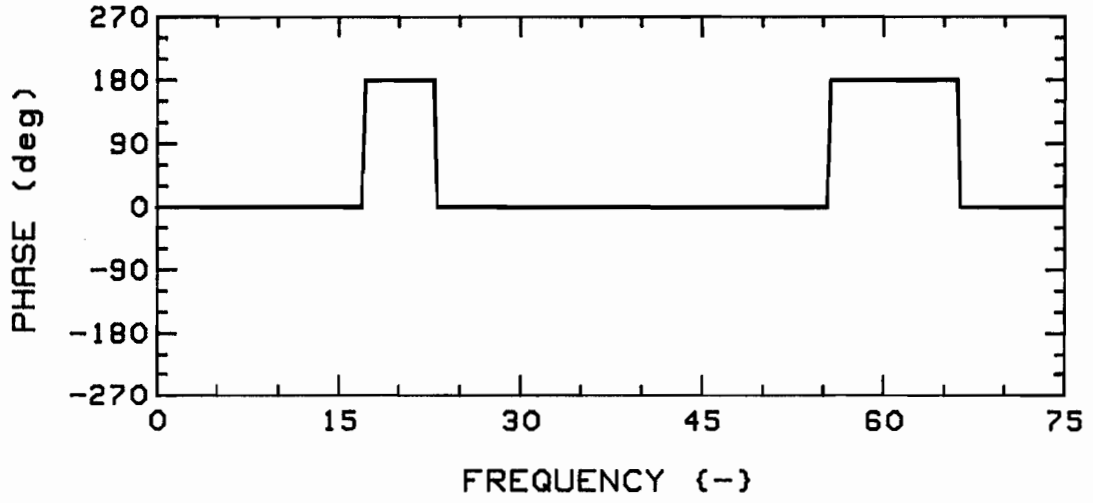

Fig.89a: Effect of modulus of elasticity of Rigid cylinders on theoretical R-R(1,3) coherence and phase of Flexible ones, for $G_c = 0.75$, 4F(1,2,3,4)/24R system; aluminium (RED) versus acetal (GREEN).

Note: Colors are superposed (identical data).

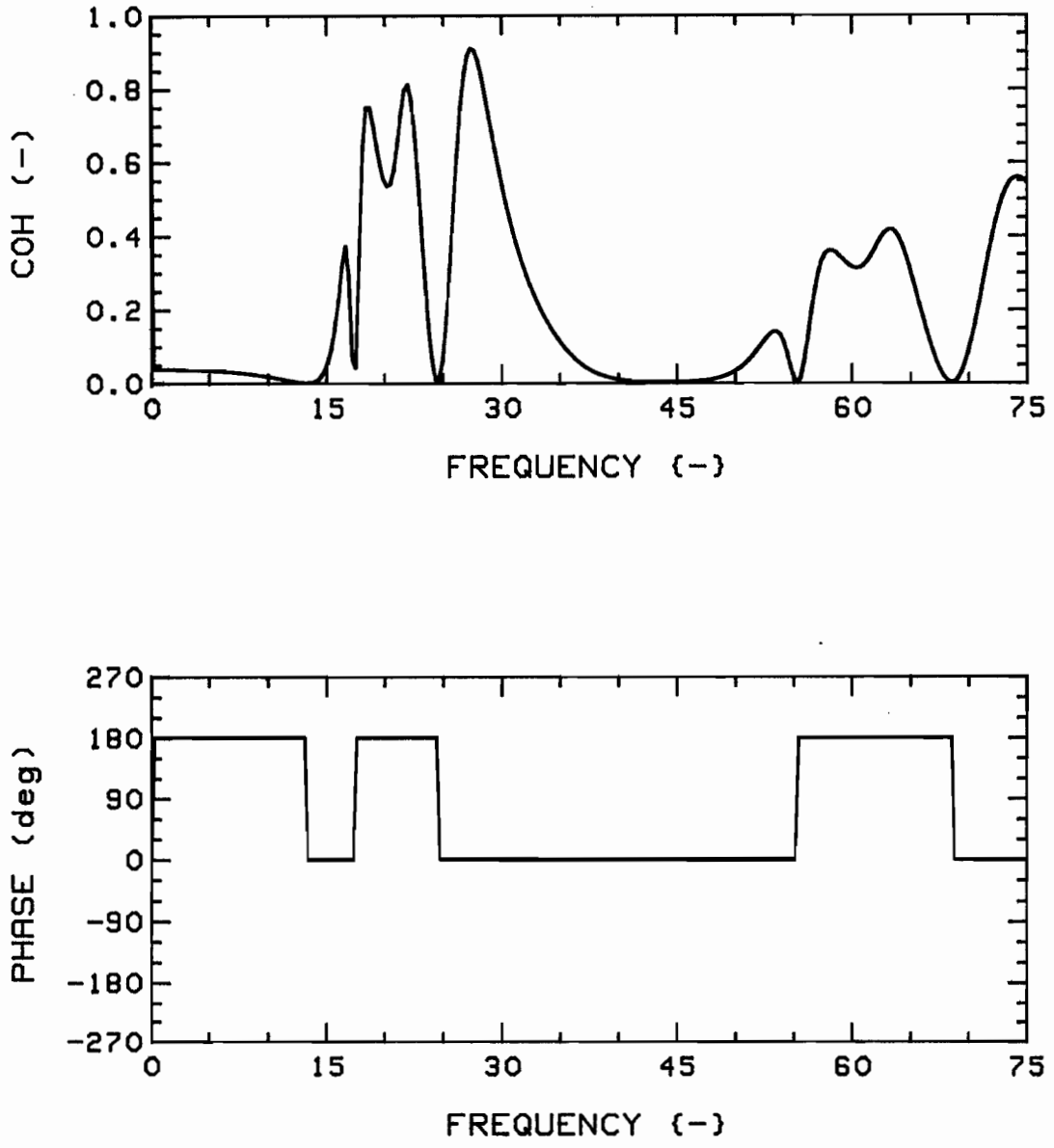

Fig.89b: Effect of modulus of elasticity of Rigid cylinders on theoretical T-T(1,3) coherence and phase of Flexible ones, for $G_c = 0.75$, 4F(1,2,3,4)/24R system; aluminium (RED) versus acetal (GREEN).

Note: Colors are superposed (identical data).

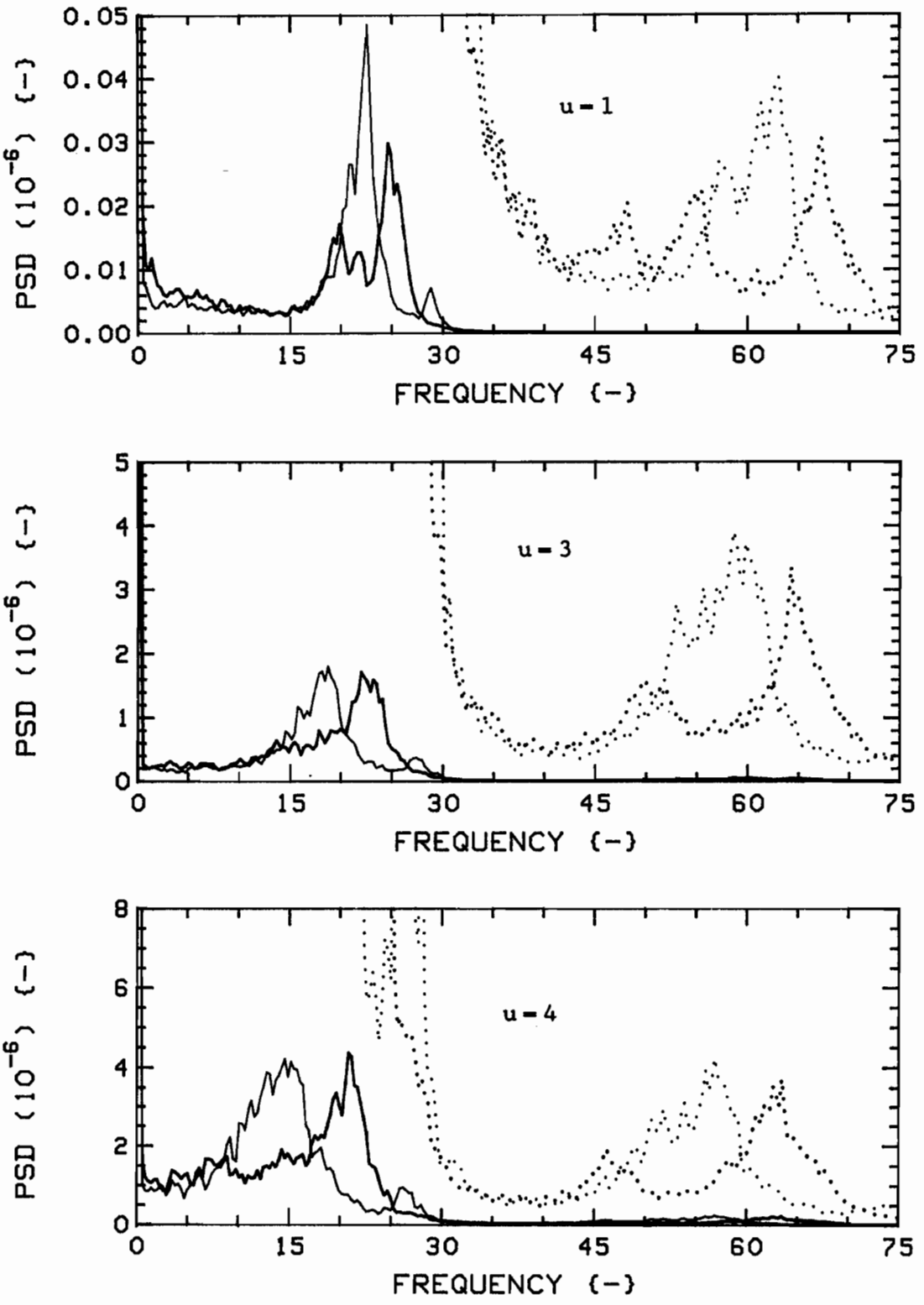

Fig.90: Measured vibration PSD's for K = 28, G_c = 0.75, 4F(1,2,3,4)/24R, Radial (RED) and Tangential (BLUE) directions.

The dotted traces are expansions of the solid ones; scales are, from top: 3.0×10^{-10}, 8.0×10^{-8}, 5.0×10^{-7}.

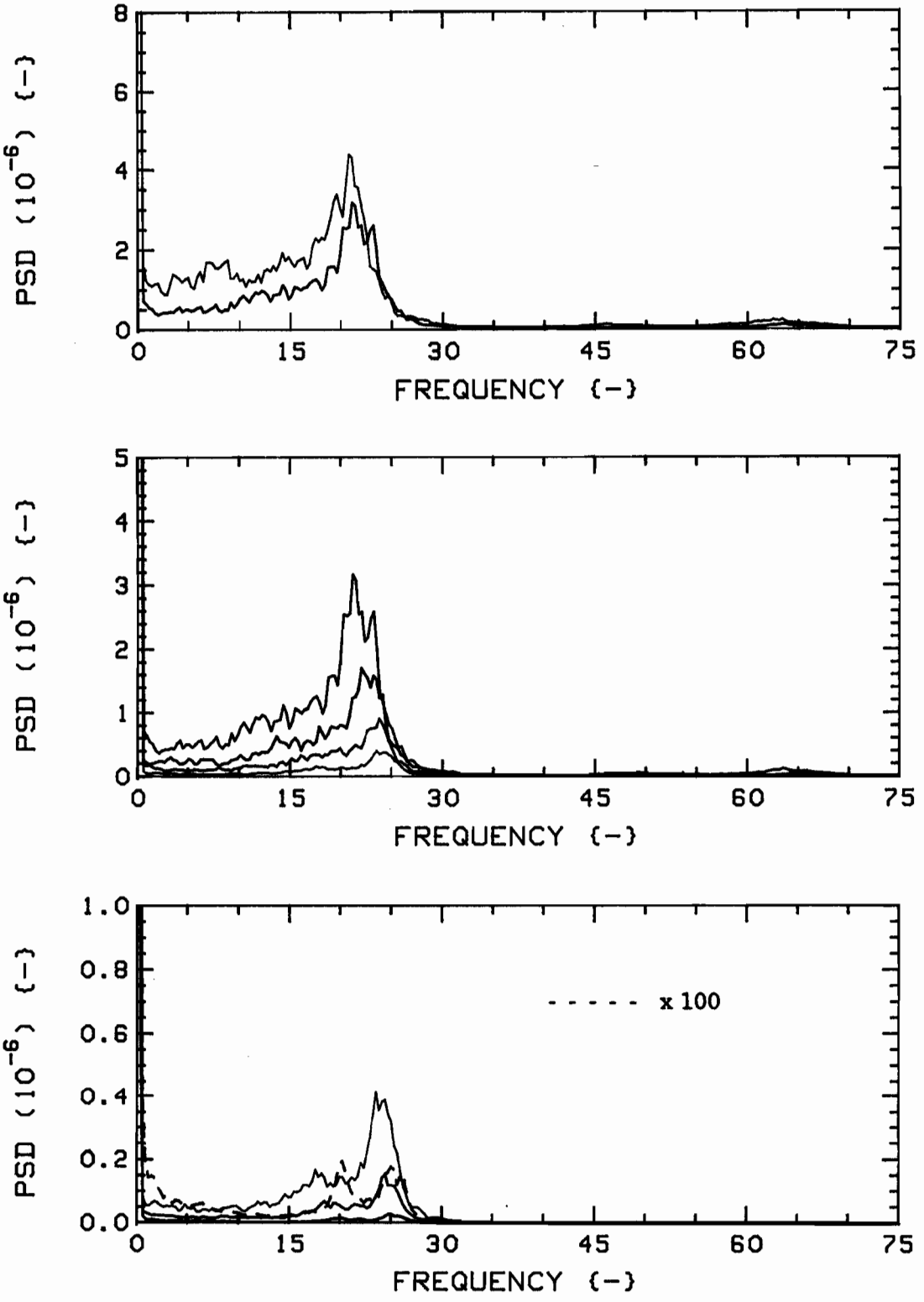

Fig.91a: Measured vibration PSD's for K = 28, G_c = 0.75, 4F(1,2,3,4) /24R, Radial direction, versus flow velocity. In descending order, u = 4.0 to 0.5, in steps of 0.5. Colour sequence: BLUE, BLACK, RED, GREEN (lowest trace of each plot is highest of the next one).

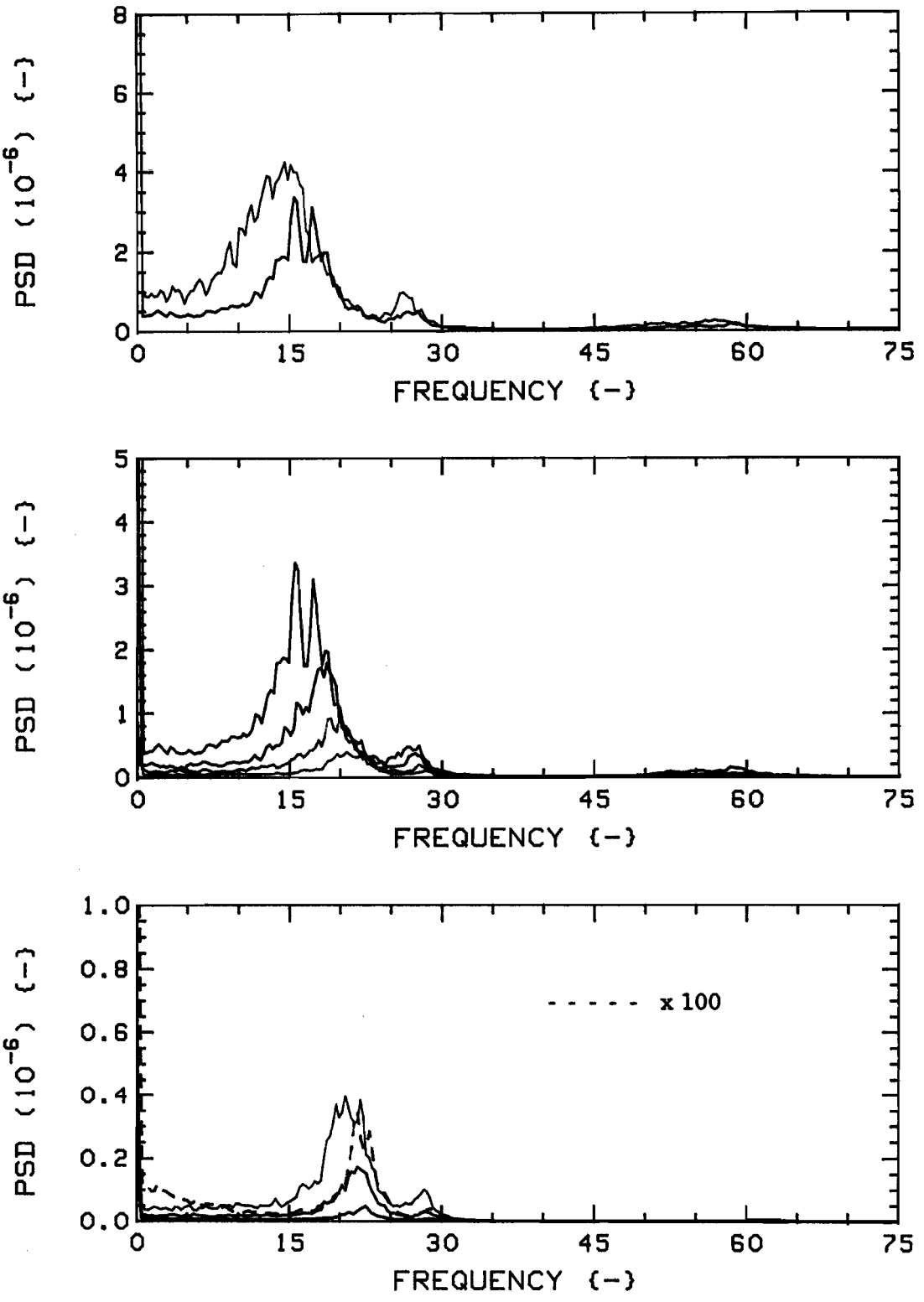

Fig.91b: Measured vibration PSD's for K = 28, G_c = 0.75, 4F(1,2,3,4) /24R, Tangential direction, versus flow velocity. In descending order, u = 4.0 to 0.5, in steps of 0.5. Colour sequence: BLUE, BLACK, RED, GREEN (lowest trace of each plot is highest of the next one).

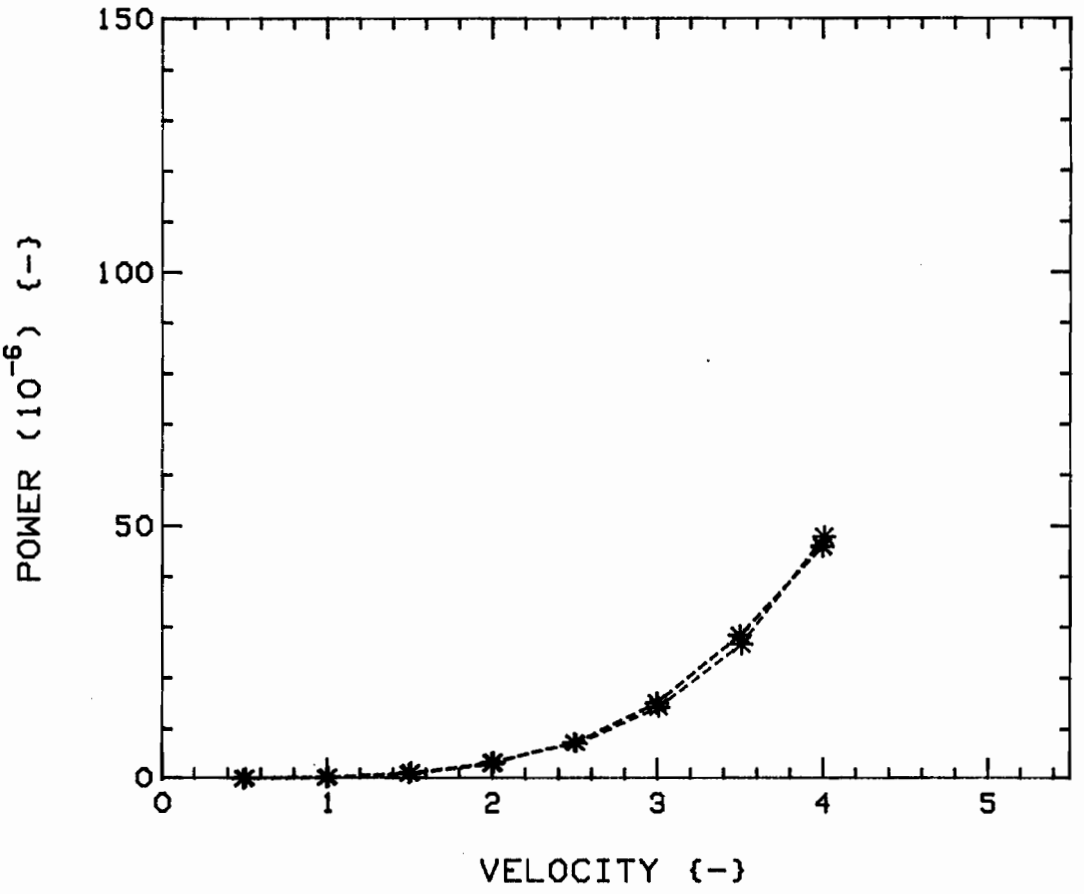

Fig.92: Powers versus flow velocity, for K = 28, G_c = 0.75, 4F(1,2,3,4)/24R, from (integrated) PSD's of Figs. 91a and 91b. Radial (RED) and Tangential (BLUE) directions.

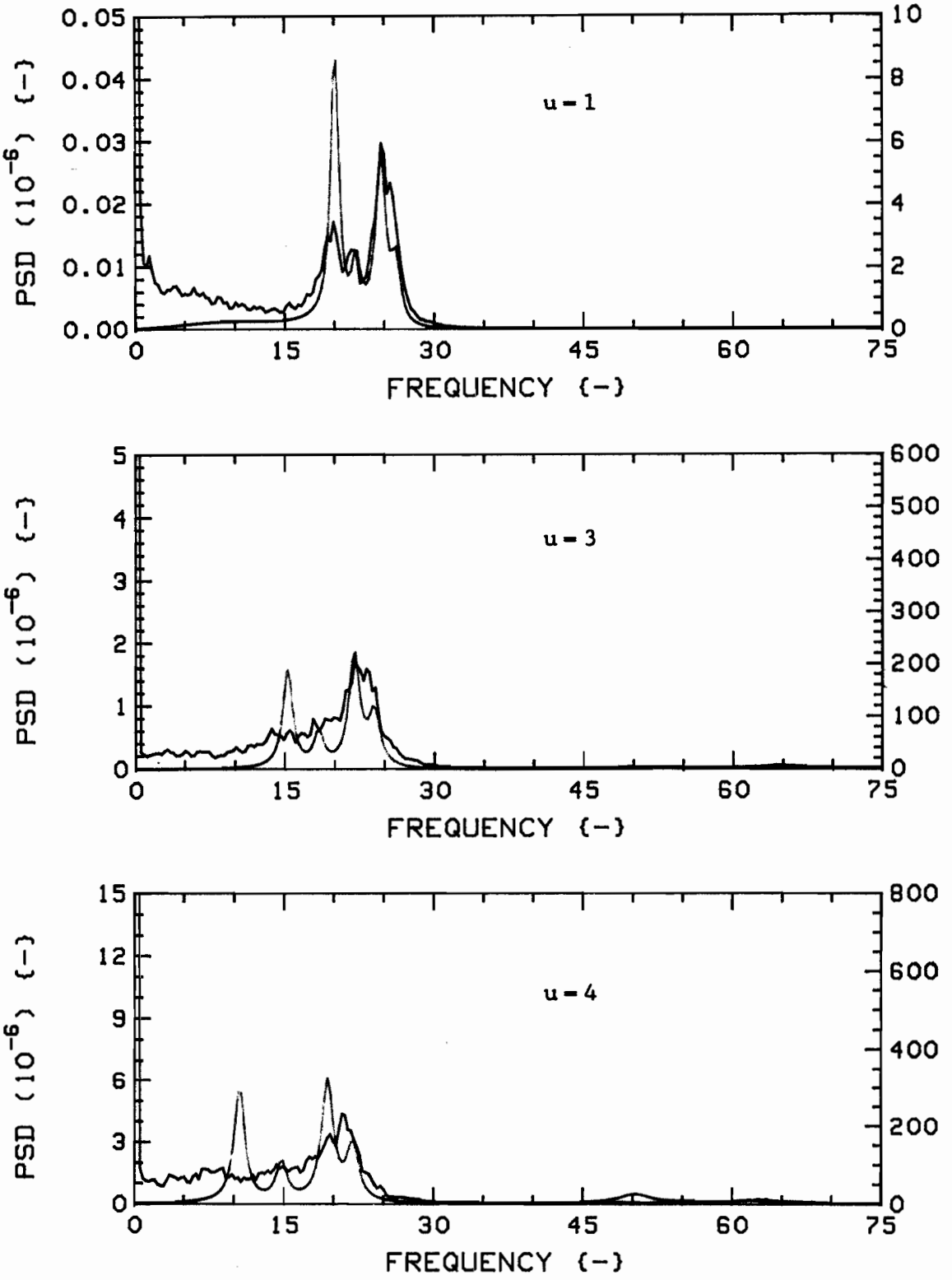

Fig.93a: Measured (RED) and theoretical (GREEN) vibration PSD's for K = 28, G_c = 0.75, 4F(1,2,3,4)/24R, Radial direction.

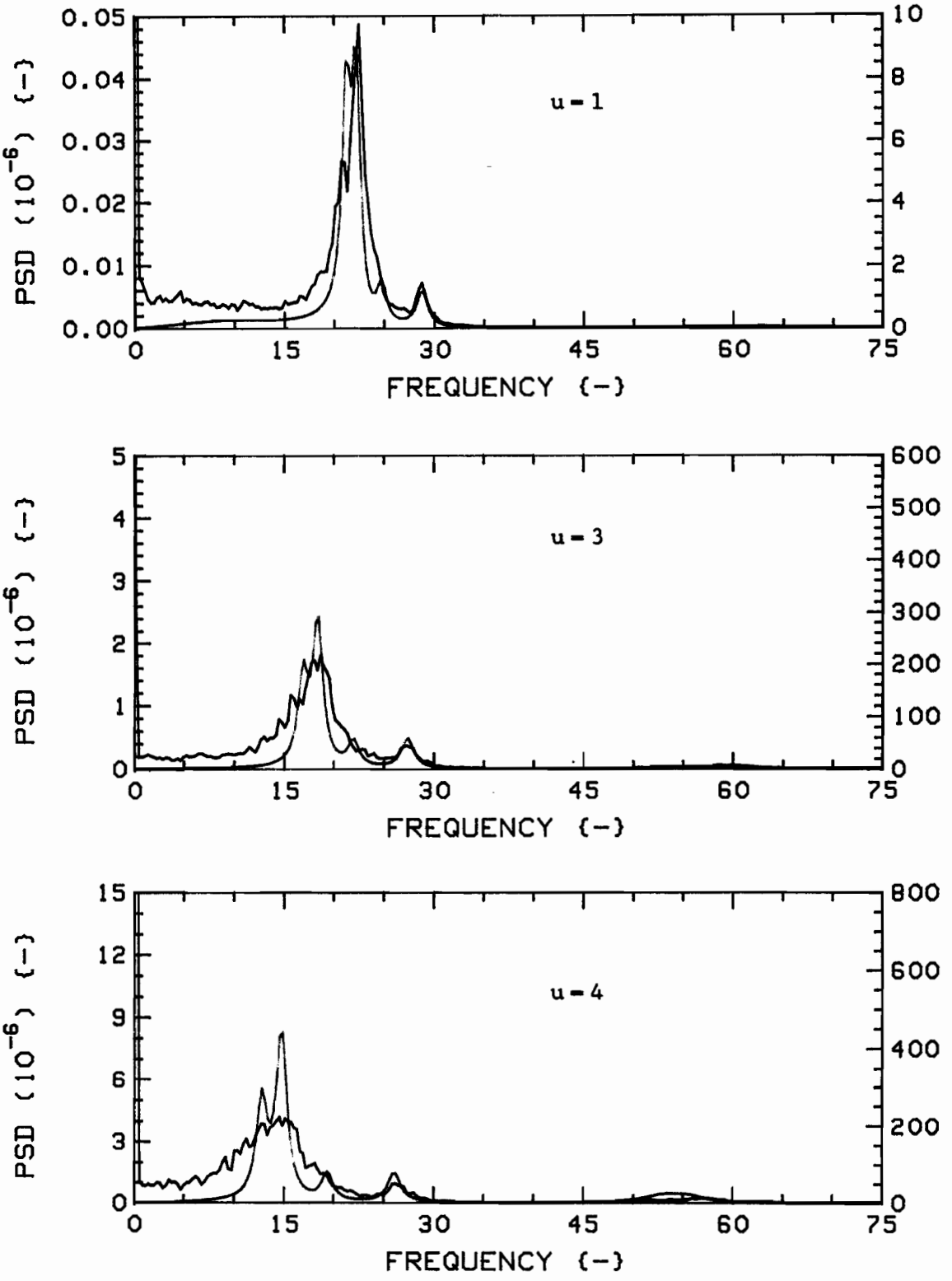

Fig.93b: Measured (RED) and theoretical (GREEN) vibration PSD's for K = 28, G_c = 0.75, 4F(1,2,3,4)/24R, Tangential direction.

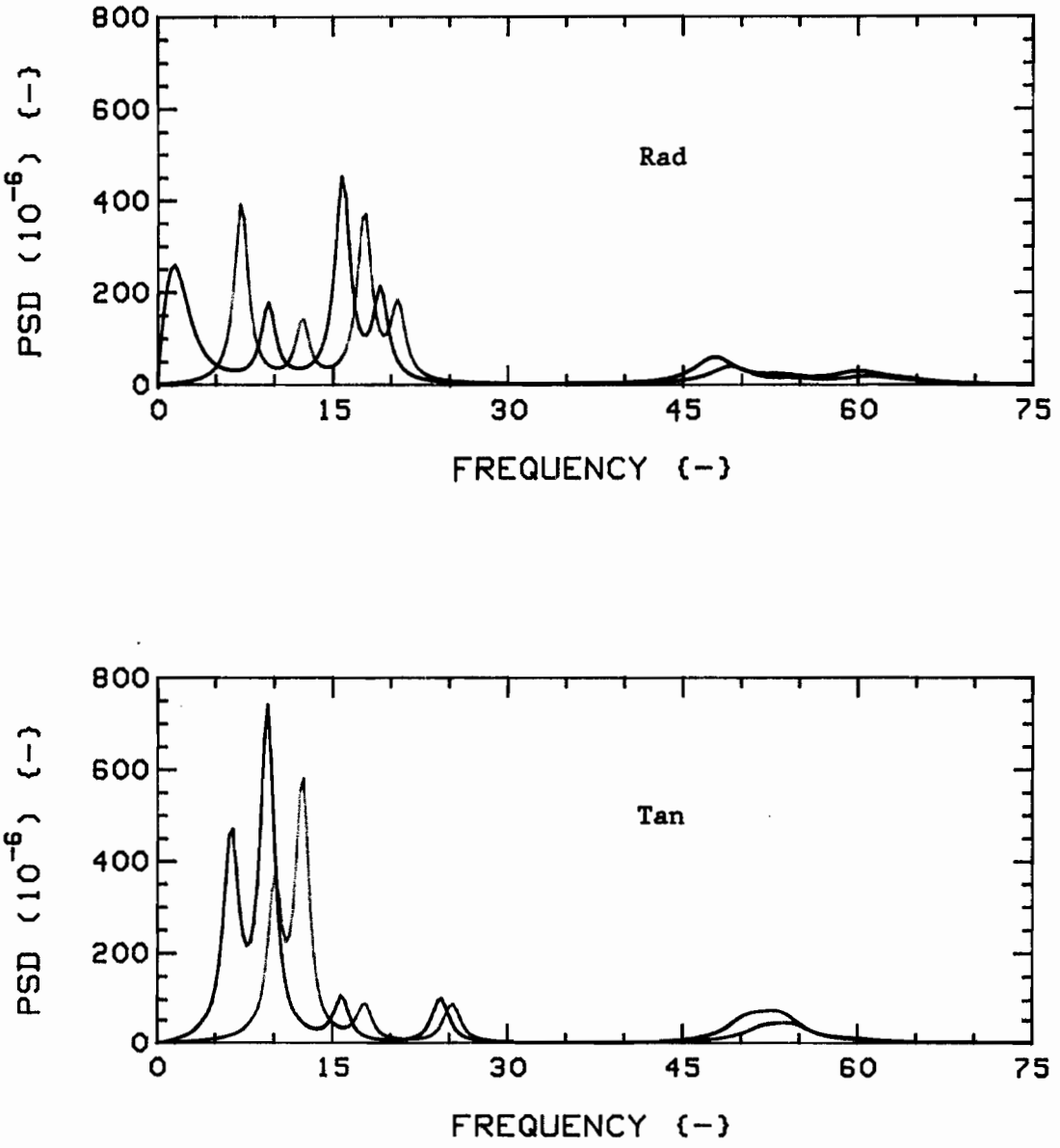

Fig.94: Theoretical PSD's for K = 28, G_c = 0.75, 4F(1,2,3,4)/24R, at u = 4.5 (GREEN) and u = 5.0 (RED).

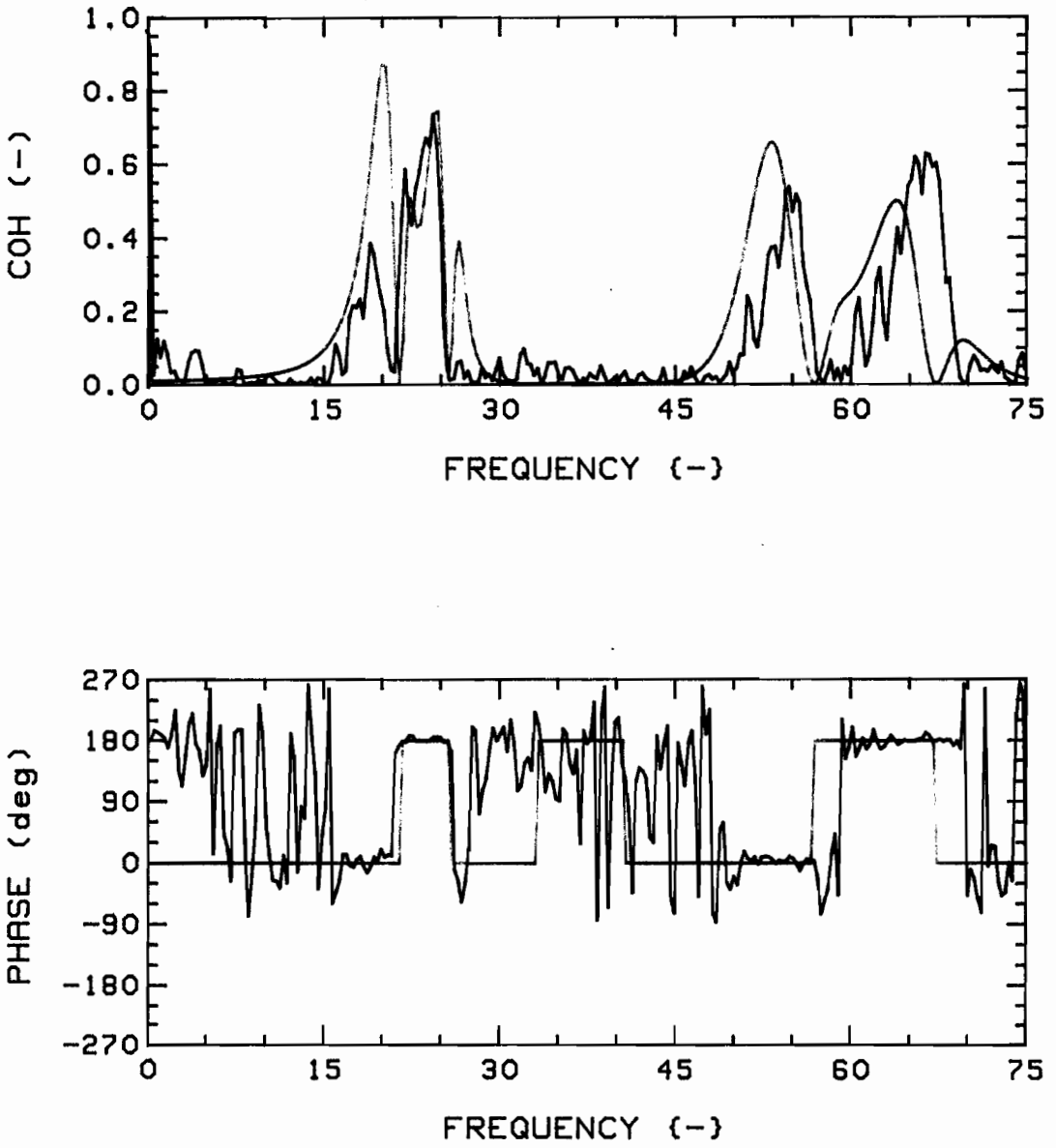

Fig.95a: Measured (RED) and theoretical (GREEN) coherence functions and phases, for K = 28, G_c = 0.75, 4F(1,2,3,4) /24R, R-R (1,3), at u = 1.

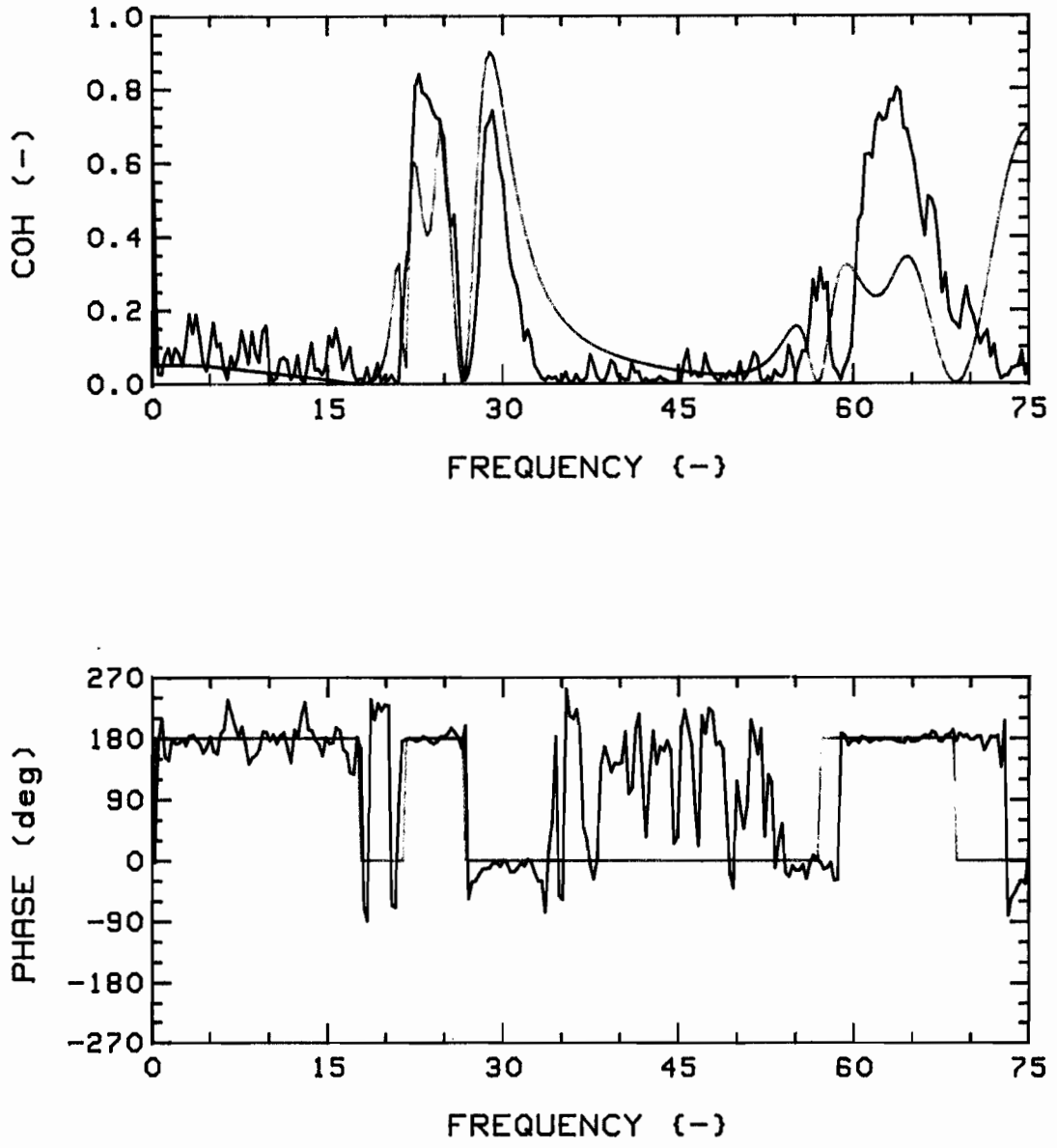

Fig.95b: Measured (RED) and theoretical (GREEN) coherence functions and phases, for K = 28, G_c = 0.75, 4F(1,2,3,4) /24R, T-T (1,3), at u = 1.

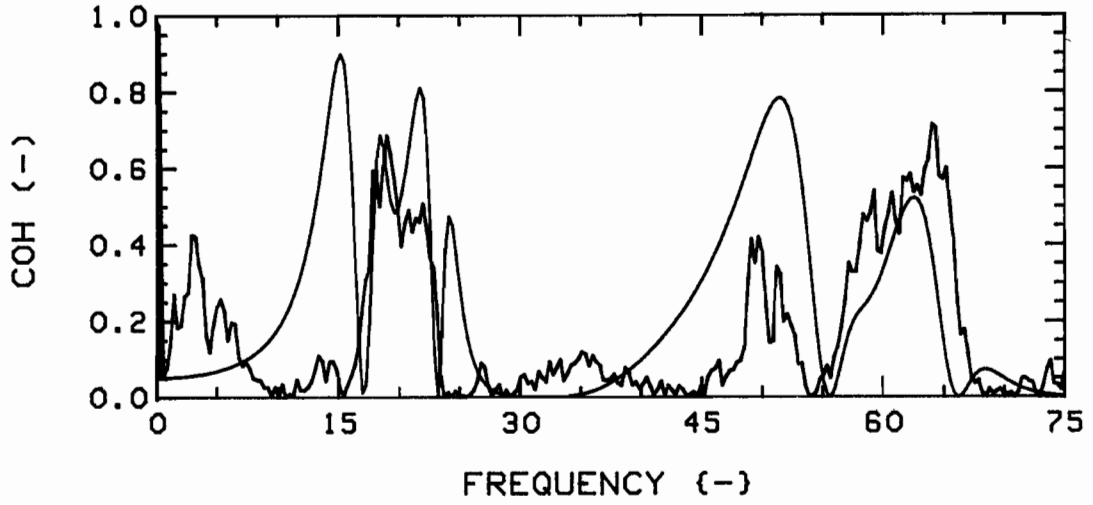

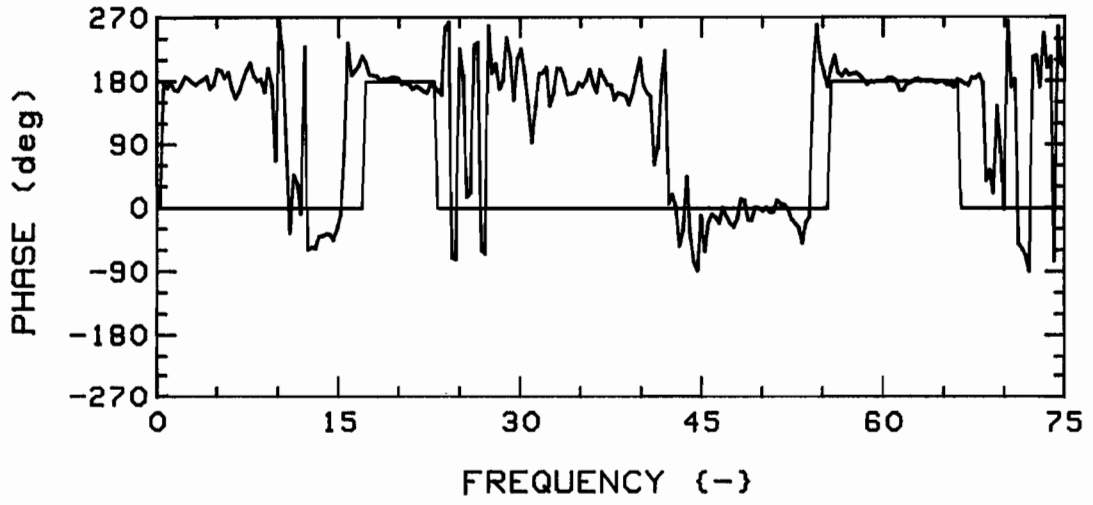

Fig.95c: Measured (RED) and theoretical (GREEN) coherence functions and phases, for K = 28, G_c = 0.75, 4F(1,2,3,4) /24R, R-R (1,3), at u = 3.

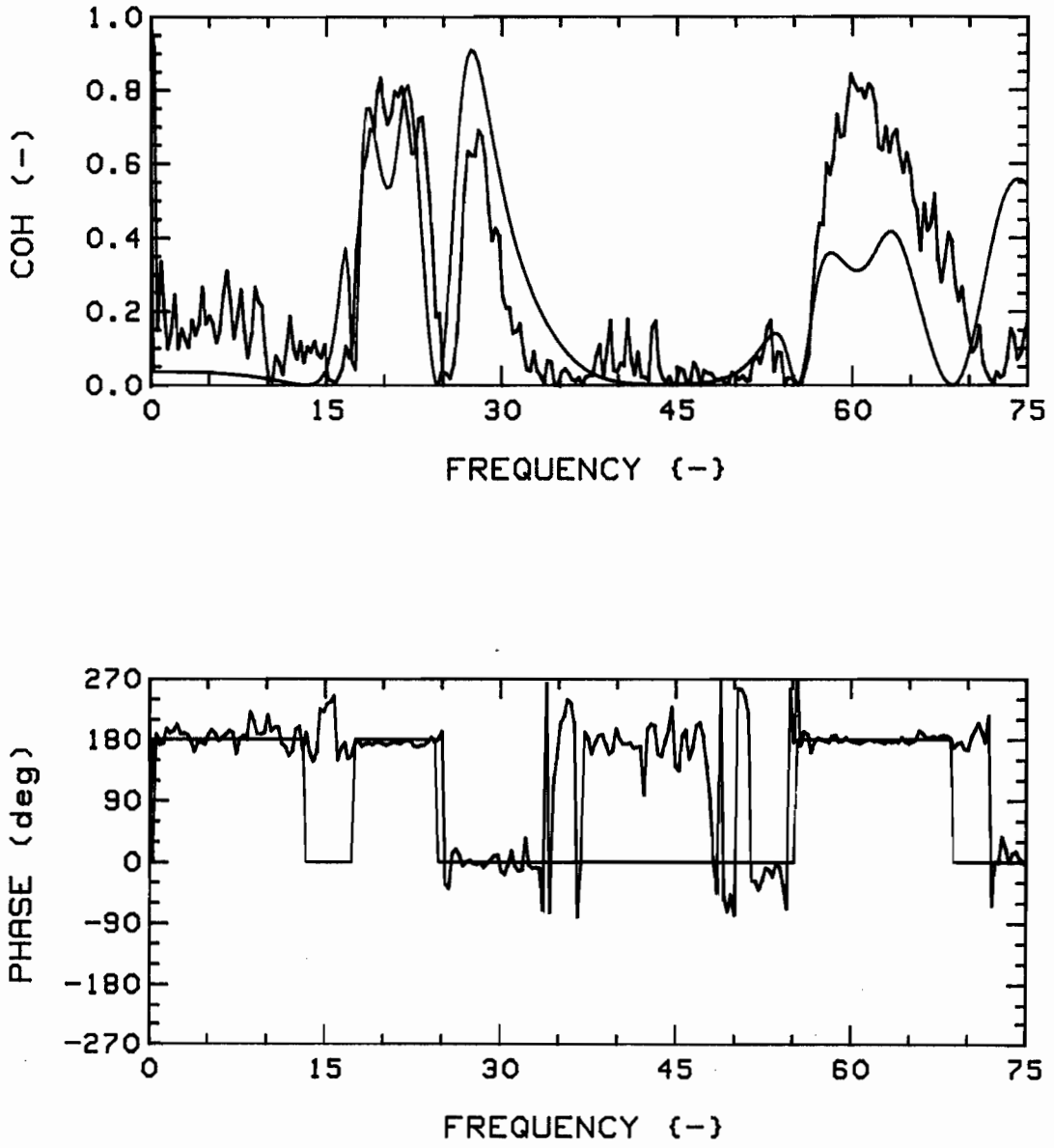

Fig.95d: Measured (RED) and theoretical (GREEN) coherence functions and phases, for K = 28, G_c = 0.75, 4F(1,2,3,4) /24R, T-T (1,3), at u = 3.

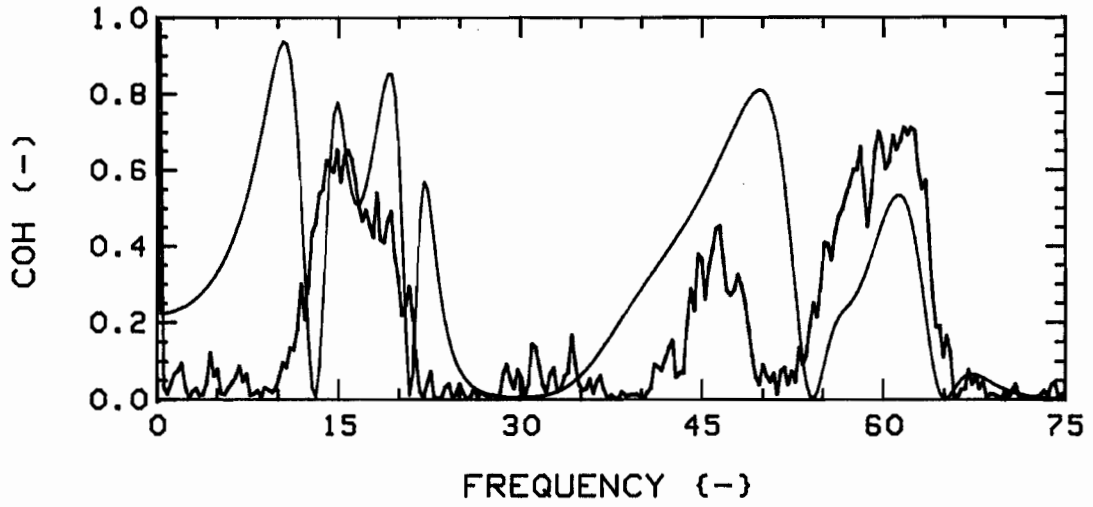

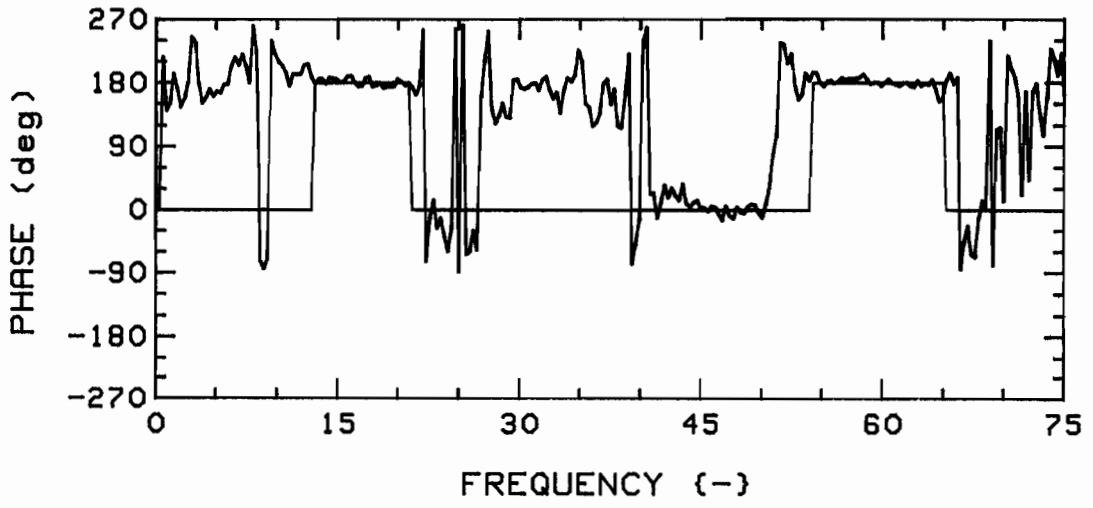

Fig.95e: Measured (RED) and theoretical (GREEN) coherence functions and phases, for K = 28, G_c = 0.75, 4F(1,2,3,4) /24R, R-R (1,3), at u = 4.

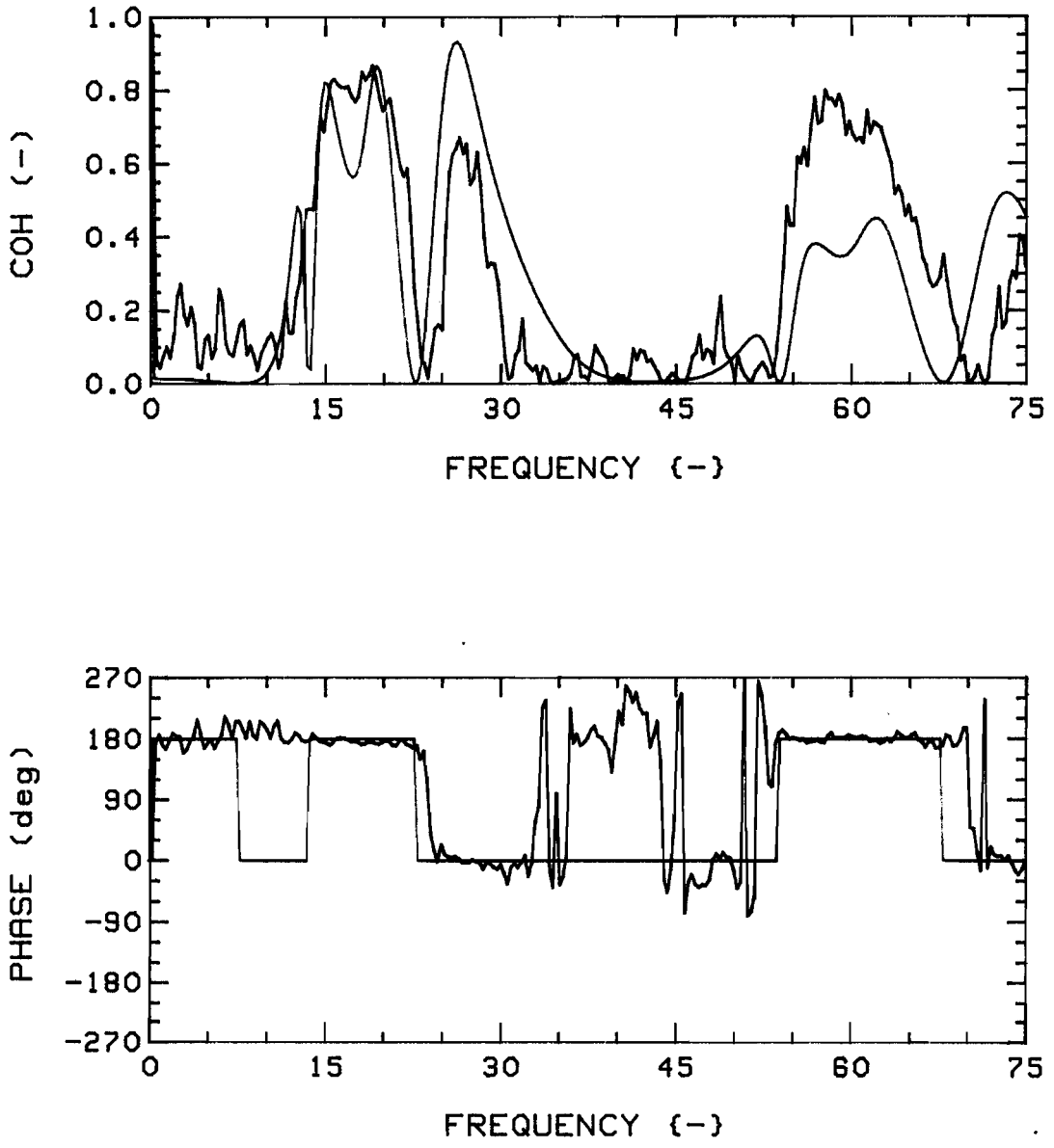

Fig.95f: Measured (RED) and theoretical (GREEN) coherence functions and phases, for K = 28, $G_c = 0.75$, 4F(1,2,3,4) /24R, T-T (1,3), at u = 4.

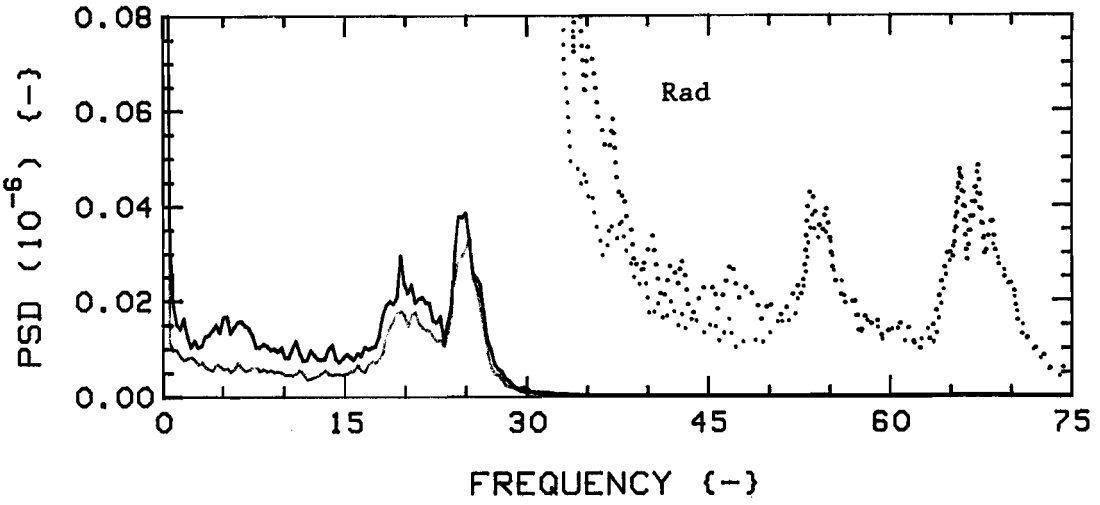

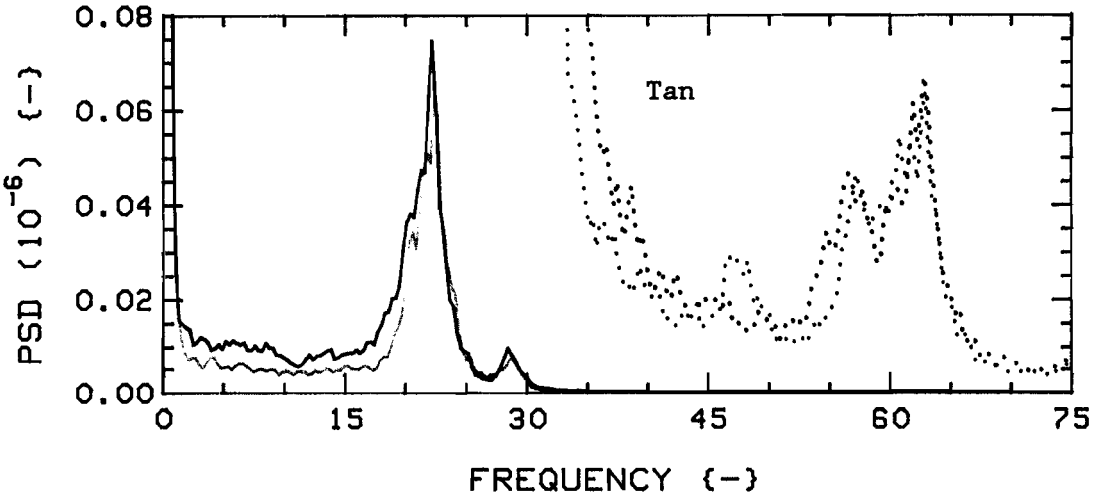

Fig.96a: Measured vibration PSD's for K = 28, G_c = 0.75, 4F(6,7,1,2) /24R, at u = 1.0; Position 7 (RED) versus Position 1 (GREEN).

The dotted traces are expansions of the solid ones, with a scale of 3.0×10^{-10}.

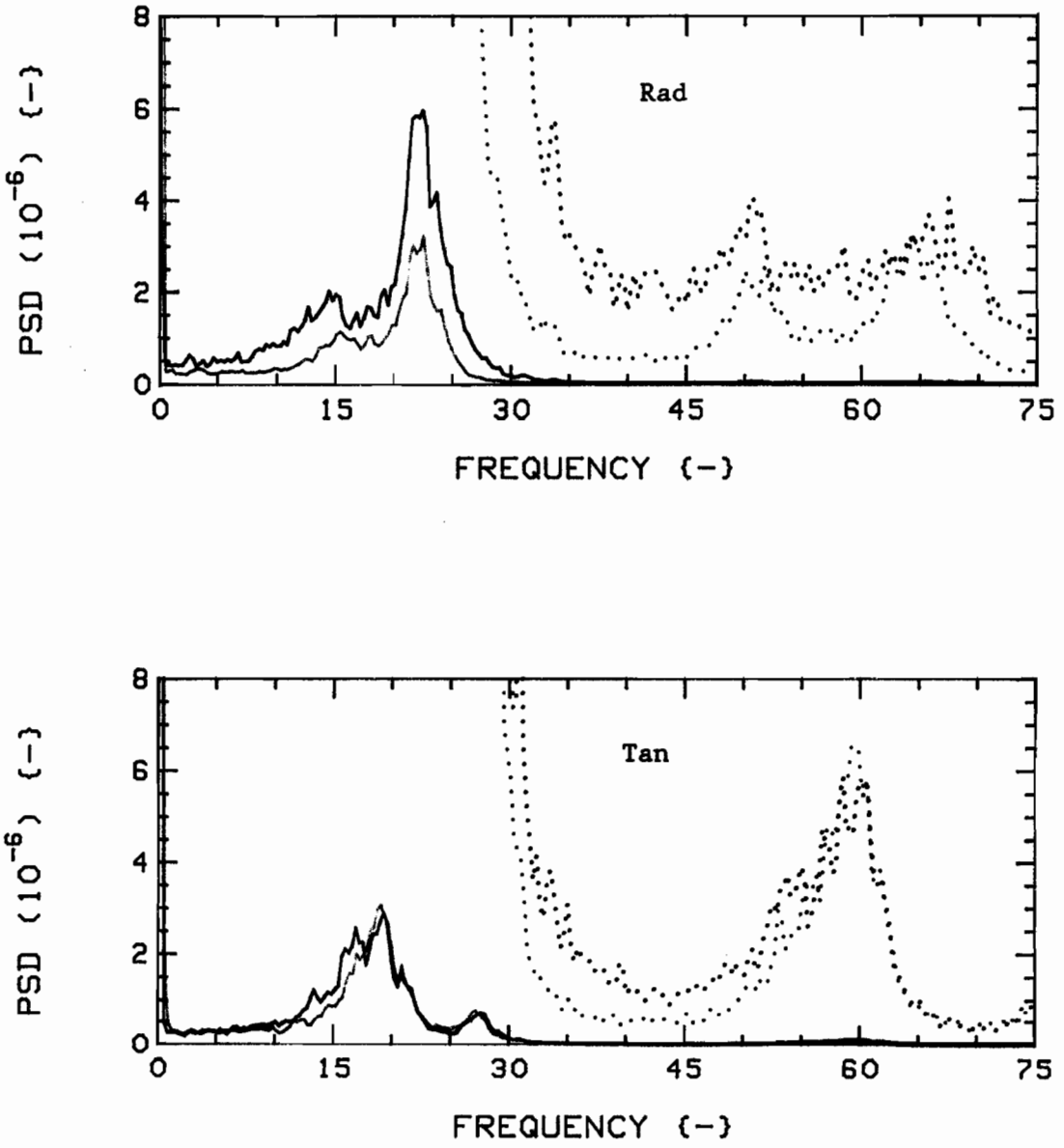

Fig.96b: Measured vibration PSD's for K = 28, G_c = 0.75, 4F(6,7,1,2) /24R, at u = 3.0; Position 7 (RED) versus Position 1 (GREEN).

The dotted traces are expansions of the solid ones, with a scale of 1.5×10^{-7}.

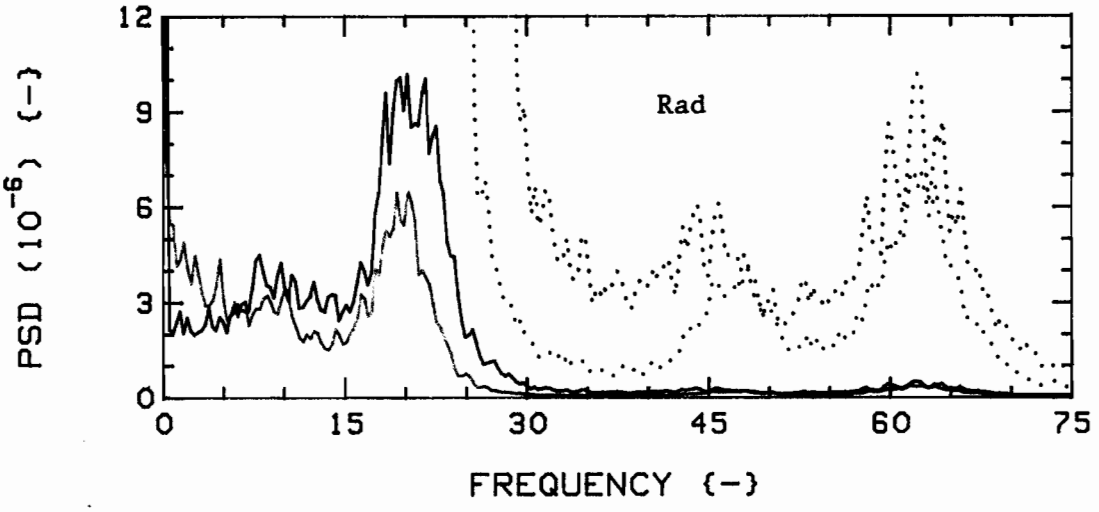

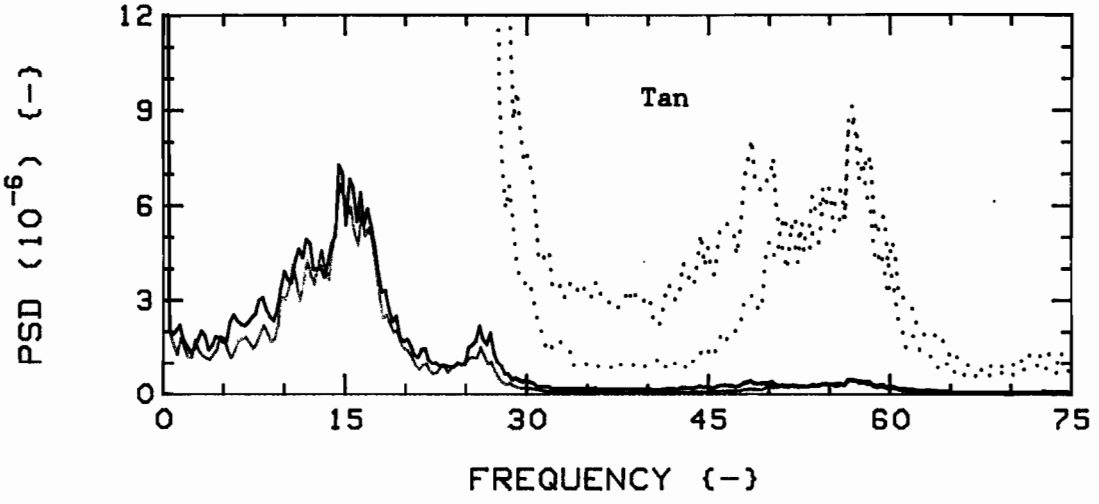

Fig.96c: Measured vibration PSD's for K = 28, G_c = 0.75, 4F(6,7,1,2) /24R, at u = 4.0; Position 7 (RED) versus Position 1 (GREEN).

The dotted traces are expansions of the solid ones, with a scale of 6.0×10^{-7}.

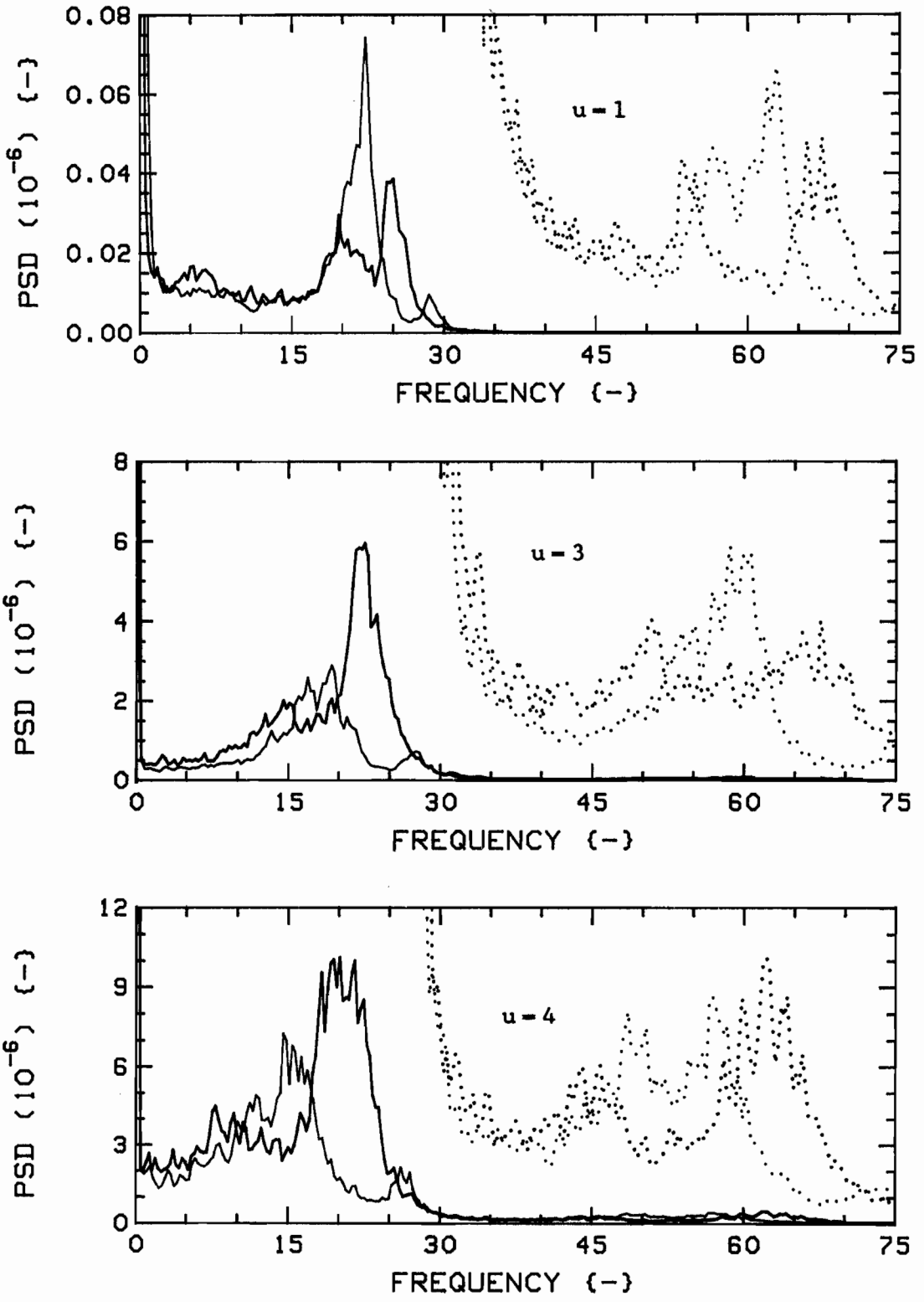

Fig.97a: Measured vibration PSD's for K = 28, G_c = 0.75, 4F(6,7,1,2)/24R, in Position 7, Radial (RED) and Tangential (BLUE) directions.

The dotted traces are expansions of the solid ones; scales are, from top: 3.0×10^{-10}, 1.5×10^{-7}, 6.0×10^{-7}.

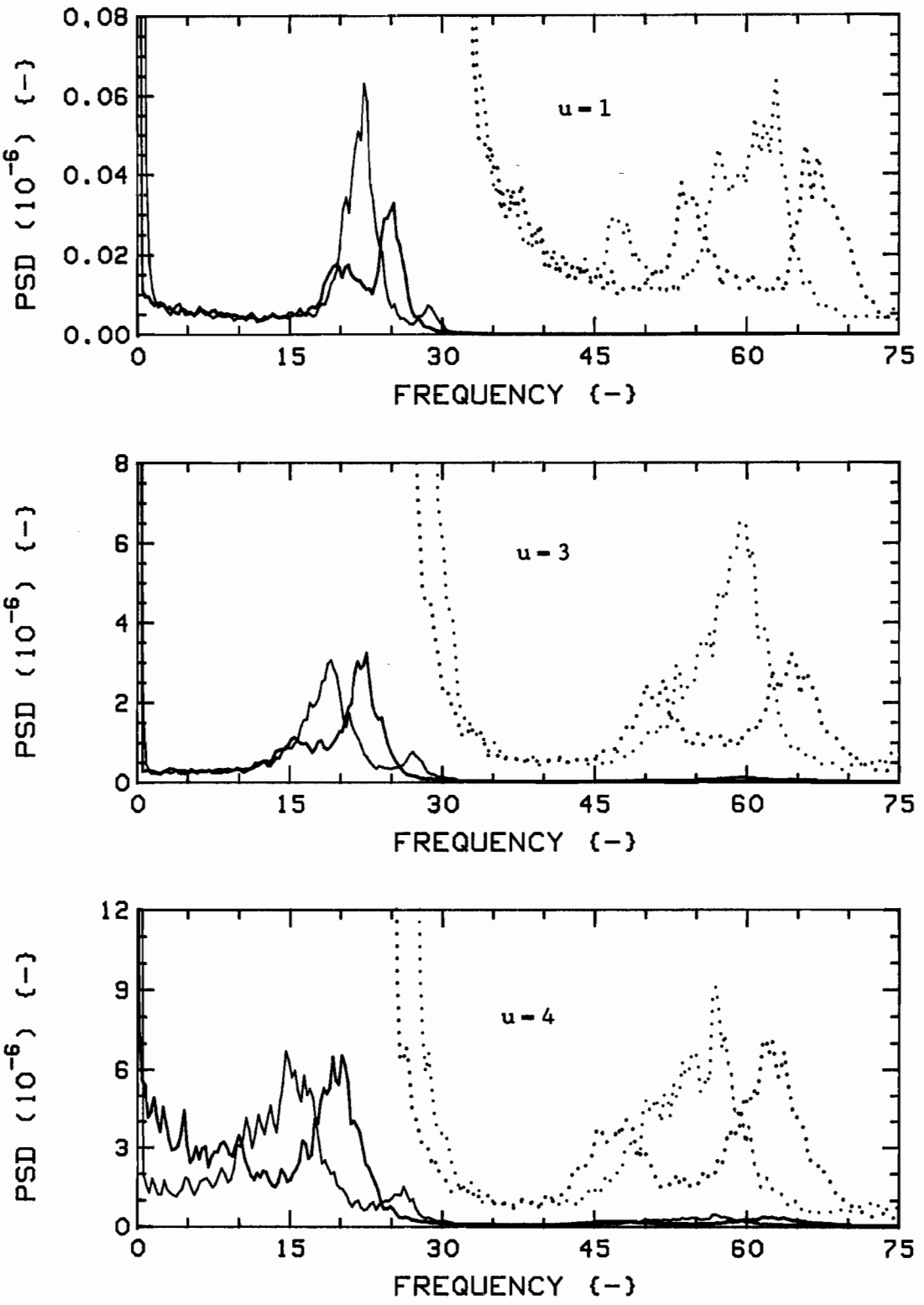

Fig.97b: Measured vibration PSD's for K = 28, $G_c = 0.75$, 4F(6,7,1,2)/24R, in Position 1, Radial (RED) and Tangential (BLUE) directions.

The dotted traces are expansions of the solid ones; scales are, from top: 3.0×10^{-10}, 1.5×10^{-7}, 6.0×10^{-7}.

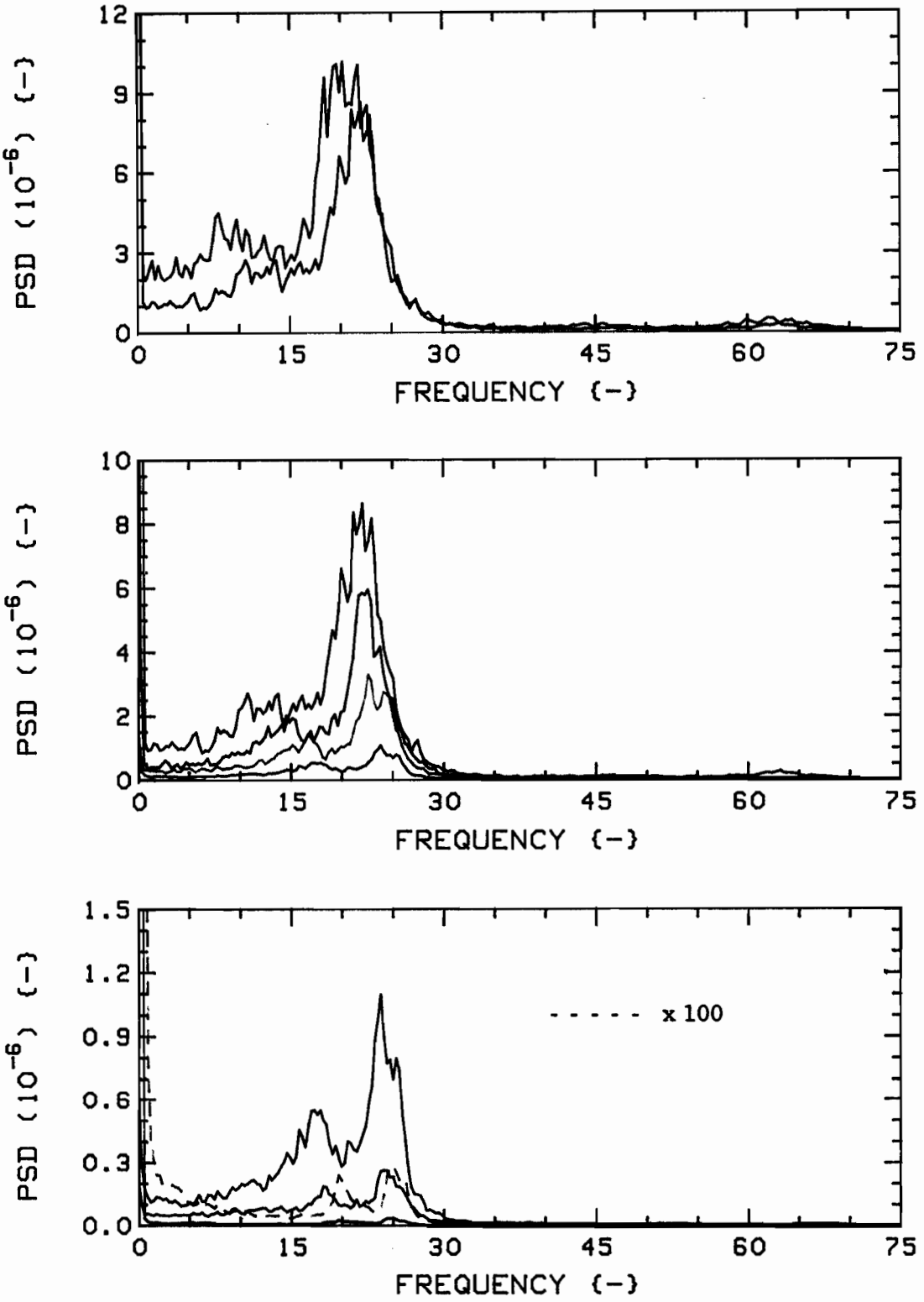

Fig.98a: Measured vibration PSD's for K = 28, G_c = 0.75, 4F(6,7,1,2) /24R, Position 7 in Radial direction, versus flow velocity. In descending order, u = 4.0 to 0.5, in steps of 0.5. Colour sequence: BLUE, BLACK, RED, GREEN (lowest trace of each plot is highest of the next one).

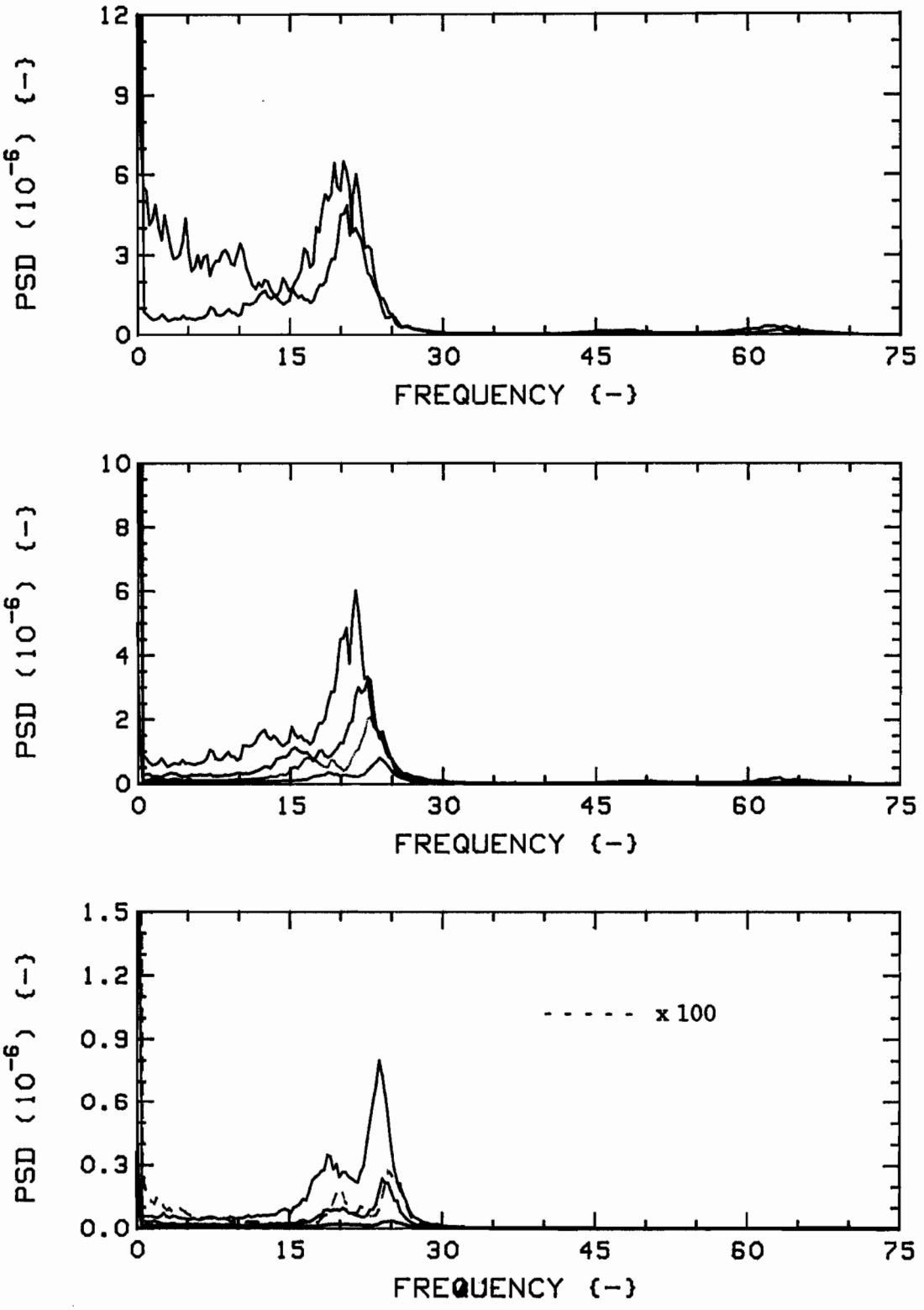

Fig.98b: Measured vibration PSD's for K = 28, G_c = 0.75, 4F(6,7,1,2) /24R, Position 1 in Radial direction, versus flow velocity. In descending order, u = 4.0 to 0.5, in steps of 0.5. Colour sequence: BLUE, BLACK, RED, GREEN (lowest trace of each plot is highest of the next one).

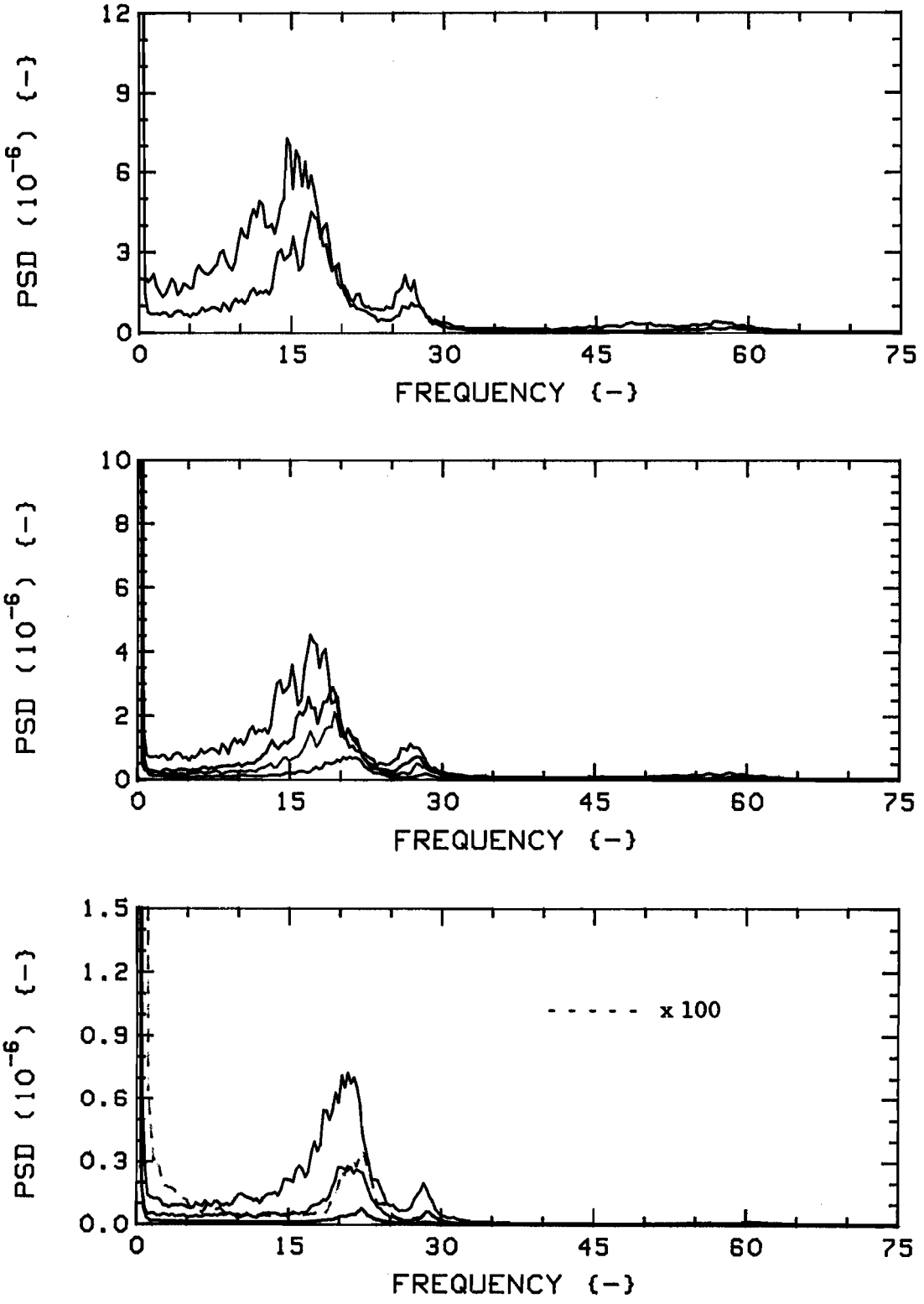

Fig.98c: Measured vibration PSD's for K = 28, G_c = 0.75, 4F(6,7,1,2) /24R, Position 7 in Tangential direction, versus flow velocity. In descending order, u = 4.0 to 0.5, in steps of 0.5. Colour sequence: BLUE, BLACK, RED, GREEN (lowest trace of each plot is highest of the next one).

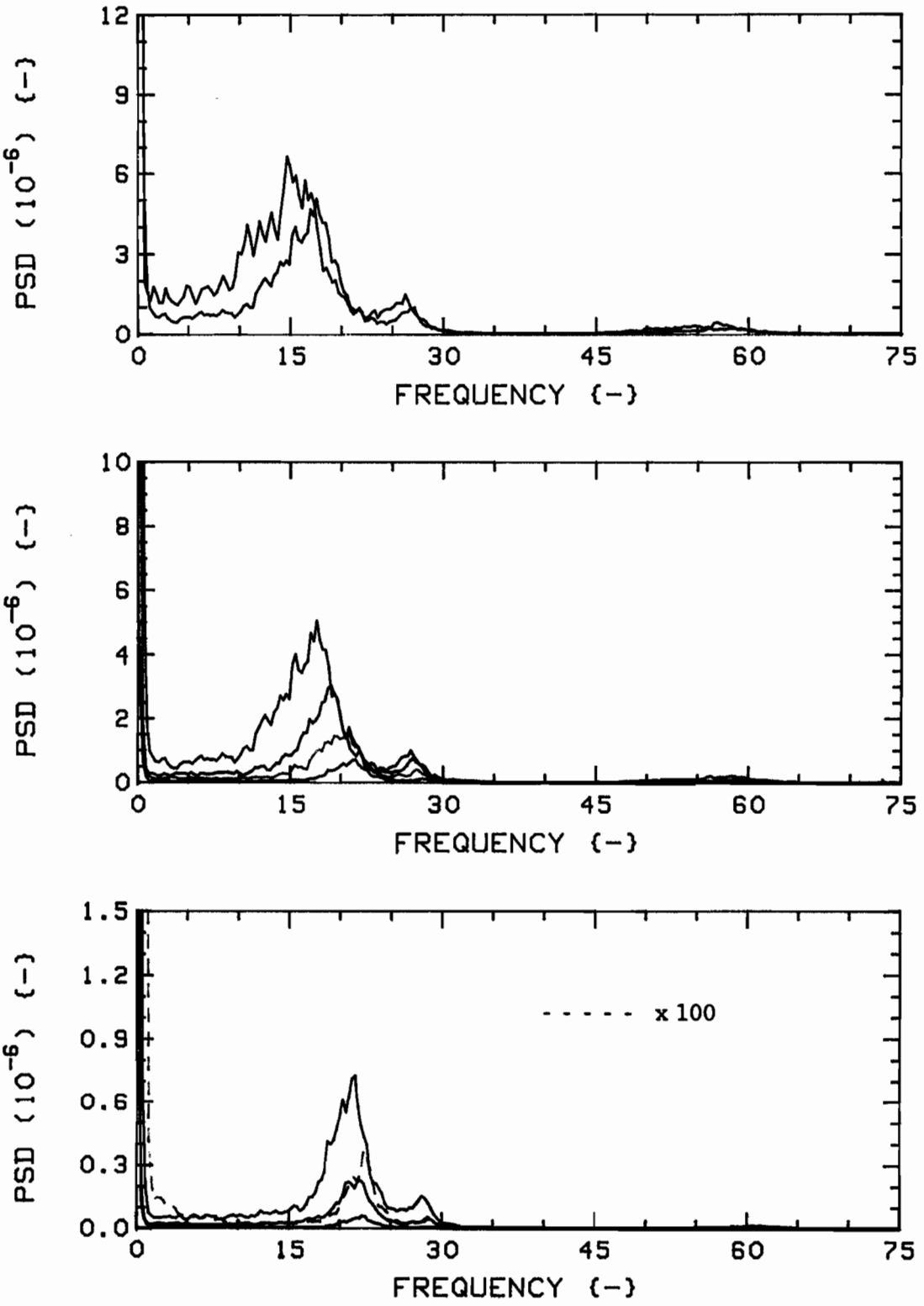

Fig.98d: Measured vibration PSD's for K = 28, G_c = 0.75, 4F(6,7,1,2) /24R, Position 1 in Tangential direction, versus flow velocity. In descending order, u = 4.0 to 0.5, in steps of 0.5. Colour sequence: BLUE, BLACK, RED, GREEN (lowest trace of each plot is highest of the next one).

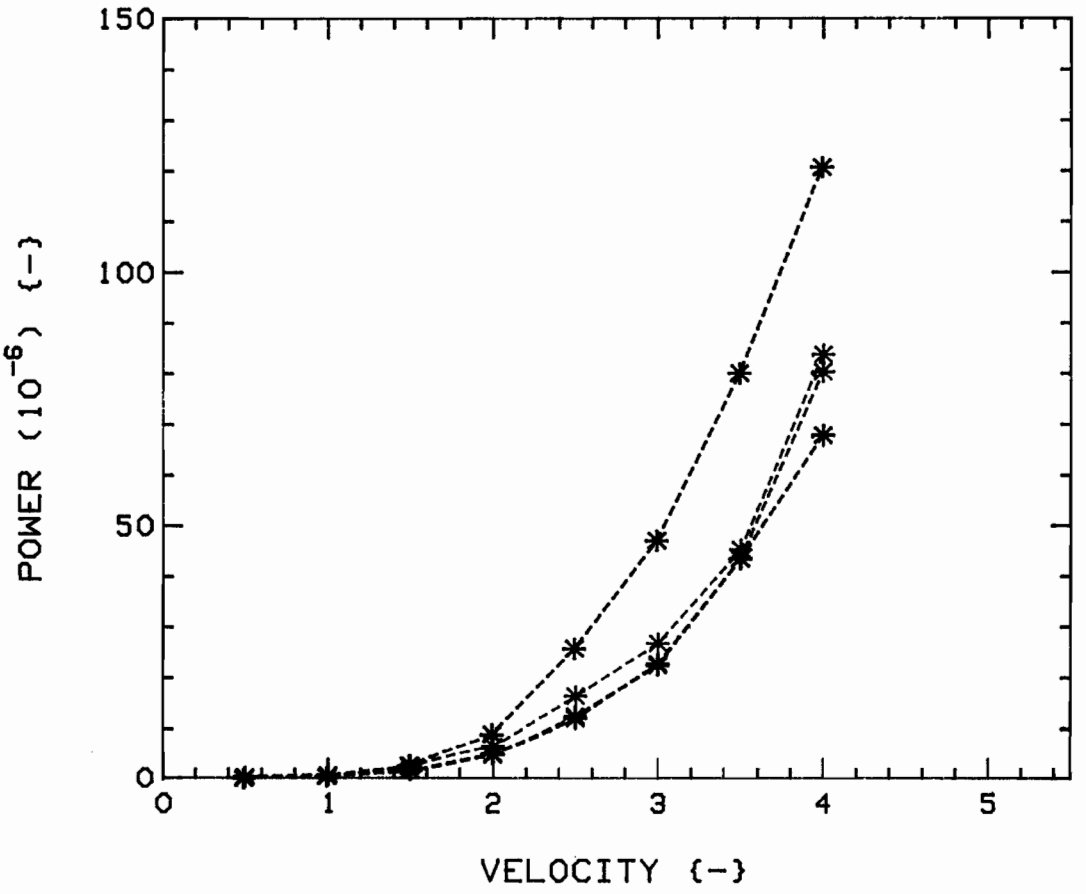

Fig.99: Powers versus flow velocity, for K = 28, G_c = 0.75, 4F(6,7,1,2)/24R, from (integrated) PSD's of Figs. 98a 98b, 98c and 98d. Radial direction, Positions 7 and 1 (RED and GREEN) and Tangential direction, Positions 7 and 1 (BLUE and BLACK).

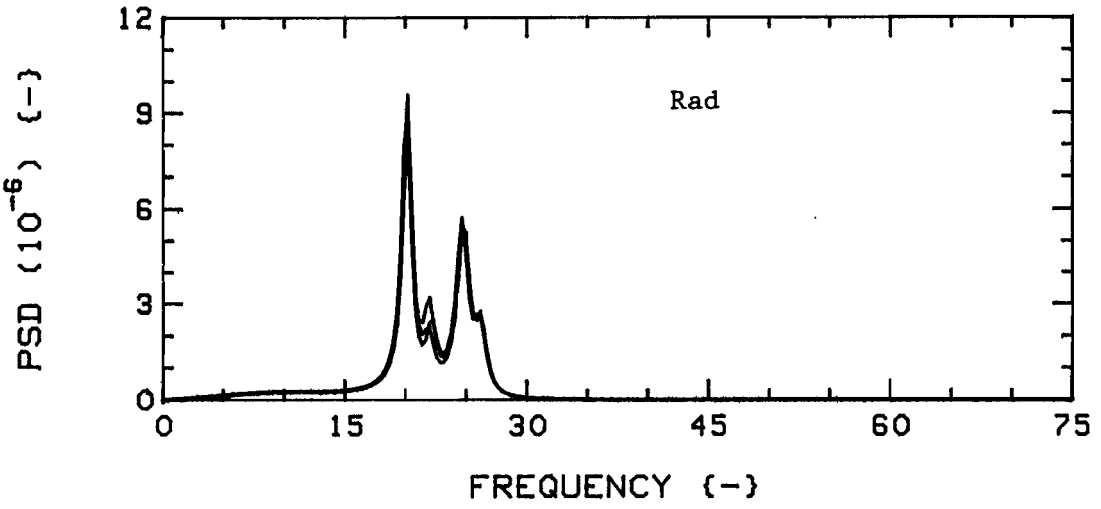

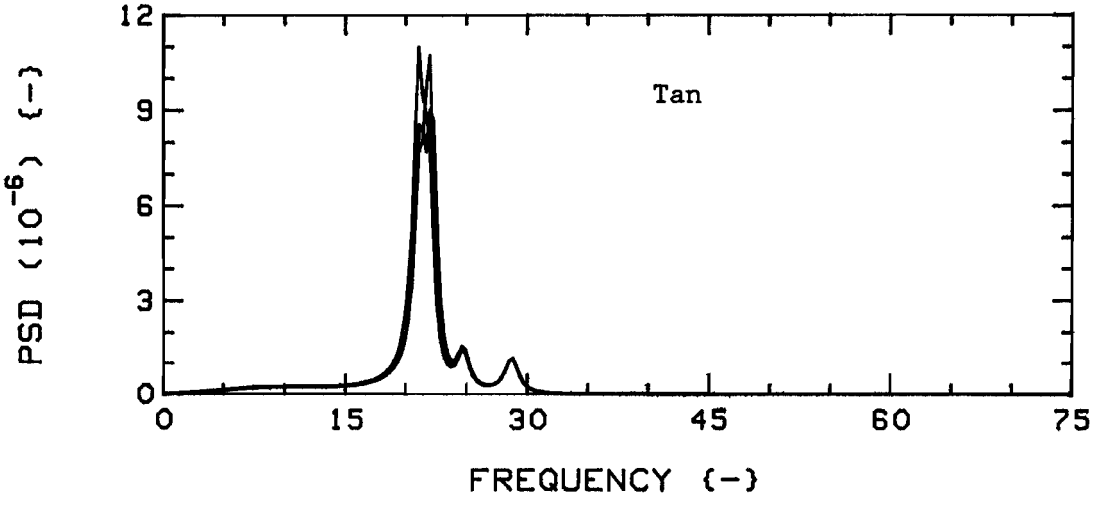

Fig.100a: Theoretical vibration PSD's for K = 28, G_c = 0.75, 4F/24R, at u = 1; central, Position 1 (RED) versus parallel offset system, Position 7 (GREEN) and Position 1 (BLUE).

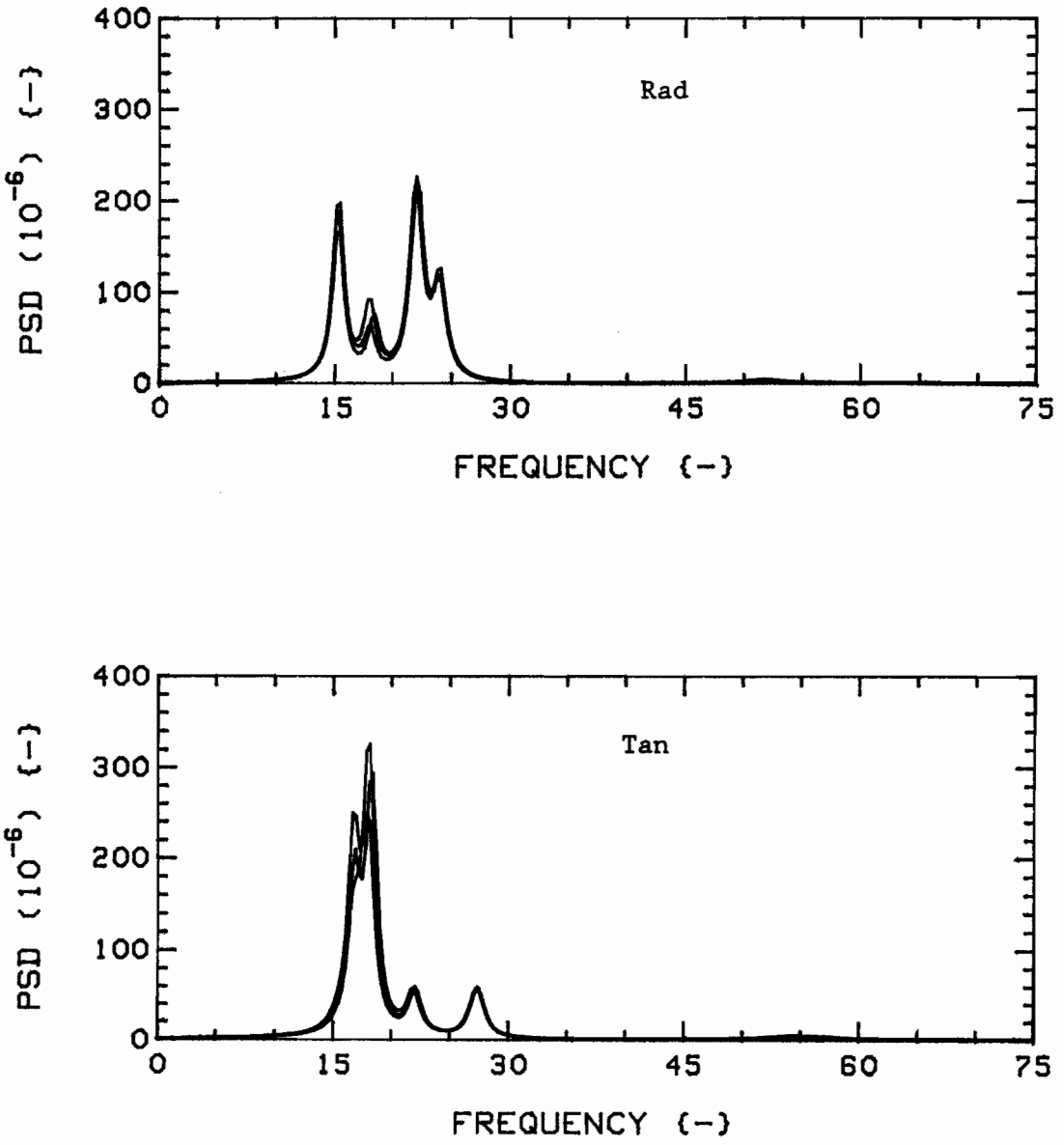

Fig.100b: Theoretical vibration PSD's for K = 28, G_c = 0.75, 4F/24R, at u = 3; central, Position 1 (RED) versus parallel offset system, Position 7 (GREEN) and Position 1 (BLUE).

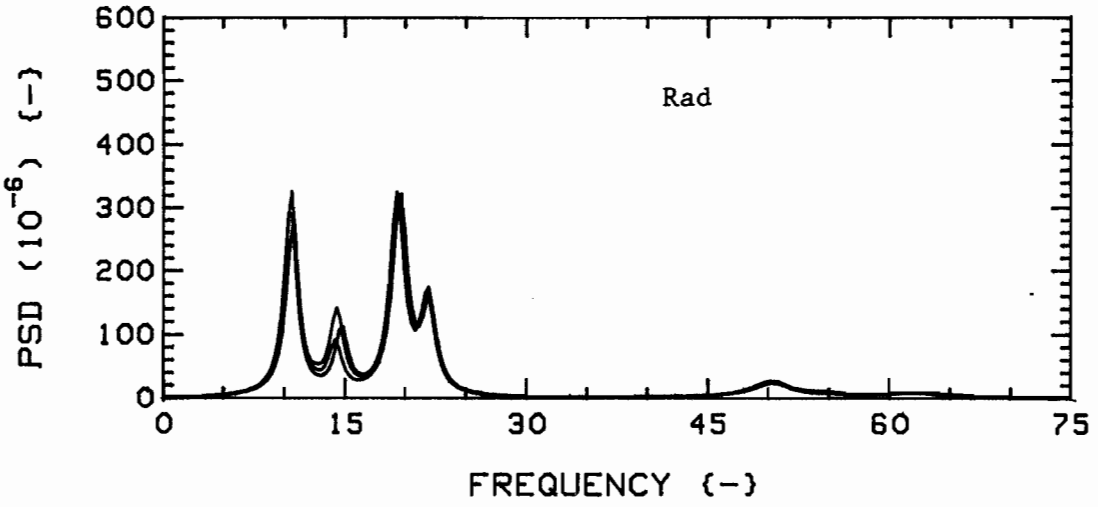

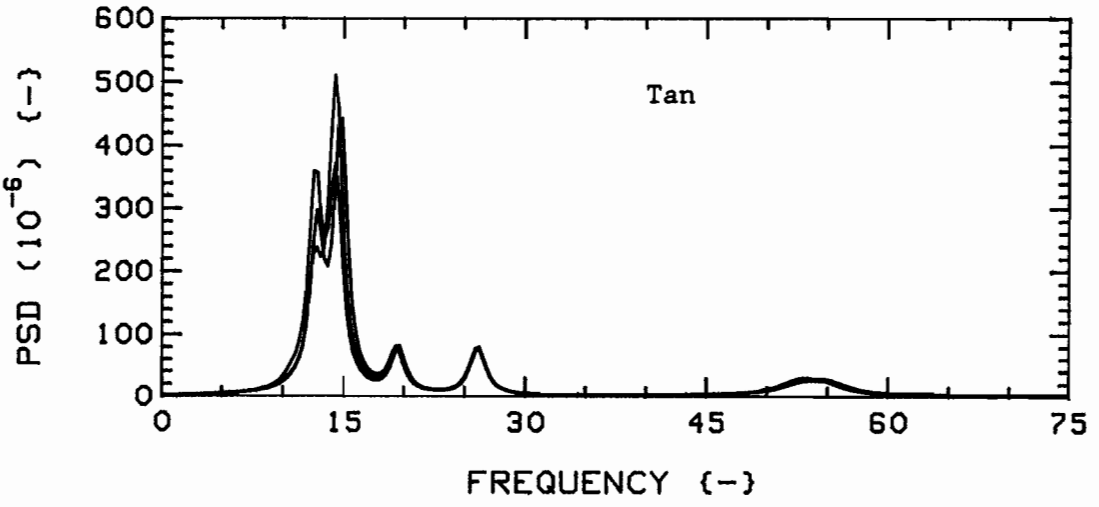

Fig.100c: Theoretical vibration PSD's for K = 28, G_c = 0.75, 4F/24R, at u = 4; central, Position 1 (RED) versus parallel offset system, Position 7 (GREEN) and Position 1 (BLUE).

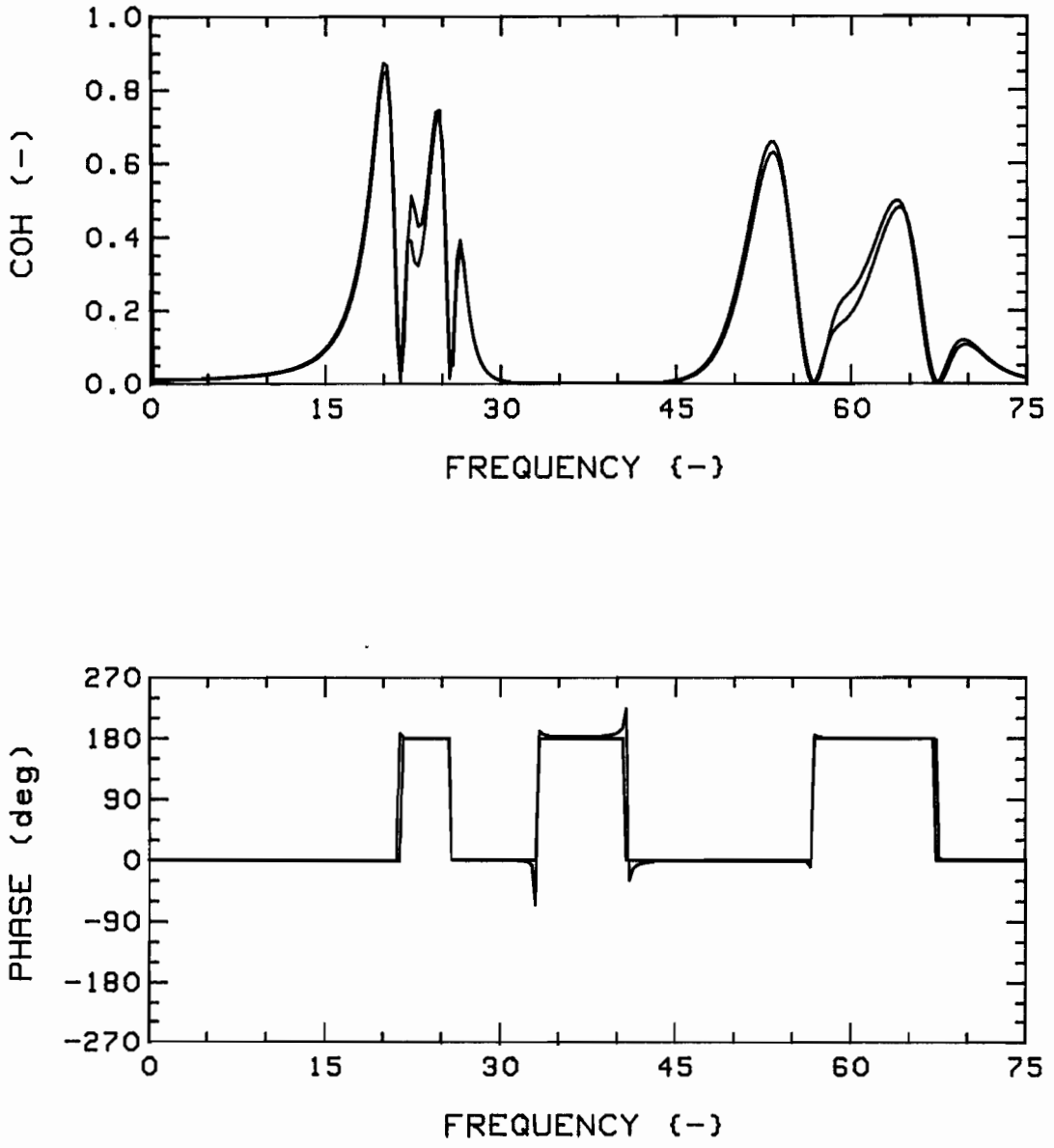

Fig.101a: Theoretical coherences for K = 28, G_c = 0.75, 4F/24R, R-R (diagonal pair), at u = 1; central (RED) versus parallel (GREEN) offset system.

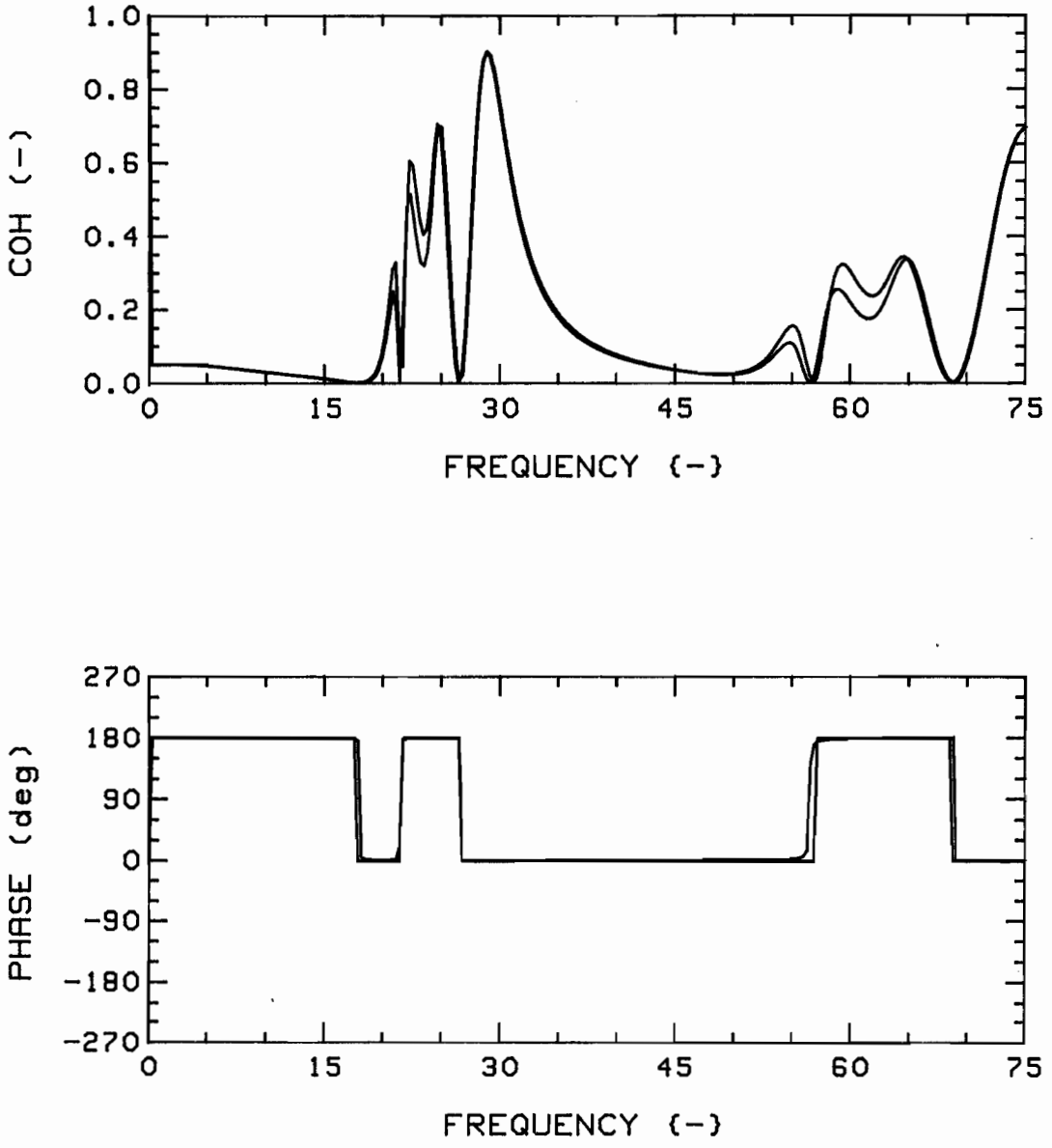

Fig.101b: Theoretical coherences for K = 28, G_c = 0.75, 4F/24R, T-T (diagonal pair), at u = 1; central (RED) versus parallel (GREEN) offset system.

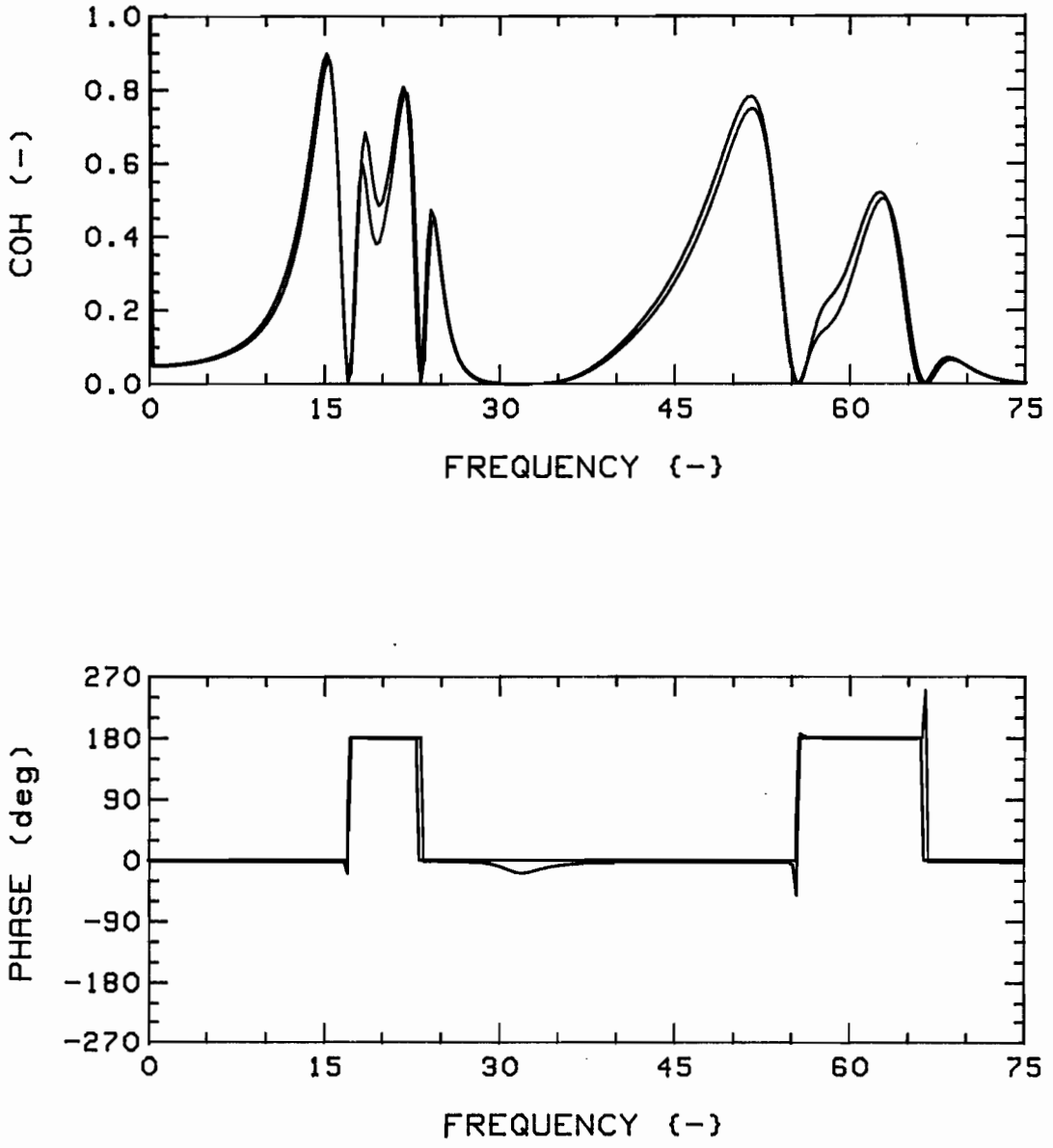

Fig.101c: Theoretical coherences for K = 28, G_c = 0.75, 4F/24R, R-R (diagonal pair), at u = 3; central (RED) versus parallel (GREEN) offset system.

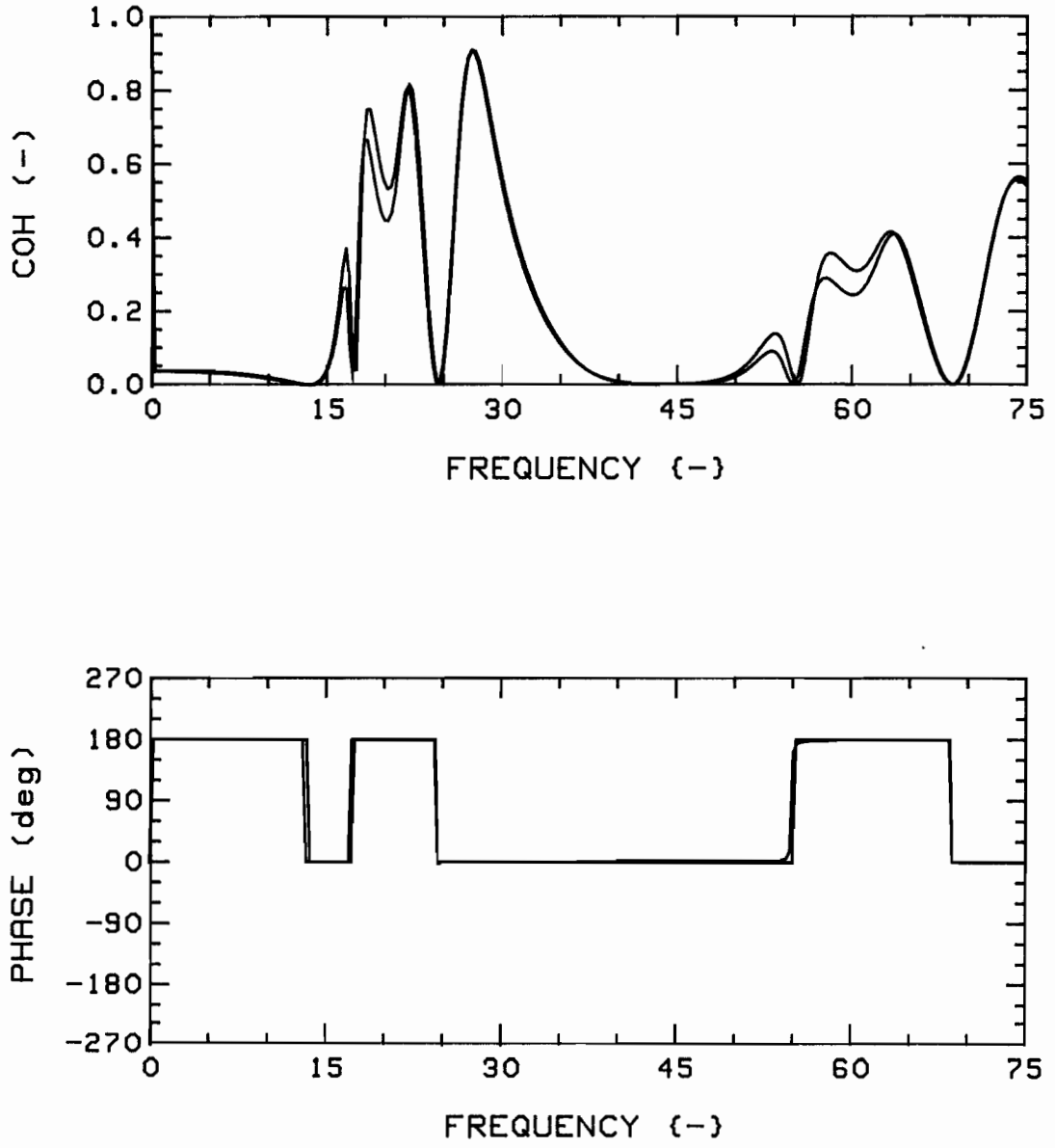

Fig.101d: Theoretical coherences for K = 28, G_c = 0.75, 4F/24R, T-T (diagonal pair), at u = 3; central (RED) versus parallel (GREEN) offset system.

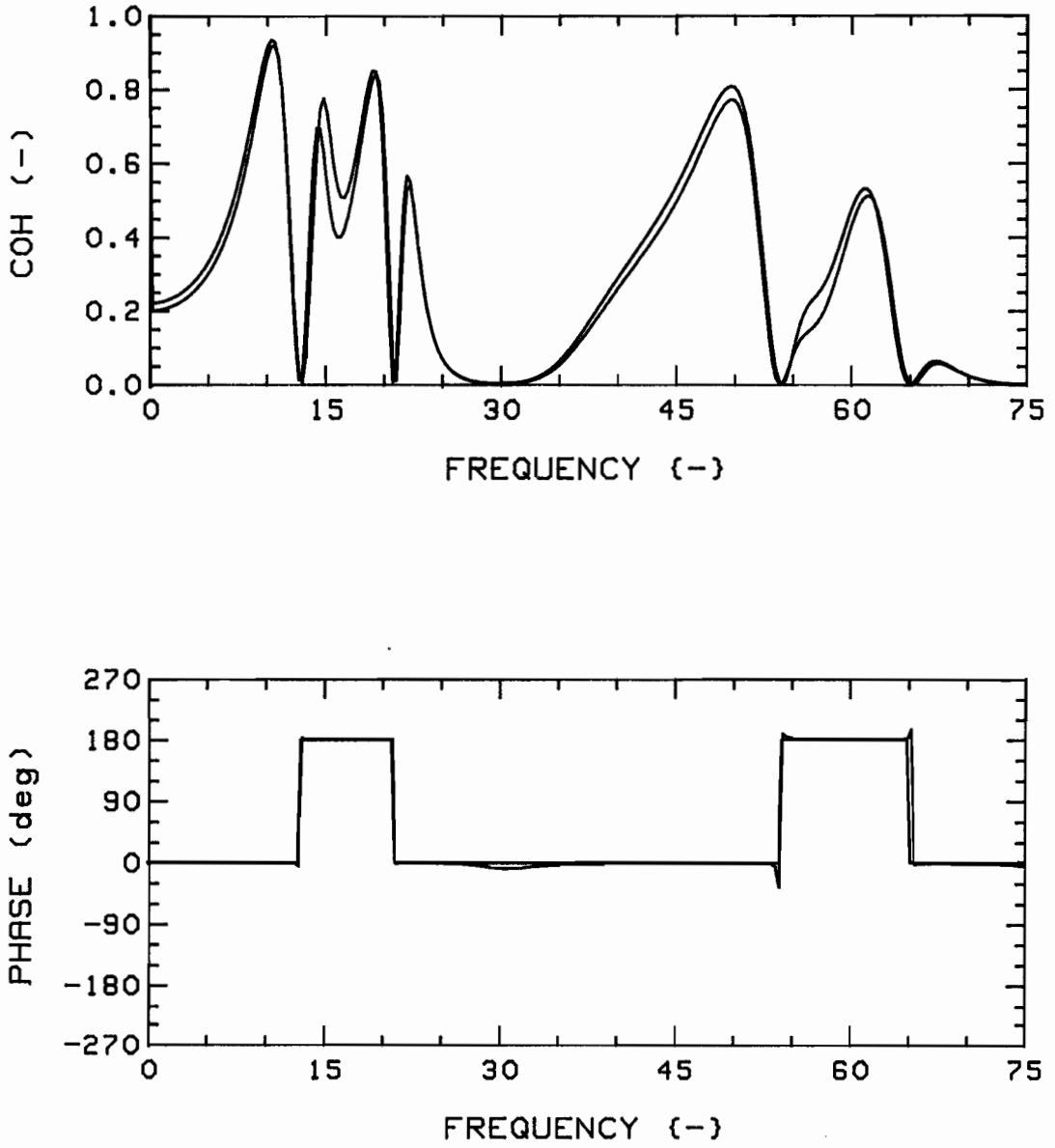

Fig.101e: Theoretical coherences for K = 28, G_c = 0.75, 4F/24R, R-R (diagonal pair), at u = 4; central (RED) versus parallel (GREEN) offset system.

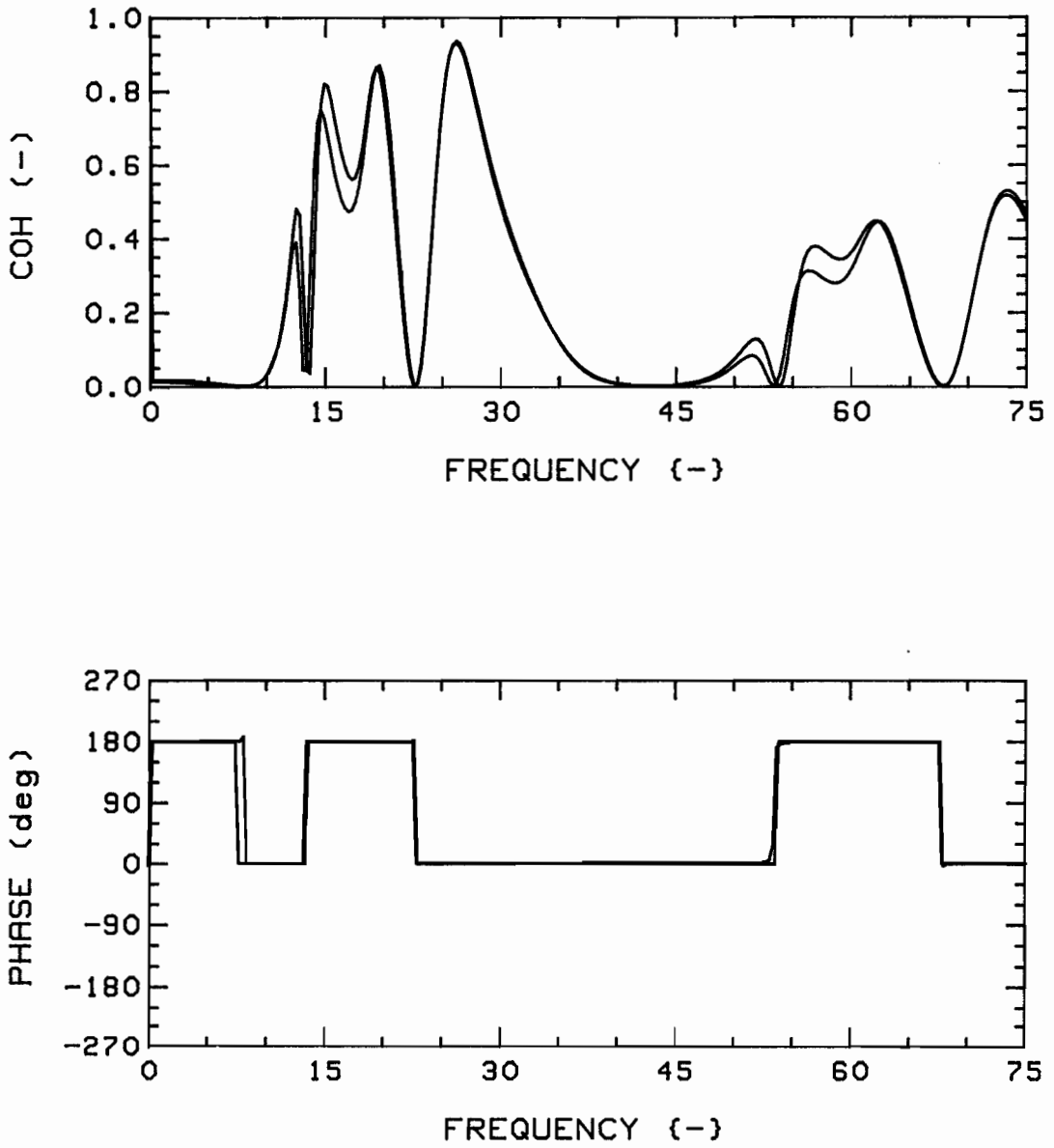

Fig.101f: Theoretical coherences for K = 28, G_c = 0.75, 4F/24R,, T-T (diagonal pair), at u = 4; central (RED) versus parallel (GREEN) offset system.

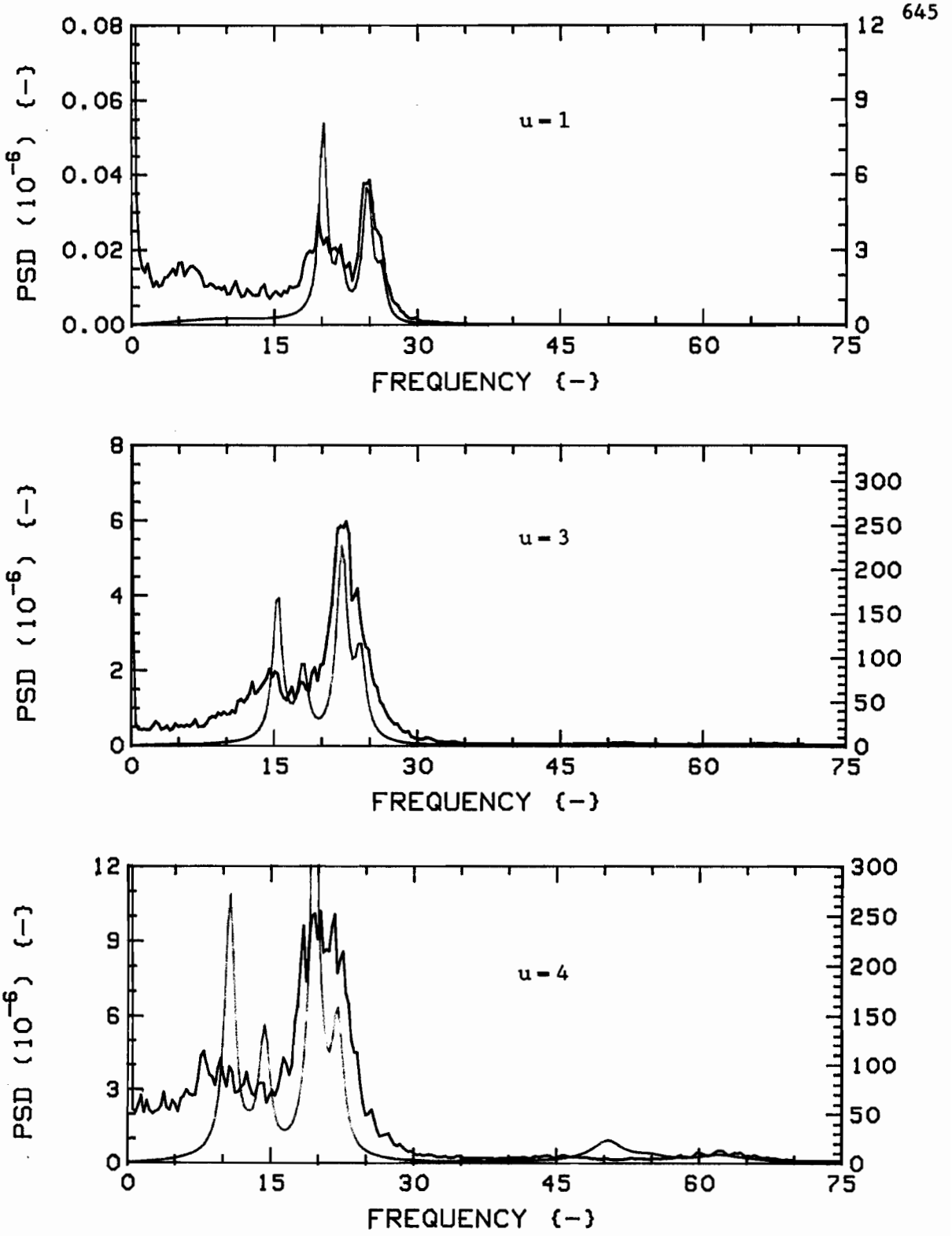

Fig.102a: Measured (RED) and theoretical (GREEN) vibration PSD's for K = 28, G_c = 0.75, 4F(6,7,1,2)/24R, Radial direction, Position 7.

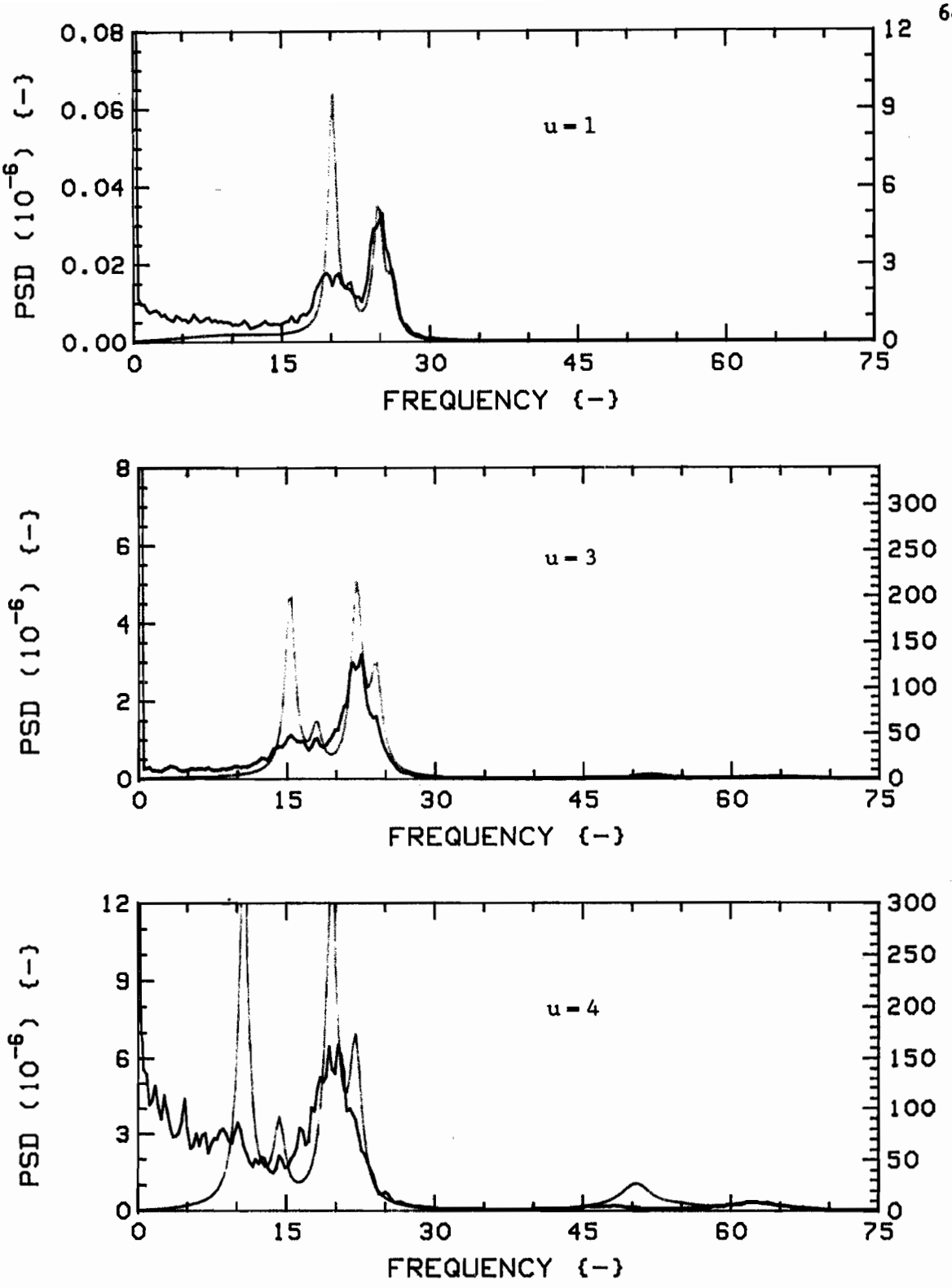

Fig.102b: Measured (RED) and theoretical (GREEN) vibration PSD's for K = 28, G_c = 0.75, 4F(6,7,1,2)/24R, Radial direction, Position 1.

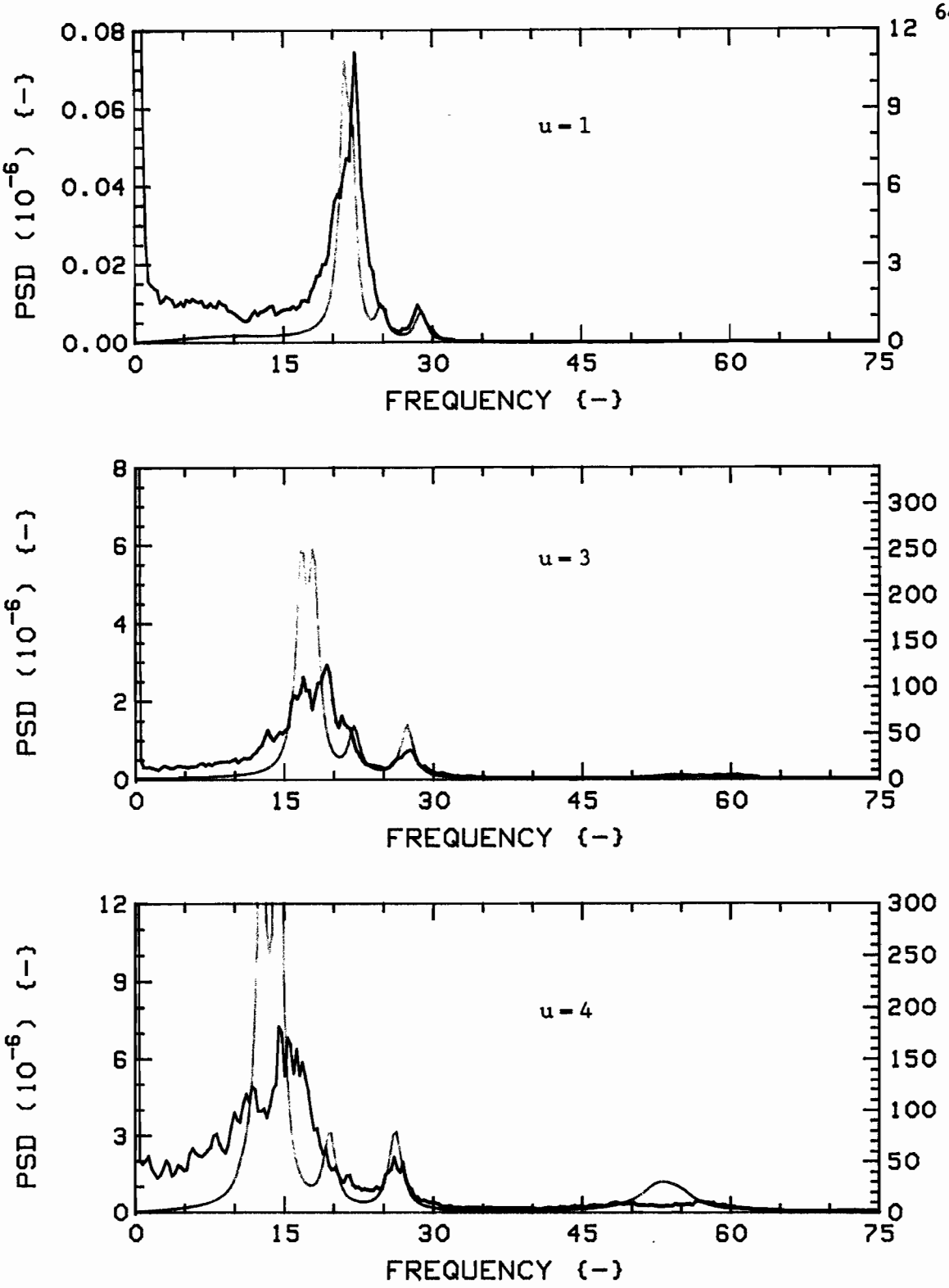

Fig.102c: Measured (RED) and theoretical (GREEN) vibration PSD's for K = 28, G_c = 0.75, 4F(6,7,1,2)/24R, Tangential direction, Position 7.

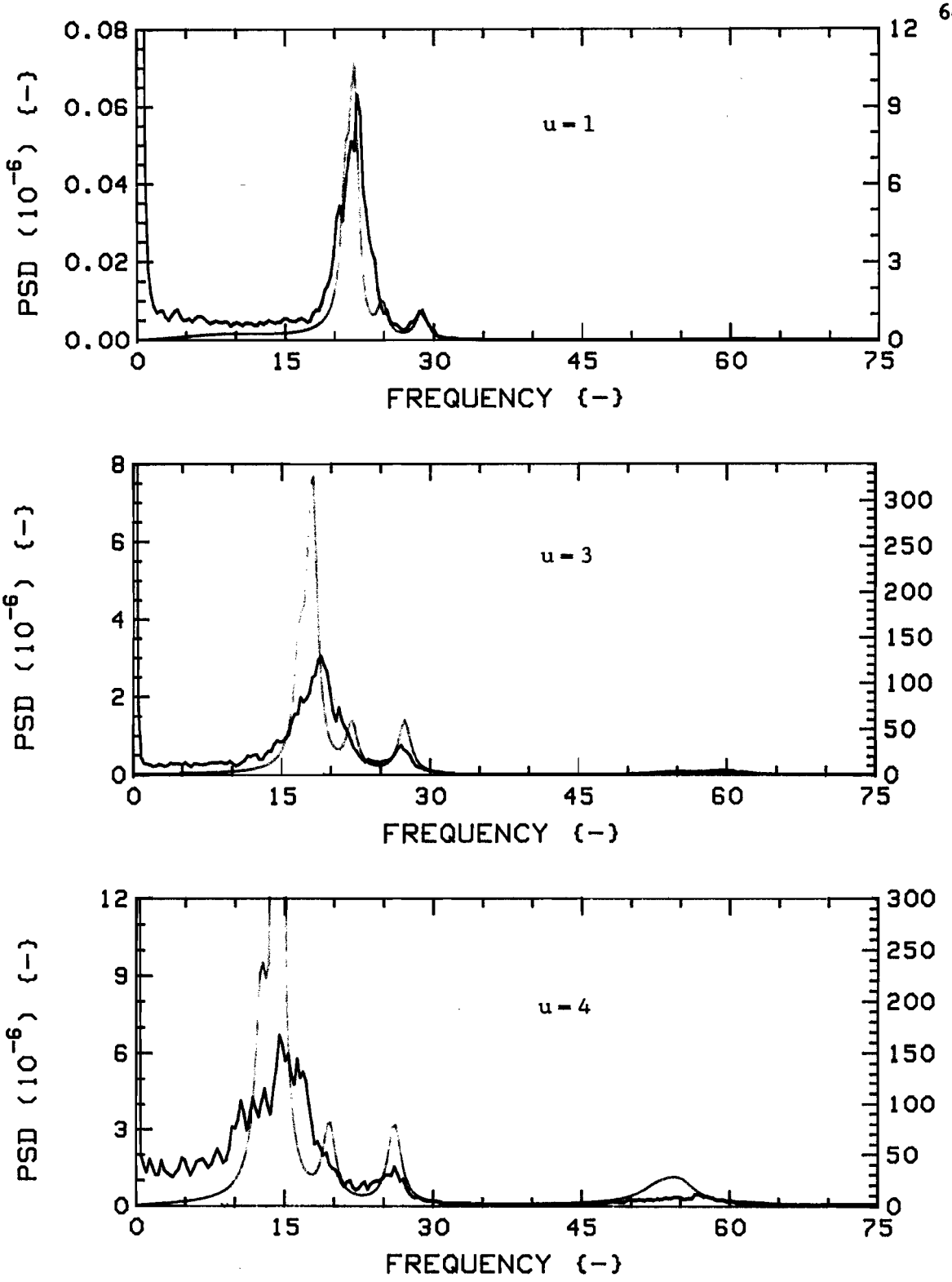

Fig.102d: Measured (RED) and theoretical (GREEN) vibration PSD's for K = 28, G_c = 0.75, 4F(6,7,1,2)/24R, Tangential direction, Position 1.

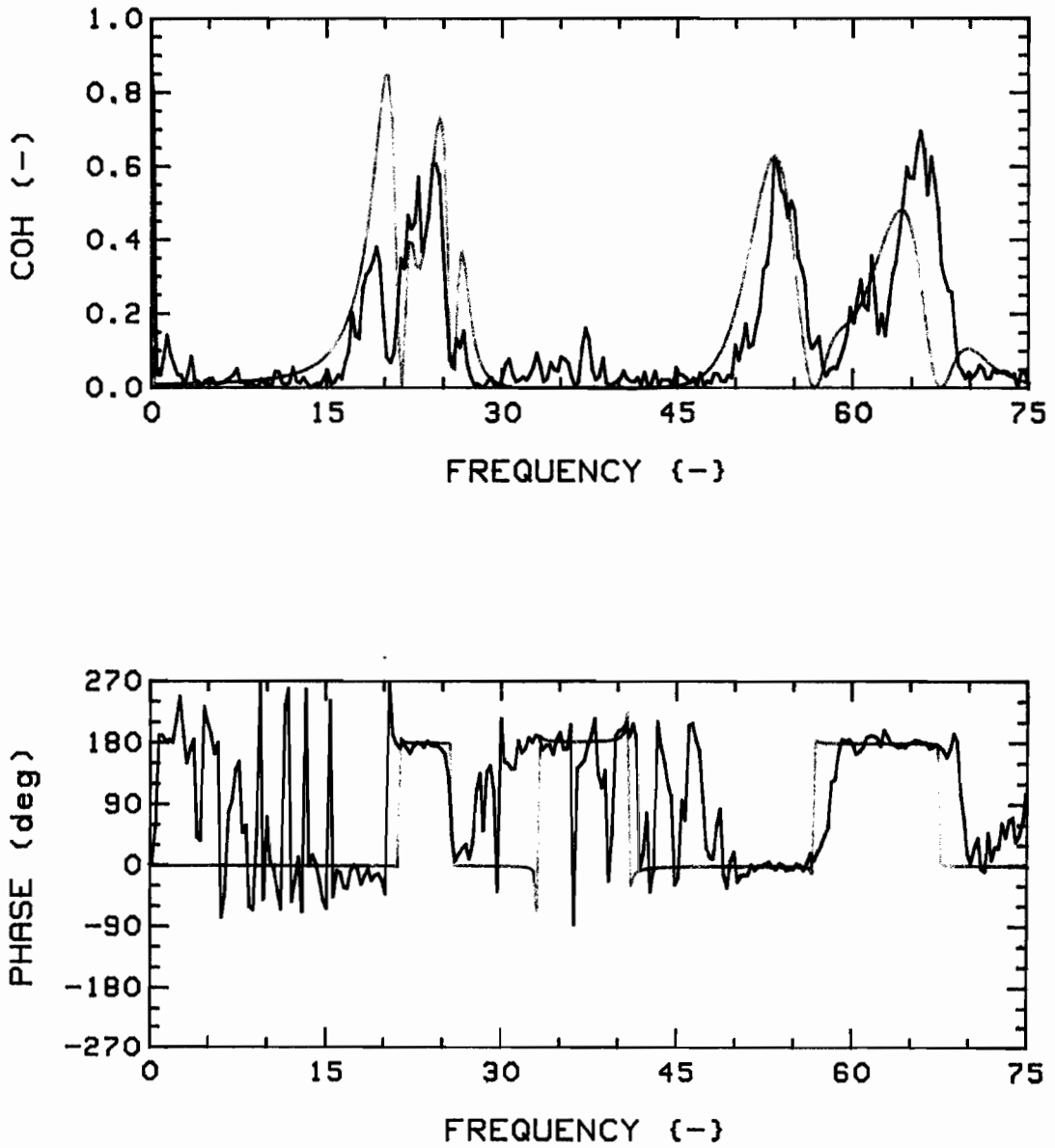

Fig.103a: Measured (RED) and theoretical (GREEN) coherence functions and phases, for K = 28, G_c = 0.75, 4F(6,7,1,2) /24R, R-R (7,1), at u = 1.

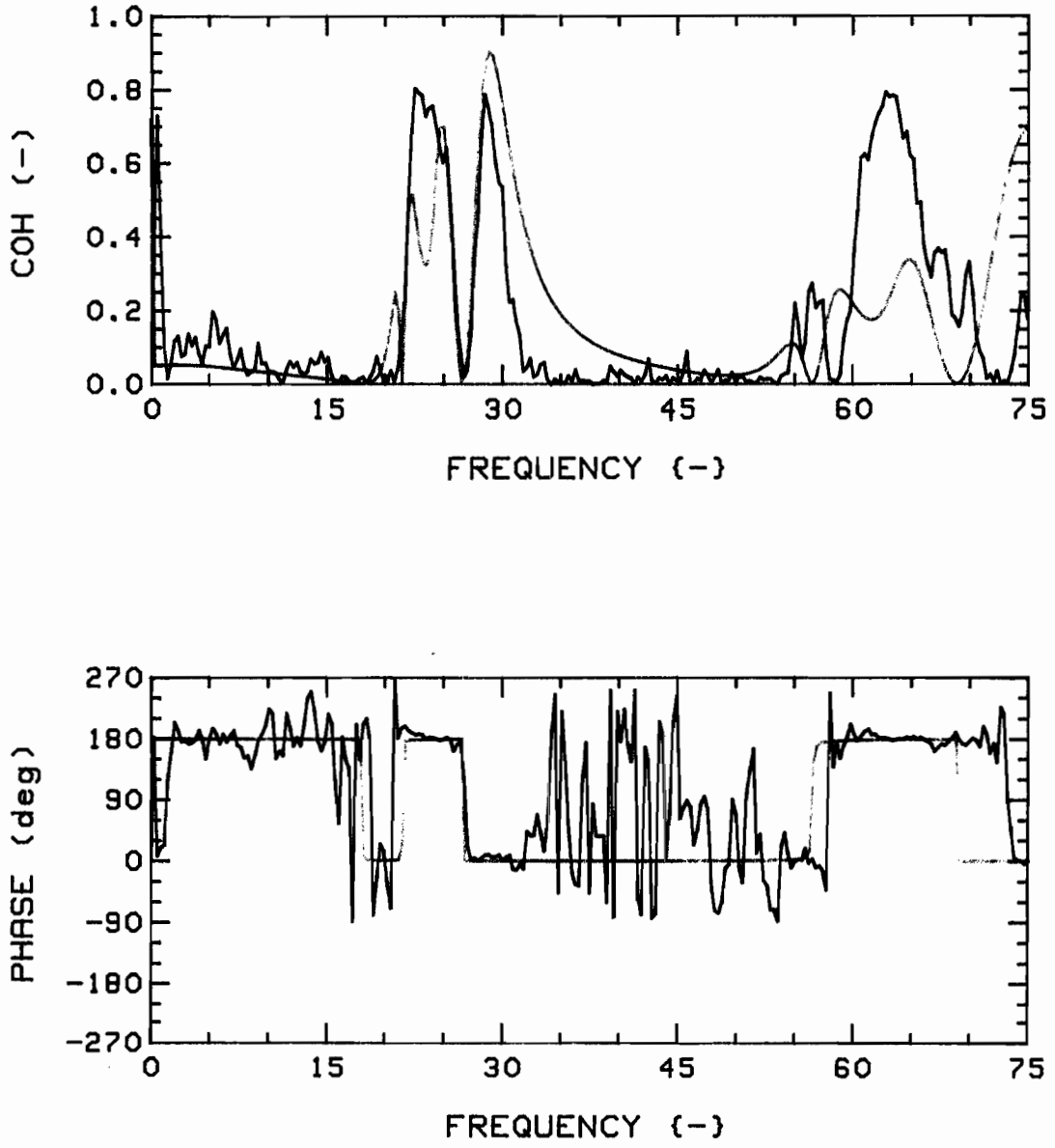

Fig.103b: Measured (RED) and theoretical (GREEN) coherence functions and phases, for K = 28, G_c = 0.75, 4F(6,7,1,2) /24R, T-T (7,1), at u = 1.

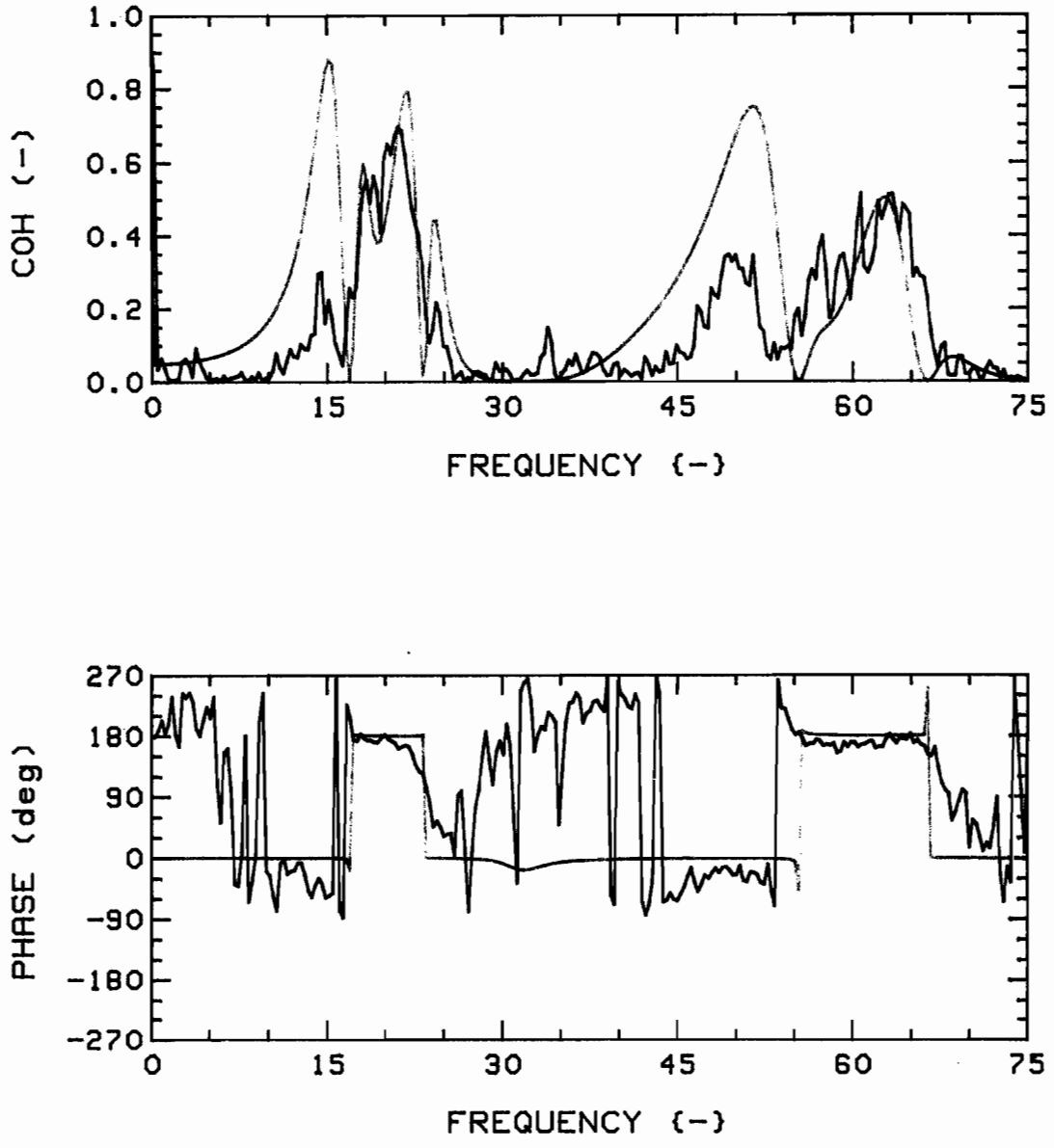

Fig.103c: Measured (RED) and theoretical (GREEN) coherence functions and phases, for K = 28, G_c = 0.75, 4F(6,7,i,2) /24R, R-R (7,1), at u = 3.

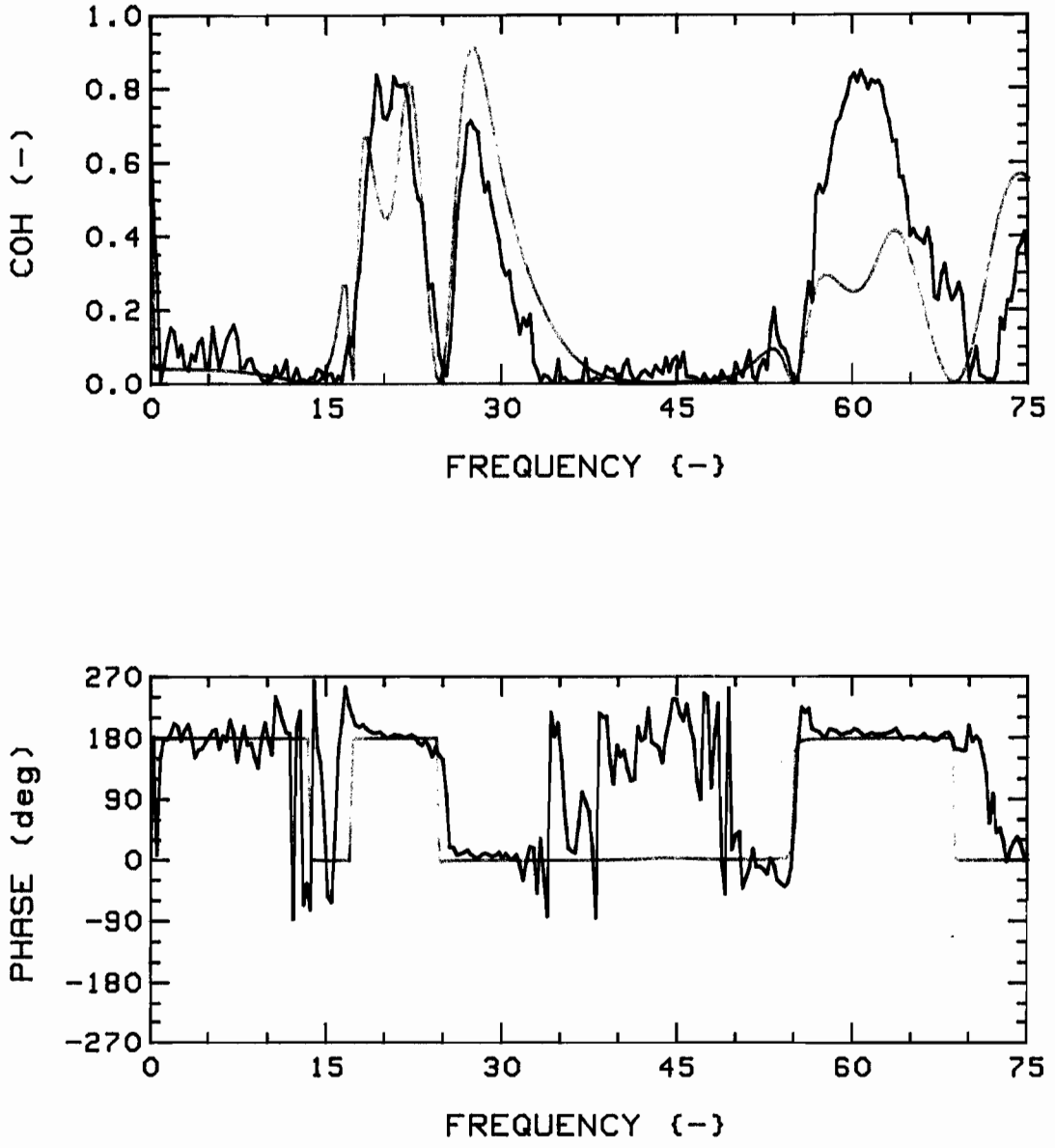

Fig.103d: Measured (RED) and theoretical (GREEN) coherence functions and phases, for K = 28, G_c = 0.75, 4F(6,7,1,2) /24R, T-T (7,1), at u = 3.

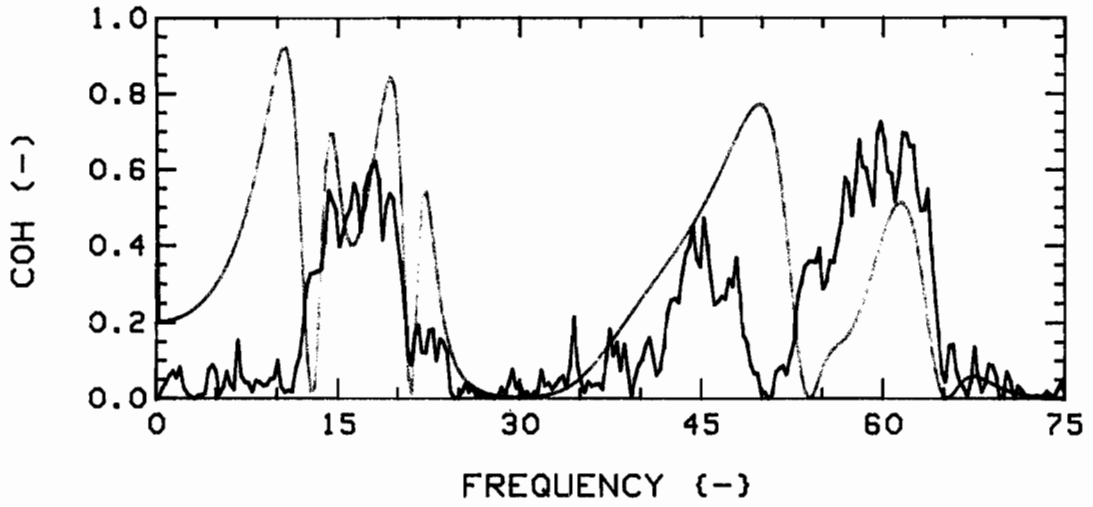

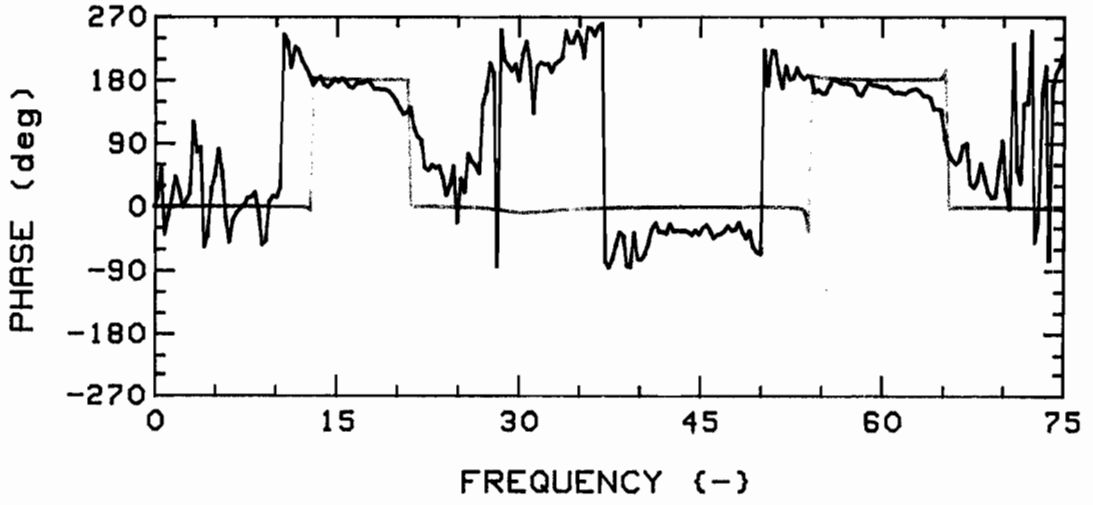

Fig.103e: Measured (RED) and theoretical (GREEN) coherence functions and phases, for K = 28, G_c = 0.75, 4F(6,7,1,2) /24R, R-R (7,1), at u = 4.

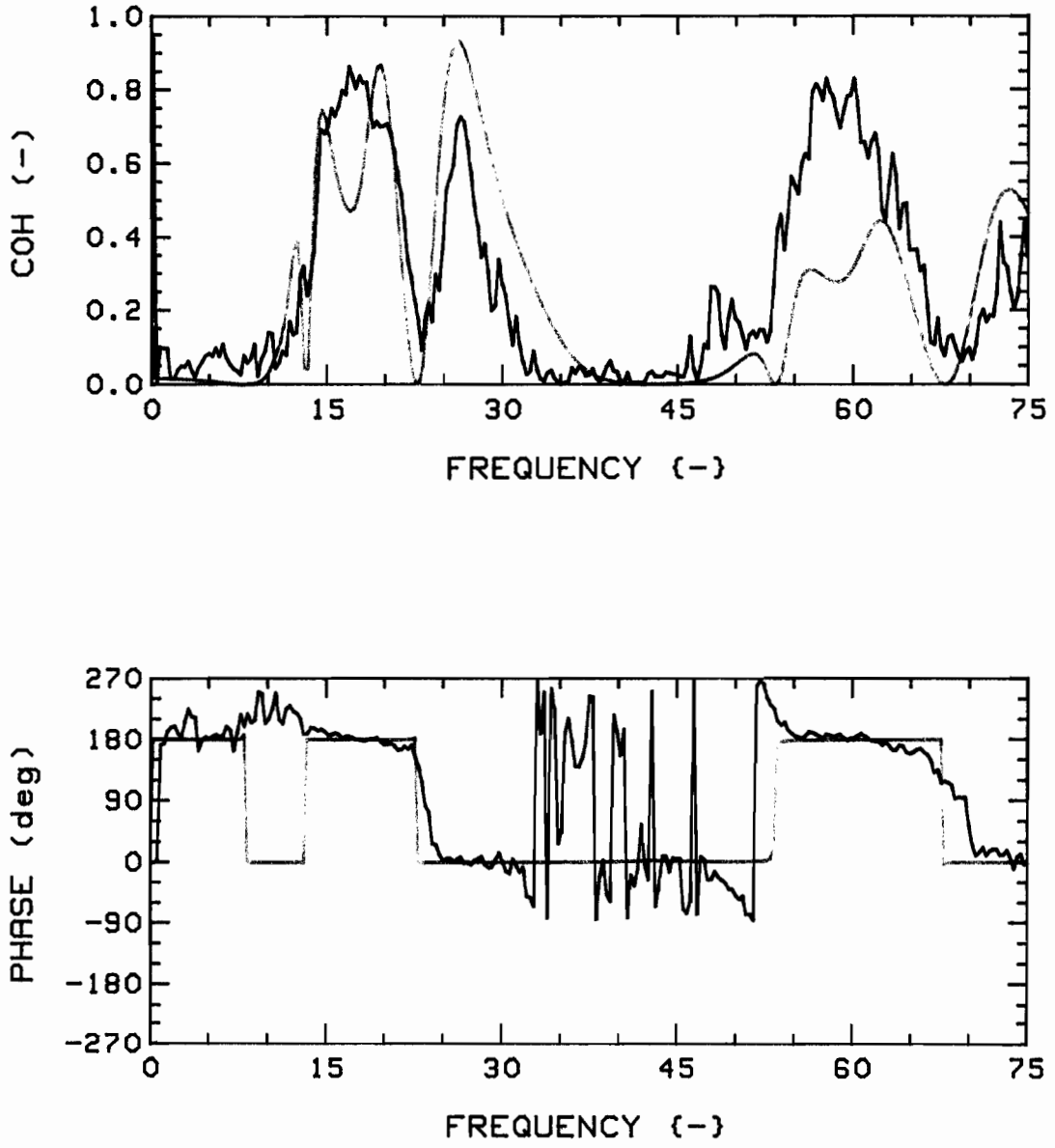

Fig.103f: Measured (RED) and theoretical (GREEN) coherence functions and phases, for K = 28, G_c = 0.75, 4F(6,7,1,2) /24R, T-T (7,1), at u = 4.

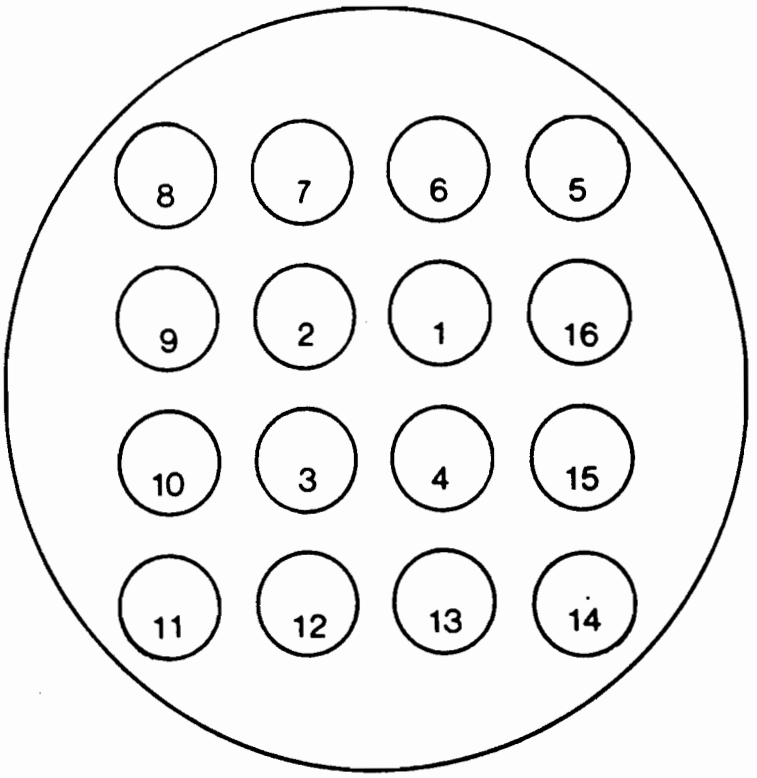

Fig.104: Reduced cluster (K = 16, G_c = 0.75, R_c = 9.40 cm), for 4F(5,6,1,16)/24R(rest) theoretical computations.

Note: See Fig. 29 for full cluster.

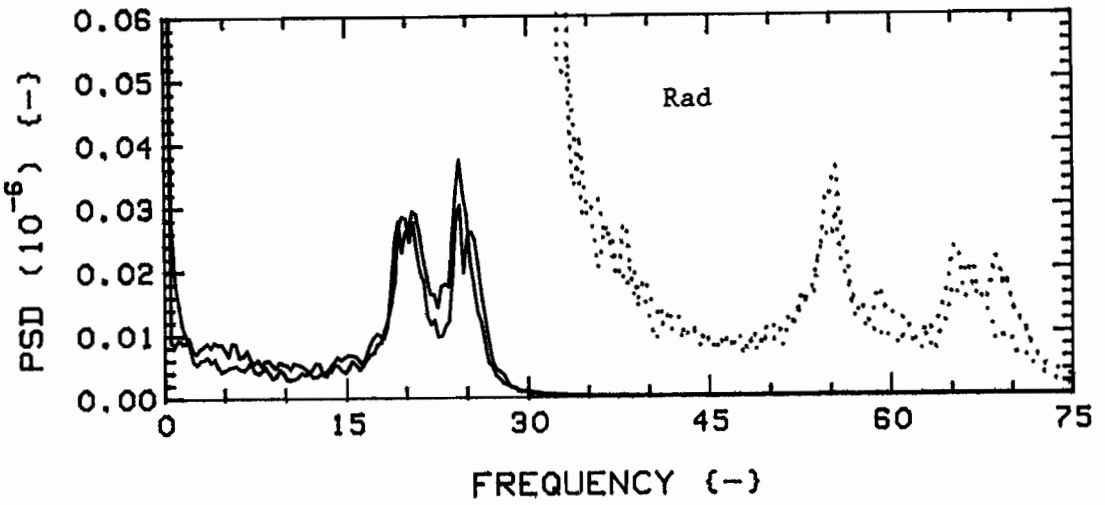

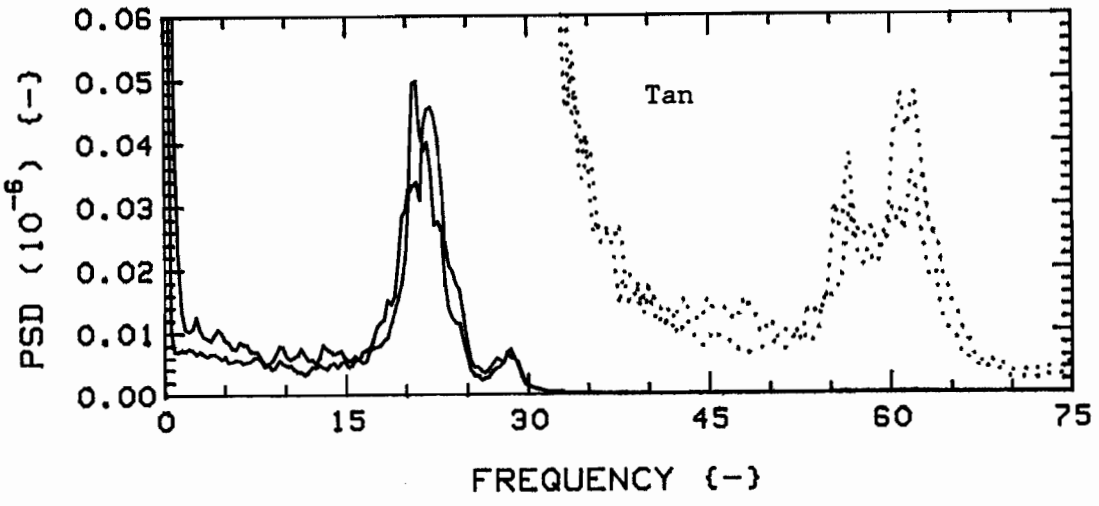

Fig.105a: Measured vibration PSD's for K = 28, G_c = 0.75, 4F(5,6,1,16) /24R, at u = 1.0; Position 5 (RED) versus Position 1 (GREEN).

The dotted traces are expansions of the solid ones, with a scale of 3.0×10^{-10}.

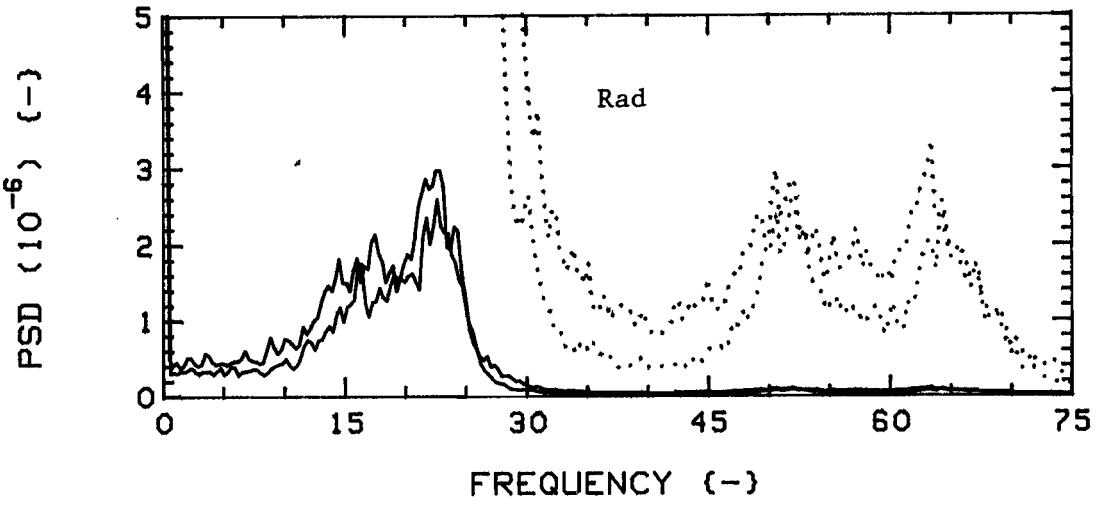

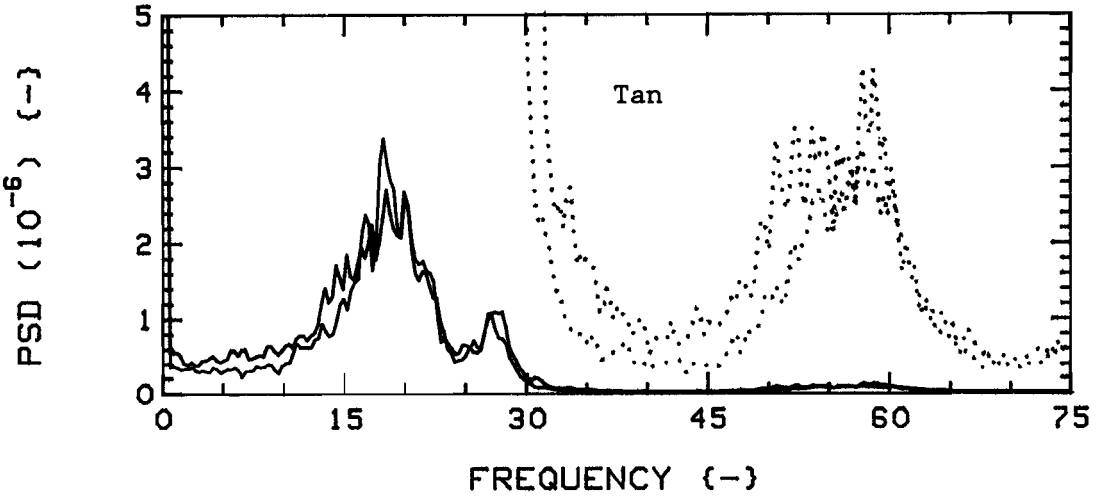

Fig.105b: Measured vibration PSD's for K = 28, G_c = 0.75, 4F(5,6,1,16) /24R, at u = 3.0; Position 5 (RED) versus Position 1 (GREEN).

The dotted traces are expansions of the solid ones, with a scale of 1.5×10^{-7}.

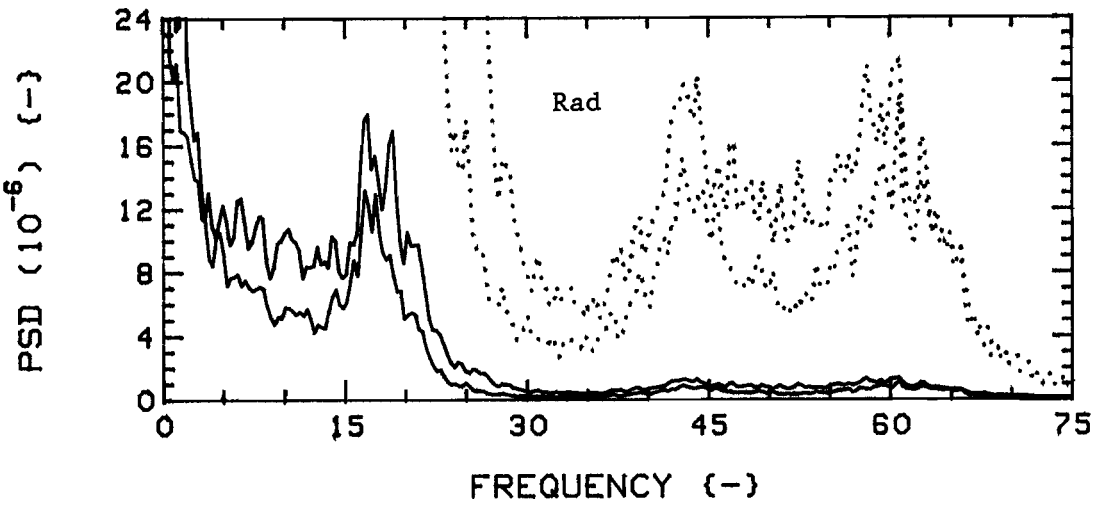

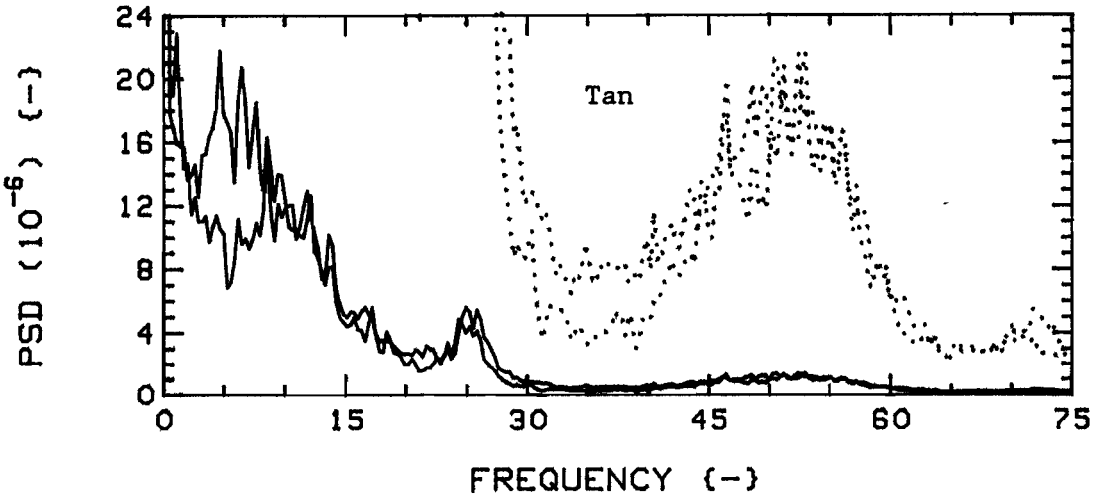

Fig.105c: Measured vibration PSD's for K = 28, G_c = 0.75, 4F(5,6,1,16) /24R, at u = 5.0; Position 5 (RED) versus Position 1 (GREEN).

The dotted traces are expansions of the solid ones, with a scale of 1.5×10^{-6}.

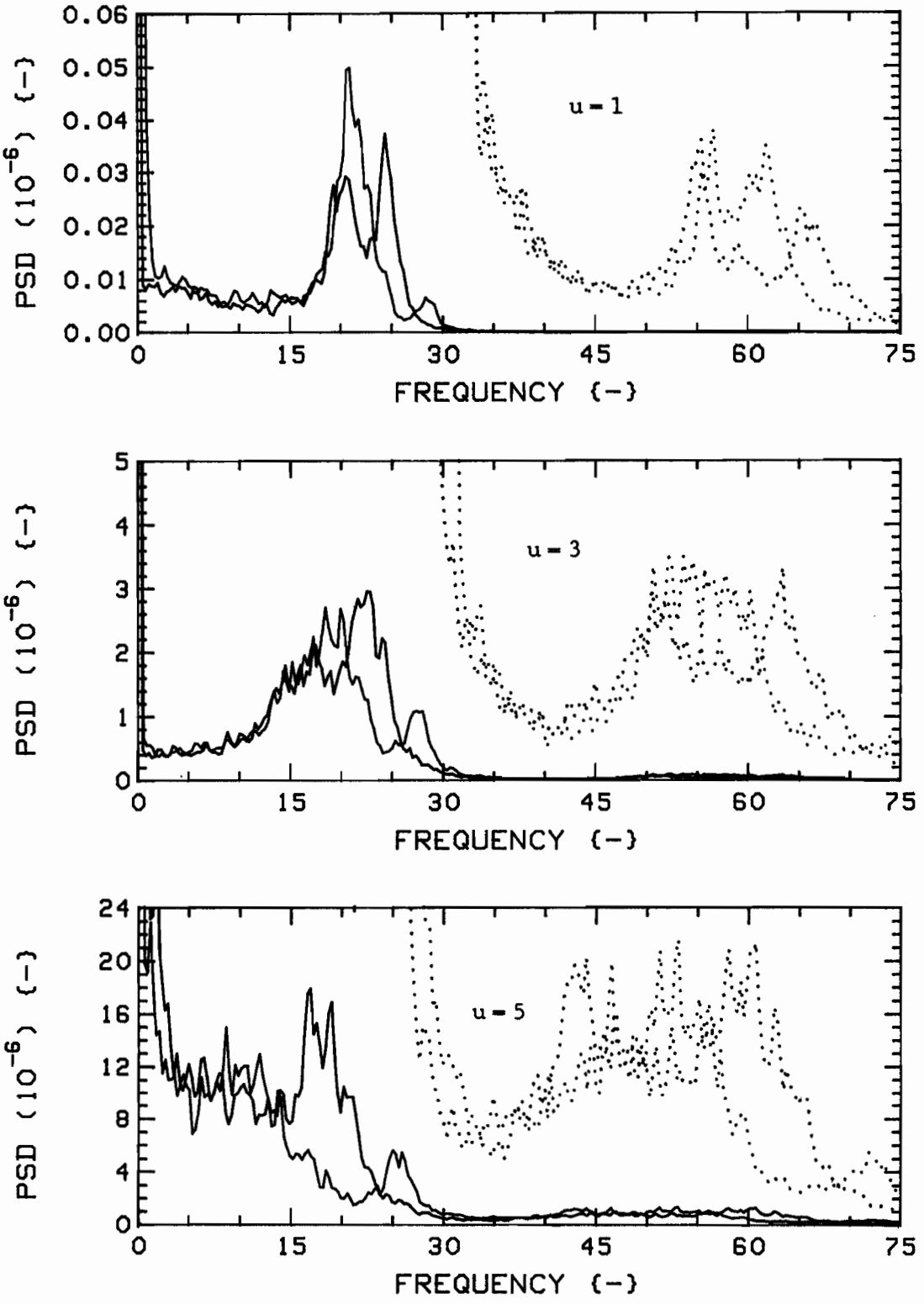

Fig.106a: Measured vibration PSD's for K = 28, $G_c = 0.75$, 4F(5,6,1,16)/24R, in Position 5, Radial (RED) and Tangential (BLUE) directions.

The dotted traces are expansions of the solid ones; scales are, from top: 3.0×10^{-10}, 1.5×10^{-7}, 1.5×10^{-6}.

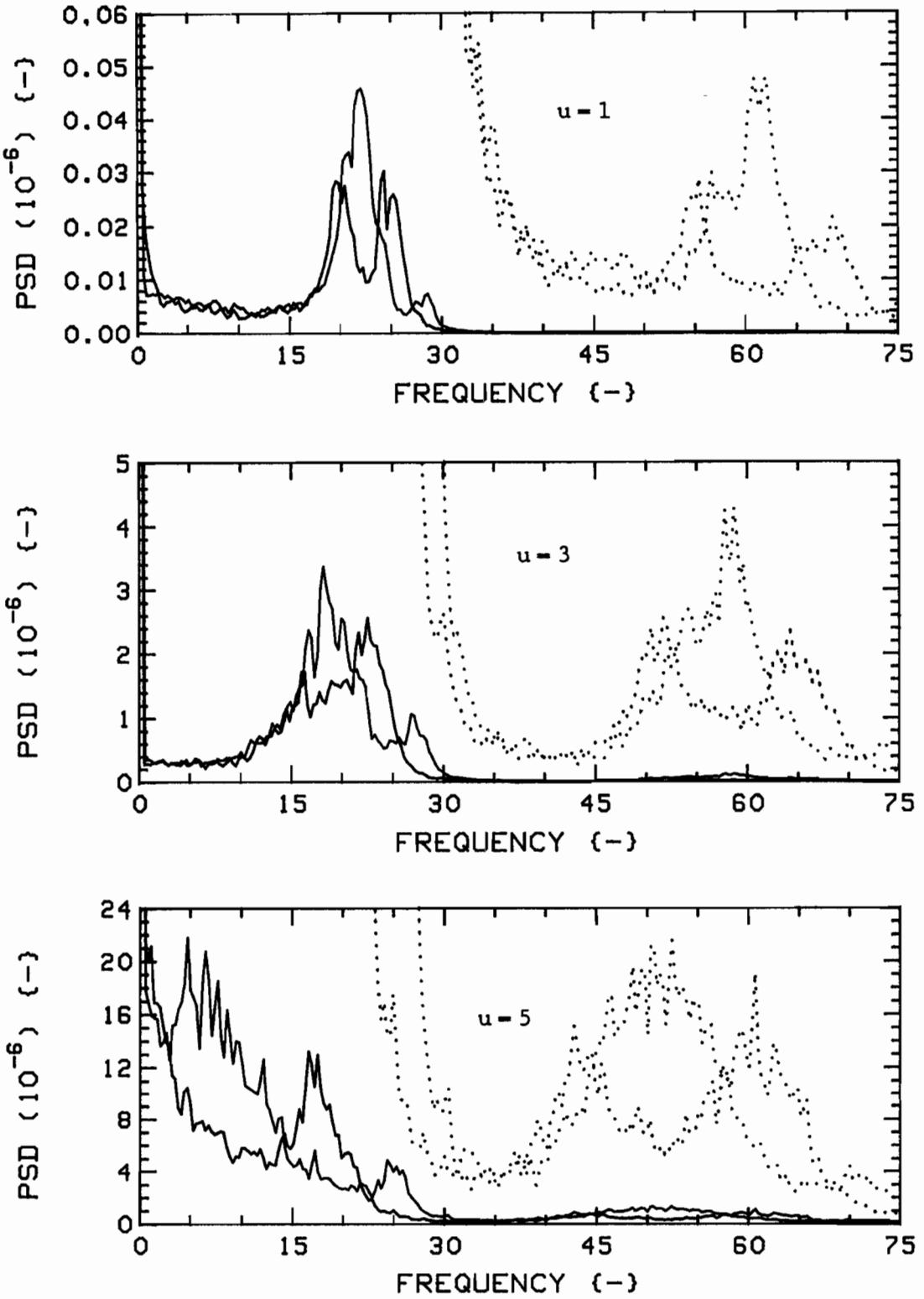

Fig.106b: Measured vibration PSD's for K = 28, G_c = 0.75, 4F(5,6,1,16)/24R, in Position 1, Radial (RED) and Tangential (BLUE) directions.

The dotted traces are expansions of the solid ones; scales are, from top: 3.0×10^{-10}, 1.5×10^{-7}, 1.5×10^{-6}.

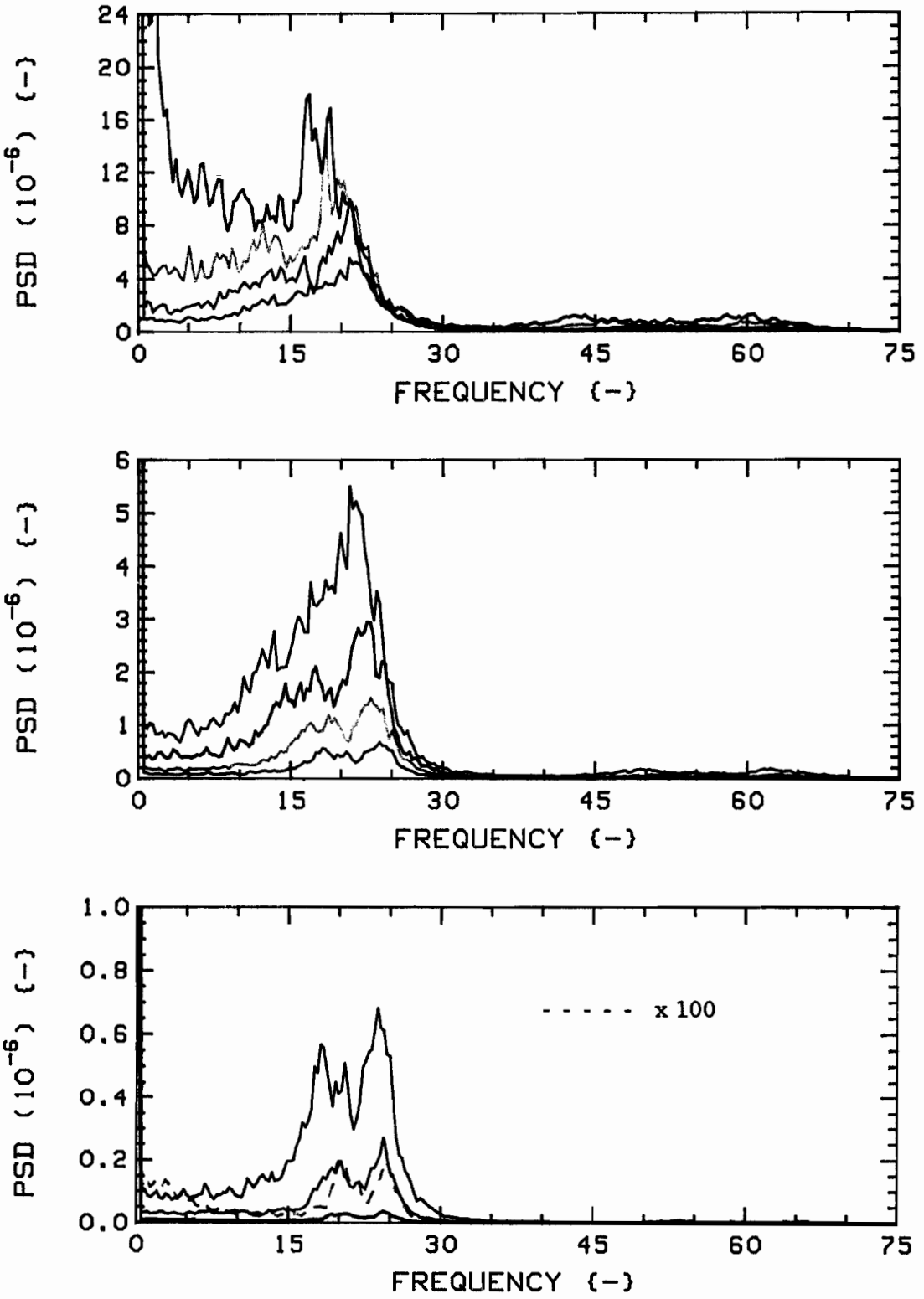

Fig.107a: Measured vibration PSD's for K = 28, G_c = 0.75, 4F(5,6,1,16) /24R, Position 5 in Radial direction, versus flow velocity In descending order, u = 5.0 to 0.5, in steps of 0.5. Colour sequence: RED, GREEN, BLUE, BLACK (lowest trace of each plot is highest of the next one).

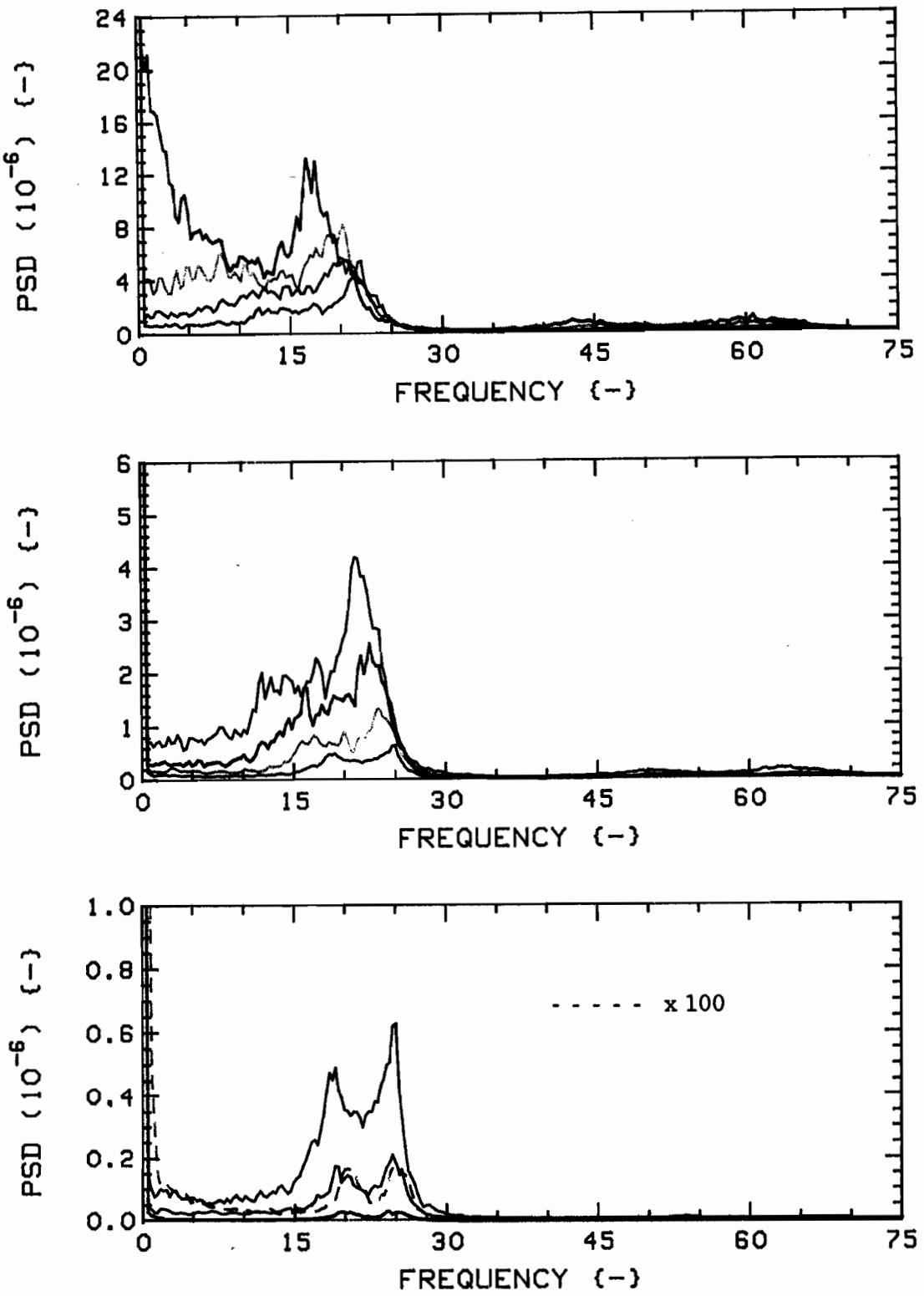

Fig.107b: Measured vibration PSD's for K = 28, G_c = 0.75, 4F(5,6,1,16) /24R, Position 1 in Radial direction, versus flow velocity In descending order, u = 5.0 to 0.5, in steps of 0.5. Colour sequence: RED, GREEN, BLUE, BLACK (lowest trace of each plot is highest of the next one).

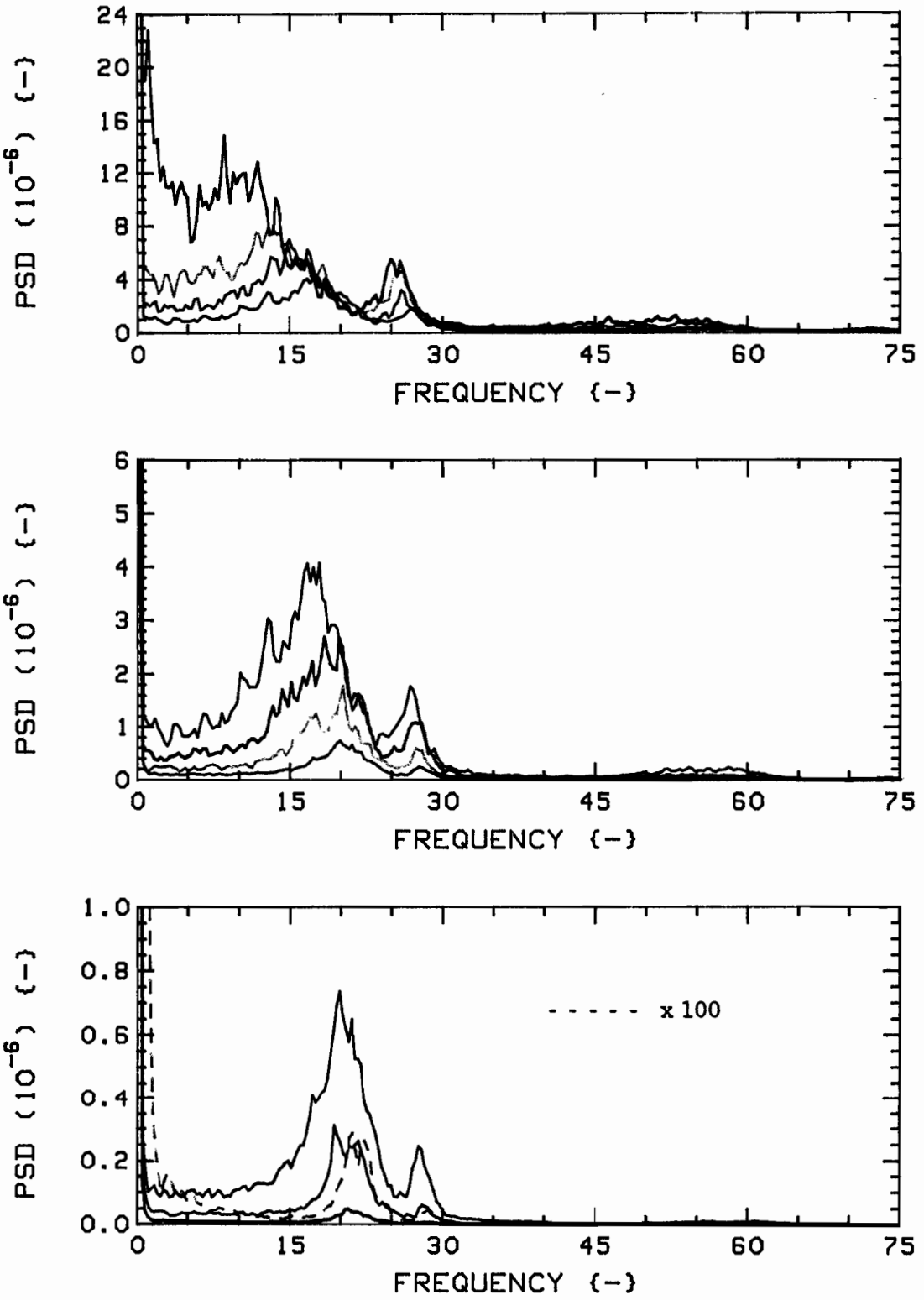

Fig.107c: Measured vibration PSD's for K = 28, G_c = 0.75, 4F(5,6,1,16) /24R, Position 5 in Tangential direction, versus flow velocity. In descending order, u = 5.0 to 0.5, in steps of 0.5. Colour sequence: RED, GREEN, BLUE, BLACK (lowest trace of each plot is highest of the next one).

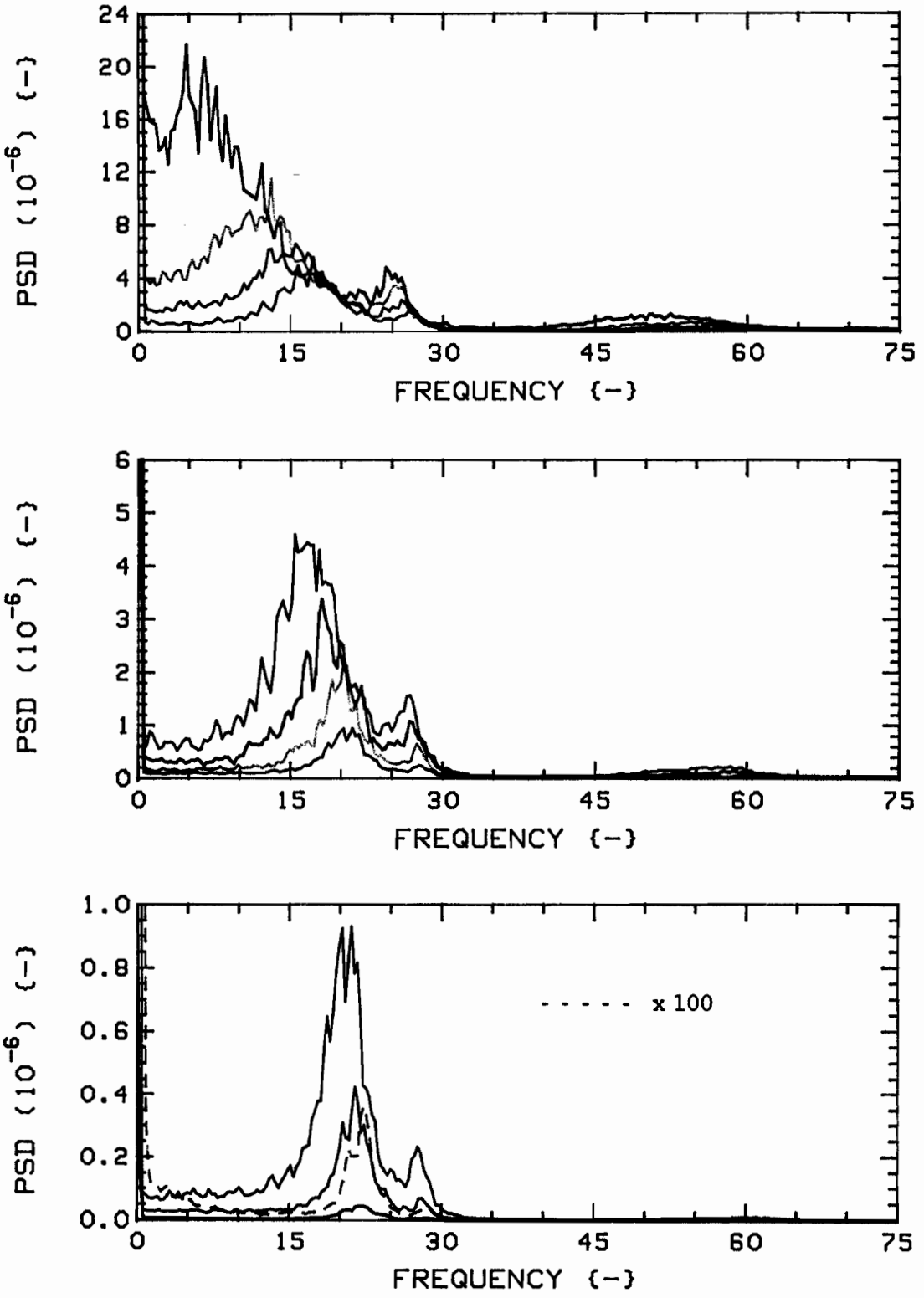

Fig.107d: Measured vibration PSD's for K = 28, G_c = 0.75, 4F(5,6,1,16) /24R, Position 1 in Tangential direction, versus flow velocity. In descending order, u = 5.0 to 0.5, in steps of 0.5. Colour sequence: RED, GREEN, BLUE, BLACK (lowest trace of each plot is highest of the next one).

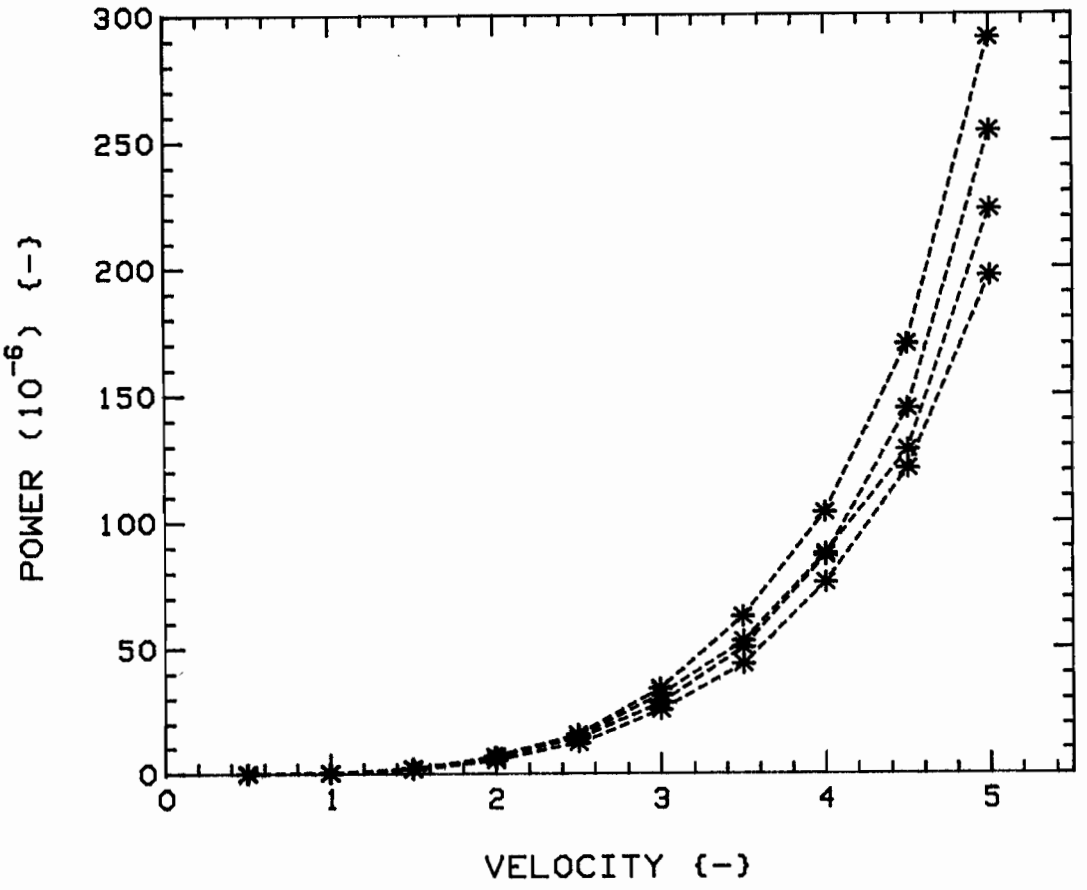

Fig.108: Powers versus flow velocity, for K = 28, G_c = 0.75, 4F(5,6,1,16)/24R, from (integrated) PSD's of Figs. 107a 107b, 107c and 107d. Radial direction, Positions 5 and 1 (RED and GREEN) and Tangential direction, Positions 5 and 1 (BLUE and BLACK).

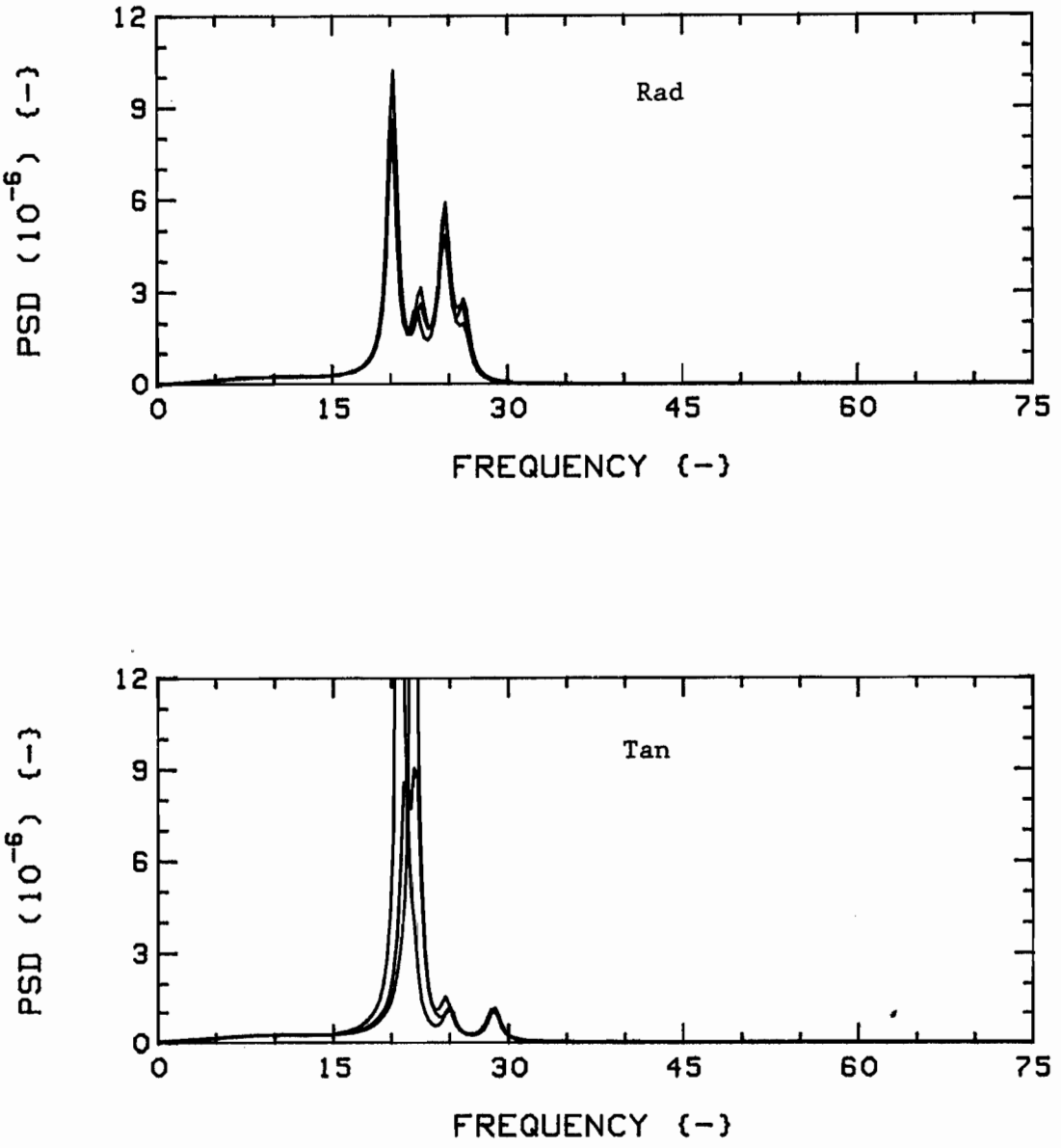

Fig.109a: Theoretical vibration PSD's for K = 28, G_c = 0.75, 4F/24R, at u = 1; central, Position 1 (RED) versus diagonal offset system, Position 5 (GREEN) and Position 1 (BLUE).

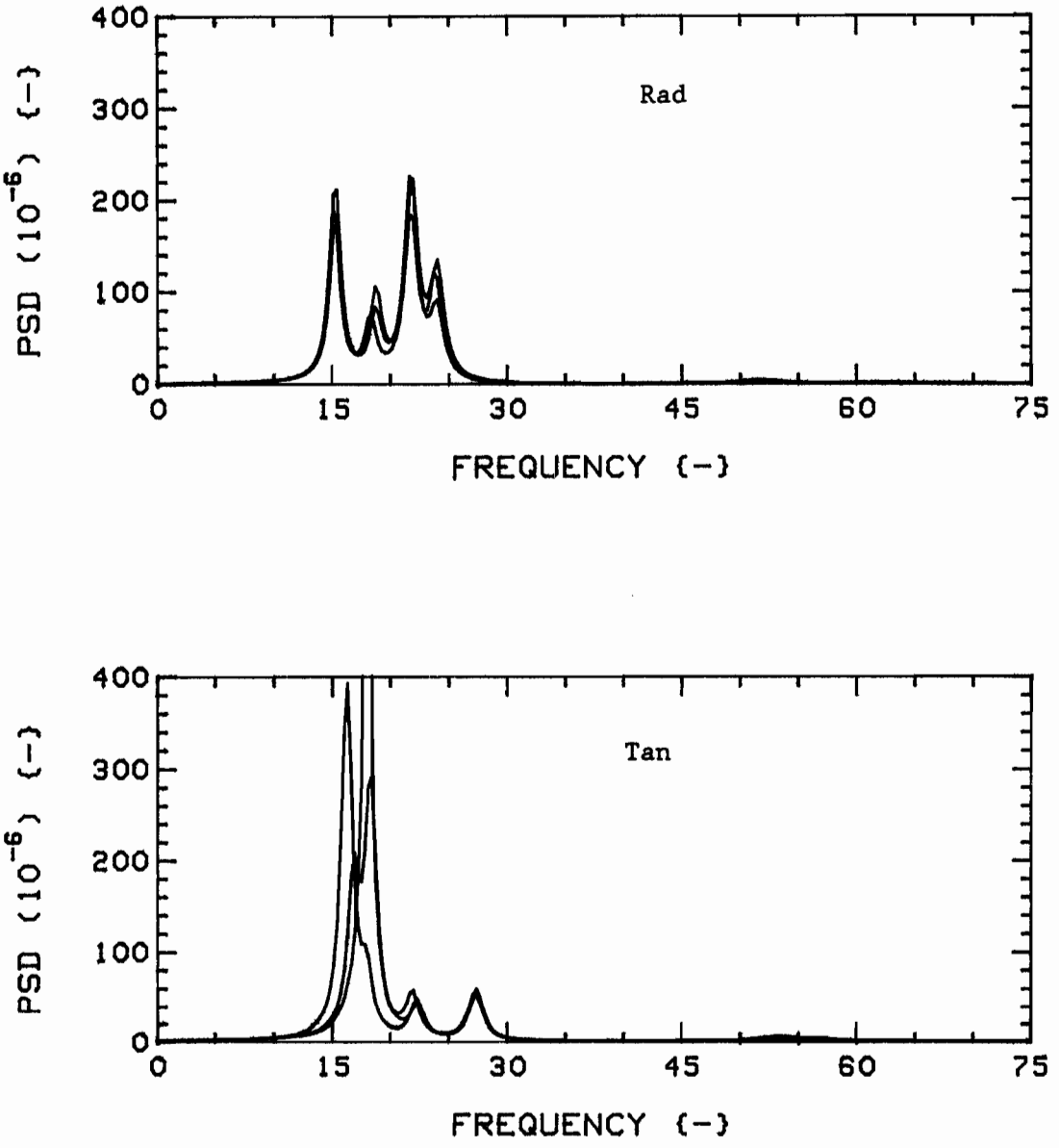

Fig.109b: Theoretical vibration PSD's for K = 28, G_c = 0.75, 4F/24R, at u = 3; central, Position 1 (RED) versus diagonal offset system, Position 5 (GREEN) and Position 1 (BLUE).

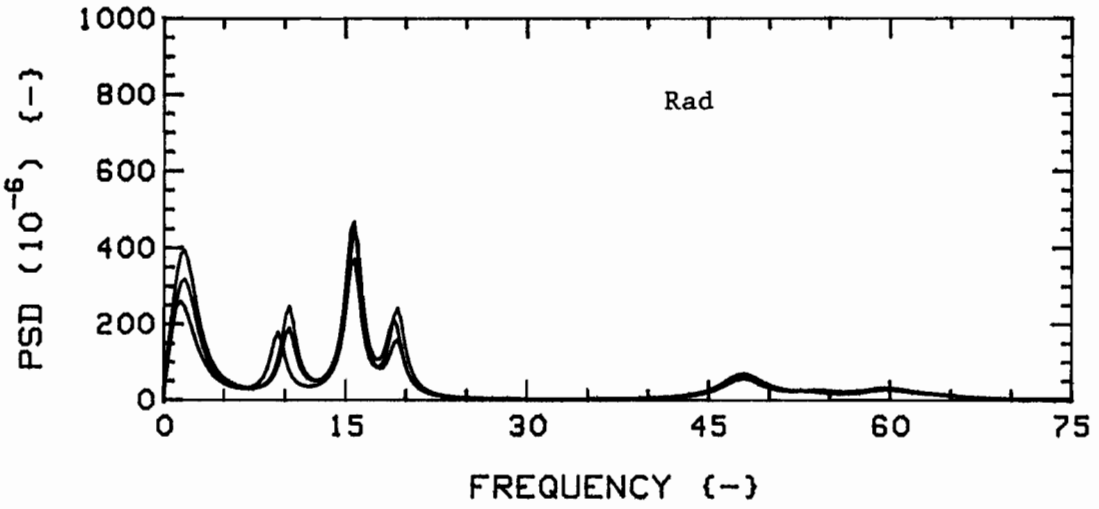

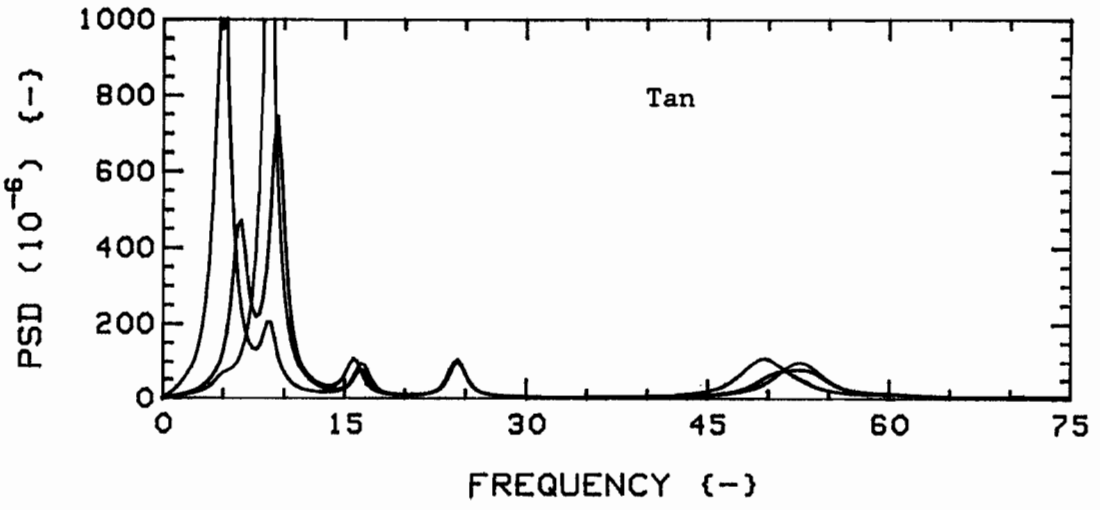

Fig.109c: Theoretical vibration PSD's for K = 28, G_c = 0.75, 4F/24R, at u = 5; central, Position 1 (RED) versus diagonal offset system, Position 5 (GREEN) and Position 1 (BLUE).

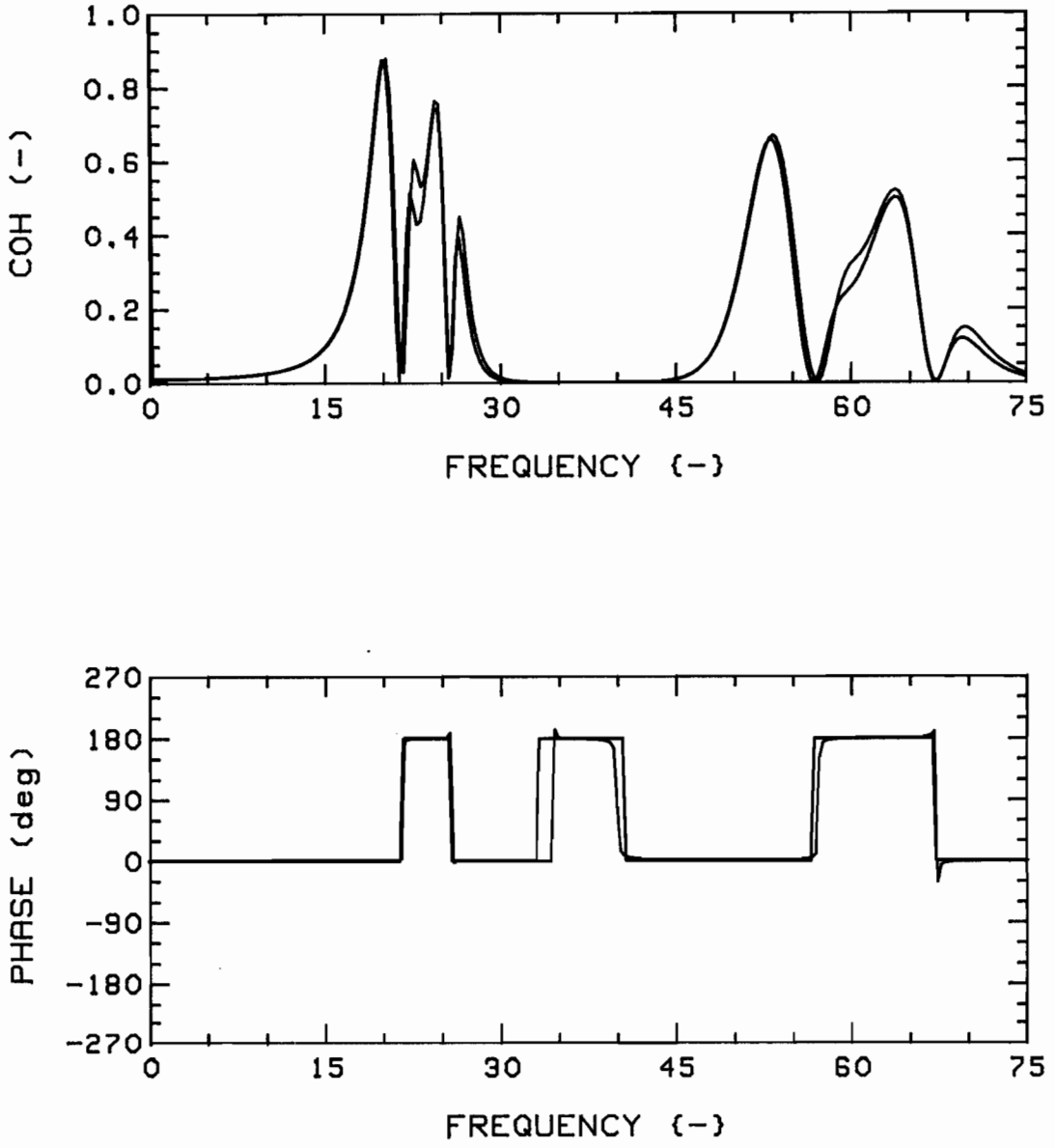

Fig.110a: Theoretical coherences for K = 28, G_c = 0.75, 4F/24R, R-R (diagonal pair), at u = 1; central (RED) versus diagonal (GREEN) offset system.

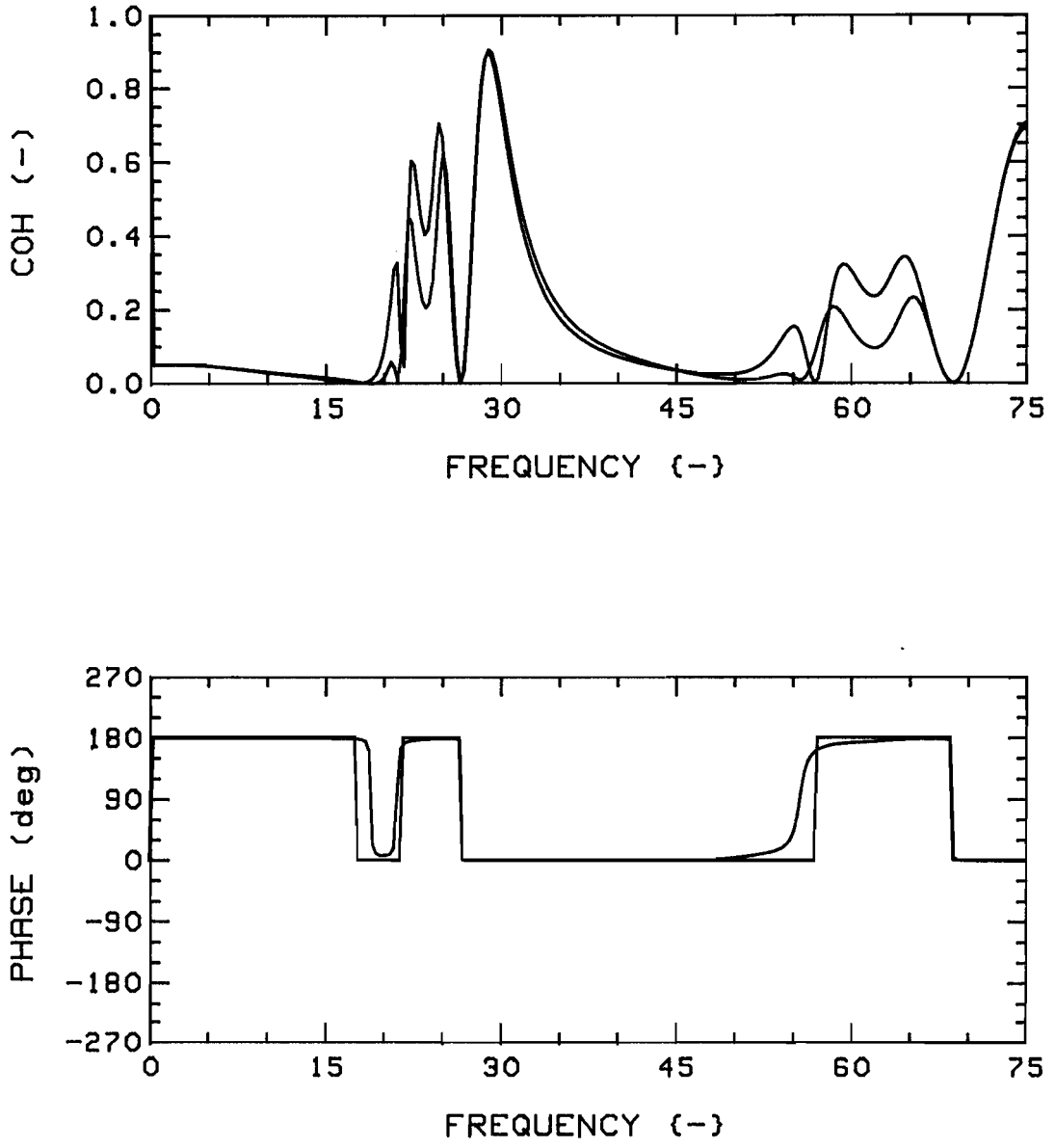

Fig.110b: Theoretical coherences for K = 28, G_c = 0.75, 4F/24R, T-T (diagonal pair), at u = 1; central (RED) versus diagonal (GREEN) offset system.

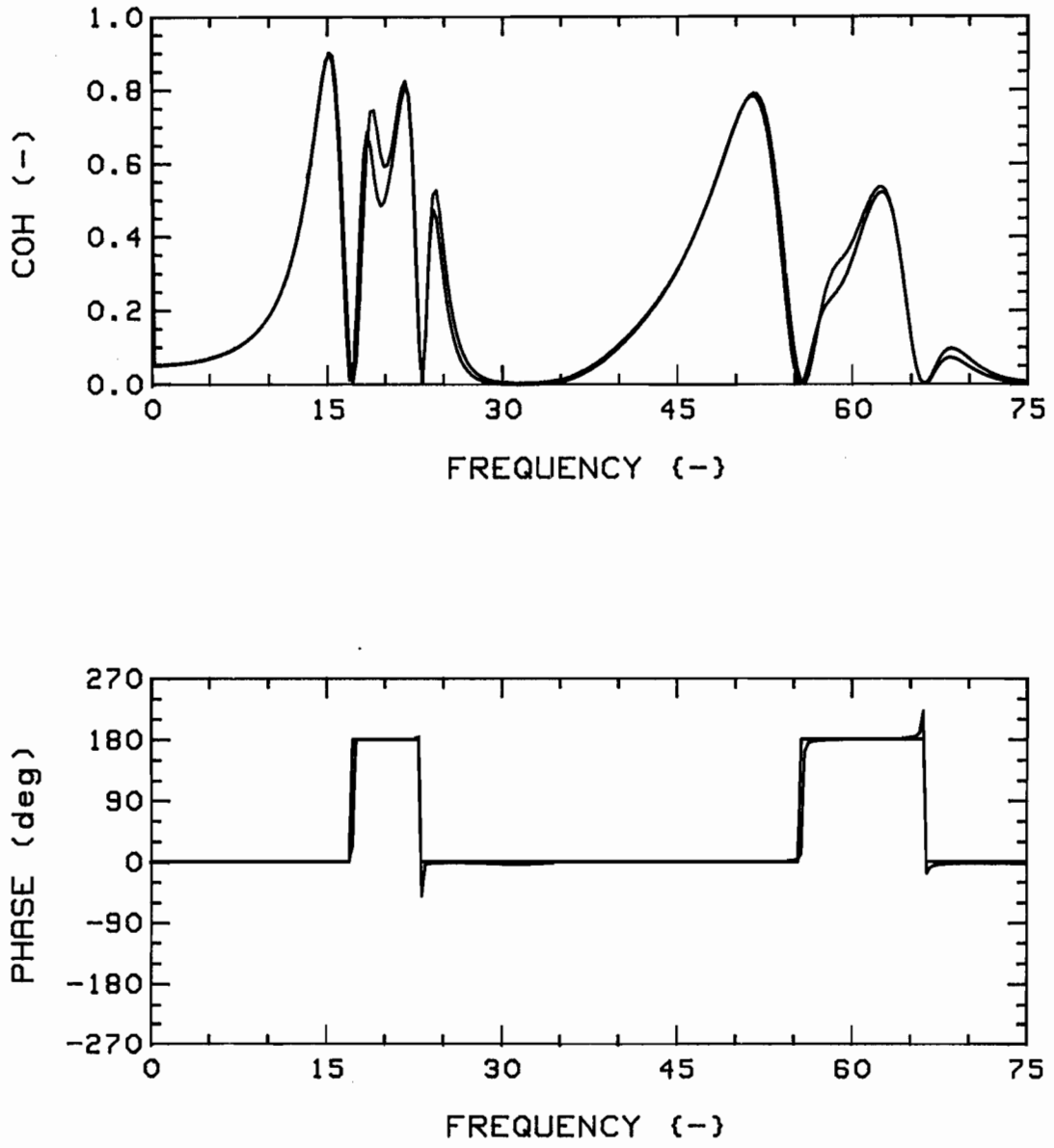

Fig.110c: Theoretical coherences for K = 28, G_c = 0.75, 4F/24R, R-R (diagonal pair), at u = 3; central (RED) versus diagonal (GREEN) offset system.

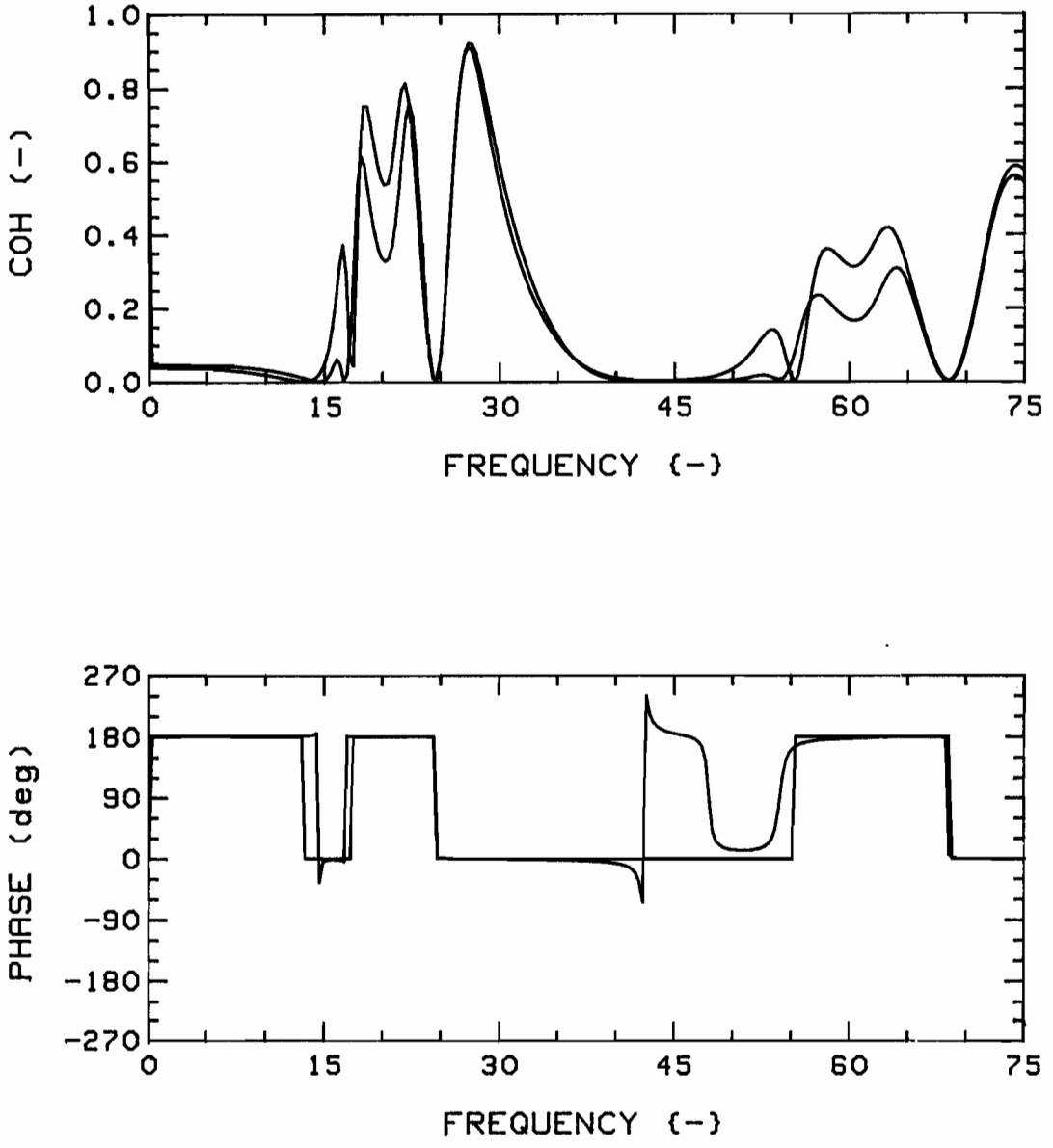

Fig.110d: Theoretical coherences for K = 28, G_c = 0.75, 4F/24R, T-T (diagonal pair), at u = 3; central (RED) versus diagonal (GREEN) offset system.

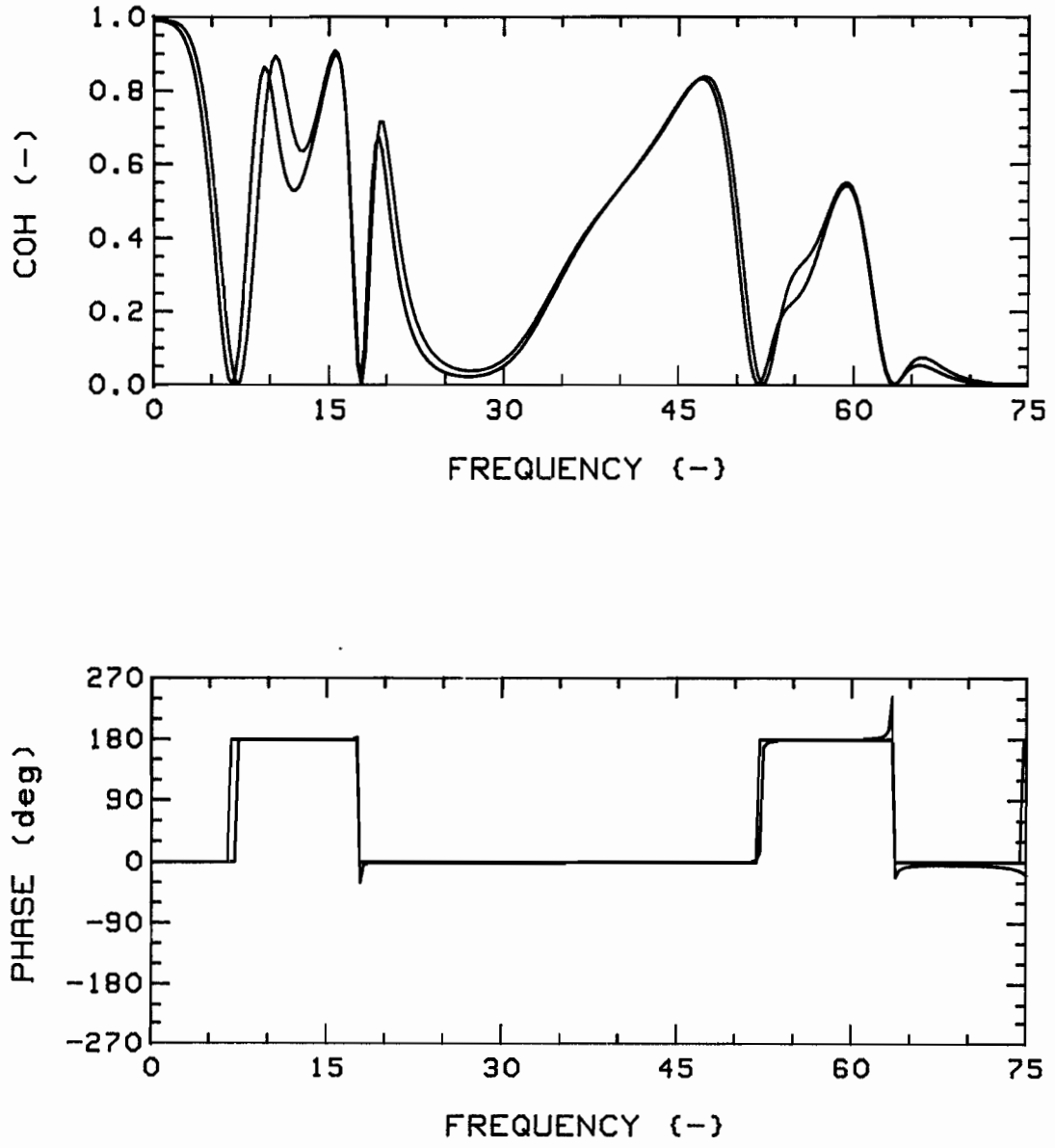

Fig.110e: Theoretical coherences for K = 28, G_c = 0.75, 4F/24R, R-R (diagonal pair), at u = 5; central (RED) versus diagonal (GREEN) offset system.

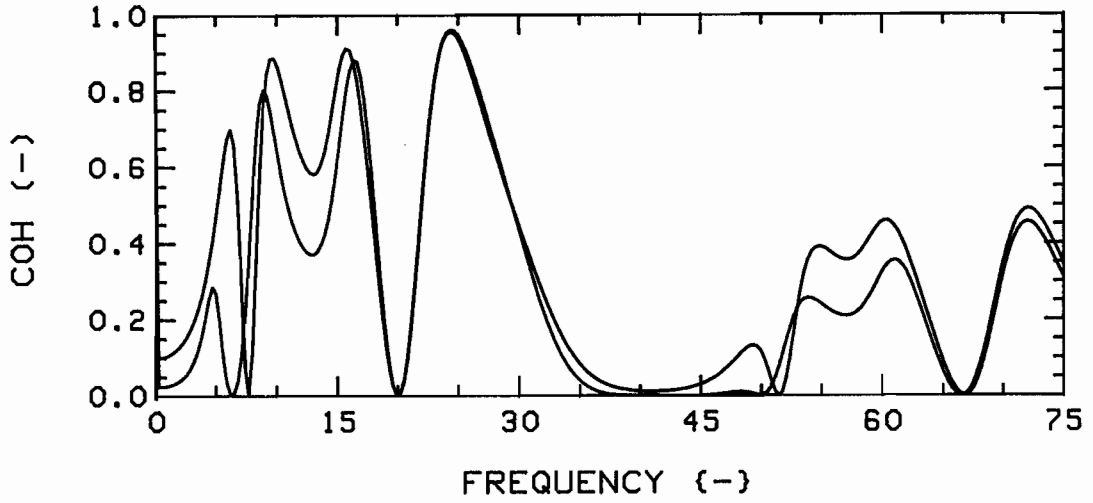

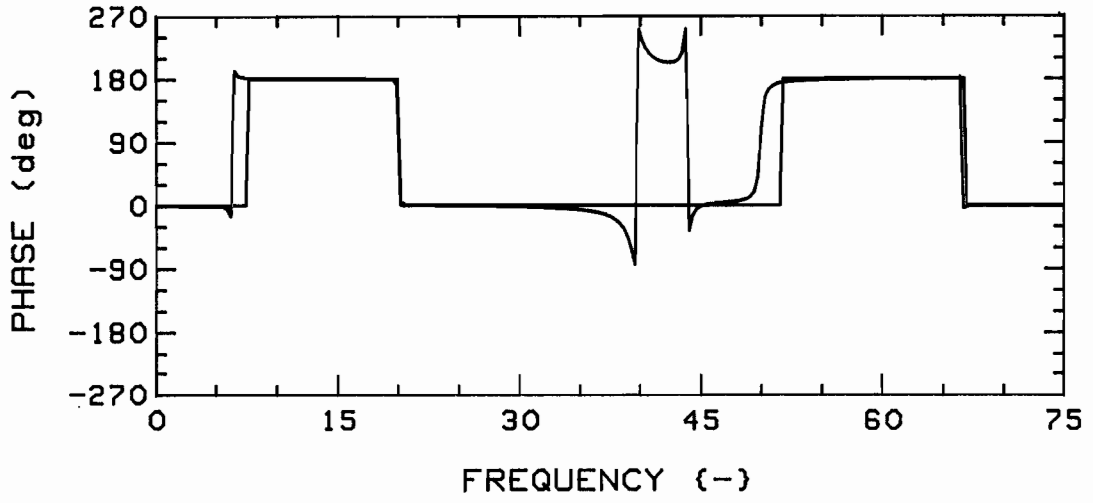

Fig.110f: Theoretical coherences for K = 28, G_c = 0.75, 4F/24R, T-T (diagonal pair), at u = 5; central (RED) versus diagonal (GREEN) offset system.

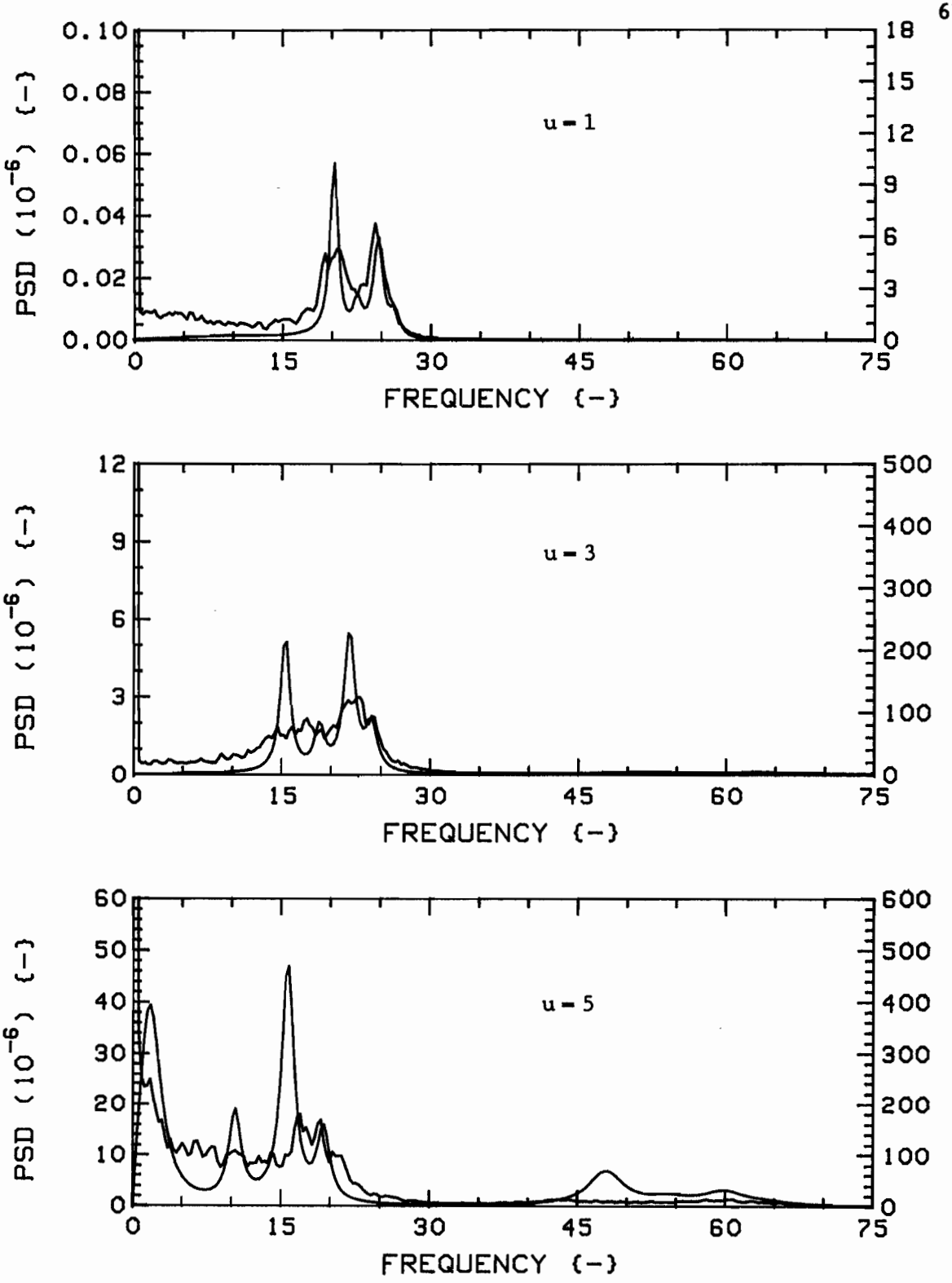

Fig.111a: Measured (RED) and theoretical (GREEN) vibration PSD's for K = 28, $G_c = 0.75$, 4F(5,6,1,16)/24R, Radial direction, Position 5.

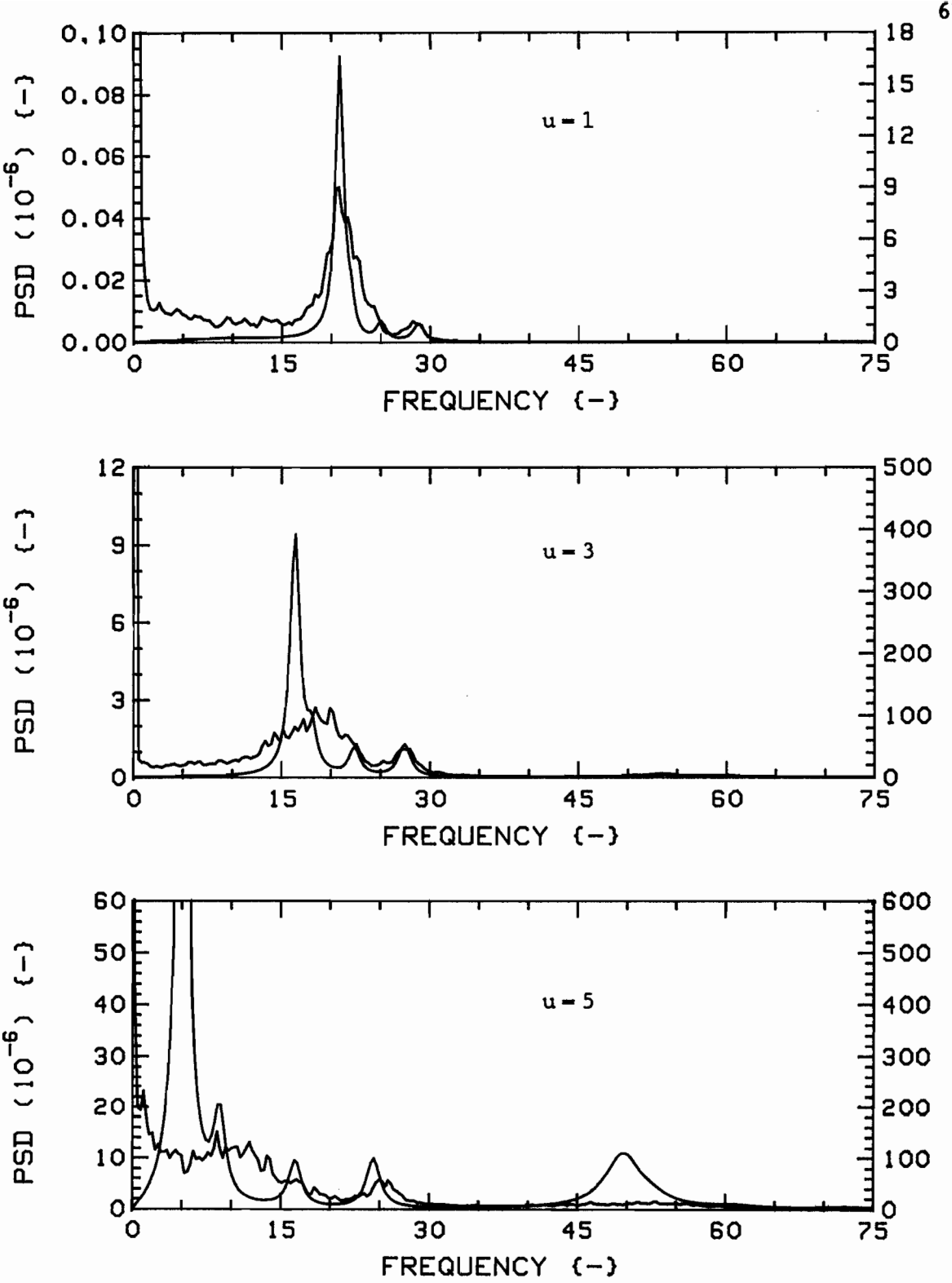

Fig.111b: Measured (RED) and theoretical (GREEN) vibration PSD's for K = 28, G_c = 0.75, 4F(5,6,1,16)/24R, Tangential direction, Position 5.

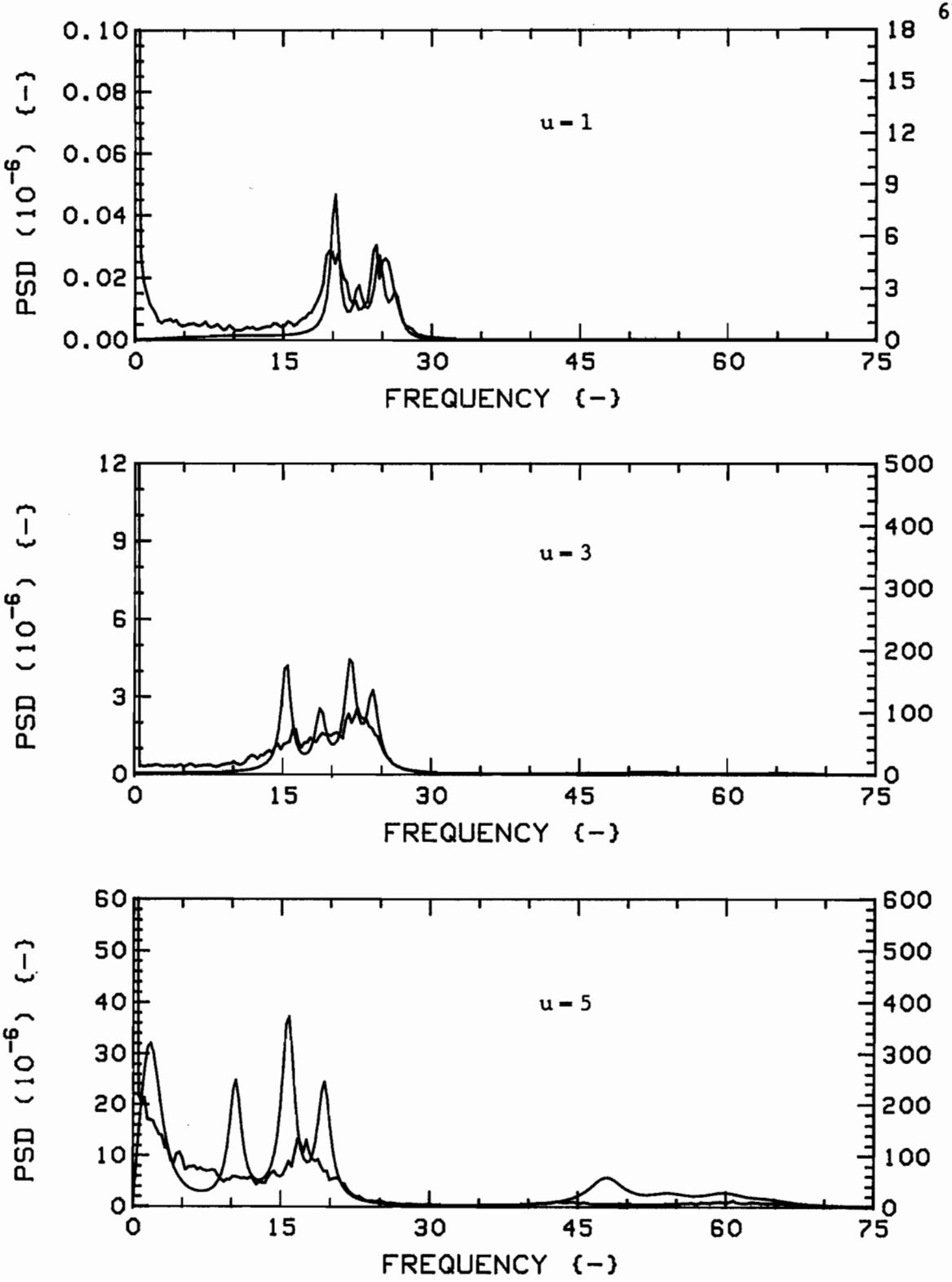

Fig.111c: Measured (RED) and theoretical (GREEN) vibration PSD's for K = 28, G_c = 0.75, 4F(5,6,1,16)/24R, Radial direction, Position 1.

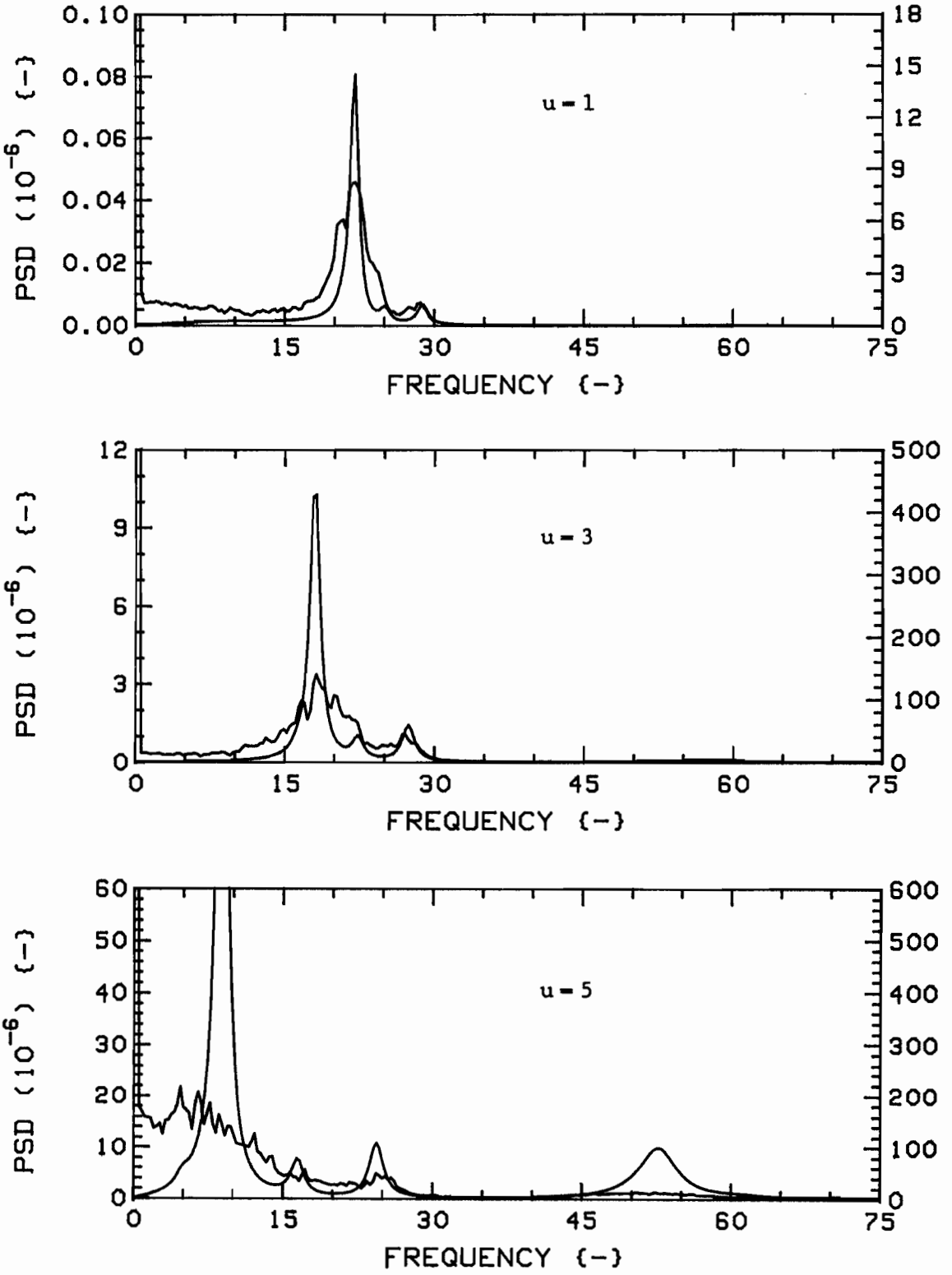

Fig.111d: Measured (RED) and theoretical (GREEN) vibration PSD's for K = 28, G_c = 0.75, 4F(5,6,1,16)/24R, Tangential direction, Position 1.

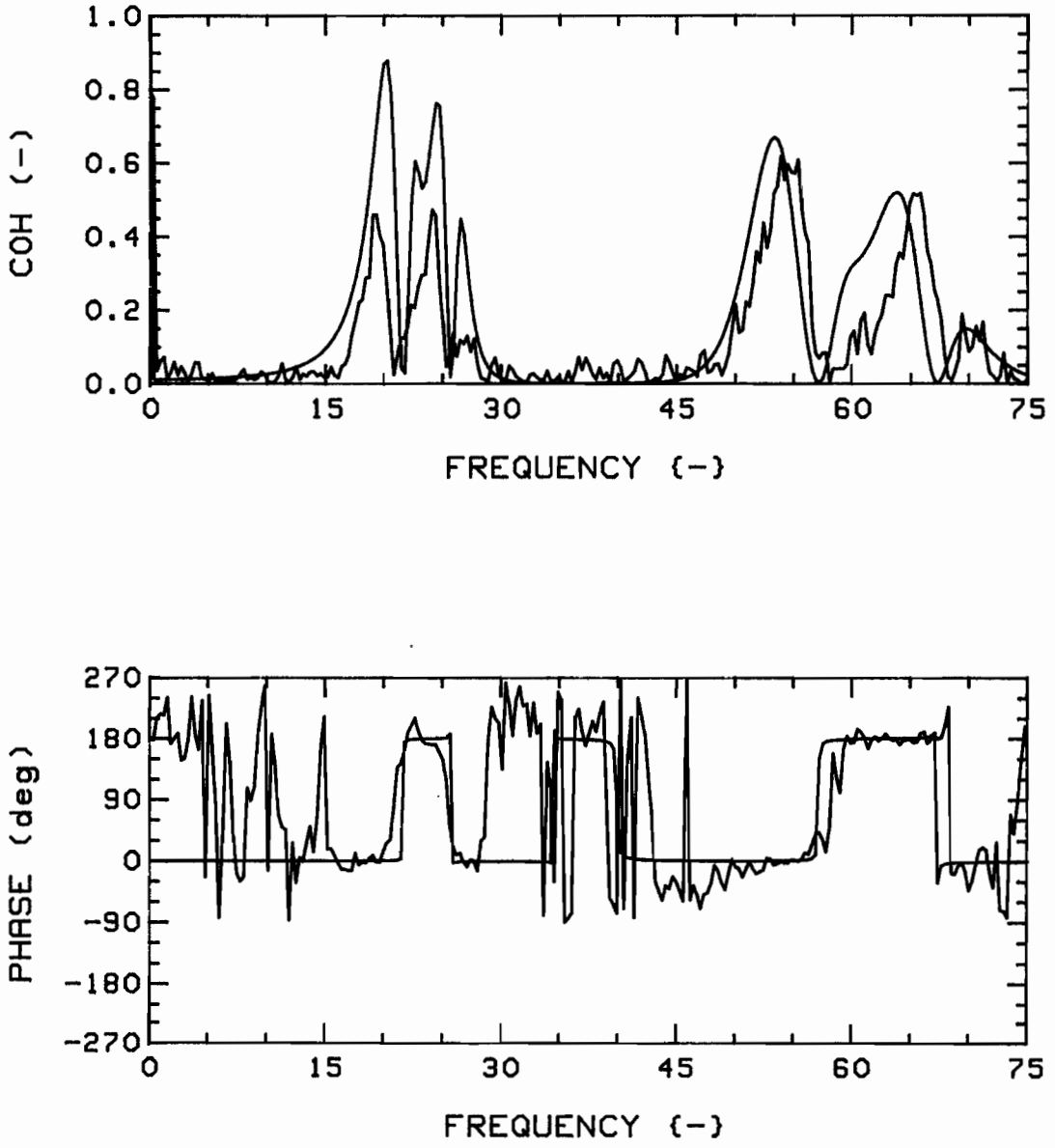

Fig.112a: Measured (RED) and theoretical (GREEN) coherence functions and phases, for K = 28, G_c = 0.75, 4F(5,6,1,16) /24R, R-R (5,1), at u = 1.

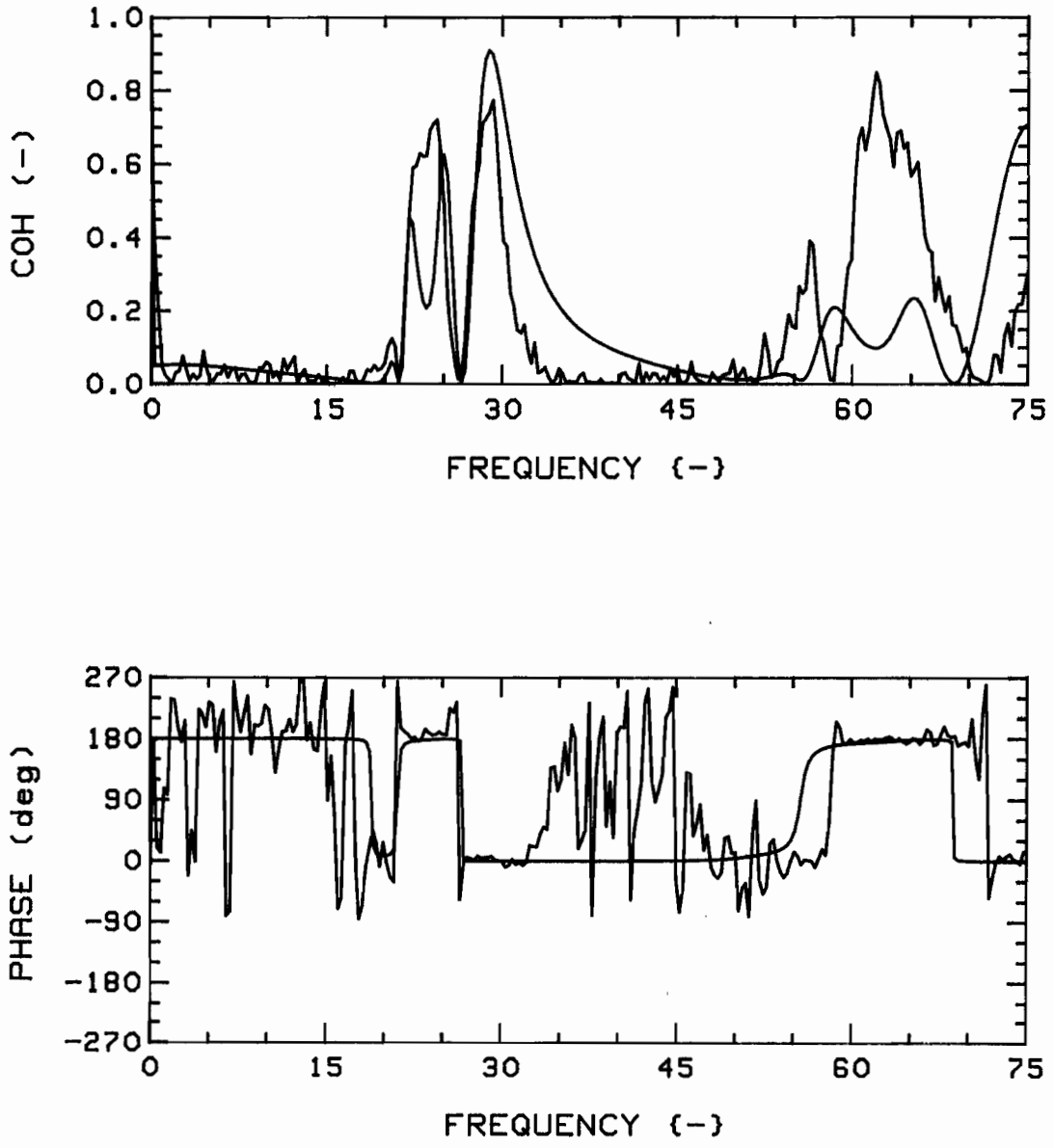

Fig.112b: Measured (RED) and theoretical (GREEN) coherence functions and phases, for K = 28, G_c = 0.75, 4F(5,6,1,16) /24R, T-T (5,1), at u = 1.

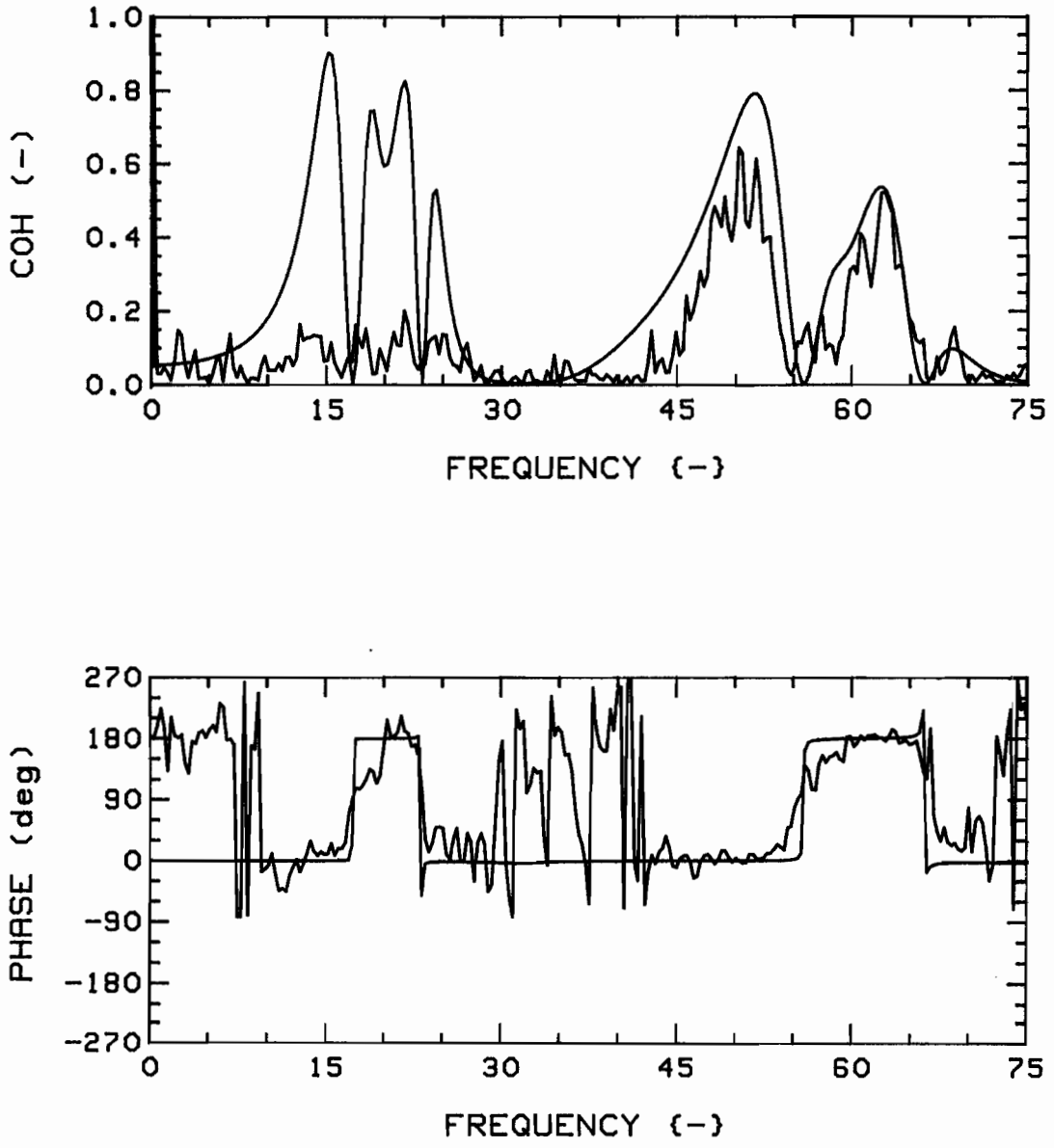

Fig.112c: Measured (RED) and theoretical (GREEN) coherence functions and phases, for K = 28, G_c = 0.75, 4F(5,6,1,16) /24R, R-R (5,1), at u = 3.

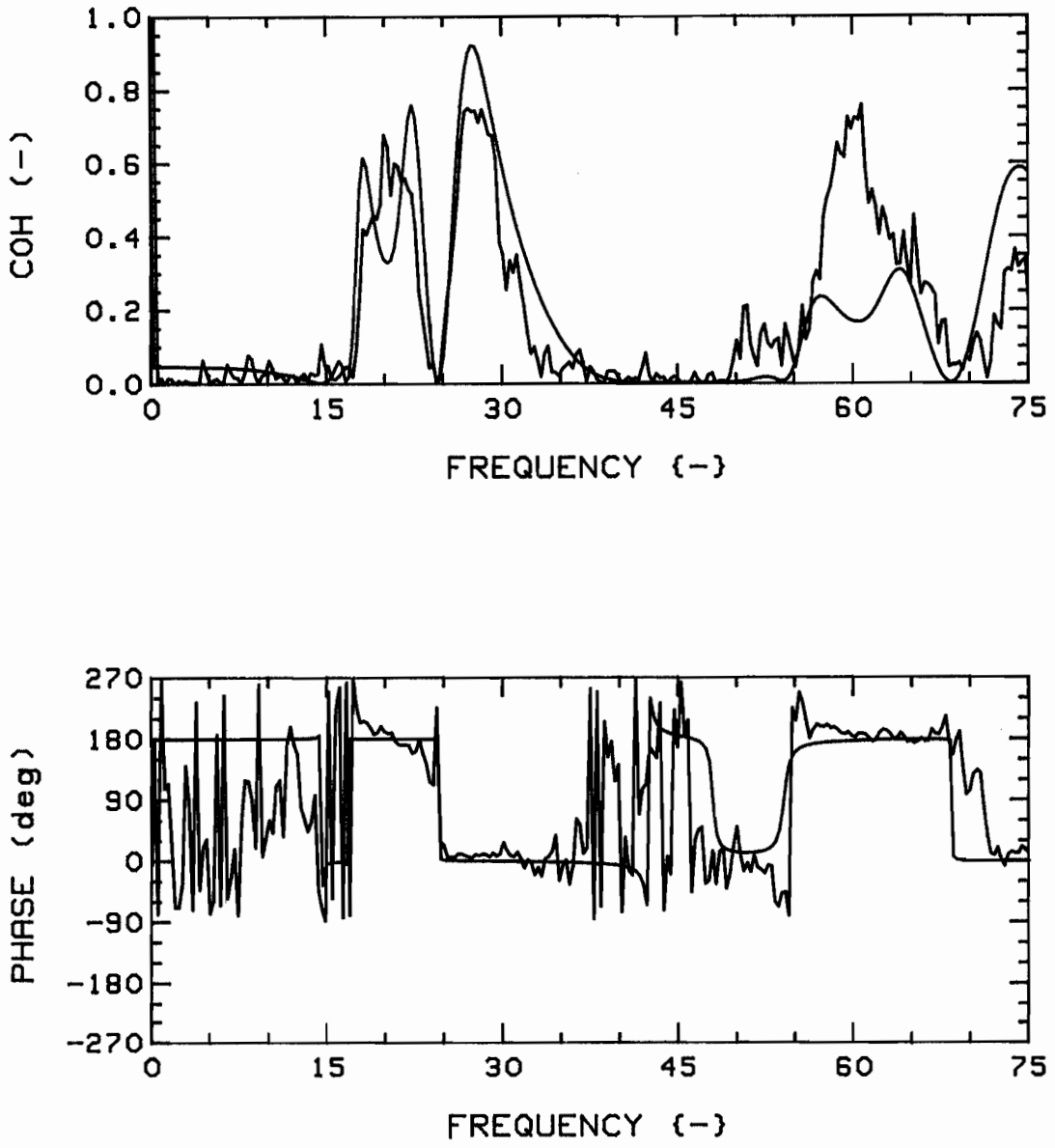

Fig.112d: Measured (RED) and theoretical (GREEN) coherence functions and phases, for K = 28, G_c = 0.75, 4F(5,6,1,16) /24R, T-T (5,1), at u = 3.

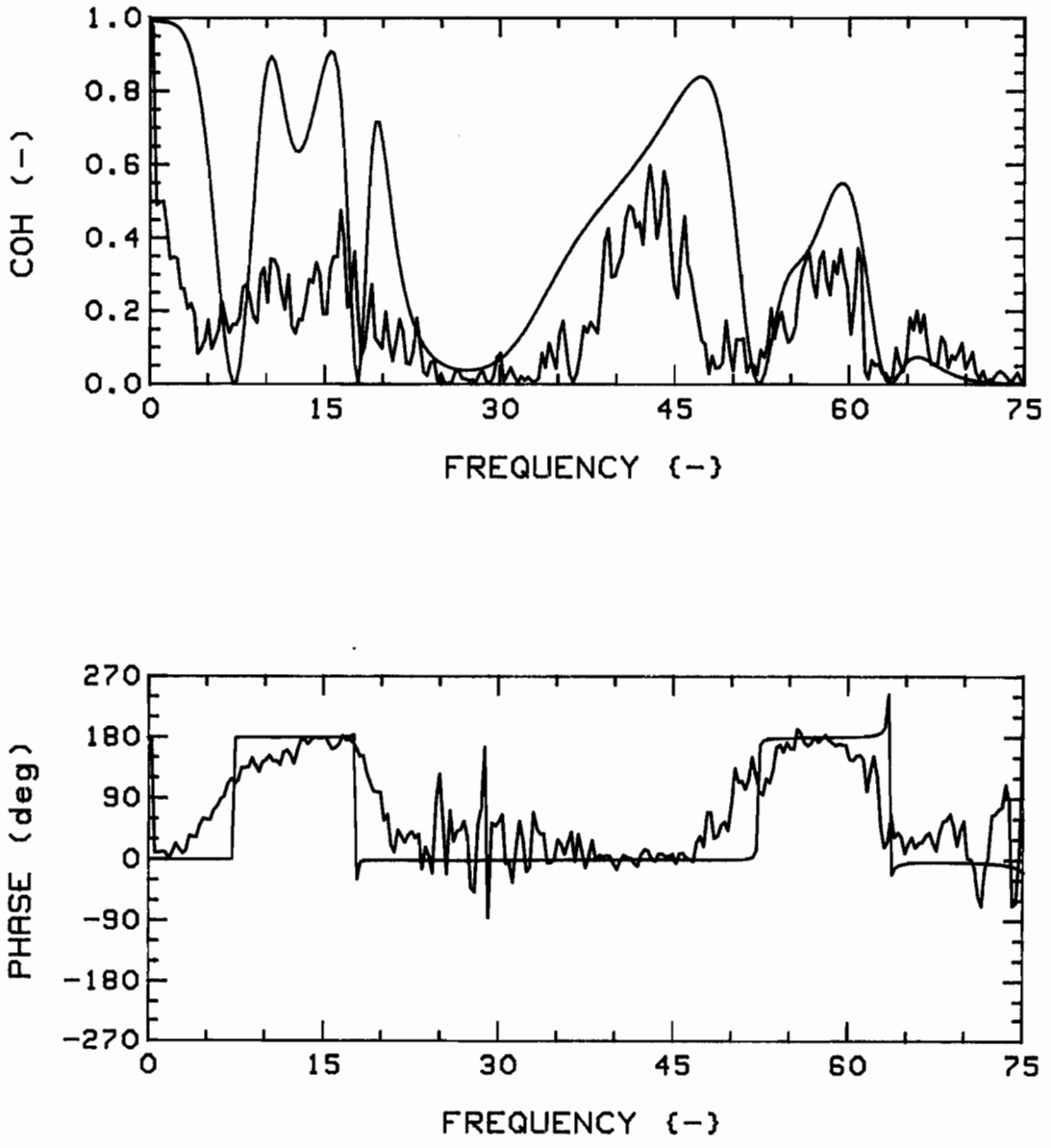

Fig.112e: Measured (RED) and theoretical (GREEN) coherence functions and phases, for K = 28, G_c = 0.75, 4F(5,6,1,16) /24R, R-R (5,1), at u = 5.

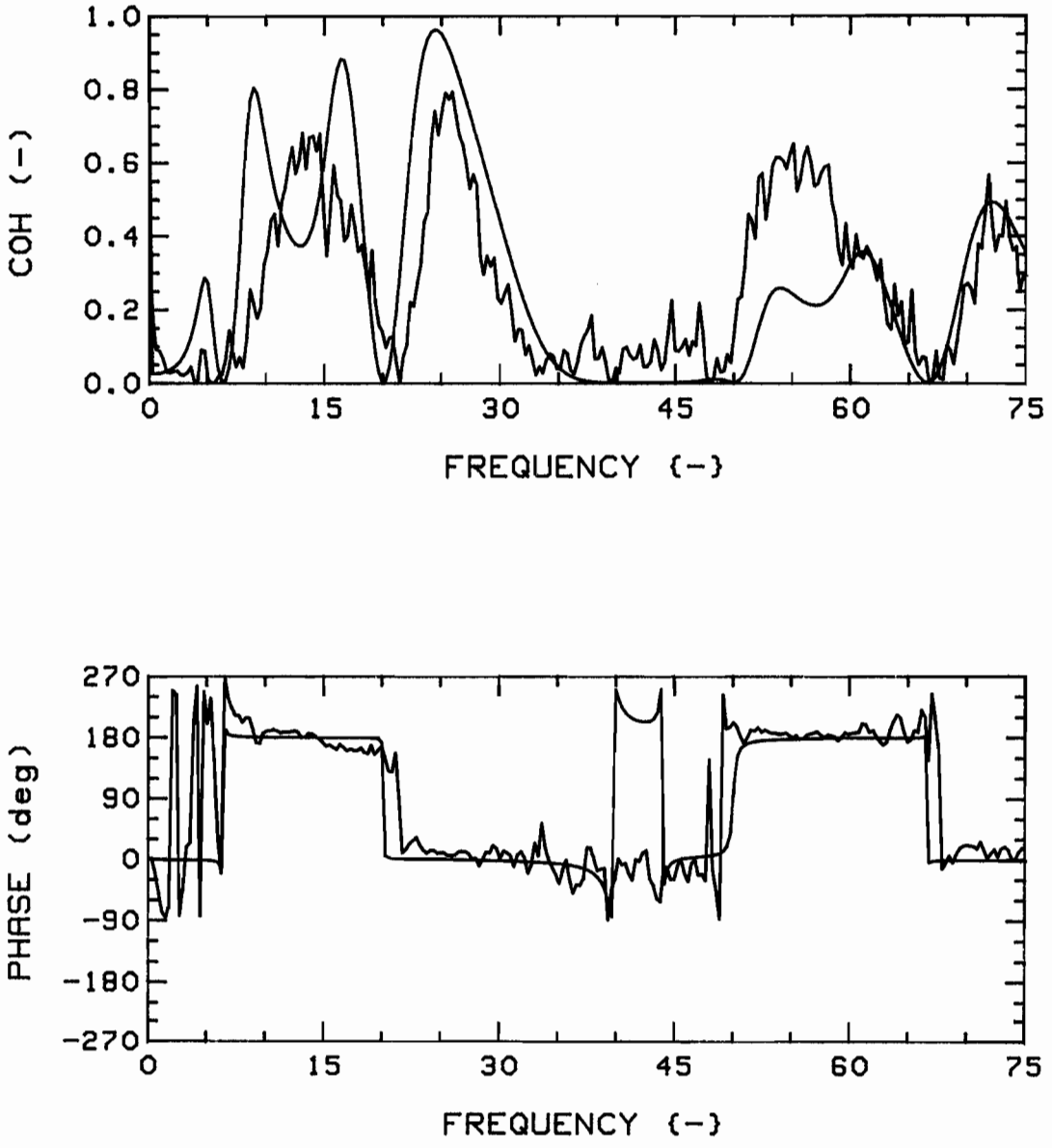

Fig.112f: Measured (RED) and theoretical (GREEN) coherence functions and phases, for K = 28, G_c = 0.75, 4F(5,6,1,16) /24R, T-T (5,1), at u = 5.

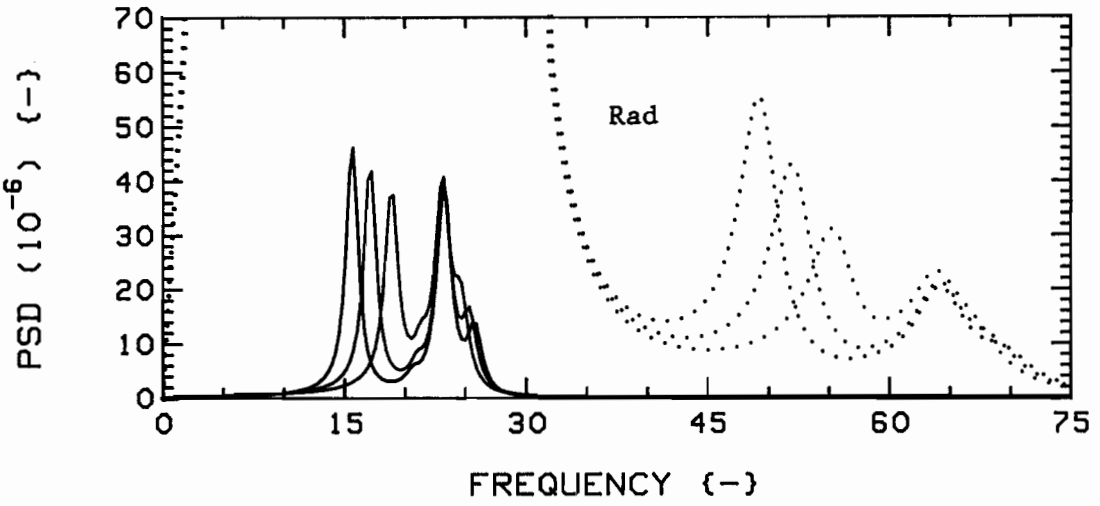

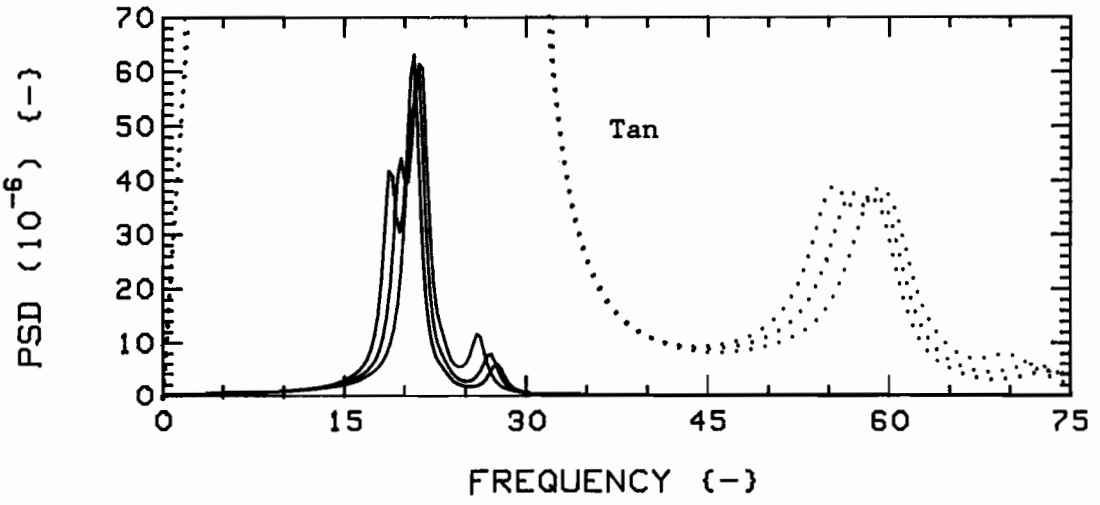

Fig.113: Effect of inter-cylinder spacing on theoretical vibration PSD's for K = 4, 4F system, at u = 3; G_c = 0.75 (RED), 1.00 (GREEN), and 1.50 (BLUE).

The dotted traces are expansions of the solid ones; scale is 2.0×10^{-7}.

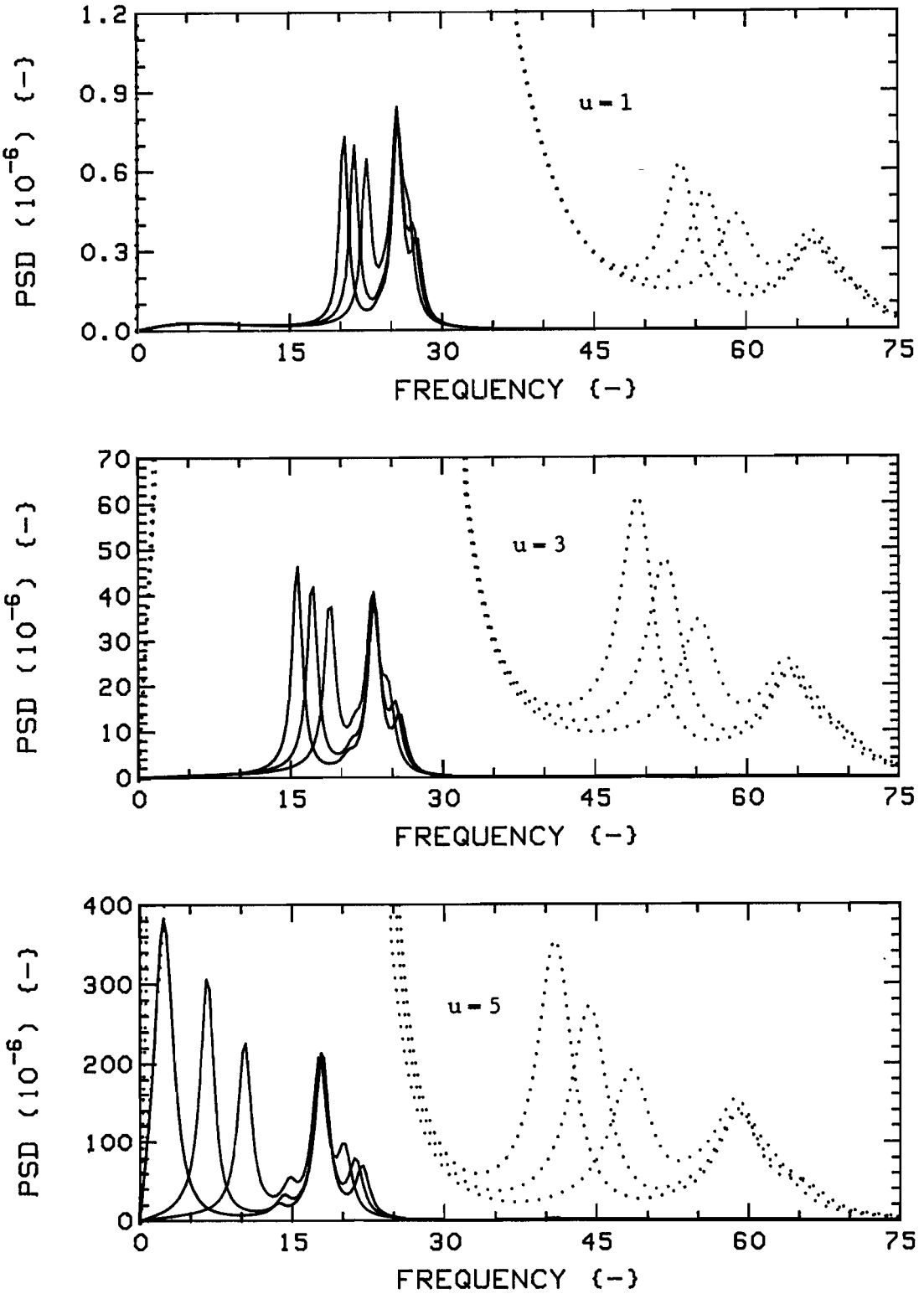

Fig.114a: Effect of inter-cylinder spacing on theoretical vibration PSD's for K = 4, 4F system, in the Radial direction; G_c = 0.75 (RED), 1.00 (GREEN), and 1.50 (BLUE).

The dotted traces are expansions of the solid ones; scales are, from top: 2.0×10^{-9}, 1.8×10^{-7}, 4.0×10^{-6}.

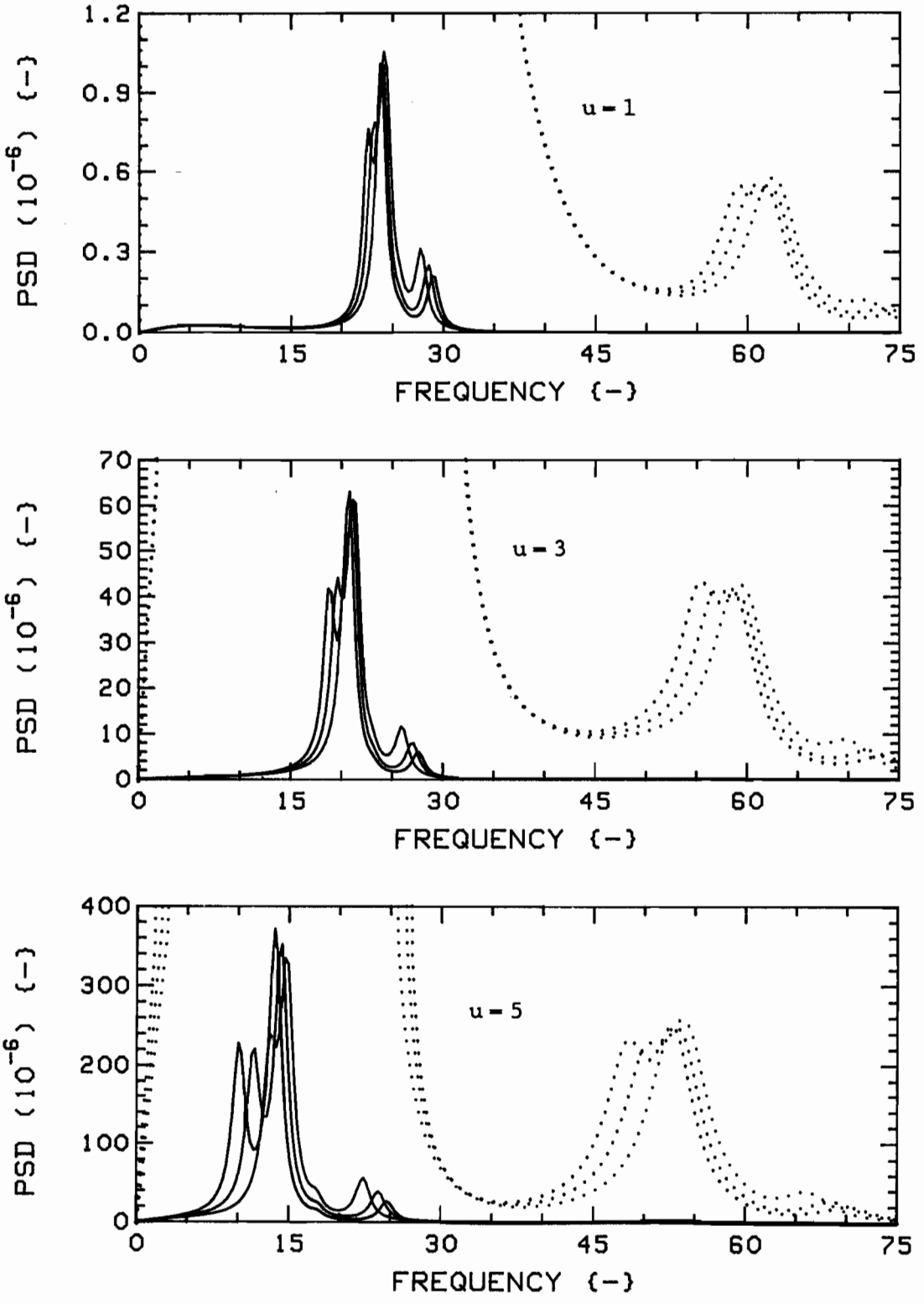

Fig.114b: Effect of inter-cylinder spacing on theoretical vibration PSD's for K = 4, 4F system, in the Tangential direction; $G_c = 0.75$ (RED), 1.00 (GREEN), and 1.50 (BLUE).

The dotted traces are expansions of the solid ones;

scales are, from top: 2.0×10^{-9}, 1.8×10^{-7}, 4.0×10^{-6}.

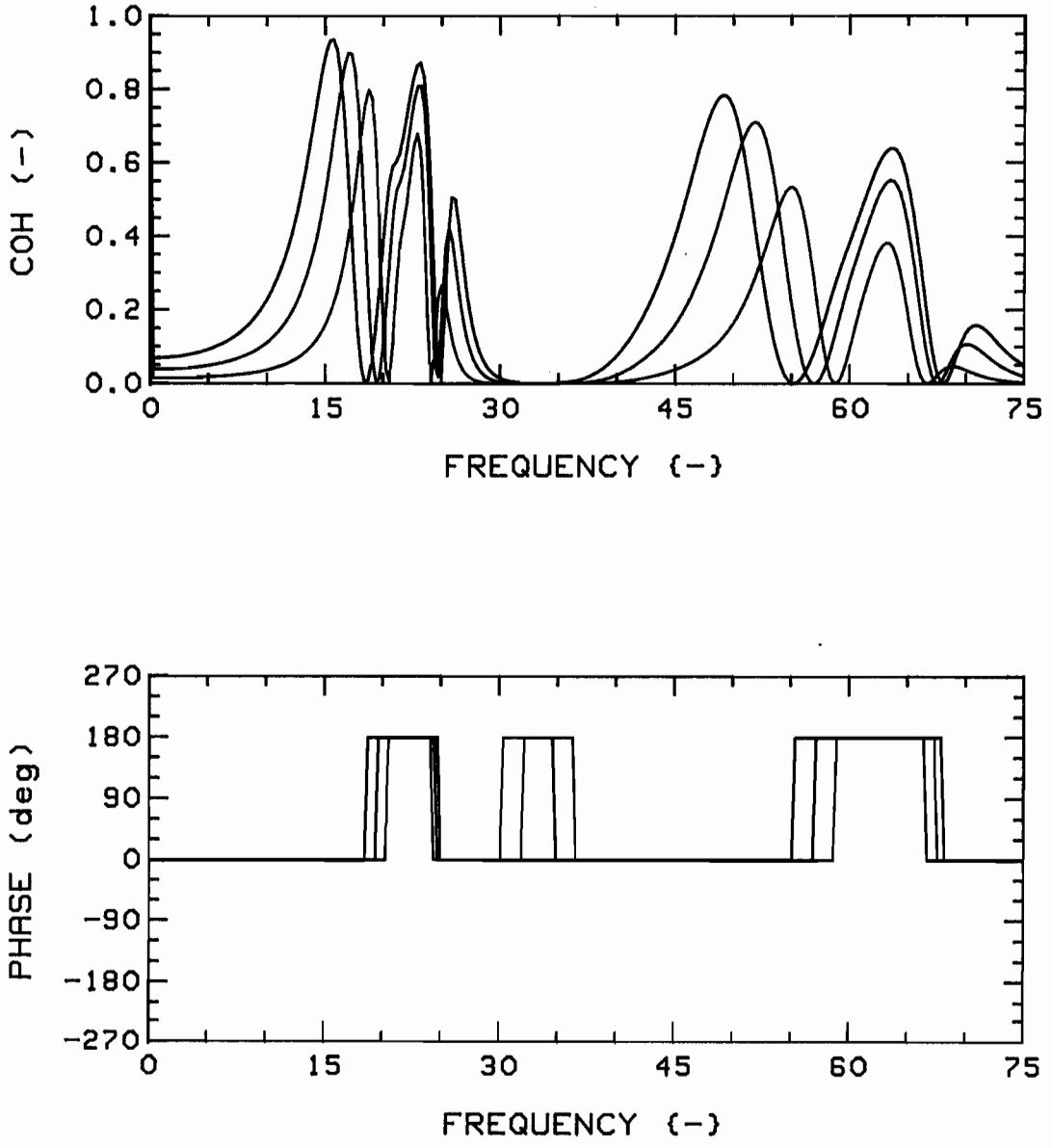

Fig.115a: Effect of inter-cylinder spacing on theoretical coherence functions and phases for K = 4, 4F system, R-R (1,3), at u = 3; G_c = 0.75 (RED), 1.00 (GREEN), and 1.50 (BLUE).

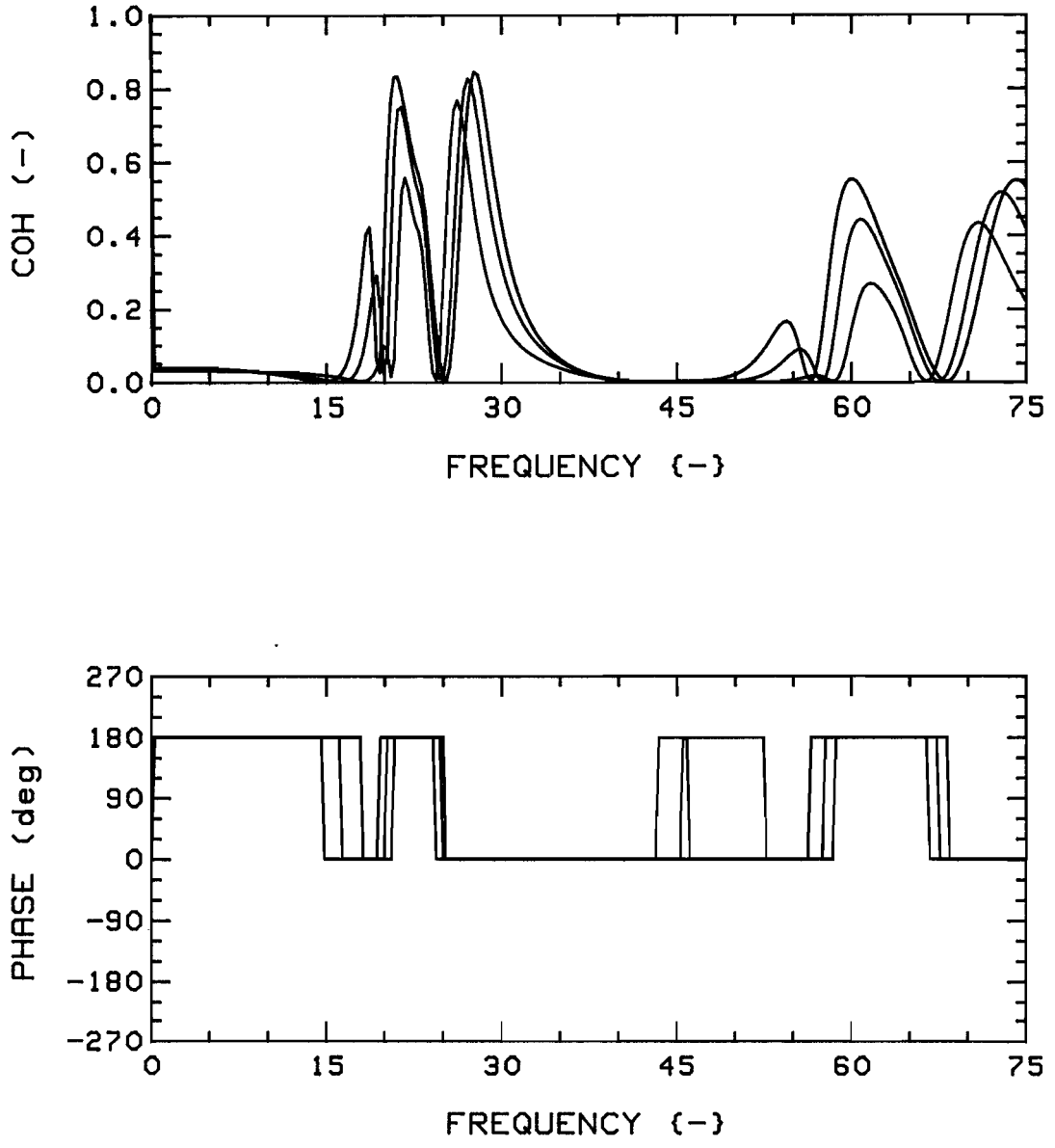

Fig.115b: Effect of inter-cylinder spacing on theoretical coherence functions and phases for K = 4, 4F system, T-T (1,3), at u = 3; G_c = 0.75 (RED), 1.00 (GREEN), and 1.50 (BLUE).

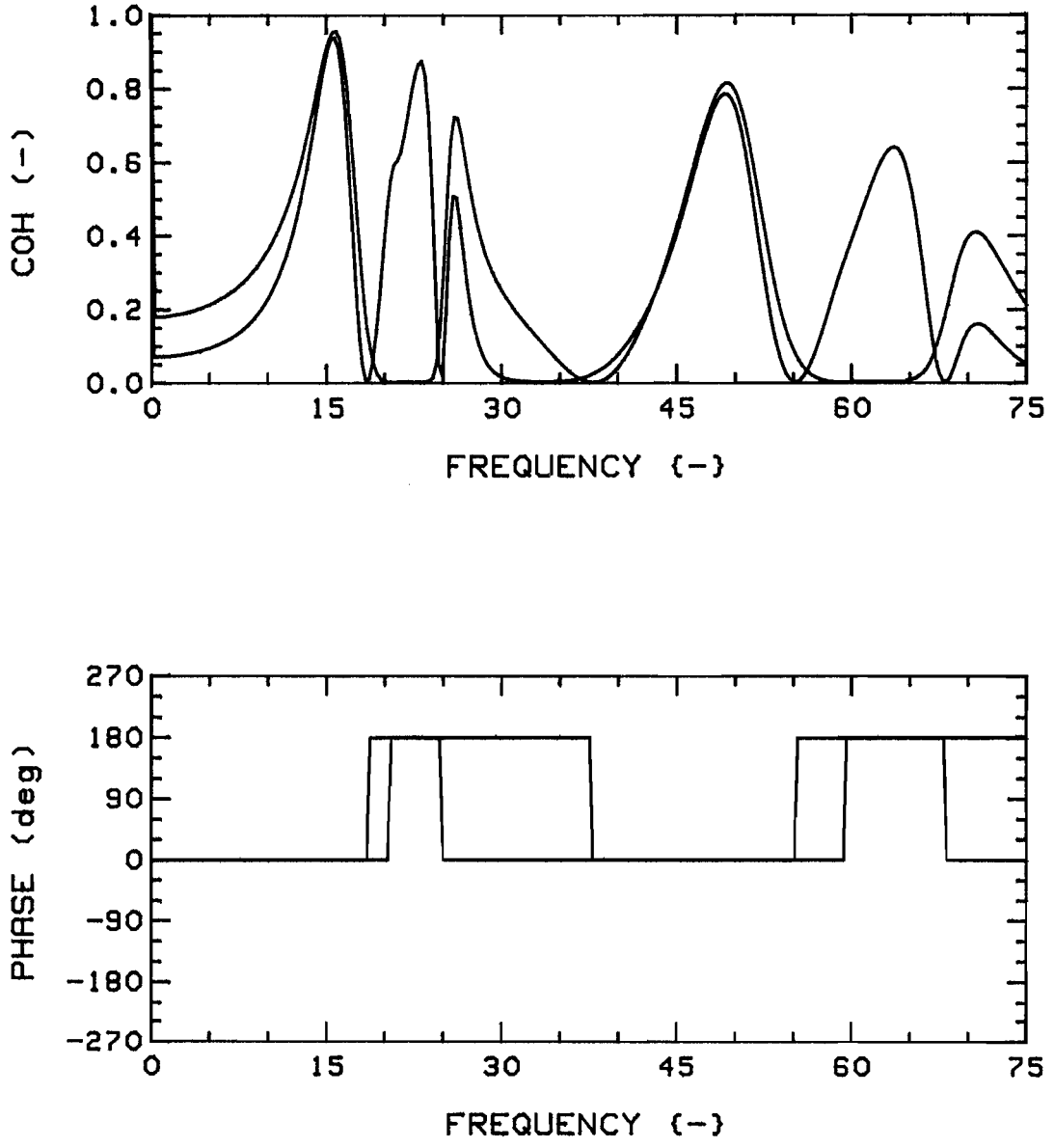

Fig.116a: Theoretical coherence functions and phases for K = 4, G_c = 0.75, 4F, at u = 3; R-R, Position pairs 1,3 (RED) and 1,2 (GREEN).

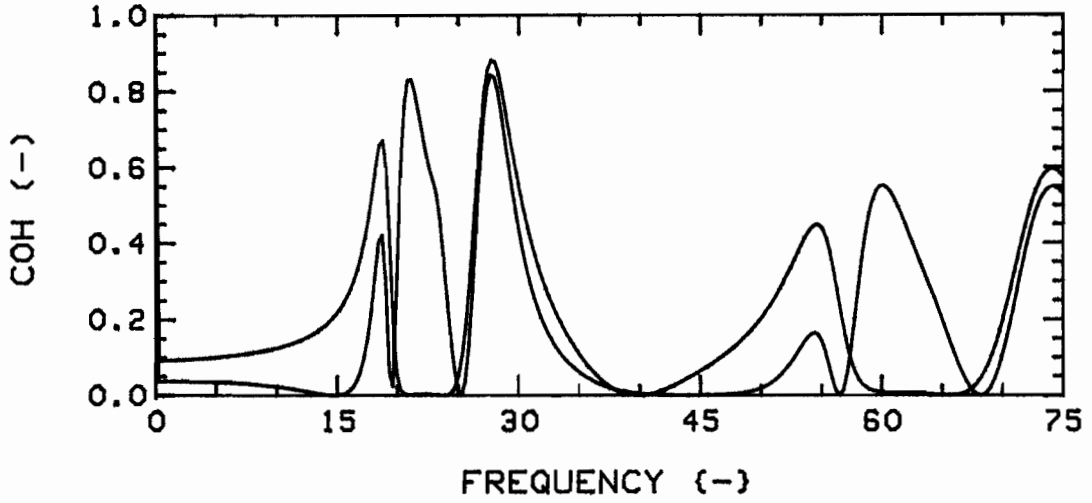

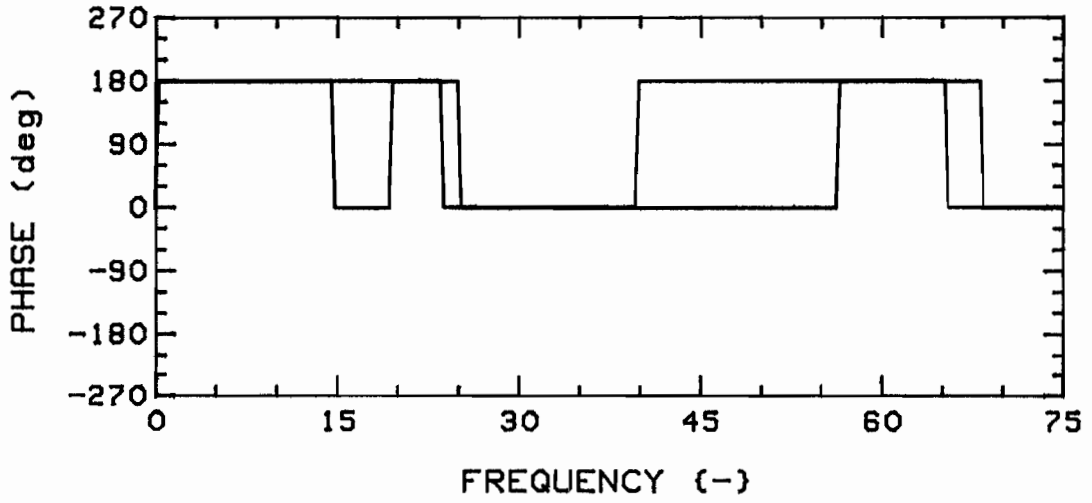

Fig.116b: Theoretical coherence functions and phases for K = 4, G_c = 0.75, 4F, at u = 3; T-T, Position pairs 1,3 (RED) and 1,2 (GREEN).

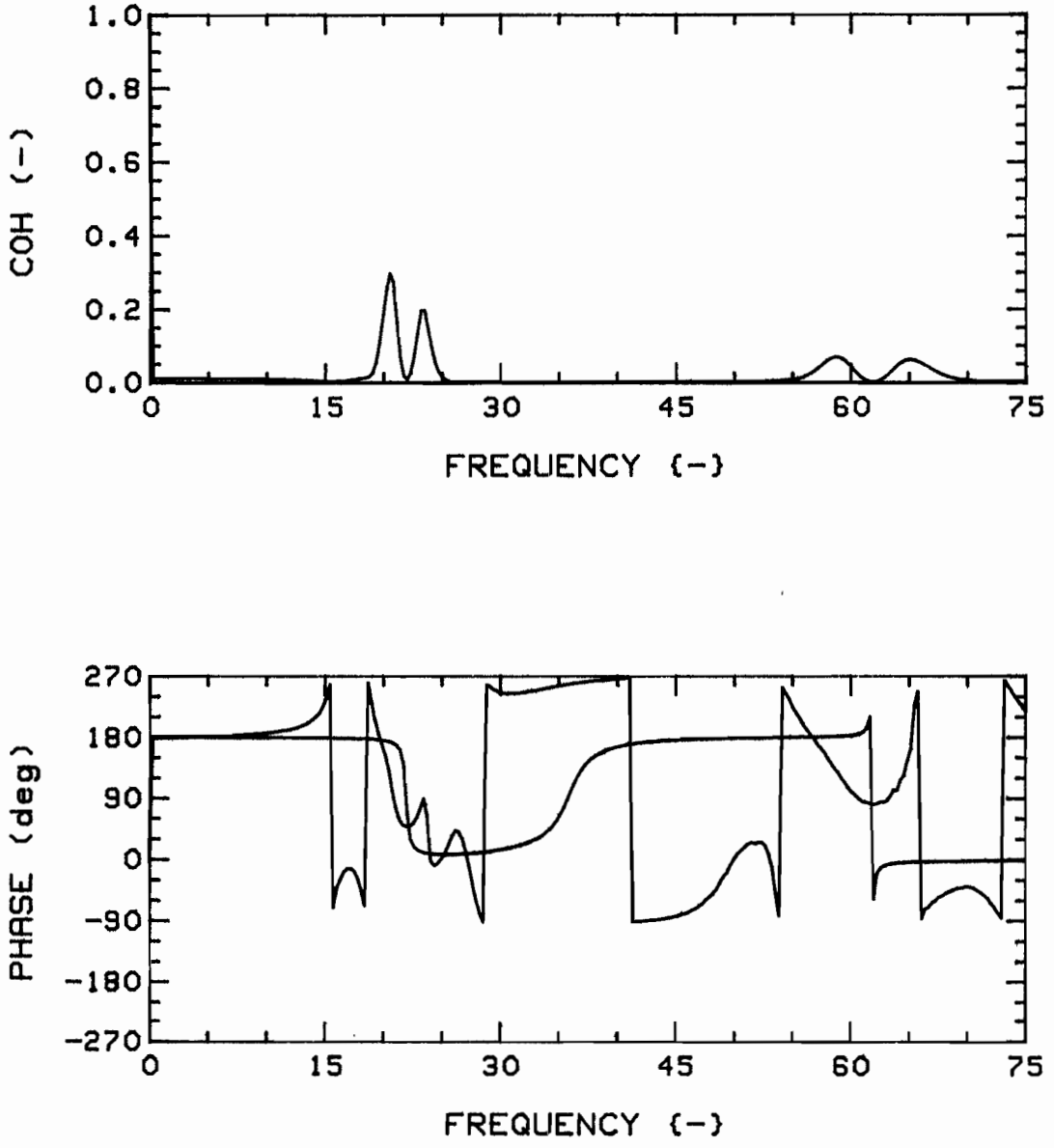

Fig.117: Theoretical coherence functions and phases for K = 4, G_c = 0.75, 4F, at u = 3; R-T, Position pairs 1,3 (RED) and 1,2 (GREEN).

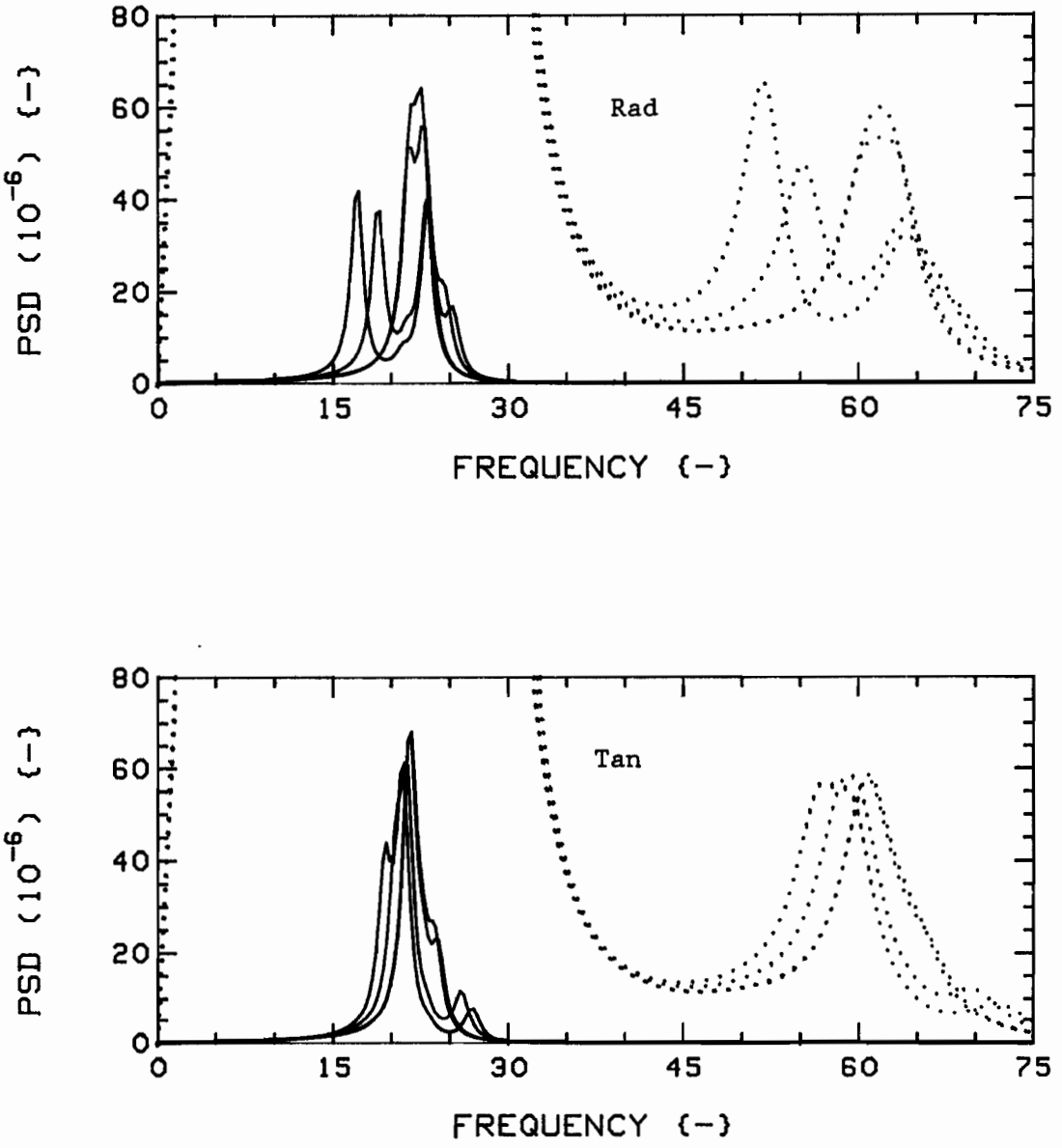

Fig.118: Effect of inter-cylinder spacing on theoretical vibration PSD's for K = 4, 4F system, at u = 3; G_c = 1.00 (RED), 1.50 (GREEN), 2.00 (BLUE), and 2.50 (BLACK).

The dotted traces are expansions of the solid ones; scale is 1.5×10^{-7}.

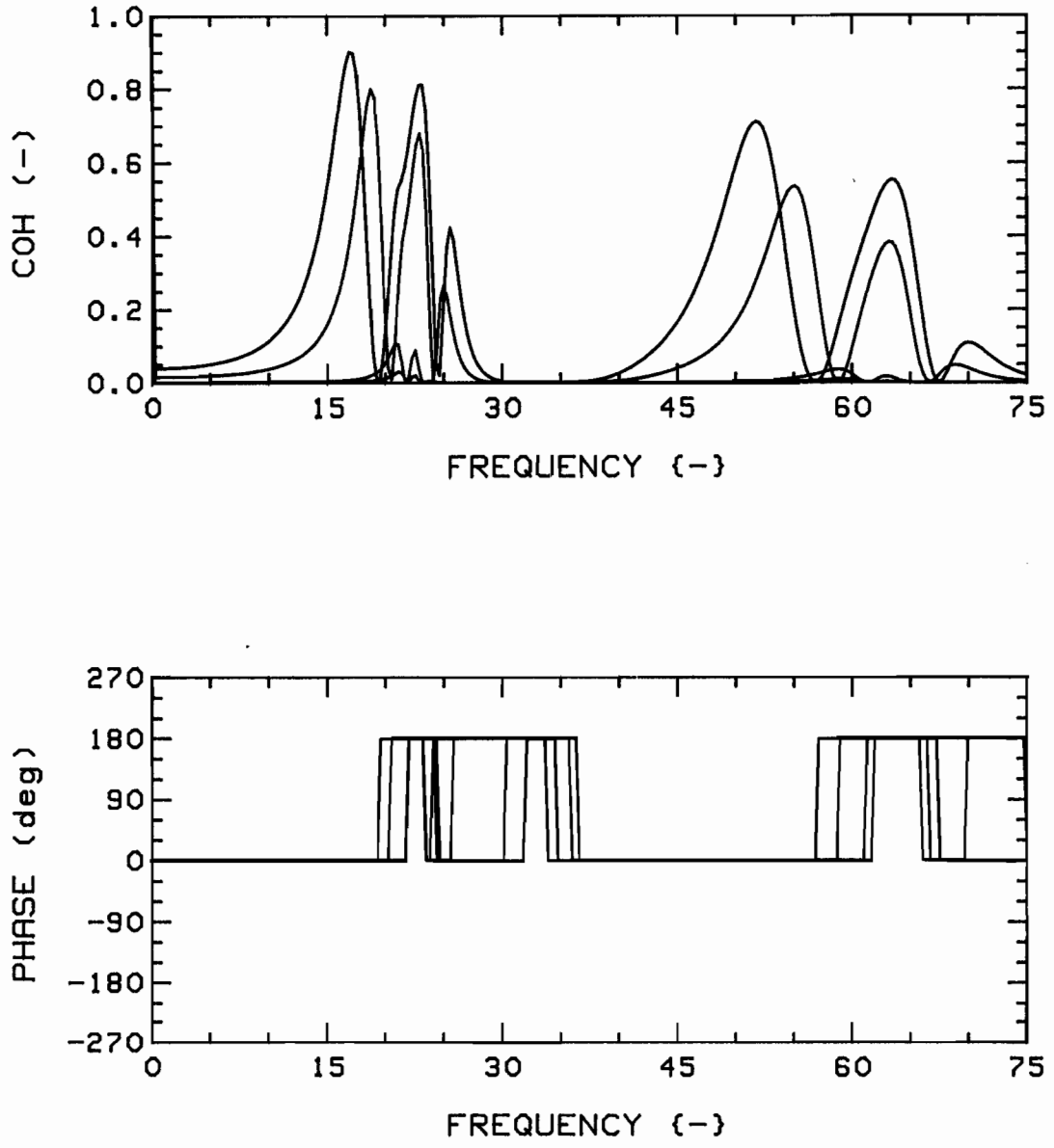

Fig.119a: Effect of inter-cylinder spacing on theoretical coherence functions and phases for K = 4, 4F system, R-R (1,3), at u = 3; G_c = 1.00 (RED), 1.50 (GREEN), 2.00 (BLUE), and 2.50 (BLUE).

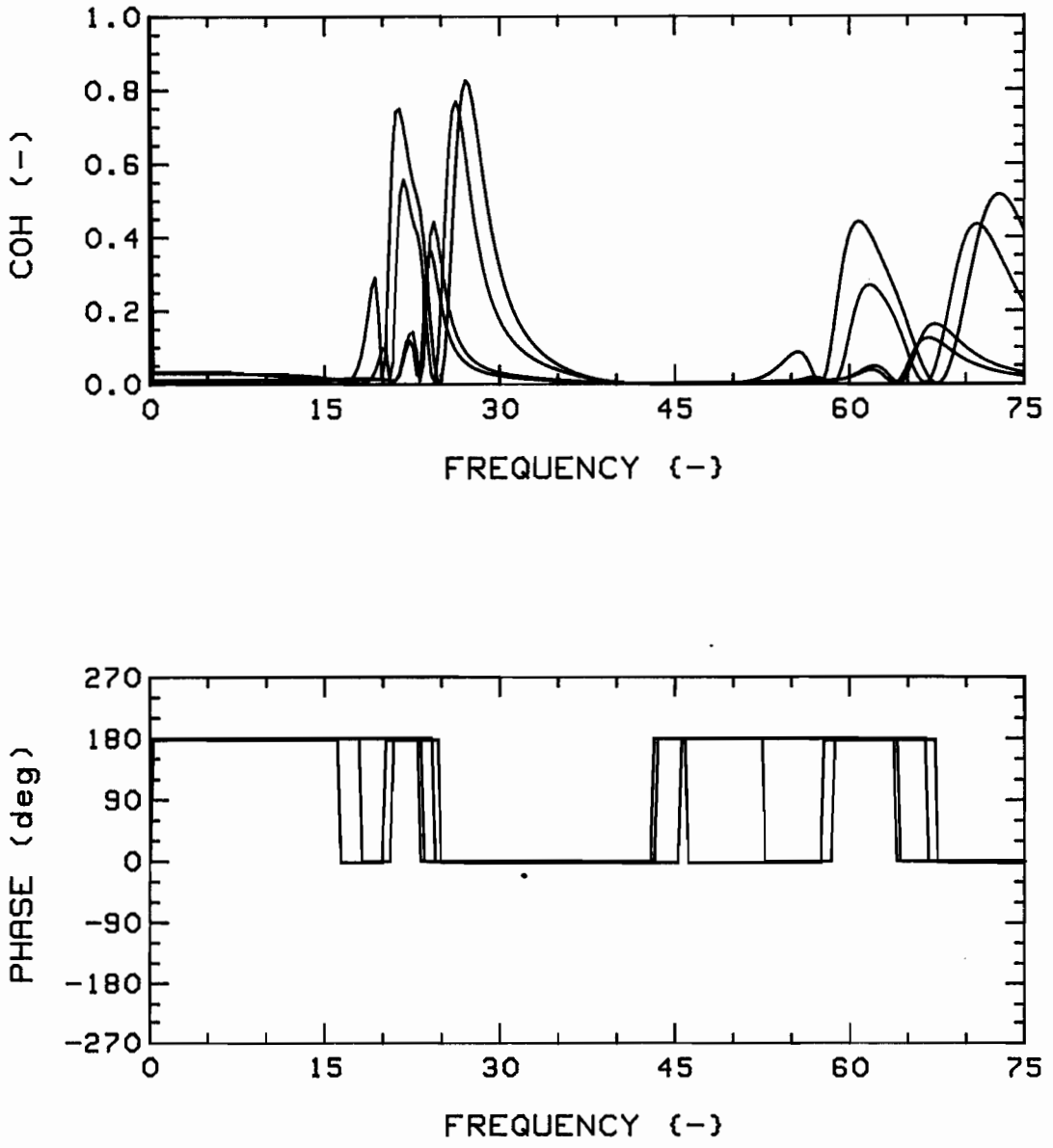

Fig.119b: Effect of inter-cylinder spacing on theoretical coherence functions and phases for K = 4, 4F system, T-T (1,3), at u = 3; G_c = 1.00 (RED), 1.50 (GREEN), 2.00 (BLUE), and 2.50 (BLUE).

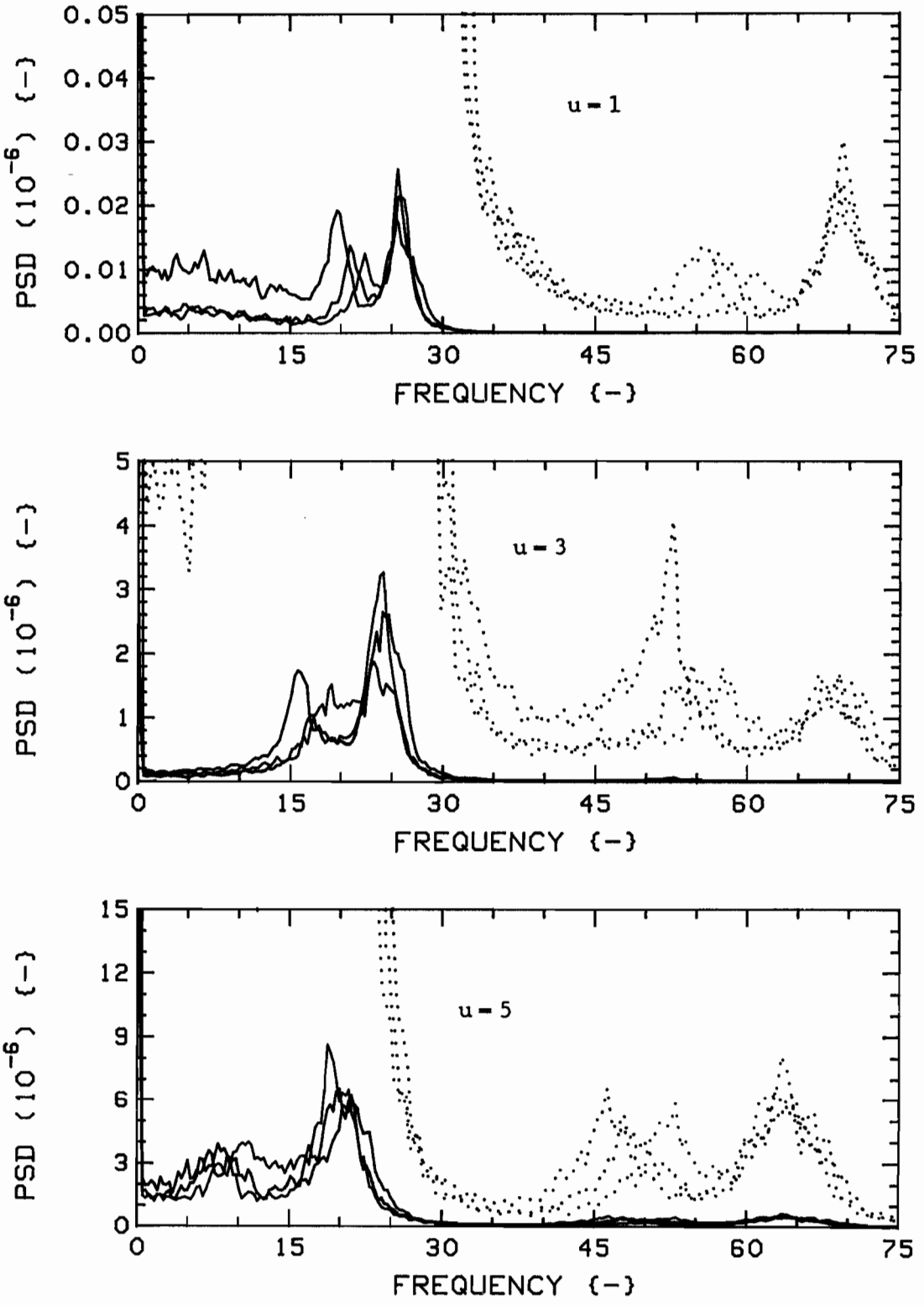

Fig.120a: Effect of inter-cylinder spacing on measured vibration PSD's for K = 4, 4F system, in the Radial direction; $G_c = 0.75$ (RED), 1.00 (GREEN), and 1.50 (BLUE).

The dotted traces are expansions of the solid ones; scales are, from top: 3.0×10^{-10}, 8.0×10^{-8}, 1.2×10^{-6}.

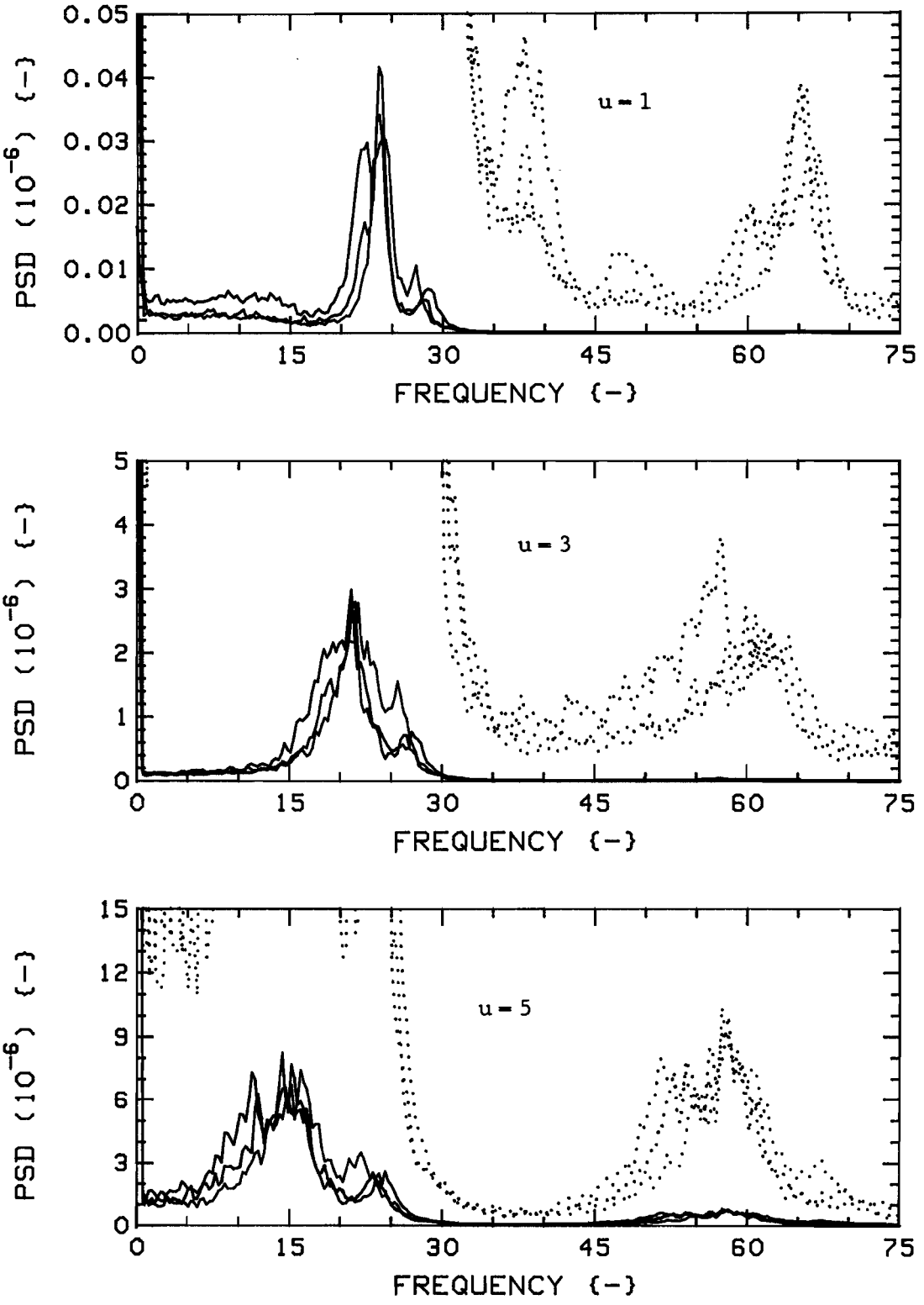

Fig.120b: Effect of inter-cylinder spacing on measured vibration PSD's for K = 4, 4F system, in the Tangential direction; G_c = 0.75 (RED), 1.00 (GREEN), and 1.50 (BLUE).

The dotted traces are expansions of the solid ones; scales are, from top: 3.0×10^{-10}, 8.0×10^{-8}, 1.2×10^{-6}.

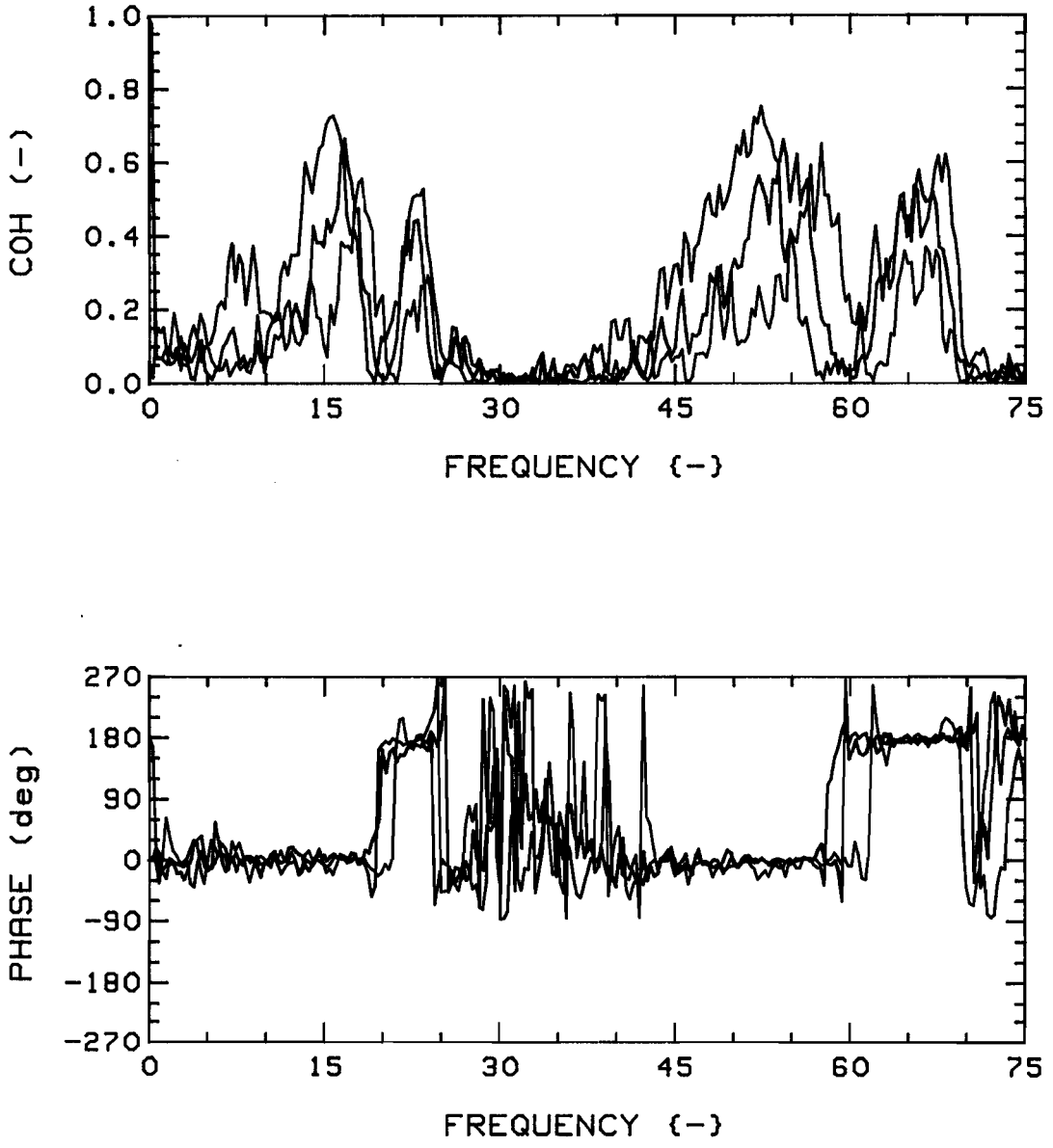

Fig.121a: Effect of inter-cylinder spacing on measured coherence functions and phases for K = 4, 4F system, R-R (1,3), at u = 3; G_c = 0.75 (RED), 1.00 (GREEN), and 1.50 (BLUE).

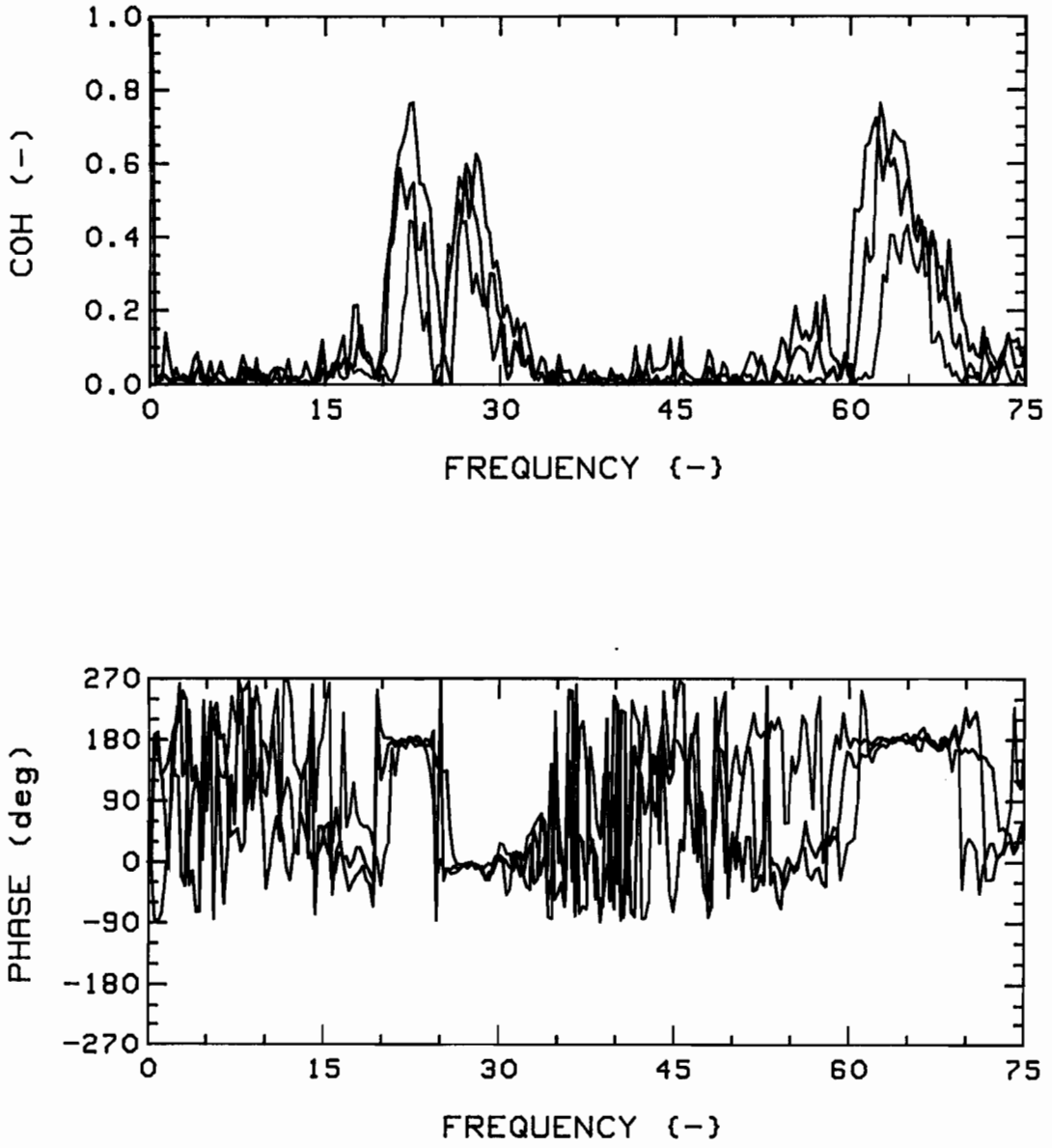

Fig.121b: Effect of inter-cylinder spacing on measured coherence functions and phases for K = 4, 4F system, T-T (1,3), at u = 3; G_c = 0.75 (RED), 1.00 (GREEN), and 1.50 (BLUE).

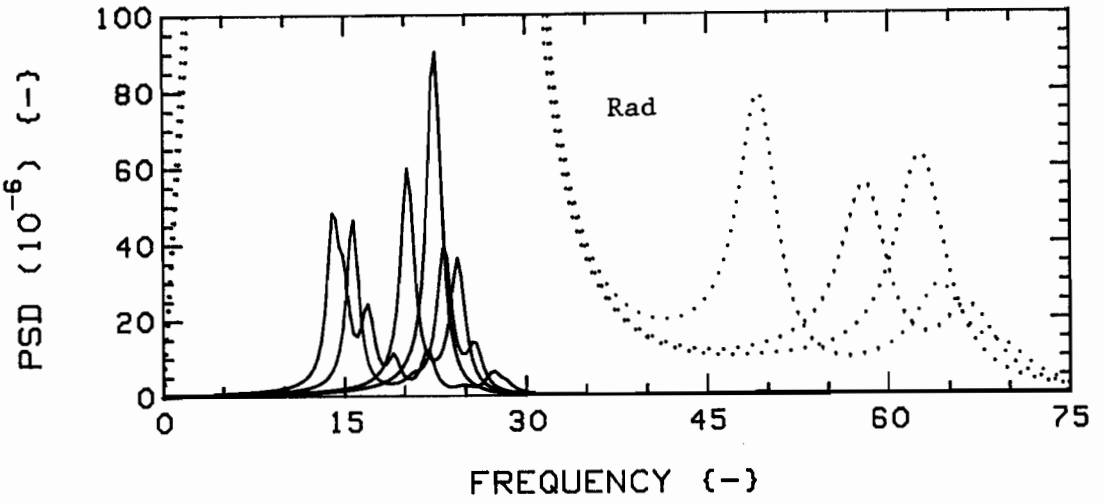

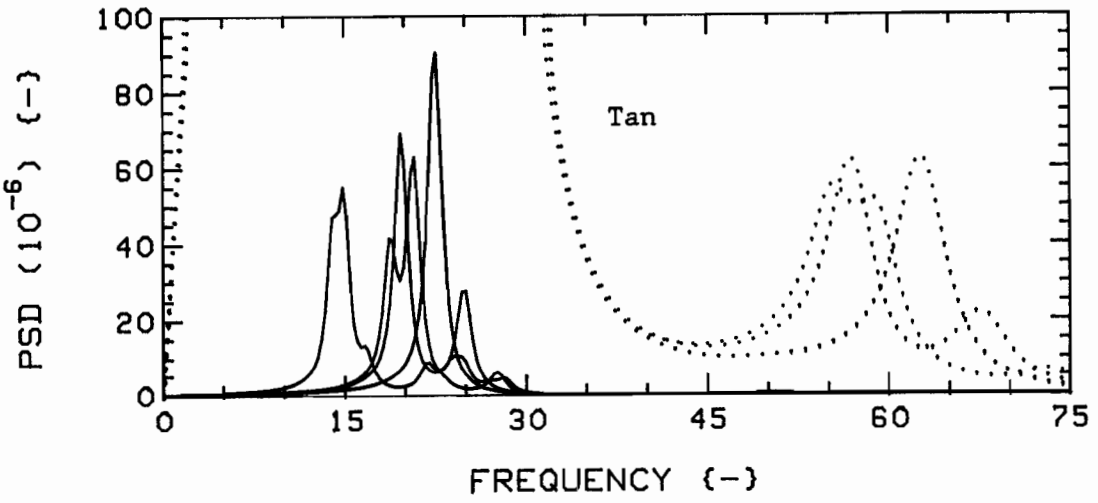

Fig.122: Effect of number of cylinders on theoretical vibration PSD's for Flexible cylinder bundles, with K = 4, G_c = 0.75 spacing, at u = 3; K = 1 (RED), 2(1,3) (GREEN), 4 (BLUE), and 12 (BLACK).

The dotted traces are expansions of the solid ones;

scale is 2.0×10^{-7}. Note that the expanded K = 12 case is not shown as N = 2 (instead of N = 3) was used in computations.

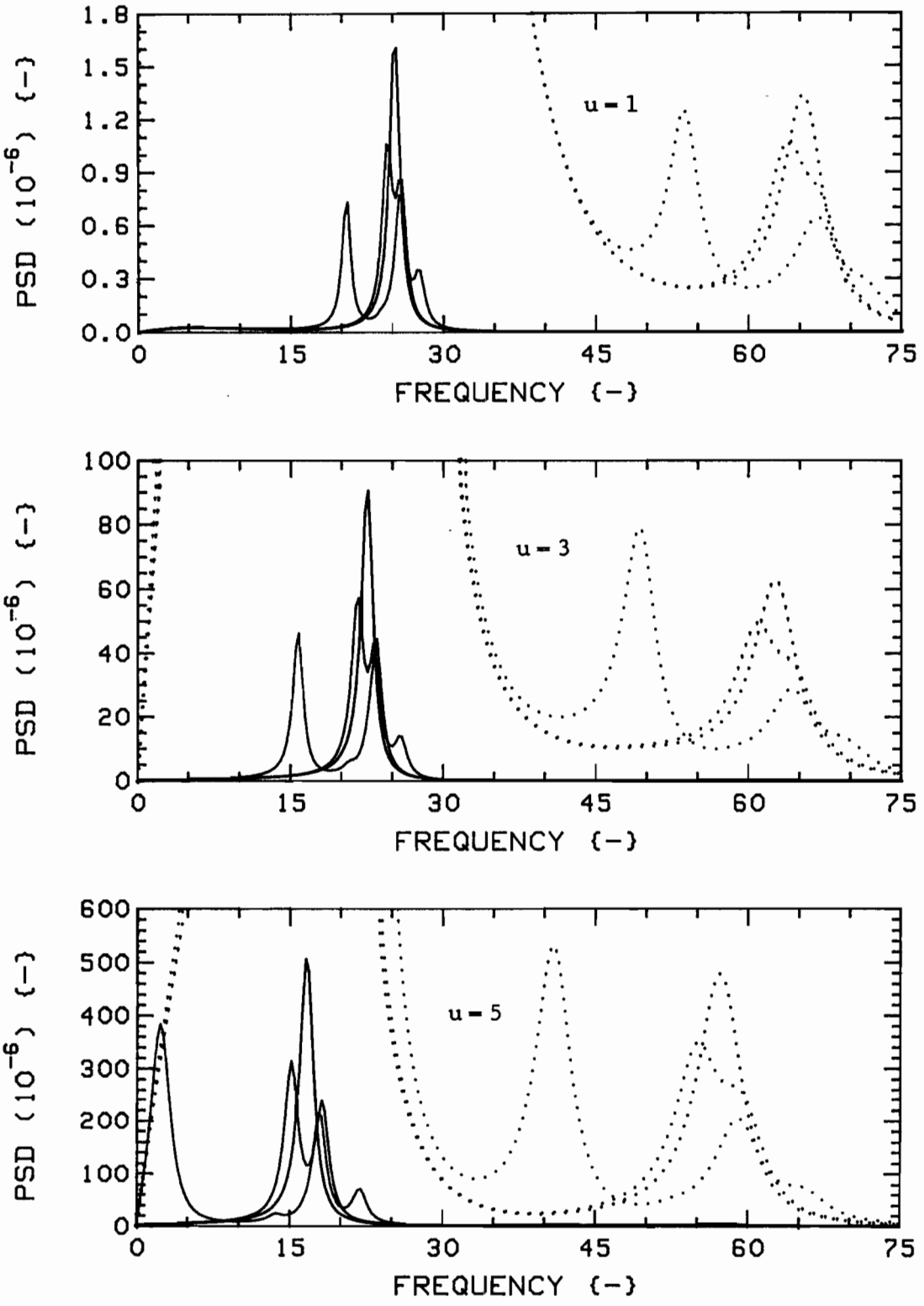

Fig.123a: Effect of number of cylinders on theoretical vibration PSD's for Flexible cylinder bundles, with K = 4, G_c = 0.75 spacing, in Radial direction; K = 1 (RED), 2(1,3) (GREEN), and 4 (BLUE).

The dotted traces are expansions of the solid ones;

scales are, from top: 1.5×10^{-9}, 2.0×10^{-7}, 4.0×10^{-6}.

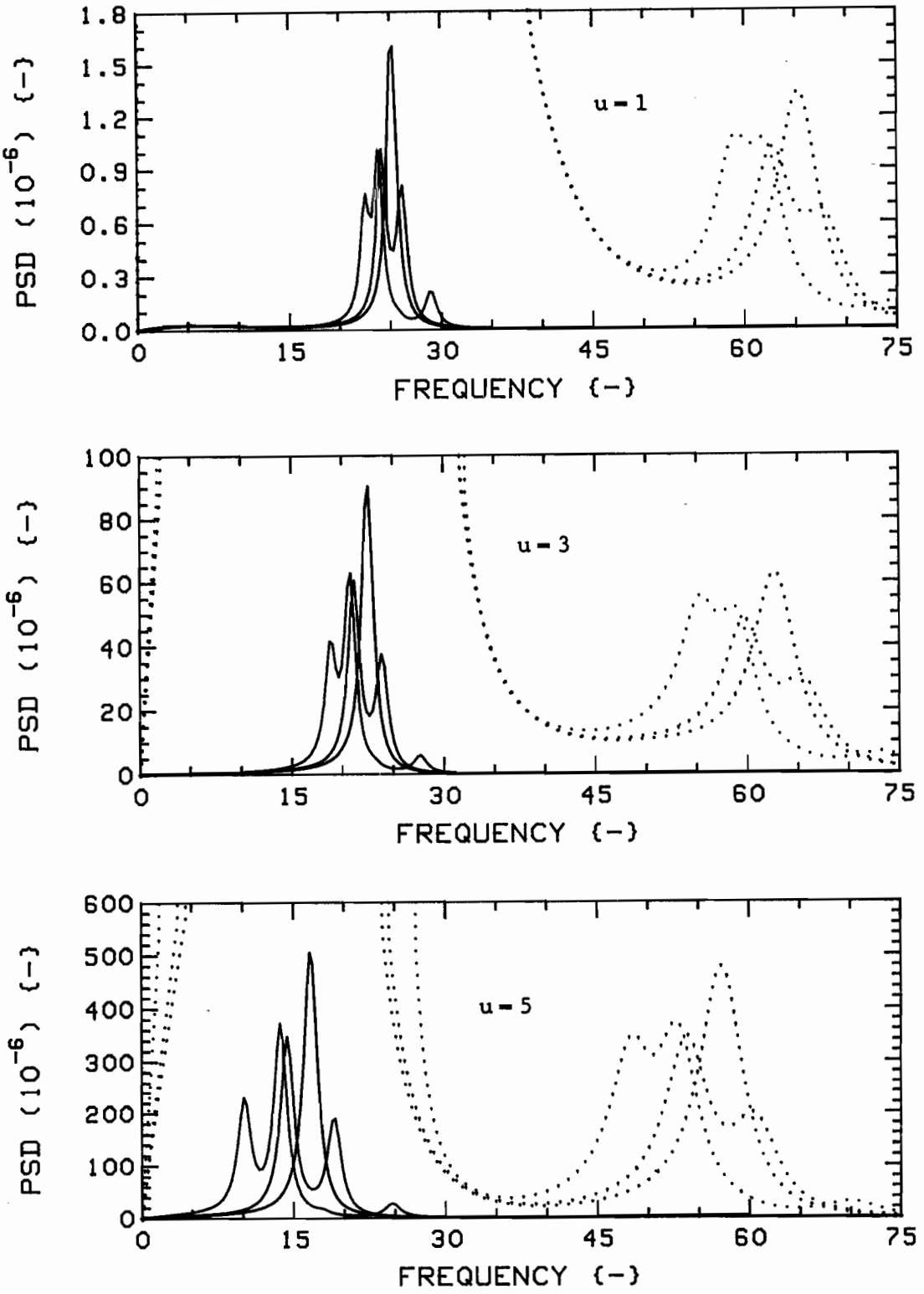

Fig.123b: Effect of number of cylinders on theoretical vibration PSD's for Flexible cylinder bundles, with K = 4, G_c = 0.75 spacing, in Tangential direction; K = 1 (RED), 2(1,3) (GREEN), and 4 (BLUE). The dotted traces are expansions of the solid ones; scales are, from top: 1.5×10^{-8}, 2.0×10^{-7}, 4.0×10^{-6}.

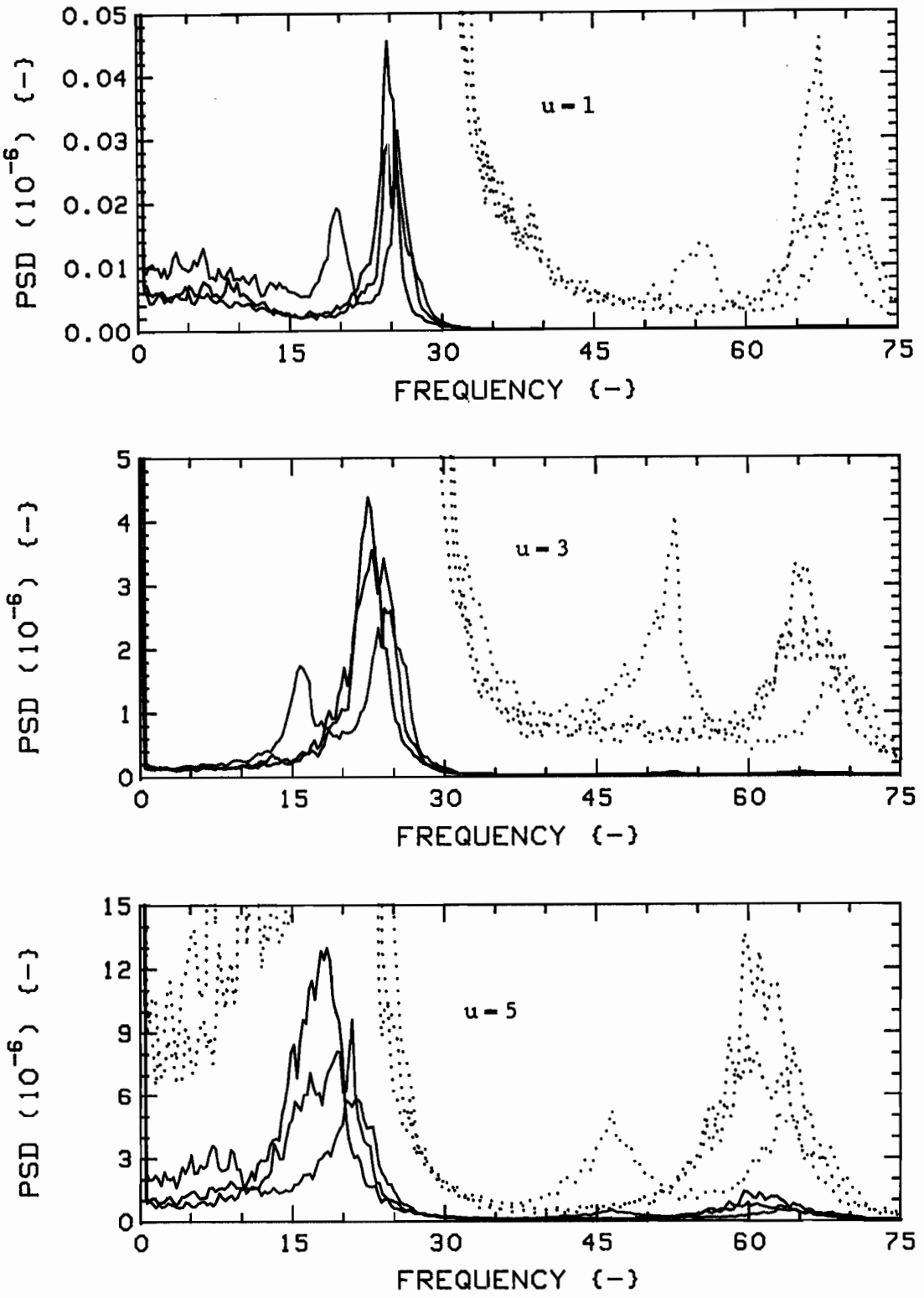

Fig.124a: Effect of number of cylinders on measured vibration PSD's for Flexible cylinder bundles, with K = 4, G_c = 0.75 spacing, in Radial direction; K = 1 (RED), 2(1,3) (GREEN), and 4 (BLUE). The dotted traces are expansions of the solid ones; scales are, from top: 3.0×10^{-10}, 8.0×10^{-8}, 1.5×10^{-6}.

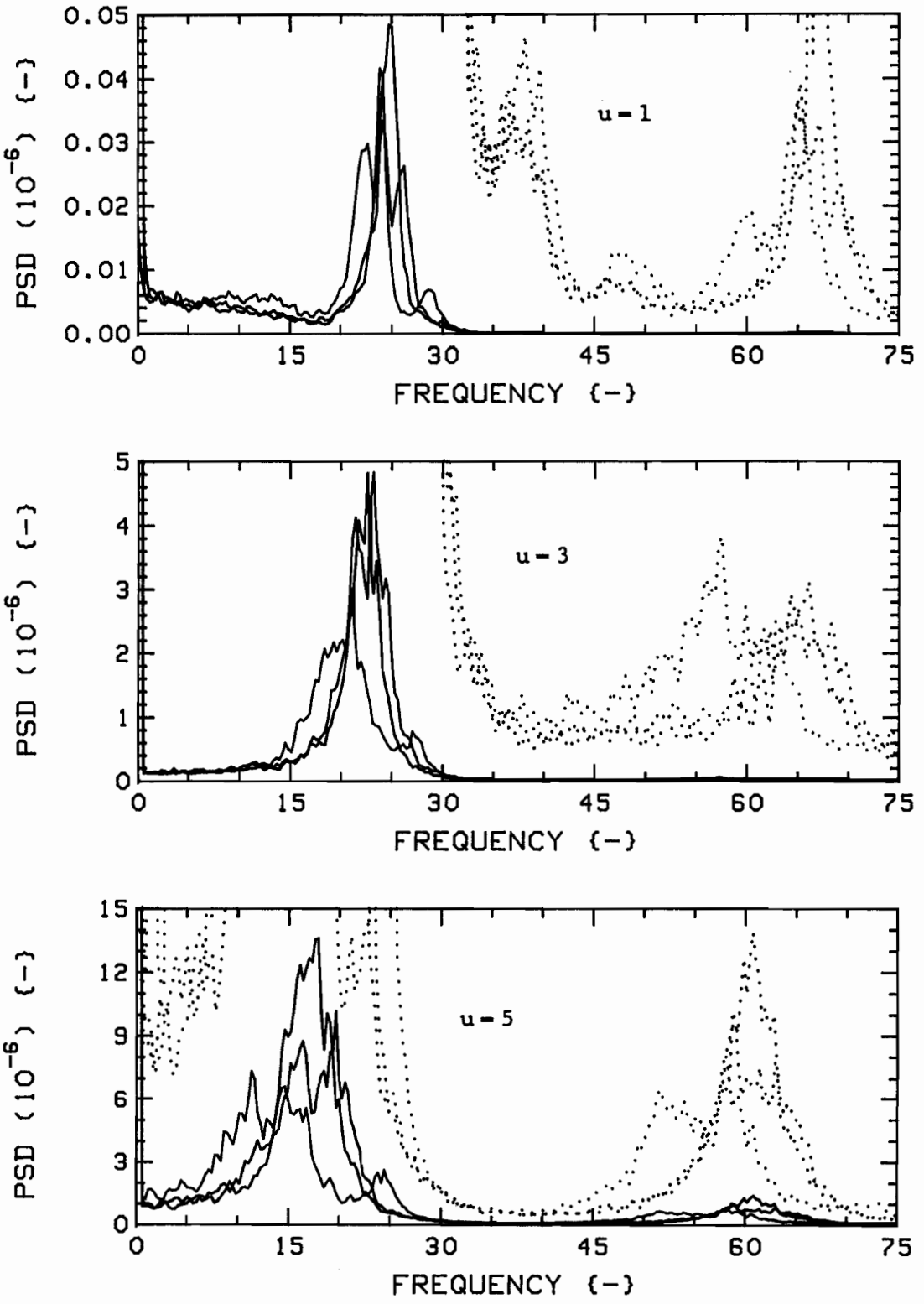

Fig.124b: Effect of number of cylinders on measured vibration PSD's for Flexible cylinder bundles, with K = 4, G_c = 0.75 spacing, in Tangential direction; K = 1 (RED), 2(1,3) (GREEN), and 4 (BLUE). The dotted traces are expansions of the solid ones; scales are, from top: 3.0×10^{-10}, 8.0×10^{-8}, 1.5×10^{-6}.

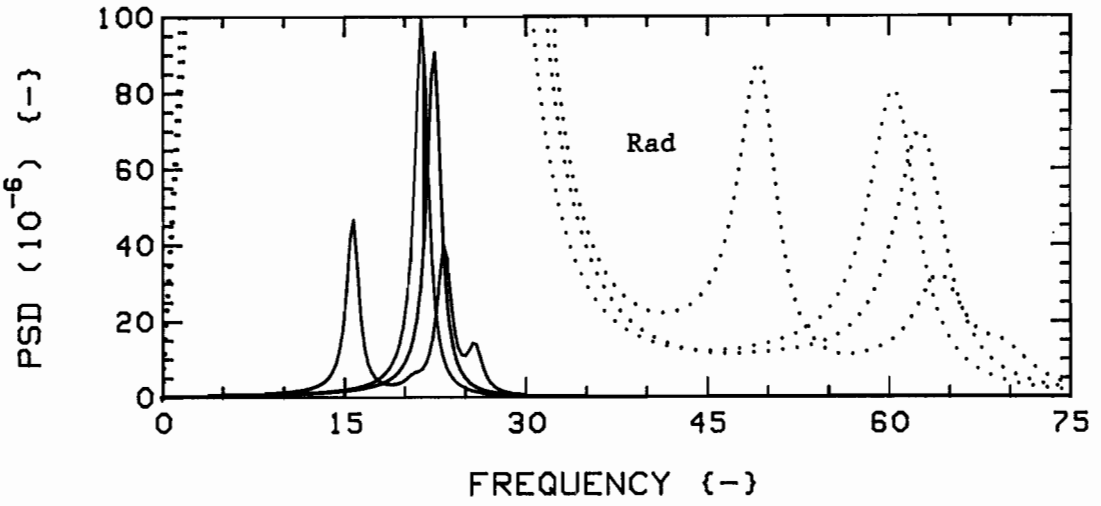

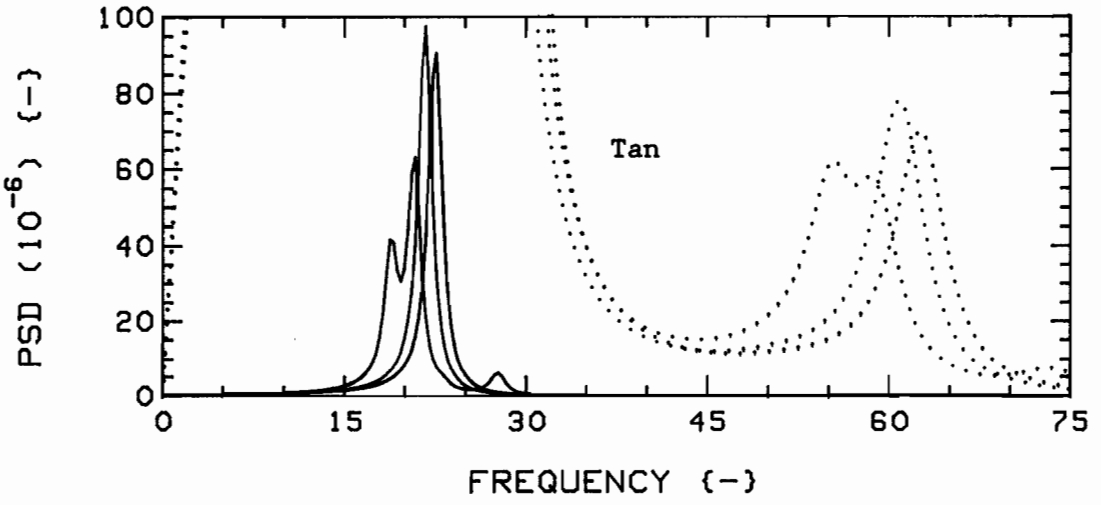

Fig.125: Effect of choice of system on theoretical vibration PSD's, with $G_c = 0.75$, at $u = 3$; K = 1, 1F (RED), K = 4, 4F (GREEN), and K = 4, 1F/3R (BLUE).

The dotted traces are expansions of the solid ones; scale is 1.8×10^{-7}.

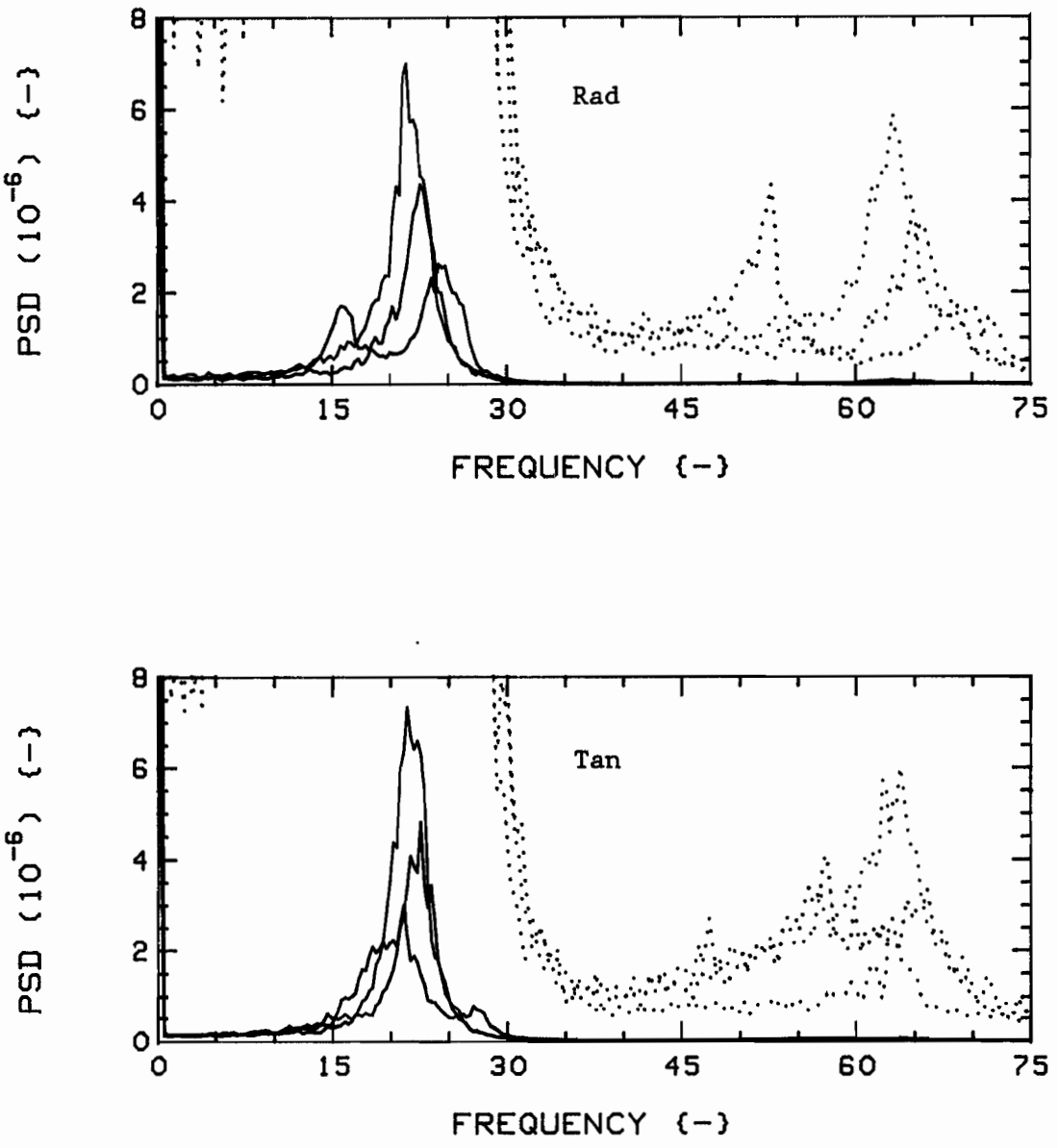

Fig.126: Effect of choice of system on measured vibration PSD's, with $G_c = 0.75$, at $u = 3$; K = 1, 1F (RED), K = 4, 4F (GREEN), and K = 4, 1F/3R (BLUE).

The dotted traces are expansions of the solid ones; scale is 1.2×10^{-7}.

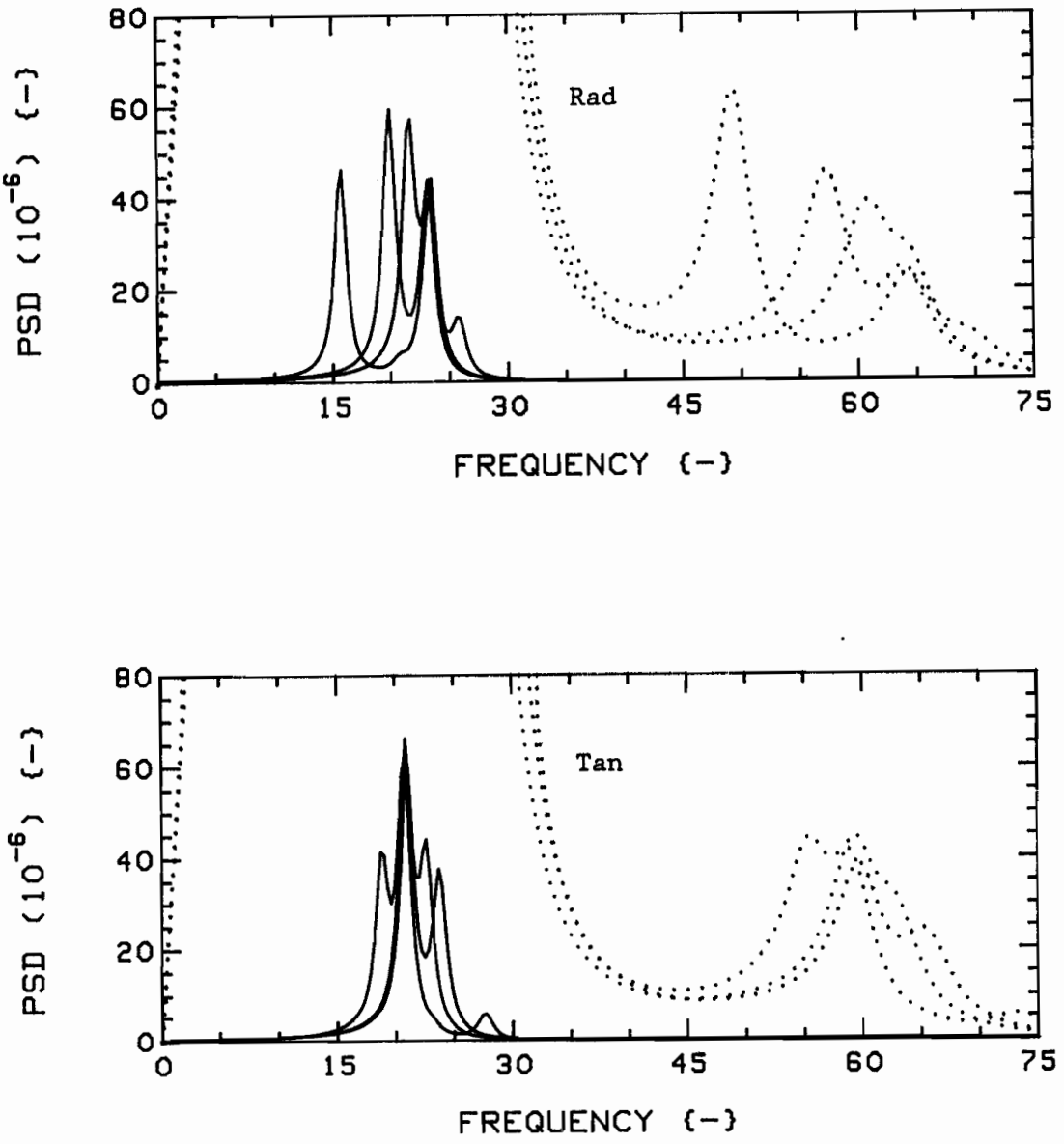

Fig.127: Effect of choice of system on theoretical vibration PSD's, with K = 4, G_c = 0.75 spacing, at u = 3; K = 2, 2F(1,3) (RED), K = 4, 4F (GREEN), and K = 4, 2F(1,3)/2R(2,4) (BLUE).

The dotted traces are expansions of the solid ones; scale is 2.0×10^{-7}.

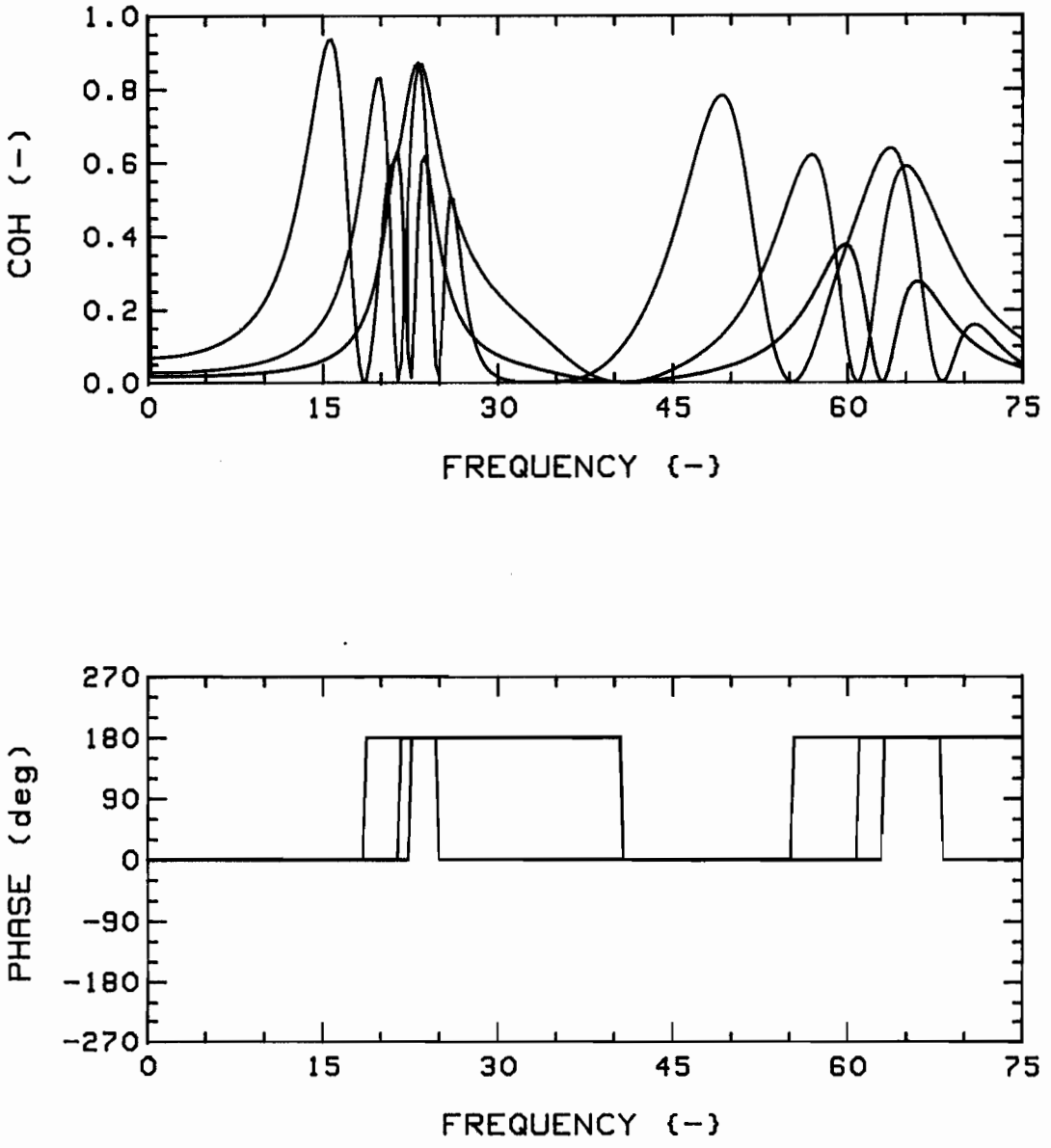

Fig.128a: Effect of choice of system on theoretical coherence functions and phases, with K = 4, G_c = 0.75 spacing, R-R (1,3), at u = 3; K = 2, 2F(1,3) (RED), K = 4, 4F (GREEN), and K = 4, 2F(1,3)/ 2R(2,4) (BLUE).

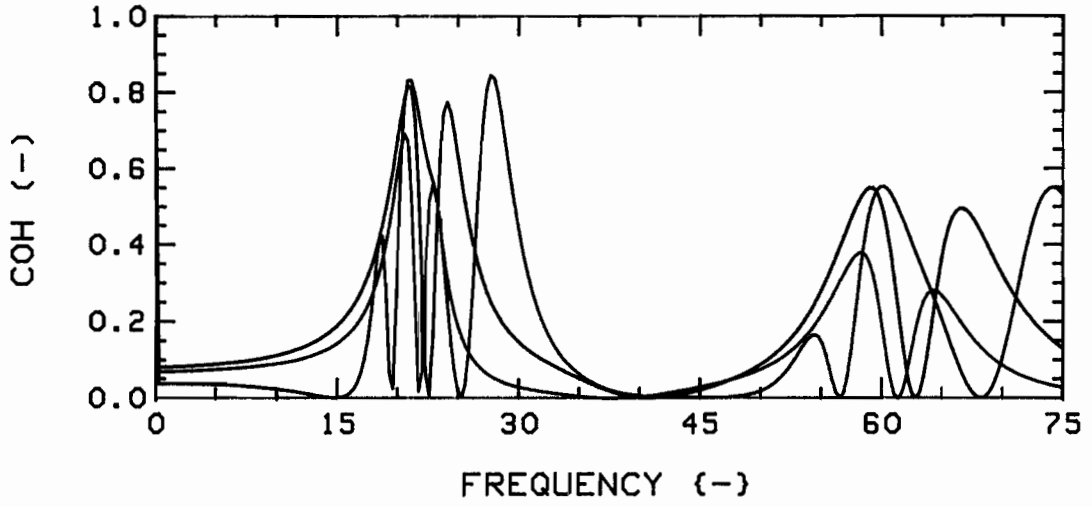

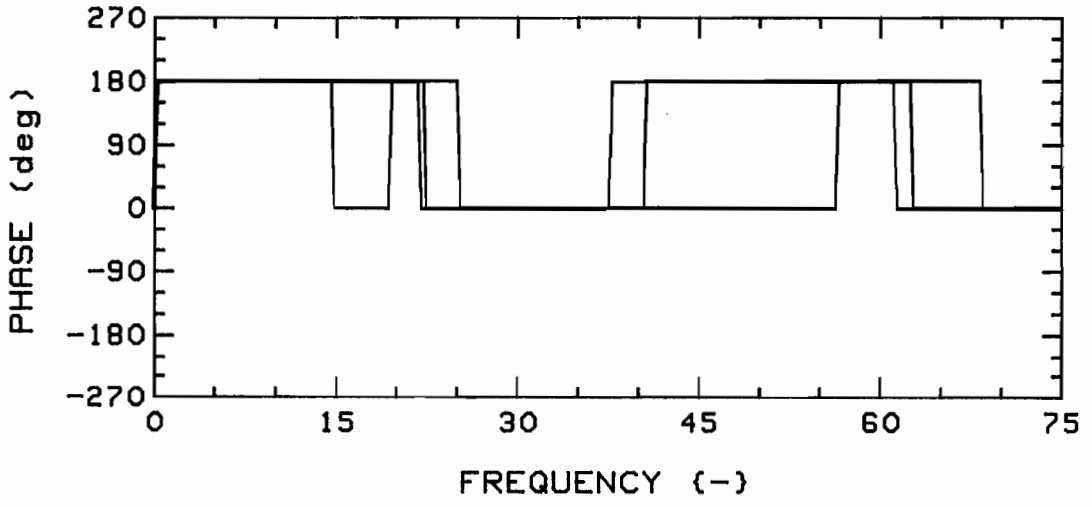

Fig.128b: Effect of choice of system on theoretical coherence functions and phases, with K = 4, G_c = 0.75 spacing, T-T (1,3), at u = 3; K = 2, 2F(1,3) (RED), K = 4, 4F (GREEN), and K = 4, 2F(1,3)/ 2R(2,4) (BLUE).

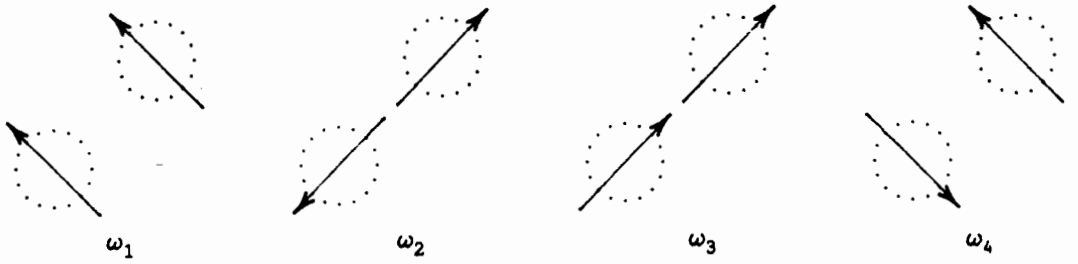

(a) 2F system

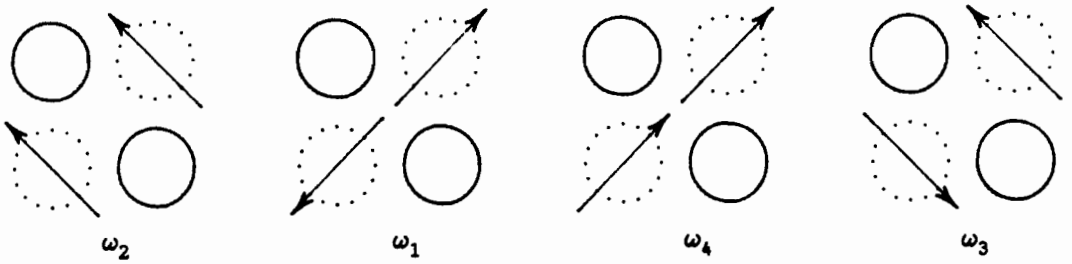

(b) 2F(1,3)/2R(2,4) system

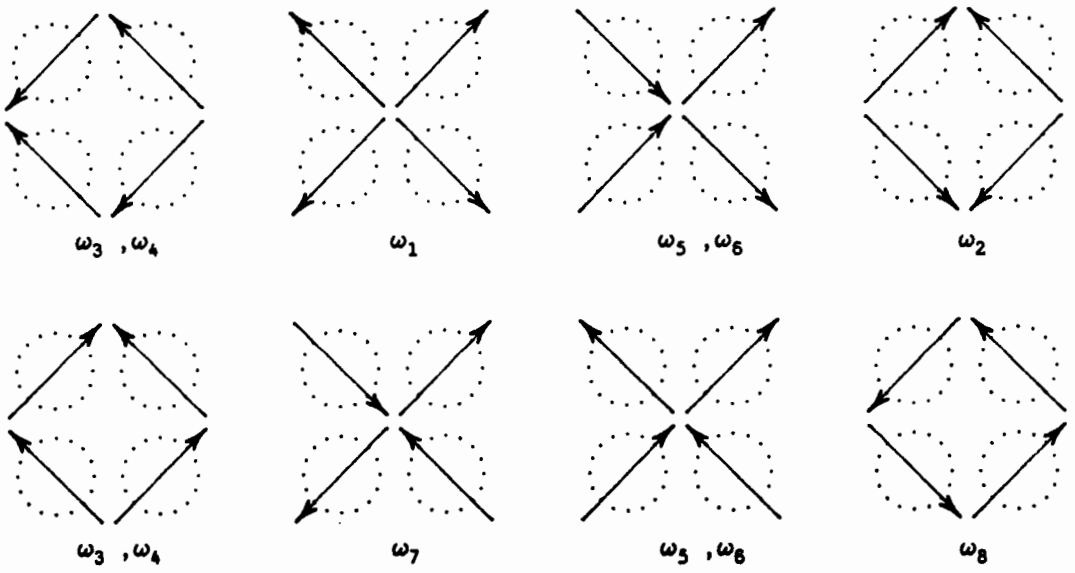

(c) 4F system

Fig. 129: Dominant cross-sectional coupling modes:
(a) 2F(1,3), (b) 2F(1,3)/2R(2,4), and 4F(1,2,3,4).

Note: $\omega_1 < \omega_2 < \omega_3 = \omega_4 < \omega_5 = \omega_6 < \omega_7 < \omega_8$.

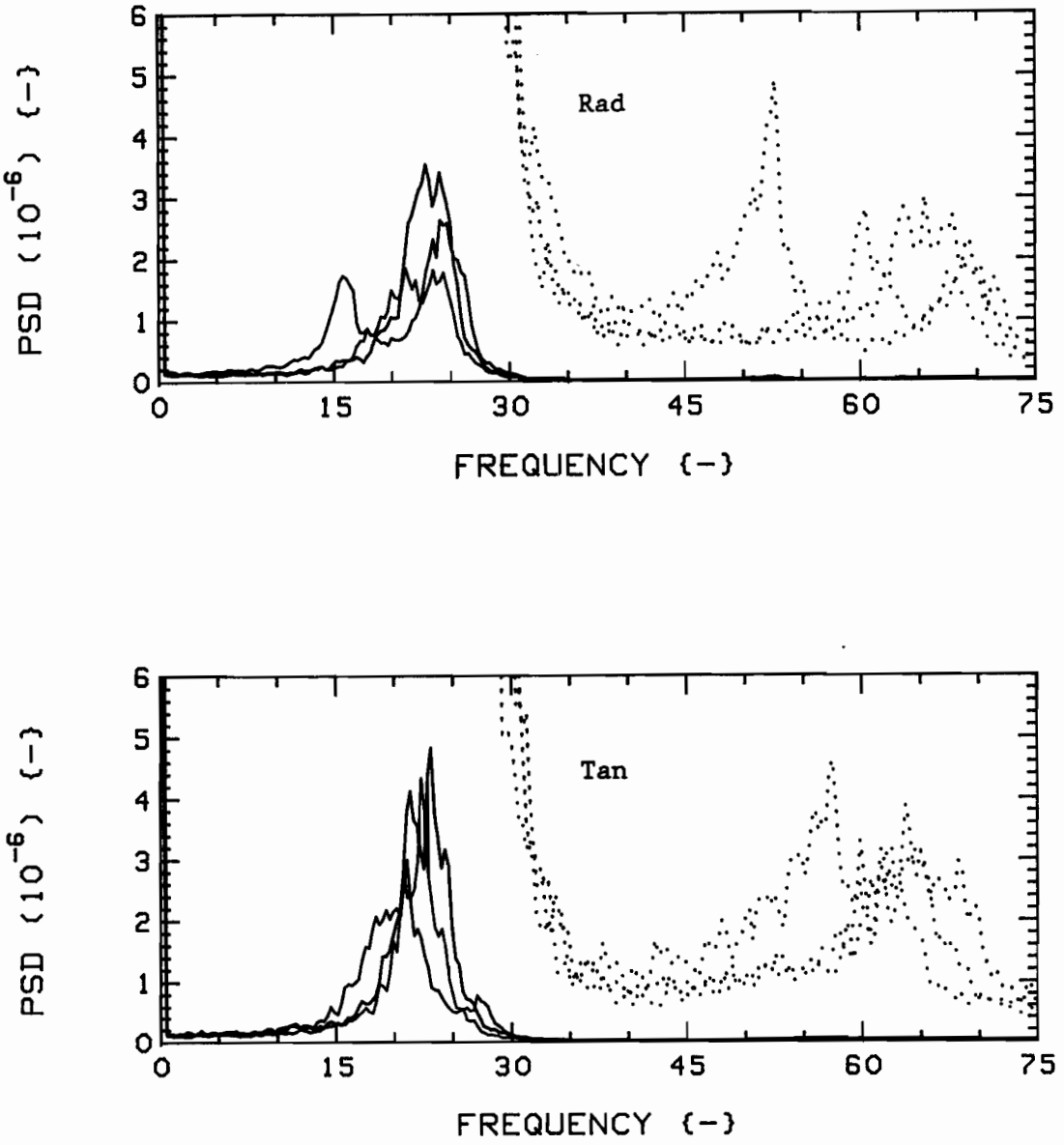

Fig.130: Effect of choice of system on measured vibration PSD's, with K=4, G_c=0.75 spacing, at u=3; K=2, 2F(1,3) (RED), K=4, 4F (GREEN), and K=4, 2F(1,3)/2R(2,4) (BLUE). The dotted traces are expansions of the solid ones; scale is 8.0×10^{-8}.

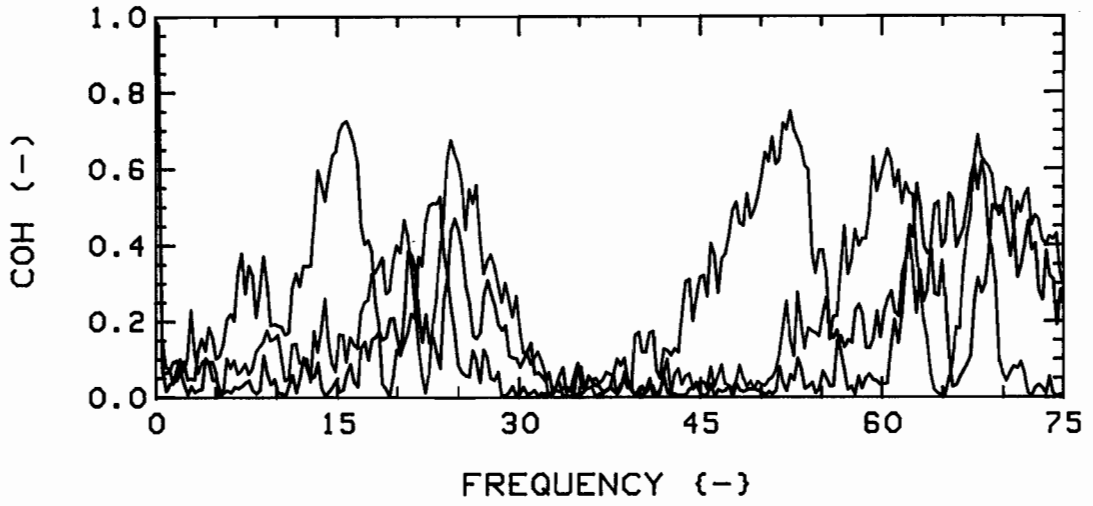

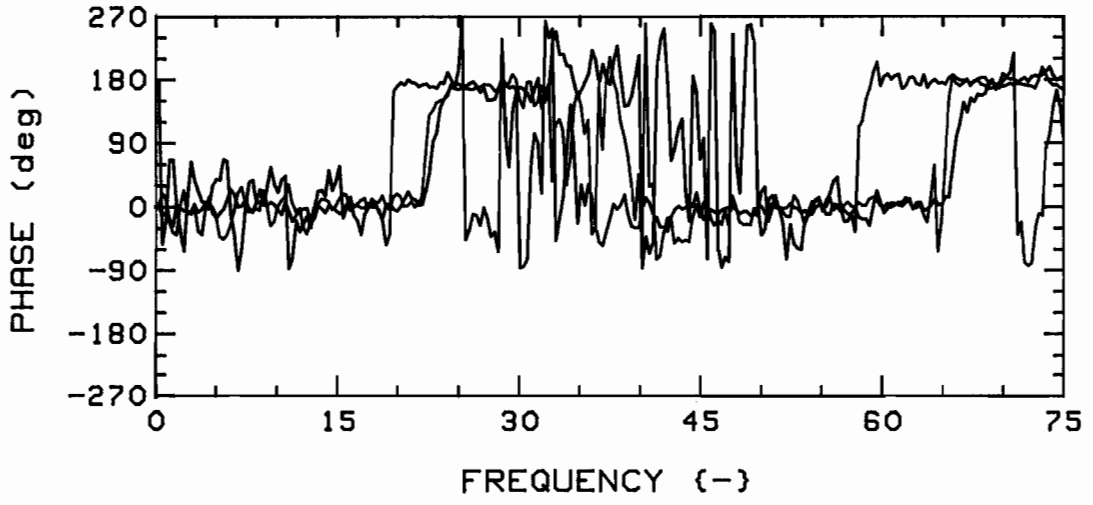

Fig.131a: Effect of choice of system on measured coherence functions and phases, with K = 4, G_c = 0.75 spacing, R-R (1,3), at u = 3; K = 2, 2F(1,3) (RED), K = 4, 4F (GREEN), and K = 4, 2F(1,3)/ 2R(2,4) (BLUE).

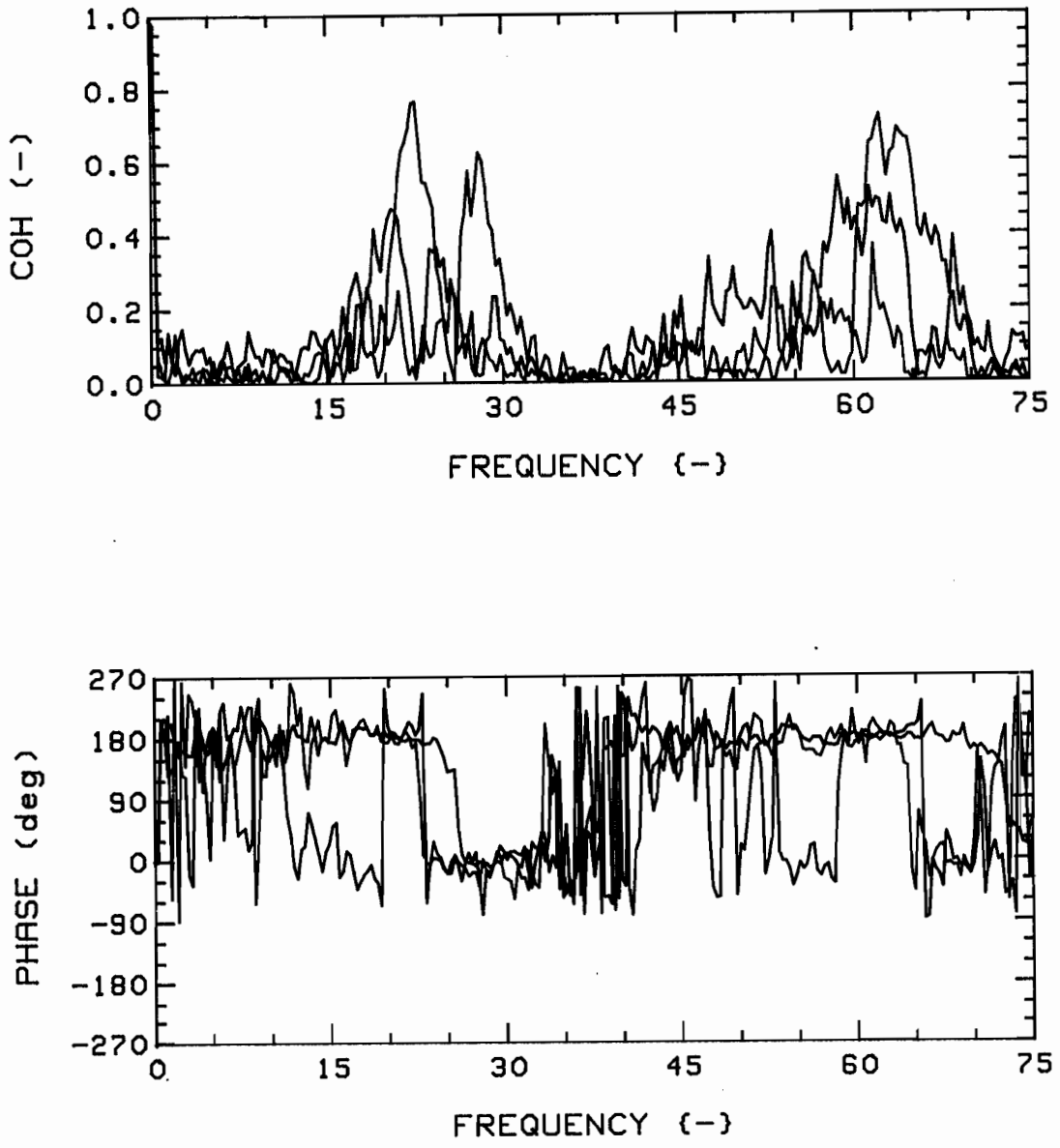

Fig.131b: Effect of choice of system on measured coherence functions and phases, with K = 4, G_c = 0.75 spacing, T-T (1,3), at u = 3; K = 2, 2F(1,3) (RED), K = 4, 4F (GREEN), and K = 4, 2F(1,3)/ 2R(2,4) (BLUE).

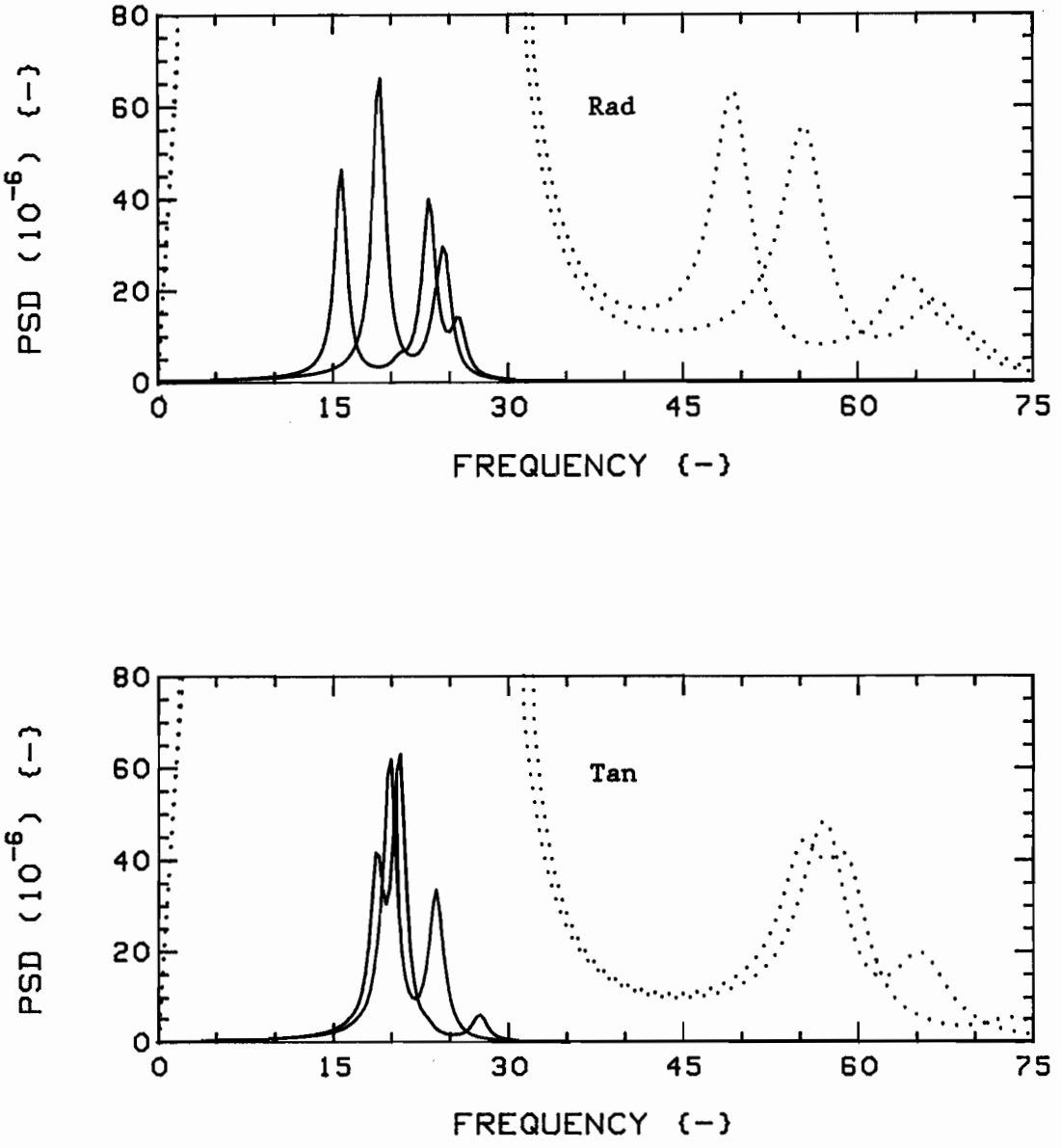

Fig.132: Effect of choice of system on theoretical vibration PSD's, with $G_c = 0.75$, at $u = 3$; K = 4, 4F (RED) and K = 4, 2F(1,2)/ 2R(3,4) (GREEN).

The dotted traces are expansions of the solid ones; scale is 2.0×10^{-7}.

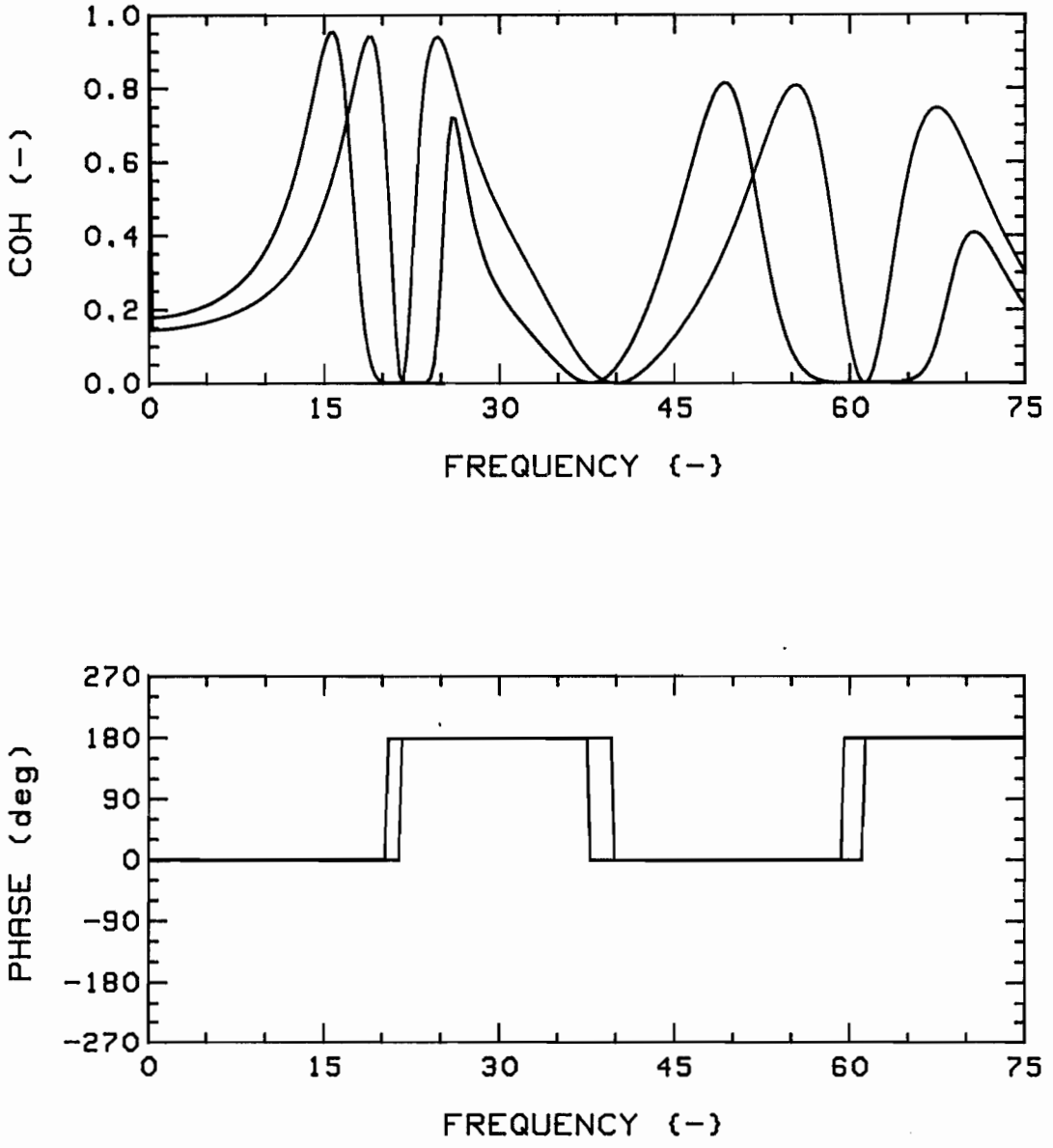

Fig.133a: Effect of choice of system on theoretical coherence functions and phases, with $G_c = 0.75$, R-R (1,2), at u = 3; K = 4, 4F (RED) and K = 4, 2F(1,2)/2R(3,4) (GREEN).

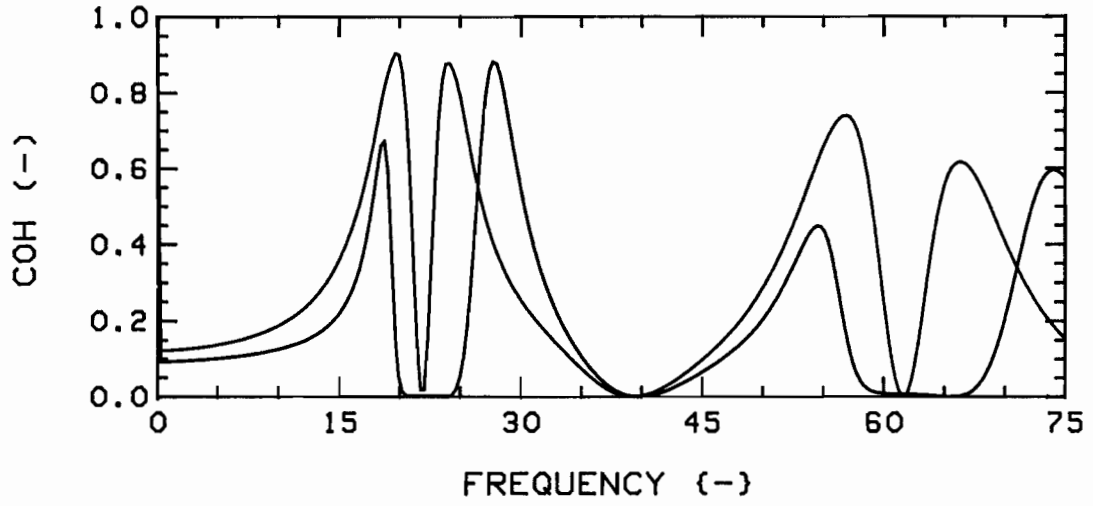

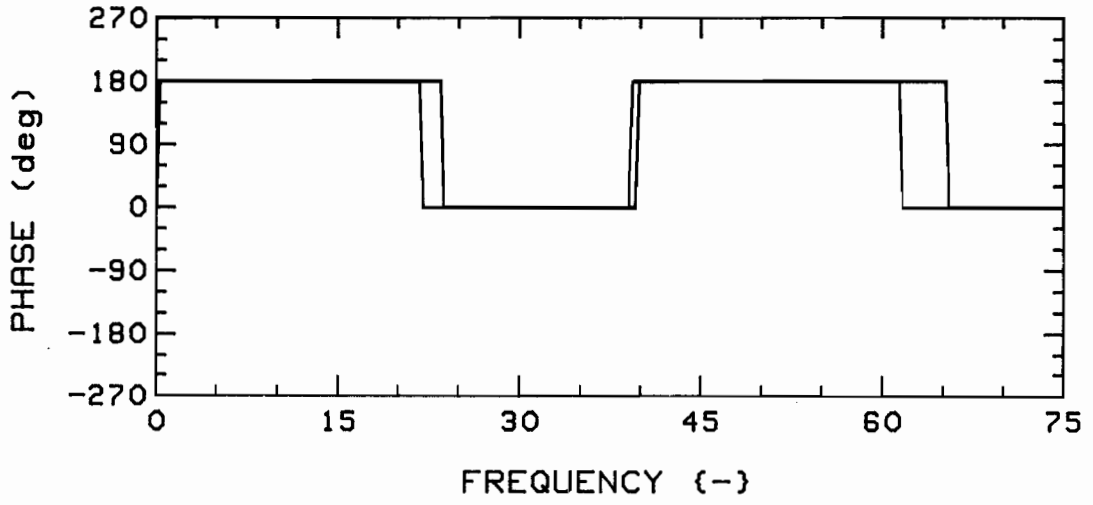

Fig.133b: Effect of choice of system on theoretical coherence functions and phases, with $G_c = 0.75$, T-T (1,2), at u = 3; K = 4, 4F (RED) and K = 4, 2F(1,2)/2R(3,4) (GREEN).

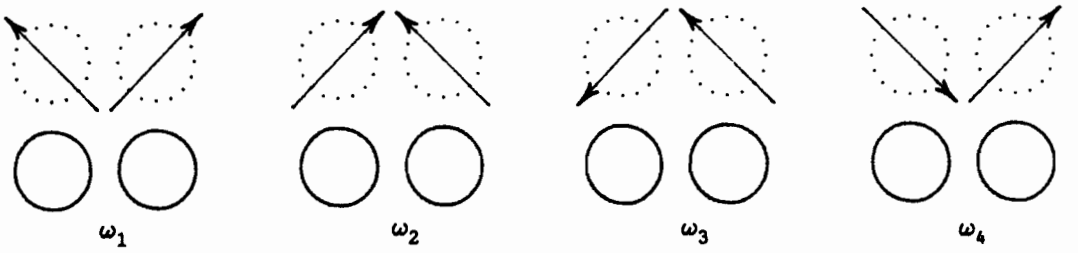

(a) 2F(1,2)/2R(3,4) system

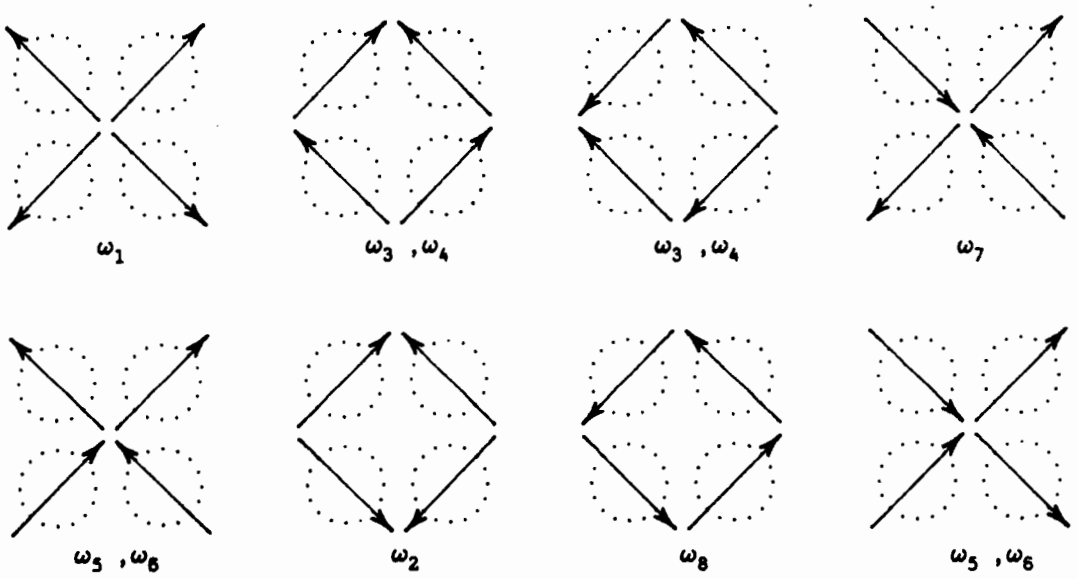

(b) 4F system

Fig. 134: Dominant cross-sectional coupling modes:
(a) 2F(1,2)/2R(3,4) and 4F(1,2,3,4).

Note: $\omega_1 < \omega_2 < \omega_3 = \omega_4 < \omega_5 = \omega_6 < \omega_7 < \omega_8$.

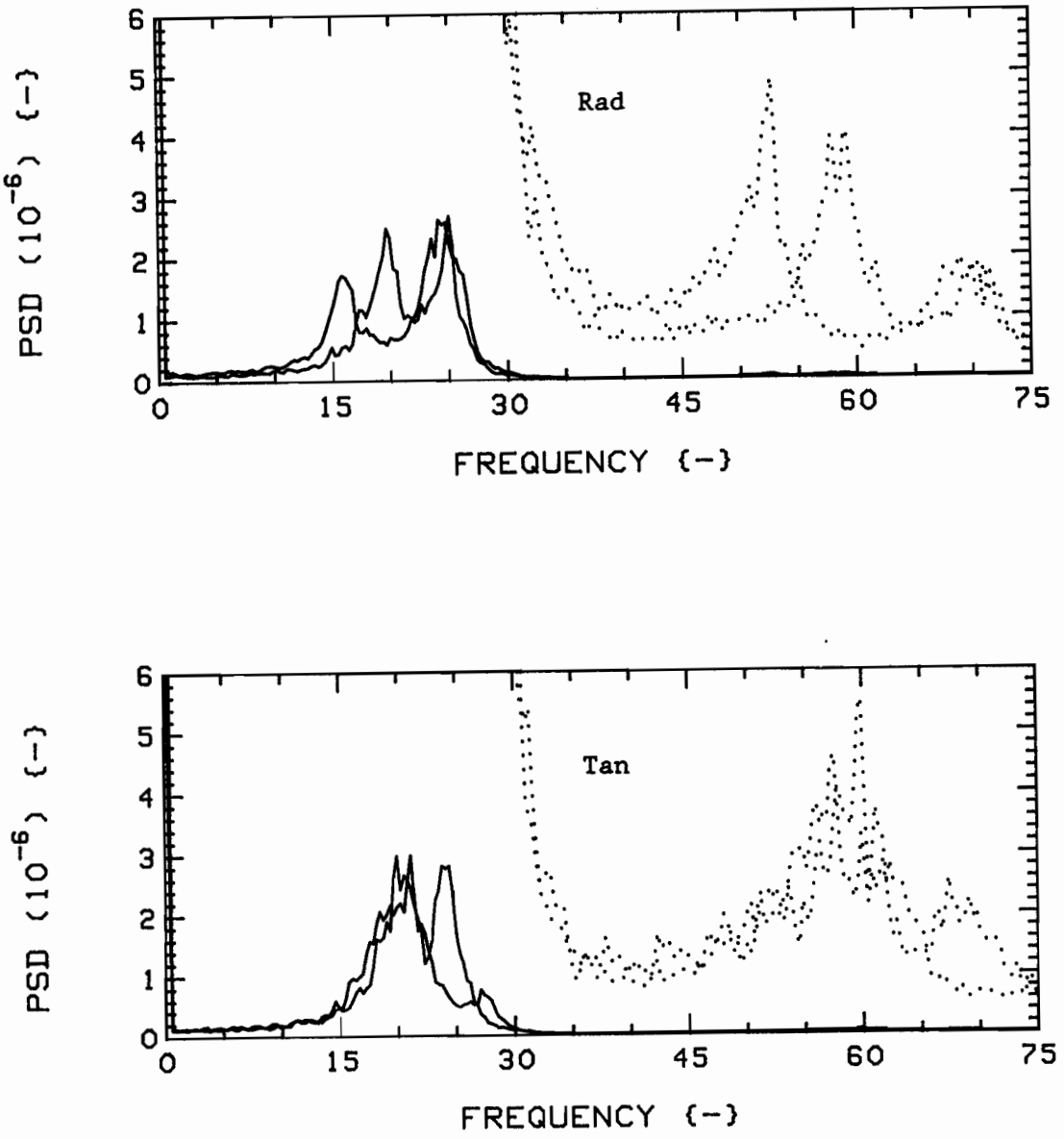

Fig.135: Effect of choice of system on measured vibration PSD's, with $G_c = 0.75$, at $u = 3$; K=4, 4F (RED) and K=4, 2F(1,2)/2R(3,4) (GREEN).

The dotted traces are expansions of the solid ones; scale is 8.0×10^{-8}.

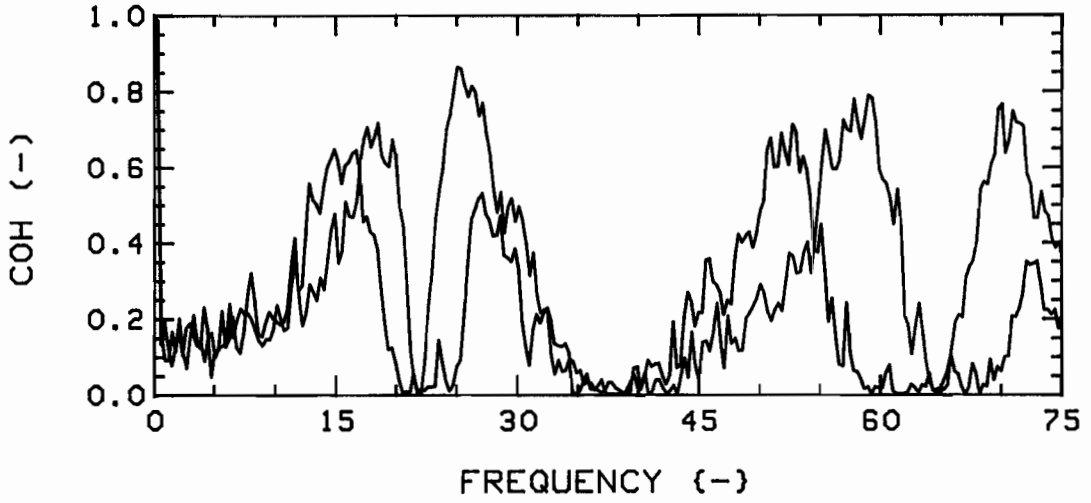

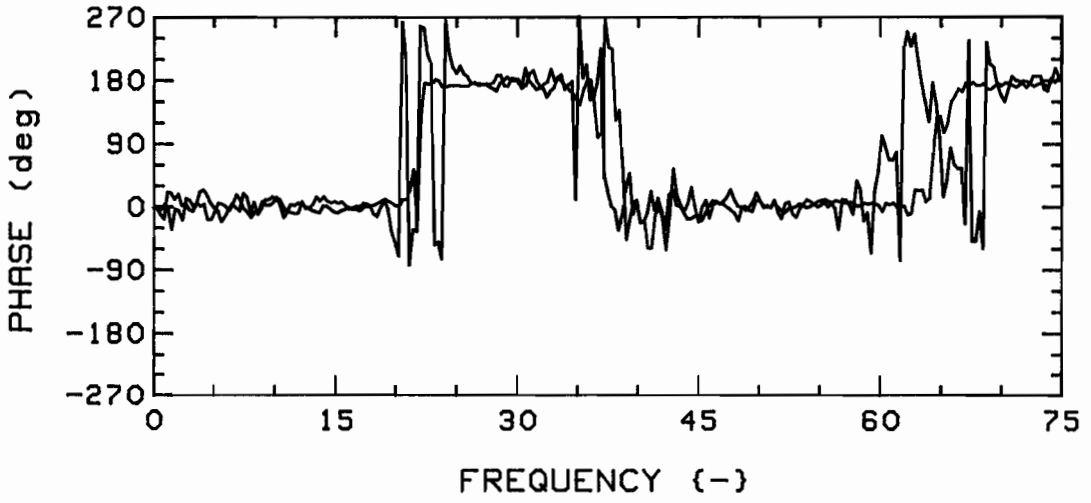

Fig.136a: Effect of choice of system on measured coherence functions and phases, with $G_c = 0.75$, R-R (1,2), at u = 3; K = 4, 4F (RED) and 2F(1,2)/2R(3,4) (GREEN).

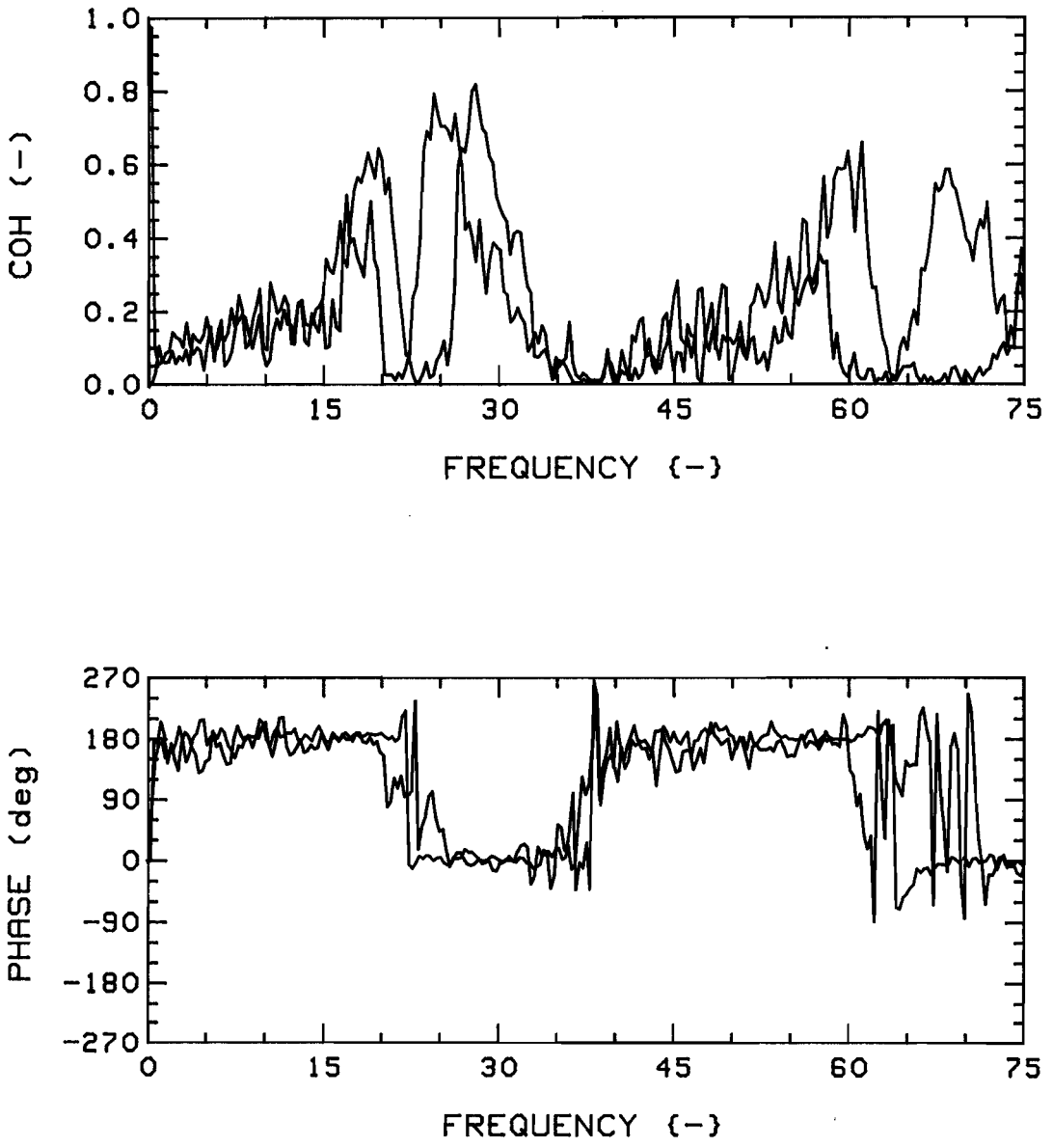

Fig.136b: Effect of choice of system on measured coherence functions and phases, with $G_c = 0.75$, T-T (1,2), at u = 3; K = 4, 4F (RED) and 2F(1,2)/2R(3,4) (GREEN).

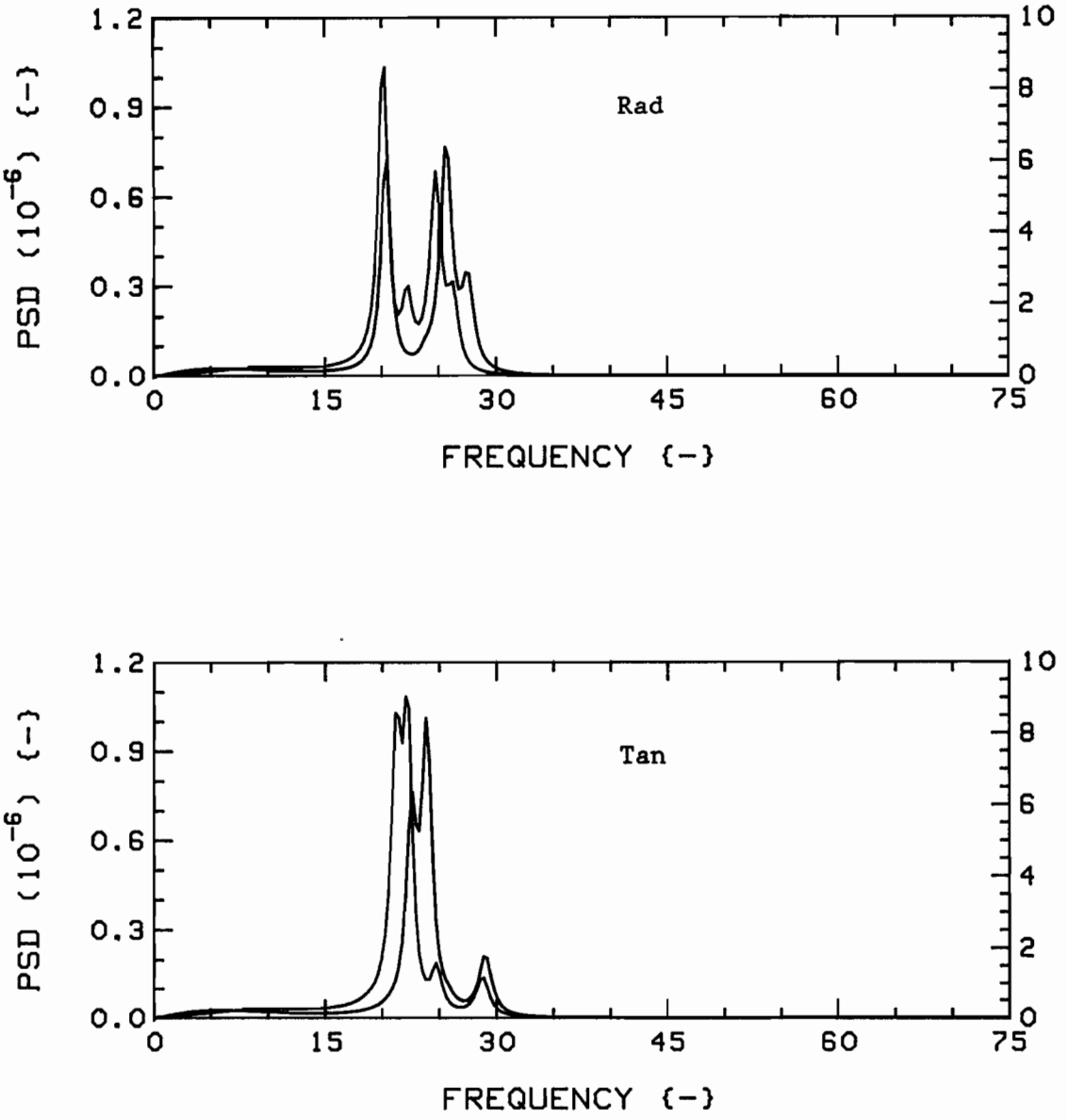

Fig.137: Effect of choice of system on theoretical vibration PSD's, with $G_c = 0.75$, at u = 1; K = 4, 4F (RED) and K = 28, 4F(1,2,3,4)/24R (GREEN).

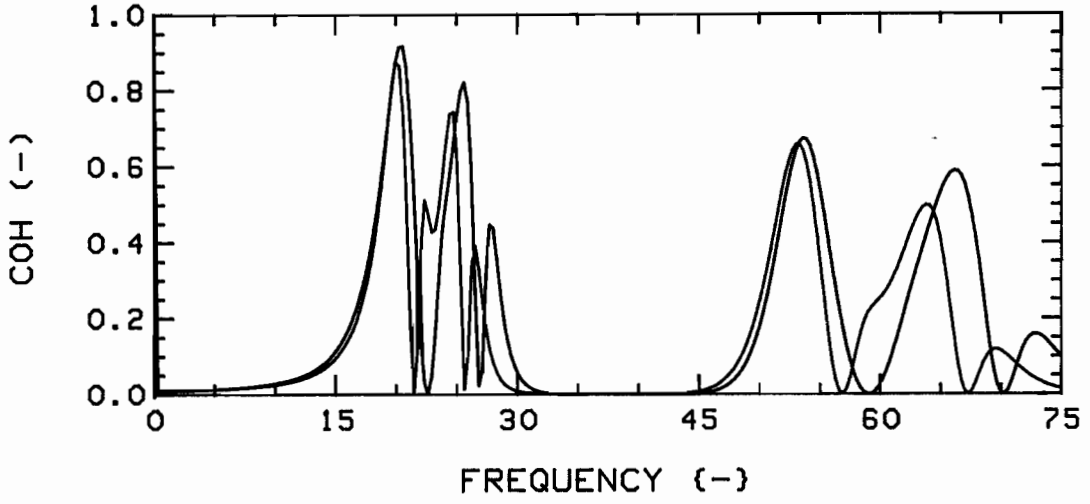

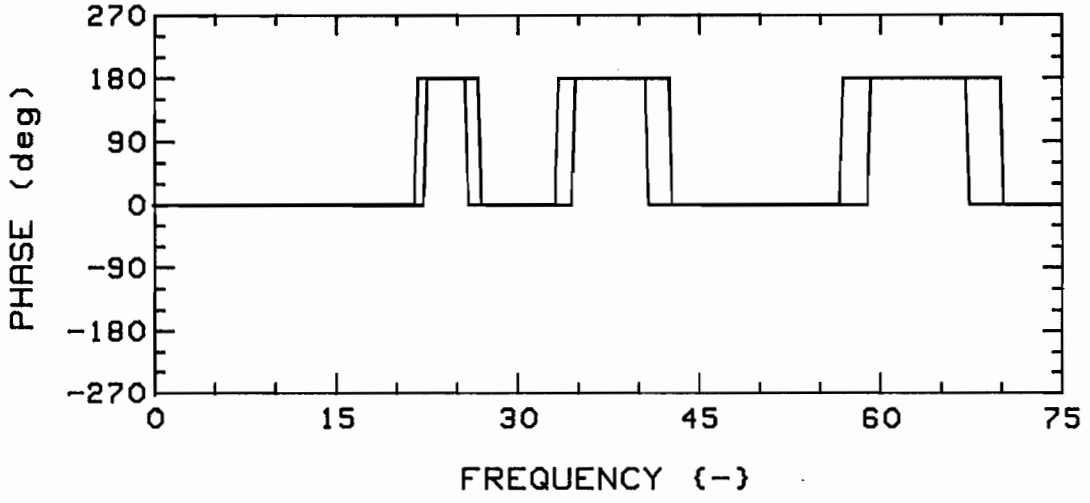

Fig.138a: Effect of choice of system on theoretical coherence functions and phases, with $G_c = 0.75$, R-R (1,3), at u = 1; K = 4, 4F (RED) and K = 28, 4F(1,2,3,4)/24R (GREEN).

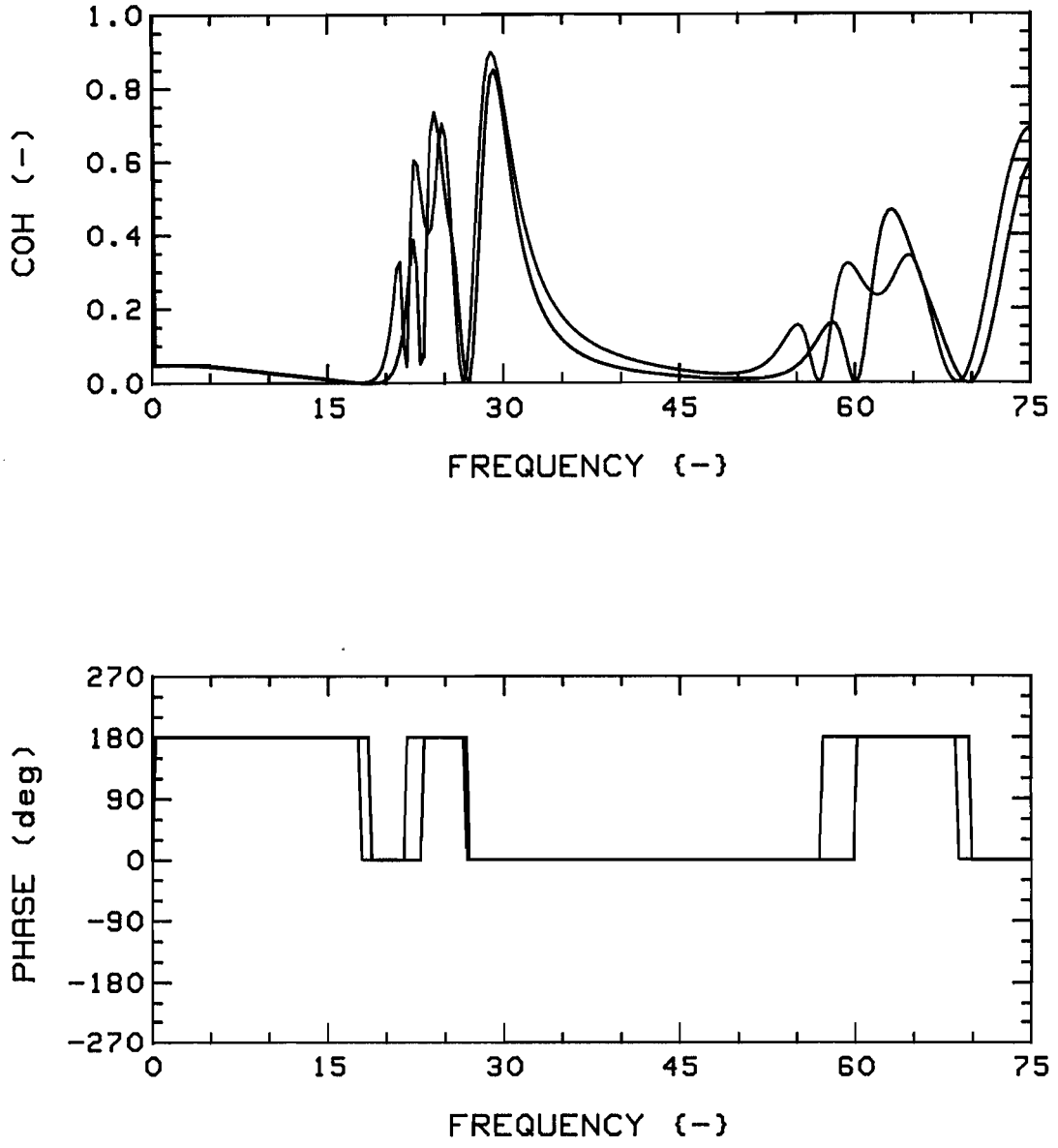

Fig.138b: Effect of choice of system on theoretical coherence functions and phases, with $G_c = 0.75$, T-T (1,3), at u = 1; K = 4, 4F (RED) and K = 28, 4F(1,2,3,4)/24R (GREEN).

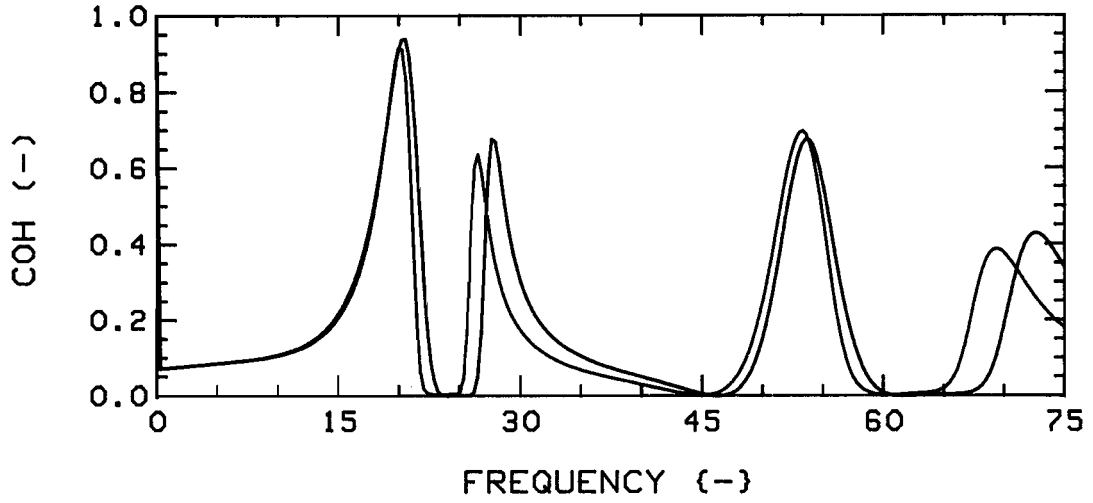

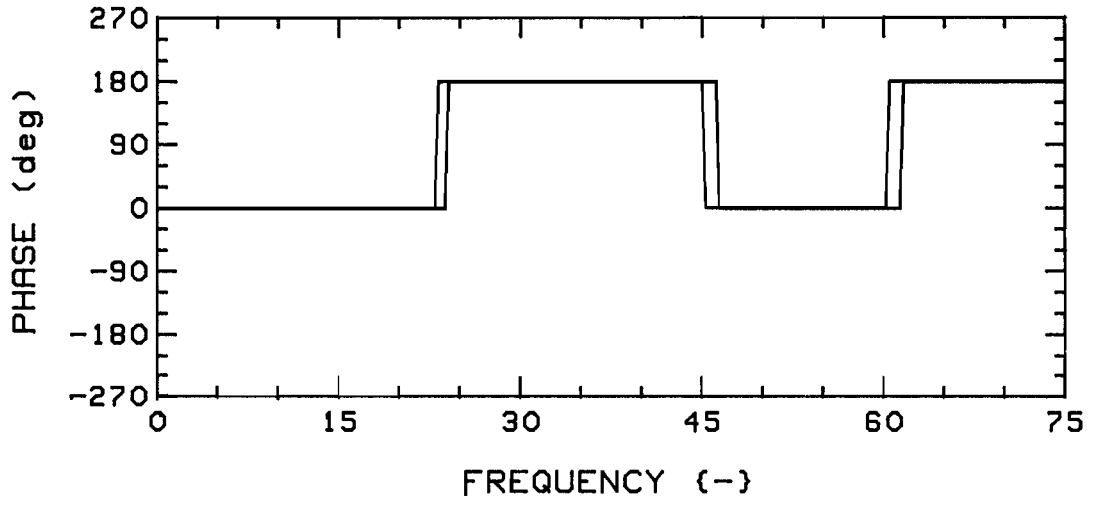

Fig.138c: Effect of choice of system on theoretical coherence functions and phases, with $G_c = 0.75$, R-R (1,2), at $u = 1$; $K = 4$, 4F (RED) and $K = 28$, 4F(1,2,3,4)/24R (GREEN).

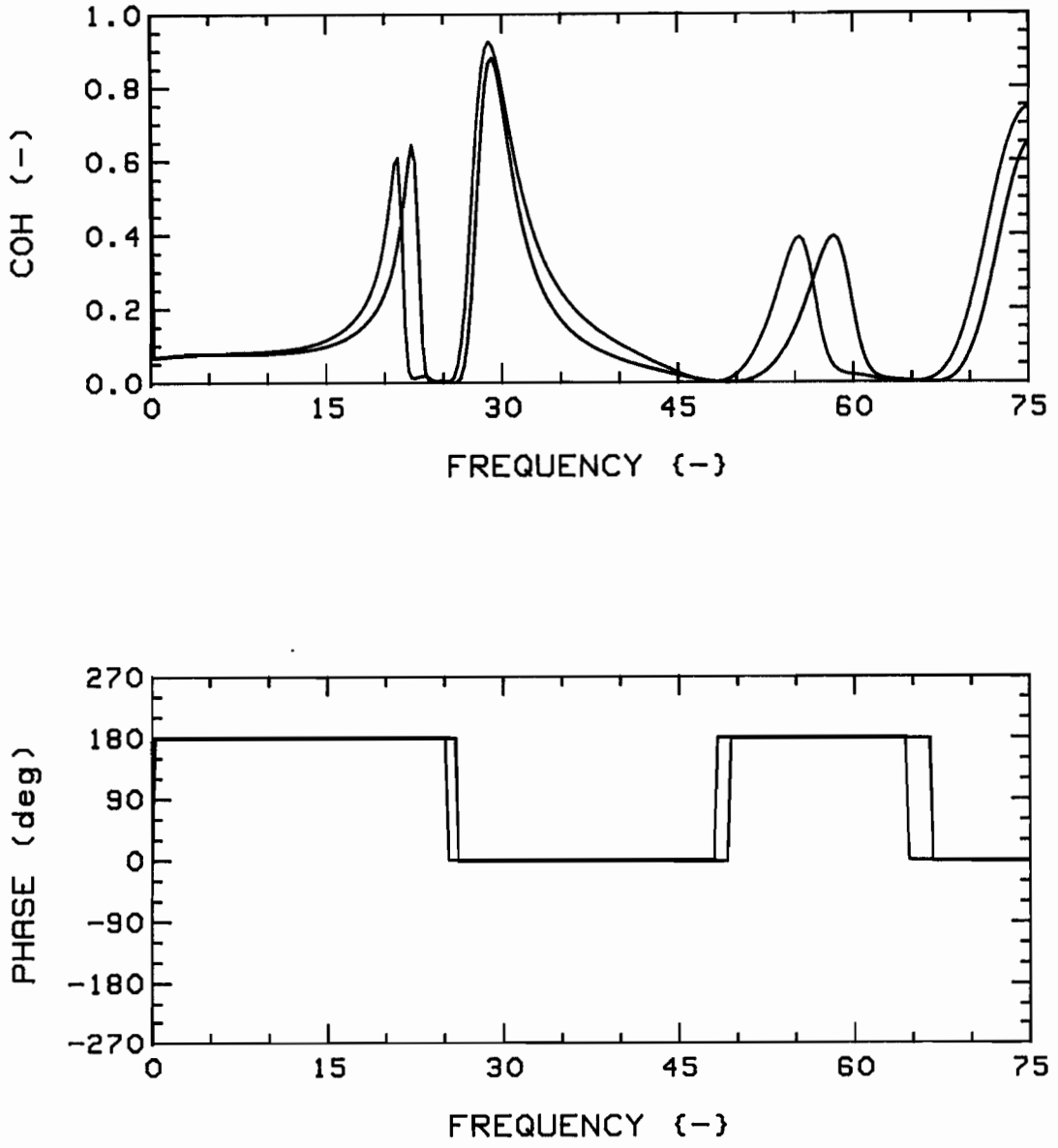

Fig.138d: Effect of choice of system on theoretical coherence functions and phases, with $G_c = 0.75$, T-T (1,2), at u = 1; K = 4, 4F (RED) and K = 28, 4F(1,2,3,4)/24R (GREEN).

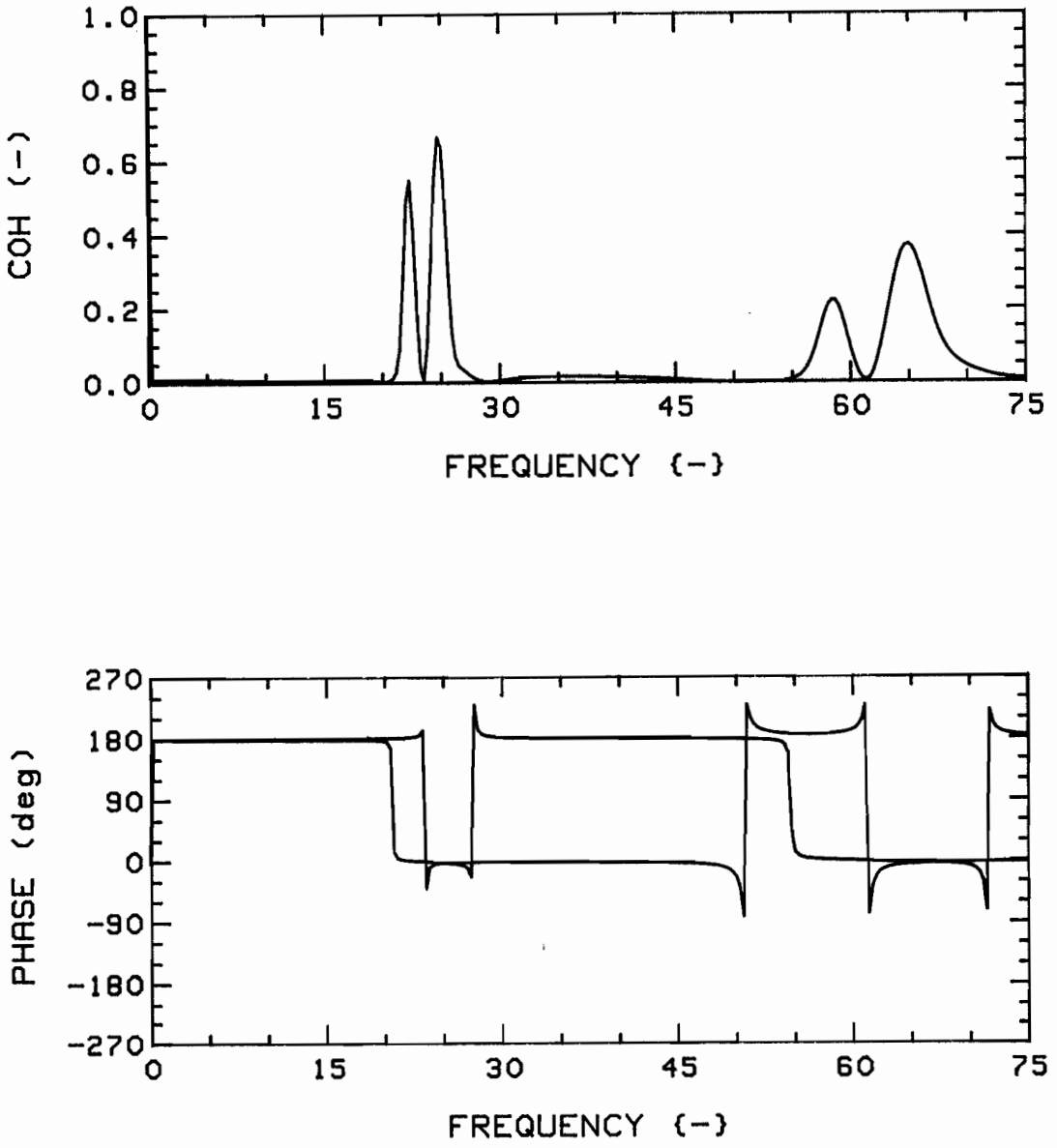

Fig.139: Coherence functions and phases for K = 28, G_c = 0.75, 4F(1,2,3,4)/24R system, at u = 1, R-T; Position pairs 1,3 (RED) and 1,2 (GREEN).

Note: The RED coherence trace is essentially zero (hence unseen).

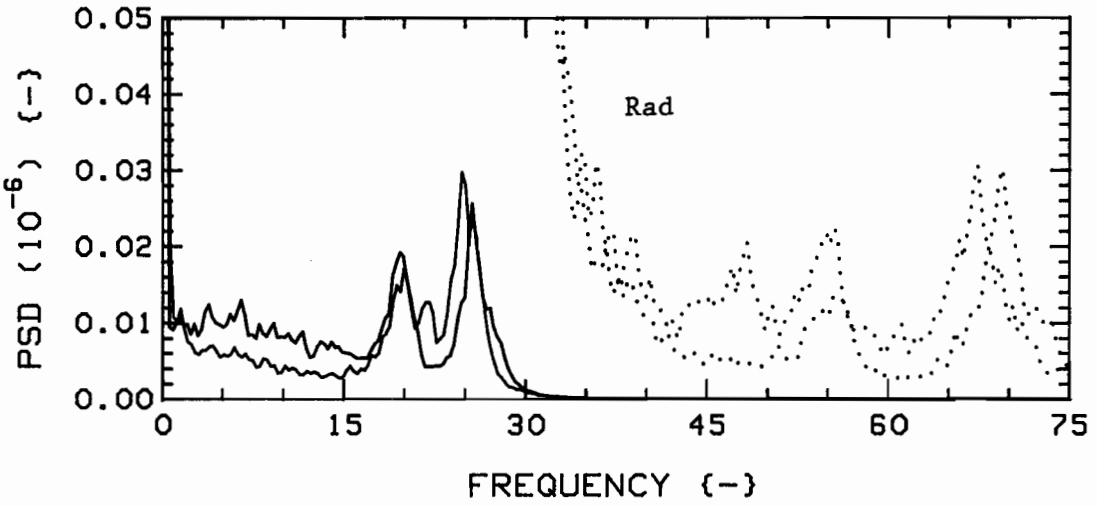

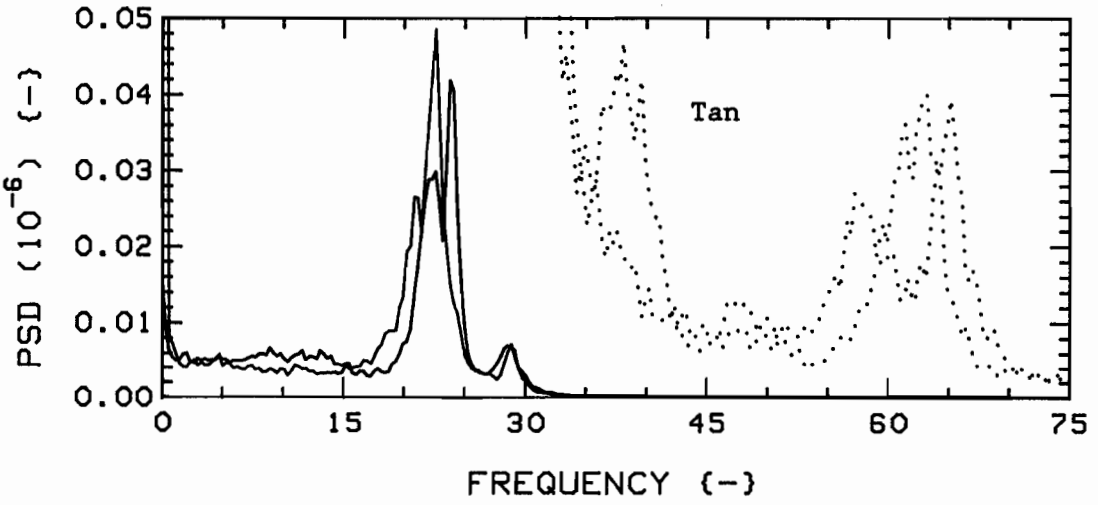

Fig.140: Effect of choice of system on measured vibration PSD's, with $G_c = 0.75$, at $u = 1$; K = 4, 4F (RED) and K = 28, 4F(1,2,3,4)/24R (GREEN).

The dotted traces are expansions of the solid ones; scale is 3.0×10^{-10}.

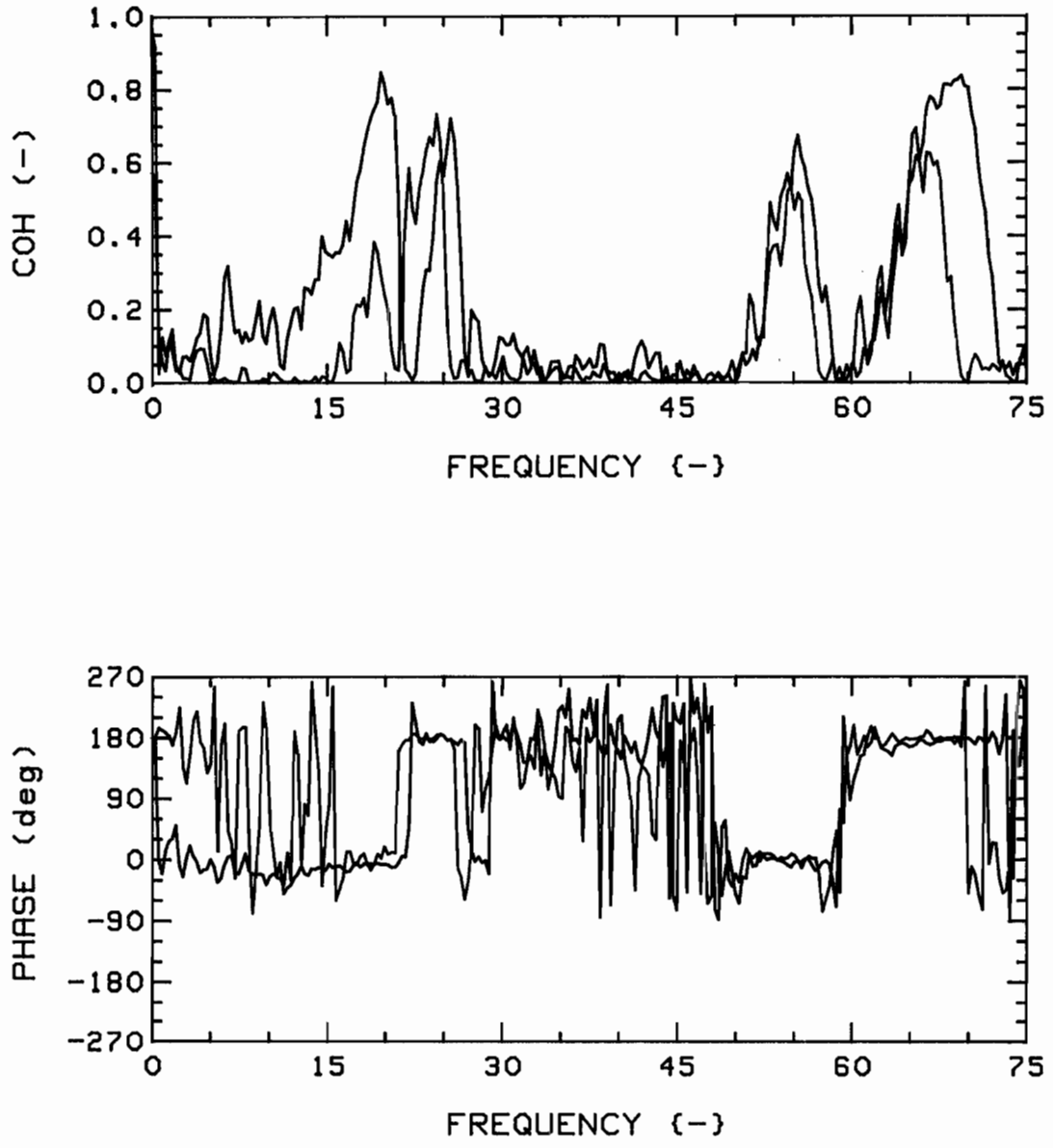

Fig.141a: Effect of choice of system on measured coherence functions and phases, with $G_c = 0.75$, R-R (1,3), at u = 1; K = 4, 4F (RED) and 4F(1,2,3,4)/24R (GREEN).

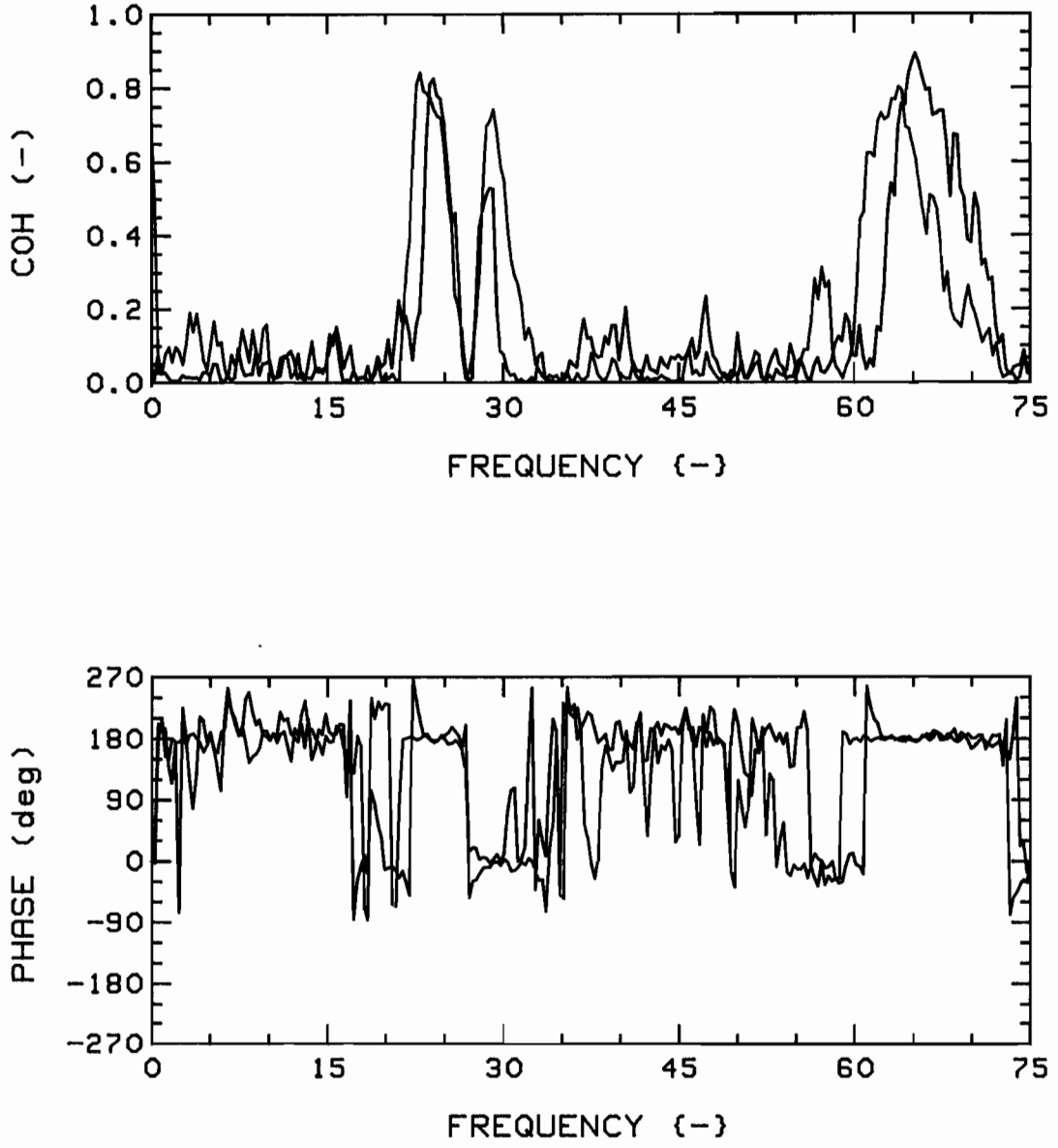

Fig.141b: Effect of choice of system on measured coherence functions and phases, with $G_c = 0.75$, T-T (1,3), at u = 1; K = 4, 4F (RED) and 4F(1,2,3,4)/24R (GREEN).

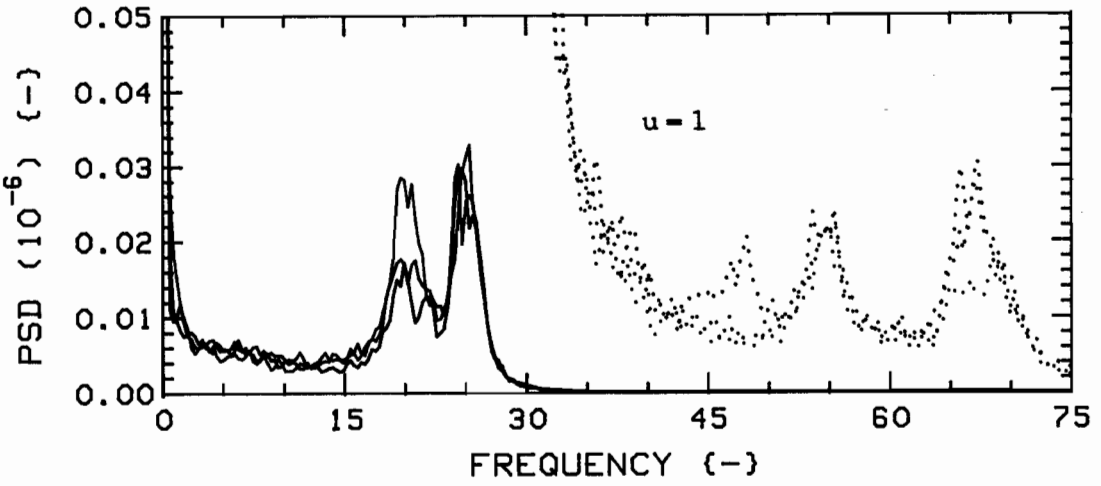

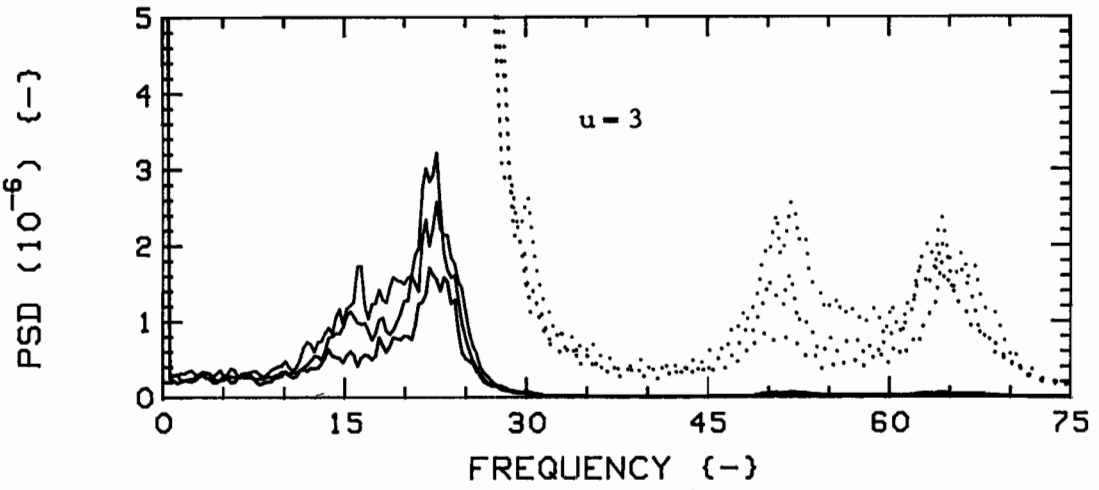

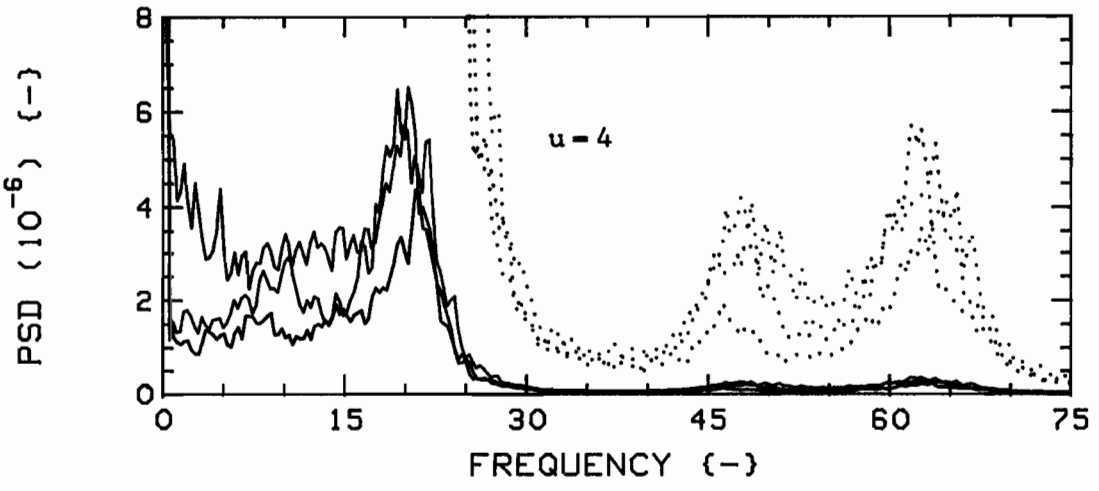

Fig.142a: Effect of choice of system on measured vibration PSD's, for 4F/24R bundles, in Position 1, with $G_c = 0.75$, Radial direction; central (RED), parallel offset (GREEN), and diagonal offset (BLUE).
The dotted traces are expansions of the solid ones;
scales are, from top: 3.0×10^{-10}, 1.5×10^{-7}, 5.0×10^{-7}.

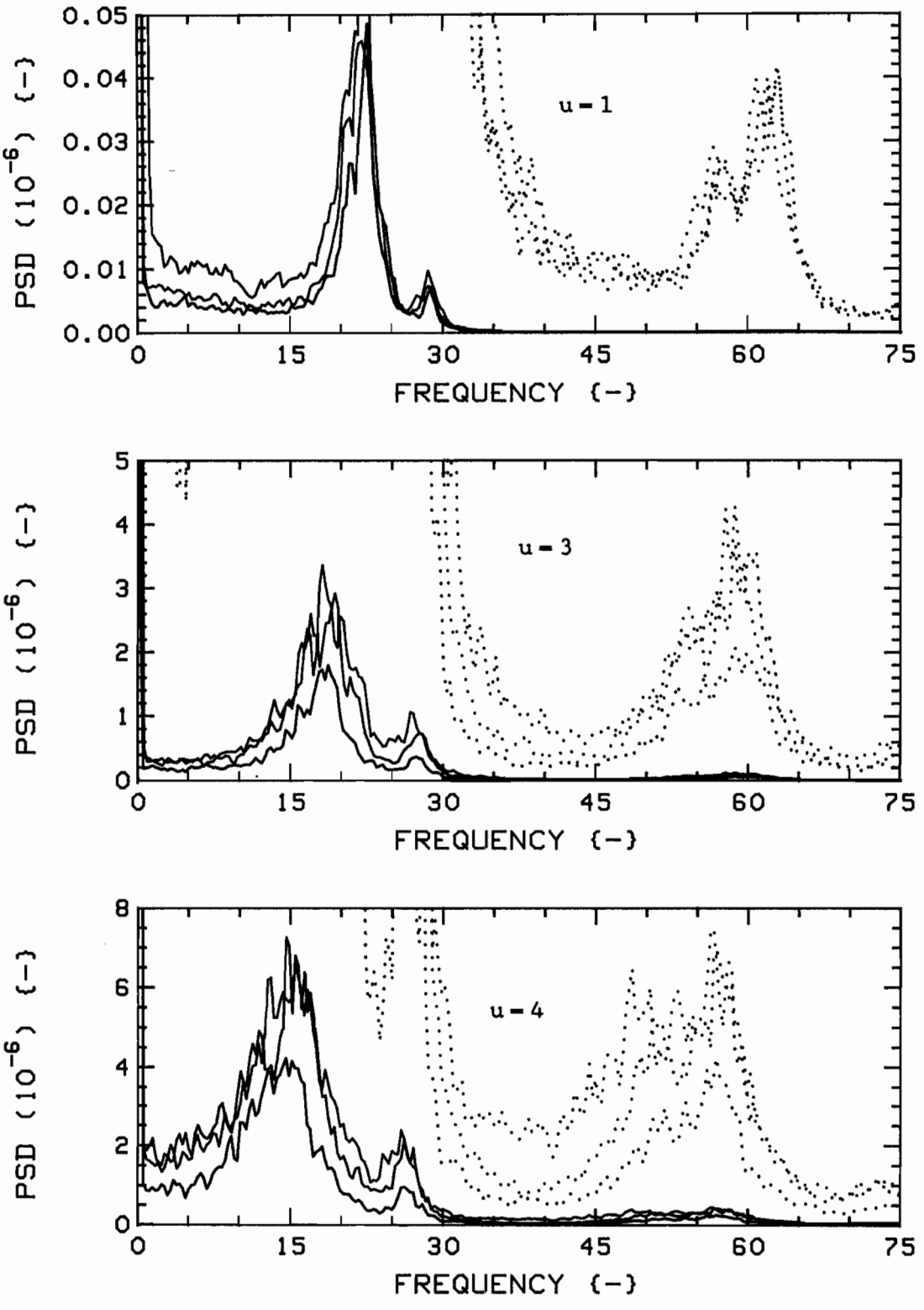

Fig.142b: Effect of choice of system on measured vibration PSD's, for 4F/24R bundles, in Position 1, with $G_c = 0.75$, Tangential direction; central (RED), parallel offset (GREEN), and diagonal offset (BLUE).
The dotted traces are expansions of the solid ones;
scales are, from top: 3.0×10^{-10}, 1.5×10^{-7}, 5.0×10^{-7}.

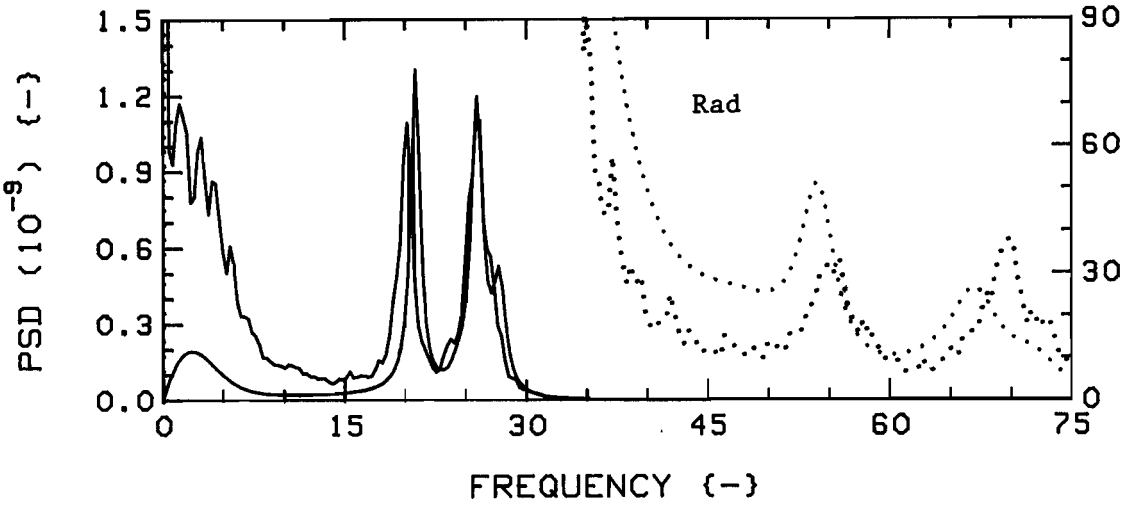

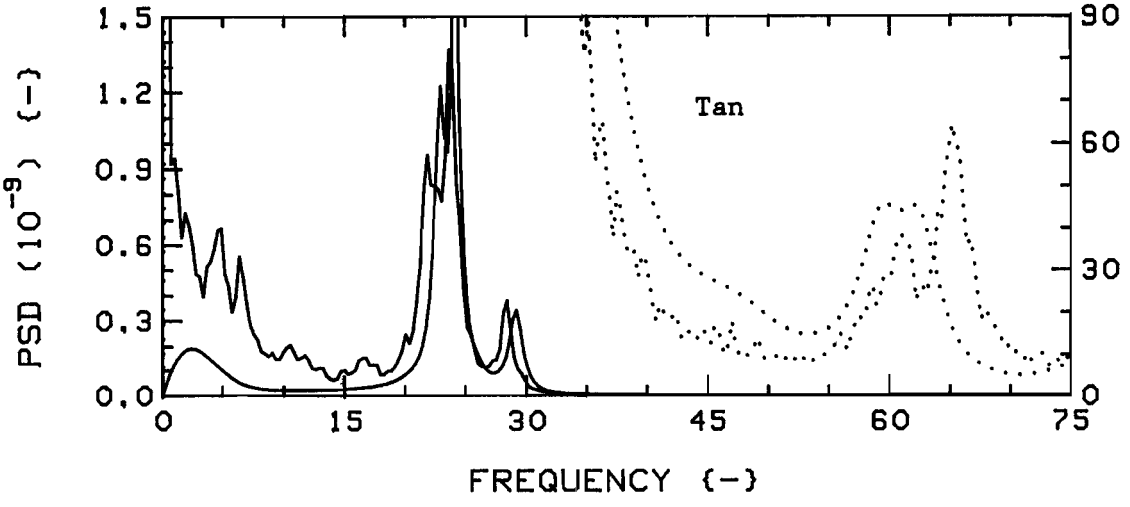

Fig.143a: Measured (RED) and theoretical (GREEN) vibration PSD's for K = 4, 4F, $G_c = 0.75$, at u = 0.5.

The dotted traces are expansions of the solid ones; scales are 5.0×10^{-12} (RED) and 1.2×10^{-10} (GREEN).

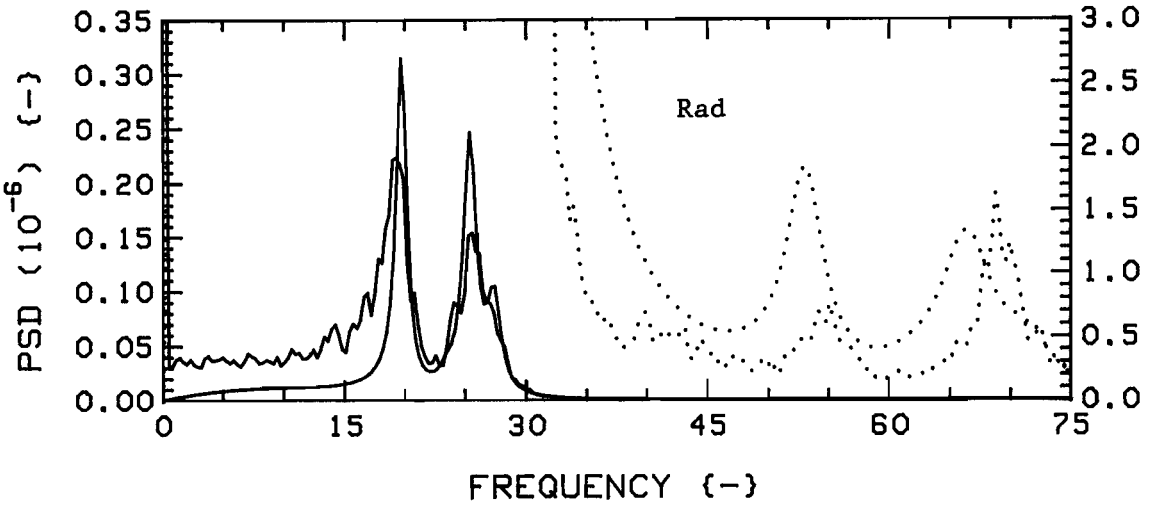

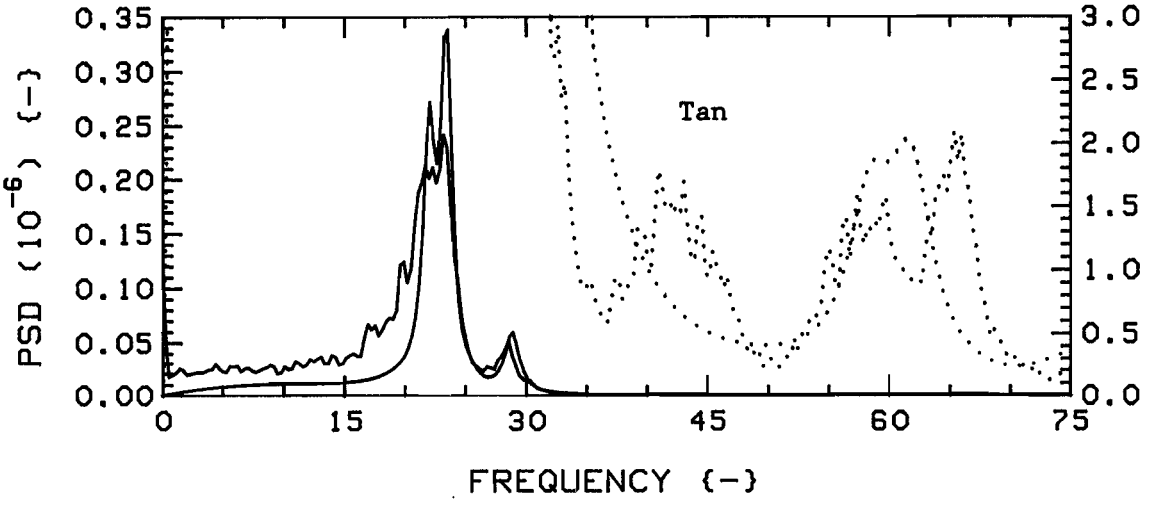

Fig.143b: Measured (RED) and theoretical (GREEN) vibration PSD's for $K = 4$, $4F$, $G_c = 0.75$, at $u = 1.5$.

The dotted traces are expansions of the solid ones; scales are 3.0×10^{-9} (RED) and 9.0×10^{-9} (GREEN).

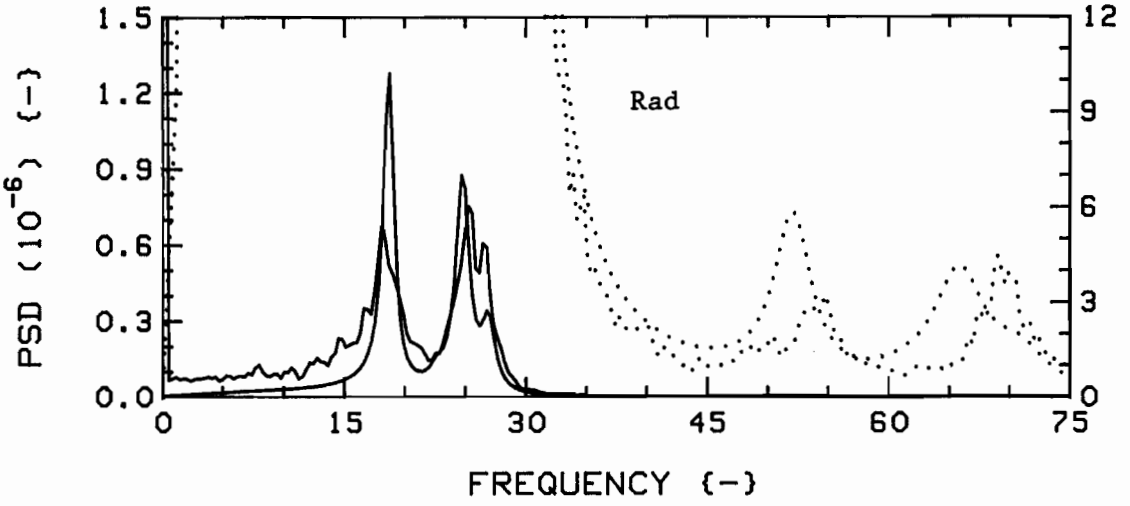

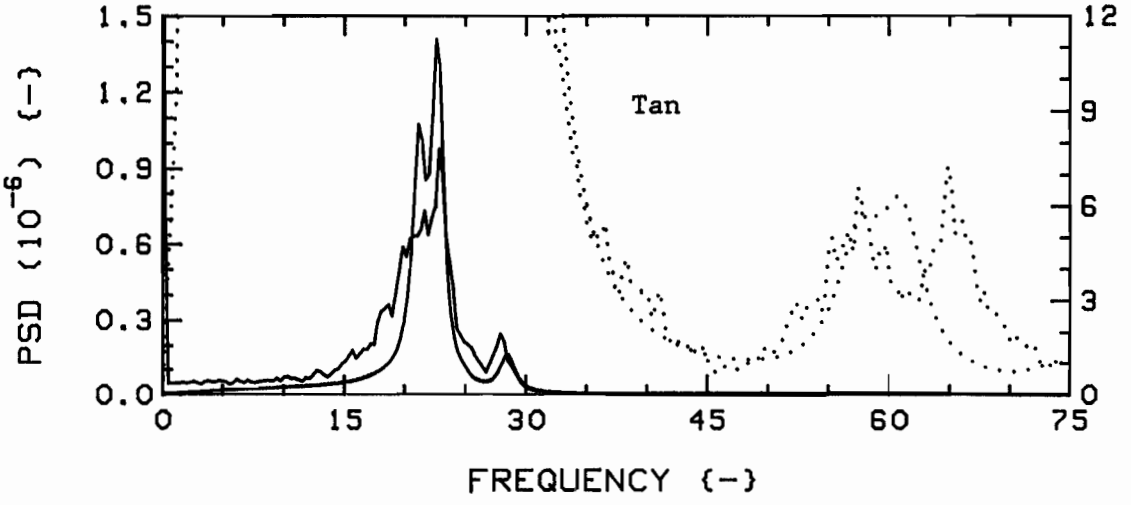

Fig.143c: Measured (RED) and theoretical (GREEN) vibration PSD's for $K = 4$, $4F$, $G_c = 0.75$, at $u = 2.0$.

The dotted traces are expansions of the solid ones; scales are 1.5×10^{-8} (RED) and 4.0×10^{-8} (GREEN).

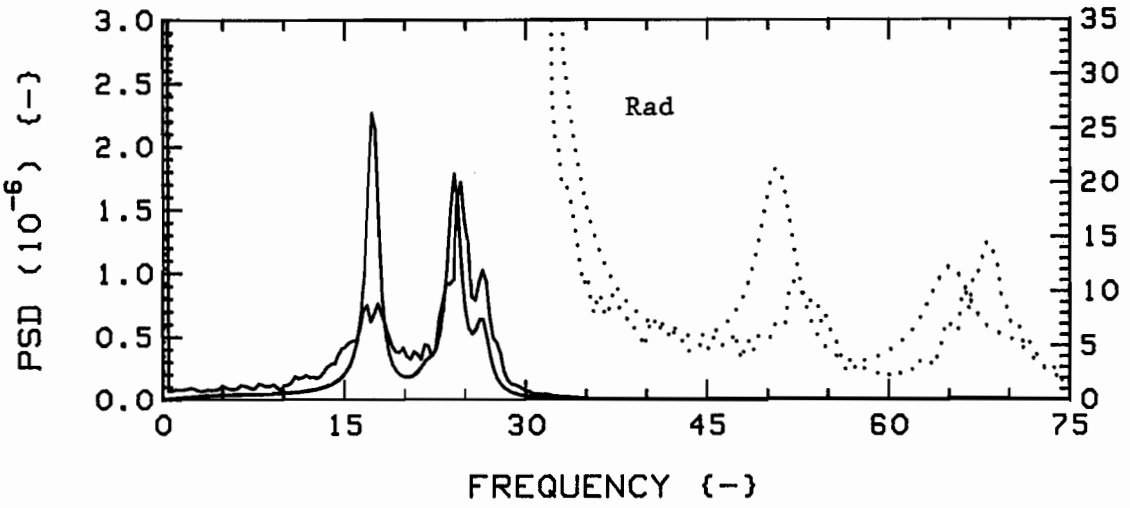

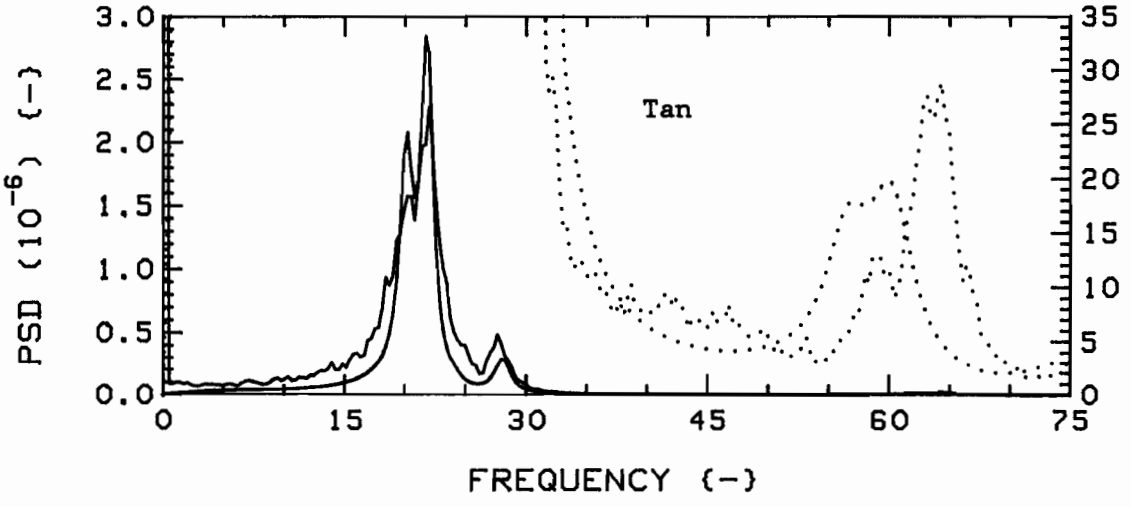

Fig.143d: Measured (RED) and theoretical (GREEN) vibration PSD's for $K = 4$, 4F, $G_c = 0.75$, at $u = 2.5$.

The dotted traces are expansions of the solid ones; scales are 4.0×10^{-8} (RED) and 9.0×10^{-8} (GREEN).

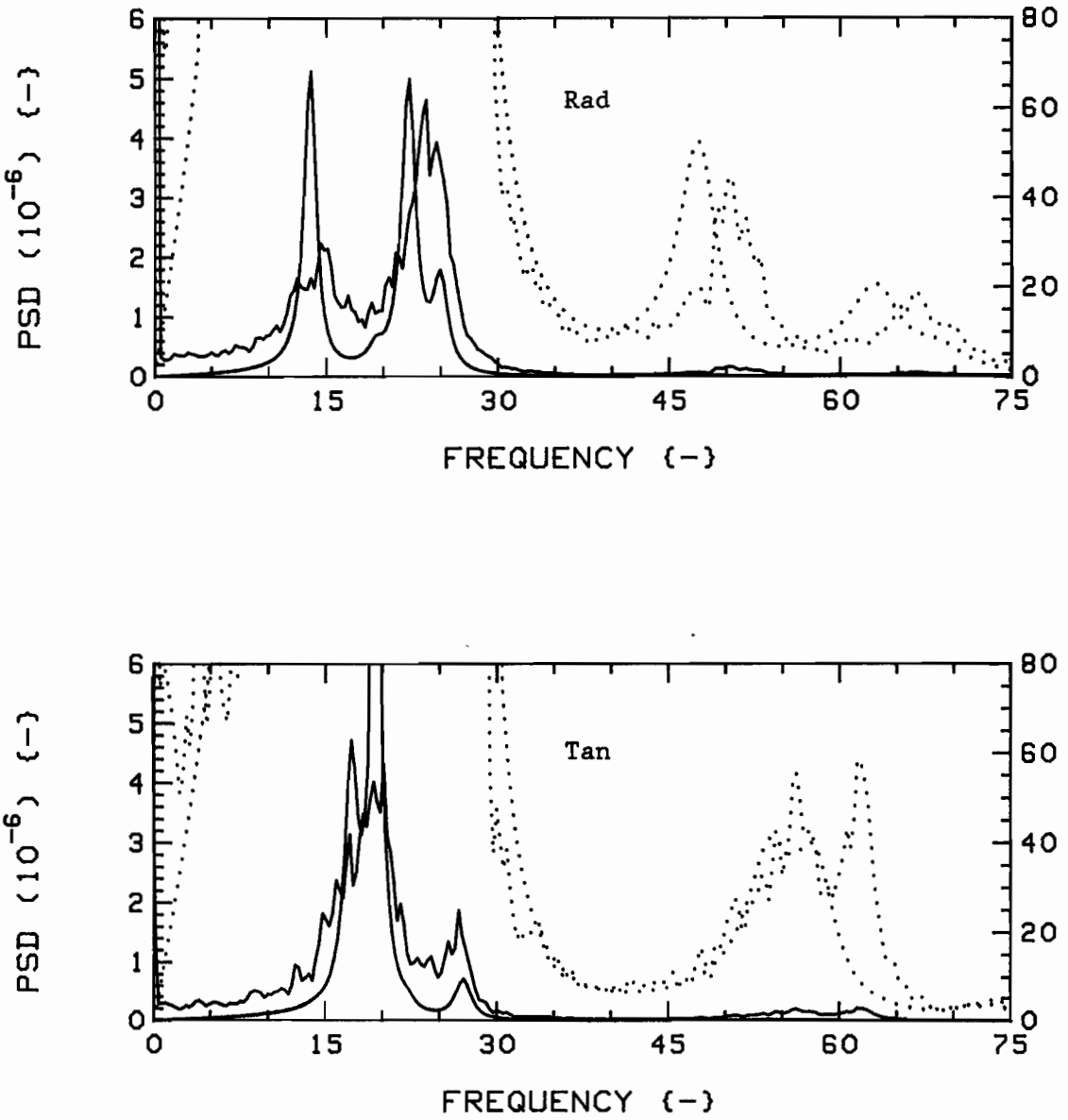

Fig.143e: Measured (RED) and theoretical (GREEN) vibration PSD's for $K = 4$, $4F$, $G_c = 0.75$, at $u = 3.5$.

The dotted traces are expansions of the solid ones; scales are 3.0×10^{-7} (RED) and 6.0×10^{-7} (GREEN).

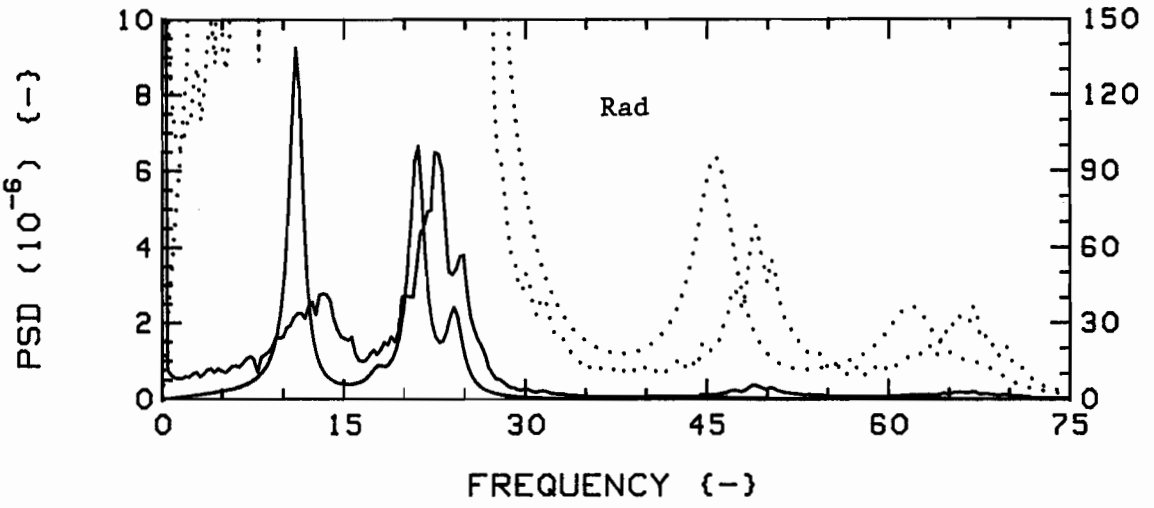

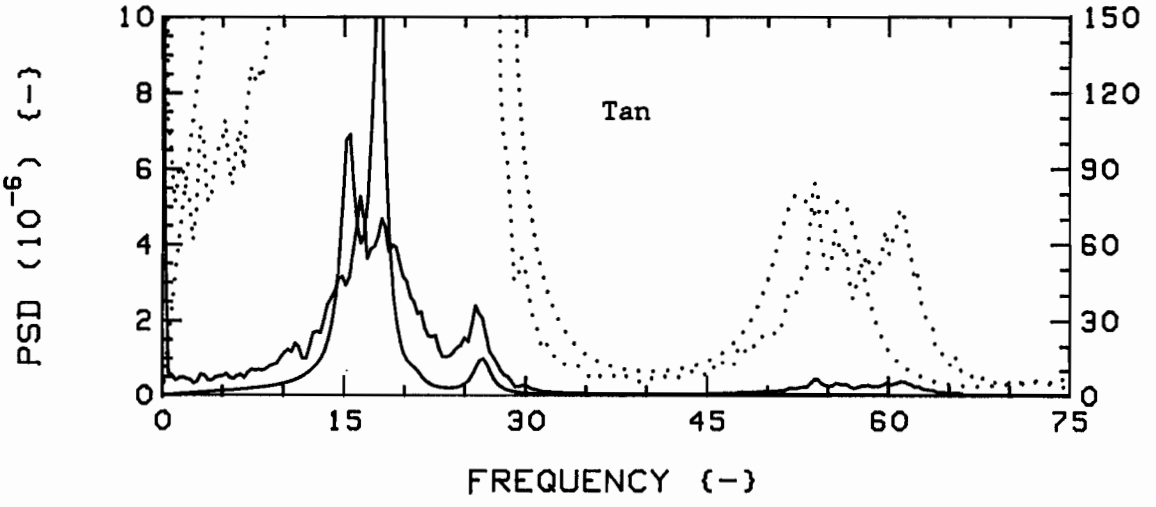

Fig.143f: Measured (RED) and theoretical (GREEN) vibration PSD's for $K = 4,\ 4F,\ G_c = 0.75$, at $u = 4.0$.

The dotted traces are expansions of the solid ones; scales are 8.0×10^{-7} (RED) and 1.5×10^{-6} (GREEN).

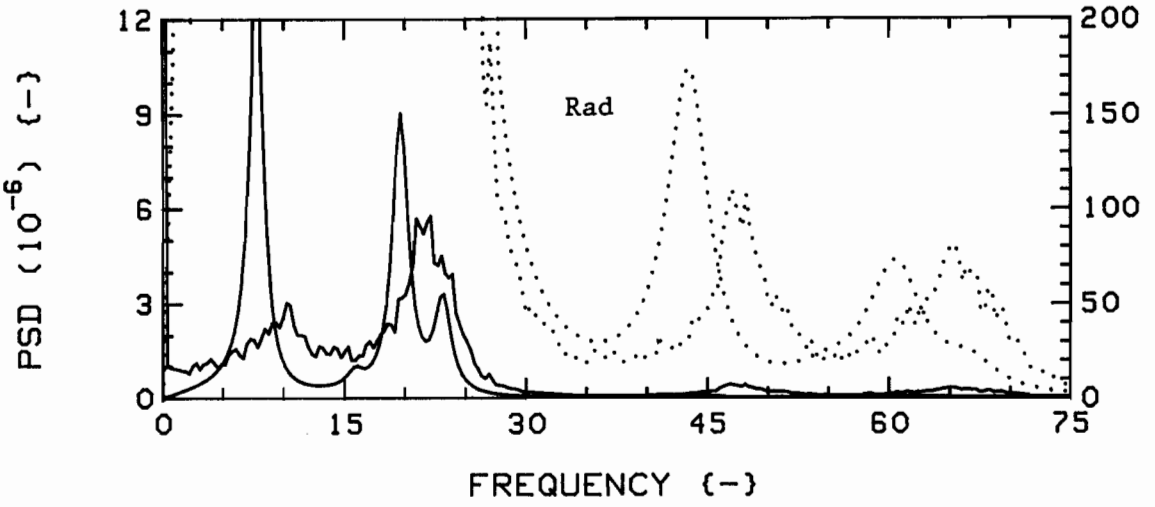

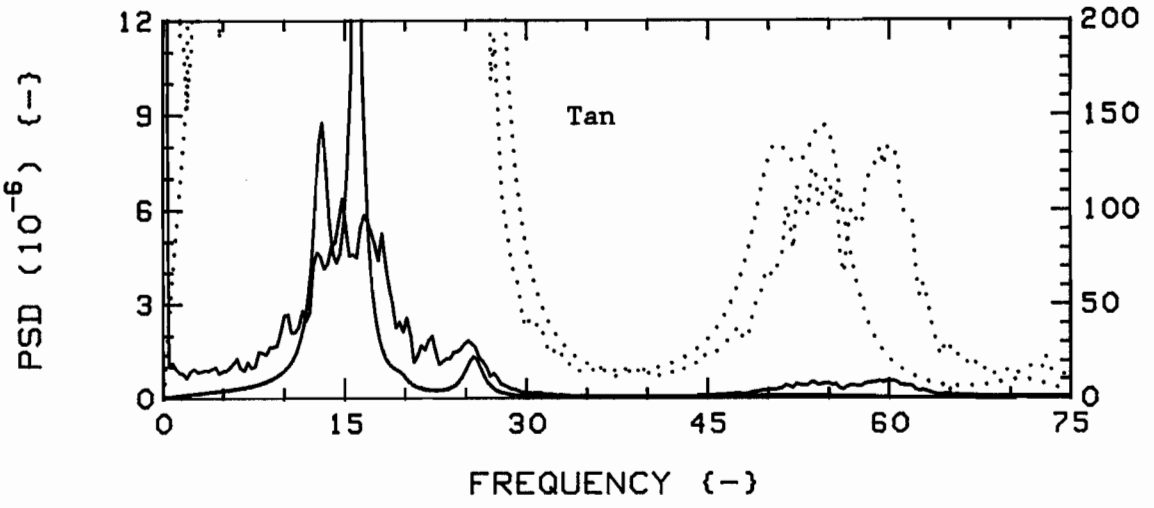

Fig.143g: Measured (RED) and theoretical (GREEN) vibration PSD's for K = 4, 4F, $G_c = 0.75$, at u = 4.5.

The dotted traces are expansions of the solid ones; scales are 8.0×10^{-7} (RED) and 2.2×10^{-6} (GREEN).

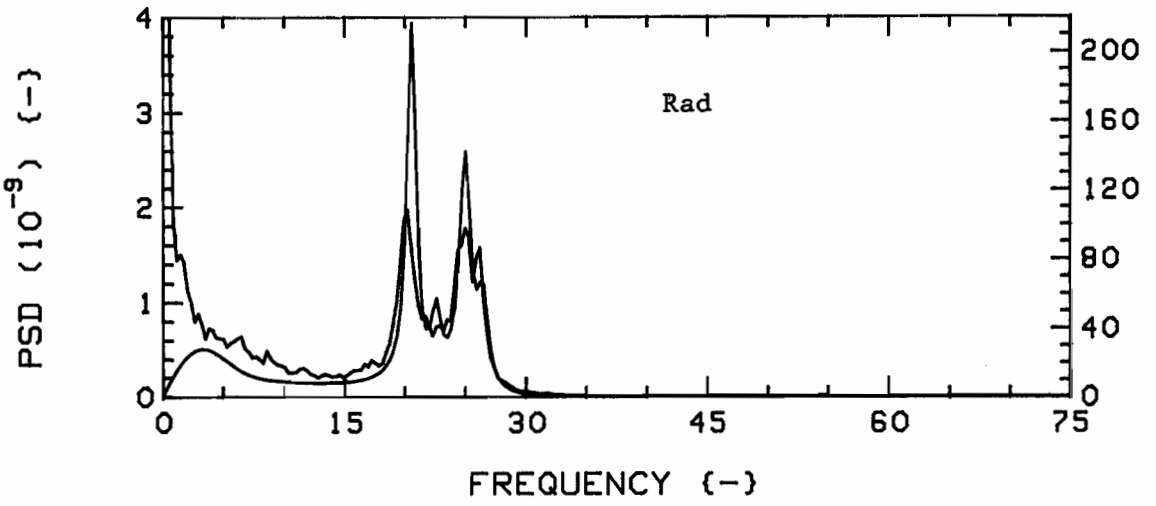

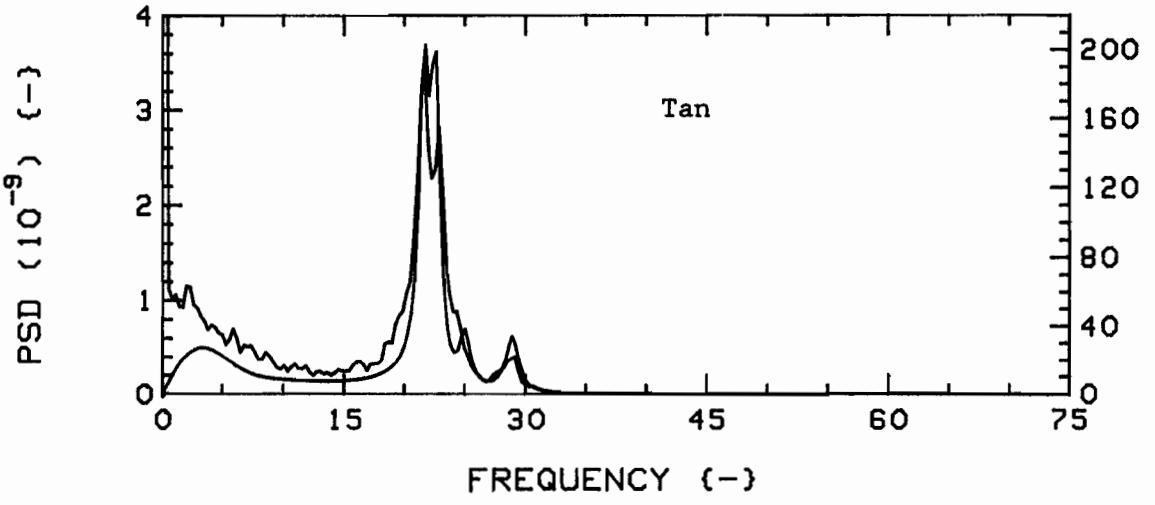

Fig.144a: Measured (RED) and theoretical (GREEN) vibration PSD's for K = 28, G_c = 0.75, 4F(1,2,3,4)/24R, at u = 0.5.

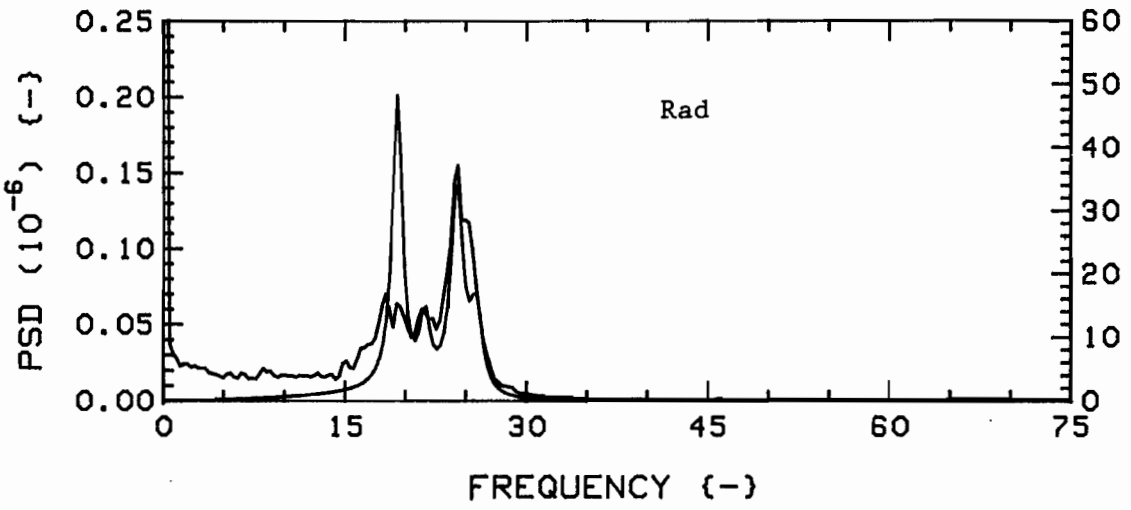

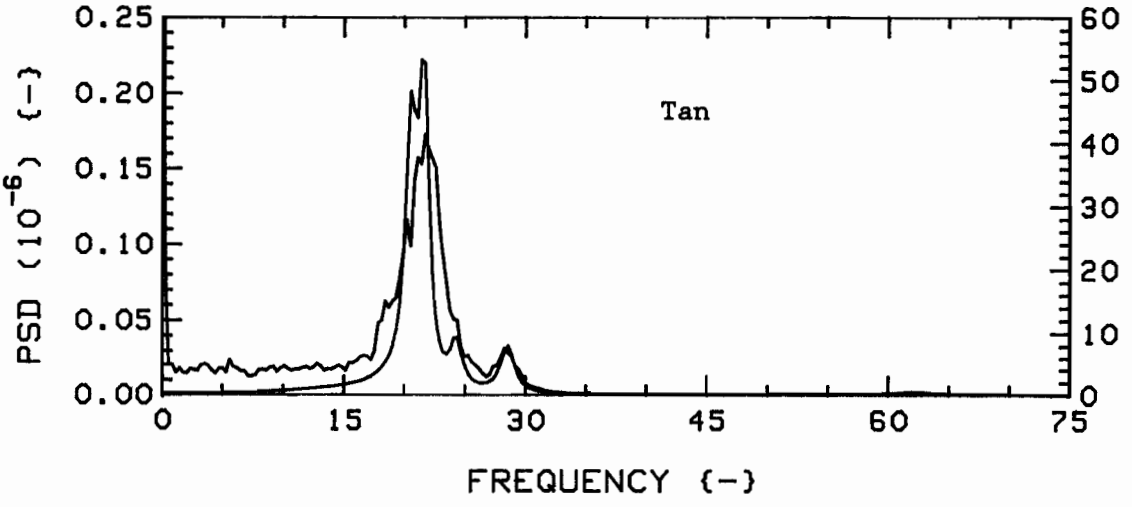

Fig.144b: Measured (RED) and theoretical (GREEN) vibration PSD's for K = 28, G_c = 0.75, 4F(1,2,3,4)/24R, at u = 1.5.

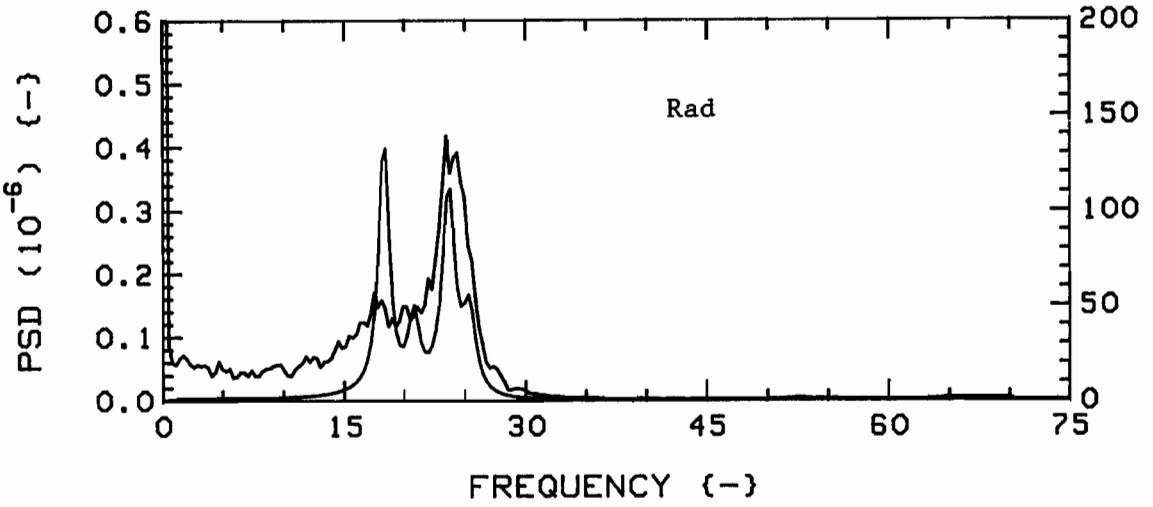

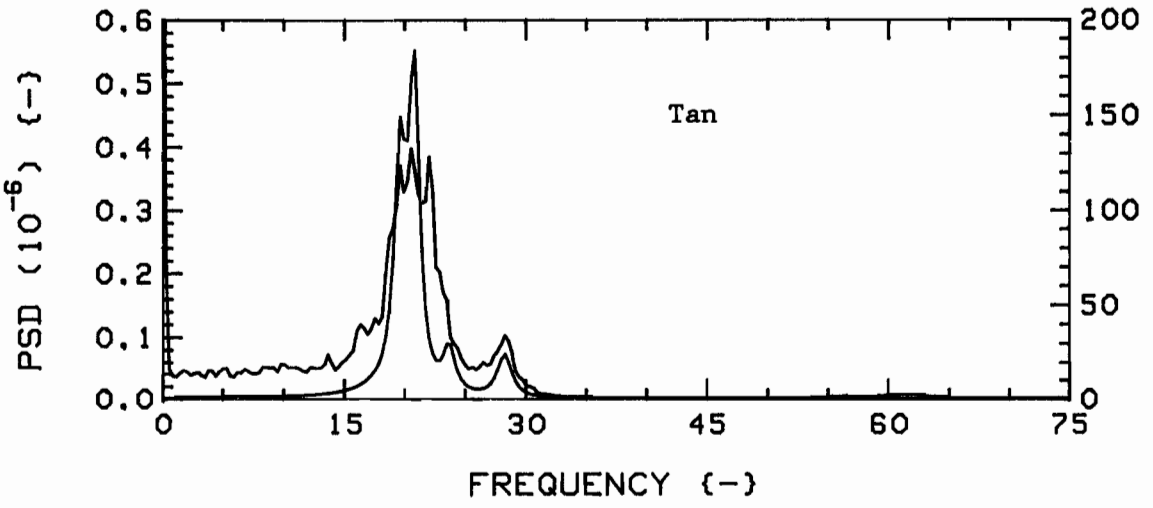

Fig.144c: Measured (RED) and theoretical (GREEN) vibration PSD's for K = 28, G_c = 0.75, 4F(1,2,3,4)/24R, at u = 2.0.

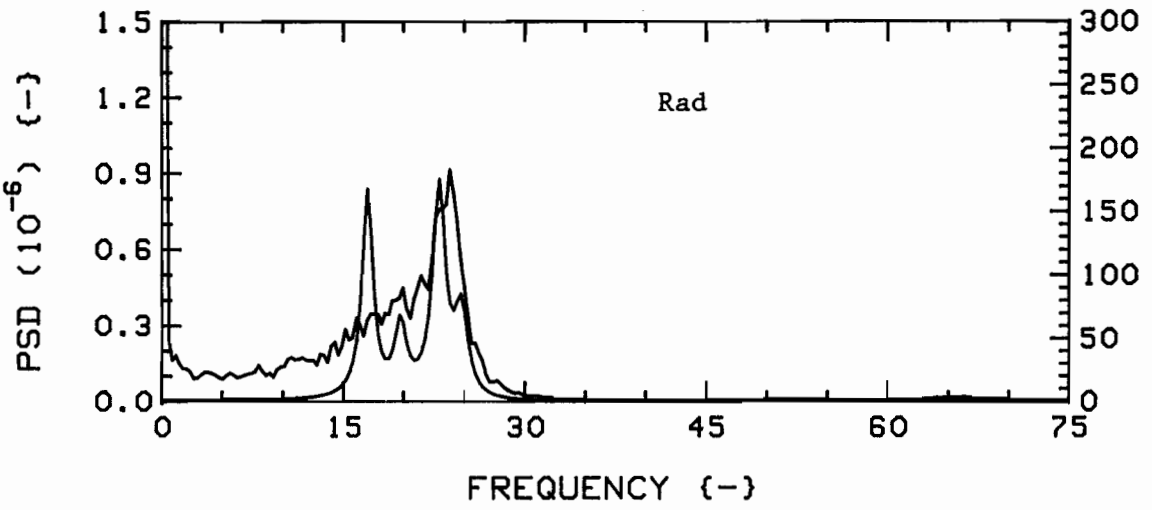

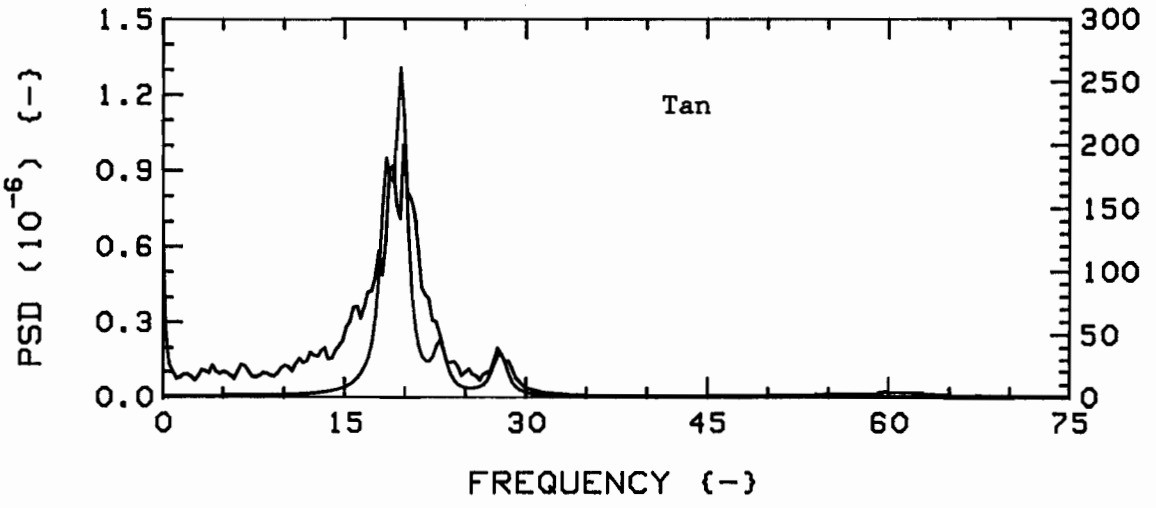

Fig.144d: Measured (RED) and theoretical (GREEN) vibration PSD's for K = 28, G_c = 0.75, 4F(1,2,3,4)/24R, at u = 2.5.

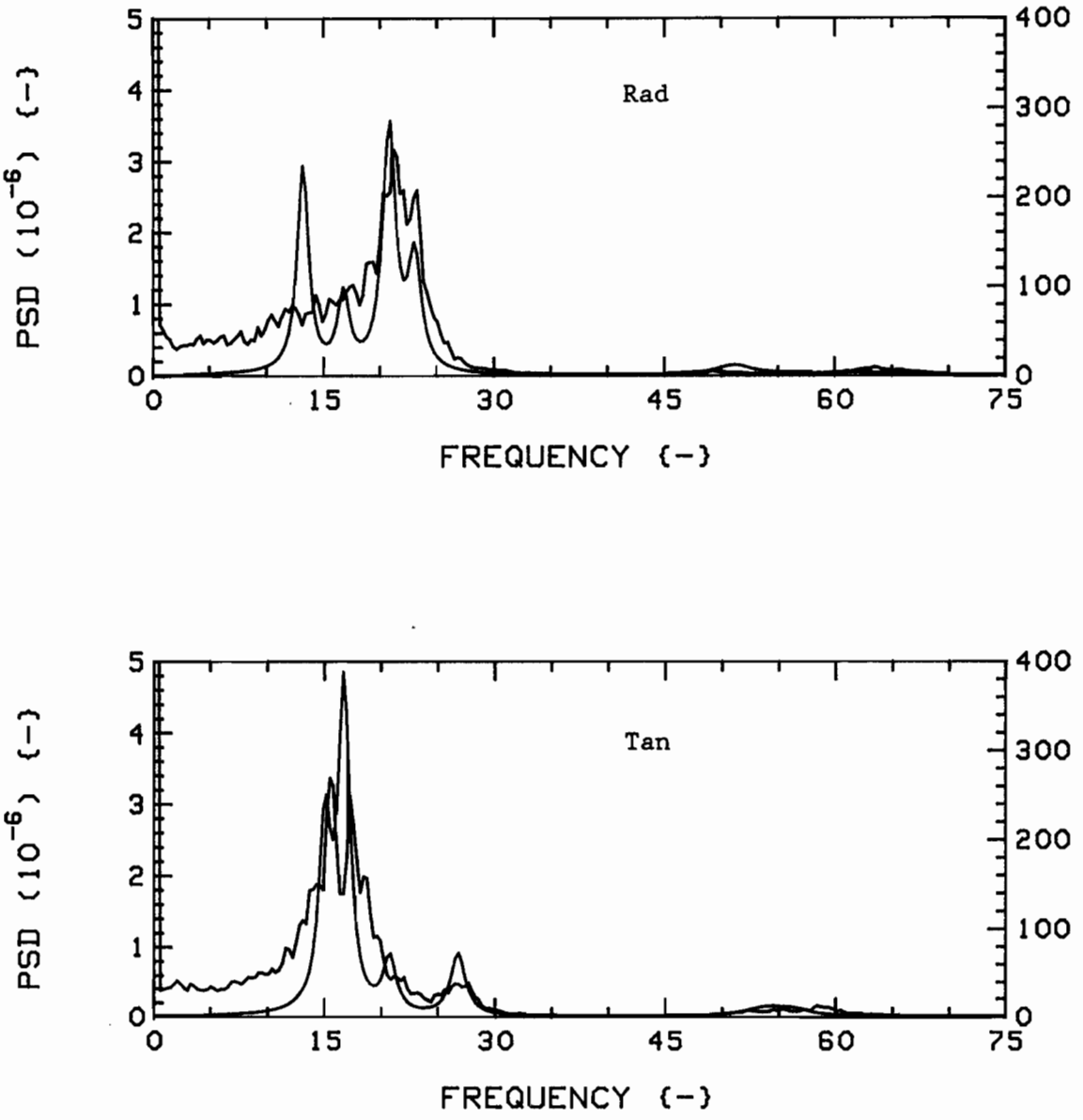

Fig.144e: Measured (RED) and theoretical (GREEN) vibration PSD's for K = 28, G_c = 0.75, 4F(1,2,3,4)/24R, at u = 3.5.

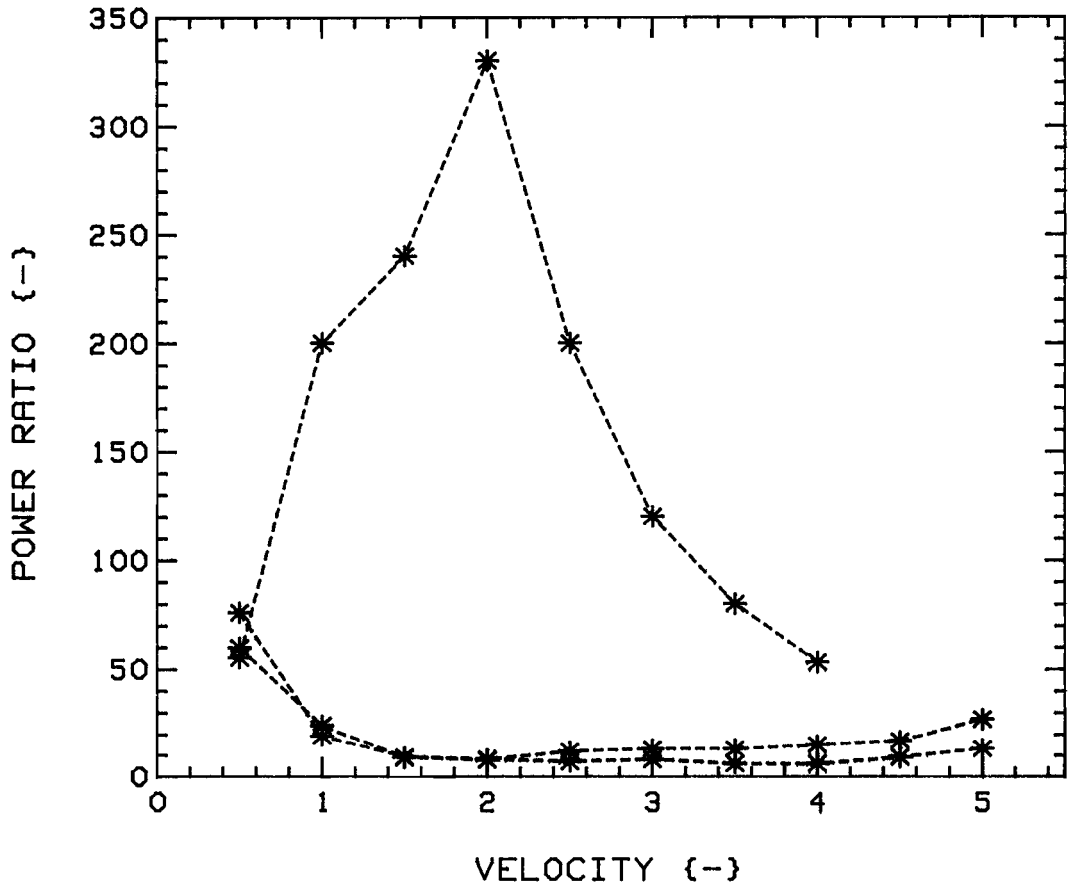

Fig.145: Theoretical to experimental vibration power ratios, versus flow velocity, for $G_c = 0.75$; K = 4, 4F, in first (RED) and second (GREEN) mode groups, and K = 28, 4F/24R, central (BLUE).

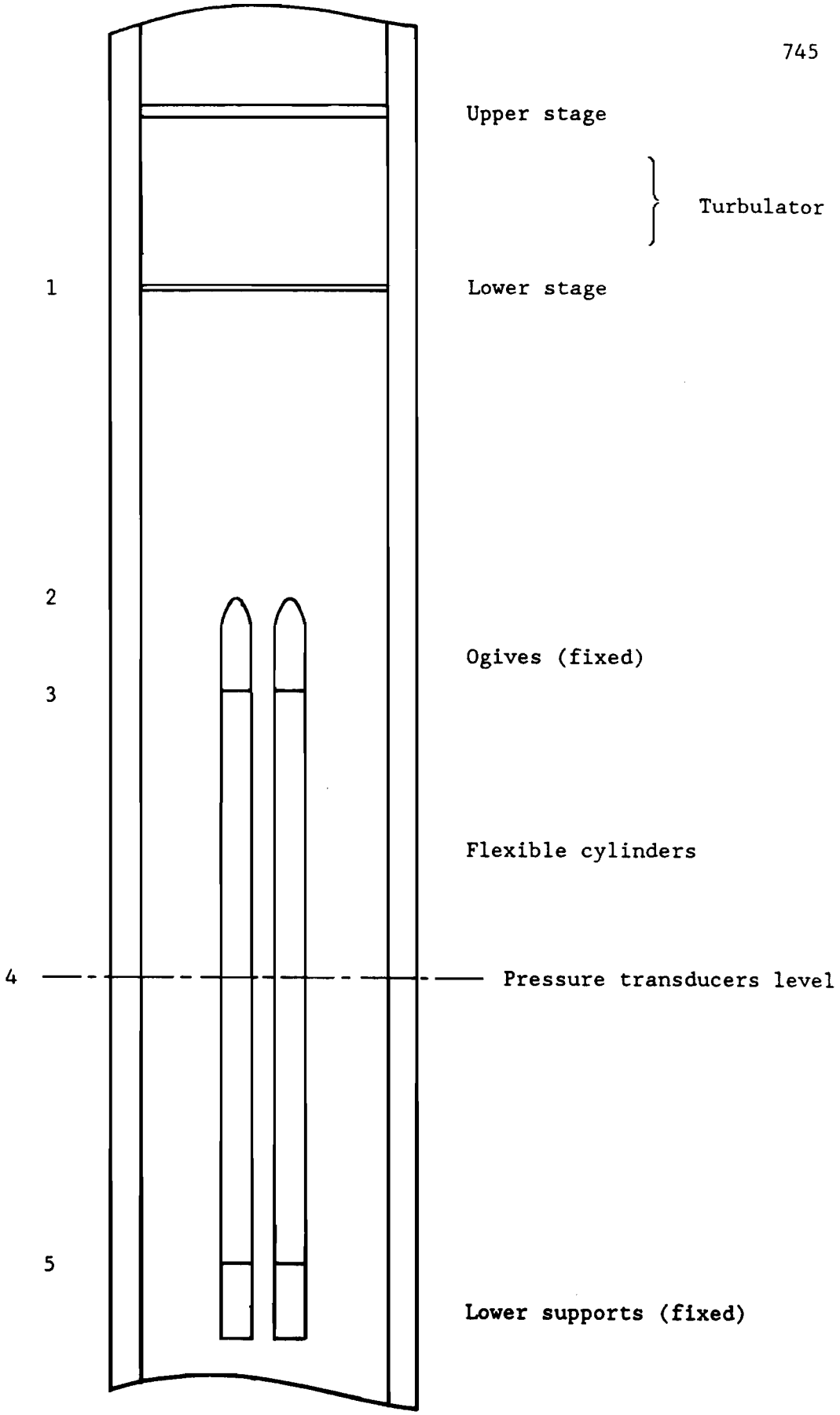

Fig.146: Water tunnel "hydraulic configuration".

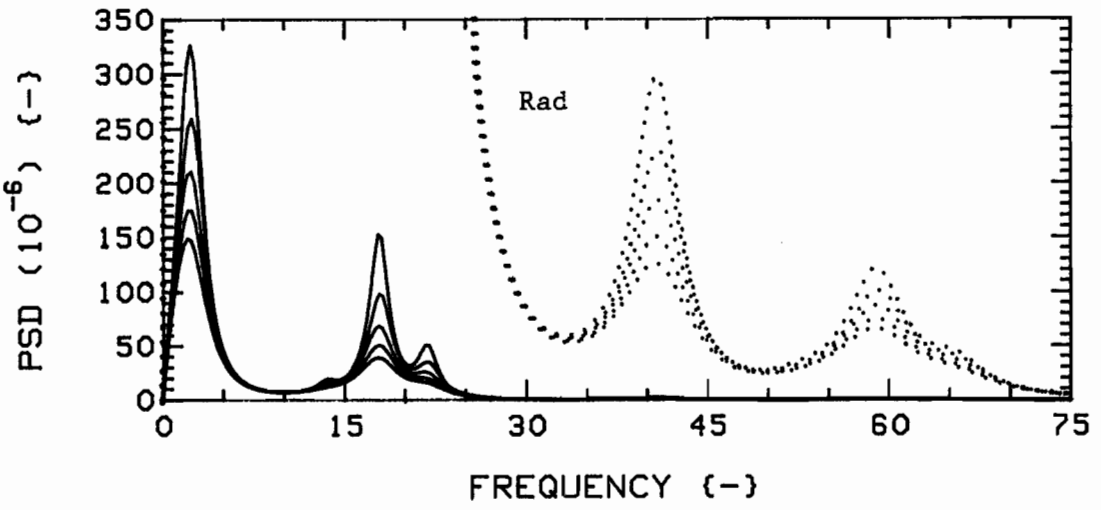

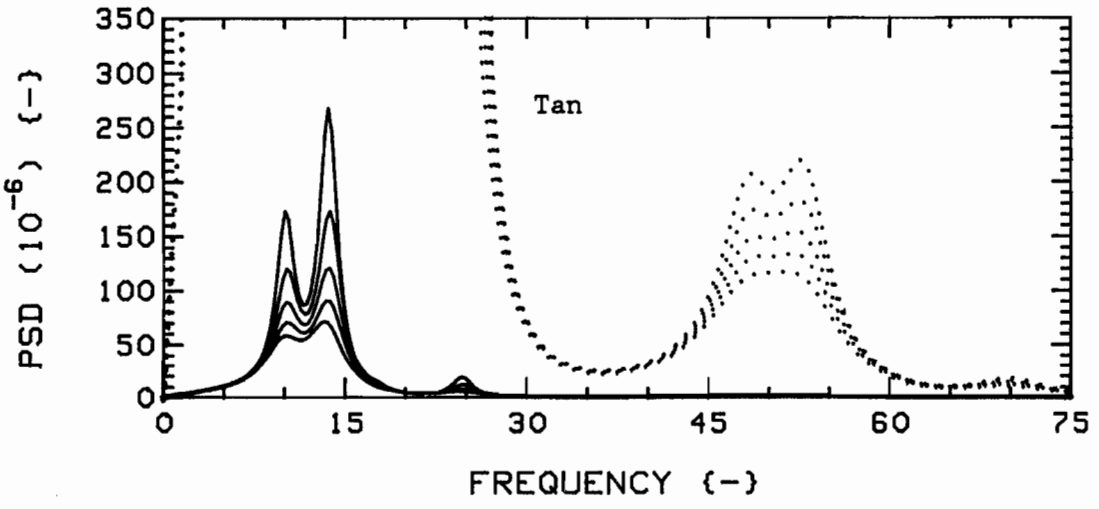

Fig.147a: Effect of varying c (fixed $c_f = 0.016$) on theoretical vibration PSD's, for K = 4, 4F, $G_c = 0.75$, at u = 5; c = 0.1 (RED), 0.2 (GREEN), 0.3 (BLUE), 0.4 (BLACK), and 0.5 (RED again).

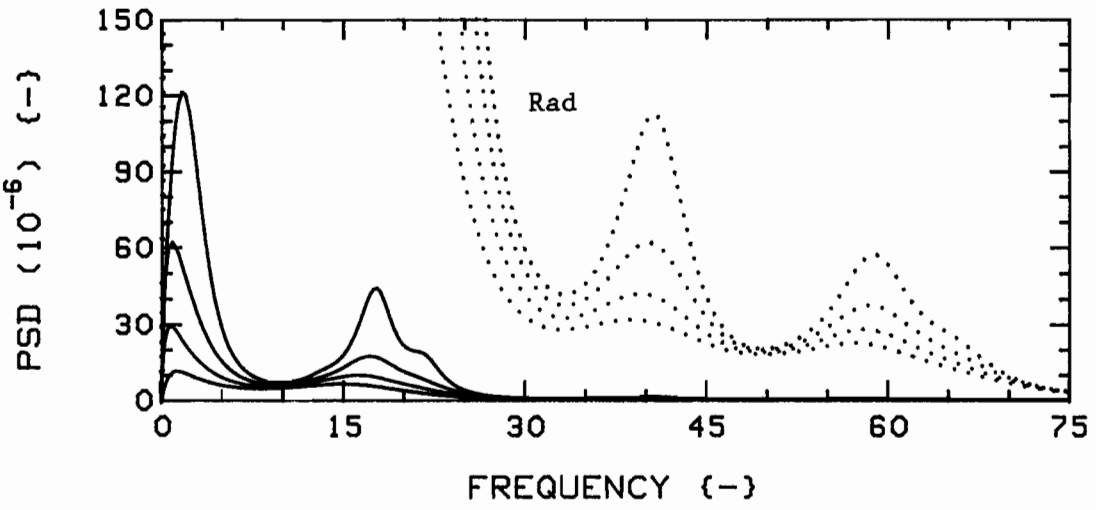

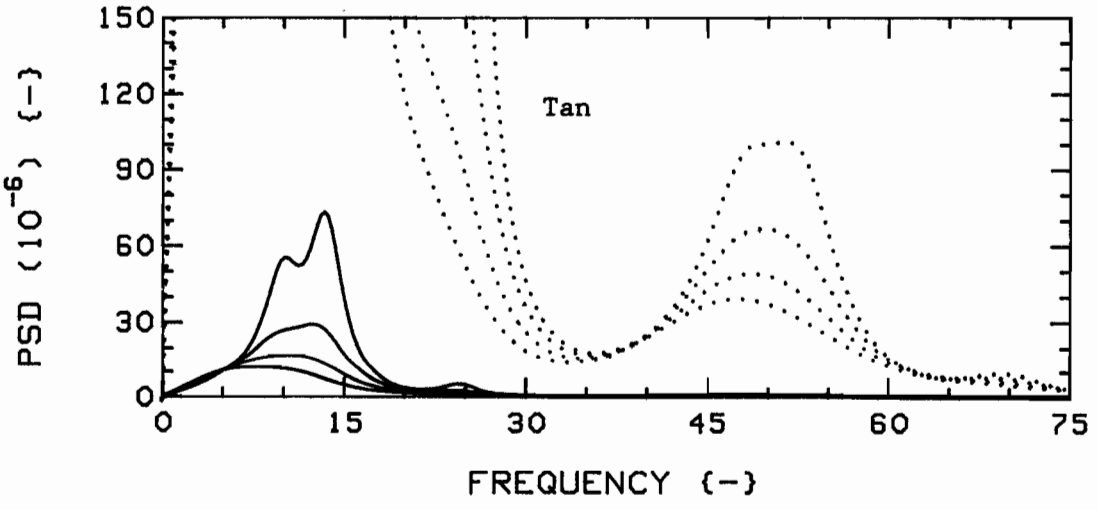

Fig.147b: Effect of varying c_f (fixed $c = 0.039$) on theoretical vibration PSD's, for K = 4, 4F, $G_c = 0.75$, at $u = 5$; $c_f = 0.1$ (RED), 0.2 (GREEN), 0.3 (BLUE), and 0.4 (BLACK).

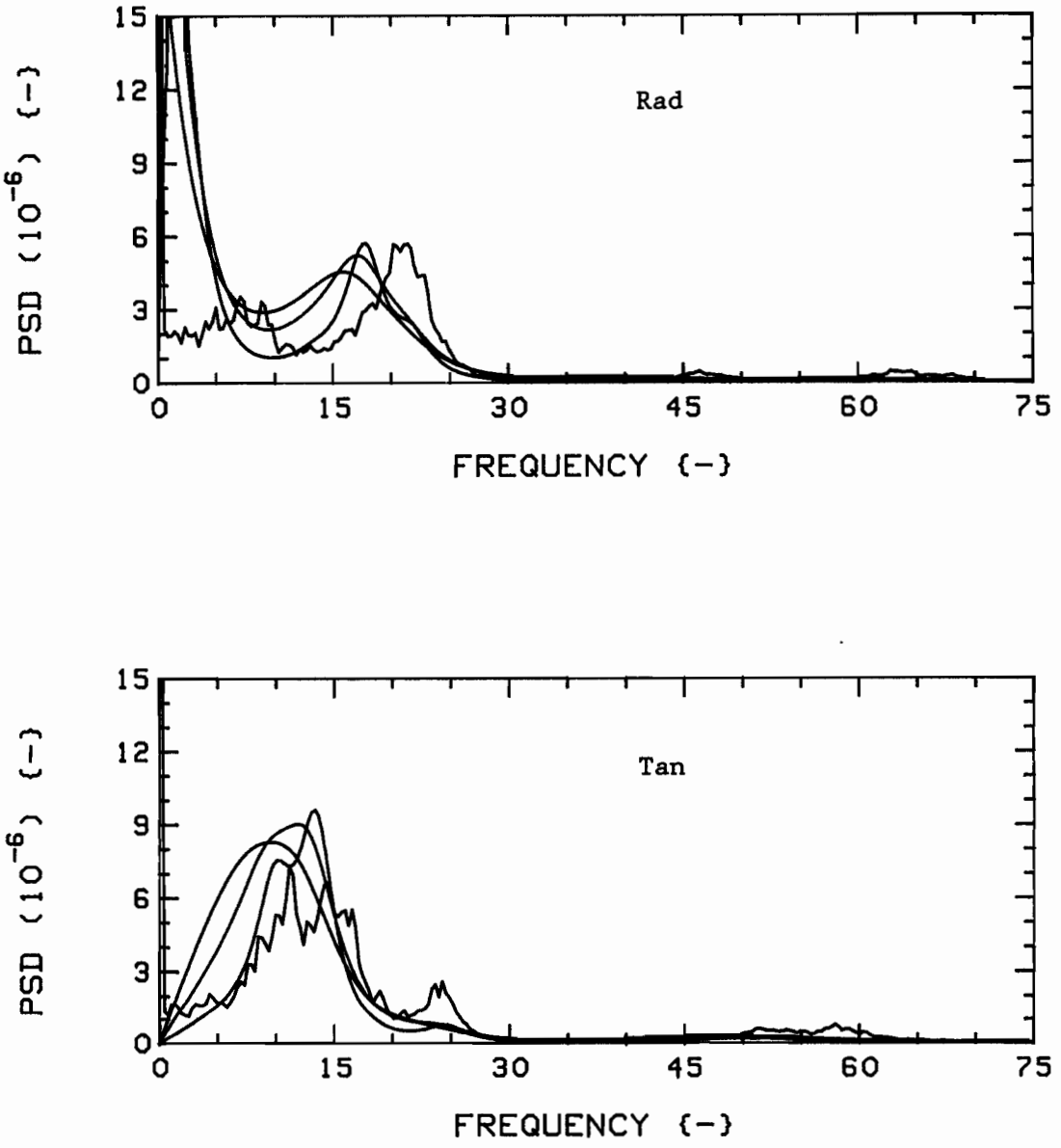

Fig.147c: Effect of varying c and c_f ($c = c_f$) on theoretical vibration PSD's, for K = 4, 4F, $G_c = 0.75$, at u = 5; experimental data shown for reference (RED); $c = c_f = 0.1$ (GREEN), 0.2 (BLUE), and 0.3 (BLACK).
Scales shown are for experimental data. Theoretical PSD scales are adjusted for comparison; they are 100×10^{-6} (GREEN), 40×10^{-6} (BLUE), and 25×10^{-6} (BLACK).

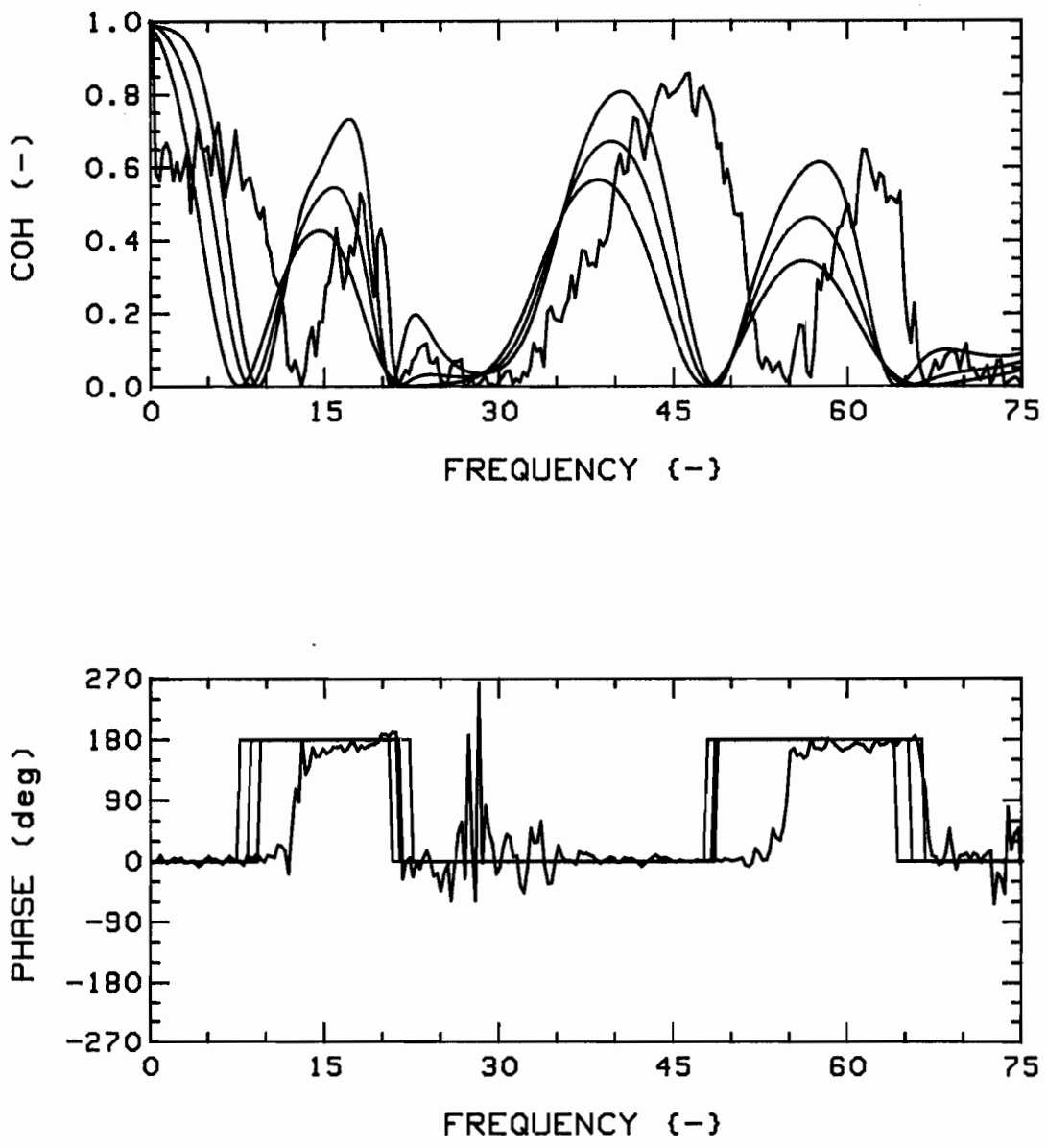

Fig.148a: Effect of varying c and c_f ($c = c_f$) on theoretical coherence function and phase, for K = 4, 4F, $G_c = 0.75$, R-R (1,3), at u = 5; experimental data shown for reference (RED); $c = c_f = 0.1$ (GREEN), 0.2 (BLUE), and 0.3 (BLACK).

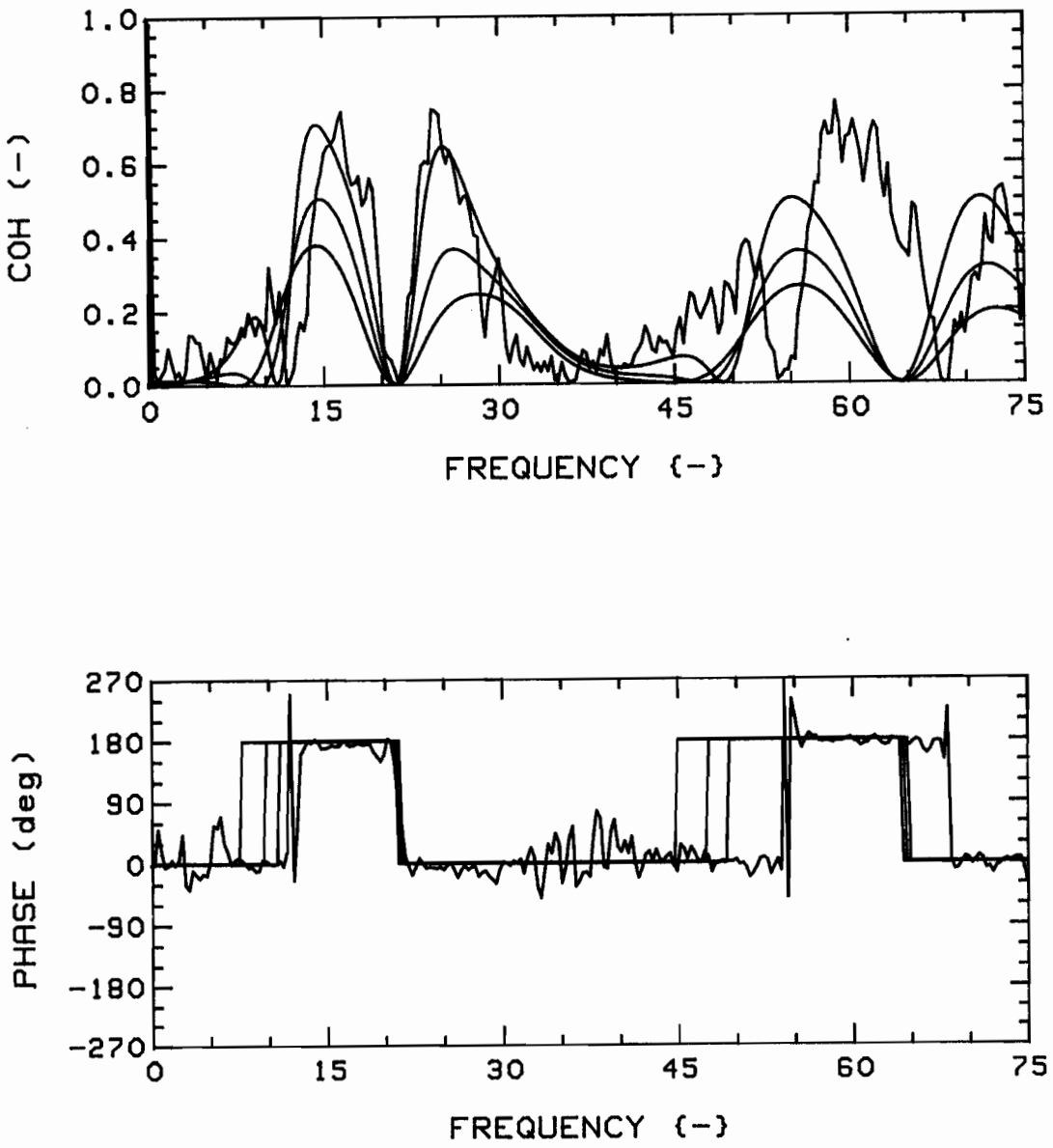

Fig.148b: Effect of varying c and c_f ($c = c_f$) on theoretical coherence function and phase, for K = 4, 4F, $G_c = 0.75$, T-T (1,3), at u = 5; experimental data shown for reference (RED); $c = c_f = 0.1$ (GREEN), 0.2 (BLUE), and 0.3 (BLACK).